AD-E801216

AD-A160 778

(1)

PROCEEDINGS
OF
SECOND SYMPOSIUM ON

THE INTERACTION OF NON-NUCLEAR MUNITIONS WITH STRUCTURES

PANAMA CITY BEACH, FLORIDA
APRIL 15-18, 1985

DTIC FILE COPY

DTIC
ELECTE
OCT 29 1985
S D
B

DISTRIBUTION STATEMENT A
Approved for public release
Distribution Unlimited

85 10 28 038

PROCEEDINGS
OF
SECOND SYMPOSIUM ON

THE INTERACTION OF NON-NUCLEAR MUNITIONS WITH STRUCTURES

PANAMA CITY BEACH, FLORIDA
APRIL 15-18, 1985

This document represents the proceedings of the Second Symposium on The Interaction of Non-Nuclear Munitions with Structures, Panama City Beach, Florida, April 15-18, 1985. The symposium was sponsored by the following U.S. Air Force agencies:

Engineering & Services Laboratory
Tyndall AFB, Florida

Armament Laboratory
Eglin AFB, Florida

Weapons Laboratory
Kirtland AFB, New Mexico

The symposium was coordinated through the University of Florida Graduate Engineering Center, Eglin AFB, Florida under USAF Contract No. F08635-83-C-0136. Dr. C.A. Ross served as the symposium coordinator for the University of Florida and Dr. P.Y. Thompson, Engineering & Services Laboratory, served as symposium coordinator for the U.S. Air Force.

All the manuscripts in this document have been approved for public release either by the author or the cognizant federal agency.

DTIC COPY INSPECTED 1

Accession For
NTIS CRA&I ☑
DTIC TAB ☐
Unannounced ☐
Justification
By
Distribution/
Availability Codes
Dist | Avail and/or Special
A-1

TABLE OF CONTENTS

A BROADER PERSPECTIVE 1
H. Norman Abramson, Southwest Research Institute

STABILITY OF WALLS AGAINST AIRBLAST FORCES 5
John R. Rempel, Center for Planning & Research, Inc. and James E. Beck, James E. Beck and Associates

EXPLOSION DAMAGE TO URBAN STRUCTURES AT LOW OVERPRESSURE 12
Hyla Napadensky, IIT Research Institute and Anatol Longinow, Illinois Institute of Technology

EXPLOSIVE FUEL IGNITION EFFECTS ON AN AIRCRAFT NOISE SUPPRESSOR SYSTEM 17
V.R. Miller, Air Force Flight Dynamics Laboratory

BLAST AND FRAGMENT RESISTANT SYSTEMS (BFR) - TEST RESULTS 24
Bernard C.J. Vienings, Hully and Associates
Pretoria, SOUTH AFRICA

ASSESSMENT OF MODULAR STRUCTURES IN BLAST AND SHOCK ENVIRONMENTS 29
Michael K.W. Wong, Air Force Weapons Laboratory

CHARACTERIZING IMPULSIVE FAILURE IN BURIED REINFORCED CONCRETE ELEMENTS 35
Timothy J. Ross, AF Weapons Laboratory

A COMPUTATIONAL PROCEDURE FOR RESPONSE OF BURIED STRUCTURES TO CONVENTIONAL WEAPONS 41
S.A. Kiger, USAE Waterways Experiment Station and J.T. Painter, Louisiana Tech University

EXPEDIENT NONLINEAR DYNAMIC ANALYSIS OF REINFORCED CONCRETE STRUCTURES 45
C. Allen Ross, University of Florida and Paul L. Rosengren, Jr., AF Engineering & Services Laboratory

STRUCTURAL RESPONSE UNDER LOCALIZED DYNAMIC LOADS 52
Theodor Krauthammer and Mehul Parikh
University of Minnesota

SIMULATION OF REAL WEAPON-EFFECTS IN MULTIPLE-DRIVER SHOCK TUBES 56
G. Hoffmann, Ernst-Mach-Institut, WEST GERMANY

DESIGN OF BURIED STRUCTURES FOR CONVENTIONAL WEAPONS THREATS 62
James T. Baylot and Sharon B. Bellue
USAE Waterways Experiment Station

DESIGN OF LAYERED STRUCTURES AGAINST CONVENTIONAL WEAPONS 68
Reuben Eytan, Eytan Building Design Ltd., ISRAEL

A CASE STUDY IN DESIGN OF UNDERGROUND SHELTERS 74
Felix S. Wong, Rudolf Y. Mak, David Kufferman and Paul Weidlinger, Weidlinger Associates

INELASTIC COLLAPSE ANALYSIS OF TRANSVERSELY LOADED CONCRETE SLABS 78
Jerzy T. Jacak and Hans Gesund, University of Kentucky

SOIL-STRUCTURE INTERACTION UNDER BLAST LOADING 84
Yu-ao He, Tianjin University, CHINA

PREDICTING CONCRETE SPALL RESULTING FROM DYNAMIC LOADING 89
William E. Wolfe, The Ohio State University and David R. Coltharp, USAE Waterways Experiment Station

BLAST RESPONSE TESTS OF REINFORCED CONCRETE BOX STRUCTURES: METHODS FOR REDUCING SPALL 95
David R. Coltharp, Sam A. Kiger, and Ken P. Vitayaudom
USAE Waterways Experiment Station and Tom. J. Hilferty, AF Engineering & Services Laboratory

DYNAMIC ANALYSIS OF A BURIED CONCRETE STRUCTURE SUBJECTED TO GAS PRESSURE LOADING 101
Fausto Citernesi and Marco Zurru
Snamprogetti SpA, ITALY and Yves Crutzen, Control Data Italia, ITALY

STRUCTURAL RESPONSE TO WEAPON LOADINGS AREAS OF APPLICATION OF EULERIAN, LAGRANGIAN AND COUPLES CODES 107
Friedhelm Scharpf, Industrieanlagen-Betriebsgesellschaft, WEST GERMANY

COMBINED FINITE ELEMENT AND LUMPED MASS TECHNIQUES FOR PARAMETRIC STRUCTURAL ANALYSIS OF STRUCTURES 112
John E. Crawford and Peter J. Mendoza
The Aerospace Corporation

INELASTIC ANALYSIS OF REINFORCED CONCRETE PANELS 117
X.L. Liu and W.F. Chen, Purdue University and T.Y. Chang, University of Akron

TRANSMISSIBILITY METHOD IN STRUCTURAL FRACTURE DIAGNOSIS 127
Mehmet Akgun and Frederick D. Ju
University of New Mexico

EXPERIMENTAL EVALUATION OF REVETMENT EFFECTS 132
Firooz A. Allahdadi and James M. Carson
New Mexico Engineering Research Institute

DEVELOPMENT AND TESTING OF IGLOO ROOF RETROFIT CONCEPTS 137
James W. Ball and David R. Coltharp
USAE Waterways Experiment Station

MODEL TESTS ON COMPOSITE SLABS OF LIGHT GAUGE METAL SHEET AND CONCRETE SUBJECTED TO BLAST LOADING 143
Peter Balazs and Bengt Vretblad, Royal Swedish Fortifications Administration, SWEDEN

THE MUST-IV (MULTI-UNIT STRUCTURE TEST) SERIES 149
Vincent A. Meyer, New Mexico Engineering Research Institute

RESPONSE OF A BURIED STRUCTURE TO HIGH INTENSE IMPULSIVE LOADING 154
J. Rick Holder, USAF Armament Laboratory

STRESS-STRAIN-STRENGTH BEHAVIOR OF PAVEMENT BASE MATERIALS 163
M.C. McVay, D. Seereeram and P. Linton
University of Florida

FRACTURE TOUGHNESS OF FIBER REINFORCED CONCRETE 169
Y.S. Jenq and S.P. Shah, Northwestern University

EXPERIMENTAL INVESTIGATION OF FIBRE AND STEEL REINFORCED CONCRETE PLATES UNDER SIMULATED BLAST-LOAD 175
Cristoph Mayrhofer and Heinz J. Thor, Ernst-Mach-Institut, WEST GERMANY

LINEAR SHAPED CHARGE PENETRATION, A PARAMETER STUDY 180
Charles E. Joachim, USAE Waterways Experiment Station

OPTIMIZATION OF A 90 MM SHAPED CHARGE WARHEAD 186
David K. Davison, Physics International Company and
Bertil K. Arvidsson, Bofors Ordnance, SWEDEN

DYNAMIC COMPRESSIVE TESTING OF CONCRETE 194
Lawrence E. Malvern, David A Jenkins, Tianxi Tang and
C.Allen Ross, University of Florida

EXPERIMENTAL PROGRAM TO INVESTIGATE RATE EFFECTS IN CONCRETE 200
Susan M. Babcock, New Mexico Engineering Research Institute

A NEW TECHNIQUE FOR STUDYING DYNAMIC TENSILE RESPONSE OF CONCRETE 206
James K. Gran, SRI International

THE TENSILE STRENGTH OF CONCRETE UNDER DYNAMIC LOADING 211
J. Weerheijm and W. Karthaus, Prins Maurits Laboratory TNO, NETHERLANDS

BEHAVIOR OF NIMS COMPOSITES DURING IMPACT LOADING 217
William E. Wolfe and R.L. Sierakowski, The Ohio State University and
Vincent P. Chiarito, USAE Waterways Experiment Station

HOPKINSON BAR SIMULATION USING DYNA2D 222
Joseph A. Smith and Tracy A. Glover, Lawrence Livermore National Laboratory

A METHOD FOR ESTIMATING ARRIVAL TIMES FOR WAVES PRODUCED BY A BURIED NON-SPHERICAL CHARGE 227
Stephen R. Whitehouse, US Air Force Academy

SPATIAL AND TIME VARIATIONS OF LOADING ON BURIED STRUCTURES BY UNDERGROUND CYLINDRICAL EXPLOSIVES 235
C.A. Ross, E.L. Jerome and L.E. Malvern
University of Florida

PROPAGATION OF SHORT DURATION AIRBLAST INTO PROTECTIVE STRUCTURES 242
J.L. Drake and J.R. Britt
Applied Research Associates, Inc.

BLAST CHARACTERISTICS RESULTING FROM INTERNAL DETONATIONS INSIDE A BLAST CHAMBER 248
Larry Mars, Computer Sciences Corporation

TESTS OF SHEAR FRACTURE AND STRAIN-SOFTENING IN CONCRETE 254
Zdenek P. Bazant and Phillip A. Pfeiffer
Northwestern University

A NONLINEAR THEORY FOR REINFORCED CONCRETE 265
G.A. Hegemier and H. Murakami, S-CUBED

A COMPOSITE FRACTURE MODEL FOR LOCALIZED FAILURE IN CEMENTITIOUS MATERIALS 272
Kaspar J. Willam and Stein Sture, University of Colorado

CONSTITUTIVE EQUATION FOR GEOLOGICAL MATERIALS UNDER HIGH DYNAMIC LOADING 278
J.K. Park and Y. Horie, North Carolina State University

AN ENDOCHRONIC PLASTICITY THEORY FOR CONCRETE 284
K.C. Valanis, University of Cincinnati and
H.E. Read, S-CUBED

A POLYMER PRESSURE GAGE FOR DYNAMIC PRESSURE MEASUREMENTS 291
Anthony J. Bur and Steven C. Roth, National Bureau of Standards

LABORATORY EVALUATION OF AN NBS POLYMER SOIL STRESS GAGE 296
Riley M. Chung and Anthony J. Bur, National Bureau of Standards and
J.R. Holder, USAF Armament Laboratory

FIELD EVALUATION OF THE POLYMER SOIL STRESS GAGE 302
J.Rick Holder, USAF Armament Laboratory and
R.M. Chung and A.J. Bur, National Bureau of Standards

ACCURACY OF ANALOG-TO-DIGITAL CONVERTERS USED FOR BLAST DATA 307
Gary P. Ganong, R&D Associates

CALIBRATION TEST OF PRESSUREMETER IN CLAY 313
An-Bin Huang, Robert D. Holtz, and
Jean-Lou A. Chameau, Purdue University

APPLICATION OF THEORIES OF MIXTURES TO BEHAVIOR OF FLUID-SATURATED DEFORMABLE POROUS MEDIA 319
Makantesh S. Hiremath and Ranbir S. Sandhu
The Ohio State University

DAMAGE PREDICTION OF IMPACTED CONCRETE STRUCTURES 326
H. Adeli, A.M. Amin, and R.L. Sierakowski, The Ohio State University

PENETRATION OF FRAGMENTS INTO SAND 333
A.J. Stilp, E. Schneider and M. Hulsewig, Ernst-Mach-Institut, WEST GERMANY

ANALYSIS OF RANDOM IMPACT LOADING CONDITIONS 338
L.A. Twisdale, Applied Research Associates, Inc.

CALCULATION OF IMPACT- AND PENETRATION-EFFECTS ON HARDENED REINFORCED CONCRETE STRUCTURES 347
R. Schwarz, P. Foros and F. Scharpf, Industrieanlagen-Betriebsgesellschaft, WEST GERMANY

FLASH X-RAY PSEUDOCINEMATOGRAPHY OF THE PENETRATION PROCESS OF BOMB-MODELS IN CONCRETE 353
A.J. Stilp, M. Hulsewig, and E. Schneider, Ernst-Mach-Institut, WEST GERMANY

EFFECT OF STRESS STATE ON VELOCITIES OF LOW-AMPLITUDE COMPRESSION AND SHEAR WAVES IN DRY SAND 358
K.H. Stokoe II, S.H.H. Lee and H.Y.F. Chu
The University of Texas, Austin

ANALYSIS OF RESPONSE OF SATURATED SOIL SYSTEMS SUBJECTED TO DYNAMIC LOADING 364
Ranbir S. Sandhu, S.J. Hong and Baher L. Aboustit
The Ohio State University

DYNAMIC PORE PRESSURE RESPONSE OF SATURATED SOIL UNDER SHOCK LOADING 371
Wayne A. Charlie, Steven R. Abt and George E. Veyera
Colorado State University

FINITE ELEMENT ANALYSIS OF FLOW AND DEFORMATION IN SATURATED SOILS 377
Ranbir S. Sandhu, Baher L. Aboustit and S.J. Hong
The Ohio State University

A VISCOELASTIC CONSTITUTIVE RELATION FOR COMPACTED COHESIVE SOIL 385
S.V. Ramaswamy and M.R.M. Alwahhab
Yarmouk University, JORDAN

AN INVESTIGATION INTO THE HIGH STRAIN-RATE BEHAVIOR OF COMPACTED SAND USING THE SPLIT-HOPKINSON PRESSURE BAR TECHNIQUE 391
C.W. Felice, Air Force Institute of Technology and
J.A. Brown and E.S. Gaffney, Los Alamos National Laboratory and
J.M. Olsen, University of Utah

SOILS AS SAMPLES FOR THE SPLIT HOPKINSON BAR 397
E.S. Gaffney and J.A. Brown, Los Alamos National Laboratory and
C.W. Felice, Air Force Institute of Technology

IMPULSE RADAR FOR DETECTION OF INTERNAL DAMAGE AND SOIL FEATURES 403
John G. Lyon, The Ohio State University and
Ted Zobeck, U.S. Department of Agriculture

EFFECTS OF STRESS STATE AND STRAIN AMPLITUDE ON SHEAR MODULUS OF DRY SAND 407
K.H. Stokoe, II and S.H. Ni, University of Texas, Austin

MEASUREMENT OF GROUND SHOCK IN EXPLOSIVE CENTRIFUGE MODEL TESTS 413
E.S. Gaffney, K.H. Wohletz and R.G. McQueen
Los Alamos National Laboratory

CENTRIFUGE MODELING OF ADVECTION AND DISPERSION PROCESSES DURING POLLUTANT TRAVEL IN SOIL 418
K. Arulanandan, N.J. Meegoda, B.L. Kutter, and
R.B. Krone, University of California, Davis and
Paul Y. Thompson, AF Engineering & Services Laboratory

DIFFICULTIES IN THE SIMULATION OF DYNAMIC EVENTS IN A CENTRIFUGE 424
A. Anandarajah, The Johns Hopkins University and
K. Arulanandan and J. Hutchinson
University of California, Davis

MODEL TESTS FOR DESIGN OF CENTRIFUGE SAFETY BARRIER 430
B.L. Kutter, University of California, Davis

CENTRIFUGE MODELING OF BURIED STRUCTURES 436
Hon-Yim Ko, Chin-Kuan Ni and Stein Sture
University of Colorado

VERIFICATION OF IN SITU PREDICTION OF STRESS-STRAIN BEHAVIOR BY LABORATORY AND CENTRIFUGE TESTS 441
Namunu J. Meegoda, Kandiah Arulanandan
University of California, Davis and
A. Anandarajah, The Johns Hopkins University

MODELING OF EXPLOSIVE-STRUCTURE INTERACTION EFFECTS IN A LARGE CENTRIFUGE 447
George B. Clark, National Technical Systems

IMPACT AND PENETRATION TESTING OF MODELED LAYERED PAVEMENT SYSTEMS 455
Phillip T. Nash and Gerald J. Friesenhahn
Southwest Research Institute and
Patricia C. Suggs, AF Engineering & Services Laboratory

LABORATORY MEASUREMENT OF WAVE PROPAGATION IN SOILS 460
James S. Wilbeck, Southwest Research Institute and
Paul Y. Thompson, AF Engineering & Services Laboratory and C. Allen Ross, Ross Engineering Associates, Inc.

ATTENUATION OF SHORT DURATION BLAST IN ENTRANCEWAYS AND TUNNELS 466
J.R. Britt, Applied Research Associates, Inc.

SOIL PROPERTIES AT DEPTH FROM SURFACE MEASUREMENTS 472
Robert Douglas and George Eller, North Carolina State University

HIGH-PRESSURE BLAST DOOR AND BLAST VALVE DESIGNS 478
David W. Hyde and Sam A. Kiger, USAE Waterways Experiment Station

NUMERICAL AND CENTRIFUGAL MODELLING OF BURIED STRUCTURE RESPONSE TO NEAR FIELD BLAST 482
F.C. Townsend, M.C. McVay, D.M. Bradley,
C.H. Cunningham and D.J. Yovaish
University of Florida

CONCRETE BREACHING DATA BASE SEARCH AND CONCRETE PENETRATION ANALYSIS 488
J.R. Wolfersberger, Goodyear Aerospace Corporation

DESIGN AND APPLICATION OF REINFORCED CONCRETE-ARMOURED DOORS 494
H.J. Hader, Ernst Balser & Partners, SWITZERLAND

AUTHOR INDEX

Aboustit, B.L., 364, 377
Abramson, H.N., 1
Abt, S.R., 371
Adeli, H., 326
Akgun, M., 127
Allahdadi, F.A., 132
Alwahhab, M.R.M., 385
Amin, A.M., 326
Anandarajah, A., 424, 441
Arulanandan, K., 418, 424, 441
Arvidsson, B.K., 186

Babcock, S.M., 200
Balazs, P., 143
Ball, J.W., 137
Baylot, J.T., 62
Bazant, Z.P., 254
Beck, J.E., 5
Bellue, S.B., 62
Bradley, D.M., 482
Britt, J.R., 242, 466
Brown, J.A., 391, 397
Bur, A.J., 291, 296, 302

Carson, J.M., 132
Chameau, J.-L. A., 313
Chang, T.Y., 117
Charlie, W.A., 371
Chen, W.F., 117
Chiarito, V.P., 217
Chu, H.Y.F., 358
Chung, R.M., 296, 302
Citernesi, F., 101
Clark, G.B., 447
Coltharp, D.R., 89, 95, 137
Crawford, J.E., 112
Crutzen, Y., 101
Cunningham, C.H., 482

Davison, D.K., 186
Douglas, R., 472
Drake, J.L., 242

Eller, G., 472
Eytan, R., 68

Felice, C.W., 391, 397
Foros, P., 347
Friesenhahn, G.J., 455

Gaffney, E.S., 391, 397, 413
Ganong, G.P., 307
Gesund, H., 78
Glover, T.A., 222
Gran, J.K., 206

Hader, H.J., 494
He, Y., 84
Hegemier, G.A., 265
Hilferty, T.J. 95
Hiremath, M.S., 319
Hoffmann, G., 56
Holder, J.R., 154, 296, 302
Holtz, R.D., 313
Hong, S.J., 364, 377
Horie, Y., 278
Huang, A.-B., 313
Hulsewig, M., 333, 353
Hutchinson, J., 424
Hyde, D.W., 478

Jacak, J.T., 78
Jenkins, D.A., 194
Jenq, Y.S., 169
Jerome, E.L., 235
Joachim, C.E., 180
Ju, F.D., 127

Karathaus, W., 211
Kiger, S.A., 41, 95, 478
Ko, H.-Y., 436
Krauthammer, T., 52
Krone, R.B., 418
Kufferman, D., 74
Kutter, B.L., 418, 430

Lee, S.H.H., 358
Linton, P., 163
Liu, X.L., 117
Longinow, A., 12
Lyon, J.G., 403

Mak, R.Y., 74
Malvern, L.E., 194, 235
Mars, L., 248
Mayrhofer, C., 175
McQueen, R.G., 413
McVay, M.C., 163, 482
Meegoda, N.J., 418, 441
Mendoza, P.J., 112
Meyer, V.A., 149
Miller, V.R., 17
Murakami, H., 265

Napadensky, H., 12
Nash, P.T., 455
Ni, C.-K., 436
Ni, S.H., 407

Olsen, J.M., 391

Painter, J.T., 41
Parikh, M., 52
Park, J.K., 278
Pfeiffer, P.A., 254

Ramaswamy, S.V., 385
Read, H.E., 284
Rempel, J.R., 5
Rosengren, Jr., P.L., 45
Ross, C.A., 45, 194, 235, 460
Ross, T.J., 35
Roth, S.C., 291

Sandhu, R.S., 319, 364, 377
Scharpf, F., 107, 347
Schneider, E., 333, 353
Schwarz, R., 347
Seereeram, D., 163
Shah, S.P., 169
Sierakowski, R.L., 217, 326
Smith, J.A., 222
Stilp, A., 333, 353
Stokoe II, K.H., 358, 407
Sture, S., 272, 436
Suggs, P.C., 455

Tang, T., 194
Thompson, P.Y., 418, 460
Thor, H.J., 175
Townsend, F.C., 482
Twisdale, L.A., 338

Valanis, K.C., 284
Veyera, G.E., 371
Vienings, B.C.J., 24
Vitayaudom, K.P., 95
Vretblad, B., 143

Weerheijm, J., 211
Weidlinger, P., 74
Whitehouse, S.R., 227
Wilbeck, J.S., 460
Willam, K.J., 272
Wohletz, K.H., 413
Wolfe, W.E., 89, 217
Wolfersberger, J.R., 488
Wong, F.S., 74
Wong, M.K.W., 29

Yovaish, D.J., 482

Zobeck, T., 403
Zurru, M., 101

A BROADER PERSPECTIVE

H. Norman Abramson

Southwest Research Institute
San Antonio, Texas

INTRODUCTION

Thirty years ago, when many of our military facilities were built, there was no significant air threat, and we had the notion that nuclear firepower could substitute for conventional weaponry. Our adversaries viewed that position and then developed an integrated plan to gain strategic victories in Europe while maintaining a "no first use" pledge on nuclear weapons. Thus, the Warsaw Pact countries have pursued with great vigor the preparations they feel are necessary to conquer Western Europe in a matter of weeks with conventional military forces. The historical goal in that battle arena is to advance quickly, destroying infrastructure, military installations, and any enemy forces encountered.

With great hope in the policy of nuclear deterrence, the U.S. also decided to develop far more effective conventional tactical weapons. Even recently, Dr. George A. Keyworth, II, the President's Science Advisor, stated the administration's position that conventional weapons are a key to the transition away from dependence on those tactical nuclear weapons deployed in the field near potential battlegrounds. The thrust is therefore to use modern technologies to improve conventional weapon lethality, with much greater accuracy and damage potential.

These evolving conventional threats have created new problems in protective structure design. Unfortunately, the bulk of the supporting technology base is empirically founded and, in some cases, obviously outdated so that recent efforts have focused on improving this base to meet modern threats. Civil engineers, who previously were responsible primarily for maintenance and services, were given the responsibility for modernizing and rebuilding that technology base and now have new challenges in meeting both readiness and regulatory requirements. Most of the papers in this symposium report efforts in these directions. However, even though current research appears to be addressing immediate needs, perhaps this is the time to take a broader look at needs and goals, how will they change in the future, and what new directions we should be taking.

THREATS FROM CONVENTIONAL WEAPONS

First, what do we perceive to be the current threats? That question can be answered in rather specific terms only by considering our opponents to have weapon technologies similar to ours. Traditionally, we think of military munitions such as projectiles, missiles, or bombs which deliver large amounts of energy on their targets either through impact and/or blast. Although there have been some enhancements in the performance of high explosives, the advancements in modern military weapons which overshadow all others are the tremendous improvements in delivery systems effectiveness and accuracy. Modern guidance techniques can place warheads on target with great precision, which has increased expected loadings on protective structures by orders of magnitudes and thus presents many new technical challenges.

When warheads were only expected to detonate at some distance from their target, loadings could be determined by choosing any equivalent charge weight and calculating overpressures, durations, and impulses by empirically derived methods. These idealizations and data bases, however, are insufficient for bombs directly impacting or detonating very close to their targets--within several charge radii, the blast environment includes intense shock waves, explosive products, and case fragments travelling at extreme velocity. This complex loading is difficult to idealize and there is very little experimental data for close-in detonations because most instrumentation simply will not survive the severe environment.

The loading is complex also for close-in ground shock even though fragment loading from the buried explosion is not as severe. When the buried charge detonates, the solid explosive is changed into an equal mass of gas at extremely high pressure which expands rapidly so that pressures at the explosive-soil interface can be hundreds of times greater than the strength of the soil, creating a zone of crushed material. If the charge detonates close enough to the structures, even the explosive products will contact the structure. Variability of soils and their properties makes it

difficult to predict accurately explosive coupling with buried structures and most instrumentation is also unable to survive this harsh environment.

The immediate problem then is to possess the capability to design or upgrade protective structures against modern threats for which expected loadings are poorly described. So far, the approach has been to attempt to improve the data base to include these more severe threats; however, the greater challenge is to expand our perceptions to the full spectrum of threats and anticipate how their future evolution will affect expected loadings and structural designs. And while we are trying to expand our perceptions, who will attempt to evaluate what new non-nuclear weaponry will appear from the SDI program to pose new threats to our present concepts of protective structural design?

TARGETS

Although we think primarily of military facilities as the structures which require protection, we must also remember that the enemy intends to destroy infrastructure. This means that virtually any significant structure, military or civilian, is subject to attack. For the most part, the civilian sector is totally unprepared to meet such threats and therefore we have an additional long term goal in providing appropriate technology applicable to non-military facilities.

Protective military structures are designed to house vital functions or equipment of extreme value. Consequently, survivability takes precedence over appearance and the structures are usually massive with soil and concrete the main building materials. Protection needs are expressed by operational users in the form of requirements; the requirements are answered from the available technology base, or extension thereof, and the need is eventually met in the consequent design. Many of the papers to be presented in this symposium reflect efforts to extend our technology base for material properties and structural response to blast and impact loads. Granted, there is a pressing need to increase our technology base to meet current user requirements, but are we producing the technical advances which will significantly improve survivability in the long term? Unfortunately, technology developments in response to user requirements often are unacceptably slow. Retired General Bryce Poe II in The Engineering and Services Quarterly Journal recalled initiating items as a Captain in 1953 which were finally constructed when he was a Lieutenant General in 1974. Because the items were important to warfighting capabilities, he concluded that national security was at risk for more than 20 years. Can we afford similar time lags in the future? Is our national security at risk today for the same reasons?

Potential targets of a non-military nature come in a variety of descriptions and can include governmental, industrial, and civilian structures. These, unlike military facilities, have no well defined survivability requirements and are not designed to provide protection from weapon attack and are usually readily accessible. For example, United States embassies have historically been designed to reflect the openness and freedom of our society. Therefore, most of them do not use restricted access, heavy barricades, or special protective features to keep visitors at a distance. Consequently, they are very vulnerable to terrorist attack. More recently, we have seen some concern for protecting government buildings in Washington, D.C., as when trucks filled with sand were used to barricade the White House against possible terrorist attack. Especially vulnerable are industrial facilities such as power plants, petrochemical facilities, storage depots, etc., which may be spread out over large areas, leaving vital components exposed. Many terrorist attacks have been targeted against U.S. businesses abroad. Other civilian lifelines such as communication networks, pipelines, bridges, and such are completely unprotected, vulnerable to attack, and are undoubtedly already targeted in the event of conflict. Complete protection of all our facilities may be an impossible task, but our vision must be broad enough to develop technologies which will enhance the survivability of both our military and non-military against all opponents.

OPPONENTS

While the Soviets have hundreds of bomber aircraft less than an hour's flight from NATO airbases, posing an evident threat, there are other opponents and threats for which we can only guess what kinds of loadings might be delivered.

Along with conventional troops, Soviet special purpose forces, SPETSNAZ, would be employed in wartime throughout Western Europe to covertly disrupt communications, destroy bridges, seize choke points, and to direct attacking aircraft to prime targets. These SPETSNAZ forces are weapons and demolition experts specially trained in infiltration tactics and sabotage methods using explosives, incendiaries, acids, and abrasives. Their realistic training includes accurate full-scale models of key targets. Their role is to operate from behind enemy lines and to attack major facilities and important weapon systems. The SPETSNAZ is suspected of having already participated in a number of covert operations, including assassinations. Their clandestine operations and expert use of explosives are tremendous threats to unprepared non-military as well as military facilities.

Since 1968, there have been more than 950 terrorist attacks against U.S. businesses, including more than 500 explosive bombings. Political extremists have exploited terrorism to attract world attention. The target of a terrorist can be anything, but the more newsworthy the better. Alarmingly, terrorists have improved arsenals with modern weapons and explosives which can be placed in close proximity to unsuspecting targets. Car bombs, for example, have proved to be capable of awesome destruction and are very difficult to defend against.

Although terrorists activities began with civilian targets, recent attacks, such as the one on our Marine barracks in Lebanon, illustrate that military installations can also be targets. Unfortunately, some nations actually sponsor international terrorism and provide training, arms, sanctuary, and advice leading to an evermore sophisticated and unknown enemy with an unlimited array of targets. The terrorist issue is well recognized by the participants of this symposium who are involved with weapon storage design, but the technologies developed to combat terrorism against military targets must be transferred to those responsible for the protection of our civilian installations and personnel as well.

CURRENT ACTIVITIES

What are we doing to provide better defensive systems? From the papers to be presented in this symposium, several topics seem to stand out. As said, definition of loads from air blast, ground shock, impact, and combinations is a major concern, and the tremendous energy deposited on structures by close-in explosions is not easily characterized by previous idealizations and new methods are being sought. We are looking for better means of measuring the extreme loadings and better understanding of the coupling with structures. Another topic of immediate concern is structural response, in which there are at least three distinct areas of research: design, analysis, and testing. Several of the standard but now outdated design manuals have recently been revised or are under revision. But, even these revisions can only reflect the technology base as it currently exists and that is believed to be seriously lacking in many respects. More than a dozen papers at this symposium will discuss analytical techniques, ranging from simple approximations to attempts at very complex descriptions. A prevailing concern relates to better descriptions of material properties and failure mechanisms. We still have no clear-cut, standard, accepted methods for accurately describing the response of structures subjected to high amplitude short duration loads, although seemingly our understanding of dynamic materials properties is advancing. As in the past, the main emphasis in structural response research is testing and development of empirical relationships. Other papers in this conference range from testing new structural systems to revisiting World War II information. In some cases, scale model testing is being used to reduce test costs, and centrifuges are being evaluated as a method for testing geotechnical problems at very small scale. Centrifuge testing is viewed as an opportunity of overcoming difficulties in modeling soil because its strength is derived through gravitational forces, although there is some controversy over the validity of the technique. Many see centrifuges as the only way to test soil-structure interaction problems at small scale while others feel scaling gravity is totally unnecessary for blast studies; however, it is more important to remember that the centrifuge is simply a modeling tool and, like any other modeling technique, can only be employed usefully within the scientific understanding of the user. Other papers describe better instrumentation techniques and a few special problems.

The real question we must ask ourselves, however, is that even if we are 100 percent successful in every area of research being pursued, how much improvement will we gain in survivability? Are we making only incremental advancements at a time when major or revolutionary new concepts and results are required? What new directions should we be taking? Considering the evolving, expanding nature of the threats, and the payoffs we expect from our current research programs, will we be in a better position of survivability 25 years hence than we are today?

THE FUTURE

Conventional weapons systems will continue to improve, and pinpoint accuracy will require facilities designed for direct hits. We can surely expect that weapons will be smarter, with substantially improved projectile lethality, and overall will possess greatly enhanced power. Threats will not always come packaged as military bombs, and special forces and terrorists will possess sophisticated weaponry and will be apt to attack a broad array of targets.

What lies ahead in protective structures design? If current research is successful, we will be more able to describe loadings from nearby detonations; dynamic properties of concrete and soil will be better understood; and perhaps new and stronger materials will be used in construction. Without the development of novel design concepts and the introduction of radically different materials and construction techniques, however, we can expect only marginal improvements over current practice--that will not be satisfactory!

The key to long term survivability is to escape the trap of attempting to solve today's problems with yesterday's technology; rather, we have to begin to develop tomorrow's technology. This requires a thorough and careful analysis of future threats. I suggest the next symposium include invited speakers from the intelligence community to describe the capabilities that our adversaries might possess in the future. Furthermore, representatives from the user communities (both military and civilian) should be asked to express their anticipated needs. To stimulate effective technical thought in the researcher, it is essential to know as much as possible about the background of the problem, why it is important, what directions should be followed in developing possible solutions, and how will the results be utilized in practice.

The research community must strive for innovative concepts, applications, and techniques. New and different materials and construction methods are needed to match their full potential against very high intensity loads. We have depended for years on passive protective structures; perhaps active protective systems could be developed for civil engineering structures as they have been for

armored vehicles, missile silos, etc. Above all, we must maintain a broad perspective and look beyond narrowly defined problems and solutions by prescription; we must focus on long term goals and objectives which, with creative and innovative thinking, could neutralize opponents.

Those persons responsible for evaluating and funding research and development efforts should studiously avoid "more of the same" and "safe" research which can lead at best only to incremental advances. Instead, they should encourage and support truly innovative and revolutionary ideas; devote more resources to concept development and less to routine testings. Dare to be bold!

Once again, I urge you to think to the future--plan your next symposium with the future as your theme. In the meantime, concentrate all your efforts to maintain the broader perspective you will need to meet the survivability challenges of the decades ahead.

Acknowledgments: I am grateful to Phillip T. Nash and Alex B. Wenzel for considerable assistance in the preparation of this paper.

STABILITY OF WALLS AGAINST AIRBLAST FORCES

John R. Rempel*
Center for Planning and Research, Inc.
Palo Alto, California

and

James E. Beck
James E. Beck and Associates
Palo Alto, California

ABSTRACT

By observing pressures, wall deflections and accelerations during collapse as well as debris distributions after collapse of several near full-scale buildings of four different types under airblast loading, we have demonstrated quantitatively the relative importance of mechanisms invoked by the collapse process. This paper outlines one of the analytical methods applied to the data and some of the results of the research program.

INTRODUCTION

Over the past eight years, experiments conducted with explosions of approximately 600 tons of ammonium nitrate have provided insight into the physical processes of wall collapse under airblast loading. Motivation for the research was a wish to explore both collapse mechanisms and debris production and distribution in the range 7 to 40 psi incident overpressures. Structures of various kinds were built and exposed to explosive airblast: load bearing masonry, half-timber, reinforced concrete tilt-up, and reinforced concrete frame with masonry infill. Wall sizes were all in the range 8 ft. high by 12 to 17 ft. long. Electronic instrumentation recorded inside and outside pressures, wall deflection, and in some cases, accelerations. Walls were all oriented perpendicularly or parallel to the blast direction (Refs. 1 - 5).

METHOD OF ANALYSIS

Since net pressure loading and horizontal wall deflection can be estimated as functions of time from the gage data, the energy deposited in the wall by the airblast can be calculated; similarly the kinetic energy (if any) of the wall at the moment of collapse can be estimated from the deflection history. The difference between these two quantities then must be accounted for by a process of "collapse". It is usually obvious from the magnitude of the difference which collapse mechanism is most likely to have been effective (e.g., brittle shear, elastic bending, compression).

In Fig. 1, interior and exterior pressure histories and the corresponding deflection history of a solid masonry wall of two clay brick wythes have been superimposed. The wall was without openings and faced Ground Zero (Refs. 3 and 4). During airblast loading the wall moved steadily inward until deflection equaled thickness at which point it was considered to "collapse". The exterior pressure was measured in the center of the 8 x 12 ft. wall; it was the result of a 37 lbf/in^2 incident blast wave striking the wall at head-on incidence. Peak reflected pressure was 140 lbf/in^2. Edge rarefactions eroded the peak in approximately 16 ms. The interior pressure shown in Fig. 1 was measured in the middle of the floor of the room directly behind the wall, i.e., approximately four and a half feet downwind from the wall. The record shows a fairly smooth, slow rise in pressure because there was no opening in the front or side walls of the room; the airblast entered the room through a hallway and a door at the rear of the room. Fig. 2 is a pre-shot photograph; a plan view is seen in Fig. 3. Pressure and deflection gage locations are indicated in Fig. 3 by the letters P and D respectively.

The measured pressure and deflection histories should be transformed to spatial averages. This has been done for this example by assuming deflection is in a "classical" failure pattern (Fig. 4) so that the average deflection equals:

$$\bar{\delta} = \tfrac{1}{2}\delta_m(1 - H/3L) = T_D\delta_m$$

where δ_m is the midpoint deflection, L and H are wall length and height, respectively. Although methods exist for transformation of exterior pressure (Ref. 6)

---

* Present Address: Westinghouse Electric Corporation, Sunnyvale, California

the effect is small when there are no openings and no transformation has been made in this example. Neglecting a small rotation the square of wall speed transforms as:

$$\bar{V}^2 = 1/3\ V_m^2(1-H/2L) = T_{KE}V_m^2$$

When the wall fails with a single midline crack the transformation factors are:

$$T_D = 0.50$$

$$T_{KE} = 0.33$$

for all values of H and L.

Although the deflection gage in the experiment failed early, its record has been extrapolated based upon previous experience.

If A is the wall area, $\delta_m(t)$, $P_{out}(t)$, and $P_{in}(t)$ are central wall deflection, inside and outside pressures as functions of time, then energy output is:

$$W = T_D \int_0^{t_f} (P_{out} - P_{in})A\ \delta_m dt$$

where t_f is the time of wall failure (when net pressure is close to zero also). P_{out} is the history produced by P5 in Fig. 3 but P_{in} is the record of P6 shifted to the right (away from the origin) to account for the separation between wall and gage. If M is wall mass, kinetic energy is (again neglecting small verical components of speed):

$$KE \approx \tfrac{1}{2}MT_{KE}V_m^2$$

Numerically in this experiment

$$W = 3.7 \times 10^5 \text{ ft-lbf}$$

and

$$KE = 4.6 \times 10^4 \text{ ft-lbf}$$

so that the difference

$$W - KE = 3.2 \times 10^5 \text{ ft-lbf}$$

represents energy of elastic and plastic deformation of the frame and wall and the removal of the simulated floor and crushing of masonry. For this R/C structure:

$$KE/W = 0.12$$

(At the base of every wall in all experiments a wood plate approximately 2 x 4 inches in cross-section was bolted to the concrete floor to simulate a built-up floor structure behind the wall.)

Although the top course of masonry in the front wall, which partially adhered to the ceiling, showed clear evidence of compressive shear fracture along its entire length (Fig. 5), we do not know exactly in what pattern or to what extent the masonry was crushed. The vertical frame members yielded (Fig. 6) and probably did not exert enough restraint to crush the masonry. However, if we postulate (1) the horizontal frame members were rigid, (2) the wall cracked in a single midline fracture, and (3) crushing occurred in four symmetical zones, (one each at top and bottom and two at the midline) then the crushing energy can be estimated. Under these conditions if the depth of crush in each zone is x, the angle of wall rotation is θ, then the width y of the zone is

$$y = \frac{x}{\tan\theta} + \frac{\tan\theta}{x}$$

and

$$x = \tfrac{1}{2}(b\sin\theta + H/2\ \cos\theta - H/2)$$

where b = wall thickness. Neglecting elastic compression, crushing work W_c is then:

$$W_c = 4\ \sigma_c\ L \int_0^{\theta_{max}} y dx$$

where σ_c is the compressive yield stress of the wall. The maximum rotation is:

$$\theta_{max} = \tan^{-1}\frac{b}{H/2}$$

By estimating the value of the integral numerically we find the crush energy under these assumptions to be approx.

$$W_c = 3.1 \times 10^5 \text{ ft-lbf}$$

(We have found brick and mortar assemblies to yield in compression at stresses intermediate between yield values of brick and mortar alone (Ref. 1). The value of W_c above has been computed using a composite value based on static testing of brick couplets.) W_c is of the order of magnitude of the difference or "dissipation" calculated above. It therefore seems likely that masonry crushing was indeed the major dissipation mechanism.

RESULTS

Other building types have been examined in this way with the results summarized in Table 1.

In particular, the pair of reinforced load-bearing masonry buildings, DNA5401 and DNA4070 (downstairs), both at nearly the same incident pressure, form an interesting contrast. A front view of the latter is seen in Fig. 7. Essentially identical except for the presence of a second story at DNA4070, analysis clearly shows the increasing restraint provided by increasing overburden. The downstairs front wall shows a dissipation

$$(W - KE)/W$$

of approximately 75%; without the second story overburden the reinforced masonry front wall collapses with only 50% dissipation.

In the case of the single story unreinforced masonry buildings DNA5401 and DNA5403, we observed ceiling slab uplift due to front wall collapse by means of accelerometers and, after allowing for 0.126 inches of elastic compression, we found crushing reduced the wall height by 0.45 and 0.12 inches, at 30 and 10-psi, respectively. Depth of crush plus elastic compression is computed as the difference between expected uplift due to rotation of wall segments and observed uplift. However, the smaller "dissipation" at lower overpressure constitutes a larger proportion of input energy than does the dissipation at higher pressure (See Table 1). But the freedom of the overburden to be uplifted reduces the dissipation (Compare DNA4071 and DNA4070 downstairs).

Removal of the floor plate occurred behind only two walls: the front ground floor of the two story building and the front wall of the R/C frame building. These were examples of greatest "dissipation" in the pressure range 30-40 psi. Apparently the vertical in-plane forces prevented shearing of the wall at the plate.

Side walls in these experiments invariably moved inward one or two inches immediately following blast arrival, but very shortly after front wall collapse (i.e., displacement equal to thickness) reversed direction strongly. Their debris was found outside the building arrayed in a direction perpendicular to the direction of blast wind. The strong differential pressure moving them outward arose in the vortices shed by the front corners of the building. The blast energy deposition during outward motion was found entirely in kinetic energy of fragments.

Rear walls moved initially inward if there were no openings in the front wall but initially outward otherwise. All eventually collapsed outward - without significant dissipation. The rear wall of DNA4071 (Fig. 3) moved outward to a maximum of two inches then returned to rest near its original position before being swept out of the building by high speed debris from the front wall.

CONCLUSIONS

Our observations of several types of building collapse have provided an understanding of collapse mechanisms such that we believe we can estimate quantitatively the behavior of these types under airblast loads other than those applied in our experiments. These collapse mechanisms will be important, for example, in assessing collapse probability and debris production under airblast loading produced by non-nuclear munitions of yields less than 500 tons. A short impulsive airblast, for example, must provide enough input energy to crush masonry at the frame or under an overburden; and the short duration will enhance any tendancy to stimulate inertial reaction forces.

This study of collapse mechanism from an energy standpoint has also been helpful in evaluating and modifying the more classical structural response models (based on force-deflection considerations) used by the authors elsewhere (e.g., Ref. 1) in predicting incipient collapse of structure.

TABLE 1

Ratio of Kinetic Energy to Input Energy, Front Walls

Expt. No.	Construction type	Incident Pressure (psi)	KE/W
5403	Load-bearing masonry (CMU)	10	0.11
5402	R/C panel, tilt-up	25	0.30
5401	Load-bearing masonry (CMU)	30	0.50
4070 (upper)	Load-bearing masonry (CMU)	40	0.58
4070 (lower)	Load-bearing masonry (CMU)	40	0.25*
4071	R/C frame, clay masonry units	37	0.15*

*floor plate removed.

REFERENCES

1. Wiehle, C. K., J. R. Rempel, and J. E. Beck, Dynamic Response of Two Types of German House Construction, SRI International for Defense Nuclear Agency, POR 6966, October 1978.

2. Rempel, J. R., J. E. Beck, and R. G. McKee, Structural Response and Debris Experiments at Operation Mill Race, SRI International for Defense Nuclear Agency POR 7077, July 1982.

3. Rempel, J. R. and J. E. Beck, Structural Response and Debris Experiments at Operation Direct Course, Center for Planning and Research, Inc. for Federal Emergency

Management Agency, in preparation.

4. Ray, J. C. and S. C. Woodson, Structural Debris Experiments, U.S. Army Experiment Station for Defense Nuclear Agency, 1984.

5. Rempel, J. R., Blast Induced Formation and Distribution of Debris, Home Office Workshop, Easingwold, England, June 21-23, 1984

6. Baity, W. M., Front Surface Loading Investigations, Ballistic Research Laboratories, Aberdeen Proving Ground, MD, September 1972.

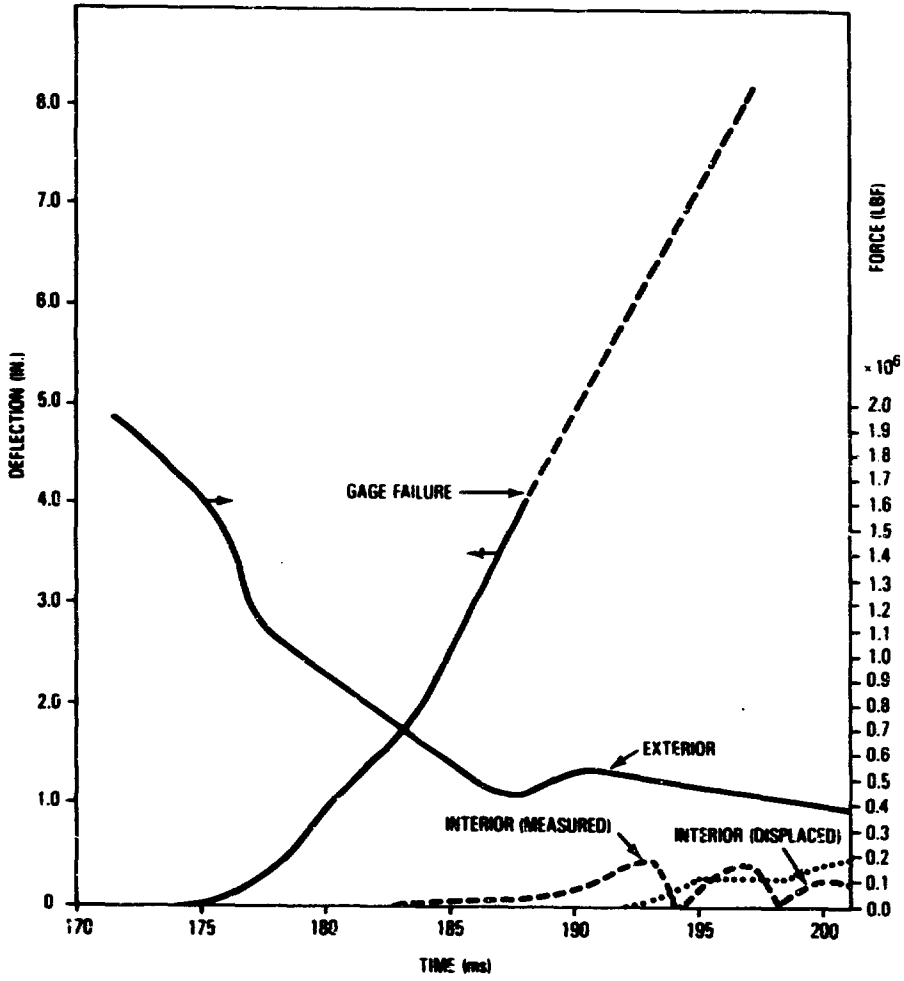

FIGURE 1 LOADING AND DEFLECTION OF A MASONRY WALL FACING GZ (DNA 4071)

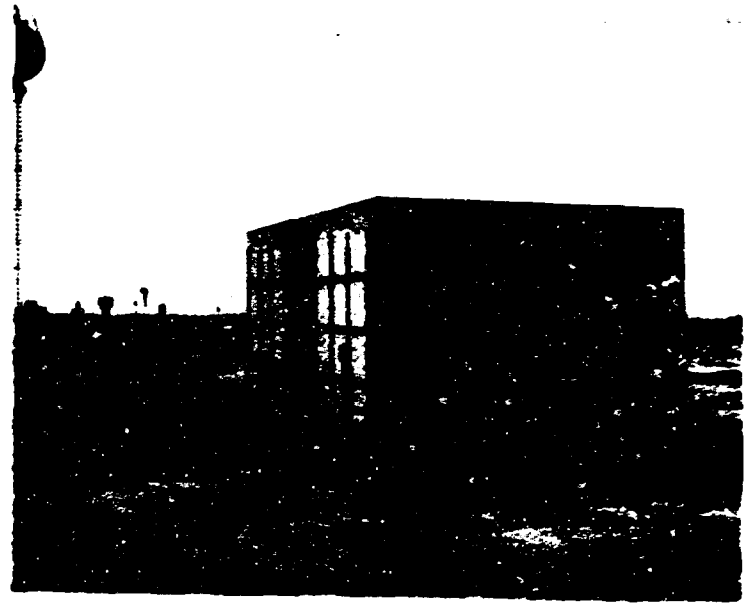

FIGURE 2. VIEW FROM REAR OF R/C FRAME BUILDING DNA4071

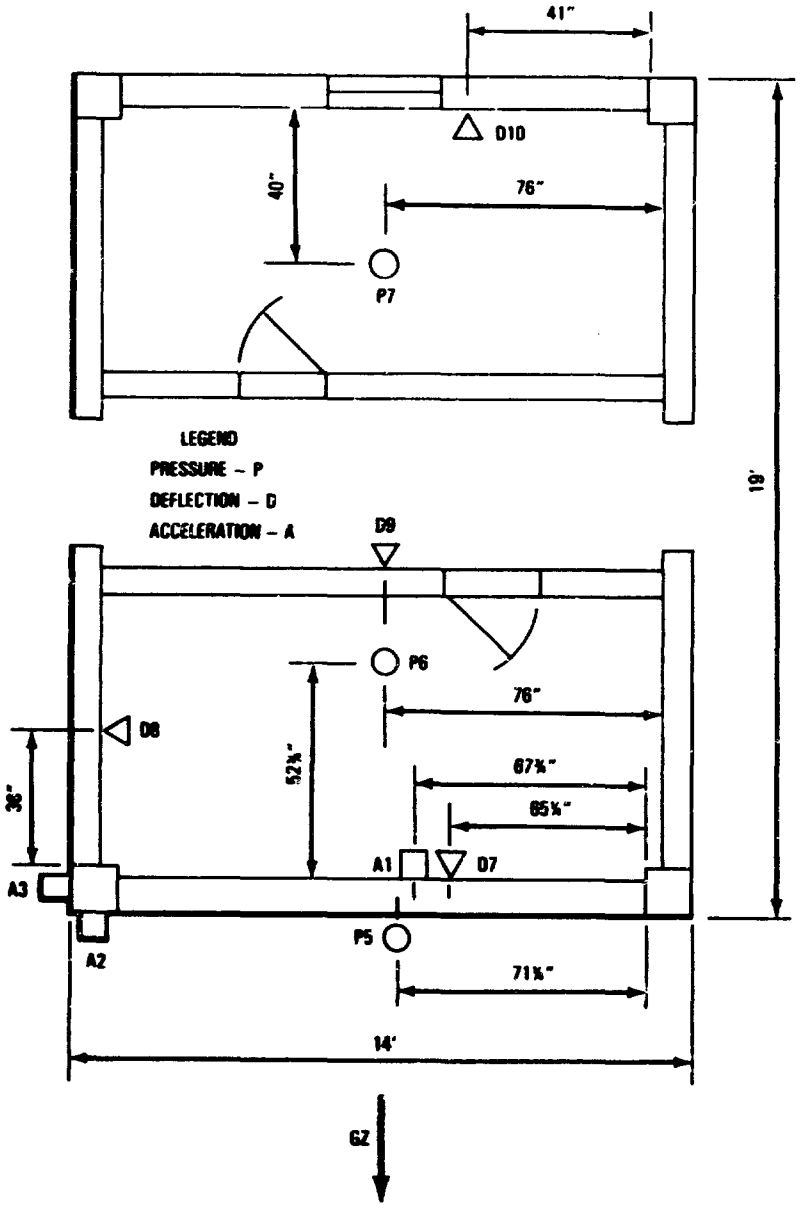

FIGURE 3. PLAN VIEW OF R/C FRAME BUILDING

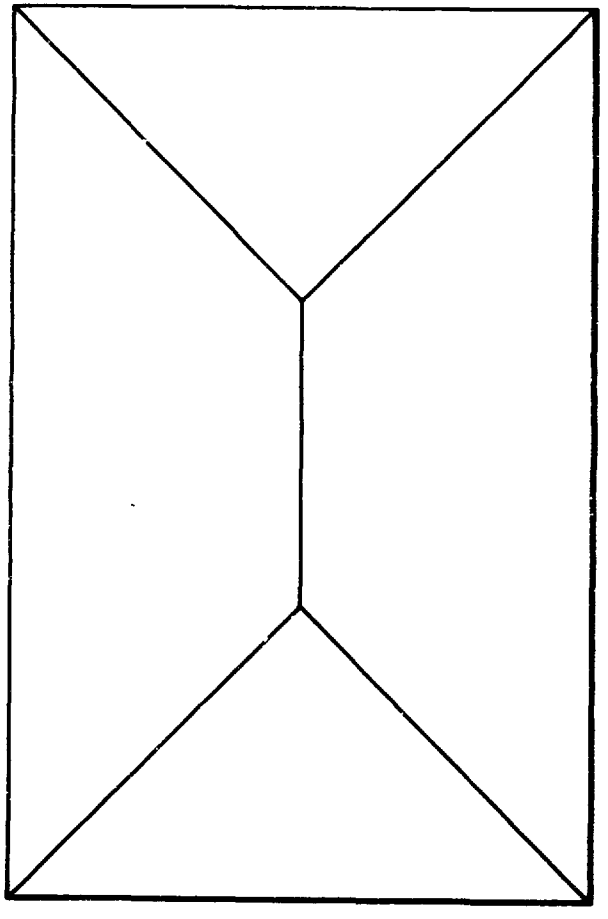

FIGURE 4. CLASSICAL WALL FRACTURE PATTERN

FIGURE 5. COMPRESSIVE SHEAR FRACTURE IN TOP COURSE, FRONT WALL, DNA4071

FIGURE 6. DISTORTED VERTICAL MEMBERS, DNA4071 POST-SHOT

FIGURE 7. FRONT VIEW OF UNREINFORCED TWO STORY CMU BUILDING DNA4070

EXPLOSION DAMAGE TO URBAN STRUCTURES AT LOW OVERPRESSURE

Hyla Napadensky
IIT Research Institute, Chicago, IL

Anatol Longinow
Illinois Institute of Technology, Chicago, IL

ABSTRACT

Manufacture, storage and transportation of chemicals capable of exploding at energy levels comparable to TNT has increased in recent years. Land areas adjoining such storage facilities and transportation routes are now more densely populated and, therefore, people in these areas are at a higher risk than previously. This paper focuses on these problems and suggests solutions so that the potential for damaging effects can be considered and mitigated by planners in the vicinity of hazardous facilities and transportation routes.

INTRODUCTION

Research studies need to be initiated to reevaluate current regulations governing the siting of "inhabited buildings" relative to stores of commercial and military explosives. One reason is that modern buildings are more vulnerable to blast effects than those for which existing regulations were developed. Many of the land areas at risk are now also more densely populated. Further, there are no Federal regulations governing the routing of materials capable of exploding and thus all structures along transportation routes carrying hazardous materials are at risk. A number of local communities have attempted to limit the transport of explosives through their environs without success.

Perhaps a more serious problem (and one for which there are no regulations, or guidelines, and essentially no awareness by structural engineers or architects) is the fact that the manufacture of chemicals capable of exploding at energy levels comparable to TNT (trinitrotoluene), has increased substantially in recent years. These are being shipped along highways and railways in large quantities and at high frequencies. These materials are not classed as explosives since their primary use is not to function by explosion. The increase in the amounts produced and the energy content of these chemicals has led to an increase in accidental explosions and, thus, an increase in risk to built-up areas in the vicinity of certain processing plants, storage facilities and respective transportation routes.

The objective of this paper is to focus attention on the problems described and to suggest possible solutions, so that the potential for damaging effects can be properly considered by individuals responsible for the planning of developments adjacent to hazardous facilities and designated transportation routes.

BACKGROUND

Existing DoD quantity-distance regulations (Refs. 1,2) used for the specification of minimum separation distances between various types and quantities of stored explosives and surrounding communities have evolved primarily from studies of actual blast damage results (Refs. 3,4,5). Each separate explosion was analyzed with respect to quantity of explosive, nature and extent of damage produced. Each result was plotted on a quantity-distance chart, and a curve was finally drawn to form an envelope on the safe side of the data points. Separation distances for quantities of explosives for which no experimental (or accident) data existed were determined by scaling existing data. In these charts damage is expressed in terms of quantity of explosive and distance to the target and is primarily related to the overpressure at the site of the target.

Current regulations (Refs. 1,2) governing storage of explosives permit conventional, inhabited buildings to be located at distances of from $40W^{1/3}$ to $50W^{1/3}$ ft ($15Q^{1/3}$ m to $20Q^{1/3}$ m). Where W is the weight of explosive in pounds and Q is in kg. The larger number applies to quantities greater than 250,000 lbs of TNT. In the weight range of 100,000 to 250,000 lb of TNT, the applicable distance is $2.42W^{0.577}$ ft. How this regulation reflects the actual response of buildings subjected to blast loads in theory and practice is discussed in the following sections.

BEHAVIOR OF STRUCTURES IN A BLAST ENVIRONMENT

The response of a structure to a blast wave induced load depends on the makeup of the structure and the character of the load. Very generally, structural characteristics of interest include the mass and mass distribution, stiffness, fundamental period, type and mode of failure.

Blast load characteristics of interest include peak load, rise time to peak load, duration and character of decay.

When the effective duration of the load is short, say less than about one third of the period, then the impulse due to the load is of major importance, and the response of the structure can be based entirely on the consideration of impulse and momentum. On the other hand, when the duration is relatively long compared with the fundamental period of the structure, say greater than about four times the period, then the loading can be treated as a step load of infinite duration. In between these two extremes, the characteristics of the loading need to be considered.

A given building is not of constant stiffness or strength throughout. Individual components such as exterior cladding, interior partitions, window panes, etc., depending on support conditions, orientation and materials, can be locally stiffer or more flexible than the primary structure, i.e., the building frame. When subjected to a given blast load, such components are therefore expected to respond in different modes than the structure as a whole.

It is evident from this brief discussion that a separation distance based on quantity of explosive alone is not necessarily a useful criterion for defining a safe condition for all cases.

Recognizing this fact, it becomes useful to characterize the strength or some critical damage level of a given building by means of a function which covers the entire range of load-time histories capable of producing that same level of damage. A peak load-impulse characterization scheme (Ref. 6) serves this purpose. It is illustrated in Fig. 1 where the function shown represents a level of damage for different combinations of peak pressure and impulse.

Procedures for evaluating the strength of buildings in a blast environment are fairly well established at this time. Making use of such structural analysis methods together with probabilistic methods, and making use of available experimental data, more reliable safe separation distances can be established.

STRENGTH OF BUILDING STRUCTURES

Analysis of the response of buildings against the effects of blast produced by accidental explosions has received a miniscule amount of attention as compared to that of other hazards, such as earthquakes. The civil engineering profession, outside of one or two government agencies has completely ignored the problem described in this paper, as has the architectural profession. Thus, information on the response of buildings to blast effects, or formal procedures or guidelines are not readily available. What does exist, and that in small quantity, is information on the strength of buildings against blast effects of nuclear weapons. This information is of limited use because nuclear weapons produce loads that have long durations. Some of this information is included in Table 1 (Ref. 7). Shown are eleven categories of buildings and corresponding "incipient failure" overpressure levels. Incipient failure means that the structure has been loaded just to the point where it will fail without additional load. Overpressures given are reference free-field overpressures at the site. Analyses performed considered corresponding reflected pressures and drag pressures as appropriate in a given case. Results are for the "composite" building. Obviously windows, doors, interior partitions, furniture, etc., will become debris at lower overpressures. Table 1 demonstrates that conventional buildings are for the most part "soft". Modern buildings, such as those using pre-fabricated components, are expected to be "softer" than corresponding buildings shown in Table 1.

A study reported in Ref. 8 was concerned with establishing safe separation distances for a number of potential civilian targets with respect to five quantities of explosives. Results for nine of the targets are given in Table 2. Included are safe separation distances, peak overpressures and impulses. Results are based on spherical charges and hemispherical blast wave data.

Results were generated by first determining what constitutes damage resulting in injury to occupants. The greatest separation distance was then determined which for the given quantity of explosive would just preclude the occurrence of

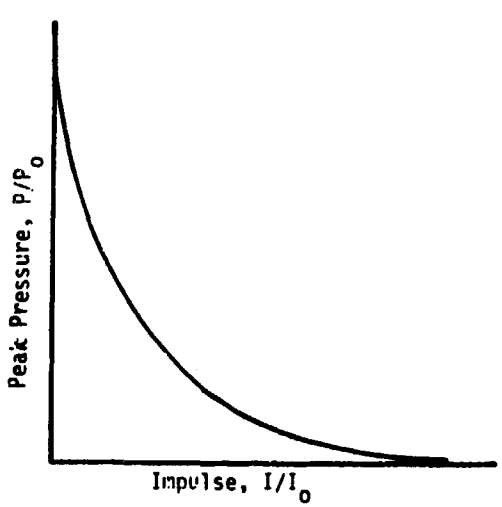

FIG. 1.-Peak Pressure-Impulse Characteization of Structural Response (I_o is the ideal impulse, P_o is the magnitude of a step load producing the same response).

TABLE 1 INCIPIENT FAILURE OVERPRESSURES (PSI)
AT SELECTED PROBABILITY LEVELS (7)

Building Category	Probability of Failure, Percent		
	10	50	90
1. Single Story Frame Residences	1.5	2.2	2.9
2. Single Story Load Bearing Residences	2.0	2.8	4.0
3. Two- or Three- Story Frame Single Residences, Row Houses, Apartments, Motels	1.6	2.3	3.1
4. Mixed One- and Two- Story "Store Front" and Light Commercial Masonry Load Bearing Wall Buildings	2.0	3.2	4.9
5. Multistory Steel Frame Apartment Buildings, Four to Ten Stories	3.5	5.2	7.5
6. Multistory Steel Frame Office and Institutional Buildings, Four to Ten Stories	3.6	5.4	8.0
7. Same as (6) except More than Ten Stories	3.6	4.9	7.5
8. One- Story Masonry Load-Bearing Wall, School and Institutional Buildings	1.8	2.8	4.6
9. Masonry Load-Bearing Wall Industrial Type Buildings, One Story	1.7	2.6	3.7
10. Light Steel Frame Industrial Type Buildings, One Story	3.7	5.0	6.8
11. Heavy Steel Frame Industrial Type Buildings, One Story	5.4	7.2	10.0

1 psi = 6.89 kPa

this level of damage. Due to the significantly different definitions of damage as well as quantities of explosives involved, the results in Tables 1 and 2 are not directly comparable.

Separation distances based on current regulations (Ref. 1) are included for comparison in the lower part of Table 2. It will be noted that in six of the cases (see asterisks in Table 2), the separation distances stipulated by the current regulation are inadequate. This occurs mostly for buildings with large span roofs. It is noted that potentially lethal effects of debris from falling neighboring buildings were not considered in the analysis described.

SELECTED ACCIDENT DATA

On June 1, 1974 an explosion occurred at the Nypro Ltd. plan at Flixborough, Lincolnshire, England (Ref. 9). The explosion followed the ignition of a cloud of cyclohexane vapor mixed with air. It resulted in 28 fatalities, numerous injuries and extensive structural damage. Structural damage extended well beyond the plant boundary. The analysis of damage concluded that the blast effect was similar to that produced by 16 metric tons (35,300 lbs) of TNT detonated at a height of 45 meters (147.6 ft). If DoD quantity-distance criteria were applied, for this quantity of explosive, inhabited buildings would be "safe" beyond about 1312 ft (400 m) scaled distances of 40 ft/lb$^{1/3}$. Damage to conventional inhabited buildings extended beyond these distances. For example, a roof collapsed at a distance of 1312 ft (400 m); ceilings collapsed at 1755 ft (535 m); 100 percent window glass breakage extended to about 2300 ft (700 m); 75% percent window glass breakage was observed at a distance of 3900 ft (1190 m); approximately 20 percent window glass breakage was observed at a range of 9005 ft (2745 m); door and window glass damage was observed at 1755 ft (535 m). The authors state that the blast load duration was long in comparison to the response time of the structures observed. The long duration was probably because this was a volume explosion (a cloud), rather than a condensed explosive (a point source). Thus, peak overpressure is directly related to damage in this case.

TABLE 2 SAFE SEPARATION DISTANCES, PEAK OVERPRESSURES AND IMPULSES FOR INDICATED QUANTITIES OF EXPLOSIVE AS DETERMINED BY STRUCTURAL ANALYSIS (8)

Target	Quantity of Explosive (lbs)											
	1,000			10,000			100,000			1,000,000		
	R	P	I	R	P	I	R	P	I	R	P	I
House (Split Level, frame-brick)	290	1.79	30	776	1.36	54	2089*	1.0	92	4500	1.0	190
Church (A-frame construction)	250	2.15	35	1185*	0.77	35	3481*	0.52	54	8000*	0.48	106
School (One-story, masonry)	180	3.64	48	496	2.49	84	1671	1.36	116	5500*	0.77	155
Office Building multi story, R/C frame, brick walls)	140	5.68	61	323	4.60	128	928	3.0	205	2500	2.15	340
Mobile Home	340	1.45	26	790	1.23	50	1900*	1.08	102	4950	0.82	172
Bus (Passenger)	230	2.45	38	550	2.10	72	1280	1.90	151	3100	1.59	272
Camper Pickup Unit	250	2.20	35	620	1.75	64	1520	1.45	128	4000	1.10	212
Commercial Jet Aircraft	200	3.00	43	539	2.15	73	1253	1.97	155	3700	1.97	315
Person (Male, 168 lbs)	230	2.5	38	496	2.50	80	1068	2.50	180	2300	2.5	370
DOD minimum distance requirements (ft):												
(a) blast hazard		400			862			1855			5000	
(b) blast and fragment hazard		1250			1250			1855			5000	

R = Separation Distance, ft.
P = Peak Overpressure, psi
I = Impulse, psi ms
1 ft = 0.3048 m, 1 psi = 6.89 kPa
*"safe" distance is greater than that required by regulations.

Fig. 2 is a compilation of data (Ref. 5) from accidental explosions, categorized by types of damage. It is seen that even at a scaled distance of 50 ft/lb$^{1/3}$ (20 m/kg$^{1/3}$) all levels of damage except "demolished" are found. Although most of such exceedences are found in the lesser damage categories, it is important to emphasize that low blast intensities cover larger land areas than do high blast intensities. The potential for damage and injuries in the larger areas of low-level blast effects can, therefore, be very significant.

On July 25, 1984 two explosions occurred within minutes of each other at the Union Oil Company refinery in Romeoville, Illinois. Seventeen workers were killed and at least twenty one were injured. Structural damage extended well beyond the plant boundaries. The blast was "felt" up to 35 miles away. It flattened buildings at the 1030 acre plant and toppled a 55 ft utility tower more than two miles away. A five foot piece of sheet metal struck a house half a mile away from the refinery. A nine month old boy was put into the Joliet hospital with head injuries sustained as a jewelry box flew across the room in his home a mile away and struck him. Minor injuries and major building damage occurred throughout the residential areas closest to the refinery (Ref. 10). Information as to the yield, i.e., the equivalent quantity of explosive involved is not available at this time.

CONCLUSIONS AND RECOMMENDATIONS

There is increasing pressure for land adjacent to hazardous facilities, previously used for agricultural purposes, to be used for commercial development. Land developers should be aware of the potential for damage near chemical and explosive manufacturing and storage facilities (e.g. tank farms), and along transportation routes (highways, railroad tracks, railroad switchyards, ports and navigable rivers) where hazardous material may be carried.

An effort should be undertaken to develop quantity-distance charts on a rational probabilistic basis; taking into account the differences in response from types of structural systems, components, connections, materials,

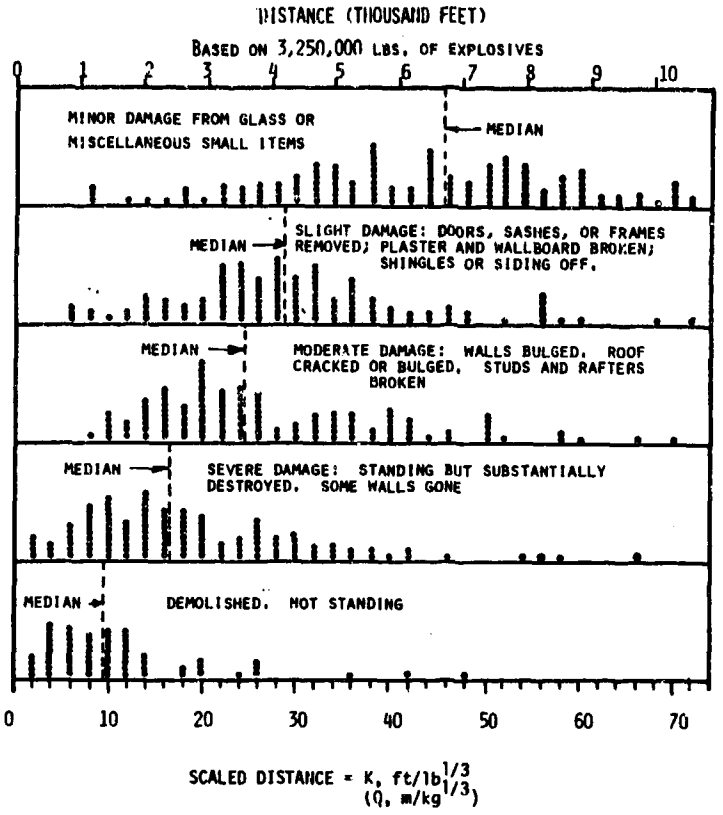

FIG 2.-Distribution Plot for Categories of Damage (5)

building orientation, etc. In those cases where buildings cannot meet stipulated separation distances, then guidelines for the design and retrofitting of buildings to resist accidental explosions should be developed.

Results of previous studies indicate that when specific protective measures are considered in the design stage of an engineered building, then such measures can be obtained at little or no additional cost (Ref. 11).

REFERENCES

1. "Ammunition and Explosives Safety Standards," Headquarters, Department of the Army, AR385-64, March, 1982.
2. "DOD Ammunition and Explosives Safety Standards", DOD Explosives Safety Board, DOD 6055.9-STD, July 31, 1984.
3. Asheton, R., "History of Explosions," Institute of Makers of Explosives, 1930.
4. Army-Navy Explosives Safety Board, Igloo Tests, Naval Proving Ground, Arco, Idaho, Technical Paper 3, 1945.
5. "Barricade Effectiveness Evaluated from Records of Accidental Explosions," Armed Services Explosives Safety Board, Department of Defense, AD 487554, July, 1966.
6. Abrahamson, G.R. and Lindberg, H.E., "Peak Load-Impulse Characterization of Critical Pulse Loads in Structural Dynamics", Dynamic Response of Structures, Pergamon Press Inc, 1971.
7. Pickering, E.E. and Bockholt, J.L., "Probabilistic Air Blast Criteria for Urban Structures", for Office of Civil Defense, Contract DAHC20-67-C-0136, OCD Work Unit 1154F, Stanford Research Institute, November 1971.
8. Custard, G.H., et al, "Evaluation of Explosives Storage Safety Criteria", Falcon Research and Development Company, March 1970.
9. Sadee, C., Samuels, D.E., and O'Brien, T.P., "The Characteristics of the Explosion of Cyclohexane at the Nypro (UK) Flixborough Plant on 1st June 1974", Journal of Occupational Accidents, 1 (1976/1977) 203-235.
10. "The New York Times", New York, Wednesday, July 25, 1984.
11. Longinow, A., " Civil Defense Shelter Options for Fallout and Blast Protection (Dual-Purpose)" Contract No. OCD-PS-64-50, Subtask 1613B, for Office of Civil Defense, IIT Research Institute, Chicago, IL, May 1967.

EXPLOSIVE FUEL IGNITION EFFECTS ON AN AIRCRAFT NOISE SUPPRESSOR SYSTEM

V.R. Miller

Flight Dynamics Laboratory
Wright-Patterson Air Force Base, Ohio

ABSTRACT

This paper presents the results from a test in which the door acceleration and the pressure environment were measured in an aircraft noise suppressor system, following the delayed ignition of the augmenter fuel of a turbofan engine such that an explosion of this fuel occurred. The system was instrumented with hydrophones, as well as accelerometers and a high temperature microphone. The resulting data were used to define the effects of the augmenter fuel explosion pressure on the noise suppressor system and its components.

INTRODUCTION

Stalls of turbofan engines are caused by afterburner hard starts caused by a missed or late light-off or blow-out. This is followed by an explosive auto-ignition of the fuel mixture a few seconds later by the hot exhaust gases. Augmenter blowouts result in an unburned fuel mixture being ignited explosively inside the augmenter section of the engine. A pressure wave propagates forward up the fan duct, and the resulting backpressure causes the fan and/or high pressure compressor to stall. In turn, the afterburner can be blown out again due to the fluctuation in flow caused by the repeated sequence of stall, hard start and stall of the fan and/or high pressure compressor. This chain of events can continue until the engine core does not have enough energy to accelerate. In the meantime, the combustor continues to pump hot gases into the turbine section which can overheat and suffer an overtemperature condition. This can result in turbine blade damage.

Stalls caused by augmenter blowouts have occurred during ground run-ups when snapping an aircraft engine throttle from idle to maximum afterburner. These blowouts have resulted in damage to noise suppressor systems. For example, bolts have been sheared, stiffeners broken, and welds cracked. A test program was performed by the Flight Dynamics Laboratory to determine the magnitude of the pressure at various locations within the secondary enclosure of a noise suppressor system (NSS) following a delayed ignition of augmenter fuel.

DESCRIPTION OF TEST ARTICLE

The NSS used during the testing is shown in Figure 1. The aircraft was positioned in the NSS such that the aft portion of the aircraft is inside of the secondary enclosure (see Figure 2). The primary air intake mufflers (PAIM) were positioned in front of the aircraft engine inlets. The PAIM reduces the noise produced by the engine compressor, which is medium to high frequency and requires minimal acoustic treatment to achieve the required noise reduction. The secondary air intake seals around the aft portion of the aircraft and provides an acoustically treated path for the cooling air which mixes with the engine exhaust in the augmenter. The augmenter, in conjunction with the engine, acts as an eductor, causing the ambient air to flow through the secondary air intake and mix with the engine exhaust. The augmenter is sized to bring in sufficient cooling air and cause adequate mixing prior to being discharged in the exhaust muffler. The exhaust muffler directs the exhaust vertically to obtain noise attenuation by spherical dispersion and includes acoustical baffles for additional noise reduction. In the forward part of the augmenter are cooling tubes which spray water into the exhaust to limit the temperatures in the exhaust muffler to 800°F during afterburner operation of the engine. The water and water tubes also break up the engine exhaust which reduces the formation of low frequency noise which is otherwise difficult to attenuate.

INSTRUMENTATION AND DATA REDUCTION PROCEDURES

The NSS was instrumented with nine 3/8 inch diameter hydrophones, one high temperature microphone, and two accelerometers. Hydrophones were used because of their excellent frequency response characteristics and are typically used in blast and shock measurements. The location of the instrumentation is shown in Figure 2. A complete description of the data acquisition instrumentation is given in Reference 1. All data were continuously

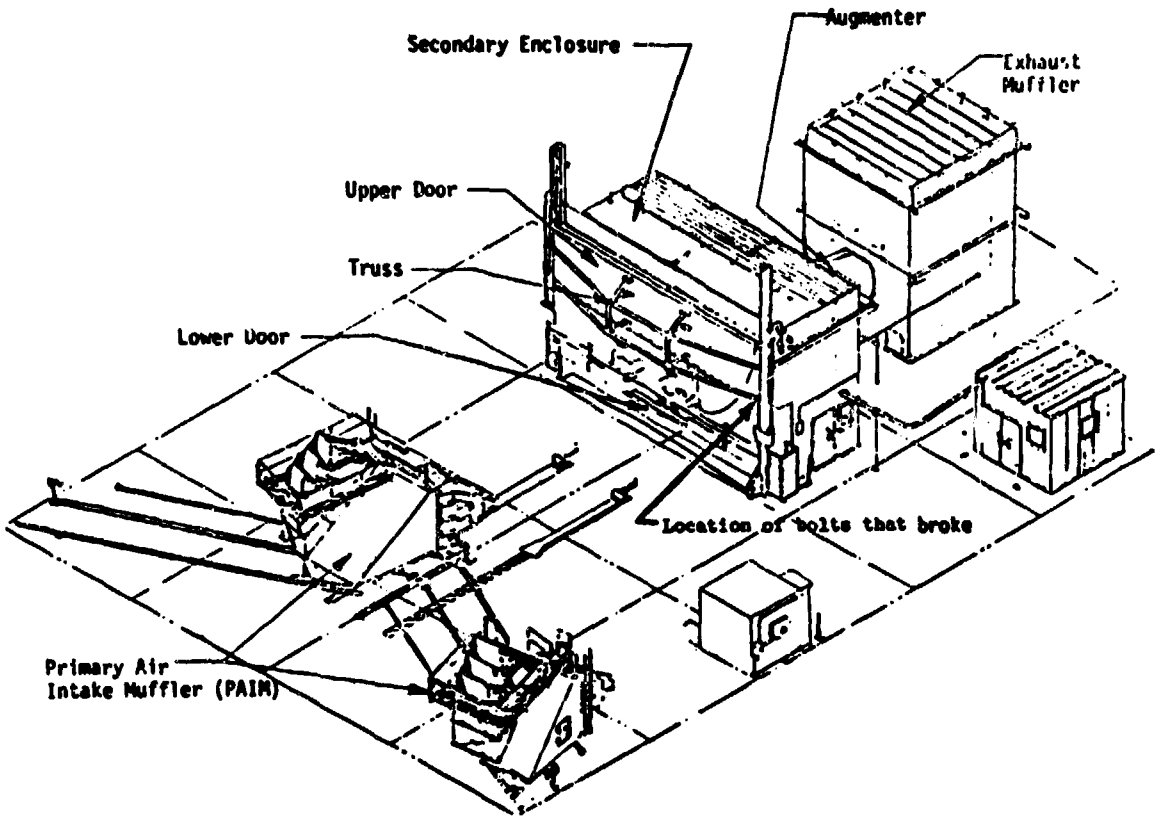

FIGURE 1 Location of Bolts Broken on Upper Door of Noise Suppressor System

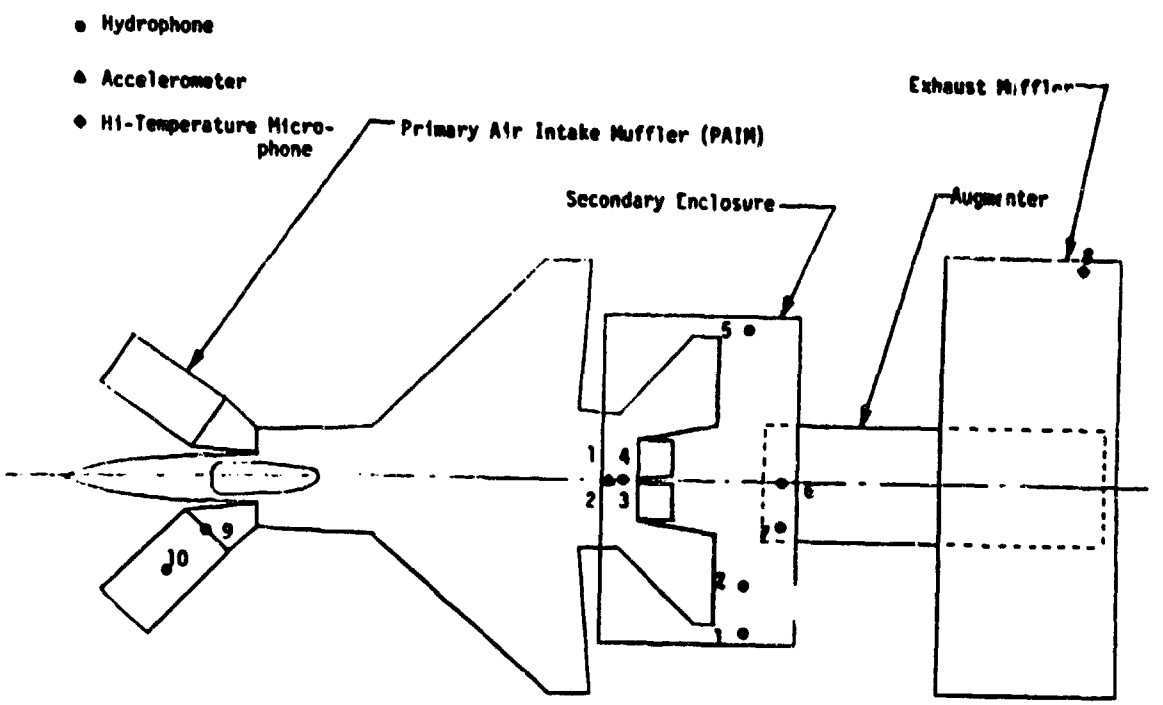

FIGURE 2 Location of Instrumentation in Noise Suppressor System

recorded on one fourteen channel tape recorder. The magnetic data tapes, recorded during testing, were analyzed on a General Radio Analyzer and Raytheon computer. Overall pressure levels were measured with one-third octave band and narrowband analyses performed for selected transducers and test conditions. Further details concerning calibration and data reduction procedures are given in Reference 1.

TEST PROCEDURES

Data were obtained by the surveys, identified in Table I as Runs 1 through 10, which include the conditions at which the aircraft was operated. All the runs were conducted without an engine shutdown. Run number 1 included running the engine in all stages of augmenter to establish baseline data. Runs 2 through 10 attempted to simulate augmenter blowouts and auto ignitions by delaying augmenter ignition. Throttle advances to each zone of augmenter power were conducted with a one second igniter delay. Runs 2 through 6 did not result in an explosion. With the igniter set for a 3 second delay, the throttle was advanced from military power to zone 2, with no explosion (Run number 7). The throttle was then snapped from idle to zone 3 (Run number 8) and then from idle to zone 5 (Runs number 9 and 10) to prevent the augmenter fuel from being ignited. Only Runs 9 and 10 resulted in an explosion (the desired simulation). During Run 10, the bolts at the lower left end of the upper door stiffener truss were broken (Figure 1).

TEST RESULTS

Two successful augmenter blowouts were achieved by snapping the engine throttle from idle to zone 5 afterburner with a 3 second augmenter igniter delay (Runs 9 and 10, see Table I). Figure 3 through 5 present pressure versus time plots from Run 10. These data indicate that at least two fan stalls and two compressor stalls occurred before the engine throttle was backed off. This sequence of stalls could have been repeated many more times [2], but were stopped for the purposes of this test program. These stalls had a duration of approximately 100 milliseconds at locations in the secondary enclosure (Figures 3 and 4). The predominant stall cycle's duration is shorter at locations in the PAIM than in the secondary enclosure (40 milliseconds, Figure 5). This is significant because there is more energy in a waveform which has a longer duration when compared to another waveform of the same pressure rise but smaller duration. A wave of longer duration will show stronger low frequency components that are important with regard to structural response and integrity. This will be shown later. These data and other unpublished data [2] show that the propagation velocity of the overpressure pulses is approximately equal to the ambient speed of sound.

Large differences in pressure and waveform were seen in comparisons between plots for which an augmenter blowout was achieved to plots were a blowout was not achieved [1]. Data from Reference 3 with engine operation in

TABLE I Summary of Test Runs

Run No.	Throttle Setting	Subsequent Throttle Movement	Augmenter Igniter
1	Military	All five augmenter zones	Normal
2	Military	To Zone 1 Augmenter	One Second Delay
3	Military	To Zone 2 Augmenter	"
4	Military	To Zone 3 Augmenter	"
5	Military	To Zone 4 Augmenter	"
6	Military	To Zone 5 Augmenter	One Second Delay
7	Military	To Zone 2 Augmenter	Three Second Delay
8	Idle	To Zone 3 Augmenter	"
9*	Idle	To Zone 5 Augmenter	"
10*	Idle	To Zone 5 Augmenter	Three Second Delay

*Cases for which explosions occurred

a normal zone 5 afterburner mode are very similar to data obtained when the engine throttle had been snapped from idle to zone 5 afterburner. This indicates that the pressure environment in the NSS is not increased by a snap throttle movement and igniter delay unless an augmenter blowout takes place.

The absolute value of the largest overpressure is plotted against a ratio of offset distance to the distance from transducer to the engine exhaust nozzle ($\frac{X}{R}$) in Figure 6 for the hydrophones located in the secondary enclosure. This figure shows that the overpressures are reasonably constant for the range of $\frac{X}{R}$ ratios measured. Based on this, it is reasonable to assume that the pressure over the upper door is uniformly distributed.

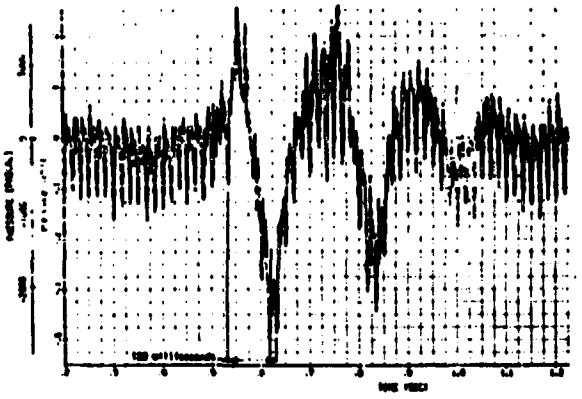

FIGURE 3 Pressure-Time Curve for Throttle Snap from Idle to A/B 5 with 3 second Augmenter Igniter Delay (Run 10) - Hydrophone 1

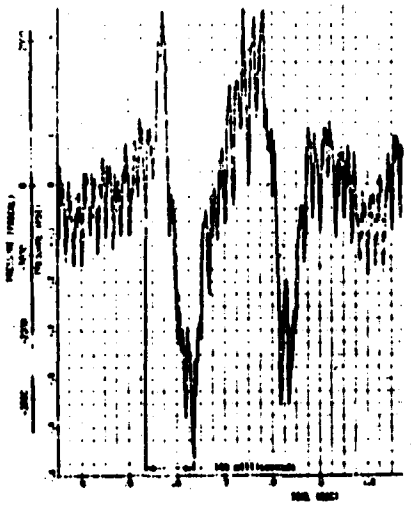

FIGURE 4 Pressure-Time Curve for Throttle Snap from Idle to A/B 5 with 3 second Augmenter Igniter Delay (Run 10) - Hydrophone 4

While it is important to know how the pressure waveform varies with time, it is equally important to know how the structure of

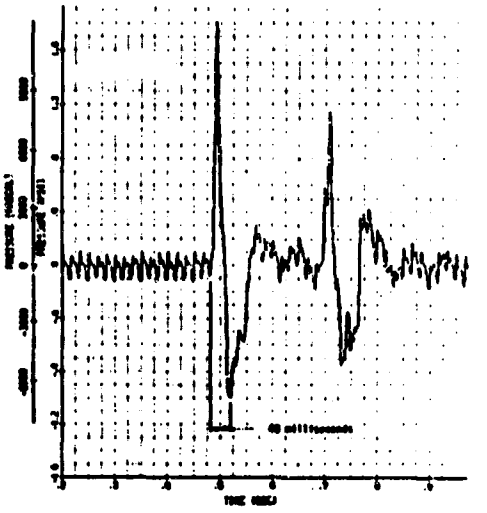

FIGURE 5 Pressure-Time Curve for Throttle Snap from Idle to A/B 5 with 3 second Augmenter Igniter Delay (Run 10) - Hydrophone 10

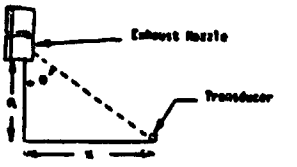

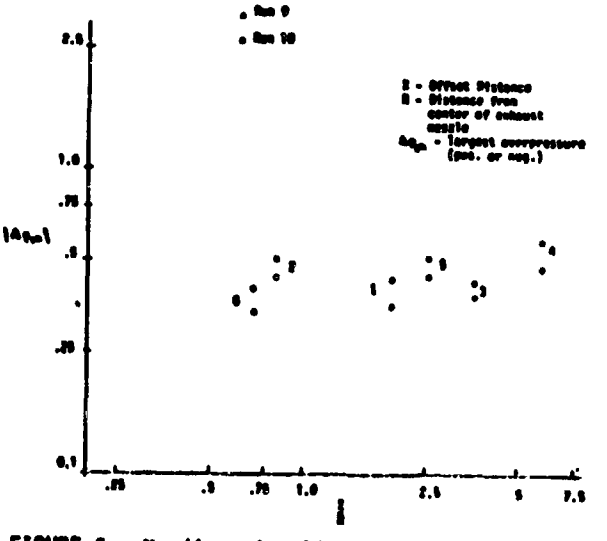

FIGURE 6 Nondimensionalized Nozzle-to-Transducer Distance as a Function of Absolute Value Of Maximum Overpressure for Hydrophones 1 through 7 from Runs 9 and 10

the NSS is affected by the overpressure. Figure 7 shows an acceleration versus time plot from Run 10 of the accelerometer located on the upper door. Note that the door experiences several very large amplitude peaks. Also note the large decrease in amplitude between the first, second, and successive positive peaks. This decay is related to the damping by the concept of energy dissipation per cycle of vibration. The acceleration is approximately a damped sinusoid and can be described by exponential and sine terms of the form $e^{-\zeta f_d t} \sin(f_p t + \psi)$ where f_d is the damped natural response frequency, ζ is the ratio of equivalent viscous damping to critical damping (damping factor), f_p is the forcing (excitation) frequency, and ψ is an arbitrary constant.

Working with the peaks identified in Figure 7, it can be shown [1] that the damping factor ζ is equal to 0.085. This factor is important because the resultant motion of the upper door depends on the amount of damping existing in the door and surrounding structure. The period of oscillation T is the time required for the door to repeat its motion. The spacing of peaks t_0, t_1, t_2 shows that the period (equal intervals of time) was approximately 0.65 seconds, which corresponds to a response frequency (f_d) of 1.5 hertz ($T = \frac{1}{f_d}$). This was the upper door's response frequency after the stiffener bolts had been broken. Because the breaking of these bolts detached the stiffener at one end, the upper door's stiffness and natural frequency were reduced. Therefore, it was necessary to calculate the natural frequency of the upper door before the bolts broke.

Using the peaks identified in Figure 7 as M and N suggests that the upper door's natural frequency before the pressure pulse broke the bolts was approximately 7 hertz ($\frac{1}{0.145}$). An analysis performed in Reference 1 verified that this frequency of 7 hertz was, in fact, the upper door's natural frequency before the bolts were broken. For this analysis, the upper door was modeled as a rectangular plate consisting of two freely-supported edges and two free edges. The approximate frequency expressions of Warburton were used [4].

Figure 8 through 10 show the power spectral density (1 hertz bandwidth) for three hydrophones from Run 10. Consideration of an envelope for the PSD's in Figures 8 and 9 reveals two distinct regions. At the very low frequencies, the spectrum varies as f^2, so that the spectrum rises at 6 dB per octave up to a maximum frequency of $\frac{\sqrt{3}}{\pi \Delta t}$ hertz as given in Reference 5. Above this maximum frequency comes a range over which the spectrum is inversely proportional to f^2 and its value falls at 6 dB per octave. The duration of the pulse Δt for the hydrophones located in the secondary enclosure (1 through 7) was found to be approximately 100 milliseconds (Figures 3 and 4) which should yield a maximum frequency of 5 to 6 hertz ($\frac{\sqrt{3}}{\pi(.100)}$). Figures 8 and 9 do show peaks in this frequency region. Frequency peaks in this region are important for structural response, this being the region where significant resonance amplification might be expected from fundamental modes of the NSS. Since it is the low frequencies that have been increased, it is expected that the stress levels produced by the peak overpressures in the structural elements of the NSS will also be increased.

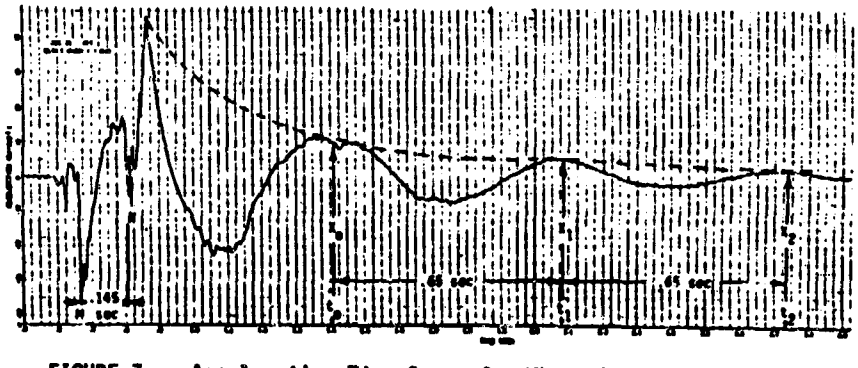

FIGURE 7 Acceleration-Time Curve for Throttle Snap from Idle to A/B 5 with 3 Second Augmenter Igniter Delay (Run 10) for Accelerometer 1 Located on Upper Door

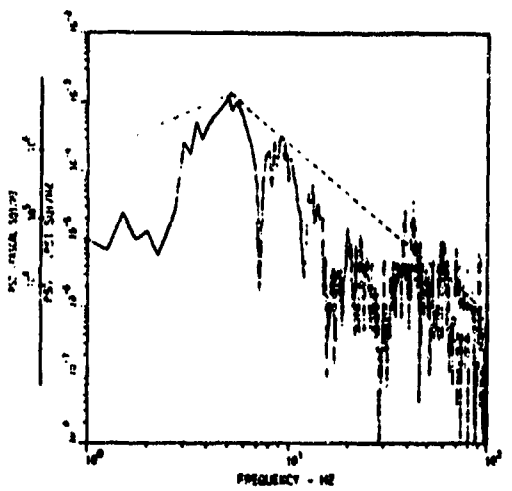

FIGURE 8 Acoustic Power Spectral Density Distribution Obtained from Throttle Snap from Idle to A/B 5 with 3 second Augmenter Igniter Delay (Run 10) - Hydrophone 1

Figure 9 shows that the peak in the frequency spectrum of the pressure pulse measured on the upper door was between 4 and 6 hertz. The dynamic effects of the upper door to the pressure pulse must be considered since the excitation frequency (4 to 6 hertz, f_p) was approximately 1/3 to 1/2 of the upper door's resonant frequency (7 hertz, f_d). This means that the deflection (or acceleration) which was caused by the pressure pulse must be multiplied by a factor to obtain the dynamic response of the upper door. This ratio of maximum amplitude (or maximum acceleration) divided by the amplitude (or acceleration) caused by the pressure pulse equal to the disturbing pressure pulse was equal to:

$$K = \frac{1}{\left(\left[1 - \left(\frac{f_p}{f_d}\right)^2 \right]^2 + \left[2\zeta \frac{f_p}{f_d} \right]^2 \right)^{0.5}}$$

This term normally is referred to as the magnification factor or frequency response function.

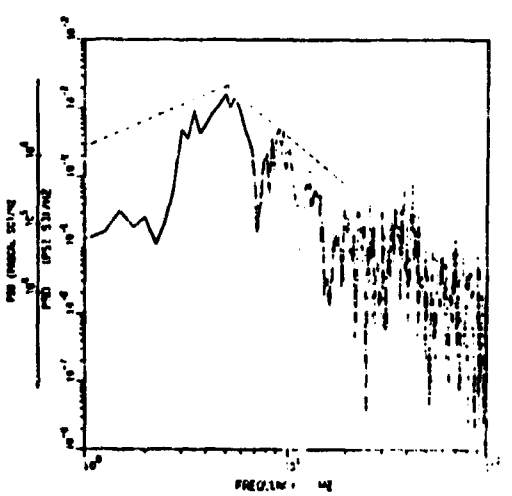

FIGURE 9 Acoustic Power Spectral Density Distribution Obtained from Throttle Snap from Idle to A/B 5 with 3 second Augmenter Igniter Delay (Run 10) - Hydrophone 4

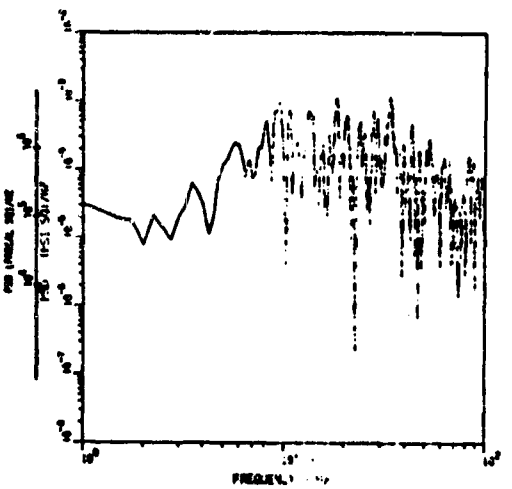

FIGURE 10 Acoustic Power Spectral Density Distribution Obtained from Throttle Snap from Idle to A/B 5 with 3 second Augmenter Igniter Delay (Run 10) - Hydrophone 10

The magnification factor for the fundamental mode has been plotted in Figure 11 with the upper door modeled as a single degree of freedom system. This figure shows the effects of various frequency ratios on the amplitude for a damping factor ζ of 0.085 when the door is subjected to a uniformly distributed pressure. For comparison, the damping factor of 0.3 was also plotted. Note that, as the frequency ratio is increased to one, the magnification factor increases. Also note that the lower the damping factor the higher the magnification factor. For the present case two frequency ratios can be considered ($\frac{4}{7} = 0.57$ and $\frac{6}{7} = 0.86$) at the damping factor of 0.085. Figure 11 shows that the magnification factor for these two frequency ratios are approximately 2 and 4.5. This means that the dynamic response of the upper door was 2 to 4.5 times the static response. If the pressure pulse had been applied statically to the upper door, it would be deflected. However, since the excitation frequency was close to the door's natural frequency, the actual deflection was increased in proportion to this magnification factor.

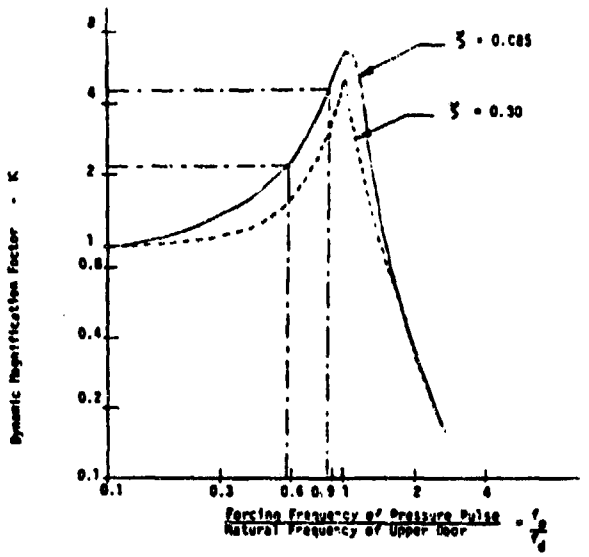

FIGURE 11 Dynamic Magnification Factor with Respect to Ratio of Forcing Frequency and Natural Frequency of Upper Door

An alternative analysis based on modeling the excitation as a single sinusoidal pulse and ignoring damping predicts the magnification factor for the two frequency ratios given above to be approximately 1.2 and 3 [6]. However, since the excitation in the form of stalls during the testing could have been allowed to continue many more times, the magnification factors, as predicted above by the steady - state analysis, are considered to be more appropriate.

It appeared that, based on the preceding discussion, the stiffening truss on the upper door increased the door's natural frequency in such a way that it was in the same general frequency region as the overpressure pulse. As a result, the door has greater response with stiffener attached than if it were unattached. The addition of more stiffening would change the door's natural frequency. However, it is estimated that it would require more than four times the present amount of stiffening to raise the door's natural frequency to at least twice excitation frequency region of the overpressure pulse. Damping could also be added to the door in the form of shear bars, shock absorbers, constrained layer treatment, etc., to be used in conjunction with the existing stiffener truss to lower the door's deflection when excited by an overpressure pulse. Another approach to designing the door would be to remove the present stiffening truss and use damping treatments, exclusively to lower the door's response. The actual fix which was used consisted of placing two rigid bars from the door to the back wall of the secondary enclosure so as to raise the door's natural frequency out of the excitation frequency region. These bars were located at the 1/3 points of the door.

CONCLUDING REMARKS

The experimental investigation reported herein indicates the following conclusions:

1. A fundamental mode (7 hertz) of the noise suppressor system's (NSS's) secondary enclosure upper door was excited by an augmenter blowout in which the engine throttle was snapped from idle to maximum afterburner with a three second augmenter igniter delay. This resulted in the failure of the bolts holding a stiffener truss on the upper door.

2. The maximum overpressure occurred in the primary air intake muffler.

3. The dynamic effects of the upper door must be considered since the excitation frequency of blowout (4 to 6 hertz) was close to the NSS upper door fundamental resonance (7 hertz). Considering these dynamic effects showed that the dynamic response of the upper door was 2 to 4.5 times the static pressure.

REFERENCES

1. Miller, et al, "Noise Suppressor Overpressurization Test," AFFDL-TM-78-114-FBE, December 1978.

2. Private communication with M. Schmidt of the Aero-Propulsion Laboratory, Turbine Engine Division, Wright-Patterson Air Force Base, Ohio.

3. Miller, et al, "Acoustic and Vibration Survey of an Engine Operating in a Test Cell," AFFDL-TM-76-99-FBE, September 1976.

4. Warburton, "The Vibration of Rectangular Plates," Proceedings of the Institute of Mechanical Engineers, Serial A, Vol. 168, No. 12, pp. 371-384, 1954.

5. Johnson and Robinson, "Loudness of Sonic Bangs," Acustica, Vol. 21, pp. 307-317, 1969.

6. Harris, C.M., and Crede, C.E., ed, Shock and Vibration Handbook, 2nd ed., p. 8-40, McGraw - Hill, New York, 1976.

BLAST AND FRAGMENT RESISTANT SYSTEMS (BFR) - TEST RESULTS

Bernard C.J. Vienings

Hulley and Associates, Pretoria.

ABSTRACT

A description with sketches is given of the Blast and Fragment Resistant (BFR) walling system, which consists of formed metal sheets joined together to constitute both the permanent formwork and the reinforcement to the concrete, which is poured into the void between the sheets. Tests are described and results outlined which were carried out with a 460 kg (1000 lb) GP air bomb, RPG 7, 68 mm aircraft rocket, explosive charges and mines. All tests results were successful within the design criteria. A static flexural test is also described.

SYSTEM DESCRIPTION

The patented Blast and Fragment Resistant (BFR)[1] walling system is a composite construction of steel and concrete, designed to provide protection against weapon effects in a more cost effective manner than does conventional reinforced concrete designed for protection.

The basic component of the BFR system is a wall element shown in Figure 1, consisting of interlocked external sheets. The two faces are tied to each other by diagonal panels shown in Figure 2 which, in zig-zag fashion, form the lattice-work of a rigid mould into which concrete is poured.

The sheets, which are presently available in three thicknesses, 0,8, 1,0 and 1,2 mm, provide the necessary reinforcement to the concrete. The sheets are presently rolled in three modules : 200 mm, 250 mm and 300 mm thick walls. The standard sheet profile is shown in Figure 3.

The sheets are pre-cut to detailed lengths, marked and delivered to site.

After conventinal concrete foundations have been cast with starting reinforcing bars to project and tie into the walls, the sheets are erected and lined-up against a kicker angle fixed to the footing.

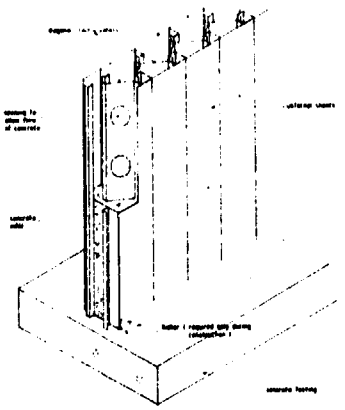

Figure 1

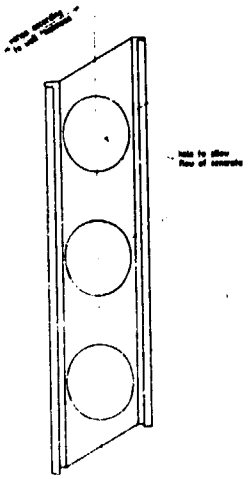

Figure 2

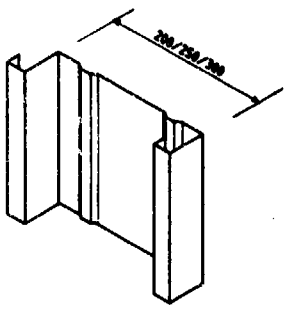

Figure 3

The external sheets easily interlock into each other at their shaped ribs in male-female fashion as shown in Figure 4. The sheets in the two external faces are staggered so that the ribs may receive the lacing panels. These lacing panels are slid in from the top and secured with self-tapping screws. The assembled sheets form a rigid mould ready to receive the concrete. The lacing panels are perforated with circular holes to allow the flow of the fresh concrete through them.

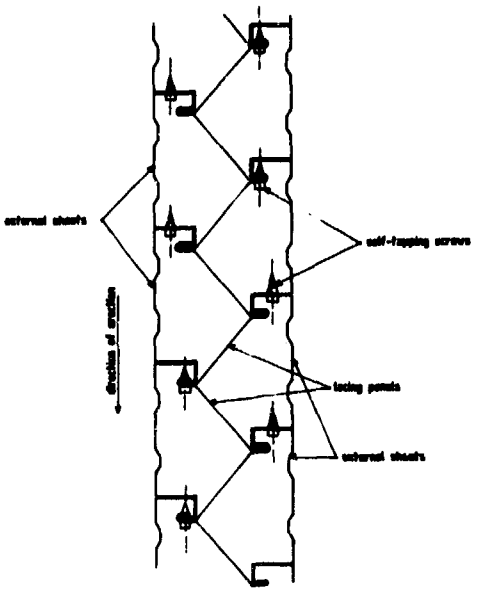

Figure 4

The external sheets form the main reinforcement to the concrete. They provide the section with symmetrical tensile and compressive reinforcement. The steel ribs are deeply embedded in the concrete, ensuring good bond between concrete and reinforcement. The lacing panels form a lattice-work properly securing the external faces to each other, and also act as a uniformly distributed shear reinforcement.

The only reinforcement bars that are necessary in the walls are the starter bars from the foundation walls, and corner bars at a connection between a wall and a roof slab.

Into the rigid steel mould which has been assembled a pumpable 30 MPa (4500 p.s.i.) mix, with slump between 100 and 150 mm is placed to complete the construction of the walling system. The system produces a strong, ductile and fragment resistant component for the construction of protective walls and hardened buildings. The sheeting forms a natural anti-spalling plate which is not available in conventional reinforced concrete walls.

A sandwich type construction has also been developed consisting of two walls 400 mm apart, with the void being filled with crushed stones usually 40 to 80 mm in size, as shown in Figure 5.

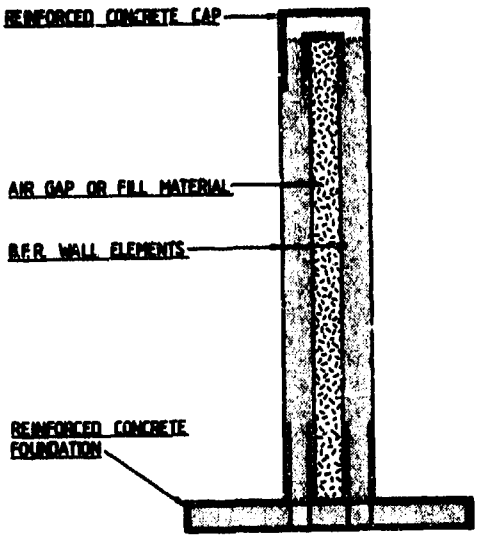

Figure 5

The walling system has been put to the following uses :

- Protective walls up to 10 m high
- Above ground buildings to resist weapon effects
- Ammunition storage magazines
- Chambers to resist effects of internal explosions ranging from 2 to 250 kg
- General protective walling systems to protect against attacks ranging from purely intrusion and bullets, to direct hits from RPG 7 rockets, light artillery of the 122 mm type, mortars and general purpose aerial bombs.

SYSTEM TESTS AND RESULTS

460 kg GP air bomb at 10 m distance

The sample tested for the above criteria was a 250 mm thick, 2 m high BFR wall used to form a 2 m long x 1,5 m wide cubicle.

The test sample was placed with the first face being 10 m away from the centreline of the bomb which was laid on a wooden trestle 1,5 m above the ground. After detonation of the bomb, the following results were observed (see Figure 6).

A number of large craters were observed having penetrated the first sheet and the concrete to a maximum depth of 40 mm. There were a multitude of small hits with no penetration. The back plate of the wall resisted any spalling and showed absolutely no signs of any damage or deflection. Damage to the first face was

Figure 6

local, with no propagation of cracks. A bikini gauge placed on the inside face of the front wall did not register any blast effects.

Direct Hits of RPG 7

The sample tested for the above criteria was a sandwich section consisting of a 200 mm BFR wall, a 400 mm gap filled with granite stones of 40 mm size and a rear 200 mm BFR wall (see Figure 7).

Several RPG 7 rockets were fired at the sample from a distance of 100 m.

All the rockets that struck the target, penetrated the outer 200 mm BFR wall, the 400 mm granite stones and about half of the inner 200 mm BFR wall, causing a heavy local plastic deformation on the exterior face of the second BFR wall. The rear metal skin of the wall prevented any spalling of the concrete.

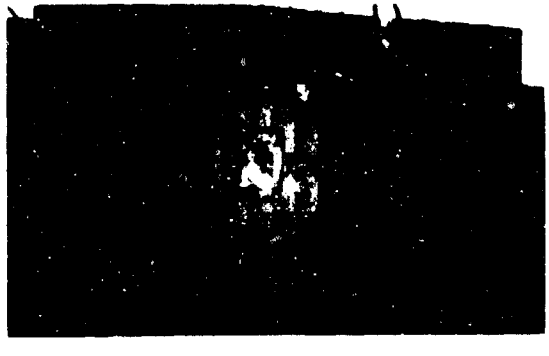

Figure 7

Direct Hits of 68 mm Aircraft Rocket

The sample tested for the above criteria was a sandwich section consisting of 200 mm BFR wall, a 200 mm gap filled with granite stones of 40 mm size and a rear 200 mm BFR wall.

Rockets were fired at the sample and two direct hits were registered.

The damage to the sample was localized to the vicinity of the hits, with the exterior metal skin being removed by the blast, and the exposed concrete pitted to a depth of 20 to 30 mm. There was no other damage to the sample, and no evidence of bulging or breaching on the back face. The exposed concrete was in no way cracked. Since only the first leaf of the sample was damaged it can be inferred that a single 200 mm BFR wall will supply 100% protection against this rocket.

Placed Explosive Charges and Mines

The BFR walls were also tested against placed explosive charges. The following was observed :

- 1,7 kg PE4 plastic explosive shaped charge does breach a 200 mm thick BFR wall with a localized opening about 400 mm x 500 mm - Damage is very local.
- 1 kg PE4 plastic explosive does crater a 200 mm thick BFR wall (200 mm x 400 mm crater) but does not penetrate the wall.
- 1,7 kg PE4 plastic explosive shaped charge does crater a 300 mm thick BFR wall but does not penetrate the wall. The crater is about 300 mm in diameter and 80 mm deep. The back skin of the tested wall was bulged outwards by $\pm$ 30 mm over an area of 0,5 m^2.
- a special charge (mine) was also detonated on the same 300 mm BFR wall sample. This mine contains about 2 kg of HE explosive but not optimally shaped. The mine caused a crater of 300 mm x 500 mm to a depth of 100 mm. The back skin was bulged outwards by $\pm$ 20 mm over an area of 0,4 m^2.

Static Moment-Rotation Tests conducted on 200 mm thick BFR walling samples

From the above blast tests it becomes apparent that the BFR section offers a great degree of ductility and is capable of deforming deeply into the plastic range, and thus can resist blast loads by absorbing large amounts of energy in internal plastic deformation work.

To assess this degree of ductility, static loading tests were performed[2] to determine the static moment-rotation relationship of the composite walling system in the direction of the "span" of the sheeting system.

Simply supported specimens, 2 m long, were loaded across the full width at mid-span by a knive edge load (see Figure 8). Support rotations were monitored by means of rotation gauges for support rotations up to 5° and larger rotations were monitored by means of a centrally located deflection gauge. Load was applied and recorded through a Macklow Smith hydraulic testing machine.

Maximum unit bending moment values were plotted against angle support rotation as shown in Figure 9.

An angle support rotation of 13,5° was observed without failure at the plastic hinge. It was not possible to pursue the loading curve as the midspan deflection of the specimen had reached the maximum clearance of the testing machine.

It is interesting to compare this large support rotation (13,5°) as against what is normally reported[3] for laced reinforced concrete (12°) and ordinary reinforced concrete (2°).

Figure 8

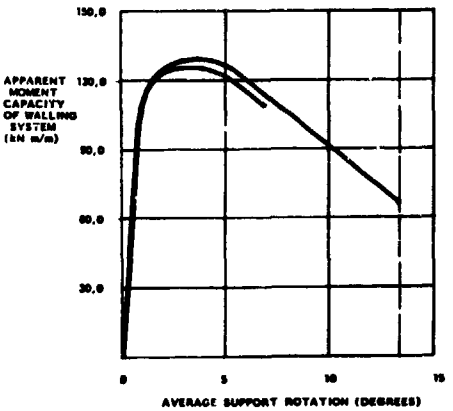

Figure 9

CONCLUSIONS

The concept of using composite laced steel sheet and concrete as used in the BFR walling system offers some definite advantages over the traditional use of concrete in protective structures.

Ductility

The most important advantage of the system is its high ductility, as illustrated by the static moment-rotation test.

Resistance to blast is achieved by the deformation mechanism of the structure whereby the externally applied energy is absorbed and converted into internal deformation work. The larger the deformation accepted by the structure without failing, the better its performane against blast.

Figure 10 shows the comparative energy absorption capabilities of BFR, laced reinforced and ordinary reinforced concrete sections.

The high ductility is mainly the result of :

- the use of commercial grade mild steel for the sheets; this allows a high percentage of elongation of the sheets before failure;
- the lacing arrangement of the sheets whereby the lacing panels hold the compression side of the sheets in position and prevent the early buckling of the compression side;
- the confinement of the concrete into triangular zones which probably contributes to an increase in concrete strength.

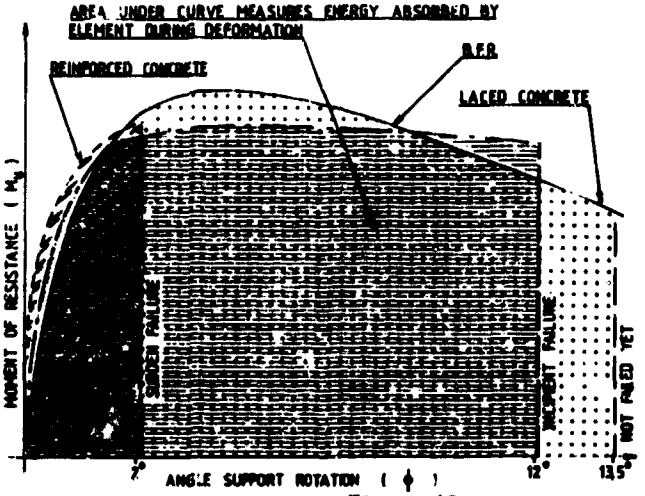

Figure 10

Resistance to Fragments

The BFR walling section has shown during the tests an excellent capability to resist fragments. This is probably due to the staggered arrangement of the external sheets and the continuous barrier presented by the diagonal panels. Also, damage is very localized. The impinging fragment is accepted and confined in the triangular zone formed by two adjacent lacing panels, and concrete destruction is localized within that triangular acceptor zone. Concrete cracks do not propagate through the wall.

Anti-Spalling

The external sheets used as permanent formwork are placed at the extreme fibers of the section and provide thus natural anti-spalling plates containing the secondary concrete fragments which are customary in reinforced concrete elements subject to blast and primary fragments.

REFERENCES

Ref. (1) - "The BFR Walling System" - Brownbuilt Metal Sections - 1984 - Johannesburg

Ref. (2) - M.G. Cross - "Report on Static Moment-Rotation Tests conducted on Brownbuilt Blast and Fragmentation Resistant Walling Specimens" - University of the Witwatersrand - Johannesburg

Ref. (3) - TM5-1300 - "Structures to Resist the Effects of Accidental Explosions" - Department of the Army, Navy and the Air Force - June 1969

ACKNOWLEDGEMENTS

1) Brownbuilt Metal Sections, a division of Dorbyl Structural Enginneering (Pty) Ltd, Johannesburg, for making information and samples available.

2) S.M. Lapage, professional engineer of Pretoria, for assistance with the paper.

ASSESSMENT OF MODULAR STRUCTURES IN BLAST AND SHOCK ENVIRONMENTS

Michael K. W. Wong

Air Force Weapons Laboratory
Civil Engineering Research Division
Kirtland Air Force Base, New Mexico

ABSTRACT

Application of a set of System Assessment Guidelines to blast and shock testing of modular structures provided the basis for development of a comprehensive test and analysis program. This program sought to characterize the blast and shock environment, determine the response of the structure, and determine its predominant modes of failure.

By conducting tests and analyzing the data, load, response, and failure mechanisms were determined. This paper will describe the role of System Assessment Guidelines in developing the objectives, purpose, and scope of the program. It will also discuss the testing and analysis efforts undertaken to study these structures.

INTRODUCTION

Structures designed to resist the effects of blast and shock are often required to protect people and equipment. However, design tools to develop such structures are generally limited. Thus, a design may not always account for major response mechanisms or dominant failure modes. Actual blast and shock testing of a prototype structure will often determine if the proper protection levels are attained. The loading environment, and response and failure modes may also be determined. Such testing, however, is often expensive and time consuming, and the resulting test data can still leave unknowns unanswered. Thus, a comprehensive approach is needed, combining field testing, data analysis, and optimization. This approach has been termed System Assessment Guidelines.

These guidelines have recently been used to develop a broad evaluation effort to determine the suitability of cylindrical and rectangular modular structures in providing a particular level of blast and shock resistance. The evaluation combined a testing program and analytical effort to characterize the blast and shock environment and to determine the loading, response, and failure mechanisms of modular, reinforced concrete structures. Testing consisted of four separate test series, each with a number of test events. Each test series was followed with detailed analysis to determine the behavior of its particular modular structure.

SYSTEM ASSESSMENT GUIDELINES

Several areas must be considered when conducting a comprehensive evaluation program. Requirements, objectives, scope, and approach must be organized in a manner which insures that they are all satisfied by testing and analysis. By designing the program according to a set of general System Assessment Guidelines, appropriate testing and analysis efforts can be assured.

The basis for the system assessment efforts starts with identification of the function and requirements for the structure. Three components must be defined: (1) the environments that the structure must function in, (2) the basic structural configuration to perform the required functions, and (3) the load and response mechanisms.

Knowing any two components allows for solution of the third. Thus, three types of system assessment problems may be formulated. The first type of problem consists of a specific environment and a given maximum level of response. The solution to this problem requires design of a suitable structure or system. The second begins with an environment and a predetermined system. Here, the solution involves determining the resulting response. This type of an effort is an analysis problem. Finally, the third type of system assessment problem occurs when a system with maximum permissible response levels is given. To solve this problem, the environment which produces the maximum response level must be determined. This type of problem could be called limit analysis.

In any particular system assessment effort, any combination of these three types of problems might have to be addressed. Very often the entire effort is iterative among all three problems.

In simple mathematical expressions the typical problem may be stated as:

$$S = f_d(E,R) \quad \text{(design)} \qquad (1)$$

$$R = f_a(E,S) \quad \text{(analysis)} \qquad (2)$$

$$E = f_l(S,R) \quad \text{(limit analysis)} \qquad (3)$$

where S is the system or structure, R is the response, E is the environment, and f_d, f_a, f_l are the functions relating the components for the various types of problems.

In an iterative cycle, Equation 2 may be substituted into either Equations 1 or 3, depending upon the type of problem. The resulting system or environment would be used to drive a subsequent analysis problem. The process would iterate until it converges to the desired solution. Thus, solution of an analysis problem is the key type of assessment effort. Figure 1 schematically outlines these processes. Testing would provide an effective tool to solve the actual problem at hand. Since test data consist of response measurements, testing can most readily meet analysis-type problems. In such a situation, the environment and system are predetermined and the response is measured. Then, f_a remains to be determined. The major load and response mechanisms characterize f_a.

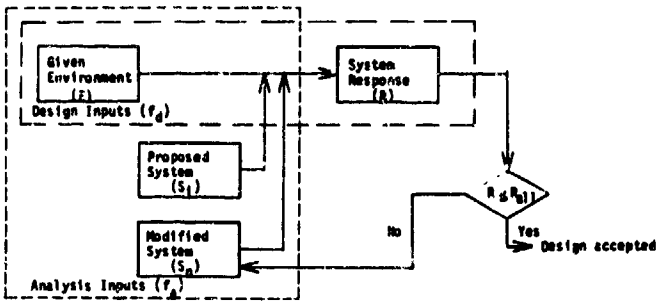

Figure 1a. Design Process

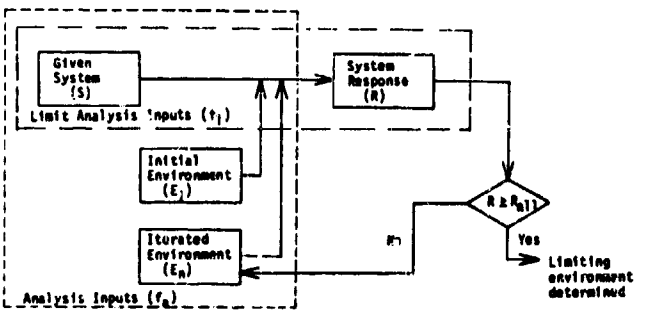

Figure 1b. Limit Analysis Process

By conducting tests, a particular system is subjected to a created environment. The interaction of the system with the environment creates the loading and response mechanisms which are recorded as test data. Thus, testing is applicable to all three types of problems.

Since testing of every system configuration and environment of interest is generally not possible, the immediate aim of the available experiments is to conduct the tests which will yield data revealing the important loading and response mechanisms. Also, the test data should indicate the predominate failure mechanisms.

By applying the results of analysis to either design or limit analysis problems, the entire spectrum of system assessment problems may be addressed. The application of this type of an assessment format has been recently applied to half-buried, modular, reinforced concrete structures.

TEST PROGRAM

General structures which have the capability of resisting the effects of high-explosive blast and shock are often needed to provide protection to people or equipment. By applying the concepts of the System Assessment Guidelines, a comprehensive program for evaluation of such structures was developed.

In this particular case, the basic system assessment problem was one of analysis. The structure or system was prespecified as being composed of cylindrical or rectangular reinforced concrete pipe sections. The sections could be assembled in a wide variety of configurations and perform a number of functions. Environments were also specified, based on the expected proximity of the structures to various detonations. Thus, the unknown system assessment component was the response.

Therefore, the initial effort in the system assessment process was to conduct testing to determine the structure's response. Based on the testing results, if the response was determined to constitute failure, a redesign effort would correct the problem, followed by iteration to an acceptable. If the response was determined to be well under the maximum allowable levels, a limit analysis process would be entered to find the limiting environment.

Since confidence in the expected behavior levels was low, a two-phased testing approach was developed. The basic system assessment framework was modified such that results from a less complicated analysis problem would follow into a more rigorous analysis effort. Phase-1 tested a simple configuration of the concrete pipe sections with limited instrumentation. The test results gave an indication of the dominant load and response mechanisms and determined which areas of the structure should be instrumented more extensively in the second phase. Phase-2 tested a more complex arrangement of the pipe sections with a greater amount of instrumentation. This phase used the knowledge gained from the first phase to determine the optimum gage and detonation locations.

With two structural shapes and two test phases, the testing program consisted of four test series named the Multi-Unit Structure Test.

MUST-I: Phase-1; Simple Cylinder
MUST-II: Phase-1; Simple Rectangle
MUST-III: Phase-2; Complex Cylinder
MUST-IV: Phase-2; Complex Rectangle

With limited instrumentation and test events in Phase-1, a relatively small amount of data was generated and analyzed quickly. The simplicity of these tests allowed some measurements of the response, given the structure and environment. The resulting Phase-2 testing was a more efficient use of resources, based on the lessons learned in

Phase-1. Mistakes were minimized, and optimum test designs were produced.

MUST-I

MUST-I featured a simple cylindrical structure, consisting of four reinforced concrete pipe sections with interior diameters of 8 ft (2.4 m) and covered with a soil berm (Figure 2).

Figure 2. MUST-I Test Article

The blast and shock environments were generated by the detonation of 1000-lb bombs. Two types of environments were generated for the test series. The first type of environment was predominately airblast, where the center-of-gravity of the charge was located on ground surface. The other type of environment was predominately ground shock. The charge was buried at a depth where most of the explosive energy would be coupled into the ground, and the largest crater would be formed. For a 500-lb (250 kg) charge weight, this depth-of-burial is 14 ft (4.3 m).

Four test events were conducted in MUST-I. They included two buried bursts alongside the structure, one surface burst alongside the structure, and one surface burst on the longitudinal axis of the structure. Figure 3 shows the test layout for the four test events.

The observations indicate that, at the ranges which the structures were tested, little damage occurred. The buried side-on burst caused some cracking at some joints. The end-on surface burst produced minor crushing where the end cap was fitted into the end pipe section. These observations provide some indication of the possible initial failure mechanisms.

In general, the severest environments were produced by the buried detonations. For such bursts, the energy of the detonation was estimated to be almost completely coupled into ground shock with the resulting stress waves propagating directly to the structure. In the case of a surface detonation, a portion of the energy went into airblast and the remainder into ground shock. The stress waves from the ground shock propagated directly to the structure. The airblast generated additional stress waves as it passed over the ground surface and berm. However, the soil did not transmit a substantial amount of the airblast energy into ground shock. Thus, the resulting surface burst environment was rather benign in comparison to the buried burst environment.

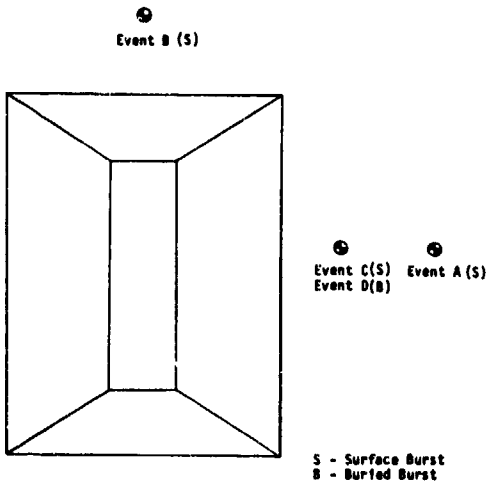

Figure 3. MUST-I Test Layout

Both types of bursts generated a variety of stress waves which induced the major load and response mechanisms. Extreme motions and excavation caused during crater formation had little effect on the load and response mechanisms, since the range of the structure to the charge was too large. For other test parameters, such as different in situ soil, larger charge weight, or closer range, crater-induced response mechanisms could become significant.

For buried bursts, the load and response mechanisms were generated by stress waves traveling through the soil. The dominant initial loading was caused by the propagation of a compression wave (P wave) from the source directly to the structure. This wave created active loading conditions on the lower upstream face as shown in Figure 4.

Structural motion away from the load provided relief from the active stress. Since the structural motion had a rigid body translation component, passive pressures developed over the downstream area to resist the motion.

Shear loads were generated by tangential passage of the P wave and the normal propagation of the S wave to the structure. Additional loads were generated at later times by the arrival of reflected P and S waves at the structure.

The resulting response mechanisms were directly related to the identified load mechanisms. The initial P wave loading was responsible for producing the major ovaling response. The P wave also caused rigid body translation. Shear waves were also responsible for rigid body effects.

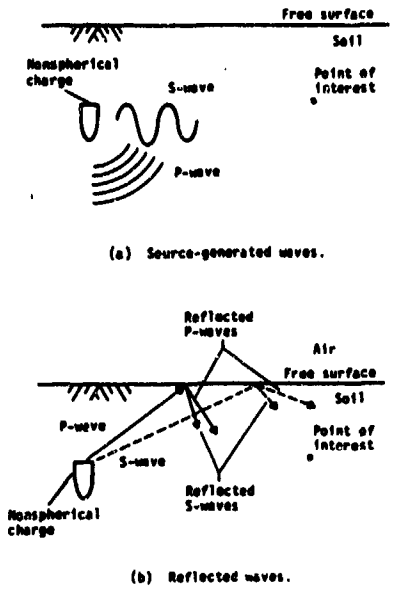

Figure 4. Waves produced by a buried charge

For the case of surface bursts, stress waves which induced the load and response mechanisms were generated by energy coupled directly into the ground and by airslap of the blast wave on the ground surface and berm. Both the direct-induced and airslap-induced ground shock produced P and S waves, including reflected and refracted P and S waves. However, since the available energy produced by the explosion was apportioned between ground shock and airblast, the magnitude and severity of the ground shock was less than for a buried burst.

Upstream-induced ground shock produced the initial loads on the structure. These were followed by downwardloads associated with airslap-induced ground shock passing through the berm. The upstream-induced ground shcok loads produced the more significant response of the structure.

Although no failure occurred, the primary potential failure mechanism for the cylindrical sections is joint failure. Relative motion between sections would have to be resisted at the joints in shear. The reduced thickness of the section to accommodate the bell-spigot joint and the absence of moment transfer due to joint dis-continuity induced a weak plane in the structure. Thus, load mechanisms which produce significant relative rigid body translation between sections would be likely to induce a failure mechanism in the joints.

MUST-II

The next series of tests were conducted under MUST-II. These tests subjected a structure, composed of four rectangular reinforced concrete pipe sections, to four test events. The test scheme is shown in Figure 5. Similar to the MUST-I tests, this series had two surface bursts and two buried bursts.

Instrumentation for the tests was similar to the MUST-I set up. Accelerometers and soil stress gages were used to measure the free-field environment. Interface pressure, strain, and acceleration gages were placed on the structure.

Figure 5a. MUST-II Test Article

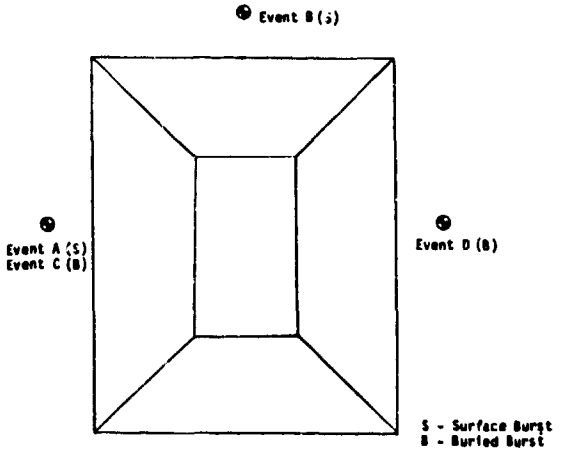

Figure 5b. MUST-II Test Layout

The observed load mechanisms were generated in the same manner. Both P and S waves were determined to cause the fundamental loading mechanisms. However, the flat surfaces of rectangular sections did not shed the normal loads as efficiently as the cylindrical shapes. Furthermore, the surface area of the rectangular sections was larger than the surface area of the cylindrical sections, providing greater loading areas. Thus, the loads on the MUST-II structure were more intense than the MUST-I structure.

For buried bursts, the upstream face was the most heavily loaded. The upstream region of the floor was subjected to a fairly heavy load. Minor loads were induced about the structure as it interacted with surrounding soil during its response.

Due to the different structural shape, the MUST-II structure exhibited different response mechanisms. Significant rigid body motion of the sections was a dominant response mechanism.

Another significant mechanism was flexure of the walls, floor and ceiling.

The rigid body motion component of the response produced observable permanent displacement in the structure. Shear loads on the surfaces of the sections produced longitudinal separation of some of the sections, allowing soil from the berm to infiltrate a joint. In addition, accelerometers on the structure, in the plane of the bomb show rigid body motion trends upward and downstream. Rigid body motion, moving the structure downstream, caused the downstream wall to flex inward as passive pressures were developed.

There was an indication from the vertical motion histories that the structure was pushed upwards and then fell under the influence of gravity, to cause additional shock as the sections rejoined with the in place soil.

The two surface burst events caused no significant behavior. The load mechanisms were similar to surface bursts created during MUST-I. The initial loads were generated by upstream-induced ground shock. They were followed by additional loads caused by airslap-induced shock waves produced by passage of the airblast on the berm.

The dominant response mechanism for the surface bursts was flexure of the walls roof, and floor. Apparently, insufficient energy was coupled into ground shock to produce significant rigid body motion.

The most likely failure mechanisms for the rectangular structures would be a failure of the joints. As with the cylindrical structure, this failure would be due to either longitudinal rigid body motion, causing opening of the joints, or downstream translation, resulting in shearing of the joint.

Additionally, the walls of the structure could be breached, constituting failure. A breach condition might be approached when rigid body motion and local flexure are insufficient to relieve the loads, and the capacity of the wall is exceeded.

Either of these failure conditions could be produced when the ground shock environment becomes sufficiently severe. Such situations would include a larger charge weight or closer range.

MUST-III & IV

Based on the preliminary findings of the Phase-1 analysis efforts, the Phase-2 test series were developed. The MUST-III structure was a configuration of cylindrical concrete pipes, similar to the MUST-I pipes, but arranged in a longer tube, with two access tubes at either end (Figure 6). Test events were both surface and buried bursts. From the Phase-1 tests, it was determined that buried bursts would be used to test the structure itself, while surface bursts would be used in testing the entrance.

The MUST-IV structure was similarly built

Figure 6a. MUST-III Test Article

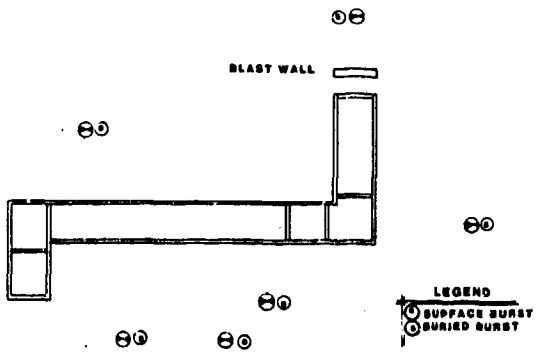

Figure 6b. MUST-III Test Layout

from concrete rectangular pipe sections. It was configured with a main tube with access tubes on either end (Figure 7).

In both of these series, the general load and response mechanisms were similar to their Phase-1 counterparts. However, due to the bends in the longitudinal axes of the Phase-2 structures, additional response was expected. Also, the existence of a number of adjacent sections implied additional restraint to rigid body translation.

As determined in the Phase-1 testing, the buried bursts against the side of the structure produced the most potential for damage. At the ranges tested, it was found that sections near the plane of the charge tended to move as a unit and were loaded similarly. The most severe joint distress was generated at joints away from the plane of the charge. At these locations, large relative motions had to be resisted by joints between sections with large differences in rigid body translation.

In the MUST-IV structure, relative rigid body rotation between the sections resulted in minor crushing of the concrete cover on the joints. The

Figure 7a. MUST-IV Test Article

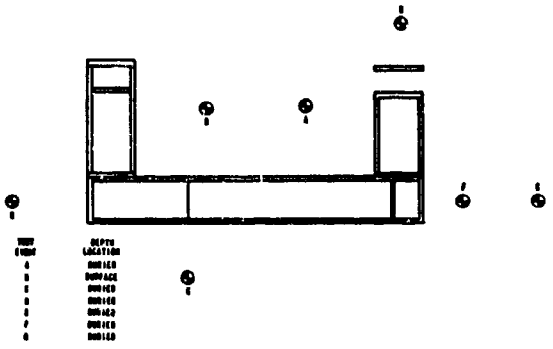

Figure 7b. MUST-IV Test Layout

MUST-III structure did not show this problem due to its cylindrical shape.

Additional structural behavior was noted in the side tubes of the MUST-IV structure when charges were located nearby. Because the entrances had no backfill or berm, no passive pressures could be developed to resist longitudinal separation of the joint. Thus, relatively large longitudinal motion was observed in the ends of the side tubes in the rectangular structure. Since the cylindrical structure could shed the loads more efficiently, no excessive longitudinal motion was recorded.

The dominant response mechanism which could lead to failure was the excessive relative motion between sections. Such motion could apply loads across the joint which exceed its resistance, causing the joint to fail. Joints on the end sections of the side tubes could open longitudinally, possibly constituting a failure mechanism.

Additionally, the wall or shell of the structure could be breached if rigid body motion and the capacity of the section are insufficient to bear the load. Such a situation may occur for a very close detonation. It would probably be accompanied by failures at adjacent joints. Finally, fragile equipment may be damaged during the response of the structure. Such equipment would have to be isolated from the structure.

SUMMARY

The results of the Phase-2 test series could be directly applied to any efforts to modify the structure's design. For the specific parameters used in the respective test series, the measured responses could be used to drive a design problem. The test results could also be used to determine if the response of the structure constituted failure. By conducting detailed analysis of the data, improved understanding of load and response mechanisms of the structure in a particular environment can be realized.

The System Assessment process for these modular structures began as a preliminary analysis problem, using simple structures in a given environment. The structural response was recorded and observed. It also allowed a more effective test setup for the more complicated phases of testing which followed.

Based on the structures in Phase-2, a more comprehensive analysis problem was approached. This particular effort provided direct identification of the behavior mechanisms. This analysis led to additional adjustments in the design and bounds on the load bearing capacity of the structure.

By having an organized approach for evaluating structures to withstand the effects of blast and shock, a proper balance of testing and analysis can be developed. The System Assessment Guidelines provide a logical basis for such an evaluation. Their application to the assessment modular, reinforced concrete structures in blast and shock environment resulted in a successful test program and a pair of structures which are capable of performing their intended functions.

REFERENCES

1. Meyer, V.A., Data Report for MUST-IV (Fourth Multi-Unit Structure Test, Full Size Rectangular Shelter), Events A through D, New Mexico Engineering Research Institute, Albuquerque NM, May 1984.

2. Whitehouse, S.R., Guidelines for Performing System Assessment Efforts, NTE-TN-83-05, Air Force Weapons Laboratory, Kirtland AFB NM, February 1983.

3. Whitehouse, S.R., Analysis Report for MUST-I (First Multi-Unit Structure Test, Generic Cylindrical Test Article), Events A through D, AFWL-TR-84-67, Air Force Weapons Laboratory, Kirtland AFB NM, February 1984.

4. Wong, M.K.W., "Blast and Shock Testing of Modular Structures," Proc. 5th ASCE Eng. Mech. Conf., Laramie, WY, August 1984, pp 652-655.

CHARACTERIZING IMPULSIVE FAILURE IN BURIED REINFORCED CONCRETE ELEMENTS

Timothy J. Ross

Air Force Weapons Laboratory
Civil Engineering Research Division
Kirtland AFB, New Mexico

ABSTRACT

An analytic procedure has been developed, using the classical elastic Timoshenko beam theory to account explicitly for shearing deformations, for defining conditions under which reinforced concrete beams and one-way slabs can fail in a direct shear mode when subjected to distributed impulsive loading from a planar source. The theory is extended to account for nonuniform loads similar to those that generally exist from closely detonated explosive point sources. The Timoshenko theory has also been extended to include rotational beam-end restraint to account for variable structural joint conditions. Failure conditions are investigated in terms of a new concept, the instantaneous shear-span ratio.

INTRODUCTION

Considerable attention is being given to the design of buried reinforced concrete structures to resist the effects of blast and shock forces which emanate from planar or point sources [3-5, 9-11]. The focus of this attention, lately, has been on the design for shearing loads which seem to be enhanced by impulsive pressures. This attention to shearing phenomena comes with good reason. As explosive disturbances are initiated at increasingly closer ranges to structures, the associated blast and shock forces on structural elements become higher in magnitude and generally quicker in rise times. Studies [6] have shown that impulsive pressure situations enhance shearing phenomena more than flexural phenomena in very early times after the shock disturbance is initiated. Shearing failures associated with direct shear at a support (Figure 1) or a generalized shear near a span interior (Figure 2) are of interest here.

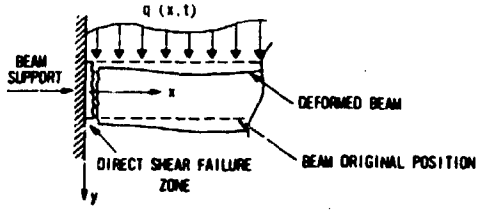

Fig.1 Direct Shear Failure

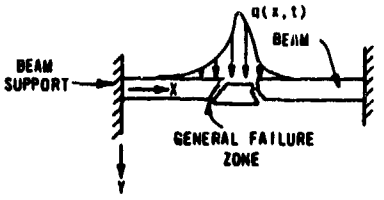

Fig.2 Generalized Shear Failure

Heretofore, most analytic procedures posed to assess structural failure phenomena under impulsive load conditions have used continuum flexural formulations such as the Bernoulli-Euler beam, the Kirchoff plate, and the Flugge shell theories, or they have decoupled the flexural and shear responses by treating each as separate single-degree-of-freedom (SDOF) models. These studies have ranged from empirically based SDOF models [3] to yield-line analyses [5,10] or multi-degree-of-freedom analyses [9] based on flexural theory. However, with impulsive loadings of ever increasing intensity, and with the associated short rise-times to peak pressure, high-frequency characteristics now dominate structural response. Because of this, it is important that the computational algorithms used to understand structural failure under impulsive loads also reflect high frequency effects in the equations of state. Such is the case when shearing deformations and rotatory inertia are included in the kinematic and constitutive relations. For example, the theories involving the Timoshenko beam, the Mindlin plate, and the Federhofer arch adequately account for the extra complexity associated with high frequency structural response. Recent studies [4,7] have attempted to assess predominantly shearing-type failures using these theories.

This paper reviews recent developments in the failure analysis of reinforced concrete beams and one-ways slabs using the Timoshenko theory and associated shear and flexure criteria [6,7]. The analytic formulation of this theory provides for an accurate assessment of the shear and moment forces in a structural element as a function of space and time. This formulation can be shown to be an adequate substitute for the exact three-

dimensional elastic theory for frequencies up to about 100,000 rad/sec. This paper also addresses the notion of an instantaneous shear-span ratio. This ratio is a function of time and provides another domain in which to assess the interrelationship among various failure mechanisms. Failure curves, defining peak pressures versus rise time domains where failures are possible, are developed and compared to experimental evidence.

ANALYTIC MODEL

The classical one-dimensional Bernoulli-Euler theory for flexural vibrations of elastic beams becomes an inadequate model when higher modes need to be considered. This theory is not suitable for transverse impulsive-type loadings because the propagation velocity of the disturbance approaches infinity as its wavelength approaches zero. Both rotatory inertia and shearing deformations become increasingly important in the higher modes. A good one-dimensional model for an assessment of high frequency influences on structural response is the Timoshenko beam model [2]. An elastic Timoshenko beam under the action of a rapidly applied triangular load is analyzed in this paper using the normal mode method. (Figure 3)

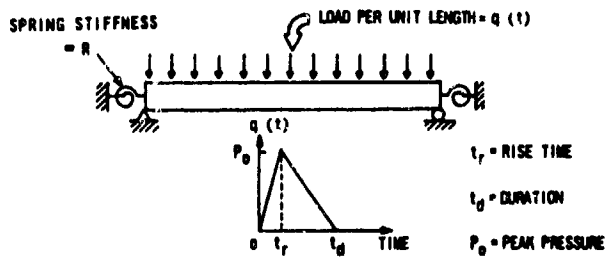

Fig.3 Timoshenko Beam Model

The well-known Timoshenko equations are solved using the assumption that the solution is characterized by harmonic motion. This assumption allows the beam vibration to be described by a series expansion of the orthogonal modes, where the temporal and space dependent features of the solution are uncoupled. In this case the solution is altered slightly because of the presence of elastic rotational beam-end constraints. The normal mode solution is a function of a parameter describing the stiffness of the rotational beam-end constraint. This parameter shows up in the description of the Timoshenko beam normal modes. Because there are two dependent variables in the Timoshenko formulation, the beam rotation due to bending ϕ and the beam transverse deflection y, there will be two types of normal modes. These two types are defined as flexure-shear modes and thickness-shear modes [7]. The normal mode solution is presented in terms of an orthogonal expansion of the normal mode shape due to deflection, Y_n, and an orthogonal expansion of the normal mode shape due to bending, Φ_n.

The bending moment M and the transverse shear force V in the beam at a general section (denoted as the coordinate x) along the beam span, can be determined from the force deformation relations

$$M = -EI\phi' \quad (1)$$

$$V = k'AG(y' - \phi) \quad (2)$$

and from the reported solutions [7] for homogeneous initial conditions for the dependent variables, y and ϕ,

$$y(x,t) = \sum_n \frac{Y_n(x)}{\omega_n} \int_0^t G_n(\tau) \sin \omega_n (t-\tau) d\tau \quad (3)$$

$$\phi(x,t) = \sum_n \frac{\Phi_n(x)}{\omega_n} \int_0^t G_n(\tau) \sin \omega_n (t-\tau) d\tau \quad (4)$$

$$G_n(t) = \frac{\int_0^L \left(\frac{q}{\rho A} Y_n + \frac{r^2 M_a}{\rho I} \Phi_n \right) dx}{\int_0^L (Y_n^2 + r^2 \Phi_n^2)\, dx} \quad (5)$$

In these relations E,G,I,A,L,r,ρ and k' are the modulus of elasticity, shear modulus, moment of inertia, cross-sectional area, length, radius of gyration, density, and shear deformation coefficient of the beam, respectively. The parameter n refers to the mode number, so ω_n is the natural frequency corresponding to the n^{th} normal mode. The beam is excited by a general transverse pressure q = q(x,t) and a general applied moment M_a which is set to zero for this study.

FAILURE CRITERIA

In this paper failure is defined to occur when a concrete element reaches its ultimate load carrying capacity. Whether this capacity is reached in terms of a shear or flexure mechanism is dependent on the state of stress in the beam and on which of the mechanisms is realized first in the beam response history.

Failure in a flexural mode is defined to occur when a beam reaches its nominal bending capacity, denoted as M_c. This capacity can be computed based on Whitney's stress block and the yield strength of the reinforcement. Criteria for three important classes of shear failures have been proposed [1], and their distinction described in terms of their relationship to certain magnitudes of the shear span ratio. These criteria are based on test results obtained in the static load domain. These classes of shear failure are termed direct shear, deep-beam, and diagonal tension. For direct shear, V_c, the failure criterion is a function which relates direct shear resistance to shear-slip along a crack plane, whether or not an actual crack exists. This criterion is valid for reinforced concrete specimens both with and without a precracked shear plane. For deep-beam and diagonal tension, the failure criteria are functions of the shear-span ratio denoted by the expression, M/Vd, where d is the effective depth of the beam.

The failure criteria for M_c and V_c are uncoupled with regard to internal forces (i.e. M_c is not a function of the shear force and V_c is not a function of the bending moment). However, the criteria for deep-beam shear and diagonal-tension are functions both of the bending moment and shear force, because of their dependence on the shear-span ratio. When assessing the likelihood of a structural element to fail in a particular mode, it is much easier to compare flexural failures to direct shear failures because of the decoupled nature of the failure criteria.

SOIL STRUCTURE INTERFACE PRESSURE

Typically, most buried structure experiments take measurements at the interface between the structure and surrounding geologic medium with the use of interface pressure gages. These interface pressures can reveal a great deal about the structural response and failure modes of buried reinforced concrete elements by displaying the spatial and temporal character of the interface loading. For example, expansive planar loads tend to engulf a structure with a plane wave, and the interface pressure is typically uniform along the span, as shown in Figure 4a. In contrast, point source interface loadings are highly localized because of a much smaller energy source compared to the planar case. Pressure distributions tend to be nonuniform and, more or less, proportional to the inverse of the square of the distance between the point source and structure as shown in Figure 4b.

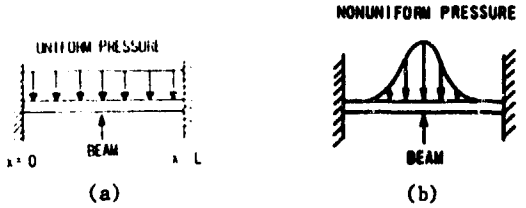

Fig.4 Symmetric Interface Pressure Distributions

For a uniform pressure, the form of Equations 3-5 is considerably simplified because the external load will be a constant in the space domain. The nonuniform pressure from a point source is more difficult because the pressure varies with space for all times; hence the resulting integrations involved in Equations 3-5 are onerous. Interface pressure records for a typical planar wave [8] are shown in Figure 5, and those for a typical point source [12] are shown in Figure 6.

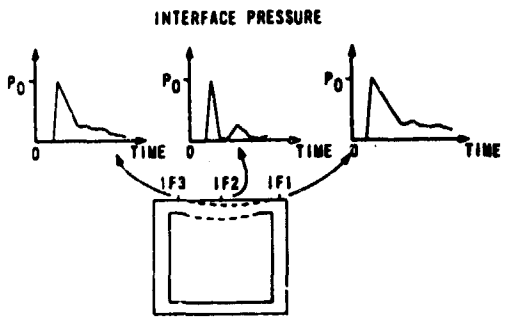

Fig.5 Interface Pressure From Planar Wave

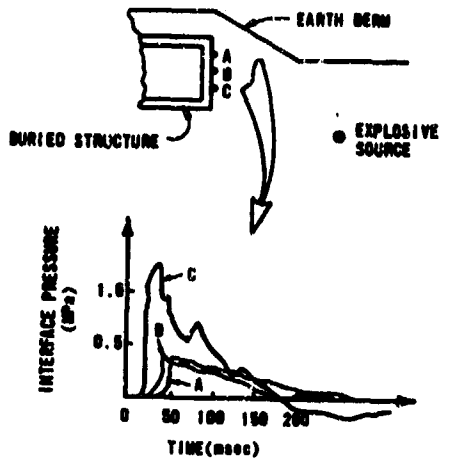

Fig.6 Interface Pressure From Point Source

NUMERICAL EXAMPLE

It is interesting to compare various failure modes of a given reinforced concrete element to impulsive loadings from a planar source and from a point source. This can be done quite conveniently for the two modes of failure classified as direct shear and flexure. To accomplish this, a comparison is made between normalized shear and moment at a beam support (x=0) as a function of time. The moment and shear are normalized to their respective nominal strength capacities, M_c and V_c. It is then possible to determine whether the beam is expected to fail in direct shear before it fails in flexure.

An example beam, with nominal mechanical and geometric properties as shown in Table 1, is selected for this analytic comparison. These results are based on an analysis of the accuracy and convergence of the normal mode solution reported [7]. The first twenty-one modes were shown to provide convergence for the example problem discussed herein. This number of modes was necessary because the higher modes are strongly influenced by the beam shearing deformations. The highly impulsive nature of the loading excites the shearing deformations because they are associated with the higher frequency thickness-shear modes alluded to earlier. By contrast, the moment relationships converged by considering the first seven modes.

TABLE 1.—Example Reinforced Concrete Beam Properties

Parameter (1)	Dimension or value (2)
Length (L)	1.14 m (44.75 in.)
Thickness (h)	0.18 m (7.25 in.)
Beam density (ρ)	2,400 kg/m³ (150 pcf)
Shear modulus (G)	13,800 MPa (2 × 10⁶ psi)
Modulus of elasticity (E)	33,100 MPa (4.8 × 10⁶ psi)
Shear deformation coefficient (k')	0.822
Poisson's ratio (ν)	0.20
Direct shear capacity (V_c)	6,140 kg (13,500 lb)
Ultimate moment capacity (M_c)	370 kg-m (32,400 in.-lb)

Figure 7 shows a plot of the normalized support shear (V/V_c) and normalized support bending moment (M/M_c) versus time for a uniformly distributed pressure with a temporal variation as shown in Figure 3, for the example elastic beam. The plot is for a fixed beam end condition and for a given rise time and load duration as shown. Several important aspects of theoretical beam behavior can be seen in this plot. In the figure, the time at which $V/V_c = 1$ is denoted as t' and the time at which $M/M_c = 1$ is denoted as t". At early times, the normalized shear curves increase at a higher rate than the normalized moment curves. However at later times, the normalized moment curves increase faster than the normalized shear curves. Therefore, the occurrence of failure in either direct shear or bending depends on whether the failure threshold (V/V_c and M/M_c equals one) intersects these curves at an early or a later time, respectively. Figure 7 shows a condition where an early time direct shear failure is indicated (t' < t").

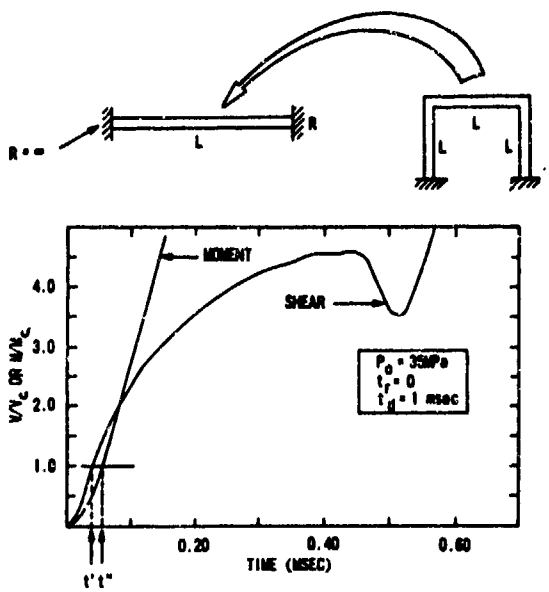

Fig.7 Normalized Forces For Fixed-End Beam

The degree of the restraint at the beam ends is another important parameter that affects elastic failure. Figure 8 shows a plot of normalized support shear and moment versus time for the example beam for a beam end restraint stiffness of R = 4EI/L. This restraint corresponds to the rotational resistance offered by a wall with the same properties and length as the beam, as shown in the schematic in Figure 8. A comparison of Figures 7 and 8 illustrates the influence of end restraint on the time parameters t' and t". In early time shear forces become more dominant over bending moments at the support as the beam end restraint decreases.

The transition from a predicted direct shear failure to no shear failure occurs when t' = t". If this transition for different combinations of rise time t_r and peak pressure P_o (for an

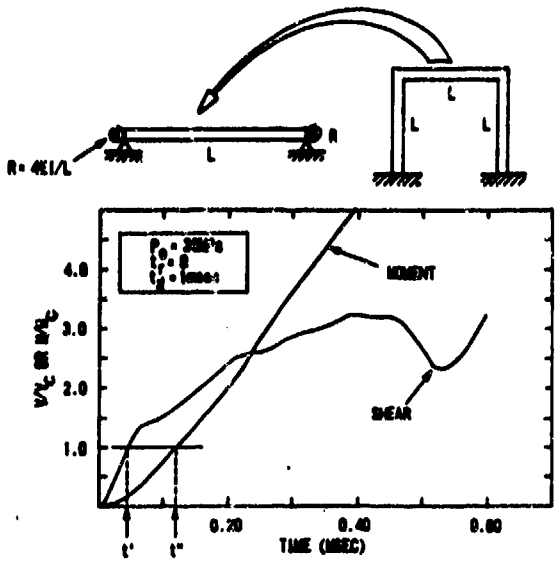

Fig.8 Normalized Forces For Elastic-End Beam

idealized triangular load shape in the time domain) is plotted in the P_o versus t_r domain, a series of points results which describes a "failure curve." Typical failure curves for the example beam with fixed ends are shown in Figure 9. These curves separate the peak pressure versus rise time domain into two regions. Combinations of peak pressure and rise time which lie in the region above a failure curve define a loading for which analysis indicates a direct shear failure. Points that lie in the region below the failure curve describe load parameter combinations which will cause either a bending failure or no failure in the beam or one-way slab.

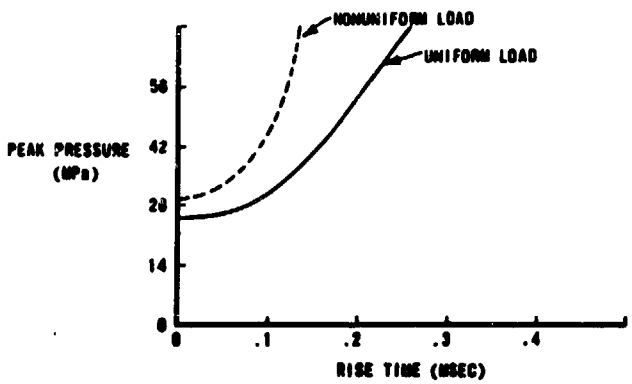

Fig.9 Failure Curves

In addition to being sensitive to certain load parameters such as the peak pressure and rise time and to certain structural parameters such as the length-to-depth ratio and the support constraints, the failure curves for a particular structural element are also sensitive to the spatial distribution of the interface pressure. Figure 9 shows the failure curves for a uniformly distributed pressure (Figure 5) and a nonuniformly

distributed pressure (Figure 6) where each pressure distribution has the same peak value and temporal distribution (i.e., a triangular shape in the time domain). The location of the curves is to be expected, with the nonuniform curve being higher, since there is less energy in the nonuniform load when compared to the uniform case. The nonuniform curve also increases with a greater slope than the uniform curve as the rise time increases. This behavior occurs because as the impulsive pressure approaches a static condition, more and more of the nonuniform pressure energy needs to be concentrated near the support for a direct shear failure situation.

The instantaneous shear-span ratio, M/Vd, is a function of time because of the temporal nature of the quantities M and V. It is interesting to look at this quantity and its relationship to the static quantities used in design procedures [1]. Figure 10 shows a plot of the instantaneous shear-span ratio versus time for the example beam and the load parameters. The two curves are both for a uniformly distributed pressure, but differ according to two different beam-end restraint conditions. If the direct shear failure time (t') for these load conditions is taken from Figure 8 for the elastic end condition and from Figure 7 for the fixed-end condition and superposed on the time scale of Figure 10, it is seen that the value of the quantity M/Vd that corresponds to direct shear failure ranges from 0.1 to 0.22. These transient values of M/Vd are less than the suggested value of 0.50 for a direct shear failure from static data [1], but they pertain to only one set of temporal and spatial (in this case uniform) load parameters.

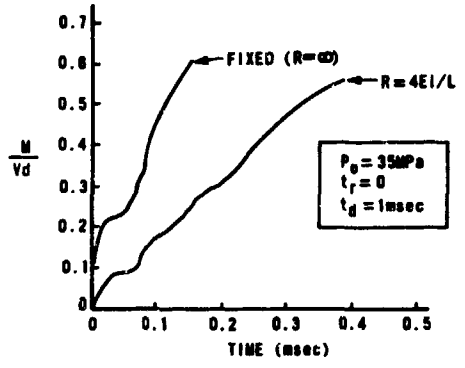

Fig.10 Instantaneous Shear-Span Ratio

For nonuniform loads, especially where the peak pressure is located closer to the center of a slab and away from a support, the analytic assessment of failure is more difficult. To assess a failure in the interior portions of a slab, the procedure described here takes on an extra variable—the location of the failure. To accomplish this, the normalized shear and moment quantities are monitored in the time domain and along the length of the beam or slab. As soon as either quantity exceeds a value of unity, both the location and time of failure are catalogued. This procedure results in a series of failure curves, each representing a different location on the beam.

An indication of the adequacy of the failure curve approach is seen in Figure 11. Points that fall above the curve are indicated by analysis to fail in direct shear at a support, and those below the curve to fail in flexure or not to fail at all. As seen, there is excellent agreement on this particular beam, except for the cases where possible mixed modes are involved. These situations may involve the other forms of failure such as deep-beam or diagonal-tension, and are under investigation.

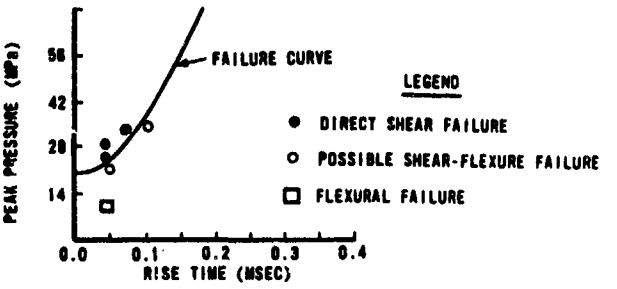

Fig.11 Comparisons of Analysis and Experimental Data

SUMMARY

An elastic Timoshenko beam model gives a clear and accurate picture of the transient influence of shear and bending moment on elastic failure behavior in impulsively loaded beams and one-way slabs. Direct shear failures precede flexural failures in the early transient response regime for certain combinations of load parameters and beam end restraint conditions. The most important load parameters affecting the failure mode are peak pressure and rise time of the impulse loading and the spatial distribution along the structural span. The beam end restraint alters the magnitude of the support bending moment much more than it alters the support shear force. Direct shear failure curves developed from elastic Timoshenko beam theory for uniformly distributed impulsive pressures are found to be in good agreement with experimental data. An approach has been outlined to assess the influence of spatial distribution on the eventual failure modes of a member under impulsive pressure. Currently this work involves the use of a failure curve and an instantaneous shear-span ratio. The utility of these parameters for distinguishing other failure modes such as deep-beam shear and diagonal-tension is being investigated.

ACKNOWLEDGEMENTS

This work was sponsored under AFOSR Task 2302Y2 and is gratefully acknowledged.

REFERENCES

[1] Hawkins, N., "Dynamic Shear Resistance of Reinforced Concrete," Letter Reports to the US Navy, 28 August and 15 September 1981.

[2] Karthaus, W. and Leussink, J.W., "Dynamic Loading: More Than Just a Dynamic Load Factor," Proc. First Symp. Inter. of Non-Nuclear Munitions with Struc., May 1983, Vol 1, pp 151-154.

[3] Krauthammer, T., "Shallow-Buried RC Box-Type Structures," ASCE Journal of Structural Engineering, Vol 110, ST3, March 1984, pp 637-651.

[4] Millavec, W.A. and Isenberg, J., "The Response of Reinforced Concrete Structures Under Impulsive Loading," Proc. Inter. of Non-Nuclear Munitions with Struc., May 1983, Vol 2, pp 88-83.

[5] Ross, C.A. and Schauble, J., "Failure of Underground Hardened Structures Subjected to Blast Loadings," US Air Force Office of Scientific Research Report, AFOSR-TR-79-0679, April 1979.

[6] Ross, T.J., "Dynamic Rate Effects on Timoshenko Beam Response," ASME, Journal of Applied Mechanics, Vol 52, No. 2, June 1985.

[7] Ross, T.J. and Wong, F.S., "Timoshenko Beams with Rotational End Constraints," ASCE Journal of Engineering Mechanics, Vol 111, EM3, March 1985.

[8] Slawson, T.R. and Kiger, S.A., "Dynamic Shear Failure of Shallow-Buried Flat-Roofed Reinforced Concrete Structures Subjected to Blast Loading," Waterways Experiment Station Technical Report, SL-84-7, April 1984.

[9] Van der Veen, C. and Blaauwendraad, J., "Structural Response of RC-Members in Case of Impulsive Loading: Failure Analysis in Bending and Shear," Proc. First Symp. Inter. Non-Nuclear Munitions with Struct., May 1983, Vol 1, pp 182-187.

[10] Vretblad, B.E., "Response of Structures to Detonations in Sand," Proc. First Symp. Interaction of Non-Nuclear Munitions with Structures, May 1983, Vol 1, pp 216-219.

[11] Wong, F.S. and Weidlinger, P., "Design of Underground Shelters Including Soil-Structure Interaction Effects," Proc. First Symp. Interaction of Non-Nuclear Munitions with Structures, May 1983, Vol 1, pp 174-176.

[12] Wong, M.K.W., "Blast and Shock Testing of Modular Structures," Proc. Fifth ASCE Eng. Mech. Conf., August 1984, Vol 1, pp 652-655.

A COMPUTATIONAL PROCEDURE FOR RESPONSE OF BURIED STRUCTURES TO CONVENTIONAL WEAPONS

S. A. Kiger

Research Structural Engineer
USAE Waterways Experiment Station Vicksburg, MS

J. T. Painter

Professor of Civil Engineering
Louisiana Tech University, Ruston, LA

ABSTRACT

Analyzing the response of a buried structure to the nearby detonation of a general purpose bomb is greatly complicated by the localized nature of the loading. Simplified single-degree-of-freedom (SDOF) models are desirable for preliminary design calculations and for vulnerability calculations, where the large plastic deflections make other analytical methods more difficult and less reliable. Two essential parameters in the SDOF model are a resistance function and an equivalent loading function. A procedure is developed for estimating the load distribution on the structure based on the weapon size, its distance from the structure, and the structural dimensions. With this load distribution, a load factor and a resistance function are derived. The resistance function is based on the yield lines expected to form for a static application of the localized load. Thus, the localized nature of the structural response can be accounted for. Several examples of computed structural response are compared with experimental data.

INTRODUCTION

There is a continuing need for simplified analysis procedures for the response of structures to conventional weapons. However, the highly transient nonuniform loads are difficult to approximate with a single "equivalent" pressure-time history. Also, the localized nature of the loading causes a complex, two-way, structural response, even in structures that are designed and reinforced to respond as one-way slabs. The scope of this paper will be limited to buried structures so that fragment loading will not be considered.

Simplified analysis methods currently in use generally give overly conservative results when used for design, and can be very misleading and nonconservative when used for vulnerability calculations. One frequently used approach to estimating a design load is to calculate the peak free-field pressure at the nearest point on the structure, multiply it by two, and design the structure to withstand that load statically. This will, in almost every case, lead to an overly conservative design. First, because it assumes an elastic response when some plastic deformation is usually allowable. Second, because it assumes a reflected pressure duration that is long when compared to the natural frequency of the responding structural element. This is not usually the case. And, finally, because it assumes a uniform pressure distribution over the entire structural element.

Specific procedures for computing more reasonable estimates for design loads are given in References 1 and 2. Reference 1 prescribes a pseudo-elastic design calculation for "moderate" damage in which the predicted peak reflected pressure on the structure at the point nearest the explosion is applied as a uniform pressure and the maximum resistance of the structural element being loaded is multiplied by 10. The multiplicative factor is determined by the damage level for which the structure is being designed. If the element just remains "elastic" in this calculation, then "moderate" damage is predicted. This empirical method is based on a large data base, and can give acceptable results so long as the calculations are for a configuration similar to the data on which the empirical factors are based. However, there is clearly room for improvement. In Reference 2 an elasto-plastic calculation is performed with an "equivalent" uniform load. The equivalent uniform load is that uniform pressure that will cause the same maximum deflection at the center of the loaded structural element as would be produced by a pressure distribution that varies as r^{-3}, where r is the slant distance from the explosion to a point on the loaded structural element. While this is an improvement, taking into account the nonuniform nature of the loading, the results are still overly conservative when compared to data. One reason is that the resistance function for the equivalent uniform load does not account for the localized nature of the response. The procedure suggested in Reference 2 corrects for this by multiplying the computed resistance by 1.5, and performing the design calculations with this increased resistance.

The procedure outlined in this paper approximates the pressure at any point on the loaded structural element as proportional to r^{-3}, where r is the slant distance from the weapon, and computes the structural resistance

based on yield lines expected to form under this pressure distribution.

ANALYTICAL PROCEDURE

Assuming a point source for the explosion, the pressure at any point on the structure wall facing the weapon can be approximated by

$$p(t) = P_o(t)\left(\frac{D}{r}\right)^3 \qquad (1)$$

where

$p(t)$ = pressure on the wall at a distance r from the weapon

$P_o(t)$ = pressure on the wall nearest the weapon (distance D)

D = perpendicular distance from the weapon to the wall

r = slant distance from the weapon to the wall

External walls of hardened structures are usually long compared to their height, and are normally reinforced as one-way slabs, heavy reinforcement in the short span, or height, and light reinforcement in the long direction. However, the localized nature of the loading will produce a two-way response, even in one-way reinforced slabs. The extent of this two-way action depends on the proximity of the weapon and the relative amount of reinforcement in the short and long directions. As a first-cut approximation, the dimensions of the responding area of the slab will be taken as the area with pressures greater than (0.1) P_o, or the actual dimensions of the slab, whichever is smaller.

The resistance of the slab will be based on a yield line analysis that includes compressive membrane effects (Reference 4) and large deflection tensile membrane resistance as shown in Figure 1. The ultimate slab resistance, R_u, is given by

$$R_u = \frac{F_t}{W_E} M_i \qquad (2)$$

where F_t is the total load on the slab, W_E is the total external work done by the applied load, and M_i is the total work done by internal forces in the deforming slab. The force F_t and the work W_E were calculated by dividing the slab into annuli as indicated in Figure 2, assuming the yield line pattern shown in Figure 3, and calculating the average load in each annulus. To calculate W_E, the annulus was further subdivided as necessary with a uniform average load used in each annulus section. Calculations for M_i include compressive membrane forces in the slab and assumes the yield line pattern shown in Figure 3. From Reference 4, as modified in Reference 5, M_i can be calculated from:

$$M_i = 4\left(0.85f'_c\beta_1 h^2 a\left\{\left[\left(\frac{1}{2}-\frac{\beta_1}{4}\right)+\left(\frac{\beta_1}{4}-\frac{3}{8}\right)\frac{\delta}{h}+\left(\frac{1}{8}-\frac{\beta_1}{16}\right)\left(\frac{\delta}{h}\right)^2\right]\right.\right.$$

$$\left.+\left[\left(\frac{1}{2}-\frac{\beta_1}{4}\right)-\left(\frac{1}{12}-\frac{\beta_1}{48}\right)\left(\frac{\delta}{h}\right)^2\right]\right\}-\frac{1}{3.42f'_c}\left[(T'_x-T_x-C'_{sx}+C_{sx})^2\right.$$

$$\left.+a(T'_y-T_y-C'_{sy}+C_{sy})^2\right]+(C'_{sx}+C_{sx})\left(\frac{h}{2}-d'_x-\frac{\delta}{4}\right)$$

$$+(T'_x+T_x)\left(d_x-\frac{h}{2}+\frac{\delta}{4}\right)+(C'_{sy}+C_{sy})$$

$$\left.\left[a\left(\frac{h}{2}-d'_y-\frac{\delta}{2}\right)+\frac{\delta}{4}\right]+(T'_y+T_y)\left[a\left(d_y-\frac{h}{2}+\frac{\delta}{2}\right)-\frac{\delta}{4}\right]\right) \qquad (3)$$

where

f'_c = compressive strength of the concrete, psi

$\beta_1 = 0.85 - 0.00005\,(f'_c - 4000)$
$0.65 \le \beta_1 \le 0.85$

h = total thickness of the slab

a = ratio of long to short span of the responding area of the slab

δ = assumed midspan slab deflection at maximum resistance. T is a steel tensile force per unit length at a yield section, C_s is a compressive steel force per unit length at a yield section, C_c is the compressive force per unit length in the concrete at a yield section, primes indicate forces at slab supports, and subscripts x and y indicate directions (length and width respectively) in the slab

d_x and d_y = distance from the compressive face of the concrete to the centroid of the tensile steel in the x and y directions

d'_x and d'_y = distance from the compressive face of the concrete to the centroid of the compressive steel in the x and y directions

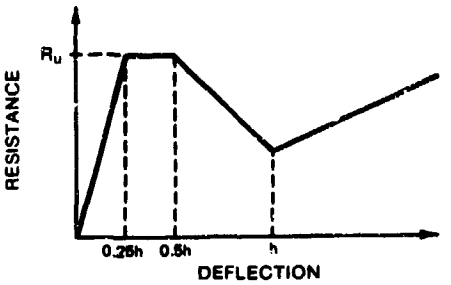

Figure 1. Resistance function.

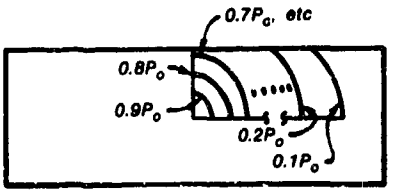

Figure 2. Constant pressure annuli.

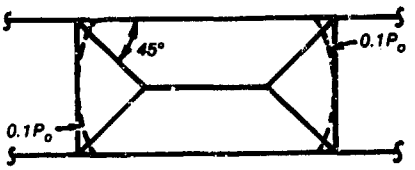

Figure 3. Yield line pattern.

As shown in Figure 1, the maximum resistance, R_u, is assumed constant between midspan slab deflections of 0.25h and 0.5h. Concrete is crushing during the resistance decay region assumed between midspan deflections of 0.5h and h. At a midspan deflection equal to h tensile membrane resistance begins along a slope given in Reference 6 as

$$K' = k_t \frac{A_{tS} f_{dy}}{(12L_S)^2} \qquad (4)$$

where

K' = slope of tensile membrane region, psi/in.

f_{dy} = dynamic yield strength of the reinforcement steel

and

$$k_t = \frac{3}{4\sum_{n=1,3,5\ldots} \frac{1}{n^3}(-1)^{(n-1)/2}\left[1 - \operatorname{sech}\left(\frac{n\pi L_L}{2L_S}\sqrt{\frac{A_{tS}}{A_{tL}}}\right)\right]}$$

The limiting value of k_t for one-way action slabs is 8.0.

L_S, L_L = length of short and long spans, respectively, ft

A_{tS}, A_{tL} = total area of steel per unit width in short and long span directions, respectively, $in.^2/in.$

The differential equation of motion to be solved for the slab response, $y(t)$ is, from Reference 7:

$$K_{LM} M_t \ddot{y}(t) + R = F(t) \qquad (5)$$

where

K_{LM} = load-mass factor

M_t = total mass of the responding slab area

R = resistance as defined in Figure 1

$F(t)$ = total force on the responding slab area

Note that the load-mass factor is computed from the nonuniform pressure distribution, $p(t)$, defined in Equation 1 and the deflected shape, $\phi(x,y)$, defined as flat plates bounded by the yield lines in Figure 3.

$$K_{LM} = K_M/K_L$$

$$K_M = \int_A m\,\phi^2(x,y)\,dA/M_t$$

$$K_L = \int_A p(t)\,\phi(x,y)\,dA/F(t)$$

A = responding slab area

m = mass per unit of slab area

$$F(t) = \int_A p(t)\,dA \qquad (6)$$

Equation 5 was numerically integrated using the Newmark β method. Details of the computer program are given in Reference 3.

COMPARISON WITH EXPERIMENTAL DATA

Calculations were performed for a series of 7 dynamic test described in Reference 3. These tests were performed on buried, reinforced concrete, slabs that were 43 inches high by 15 feet long by 4.3- or 8.6-inches thick. The explosive used was 15.4 lb of C4 in a steel cylinder which simulated, assuming a 1/3-scale wall, an earth penetrating 1000 lb bomb. The simulated bombs were detonated at various standoff distances.

Test results are shown in Table 1. The numbering scheme is in keeping with that in Reference 3, and the range is the perpendicular distance, D , between the center of gravity of the charge and the slab.

Results of the calculations are also shown in Table 1. Calculations for M_1 , on which the maximum resistance depends, were based on the assumption that the maximum slab resistance occurs at a midspan deflection equal to 0.5 times the slab thickness. Loads used in the calculations were computed using Equation 1 with $P_o(t)$ taken from the measured data in Reference 3. Results in Table 1 indicate good agreement between calculated maximum response and the experimental data.

Table 1. Calculations and Data from Reference 3.

Test No.	Range (D) ft	Maximum Deflection (in.) Data	Calculation
4	10	0.38	0.31
5	5	2.13	2.80
5A	3.75	Breach	12.5
6	5	1.56	1.58
7*	5	0.63	0.44
9	5	2.94	5.20
10	5	1.69	1.50

* Slab 7 was 8.6 inches thick. All other slabs were 4.3 inches thick.

CONCLUSIONS

The computational procedure described here accounts for the nonuniform pressure distribution on a buried structure generated by the nearby detonation of an earth penetrating bomb. The computed resistance of the responsing structural wall is based on yield line theory, it includes compressive membrane effects, and it accounts for the localized two-way response of the wall. Predicted maximum responses using this procedure agree well with data from a series of dynamic tests using simulated 1000-lb bombs. The simplified procedure outlined in this paper represents a significant improvement over those simplified methods that are in general use at the present time.

ACKNOWLEDGEMENT

This work was sponsored by the U.S. Air Force Engineering and Services Center (AFESC) at Tyndall Air Force Base, Florida. The Project Monitor was Mr. Walter C. Buchholtz (AFESC).

REFERENCES

1. Department of the Army Technical Manual, TM5-855-1, "Fundamentals of Protective Design (Non-Nuclear)," Headquarters, Department of the Army, July 1965.

2. Department of the Army Technical Manual, TM5-855-1, Revision in publication.

3. Baylot, J. T.; Marchand, Kirk; Kiger, S. A.; and Painter, J. T.; "Response of Buried Structures to Earth-Penetrating Conventional Weapons," Air Force Engineering and Services Laboratory, Technical Report, Tyndall, AFB, FL (in preparation).

4. Park, R. and Gamble, W. G.; "Reinforced Concrete Slabs," Chapter 12, John Wiley and Sons, 1980.

5. Guice, L. K.; Louisiana Tech University, Ruston, LA; Private Communication, Nov 1984.

6. Wiehle, C. K. and Bockholt, J. L. "Dynamic Analysis of Reinforced Concrete Floor Systems"; Technical Report, May 1973; Stanford Research Institute, Menlo Park, Calif.

7. Biggs, J. M. "Introduction to Structural Dynamics," McGraw-Hill Book Co., New York, NY, 1964.

EXPEDIENT NONLINEAR DYNAMIC ANALYSIS OF REINFORCED CONCRETE STRUCTURES

C. Allen Ross
University of Florida Graduate Engineering Center
Eglin AFB, Fl

Paul L. Rosengren, Jr.
Air Force Engineering and Services Laboratory
Tyndall AFB, Fl

ABSTRACT

This paper presents the application of the nonlinear dynamic analysis computer code, REICON, to two specific types of survivability problems: Underground hardened shelters and runway damage assessment.

The computer program REICON was used to analyze a generic reinforced concrete structure to determine its survivability at various weapon stand-off distances. Localized shear failure and flexural response calculations are performed using fourth-order Runge-Kutta and Newton-Cotes numerical integration techniques to solve the differential equations of motion and energy. Runway damage analysis was performed for both vertical and horizontal buried cylindrical charges. The crater radius and apparent center-point displacement versus the charge center of gravity were obtained for a generic concrete runway section. The paper concludes that REICON provides reasonable analytical results with a minimum of data preparation and computer execution time.

INTRODUCTION

The problem of predicting response of reinforced concrete structures to localized underground explosives is rather complicated if all the parameters of the material, structure and loading function are taken into account. A finite element program could possibly handle all the parameters required for the analysis; however, many of the parameters associated with the dynamic properties of concrete and soil/structure interaction loads are just not available. Couple these problems with all the other standard large deflection, large strain, nonlinear material, nonlinear geometry problems; these codes become almost economically prohibitive to run.

This paper describes a rather simplified computer code with very short running time that uses a response failure mechanism based on the method of plastic hinges or yield lines. A very brief description of the computer model and the results of two examples of its use are given in the following sections.

COMPUTER PROGRAM

The computer program REICON [1] is based on energy principles using static and travelling plastic hinges and a rigid perfectly plastic constitutive relation between the hinge moment and its angle of rotation. For flexure the basic assumption is that the failure mechanism is by plastic hinges; and failure, defined by actual material separation, results from gross rotation with reinforcement tensile failure. Shear failure is assumed to occur early in the dynamic loading process and is based on a critical velocity associated with a critical impulse.

The flexural response for plates will be described here briefly and details of the analysis for plates and beams are given in the references [1-3]. The failure mechanisms for plates are shown schematically in Figure 1 and the details for the plate are shown in Figure 2. Similar mechanisms are assumed for beams. Using Figure 2 the equations of motion for the assumed plastic hinge response may be written. For the inclined portions (1) and (2) the equation of motion becomes

$$\left.\begin{aligned} &\ddot{m}\theta a^4\overline{AR}\chi^3\left[\frac{1}{3}(z^2\overline{AR}+1)-\frac{\chi_r}{\chi}(z\overline{AR}+1)\right] \\ &= f(t)\int_0^{\chi_h}\int_{\frac{zb\chi}{a}}^{b} p(x,y)\,x\,dy\,dx \\ &+ f(t)\int_0^{zb\chi_h}\int_{\frac{a\chi}{zb}}^{a} p(x,y)\,y\,dx\,dy \\ &- nwa^3\overline{AR}\chi^2\left[\overline{AR}z^2\left(\frac{1}{2}-\frac{\chi}{3}\right)+\frac{1}{2}-\frac{z\chi}{3}\right] \\ &- FM_u(1+\overline{AR})a \quad , \end{aligned}\right\} \quad (1)$$

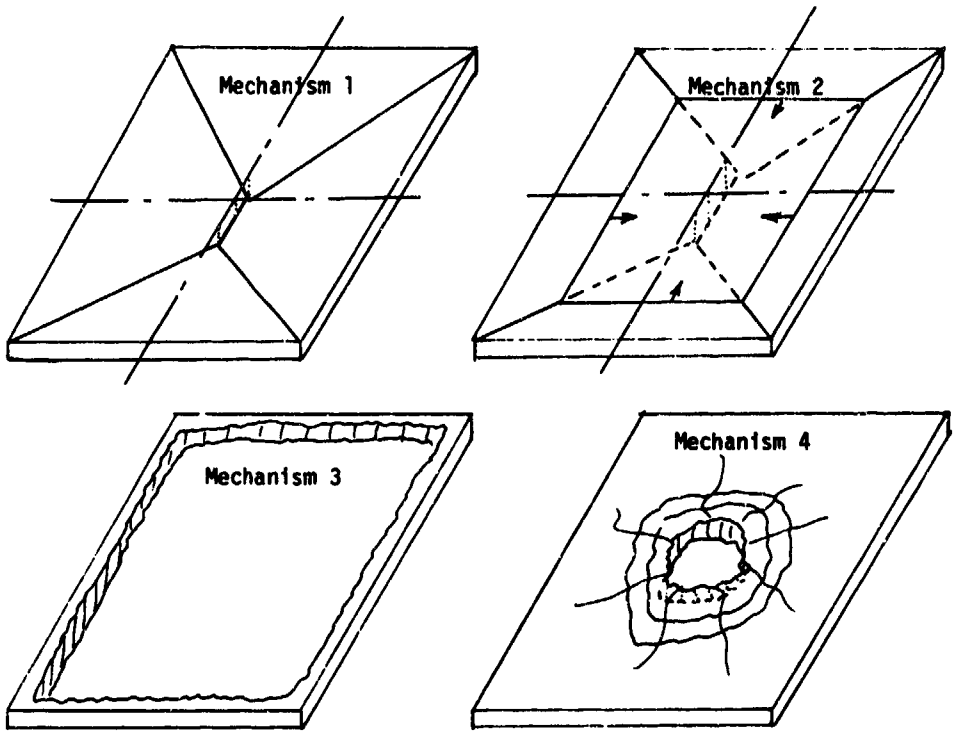

Figure 1. Plate response and failure mechanisms.

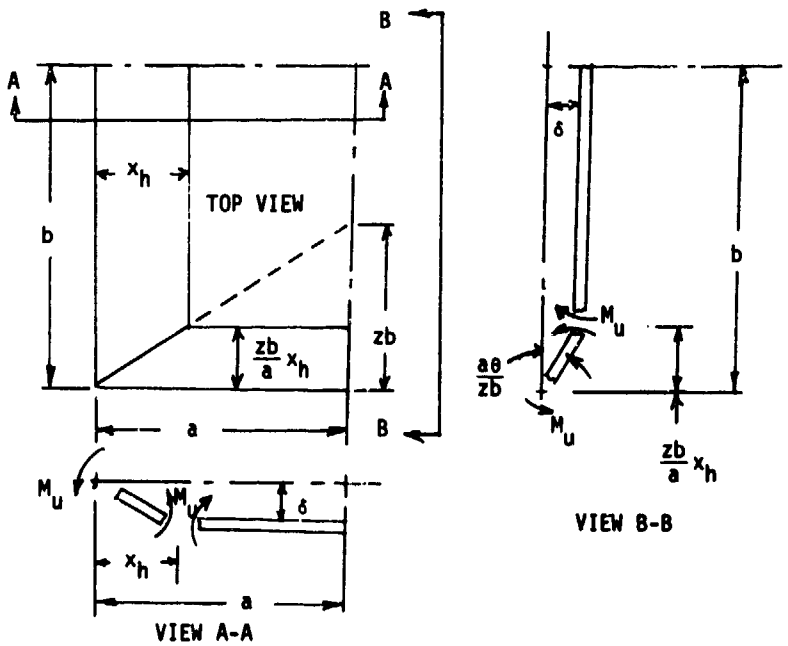

Figure 2. Schematic of plate response.

and for the flat portion (3) the equation of motion is

$$\left.\begin{aligned} & m(1-X)(1-zX)ab\ddot{\delta} \\ & = f(t)\int_{x_h}^{a}\int_{\frac{zbx_h}{a}}^{b} p(x,y)dydx \\ & - nw(1-X)(1-zX)ab \end{aligned}\right\} \quad (2)$$

where:

m	mass per unit area
$\overline{AR}$	aspect ratio = b/a
X	x_h/a
zb	final hinge position
f(t)	time variation, load function
p(x,y)	spatial variation, load function
F	hinge moment multiplier, natural hinge F = 1, fixed edge F = 2
M_u	plastic hinge moment/unit dist.
a,b	plate dimensions
n	loading direction, loaded below n=1.0, loaded above n=-1.0
x_h	hinge length
x,y	plate coordinates
θ	hinge rotation angle
w	weight per unit area
δ	center point deflection

The initial position of the hinge may be determined by the initial conditions

$$\left.\begin{aligned} & \ddot{\theta}ax = \ddot{\delta} \\ & f(t) = 1.0 \end{aligned}\right\} t = 0.0 \quad (3)$$

If the initial response is a Mechanism 2 then the hinge motion is towards the Mechanism 1 mode as shown in Figure 1. The spatial integration of Equations (1) and (2) are performed numerically using a method of Reference [4] and resulting differential equations are solved numerically using a fourth order Runge-Kutta method of Reference [5]. Failure is assumed to occur when a reinforcing element fails in tension. This criterion is incorporated into the computer model.

Edge shear failure, defined as complete severance of the plate from the supports at the edges is assumed to occur when the internal hinge forms at the edges. This may be analyzed in a fashion similar to a metal beam analysis of Reference [6] where a critical velocity for complete severance at the edges is calculated. The result of this analysis gives the critical velocity as

$$\dot{\delta}_{cr} = (2\sqrt{2}/3)(\sigma_{ud}/\rho)^{\frac{1}{2}} \quad (4)$$

which is independent of the dimensions of the plate and depends entirely on σ_{ud}, the ultimate dynamic tensile strength of the reinforced concrete slab and the slab density ρ. The critical specific impulse, I_{cr}, required to cause shear failure may be expressed as

$$I_{cr} = \rho h\dot{\delta}_{cr} = (2\sqrt{2}/3)(\rho\sigma_{ud})^{\frac{1}{2}} \quad (5)$$

where h is the slab or plate thickness. Using a linear rule of mixtures for density and dynamic tensile strength σ_{ud} the critical impulse becomes

$$I_{cr} = (2\sqrt{2}/3)h\left\{\left[(1-q)\rho_c+q\rho_r\right]\left[(1-q)\sigma_{cd}+q\sigma_{rd}\right]\right\}^{\frac{1}{2}} \quad (6)$$

where q is the volume ratio of reinforcing element and subscripts c,r refer to concrete and reinforcing element respectively. The applied specific impulse is given generally as

$$I_{ap} = \int_0^{\tau_{cr}} p(t)dt \quad (7)$$

where p(t) is the time varying uniform load and τ_{cr} is a critical time for shear response, on the order of a quarter period of the fundamental flexural mode or the period of the third or fourth flexural mode. When I_{ap} exceeds I_{cr}, then shear failure at the edges is assumed to occur.

For localized shear failure, a static localized hinge mechanism given in Reference [7] and shown in Figure 3 was used. Again the critical velocity/impulse criterion was used in the following manner.

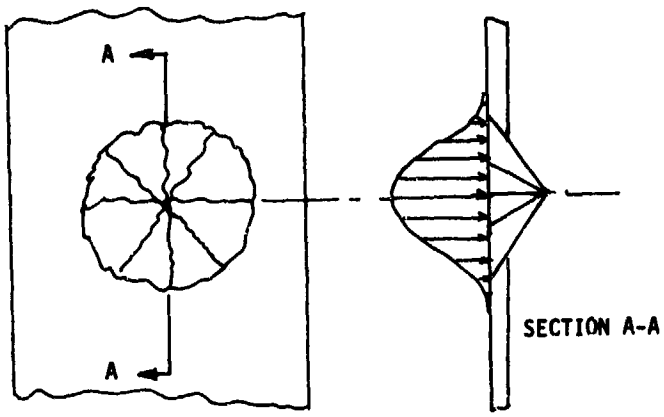

Figure 3. Schematic of localized breach by shear.

1. A loading symmetric about either axis through the plate center was assumed.

2. Starting with an initial radius equal to the thickness of the plate, an average specific impulse $\bar{I}$ is determined by

$$\bar{I} = \frac{4}{\pi h^2}\int_0^{t_{cr}}\int_0^{h}\int_0^{2\pi} p(\beta,r,t)\,d\beta\,dr\,dt \qquad (8)$$

3. If $\bar{I}<I_{cr}$ then localized shear is assumed not to occur. If $\bar{I}>I_{cr}$ then increment h to h+dh and recalculate $\bar{I}$ until $\bar{I}<I_{cr}$.

4. The value of h+dh where $\bar{I}$ is slightly greater than I_{cr} becomes the breach radius for localized shear.

Localized shear failure coupled with flexural response is of interest where a slab is resting on soil containing a localized explosion. This problem is treated by determining the breach radius and then removing the breached volume and associated loading. The flexural response using a Mechanism 1 response is then used to calculate the upheaval of the remaining slab.

The loading function is written generally so that either cylindrical or spherical explosive shapes may be used. Details of these functions are given in Reference [1].

BURIED RECTANGULAR STRUCTURES

A typical analysis was performed on a generic reinforced concrete rectangularly shaped personnel shelter approximately 8 feet high, 12 feet wide, 100 feet long and 12 inches thick. The structure wall was assumed to behave as a simply-supported plate with the explosive charge fully coupled into the soil. The load on the structure was characterized by an exponentially decaying pressure-time history with a user-defined decay constant. The spatial variation of pressure was characterized by the Hopkinson or "cube root" scaling function with user defined constants [Reference 8]. The explosive charge was idealized as an uncased spherical charge located at various standoff distances from the structure [Reference 9]. Figure 4 contains the complete input and output data for one such analysis. The standoff distances (Z1 and Z2) and the pressure durations were varied as the charge was moved from 10 to 40 feet from the structure wall. Additional examples are contained in Reference [1].

RESULTS FOR BURIED RECTANGULAR STRUCTURES

The results of the individual analyses are summarized in Figure 5. As the weapon is moved away from the wall, the structural response becomes progressively less until there is insufficient pressure to give a response. The fact that the tension reinforcement fractures in flexure indicates that the centerline deflection is excessive. When the results are tabulated in this manner, the response spectrum is readily apparent and easily quantified. Approximately 35 minutes of central processor time was required for all eleven analyses. Reference [1] contains additional examples with favorable comparisons to experimental data.

Weapon Standoff (feet)	Breach Radius (inches)	Tension Reinforcement Fracture in Flexure	Max Centerline Deflection (inches)
10	48.0	YES	N/A
13	48.0	YES	N/A
16	35.5	YES	N/A
19	NONE	YES	N/A
22	NONE	NO	11.89
25	NONE	NO	4.83
28	NONE	NO	1.63
31	NONE	NO	0.39
34	NONE	NO	0.04
37	*	*	*
40	*	*	*

*Insufficient pressure to give response.

Figure 5 Summary of Results for a Buried Rectangular Structure

CALCULATIONS ON A CONCRETE PLATE
BURIED RECTANGULAR STRUCTURE (SPHERICAL CHARGE) 10 03/01/11. 11.29.44

INPUT VALUES

PLATE HALF WIDTH OR BEAM HALF SPAN, IN.	(A)	48.000000
BEAM OR PLATE THICKNESS, IN.	(H)	12.000000
LENGTH TO WIDTH RATIO, DIMENSIONLESS	(AR)	1.5000000
MASS PER UNIT AREA, LBS-SEC.SQ/IN.CUBED	(SMALLM)	.27000000E-02
POWER FROM PRESSURE-LAMBDA CURVE	(EN)	3.0000000
UNIFORM PRESSURE LOAD, PSI	(PU)	0.
PRESSURE DECAY, DIMENSIONLESS	(ALPHA)	5.0000000
PRESSURE DURATION, SEC.	(TAU)	.25000000E-01
SUPPORT FACTOR: 1=SIMPLY, 2=CLAMPED	(F)	1.0000000
WAVE FUNCTION: 1=GENERAL, 2=SQUARE	(WAVEFN)	1.0000000
WEIGHT VECTOR: 0=YES, 1=EXP BLW, -1=EXP ABV	(SMALLN)	0.
REINFORCEMENT DENSITY, LB.-SEC.SQ./IN.**4	(RHOR)	.73400000E-03
CONCRETE COMPRESSIVE STRENGTH, PSI	(SIGMAC)	4000.0000
REINFORCED STEEL YIELD STRESS, PSI	(SIGMAR)	60000.000
REINFORCEMENT RATIO IN TENSION, DIMENSIONLESS	(Q)	.65400000E-02
REINFORCING DISTANCE, IN.	(D)	11.000000
DIAMETER OF EXPLOSIVE, IN.	(BIGD)	25.740000
PRESSURE INTERCEPT ON P-LAMBDA CURVE	(SMALLP)	3812.0000
EXPLOSIVE WEIGHT, LBS.	(BIGW)	300.00000
LENGTH OF EXPLOSIVE, IN.	(BIGL)	25.740000
X 1 OF EXPLOSIVE, IN.	(EX1)	48.000000
X 2 OF EXPLOSIVE, IN.	(EX2)	96.000000
Y 1 OF EXPLOSIVE, IN.	(EY1)	72.000000
Y 2 OF EXPLOSIVE, IN.	(EY2)	72.000000
Z 1 OF EXPLOSIVE, IN.	(EZ1)	120.00000
Z 2 OF EXPLOSIVE, IN.	(EZ2)	120.00000
SHEAR STIRRUP REINFORMENT RATIO	(QI)	.16350000E-02
TIME INCREMENT, SEC.	(TINCR)	.10000000E-03
TIME MAXIMUM, SEC.	(TMAX)	.10000000E-01
TIME STEP INTERVAL PER PRINTED LINE, SEC.	(TPRINT)	.50000000E-03
CRITICAL TIME, SEC.	(TCR)	.25000000E-01

COMPUTED CONSTANT VALUES

PLATE HALF LENGTH, IN.	(B)	72.000000
RATIO OF FINAL HINGE LOC TO B, DIMENSIONLESS	(Z)	.83142233
HINGE MOMENT, IN.-LBS./IN.	(BIGRU)	40259.024
WEIGHT PER UNIT AREA, LBS./IN.SQ.	(W)	1.0432000
ORIGINAL HINGE LOCATION, IN.	(XH)	12.000096

SIMPLY-SUPPORTED GENERAL TIME FUNCTION VERTICAL WALL BLAST LOAD

CALCULATIONS ON A CONCRETE PLATE LOCALIZED SHEAR FAILURE CALCULATION

BURIED RECTANGULAR STRUCTURE (SPHERICAL CHARGE) 10 03/01/11. 11.29.44
SIMPLY-SUPPORTED GENERAL TIME FUNCTION VERTICAL WALL BLAST LOAD

BREACH RADIUS	I BAR	I CRITICAL
12.000000	13.601092	4.8161584
48.000000	13.821018	4.8161584

CALCULATIONS ON A CONCRETE PLATE FLEXURAL RESPONSE ASSUMING NO LOCALIZED SHEAR FAILURE

BURIED RECTANGULAR STRUCTURE (SPHERICAL CHARGE) 10 03/01/11. 11.29.44
SIMPLY-SUPPORTED GENERAL TIME FUNCTION VERTICAL WALL BLAST LOAD

TIME (SECONDS)	THETA (RADIANS)		MIDPT. VEL. (IN./SEC.)	MIDPT. DELTA (INCHES)	PRESSURE WORK (IN.-LBS.)	PLASTIC WORK (IN.-LBS.)	KINETIC ENERGY (IN.-LBS.)	HINGE LOCATION (INCHES)
0.	0.		0.	0.	0.	0.	0.	
.10000C000E-03	.11259781E-01		1867.52248	.18453432	.44299879+5	.30279B8.39	.4229910.1	
.20000C000E-03	.45282701E-01		1873.4622	.55712608	.13156807E+06	.9171975.15	.1269874.5	
.30000C000E-03	.92503780E-01		1873.9966	1.2086569	.26913806E+06	.1868045.0	.2584911.3	
.40000C000E-03	.15743940		1875.0015	2.0728117	.45000875E+06	.2811232.4	.3871993.2	
.50000C000E-03	.23487685		1881.7665	3.1292059	.6799972E+06	.4194291.1	.5774124.1	
.60000C000E-03	.32312117		1899.0280	4.3478233	.9021454E+06	.5611228.1	.7727124.1	
.70000C000E-03	.42013239	*	1931.0269	5.7193293	.1170320E+07	.7261102.1	.9977124.1	
.80000C000E-03	.52334225	*	1981.0669	7.2228244	.1457126E+07	.9041102.1	.1242124.1	
.90000C000E-03	.63248178	*	2054.0369	8.8981259	.1781812E+07	.1104102.1	.1517124.1	
.10000C000E-02	.74268805	*	2151.7716	10.817855	.2144785E+07	.1329102.1	.1826124.1	
.11000C000E-02	.85294723	*	2270.6078	12.967133	.2545967E+07	.1577102.1	.2167124.1	
.12000C000E-02	.96328075	*	2401.9368	15.346733	.2985350E+07	.1849102.1	.2541124.1	
.13000C000E-02	.10735170	*	2537.9965	17.956710	.3462933E+07	.2144102.1	.2947124.1	
.14000C000E-02	.11837177	*	2671.1648	20.797210	.3978717E+07	.2463102.1	.3386124.1	
.15000C000E-02	.12937138	*	2794.5548	23.868310	.4532701E+07	.2805102.1	.3858124.1	
.16000C000E-02	.14034847	*	2904.1289	27.170114	.5124886E+07	.3171102.1	.4363124.1	
.17000C000E-02	.15130497	*	2997.8017	30.702717	.5755272E+07	.3561102.1	.4901124.1	
.18000C000E-02	.16224087	*	3075.5117	34.466210	.6423858E+07	.3974102.1	.5472124.1	
.19000C000E-02	.17315618	*	3138.2127	38.460686	.7130645E+07	.4412102.1	.6076124.1	
.20000C000E-02	.18405090	*	3187.0000	42.686234	.7875632E+07	.4874102.1	.6713124.1	

TIME EXCEEDED

AN ASTERISK INDICATES THAT A REINFORCING ELEMENT HAS FRACTURED

Figure 4. Example Input and Output Data from REICON

RUNWAY DAMAGE ASSESSMENT

When an explosive device is placed in the soil directly beneath a concrete slab, the response may be one of the following:

a. breach or complete shear of a portion of the slab without appreciable damage to the other portions of the slab,

b. flexural response usually in a Mechanism 1 mode, or

c. combination of a and b.

An optimum depth of burial of the explosive below the concrete slab will give maximum upheaval. This optimum depth may be determined analytically by REICON by initially placing the explosive device in contact with the slab and progressively increasing the distance of the explosive from the slab. At each depth both the breach or shear radius and height of upheaval are calculated. This calculation was performed for an unreinforced concrete slab 20 x 20 ft, 1.0 ft thick resting on sandy soil containing a cylindrical explosive of 6.7 lb located directly beneath the center of the slab. Figure 6 shows the results of this calculation and the significant result shows that the optimum depth for maximum upheaval occurs where the breach radius goes to zero. The experimental results of explosive cylinders, inclined at approximately 30° to the slab normal, show an optimum depth of 34 inches as compared to the average of approximately 35 inches for the curves of Figure 6. This depth is referenced to the midplane of the slab. All the necessary data required for this calculation are found in Reference [1].

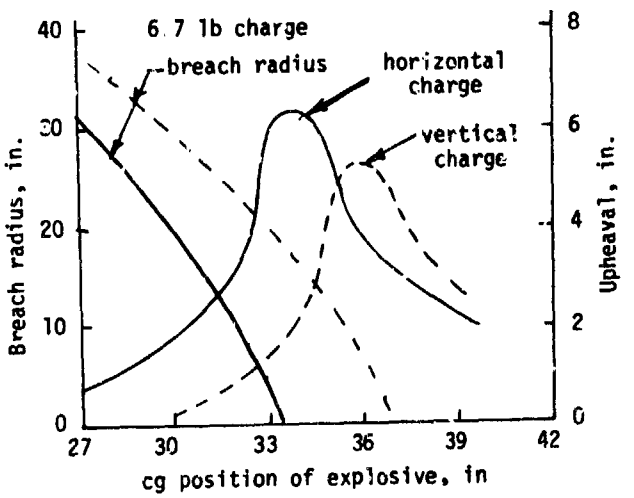

Figure 6. Breach radius and height of upheaval vs cg of explosive below midplane of slab.

CONCLUSIONS

While finite element techniques are very powerful, they usually require large computers and long execution times. Traditional numerical integration techniques coupled together with explicit expressions for the differential equations of motion and energy offer an efficient alternative to solve the structural response of nonlinear dynamic systems. When one considers the accuracy with which most material and loading parameters are known, time consuming analytical calculations are often not justified. The computer program REICON [1] provides a quick and efficient alternative to large, general purpose finite element computer programs and requires a minimum of data preparation and computer execution time.

ACKNOWLEDGEMENTS

The authors wish to express their appreciation for the efforts of the Air Force Armament Laboratory for their assistance in developing and installing the computer code REICON and providing experimental test data.

REFERENCES

1. Ross, C. A., Sierakowski, R. L., and Schauble, C. C., "Concrete Breaching Analysis," AFATL-TR-81-105, USAF Armament Laboratory, Eglin AFB, Florida, December, 1981.

2. Ross, C. A., and Schauble, C. C., "Failure of Underground Hardened Structures Subjected to Blast Loadings," AFOSR TR-79-0679, US Air Force Office of Scientific Research, Bolling Air Force Base, D.C., April, 1979.

3. Ross, C. A., Schauble, C. C., and Nash, P. T., "Response and Failure of Underground Reinforced Concrete Plates Subjected to Blast," The Shock and Vibration Bulletin No. 50, Part 3, Shock and Vibration Information Center, Naval Research Laboratory, Washington, D. C., pp. 71-81, September, 1980.

4. Hildebrand, F. B., Introduction to Numerical Analysis, McGraw-Hill Publishing Company, New York, New York, pp. 71-76, 1956.

5. Hildebrand, F. B., Introduction to Numerical Analysis, McGraw-Hill Publishing Company, New York, New York, pp. 236-239, 1956.

6. Jones, N., "Plastic Failure of Ductile Beams Loaded Dynamically," Trans. ASME Vol 98 Series B No 1, pp. 131-136, February, 1976.

7. Szilard, R., Theory and Analysis of Plates, Classical and Numerical Methods. Prentice-Hall, Inc., Englewood Cliffs, New Jersey, p. 601, 1974.

8. Drake,, J. L. and Little,, C. D. Jr., "Ground Shock from Penetrating Conventional Weapons," Proceedings of Symposium on The Interaction of Non-Nuclear Munitions with Structures, USAF Academy, CO., May 1983.

9. "A Manual for the Prediction of Blast and Fragment Loadings on Structures," DOE/TIC-11268, U.S. Department of Energy, Pantex Plant, Amarillo, Texas, November, 1980.

STRUCTURAL RESPONSE UNDER LOCALIZED DYNAMIC LOADS

Theodor Krauthammer and Mehul Parikh

Department of Civil and Mineral Engineering
University of Minnesota, Minneapolis, Minnesota 55455

ABSTRACT

Studies at the Waterways Experiment Station on the response of reinforced concrete box-type structures under the effects of simulated nuclear detonations and under localized high explosives detonations provided the required data for comparing the structural responses. Analytical studies at the University of Minnesota may provide additional information that can be combined with the experimental results for explaining the nature of the observed behavior and the reasons for such differences. This paper is aimed towards highlighting the two types of behavior, and providing brief discussions on the results of recent experimental and analytical studies.

INTRODUCTION

Current design procedures for protective structures to resist conventional weapon effects are primarily based on WWII technology, and are similar to those described in Ref. (2). The quality of a design procedure can be enhanced by comparison to actual system behavior and by modifying the design recommendations accordingly. As a result it seems to be quite important to be able to accurately describe structural behavior under the effects in which one is interested. At this time there are questions regarding the accuracy of the description and definition of effects and environment, as presented in Ref. (2) or similar documents, but this issue is not under consideration in this paper. One may employ information from other sources, for example Refs. (3,10) in order to better define the anticipated loading conditions, and to provide the designer with more realistic information and recommendations. Furthermore, the purpose of this paper is to discuss and demonstrate the differences in structural response between the cases that were loaded by a simulated nuclear environment and cases where the loading was locally induced by HE devices.

Since the end of WWII most of the research on hardened structural response in the U.S. was devoted to protection from nuclear detonations, and only in the last five years there was a revival of activity in the area of hardening against conventional weapons. In order to understand the nature of the differences between these two environments, as related to blast and shock effects, one has to study the expected loading conditions that could be associated with such events, and to evaluate the structural response accordingly. For nuclear detonations the blast and shock will produce high intensity stress waves that propagate in the ground and reach the structure under consideration. The stress field will interact with the entire structure since the nuclear effects are acting on a large zone in the medium where the structure is located. Under these conditions one may assume that the analysis can be performed by considering the variation of load (i.e. pressure) with time while no significant spatial variation needs to be considered. On the other hand, when conventional detonations are considered the pressure wave propagates from the source of detonation which is located near the structure (in cases where the weapon is far from the structure the loads are rather small due to the steep decay of pressure with distance), and therefore the applied loads are acting on a relatively small area of the entire structure. The loading conditions under conventional weapon effects are therefore defined by a pressure-time history combined with a spatial distribution, and the nature of the structural response is considerably different from that in the nuclear domain.

In order to study and demonstrate the differences in the structural response under these two loading conditions it was decided to obtain test data from field experiments, and to compare analytical with experimental results. Fortunately, such tests were conducted on the same type of structures where the main differences were related to the source of loads. In two series of tests seven reinforced concrete box-type structures were subjected to simulated nuclear blast by employing the HEST technique (1,4, and 6), while in another series similar structures were subjected to the blast and shock effects from the detonation of 9.5kg spherical TNT charges (5). These cases were analyzed by employing an advanced single-degree-of-freedom (SDOF) numerical technique, and the results were compared to the experimental data. Previous studies at the University of Minnesota led to the development of SDOF procedures for studying the response of reinforced concrete structural systems under severe dynamic loads, and the results obtained by such evaluations were quite accurate, as compared to experimental data (1, 4, 7, and 8). As a result, it was decided to employ the same technique for the analysis of the present structural specimens in order to ensure that any difference in results between the two cases will be due to the type of loading condition to be imposed on the structures.

ANALYTICAL APPROACH

The systems under consideration are shallow-buried reinforced concrete box-type structure, as described in Refs. (5, 6, and 7). The response under simulated nuclear blast environment was discussed in Refs. (6 and 9), while the response under HE charges was presented in Ref. (5). The application of SDOF techniques for the analysis of such systems was discussed in Refs. (1, 4, 7, and 8), and is briefly described next.

The structure was represented in the analysis by two resistance functions - one for the flexural response and another for the shear response. In the computation a typical loading function was applied to a SDOF system that included an effective mass, characteristic system damping, and the first resistance function. At each time step various parameters were computed and the flexural central acceleration was used to derive an effective inertia force acting on the slab. That inertia force was applied to a second SDOF system that included the total mass, characteristic structural damping, and the shear resistance function in order to compute the shear response of the slab. In those cases the pressure-time histories that were employed to represent the loading functions for the flexural computations were assumed to be uniformly distributed over the entire slab.

The structural systems under consideration were reinforced concrete box-type structures with internal dimensions of about 4 ft X 4 ft X 16 ft (1.2 m X 1.2 m X 4.8 m) and a wall thickness of 5.6 in (140 mm). The nuclear load simulation was generated by a High Explosive Simulator Technique (HEST) applied to the soil free surface located about 2 ft (0.6 m) above the structure, while the localized HE environment was generated by the detonation of 21 lbs (9.5 kg) of spherical TNT charges at various horizontal distances from the side wall mid-height point. Structural mechanisms for these structures have been described in the literature (1, 4, 7, and 8), and therefore the information will not be repeated here. Nevertheless, the issue of the loading function has to be discussed in order to highlight the differences between the system responses, as presented next.

For the analysis of the structures under the simulated nuclear effects it was assumed to employ a pressure-time history where the peak pressure was the average peak pressure from all pressure gauges. That load was applied as a uniformly distributed pressure over the entire slab. When the localized effects have to be considered, the previous technique for representing the loads is no longer accurate since the pressure function includes a spatial distribution as well as a time variation. If one employs the load definition function from the nuclear domain for the localized (i.e., conventional) problem, the resulting structural behavior, as represented by data from the same numerical approach, will be much more severe than observed experimentally. This is a clear indication that the previous approach for the load definition tends to overestimate the applied loads, and therefore cannot be employed for studying localized effects without fundamental changes.

In order to include the effects of the load spatial distribution on the structural behavior it was proposed to "normalize" the applied pressure through the ratio of the loaded area divided by the total area which is exposed to the ground shock. This procedure has been performed by computing the pressure-time

histories for unit areas of the slab, and including the time-of-arrival of the load at the area of interest. These pressures were integrated over the subareas, and an effective history was computed for the slab. That loading function was applied to the simulated structure for computing the system response.

RESULTS

Structural response under simulated nuclear blast effects, and the comparison to experimental data, is presented in Table 1. A similar comparison has been performed for the structures under the effects of the spherical TNT charges, and the results are presented in Table 2. These results may demonstrate the effectiveness of the proposed approach both for cases in the nuclear domain, and under the HE generated loads. At this time the present effort continues towards modification of the method, and introduction of improved models for loading functions and structural response. Further studies will be performed on the soil-structure interaction issue.

ACKNOWLEDGMENTS

The authors wish to thank Dr. S. A. Kiger from the Waterways Experiment Station for his cooperation. Also, the support of the University of Minnesota Computer Center is gratefully acknowledged.

REFERENCES

1. Bazeos, N., and Krauthammer, T., "An Improved Numerical Approach for the Analysis of Reinforced Concrete Slabs Under the Effects of Dynamic Loads", Structural Engineering Report No. 83-01, Department of Civil and Mineral Engineering, University of Minnesota, March 1984.

2. Crawford, R.E., et al., "Protection from Nonnuclear Weapons", Air Force Weapons Laboratory, Technical Report No. AFWL-TR-70-127, February 1971.

3. Henrych, J., "The Dynamics of Explosion", Elsevier 1979.

4. Holmquist, T.J., and Krauthammer, T., "A Modified Method for the Evaluation for Direct Shear Capacity in Reinforced Concrete Slabs Under the Effects of Dynamic Loads", Structural Engineering Report No. 83-02, Department of Civil and Mineral Engineering, University of Minnesota, May 1984.

5. Kiger, S.A., and Albritton, G.E., "Response of Buried Hardened Box Structures to the Effects of Localized Explosions", U.S. Army Engineer Waterways Experiments Station, Technical Report SL-80-1, March 1980.

6. Kiger, S.A., Getchell, I.V., Slawson, T.R., and Hyde, D.W., "Vulnerability of Shallow-Buried Flat Roof Structures", U.S. Army Engineer Waterways Experiment Station, Technical Report SL-80-7, Reports 1 through 6, Septmeber 1980 through September 1984.

7. Krauthammer, T., "Shallow-Buried RC Box-Type Structure", Proc. ASCE Journal of Structural Engineering, Vol. 110, No. 3, March 1984.

8. Krauthammer, T., "Simplified Analytical Models for Preliminary Evaluations", Proc. 6th International Symposium of Protective Structures, Mannheim, September 25-27, 1984.

9. Parsons, R., and Rinehart, E., "Kachina Test Series: Butterfly Maiden", Air Force Weapons Laboratory, Final Report AFWL-TR-82-132, Vol. I, II, June 1983.

10. Vredblad, V., "Versuche mit Ladungen in Boden - Ergebnisse", Proc. 6th International Symposium on Protective Structures, Mannheim, Spetember 25-27, 1984.

TABLE 1 SUMMARY OF RESULTS: NUCLEAR DOMAIN

Event	Experiment Structural Behavior or Failure Mode	Measured Permanent Deflection Δ (mm)	Average Peak Pressure (MPa)	Computed Permanent Deflection Δ 1 (mm)	Δ1/Δ	Analytical Shear Slip Attained (mm)	Failure Shear Slip (mm)	Time of Failure (m sec)
No. 1*	Flexure	12.7	9.0	16.2	1.28	0.14	5.6	—
No. 2*	Shear	Failed	36.2	Failed	1.0	5.0	5.0	1.02
No. 3*	Flexure	152.4	18.3	152.4	1.0	0.16	4.8	—
No. 4*	Flexure	304.8	20.0	309.9	0.98	0.4	6.0	—
No. 5*	Flexure	78.4	79.0	81.5	1.03	20.3	29.7	—
No. 6*	Shear	Failed	80.2	Failed	1.0	5.8	5.8	1.06
LB**	Flexure	185.4	8.0	182.9	0.99	0.33	3.8	—
				Average:	1.04			

* Data from Ref. [6]

** Data from Ref. [9]

TABLE 2 RESULTS FOR HE ENVIRONMENT

Case	Range [ft]	Analytical Residual Displacement [in]	Analytical Behavior	Observed Experimental Behavior
3C1	8	0.89	No failure	Similar residual displacement No failure
3C2	6	2.35	No failure	Flexural cracking
3C3(1)	4	Computation stopped at 10.61 inches, 0.0116 sec.	Steel failure at 0.0116 sec. with displacement of 10.61"	Flexural failure Excessive permanent deflection of 10.5"
3C5(2)	2.7	Shear failure	Instant shear failure	Massive concrete failure
3D1	8	0.53	No failure	No failure
3D2	6	1.27	No failure	No failure
3D6	4	4.24	No failure	Flexural cracking
3D7(1)	2.7	Excessive deformation of 18.19"	Steel Failure at 0.0061 sec.	Flexural cracking
3D8(2)	2	Shear failure	Instant Shear Failure at 0.0028 seconds	Shear failure

(1) In the experiment, accelerometer was on the opposite side of the slab under observation.

(2) In the experiment, charge was placed horizontally away from the center of the slab.

Simulation of Real Weapon-Effects in Multiple-Driver Shock Tubes

G. Hoffmann

Fraunhofer-Institut für Kurzzeitdynamik
ERNST-MACH-Institut
Eckerstr. 4
7800 Freiburg, Germany

ABSTRACT

To estimate the reaction of structures against weapon effects concerning the pressure caused by their detonation the pressure-time-history must be known. It can by obtained in free-field tests; in the same way the reaction can be achieved. In most cases it is more advantageous to do this in a simulation device e.g. in a shock tube. Assumption is then the agreement of the pressure-time-histories in the free-field and in the device. There are no problems with relatively small shock tubes of constant diameter. But in large facilities this condition is not fulfilled. Constructive aspects force the use of a multiple driver. The consequence is a step in the cross section of the expansion tube. This causes unwanted effects in the pressure decay: So-called pressure spikes arise after the first peak-overpressure, and this is no real weapon effect. In experiments with a model shock tube with an extreme tube step it should be investigated, if there is a possibility of damping or eliminating these spikes. The means developed are described.

1. INTRODUCTION

The pressure-time-history of a detonating weapon at a given distance from the detonation center can be achieved in free-field tests. But in most cases it is more advantageous to simulate those weapon effects e.g. on account of cost, security and reproducibility especially considering large charges. Wellknown means for simulations for this purpose are shock-tubes. The knowledge of their function is presupposed. Generally, there are no problems with small tubes of constant diameter from the beginning in the driver part up to the measuring point in the expansion part.

On account of several reasons shock tubes with diameters of some meters cannot be driven by a same diameter driver-tube. It must consist of single tube elements of small diameter (≤ 1 m). Fig. 1 sketches such a device. Examples are the facilities of the REITER-ALPE in Germany and of GRAMAT /2/ in France. Installing several driver tubes it is obvious that there must be a discontinuous extension in the cross section. The consequence is that the shock fronts emerging from the driver tubes are diffracted, which causes an unwished effect in the pressure-time-history, not found in one of a free detonation.

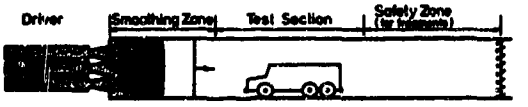

Fig. 1 Multiple Driver Shock Tube/2/

Fig. 2 shows the ideal free-field pressure profile of a weapon, while Fig. 3 presents that one simulated in a shock tube of constant diameter, and Fig. 4 gives an example of the effect in a simulator of the above mentioned kind, where several spikes occur as a result of diffraction and reflection processes. In the interaction with structures, these spikes may cause effects which are different from those of figs. 2 and 3 resp.

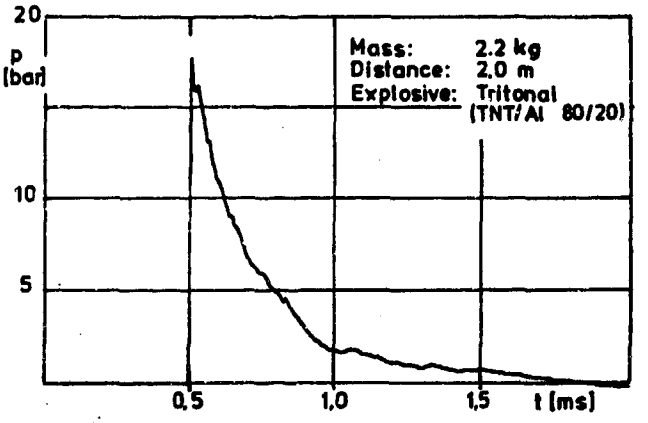

Fig. 2 Pressure-time-history of a Real Weapon

The aim of the investigation is to find constructive means to avoid the spike or at least to damp it to a tolerable value. The most simple way to do so is to lengthen the driven tube to more than ten times the diameter. But at large diameters this would lead to very long devices. This would increase cost and space and not at last it would necessitate a stronger propulsion to get in the farer distance the same peak overpressure as close to the membrane. On the other

hand this can only be a theoretical consideration because in practice diaphragms of meters in diameter are not manufactured.

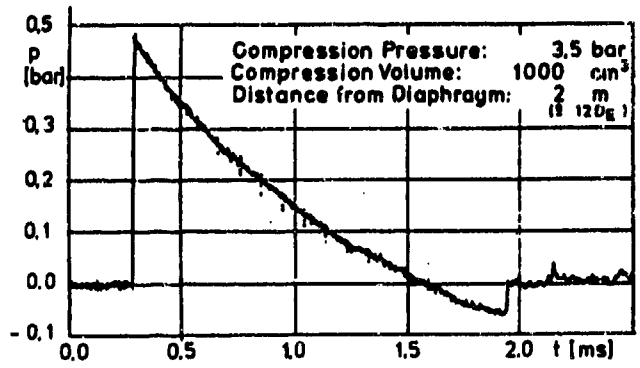

Fig. 3 Pressure-time-history in a Shock Tube of Constant Diameter

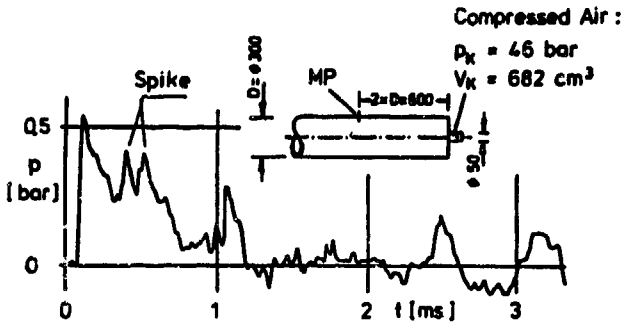

Fig. 4 Pressure-time-history in a Shock Tube with Discontinuous Cross-Section

2. MODEL DEVICE AND EXPERIMENTS

To minimize the costs studies were carried out with a simplified model tube the scaling factor of which was 1:63 in comparison to the GRAMAT device. The simplification consists of only one driver tube instead of several ones but with the same geometric relationship of the cross sections. In Fig. 5 the mean dimensions are sketched. In this version they agree with the GRAMAT device, except for the adaption of tube extension. This was necessary to get a spike-free base curve in the same tube. In this way it can be seen that a diverging one with a small opening angle of 6° from the compression to the expansion tube is another mean to get the wanted pressure profile. But it must also remain out of consideration on account of the long tube extension. The first test had the aim to change the geometry of the tube in such a manner that a very marked spike should arise in the pressure decay.
This was found

- in the case of an unsteady step from a small to a large diameter in the expansion tube (in the described case the relationship of the cross section was a_s = 28.7),
- the nearer the pressure transducer was installed to the diaphragm (therefore, the measuring points were changed to A: 3.2 D_E, B: 5.6 D_E, C: 7.2 D_E),
- the smaller the compression volume (but not too small) and the higher the compression pressure was chosen (best values have been V_K = 25 cm³, p_k = 20 bar).

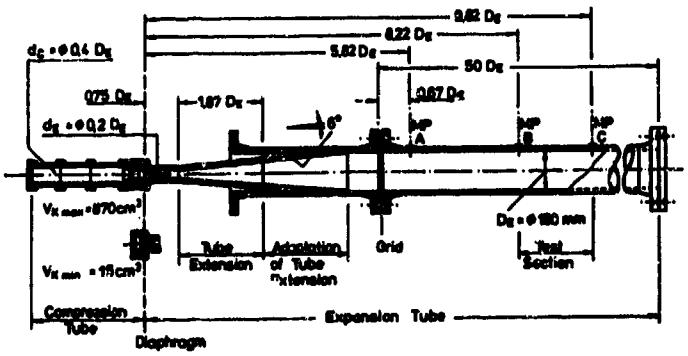

Fig. 5 Model Shock Tube

In an extensive research program a lot of means like mesh wire grids, baffles, multiple cones etc. were tested. But these means turned out not to be very succesful, because they reduced the free cross section in such a way that the peak overpressure and the duration of the overpressure were untolerably diminished.

The essential results of this first test is presented in Fig. 6. The pressure-time-history would only be received at the measuring point B on account of the long divergent nozzle. Curve I shows that an excellent pressure decay, very similar to the one caused by a weapon, is obtained which such a construction. It serves in the latter as the above mentioned base curve. Looking on the diagrams it must be mentioned that the time scale is unallowably extended in order to get a better mark of the spike. In this regard, the second peak, very close to the first peak overpressure, i.e. 0,01 ms later, is absolute an effect of the eigenfrequency of the pressure gage -as it was proved- and, therefore, can not be interpreted as a spike. Comparing the pressure-time-histories II and III the damping effect of the baffles is obvious, but the results are not satisfying since the curve is transmitted to small values, i.e. the reduction is about 50 %. In order to compensate for the pressure in the driver should be enlarged. But the question remains then is this worth to do or are there better means?

After some considerations how to avoid this disadvantage and after some experiments the answer was found in a certain construction which proved to be

successful. To find this construction a second test series was conducted, at the beginning of which was overthought that the pressure-time-history measured at the wall of the tube is only of theoretical interest since in practice a test object is hardly installed there, but on a plane platform near the tube axis. There the pressure profile can differ especially at the beginning of the shock when the front is not yet plane, as it was subsequent experimentally confirmed; see Fig. 7.

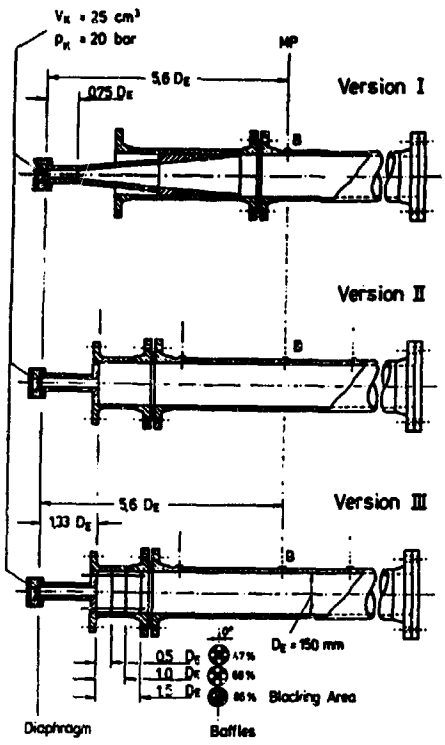

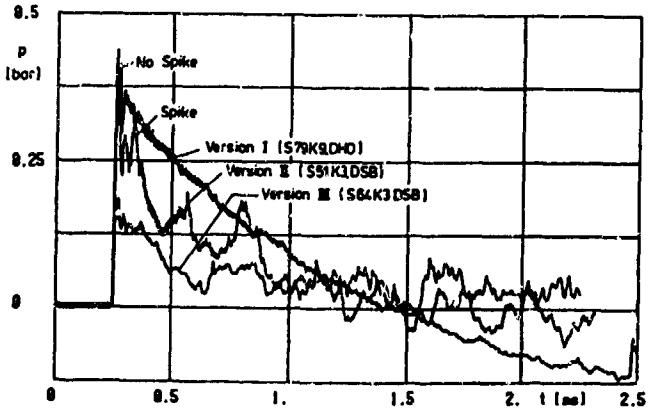

Fig. 6 Comparison of Pressure-time-histories Spike-free (I), Marked Spike (II) Spike-damped (III)

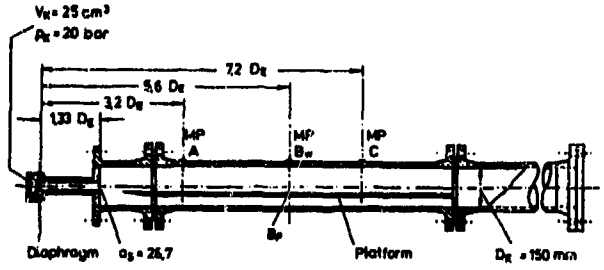

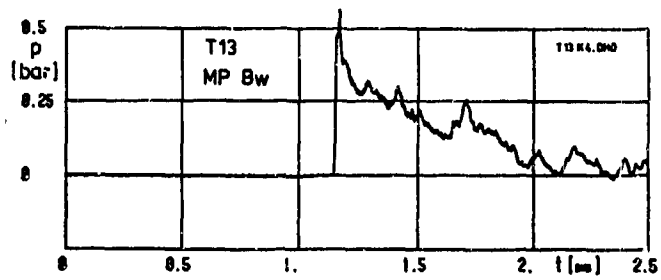

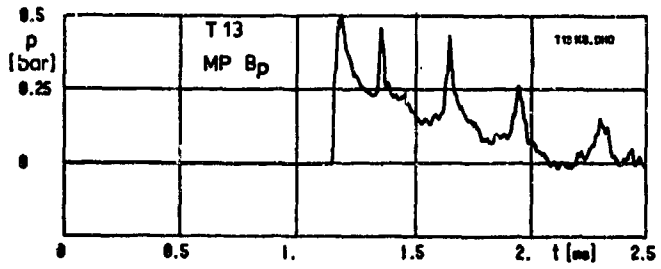

Fig. 7 Pressure-time-histories in the Same Cross Section at the Tube-Wall and at the Platform

Fig. 8 visualizes how the spike develops. It shows a section of the tube beginning at the transmission from small to large diameter (left side) up to the right of the cross section where the transducers "A" are installed. This cut was chosen -instead of "B"- because here the shock fronts are very clear. In the left picture -taken from a 24 pictures-serie- the incident shock front has just reached the edge of the measuring platform; in the meantime fronts reflected at the tube wall are walking to the axis, which are contacting in the next picture the vortices at the mouth of the small tube. The important shadowgraph for the spike is the right one. The incident -now nearly plane- shock front is running over the gage, installed in the middle of the support of the platform (black square). This front causes the overpressure peak; that one at the upper wall is produced by a MACH-stem. The spike will arise when the foot point of the reflected front, which is connected to the MACH-stem, overruns the gage. It is now very obvious that the spike is no real weapon effect but involved to the simulator and therefore it must be damped or eliminated for a correct simulation.

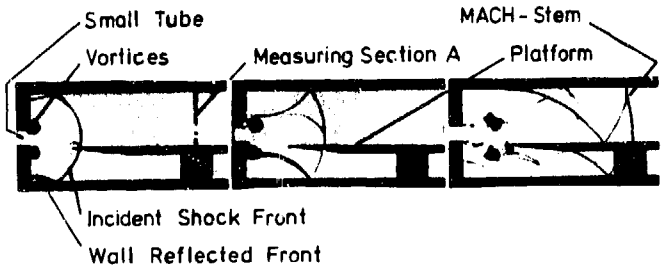

Fig. 8 Shadowgraphs of the Shock

From this picture it can also be derived where one has to start against the spike: On the one hand at the small tube mouth on the other at the tube wall. Consequently a lot of ideas were developped in this direction. The most striking constructions are shown in Fig. 9 and Fig.10. To smoothen the unsteady transition from small to large diameter two kinds of short cones with a "wave-breaking" surface were inserted. One of them has the coarse profile of a comb or a series of teeth in its cross section -it is, therefore, called "tooth cone"- the other one with fine triangle spikes in its profile is called "spike cone". In one test serie on the platform a board as a test object was inserted at the measuring point. This board contained also pressure gages at the side wall, on the roof and the front wall. Unfortunately a splinter of the diaphragm destroyed the front wall gage and, therefore, a wide meshed splinter barrier grid was installed. Fortunately having also smoothing effect on the spike it was retained in the further. Fig. 9 gives an idea of these means.

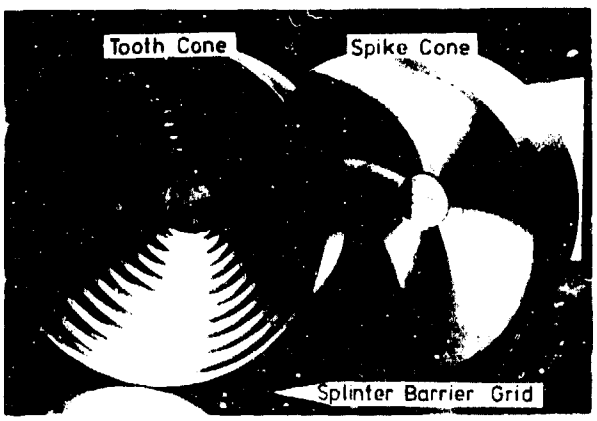

Fig. 9 Special Extension Cones

In order to disturb the reflection at the wall an inner coating of it was assigned consisting of perforated sheets and mesh grids. The perforated tunnels were manufactered with two bores, one 10 mm diameter the other 5 mm. The distance to the wall was chosen with 10 mm. The grid tunnel could be combined with the perforated tunnels as another, inner coating of them, as Fig.10 shows. The length of the tunnels were the same as that one of the platform. With the perforation it should be achieved that a part of the shock front is earlier reflected at the coating sheet,another -passing the bores- not before striking the tube wall. In this way the shock fronts are "minced" and the "pieces" are following another in short time distances and superposing themselves; thus a damping effect is obtained.

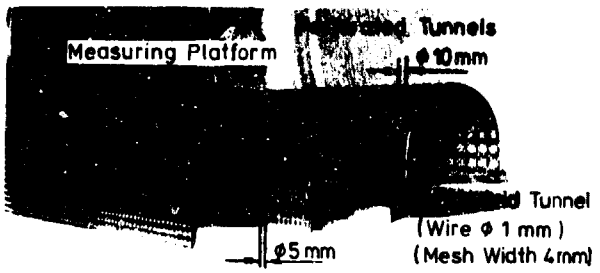

Fig.10 Damping Tunnels

All these constructive components, presented in Fig. 9 and Fig.10, were combined in a convenient manner. The pressure-time-histories were registered at the wall and on the platform in the three cross sections A,B,C, already mentioned. The best results were achieved with the components as they have been installed in the tests numbered T 53, T 56, T 59.To evaluate the improvement the best method is to compare all the pressure-time-histories because the whole decay gives the best overview, but on account of so many plots it is not very easy to survey especially in this presentation.

Construction		Platform			
		Splinter Barrier Grid			
		Tooth Cone		Spike Cone	
Legend: p, p_{so}, p_{ws}, t	without	-		Perf.Tun.10	Perf.Tun. 5
		Mesh Grid T.		-	Mesh Grid T.
	T 19	T 53		T 56	T 59
Meas. Point		Pressure relation p_{so}/p_{ws}			
Wall A		1,42		1,14	1,17	1,17
Wall B		1,52		1,09	1,56	NS
Wall C		1,17		NS	NS	NS
Platform A		6,82		6,25	5,32	5,34
Platform B		1,75		1,24	1,39	1,39
Platform C		1,74		1,32	1,19	1,17

Table 1: Relation of Spike Overpressure p_{so} to the Pressure p_{ws} without Spike for Different Components (NS ≙ NO Spike)

At the point where the most striking spike arises a discrete degree of evaluation can be seen in the relation of the spike overpressure p_{so} to that pressure p_{ws} in the decay , which would be obtained if no spike occured at this time. These values are gathered in table 1, separated for the measuring point at the wall and on the platform, resp. If the relation $p_{so}/p_{ws} = 1.00$ the spike is completely eliminated, i.e at no time the point p_{so} can be found in the curve decay and, therefore, it is marked with NS (No Spike). To be able to estimate the improvement the values of the test (T 19) without

any installed component is included in table 1. As can it be seen, the damping effect is considerably good especially at the wall, also at measuring point A_W which is very close to the tube step. An exception seems to be MP B_W for test T 56. But looking at the whole pressure profile plotted in Fig.11 it can be neglected because the spike appears very late at a small pressure level and that is why the relation is so bad. The more important pressure-time-histories on the platform are not improved as well, but nevertheless it can be called a good progress. From Fig. 11 also can be seen that there is no big difference between T 56 and T 59. What is very striking in table 1 are extremely high relation values for MP A_p (platform). They are obtained because the peak overpressure is unexpectedly low -about the half or even less of the normal hight- and the spike is extremely high.

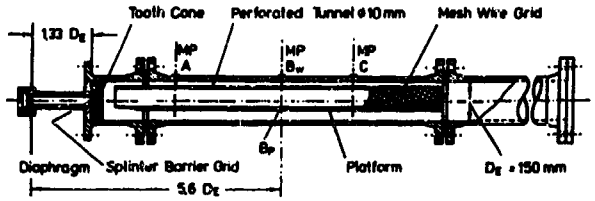

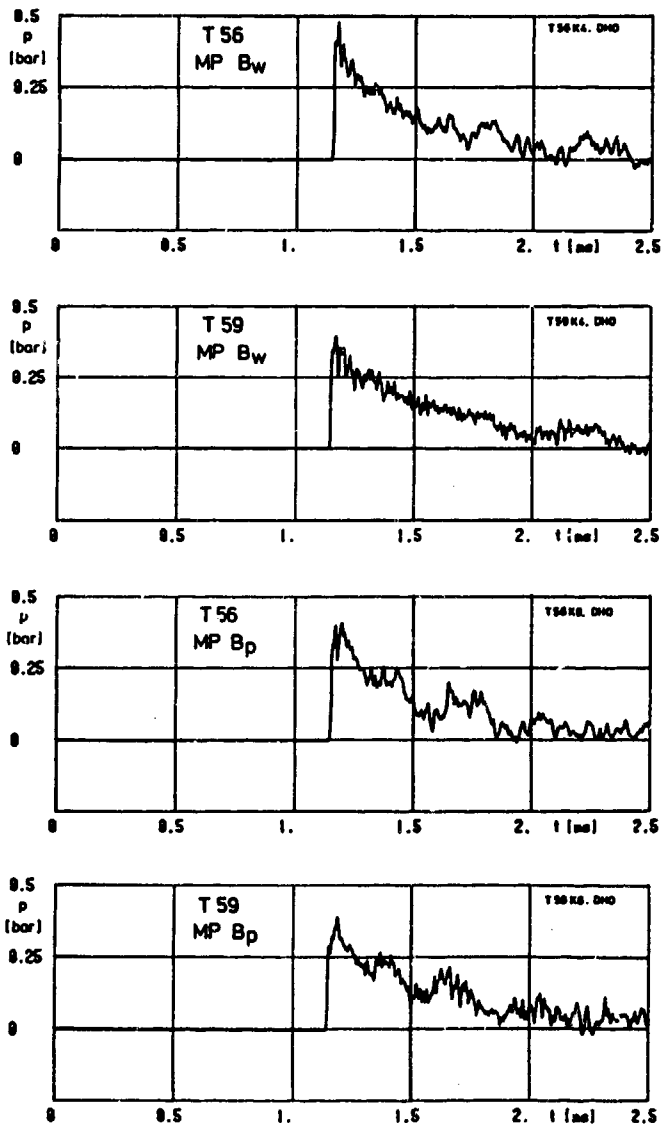

Fig. 11 Spike Damped Pressure-time-history

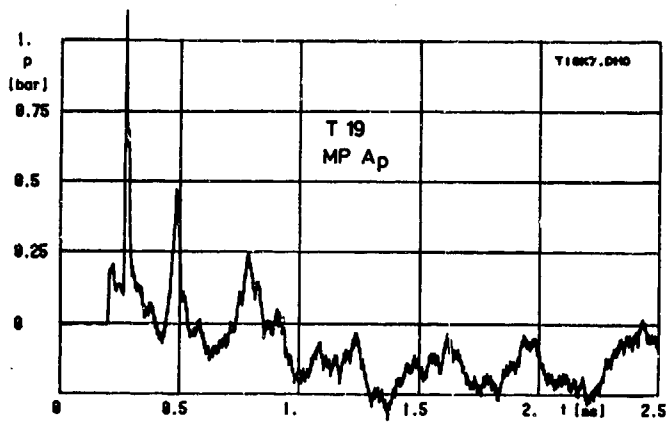

Fig. 12 Pressure-time-history at MP A_p (Platform) without Components (T 19)

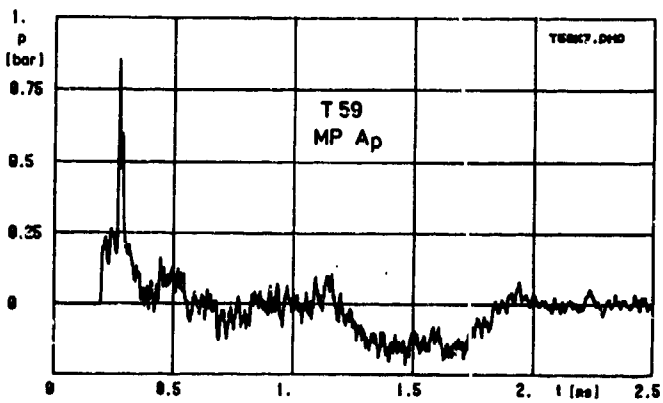

Fig. 13 Pressure-time-history at MP A_p (Platform) with Components (T 59)

Fig. 12 and Fig. 13 show the appertaining pressure-time-histories to this measuring point. The damping effect is remarkable, too, but only for the second spike and so on. It is also obvious from these plots that it is not opportune to install a test object so close to the step (in this case nearer then 3.2 D_E) because one is amidst in the diffraction zone where the shock front is not yet well formed. Perhaps the first spike could be better damped if the

tunnel was extended to the cross section of the tube step. This is not yet tried being of no great interest.

In the beginning of this presentation the argument was given why the time-scale for all the pressure-time-histories was inadmissably enlarged. Therefore, finally the representative pressure-profiles are plotted time-correctly in Fig. 14 and Fig. 15.

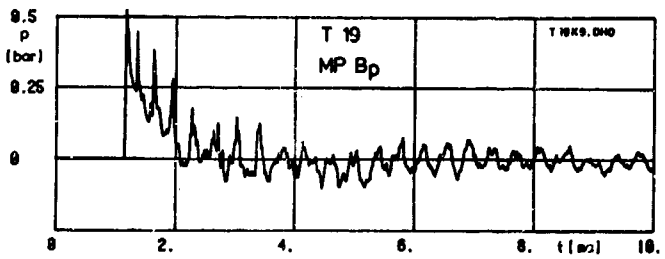

Fig. 14 Time-correct Pressure-time-history on the Platform without any Component

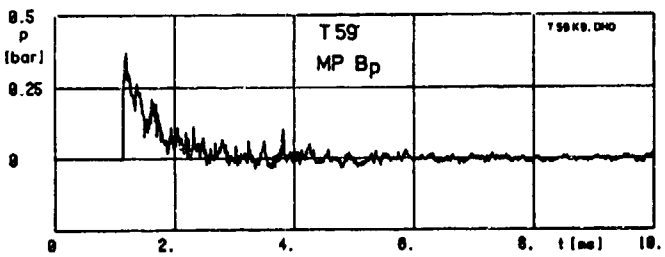

Fig. 15 Time-correct Pressure-time-history on the Platform with Components According to Test T 59

The example shows the measurements on the platform at the measuring point B, i.e. in a distance of 5.6 D_E from the diaphragm. In the contrast of these diagrams the remarkable progress in damping the spikes is obvious. Not yet as smooth as the pressure-time-history of non-stepped shock tube (see Fig. 3) it encourages to do more work in this field.

3. CONCLUSIONS

The described experiments have shown that there are constructive means installed in a shock tube with unsteady stepped cross section which can damp or even eliminate spikes in the pressure decay. Thus it is possible to simulate real weapon effects whose pressure profile is " spikeless" more accurate as before. The studies are just at the beginning; much work has still to be done to optimize the results. Points of investigation will be

- to change the volume and pressure in the driver of the tube in order to simulate any weapon,
- to improve or simplify, resp. the components
- to enlarge the model tube on account of scaling effects,
- to use more than one driver as it is necessary for large simulation facilities.

4. REFERENCES

/1/ Gratias, S., Monzac, I.B.G.
Le Simulateur de Souffle a Grand Gabarit du Centre d' Etudes de GRAMAT: Conception, Etudes Performances
7. Int. Symp. on Milit. Appl. of Blast Simulation
Canada,July 1981

Cadet, H., Monzac, I.B.G.
Le Simulateur de Souffle a Grand du Centre d'Etudes de GRAMAT: Description et Utilisation Operationelle
7. Int. Symp. on Milit. Appl. of Blast Simulation
Canada, July 1981

/2/ Amann, H.O.
Personal Information
Ernst-Mach-Institut, Freiburg
Germany, 1984

DESIGN OF BURIED STRUCTURES FOR CONVENTIONAL WEAPONS THREATS

James T. Baylot
and
Sharon B. Bellue

USAE Waterways Experiment Station
Vicksburg, Mississippi

ABSTRACT

TM 5-855-1, "Fundamentals of Protective Design for Conventional Weapons," has been revised to include recent test data and design methodology on conventional weapons effects. This manual provides methods for determining loads on buried structures from conventional weapons and outlines procedures for designing those structures. These procedures are discussed, and a typical roof slab design example is presented. Methods of designing exterior and interior walls are discussed.

INTRODUCTION

TM 5-855-1, "Fundamentals of Protective Design for Conventional Weapons," has recently been revised and is currently being reviewed. This manual provides information on a wide variety of weapons effects as well as information on how to design structures to resist the loads transmitted to them by these weapons. Some of the subjects covered include:

Non-Nuclear Weapon Characteristics
Ground Shock Cratering and Ejecta
Loads on Structures
Mechanics of Structural Elements
Dynamic Response of Structures

The purpose of this paper is to provide an example of how the information contained in TM 5-855-1 may be used to design a buried structure. A design example is presented, and the methods used are discussed and evaluated.

Figure 1 shows a plan view of the structure which was analyzed. This is a reinforced concrete structure that is buried under 7 ft of earth, which is in turn covered by a 3-ft-thick detonation slab. The structure was designed for a direct hit from a 500-lb general purpose (GP) bomb. Design calculations for the roof slab and interior walls are presented, and the design of the exterior wall is discussed. Information concerning weapon penetration and detonation slab design is provided in the manual but will not be covered in this paper. The worst case for design of the roof slab would be the 500-lb bomb detonating directly over the center of Room A, as shown in Figure 1.

DESIGN OF ROOF SLAB OF ROOM A

Normally, the design of a hardened structure is a trial-and-error procedure. A trial section is selected and analyzed. A new trial section is then selected based on the results of the analysis. Only the final analysis is presented in this paper. Equation, figure, table, and section numbers refer to those of the revised version of TM 5-855-1.

The following values were used in the design:

Long span length (L_L)	- 87 ft
Short span length (L)	- 33 ft
Roof thickness (t)	- 48 in.
Effective depth (d)	- 45.5 in.
Tensile steel ratio (p)	- 0.004
Tensile strength of steel (f_y)	- 60 ksi
Unconfined compressive strength of concrete (f'_c)	- 4 ksi
Weapon penetration into detonation slab (X)	- 24 in.

The following characteristics of a 500-lb GP bomb were taken from Table 2-4:

Total gross weight	- 520 lb
Charge-to-weight ratio	- 51%
Length	- 45 in.

DESIGN PROCEDURE

The following procedure was used to check the design of the roof slab:

1. Determine loading on roof.
2. Determine natural period of roof.
3. Determine equivalent static load.
4. Check capacity of roof slab in flexure.
5. Check shear capacity of slab.
6. Determine support reactions.

ROOF SLAB LOADING

Coupling Factor

For a 45-in.-long bomb and a 24-in. penetration, the center of gravity of the charge will be located near the top surface of the slab. The procedure from Section 5-1.d.3 may be used to

calculate the coupling factor for a charge in contact with more than one material. Figure 5-3 (Figure 2) was used to calculate the coupling factor for each material, using a depth of penetration (d) of 0 ft. Equation 5-6 was then used to obtain the overall coupling factor.

From Figure 5-3

Coupling factor for concrete (f_c) = 0.85
Coupling factor for air (f_a) = 0.14

Equation 5-6 averages the coupling factors based on the weight of the charge in contact with each material.

For the two materials considered:

$$f = f_a\left(\frac{W_a}{W}\right) + f_c\left(\frac{W_c}{W}\right)$$

where W_a and W_c are the weights of charge in contact with air and concrete, respectively

W = Total charge weight

Assuming half the charge is in contact with each material, and substituting f_a and f_c:

$$f = 0.14(.5) + 0.85(.5) = 0.495$$

Peak Pressure at Center of Slab

Free-field pressures and impulses may be computed using equations from Chapter 5. From Table 5-1, the soil properties for calculating ground shock parameters for a dry sand are:

Seismic velocity (c) = 1,000 fps
Acoustic impedance (ρc) = 22 psi/fps
Attenuation Coefficient (n) = 2.75

Peak pressure is calculated using Equation 5-5a. Charge weight (W) is 0.51 x 520 = 265 lb. R is the distance from the bomb center of gravity to the roof, in feet.

$$P_o = f(\rho c)160\left(\frac{R}{W^{1/3}}\right)^{-n} \qquad (5\text{-}5a)$$

The peak pressure (P_c) at the center of the slab is calculated using Equation 5-5a and a range (R) of 10 ft.

$$P_c = (0.495)(22)(160)\left(\frac{10}{265^{1/3}}\right)^{-2.75} = 515.8 \text{ psi}$$

Duration of Pressure Pulse

The positive phase duration varies across the slab. The duration is short near the center and longer near the supports. The equivalent triangular duration at the quarter point of the slab was used as an average duration for design; therefore, this duration was computed. The range from the weapon to the quarter point of the span is 12.96 ft. The pressure P_{qp} is calculated by substituting into Equation 5-5a.

$$P_{qp} = 252.6 \text{ psi}$$

The total impulse (I_o) is calculated using Equation 5-5e.

$$\frac{I_o}{W^{1/3}} = (f)(p_o)(1.1)\left(\frac{R}{W^{1/3}}\right)^{(-n+1)} \qquad (5\text{-}5e)$$

$$\rho_o = 144\left(\frac{\rho c}{c}\right)$$

$$I_{qp} = (265)^{1/3}(.495)(144)\left(\frac{22}{1,000}\right)(1.1)\left(\frac{12.96}{(265)^{1/3}}\right)^{-1.75} = 3.24 \text{ psi-s}$$

For a triangular pressure pulse, the duration is given by

$$t_d = \frac{2I}{P}$$

Therefore

$$t_{qp} = \frac{2I_{qp}}{P_{qp}} = \frac{2(3.24)}{252.6} = 0.0256 \text{ sec} = 25.6 \text{ msec}$$

Equivalent Uniform Pressure

The loads on the roofs of underground structures are not uniform, especially if the depth of burial (DOB) is shallow. However, uniform loads are needed for the single-degree-of-freedom analysis. Figure 8-1 can be used to obtain an equivalent uniform load. These equivalent uniform load factors were obtained by performing a series of static finite-element analyses. In these analyses, the equivalent uniform load is one that will produce the same midpoint deflection as the distributed load given in Equation 8-1.

$$P_R = P_{or}(D/R_S)^3 \qquad (8\text{-}1)$$

where

P_R = Pressure on roof at a distance of R_S away from weapon
P_{or} = Pressure on the roof directly below the weapon
D = Depth from weapon to roof
R_S = Slant distance from weapon

Using Figure 8-1.b (Figure 3) and a ratio of standoff to short span, (D/A) = 10 ft/33ft = 0.3 and a ratio of short to long span (A/B) = 33 ft/87 ft = .38, the ratio of uniform load to peak stress is 0.43. The equivalent uniform pressure is 0.43 P_c = 0.43(515.8) = 221.8 psi.

Reflected Pressure

From Section 8-1.a, the reflected pressure is 1.5 times the equivalent uniform pressure.

$$P_r = 1.5 \times 221.8 \text{ psi} = 332.7 \text{ psi}$$

The duration of the reflected pressure is six wave transit times through the roof (8-1.a). The speed of the wave in concrete is 10,000 fps. Therefore, the duration (t_{d1}) of the reflected pressure is:

$$t_{d1} = \frac{12 \times 4 \text{ ft}}{10{,}000 \text{ fps}} = 4.8 \times 10^{-3} \text{ s} = 4.8 \text{ ms}$$

Design Pressure Pulse

The design pressure pulse is the combination of the reflected pressure pulse and the equivalent uniform pressure, as shown in Figure 4.

NATURAL PERIOD OF THE ROOF

From Equation 10-10, the natural period (T) is given by:

$$T = 2\pi\sqrt{K_{LM}M/K} \qquad (10\text{-}10)$$

where

K_{LM} = Load mass factor
M = Mass
K = Stiffness

From Table 10-2, the effective stiffness and load mass factor of a uniformly loaded one-way slab in the elastic-plastic strain region are given by:

$$K = 307EI/L^3$$

$$K_{LM} = 0.78$$

From Equation 9-2, the modulus of elasticity (E) of the concrete is given by:

$$E = 57{,}000\sqrt{f'_c} = 57{,}000\sqrt{3{,}000} = 3.122 \times 10^6$$

The average cracked-uncracked moment of inertia (I) is given by Equation 9-38:

$$I = \frac{bd^3}{2}(5.5p + 0.083) \qquad (9\text{-}38)$$

for a 1-in.-wide section:

$$I = \frac{1(45.5)^3}{2}(5.5(0.004) + 0.083) = 4{,}945 \text{ in.}^4/\text{in.}$$

The mass is the total mass of a 1-in.-wide strip of the slab.

$$M = (33 \text{ ft})(4 \text{ ft})\left(\frac{1}{12} \text{ ft}\right)\frac{150 \text{ lb/ft}^3}{386.4 \text{ in./s}^2}$$

$$= 4.27 \text{ lb s}^2/\text{in. per unit of width}$$

Substituting into Equation 10-10 gives the fixed-fixed natural period:

$$T_{fixed} = 2\pi\sqrt{\frac{.78(4.27)}{76{,}327}} = .042 \text{ s} = 42 \text{ ms}$$

Since the boundary conditions are somewhere between fixed and simple supports, an average period between fixed and simple supports was used.

$$T = 1.5(T_{fixed}) = 1.5(42) = 63 \text{ ms}$$

Section 10-3.b.7 recommends that the period of the slab not be modified to account for the mass of the soil; therefore, the 63-ms period was used for calculations.

EQUIVALENT STATIC LOAD

The procedure outlined in paragraph 10-2b(2)(e) was used to determine the equivalent static load on the structure from a two-part pressure pulse. If a bilinear pressure-time history (similar to the one shown in Figure 4) is used, the following approximate relationship conservatively predicts the response:

$$\frac{(F_1)_1}{R_m}C_1(\mu) + \frac{(F_1)_2}{R_m}C_2(\mu) = 1 \qquad (10\text{-}8)$$

$C_1(\mu)$ and $C_2(\mu)$ are the values of R_m/F corresponding to a certain value of ductility ratio (μ) and the ratios of duration to period t_{d1}/T and t_{d2}/T, respectively. This equation when solved for R_m results in:

$$R_m = (F_1)_1 C_1(\mu) + (F_1)_2 C_2(\mu)$$

From Figure 4

$(F_1)_1 = 332.7 - 221.8 = 110.9$
$(F_1)_2 = 221.8$
$t_{d1} = 0.0048$
$t_{d2} = 0.0256$
$t_{d1}/T = 0.0048/0.063 = 0.076$
$t_{d2}/T = 0.0256/0.063 = 0.40$

From Figure 10-3 (Figure 5), for a ductility ratio of 10:

$$R_m/(F_1)_2 = 0.24$$

$$C_2(10) = 0.24$$

$(F_1)_1$ is impulsive, and Figure 5 may not be used.

For an impulsive load:

$$R_m = \frac{I\omega}{\sqrt{2\mu-1}} \qquad (10\text{-}4)$$

For a triangular load, Equation 10-4 may be reduced to:

$$R_m/(F_1)_1 = \frac{\pi t_{d1}/T}{\sqrt{2\mu-1}}$$

$$= \frac{\pi(0.076)}{\sqrt{2(10)-1}}$$

$$= 0.055$$

$$C_1(10) = 0.055$$

$$R_m = (110.9)(0.055) + (221.8)(0.24) = 59.3 \text{ psi}$$

The manual recommends that the design load be divided by 1.5 to account for some of the conservatism built into the analysis procedure. Therefore, equivalent static design blast load is:

$$P_b = \frac{59.3}{1.5} = 39.6 \text{ psi}$$

The dead load should be added to this value. The dead load for 7 ft of concrete and 7 ft of soil is 12.4 psi. The total design pressure is 39.6 + 12.4 = 52 psi.

CHECK CAPACITY OF SLAB IN FLEXURE

Equation 9-18 was used to determine the plastic moment capacity of the section.

$$M_p = pf_y\, bd^2(1 - 0.59pf_y/f'_c) \qquad (9\text{-}18)$$

This equation determines the static capacity and should be modified to account for dynamic strength increases.

Based on Sections 9-2 and 9-3, dynamic strength increase factors for steel and concrete are 10 percent and 20 percent, respectively.

Therefore

$$M_p = (0.004)(1.1)(60)(12)(45.5)^2\left(1 - 0.59(0.004)\frac{1.1(60)}{1.2(4)}\right)$$

$$= 5{,}673 \text{ in.-kips/ft} = 523 \text{ ft-kips/ft}$$

The capacity of the slab is given by Table 10-2 as:

$$R_m = \frac{8}{L}(M_{ps} + M_{pm})$$

where

M_{ps} = Plastic moment capacity at supports
M_{pm} = Plastic moment capacity at middle

$$M_{ps} = M_{pm} = 523 \text{ ft-kips/ft}$$

$$R_m = \frac{8}{33}(523 + 523) = 254 \text{ kips/ft width}$$

or

$$R_m = \frac{254 \text{ kips/ft} \times 1{,}000 \text{ lb/kip}}{(12 \text{ in.})(33 \text{ ft})(12 \text{ in./ft})} = 53.4 \text{ psi}$$

Since the capacity of 53.4 psi is greater than the required capacity of 52 psi, the slab is adequate in flexure.

CHECK SHEAR CAPACITY OF SLAB

The shear capacity should be determined for a uniform load equal to the flexural capacity. For a slab of normal thickness, the critical section for shear is a distance d away from the supports. The shear stress (v) at d from the support of a uniformly loaded one-way slab is:

$$v = \frac{L - 2d}{L}(0.5L)\, R_m/d$$

$$= \frac{33 \text{ ft} \times 12 \text{ in./ft} - 2(45.5)}{(33)(12)}(0.5)(33)(12)(53.4)/45.5$$

$$= 179 \text{ psi}$$

Because the slab is not actually a one-way slab and the load is not uniform, the use of Equation 9-39 in predicting the shear stress capacity of the concrete is overly conservative. Therefore, the shear stress capacity is taken as the limit value of:

$$v_c = 3.5\sqrt{f'_c} = 3.5\sqrt{3{,}000} = 192 \text{ psi}$$

Since the applied shear stress is less than the shear stress capacity of the concrete, no shear steel is required. However, the manual recommends that an additional shear stress capacity of 50 psi be provided in the form of stirrups.

DETERMINE SUPPORT REACTIONS

Dynamic support reactions must be determined so that interior load-bearing walls can be designed. The exterior walls must also be checked for the axial load plus bending moment that is transferred to them from the roof slab.

The reaction which occurs at the ends of a uniformly loaded fixed-fixed one-way slab in the plastic response region is given in Table 10.2 as:

$$V = 0.38\, R_m + 0.12P$$

V is the dynamic reaction as a function of time, and this equation is only valid when the slab is responding in the fully plastic mode. P is the

dynamic load as a function of time, and R_m is the ultimate capacity of the slab. The peak reaction will occur at the time when the slab reaches its ultimate capacity. The maximum support reaction is determined by substituting the value of R_m and the value of P at the time the slab reaches ultimate capacity. Since the duration of the reflected pulse is very short compared to the natural period of the slab, it is unlikely that the slab will reach its ultimate capacity before the reflections are relieved. Therefore, it is conservative to determine the peak reaction using the equivalent uniform incident pressure. These pressures must be multiplied by the area over which they act in order to determine the maximum reaction.

$$V = [0.38(53.4) + 0.12(221.8)]\ 33(12)(1)$$

$$= 18,575\ \text{lb/in.}$$

$$= 223\ \text{kips/ft}$$

The interior and exterior walls should be designed to resist this load.

DESIGN OF EXTERIOR WALLS

The exterior walls must be designed for the weapon penetrating the soil and detonating opposite the wall. Procedures are outlined in the manual for determining the path the bomb will take after it enters the soil. Using this information, a detonation slab can be designed to keep the weapon at any desired standoff distance from the wall. Once the standoff is determined, the procedure for designing the wall is similar to the one used for the roof slab.

More than likely, the bomb will penetrate deep enough to detonate opposite the center of the wall, and the charge will be fully coupled at that depth. The same procedure used to determine the roof slab loading is used to determine the wall loading. With the normal wall heights and weapon standoff, the equivalent uniform load factor will be almost 1.0, since the pressure is almost uniform.

The reflected pressure is 1.5 times the incident pressure, but the procedure for calculating the reflected pressure duration may be different than the procedure used for the roof slab. If the wall is relatively thick and short, the reflection may be cut off by a relief wave coming in from the free edge of the structure. This relief time is given by:

$$t_r = \frac{Z_f - D}{C_L} + \frac{X_f}{C_u}$$

where

t_r = Duration of reflected pressure
Z_f = Slant range from weapon to free edge
D = Distance from weapon to center of structure
C_L = Loading wave velocity
X_f = Distance from center of slab to nearest free edge
C_u = Unloading wave velocity

The relief time should be calculated using the procedure above and the procedure used for the roof slab. The smaller number should be used.

The walls will normally be one-way slabs and may be considered deep slabs. If the span-to-effective-depth ratio is less than or equal to 5, the slab should be analyzed using the procedures in Section 9-5e(2).

The required moment capacity of the wall may be controlled by the moment transferred to it from the roof slab. If this is the case, the bomb should probably be allowed to detonate closer to the wall. However, shock levels inside the structure should be checked before the design standoff is changed.

DISCUSSION OF DESIGN PROCEDURES

The procedures for designing buried structures presented in the latest edition of TM 5-855-1 have been changed significantly from the previous edition. The equations defining the load-time history of the structure have been changed to include recent data. In the previous edition, the peak reflected pressure and duration of the half-sine wave pulse can be computed. In the new manual, the incident as well as reflected pressures and durations may be calculated. Using this procedure, the reflected pressure is applied to the structure for a much shorter period of time.

In the previous edition of the manual, the load is applied uniformly over the slab. In the revised manual, a procedure is provided for averaging the load over the slab. This can significantly reduce the design loading for a close-in detonation.

In the previous manual, an impulsive elastic analysis is performed. An elastic analysis is performed, and if the maximum stress remains below a fictitious yield stress, the design is acceptable. This fictitious yield stress is a function of the amount of damage allowable. This method was presented because of its ease of use and should produce good designs if the load is truly impulsive.

In the revised manual, a simplified method of performing a linear elastic-plastic dynamic analysis is presented. This procedure is no more complicated than the impulsive elastic analysis but is accurate for a wide range of problem types. This procedure should be much more accurate for longer duration loads.

There are several factors which are not considered in the simplified methods presented in the manual. Compressive membrane action, time phasing of the load, the localized nature of the structural response, and soil-structure interaction can significantly affect the response of the structure. Each of these factors can increase the hardness of the structure, and if neglected, the design of the structure will be overly conservative. For this reason, the loads are divided by 1.5 before they are applied to the structure. These procedures will produce conservative results even after application of this factor.

A computer code to analyze structures subject to conventional weapons effects is currently being developed at the Waterways Experiment Station. This code will consider those factors neglected in the manual and should allow for less conservative designs.

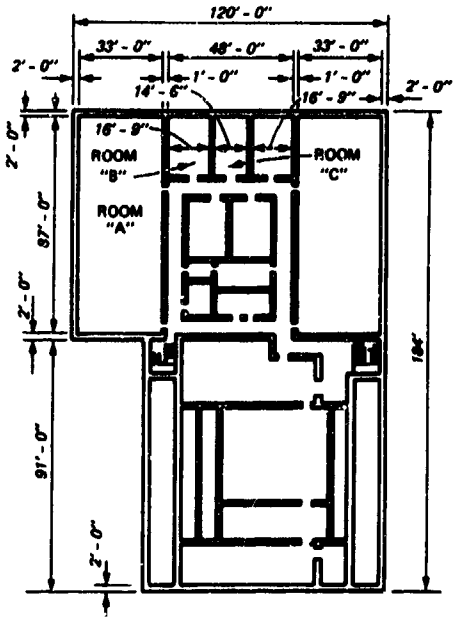

Figure 1. Building plan.

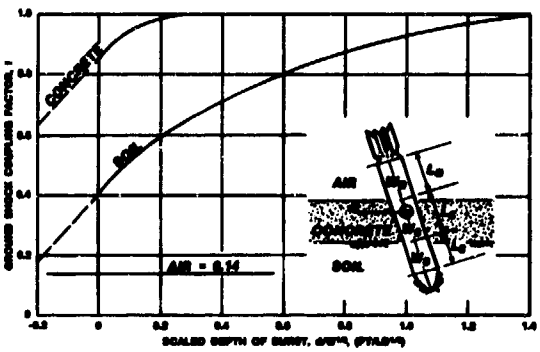

Figure 2. Ground shock coupling factor.

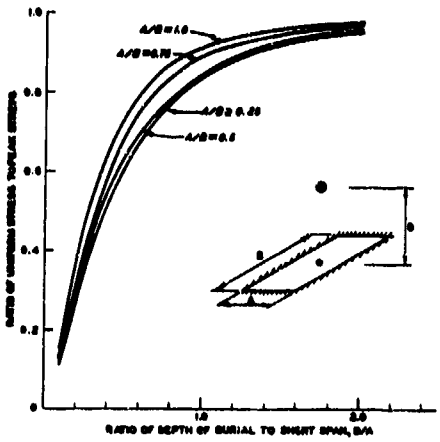

Figure 3. Equivalent uniform load in flexure with fixed supports.

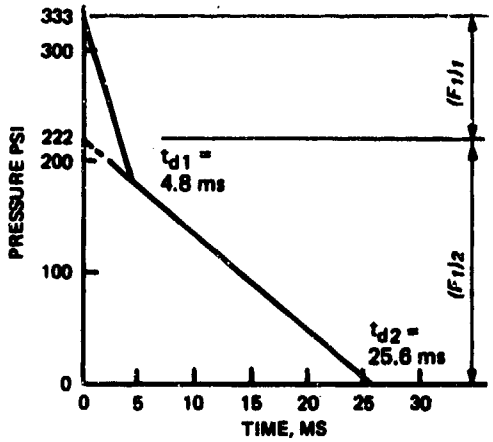

Figure 4. Uniform pressure versus time for the roof load.

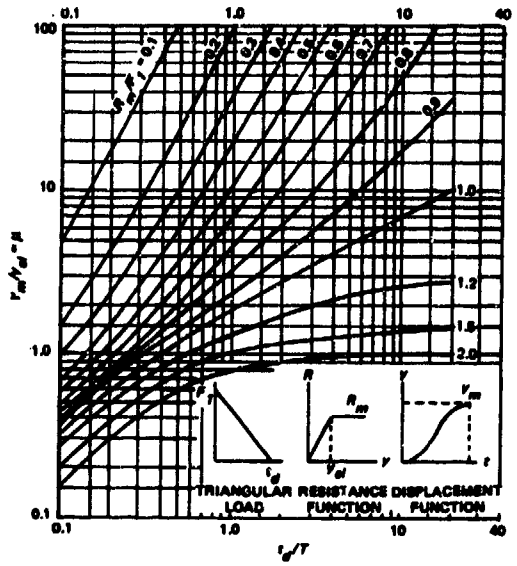

Figure 5. Response curve.

DESIGN OF LAYERED STRUCTURES AGAINST CONVENTIONAL WEAPONS

Reuben Eytan

Eytan Building Design Ltd.
Tel Aviv, Israel

ABSTRACT

The design of layered structures against conventional weapons effects is presented and compared to the design of conventional hardened structures. Several types of layers configurations such as concrete-air-concrete, concrete-soil-concrete, concrete-rocks-concrete, steel-soil-steel and steel-concrete-steel are presented and discussed. The design concepts and advantages of the above layered structures against direct hits and near misses of conventional weapons such as artillery shells, air bombs and shaped-charge projectiles for both aboveground and underground structures are described. Based on practical experience, the optimal applications of layered structures are presented.

INTRODUCTION

In this paper three types of conventional weapons attack are considered:

- direct hits of artillery shells.
- near misses of air bombs.
- direct hits of shaped-charge projectiles.

Artillery shells include high-explosive projectiles fired by mortars, guns or rocket launchers.

Air bombs include fragmentation/blast air bombs or warheads (ground-to-ground).

Shaped-charge projectiles include projectiles fired from portable weapons (RPG etc.), anti-tank weapons, recoilless guns or air-to-ground launchers.

The attacks are considered to occur on aboveground or underground structures and the main impact of the weapons effects will be on the following structural elements:

- the structure's roof in the case of a direct hit of an artillery shell (aboveground or underground structure)
- the structure's walls in the case of a near miss of an air bomb (aboveground or underground structure).
- the aboveground structure's walls in the case of a direct hit of a shaped-charge projectile.

CONVENTIONAL DESIGNS

The configurations of "conventional designs" for three types of attack are illustrated in Figures 1, 2 and 3.

The conventional design of an aboveground or underground structure against a direct hit of an artillery shell consists of providing protective layers above the structure:

- a penetration layer (burster layer), made usually of hard materials such as concrete, rocks, etc. which stop the shells' penetration and induce it's explosion.
- an absorption layer, made usually of soil which absorbs the energy released by the shell's explosion.

The conventional design of an aboveground or underground structure against a near miss of an air bomb consists simply of a hardened structure with monolithic walls and roof.

The conventional design of an aboveground structure against a direct hit of a shaped-charge projectile consists of one of the following solutions:

- the provision of a thick monolithic structure capable of absorbing fully the jet effects.
- the provision of an "activator" element at a certain distance in front of a monolithic structure.

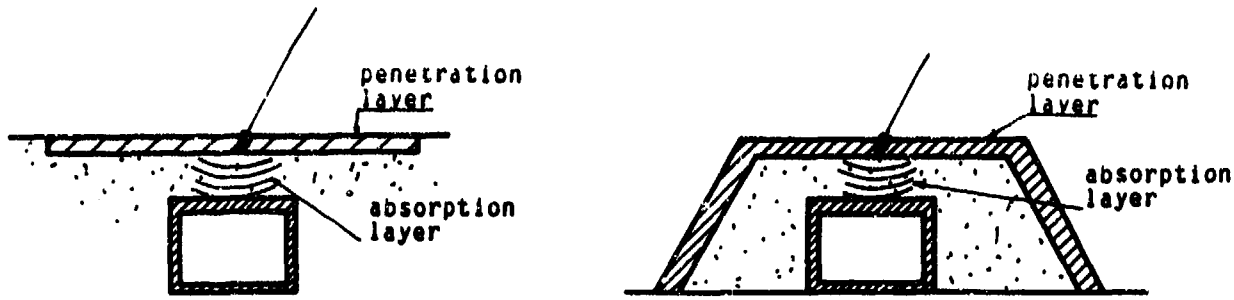

a) Underground hardened structure

b) Aboveground hardened structure

Figure 1. Conventional designs against direct hits of artillery shells.

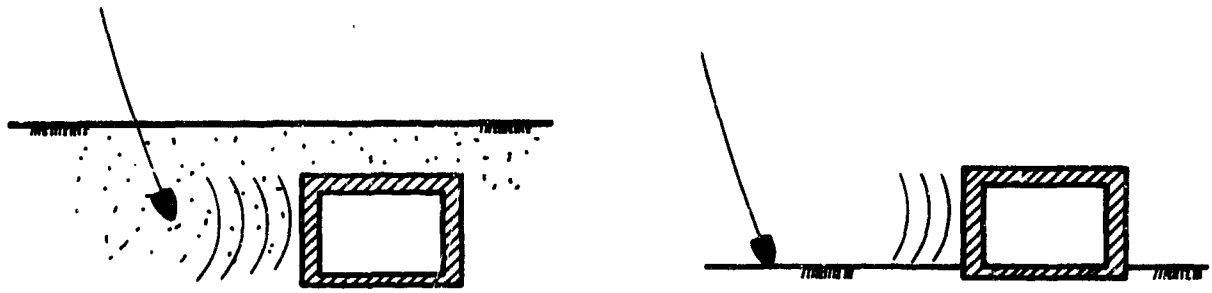

a) Underground hardened structure

b) Aboveground hardened structure

Figure 2. Conventional designs against near misses of air bombs

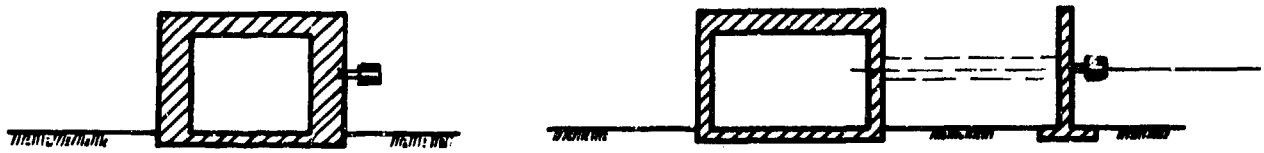

a) Single monolithic structure

b) Activator element in front of the structure

Figure 3. Conventional designs against direct hits of shaped-charge projectiles.

THE LAYERED STRUCTURES CONCEPT

To replace the above described conventional designs, the layered structures concept was developed.

The layered structures consist of several layers of different materials acting togetner in withstanding the weapons effects and the normal static loads.

In this paper five types of layered structures described in Figure 4 are discussed:

- reinforced concrete-air-reinforced concrete.
- reinforced concrete-soil-reinforced concrete.
- reinforced concrete-rocks-reinforced concrete.
- steel-soil-steel.
- steel-concrete-steel.

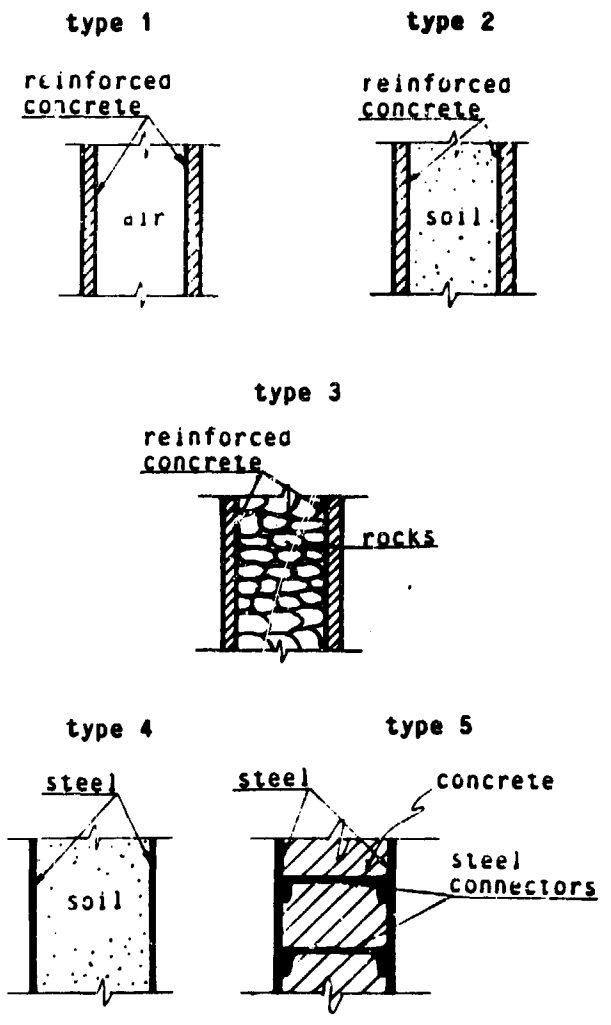

Figure 4. Layered Structures

OPTIMAL APPLICATIONS OF LAYERED STRUCTURES

The optimal applications of layered structures regarding the type of attack, aboveground or underground location of the structure and the type of layers configuration are presented in Table 1.

Structure location	Type of attack	Layered structures				
		Type 1	Type 2	Type 3	Type 4	Type 5
Underground structure	Near miss of an air bomb	*	*			
Aboveground structure	Direct hit of an artillery shell	*				
	Near miss of an air bomb	*	*			*
	Direct hit of a shaped -charge projectile		*	*	*	

Table 1 - Optimal applications of layered structures

The layered structures in the above described applications were developed, tested on full-scale and constructed in different locations and in large numbers so that it can be now stated that practical experience for the layered structures presented in this paper has been gained.

DESIGN CONSIDERATIONS FOR LAYERED STRUCTURES

In the design of layered structures to withstand the conventional weapons effects the following considerations were applied:

Layered Structure Type 1
(reinforced concrete-air -reinforced concrete)

In the case of a direct hit of an artillery shell the layers are designed as follows:

- the outer reinforced concrete layer: to stop the penetration of the projectile and to induce it's explosion.
- the air gap: to prevent direct shock transfer to the inner reinforced concrete layer.
- the inner reinforced concrete layer: to withstand the blast effects going through the outer layer and to absorb all secondary concrete fragments of the outer layer.

In the case of a near miss of an air bomb the layers are designed as follows:

- the outer reinforced concrete layer: to withstand fully or partially the fragments penetration and/or the blast effects.
- the air gap: to prevent direct shock transfer to the inner reinforced concrete layer.
- the inner reinforced concrete layer: to withstand the remaining fragments penetration and/or blast effects going through the outer layer and to absorb all secondary concrete fragments of the outer layer.

Layered structure type 2
(reinforced concrete-soil -reinforced concrete)

In the case of a near miss of an air bomb the layers are designed as follows:

- the outer reinforced concrete layer: to withstand partially the fragments penetration and/or the blast effects.
- the soil fill: to stop the primary fragments penetration and/or the secondary concrete fragments of the outer layer and to partially absorb the shock transfered from the outer layer.
- the inner reinforced concrete layer: to withstand the remaining shock effects transfered through the soil fill.

In the case of a direct hit of a shaped-charge projectile the layers are designed as follows:

- the outer reinforced concrete layer: to activate the projectile.
- the soil fill: to absorb partially the jet effects.
- the inner reinforced concrete layer: to withstand the remaining jet effects.

Layered structure type 3
(reinforced concrete-rocks -reinforced concrete)

In the case of a direct hit of a shaped-charge projectile the layers are designed as follows:

- the outer reinforced concrete layer: to activate the projectile.
- the rock fill: to absorb partially the jet effects.
- the inner reinforced concrete layer: to withstand the remaining jet effects.

Layered structure type 4
(steel-soil-steel)

In the case of a direct hit of a shaped-charge projectile the layers are designed as follows:

- the outer reinforced steel layer: to activate the projectile.
- the soil fill: to absorb all the jet effects.
- the inner steel layer: to hold the soil fill in place.

Layered structure type 5
(steel-concrete-steel)

In the case of a near miss of an air bomb the layers are designed as follows:

- the outer steel layer: to contain the concrete fill, to reduce the fragments penetration and to be part of the blast-resistant structure.
- the concrete fill: to withstand the fragments penetration.
- the steel connectors: to ensure the overall structural blast resistance.
- the inner steel layer: to contain the concrete fill and to be part of the blast-resistant structure.

LAYERED STRUCTURES COMPARED TO CONVENTIONAL DESIGNS

Case 1 - Aboveground structure against a direct hit of an artillery shell

Let us compare a layered structure type 1, as illustrated in Figure 5, to the conventional design described in Figure 1b.

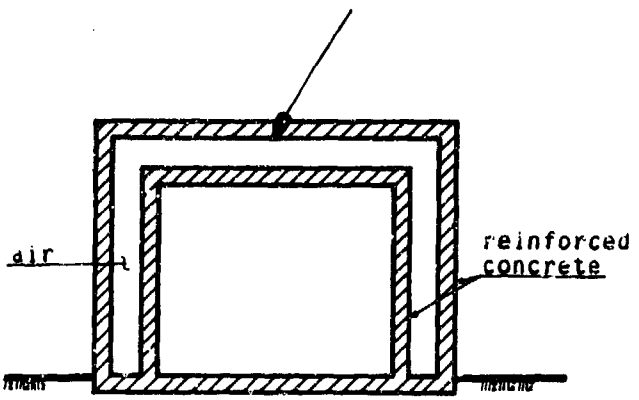

Figure 5. Aboveground layered structure type 1

The advantages of the layered structure, as compared to a monolithic reinforced concrete structure, are:

- the overall dimensions of the structure are significantly reduced.
- the dead loads are much lower, resulting in a lighter structure.
- the air gap can be used for services, equipment, storage, etc.
- the design of the layout of service ducts, pipes, cables, etc and their penetrations through the structural elements is much simpler.
- the construction is easier and quicker.
- the supervision and maintenance of all the services is much easier.

Case 2 - Underground structure against a near miss of an air bomb

Let us compare a layered structure type 2, as illustrated in Figure 6, to the conventional design described in Figure 2a.

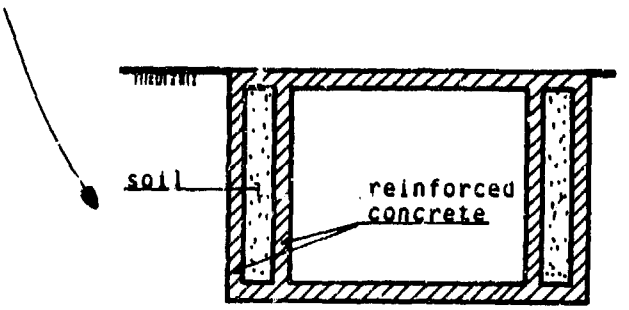

Figure 6. Underground layered structure type 2

The advantages of the layered structure, as compared to a monolithic reinforced concrete structure, are:

- the overall thickness of the double concrete wall is less than the thickness of the equivalent monolithic wall.
- the shock transfer through the walls is greatly reduced.
- there is no danger of spalling and therefore no need for anti-spalling measures.
- the waterproofing performance of the layered structure is higher.

Case 3 - Aboveground structure against a direct hit of a shaped -charge projectile

Let us compare a layered structure type 3, as illustrated in Figure 7, to the conventional design described in Figure 3a.

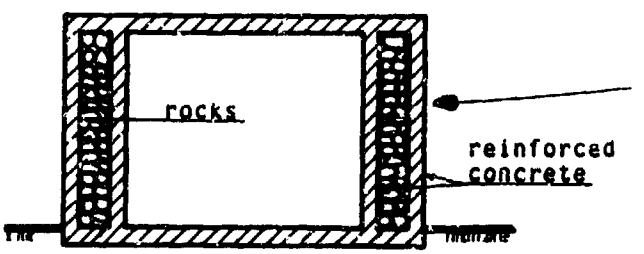

Figure 7. Aboveground layered structure type 3

The advantages of the layered structure, as compared to a monolithic reinforced concrete structure, are:

- the overall thickness of the double concrete wall is less than the thickness of the equivalent monolithic wall.
- the construction and long-term performance problems of very thick concrete walls are eliminated.

COST-BENEFIT

In different practical applications of layered structures it was found that they are more cost-effective than the equivalent conventional designs.

SUMMARY AND CONCLUSION

The design concepts and advantages of layered structures were presented in comparison to conventional designs of hardened structures.

The layered structures discussed are not theoretical but have been constructed and therefore should be regarded as feasible and practical designs.

The purpose of the paper was to present the layered structures as compared to conventional designs but it is not the author's intention to generalize and claim that layered structures are always better and cheaper than conventional hardened structures. It remains the designer's task to decide which is the optimal solution for the given set of threats, site conditions and constraints and the structure type.

However, as shown here, the layered structures present an attractive alternative in the right environment and due to the present experience it is the author's belief that in the future the layered structures will gradually "establish" themselves as conventional solutions for hardened structures against conventional weapons.

A CASE STUDY IN DESIGN OF UNDERGROUND SHELTERS

Felix S. Wong, Rudolf Y. Mak, David Kufferman and Paul Weidlinger

Weidlinger Associates
Palo Alto, California and New York, New York

ABSTRACT

A design methodology developed previously has been applied to the design of several underground shelters. The methodology accounts for the effect of structure-medium interaction (SMI) but requires little extra expense beyond that of a conventional design, e.g. the design of an aboveground shelter. Results of a case study are presented in this paper to illustrate the methodology and its potential impact on the design of underground shelters.

INTRODUCTION

The design of underground shelters against non-nuclear munitions should incorporate the effects of dynamic SMI, i.e. the coupling between the response of the buried structure and the load exerted by the medium on the structure. This interaction is known to change significantly the magnitude and distribution of the structural loading from that of the free-field soil [1]. The design of the underground shelter is correspondingly affected.

An exact method to include the effect of soil-structure interaction on shelter design involves the use of dynamic finite element models of the complete soil-structure configuration, in order to capture the complex wave mechanics. Such finite element analyses are, in general, too expensive for design purposes, since several iterations are usually necessary. Through our research effort a design methodology is developed whereby the effect of SMI is incorporated in the design procedure, but which requires little extra expense beyond that of a conventional design, e.g. the design of a conventional shelter. This methodology makes use of the transient nature of the munition source, the spatial and soil attenuation of the blast wave from such a source, and an approximate SMI algorithm. This design methodology will be referred to as the SMI design methodology to distinguish it from conventional design methods. It consists of two steps shown schematically in Fig. 1. The modification of the structural characteristics in step (ii) to account for the effect of interaction is accomplished in a systematic manner, and is based on the properties of the medium and structural materials and the mechanics of dynamic SMI. Except for this modification, the procedure is identical to that for a bare structure in a conventional design. Hence, the cost of the design is basically the same as for the conventional design. Details can be found in [2].

CASE STUDY

The prospective shelter to be designed is a two-story, fairly rectangular, reinforced concrete building, which is referred to as the ADCC building (see Fig. 2). The preliminary plan for the building includes twelve distinct roof slabs and wall panels which must be sized. Sizing involves the determination of the rebar percentage and slab/panel thickness, since the concrete and rebar types, as well as the overall dimensions of the slab/panel and munition threat, are predetermined by construction and operational requirements. The shelter is to be buried in sand.

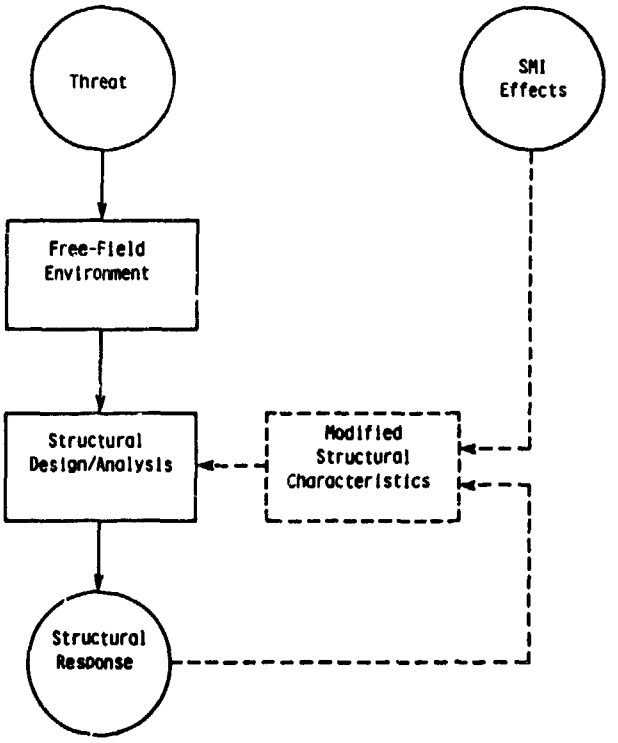

Fig. 1 SMI design methodology.

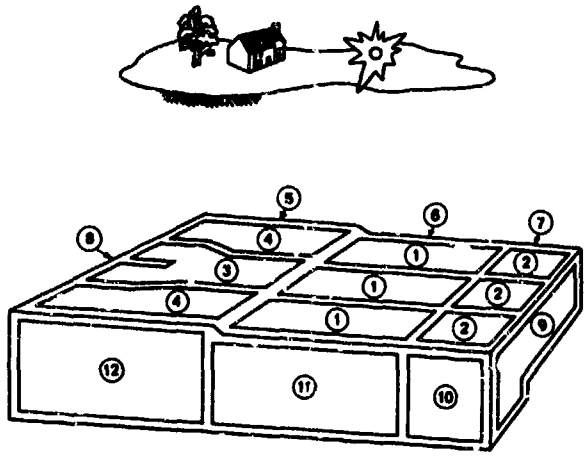

Fig. 2 Layout of ADCC structure.

All slabs and panels were analyzed using inelastic finite element models with 20 elements along the length, 10 elements along the width and 4 elements in the thickness direction. Space limitations do not permit all the results to be included herein. Since results of all slab/panel analyses are fairly similar, they will be illustrated by using results for Case [illegible], i.e. the design of roof slab 2 subjected to threat A, and the source is directly above the center of the slab. In particular, results obtained by using the SMI design methodology will be compared with results of a conventional approach. In the latter, the ground shock is simply amplified by a factor of two and then applied to the structure. This should be contrasted with the SMI design approach where the load depends on the structural response at that time. It can be shown that the mechanism of interaction is also equivalent to the addition of (radiation) damping to the structural response [3].

All results presented in what follows are based on a preliminary slab configuration with 4 ksi concrete and 60 ksi steel rebars. Reinforcement is 0.5 percent top and bottom in the vertical and horizontal directions. The sand medium is assumed to have unit weight of 120 pcf, a loading wavespeed of 1000 fps and an unloading wavespeed of 3000 fps.

Structural Load--The difference between the loadings delivered to the slab according to the SMI and conventional methodologies can be ascertained by comparing the pressure contour plots shown in Fig. 3. In the conventional approach, the applied load is not affected by the response of the structure and the pressure contour surface is strictly convex (Fig. 3a). The peak pressure occurs at the point nearest the source, i.e. at midspan, and the decay of pressure with range and time is monotonic. On the other hand, in the SMI method, deflection of

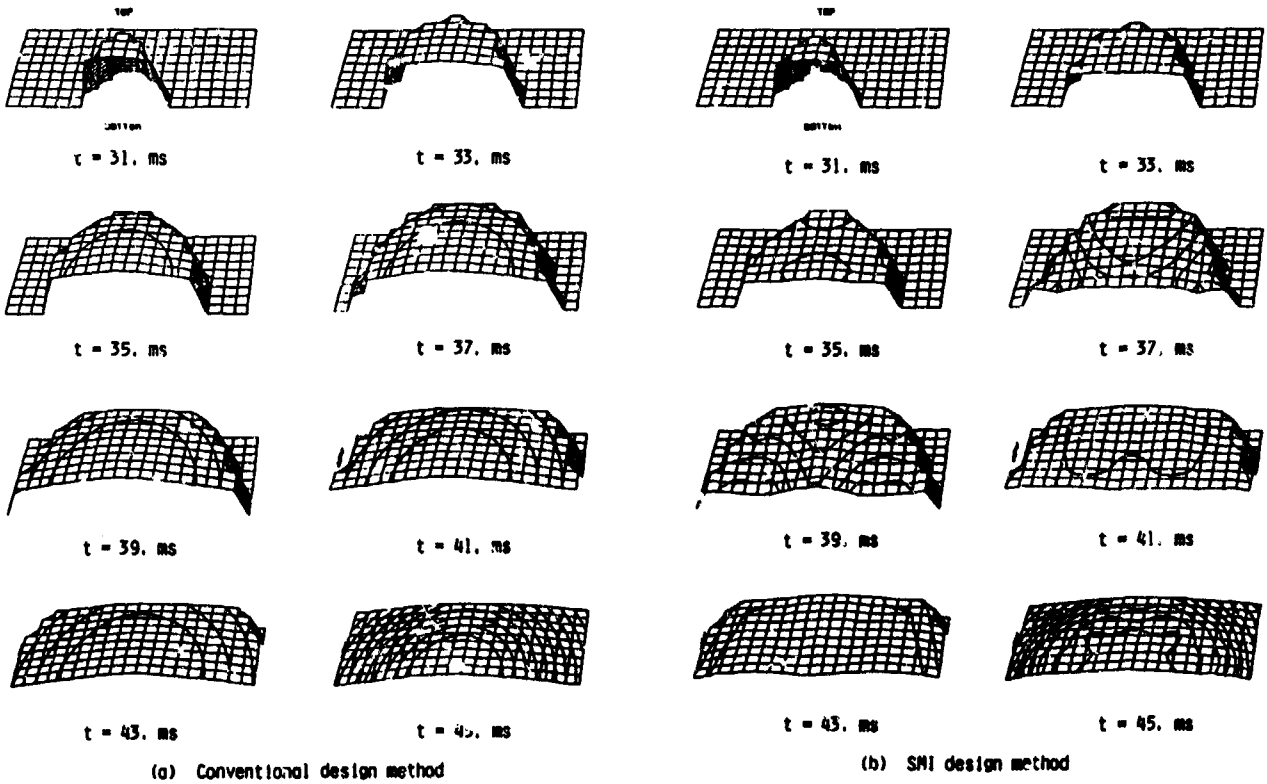

(a) Conventional design method

(b) SMI design method

Fig. 3 Comparison of loadings on structure according to conventional and SMI design methods.

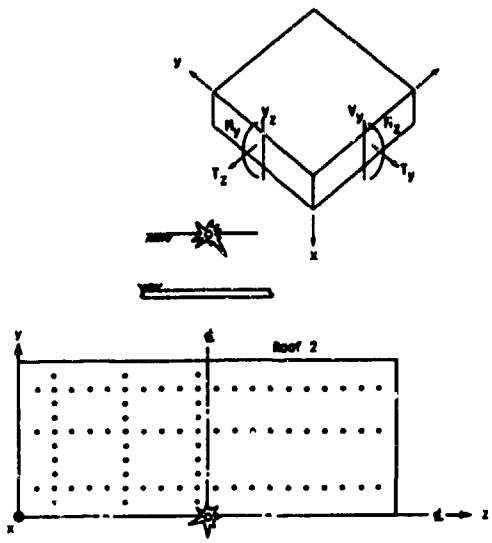

(a) Output stations and sign convention

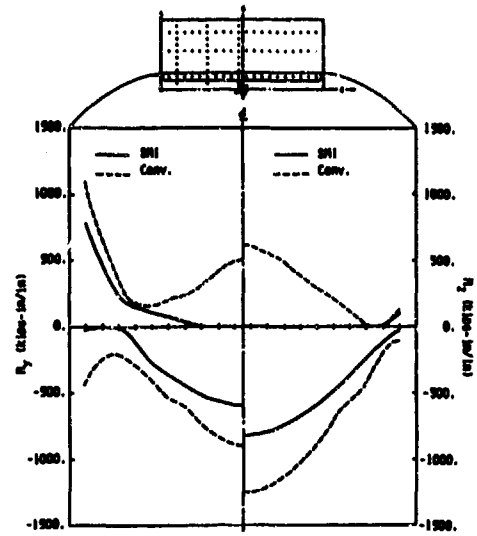

(b) Moment distribution along horizontal line near plane of symmetry

Fig. 4 Comparison of results from SMI and conventional design analyses.

the slab relieves the loading acting on it. Since the loading is the highest at midspan, deflection of the midspan is also largest. Relief is large, which, in turn, counteracts the high loading. Hence, once the structure begins to respond to the initial applied load, the pressure contour surface has a crater shape (Fig. 3b). By comparing Figs. 3a and 3b, it is seen that both the magnitude and the spatial distribution of the load are very different in the two cases. At later times, peak pressure in the SMI case tends to occur near the support, since the support corresponds to "hard" points which are not capable of any load relief.

Moment and Shear--Because of the effects due to SMI on the magnitude and distribution of the load, the maximum shear and moment in the slab computed by using the SMI methodology will be different from that computed by using conventional procedures. The difference is qualitative as well as quantitative, as the comparisons in Fig. 4 show. In this figure, the solid line corresponds to the SMI method and the dashed line the conventional method, as described previously. The sign convention for the moments My and Mz, and for the shears Vy and Vz is described in Fig. 4a. Structural response data are obtained for three lines with constant values of y, i.e. horizontal lines on the slab, and for three lines with constant values of z, i.e. vertical lines on the slab. However, only some representative results can be presented here.

With reference to the comparison of moments along the horizontal plane of symmetry of the slab shown in Fib. 4b, the magnitude of the minimum or maximum moment by the SMI method is uniformly smaller than that by the conventional method. The difference is approximately 40 percent for the peak negative moment, while the difference for the peak positive moment is much larger. The former is due to the load relief effect of the interaction. The latter is due to the damping effect of the interaction. The rebound in the slab is greatly diminished due to radiation damping, as will be described presently. The difference in shears follows the same pattern as the difference in moments, but will not be illustrated.

Instructure Motion--Another important SMI effect which is often ignored in conventional design can be described with reference to Fig. 5. In this figure, a representative slab velocity/time trace is compared with its counterpart obtained using the conventional method. Recall in the conventional method being discussed, the blast load is simply amplified by a factor of two. Since the source is directly above the center of the slab in this case, the slab response is fairly stiff for this threat environment, and no structural damping is assumed,

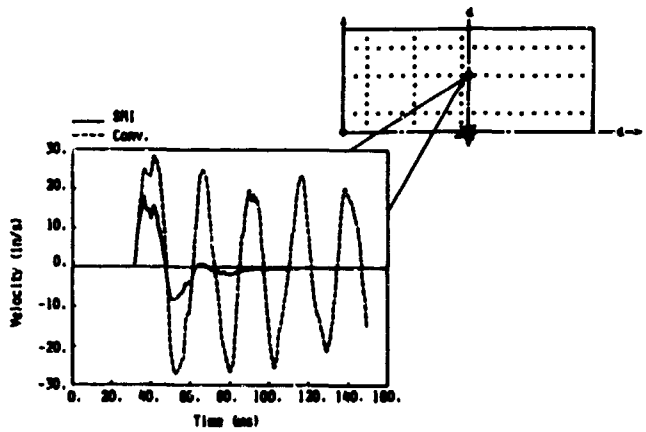

Fig. 5 Comparison of velocity-time traces from SMI and conventional design analyses.

the time trace corresponding to the conventional method (dashed line in Fig. 5) is the response of an undamped elastic system subjected to impulsive loading. The SMI response shown as the solid line, on the other hand, exhibits very strong damping which not only contributes to the reduction of the peak velocity in the first half of the loaded cycle, but also changes the subsequent response very significantly. This phenomenon is called radiation damping and can be traced directly to the interaction mechanics [3]. It is clear that the spectral contents of the solid and dashed lines in Fig. 5 are very different. Hence, equipment attached to the roof or wall will be subjected to very different excitations according to these design methods, with important consequences on their shock-isolation requirements.

SUMMARY

The effects of dynamic SMI can change significantly the magnitude and distribution of the structural loading and, hence, should be considered in the design of underground shelters. In addition to structural survivability, these effects can impact other system design considerations as well. The SMI design methodology illustrated herein by using a case study incurs little extra cost when compared with conventional design procedures. However, it may lead to significant savings by providing more realistic estimates of the design loads and peak structural response.

REFERENCES

[1] Wong, F.S. and Richardson, E., "Transfer Function Analysis for Statistical Survivability/Vulnerability Assessment of Protective Structures," AFWL-TR-82-32, October 1982.

[2] Wong, F.S. and Weidlinger, P., "Design of Underground Shelters Including Soil-Structure Interaction Effects," Proc. Symp. Interaction of Non-Nuclear Munitions with Structures, Colorado Springs, CO, May 1983.

[3] Wong, F.S. and Weidlinger, P., "Damping of Shallow-Buried Structures due to Soil-Structure Interaction," Shock and Vibration Bulletin, 52, Part 5, May 1982.

INELASTIC COLLAPSE ANALYSIS OF TRANSVERSELY LOADED CONCRETE SLABS

Jerzy T. Jacak
and
Hans Gesund

University of Kentucky

Lexington , Kentucky

ABSTRACT

The flexural strength of orthotropically reinforced flat plate floor systems subjected to combinations of distributed and concentrated loads is analyzed. Several upper bound solutions corresponding to different yield line patterns are obtained. Both column reactions and concentrated panel loads are assumed to act over finite areas rather than point loads. The analysis is limited to interior panels of an infinite system, with all panels identical and subjected to identical loadings. It has been found that a series of critical patterns emerges, whose geometry depends on the geometry of the structure, the distribution of the reinforcement, and the locations, shapes and sizes of the patch loads.

LIST OF SYMBOLS

a_1 to a_4 — x direction dimensions of elliptical fans in collapse mechanisms

b_1 to b_4 — y direction dimensions of elliptical fans in collapse mechanisms

c , λc — side dimensions of a column in the x and y directions, respectively

$K = w\lambda l^2/m\Sigma k$ — coefficient related to the yield line pattern

$k_x m$ — negative yield moment per unit length provided by top tension reinforcing bars placed parallel to the x axis

$k_x' m$ — positive yield moment per unit length provided by bottom tension rebars placed parallel to the x axis

$k_y m$ — negative yield moment per unit length provided by top tension rebars placed parallel to the y axis

$k_y' m$ — negative yield moment per unit length provided by bottom tension rebars placed parallel to the y axis

l , λl — side dimensions of a panel in x and y directions, respectively

l_x, l_y — coordinates of the centroid of the concentrated load within a panel

m — unit yield moment per unit length

$m \Sigma k = m(k_x' + k_x + k_y' + k_y)$ = total positive plus negative moment resisting capacity of the slab in two orthogonal directions

P = applied concentrated load

s , $\lambda_s s$ — side dimensions of the area covered by a concentrated load

w = collapse load per unit area

$\mu = (k_x' + k_x)/(k_y' + k_y)$ coefficient of orthotropy

$\omega = w\lambda l^2/P$ load ratio

INTRODUCTION

Column supported, reinforced concrete flat slabs or flat plates are subjected to large bending moments and shearing forces at their connections with the columns. Either or both of these effects can cause failure by punching of the slab. Such slabs are typically designed for distributed loads. However, they are frequently also loaded with concentrated or patch loads such as machinery, forklift trucks, etc., and, in the dynamic range, missiles or explosives. The flexural strength and collapse mechanisms of such slabs when subject to combinations of distributed and concentrated loads, have not previously been reported on in the literature.

Reinforced concrete slabs with usual reinforcement ratios exhibit a great deal

of ductility in flexure. Tests on slabs show that extensive deformations occur before their ultimate strength is reached and that the tension reinforcement in the vicinity of concentrated loads or supports yields before punching, thus permitting large rotations to occur. This ductile behavior enables slab systems to redistribute moments prior to collapse, provided that shear failure is prevented. The research reported herein is concerned with the inelastic analysis of the flexural strength of orthotropically reinforced slabs supported on columns and loaded with combined distributed and concentrated loads. Shear strength has been dealt with frequently in the literature and is not considered. It is obvious, however, that flexural distress is unlikely to enhance shear resistance.

DESIGN METHODS

Sect. 13.3.1 of the ACI (318-83) Code states that "A slab system may be designed by any procedure satisfying conditions of equilibrium and geometric compatibility..." and Sect. 13.3.1.1 names two methods of design of slab systems subjected to gravity loads only. However, concentrated loads cannot be handled correctly by these methods and elastic, e.g. finite element, methods give unrealistic results at corners of patch or concentrated loads, or supports, i.e.the very locations where failure usually initiates.

The flexural limit strength of reinforced concrete slabs can generally be predicted quite accurately by making use of the yield line theory. This method is also ideally suited for dealing with corners of concentrated loads or supports by means of yield fan mechanisms and has given good correlation with a large number of experiments.

The yield line theory will therefore, be used here.

THE ANALYTICAL MODEL

The slab system to be analysed is supported on columns so arranged as to divide it into rectangular panels. See Fig. 1. A concentrated load, P, will be assumed to be distributed over a small rectangular area of dimensions s and $\lambda_s s$, as shown. The entire slab, including the area beneath P, will carry a uniformly distributed load of magnitude w per unit area which may be self weight plus any additional distributed surcharge.

The analysis will be limited to interior panels. It is also assumed that all interior panels are identical and are identically loaded. Concentrated load will be assumed to be distributed over small rectangular areas, as is the case in many real situations, and magnitudes and footprint areas, as well as locations within

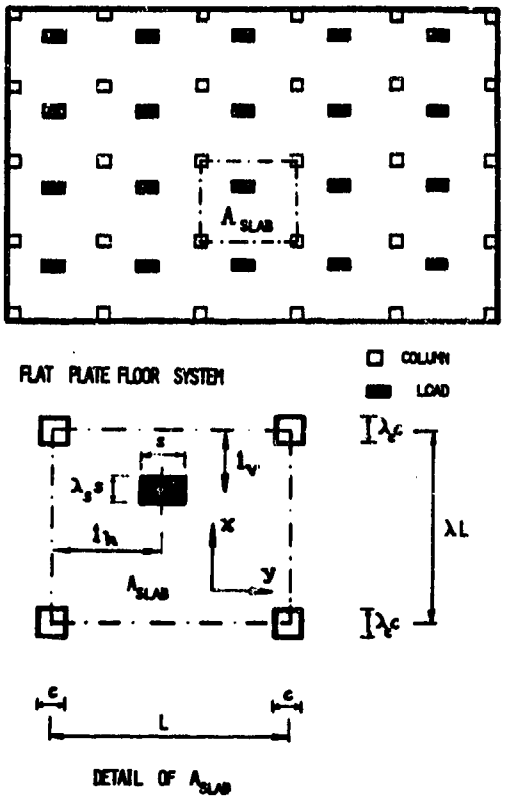

a panel, are arbitrary.

MODES OF COLLAPSE IN THE SLAB

The yield line analysis has been carried out using the virtual work method as presented by Johansen [3]. The method is based on a postulated geometrically admissible collapse mechanism.

In any analysis of flexural strength by means of yield line theory it is necessary to consider all reasonable, geometrically admissible collapse mechanisms. The one giving the lowest upper bound on the collapse load will control.

Among the many factors which can influence the flexural collapse of flat slabs, those being studied, are:

1) the coefficient of orthotropy,
2) the geometry of the panel,
3) the aspect ratios and sizes of columns and the footprints of the concentrated loads,
4) relative magnitudes of the concentrated and distributed loads,
5) the locations of the concentrated loads in a panel, and
6) the relationships between total yield moment resistance available in the slab and the loads.

Since the yield line mechanisms for the problem under investigation may involve yield fans forming both at column

reactions and around concentrated loads, a question arises regarding possible interactions among the fans. This problem has never previously been addressed.

The most likely, geometrically admissible yield line patterns for the problem at hand are shown in Fig. 2. They include both simple overall folding-type yield line mechanisms (Cases A and B), simplified straight line mechanisms (Cases C,D,E and F) and standard fan-shaped flexural punching mechanisms (Cases G and H), as well as more complex mechanisms involving interacting elliptical fans in simultaneously forming load and column punching mechanisms (Cases I,J,K and L). A positive yield line is defined as a plastic hinge in which the rotation is convex down. The reverse is true for a negative yield line . Positive yield lines are shown in Fig.2 as dashed lines, negative as thin solid lines.

The governing equations, expressing the relationship between the yield moment capacities of the slab and the collapse load for a particular pattern of yield lines, were derived and solved by numerical minimization schemes [4].

RESULTS OF THE YIELD LINE ANALYSIS

As an illustration, an isotropically reinforced system with square panels and point columns and loads (to compare with known solutions for extreme values of ω) [1,3,5], was analyzed.

Two locations of concentrated load are analyzed: when the centroid of the concentrated load falls on the top left quarter point of a panel and when it falls on middle point of a panel.

The results are presented in terms of the coefficient K in Tables 1 and 2, wherein $K = w\lambda l^2/m\Sigma k$. They are also plotted using a logarithmic scale in Fig.3 and Fig.4, respectively. The formulae for K as derived by yield line analysis are not given here for lack of space, but are available to interested parties upon request.

As can be seen from the graphs, when the concentrated loads are applied in the middle of panels, the folding-type mechanisms (Case A ,or B) give the lowest values for the load ratios of up to, approximately, equal to 2. For higher ratios of ω the column punching mechanism will control the collapse.

For concentrated loads applied at quarter points of panels the combined column and load flexural punching mechanism (Case K, or L) governs for load ratios ω up to, approximately, equal to .75. For higher ratios of again the column punching mechanisms will control the collapse.

The influence of other parameters, e.g. the ratio of transverse to longitudinal reinforcement in the slab (i.e. coefficient of orthotropy), size of the footprint of the concentrated load and other locations of the concentrated loads can be found in [2].

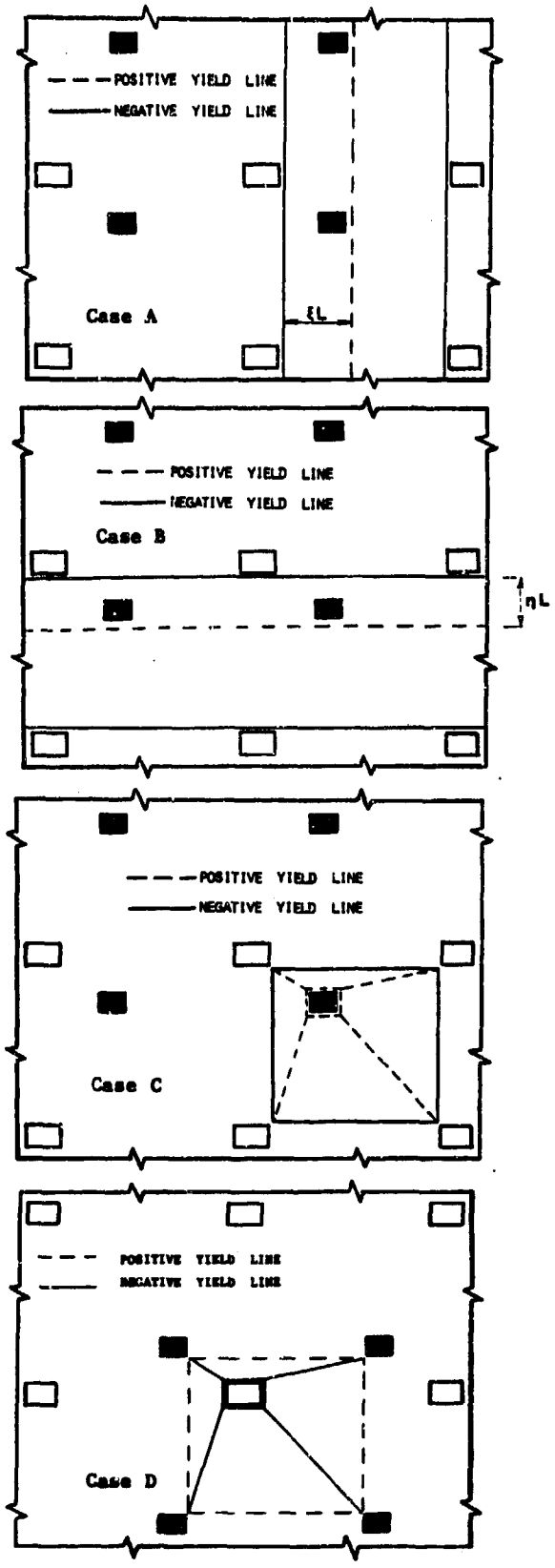

Fig. 2 Yield Line Patterns for Flat Plate Floor System

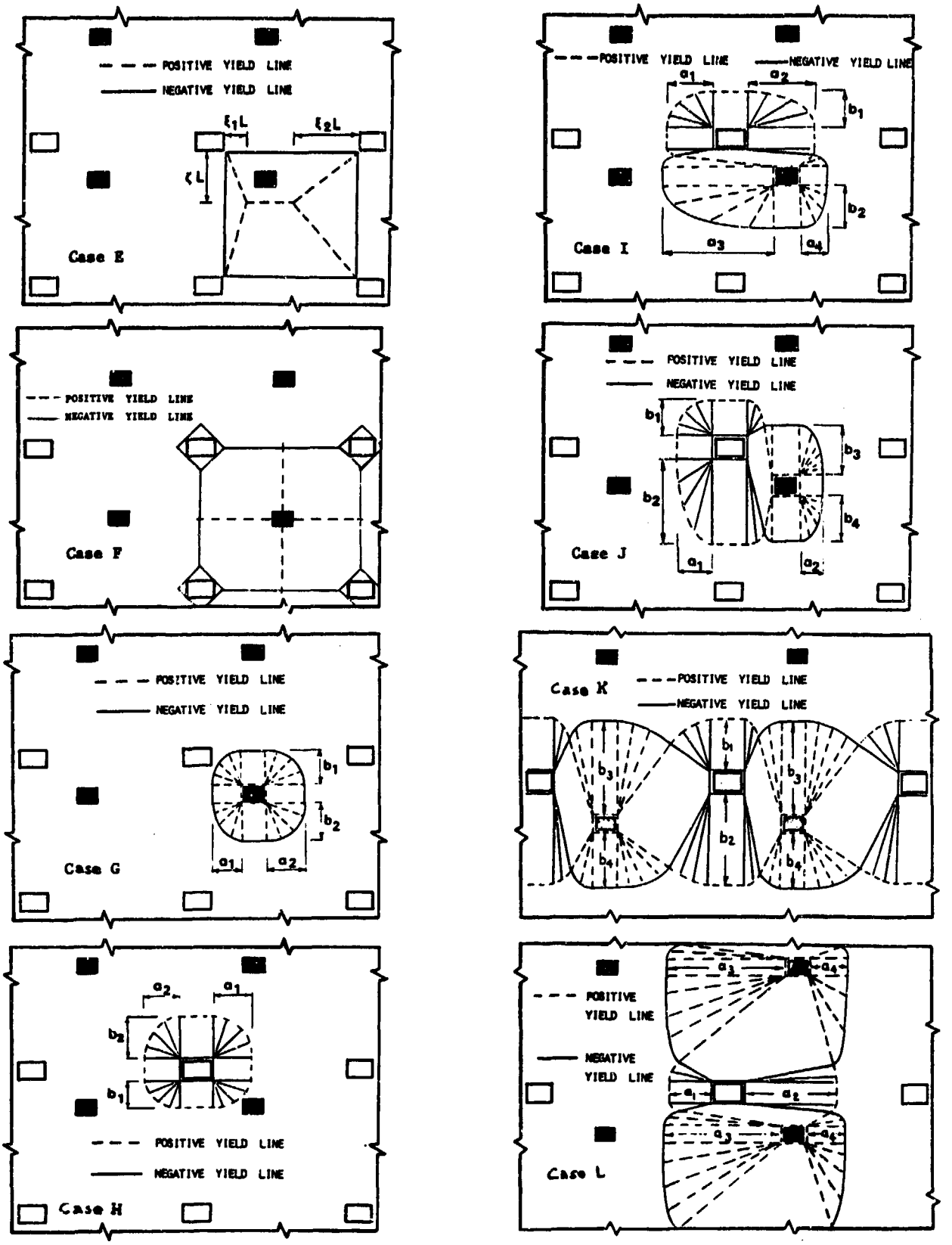

Fig. 2 Yield Line Patterns for Flat Plate Floor System

Table 1 Values of K for concentrated load at quarter point of panels

μ=1 ,λ=1 , $l_h = l_v$ = .25 Point loads and supports									
Case	ω = .010	.025	.100	.250	.500	1	10	100	1000
A , B	.027	-	.254	-	-	1.781	3.635	3.968	4.004
C	.053	-	.517	-	-	4.010	12.346	15.586	16.006
D	.053	-	.501	-	-	3.207	6.970	7.896	8.003
E	no		no			no	10.314	11.821	11.982
G	.0314	.078	.313	.774	-	2.734	-	-	-
H	.0312	.077	.287	.634	1.058	1.589	2.896	3.155	3.184
I , J	.0224	.056	.220	.533	1.036	no	no	no	no
K , L	.0219	.055	.218	.540	.951	no	no	no	no

(-) - value was not calculated
no - mechanism will not form

Table 2 Values of K for concentrated load at quarter point of panels

μ=1 ,λ=1 , $l_h = l_v$ = .5 Point loads and supports									
Case	ω = .010	.025	.100	.250	.500	1	10	100	1000
A , B	.020	-	.191	-	-	1.336	3.340	3.929	4.000
C	.040	-	.388	-	-	3.004	9.247	11.674	12.000
D	.040	-	.375	-	-	2.402	5.220	5.914	6.000
E	.040	-	.387	-	-	3.000	9.231	11.650	12.000
G	.0314	.078	.307	.742	1.397	-	-	-	-
H	.0312	.077	.287	.634	1.058	1.589	2.896	3.155	3.184
I , J	.0314	.078	.311	.773	2.044	no	no	no	no
K , L	.0269	.067	.264	.673	no	no	no	no	no
F	.154	-	-	-	-	3.206	3.910	3.998	4.000

(-) - value was not calculated
no - mechanism will not form

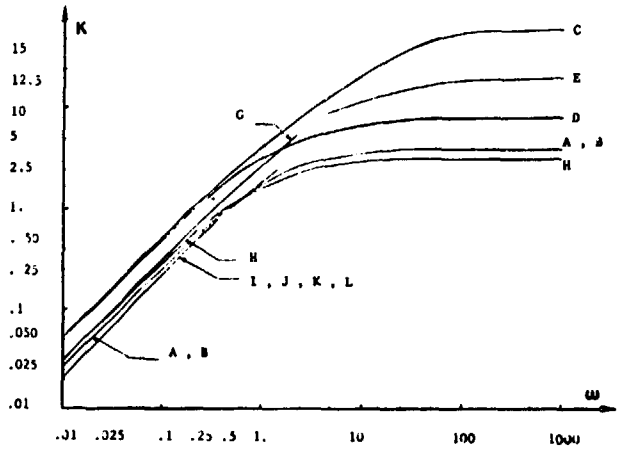

Fig. 3 Collapse load vs. load ratio for different Yield Line Patterns for $l_h = l_v$ = .25

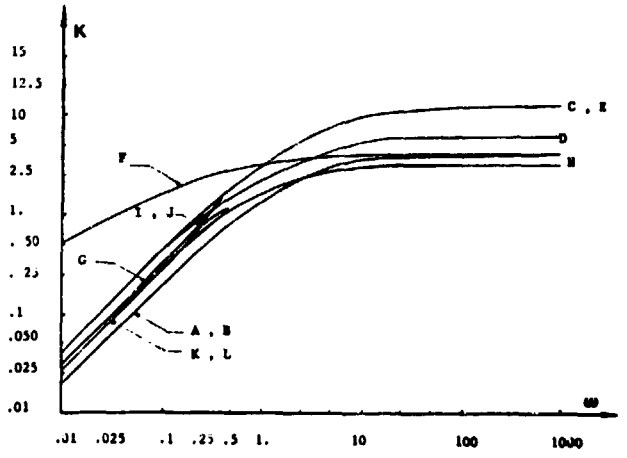

Fig. 4 Collapse load vs. load ratio for different Yield Line Patterns for $l_h = l_v$ = .5

CONCLUSIONS

It has been found that different mechanisms can control the collapse. Which particular mechanism becomes critical depends on the combinations of variables which characterize a particular slab system. Some of the equations derived constitute a generalization of elliptical fan equations derived by Sawczuk and Jaeger, and equations derived by Gesund for cases of flexural punching of column supported slabs subjected to distributed load only, and boundary supported slabs subjected to combined loadings.

Further study is needed 1) to evaluate the effect of these parameters, for exterior and corner panels, 2) to develop reasonably accurate but simple strength predictions which can be readily used by the engineering profession, and 3) extend the work to irregular layouts of columns and loads.

Some experimental verification has been carried out [2], but more would be desirable to assure that no possibly critical mechanisms have been overlooked. Knowing how gently curved the solution surfaces obtained from Yield Line Theory are, however, it is extremely unlikely that any alternate mechanism could give an upper bound on the collapse load which would be as much as 25% less than the lowest presented here.

REFERENCES

1. Gesund, H., "Limit Design of Slabs for Concentrated Loads",J.Struct.Div., ASCE, Vol. 107, No. ST9, Proc. Paper 16504, Sept., 1981, pp.1839-1856.
2. Jacak, J.T., "Inelastic Analysis of the Flexural Strength of Flat Plate Floor Systems Subjected to Distributed and Concentrated Loads", Ph.D. Diss., Directed by H. Gesund, University of Kentucky, 1985.
3. Johansen, K.W., "Yield Line Theory", London. Cement and Concrete Association, 1962, pp.181.
4. Kuester J.L. and Mize J.H., "Optimiza tion Techniques with FORTRAN ", McGraw Hill, 1973, pp.500.
5. Sawczuk, A. and Jaeger, T., "Grenztrag fahigkeits-Theorie der Platten", Sprin ger Verlag, Berlin, 1963, 522 pp.

SOIL-STRUCTURE INTERACTION UNDER BLAST LOADING

Yu-ao He

Tianjin University
Tianjin, CHINA

ABSTRACT

Through the analysis of beam-type underground-structure, a new model for the interaction between back filling soil and underground-structure under blast loading is presented. Such that the underground-structure can be predicated correctly.

A Finite Element-Curve Fitting method for determining the rigidity of back filling soil, which is a basic component factor of the model, is also given in this paper.

The calculated results based on this proposed model and the dynamic experiments of shallow-embedded beams were in good agreement.

INTRODUCTION

The model of soil-structure interaction (SSI) of underground-structure, according to that by means of which part of the SSI system discussed was taken from , may be divide into two forms: associated and disassociated. The associated model is that in which the medium/structure should be considered as a whole and analysed by using the finite element method in an ordinary way. On the contrary, the disassociated model is actually the structure itself separted from medium and while analysed the influence of SSI should be taken account in.

It is obvious that the analysis for underground-structure by the associated model is more complicated than the disassociated. So it needs further laborious works and requires the computer with more large storage.

The disassociated model has been studied in different way by some researchers. In this paper, a new disassociated model for the dynamical analysis of underground-structure under blast loading is given.

DESCRIPTION OF MODEL

Take the beam-type structure, show in Fig. 1 which might be the top slab of subway, as an object of study. And take it as the plane strain problem when the surface of earth was overspread with distributed loads.

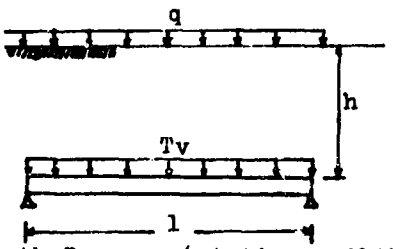

A. Earth Pressure(static equilibrium)

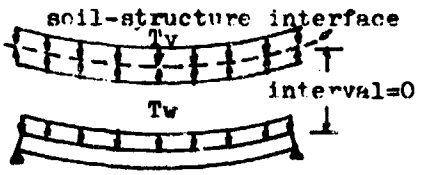

B. Earth Pressure(dynamic displacement)

Fig. 1 Earth Pressure on the Beam

Before the blast loads acting, the earth pressure can be obtained by the conventional formulae in the soil mechanics. For the shallow-embedded structures constructed by the cut-and-cover method, the earth pressure should be using Terzaghi's formula that is well known.

It is should denoted here that these formulae given by soil mechanics of today are only suitable for the state of static equilibrium. While the displacements dynamically occurring, the original earth pressure Tv is no longer keeping unalternated and should be equal to the contact pressure Tw between soil and beam, obtained by the conditions of compatibility in the static sense under the pressure Tv. The pressure Tw should be maintained until the dynamical displacements vanished. So that, in the period of dynamic exciting, the effects of the contact pressure Tw on the

responses of the beam equivalent to some mass added upon the beam. The mass is equal to Tw/g and may be called as " Equivlence mass " conveniently. (g is the acceleration of gravity)

The procedure of the responses of the beam under blast loading may be illutrated by the concept of wave dynamics. The procedure might be divided into two phases (He 1979): constrained and unconstrained. In the constrained phase, suppose that the beam is applied by an imaginary " fixed-rigid " constraint, shown in Fig. 2 .

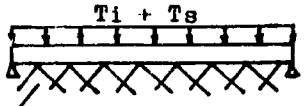

A. Constrained Phase

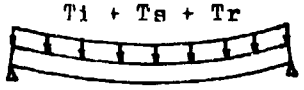

B. Unconstrained Phase

Fig. 2 Dynamic Loads on the Beam

While the incident stress wave impinging upon the upper surface of the beam, the scattered wave should be generated. Let the incident and scattered stresses represented by Ti and Ts respectively.

Next, the unconstrained phase, to free the beam from the imaginary constraint, the deformation and the displacement should happen. These disturbs will input forcefully into the medium. Then the radiated wave will generate. Let the radiated stress beween the soil and the upper surface of the beam represented by Tr . Generally, the expression for it might be represented by the following formula (He 1979*,1980):

$$Tr = - (KU + C\dot{U}) \qquad (1)$$

where U = disturb(displacement or deformation of beam)

$\dot{U}$ = rate of change of disturb with respect to time

K = rigidity function of soil

C = damping function.

From theoretical analysis, it had been known that the functions depend on the properties of soil, the geometrical parameters of where discussed on the beam, the height of soil covered over the beam (as a semispace problem) and the frequency of disturb.

The stress Ti should be given certainly in practice, and then the stress Ts may be obtained theoretically. But the stress Tr is almost unknown, it is a function of U and $\dot{U}$ mentioned above.

In essence, the SSI is equal to the radiated stress plus the action of inertia of equivalent mass M . Therefore, the new SSI model proposed this paper can be generally expressed in the following form:

$$(SSI) = - (KU + C\dot{U} + M\ddot{U}) \qquad (2)$$

If let the proposed model discrete for numerical analysis, a schematic diagram for the beam is shown in Fig. 3 .

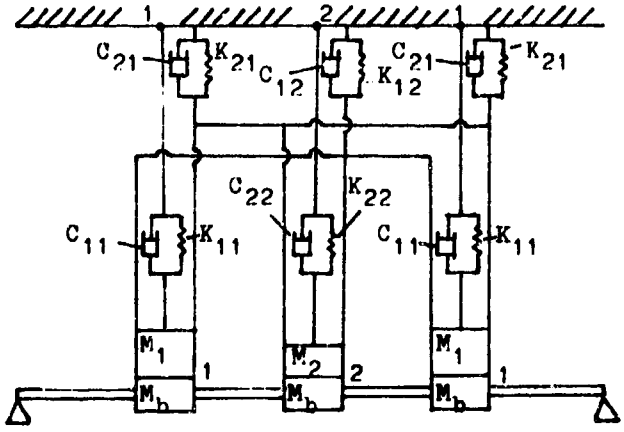

Fig. 3 A Schematic Diagram for SSI

In the figure, $K_{ij} = abK'_{ij}$, a = distance between joint i and j on the beam, b = width of the beam, K'_{ij} = distributed rigidity function. The K'_{ij} function means that the distributed force to be needed for generating an unit displacement at point i; the distributed force acts on the soil at a range just length a with the midpoint of point j . Similar definitions for C_{ij} , M_b, M_1 and M_2 may be given.

In the following, function K is found by static elasticity. So that the proposed SSI model belongs to quasi-static.

SOIL RIGIDITY FUNCTION

From that indicated above, the rigidity function for any discrete point i can be written as $K_{ij}(h/l, E, \nu)$. It is depend-

ing on the relative height of covered soil h/l and the property of soil (Young's modulus E and Poisson's ratio ν). In which, h is the height of covered soil and l is the span of beam.

The Finite Element-Curve Fitting method for detemination of the rigidity function is shortly mentioned below. The method is divided into two steps. First, by using finite element method, the values of K_{ij} for discrete points h/l = .25, .50, .75, 1.00, 1.25, 1.50 are obtained. And then the rigidity functions should be given by using the curve fitting method for these discrete values. Conveniently, let ν = 1/3.

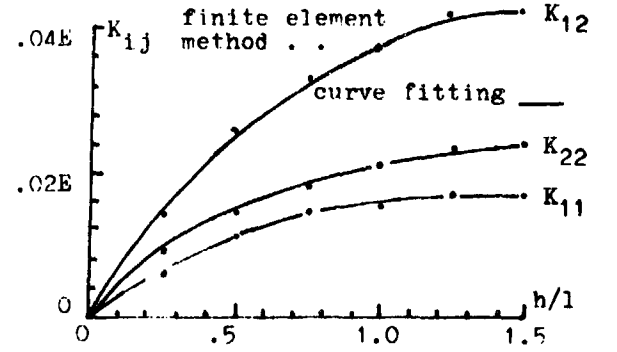

Fig. 4 Soil Rigidity Functions

These functions should be written as the following:

$$K_{11}(h/l, E, \nu) = E(.03297(h/l) - .024231(h/l)^2 + .006566(h/l)^3) \quad (3)$$

$$K_{21}(h/l, E, \nu) = E(.03141(h/l) - .016491(h/l)^2 + .003253(h/l)^3) \quad (4)$$

$$K_{22}(h/l, E, \nu) = E(.04315(h/l) - .028451(h/l)^2 + .006713(h/l)^3) \quad (5)$$

$$K_{12}(h/l, E, \nu) = 2K_{21}(h/l, E, \nu) \quad (6)$$

NONLINEARITY OF SOIL

The rigidity functions given above are based on the hypothesis of linear elasticity. But the strains of soil might be larger than 1/10000 while the blast loads acting on; the nonlinearity would be appeared. So that the influences of it must be considered. It may be treated with the Newton-Raphson method for modifying the modulus E.

The equivalent strains of soil under the giving loads q(kg/cm^2) can be calculated by the Finite Element-Curve Fitting method also:

$$\gamma = ql^2/\beta(h/l)E \quad (7)$$

where $\beta(h/l)$ = strain function

$$\beta(h/l) = 4050(h/l) - 615(h/l) + 245(h/l) \quad (8)$$

The secant modulus E(kg/cm^2) of soil is obtained by the Newton-Raphson method from the stress-strain curve and Equ. 7 . After some circles of iteration, the precise value of E corresponing with actual strain of soil is obtained. Then substituting E in Equ. 3 - 6, the modified rigidifuntions are given.

EQUIVALENT MASS

From Terzaghi's formula for soil pressure, the soil weight acting on the joint 1 or 2 of the beam (shown in Fig. 3) is:

$$W = abTv \quad (9)$$

By the conditions of compatibility, the equivalent masses at joint 1 and 2 can be obtained:

$$M_1 = W((1/k_{12}+1/K_{12})(1/K_{21}+1/K_{22})-(1/k_{22}+1/K_{22})(1/K_{11}+1/K_{12}))/g((1/k_{21}+1/K_{21})(1/K_{12}+1/k_{12})-(1/k_{11}+1/K_{11})(1/k_{22}+1/K_{22})) \quad (10)$$

$$M_2 = W((1/k_{21}+1/K_{21})(1/K_{12}+1/K_{11})-(1/k_{11}+1/K_{11})(1/K_{22}+1/K_{21}))/g((1/k_{21}+1/K_{21})(1/K_{12}+1/k_{12})-(1/k_{11}+1/K_{11})(1/k_{22}+1/K_{22})) \quad (11)$$

where k_{ij}= rigidity of the beam. Its definition is similar to K_{ij}.

Discussion on Equ. 10 and 11:

1. If soil is more rigid than beam, $K_{ij} \gg k_{ij}$ then $M_1 = M_2 = 0$
2. If the rigidity soil and beam is equal to each other, $K_{ij} = k_{ij}$ then $M_1 = M_2 = W/2g$
3. If beam is more rigid than soil, $k_{ij} \gg K_{ij}$ then $M_1 = M_2 = W/g$.

From above, the general aspects variations for the equivalent mass may be found out.

After some statistical simplifications , Equ. 10 and 11 might be written in following forms:

1. For the simply supported beam

$$M_1 = (6.69\ 10^{-3}\theta K_{11} + .3512)/(23.72\ 10^{-6}\theta^2 K_{11}^2 + 10.94\ 10^{-3}\theta K_{11} + .3512) \quad (12)$$

$$M_2 = -(7.34\ 10^{-3}\theta K_{11} - .3512)/(23.72\ 10^{-6}\theta^2 K_{11}^2 + 10.94\ 10^{-3}\theta K_{11} + .3512) \quad (13)$$

2. For the fixed end beam

$$M_1 = (3.11\ 10^{-3}\theta K_{11} + .3512)/(3.05\ 10^{-6}\theta^2 K_{11}^2 + 2.91\ 10^{-3}\theta K_{11} + .3512) \quad (14)$$

$$M_2 = -(2.20\ 10^{-3}\theta K_{11} - .3512)/(3.05\ 10^{-6}\theta^2 K_{11}^2 + 2.91\ 10^{-3}\theta K_{11} + .3512) \quad (15)$$

where $\theta = (E/\underline{E})(h/d)^3$; relative rigidity parameter

d = height of beam

$\underline{E}$ = Young's modulus of material for beam.

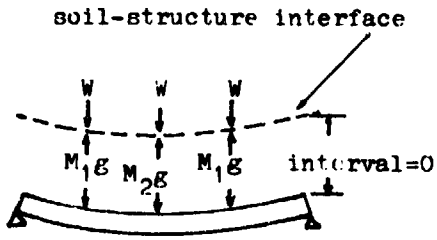

Fig. 5 Contact Forces

Illustrative example: Suppose a steel beam with span l=100cm, height d=2cm and modulus $\underline{E}$=2100000kg/cm². The distributed blast loading q=1kg/cm². The modulus of soil(for initial) E=200kg/cm². Find the equivalent masses for the different heights of covered soil.

By using Equ. 12-15, the equivalent masses should be obtained. And then, the varied relations between the relative equivalent mass (M_1/M , M_2/M) and the relative height of covered soil (h/l) are given in Fig. 6 for observing and comparing conveniently. In which $M = W/g$.

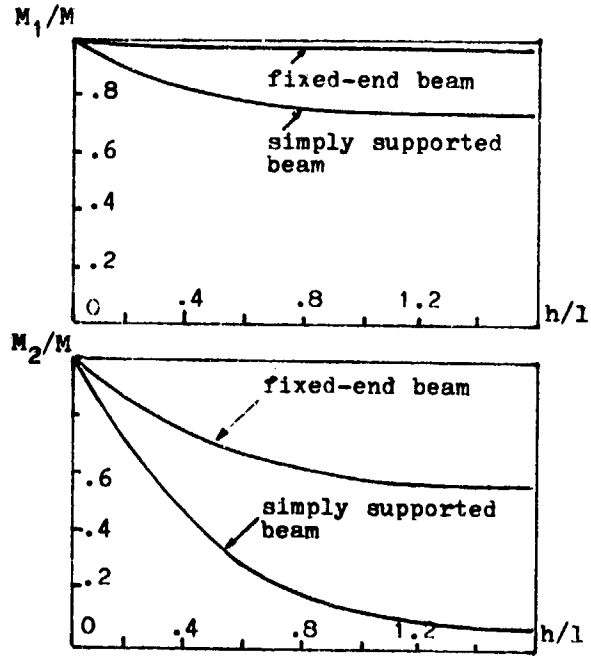

Fig.6 Relative Equivalent Mass

COMPARISONS WITH EXPERIMENTS

The data of the experiments were known as that: the span and height of the steel beam is 70cm and 2cm respectively; the weight per unit volume and modulus(initial) of soil is .00143kg/cm³ and 1000kg/cm² for sand(Experiment No. 1), and .00189kg/cm³ and 200kg/cm² for clay(Experiment No. 2) respectively.

For verifying the proposed model, the comparisons with experiments are given. It is convenient to choose the fundamental frequency of structure for comparing.

The fundamental frequency can be determined by the following formula obtained by using the proposed model for the beam as well as that shown in Fig. 3.

$$\omega = ((A - (A^2 - 4\alpha B)^{\frac{1}{2}})/2(M_b + M_2)B)^{\frac{1}{2}} \quad (16)$$

where $A = 1/(K_{11} + k_{11}) + 1/(K_{22} + k_{22})$

$$B = 1/(K_{11} + k_{11})(K_{22} + k_{22}) - 1/(K_{21} + k_{21})(K_{12} + k_{12})$$

$$\alpha = (M_b + M_2)/(M_b + M_1)$$

M_b = concentrated discrete mass of beam at joint 1 and 2 .

In Equ. 16, the damping had been neglected.

If let K_{ij}=0, then the fundamental frequence for the beam of uncovered soil, ω_*, will be given.

The coparisons are given in Fig. 7-8.

It is shown that the calculated based on the proposed model were in good agreement with the results of the experiment No. 1 and No. 2.

CONCLUSIONS

The new SSI model proposed in this paper can correctly reflects the practicl behaviours of the underground-structures under blast loading. And then it is effective and useful for the purpose of analysing and designing in a simple way.

ACKNOWLEDGEMENT

The results of experiment used in this paper for comparisons are adoped from Ref.4 . It is gratefully acknowledged by the author.

REFERENCES

1. He, Y.-A.,(1979), "Study on the Dynamical Responses of Underground-Structures", Underground Engineering, No.5, May. (In Chinese).

2. He, Y.-A.,(1979*), "The Radiated Stress around a Circular Hole at the Infinite Plane", ibid., No.2, February.

3. He, Y.-A.,(1980), "The Mixed Boundary Problems of Radiated Stress around a Circular Hole", ibid., No.9, September .

4. Li, G.-H., et al.,(1979), "Study of the Nature Frequency for Shallow-Embedded Underground Beam", J. Tung Chi University, December. (In Chinese) .

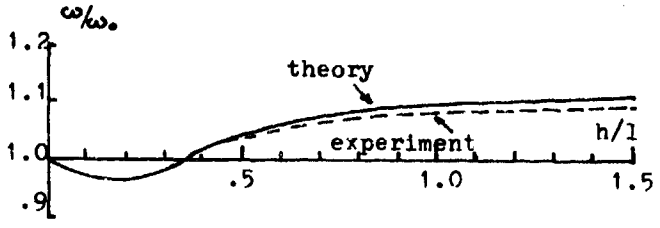

Fig.7 Comparisons with Experiment No. 1

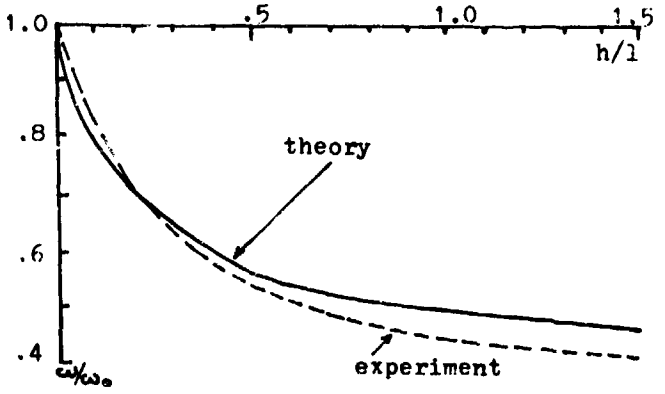

Fig.8 Comparisons with Experiment No. 2

PREDICTING CONCRETE SPALL RESULTING FROM DYNAMIC LOADING

William E. Wolfe
The Ohio State University, Dept. of Civil Engineering
Columbus, Ohio 43210
and

David R. Coltharp
U.S. Army Engineer Waterways Experiment Station Structures Laboratory
Vicksburg, Mississippi 39180

Whether spalling will or will not take place as a consequence of a dynamic load is of considerable importance to the designers of protective structures and therefore has been the subject of a number of research projects. However, due to the complexity of the problem, available analyses rely on either highly idealized boundary and loading conditions or on empirical expressions derived by fitting curves to a limited amount of experimentally obtained data. A review of the methods most commonly used to calculate spalling of the backface of concrete slabs is presented. Limits to the applicability of the predictive procedures are discussed.

1. INTRODUCTION

The dynamic response of a concrete structure can be divided in a broad sense into two categories: 1) structural or global behavior, and 2) local behavior. Local behavior can in turn be divided into a number of separate study areas. included among these sub-areas are; a) cratering, b) penetration, c) perforation, d) cracking and e) spalling. The primary subject of interest of this paper is spalling. Other local effects will only be introduced when necessary to describe the spalling phenomenon.

Spalling, as used in this paper, refers to the ejection of pieces of concrete from the back (unloaded) face of a concrete structure which has been subjected to a dynamic load. When ejected, these concrete particles typically possess velocities large enough to cause severe injury to personnel and/or damage to equipment housed within the structure. Spall is the result of a tensile failure in the target material. The process of loading which leads to spalling is shown schematically in Figure 1. In this illustration, a load pulse in the concrete resulting from a specified dynamic load is idealized as a plane triangular compression wave and the target is assumed to be a planar wall of some finite thickness. The incident pulse is shown in the figure as passing through the target without change in either shape or magnitude. Upon reaching an interface between two materials, the incident wave would in general be both reflected and refracted. However, if the interface is a free surface only a reflected wave would be generated. For an arbitrary angle of incidence, a stress free boundary can only be insured if a rarefaction and a distortional wave are generated at the interface. However, if the angle of incidence is normal to the free surface, the necessary boundary conditions can be satisfied by a reflected tensile wave equal in shape and magnitude to the incident compression wave. The actual stress state at a point in the concrete target is determined by taking the sum of the stresses induced by the incident compressive pulse and the reflected tensile pulse at that point. For a target consisting of a material which has a much lower strength in tension than in compression, a tensile failure will occur at some plane in the target when the amplitude of the reflected tensile stress wave exceeds the dynamic tensile strength. The location of the failure surface is a function of the shape and magnitude of the incident pulse. For the example shown in Figure 1 where the shape of the stress wave is triangular and the magnitude is just equal to the dynamic tensile strength, the distance from the free surface to the spall plane is one-half the wavelength. For larger incident wave amplitudes, the failure strength would be reached sooner and the initial spall thickness would be less, but multiple spall zones would develop. When failure does occur, the material between the original free surface and the newly created fracture surface will possess an amount of entrapped momentum equal to the mass of the spalled material times the particles' velocity in the spalled zone. It is this trapped momentum that gives the spalled material its ejection velocity.

The incident compressive wave can be the result of an impact of a solid body, an overpressure such as would be caused by a blast wave, or a combination of impact and impulse resulting from the nearby detonation of a cased explosive charge. Predictions of spall thickness have typically been either empirical in nature, i.e., the approach taken is one of determining the best fit to a set of experimental data, or theoretical in which the formulation requires that a signficant number of simplifying assumptions be

made in order to make the problem solvable. The approach chosen is usually dependent upon which of the above loading conditions is considered to be the design threat. Since more data exist for the problem of response due to impact of a projectile, solution techniques for the impact problem have largely been empirical. On the other hand, because the amount of data on the spall of concrete slabs from blast loading is much more limited, the solutions to this type of loading have tended to be theoretical.

2. RESPONSE TO AN IMPULSIVE LOAD

When an explosive charge is denotated near a concrete wall a compressive stress wave is generated that is transmitted through the structure. As was observed in the introduction when this compressive wave reaches a free surface, it is reflected. The reflected wave will have a tensile component whose amplitude is proportional to the amplitude and a function of the angle of incidence of the compression wave. A comparison of the state of stress induced by the incident and reflected waves with the dynamic material properties of the concrete must be made in order to assess the liklihood of spall. Peak incident pressures can be calculated if the magnitude of the explosive source and its distance from and orientation to the target are known (7, 8, 30). Accurate spall calculations require a detailed knowledge of more than just the magnitude of the incident wave however. The stress time history must also be known or assumed. One possible wave form which has been widely used is a triangle such as the one which was shown in Figure 1. Another is an exponential relationship such as the one proposed by Kot et. al. (20) which they found to be in somewhat better agreement with available observations than the simple triangular pressure distribution. A plot showing a triangular pulse and Kot's exponential decay pulse together with a pressure time history measured during tests reported by Coltharp (6) is presented in Figure 2. There does not appear to be a great deal of difference among the three plots and either of the two idealizations would be expected to simulate the important characteristics of the actual pressure wave in sufficient detail for design. Predicted first spall thickness for the exponential stress pulse as presented by Kot et. al. (20) is given as:

$$\delta_1 = \frac{V_p t_+}{2} \left(\frac{\sigma_t}{p_o}\right)^{1/\gamma} \qquad (1)$$

The symbols used in this and subsequent equations are defined in the glossary at the end of the paper.

Dynamic Tensile Strength

Spall occurs when the net tensile stress exceeds the dynamic tensile strength of the concrete. Several investigators (3, 22, 24, 29, 31, 32) have reported dynamic tensile strengths as much as 2.2 times the measured static concrete tensile strength. Despite these observations, design procedures currently being used (27, 30) do not allow for an increase in design strengths to account for dynamic loads.

3. BEHAVIOR OF SLABS SUBJECTED TO IMPACT LOADS

Although the mechanics of projectile penetration has been studied since the early eighteenth century, a completely adequate theoretical description of the behavior of a target as it is impacted by a high speed missile has not yet been proposed (2). There are however, a number of empirical and semi-empirical methods for predicting the response of a concrete target, including spalling, to a missile impact. Each is a best fit to a limited number of observations and being empirical, each varies in its ability to predict the onset of spall.

3a. The first of the spall thickness expressions was the Petry Formula which appeared in its original form in 1910. In the revised form currently in use (1, 7, 19), spall thickness is calculated as a function of the strength of the concrete and the weight and velocity of the missile. The Modified Petry Formula is given as:

$$S = 26.4\, K_p A_p \log\,(1 + V^2/0.0215) \qquad (2)$$

3b. The Corps of Engineers (COE) Formula (7, 9, 17) was developed from test results obtained by impacting concrete slabs with artillery shells of four different sizes. The expression for spall thickness is given as:

$$s = 2.12d + 1.36x \quad \text{for } 3d < s < 18d \qquad (3)$$

where:

$$x = \frac{222 P_p\, d^{0.215}\, V^{1.5}}{\sqrt{f_c}} + d/2 \qquad (4)$$

3c. The National Defense Research Committee (23) developed a spalling formula by observing that in a large number of tests, spalling would take place when the projectile penetrated at least 50% of the target thickness. A prediction of the amount of penetration to be expected was made by assuming that the force resisting projectile penetration at any time t is proportional to the missile velocity at that time t times the depth of penetration. The NDRC formula for spall is given as:

$$s = 7.91x - 5.06\frac{x^2}{d} \qquad x < 0.65d \quad (5)$$

where:

$$x = (4KNd^{2.2}\, DV^{1.8})^{0.5} \qquad x < 2d \quad (6)$$

$$x = KNd^{1.2}\, DV^{1.8} + d \qquad x > 2d \quad (7)$$

The NDRC formulation will predict spall thicknesses in the range of s<3d which is appropriate for thin targets or large projectiles. For thicker targets (s > 3d) the NDRC formula takes on the form of the Corps of Engineers equation for spall.

3d. The Amman and Whitney formula was developed (13, 14, 15) to characterize the damage to concrete structures resulting from the impact of explosively generated fragments. In the original forms the equations for spall were strictly applicable only for missiles having impact velocities greater than 1000 feet/sec. The formulas have been modified and now appear to give reasonable estimates for spall caused by missiles impacting at lower velocities (13). Spall thickness is given by the modified Amman and Whitney formula as:

$$s = 1.215xd^{0.1} + 2.12d \qquad (8)$$

The form of the penetration equation is that of the NDRC equations (equations 6 and 7) but with $K_{AW} = 1.15K_{NDRC}$. The Amman and Whitney penetration equations are often expressed in terms of fragment weight. When given in this form the penetration is calculated as:

$$x = 0.91\, W_f^{0.37}\, V^{0.9} \qquad x < 2d \quad (9)$$

$$x = 0.3\, W_f^{0.4}\, V^{0.9} + 0.575 W_f^{0.33} \qquad x > 2d \quad (10)$$

3e. Kar (17, 18) has developed a set of expressions that utilize the same format as the NDRC equations but provide for additional parameters in the formulation. These additions to the spall equations include the effects of missile material properties and cross sectional area and the size of the aggregate in the concrete. The spall thickness is calculated by the following expressions:

$$s\text{-}a = \beta\left(7.91x - 5.06\,\frac{x^2}{d}\right) \qquad (11)$$

where:

$$x = \left(4KNd^{2.2}\, DV^{1.8}\,\frac{d}{d_o}\right) \qquad x<2d \quad (12)$$

$$x = KND^{1.2}D\, V^{1.8}\,\frac{d}{do} + d \qquad x > 2d \quad (13)$$

3f. Chang (5) postulated that particle spall resulted from local bending failure of the concrete target. A spall thickness was defined as the wall thickness at which the kinetic energy of the impacting missile equalled the strain energy capacity of the portion of the wall affected by the impact. The resulting expression developed by Chang is:

$$S = Y\left(\frac{u}{v}\right)^{0.4a}\,\frac{\left(\frac{W_p}{g}V^2\right)^{0.4}}{d^{0.2} f_c^{0.4}} \qquad (14)$$

3g. Hughes (16) nondimensionlized the NDRC equations by proposing an impact factor (similar to the impact factor proposed independently by Haldar and Miller (12)). According to Hughes, spall thickness can be calculated from the following

$$s = 1.74x + 2.5d \qquad (15)$$

where:

$$x = \frac{0.19Id}{f_c} \qquad (16)$$

and:

$$I = \frac{W_p V^2}{gd^3 f_c} \qquad (17)$$

In the Hughes model the impact force increases linearly to a maximum value which corresponds to the onset of spall. The load then decreases parabolically to zero at maximum penetration. In the equations presented by Hughes the missile must be non-deformable, energy cannot be dissipated at the point of impact except in deforming the target and the effects of reinforcement cannot be accounted for. Hughes presents data (16) comparing calculated values of spall thickness with available data. The figures show good agreement between predictions and observations with the predictions tending to be somewhat conservative. The predicted values appear to become increasingly conservative as the impact factor decreases.

3h. A series of tests performed for the Bechtel Corp. (1, 9, 28) in which both deformable and non-deformable large diameter cylinders impacted concrete slabs resulted in the development of a new set of empirical equations for calculating spall thickness. For non-deformable missiles the Bechtel equation for spall is:

$$s = \frac{15.5}{\sqrt{f_c}}\,\frac{W_p^{0.4}\, V^{0.5}}{d^{0.2}} \qquad (18)$$

For deformable cylinders the spalling thickness is:

$$s = \frac{5.42}{\sqrt{f_c}}\,\frac{W_p^{0.4}\, V^{0.65}}{d^{0.2}} \qquad (19)$$

3i. Stone and Webster performed a series of tests similar to the Bechtel tests (1, 9, 19). As with the Bechtel equations, spall thickness for either rigid or deformable cylinders can be obtained. The Stone and Webster equation for spall thickness is given as:

$$s = \left(\frac{W_p V^2}{C}\right)^{0.33} \qquad (20)$$

4. COMPARISION OF THE IMPACT FORMULAS

Figure 3 is a plot of the predicted spall thickness as a function of impact velocity. A prediction of the spall thickness for two different projectiles is presented for each of the empirical spalling procedures reviewed above. The first, shown in Figure 3a, might be considered to

be a typical fragment with a projectile weight = 0.68 kg, and a diameter = 2.5 cm. The second projectile, shown in Figure 3b, weighs 160 kg and the diameter is 15.2 cm. The target consists of 5000 psi concrete. It can be seen that for both large and small projectiles the Corps of Engineers Formula gives the most conservative estimate of spall thickness with the degree of this conservatism increasing with increasing projectile velocity. Superimposed on both figures is a shaded area indicating the general region in which most of the available data fall. Within this range the NDRC formulas have been shown to be adequate, though, conservative, predictors of spall for small missiles. The NDRC equations are quite conservative for large missiles (9). Observed behavior has been shown to be more satisfactorily predicted by the Bechtel equations for these missiles (9).

5. COMBINED IMPACT AND IMPULSE

The equations reviewed above have all considered damage to be the result of either a single load either impulse or impact. An important consideration in the determination of the dynamic response of a concrete wall is the effect on that wall of a combined blast and fragmentation load typical of that delivered by explosive munitions. The results of recent tests in which concrete walls were subjected to loads from both cased and uncased charges indicate that damage due to the combined load is much more extensive than would be predicted by current methods. Kropatscheck (21) and Hader (11) clearly show that fragment impact causes damage in addition to that caused by dynamic overpressures alone. Hader's results showed that wall thicknessess had to be tripled for cased explosion tests in order to reduce the wall damage to that found for uncased charges with the same scaled distance. Coltharp (6) has presented results of tests using cased charges which show the greatest amount of spall occurs in the area subjected to fragment impact. Canada (4) has proposed a method for combining the procedures discussed above for determining the effects of an impulse with the empirical Amman and Whitney formula for fragment impact to estimate the spall that would be expected when a target is subjected to both threats.

6. GLOSSARY OF TERMS

The symbols used in this report along with customary units are given below.

- t_+ = duration of positive phase of stress wave (sec)
- γ = constant -Kot
- δ_1 = thickness of first spalled layer (in)
- P_o = peak positive normal reflected pressure (peak compressive pressure at near face in concrete) (psi)
- s = spall thickness (in)
- x = penetration (in)
- V_p = dilatational wave velocity (in/sec)
- σ_t = concrete tensile strength (lb/in^2)
- d = projectile diameter (in). For projectiles with non-circular cross-sections, d = equivalent diameter (same contact area)
- d_c = outside diameter of missile (in) -Kar
- W = projectile weight (lbs)
- W_f = fragment weight (oz) -Amman & Whitney
- g = acceleration due to gravity (ft/sec^2)
- N = missile shape factor $0.72 < N < 1.14$
- N = missile shape factor $0.72 < N < 1.17$ -Kar
- V = missile impact velocity (1000 ft/sec)
- f'_c = concrete compressive strength (lb/in^2)
- K_p = penetrability coefficient -Petry
- K = $180/\sqrt{fc}$ -NDRC
- K = $(180/\sqrt{fc})\beta^{1.25}$ -Kar
- A_p = missile wieght/unit projected area (lb/ft^2)
- D = missile calibre density = W/d^3 (lb/ft^3)
- P_p = sectional pressure of missile $1.27\ W/d^2$ (lb/ft^2)
- E_m = modulus of elasticity of missile (lb/in^3)
- E_s = modulus of elasticity of steel $= 29X10^6\ lb/in^2$
- α = maximum aggregate size (in) -Kar
- β = coefficient = Em/Es -Kar
- Y,a = coefficients -Chan
- v = reference velocity = 200ft/sec -Chan
- I = impact factor -Hughes, Haldar
- $\dot{\varepsilon}_s$ = strain rate factor $1 + 12.3\ (\ln(1 - 0.03I))$ -Hughes
- C = coefficent reflecting missile shape -Stone & Webster

7. REFERENCES

1. ASCE Technical Committee on Impactive and Impulsive Loads, Preliminary Draft Report, Volume V, proceedigns of the Second ASCE Conference on Civil Engineering and Nuclear Power, Knoxville, Tennessee, September 15-17, 1980.
2. Backman, M.E. and Goldsmith, W., "The Mecanics of penetration of Projectiles into Targets," International Journal of Engineering Science, Volume 16, Number 1, 1978, pp. 1-99.
3. Birkimer, D.L. and Lindemann, R., "Dynamic Tensile Strength of Concrete Materials," American Concrete Institute Journal, Jan., 1971, pp. 47-49.
4. Canada, C.E., "Combined Blast and Fragment Loading of Reinforced Concrete," Report to SCEEE, August, 1984.
5. Chang, W.S., "Impact of Solid Missiles on Concrete Barriers," Journal of the Structural Division, ASCE, Vol. 107, No. ST2, February, 1981, pp. 257-271.
6. Coltharp, D.R., "Blast Response Tests of Reinforced Concrete Box Structures," Proceedings of the Symposium on the Interaction of Non-nuclear Munitions with Structures, Part 2, U.S. Air Force Academy, Colorado, May 10-13, 1983, pp. 133-138.
7. Department of the Army, Fundamentals of Protective Design (Non-Nuclear), TM 5-855-1, July, 1965.

8. Department of the Army, Structures to Resist the Effects of Accidental Explosions, TM 5-1300 (also NAVFAC P-397 and AFM 88-22), Departments of the Army, Navy and Air Force, June, 1969.
9. Florence, A.L., "Designing Nuclear Power Plants to Withstand Pulse and Impact Loads," Minutes of the Eighteenth Explosive Safety Seminar, San Antonio, TX, pp. 1809-1863.
10. Glasstone, S. and Dolan, P.J., The Effects of Nuclear Weapons, Revised Edition, Department of the Army Pamphlet No. 40-3, March, 1977.
11. Hader, H., "Effects of Bare and Cased Explosives Charges on Reinforced Concrete Walls," Proceedings of the Symposium on the Interaction of Non-Nuclear Munitions with Structures, U.S. Air Force Academy, Colorado, May 10-13, 1983, pp. 221-226.
12. Halder, A. and Miller, F.J., "Local Effects Evaluation of Concrete Structures," Proceedings of the Symposium on Concrete Structures Under Impact and Impulsive Loading, Berlin, June 2-4, 1982, pp. 345-357.
13. Healey, J.J. and Dobbs, N., "Discussion of 'Assessment of Empirical Concrete Impact Formulas' by G.E. Sliter," Journal of the Structural Divison, ASCE, Vol. 107, No. ST5, May, 1981, pp. 1015-1016.
14. Healey, J.J. and Weissman, S., "Discussion of 'Local Effects of Tornado-Generated Missiles', by A.K. Kar," Journal of the Structural Division, ASCE, Vol. 105, No. ST6, June, 1979, pp. 1212-1215.
15. Healey, J., Werner, H., Weissman, S. and Dobbs, N., "Primary Fragment Characteristics and Impact Effects on Protective Barriers," Technical Report 4903, Ammann and Whitney Consulting Engineers, December, 1975.
16. Hughes, G., "Hard Missile Impact on Reinforced Concrete," Nuclear Engineering and Design, Vol. 77, 1984, pp. 23-35.
17. Kar, A.K., "Local Effects of Tornado-Generated Missiles," Journal of the Structural Division, ASCE, Vol. 104, No. ST5, May, 1978, pp 809-816.
18. Kar, A.K., "Closure to 'Local Effects of Tornado-Generated Missiles'," Journal of the Structural Division, ASCE, Vol. 106, No. ST1, January, 1980, pp. 354-359.
19. Kennedy, R.P., "A Review of Procedures for the Analysis and Design of Concrete Structures to Resist Missile Impact Effects", Report NSS 5-940.1 Holmes and Narver, Inc., Anaheim, California, September, 1975.
20. Kot, C.A., Valentin, D.A., McLennan, D.A. and Turula, P., "Effects of Air Blast on Power Plant Structures and Components," Argonne National Laboratory, Report No. ANL-CT-78-41, October, 1978.
21. Kropatscheck, M.O., "Test and Evaluations of Close-In Detonations," Proceedings of the Symposium on the Interaction of Non-Nuclear Munitions with Structures, U.S. Air Force Academy, Colorado, May 10-13, 1983, pp. 227-236.
22. Mlaker, P.F., Vitaya-Udom, K.P. and Cole, R.A., "Concrete Behavior Under Dynamic Tensile-Compressive Load," Technical Report SL-84-1, U.S. Army Engineer Waterwasy Experiment Station, Vicksburg, MS, January, 1984.
23. National Defense Research Committee, Effects of Impact and Explosion, Volume 1, Office of Scientific Research and Development, Washington, D.C., 1946.
24. Read, H.E. and Maiden, C.J., "The Dynamic Behavior of Concrete," Topical Report, Systems, Science and Software, LaJalla, CA, August 1971.
25. Sliter, G.E., "Assessment of Empirical Concrete Impact Formulas," Journal of the Structural Division, ASCE, May, 1980, pp. 1023-1045.
26. Sliter, G.E., "Residual Velocity of Missiles Perforating Concrete," Second ASCE Conference on Civil Engineering and Nuclear Power, Vol. iv, Knoxville, Tennessee, 1980.
27. Southwest Research Institute, A Manual for the Prediciton of Blast and Fragment Loadings on Structures, Preliminary Edition, November, 1980.
28. Stephenson, A.E. and Sliter, G.E., "Full-Scale Tornado-Missile Impact Tests," Transactions of the Fourth International Conference on Structural Mechanics in Reactor Technology, J10/1, Vol J(b), 1977.
29. Suaris, W. and Shah, S.P., "Rate Sensitive Damage Theory for Brittle Solids," Journal of Engineering Mechanics, ASCE, Vol. 110, No. 6, June 1984, pp. 985-997.
30. U.S. Army Engineer Waterways Experiment Station, Structures Laboratory, Fundamentals of Protective Design for Conventional Weapons, July, 1984.
31. Watson, A.J., and Sanderson, A.J., "The Fracture of Concrete Under Explosive Shock Loading, "Proceedings of the Symposium on Concrete Structures Under Impact and Impulsive Loading, Berlin, June 2-4, 1982, pp. 379-392.
32. Zielinski, A.J. and Reinhardt, H.W., "Stress-Strain Behaviour of Concrete and Mortar at High Rates of Tensile Loading, "Cement and Concrete Research, Vol. 12, 1982, pp. 309-319.

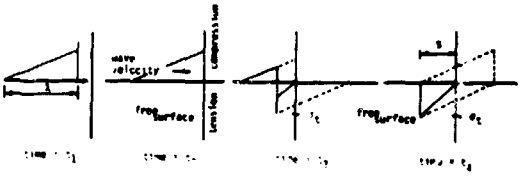

Figure 1. Triangular Pressure Distribution Resulting from an Idealized Load

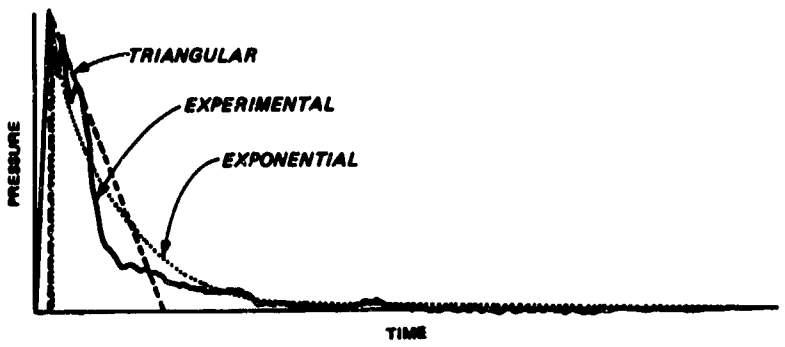

Time (msec)

Figure 2. Comparison of Idealized Waveforms with an Observed Time History

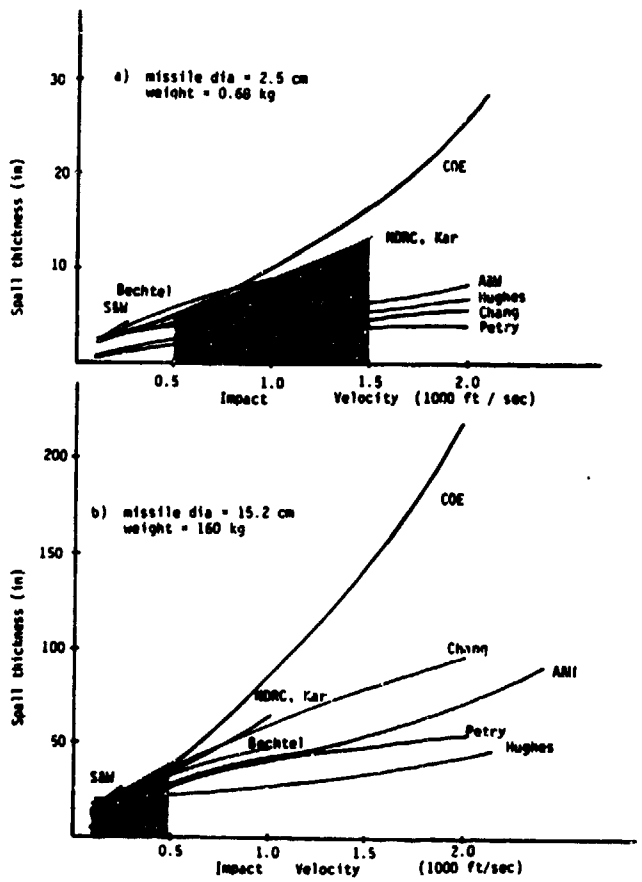

Figure 3. Comparison of Spall Thickness Predictions

BLAST RESPONSE TESTS OF REINFORCED CONCRETE BOX STRUCTURES: Methods for Reducing Spall

David R. Coltharp, Sam A. Kiger, Ken P. Vitayaudom
USAE Waterways Experiment Station
Vicksburg, Mississippi

Tom J. Hilferty
U. S. Air Force Engineering and Services Center
Tyndall AFB, Florida

ABSTRACT

Nine explosive tests were conducted against reinforced concrete walls to determine the effectiveness of: (a) earth berms, (b) spall plates, and (c) increased wall thickness, on reducing or eliminating spalling of the wall. The test items were reinforced concrete box-type structures, and the two opposite walls on each structure were tested. Cased explosive charges were detonated on the ground near the structures, and instrumentation recorded blast-pressure loading, steel strains, wall deflection, and in-structure motion. Three tests used earth berms placed halfway up the exterior of the 32.5-cm-thick walls. Three tests used spall plates on the interior of the 32.5-cm-thick walls. Three tests used thicker walls (40 cm, 47.5 cm, and 55 cm). All three methods were effective in reducing or eliminating spalling of the interior of the wall. Test results and the relative advantages and disadvantages of each method are discussed.

INTRODUCTION

Background

In August-September 1982 a series of six tests were conducted to determine the response of concrete walls with various amounts of reinforcement to nearby detonations. Results of this program are reported in Reference 1 and identify spalling of the interior of the walls as the major damage mechanism. In November-December 1983 a second series of wall tests were conducted to evaluate methods of reducing this spall. Nine scale model tests were conducted at Tyndall AFB, Florida, by the Air Force Engineering and Services Center in conjunction with the U. S. Army Engineer Waterways Experiment Station. This paper presents the results of those tests. A detailed description of both test series is given in Reference 2.

Objective and Approach

The primary objective of the second testing program was to evaluate three separate methods of reducing or eliminating spall: (a) use of earth berms on the exterior of the wall to attenuate the peak stress and distribute the loading resulting from the blast, (b) spall plates on the interior of the wall to trap the concrete spall particles, and (c) increased wall thickness to attenuate the stress wave below the spall threshold value.

Secondary objectives included evaluating the effect of an open versus closed shear stirrup design in the wall reinforcement and examining the effect of a charge detonated with its axis 60° from horizontal versus 90°.

Nine tests were conducted with cased explosive charges detonated at a given standoff from one-half scale model structures. All tests were instrumented with active gages and high-speed photography to obtain data on the loading and response of the test walls.

EXPERIMENTAL PROCEDURES

The procedure was similar than that used in the first test series (Reference 1). Four box structures were constructed for use as test specimens (Figure 1). Each had a floor, roof, and two test walls and were 4 m long with interior dimensions of 1.65 m (height) by 1.65 m (width). The steel reinforcement design for the roof and floor was similar to the first test series (Reference 1). Principal steel ratios for the test walls varied and are discussed later. Single leg, open shear stirrups were used in all but one of the walls. Stirrup spacing was based on the static flexural capacity of the wall. The transverse steel ratio for all walls was 0.1 percent. All steel was specified to be ASTM A615-68, Grade 60, having a minimum yield of 414 MPa. Tests showed yield to be approximately 497 MPa. The concrete compressive strength was approximately 38 MPa.

Each box was placed in a reaction structure to minimize rigid body motion and exposed to the nearby detonation of a cased cylindrical charge. The charge design and standoff was the same as used for the first test series and was chosen to simulate a scaled specified weapon. All charges were detonated on the ground surface with their axis vertical except for test No. 3 which used a charge with its axis 60° from horizontal in a plane containing the midplane of the box structure.

Test Description

Table 1 presents the primary test parameters. Figure 2 shows the protection methods tested. Berms were used in the first three tests. They had been tried successfully in previous tests (Reference 3) and consisted of local soil placed on a 1:1.5 slope against the exterior of the wall. Two berm heights were tested with walls having minimum reinforcement. Since no significant wall damage

Table 1. Test Sequence And Parameters.

Test No.	Wall Thickness cm	Principal Steel Percentage	Spall Protection Method
1	32.5	0.09	0.7-m-high berm
2	32.5	0.09	1.0-m-high berm
3*	32.5	0.09	1.0-m-high berm
4	32.5	0.50	Spall plate
5	32.5	0.25	Spall plate
6	40.0	0.15	Increased thickness
7	55.0	0.08	Increased thickness
8	47.5	0.11	Increased thickness
9**	32.5	0.25	Spall plate

* 60 degree orientation, same wall as used in Test No. 2.
** Closed stirrups versus open

resulted from test No. 2, this wall was retested with a 60° charge orientation so that fragments would impact above the berm and possibly produce more damage.

One-millimeter-thick spall plates were used on three tests. They were attached to the wall interior with approximately 19 bolts/m^2 and extended from the floor to the midpoint of wall. Steel percentages for these walls were chosen to compare with two of the walls that were tested in the first series (Reference 1). A closed stirrup design was used in one of these walls.

Test Nos. 6-8 used thicker walls in an effort to attenuate the stress wave in the wall to such an extent that spalling would not occur. Thicknesses were chosen based on predictions of Reference 4. The steel percentage was chosen such that each of the thick walls had the same flexural capacity as a 32.5 cm thick wall with 0.25 percent reinforcement.

Measurements

The gage layout for the tests is shown in Figure 3. The gages were used to measure: (a) loading of the wall from the airblast and (for the berms tests) ground shock; (b) strain in the reinforcement steel; (c) in-structure motion (acceleration, velocity, displacement); and (d) relative displacement of the wall and roof. High-speed cameras were used inside the box structures to record crack formation, wall motion, and concrete spall velocities.

TEST RESULTS

Pressure Data

The peak pressure versus distance up the wall is shown in Figure 4. The graph is plotted for the center vertical gage line and compares the results of the first series with data from the second series. Also shown is the predicted pressure for a spherical charge (using Reference 5). Note that the pressure near the bottom of the wall for the berm tests is dramatically reduced due to the wave attenuation of the soil. Figures 5 and 6 show the spatial distribution of peak pressures on the wall for the shots without and with berms, respectively. These graphs again show the dramatic reduction in peak pressure due to the berm.

Acceleration Data

Peak acceleration data for the various gages is given in Table 2. The berm Test Nos. 1 and 2 show decreased accelerations. The same decrease in response can be seen in the shock spectra plotted in Figure 7. (An upper bound acceleration for these spectra can be approximated from the peak values given in Table 2).

Deflection Data

The peak midspan deflections for the tests are given in Table 3. Test Nos. 4 and 5 were similar to Test Nos. 2 and 6, respectively, of the first test series. Note from the table that even with much less steel percentages, the deflections for walls with berms were significantly less. Note also that the thicker walls deflected less than Test No. 5 with the same capacity 32.5-cm wall. Test No. 9 which used closed stirrups also deflected considerably less than Test No. 5 with open stirrups.

Fragmentation Effects

As with the first test series, fragment impacts on the test walls were concentrated near the bottom except for Test No. 3 with the 60° charge configuration where they were near the midspan. The berms in Tests 1 and 2 stopped all fragments from reaching the wall (Figure 8) while fragments for other tests penetrated 4-5 cm into the wall and exposed the exterior layer of reinforcing (Figure 9).

Spallation and Structural Damage

No spalling occurred for the three berm tests. The walls appeared to respond in a flexural mode judging from the cracks near the midspan of the wall interior (Figure 10). Structural damage for these tests was minor.

The spall plates functioned properly in all three tests in which they were used. As anticipated, spalling occurred only on the lower portion of the wall. The plates suffered a large membrane deformation (~20 cm) but contained most of the spall particles (Figure 11). Structural damage was highly localized to the lower middle of the wall and was similar to that seen for the first test series.

Figures 12 thru 14 show the spalling of the three thicker walls tested and how it decreased with increased wall thickness. Noting that the spall fragments for Test Nos. 7 and 8 were located only a few feet from the wall, it was judged that the spall area and velocity for the 47.5 cm and 50 cm wall were reduced to acceptable levels. Structural damage was light.

CONCLUSIONS

All three methods, spall plates, added wall

Table 2. Peak Accelerations, g's.

Test No.	AWHM	ARV	ARH	AFV	AFH
1	+3,100/-2,900	+84/-86	+88/-80	+80/-88	+180/-150
2	+2,800/-2,600	+72/-90	+84/-82	+82/-86	+150/-150
3	+17,500/-15,000	+390/-400	+420/-400	+370/-400	+350/-290
4	+22,500/-12,500	+1,490/-1,498	+1,100/-1,300	+1,600/-1,800	+2,500/-3,500
5	+14,000/-10,000	+780/-1,180	+580/-950	--	+3,500/-4,700
6	+9,500/-6,000	+1,500/-1,490	+1,000/-980	+4,000/-3,100	+2,600/-2,300
7	+8,000/-6,000	+1,300/-1,200	+1,200/-1,000	+4,300/-4,300	+4,000/-4,000
8	+17,500/-10,000	+1,500/-1,800	+2,500/-2,000	--	+12,000/-8,000
9	+14,000/-7,500	+1,000/-1,100	+900/-850	+4,000/-2,700	+8,800/-6,000

Table 3. Peak Midspan Deflections.

Test No.	Steel Percentage	Wall Thickness cm	Berm	Midspan Deflection mm
1	0.09	32.5	X	6.4
2	0.09	32.5	X	3.6
3	0.09	32.5	X	10.2
4	0.50	32.5		20.1 (23)*
5	0.25	32.5		44.5 (37)*
6	0.15	40.0		24.1
7	0.08	55.0		12.7
8	0.11	47.5		10.9
9	0.25	32.5		24.1**

* Corresponding data from first test series.
** Used a closed stirrup design.

thickness, and earth berms, were effective in reducing or eliminating spall. Each offers advantages and disadvantages.

Interior spall plates contain the concrete fragments, but the exterior and interior of the walls are still damaged resulting in reduced section capacity. Steel spall plates provide EMP protection and are a good retrofit technique.

Increasing the wall thickness to 40 cm reduces the area of spall and spall velocity, but still not to acceptable levels. Wall thicknesses of 47.5 cm and 55 cm reduce the area and velocity of spall fragments to acceptable levels. Increased thickness also offers added protection from direct hit penetrating weapons.

Exterior sand berming is very effective in reducing the blast pressure and fragmentation loading. The interior suffers no spall damage and only minor flexural cracking. Berming permits the use of lower steel ratios, produces a more flexural-type response, and is the most coat effective solution.

REFERENCES

1. Coltharp, David R., "Blast Response Tests of Reinforced Concrete Box Structures," Proceedings of the Symposium on the Interaction of Nonnuclear Munitions with Structures, Part 2, p 133, May 10-13, 1983.

2. Coltharp, D. R., Vitayaudom, K. P., and Kiger, S. A., "Response of Semihardened Facility Walls to Nearby Detonations," Air Force Engineering and Services Center, Technical Report, Tyndall AFB, FL (in preparation).

3. Loos, G., and Pahl, H., "Explosive Tests on Underreinforced Model Structures in Incirlik (Republic of Turkey) and Meppen (Federal Republic of Germany)," Infrastrukturstab der Bundeswehr, TB-82-01, January 1982.

4. Hader, Hansjörg, "Effects of Bare and Cased Explosive Charges on Reinforced Concrete Walls," Proceedings of the Symposium on the Interaction of Nonnuclear Munitions with Structures, Part 1, p 22, May 10-13, 1983.

5. Department of the Army, TM 5-1300, "Structures to Resist the Effects of Accidental Explosions," June 1969.

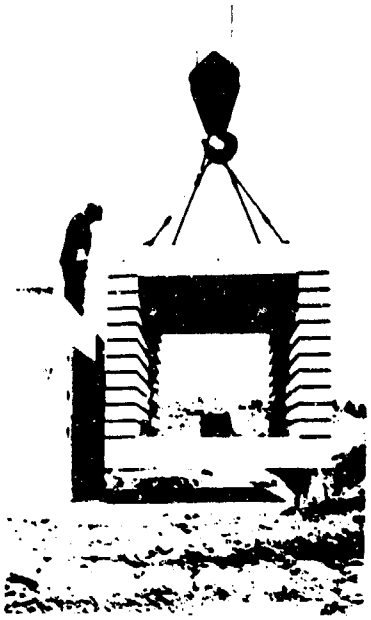

Figure 1. Placement of box structure.

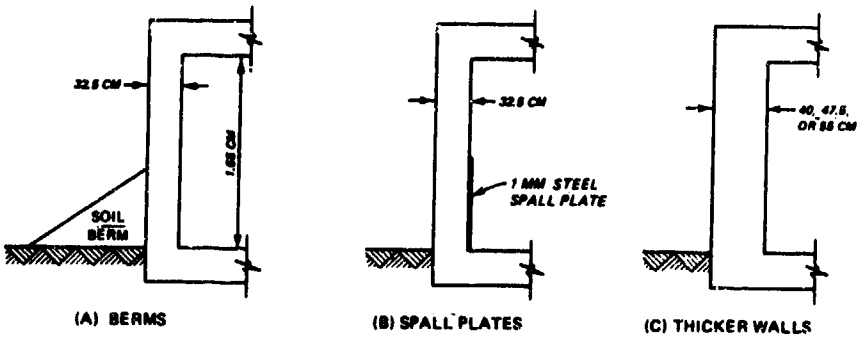

Figure 2. Spall protection methods.

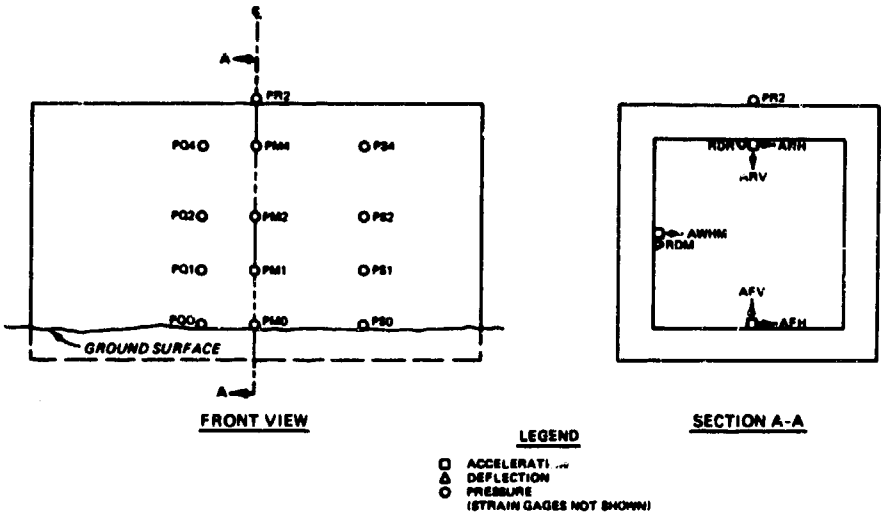

Figure 3. Gage location.

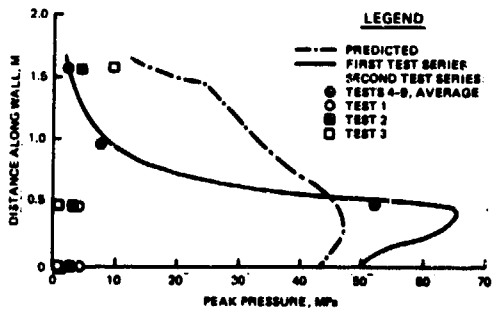

Figure 4. Peak pressure distribution along vertical gage line.

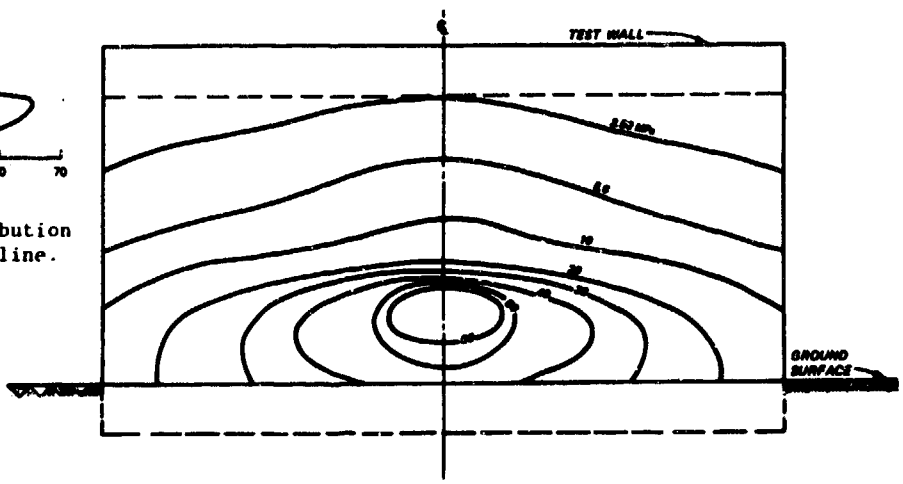

Figure 5. Average spatial distribution of peak pressure for tests without berms.

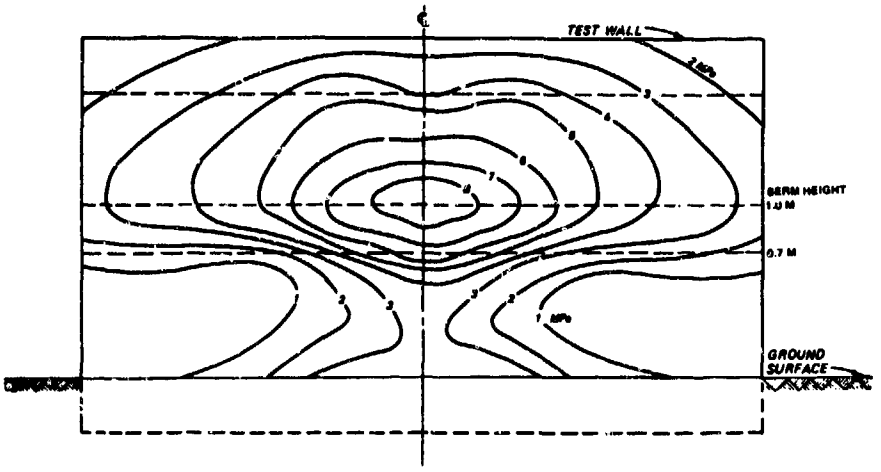

Figure 6. Average spatial distribution of peak pressure for Tests 1 and 2 (bermed).

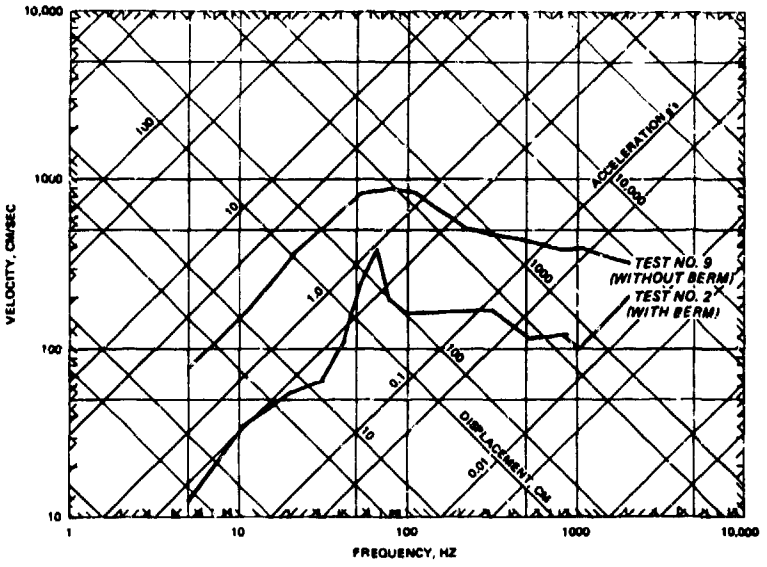

Figure 7. Shock spectra for 5% damped oscillator subjected to acceleration at midspan of test wall (gage AWHM).

Figure 8. Typical damage for bermed wall.

Figure 9. Typical damage for wall without berm.

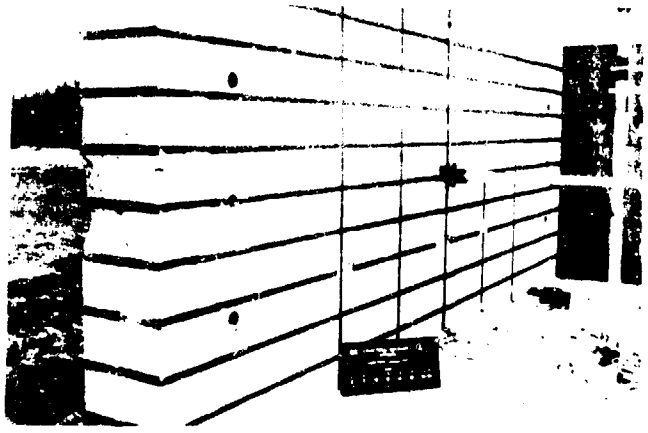

Figure 10. Flexural cracks on bermed wall (Test No. 1).

Figure 11. Deformation of spall plate (Test No. 4).

Figure 12. Spalling of 40-cm wall (Test No. 6).

Figure 13. Spalling of 47.5-cm wall (Test No. 8).

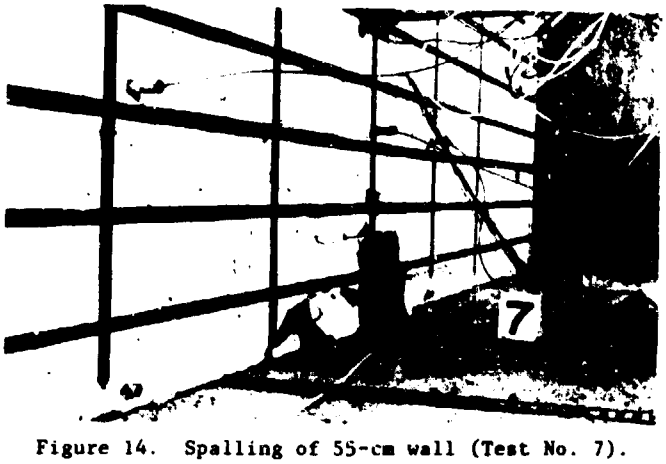

Figure 14. Spalling of 55-cm wall (Test No. 7).

DYNAMIC ANALYSIS OF A BURIED CONCRETE STRUCTURE SUBJECTED TO GAS PRESSURE LOADING

Fausto Citernesi
and
Marco Zurru

Snamprogetti SpA
S.Donato Milanese (MI),Italy

Yves Crutzen

Control Data Italia
Segrate (MI), Italy

ABSTRACT

This paper adresses the highly nonlinear problem of extreme accident analysis of a buried concrete member subjected to impulsive loading. A reinforced concrete wall is designed for environment protection against nearby pipeline explosion and its structural behaviour is analysed by means of the modern finite element nonlinear program ABAQUS. In this paper, some general features of the computer program are first presented. Then its use in the field of structural strength assessment is described by the following applications:

- pressure wave propagation study;
- reinforced concrete wall behavior analysis
- surrounding ground behaviour evaluation.

INTRODUCTION

The design of highly pressurized pipelines is more and more related to requirements of environment protection. A typical case is given by the damage effects that might arise from a gas explosion in a pipeline buried in an earth structure like a dam. In order to increase the safety factor in such a critical situation by preventing the dangerous movement of soil portions in the direction of civil constructions , a concrete protective wall is incorporated in the earth structure. In Fig.1, an earth embankment containing a gas pipeline is partially surrounded by a buried concrete wall. As the dimensions of the concrete structure and its reinforcement percentage have been previously determined, the principal aim of this study is to estimate the concrete strength limit and the earth structure integrity. The general assumption is that plane strain analyses are performed for reasons of computer costs and conservative considerations even if, on the base of recent experimental results, the length of crack propagation in pressurized pipelines are not infinite but of about six pipe diameters.

COMPUTER PROGRAM CAPABILITIES

The modern computerized analysis is applied for the investigation of the behaviour of the earth and buried concrete structures in presence of this extreme dynamic loading phenomena. The modern structural analysis system ABAQUS, developed by HIBBITT, KARLSSON & SORENSEN, INC., [1] is extensively used for this purpose. Generally regarded as one of the most advanced finite element analysis programs, ABAQUS has implemented powerful material, geometry and boundary nonlinear engineering modeling capabilities. Moreover, ABAQUS includes the automatic control of load increment and time step size, based on tolerance definitions,that represents a quite challenging feature in nonlinear static and dynamic analyses.

Concerning reinforced concrete structures, the program contains a general capability for modeling plain and reinforced concrete in all types of structures. Separate modeling is used for concrete and reinforcement so that rebar direction,location, size and spacing can be defined in detail. Rebar is usually treated as an elasto-plastic metal. The concrete behaves in agreement with an elasto-plastic failure theory principally based on Chen & Chen's model that utilizes a uniaxial stress-strain curve where the yield surface and the failure surface are related to the uniaxial and biaxial compressive strengths. As shown in Fig. 2, the salient feature of concrete is the difference in response under tensile and compressive stresses.

Crushing and cracking failures are determined by reaching critical stresses. But, in tension, and additional strain failure criterion is introduced to check more accurately the cracking failure. In cracked zones, a strain softening model is assumed for the direct stress across the crack due to rebar-concrete interaction and a variable shear stiffness can be introduced in presence of aggregate interlocking [1]. These arguments have been also discussed, together with numerical applications of partial damage and disintegration of reinforced concrete components, in a previous presentation at the First Symposium on The Interaction of Non-Nuclear Munitions with Structures [2].

PRESSURE WAVE PROPAGATION STUDY

The distribution in space and the variation in time of the impulsive dynamic loading applied on the protective wall strictly depends upon the following determinations:

- gas-soil interaction effects;
- elastic pressure wave propagation in surrounding ground.

Assuming the lump of soil that covers the pipeline to behave and to move high up like a rigid body and assuming that the gas volume dilatation is directly correlated with soil displacement, the following differential equation can be written on the basis of gas dynamics [3]:

$$m \ddot{x} = f(x)\, p(x,\dot{x},t) - gm \qquad (1)$$

where:

m is the soil lump mass;
x is the vertical displacement;
f is the effective surface exposed to gas pressure;
p is the gas pressure;
g is the gravity acceleration;
$\dot{x}$ is the vertical velocity;
t is the time parameter(ms).

The solution of equation (1) gives the pressure variation in time (time history) as shown in Fig.3. It should be noted that, for this application, the pressure decreases after the first period of 6 ms and it has half of its original value after a period of 29 ms. These results have been used as input for an ABAQUS run with the following goals:

- verify the assumptions made;
- calculate the pressures acting on the concrete wall.

The finite element model used for the calculation is shown in Fig. 4 and utilizes simplified soil properties: the soil material assumes a linear elastic behaviour with no tension strength. The gas pressure is applied uniformly in the pipe hole neglecting the pipe wall. The buried concrete wall is assumed to be rigid in confront with the deformation of the soil. A comparison between the solution of the differential equation (1) and the nodal displacements calculated by ABAQUS for one interesting point shows a quite good agreement (see Fig. 5). The gas volume variation in time is also similar for both calculations. The deformations of the soil lump laying around the pipe are shown for two real times (1.07 ms and 6.3 ms) in Fig. 6. This numerical simulation only covers a time interval of about 7 ms because, after that time, the soil breaks into small fragments and, thus, the initial hypothesis is no more acceptable. But, after that time, the gas pressure drops to very low values.

The integration of stresses obtained inside the soil elements close to the concrete wall permits to define the input pressure loading that vary in space and time. The analysis related to the concrete wall strength assessment utilizes an ABAQUS model defined by a few 8-nodes plane strain elements in connection with a CONCRETE constitutive relationship and a REBAR element behaviour. As far as the imposed boundary conditions on the wall model are concerned, different springs are defined to easily simulate the soil deformability and the foundation interaction effects [4,5,6] (Fig. 7).

Every time increment within an history step, ABAQUS gives the values of the nodal variables, e.g., displacements, velocities, accelerations, reaction forces, and the element variables values, e.g., stresses, strains, section forces, ecc. Moreover, in presence of reinforced concrete material, steel yelding and concrete cracking and crushing messages are printout in order to accurately observe the propagation of the pressure waves, the growth of plasticity, the extension of craking and the progressive disintegration of the composite material. Fig.8 shows the structural deformation and Fig. 9 illustrates the state of partial damage in both concrete and reinforcement bars at 5.77 ms.

As illustrated in the last picture, a large amount of external energy is dissipated through the inelastic material deformations of concrete and steel. The main consequence for the buried wall is its protective action by absorbing and dissipating a large amount of the total input energy and by drastically reducing the impulsive loading effect in the surrounding soil of the earth structure.

EFFECTS ON EARTH STRUCTURES

The next step is related to the evaluation of the dynamic residual effect of the gas explosion on the earth structure containing pipeline and wall.
Having a soil stiffness much smaller than that of the concrete material,we assume the wall to behave like as a rigid body.
A linear ABAQUS analysis is defined for the earth structure response in order to verify that soil displacements and stresses are within the linear elastic range.
Fig. 10 shows a typical deformation shape of the dam. It can be noted that the displacements are only meaningful near the wall with the introduction of a magnification factor. Fig. 11 illustrates the effect of the high pressure wave propagation through the earth structure in 3 particular points below the buried wall (see Fig. 10).

CONCLUSIONS

The computerized approach based on the finite element method confirms its general use for a wide range of challenging engineering problems like this optimal environment protection design case.
The subdivision of the global analysis into different steps has permitted to obtain a clear understanding of the development of the physical phenomena.
ABAQUS computer program has proven to be highly efficient and able to account for the severe non-linearities occurring during a fast-transient dynamic event like the present gas pipeline explosion in an earth structure.

REFERENCES

[1] ABAQUS User's,Example Problems,Theory Manuals, Hibbitt, Karlsson & Sorensen, Inc., Providence, R.I., USA, 1982

[2] Crutzen, Y., Extreme Dynamic Loading Effects on Steel and Concrete Shell Structures, First Symposium on the Interaction of Non-Nuclear Munitions with Structures, USAF Accademy, Colorado, USA, 1983.

[3] Landau, L.D., Lifshitz, E.M., Fluid Mechanics, Pergamon Press, London,1959

[4] Barkan,D.D.,Dynamics of Bases and Foundations, Mc. Graw-Hill, New York (USA) 1962

[5] Bowles, J.E., Foundation Analysis and Design (2.nd edition), Mc. Graw-Hill Kogakusha Ltd., Tokyo, 1977.

[6] Prakash, S., Soil dynamics, Mc Graw-Hill, New York (USA), 1981.

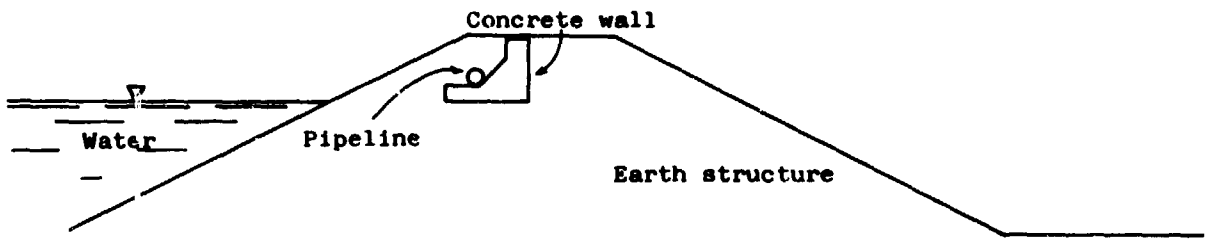

Figure 1. Description of the problem

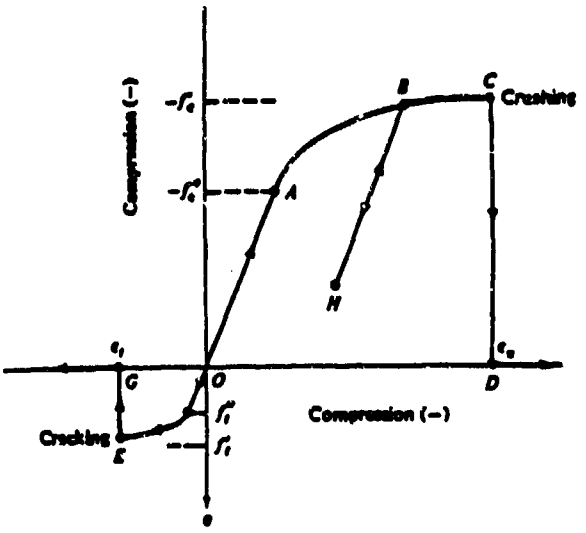

Figure 2. Concrete stress-strain constitutive relationship

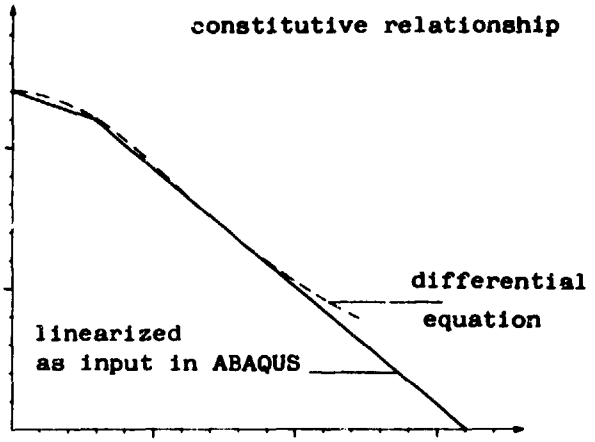

Figure 3. Gas pressure variation in time

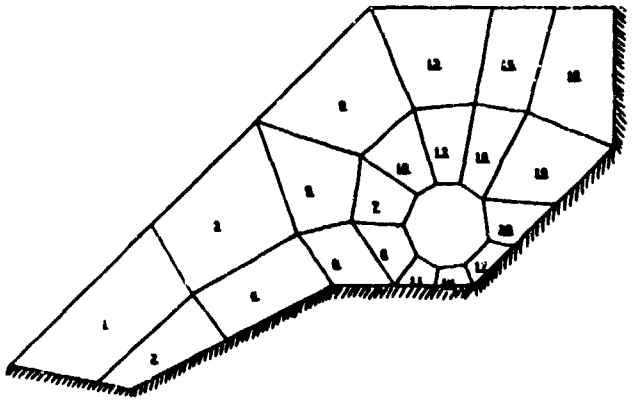

Figure 4. Mesh used for first ABAQUS run

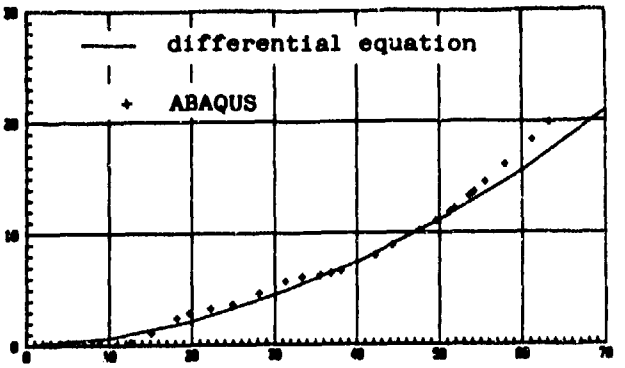

Figure 5. Comparison between analytical and ABAQUS results for a typical point

Magnificatcn factor = 13.

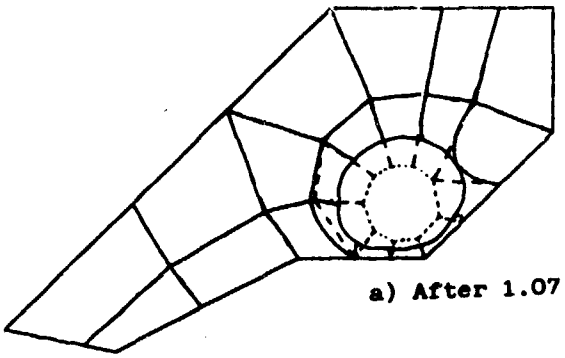

a) After 1.07 ms

Magnification factor = 2.5

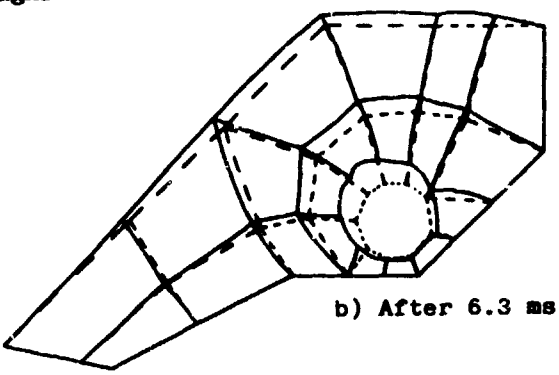

b) After 6.3 ms

Figure 6. Soil deformation

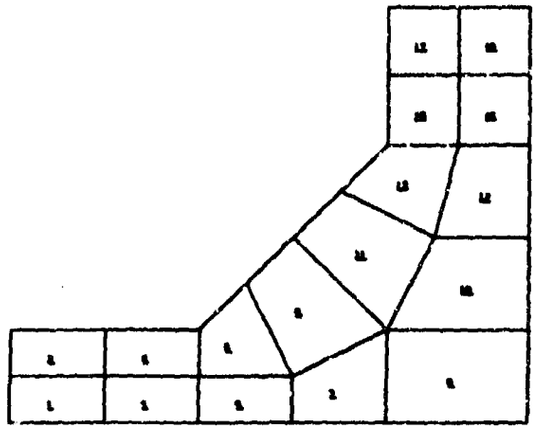

Figure 7. Mesh for reinforced concrete wall analysis with ABAQUS

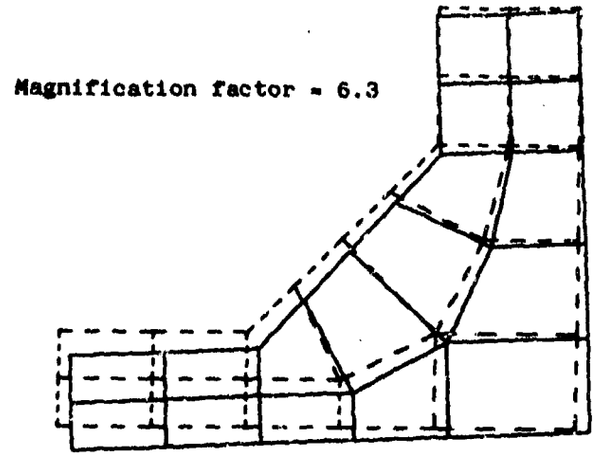

Figure 8. Typical deformation of concrete wall

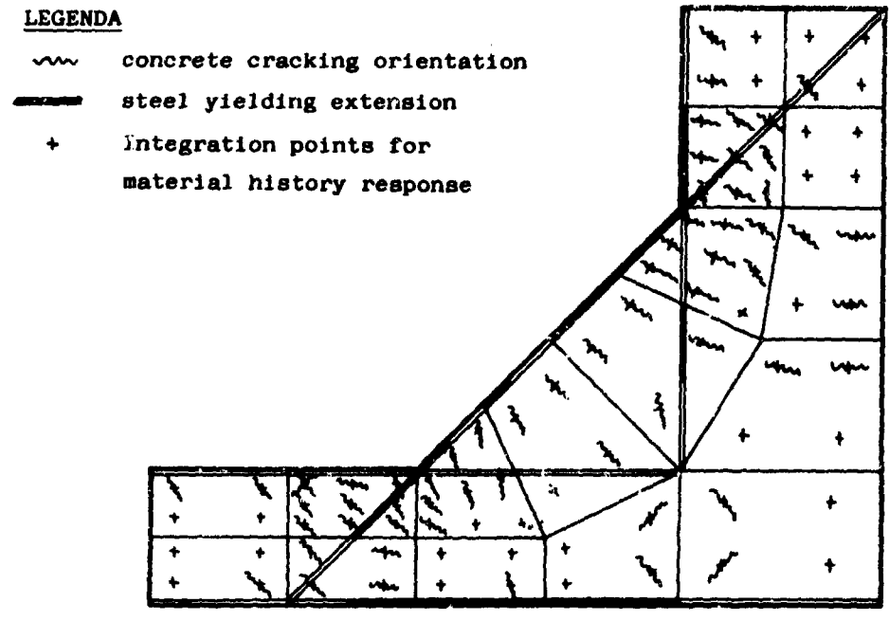

Figure 9. Steel yielding and concrete cracking after 5.75 ms

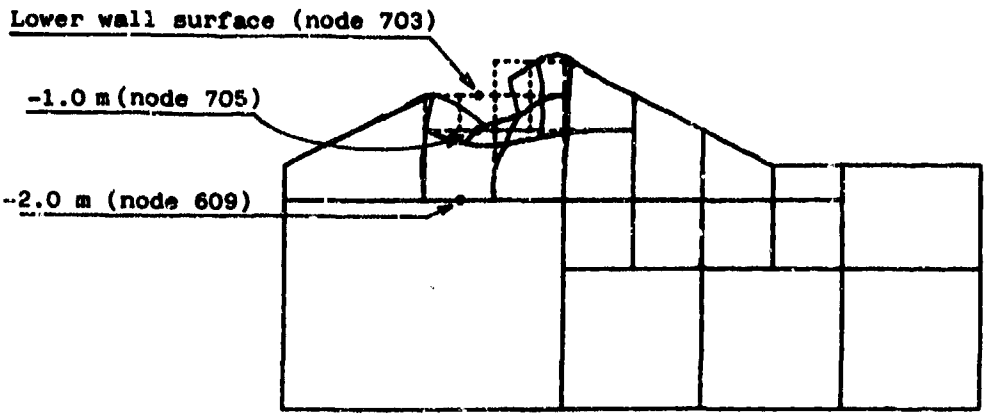

Figure 10. Typical earth structure deformed (ABAQUS plotting)

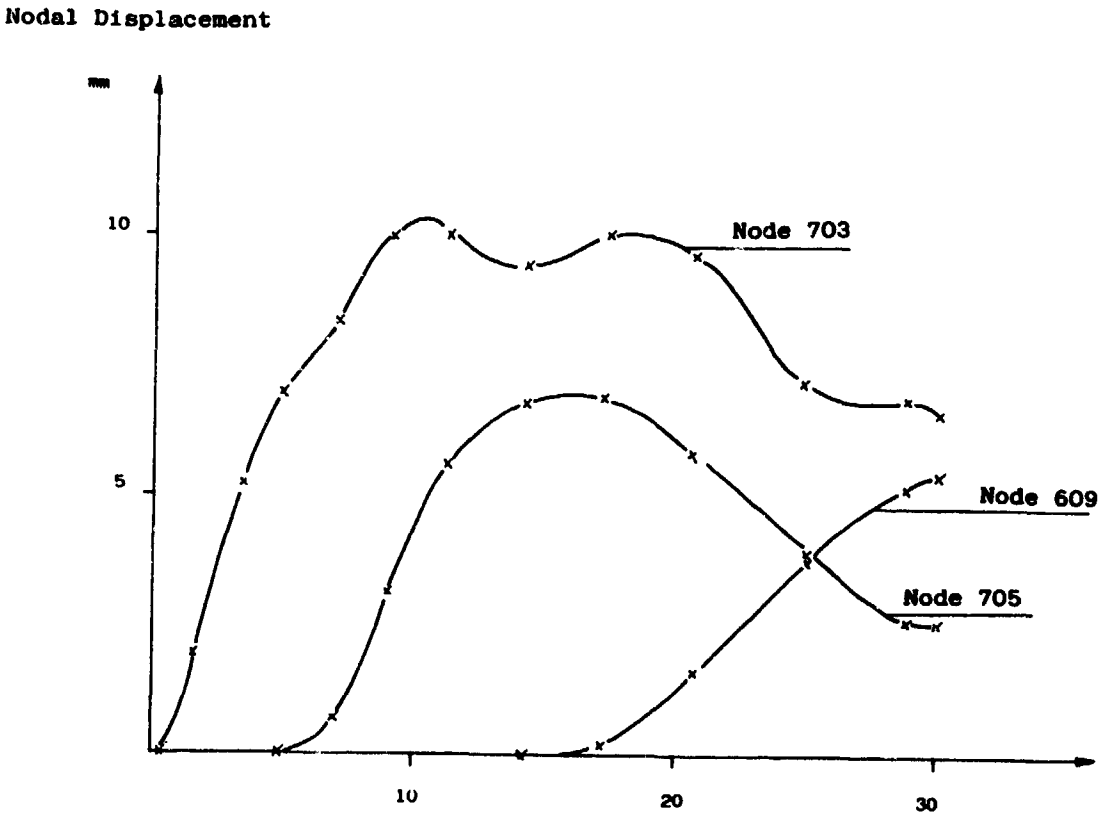

Figure 11. Displacements vs. time in the ground under the wall

STRUCTURAL RESPONSE TO WEAPON LOADINGS
AREAS OF APPLICATION OF EULERIAN, LAGRANGIAN AND COUPLED CODES

Friedhelm Scharpf

Industrieanlagen-Betriebsgesellschaft mbH, West Germany

ABSTRACT

In order to calculate the structural response to weapon loadings Eulerian and Lagrangian codes can be used. In this paper the areas of application of the different codes are demonstrated including coupled codes. For impact and penetration problems an idea for an improved model is outlined combining the advantages of Eulerian and Lagrangian codes.

INTRODUCTION

The interaction of ammunition with structures is a transient process, mainly in the extreme short time range with very high loadings. Exacting requirements are set on computer codes for application in this area. They have to account for nonlinear material behavior with plasticity and failure models, for nonlinear geometric behavior and even for dynamic change of the whole system, calculating post-failure behavior or updating contact areas in penetration problems.

Extreme nonlinearity leads to explicit formulations where the equations of motion are integrated independently from the material response within each time step. The Lagrangian formulation with the conservation of mass by definition is suitable for an accurate material description. If large material flow is expected it is advantageous to use the Eulerian formulation, where the mesh remains fixed in space and time. However there are a lot of applications, where only parts should be mapped in Eulerian coordinates, such as explosives, while other parts, like structures, are better mapped in Lagrangian coordinates. This can be solved by either uncoupled or coupled calculations. Especially in three-dimensional cases where the computing costs are seldom negligible it is very important to use the suitable formulation setting up the problem.

All the codes in this area can still be called "young". As they are all demanding for a fast and inexpensive computer with large storage capacity, the development of these codes has to be seen in relation to the extraordinary hardware development of the last years. Many two-dimensional and a smaller but growing number of three-dimensional codes are already known (1).
Examples in this presentation are calculated with codes of the DYSMAS-family (DYNAMIC SYSTEM MECHANICS ADVANCED SIMULATION), developed in Germany (2). The program-family consists of the codes DYSMAS/L, a FE-Lagrangian code, DYSMAS/E, a FD-Eulerian code, and DYSMAS/ELC, an Euler-Lagrange coupled code, each with both two- and three-dimensional versions.

APPLICATION OF EULERIAN CODES

Eulerian codes are often called "Hydro-Codes" because they are mainly used to solve fluid dynamics. The accurate description of plastic flow is not so important in this area of application as pressure is dominant in comparison to deviatoric stresses. On the other hand severe fluid flow requires the fixed grid of the Eulerian formulation. For these reasons hydro-codes are also used to calculate explosives including shaped charges.

A wide range of application of Eulerian codes is the calculation of the structural loading. An example of a blastwave impacting a shelter door which is shielded by a mound is shown in Fig.1.

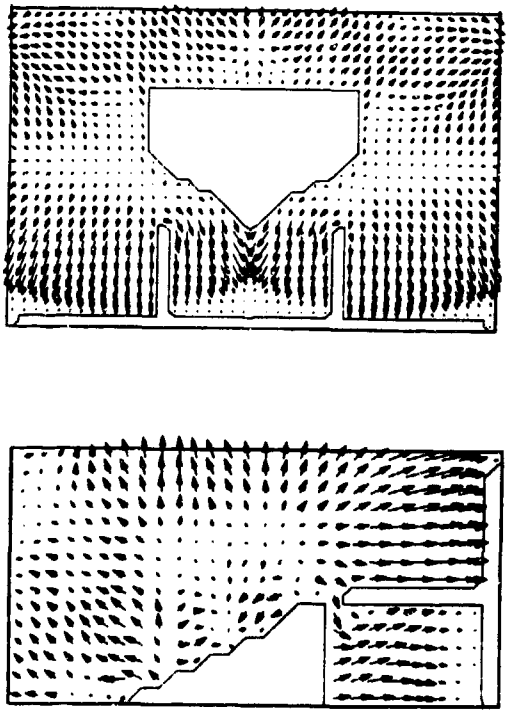

Fig. 1 Numerical Simulation of Blast Wave Impacting a Shelter Construction
Above: Ground-Level Section (Top View)
Below: Mid-Plane Section (Side View)

The velocity distribution of the three-dimensional problem is shown at the arrival time of the blastwave at the door. This problem can be calculated purely Eulerian (with a rigid structure as a boundary condition) if the motion of the structure has only little effect on the loading during the calculated time. In this case the structure is stiff and small movements of the structure are not causing significant changes of the air pressure wave. The time history of pressure at the surface of the structure is recorded and can be used later as the loading function for design.

APPLICATION OF LAGRANGIAN CODES

The response of structures to weapon loadings can be calculated with Lagrangian codes. These codes should model material and geometric nonlinearity. Distortions of the mesh are allowed within the limits of the basic assumptions of the numerical model. There should be no restrictions to rigid body motion. Many Lagrangian codes can also be used for the calculation of two or more bodies impacting each other, if an adequate contact processor is built into the program.
Geometrically complex structures can best be modelled by Finite Elements. Most of the newer codes are using Finite Element formulations for the discretization of space instead of difference equations.

An example of a shelter door loaded by air blast demonstrates the application of a Lagrangian code. The Finite Element discretization of the shelter door is shown in Fig.2. The door is loaded by the detonation of a bomb. The pressure functions were calculated separately with the Eulerian code. The door is in contact

with the shelter, but it opens after the pressure impact which can be seen from the displacement transient in Fig.3.

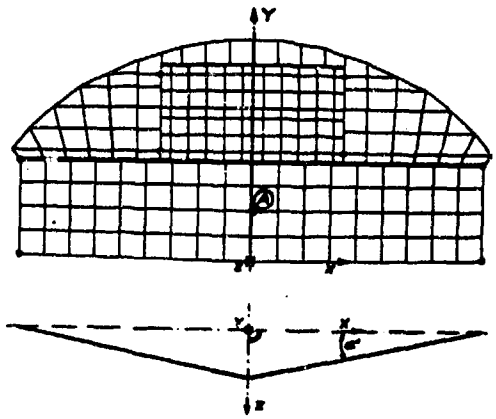

Fig. 2 Shelter Door, Finite Element Discretization

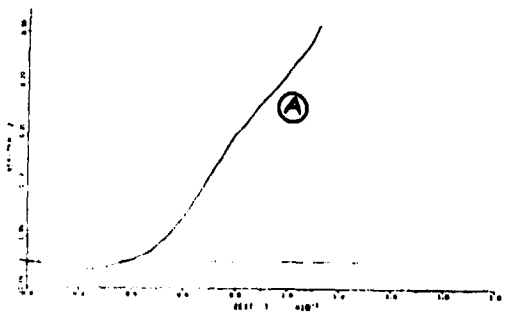

Fig. 3 Displacement Transient in Z-Direction at the Lower Door Joint with Opening after 40 ms

COUPLED CALCULATIONS

Often the loading process acting upon a structure is not only caused by an external energy source but also influenced by the interactive response of the structure itself. In these cases it is not possible to run the Eulerian code for calculation of the loading and the Lagrangian code for calculation of the response in succession.

A wide field of application for coupled calculations are underwater explosions against ships. Fig.4 shows a result of a numerical simulation of a torpedo shot against a frigate at a real time of about 60 msec.

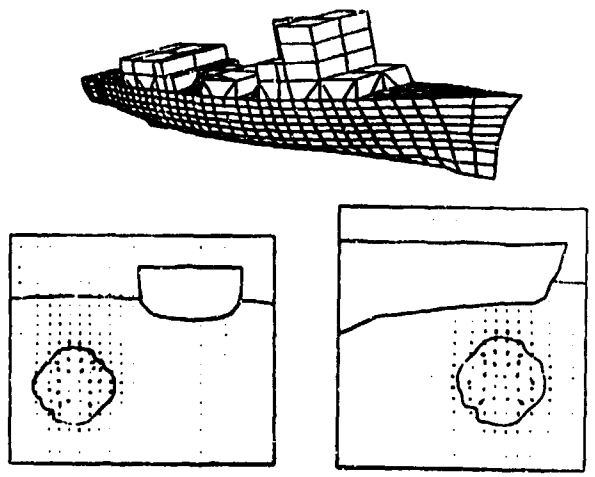

Fig. 4 Numerica' Simulation of an Underwater Detonation against a Vessel-Undeformed Structure, two Plane Sections Through the Gasbubble

A sudden motion of a structure against water causes high pressure due to the nearmost incompressibility of water. A sudden motion of this structure in the other direction causes immediate cavitation in the water with a pressure collapse. In the case of a torpedo shot the ship structure locally moves more than one meter within the initial loading time. So loading and response is an interactive process, which means that a coupling processor has to exchange information between fluid- and structure within each time step.The Eulerian code needs the information about the actual position of the structure as a geometric boundary condition. The Lagrangian code requires forces depending on the actual pressure distribution at the submerged parts of the structural interface.

If the motion of the structure is small a coupling model can be used, where the structure is only allowed to move within one row or column of the Eulerian grid. Such a model can be used to solve e.g. hydraulic ram problems with small structural movements. If, however, one has to calculate the penetration of a fragment through the wall of an aircraft tank, a coupling processor has to be chosen allowing arbitrary motion of the structure like in the example above.

Beside other classical areas of coupled problems like soil-structure interaction (buried charge exploding near a shelter) there are a lot of special problems asking for a coupled code like calculations of an active armor.

CODES FOR THE CALCULATION OF PENETRATION PROCESSES

In most cases a penetration model requires a very accurate material description. For this area of application, the use of Lagrangian codes (with contact processor) is advantageous. Good results can be expected for impact problems. Material failure can be accounted for by modification of the stress tensor.

Difficulties arise in cases of complete penetration, where the target mesh has to be cut or opened. To overcome the numerical problems caused by large distortion of failed elements, sometimes the only way is to set up this problem in Eulerian description or to use a coupled code with an Eulerian target and a Lagrangian penetrator.

At present there are models for the post-failure behavior of Lagrangian material by separating elements or meshlines from each other, as the slide line model, the model for arbitrary crack opening, or the erosion model. The latter model is demonstrated in the calculation of the penetration of a two-plate target in Fig.5.

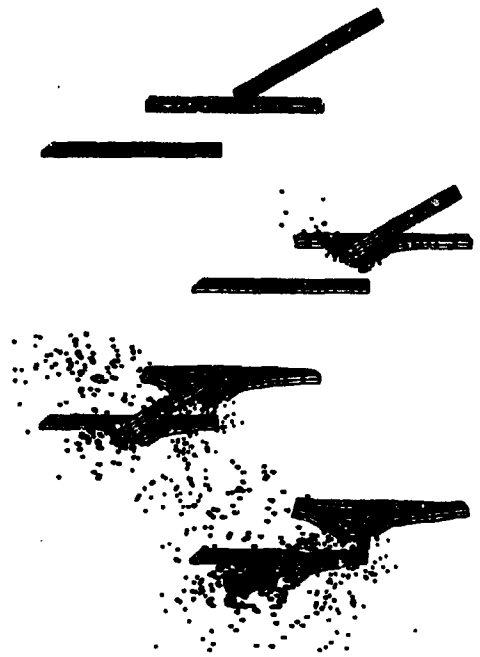

Fig. 5 Penetration of a two-plate Target

In this model, failed elements are erased dynamically. But the masses of the elements still remain in the system as single masses controlled by the contact processor and exchanging kinetic energy with surfaces henceforth.

Analyzing thick targets (in relation to the caliber of the projectile) numerical trouble can still occur with the erosion model if the mesh is too coarse. When a failed element is eroded there is a sudden gap and it takes some cycles of calculation until this gap closes again.

Especially in expensive three-dimensional problems, where the mesh in many cases cannot be as fine as desirable numerical troubles with those artificial discontinuities may occur.

An idea for an improvement is to combine the advantages of the Lagrangian and the Eulerian description. This model should calculate as long as possible in Lagrangian coordinates. However when failed material causes severely distorted elements, this material has to be transformed dynamically into an Eulerian grid. This model requires a Lagrangian code, an Eulerian code and a coupling module which is able to redefine the interface between the Lagrangian mesh and the Eulerian mesh automatically. Of course this model should be three-dimensional as most of the interesting penetration problems are three-dimensional. So the idea might be quite simple but the realization will certainly be an extensive work.

CONCLUSIONS

For the field of structural response to weapon loadings, guidelines were given for the choice of an appropriate code formulation depending on the physical nature of the problem to solve. The use of the adequate code formulation is essential to get proper results and necessary to keep the computer costs at a level as low as possible which is at least in three-dimensional calculations also a very important aspect.

REFERENCES

(1) Zukas J.A., Impact Dynamics, John Wiley & Sons, New York (1982)

(2) The Program Family DYSMAS, B-TF-V197, IABG, Munich (1984)

COMBINED FINITE ELEMENT AND LUMPED MASS TECHNIQUES FOR PARAMETRIC STRUCTURAL ANALYSIS OF STRUCTURES

John E. Crawford
Peter J. Mendoza

The Aerospace Corporation
El Segundo, California

INTRODUCTION

The analysis of structures built to survive blasts entails a large number of highly nonlinear response computations to determine the blast pressure at which the structure fails. The large number of computations is needed to account for the effects of parametrically varying the structural properties and weapon types. With their simplicity and economy of operation, lumped mass approximations are commonly employed for these computations in the form of either single or multiple degree-of-freedom idealizations (SDOF and MDOF). Although the SDOF and MDOF idealizations have proven effective when applied to simple conventional structures, for complex structures these idealizations are often only superficially based on the actual structures' behavior.

This paper outlines a new strategy for defining and evaluating lumped mass approximations. The strategy consists of utilizing the finite element method to improve these idealizations in two ways. First, for the structure, the static load-deflection relation and the associated shape function are determined from a high fidelity nonlinear finite element calculation. Secondly, the errors introduced by the lumped mass approximation can be isolated and explicitly assessed using the improved input provided by the static finite element calculation and by comparison with the "exact" results provided by the nonlinear dynamic finite element calculation. Thus, a sophisticated analysis technique (i.e., the finite element method) is used to generate "experimental-like" data that in turn are used to define the relatively simple lumped mass idealization, potentially resulting in an economical solution to a highly complex problem.

To demonstrate the effectiveness of this new strategy, vis-a-vis the combination of finite element and lump mass procedures, an SDOF idealization is used to compute the response of a stiffened circular plate. These results are compared to those from a nonlinear dynamic, finite element computation. The paper also describes the basis for the SDOF idealization, the results from the finite element analyses, and the manner in which those results are used to develop the SDOF idealization.

FRAGILITY ANALYSIS

The fragility of a structural system, whose properties are defined by random variables, is measured probabilistically. The fragility indicates the likelihood that a system's functional failure will be caused by a particular blast load. Typically, fragility is expressed in terms of the peak overpressure P_{so} of the blast load, e.g., that P_{so} which has a 25 percent chance of causing failure. Also typical is the representation of a structure's fragility through the development of a fragility curve, which defines P_{so} as a function of the probability of failure for a specific weapon type. Generally, some "key" displacement value is chosen to indicate failure; such as the maximum vertical deflection at the midspan of a structure.

Generation of fragility curves using either a Monte Carlo or some other statistical method involves a substantial number of nonlinear structural response computations. The quantity of computations must be sufficient to enable determination of the effects of variations in the structure's properties and weapon types. This, along with the iterative computation of P_{so} for each specific set of structural properties and weapon types, usually results in such a large number of computations as to preclude the use of dynamic finite element computations.

Because of their simplicity and economy of operation, lumped mass approximations are often employed for these probabilistic computations in the form of either SDOF or MDOF idealizations. For complex structures, however, these idealizations are often only superficially based on the actual structural behavior because of either lack of test data or any clear understanding of structural performance; e.g., how the structure is affected by the variation in a web's thickness or yield strength.

Finite element calculations can improve the fragility analysis in three ways: (1) by providing shape and resistance functions for the SDOF and MDOF models, (2) by determining the effects of parameter variations on these functions, and (3) by assessing the systematic errors introduced by the SDOF and MDOF idealizations. The remainder of this paper describes the manner in which

the results from finite element calculations are used in conjunction with the SDOF idealization. Also mentioned is a validation case which illustrates the efficacy of this procedure.

SINGLE DEGREE-OF-FREEDOM MODELS

The intent of the SDOF idealization is to replicate the displacement history of any specific point in the actual structure. To develop the idealization requires two fundamental pieces of information: a force deformation relation for a specific point and its associated shape function. For an SDOF idealization, the equation of motion is written in terms of an effective mass, stiffness, and force

$$m_e \ddot{\delta} + k_e \delta = f_e(t) \qquad (1)$$

where these effective properties are defined in terms of the actual structural properties and the shape function

effective mass: $m_e = K_M M_T$ (2)

effective stiffness: $k_e = K_L R(\delta)$ (3)

effective force: $f_e(t) = K_L F(t)$ (4)

where

K_M = mass factor, which is a function of ϕ

K_L = load factor, which is a function of ϕ

M_T = total mass of structure

R = stiffness of structure, often denoted as the resistance function

F = dynamic force applied to structure

δ = displacement for the SDOF idealization or the "key" displacement within the real structure

$\ddot{\delta}$ = acceleration

See reference [1] for a more complete description of the method.

For nonlinear systems, the stiffness of the structure is approximated as a piecewise linear function and is generally denoted as the resistance function $R(\delta)$. The load and mass factors are derived from the shape function ϕ, which is itself dependent on δ and the spatial coordinates.

To better understand the effect of the shape function, Equation (1) is recast in terms of the actual system parameters

$$K_S(\delta) M_T \ddot{\delta} + R(\delta) \delta = F(t) \qquad (5)$$

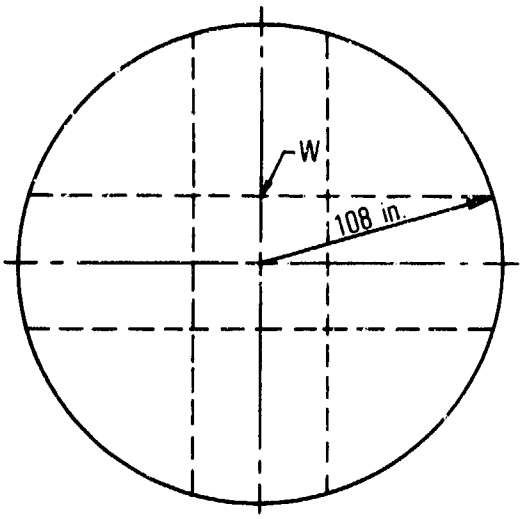

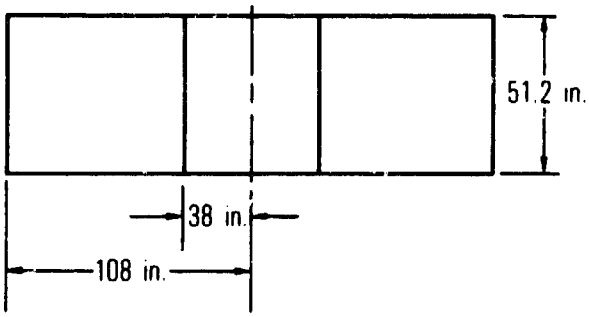

"W" denotes location of maximum web deflection

Figure 1. Generic Stiffened Plate

where

$$K_S(\delta) = K_M/K_L \qquad (6)$$

From this form, it is clear that as the factor K_S becomes negligible, Equation (5) reverts to a static condition. This equation can also be used to evaluate the effect of various shape functions, where smaller values of displacement will be computed as the value of K_S increases.

Shape and Resistance Function Computations. Static finite element calculations are used as the basis from which the resistance R, and its associated shape function ϕ, are derived. The static force used in the finite element model must replicate the spatial distribution of the dynamic force applied to the actual structure. Also, some error occurs if the applied dynamic load is not in phase everywhere on the actual structure, such as for a traveling wave.

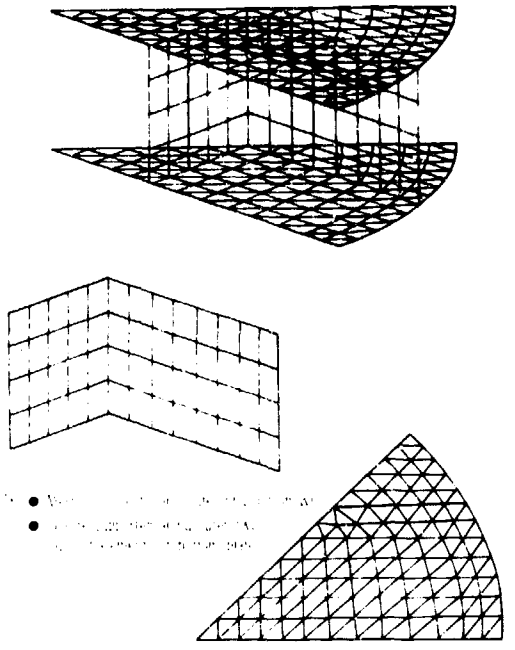

Figure 2. Structure Mesh

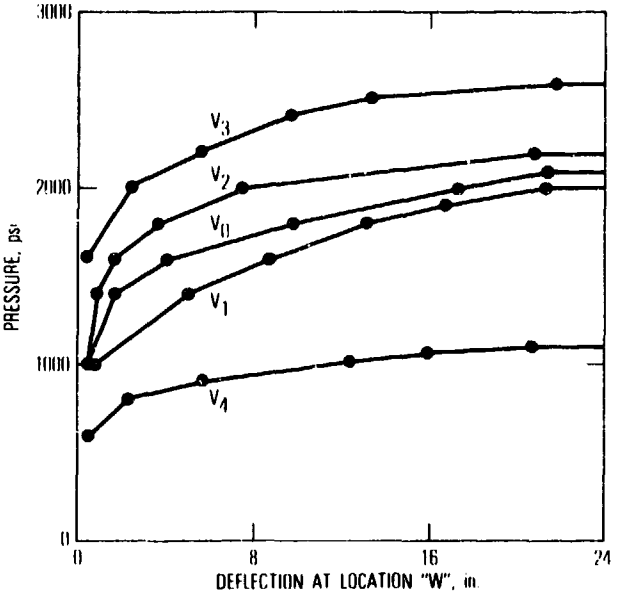

Figure 3. Computed Resistance Function for STRUCTURES V0 through V4

To illustrate the process for deriving R and ϕ, a finite element computation for a stiffened plate is presented. The design is shown in Figure 1; hereafter it is referred as the STRUCTURE. The properties of the constituent materials for this baseline STRUCTURE are given in Table 1 in the horizontal column V0. To examine the effect of different geometric and mechanical properties on the STRUCTURE's response, several variations from the baseline configuration are defined. These are also shown in Table 1 and are denoted as STRUCTURES V1 through V4. The premise for these variations is maintenance of a constant weight. All calculations are done with ADINA (reference [2]) using nonlinear material properties and finite strains; the loading is a uniform pressure applied to the top surface of the STRUCTURE.

Figure 2 depicts the mesh used for the finite element computation; because of symmetry, only one-eighth of the STRUCTURE is modeled. The top and bottom plates are modeled as shells and the webs are modeled as membranes. The resistance functions, i.e., applied pressure versus maximum web displacement, for STRUCTURES V0 through V4 are shown in Figure 3, while the maximum resistance for each variation is listed in Table 1. For STRUCTURE V0, the deformations along the top of the web are depicted in Figure 4, where they are normalized with respect to their maxima. The normalized deformations constitute the shape functions ϕ.

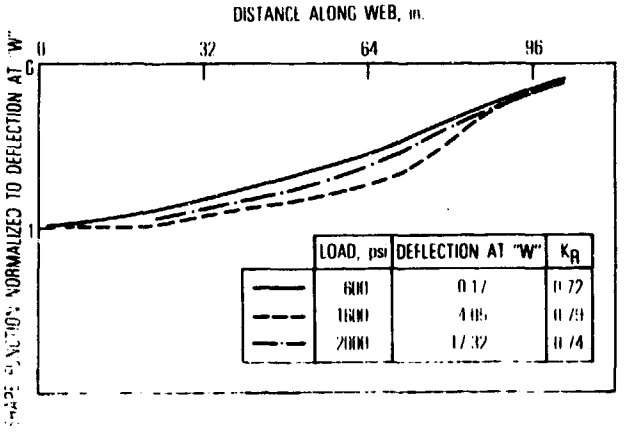

Figure 4. Shape Function for STRUCTURE V0

The mass and load factors are computed from the shape function. Since the STRUCTURE experiences deformations into the plastic range, ϕ will change as a function of the load as shown in Figure 4. Using this figure, an expression for ϕ as a function of the STRUCTURE's centerline displacement can be derived, i.e., $\phi \equiv \phi(\delta)$ where δ also is the SDOF displacement variable for the STRUCTURE. In the limit, a continuous curve for the K_g factor versus δ could be generated. From a practical standpoint, it is adequate to compute only average values of K_g associated with each linear portion of the resistance function. Thus, for the elastic range of resistance, a value of K_g is computed; while for the plastic range, several values may be computed.

Table 1. Properties and Response for STRUCTURE Variations

STRUCTURE	Core Wt. (lb)	Web			Top Plate			Bottom Plate			Outer Ring			Max Resistance	K_S at	
		Thickness (in)	Wt. (lb)	σ_y (ksi)	Thickness (in)	Wt. (lb)	σ_y (ksi)	Thickness (in)	Wt. (lb)	σ_y (ksi)	Thickness (in)	Wt. (lb)	σ_y (ksi)	psi	600 psi	Max Load
V0: As shown in Figure 1	1734	2.0	365	50	3.0	486	40	1.00	173	37	1.00	166	37	2150	0.72	0.74
V1: 30% reduction, σ_y web	1734	2.0	365	35	3.0	486	40	1.00	174	37	1.00	166	37	2050	0.68	0.66
V2: 30% increase σ_y web	1734	2.0	365	65	3.0	486	40	1.00	173	37	1.00	166	37	2250	0.68	0.75
V3: 30% reduction in web height	1208	4.16	531	50	4.3	698	40	1.55	250	37	2.13	237	37	2600	0.75	0.75
V4: 30% increase in web height	2252	0.80	205	50	1.7	275	40	0.60	96	37	4.72	96	37	1100	0.76	0.76

Table 1 contains the K_S factors for the several STRUCTURE variations. The K_S varies only minimally with increasing pressure for STRUCTURE V0; it starts from a value similar to that for an elastic circular plate (reference [1]) and increases in value about 10%. In the plastic range, the variation in K_S is in sharp contrast to the result obtained in reference [1], where the plastic K_S for a circular plate decreases by about 30%. The reason for this discrepancy is that the K_S of reference [1] is based on a bending mechanism, while the mechanism associated with the STRUCTURE is that of shear failure.

SDOF Validation. The preceding methodology provides an SDOF idealization based on a consistent and relatively accurate set of parameters. The remaining and prominent source of error in the SDOF approximation is the inherent weakness of computing a dynamic response with an SDOF. This is particularly pronounced for stiffened plates which may require very high pressures to fail. Associated with the high pressure blast is a very short duration wave front, so that much of the energy is not converted to motion because of the typically lower frequency of the SDOF system. That is, the frequency mismatch between the load and the SDOF system causes underprediction of the motion.

To obtain some estimate of the error associated with the SDOF idealization, a nonlinear dynamic finite element response was computed for the STRUCTURE V0 and is shown in Figure 5. The corresponding SDOF calculation is also shown. The resistance function for this calculation is based on a bilinear approximation taken from Figure 3 for STRUCTURE V0, and 0.79 is used for K_S. As expected, the SDOF underpredicted the "exact" finite element result, in this case by 7%.

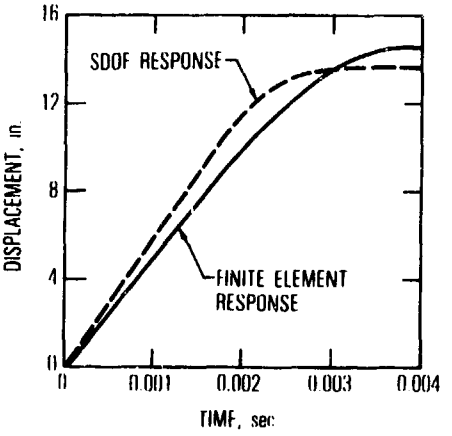

Figure 5. Comparison of SDOF and Finite Element Response

CONCLUSION

This paper presents a methodology for defining the SDOF model based on static responses computed from a high fidelity finite element model. By also performing a few dynamic finite element computations, the SDOF results can be evaluated for accuracy and possibly be corrected to provide ultimately better fragility curves. In summary, the strategy presented provides a basis upon which the efficacy of using the SDOF model in fragility calculations may be judged.

The calculations for the STRUCTURE indicate that the SDOF can yield an adequate result when compared to a high fidelity dynamic finite element solution. Also demonstrated is the importance of understanding the mechanism in which the structure fails. For the STRUCTURE

used in this paper, the SDOF factor K_g is quite different from that reported in the standard references. The differences in ϕ, R, and K_g for the parametric variations V0-V4 of the STRUCTURE's properties indicate that for parametric studies K_g and R must be taken as functions of the structural variables.

The benefits of the SDOF model are ease of use and a robust solution process; that is, unlike finite element solutions, little expertise is needed to get good results. On the downside is the lack of accuracy in the response, where it is expected that peak deformation will be underpredicted. This conclusion is based on the inherent lack of coupling between the blast load and the lower frequency SDOF model. The SDOF method is especially suited for the development of fragility curves where parametric calculations are needed and only moderate accuracy is required.

REFERENCES

1. Biggs, John M., Introduction to Structural Dynamics, McGraw-Hill Book Co., New York, NY, 1964.

2. "System Theory and Modeling Guide," Report AE83-4, September 1983, ADINA Engineering AB.

INELASTIC ANALYSIS OF REINFORCED CONCRETE PANELS

X. L. Liu[1], W. F. Chen[2], T. Y. Chang[3]

[1]Research Asst., School of Civ. Engr., Purdue Univ., W. Lafayette, IN
[2]Prof. & Head of Struc. Engr. Dept., Sch. of Civ. Engr., Purdue Univ., W.Lafayette, IN
[3]Prof., Dept. of Civ. Engr., Univ. of Akron, Akron, OH

ABSTRACT

Recently, the results of 21 reinforced concrete shear panel tests were reported by the University of Toronto. This paper attempts to compare several analytical predictions with these Toronto's tests. These include: (1) a simplified analysis method; (2) a refined finite element method; and (3) a summary of other investigators' results using different constitutive models for reinforced concrete materials. It is found that, for practical use, the simplified method excluding the effect of concrete tension stiffening appears to give an adequate prediction of the behavior and strength of shear panels. The refined finite element method is found to give a better prediction for the case of anisotropically reinforced concrete panels.

1. INTRODUCTION

Reinforced Concrete Planar elements often form part of a complex structural system, such as shear walls in multistory building frames, box girders or V-folded plate roofs.

Generally speaking, the analytical methods developed for these types of structures can be grouped into two approaches. The first approach treats the panel as an ordinary beam, while the second approach considers the planar element as a general plane stress problem, using elastic homogeneous and isotropic idealizations for the material. Recently, through experimental studies and engineering approximation, the effects of cracking of concrete, yielding of reinforcing steel and the nature of failure mechanism have been incorporated.

With the present state of development of finite element computer method, analytical solutions for any properly formulated constitutive laws for reinforced concrete materials can be obtained. Within the mechanics of finite element, however, the trend has been toward the use of higher-order element and/or more complex material models. As a result, computational time has been drastically increased.

The aim of this paper is to present a simplified method and to compare the results with that of a refined finite element method. The proposed method enables designers to assess the response of reinforced concrete panels throughout the entire range of loading up to ultimate strength including the post-failure behavior.

Recently, some test data and several calculated results were made available to the investigators through the International Competition Committee on the Prediction of Structural Response of Reinforced Concrete Panels. These panels were tested at the University of Toronto in the summer of 1981[5]. This paper attempts to compare the predictions based on the simplified method with that of Toronto's tests as well as those predictions made by other investigators using different constitutive models for reinforced concrete materials.

All reinforced concrete panels considered in the present study have the same thickness with two layers of reinforcements. Only in-plane loads are considered. Herein, for simplicity, the panel is treated as a plane stress problem.

The first part of this report describes briefly the tests that were conducted at the University of Toronto, followed by the presentation of the simplified analysis method and the refined finite element method. The comparisons between calculated results and tests and between the simplified method and the refined finite element solution are then presented.

2. TEST PANEL AND TEST SET-UP

2.1 Test Panels

The panels tested at the University of Toronto were 890 x 890 x 70 mm plates with two layers of welded wire fabric (Fig. 1). The clear concrete cover to the outer reinforcement (the χ direction steel is on the outside) is 6 mm. The wires were spaced at 50 mm center to center. At each edge of the specimen, five steel shear keys, anchored with shear studs, were cast. Brass strain targets were fixed onto the reinforcing steel and protruded to the surfaces of the specimen. Sixteen targets, on

a 200 mm grid, were used on each side of the specimen to read strains in the longitudinal, transverse, and the 45° directions. Table 1 summarizes the parameters and observations of the tested specimens[4].

2.2 Testing Set-Up

Every specimen was loaded by links pinned to the steel shear keys. Each key was acted upon by two inclined links (Fig. 2). When one link pulled, while the other pushed with the same force, a resultant force parallel to the edge was produced. If the other also pulled with the same force, a resultant force normal to the edge would be produced.

The forces in the 40 links (2 x 5 x 4) were produced by 37 double-acting hydraulic jacks acting on 37 of the links. The remaining three links were fixed in length to stabilize the overall position of the specimen within the rig.

To prevent out-of-plane movement of the panel the shear keys were attached to an auxiliary frame by means of tie-rods with spherical rod ends[4].

3. SIMPLIFIED METHOD

3.1 Material Models

Concrete: The uncracked concrete is assumed to be an elastic, isotropic, homogeneous material. The direction of crack is assumed to occur perpendicular to the maximum principal tensile stress in the concrete just prior to the formation of cracks. After the formation of cracks, they are assumed to be fixed in the panel. Further, the cracked concrete is assumed to be a transversely isotropic (or orthotropic) material with one of the material axes being oriented along the direction of cracking. The reserved shear-strength in the cracked concrete due to aggregate interlocking is accounted for by retaining a portion of the shear modulus.

In modeling the cracks, the smeared-cracking approach is used[1]. In this approach, a crack is treated as an infinite number of parallel fissures across that part of the single element as sketched in Fig. 3. Two approaches for tensile stress built-down across the cracks are used: one considers the influence of concrete tension stiffening as shown in Fig. 4a, the other treats the concrete as a purely brittle-fracture material.

Steel: The reinforcements are treated as a continuous layer. Thus, no individual bar is considered. The reinforcement is assumed to take only axial stress and its stress-strain relationship is idealized as the elastic-perfectly plastic type.

Reinforced Concrete: Perfect compatibility of deformation between concrete and steel is assumed. The uncracked and unyielded reinforced concrete can therefore be considered as an elastic isotropic, homogeneous material. After cracking occurs, it can be visualized as a planar latticed structure with infinitesimal mesh size. One set of lattice links is formed by concrete columns and other set is formed by reinforcements for each of the reinforcement directions, in which only internal normal forces can be transmitted[1,2].

3.2 Material Stiffness

The material stiffness of the composite element is obtained by the simple superposition of material stiffnesses of concrete to that of reinforcement. This is summarized in the forthcoming.

Elastic uncracked concrete: If the influence of reinforcement area is included, the matrix $[D]_c$ for the special case of plane-stress condition is, in the usual notation,

$$\begin{bmatrix} \tau \\ \sigma_y \\ \tau_{xy} \end{bmatrix} = [D]_c \begin{bmatrix} \varepsilon_x \\ \varepsilon_y \\ \varepsilon_{xy} \end{bmatrix} \tag{1}$$

where

$$[D]_c = \frac{E_c}{1-\nu^2} \begin{bmatrix} (1-\rho_x) & \nu & 0 \\ \nu & (1-\rho_y) & 0 \\ 0 & 0 & 1-\nu \end{bmatrix}$$

in which ρ_x and ρ_y are steel ratios in x- and y-direction respectively and E_c and ν are Young modulus and Poisson's ratio of concrete respectively.

Elastic cracked concrete: In this case, it is further assumed that a crack forms in the plane perpendicular to the maximum principal-tensile-stress direction. As mentioned previously, for the case of purely brittle-fracture model, only the normal stress perpendicular to the cracked plane and part of the shear stress parallel to the cracked direction are released; the other stresses are assumed to remain unchanged (Fig. 5a). Thus, the stress state in a cracked concrete is essentially an uniaxial stress state parallel to the cracked direction. The sliced concrete between two adjacent cracked planes behaves as a single column. For a cracked concrete, we have, referring to the x'y' coordinate system (Fig. 3)

$$\begin{bmatrix} \Delta\sigma'_x \\ \Delta\sigma'_y \\ \Delta\tau'_{xy} \end{bmatrix} = \begin{bmatrix} E_c & 0 & 0 \\ 0 & 0 & 0 \\ 0 & 0 & 2\beta G_c \end{bmatrix} \begin{bmatrix} \Delta\varepsilon'_x \\ \Delta\varepsilon'_y \\ \Delta\varepsilon'_{xy} \end{bmatrix} \tag{2}$$

where G_c is the shear modulus of concrete, and β is the reduction factor of shear modulus ($0 < \beta < 1$). Using Cauchy's formula for stress transformation, we obtain the incremental stress-strain relationship in x-y coordinate system (Fig. 3)

$$\begin{bmatrix} \Delta\sigma_x \\ \Delta\sigma_y \\ \Delta\tau_{xy} \end{bmatrix} = [D]_c \begin{bmatrix} \Delta\varepsilon_x \\ \Delta\varepsilon_y \\ \Delta\varepsilon_{xy} \end{bmatrix} \tag{3}$$

where $[D]_c$ =

$$\begin{bmatrix} C^4E_c+2C^2S^2\beta G_c & C^2S^2E_c-2C^2S^2\beta G_c & 2C^3SE_c-2CSM\beta G_c \\ C^2S^2E_c-2C^2S^2\beta G_c & S^4E_c+2C^2S^2\beta G_c & 2CS^3E_c+2CSM\beta G_c \\ C^3SE_c-CSM\beta G_c & CS^3E_c+CSM\beta G_c & 2C^2S^2E_c+M^2\beta G_c \end{bmatrix}$$

where $C = \cos\phi$, $S = \sin\phi$, $M = C^2 - S^2$, the angle ϕ indicates the direction of cracks (Fig. 3).

On the other hand, for the case of concrete tension stiffening model, the stress state in a cracked concrete is assumed to be in a biaxial stress state. The sliced concrete between two adjacent cracked planes behaves as an orthotropic planar element. In this case, following Eq. (2) and assuming $\nu_x = \nu_y = \nu$, we have

$$\begin{bmatrix} \Delta\sigma'_x \\ \Delta\sigma'_y \\ \Delta\tau'_{xy} \end{bmatrix} = \begin{bmatrix} \frac{E_c}{1-\nu^2} & \frac{\nu E_c}{1-\nu^2} & 0 \\ \frac{\nu E_t}{1-\nu^2} & \frac{\nu E_t}{1-\nu^2} & 0 \\ 0 & 0 & 2\beta G_c \end{bmatrix} \begin{bmatrix} \Delta\varepsilon'_x \\ \Delta\varepsilon'_y \\ \Delta\varepsilon'_{xy} \end{bmatrix} \quad (4)$$

similarly, we have Eq. (3) and the elements in the matrix $[D]_c$ are defined as

$$D_{11} = D_{22} = C^2(C^2+S^2\nu)E_c + S^2(S^2+C^2\nu)E_t + 4C^2S^2\beta G_c$$

$$D_{12} = D_{21} = S^2(C^2+S^2\nu)E_c + C^2(C^2+S^2\nu)E_t - 4C^2S^2\beta G_c$$

$$D_{31} = CS(C^2+S^2\nu)E_c - CS(S^2+C^2\nu)E_t - 2CS(C^2-S^2)\beta G_c$$

$$D_{32} = CS(S^2+C^2\nu)E_c - CS(C^2+S^2\nu)E_t + 2CS(C^2-S^2)\beta G_c$$

$$D_{13} = 2C^3S(1-\nu)E_c - 2CS^3(1-\nu)E_t - 4CS(C^2-S^2)\beta G_c$$

$$D_{23} = 2CS^3(1-\nu)E_c - 2C^3S(1-\nu)E_t + 4CS(C^2-S^2)\beta G_c$$

$$D_{33} = 2C^2S^2(1-\nu)E_c + 2C^2S^2(1-\nu)E_t + 2(C^2-S^2)^2\beta G_c$$

where E_t is the initial tension modulus of elasticity of concrete.

Elastic Reinforcement: Since the reinforcements are assumed to take only axial stress, the material stiffness matrix for reinforcements is similar to that of cracked concrete (Fig. 5b). Denoting the inclination angle of reinforcement bars with x-axis as α, it is found that

$$\begin{bmatrix} \Delta\sigma_x \\ \Delta\sigma_y \\ \Delta\tau_{xy} \end{bmatrix} = [D]_s \begin{bmatrix} \Delta\varepsilon_x \\ \Delta\varepsilon_y \\ \Delta\varepsilon_{xy} \end{bmatrix} \quad (6)$$

where

$$[D]_s = \rho \begin{bmatrix} C^4E_s & C^2S^2E_s & C^3SE_s \\ C^2S^2E_s & S^4E_s & CS^3E_s \\ 2CS^3E_s & 2CS^3E_s & 2C^2S^2E_s \end{bmatrix}$$

$C = \cos\alpha$ $S = \sin\alpha$. ρ is steel ratios in x' direction.

Plastic Reinforcement: Similar to the cracked concrete, but with the modulus E_s equal to zero, the component material stiffness matrix for a plastic reinforcement is

$$[D]_s = [0] \quad (7)$$

3.3 Single Element Analysis

The stress-strain relations expressed previously in terms of stiffness matrices can now be incorporated in the analysis of reinforced concrete panels using a single square element to approximate the actual tests. The numerical analyses have been performed for the cases shown in Table 2.

Cracking in Concrete: Before cracking, the specimen behaves as a linearly elastic isotropic material and its stiffness matrix is obtained by a simple superposition of the material stiffnesses of concrete to that of reinforcements in x-, y- directions. For example, by substituting $\alpha = 0$ and 90^o into Eq. (6) and adding Eq. (1), we obtain the uncracked stiffness matrix of the reinforced concrete specimens.

Using the Mohr's circle construction, the crack direction, which is assumed to develop perpendicular to the principal tensile strain in an uncracked concrete, can be determined.

When the maximum principal-tensile-strain reaches the critical values ε_o^c (Fig. 4), cracks occur in concrete. After the formation of cracks, the stiffness matrix of a cracked specimen must be used. If the concrete tension stiffening is ignored, the stiffness of the panel is obtained by the superposition of the stiffness of cracked concrete (Eq. 3) to that of reinforcements, the later is the same as that of uncracked specimen before yielding of steel.

Beyond the initial crack point 1 (Fig. 6), there are two extreme loading paths to follow: either point 3 or point 2. For a load-controlled analysis, the loading will remain on the same level as that of the uncracked case, while the displacement or strain must increase significantly as the element stiffness reduces. This corresponds to point 3 in Fig. 6. Since both the compressive concrete and the tensile steel are still in the linear range, it is a simple matter to determine point 3 directly from point 0.

For a displacement - control analysis, we must allow the redistribution of the released stresses in a cracked element during the sudden formation of cracks. This corresponds to loading path 1-2 (Fig. 6). The released stresses $\{\sigma_o\}$ can be represented in the x'y' coordinate system as

$$\{\sigma'_o\} = \begin{bmatrix} \sigma'_x \\ \sigma'_y \\ \tau'_{xy} \end{bmatrix} - \begin{bmatrix} \sigma'_x \\ 0 \\ \beta\tau'_{xy} \end{bmatrix} = \begin{bmatrix} 0 \\ \sigma'_y \\ (1-\beta)\tau'_{xy} \end{bmatrix} \quad (8)$$

where β again is the reduction factor of shear stress. With respect to the x-y coordinate system, Eq. (8) has the form

$$\{\sigma_o\} = \begin{bmatrix}\sigma_x\\ \sigma_y\\ \tau_{xy}\end{bmatrix} - [T]\begin{bmatrix}\sigma_x\\ \sigma_y\\ \tau_{xy}\end{bmatrix} = ([I]-[T])\begin{bmatrix}\sigma_x\\ \sigma_y\\ \tau_{xy}\end{bmatrix} \quad (9)$$

where $[T] =$

$$\begin{bmatrix} c^4 + 2c^2s^2\beta & c^2s^2-2c^2s^2\beta & 2c^3s-2cs(c^2-s^2)\beta \\ c^2s^2-2c^2s^2\beta & s^4+2c^2s^2\beta & 2cs^3+2cs(c^2-s^2)\beta \\ c^3s-cs(c^2-s^2)\beta & cs^3+cs(c^2-s^2)\beta & 2c^2s^2+(c^2-s^2)^2\beta \end{bmatrix}$$

It should be noted the $\{\sigma_o\}$ is the released stress vector for concrete only. Before cracking, the total stresses $\{\sigma\}$ in an element may be separated into

$$\{\sigma\} = [\{\sigma\}_c + \{\sigma\}_s]\{\varepsilon\}$$
$$= [D]_c\{\varepsilon\} + [D]_s\{\varepsilon\} \quad (10)$$

where the first term represents the stress in concrete and the second the stress in steel.

After cracks developed, the total stress change $\{\Delta\sigma\}$ in the panel can be written as

$$\{\Delta\sigma\} = \{\sigma\} - \{\sigma_o\} = [D]_c\{\varepsilon\} + [D]_s\{\varepsilon\} - \{\sigma_o\}$$
$$= [[D]_c\{\varepsilon\} - \{\sigma_o\}] + [D]_s\{\varepsilon\} \quad (11)$$

where the first two terms represent the stress changes in concrete.

For the case of tension stiffening model, the stiffness matrix of the cracked specimen is obtained by a simple superposition of Eq. (5) and Eq. (6). For simplicity, we assume that after cracking the concrete modulus is approximately equal to the secant modulus until the tensile-strain of concrete exceeds a certain value, at which E_c is taken to be zero (Fig. 4a). Further, it is assumed that, when the maximum principal tensile strain of concrete reaches the value ε_o, or the maximum principal compression strain of concrete reaches the value $\kappa\varepsilon_c$, the stiffness matrix Eq. (5) is reduced to Eq. (3).

Yielding in Steel: The yielding of steel is one of the possible failure modes in a specimen. It is therefore necessary to check the strain in the axial direction of the reinforcements. When the axial strain in the longitudinal or transverse steels reaches the yield value ε_o^s, the steel yields.

Crushing in Concrete: In some cases, the uniaxial compressive strain of the sliced concrete between two adjacent cracked planes need to be checked. As it reaches the critical value ε_o^c (Fig. 4a) corresponding to the uniaxial stress level $\kappa f_c'$, where κ is a reduction factor usually taken to be 0.85, the concrete crushes. Note that due to aggregate interlocking, a part of shear force will still exist, as shown in Fig. 5a. This implies that, to some extent, the "uniaxial" compressive strength of concrete depends on the reduction factor β.

Since all the stress-strain relationships, including cracked concrete, are linear, a direct analytical solution of stresses and strains for this type of problems can be achieved without the recourse to a step-by-step calculation.

4. REFINED FINITE ELEMENT METHOD

4.1 Material Models

Concrete: The uniaxial stress-strain curve of concrete under compression is assumed to be of the form

$$\sigma = \frac{E_c\varepsilon}{1+(E_c\,\varepsilon_o/f_c' - 2)(\varepsilon/\varepsilon_o)-(\varepsilon/\varepsilon_o)^2} \quad (12)$$

Under uniaxial tension, a linear stress-strain relationship with and without concrete tension stiffening is used. Herein, the concrete tension stiffening model is considered as shown in Fig. 4b.

In the present analysis, we use the failure criterion of concrete proposed by Chen and Chen[6]. In the compression-compression region:

$$f_u(\sigma_{ij}) = J_2 + A_uI_1/3 - \tau_u^2 = 0 \quad (13)$$

In the tension-tension or tension-compression region:

$$f_u(\sigma_{ij}) = J_2 - I_1^2/6 + A_uI_1/3 - \tau_u^2 = 0 \quad (14)$$

where
a, b and τ_u = material constants

Steel: As for steel, an elastic-perfectly plastic von Mises type of yield criterion was assumed. In the case of biaxial stress state, the von Mises criterion reduces to

$$\sigma_1^2 - \sigma_1\sigma_2 + \sigma_2^2 = f_y^2 \quad (15)$$

where σ_1, σ_2 = principal stresses. f_y is the yield stress of steel.

Thus, the influence of shear stress on the strength of steel is included in the refined analysis.

4.2 Finite Element Analysis

A model consisting of four node plane stress elements was used. The numerical analysis is performed by load increments as shown in Fig. 7a. The solution within one load increment is obtained by solving the matrix equation

$$\{\Delta x\} = [K]\{\Delta U\} \quad (16)$$

where $\{\Delta x\}$ is incremental load vector, and $\{\Delta U\}$ is the incremental unknown displacement vector. The dimension of these vectors is equal to the number

of discrete displacements considered in the analysis.

The stiffness matrix [K] is assembled from the element stiffness [k] matrices by the direct stiffness procedure. The element stiffness matrix depends on the material properties of the element, and is given by the matrix triple product

$$[K] = \int_V [B]^T [D][B]dv \qquad (17)$$

Matrix [B] specifies the strain-dislacement relations. The material properties are introduced by means of the material stiffness matrix [D]. The element stiffness matrix changes with the change of the material stiffness, such as, for example, during the transition from the uncracked to the cracked state.

The iteration procedure for one load increment is illustrated in Fig. 7a. The solution is first performed assuming an initial stiffness (point 2 in Fig. 7a). Then all material criteria are checked in all elements. For those elements whose tensile strength or yield stress is exceeded, the material stiffness and thus the element stiffness matrices are updated. The unbalanced forces are redistributed to the entire system in order to maintain equilibrium. This may take several displacement solutions (between points 2 and 3), before all material criteria are satisfied. In This procedure, any number of elements can be treated simultaneously for cracking or plasticity during one load increment.

If the displacement (instead of force) increment is specified, a typical load-dislacement diagram is shown in Fig. 7b. Such curves may occur either just after the formation of cracks or at the limit load. Details of this calculation procedure are given elsewhere (see in Ref. [1]). The present refined analysis was conducted using a finite element program called NFAP, which is an in-house research computer code at the University of Akron. All computer runs were made on an IBM 360-158 computer.

5. NUMERICAL RESULTS

5.1 Simplified Method

Using somewhat different material parameters, the numerical results predicted by eight Purdue graduate students using the simplified inelastic analysis without concrete tension stiffening are summarized in Table 2 together with the average values of the four tested panels reported by University of Toronto and the range of 20 analytical predictions made by 24 authors from 11 different countries around the world.

The simplified method appears to predict the failure stress of panels reasonably well, especially for those under same loading system. As compared with various predicted results of the International Competition, the predicted failure strengths by the simplified method are seen closer to the average value than those based on computer models. A sketch of comparisons between the present results based on the simplified method with those computer solutions based on different constitutive models are shown in Figs 8 to 11 for the four types of panels.

As for the aggregate interlocking, it is found that it has a significant effect for the non-isotropically reinforced concrete panels, such as panels PV19 (Fig. 12) and PV29. In fact, the aggregate interlocking factor β is found to improve significantly the softening behavior of a cracked concrete specimen. The value of this factor depends on the level of loads and the amount of steel ratio. For the present cases, it is found that if the value of β is limited in the range 0.5 to 0.8, the solution that describes the post-cracking behavior of panels is generally acceptable.

If the tension stiffening of concrete is considered, as shown in Figs. 8 to 11, the calculated curves are closer to test curves, but the failure points do not change much.

5.2 Refined Finite Element Method

The predicted results including the consideration of concrete tension stiffening are summarized in Table 3 by comparing with both the tests and the predicted results of the International Competition and the simplified method. Some typical plots are shown in Figs. 13 to 16. Since the refined finite element method considers a more realistic material model, the results are better than those of the simplified method. The refined method can also predict the progressive failure during the loading process. For example, it describes the details of the cracking development as shown in Fig. 17. The results of the refined method, especially those considering the effect of concrete tension stiffening, are quite close to the average values of the test results.

5.3 Error of Predicted Results

The predicted failure stresses for panels are generally found to be higher than that of test results (Table 2 and 3). Further information about the details of the tested specimens is necessary before a definite conclusion can be made. As a typical example, from the crack picture of panel PV29 (Fig. 18), it is found that though the crack patterns are in consistent with our computations, the failure modes of specimens at ultimate strength were quite different. In some cases, the actual failure is caused by the transversal pull-out of reinforcement bars, which, in turn, causes brittle sliding shear failure of concrete. Most of the predictions reported by the International Competition team also had a much higher failure prediction for panel PV29 than that of tests. Furthermore, it is seen from Fig. 18, that the transversal bars are not exactly vertical. This will certainly have an influence on the post-cracking behavior of panel PV29. These phenomena, can also be found in many other panels (Figs. 13,14,15).

It is difficult to conduct a pure shear stress test in a laboratory set-up. The problems

associated with this type of tests are, among many others, (1) How to control the whole set of jacks with a concerted action (Fig. 2); (2) How to keep the exact direction of the jack action, especially near the state of failure; and (3) How to avoid various kinds of local failure including the local pull-out of the shear keys, local yielding of steel, wire rupture at welds etc. In the preliminary results reported[4] by the University of Toronto, 53.3 percent of these tested specimens failed prematurely due to local failure.

6. CONCLUSIONS

(1) The important parameters in the panel study are the aggregate interlocking factor β, and the reduction factor of the uniaxial strength of concrete κ. For the present analysis cases, the values of β are limited in the range 0.5 to 0.8, and κ are taken to be 0.85.

(2) The finite element method is found to give a better prediction for the case of anisotropically reinforced concrete panels.

(3) The inclusion of tension stiffening in the concrete material model improves the accuracy of the results. For concrete panels, the range of post peak[6] of concrete tensile strain may be taken around $10\varepsilon_o^t$.

(4) Except for the cases of local failure, the simplified model excluding the effect of concrete tension stiffening appears to give an adequate prediction of the behavior and strength of shear panels for practical use.

REFERENCES

1. Chen, W. F., "Plasticity in Reinforced Concrete", McGraw-Hill, New York, 1982.

2. Cervenka, V. and Gerstle, K. H., "Inelastic Analysis of Reinforced Concrete Panels: Theory", Publ. Int. Assoc. Bridge Struc. Eng., Vol. 31-II, pp. 31-45.

3. Chang, T. Y., Tangucki, H., Chen, W. F., "Prediction of Structural Response of Reinforced Concrete Panels", University of Akron, CE Dept., 1982.

4. Vecchio, F. and Collins, M. P., "The Response of Reinforced Concrete to In-plane Shear and Normal Stresses", ISBN 0-7727-7029-8, Publication No. 82-03, Univ. of Toronto, CE Dept., March 1982.

5. Collins M. P., "Memorandum about prediction competition", University of Toronto, Canada, Sept. 18, 1981.

6. Chen, A. C. T. and Chen, W. F., "Constitutive Relations for Concrete", J. Engrg. Mech. Div., ASCE, Vol. 101, No. EM4, Aug. 1975, pp 465-481.

7. Chang, T. Y., "A Nonlinear Finite Element Analysis Program - NFAP", Department of Civil Engrg., University of Akron, Oct. 1, 1980.

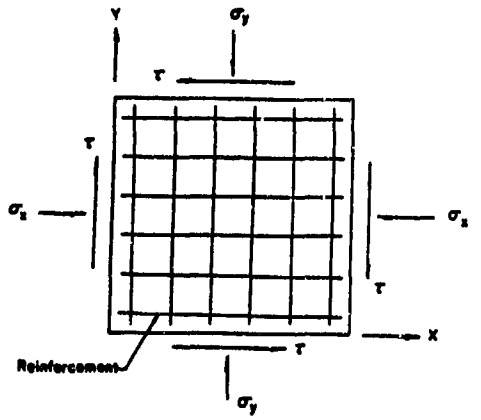

Fig 1 TEST PANEL

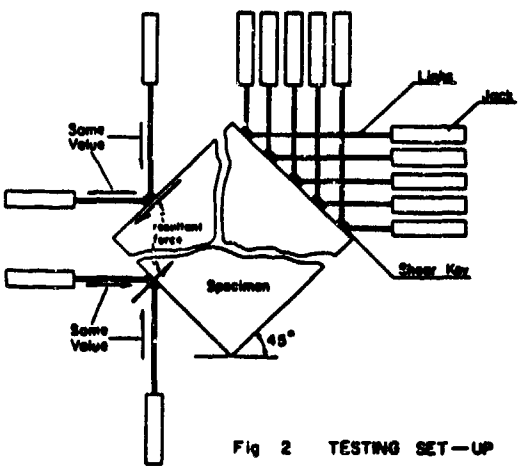

Fig 2 TESTING SET—UP

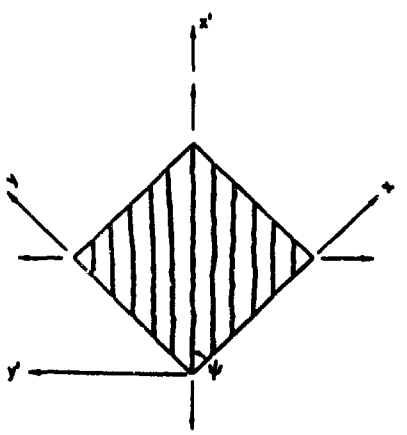

Fig 3 SMEARED CRACKING

TABLE 1. SPECIMEN PARAMETERS AND TEST OBSERVATIONS

Specimens	PERCENTAGE OF STEEL REINFORCEMENT		STEEL YIELD STRENGTH (MPa)		CONCRETE STRENGTH f_c' (MPa)	CYLINDER STRAIN AT PEAK ε_o^c ($\times 10^{-3}$)	LOADING PATH	τ_{cr} (Mpa)	τ_u (Mpa)	REMARKS
	Long.	Trans.	Long.	Trans.						
PV2	0.18	0.18	430	430	23.5	2.25	$0<\tau<\tau_u$ $\sigma_x=\sigma_y=0$	1.10	1.16	Cracking*
PV3	0.48	0.48	660	660	26.6	2.30	"	1.66	3.07	Steel rupture**
PV16	0.74	0.74	250	250	21.7	2.00	"	2.07	2.16	Yielding
PV5	0.74	0.74	620	620	28.3	2.50	"	1.73	4.24	Pull-out
PV4	1.06	1.06	240	240	26.6	2.50	"	1.79	2.89	Yielding
PV14	1.79	1.79	460	460	20.4	2.23	"	1.93	5.24	Pull-out
PV6	1.79	1.79	270	270	29.6	2.50	"	2.00	4.55	Local Yielding
PV7	1.79	1.79	450	450	31.3	2.50	"	1.93	6.81	Pull-out
PV8	2.62	2.62	460	460	29.8	2.50	"	1.73	6.67	Pull-out
PV13	1.79	-	250	-	18.2	2.70	"	1.73	2.01	Concrete shear
PV12	1.79	0.48	470	270	16.0	2.50	"	1.73	3.31	"
PV10	1.79	1.06	260	280	14.5	2.70	"	1.86	3.97	"
PV11	1.79	1.31	240	240	15.6	2.60	"	1.66	3.56	Local Yielding
PV1	1.79	1.68	480	480	34.5	2.20	"	2.21	8.00	Pull-out
PV9	1.79	1.79	460	460	11.6	2.80	"	1.38	3.76	Concrete Shear
PV15	0.74	0.74	250	250	21.7	2.00	$0<\tau<\tau_u$ $\sigma_y=\tau=0$		***	No failure
PV17	0.74	0.74	250	250	20.4	2.00	"		$\sigma_{u_{21.2}}$	explosive failure of concrete
PV27	1.785	1.785	442	442	20.4	1.90	$0<\tau<\tau_u$ $\sigma_x=\sigma_y=0$		6.3	
PV25	1.785	1.785	466	466	19.2	1.80	$0<\tau<\tau$ $\sigma_x=\sigma_y=0.69\tau$		9.1	
PV19	1.785	0.713	458	299	19.0	2.15	$0<\tau<\tau_u$ $\sigma_x=\sigma_y=0$		4.0	
PV29	1.785	0.885	441	324	21.6	1.80	$0<\tau<3.86$Mpa: $\sigma_x=\sigma_y=0$ $\tau\geq 3.86$Mpa: $\sigma_x=\sigma_y=(\tau-3.86)$		5.9	

* Initially cracked at 90°
** Non-stress relieved wires ruptured at welds.
*** to be halted prior to failure

TABLE 2 NUMERICAL RESULTS OF SIMPLIFIED METHOD
BY PURDUE GRADUATE STUDENTS

STUDENT NAMES	PARAMETERS							PREDICTED FAILURE STRESS (MPa)			
	CONCRETE						STEEL				
	E_c(MPa)	f_t'(MPa)	ε_o^c	ν	β	k	E_s(MPa)	PV27	PV25	PV19	PV29
1 H.Sugimoto	$4733\sqrt{f_c'}$	$0.09f_c'$	$\frac{f_t'}{E_c}$	0.18	0.5	1	206850	7.891	9.893	5.153	10.776
2 D.J. Han	$4733\sqrt{f_c'}$	$0.09f_c'$	$\frac{f_t'}{E_c}$	0.19	0	1	207000	7.88	-	-	-
	"	"	"	"	0.5	"	"	7.935	-	5.14	-
3 E.M. Lui	$4730\sqrt{f_c'}$	$0.09f_c'$	$\frac{f_t'}{E_c}$	0.20	0.5	1	207000	8.67	11.30	3.95	12.75
4 X.L. Liu	$2f_c'/\varepsilon_o^c$	$0.09f_c'$	$\frac{f_t'}{E_c}$	0.20	0	0.85	200000	7.6787	9.6568	2.0856	2.7860
	"	"	"	"	0.5	"	"	7.5030	"	3.8235	11.11
	"	"	"	"	0.8	"	"	7.3958	"	3.7661	11.11
5 N. Saha	$2f_c'/\varepsilon_o^c$	$0.09f_c'$	f_t'/E_c	0.18	0.6	1	204083	8.261	9.870	7.706	10.699
6 S. Saigal	$2f_c'/\varepsilon_o^c$	$0.09f_c'$	f_t'/E_c	0.20	0.8	1	204800	8.257	11.360	5.588	12.730
7 D. Boteca	$2f_c'/\varepsilon_o^c$	$0.09f_c'$	f_t'/E_c	0.20	0.5	1	199955	7.53	11.36	5.64	12.730
8 D. Escolar	$2f_c'/\varepsilon_o^c$	$0.09f_c'$	f_t'/E_c	0.20	0.7	1	200000	7.81	11.36	4.04	12.730
EXPERIMENTAL VALUES								6.3	9.1	4.0	5.9
INTERNATIONAL PREDICTION COMPETITION							Range	4.4~8.8	3.9~15.2	2.1~5.7	3.7~16.5
							Average and S. Dev.	7.1±1.2	9.0±2.9	3.2±0.3	9.3±3.2

TABLE 3. SUMMARY OF PREDICTED AND TESTED DATA

SOURCE		DATA			
		PV27	PV25	PV19	PV29
EXPERIMENTAL VALUES		6.3	9.1	4.0	5.9
INTERNATIONAL PREDICTION COMPETITION	RANGE	4.4-8.8	3.9-15.2	2.1-5.7	3.7-16.3
	AVERAGE & S. DEV	7.1±1.2	9.0±2.9	4.2±0.3	9.3±3.2
SIMPLIFIED METHOD (β=0.6, k=0.85)	No Concrete Tension Stiffening	7.4	9.7	3.8	11.1
	With Concrete Tension Stiffening	"	"	"	"
REFINED FINITE ELEMENT METHOD (MEAP)	No Concrete Tension Stiffening	8.0	9.4	3.5	10.4
	With Concrete Tension Stiffening	7.8	9.7	4.5	7.3

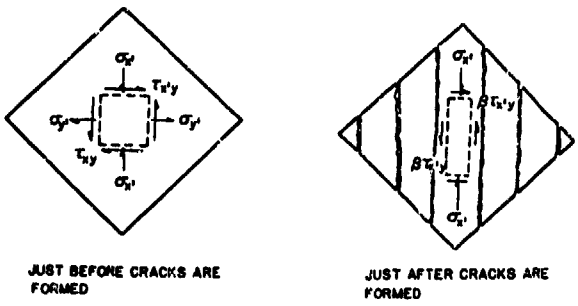

(a) STRESS CHANGE IN CONCRETE DUE TO CRACKING

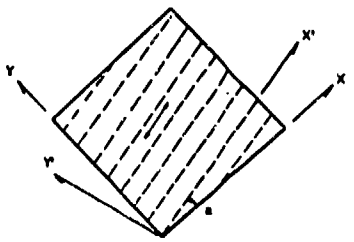

(b) STRESS CONDITION OF STEEL

FIG 5: STRESS CONDITION

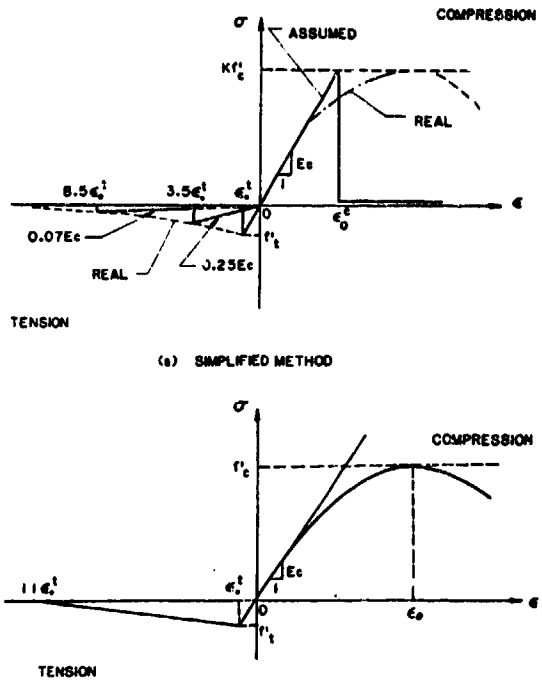

(a) SIMPLIFIED METHOD

(b) REFINED METHOD

FIG 4: UNIAXIAL BEHAVIOR OF CONCRETE

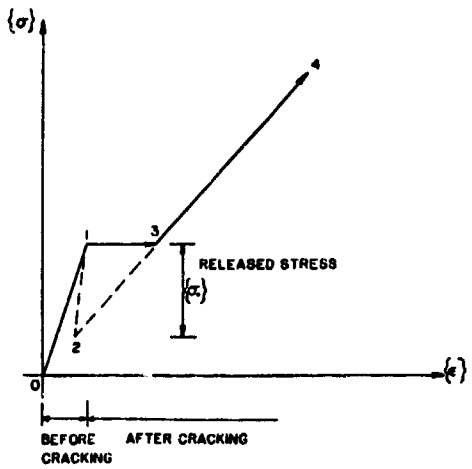

FIG 6: TWO LOADING PATHS

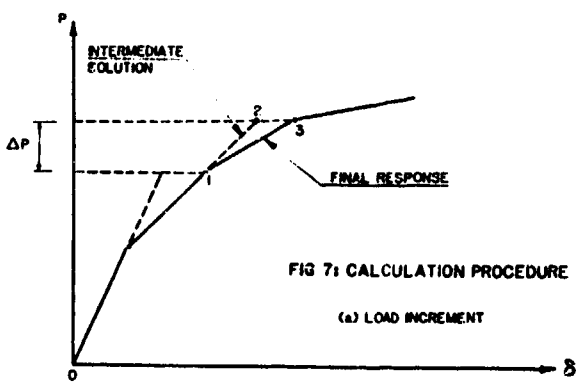

FIG 7: CALCULATION PROCEDURE

(a) LOAD INCREMENT

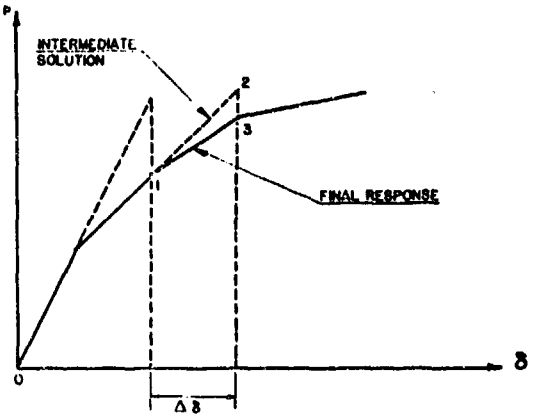

FIG 7: CALCULATION PROCEDURE

(b) DISPLACEMENT INCEMENT

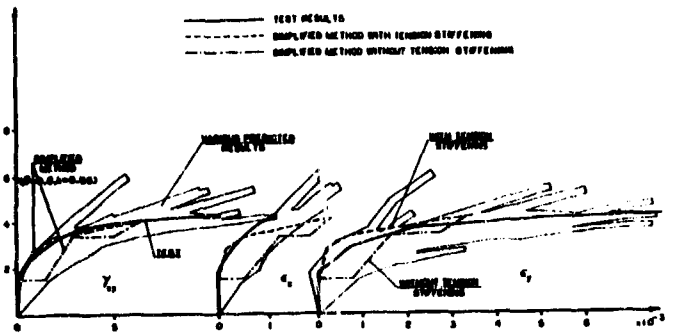

FIG. 10 COMPARISON OF PREDICTION WITH TESTS
PANEL PV19 (ANISOTROPIC, PURE SHEAR)

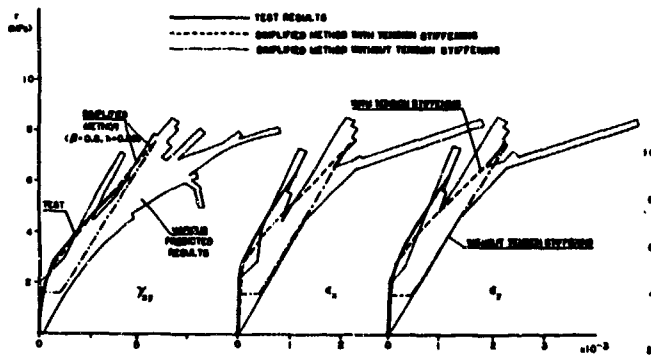

FIG. 8 COMPARISONS OF PREDICTIONS WITH TESTS
PANEL PV27 (ISOTROPIC, PURE SHEAR)

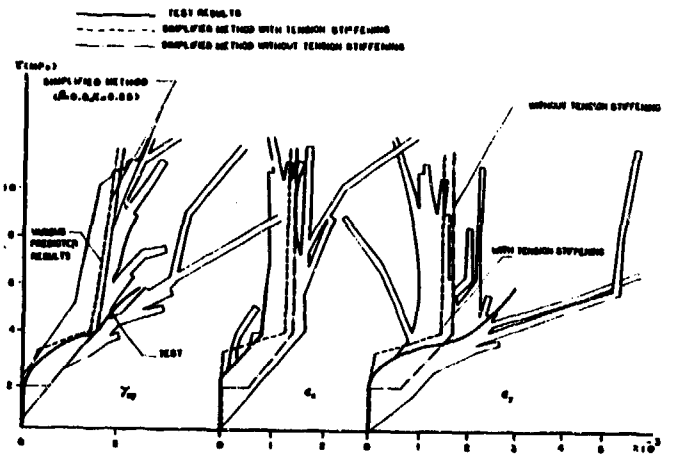

FIG 11: COMPARISON OF PREDICTIONS WITH TESTS PANEL PV-29 (ANISOTROPIC, NONPROPORTIONAL LOADING: a. $0<\tau\leq 3.86$ MPA $\sigma_x=\sigma_y=0$;
b. $\tau\geq 3.86$ MPA $\sigma_x=\sigma_y=(\tau-3.86)$)

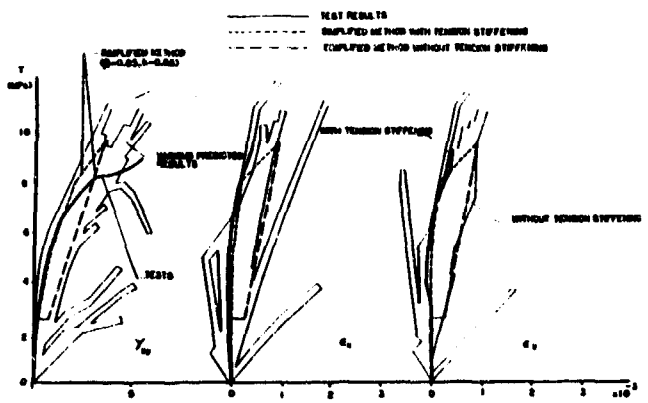

FIG 9: COMPRESSION OF PREDICTIONS WITH TESTS
PANEL PV25 ISOTROPIC $\sigma_x=\sigma_y=0.69$ τ , $0\leq\tau\leq\tau_y$)

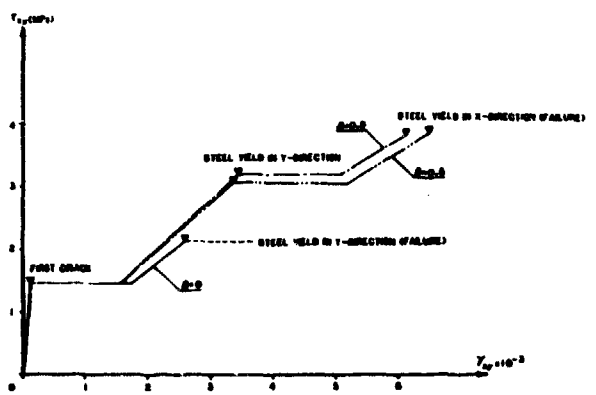

FIG. 12 THE EFFECT OF THE AGGREGATE INTERLOCKING FACTOR β
(PANEL PV19)

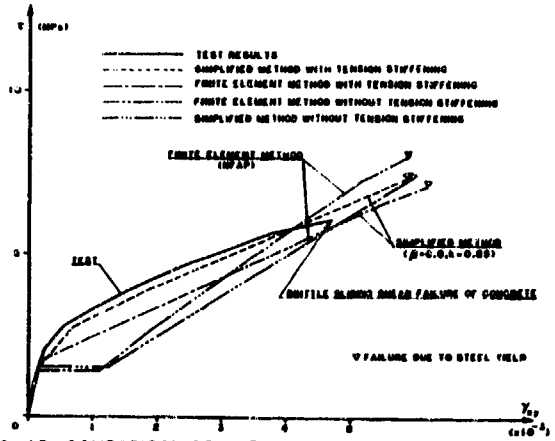

FIG. 13 COMPARISON OF F. E. METHOD, SIMPLIFIED METHOD WITH TESTS (PANEL PV27 ISOTROPIC, PURE SHEAR)

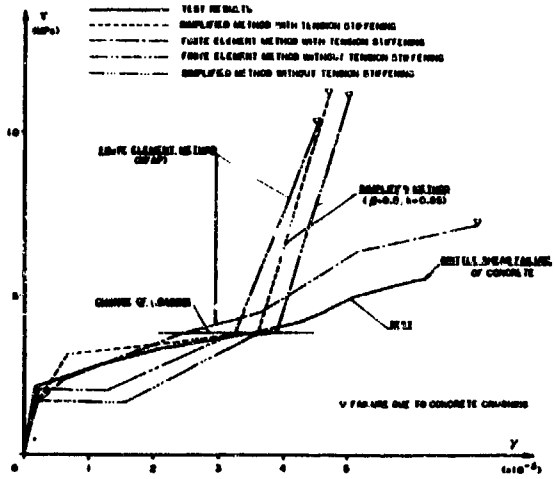

FIG. 16 COMPARISON OF F. E. METHOD, SIMPLIFIED METHOD WITH TESY PANEL PV29 (ANISOTROPIC, NONPROPORTIONAL LOADING: a. $0<\tau\leq3.86$ MPa $\sigma_x-\sigma_y=0$; b. $\tau=3.86$ MPa $\sigma_x-\sigma_y=(\tau-3.86)$)

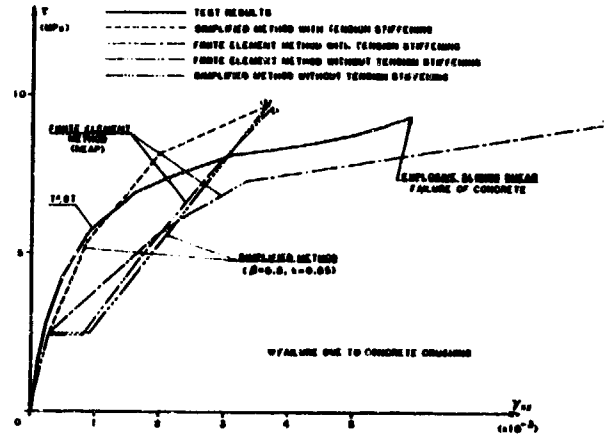

FIG. 14 COMPARISON OF F. E. METHOD, SIMPLIFIED METHOD WITH TESTS (PANEL PV25 ISOTROPIC, $\sigma_x=\sigma_y$ 0.69T, $0<\tau<\tau_0$)

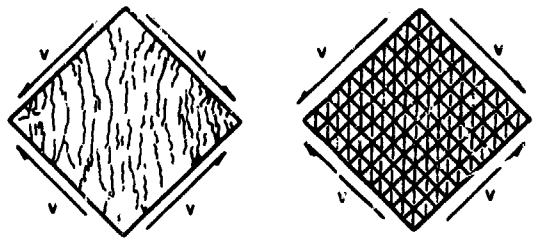

(a) REAL CRACK PATTERN V=4.90 MPa

(b) CALCULATED CRACK PATTERN V=4.90 MPa

FIG 17: COMPARISON OF CALCULATED CRACK PATTERN WITH TESTS (PV27)

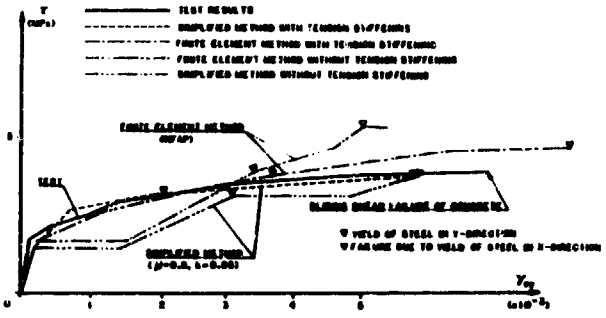

FIG. 15 COMPARISON OF F. E. METHOD, SIMPLIFIED METHOD WITH TESTS (PANEL PV19 ANISOTROPIC, PURE SHEAR)

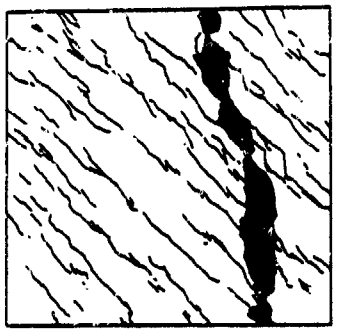

Fig 18 FAILURE OF PANEL PV29

TRANSMISSIBILITY METHOD IN STRUCTURAL FRACTURE DIAGNOSIS

Mehmet Akgün, Research Assistant
and
Frederick D. Ju, Professor

Mechanical Engineering Department
University of New Mexico
Albuquerque, New Mexico 87131

ABSTRACT

In this paper, transmissibility changes in a large frame structure caused by damage are utilized to diagnose the structural damage from cracking. Transmissibility, for the purpose of the present study, is defined as the ratio of the peak acceleration at the response location to the amplitude of the sinusoidal excitation in a plane frame structure. Transmissibilities at different locations in an undamaged structure and in a corresponding structure with known damage are computed and the results are compared to establish a trend among the changes in transmissibilities in relation to the damage. Transmissibility is a function of the load frequency and has maxima at the modal frequencies of the structure. In a field application, transmissibilities before and after the damage occurs can be measured. The damage location can be predicted with a minimum number of response locations where transmissibilities are computed (or measured).

INTRODUCTION

Nondestructive damage diagnosis is an important component of structural safety analysis. The reliability of a fractured structure depends on the accurate diagnosis of the location and of the severity of the fracture damage. Standard methods of fracture inspection available in ASME code [1], which specifies visual, surface and volumetric techniques, are all applicable to relatively simple structures or to large complex structures with known and readily accessible fracture locations. Otherwise, special methods based on a sound structural theory are needed. The present method is one of those utilizing the changing dynamic characteristics due to the presence of cracks on some structural members. It is desirable to apply in the diagnostic test the dynamic characteristics that relatively minor fracture damage would render large changes in their values. The present paper illustrates the use of transmissibility change for assessment of fracture damage especially in large structures.

Earlier work by Ju et al [2,3] utilizes the changes in modal frequencies for fracture damage diagnosis. There, the method applies readily to simple frame structures. For complex structures or structures with multiple cracks, the frequency method encounters uncertainties [4,5], that a probabilistic assessment becomes necessary and is yet to be developed. Those uncertainties arise from a myriad of measurement problems; such as: small frequency changes for a small number of cracks, differences in frequency changes within measurement error for different damage configurations and crossover (frequency of predamage higher mode drops below that of lower mode after damage). Transmissibility change is proposed as a better means of damage diagnosis [6,7]. Transmissibility is defined as the ratio of the response at a point on the structure to a sinusoidal excitation at another point. Significant changes in transmissibility can result at optimal response and excitation locations.

In this method, damage to a Mode I type crack in bending, is modeled as a fracture hinge [2]. Internal damping is incorporated into the structural model by means of complex Young's moduli for sinusoidal excitation. Governing equations for the beam elements which make up the structure are therefore of the same form as that for a Bernoulli-Euler beam with complex coefficients. The dynamic analysis of frame structures may then use the circuit analogy developed by Akgun, Ju and Paez [5,8,9]. Each uniform beam element is represented by an analog π-circuit. A fracture hinge, that is, the mechanical analog of a crack, is simulated by a "crack resistor."

TRANSMISSIBILITY

For a structure excited by a sinusoidal force at a specific point, the transmissibility across the structure at an arbitrary point (a measuring station) is defined as

$$T = |A/F| \tag{1}$$

where A is the transverse acceleration at the response station and F is the force at the excitation station. When F is sinusoidal, transmissibility becomes

$$T = \Omega^2 y/F_m \tag{2}$$

where Ω, y and F_m are the excitation frequency, the magnitude of the transverse deflection, and the amplitude of the excitation, respectively. Transmissibility, hence, is a function of the frequency and has peaks at the natural frequencies of the structure. Its value at a particular location and frequency will, in general, change if damage occurs to the structure. The relative transmissibility change at a location is defined as

$$R_T = (T_c - T_o)/T_o \qquad (3)$$

where T_o and T_c denote the pre- and post-damage transmissibilities, respectively. The relative transmissibility change, R_T, is a function of the location of excitation, excitation frequency, location where the response is measured, and the damage parameters, i.e., crack location and intensity.

It is desirable to have large values of R_T corresponding to relatively small cracks. Such values are obtained in the vicinity of the modal frequencies of the structures. On the other hand, if the deflected shape has a "pseudo-node point" (PNP) under the excitation (the point with smallest magnitude of transverse deflection), this point will, in general, shift after the damage has occurred. The numerical results indicate that largest changes in transmissibility are obtained in the vicinity of, but not exactly at, the pseudo-note points of the undamaged structure [7]. In general, then,

$$-1 < R_T < \infty \qquad (4)$$

where the lower limit is approached if the transmissibilities are computed near the pseudo-node points of the damaged structure. It should be noted that the pseudo-note points of the undamaged and damaged structure are very close. R_T is, therefore, very sensitive to the location of the response station in the vicinity of the pseudo-node points.

COMPUTATION OF DEFLECTIONS

Under sinusoidal excitation, internal damping in a beam can be represented by the complex Young's modulus [10], namely,

$$E = E_o(1 + i\delta) \qquad (5)$$

where E_o and δ are the dynamic Young's modulus and the damping factor, respectively. A damped Bernoulli-Euler beam under concentrated load can be simulated by an analog π circuit. A planar frame, n stories by m spans, is then represented by an interconnection of π circuits simulating columns and girders [5,7]. In this paper, only one major crack is assumed to exist on the structure. The beam element with the crack is simulated by two π circuits joined by the "crack resistor." Crack intensity is represented by a non-dimensional variable ($\theta = 3\pi(1 - \nu^2)(b/L) \int_0^\gamma \lambda[f(\lambda)]^2 d\lambda$) called the "sensitivity number," [2,3] which is a function of the crack depth (γ) and the slenderness ratio (b/L) of the beam element on which the crack is located. Solution of the circuit equations yield the transverse deflection at the desired locations on the structure.

The application of the transmissibility method will be illustrated with an example of a three-story four-span frame (Figure 1). Without loss of generality, all the beam elements are taken to be of equal length and the properties are uniform throughout the frame. The fundamental undamped characteristic value of this frame is computed to be 0.9653 without any crack. Since exciting the frame near the fundamental modal frequency yields the largest changes in transmissibility, the frame is excited at a frequency corresponding to a characteristic value of 0.96, slightly less than the fundamental characteristic value of the pre-damage structure. One of the outer ground-floor columns, being most easily accessible, is where the excitation is applied. The optimum locations of the excitation on these columns for the maximum change in transmissibility are found to be near the junctions with the girders. The location of the excitation is thus chosen to be at a relative distance of 0.95 from the ground. One of the objectives of the study is to accomplish damage assessment with as few transducers as possible. To that end, the "pseudo-node points" (PNP) of the girders 16, 19, 21, 24, and 27 (Fig. 1) are computed accurately in order to place the response transducers. Knowledge of the transmissibility changes at these five stations is found adequate to isolate the damage to within one or two cells of the frame. The computed relative positions of the pseudo-node points (PNP) of the above girders, measured from the left end of each girder, for an excitation at the fundamental characteristic value .96 applied on column 1 (Fig. 1) at 0.95 relative position are given in the following table. The transducer locations (TL) used in the analysis to follow are shown in the last row.

Girder	16	19	21	24	27
PNP	.6062	.3913	.4899	.6183	.3811
TL	.61	.39	.49	.62	.38

Figures 2 and 3 depict the transmissibility changes corresponding to a crack on girders 17 and 26 (Fig. 1), respectively, as functions of the crack location. Transmissibility change at the station 27 (on girder 27) for a crack on girder 17 is very small. Changes at the stations 16 and 19 for a crack on 26 are also very small. These transmissibility charges are, therefore, not shown in the figures. The damping factor, δ, is taken as .01 in the computations. The sensitivity number, θ, for the crack is .01. θ is a function of the crack depth and the slenderness ratio of the beam on which the crack is located [8,3]. For

beams with slenderness ratios (length to beam-depth ratio) of 10 and 20, $\theta = .01$ corresponds to relative crack depths of .20 and .28, respectively.

Figures 2 and 3 demonstrate that the transmissibility change at a station varies significantly with respect to the crack location. The large variations are predominantly due to two reasons. First, a crack in the vicinity of an inflection point of the modal shape causes a very small change in the transmissibility. Secondly, the locations of the pseudo-node points of the damaged structure, which are close to the pseudo-node points of the undamaged structure, depend on the location of the crack. Small changes in the locations of the pseudo-node points hence cause large variations in transmissibility at a given station.

The objective of the study is to find general trends among the values of the transmissibility changes, which can, in practice, be used to locate damage, given the transmissibility changes computed from the measured responses at the response stations. To that end, transmissibilities at all five stations on the frame of Figure 1 were computed with and without any crack, with the crack location varied throughout the frame. The results of comparing the relative transmissibility changes at the five stations, when the frame is excited at column 1, are summarized below, where R_j stands for the relative transmissibility change at the station on element j.

a) A crack close to a joint or an anchor renders larger transmissibility changes than a crack in the mid-region of a beam element.

b) If the crack is far from the jth transmissibility station (on element j), R_j is very small compared to the other R values. Specifically,

i) $R_{16} \approx 0$ for a crack on elements 3, 6, 9, 10 through 15, 19, 22 through 27.
ii) $R_{19} \approx 0$ for a crack on elements 1 through 6, 9, 20, 24 through 27.
iii) $R_{24} \approx 0$ for a crack on elements 10, 13 through 15, 18, 23, 27.
iv) $R_{27} \approx 0$ for a crack on elements 1, 3, 4, 17.
v) R_{21} is almost always significant when the crack is not at an inflection point of the modal shape.

These results are for a θ value of .01. R_j is considered near zero if its magnitude is less than 10% for the crack located anywhere on the particular beam element. $|R_{27}|$, for example, is less than 10% for a crack located at most anywhere on the girder 24. However, 24 is not listed in (iv) since $R_{27} > 10\%$ when the crack is near the right end of the girder 24. For larger values of θ, i.e., for deeper cracks or for less slender beams, magnitudes of the above R_j values may exceed 10% but they would still remain much smaller than those of the other significant R_j values.

c) If R_{16} and R_{21} are the largest two or are negative and the lowest two, the crack is on one of the elements 1, 2, 4, 5, 16, 17.

d) If R_{19} and R_{21} are the most significant values among all R_j (i.e., they are the largest two, or one is the largest and the other is negative and the lowest), the crack is on the element 7, 8, 10, 12, 14, 18, or 19. If, in addition, $R_{19} > R_{21} > 0$, the crack is not on the element 7, 8, or 12.

e) If R_{21} and R_{24} are the only significant values (i.e., positive and large, or negative and low) while the others are small in magnitude, the crack is on the element 2, 3, 5, 6, 20 through 22, or 24. If, in addition, R_{27} is also significant, the crack is on the element 25 or 26.

f) If $R_{21} > R_{27} > 0$, the crack is on the element 9, 11, 12, 19, 21, 22, or 24.

g) If $R_{27} > R_{21} > 0$, the crack is on the element 9, 11, 12, 15, 23, 26, or 27.

h) If R_{21} and R_{27} are negative and the only significant values, the crack is on the element 12, 14, 22, 23, 25, 26, or 27.

i) If R_{19} and R_{27} are the most significant values among all R_j the crack is on the element 10, 13, 14, 18, 19, or 23.

If no conclusion is reached as a result of exciting structure on column 1, the frame may be excited on column 13 and a diagnosis may be reached.

CONCLUSIONS

The present paper establishes the technique of transmissibility method in the diagnosis of fracture damage in structures. The analysis is an extension of the circuit analogy method which was developed for the frequency method in damage diagnosis. The extension involves the incorporation of damping and the insertion of the excitation and the response stations. The paper also proposes the optimal locations on beam elements in the structure for the mountings of response transducers. It is found that, in the neighborhood of pseudo-node points in the structure at the particular excitation frequency, the transmissibility change can be large even with

small cracks. With the influence of damping and changes in dynamic characteristics, the difference in relative transmissibility changes (R_1) can lead to the accurate location of the fracture damage and thus an assessment of the intensity of the crack damage.

REFERENCES

1. ASME Boiler and Pressure Vessel Code, Sec. XI. Art. IWA-2000, 1974.

2. Ju, F. D., Akgun, M., Wong, T. E., and Paez, T. L., "Modal Method in Diagnosis of Fracture Damage in Simple Structures," Productive Applications of Mechanical Vibrations, ASME-EMD-V. 52, 1982, pp. 113-125.

3. Ju, F. D., Akgun, M., Paez, T. L., Wong, T.E. "Diagnosis of Fracture Damage in Simple Structures," UNM Report CE-62(82) AFOSR-993-1, AFOSR Report No. AFOSR-TR-83-0049, October 1982.

4. Ju, F. D., Akgun, M., Paez, T. L. "Diagnosis of Multiple Cracks on Simple Structure," ASCE Annual Convention Applied Fracture Mechanics Session, San Francisco, CA, October 1-5, 1984.

5. Akgun, M., Ju, F. D., Paez, T. L. "A General Theory of Circuit analogy in Fracture Diagnosis," UNM Report ME-124(84) AFOSR-993-1, AFOSR Report No. AFOSR-TR-84-0910, March 1984.

6. Akgun, M., Ju, F. D., Paez, T. L. "Transmissibility as a Means to Diagnose Damage in Structures," Proc. 3rd IMAC Conference, Orlando, FL, January 27-31, 1985.

7. Akgun, M. "Structural Theory of Fracture Damage Diagnosis," Ph.D. dissertation, UNM (in preparation).

8. Akgun, M., Ju, F. D., Paez, T. L. "Fracture Diagnosis in Structures Using Circuit Theory," Proc. Interaction of Non-Nuclear Munitions with Structures, 1983, pp. 146-150.

9. Ju, F.D., Akgun, M., Paez, T. L. "Fracture Diagnosis in Beam-Frame Structure Using Circuit Analogy," Recent Advances in Engrg Mechanics, ASCE, May 1983.

10. Snowdon, J. C. Vibration and Shock in Damped Mechanical Systems, Wiley, 1968, pp. 3-7.

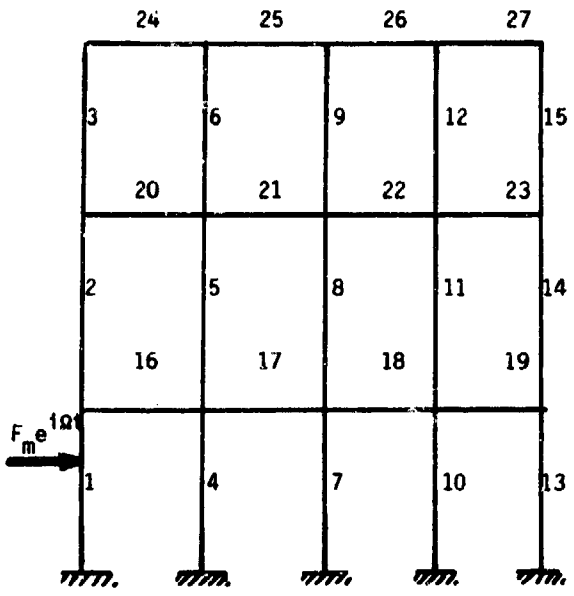

Figure 1. Three-Story Four-Span Frame.

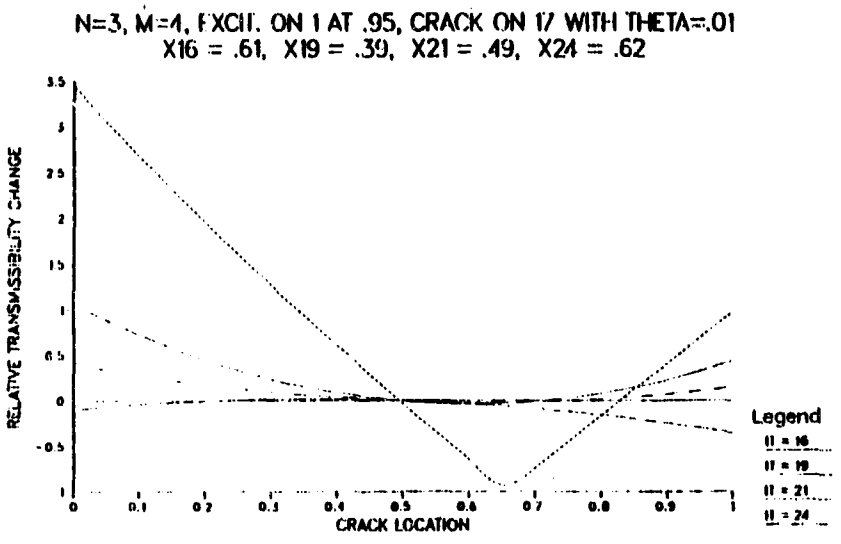

Figure 2. Relative Transmissibility Changes at Stations 16, 19, 21, and 24 for a Crack on Element 17.

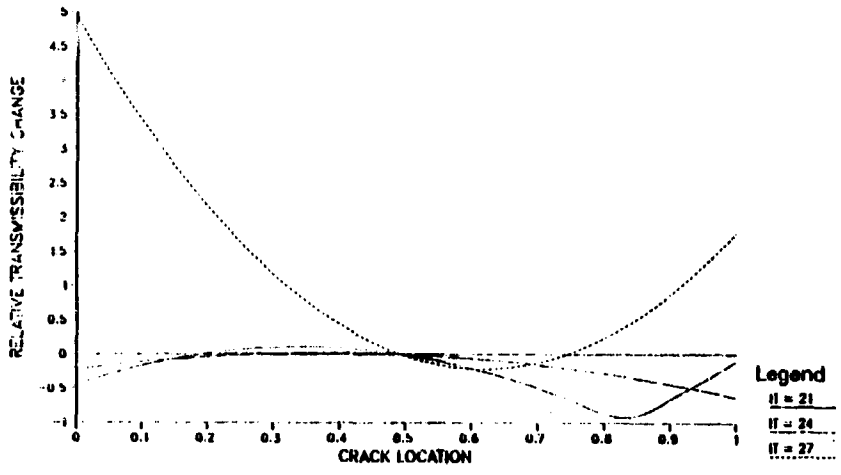

Figure 3. Relative Transmissibility Changes at Stations 21, 24, and 27 for a Crack on 26.

ACKNOWLEDGEMENT

The research is performed under AFOSR Grant No. 81-0086. Col. Lawrence D. Hokanson is the contract monitor officer.

EXPERIMENTAL EVALUATION OF REVETMENT EFFECTS

Firooz A. Allahdadi
and
James M. Carson

New Mexico Engineering Research Institute
University of New Mexico
Albuquerque, New Mexico

ABSTRACT

Effects of revetments in reducing airblast loading on aboveground structures as a function of scaled distance, $ft/W^{1/3}$, where W is the explosive weight in pounds, are investigated experimentally. Two sets of ad hoc model tests were designed. The objectives were to determine the least scaled distance from the explosive source to a "structure" behind the revetment while maintaining a desired 3.5-lb/in^2 peak overpressure environment. Analysis of the data showed that revetments effectively reduce the peak pressure immediately behind the revetment. However, a transition region exists behind the revetment where the pressure field recovers and approaches the free-field value, thus nullifying the effect of the revetment.

I. INTRODUCTION

Current explosive safety criteria for structures in the vicinity of stored explosives are based on the quantity of the explosive and the distance from the explosive source. The term relating these two conditions is called a K-factor, which is equal to this distance in feet divided by the cube root of the net explosive weight (TNT equivalent) in $lb^{1/3}$. Current standards for intraline distances call for a peak side-on overpressure of 3.5 lb/in^2 and a K-factor of 18. Intraline distances apply to facilities closely related in mission to the explosive source.

Economic and land considerations motivated the design of two sets of small scale revetment tests to investigate the possibility of reducing the K-factor using a bin revetment, while maintaining the 3.5- lb/in^2 overpressure ceiling. The tests were also designed to provide baseline data regarding free-field environments, airblast/revetment shock interaction, and blast loading definition.

The small-scaled tests (1/26 scale) involved surface bursts of a 0.5-lb (C-4) hemispherical explosive charge, scaled revetments, and mock structures. The K-factors ranged from 5.4 to 13.2 for the first series of four tests, and from 10.7 to 19 for the second series of eight tests. The first series used a simple stationary bin revetment. The second test series involved a movable revetment and mock structure to accomodate various configurations.

Three basic configurations were used.

1. Free-field measurements (Tests 1 and 2)--Tests involved no revetment; the mock structure was located at one side of the gage field.

2. Revetment/Structure tests (Tests 3, 4, and 5)--Tests involved a revetment and the mock structure located a scaled 15 ft behind the revetment (e.g., spacing for a road).

3. Revetment/Structure tests (Tests 6, 7, and 8)--Tests involved a revetment and the mock structure located a scaled 4 ft behind the revetment (e.g., spacing for a sidewalk).

The revetments are relatively close (4 to 15 ft full scale) to the structure on these tests (Fig. 1).

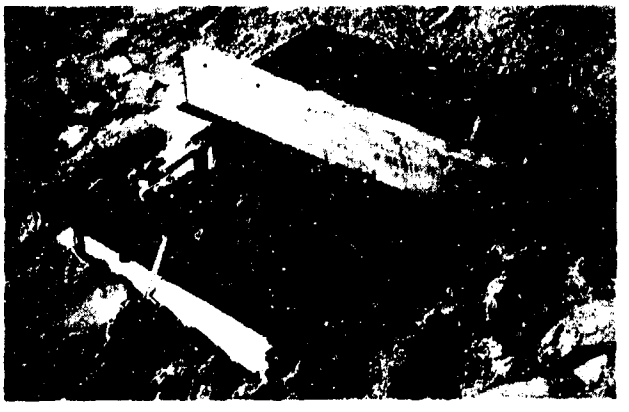

Figure 1a. Movable mock structure.

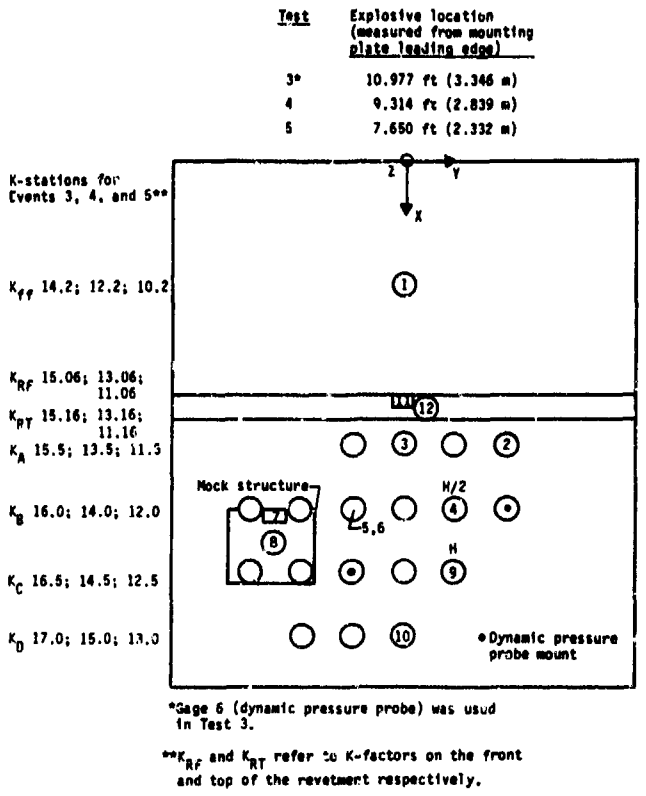

*Gage 6 (dynamic pressure probe) was used in Test 3.

**K_{RF} and K_{RT} refer to K-factors on the front and top of the revetment respectively.

Figure 1b. SSRT-II gage mounting plate (36 by 42 in^2) and explosive locations for Tests 3, 4, and 5; mock structure at scaled 15 ft.

The airblast environment behind and in front of the revetment and the revetment-mock structure shock interaction were measured using Kulite pressure transducers. To monitor planarity of the shock front and vertical pressure gradient, some pressure transducers were mounted on risers at two elevations, H and H/2 (Fig. 1b), where H is the revetment height.

The principles and analysis of the test data are outlined in Section II; conclusions are presented in Section III.

II. TEST RESULTS

The first test series established the lower bound for K-factor. The results of the first test series showed that a K-factor larger than 13 is required to achieve a 3.5-lb/in^2 overpressure behind the revetment. The thrust of the second small test series was to determine the minimum K-factor that would not exceed the desired peak overpressure environment behind the revetment.

1. Analysis of the data demonstrated that a revetment could effectively reduce the peak side-on overpressure and lower the required K-factor. A quantitative measurement of the revetment effects in reducing the peak side-on overpressure versus scaled distance (K) is illustrated in Figure 2. This reduction in overpressure at a particular range due to a revetment is shown by

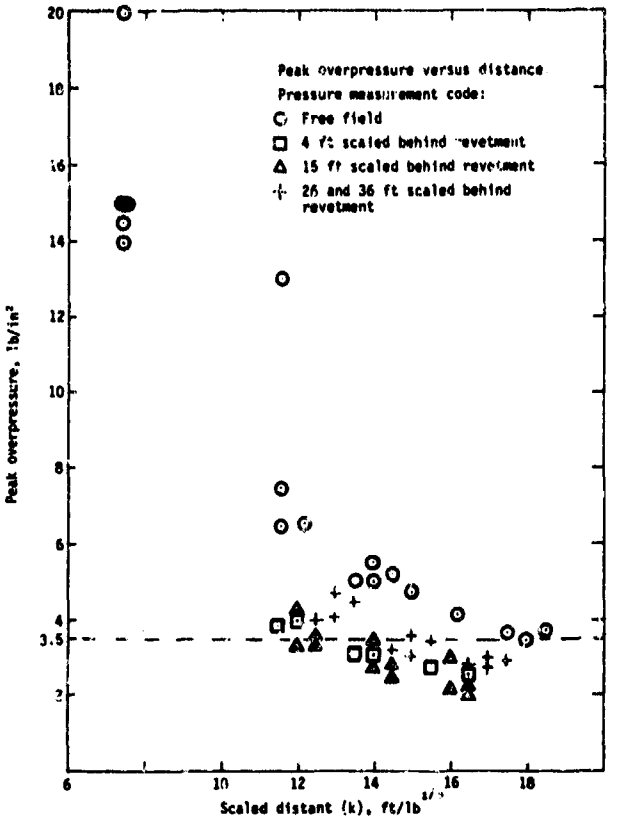

Figure 2. Pressure versus distance.

comparing the free-field measurements (circles) to measurements behind the revetment (squares and triangles). Immediately behind the revetment a nearly 2 lb/in^2 pressure drop is seen. It is important to observe that farther behind the revetment (at a distance approximately equal to 4 to 5 revetment heights) the peak side-on overpressure tends to recover and approach its free-field value. This phenomenon is demonstrated by the response of the gages farthest behind the revetment and shown as + symbols in Figure 2. It is interesting that the free-field pressure measurements reach 3.5 lb/in^2 at a range approximately equal to K-18, thus correlating with the current design manual (Ref. 1).

2. The airblast load on the mock structure at scaled distances of 4 and 15 ft behind the revetment was monitored. Investigation of the pressure history records of the mock structure revealed a great deal of shock interaction occurring between revetment and mock structure (Fig. 3). A summary of free-field measurements and the mock structure loading with the corresponding K-factors is given in Table 1. Note that there is a decrease in the free field overpressure (gages 1, 3 through 5, 9 through 10) with increasing range in both tests. Also note that gage 7 located on the front face of the mock structure recorded a reflected pressure over twice the incident overpressure.

The strong shock interactions observed between the mock structure and revetment suggest that the

TABLE 1. MOCK STRUCTURE AND FREE-FIELD BLAST ENVIRONMENT

		Test No. 1			Test No. 2		
Gage No.	Elevation, in	K, ft/lb$^{1/3}$	P, lb/in^2	I, lb/in^2-s x 10^{-3}	K, ft/lb$^{1/3}$	P, lb/in^2	I, lb/in^2-s x 10^{-3}
1	0.0	16.20	4.20	3.54	12.2	6.56	4.56
3	0.0	17.50	3.68	3.60	13.5	5.07	4.17
4	3.0	18.0	3.0	3.80	14.0	5.52	3.94
5	0.0	18.0	3.5	3.20	14.0	4.95	3.83
[a]6	6.7	18.0	2.8	0.5	--	--	--
[b]7	2.5	18.0	7.54	≈3.0	14.0	11.50	3.25
8	5.0	18.25	3.4	0.95	14.25	5.20	1.27
9	6.0	18.5	3.5	2.98	14.50	5.20	3.68
10	0.0	19	--	--	15.0	4.69	3.29
[c]--							

[a]Dynamic pressure measurement.

[b]Reflected pressure measurement.

[c]No revetment used in Test 1 and 2. Gage locations 11 and 12 not used (Fig. 1b).

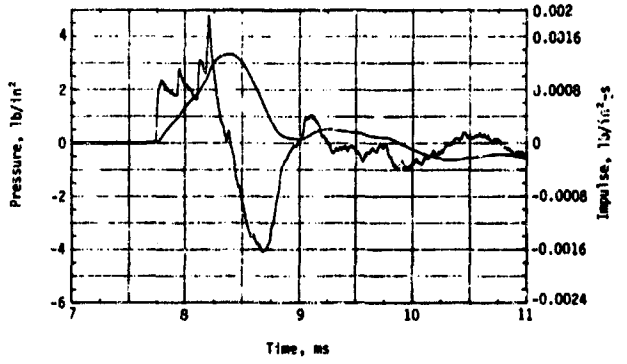

(a) Scaled 4-ft spacing.

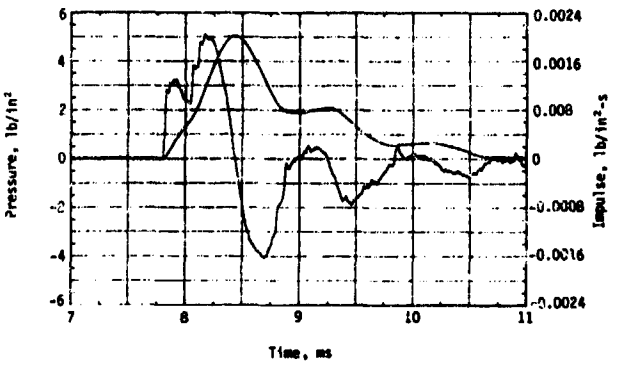

(b) Scaled 15-ft spacing.

Figure 3. Revetment/Structure shock interaction at scaled 4-ft and 15-ft spacing.

incident peak overpressure criteria alone may not be sufficient to fully determine the total load on a structure or to ensure its survivability. These interactions, i.e., multiple reflections and diffractions, effectively contribute to the total load on the structure and their impact should be considered in the criteria for selecting a viable K-factor. Criteria based on other parameters such as blast pressure waveforms and impulse functions should be considered. Note that there exists an enhancing effect caused by multiple reflection of the shock between mock structure and revetment which greatly influences the loading definition on the structure.

3. A pressure decrease with elevation was detected. However, this gradient was less than 10 percent.

4. In general a comparative analysis of the pressure traces demonstrated the reproducibility of the free and perturbed airblast environment ahead and behind the revetment. The pressure records provided by transducers positioned at various locations relative to the revetment were investigated and compared with theoretical prediction. As predicted by theory (Ref. 2), for a low overpressure region, the gages ahead of the revetment recorded consistently the same normal peak reflected pressure as the incident overpressure (Fig. 4). The pressure measurement provided by the gages mounted on the risers displayed a double peak pulse indicative of the reflection waves from the flat base plate (Fig. 5). The flush mounted gages located immediately behind the revetment showed flat top traces attesting to the diffraction of the blast wave around the revetment (Fig. 6). The initial broadening of the pressure pulse due to vorticity effects behind the blast wave (Ref. 3) on top of the revetment is compared with the free-

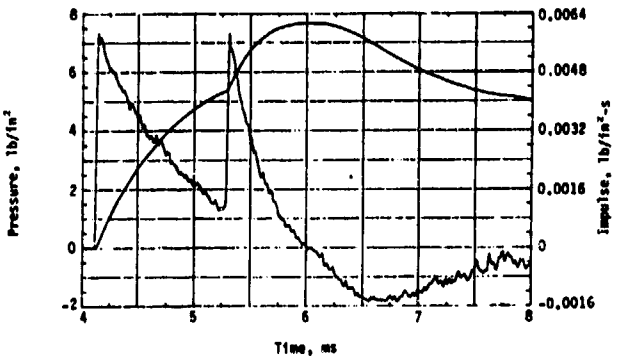

(a) SSRT-II-8

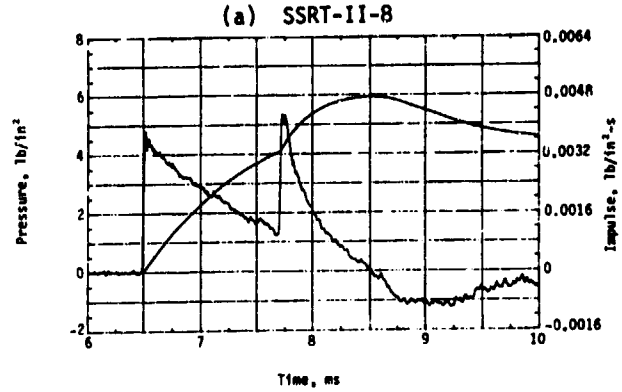

(b) SSRT-II-3

Figure 4. Incident overpressure followed by reflection from revetment.

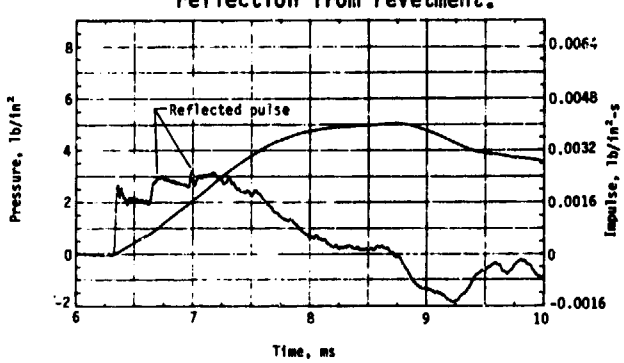

(a) Reflected pressure from base plate, SSRT-II-4, No. 4.

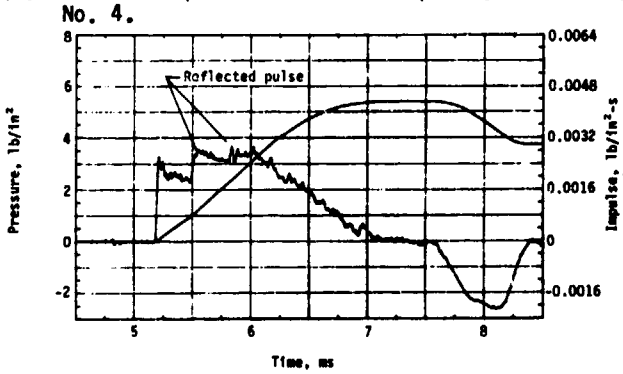

(b) Reflected pressure from base plate, SSRT-II-5, No. 4.

Figure 5. Reflected pressure provided by gages mounted on risers.

field pressure environment (Fig. 7). Qualitative comparison of the two records shows that, for nearly identical incident peak overpressures, the impulse related to the pressure pulse on top of the revetment peaks much sooner, due to the vorticity modified pressure pulse shape. The measured dynamic pressure showed that at low overpressure the peak dynamic pressure, at best, has the same magnitude as peak static overpressure (Fig. 8). This behavior is in accordance with the findings outlined in Reference 4.

CONCLUSIONS

Analysis of the data demonstrated that revetments are effective in reducing distances while maintaining a desired peak 3.5-lb/in^2 overpressure. Depending on location of the structure behind the revetment, the current K-18 can be reduced to a value between 13.5 and 16. It is concluded that load definitions based on peak overpressure are not a sufficient criteria; for accurate definitions of load other airblast parameters such as impulse and reflected pressure should be considered as well.

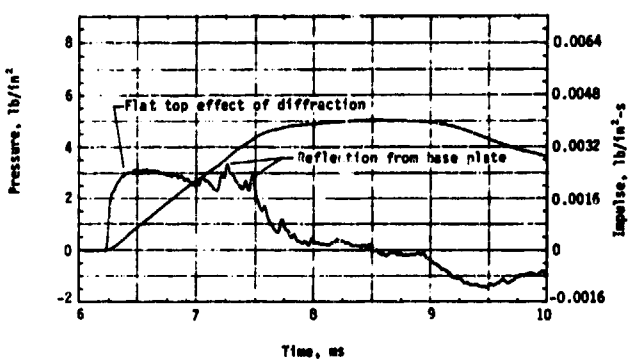

(a) Free field blast environment behind the revetment, SSRT-II-4, No. 3.

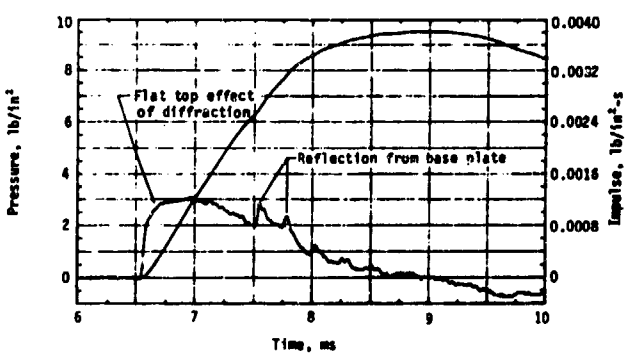

(b) Free field blast environment behind the revetment, SSRT-II-5, No. 3.

Figure 6. Free field pressure environment behind the revetment.

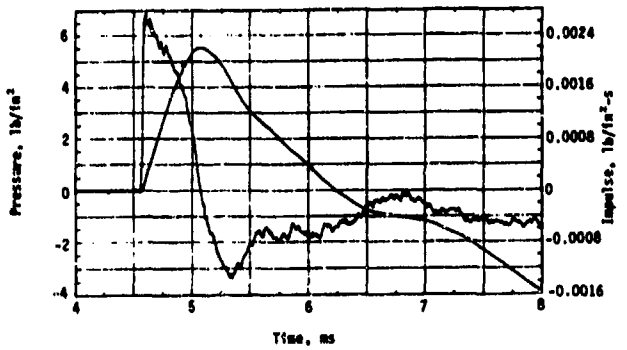

(a) Record of pressure field on the revetment, SSRT-II-6, No. 2.

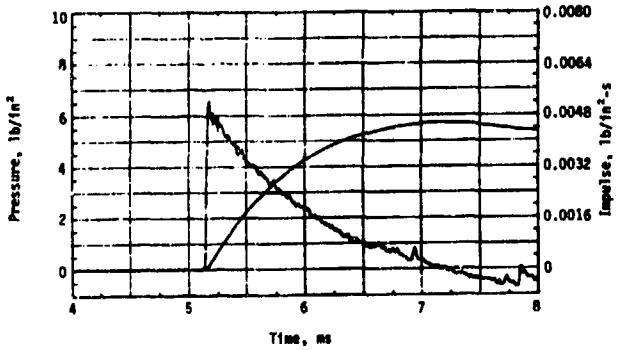

(b) Free field overpressure record, SSRT-II-2, No. 1.

Figure 7. Comparison of the pressure field on the revetment roof and free field.

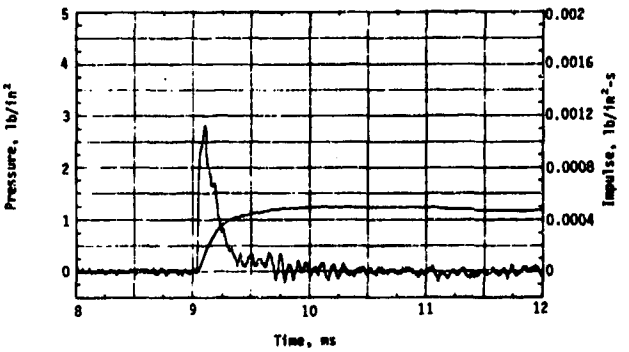

(a) Dynamic pressure record, SSRT-II-1, No. 6.

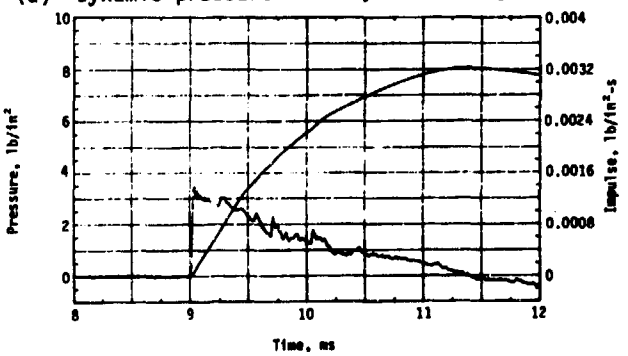

(b) Static overpressure record, SSRT-II-1, No. 5.

Figure 8. Comparison of dynamic pressure with static overpressure for low overpressure environment.

REFERENCES

1. Crawford, Robert F., et al, Protection from Nonnuclear Weapons, AFWL-TR-70-127, Air Force Weapons Laboratory, Kirtland Air Force Base, New Mexico, 1971.

2. Carpenter, H. J., Kuhl, A., and Srinivasa, D., Evaluation of Airblast Loading Prediction Techniques, AFWL-TR-80-27, Air Force Weapons Laboratory, Kirtland Air Force Base, New Mexico, 1980.

3. Glasston, S., ed., The Effects of Nuclear Weapons, prepared by U. S. Department of Defense, published by U. S. Atomic Energy Commission, April 1962.

4. Hartenbaum, B., The Determination and Use of Dynamic Pressure in Airblast Tests, Hi-Tech Lab. Inc., P.O. Box 1686, Santa Monica, California.

DEVELOPMENT AND TESTING OF IGLOO ROOF RETROFIT CONCEPTS

James W. Ball
and
David R. Coltharp

U. S. Army Engineer Waterways Experiment Station
Vicksburg, Mississippi

ABSTRACT

A variety of roof retrofit cover concepts were developed and tested as a means of preventing personnel using explosives from gaining access to ammunition storage igloos. Four passive cover concepts, which were used in conjunction with the existing cover over the roof of the igloo, consisted primarily of: (1) 3-ft-thick concrete, (2) rock rubble, (3) 2-ft-thick concrete, and (4) additional soil. A single active cover concept consisted of a foaming liquid designed to fill the crater that resulted from "first shot" detonations. Seventeen explosives tests were conducted using shaped and platter charges with up to 40 lb of explosives. For each test, pressure measurements were recorded inside and outside the igloo, along with accelerations of the igloo's floor slab. A high-speed movie camera, focused on the inside of the igloo, recorded all roof perforations. All retrofit covers proved adequate in denying personnel access through the roof of the igloo. Sympathetic detonation inside the igloo due to fragment mass and velocity is more likely with the soil cover. It is less likely with the 3-ft-thick concrete cover.

INTRODUCTION

Background

Current ammunition storage igloos offer limited protection against forcible penetration with various tools and explosives. As part of a program to upgrade the igloos against forcible entry, the U. S. Army Engineer Waterways Experiment Station (WES) developed and tested four passive roof retrofit concepts for prototype igloos against persons using up to 40 lb of explosives in the form of shaped charges and platter charges. In conjunction with these passive concepts, the U. S. Army Construction Engineering Research Laboratory (CERL) designed and tested an active delay system that consisted of filling craters formed from "first shot" charges with foam, thus denying early emplacement of "second shot" charges close to the roof surface.

Preliminary tests were conducted on existing reinforced concrete elements at Fort Polk, La., and Camp Shelby, Miss. Results of these tests were used to design four cover concepts that were constructed and tested on a prototype igloo at the Sierra Army Depot (SIAD) in Herlong, Calif.

Objectives

The primary objective of this investigation was to develop and test the effectiveness of passive and active retrofit cover concepts in preventing personnel (using up to 40 lb of explosives) from entering an ammunition storage igloo through the roof. Secondary objectives included obtaining pressure, acceleration, and fragmentation data for comparison against criteria for sympathetic detonations.

Design Assumptions and Charge Threats

It was assumed that a terrorist team would attempt a surgical entry versus a structural breaching or collapse of the igloo. Also, it was assumed that the cover designs would prevent the attack team from digging and placing the explosive charge close to the roof of the igloo. Primary materials considered in the design of the passive retrofit covers included (1) added soil cover, (2) concrete, (3) rock rubble, and (4) gravel.

The primary explosive threats considered in the design of the retrofit covers consisted of an M3 40-lb shaped charge and a 40-lb platter charge. Pertinent information on the M3 40-lb shaped charge is presented in Table 1. The platter charge consisted of 40 lb of C-4 that was placed on one side of a circular steel flyer plate.

TEST PROCEDURES

Test Structure

Design and construction of modifications to an existing damaged igloo (Fig. 1) at the SIAD in Herlong, Calif., were accomplished by the U. S. Army Corps of Engineers District at Sacramento, Calif., during the period 10 March through 10 August 1983. These modifications included: (1) repairing three existing holes in the roof, (2) repairing cracks in the arch, (3) adding four roof retrofit covers, and (4) constructing internal bracing to support the added weight of the retrofit covers. The front headwall of this igloo, almost entirely removed from past damage, was not included in the modification. However, the remaining headwall was completely removed for test purposes.

The existing igloo is a lightly reinforced concrete arch (Fig. 2) that is 81 ft long. Principal reinforcing steel of the arch consists only of 0.5-in-diam steel rods that are spaced on 12-in centers. The concrete thickness of the arch varies from 16 in at the base to 6 in at the crown. Therefore, the percentage of principal reinforcement varies from approximately 0.10 percent at the

base to 0.27 percent at the crown of the arch.

Based on the preliminary tests at Fort Polk, La., and Camp Shelby, Miss., four passive retrofit cover sections were constructed over the roof of the igloo. To support the added weight of the retrofit covers, the lightly reinforced concrete arch was supported with internal bracing. A cross-section of each cover along with the internal bracing is shown in Fig. 3. The four cover sections consisted mainly of (1) 3 ft of concrete, (2) 3 ft of rock rubble, (3) 2 ft of concrete, and (4) 2.5 ft of soil. For testing the CERL's active foaming system, 1-in-diam PVC pipes spaced on 12-in centers were embedded in the 3-ft concrete and rock rubble sections. Fig. 4 shows the four constructed retrofit covers. Plywood forms used for concrete placement in the first and third cover sections were left in position for the tests to prevent the soil overburden from sloughing. As another means of preventing sloughing, boards were placed on the side slopes at the terminated ends of the rock rubble and sand cover sections.

Test Shots and Locations

Test shot locations are shown in Fig. 5. The first test shot at each location is numbered from one to nine. The second test shot at the same location as the first is designated with the letter "A". Two "first shots" and one "second shot" were conducted on the 3-ft concrete section; three first shots and three second shots on the rock rubble section; two first shots and two second shots on the 2-ft concrete section; and two first shots and two second shots on the sand section. All first shots were either 40-lb shaped charges or 40-lb platter charges. All 40-lb shaped charges were identical to those whose characteristics were previously defined in Table 1. All 40-lb platter charges consisted of 40 lb of C-4 that was placed on one side of a 0.5-in-thick steel plate with a diameter of 19 in. All second shots were planned to be only 20-lb platter charges (20 lb of C-4 placed on one side of a 0.25-in-thick steel plate with a diameter of 19 in). However, after Test 5A, it was concluded that these charges were having no effect in perforating the retrofit covers. Therefore, 40-lb platter charges were used for Tests 6A, 7A, and 8A. For Test 9A, the last shot, a 20-lb platter charge was used.

CERL's Foaming Operation

CERL personnel foamed the craters formed by Test Shots 2, 3, and 4 prior to Test Shots 2A, 3A, and 4A, respectively. This procedure entailed attaching an adapter to the end of a pipe that had been broken from the first shot detonation and resulting cratering action. Two hoses were connected to the adapter. The other ends of the hoses were connected to two pressurized tanks containing the foaming liquid. The tanks were located on a truck at the base of the igloo. A valve was turned on and the liquid foam from the tanks passed through the hoses and out the broken pipe into the crater. The liquid began to foam, filling the crater and hardening. The amount of time required for the foam to harden is determined by the exact mixture of the foaming liquid.

Placement of Test Charges

Prior to each test shot, an explosive ordnance team (EOT) from First Special Operations Command of Fort Bragg, N. C. placed each test charge at each test location. Each shaped charge was placed in the standard-issued metal tripod that provided a 15-in standoff distance. With the exception of Tests 2A and 4A, all platter charges were placed on a wood stand that provided a 2-ft standoff distance. Since each charge was placed on the side slope of the retrofit covers instead of the crown, care was taken to align the charge perpendicular to the roof of the arch. Prior to Test 2A, after foaming the crater formed from Test 2, the EOT shoveled off the foam within 2 feet of the bottom of the crater and placed the platter for Test 2A directly on the foam. For Test 3A, the foam was shoveled out of the way and the wood stand with the 20-lb platter was placed in the crater that had resulted from Test 3. The same procedure was used for removing the foam prior to Test 4A. However, this time the foam was removed to the level of the original retrofit cover and the 20-lb platter placed directly on the foam. All other second test shot platters were placed on the wood stand in the craters resulting from the first shots.

Damage Survey

Measurements of the crater in the retrofit covers, measurements of the perforated holes in the roof of the igloo, still photographs, and a visual inspection were made following each test shot to assess damage.

Electronic Transducer Measurements

Five channels of data were obtained from electronic instrumentation for each test shot. Two channels recorded the pressure inside and outside the igloo. Three channels recorded the vertical, longitudinal, and transverse accelerations of the igloo's floor slab. The outside pressure gage was located on the centerline of the igloo's apron 2 ft outside the open end. The pressure gage inside the igloo was placed on the igloo's floor. It was transversely located in line with each test shot location (6 ft from the igloo's centerline). For test shots 1-2A, 3-4A, 5-5A, 6-7A, and 8-9A, the inside pressure gage was located longitudinally from the outside pressure gage at distances of 67, 72, 63, 47, and 24.5 ft, respectively. The accelerometers were located on the centerline of the igloo's floor slab at the same longitudinal distances from the open end as the test shots.

Particle Size and Velocity Measurements

A measurement was made of the particle sizes and velocities of fragments that perforated the roof inside the igloo for each test shot. These measurements were recorded by a high-speed movie camera (1,000 frames per second) positioned 165 ft in front of the igloo focused on the front post (Fig. 6) and endwall (Fig. 7) inside the igloo. The post and endwall were painted white with black stripes spaced on 2-ft centers.

RESULTS AND DISCUSSION

Damage Survey

Results of the damage survey revealed that all

retrofit covers were adequate in denying personnel access to the interior of the igloo. Only "first shot" 40-lb shaped charges were successful in perforating the roof of the igloo. This occurred for all cover sections with the exception of the 3-ft-thick concrete section. The perforated holes were small with diameters that ranged from 4.5 to 6 in.

Electronic Transducer Measurements

As would be expected, peak recorded pressures inside and outside the igloo occurred with the largest charges, i.e., 40-lb platter and shaped charges. Peak pressure measurements of "first shot" tests using these charges are shown in Table 2. The table also gives the time of arrival of the pressure wave at each gage location. As shown in this table, peak pressures inside the igloo range from 0.2 to 2.25 psi. Also, peak pressures outside the igloo range from 0.47 to 6.5 psi. Pressures inside and outside the igloo increase as the charge locations are moved closer to the open end of the igloo, the location of the outside pressure gage. With the exception of Test 9, there was no measurable pressure inside the igloo that was induced through the igloo's roof. This is evident in Table 2 when a comparison is made between the arrival times of the pressure wave inside and outside the igloo. For each test, with the exception of Test 9, the pressure wave arrives at the outside gage location before it arrives at the inside gage location. Thus, the peak pressure inside the igloo results from the pressure wave that enters the open end of the igloo. A comparison of the pressure-time histories for Test 9 inside and outside the igloo (Fig. 8) shows that the arrival time of the first pressure wave at both locations occurs at 10 ms. The first peak pressure spike of 2 psi inside the igloo is associated with the pressure that is induced through the perforated hole in the roof. The second pressure spike of 2.25 psi is associated with that pressure wave that enters the open end of the igloo. The pressure induced through the roof is consistent with the observation made with the high-speed movie camera that was focused on the inside of the igloo. The camera observed the jet from the shaped charge entering the igloo through the perforated hole in the roof. This jet was not observed with the camera for any other test.

The low level response of the floor slab that was indicated by the recorded acceleration time histories is consistent with the observation of no damage to the igloo as a result of structural motion. It should be noted that the measured response would be different for an igloo that contained no internal bracing and whose endwall was not missing. It is believed that the response of the test igloo with these differences is higher than it would be without them.

Particle Size and Velocity Measurements

The individual mass of particles (fragments) and their corresponding velocities were undetectable with the high-speed movie camera focused on the inside of the igloo. The camera did show that only the shaped charge detonations of Tests 4, 5, 7, and 9 would induce fragments inside the igloo that would be of concern to sympathetic detonations. With the exception of Test 9, the camera recorded a dark mass of debris that entered the perforated holes in the igloo's roof and impacted the floor slab. For Test 9, the jet from the shaped charge entered the inside of the igloo through the perforated hole in its roof.

Average velocities of the mass of debris inside the igloo resulting from Tests 4, 5, and 7 were calculated to be 494, 517, and 242 ft/s, respectively. The average velocity of the jet from Test 9 was calculated to be 2,282 ft/s.

CONCLUSIONS

The following conclusions were obtained from the test results.

1. All retrofit cover designs were proved adequate in denying access through the roof of the igloo to personnel using "first shot" and "second shot" 40-lb shaped and platter charges.

2. All retrofit covers, with the exception of the 3-ft-thick concrete cover, permitted perforation of the igloo's roof. The perforated holes range in diameter from only 4.5 to 6 in.

3. All retrofit covers, with the exception of the soil cover, prevented pressure from being induced through the roof of the igloo.

4. The applied dynamic loads resulted in no damage to the igloo, other than perforated holes in the roof.

5. Sympathetic detonation inside the igloo due to fragment mass and velocity is more likely with the soil cover. It is less likely with the 3-ft-thick concrete cover.

6. Test results provided pressure and acceleration data that can be used for comparison against criteria for sympathetic detonations.

Table 1. Characteristics of the M3 shaped charges.

Total Weight lb	Explosive Weight lb	Type of Explosive	Charge Diameter in	Charge Height in	Container Material	Cone Liner				
						Material	Thickness in	Angle deg	Outer Diameter in	Weight lb
40	30	Comp B	9.5	15.5	Sheet Metal	Steel	0.150	60	9	5.6

Table 2. Peak pressure measurements.

Retrofit Cover Section	3 ft Concrete				Rock Rubble					
Test Charge	40-lb Platter		40-lb Shaped		40-lb Platter		40-lb Shaped			
Test No. Location	1-I	1-O	2-I	2-O	3-I	3-O	4-I	4-O	5-I	5-O
Peak pressure, psi	0.25	0.63	0.20	0.47	0.30	0.78	0.23	0.62	0.31	0.8
Pressure wave arrival time, ms	110	62	110	50	100	50	100	48	80	42

Retrofit Cover Section	2 ft Concrete				2.5 ft Soil			
Test Charge	40-lb Shaped				40-lb Platter		40-lb Shaped	
Test No. Location	6-I	6-O	7-I	7-O	8-I	8-O	9-I	9-O
Peak pressure, psi	0.45	1.3	0.41	1.3	1.20	4.0	2.25	6.5
Pressure wave arrival time, ms	59	28	59	28	28	15	10	10

Note: I's denote inside; O's denote outside.

Fig. 1. Existing Damaged Igloo.

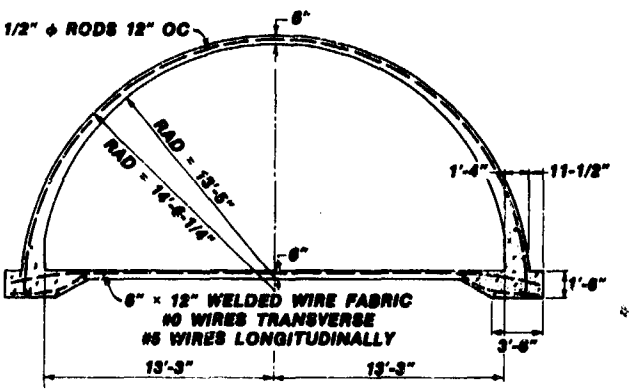

Fig. 2. Cross Section of Existing Igloo.

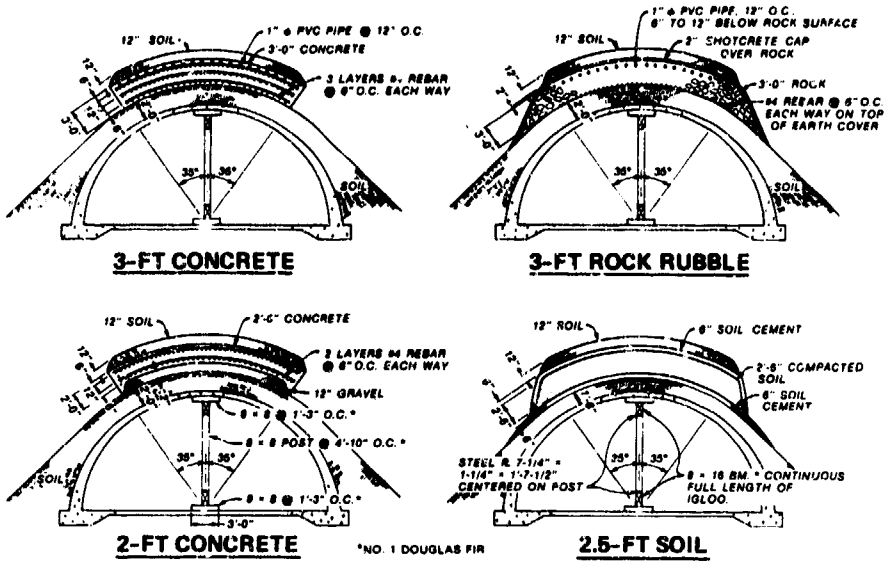

Fig. 3. Cross Section of Cover Sections and Internal Bracing.

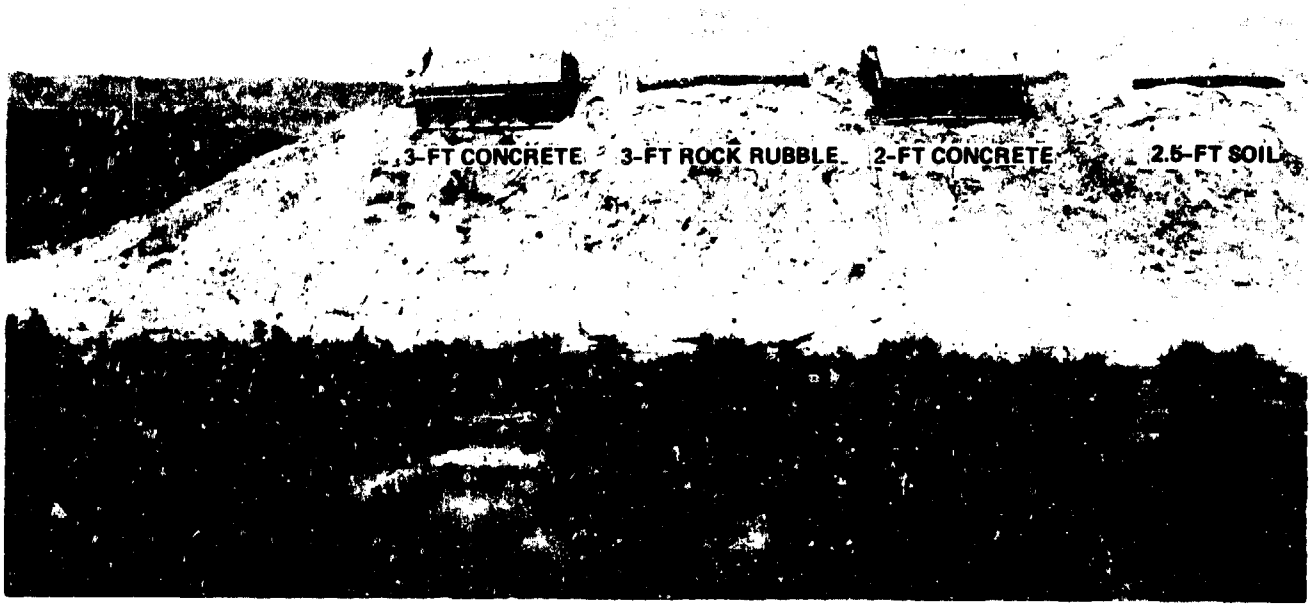

Fig. 4. Constructed Retrofit Covers.

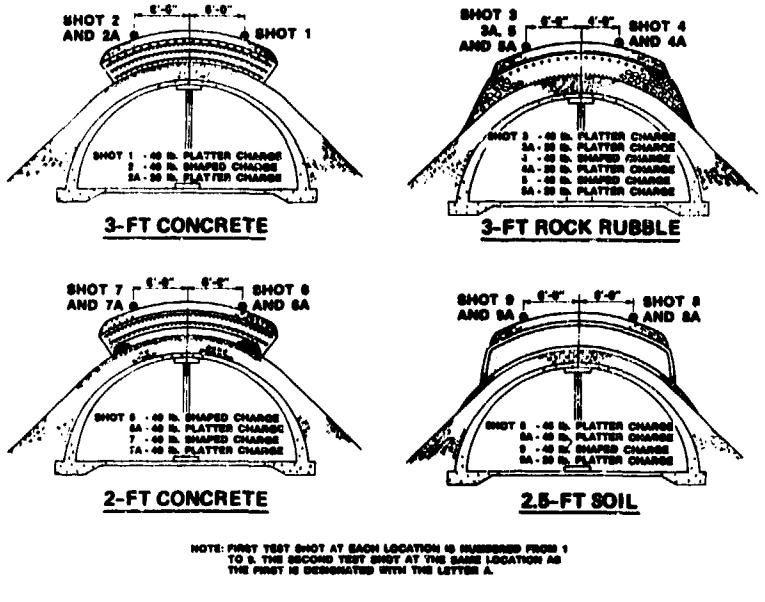

Fig. 5. Test Shot Locations.

Fig. 6. Movie Camera in Front of Igloo Focused on Striped Post.

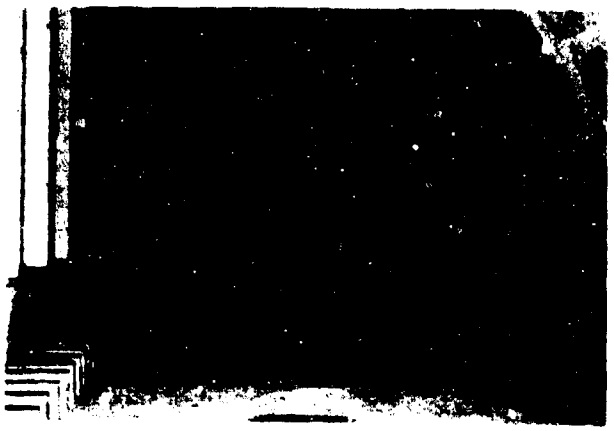

Fig. 7. One-half of Striped Endwall.

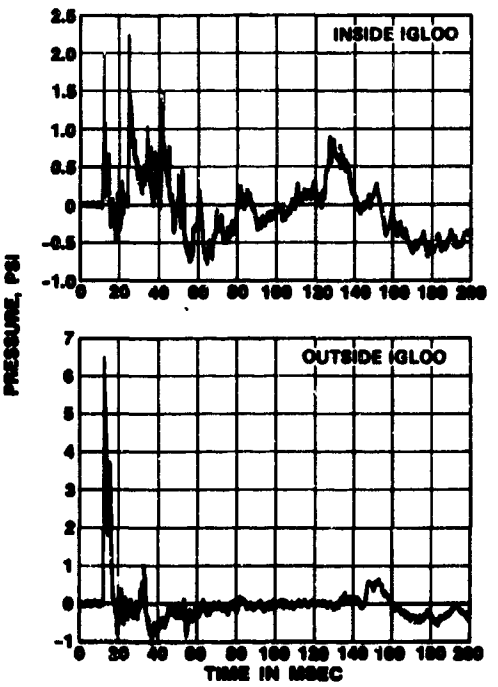

Fig. 8. Pressure-Time Histories for Test 9.

MODEL TESTS ON COMPOSITE SLABS OF LIGHT GAUGE METAL SHEET AND CONCRETE SUBJECTED TO BLAST LOADING

Peter Balazs
and
Bengt Vretblad

FortF - Swedish Fortifications
Research Department
Eskilstuna, Sweden

Summary

Model tests have been carried out at the Research Department of the FortF - Swedish Fortifications on composite slabs of light gauge metal sheet and concrete, using welded studs as shear connectors. Tests were also carried out on corresponding conventionally reinforced concrete slabs. Slabs were subjected to blast load and - as a reference - to static load. The results to date are given in the report. They indicate that composite action between sheet metal and concrete is possible in slabs subjected not only to static, but also to dynamic loading.

1. Introduction

The main interest of the research program concerning composite structures subjected to dynamic loading presently in progress at the Research Department of the FortF - Swedish Fortifications has been concentrated on the composite action of concrete in conjunction with other materials. The use of composite structures in the field of fortifications is of great interest in two areas especially, that is to say in the strengthening of existing hardened structures and in the construction of new structures that are to withstand electro-magnetic pulse (EMP).

When strengthening existing structures through - for example - the addition of in-situ concrete onto the original concrete structure, the composite action of the two materials will determine the strength of the structure. The shear connecting devices are of major importance in composite action. Theoretical and experimental investigations of shear connectors and interfaces subjected to dynamic loading is at present being conducted at the FortF. The results of the investigations are to be published at a later date.

One of the conditions that several hardened structures must fulfill, is that they should - besides withstanding blast loads - be fitted with a complete EMP protection. This means that the structure must be encased with metal. The question is: is it possible to use the same sheet also in a loadbearing capacity? A preliminary investigation on whether or not conventional reinforcement and lightgauge sheet may be replaced by a thicker sheet with welded headed bolts (studs) has been carried out. The results from this investigation show that the composite structure is economically advantageous when compared with a conventionally designed structure.

Model tests of composite slabs of light gauge sheet metal and concrete have been carried out in accordance with the objectives of the research program. The aim of the investigation is to

- experimentally investigate the possibilities of using composite structures of concrete and sheet metal with welded studs during blast loading
- study the relationship between load and deformation, and the ultimate load behaviour of longitudinal slab sections (simply supported and restrained) during both blast and static loading, and compare composite slabs and conventionally reinforced concrete slabs.

2. Experimental Investigation

2.1 Test specimens

In all, four slabs were manufactured; two composite slabs (S1 and S2) and two conventionally reinforced concrete slabs (A1 and A2). Four frames were made, three of which were of composite construction (S3, S4 and S5) and one of conventional reinforced concrete (A3). Their appearance and dimensions are shown in FIG 1.

Steel sheet of nominal thickness 1.5 mm was used in all test specimens S1 - S5, with 25 mm studs of type M4. The choice of sheet thickness and stud dimension was determined partly on the basis of practical aspects, and partly on the request that the ratio of stud diameter to sheet thickness be in the order of 2.5.

The number of studs in slabs S1 and S2 was determined so that the total anchoring force, that is to say the number of studs multiplied by the design value for a stud (according to the Swedish Code for Light Gauge Metal Structures) be equal the tension forces in the sheet at yield. In order to withstand the effect of suction from the blast, the slabs were further

reinforced with primary hogging reinforcement 5 ⌀ 6 mm and 8 ⌀ 6 as crossbars.

The slabs A1 and A2 were for reference purposes, which is why they were manufactured with conventional reinforcement only. Primary and crossbar reinforcement consisted of 6 ⌀ 8 mm (ribbed bar, yield stress 400 MPa) and 9 ⌀ 6 mm respectively. The remaining reinforcement (hogging) was the same as that in slabs S1 and S2.

The number of studs in frames S3, S4 and S5 was determined on the basis of the total anchor force - based on the design value of the studs - being compatible to the force in the sheet due to a moment which was equal to the yield moment at midspan in the conventionally reinforced slab. In order to achieve rigid restraint of the slab from the vertical part, the corner of the frame was reinforced with 6 ⌀ 8 mm (ribbed bar, 400 MPa). All crossbar reinforcement was ⌀ 6 mm, the number given in FIG 1.

The conventionally reinforced frame, A3, was reinforced with 7 ⌀ 8 mm (ribbed bar, 400 MPa) as sagging reinforcement in the slab, all other reinforcement being identical to that of frames S3 - S5.

2.2 Loading

The tests were carried out in two series. The slabs were tested in test series no. 1, and the frames in test series no. 2, see FIG 2.

Slabs A1 and S1 were tested in test series no. 1 with static loading only in the form of four knife-edge loads placed as shown in FIG 2 or one central knife-edge load (S1 only). Slabs A2 and S2 were tested in a shock tube where they were subjected to a blast load. The general shape of the pressure-time relationship of the load is shown in FIG 7.

Frame S4 in test series no. 2 was tested, as was specimen S2, with a static load with four respectively one knife-edges. Frames A3, S3 and S5 were subjected to blast loading. The blast was "side-on" that is of the type shown in FIG 9 that passes over the top side of the frame.

The specimens subjected to static testing were loaded with a hydraulic jack (through a system of linked beams that transferred the load into four knife-edge loads) where the load was measured by means of a load-cell. The deformations (deflections) were measured partly electronically and partly through mechanical deflection gauges. Strain measurement were recorded for the reinforcement and for the sheet.

3. Test results and evaluation

3.1 Deformation

FIGS 3-6 show the deformation due to static loading in the form of load-deflection curves, one for each test. In all cases the maximum deflection is shown, that is to say the deflection of the centre of the slab.

FIG 3 shows the load-deflection curve for slabs S1 and A1 for the same load case. FIG 4 shows the deformation of these slabs when subjected to different loading cases, which is why the deflection is related to the mid-span moment. FIG 5 shows the load-deflection curve for slab S1 again. Besides the measured deflection, δ, even the calculated values are shown, whereby complete composite action was assumed to exist between the concrete and the sheet (constant EI). FIG 6 shows the load-deflection curve for test specimen S4, where, as in FIG 5, even the calculated values are shown. Besides the assumptions made in FIG 5, it was even assumed that the corner reinforcement was of ideal elasto-plastic material of infinite ductility. These four figures show that, under static loading, the expected demands as regards deflection of the composite structure, were fulfilled.

FIGS 7-10 show some of the results from the blast tests. The deformation curves show, in all cases, deflection of the centre-line of the slabs as a function of time.

FIGS 7, b and c show the maximum deflection before decay of slabs S2 and A2 respectively during the loading sequence shown in FIG 7a. It is apparent, as is also the case during static loading, that even here there is a noticable difference in the deflection vs time of each slab. The maximum deflection of slab A2 is approximately four times greater than that of slab S2, and at the same time the remaining deformation of A2 is 15 mm and negligable in S2.

The testing of slab S2 was repeated with increased load intensity, see FIG 8a. It was not until this latter load, at considerably higher pressure and impulse levels, that the maximum and the remaining deformation was of the same order as that of slab A2. Compare FIGS 8b and 7c.

Finally FIG 9 and 10 show the deformation vs. time of the frames during the load sequence shown in FIG 9a and 10a. These figures show again, as in the previous cases, that the composite structures show less maximum and less remaining deformation than a conventionally reinforced test specimen, due to greater stiffness (in this particular instance).

3.2 Load capacity

For a shelter structure both elastic and plastic behaviour is of importance. Ultimate load behaviour is often of considerable interest. This test series has resulted in ductile as well as brittle failures.

The shear connectors in the composite slabs S1 and S2 were designed so that composite action between the concrete and the sheet existed even when yield stresses were reached in the sheet. Ductile failure was obtained under both the static and the dynamic loading of these slabs. The

appearance of the slabs after blast loading is shown in FIG 11. The total anchor capacity in the shear connectors has, during the entire loading sequence, been greater than the the force in the sheets. In this way, not only the ultimate load but even the total ultimate deflection of the test specimen have been determined, through the strain properties of the sheet material.

Frames S3 and S4 were designed so that their load capacity should be equivalent to that of the conventionally reinforced frame A3. In this case the shear connector must exhibit plastic behaviour before plastic behaviour is possible in the sheet. The design did not permit movements between the concrete and the sheet to allow for plastic behaviour in all the connectors, however. The sheet was even restrained through spot-welding to embedded angle sections, which contributed to the limiting of movement between the concrete and the sheet. The total anchor force at the moment of failure was therefore greater than the sum of the forces in the shear connectors.

When failure occurred in the row of spot welds, all shear connectors between the support and mid-span failed simultaneously. The composite frames therefore failed instantaneously both under static and dynamic loading. The appearance of the test specimens at failure is shown in FIG 12.

S5 was made identical with S3 and S4 with the one exception that instead of spot welds between steel sheet and the angle sections at the supports continous welding was used. This did not change the mode of failure but changed the load at failure.

To sum up, the results of the investigation indicate that composite action between concrete and sheet metal may be obtained in slabs subjected to static and dynamic loading. If the total anchor force in the shear connector is less than the force that is equivalent to failure in the sheet, then an instantaneous failure is shown by the structure. The shear connectors must be designed so that their total load capacity is greater than the force required for failure in the sheet, in order to obtain ductile failure in the structure.

References

Balazs, P., "Model tests on composite slabs of light-gauge metal sheet and concrete subjected to blast loading". (To be published)

Ramsden, J.A., "Samverkansbjälklag av tunnplåt och betong - inventering och nulägesrapport". SBI Rapport 103:3, juli 1982. Swedish.

The Swedish Code for Light-Gauge Metal Structures (English translataion) SBI. Stockholm 1993.

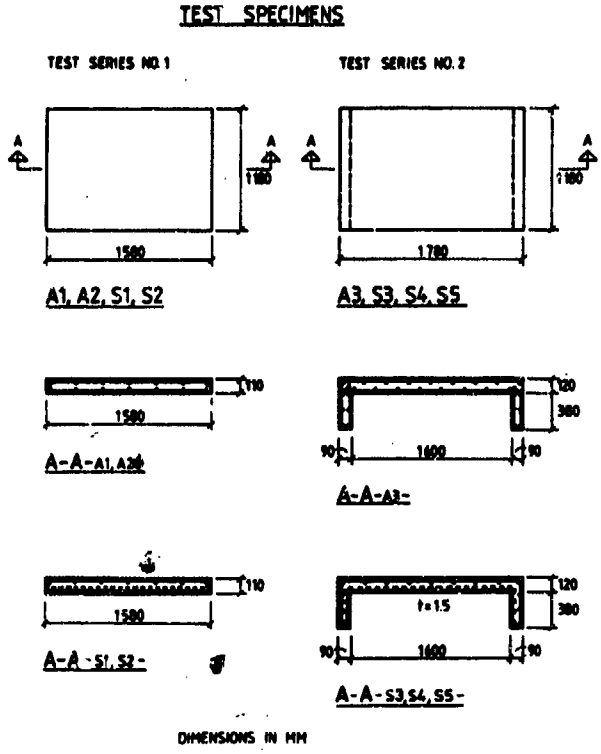

FIG 1. Test specimens.

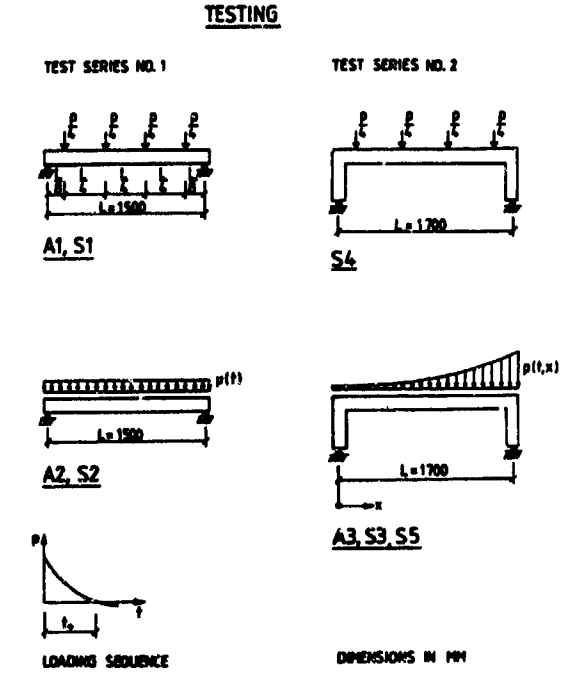

FIG 2. Loading of test specimens.

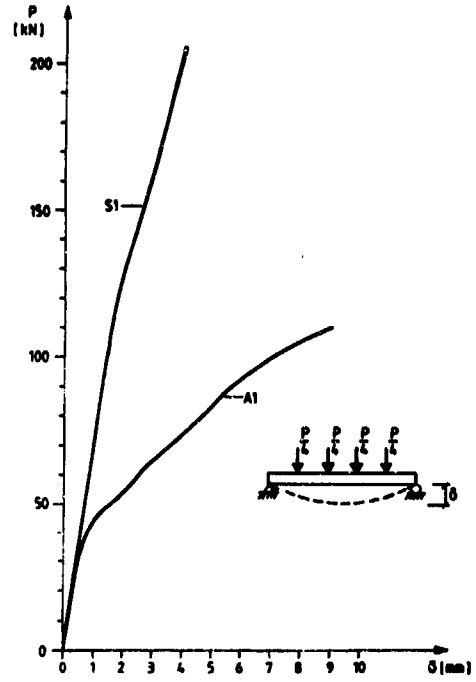

FIG 3. Load-deflection curve for slabs S1 and A1 (static loading).

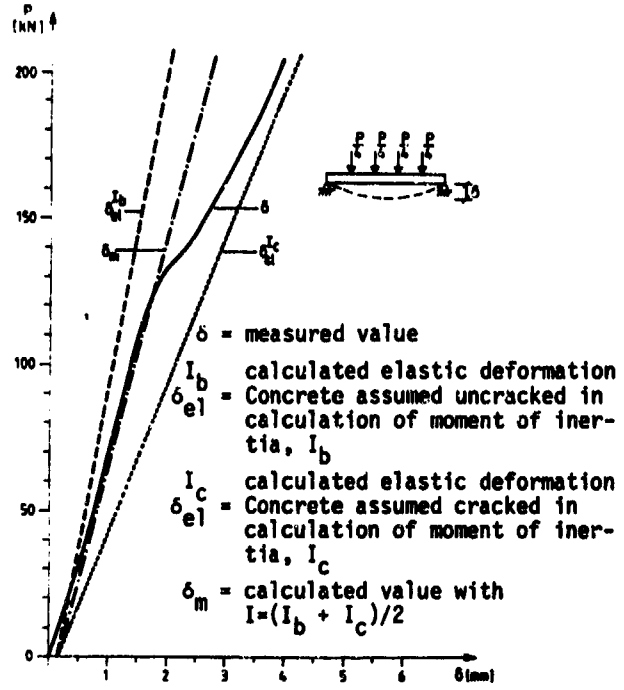

FIG 5. Load-deflection curve for slabs S1.

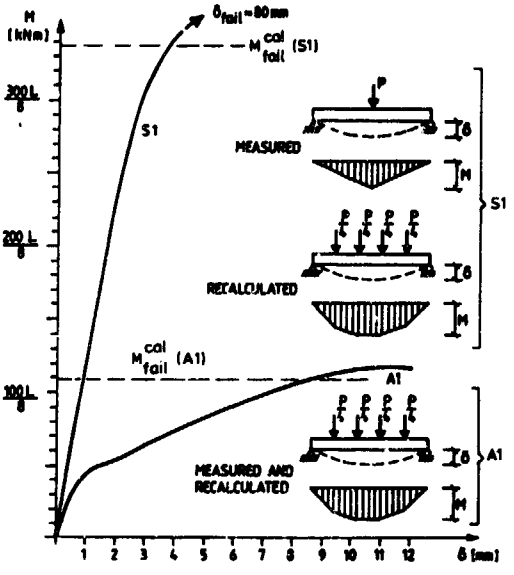

FIG 4. Moment-deflection curve for slabs S1 and A1. Comparison between deflection in each test specimen related to moment at mid span with alternative loading (A1=four knife-edge loads, S1=one knife-edge load). Both curves are calculated for four knife-edge loads.

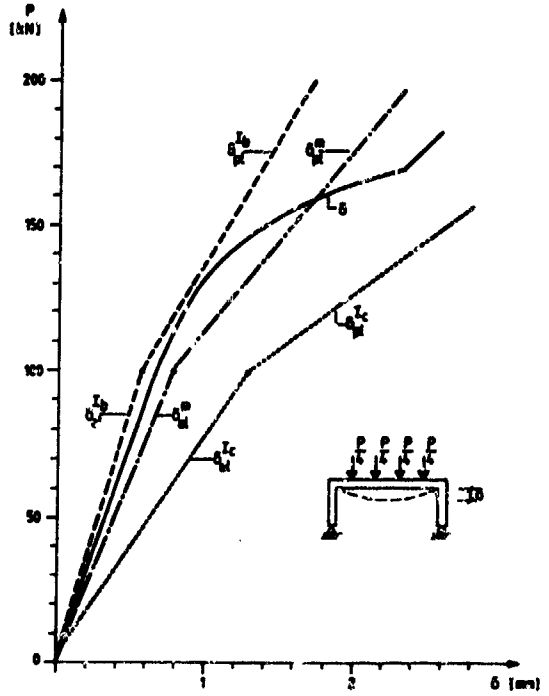

FIG 6. Load-deflection curve for frame S4
Index el = elastic deformation
pl = elasto-plastic deformation (stresses in reinforcement = yield stress)
Other symbols - see FIG 5

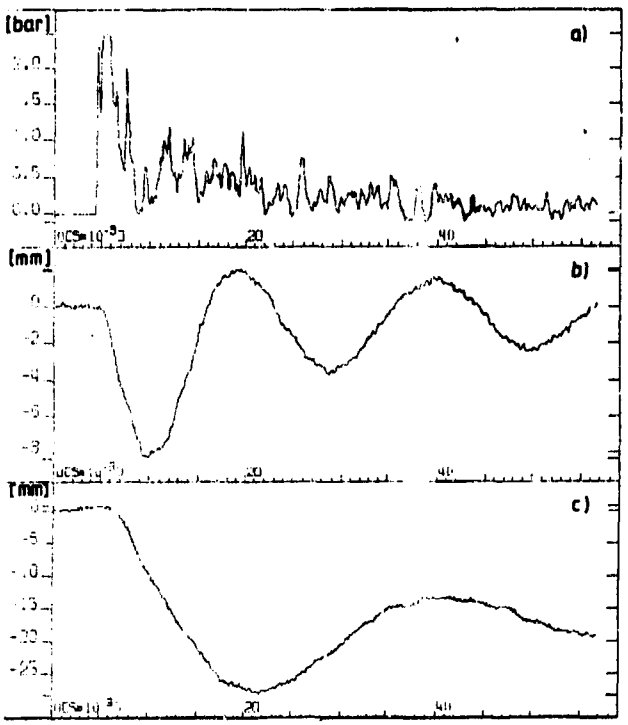

FIG 7. Blast loading of slabs S2 and A2 (6x10g, 1.47 m from test specimen).
a) Pressure time curve of load sequence.
b) Deflection curve (midspan) as a function of time for S2.
c) Deflection curve as a function of time for A2.

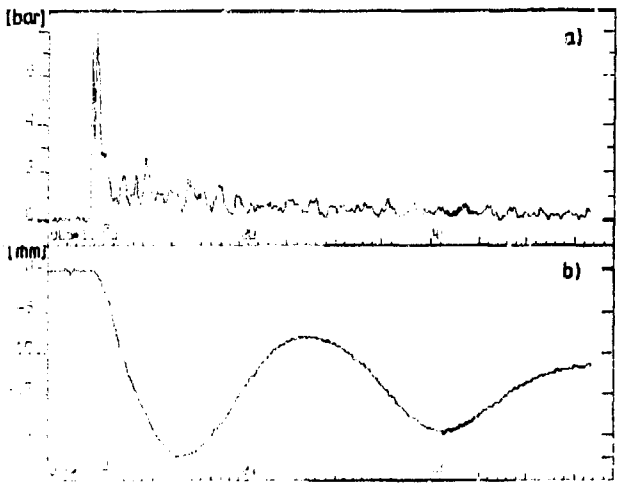

FIG 8. Blast loading of slab S2 (6x30g, 1.0 m from test specimen).
a) Pressure time curve of load sequence.
b) Deflection curve (midspan) as a function of time.

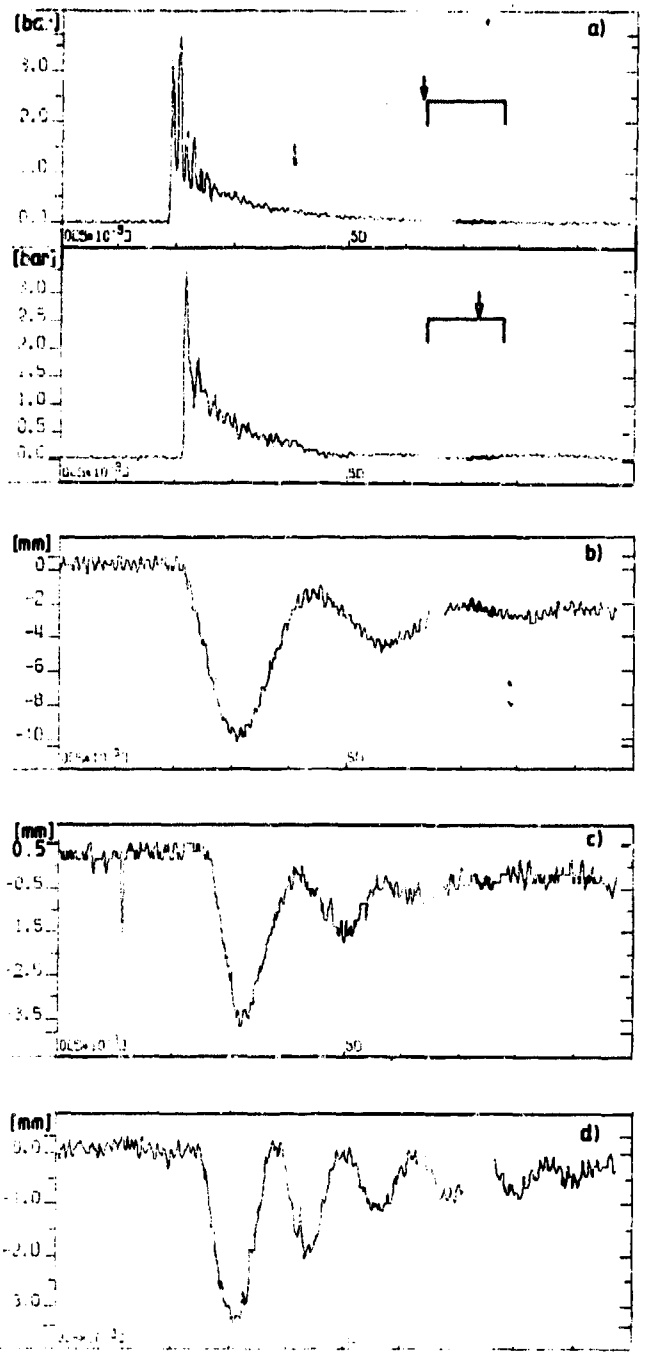

FIG 9. Blast loading of frames A3, S3 and S5 (6x100g, 3.0 m from front edge of test specimen).
a) Pressure time curve of load sequence.
b) Deflection curve (midspan) as a function of time for frame A3.
c) Deflection curve (midspan) as a function of time for frame S3.
d) Deflection curve (midspan) as a function of time for frame S5.

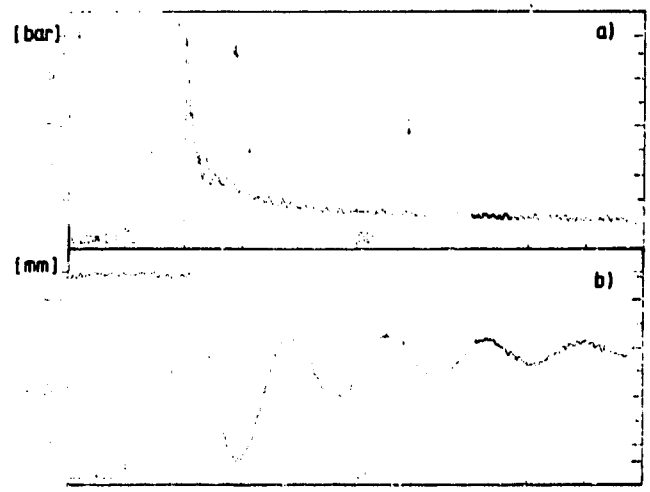

FIG 10. Blast loading of slab S5 (6x500g, 3.5 m from test specimen)
a) Pressure time curve of load sequence
b) Deflection curve (midspan) as a function of time

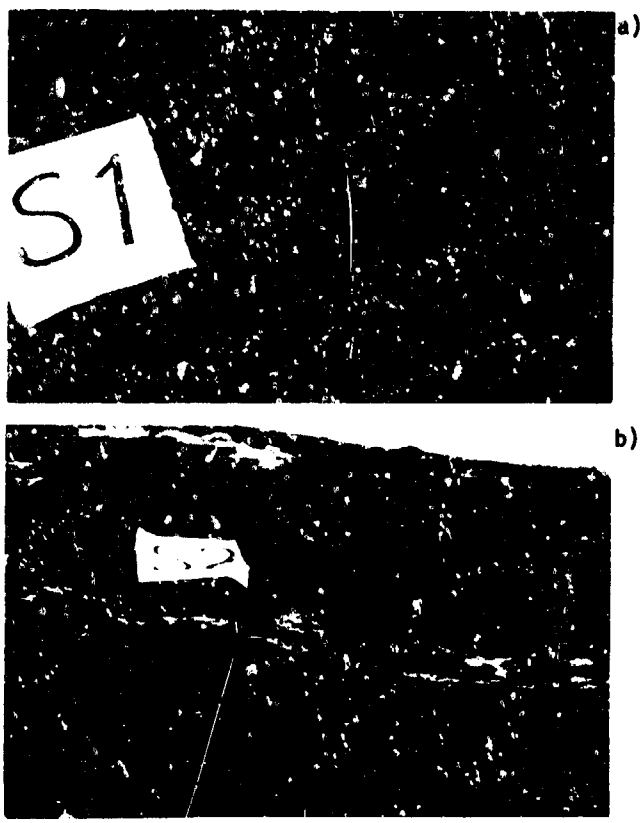

FIG 11. Appearance of composite slabs after loading. Failure load.
a) Slab S1 (static load, P=190 kN center load
b) Slab S2 (blast load, max impulse ≃ 3 kPa·s

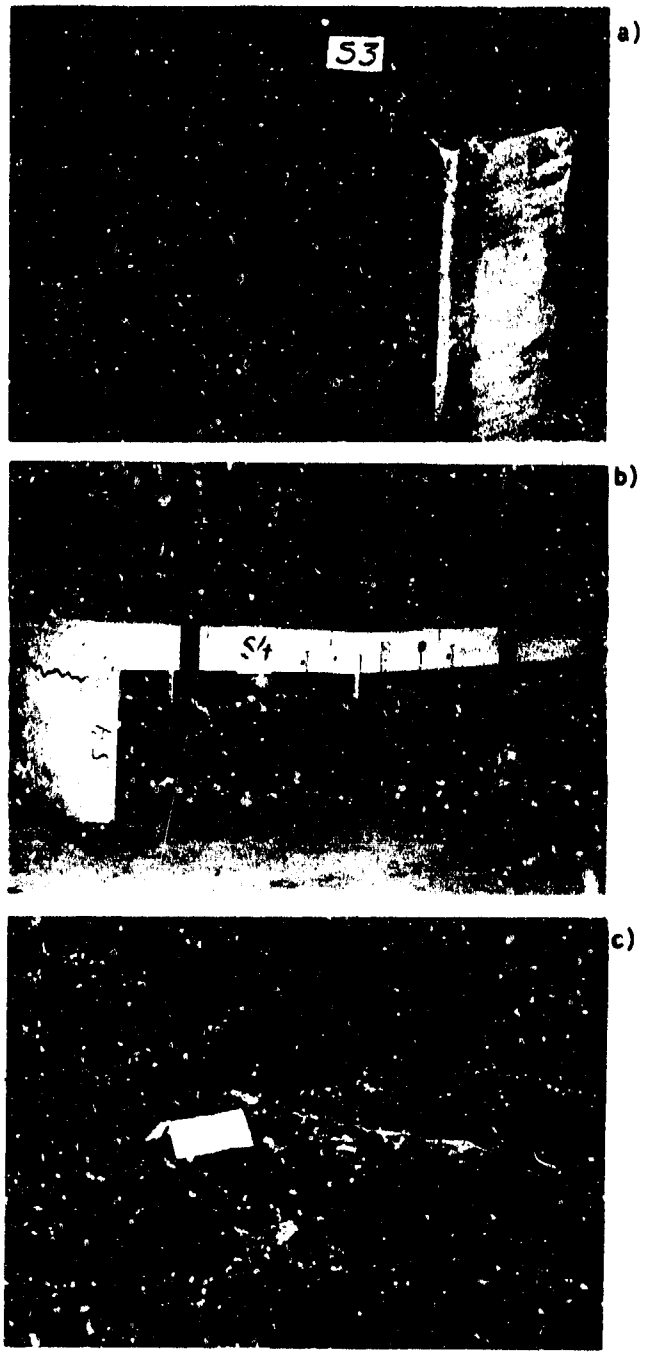

FIG 12. Appearance of composite frames after loading. Failure load.
a) Frame S3 (blast load, max impulse ≃ 5 kPa·s)
b) Frame S4 (static load, P=180 kN center load)
c) Frame S5 (blast load, max impulse ≃ 7 kPa·s

THE MUST-IV (MULTI-UNIT STRUCTURE TEST) SERIES

Vincent A. Meyer

New Mexico Engineering Research Institute
Albuquerque, New Mexico

ABSTRACT

The MUST-IV Test Series was designed to evaluate the survivability of a reinforced concrete personnel shelter in a blast and shock environment. The shelter consisted of precast, modular segments with bell and spigot joints. It was rectangular in cross section and contained complete mechanical and electrical subsystems for a self-contained power and air supply system. The blast and shock environment was generated using 1000-lb and 500-lb general purpose bombs. This paper examines the testbed construction, test program, and test results of this series.

INTRODUCTION

Protection of personnel in chemical environments is required to support United States Air Force (USAF) operations. Because conventional-weapon environments are expected to accompany these chemical environments, personnel shelters must be able to function when exposed to the blast and shock effects generated by conventional weapons. Failure of the shelter system is defined by the following:

1. Collapse of the structural elements under blast or shock loads.

2. Failure of the structural envelope to hold a positive pressure against the chemical environment.

3. Failure of the air supply system due to equipment failure from blast or shock loads.

4. Injury to personnel from blast or shock loads.

The entire MUST series consisted of two phases. In Phase I, generic cylindrical and rectangular structures were tested and evaluated. In Phase II, full-scale, fully equipped, cylindrical and rectangular shelters were tested and evaluated The MUST-IV test article was the rectangular shelter tested in Phase II.

The MUST-IV shelter was subjected to a series of tests that specifically challenged the shelter in order to evaluate it against the failure modes. Other objectives of the MUST-IV test events were

1. Identify critical load and response mechanisms for the shelter and equipment in a conventional weapon environment.

2. Provide data to verify, establish, or modify criteria for the identified modes of failure.

The evaluation of the shelter was done on a systems assessment basis. This evaluation approach begins with the identification of the functional requirements of the system. The three components that must be defined are the environment, the structure, and the response mechanism. If two of the components are known or given, then the third can be solved for by the use of one of three equations. The design equation is used when the environment and response are given and the structure is the unknown. The analysis equation is used when the structure and the environment are given and the response is the unknown. The limit states equation is used when the structure and response are given and the environment is the unknown. The MUST-IV test series primarily involved the analysis equation. The details of this assessment are being addressed in another paper at this symposium presented by Lt. Michael K. W. Wong of the Air Force Weapons Laboratory (AFWL), Albuquerque, New Mexico. To define the three functional components, data were collected pretest, posttest, and during the event. The data consisted of the output from active free-field soil stress, acceleration, and blast pressure gages; active structural concrete strain, steel strain, interior pressure, and soil/structure interaction gages; active equipment acceleration, voltage measurement, current measurement, intake and exhaust pressure, and generator shaft revolution-per-minute measurement gages; passive structural displacement gages; and structural element gap measurements.

TEST ARTICLE

The MUST-IV test article was a precast, modular, reinforced concrete shelter that had a rectangular cross section. The modular system of construction is considered to have the following advantages over a cast-in-place concrete structure:

1. Plant-cast concrete quality control and material savings due to production line techniques.

2. Field labor savings and material savings due to elimination of bulky framework.

3. Flexibility in shelter layout.

4. Blast and shock load energy absorption through structure displacement.

Nineteen modules, six end caps, and two interior bulkheads were assembled to form the completed test structure. In plan view the assembled structure was roughly U-shaped (Fig. 1).

CONSTRUCTION

The MUST Test Series was conducted at the McCormick Ranch Test Area. McCormick Ranch is a 600-acre test site located adjacent to Kirtland Air Force Base in Albuquerque, New Mexico. Reference [1] details the soil conditions at the testbed. From the surface to a depth of 6 m (19.7 ft), the soil is a uniform, medium-to-fine, nonplastic sand. Intense soil cementation has been observed in some excavations, but does not occur uniformly over the testbed area. Also, the surface soils have been deposited from alluvial action so that a nonisotropic condition exists. Wave speeds in the soil are faster in the north-south direction than in the east-west direction.

Preparation of the testbed consisted of surveying and grading an area 45.72 m (150 ft) by 30.48 m (100 ft) within an already established shrub-free area. The corners of the main segment trench and entrance and exit trenches were then established and excavated to the required depth and levelness. All free-field instrumentation packages located under the structure or in the near free field to the structure were then placed. A sand bed was placed and leveled in the trench. This sand bed allowed the structure to be placed with its midline at the final grade of the testbed.

To assemble the structure, construction techniques typical of large diameter pipe laying were used. Each module and interior bulkhead had a male (spigot) and female (bell) end for mating of the modules and bulkheads. End caps were bolted to flat ends on the specific modules. All joints were assembled with an elastomeric gasket material and sealing lubricant. The lubricant also aided in the assembly process. A 140-ton capacity mobile crane was used to place the individual pieces of the test article in the trenches. The modules, bulkheads, and end caps were pulled together by cable come-alongs secured to cast-in anchors along the sides of the pieces.

The trench was backfilled to the final grade of the testbed using in situ soil. Mechanical tampers and a roller compactor were used to compact the backfill to 95 percent of the maximum density as determined by ASTM D698-70 at a± 2 percent of optimum moisture.

After completion of the backfill, the remaining free-field gages were placed. The structure was then covered with a loose, uncompacted soil berm. In cross section the berm was trapezoidal. See Figure 2.

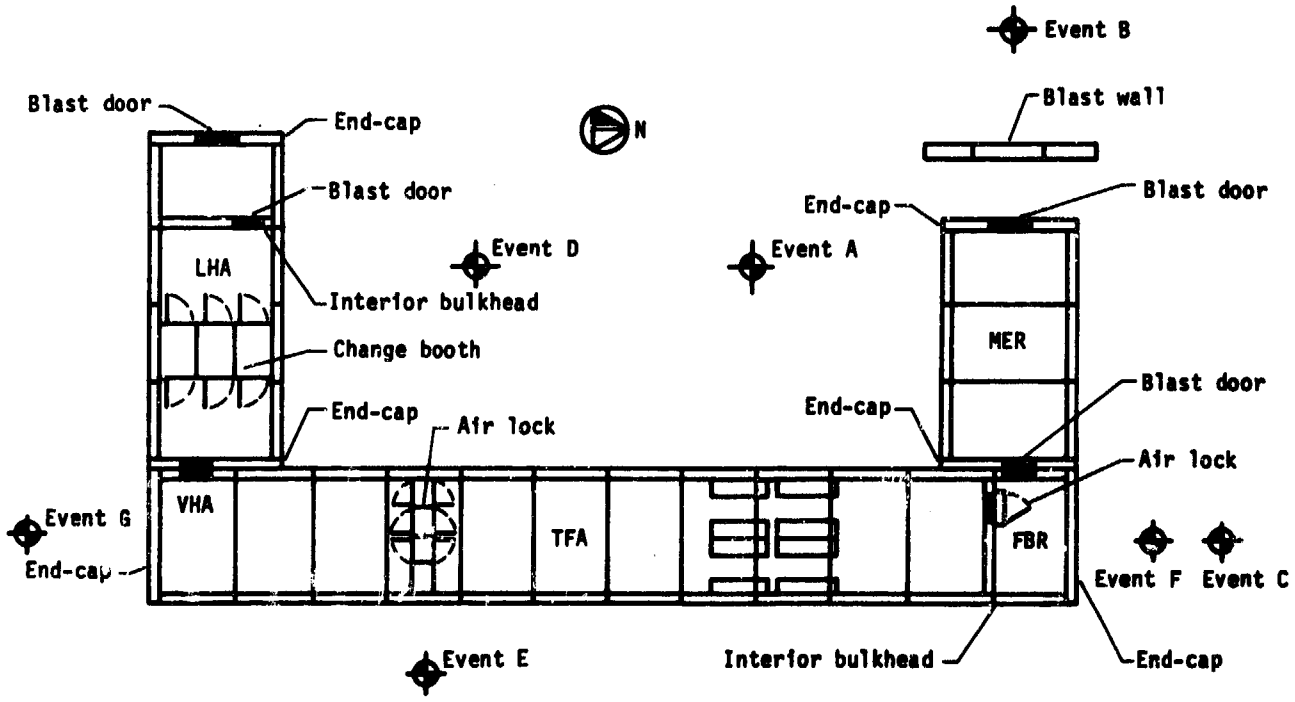

Figure 1. MUST-IV general shelter layout.

All major interior equipment for the mechanical and electrical subsystems was mounted on shock-isolated frames with the exception of the fuel oil tank that supplied the unit heater and diesel generator. The shock isolation system had been designed based on the expected shock environment and the frequencies of each individual piece of equipment. The fuel tank and minor equipment were hard-mounted to the floor, walls, or ceiling as appropriate.

DATA ACQUISITION

Transducers and hardware commonly used for conventional blast and shock testing were used on the MUST-IV test events. Free-field acceleration was measured with four types of Endevco accelerometers cast in epoxy minicanisters. Structure acceleration was measured with Endevco accelerometers attached to aluminum mounting blocks. Soil pressure measurements were made with Kulite transducers having a range of 20.69 MPa (3000 lb/in^2). Pressure at the soil-structure interface was measured with Kulite WAM transducers mounted in a New Mexico Engineering Research Institute (NMERI) normal stress mount. Concrete strain was measured with BLH strain gages which have a resistance of 120 Ω. Steel strain was measured with Ailtech weldable strain gages which have a resistance of 350 Ω. Airblast pressure measurements were made with Kulite pressure transducers mounted in standard AFWL hardware that had been cast in concrete blast pressure pads (external blast pressure) or had been mounted on threaded flanges (interior pressure).

The basic measurement system consisted of the transducers, the cable from the transducers to the junction box and forward amplifiers, the junction box, the cable from the junction box to the recording van, and the recording van.

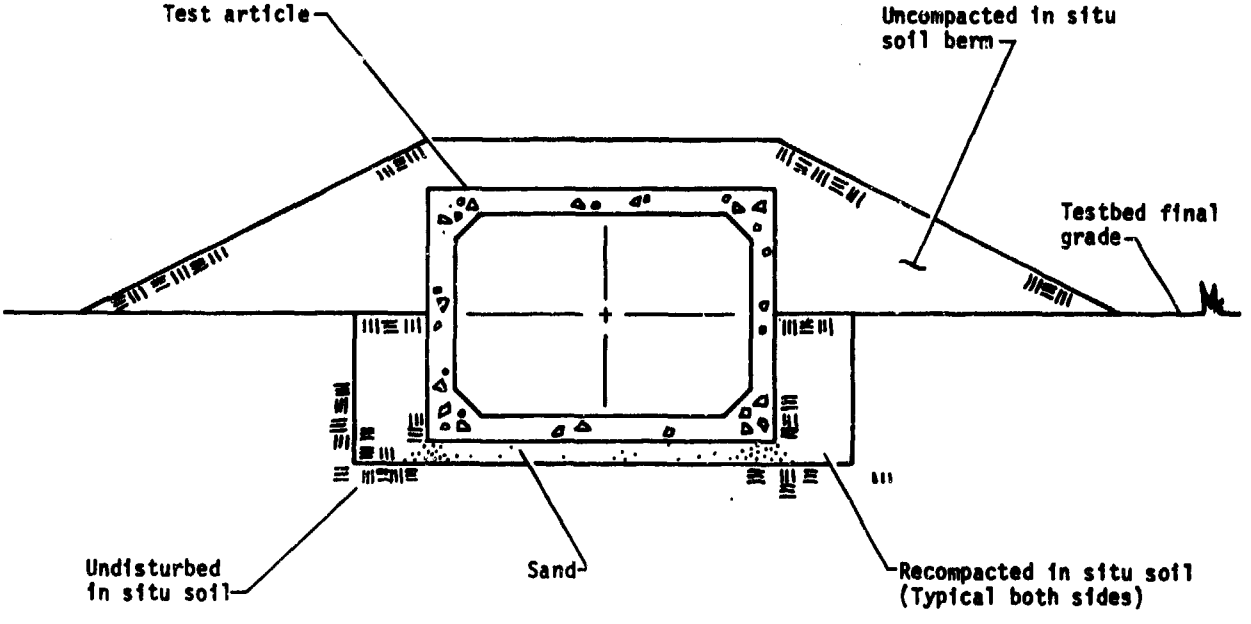

Figure 2. Typical cross section of test facility.

The junction box was approximately 99 m (325 ft) from the structure, where ISD-230 amplifiers were located. Amplification was required for most of the structural gages, and this closely coupled amplification provided the maximum signal-to-noise ratio and data recovery. Signals were relayed from the junction box to the instrumentation van through 20-pair cables. The junction box also served to connect the unamplified structure gages and the free-field 2-pair cables to the 20-pair cables running from the junction box to the instrumentation van.

The data were recorded on 28-track Ampex 2230 recorders in a multiplex record format.

In addition to the active and passive gages used in each test event, interior and exterior motion picture cameras were used to document the behavior of the test article during the test. The high-speed exterior cameras recorded the blast, ejecta, and dust cloud formation while the interior high-speed cameras recorded structure and equipment response.

TEST PROGRAM

As in the previous phases of the MUST series, 1000-lb and 500-lb general purpose bombs were used to generate the blast and shock environments. These general purpose bombs were placed as a surface burst, with the bomb center-of-gravity at testbed grade level or as a buried burst, with the bomb center-of-gravity at a specified distance below grade.

The evaluation of the Phase I test events and the cylindrical shelter in the first part of Phase II had shown that for a partially buried, bermed, multi-unit structure, the surface burst did not place critical loads on the structure or equipment. Therefore, the test plan for the MUST-IV structure emphasized the buried bursts. The locations of the bomb center-of-gravities were chosen to test the system failure modes. They were also chosen to attempt to repeat some of the bomb-to-structure locations. Bomb center-of-gravity locations are shown in Figure 1. The test event schedule is given in Table 1. Events A and D were located in similar positions to the main segment and the entrance and exit segments. Events C, F, and G were located at varying distances from the main segment end caps.

TABLE 1. MUST-IV TEST SCHEDULE

Test Event	Test Date	Bomb Location
A	17 Feb 84	Buried
B	24 Feb 84	Surface
C	2 Mar 84	Buried
D	9 Mar 84	Buried
E	16 Mar 84	Buried
F	23 Mar 84	Buried
G	25 May 84	Buried

TEST RESULTS/ANALYSIS

The single surface burst event was not expected to provide the most severe environment for the structure. The event did test a proposed blast wall, the blast valves, a blast-resistant door, the exhaust and vent pipes for the mechanical equipment, and the exposed end cap of the exit segment. The blast wall provided some attenuation of the peak pressures and experienced significant distress, but performed as designed. The door failed in rebound when some bolts had their threads stripped by the nuts, thus allowing the door to swing open. Because of the timing of the failure and the design of the airflow through the structure, this failure did not qualify as a system failure. The exhaust and vent pipes, and the end cap performed as designed. The airblast load on the end cap and the ground shock environment were the major loads on the structure from this event, while very little of the structure response was attributed to airslap through the berm.

The failure modes of major concern with regard to the buried burst events were the failure of the structural elements, in particular the bell and spigot joints, and the failure of the equipment.

Test events A, D, and E provided the environments to primarily challenge the structural elements and the joints. In addition, event A also challenged the mechanical equipment. Test events C, F, and G provided the environments to primarily challenge the mechanical equipment but also tested the end cap.

The individual wall, floor, and roof elements of each module responded to the environment with an elastic behavior. The corner details at the intersection of the walls with the floor and the walls with the roof had been designed to be moment-resistant. This stiff corner successfully transmitted flexural forces between elements. No evidence was found of any tensile cracks on any face of any of the individual elements.

Each module generally responded to the environment with a rigid-body rotation and translation. The geometry of partially burying the structure with a loose berm allows the structure to positively respond to the horizontal and vertical components of the shock load. The partial burial with a controlled, compacted backfill holds the structure in place so that the horizontal component of the load pushes the structure into the in situ soil and backfill (translation). Since this backfill is only up to the structure midline with a loosely placed berm above it, the structure is not as constrained at the top downstream corner as it is at the bottom downstream corner. With nothing but a loose berm above it, the structure responds to the vertical component of the shock load by moving up. The acceleration data plots show the -1 g trace as the structure "falls" back after the loading and the interface pressure data plots show the point at which the structure rejoins the ground below it. This combination of load components with a constrained bottom downstream corner is thought to be the mechanism that produces rigid-body rotation.

Also contributing to the structure response is the interconnection of adjacent modules. If the structure was continuous, one would expect a response similar to a beam on an elastic foundation. However, each bell and spigot joint allows some degree of freedom for movement between modules. Insufficient data were generated from this test series to identify the exact nature of the interaction of the modules at the joints. Comparison of data from gages in adjacent modules confirms that differences exist. The steel strain gages that had been placed in certain joints, and that may have contributed some information as to what was occurring at the joints, were either not functional at the time of testing or produced unusable data. When evaluated against the system failure modes, however, the joints did not fail. They did exhibit three types of distress, but with the exception of event F, none of these joint-damage types would qualify as a system failure. The three joint-damage types were crushing and spalling of the joint edges due to rotation and closure, cracking of the bell or spigot due to relative rigid-body motion, and longitudinal separation of the joints. This last type of joint failure did qualify as a system failure in event F. The center-of-gravity of the bomb had been intentionally moved closer to the structure to create a more severe environment on the Filter Blower Room (FBR) and end cap. As a result of the bomb location, the last three modules in the main segment were lifted up by the blast, longitudinally separated, and when they fell back, the FBR module tilted partially into the crater.

CONCLUSION

A partially buried, bermed, multi-unit reinforced concrete structure was directly evaluated for the failure modes in a conventional weapons environment. While the structure did show some distress at some elements, it did not fail under the specified criteria and miss distances. The shelter responds to the loading environment by flexure of the walls, roof and floor, and translation and rigid-body rotation of the modules. The shock isolation mounting of the equipment protected it from the blast and shock loads. The module joints are the critical elements of this structure and further study of the exact nature of the joint interaction is suggested.

REFERENCES

1. Bedsun, David A., and Logan, J. W., Soil Index Properties and Material Models for Subsurface Soil at Multi-Unit Structure Test (MUST) Sites, AFWL-TR-84-29, Air Force Weapons Laboratory, Kirtland Air Force Base, New Mexico, February 1984.

2. Meyer, Vincent A., Data Report for MUST-IV (Fourth Multi-Unit Structure Test, Full-Size Rectangular Shelter), Events A through G, AFWL-TR-84-120, Air Force Weapons Laboratory, Kirtland Air Force Base, New Mexico, December 1984.

3. Morrison, Dennis, Bacon, Pamela C., and Meyer, Vincent A., Analysis Report for MUST-IV (Fourth Multi-Unit Structure Test, Full-Size Rectangular Shelter), Events A through G, AFWL-TR-84-137, Air Force Weapons Laboratory, Kirtland Air Force Base, New Mexico, (in publication).

4. Harris, Keith L., Power System Report for MUST IV (Fourth Multi-Unit Structure Test, Full-Size Rectangular Shelter), Events A through F, AFWL-TR-84-XXX, Air Force Weapons Laboratory, Kirtland Air Force Base, New Mexico, (in publication).

RESPONSE OF A BURIED STRUCTURE TO HIGH INTENSE IMPULSIVE LOADING

J. RICK HOLDER

USAF Armament Laboratory
Vulnerability Assessments Branch
Eglin AFB, Florida 32542-5000

ABSTRACT

A 1/3 scaled buried multiroomed concrete structure was subjected to a series of internal high explosive tests. The purpose of the tests was to gather empirical data necessary to: (1) develop methods to predict internal wall breach from internal high intense impulsive loading, (2) develop methods to predict internal pressure migration from internal high explosions, and (3) determine overall component structural integrity. Impulsive loading was obtained from detonations of 0.1 to 2.0 pound charges. A large amount of structural response data was gathered which can be applied to problems involving dynamic loading of reinforced concrete structures. The data gathered during this test program will be presented.

INTRODUCTION

Background

The Air Force Armament Laboratory (AFATL) has responsibility within the Air Force for the lethality evaluation of conventional munitions against ground and air targets. Hardened, high value targets such as radar sites, airfields, and command control centers represent high priority target threats in a tactical scenario, and are consequently of high interest in current Air Force munition development programs. Part of the engineering knowledge necessary to evaluate the lethality of conventional munitions against high value targets includes internal detonations of explosive against internal concrete walls, floors, and roofs. Problems presently exist due to the lack of data measuring blast pressures placed on internal walls, floors, and roofs due to the detonation of explosives internally. Therefore, it is important to collect such empirical data and to develop methods to predict internal wall breach and pressure migration from internal high explosions.

In response to this need, the USAF Armament Laboratory planned, constructed, and tested a buried, multiroomed reinforced concrete structure. This paper describes the results of field testing the concrete structure at Eglin AFB range facilities.

OBJECTIVE and APPROACH

The objective of this series of tests was to gather empirical data from internal high explosive detonations. Blast pressure, impulse, wall and equipment acceleration, and wall deflection was measured. Tests were conducted with explosive charges detonated at different standoffs from different walls within a buried multiroomed concrete structure. Each room had either a steel or wooden door. All rooms had some type of equipment with internal electronic components. Some tests had the doors open, some closed, some with a mixture of the doors open and closed. Each room was instrumented with a pressure transducer. Selected walls and/or roofs were instrumented with an accelerometer. Selected equipment was also instrumented with an accelerometer. Walls surrounding the room where the event took place were instrumented with deflection gages. After each test a damage assessment was performed on all structural components of the target.

EXPERIMENTAL PROCEDURES

Test Structure

One reinforced concrete multiroomed box-type structure was constructed for use an the test specimen. The structure had eight rooms, floor, roof, and a hallway running the entire length of the structure (Figure 1). Each room had two full internal walls fixed on four edges, one external wall and one internal wall with a door opening. All internal walls were 0.33 feet thick, 5.0 feet in length, and 4.0 feet in height. The floor, roof, and external walls were 0.67 feet thick. The test structure represented a 1/3 scale model of a full-scale generic structure. The steel reinforcement percentages for the interior walls was 0.027 and 0.013 for the exterior walls, floor, and roof. The reinforcement design did not use shear stirrups or shear dowels; however, development lengths of the reinforcing bars were used to tie the walls to the roof and floor slabs. Reinforcement details are shown in the section drawings of Figure 1. The test structure was constructed on Eglin AFB range facility. The structure was built with the roof at ground level. Once constructed, 5.0 feet of compacted earth was placed over the structure. This structure was

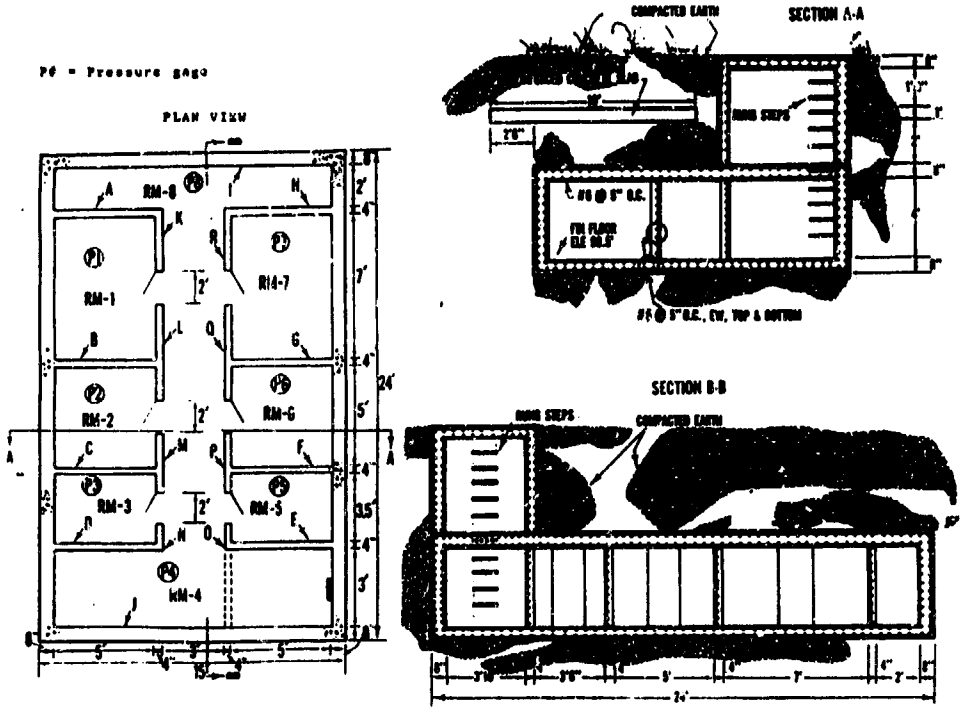

Figure 1. Test structure and gages, walls location.

completed in 1977 and allowed to set until testing, June 1984.

Material and Structural Properties

The concrete mixture used for the structure was designed to give a 28-day compressive strength of 4000 psi. Actual data from test cylinders gave an average compressive strength of 6400 psi at 28-days. Table 1 indicates actual wall compressive strength using the Swiss Hammer method. For identification each wall is labeled by letters (see Figure 1). The cement used met ASTM Specification C150-71, Type I. The course aggregate used was crushed limestone which met ASTM C-33, #57.

The reinforcement steel was specified as ASTM A615-68, Grade 40, having a design minimum yeild of 40,000 psi.

Measurements

The gage layout for the active instrumentation used is presented in figure 1. The gage layout was chosen and located to measure:

a. Airblast load imposed on the walls, roof, and floor surfaces.

b. In-structure motion (Acceleration, Velocity, and Displacement).

In addition to the active gages, passive scratch gages were used to measure the peak and permanent displacement of the wall.

Wall NO.	Compressive Strength (PSI)
A	7500
B	7300
C	6900
D	6500
E	5800
F	6000
G	6500
H	6400
I	6800
J	6400
K	6200
L	7000
M	7400
N	6700
O	5800
P	6200
Q	5800
R	5600
Roof	6400
Floor	6400

Table 1. Interior Wall Compressive Strengths

Instrumentation

PCB pressure and velocity transducers were used to make the active measurements. These transducers were attached to RG-62 coaxial cable which ran approximately 300 feet to the following recording sequence:

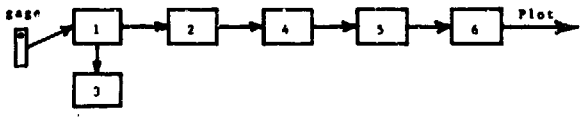

1. PCB 463A Charge Amplifier

2. VR 3700-Wide Band Group II-Frequency Modulator Tape Recorder

3. Bell and Howell 5-133 Oscillograph

4. Hewlett Packard 5180 Waveform Recorder

5. Hewlett Packard 9825 Computer

6. Hewlett Packard four-pen plotter

When the charge was detonated a loading was placed on the concrete walls, floor, and roof of an individual room. The pressure was then formed throughout the structure and exited through the entrance. The gages reacted causing an electrical signal to move through the cable to the charge amplifier. At this point, the signal is amplified and moved to the frequency modulator and oscillograph. The oscillograph allows a quick look at the wave form. The frequency modulator stores the signal on analog tape. The signal is then transfered from the tape to the computer where its software calculates the pressure-time history curve, impulse, and acceleration. Peak pressure and impulse are also determined by the computer program. This data is then plotted for permament record.

Explosive Charges

All charges were fabricated by forming composition C-4 explosive into a sphere. The charge weight varied from 0.1 to 2.0 pounds.

Test Procedure

Prior to the start of testing, stands were constructed to house the pressure transducers. The stands were designed so as to locate the pressure sensing element 24.0 inches above the floor slab in all locations. The charge was also placed 24.0 inches above the floor slab in all tests. Various standoffs were used in testing the different walls. Velocity transducers were placed on different areas within the test structure depending on the charge location. Preparation for the individual tests proceeded as follows:

a. The structure was cleaned of any debris.

b. Instrumentation was prepared and calibrated for each test.

c. Door position of individual rooms was selected.

d. The charge was emplaced and armed.

e. Final checks were made, the final countdown began, and the
charge was detonated.

f. After each detonation, a mechanical fan was placed on the
structure's entrance to remove the explosive gases and the
aerial debris.

g. An explosive expert insured complete detonation.

h. Still photographs were taken of the damage to all interior
walls, floor, roof, doors, and equipment that was located
in the various rooms.

i. Measurements were made of the damaged areas.

j. Major cracks were marked and a drawing was made of the
interior damage.

TEST RESULTS

Twentytwo successful tests took place. The following tables indicate each test's charge weight and location, test wall and room, pressure, impulse, deflection, and acceleration measurements, and a damage assessment after each shot.

TEST 1

Charge Weight	.1	(LBS)
Charge Location	1	(ROOM)
Test Wall	A	(WALL)
Charge Standoff	21	(INCHES)
Charge X-coordinate	30	(INCHES)
Charge Y-coordinate	24	(INCHES)

Transducer Location	P1	P2	P3	P4	P5	P6	P7	P8
Peak Pressure (PSIG)	*	*	*	*	*	*	*	*
Impulse (PSI-MSEC)	*	*	*	*	*	*	*	*

BASE LOCATION	WALL	WALL
	A	K
Deflection (in)	0.0	0.0

BASE LOCATION	WALL	WALL	EQUIP
	K	ROOF	RM 2
Acceleration (g's)	9.1	2.9	1.7

DAMAGE: * EQUIPMENT NOT SET PROPERLY - NO DATA. ALL DOORS TO EACH ROOM WERE CLOSED THE METAL DOOR AND FRAME OF ROOM 1 WAS BLOWN INTO ROOM 7. DOOR WAS BENT, NON-USEABLE. ELECTRICAL LIGHT FIXTURES AND CONDUIT IN ROOM 1 AND IMMEDIATE HALLWAY WERE DESTROYED. NO STRUCTURAL DAMAGE OCCURRED.

TEST 2

Charge Weight	.25	(LBS)
Charge Location	1	(ROOM)
Test Wall	A	(WALL)
Charge Standoff	27.5	(INCHES)
Charge X-coordinate	20.5	(INCHES)
Charge Y-coordinate	24	(INCHES)

Transducer Location	P1	P2	P3	P4	P5	P6	P7	P8
Peak Pressure (PSIG)	*	*	*	*	*	*	*	*
Impulse (PSI-MSEC)	*	*	*	*	*	*	*	*

GAGE LOCATION	WALL	WALL
	A	K
Deflection (in)	.063	0.0

GAGE LOCATION	WALL	WALL	EQUIP
	K	ROOF	RM 2
Acceleration (g's)	*	*	*

DAMAGE = EQUIPMENT NOT SET PROPERLY - NO DATA ALL DOORS WERE LEFT OPEN. NO STUCTURAL DAMAGE OCCURRED.

TEST 3

Charge Weight	.25	(LBS)
Charge Location	1	(ROOM)
Test Wall	A	(WALL)
Charge Standoff	15	(INCHES)
Charge X-coordinate	38	(INCHES)
Charge Y-coordinate	24	(INCHES)

Transducer Location	P1	P2	P3	P4	P5	P6	P7	P8
Peak Pressure (PSIG)	*	*	*	*	*	*	*	*
Impulse (PSI-MSEC)	*	*	*	*	*	*	*	*

GAGE LOCATION	WALL	WALL
	A	K
Deflection (in)	.125	0.0

GAGE LOCATION	WALL	WALL	EQUIP
	K	ROOF	RM 2
Acceleration (g's)	0.4	4.2	1.3

DAMAGE: * EQUIPMENT NOT SET PROPERLY - NO DATA ALL DOORS LEFT OPEN. NO STRUCTURAL DAMAGE FIVE KEYS WERE KNOCKED FROM THE TERMINAL KEYBOARD LOCATED IN ROOM 2.

TEST 4

Charge Weight	.25	(LBS)
Charge Location	1	(ROOM)
Test Wall	A	(WALL)
Charge Standoff	15	(INCHES)
Charge X-coordinate	38	(INCHES)
Charge Y-coordinate	24	(INCHES)

Transducer Location	P1	P2	P3	P4	P5	P6	P7	P8
Peak Pressure (PSIG)	*	*	*	*	*	*	*	*
Impulse (PSI-MSEC)	*	*	*	*	*	*	*	*

GAGE LOCATION	WALL	WALL
	A	K
Deflection (in)	.13	*

GAGE LOCATION	WALL	WALL	EQUIP
	K	ROOF	RM 2
Acceleration (g's)	3.5	0.8	1.0

DAMAGE: * GAGE MALFUNCTION - NO DATA. ALL DOORS WERE OPEN. NO STRUCTURAL OR EQUIPMENT DAMAGE OCCURRED.

TEST 5

Charge Weight	.25	(LBS)
Charge Location	1	(ROOM)
Test Wall	A	(WALL)
Charge Standoff	6.8	(INCHES)
Charge X-coordinate	38	(INCHES)
Charge Y-coordinate	24	(INCHES)

Transducer Location	P1	P2	P3	P4	P5	P6	P7	P8
Peak Pressure (PSIG)	*	2.33	3.83	5.93	3.66	4.91	6.58	9.47
Impulse (PSI-MSEC)	*	**	**	**	**	**	**	**

GAGE LOCATION	WALL	WALL
	A	K
Deflection (in)	.19	*

GAGE LOCATION	WALL	WALL	EQUIP
	K	ROOF	RM 2
Acceleration (g's)	63.9	12.2	2.5

DAMAGE: * GAGE MALFUNCTION - NO DATA. ALL DOORS WERE OPEN. NO STRUCTURAL OR EQUIPMENT DAMAGE OCCURRED. ** IMPULSE COULD NOT BE CALCULATED.

TEST 6

Charge Weight	.25	(LBS)
Charge Location	1	(ROOM)
Test Wall	A	(WALL)
Charge Standoff	3.8	(INCHES)
Charge X-coordinate	38	(INCHES)
Charge Y-coordinate	24	(INCHES)

Transducer Location	P1	P2	P3	P4	P5	P6	P7	P8
Peak Pressure (PSIG)	24.6	4.89	1.49	6.8	7.8	7.63	8.39	9.54
Impulse (PSI-MSEC)	**	**	**	**	**	**	**	**

GAGE LOCATION	WALL	WALL
	A	K
Deflection (in)	.44	*

GAGE LOCATION	WALL	WALL	EQUIP
	K	ROOF	RM 2
Acceleration (g's)	9.7	3.6	2.09

DAMAGE: * GAGE MALFUNCTION - NO DATA. ALL DOORS WERE OPEN. NO STRUCTURAL OR EQUIPMENT DAMAGE OCCURRED. ** IMPULSE COULD NOT BE CALCULATED.

TEST 7

Charge Weight	.25	(LBS)
Charge Location	1	(ROOM)
Test Wall	A	(WALL)
Charge Standoff	1.8	(INCHES)
Charge X-coordinate	38	(INCHES)
Charge Y-coordinate	24	(INCHES)

Transducer Location	P1	P2	P3	P4	P5	P6	P7	P8
Peak Pressure (PSIG)	37.5	3.90	1.77	10.8	4.85	*	*	*
Impulse (PSI-MSEC)	**	**	**	**	**	*	*	*

GAGE LOCATION	WALL	WALL
	A	K
Deflection (in)	*	*

GAGE LOCATION	WALL	WALL	EQUIP
	K	ROOF	RM 2
Acceleration (g's)	*	*	*

DAMAGE: * GAGE MALFUNCTION - NO DATA ALL DOORS WERE OPEN. CONCRETE SPALLED FROM WALL A OF ROOM 1 MEASURING 8.75" WIDE BY 8.25" HIGH BY 1.31" DEEP. CONCRETE SPALLED FROM WALL A OF ROOM 8 MEASURING 17.8" WIDE BY 32.8" HIGH BY 2.5" DEEP. TWO VERTICAL AND ONE HORIZONTAL REINFORCEMENT BARS WERE VISIBLE. ** IMPULSE COULD NOT BE CALCULATED.

TEST 8

Charge Weight	.46	(LBS)
Charge Location	1	(ROOM)
Test Wall	B	(WALL)
Charge Standoff	42	(INCHES)
Charge X-coordinate	38	(INCHES)
Charge Y-coordinate	24	(INCHES)

Transducer Location	P1	P2	P3	P4	P5	P6	P7	P8
Peak Pressure (PSIG)	*	*	*	*	*	7.8	9.2	11.8
Impulse (PSI-MSEC)	*	*	*	*	*	2.87	4.88	4.18

GAGE LOCATION	WALL	WALL
Deflection (in)	K	E
	.875	.75

GAGE LOCATION	WALL	WALL	EQUIP
Acceleration (g's)	K	ROOF	RM 2
	101	7.8	1.8

DAMAGE: ▼ GAGE MALFUNCTION - NO DATA, NO VISIBLE STRUCTURAL DAMAGE INSIDE ROOM 1. APPROXIMATELY .5 lb OF CONCRETE MEASURING 4"X2.5" SPALLED FROM WALL A IN ROOM B, THE RIGHT SIDE OF ROOM 7' DOOR FRAME BROKE LOOSE FROM THE WALL AND PROTRUDED INTO THE HALLWAY 8.5 INCHES. ALL DOORS WERE OPEN.

TEST 9

Charge Weight	.45	(LBS)
Charge Location	1	(ROOM)
Test Wall	B	(WALL)
Charge Standoff	21	(INCHES)
Charge X-coordinate	38	(INCHES)
Charge Y-coordinate	24	(INCHES)

Transducer Location	P1	P2	P3	P4	P5	P6	P7	P8
Peak Pressure (PSIG)	*	*	*	*	*	3.9	9.1	39.0
Impulse (PSI-MSEC)	*	*	*	*	*	2.12	3.70	10.3

GAGE LOCATION	WALL	WALL
Deflection (in)	B	L
	.81	.88

GAGE LOCATION	WALL	WALL	EQUIP
Acceleration (g's)	L	ROOF	RM 2
	*	3.5	1.0

DAMAGE: ▼ GAGE MALFUNCTION - NO DATA. NO VISIBLE STRUCTURAL DAMAGE INSIDE ROOM 1. NINE PIECES OF CONCRETE MEASURING 6" BY 3" EACH SPALLED FROM WALL A IN ROOM B. THIS SPALL INCREASED THE CRATER TO 28.75" WIDE BY 22" HIGH BY 2.63" DEEP. REINFORCEMENT WAS VISIBLE. ROOM 7'S DOOR FRAME WAS BROKEN COMPLETELY FROM THE WALL. AN ADDITIONAL SEVEN KEYS WERE KNOCKED FROM THE TERMINAL KEYBOARD LOCATED IN ROOM 2. ALL DOORS WERE OPEN.

TEST 10

Charge Weight	.5	(LBS)
Charge Location	1	(ROOM)
Test Wall	B	(WALL)
Charge Standoff	6	(INCHES)
Charge X-coordinate	38	(INCHES)
Charge Y-coordinate	24	(INCHES)

Transducer Location	P1	P2	P3	P4	P5	P6	P7	P8
Peak Pressure (PSIG)	*	1.2	2.1	2.5	2.58	16.5	32.8	*
Impulse (PSI-MSEC)	*	.42	1.0	1.83	1.47	4.58	13.3	*

GAGE LOCATION	WALL	WALL
Deflection (in)	B	L
	.63	.63

GAGE LOCATION	WALL	WALL	EQUIP
Acceleration (g's)	L	ROOF	RM 2
	*	12.3	*

DAMAGE: ▼ GAGE MALFUNCTION - NO DATA. ALL DOORS WERE OPEN. ADDITIONAL CONCRETE SPALLED FROM WALL A OF ROOM B EXPANDING THE CRATER TO 28.75" WIDE BY 22" HIGH BY 2.75" DEEP. A CRATER WAS FORMED ON WALL A IN ROOM 1 MEASURING 8.5" WIDE BY 6.25" HIGH BY 1.63" DEEP. REINFORCEMENT WAS VISIBLE ON WALL A IN ROOM 1. A CONCRETE PLUG MEASURING 2.38" WIDE BY 1.75" HIGH BY .25" DEEP SPALLED FROM WALL B IN ROOM B. OSCILLOSCOPE COVER BEGAN TO SEPARATE IN ROOM 2. CASING ON EQUIPMENT IN ROOM B BEGAN TO SEPARATE.

TEST 11

Charge Weight	.5	(LBS)
Charge Location	1	(ROOM)
Test Wall	B	(WALL)
Charge Standoff	3	(INCHES)
Charge X-coordinate	38	(INCHES)
Charge Y-coordinate	24	(INCHES)

Transducer Location	P1	P2	P3	P4	P5	P6	P7	P8
Peak Pressure (PSIG)	75.1	1.5	7.1	2.4	1.7	5.8	88.1	*
Impulse (PSI-MSEC)	7.53	.74	3.4	2.75	1.41	2.65	15.7	*

GAGE LOCATION	WALL	WALL
Deflection (in)	B	L
	**	.63

GAGE LOCATION	WALL	WALL	EQUIP
Acceleration (g's)	L	ROOF	RM 2
	*	33.2	*

DAMAGE: ▼ GAGE MALFUNCTION - NO DATA. ** DEFLECTION GAGE MEASURED 8.63". SPALL FROM WALL B CAUSED THIS LARGE READING. ALL DOORS WERE OPEN. WALL A WAS BREACHED. A HOLE MEASURING 3" IN DIAMETER WAS FORMED. THE CRATER ON WALL A OF ROOM B WAS UNCHANGED. ADDITIONAL CONCRETE SPALLED FROM WALL A IN ROOM 1 EXPANDING THE CRATER TO 8.25" WIDE BY 5.94" HIGH. A CRATER FORMED ON WALL B OF ROOM 1 MEASURING 5.63" WIDE BY 2.75" HIGH BY .13" DEEP. ADDITIONAL CONCRETE SPALLED FROM WALL B IN ROOM 2 EXPANDING THE CRATER TO 18" WIDE BY 15.56" HIGH BY 2.13" DEEP. NO ADDITIONAL DAMAGE TO EQUIPMENT IN ROOM 2 OR ROOM B.

TEST 12

Charge Weight	.5	(LBS)
Charge Location	1	(ROOM)
Test Wall	B	(WALL)
Charge Standoff	1.25	(INCHES)
Charge X-coordinate	38	(INCHES)
Charge Y-coordinate	24	(INCHES)

Transducer Location	P1	P2	P3	P4	P5	P6	P7	P8
Peak Pressure (PSIG)	71.1	1.68	5.88	1.38	1.78	29.8	43.0	*
Impulse (PSI-MSEC)	7.81	1.84	1.74	.75	1.41	9.88	11.23	*

GAGE LOCATION	WALL	WALL
Deflection (in)	B	L
	*	*

GAGE LOCATION	WALL	WALL	EQUIP
Acceleration (g's)	L	ROOF	RM 2
	*	12.3	*

DAMAGE: ▼ GAGE MALFUNCTION - NO DATA. ALL DOORS WERE OPEN. THE HOLE IN WALL A INCREASED IN SIZE TO MEASURE 5.8" WIDE BY 4.8" HIGH. ADDITIONAL CONCRETE SPALLED FROM WALL A OF ROOM B TO MEASURE 22.8" WIDE BY 22.8" HIGH. ADDITIONAL CONCRETE SPALLED FROM WALL A OF ROOM 1 TO MEASURE 9.8" WIDE BY 7.8" HIGH. A CRACK MEASURING 42.5" HIGH DEVELOPED FROM THE FLOOR AT THE CORNER OF WALL A AND WALL B IN ROOM 1. OTHER FINE CRACKS DEVELOPED ON BOTH FACES OF WALL A IN THIS GENERAL AREA. A SPALL AREA OF 34.8" HIGH BY 5.8" WIDE BY .25" DEEP ALSO DEVELOPED IN THIS AREA. AT THE DOOR OPENING OF WALL B IN ROOM 1, CONCRETE SPALLED MEASURING 4.8" WIDE BY 58.8" HIGH. WALL B WAS BREACHED. A HOLE MEASURING 7.8" WIDE BY 8.5" HIGH WAS FORMED. TWO VERTICAL AND ONE HORIZONTAL BAR WAS DEFLECTED .88" TOWARDS ROOM 2. ADDITIONAL CONCRETE SPALLED FROM WALL B OF ROOM 1 EXPANDING THE CRATER TO 18.8" WIDE BY 18.24" HIGH. ADDITIONAL CONCRETE SPALLED FROM WALL B OF ROOM 2 EXPANDING THE CRATER TO 21.8" WIDE BY 21.8" HIGH.

TEST 13

Charge Weight	.75	(LBS)
Charge Location	7	(ROOM)
Test Wall	H	(WALL)
Charge Standoff	42	(INCHES)
Charge X-coordinate	38	(INCHES)
Charge Y-coordinate	24	(INCHES)

Transducer Location	P1	P2	P3	P4	P5	P6	P7	P8
Peak Pressure (PSIG)	8.8	v	6.8	5.8	4.8	8.2	v	v
Impulse (PSI-MSEC)	1.86	v	3.13	3.01	1.98	5.57	v	v

GAGE LOCATION	WALL	WALL
	G	H
Deflection (in)	*	.6 vv

GAGE LOCATION	WALL	WALL	EQUIP
	R	ROOF	RM 6
Acceleration (g's)	125	10.7	*

DAMAGE: v GAGE MALFUNCTION - NO DATA. ALL DOORS WERE OPEN. vv GAGE WAS DISLOCATED. POSSIBLE ADDITIONAL DEFLECTION LENGTH DUE TO MOVEMENT. NO STRUCTURAL DAMAGE TO ROOM 7, EQUIPMENT IN ROOM 7 HAD INTERNAL DAMAGE. CRT WAS DISLOCATED FROM EQUIPMENT. EQUIPMENT FRAMES WERE BENT AND BROKEN.

TEST 14

Charge Weight	.75	(LBS)
Charge Location	7	(ROOM)
Test Wall	H	(WALL)
Charge Standoff	18	(INCHES)
Charge X-coordinate	38	(INCHES)
Charge Y-coordinate	24	(INCHES)

Transducer Location	P1	P2	P3	P4	P5	P6	P7	P8
Peak Pressure (PSIG)	18.0	18.[illegible]	3.58	4.08	4.18	17.1	83.2	v
Impulse (PSI-MSEC)	5.2	3.77	2.45	3.11	3.85	8.48	12.16	v

GAGE LOCATION	WALL	WALL
	C	H
Deflection (in)	.63	.75

GAGE LOCATION	WALL	WALL	EQUIP
	R	ROOF	RM 6
Acceleration (g's)	109	10.7	*

DAMAGE: v GAGE MALFUNCTION - NO DATA. ALL DOORS WERE OPEN. NO STRUCTURAL DAMAGE TO ROOM 7, EQUIPMENT IN ROOM 7 WAS FURTHER DESTROYED. NO LONGER REPAIRABLE.

TEST 15

Charge Weight	.75	(LBS)
Charge Location	7	(ROOM)
Test Wall	H	(WALL)
Charge Standoff	6.8	(INCHES)
Charge X-coordinate	38	(INCHES)
Charge Y-coordinate	24	(INCHES)

Transducer Location	P1	P2	P3	P4	P5	P6	P7	P8
Peak Pressure (PSIG)	18.1	v	8.28	13.8	3.58	3.48	v	12.9
Impulse (PSI-MSEC)	7.68	v	2.45	1.88	2.81	2.81	v	4.45

GAGE LOCATION	WALL	WALL
	C	H
Deflection (in)	*	1.75vv

GAGE LOCATION	WALL	WALL	EQUIP
	R	ROOF	RM 6
Acceleration (g's)	*	51.5	*

DAMAGE: v GAGE MALFUNCTION - NO DATA. ALL DOORS WERE OPEN. vv LARGE DEFLECTION PROBABLY DUE TO CONCRETE SPALL. NO STRUCTURAL DAMAGE TO ROOM 7, HOWEVER, CONCRETE SPALLED FROM WALL H OF ROOM 8 MEASURING 12.5" WIDE BY 12.8" HIGH BY 2.13" DEEP. CRACKS ALONG WALLS A AND R HAVE ENLARGED. FIVE REINFORCEMENT BARS AT THE JUNCTION OF WALLS A AND R ARE VISIBLE. ROOM 2 DOOR FRAME CAME LOOSE FROM WALL AT THE BOTTOM RIGHT SIDE OF ENTRANCE.

TEST 16

Charge Weight	.75	(LBS)
Charge Location	7	(ROOM)
Test Wall	C	(WALL)
Charge Standoff	3.8	(INCHES)
Charge X-coordinate	38	(INCHES)
Charge Y-coordinate	24	(INCHES)

Transducer Location	P1	P2	P3	P4	P5	P6	P7	P8
Peak Pressure (PSIG)	22.7	8.48	*	18.3	2.78	*	*	47.8
Impulse (PSI-MSEC)	3.76	8.47	*	1.22	1.62	*	*	11.5

GAGE LOCATION	WALL	WALL
	C	O
Deflection (in)	*	.88

GAGE LOCATION	WALL	WALL	EQUIP
	K	ROOF	RM 6
Acceleration (g's)	75.0	*	*

DAMAGE: v GAGE MALFUNCTION - NO DATA DOOR 6 WAS CLOSED. THE REMAINING DOORS WERE OPEN. ADDITIONAL CONCRETE SPALLED FROM WALL H IN ROOM 8 MEASURING 18.5" WIDE BY 14.5" HIGH BY 2.13" DEEP. ONE VERTICAL AND TWO HORIZONTAL REINFORCEMENT BARS WERE VISIBLE NO BAR DEFORMATION. EQUIPMENT IN ROOM 8 HAD CONCRETE SPALL COVERING IT, HOWEVER, NO APPARENT DAMAGE. CONCRETE CORNER OF WALLS A AND R IN ROOM 8 HAS BROKEN LOOSE MEASURING 14.8" WIDE BY 28.8" HIGH BY 2.58" DEEP. CONCRETE SPALLED FROM WALL H OF ROOM 7 MEASURING 8.8" WIDE BY 2.8" HIGH BY .38" DEEP. CONCRETE SPALLED FROM WALL R OF ROOM 7 MEASURING 15.8" WIDE BY 18.8" HIGH BY 1.44" DEEP. ALSO, CRACKS RUNNING 45° ALL THE WAY THROUGH WALL R MEASURED 24" FROM LEFT TO RIGHT. CONCRETE SPALLED FROM WALL C OF ROOM 7 MEASURING 4.5" WIDE BY 5.75" HIGH BY .63" DEEP. CONCRETE SPALLED FROM WALL O OF ROOM 7 MEASURING 2.8" WIDE BY 6.8" HIGH BY .63" DEEP. THIS SPALL APPEARED AT THE DOORWAY AND MOVED LEFT TOWARDS THE CORNER. CONCRETE SPALLED FROM WALL C OF ROOM 8 MEASURING 28.8" WIDE BY 24.8" HIGH BY 3.8" DEEP. EQUIPMENT IN ROOM 8 WAS SHAKEN BUT THERE WAS NO VISIBLE DAMAGE.

TEST 17

Charge Weight	1.8	(LBS)
Charge Location	2	(ROOM)
Test Wall	C	(WALL)
Charge Standoff	38	(INCHES)
Charge X-coordinate	38	(INCHES)
Charge Y-coordinate	24	(INCHES)

Transducer Location	P1	P2	P3	P4	P5	P6	P7	P8
Peak Pressure (PSIG)	21.7	v	2.88	18.8	19.7	38.8	6.78	*
Impulse (PSI-MSEC)	14.8	v	1.87	.84	7.18	3.58	2.37	*

GAGE LOCATION	WALL	WALL
	C	M
Deflection (in)	.75	*

GAGE LOCATION	WALL	WALL	EQUIP
	M	ROOF	RM 6
Acceleration (g's)	140	4.2	*

DAMAGE: v GAGE MALFUNCTION - NO DATA. DOOR 2 WAS CLOSED AND REMAINING DOORS WERE OPEN. WALL B BREACHED. BREACH OF WALL B IN ROOM 1 MEASURED 24.5" WIDE BY 18" HIGH. THREE VERTICAL AND THREE HORIZONTAL REINFORCEMENT BARS WERE EXPOSED. NO DEFLECTION IN REINFORCEMENT. CONCRETE SPALLED FROM THE CORNER OF WALLS K AND A CREATING A BREACH MEASURING 9.8" WIDE BY 15.8" HIGH. ADDITIONAL CONCRETE SPALLED FROM WALL R OF ROOM 7 MEASURING 18.8" WIDE BY 18.8" HIGH BY 2.25" DEEP. ADDITIONAL CONCRETE SPALLED FROM WALL C OF ROOM 8 MEASURING 28.8" WIDE BY 23.8" HIGH BY 2.88" DEEP. DOOR AND FRAME TO ROOM 8 WAS BLOWN INTO ROOM 8 AND BENT THE EQUIPMENT. KNOBS COULD FUNCTION. NO APPARENT DAMAGE TO EQUIPMENT. ALL EQUIPMENT IN ROOM 2 WAS COMPLETELY DESTROYED ALONG WITH THE DOOR AND FRAME. THE FRAME WAS BENT AND LOCATED IN ROOM 8. NO DAMAGE TO WALL C IN ROOM 2.

TEST 18

Charge Weight	1.8	(LBS)
Charge Location	2	(ROOM)
Test Wall	C	(WALL)
Charge Standoff	15	(INCHES)
Charge X-coordinate	38	(INCHES)
Charge Y-coordinate	24	(INCHES)

Transducer Location	P1	P2	P3	P4	P5	P6	P7	P8
Peak Pressure (PSIG)	*	116	34.3	126	30.9	78.7	*	*
Impulse (PSI-MSEC)	*	11.9	12.8	9.81	6.55	41.2	*	*

GAGE LOCATION	WALL	WALL
	C	M
Deflection (in)	1.5	*

GAGE LOCATION	WALL	WALL	EQUIP
	M	ROOF	RM 6
Acceleration (g's)	96.2	9.7	*

DAMAGE: * GAGE MALFUNCTION - NO DATA. DOOR TO ROOM 3 WAS CLOSED. REMAINING DOORS WERE OPEN. NO CHANGE TO DAMAGE IN ROOM 2. CONCRETE SPALLED FROM TOP RIGHT OF DOORWAY TO WALL P IN ROOM 6 MEASURING 3.25" WIDE BY 18.5" HIGH BY 4.5" DEEP. ADDITIONAL CONCRETE SPALLED FROM WALL C OF ROOM 6 MEASURING 8.8" WIDE BY 14.8" HIGH BY 2.25" DEEP. DOOR EDGE OF WALL R IN ROOM 7 SHEARED OFF MEASURING 4.5" WIDE BY 28.8" HIGH BY 4.5" DEEP.

TEST 19

Charge Weight	1.8	(LBS)
Charge Location	2	(ROOM)
Test Wall	C	(WALL)
Charge Standoff	6	(INCHES)
Charge X-coordinate	38	(INCHES)
Charge Y-coordinate	24	(INCHES)

Transducer Location	P1	P2	P3	P4	P5	P6	P7	P8
Peak Pressure (PSIG)	*	48.3	3.88	29.1	13.5	5.88	*	*
Impulse (PSI-MSEC)	*	5.78	1.85	3.11	1.58	3.38	*	*

GAGE LOCATION	WALL	WALL
	C	M
Deflection (in)	*	.63

GAGE LOCATION	WALL	WALL	EQUIP
	M	ROOF	RM 6
Acceleration (g's)	107	19.0	*

DAMAGE: * GAGE MALFUNCTION - NO DATA. ALL DOORS WERE OPEN. ADDITIONAL CONCRETE SPALLED FROM WALL B OF ROOM 1 MEASURING 27.5" WIDE BY 18.8" HIGH. RADIAL CRACKING SURROUNDED THE BREACH IN THIS WALL. ROOF JOINT AT WALL B IN ROOM 1 HAS DEVELOPED A CRACK ITS ENTIRE LENGTH. ADDITIONAL CONCRETE SPALLED FROM WALL B OF ROOM 2 MEASURING 22.8" WIDE BY 22.8" HIGH. A CRACK DEVELOPED DIRECTLY ABOVE THIS SPALL AREA ON WALL B IN ROOM 2 MEASURING 42.8" WIDE BY 2.5" HIGH BY .53" DEEP. A CRACK DEVELOPED ON WALL P OUTSIDE OF ROOM 6 MEASURING 8.86" WIDE BY 26.8" HIGH. EQUIPMENT IN ROOM 6 RECEIVED MINOR DAMAGE BUT COULD BE REPAIRED. THREE LARGE CONCRETE PIECES SPALLED FROM WALL R OF ROOM 7'S ENTRYWAY MEASURING 5.8" WIDE BY 26.8" HIGH BY 4.5" DEEP (ENTIRE THICKNESS OF THE WALL). CONCRETE SPALLED FROM WALL C OF ROOM 3 MEASURING 18.8" WIDE BY 14.8" HIGH BY 4.75" DEEP.

TEST 20

Charge Weight	1.8	(LBS)
Charge Location	6	(ROOM)
Test Wall	F	(WALL)
Charge Standoff	3.8	(INCHES)
Charge X-coordinate	38	(INCHES)
Charge Y-coordinate	24	(INCHES)

Transducer Location	P1	P2	P3	P4	P5	P6	P7	P8
Peak Pressure (PSIG)	*	114	1.98	21.6	*	*	25.1	*
Impulse (PSI-MSEC)	*	17.5	8.36	3.16	*	*	3.04	*

GAGE LOCATION	WALL	WALL
	E	P
Deflection (in)	.13	*

GAGE LOCATION	WALL	WALL	EQUIP
	P	ROOF	RM 3
Acceleration (g's)	129	13.6	*

DAMAGE: * GAGE MALFUNCTION - NO DATA. DOOR 5 WAS CLOSED. REMAINING DOORS WERE OPEN. ADDITIONAL CONCRETE SPALLED FROM WALL B OF ROOM 1 MEASURING 31.8" WIDE BY 22.9" HIGH BY 2.5" DEEP. THE BREACH IN THIS WALL ALSO INCREASED TO MEASURE 12.8" WIDE BY 14.8" HIGH. THREE VERTICAL AND TWO HORIZONTAL REINFORCEMENT BARS ON WALL B IN ROOM 1 ARE TOTALLY EXPOSED. NO DEFORMATION OCCURRED. ADDITIONAL CONCRETE SPALLED FROM WALL C OF ROOM 2 MEASURING 16.8" WIDE BY 18.8" HIGH BY 2.5" DEEP. SOME HAIRLINE RADIAL CRACKING DEVELOPED FROM THIS SPALL AREA. THREE HORIZONTAL AND ONE VERTICAL BAR WAS EXPOSED. CONCRETE SPALLED FROM WALL F OF ROOM 5 MEASURING 23.75" WIDE BY 28.5" HIGH BY 3.38" DEEP. TWO VERTICAL AND THREE HORIZONTAL REINFORCEMENT BARS WERE EXPOSED. HAIRLINE RADIAL CRACKING OCCURRED SURROUNDING THE SPALL AREA. TWO WALL BREACHES OCCURRED IN WALL C OF ROOM 6 WITHIN A CONCRETE SPALL AREA MEASURING 22.8" WIDE BY 24.8" HIGH BY 2.8" DEEP. THE FIRST HOLE MEASURED 2.5" BY 3.8". THE SECOND HOLE MEASURED 18.8" BY 16.8". ON THE SECOND HOLE, THREE HORIZONTAL AND ONE VERTICAL REINFORCEMENT BAR WAS EXPOSED. NO DEFORMATION OCCURRED. ADDITIONAL CONCRETE SPALLED FROM WALL C OF ROOM 7 AT THE BREACH MEASURING 31.8" WIDE BY 28.5" HIGH BY 2.8" DEEP. FIVE HORIZONTAL AND THREE VERTICAL REINFORCEMENT BARS WERE EXPOSED. ADDITIONAL CONCRETE PIECE FROM THE DOORWAY OF WALL R IN ROOM 7 BROKE OFF MEASURING 7.8" WIDE BY 15.8" HIGH BY 4.5" DEEP.

TEST 21

Charge Weight	2.8	(LBS)
Charge Location	3	(ROOM)
Test Wall	D	(WALL)
Charge Standoff	6.8	(INCHES)
Charge X-coordinate	38	(INCHES)
Charge Y-coordinate	24	(INCHES)

Transducer Location	P1	P2	P3	P4	P5	P6	P7	P8
Peak Pressure (PSIG)	*	*	59.7	47.3	84.4	*	43.8	*
Impulse (PSI-MSEC)	*	*	6.37	13.1	19.5	*	17.7	*

GAGE LOCATION	WALL	WALL
	C	D
Deflection (in)	*	*

GAGE LOCATION	WALL	WALL	EQUIP
	M	ROOF	RM 5
Acceleration (g's)	*	28.7	*

DAMAGE: * GAGE MALFUNCTION - NO DATA. ALL DOORS WERE OPEN. ADDITIONAL CONCRETE SPALLED FROM WALL C OF ROOM 2 MEASURING 23.8" WIDE BY 23.5" HIGH BY 3.8" DEEP. THE BREACH IN THIS WALL EXPANDED TO 19.8" WIDE BY 9.8" HIGH. THE WALL APPEARED TO BE VERY WEAK. MULTIPLE CRACKING OVER ENTIRE WALL C. ADDITIONAL CONCRETE SPALLED FROM WALL C OF ROOM 3 MEASURING 42.8" WIDE BY 34.8" HIGH BY 3.25" DEEP. ADDITIONAL CONCRETE SPALLED FROM WALL B OF ROOM 2 MEASURING 22.8" WIDE BY 27.5" HIGH BY 2.8" DEEP. THE BREACH IN WALL B IN ROOM 2 EXPANDED TO MEASURE 14.8" WIDE BY 14.8" HIGH. ALL EQUIPMENT IN ROOM 2 WAS DESTROYED. CRACKS HAVE DEVELOPED ALL THROUGH WALL M OF ROOM 2. ALL CONCRETE ON WALL N IN ROOM 3 WAS SPALLED AWAY FROM THE REINFORCEMENT. THE REINFORCEMENT WAS NOT DEFORMED. TWO SPALL AREAS DEVELOPED IN WALL B IN ROOM 3. THE FIRST MEASURED 45.8" WIDE BY 5.5" HIGH BY .63" DEEP. THE SECOND AREA MEASURED 18.25" WIDE BY 6.25" HIGH BY 1.5" DEEP. RADIAL CRACKING DEVELOPED THROUGH THE ENTIRE WALL. ALL EQUIPMENT IN ROOM 4 WAS DESTROYED. ADDITIONAL CONCRETE SPALLED FROM WALL D OF ROOM 4 IN TWO PLACES. THE FIRST MEASURED 28.8" WIDE BY 16.8" HIGH BY 2.25" DEEP. THE SECOND MEASURED 9.8" WIDE BY 11.8" WIDE BY 1.62" DEEP. CRACKS OCCUR AT BOTH ROOF AND FLOOR JOINTS OF WALL D. THE BREACH IN WALL C IN ROOM 6 INCREASED TO 14.8" WIDE BY 16.8" HIGH. ADDITIONAL CONCRETE SPALLED FROM WALL F OF ROOM 6 MEASURING 7.8" WIDE BY 9.25" HIGH BY 1.8" DEEP. A BREACH OCCURRED IN WALL F IN

ROOM 6 MEASURING 3.8" WIDE BY 3.9" HIGH. A BREACH OCCURRED IN WALL P IN ROOM 6 AT THE EDGE OF THE DOORWAY MEASURING 8.9" WIDE BY 8.5" HIGH. CONCRETE SPALLED IN THIS AREA MEASURING 13.8" WIDE BY 19.8" HIGH BY 1.9" DEEP. EQUIPMENT IN ROOM 6 WAS DENT WITH POSSIBLE REPAIR NEEDED. ADDITIONAL CONCRETE SPALLED FROM WALL P OF ROOM 5 MEASURING 23.8" WIDE BY 28.5" HIGH BY 2.5" DEEP. A SECTION OF WALL P IN ROOM 5 WAS BROKEN OFF. THIS CONCRETE SPALL MEASURED 2.5" WIDE BY 48.0" HIGH BY 4.5" DEEP. THERE WAS NO REINFORCEMENT IN THIS SECTON.

** THIS GAGE WAS PLACED JUST OUTSIDE THE DOORWAY TO ROOM 3

TEST 22

Charge Weight	2.8	(LBS)
Charge Location	5	(ROOM)
Test Wall	E	(WALL)
Charge Standoff	3.8	(INCHES)
Charge X-coordinate	38	(INCHES)
Charge Y-coordinate	24	(INCHES)

Transducer Location	P1	P2	P3	P4	P5	P6	P7	P8
Peak Pressure (PSIG)	*	99.3	78.3	180	*	214	13.8	9.99
Impulse (PSI-MSEC)	*	3.99	89.5	61.8	*	39.8	10.8	1.91

GAGE LOCATION	WALL	WALL
	E	O
Deflection (in)	*	*

GAGE LOCATION	WALL	WALL	EQUIP
	M	ROOF	N/A
Acceleration (g's)	*	4.8	N/A

DAMAGE: * GAGE MALFUNCTION - NO DATA. ALL DOORS WERE OPEN. ADDITIONAL CONCRETE SPALLED FROM THE AREAS IN ROOMS 2,3,5,6, AND 7. THE BLAST HAS WEAKENED THE CONCRETE IN THESE WALLS. ALL EQUIPMENT IN ROOMS 2,4, AND 8 WERE COMPLETELY DESTROYED. THE CONCRETE IN WALLS P AND O IN ROOM 5 WAS COMPLETELY REMOVED BY THE BLAST. WALL O'S REINFORCEMENT WAS DEFORMED OUTWARDS 17.5". WALL E IN ROOM 5 WAS PUSHED OUTWARD 3.8" FROM ITS ORIGINAL POSITION. WALL E IN ROOM 4 SHOWS MANY STRESS CRACKS AND ALSO SEPARATION FROM THE FLOOR AND ROOF CONNECTIONS. THIS WALL APPEARS AS IF IT WAS NOT TIED INTO THE ROOF SLAB. DUE TO THIS SEPARATION, SOIL FROM THE EXTERIOR FELL INTO ROOMS 4 AND 5.

THE BREACH IN WALL E IN ROOM 5 MEASURED 58.8" WIDE AND 5.8" HIGH. CONCRETE SPALLED FROM WALL E OF ROOM 4 IN TWO PLACES. THE FIRST AREA MEASURED 20.8" WIDE BY 24.8" HIGH BY 1.75" DEEP. THE SECOND AREA MEASURED 68.8" WIDE BY 38.5" HIGH BY 2.5" DEEP. CONCRETE SPALLED FROM WALL E OF ROOM 5 MEASURING 51.8" WIDE BY 4.8" HIGH BY 38" DEEP. ADDITIONAL CONCRETE SPALLED FROM WALL F OF ROOM 5 MEASURING 48.8" WIDE BY 34.8" HIGH BY 2.56" DEEP. THE BREACH IN THIS WALL INCREASED TO MEASURE 58.8" WIDE BY 5.8" HIGH.

CONCLUSIONS

Loading

The blast-pressure loading on the walls, floor, and roof in the room of the event was a result of reflected overpressure and reflected specific impulse. When a charge is detonated inside a room, the initial shock wave is identical with that obtained in the open air. However, once this shock wave strikes the walls that surround the charge it is reflected and the reflected wave bounds back and forth among the walls, floor, and roof until its energy has been completely transformed into heat, vented, or until the confining walls fail due to the loading. In most tests the doors were left open in the rooms; therefore, one must consider these rooms partially vented. The door openings were small compared to the total surface area; therefore, full venting of the contained explosion did not occur. This confinement increased the interior pressures, impulses, and duration. In addition to the initial shock wave and its reflections, the accumulation of gases from the explosion resulted in a pressure buildup, and since the venting area was limited, the duration of the pressure was prolonged. This could be observed from the pressure-time curve histories obtained by the placement of a pressure gage in each of the rooms of the test structure. A typical pressure-time curve for a point on a wall of a partially vented room is shown in Figure 2. The high peaks are the multiple reflections of the initial shock wave. The mean pressure has a lower pressure reading than the peak pressure reading and a long duration when compared to the duration of the shock wave pressures. In this test program, the peak pressure and specific impulse were more important in the loading of the structure rather than a long duration loading since the venting process was a governoring factor. It is obvious that the pressure from the detonation moved throughout the structure. The gages in each of the rooms measured some increase in pressure as the pressure vented from the room of detonation. The peak pressures were higher in the room of the event than the surrounding rooms. The pressure decayed rapidly as it migrated to the other rooms. As the distance increased from the detonation the peak pressure decreased. The recorded pressures were lower than those predicted using the equations for blast in an enclosed room. This could be a result of the rooms being partially vented. The venting of each test could be observed. The main entrance to the test structure was always left open during each test.

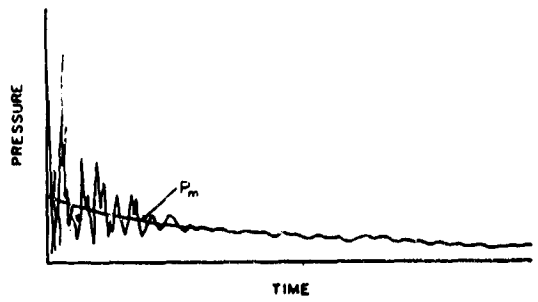

Figure 2. Pressure-time variation for a partially vented explosion.

The pressure resulting from the charge detonation traveled throughout the structure and finally vented out the entrance. Looking at the pressure data, one could see how the migration of pressure occurred. If a door to a room was closed and undamaged from the detonation event the pressure moved around that particular room. If the door to a room was open, the pressure would move into the room then move out again looking for a location to disperse, normally out the entrance of the test

structure. The pressure migration and the loading function obtained from this series of internal detonation of explosives and the effects it has on equipment, personnel, and the overall structure is needed to develop predictive models. However, further numerical studies including comparisons with experimental data, will be needed to develop a predictive model for pressure migration and loading method for this type of structure.

Spallation

Test results indicated the spall occurred primarily due to direct results of interference, near the free surface (that area between the wall reinforcement and the outside edge of the wall know as concrete cover), between the tail of an oncoming incident compressive wave (not yet reflected) and the reflected tensile wave. The concrete usually spalled from the opposite side of the wall from charge placement. This spall normally was as thick as the concrete cover. Only the larger, close-in charges create spall on the interior wall faces. In a few cases a punch through occurred. This punch through usually was a concrete plug sheared from the reinforcement pattern. Spall size and pattern enlarged in size as the charge weight increased and the standoff became less. After each test the previously spalled areas increased in size. This was the result of the interface between the additional loading of the structure and the previously spalled areas. The normal spall pattern was in a conical shape. Radial cracking surrounding the pattern area after the initial spall occurred. In some cases of nonreinforced areas, such as door jams, large sections of concrete broke off. No spall occurred to the floor, roof or exterior walls.

Structural Response

In all of the tests, the response of the walls were similar, differing only in severity. It consisted of a local area of damage opposite the placement of the charge. There was no structural damage to the roof, floor, or exterior walls during any tests. In the final test, one interior wall did pull away from the roof causing a separation in concrete and roof reinforcement. The interior wall movement due to charge detonation indicated the walls reacted in an overall flexure response, typical for a two-way supported slab under uniform loading conditions. The walls tested were oblong in shape and when loaded they deflected in a platterlike shape. This was expected since the moment distribution is applied in the same pattern. The damage mechanism is a result of point source loading. The damage area was in a circular pattern with radial cracking in a localized area with some cracking along the wall support edges. Since the charges were bare and spherical in shape this type of damage was expected. Therefore failure of the concrete begins before any appreciable overall response occurs and the concrete and reinforcing elements fail locally as the test results indicate.

REFERENCES

1. Department of the Air Force, AFM 88-22, "Structures to Resist the Effects of Accidental Explosions," June 1964.

2. National Defense Research Committee, "Effects of Impact and Explosion," Summary Technical Report of Division 2, Vol. 1, Washington,D.C., 1946.

3. Ferguson, P.M., "Reinforced Concrete Fundamentals," John Wiley & Sons,Inc., New York, 1973.

4. Department of Energy, DOE/TIC-11268, "A Manual for the Prediction of Blast and Fragment Loadings on Structures," November 1980.

STRESS-STRAIN-STRENGTH BEHAVIOR OF PAVEMENT BASE MATERIALS

M. C. McVay[1], D. Seereeram[2], P. Linton[3]

UNIVERSITY OF FLORIDA

ABSTRACT

Present analysis/design of base courses beneath runway pavements relies on simple compressive laboratory tests to determine resilient and permanent deformation behavior. The results and approach are shown to be unconservative, and improved analytical representation is warranted. Since a moving wheel load involves continuous principal plane rotations, the significance of anisotropy on the stress-strain-strength response of sands under a general loading program is reported. The paper concludes with present "state-of-the-art" analytical characterization of arbitrary loading, and the ongoing research at the University of Florida in the development of improved constitutive relationships for granular materials subject to moving wheel loads.

INTRODUCTION

One of the most significant factors affecting the serviceability of pavement systems is the physical and mechanical characteristics of the soil over which the pavement is constructed. Common modes of distress, such as fatigue, fracture, distortion, and rutting, may in many cases be directly linked to the behavior of the underlying supportive soil (1,2).

Current methods of pavement design and analysis depend heavily on a combination of multiple elastic layer theory and laboratory tests (1,3,4). The elastic theory is used to determine the states of stress and strain in the soil-structure system, and laboratory tests are in turn employed to determine the fatigue, rutting, and distortion (resilient) characteristics of the pavement and the supportive material. A typical sequence in the prediction of rutting and distortion of the base course is as follows (3): 1) representative elastic parameters of the material are selected based on experience, 2) using linear elastic theory, the stresses beneath a stationary flexible quasi-static circular load are determined for a representative point in the ground, and 3) a Resilient Modulus Test (2,5) is subsequently performed with the prescribed stresses ascertained from Step Two to obtain the permanent deformation (rutting), and an elastic resilient modulus for later use in multilayer analysis (distortion) (4).

However, the present approach of characterizing the base course with regards to analysis and design suffers from a number of severe limitations. For example, the laboratory Resilient Modulus Test uses only cyclically varying axial compressive loading with fixed principal planes, whereas the actual field behavior may involve extension stress states as well as large rotation of principal planes. Figure 1 depicts the stress paths obtained at two representative fixed points in the ground from quasi-static elastic theory due to an approaching circular load (moving wheel).

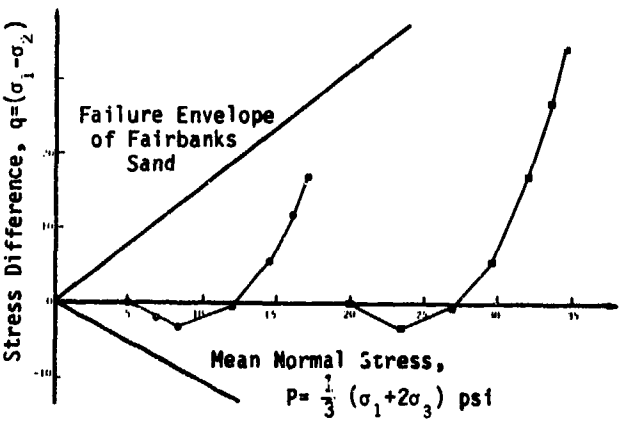

Figure 1. Stress Paths for Moving Wheel Loading.

Since the resilient test only varies the axial load, the positive portion of each stress path in Figure 1 is commonly cycled in a triaxial environment. Figure 2 plots the response of such a test on a typical Florida sand (7). Shown in

(1) Assistant Professor, Department of Civil Engineering, University of Florida
(2) Ph.D. Candidate, Department of Civil Engineering, University of Florida
(3) M.S. Candidate, Department of Civil Engineering, University of Florida

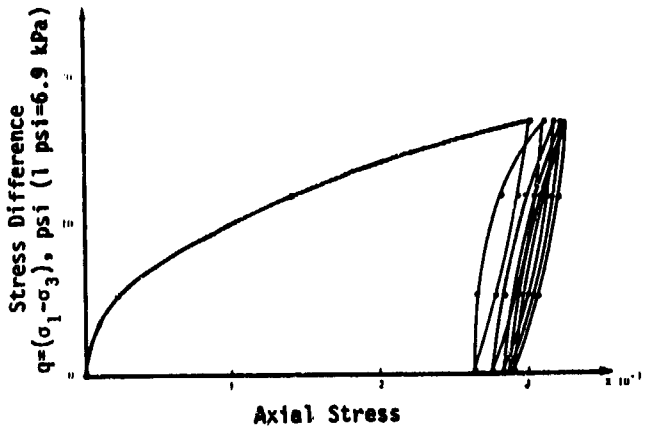

Figure 2. Stress-Strain Response of Fairbank's Sand Undergoing Cyclic Compressive Loading, Initial Stress 12.5 psi.

Figure 3 is the measured stress-strain behavior for the complete stress path (Fig. 2) which has undergone six cycles of loading (7). Evident from a comparison of the two figures is that the permanent deformation (rutting) is about one and one half times greater in the moving wheel test (Fig. 3) than in the Resilient modulus test (Fig. 2), and the resilient modulus is approximately twice the value calculated in the moving wheel experiment. Since the measured behavior is on the unconservative side, the results suggest that improved methods in the analysis and design of the base courses are warranted.

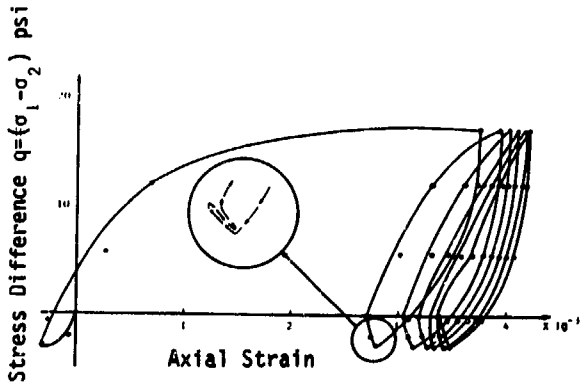

Figure 3. Stress-Strain Response of Fairbank's Sand Undergoing Moving Wheel Stress Path, Initial Stress 5 psi.

The design of optimum runway pavements is a coupled boundary value problem involving the interaction of the pavement, base course, and in situ soil. In order for the design to be viable, improved consititutive relations for the soil must be developed which includes the capability of simulating permanent strain buildup, as well as resilient behavior during cyclic loading. Since the characteristics of soil is highly dependent upon past history, composition, and current stress-strain state, such a model must have the capacity of representing rotation of planes, inherent, and stress-induced anisotropy, but should remain simple enough to obtain model parameters from readily available triaxial test. Reported herein is the ongoing research at the University of Florida in the development of a cyclic, phenomenological, elasto-plastic Bounding Surface constitutive model for granular material which explicitly (or implicitly) accounts for the influence of anisotropy on: 1) the plastic flow rate direction, 2) the plastic modulus, and 3) the strength variation that results from a rotation of the principal stress axes. Specifically, the paper reports on the experimental observed stress-strain and strength behavior of soils exhibiting anisotropy subject to rotation of planes, and the ability of present "state of the art" constitutive relationships in predicting such behavior. Since most pavement base and subbase materials are granular, the investigation dealt only with dry sands.

EXPERIMENTAL

In 1944 Casagrande and Carillo (7) distinguished between two forms of anisotropy in soils-inherent, and stress-induced. Inherent anisotropy was defined as "physical characteristics inherent in the material, and entirely independent of the applied strains," whereas induced anisotropy was stated as "due exclusively to the strains associated with the applied stresses." Although these definitions were developed to describe strength, Arthur et al. (8) considers them equally applicable to stress-strain behavior. The

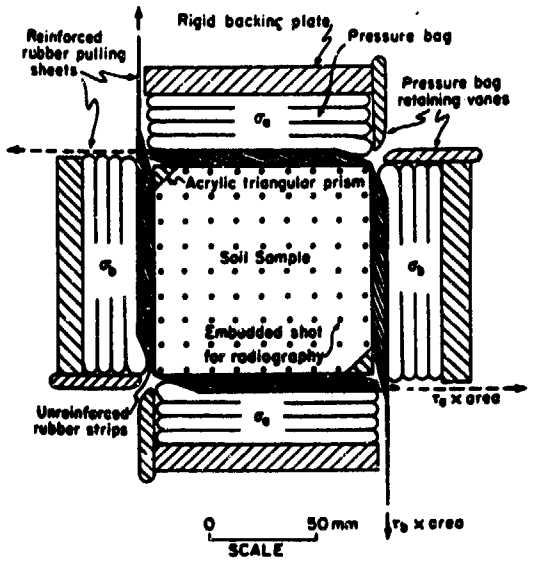

Figure 4. Directional Shear Cell Apparatus, Arthur (9).

complexity of characterizing inherent and stress induced anisotropy in combination with principal plane rotations indicates that the phenomenon is most appropriately investigated by studying each separately.

A testing apparatus, developed specifically to investigate anisotropy, is depicted in Figure 4. The Directional Shear Cell (9), sometimes referred to as DSC device, allows the investigation of inherent or stress-induced anisotropy independently of one another under a controlled rotation of the principal planes. As seen from the figure, orientation of the principal axes is controlled by the tension in the pulling sheets and flexible pressure bags. Plotted in Figure 5 is the measured stress strain responses of dense pluviated (air rained) Leighton Buzzard sand specimens tested in the DSC under a number of horizontal principal plane rotations. The measured response, within limits, gives a unique stress-strain curve independent of principal plane orientation. Based on such behavior, Arthur (9) reports that most sands, if deposited from a vertical direction, and subsequently sheared under horizontal monotonic loading, exhibit transverse isotropic material response. If however, the sand

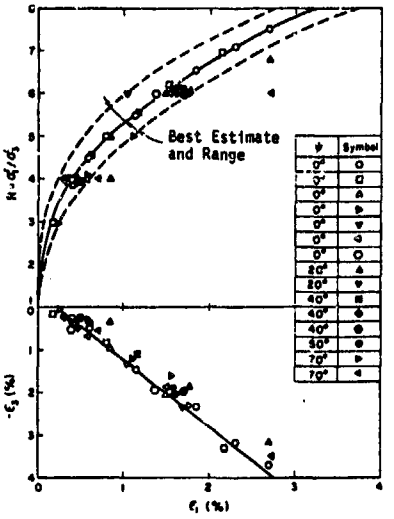

Figure 5. Stress Ratio Versus Principal Strain, Under Monotonic Loading with Principal Plane Orientation, ψ, Arthur (9).

specimen is subject to a prior loading, the stress-strain response is completely altered as illustrated in Figure 6. The results presented in the figure, are the measured stress-strain curves obtained from loading to sixty percent of failure under various principal plane orientations, followed by unloading, and subsequent reloading along new principal plane orientations (see legend). Inspection of the figure illustrates the significant influence stress-induced anisotropy has on the measured stress-strain behavior. Similar results have been observed by other researchers in different testing apparatuses (10).

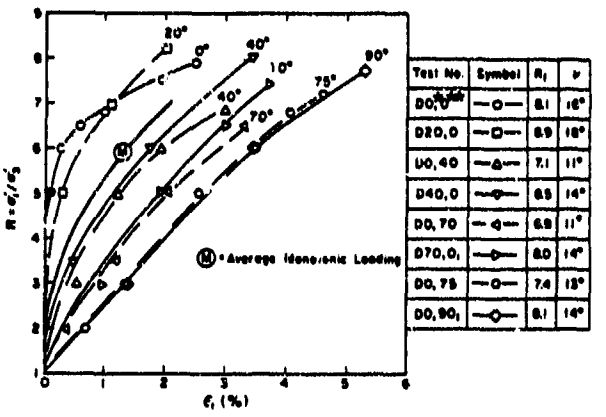

* Principal plane orientation for first load
** " " " " second "

Figure 6. Stress-Induced Anisotropic Response in Second Load Application for Leighton Buzzard Sand, Arthur (9).

Inherent anisotropic material response is usually attributed to the soil's composition (particle shape, gradation, etc.) and fabric (11,12). The latter is directly related to the mechanical processes under which a soil is formed or artificially constructed. For example, Oda (11) used pluviation (pouring through air) to construct sand (Toyoura) specimens for a cubical plane strain apparatus oriented with different bedding angles from the horizontal and was clearly able to demonstrate the influence of the inherent anisotropic phenomena on the material's strength (Fig. 7). Depicted in Figure 8 is the monotonic

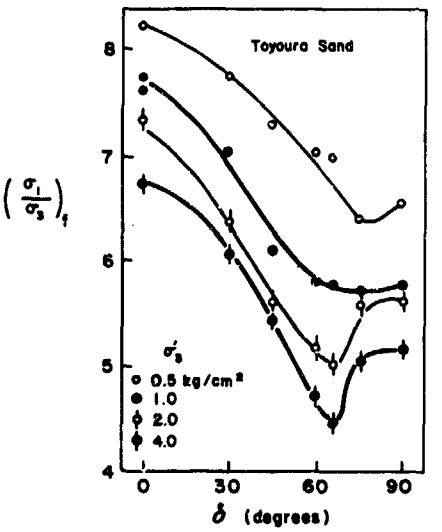

Figure 7. Variation in Strength Due to Bedding Orientation, δ, Oda (11).

response of dense Reid Bedford sand specimens tested in a hollow cylinder apparatus, under a general loading program (12). Also shown in the figure, are the principal plane orientations for each test. Since moving wheel stress paths

involve continuous rotation of the principal planes, the tests lend considerable insight into the stress-strain response of an inherent anisotropic sand prior to the stress-induced influences (cyclic loading). Presented in Figure 9 is an in-

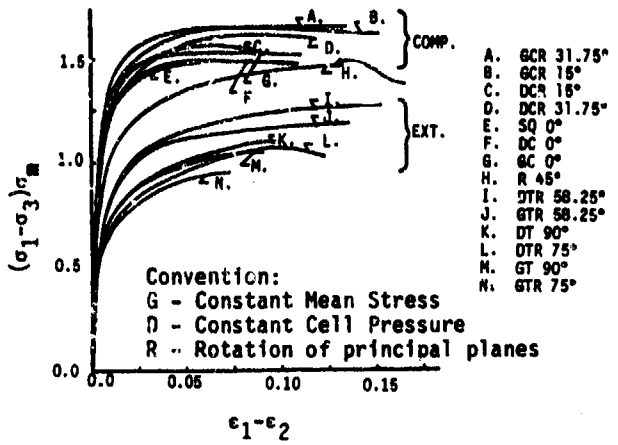

Figure 8. Principal Stress Versus Strain Difference of Monotonically Loaded Reid Bedford Sand Under General Principal Plane Orientation, Saada (12).

house study on the influence of the magnitude of prior shearing (amount of stress-induced anisotropy) on spherical loading strain ratios for the same Reid Bedford sand presented earlier. The loading is semi-representative of a moving wheel passing points of different elevation in the field. The prior axial compression load was zero, twenty, forty, and sixty percent of the Mohr-Coulomb compressive strength. The figure also depicts the response for isotropic material behavior. Apparent from the figure is the inherent and stress-induced anisotropic influences and some support for the belief that stress-induced anisotropy may be erased under extremely high isotropic loading if prior shearing isn't excessive.

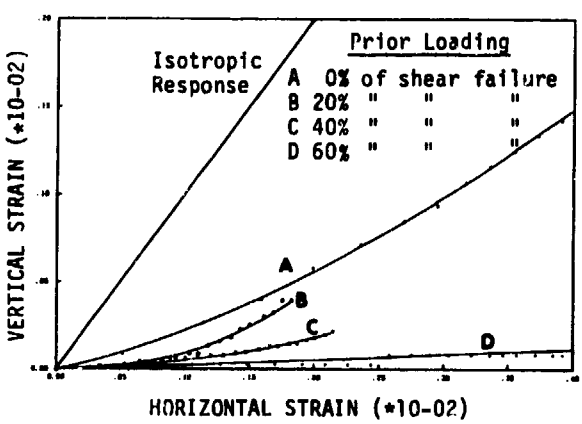

Figure 9. Vertical Versus Horizontal Strain Response of Reid Bedford Sand Under Spherical Loading with Prior Shears.

Based on the presented experimental results, one can say with confidence that anisotropy plays a significant role in the stress-strain and strength behavior of a granular media. Due to the nature of construction (vertical vibration in direction of deposition) and loading (cyclic moving wheel stress path) it is reasonable to expect that base materials will exhibit considerable anisotropic behavior during their service life. Therefore, for improved analysis/design of runway-base systems, the constitutive characterization of the base material must be capable of capturing anisotropy. Presented next is a current "state of the art" prediction of a generalized loading response observed in the hollow cylinder device. Note, this does not involve cyclic loading but only investigates the behavior of an initially inherent anisotropic specimen subject to a monotonic load with a fixed principal plane direction other than its material fabric alignment; the first step before cyclic loading in the simulation of a passing moving wheel.

ANALYTICAL

A review of the literature on phenomenological plasticity theory, as it relates to soil mechanics, uncovered only a single model which was capable of realistically simulating the nonlinear, anisotropic, elasto-plastic hysteretic, path dependent, and, in particular, cyclic stress-strain behavior of sand: the Prevost pressure-sensitive, isotropic/kinematic hardening model (13). This model may appear intractable and too complex to many practitioners, but stress-induced as well as inherent anisotropy is accounted for in a realistic manner, and it may be the simplest yet most complete analytical representation of elasto-plastic anisotropic hardening (14).

The anisotropic hardening behavior in the model is described through a field of plastic shear moduli and a corresponding set of nested yield surfaces in stress space as depicted in Figure 10. The yield surfaces are both free to translate and change size in stress space at the same time. Individual plastic moduli are constant

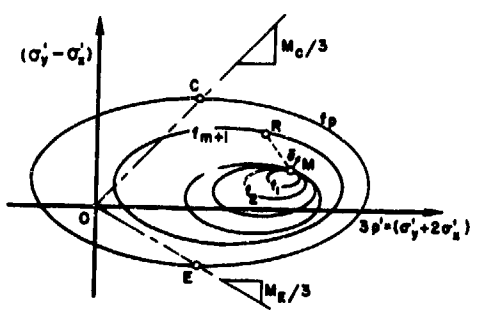

Figure 10. Prevost's Multi-Yield Surfaces in Axial Stress Space.

on each surface, however the complete description of the constitutive behavior is dependent on the stress path between the surfaces

and the relative configuration of the surfaces with respect to one another. Evaluation of the model constants requires the initial positions and sizes of relevant yielding surfaces from consolidation data and conventional triaxial compression (increased axial load, CTC) and extension (decreased axial loading, RTE) tests at the consolidation stress level of interest. The model has been independently coded and verified at the University of Florida.

Fifteen presently unpublished hollow cylinder tests, subject to a general loading program (Fig. 9) were made available from Saada at Case Western Reserve University. Two of these tests, the RTC and CTC, and a published series of K_o consolidation tests performed at the U.S. Army Waterways Experimental Station, WES (15), were used to obtain the model's parameters. The rest of the hollow cylinder results were predicted with the Prevost pressure sensitive model. Figure 11 shows the model's exact reproduction of the conventional triaxial compression data (CTC) used in the calibration.

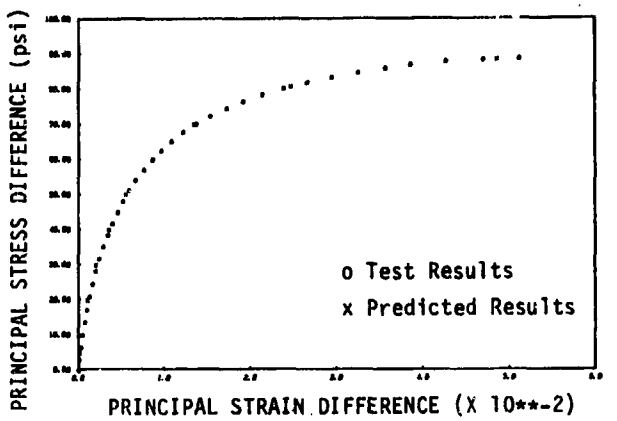

Figure 11. Measured and Predicted Principal Stress Versus Strain Difference of Reid Bedford Sand Under Conventional Triaxial Compression Loading

Figure 12 depicts the model's prediction of a constant mean stress (30 psi) test in which the principal planes were oriented 31.75 degrees from the vertical.

Obviously, such a brief investigation is not sufficient for judgment, but preliminary indications are that the Prevost analytical representation does not qualitatively or quantitatively simulate the observed behavior; this outcome underscores the need for continued fundamental research.

Presently, research is underway at the University of Florida in the development of an improved bounding surface plasticity model which specifically addresses anisotropy and rotation of planes with regards to a passing moving wheel load. Even though an earlier model (6) had some success in characterizing a cyclic ninety degree jump in principal stresses, the newer version will incorporate a number of improvements: 1) a more

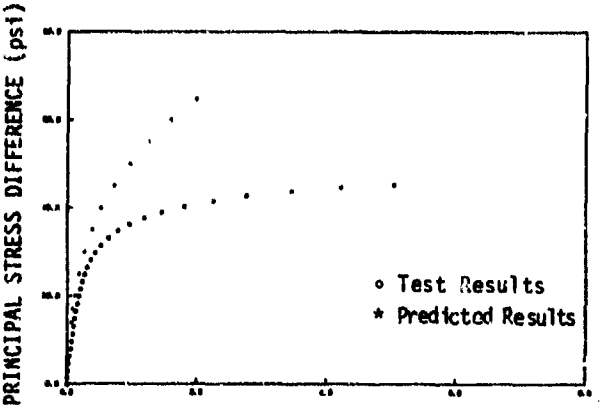

Figure 12. Correlation Between Measured and Predicted Principal Stress Versus Strain Difference for Reid Bedford Sand with Principal Planes Oriented 31.75° and a Constant Mean Stress of 30 psi.

tractable functional representation of the isotropic consolidation surface along its meridional axis, 2) an allowance for the influence of intermediate principal stress by replacing the Mises circle on the octahedral plane with a more realistic representation (17), 3) parametric control of the size of the bounding surface which will be useful in modeling jump rotations of the principal stress axes, 4) incorporation of the soil "fabric" tensor to capture the sysmmetry and intensity of the stress-induced as well as inherent anisotropy, and 5) an option for predicting flow using a varying non-associated flow rule (18). In regards to tasks 3 and 4, it is envisioned that, depending upon the angle between the spatial mobilized plane and minor eigenvector of the fabric tensor, a functional relationship between strength and this angle can be proposed. Variations in strength are, of course, manifest in purely isotropic processes of the bounding surface. From physical intuition, we also expect that this level of strength variation will depend on the intensity of the anisotropy (mathematically depicted in terms of, say, the second invariant of the deviatoric tensor). This refined model will subsequently be used to predict all laboratory obtained hollow cylinder, Directional Shear Cell, and in-house cyclic tests.

CONCLUSIONS

Current methods of predicting pavements' subbase and base deformation relies almost exclusively on cyclic laboratory tests involving only variations in axial load. However, using more realistic representation of the moving wheel stress path (ninety degree jump rotations in principal planes) reveals that the present methods of predicting permanent deformation and resilient behavior to be unconservative by as much as a factor of two. These variations are attributed to the complex nature of the soil in which its response is controlled by past history, current state, composition, and method of formation. All may lead to the development of anisotropy, and

under a general loading program, have a significant influence on the stress-strain and strength behavior of granular materials. In order for present design to be improved, a more complete analytical statement on anisotropy under cyclic principal plane rotation must be developed. A review of a present "state of the art" analytical characterization, reveals its inability to capture strength under a general monotonic loading. With laboratory obtained hollow cylinder data, Directional Shear Cell results, and presently ongoing in-house cyclic triaxial tests, an improved phenomenological bounding surface plasticity mode is under development at the University of Florida which should result in a more realistic pavement-base analysis and design.

ACKNOWLEDGEMENTS

This research was sponsored by USAF/AFSOR, Bolling AFB, Washington under project AFOSR-84-0108, "Stress-Strain Behavior of Runway Base Materials Subject to Cyclic Moving Wheel Loads." The cooperation and guidance provided by Lt. Col. Lawrence Hokanson is greatly appreciated. The assistance of Dr. D. Bloomquist and R. Failmezger, University of Florida, contributed substantially to this project and is recognized.

REFERENCES

1. Monismith, C.L., and Finn, F.N., "Flexible Pavement Design: State of the Art," ASCE Journal of the Transportation Engineering Division, Jan. 1977, TE1, pp. 1-53.

2. Seed, H.B., Chan, C.K., and Lee, C.E., "Resilience Characteristics of Subgrade Soils and Their Relation to Fatigue Failures in Asphalt Pavements," Proc., 1st International Conference on Structural Design of Asphalt Pavements, Ann Arbor, Mich. 1962.

3. Brabston, W.N., "Investigation of Compaction Criteria for Airport Pavement Subgrade Soils," Technical Report GL-81-U, U.S. Army Engineer Waterways Experiment Station, C.E. Vicksburg, Miss., Oct. 1981.

4. Crawford, J.E., "An Analytical Model for Airfield Pavement Analysis (AFPAV), Technical Report 71070, Air Force Weapons Laboratory, Kirtland Air Force Base, N. Mex., 1971.

5. "Resilient Modulus Test," Standard presently under consideration for ASTM, 1984.

6. McVay, M.C. and Taesiri, Y., Cyclic Behavior of Pavement Base Materials," Journal of the Geotechnical Engineering Division, ASCE, to be published in January, 1985.

7. Casagrande, A. and Carillo, N., Boston Society of Civil Engineers, Vol, 31, 1966, pp. 74-87, 1944.

8. Arthur, J.R.F., Chua, K.S., and Dunstan, T., Geotechnique, Vol. 27, No. 1, 1977, pp. 13-36.

9. Authur, J.R.F., Bekenstein, S. Germaine, J., and Ladd, C.C., "Stress Path Tests with Controlled Rotation of Principal Stress Directions," Laboratory Shear Strength of Soil, ASTM STP 740, Chicago, 1980, pp. 516-540.

10. Mould, J.C., Sture, S., Ko, H., "Modeling of Elasto-Plastic Anisotropic Hardening and Rotating Principal Stress Directions in Sand," IUTAM Conference on Deformation and Failure of Granular Materials, Delft Netherlands, 1982, pp. 431-439.

11. Oda, M., "Initial Fabrics and Their Solutions to Mechanical Properties of Granular Material," Soils and Foundations, Japanese Society of Soil Mechanics and Foundation Engineering, Vol. 12, No. 1, 1972, pp. 17-36.

12. Saada, A.S., Bianchine, G.F., Piero, P.M., "The Mechanical Properties of Anisotropic Granular Soils," Colloque International In C.N.R.S., No. 351, Grenoble, France, 1983.

13. Prevost, J.H., "Constitutive Theory for Soil," in Proceedings of the Sysmposium on Limit Equilibrium, Plasticity and Generalized Stress-Strain Applications in Geotechnical Engineering, ed. Raymond Yong and E.T. Selig, New York, NY; ASCE 1980.

14. Ko, Hon-Yim, Sture, S., "State of the Art: Data Reduction and Application for Analytical Modeling," in Laboratory Shear Strength of Soil, ed. Raymond Yong and Frank C. Townsend, 1916 Race Street, Philadelphia, PA; ASTM STP 740, 1980.

15. Al-Hussaini, M.M., Townsend, F.C., Investigation of K_o Testing in Cohesionless Soils, Vicksburg, Mississippi; U.S. Army Engineers Waterways Experiment Station, 1975.

16. Dafalias, Y.F. Popov. E.P., "Plastic Internal Variables Formalism of Cyclic Plasticity," Journal of Applied Mechanics, Vol. 98, No. 4, Dec. 1976, pp. 645-651.

17. Gudehus, G., "Elastoplastische Stoffgleichungen fur trockener Sand," Ingenieur Archiv. Vol. 42, 1973.

18. Dafalias, Y.F., "Initial and Induced Anisotropy of Cohesive Soils by Means of a Varying Non-Associated Flow Rule," in Proceedings sur "Le Conportement Plastique des Solides Anisotropes", Colloque International die D.N.R.S No. 319, Villard-de-Lans, France, July 1981.

FRACTURE TOUGHNESS OF FIBER REINFORCED CONCRETE

BY

Y.S. Jeng[1] and S. P. Shah[2]

Department of Civil Engineering
Northwestern University
Evanston, Illinois 60201

ABSTRACT

A fracture mechanics based theoretical model is presented to predict the crack propagation resistance of fiber reinforced cement based composites. Mode I crack propagation and steel fibers are treated in the proposed model. The mechanism of fracture resistance for FRC can be separated as: subcritical crack growth in matrix and beginning of fiber bridging effect; post critical crack growth in matrix such that $K_I = K^s_{Ic}$ where K_I is the net stress intensity factor due to the applied load and the fiber bridging closing stresses; and a final stage where the resistance to crack separation is provided exclusively by fibers. The response of FRC during all these stages was successfully predicted from the knowledge of matrix fracture properties and the pull-out load vs. slip relationship of single fiber. The model was verified with the results of experiments conducted on notched beams reported here.

INTRODUCTION

Research conducted during the last twenty years has shown that the addition of fibers significantly improves penetration, scabbing and fragmentation resistance of concrete. The possible application of fiber reinforced concrete (FRC) include explosion and shock resistant protective structures. Even though the enhanced "cracking resistance" is the most important attribute of FRC, there are no rational methods of measuring or predicting this important material property.

In this paper a fracture mechanics based theoretical model is presented. To aid in development of the proposed theoretical model, experiments were conducted on unreinforced and steel fiber reinforced notched beam specimens of various sizes.

[1] Graduate Research Assistant, Northwestern University, Evanston, IL 60201

[2] Prof. of Civil Engineering, Northwestern University, Evanston, IL 60201

PROPOSED MODEL FOR CRACK PROPAGATION

The fracture resistance of fiber reinforced concrete is dominated by the coupling effects between fiber and matrix. As cracks start propagating in matrix, fibers tend to resist further crack propagation. To accurately predict this fiber bridging mechanism, the crack propagation in unreinforced matrix is first described.

Unreinforced Matrix

Crack propagation (only Mode I is considered here) in plain matrix (portland cement paste, mortar and concrete) can be separated into four stages. Prior to crack initiation, the load vs. load-point deflection response can be considered essentially linear (Fig. 1a) when the stress intensity factor (K_I) is less than half the critical stress intensity factor (K^s_{Ic}).

The shape of the load vs. load-point curve becomes nonlinear and significant permanent displacements are observed upon unloading in the nonlinear range (Fig. 1b). The inelastic displacement during crack growth in cement based composites is primarily due to friction associated with roughness of cracks and geometrical interlock.

The structure reaches its critical load carrying capacity when the critical stress intensity factor K^s_{Ic} is reached (Fig. 1c). Note that the value of the critical stress intensity factor as defined here depends on the effective crack length (a) which is the sum of the effective nonlinear crack growth (ℓ_{ec}) and the initial notch (a_o). To calculate the critical stress intensity factor inelasatic displacements must be separated from the total response as will be detailed later.

If the structure is loaded at a moderate rate using the displacement control, then cracks propagate in a steady state (in the sense of K_I) condition and the softening type of post-peak response is observed (Fig. 1d). During this state, the stress intensity factor continues to be equal to K^s_{Ic}, the crack continues to grow while the load is dropping.

Fiber Reinforced Composites

The prediction of the response of the fiber reinforced composites (FRC) containing an initial notch of length a_0 can be facilitated by dividing the response into three stages (Fig. 2).

(a) Linear Range:

Within the linear range of the unreinforced matrix (Fig. 1a) the FRC also behaves linearly. The initial Young's modulus for FRC may be different than that for matrix depending upon the amount of fibers.

(b) Nonlinear Crack Growth:

When the stress intensity factor (calculated using the conventional linear elastic fracture mechanics - LEFM) becomes greater than half the critical stress intensity factor (K^s_{Ic}) nonlinear crack growth commences and the fibers will tend to resist this growth. The fiber bridging forces will depend on the total crack opening displacement while the calculations of stress intensity factor will depend on the effective crack growth and the elastic crack opening displacement. It is assumed that the crack profile and the critical effective crack extension remain the same for FRC as those for unreinforced matrix.

The total load P acting on the composite structure can be divided into three parts (Fig. 3):

$$P = P^M + P^f_k + P^f_s \qquad (1)$$

where M is the contribution due to matrix and is related to K_I, P^f_k is related to K^f_I and accounts for the singularity effect due to fiber bridging, and P^f_s satisfies global equilibrium due to fiber bridging forces (Fig. 3).

Note that the value of P for FRC does not necessarily attain a maximum when K_I just reaches K^s_{Ic}. Depending upon the volume of fibers, the maximum load for FRC may occur for a larger crack length than that corresponding to the peak load in the unreinforced matrix (Fig. 2).

(c) Completely cracked matrix:

When the crack opening displacement (CMOD in Fig. 2) becomes very large, the resistance offered by matrix becomes negligible and eventually the stress intensity factor (K_I) becomes zero. Further crack separation is now mainly resisted by fibers. At this stage the load (P) and the corresponding CMOD can be calculated from only the global equilibrium consideration. That is:

$$P = P^f_s \qquad (4)$$

DETERMINATION OF CRITICAL STRESS INTENSITY FACTOR (K^s_{Ic}) AND CRITICAL CRACK TIP OPENING DISPLACEMENT ($CTOD_c$)

The proposed model is applicable in general to specimens or structures of any geometry. To experimentally verify and numerically demonstrate the model, notched beam specimens which were simply supported and centrally loaded (the so-called three-point bend specimen) were tested. To demonstrate the validity of K^s_{Ic} as a valid material parameter, specimens of varying sizes and made with cement paste, mortar and concrete were tested.

As a result of the nonlinear slow crack growth prior to the peak load one cannot use the initial notch length (a_0) to calculate K_{Ic} from measured maximum load and using LEFM. An effective crack length $a = a_0 + \ell_{ec}$ was defined such that the measured elastic crack mouth opening displacement ($CMOD^e$) and that calculated using this length, measured load and LEFM were equal. Once the effective crack length is determined (an iterative procedure was employed) then the values of K^s_{Ic} and $CTOD_c$ can be calculated using LEFM. From the experimental results and calculations it was observed that: 1. The value of K^s_{Ic} calculated as proposed is essentially independent of the geometry of the beam specimens. This was not true for the conventional method of calculating fracture toughness based on a_0 and P_{max} [1,2]. 2. The values of the critical crack tip opening displacement for mortar specimens ($CTOD_c$) can be approximately considered independent of the dimensions of the beams [3].

RESISTANCE PROVIDED BY FIBERS

The resistance offered by fibers (only steel fibers are considered here) depends primarily on the interfacial bond between the fibers and the matrix. This is because of the short length (of the order of 25mm) of the fibers and rather weak zone in the matrix that is observed in surrounding fibers. It is assumed that the fiber-bridging forces can be calculated from the pull-out test results of single, aligned fibers.

From the experimental results of the pull-out tests [4, 5] it was observed that the pull-out load vs. slip relationship can be expressed only as a function of the maximum pull-out stress and the length of the fiber.

The maximum pull-out stress will depend on the number of fibers crossing the cracked surfaces, that is, on the volume fraction of fibers.

CALCULATION OF LOAD-CMOD CURVES FOR FIBER REINFORCED COMPOSITES

The procedure involves calculating the applied load and the corresponding CMOD for a fixed value of the effective crack extension ($a_0 + \ell_e$). The procedure is repeated for different increasing values of ℓ_e and the associated

value of K_I (which is a function of ℓ_e) to obtain the entire P-CMOD response. For example, in the steady state, for any given ℓ_e ($\ell_e > \ell_{ec}$) and K^s_{Ic}, the CMOD can be calculated using LEFM formula. The associated P^M in Eq. (1) (see Fig. 3) can be related to $\underline{a}$ and K^s_{Ic} as =

$$P^M = \frac{K^s_{Ic}\, b^2\, t}{1.5\, \sqrt{\pi a}\, F_1\left(\frac{a}{b}\right)} \qquad (3)$$

To determine the stress intensity factor (K^f_I) due to fiber bridging, the stress intensity factor of a crack in an infinite strip of unit thickness subjected to a unit point load was used as Green's function and integrated over the closing pressure zone. Similarly, P^f_y and K^f_I can be related by Eq. 3. The value of P^s_y is determined from global equilibrium condition.

CALCULATIONS OF LOAD-DEFLECTION RESPONSE OF FRC

To relate the loads with the load-point deflection analytically, the concept of global energy balance was used. The total strain energy release rate (termed G_R) for the critical section can be derived and expressed as elastic and inelastic energy consumption during new crack formation.

For a certain amount of increment of effective crack extension, the total energy absorbed determined from G_R vs. ℓ_e is equated to that obtained from the load vs. load-point deflection curve. From this equality and knowing the R-curve, deflections can be determined. It was assumed that unloading was elastic prior to peak whereas for load-deflection curve beyond the peak, it was assumed that the elastic deflection after unloading remained constant and was equal to that at the peak. More details about the derivation of load-deflection and load-CMOD relationship are given in Ref. 6.

TEST PROGRAM

Three point bend test was used to verify the validity of the proposed model. Fiber reinforced beams with dimensions 11 in (280mm) x 3 in (76mm) x 6.75 in (19.1mm) (span x depth x thickness) and different fiber volume fractions (ranging from 0% to 1.5%) were prepared. One inch long brass coated smooth steel fibers with 0.016 in diameter were used. Four different series with the same mortar matrix were cast.

DISCUSSION OF TEST RESULTS

The material properties of unreinforced matrix were directly calculated from the experimental results.

To account for distribution of fibers from section to section of the beam, from beam to beam and to include spatial distribution at a given section an effective volume fraction V_{ef} rather than global volume fraction, V_f was used in the theoretical analysis.

The experimental results of load-CMOD curves for beams made with different fiber volume fractions (including unreinforced matrix) are plotted in Fig. 4 and compared with the theoretical prediction. The theoretical prediction is judged to be quite satisfactory. Good agreement was also found between the theoretical prediction and experimental results of load-deflection curves (Fig. 5). Fig. 6 shows a plot of peak load values vs. effective fiber volume fractions. The strength of FRC beams with effective fiber volume fraction of 2.5% is about twice the strength of unreinforced matrix. The G_R values at ℓ_e equals 1.9 in. (a/b = 0.933) are plotted in Fig. 7 for different values of V_{ef}. It can be seen that the energy absorption ability for beams with V_{ef} = 2.5% is about 30 times that of unreinforced matrix. In comparison to the improvement of energy absorption, the strength improvement due to addition of fibers is less significant. This was also shown by Shah and Rangan [7].

ACKNOWLEDGEMENT

This investigation was sponsored by the Air Force Office of Scientific Research under Grant No. AFOSR-82-02-43 [Lt. Col. Lawrence D. Hokanson, Program Manager].

REFERENCES

1. Jenq, Y.S., and Shah, S.P., "Nonlinear Fracture Parameters for Cement Based Composites; Theory and Experiments" in Application of Fracture Mechanics to Cementitious Composites, ed. by S. P. Shah, to be published by Martinus Nijhoff Publishers, 1985.

2. Jenq, Y.S., and Shah, S.P., "A Fracture Toughness Criterion for Concrete," Engineering Fracture Mechanics (to appear).

3. Jenq, Y.S., and Shah, S.P., "A Measure for the Fracture Toughness of Cement-Based Material," Proceedings of Symposium of Material Research Society, Boston, 1984.

4. Stroeven, P., Shah, S.P., deHaan, Y.M., and Bouter, C., "Pull-out Tests of Steel Fibers," Proceedings, International Symposium, RILEM-ACI-ASTM, SHEFFIELD, Sept. 1978, pp. 345-353.

5. Naaman, A.E., and Shah, S.P., "Pull-out Mechanism in Steel Fiber Reinforced Concrete," Journal of ASCE-STD, August 1976, pp. 1537-1548.

6. Jenq, Y.S. and Shah, S.P., "Crack Propagation Resistance of Fiber Reinforced Concrete," submitted for publication.

7. Shah, S.P., and Rangan, B.V., "Fiber Reinforced Concrete Properties," ACI Journal, Vol. 62, No. 2, Feb. 1071, pp. 126-135.

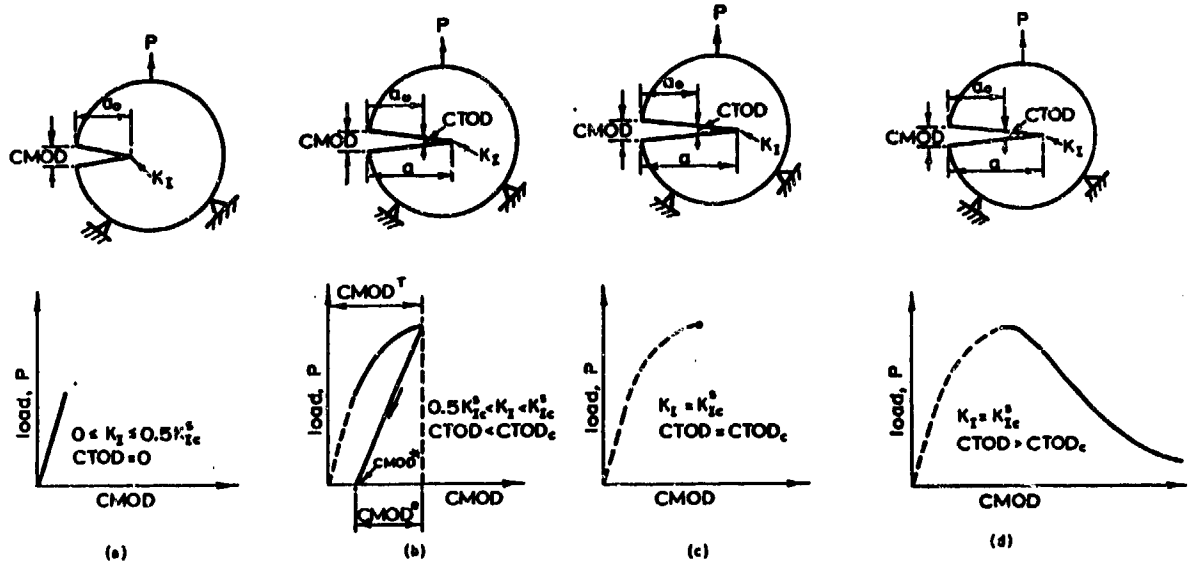

Fig. 1- Fracture Resistance Stages of Unreinforced Matrix

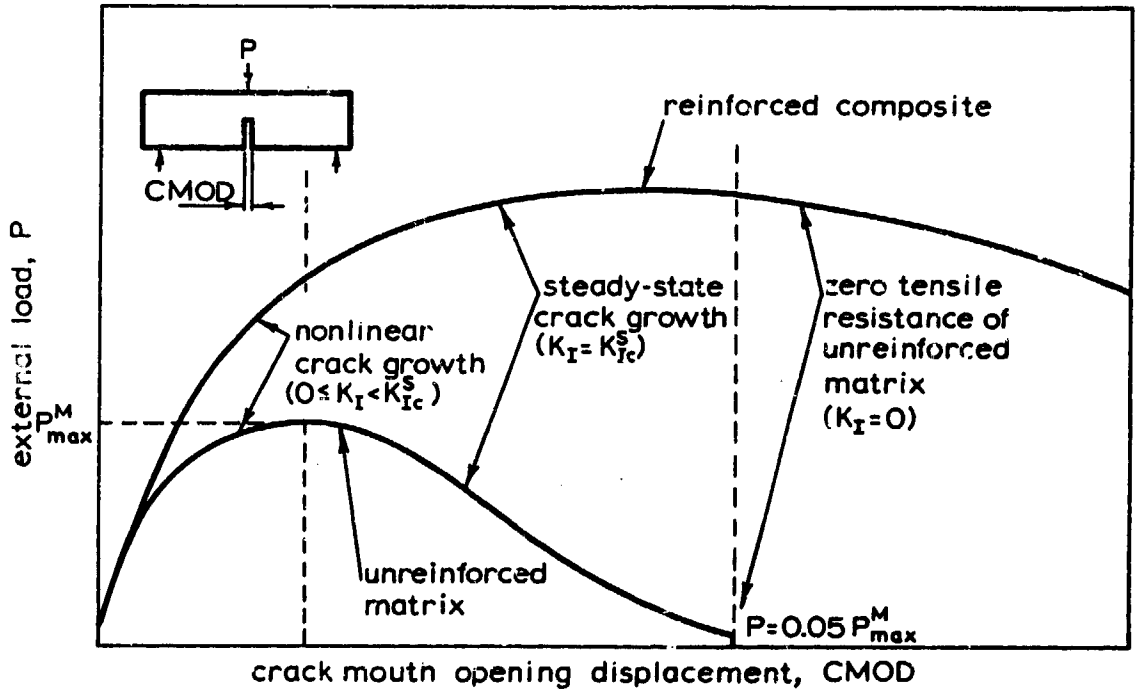

Fig. 2- Fracture Resistance Mechanisms of Fiber Reinforced Concrete

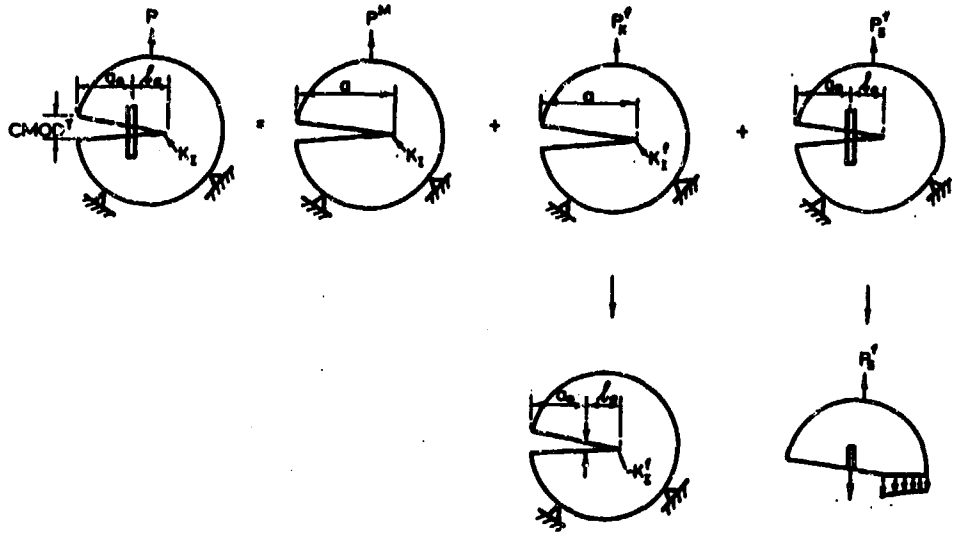

Fig. 3- Compositions of External Load Applied on a Fiber Reinforced Structure

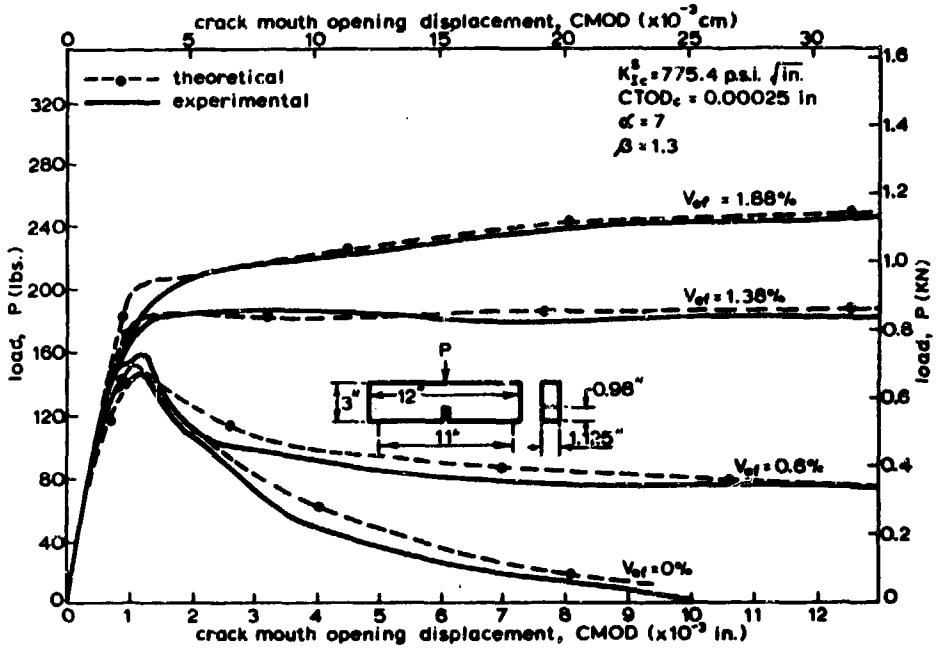

Fig. 4- Comparison of Theoretical Prediction and Experimental Results of Load-CMOD curves

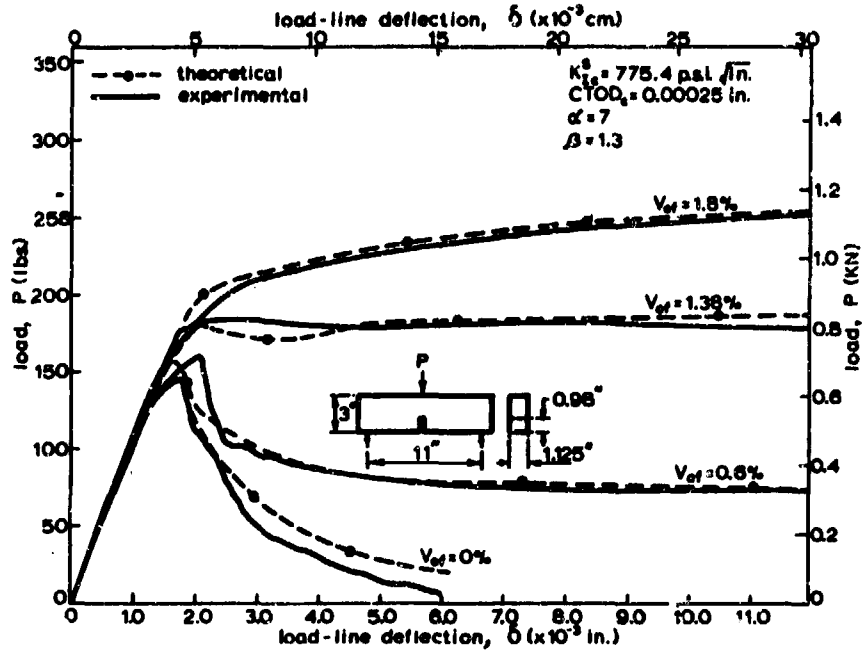

Fig. 5- Comparison of Theoretical Prediction and Experimental Results of Load-deflection Curves

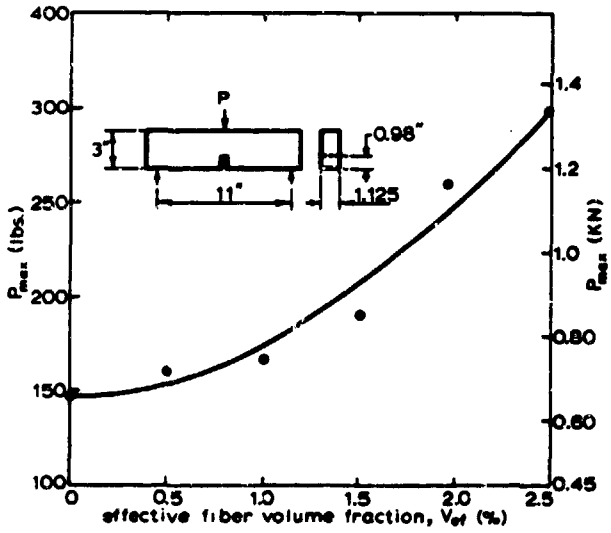

Fig. 6 - Relationship between Peak Load and Effective Fiber Volume Fraction

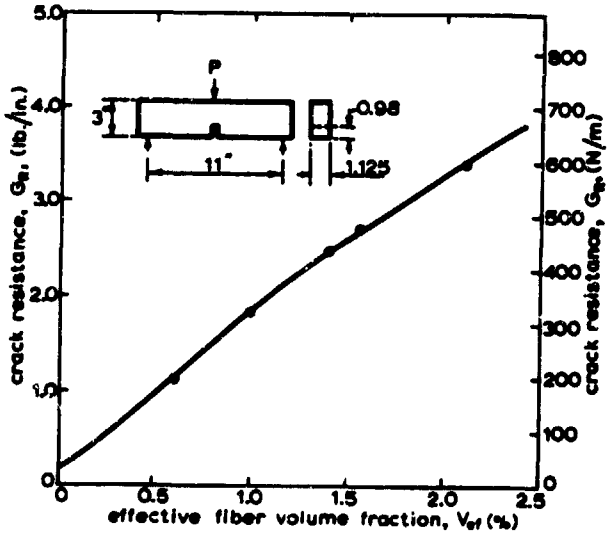

Fig. 7 - Relationship between Crack Resistance Energy and Effective Fiber Volume Fraction

EXPERIMENTAL INVESTIGATION OF FIBRE AND STEEL REINFORCED CONCRETE PLATES UNDER SIMULATED BLAST-LOAD

Christoph Mayrhofer
and
Heinz J. Thor

Fraunhofer-Institut für Kurzzeitdynamik
Ernst-Mach-Institut, Freiburg, West-Germany

ABSTRACT

Concrete plates reinforced by steel an fibre have been experimentally investigated in a blast-load-simulator. The influence of the content of fibre on the load carrying capacity is calculated for the static and dynamic case compared with experiments. The results of yield-line-theory are applied for the determination of static behavior, whereas the dynamic response is computed on the basis of a one-degree-of freedom system with elasto-plastic resistance function. The loading with an ideal blast-wave is compared with the experimental results obtained in the simulator.

INTRODUCTION

The advantageous physical properties and the large working capacity of fibre reinforced concrete lead to the investigation of its application in the case of bending stress and area loading. Beside the behaviour under static load, the dynamic response is of primary interest.

Since the fibre cuts are oriented at random their effectivity especially under multiaxial stress is expected to be good. For the study of this behaviour scaled experiments were carried through with slabs of different geometry and supports.

Aim of the investigation was to determine the behaviour of fibre concrete under flexural stress and the conditions which allow its application e.g. in the construction of shelters. The basis for the comparison are the properties of reinforced concrete plates. The results of tests where reinforced concrete have been compared are available in a report /1/.

TEST-PROGRAM

For the experimental program a total of hundred model slabs has been cast and tested. Thirty-five slabs thereof and the same quantity of additional model beams were available to test the efficiency under different stress modes. One-and-two-dimensional (1-D,2-D) stresses were analysed. A compilation of the slabs and beams under test together with their supports is found in Tab. I.

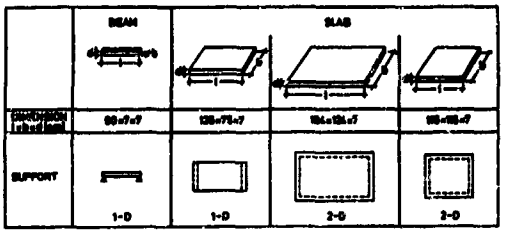

Tab. I Beam and slab dimensions

The test objects were cast correspondingly in fibre and steel reinforced concrete. The length of the fibre cuts varied from 25 mm to 55 mm, their length to diameter ratio from 35 to 125. The reinforcement mesh corresponded to steel type 420/500, the concrete quality to Bn 45, screening of aggregates 0/8. Four types of plates were tested, -fibre concrete, -reinforced fibre concrete, -concrete, -reinforced concrete, with variation of the fraction of fibre and steel reinforcement.

The plates were subjected to static and dynamic loads on a blast-wave simulator (Fig.1). The device consists in principle of a pressure chamber, which is divided into two parts by the plate. At the start of the load test both sections are inflated to the same pressure. By venting both chambers with different flowrates, the plate is loaded by a resulting force proportional to the time-dependent difference-pressure . Force and impulse corresponding to a large range of TNT-equivalent can be simulated by an adequate dimensioning of the test parameters. The fastest rise time of the pressure pulse is in the range of 3-5 ms, for the simulation of static load this risetime is extended to 4 minutes. Pressure measurements are carried through on the strain gage principle, whereas the plate-deflection is monitored by an inductive displacement pick up.

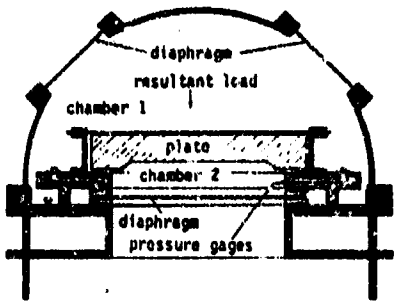

Fig. 1 Schematic of Blast Simulator

RESULTS

Since the experiments only allow a limited variation of the different parameters a numerical analysis is required. The ultimate load $p_{f,b}$ of a fibre specimen is normalized by the maximum load p_e of a corresponding reinforced concrete model. This leads to the following definition of the efficiency, comparing the same type of systems:

$$(1) \qquad \varkappa = p_{f,b} / p_e = M_{Br}^{f,b} / M_{Br}^{e}$$

Only the ratio of the ultimate resistance moments is of signifance , other system parameters do not matter. The moments are calculated on the basis of Equs. 2-4:

$$(2) \qquad M_{Br}^{e} = \sigma_e \cdot \mu \cdot h_m^2 \left(1 - \frac{\sigma_e \cdot \mu}{\beta_w \cdot 2}\right)$$

$$(3) \qquad M_{Br}^{f,b} = \beta_w \cdot \frac{d^2}{3} \cdot \beta_{BZ}^{f,b} / \left(\beta_w + \beta_{BZ}^{f,b}\right)$$

$$(4) \qquad \beta_{BZ}^{f,b} = \beta_{BZ}^{b} \cdot 0{,}97 \left(1 - V_f\right) + 3{,}41 \cdot V_f \cdot \frac{l_f}{d_f}$$

where

d	=	slab thickness
β_w	=	cube strength
β_{BZ}^{b}	=	bending tensile strength (concrete)
$\beta_{BZ}^{f,b}$	=	bending tensile strength (fibre concrete)
σ_e	=	tensile stress (steel)
V_f	=	fibre content
μ	=	steel content
l_f/d_f	=	length to diameter ratio (fibre)

Due to the difference in tension zones in concrete reinforced by bars and by fibres, the effectivity factor $\varkappa$ is multiplied with the square of the ratio height h_m to the thickness d (Fig.2,3). These figures present the calculated value of $\varkappa$ as function of the percentage of steel reinforcement μ for two values of fibre content V_f. The calculation based on the one-dimensional case (Eq.4) overestimates the efficiency factor $\varkappa$ as can be seen in comparison with the experimental results for beams and slabs supported on two sides.

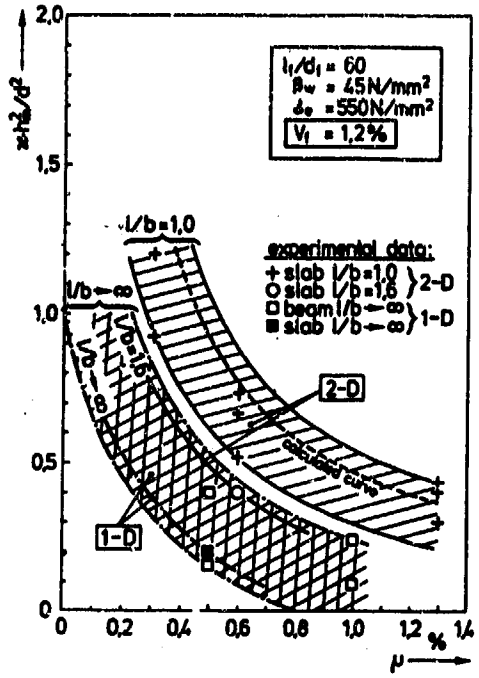

Fig. 2 Effectivity factor for fibre content V_f = 1.2 %

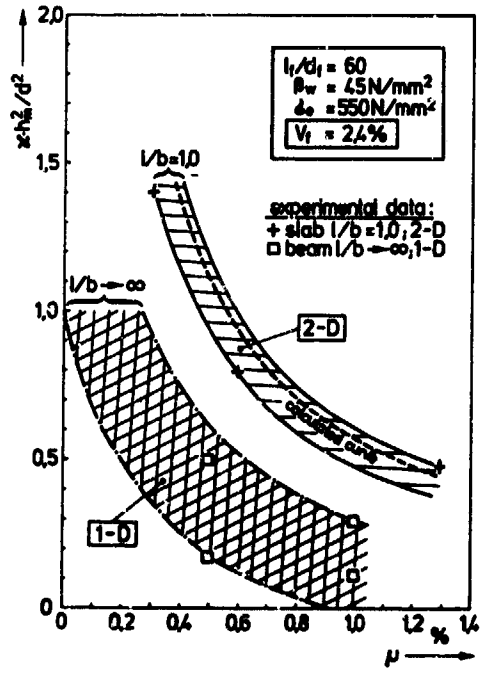

Fig. 3 Effectivity factor for fibre content V_f = 2.4 %

The experiments clearly display the difference between one- and two-dimensional loading. The efficiency factor is higher in the latter case. Also can be observed that the influence of the length to width ratio l/b is essential. This parameter varies for the slabs under examination from 1 to 1.6, thus forming the upper and lower bounds of the test results.

As Fig. 2 and 3 display equal load capacity for both types of support is only achieved for a low percentage μ of steel reinforcement. Since μ is given for the one-dimensional case this implies that the total steel content is twice as high in the two-dimensional cases tested here. For a constant value of $\varkappa \cdot (h_m/d)^2 = 1$ for both systems in Fig. 4 the content of fibre is compared to the total amount of steel. In the 1-D-system the percentage of fibre is higher than that of steel. Since $V_f = 3$ % is a limiting value for the fibre component which can be handled in the casting process /2/, the maximum load capacity is comparable to a steel reinforcement $\mu < 0{,}3$ %.

The 2-D-system contains a range between 0,3 % $< \mu < 1$ %, which is of interest under an economical point of view. Here the fibre content is equal or less than the amount of steel. The limit for the substitution of steel is 1,1 % $< \mu < 1{,}3$ % because the maximum of $V_f = 3$ % is reached.

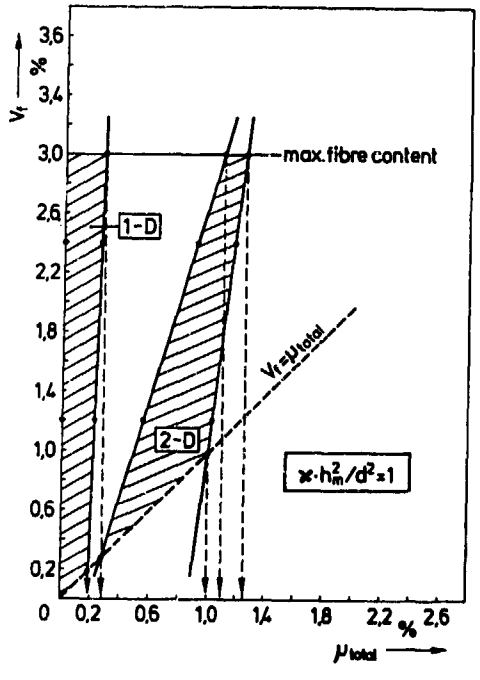

Fig. 4 Fibre and steel content for equal ultimate load

The static load capacity together with the static deflection behaviour is the basis for the theoretical discussion of the dynamic response. Typical displacement curves as functions of applied pressure are shown in Figs. 5 and 6. A concrete plate without reinforcement (Fig.5) points out an almost ideal elastic behaviour, whereas the example in Fig. 6, a fibre concrete slab, shows a pronounced elasto-plastic behaviour. This is the same typical deformation as it is known for reinforced concrete slabs, also the working capacity of the fibre concrete is comparable to that of reinforced concrete plates.

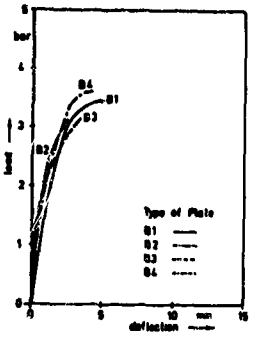

Fig. 5 Load vs deflection (concrete)

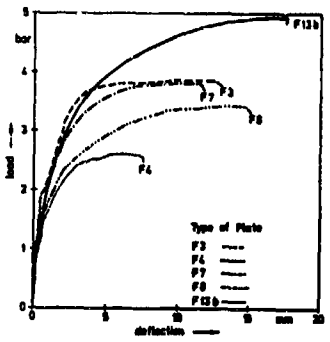

Fig. 6 Load vs deflection (fibre concrete)

The dynamic response of slabs under simulated blast load is calculated on the basis of a one-degree-of-freedom system /3/. The result for the case of the given load history and nonlinear resistance function presents Fig. 7. Here the maximum deflection is displayed vs. time in normalized scales. The nonlinearity causes a field of curves with the parameters λ, the ratio of peak load p_1 to maximum resistance force R_0. Another characteristic set of curves is obtained by connecting the points of multiples of the elastic deflection $1/\lambda$.

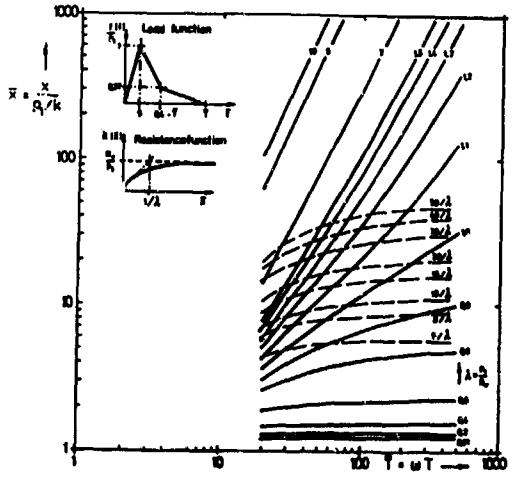

Fig. 7 Maximum normalized displacement $\bar{x}$ vs dimensionless time $\bar{T}$

By comparing these values to the actual ultimate deflection of a beam or slab, it is possible to construct iso-damage curves as shown in Fig. 8-10.

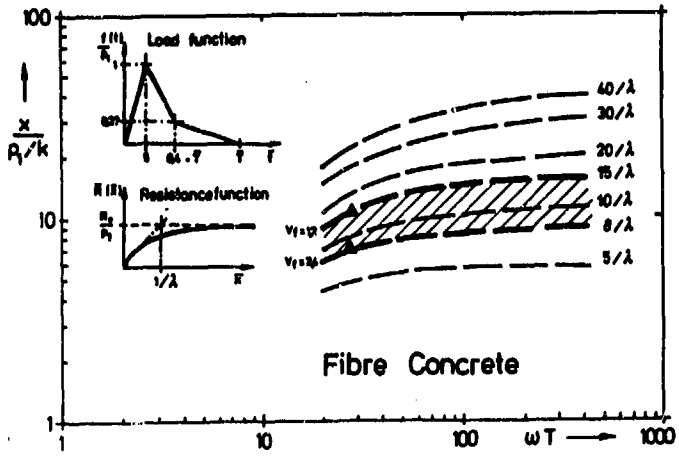

Fig. 8 Iso-damage curves for fibre concrete

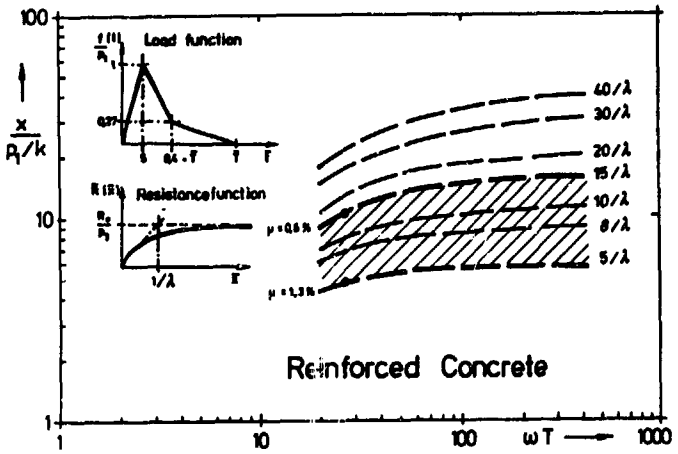

Fig. 9 Iso-damage curves for reinforced concrete

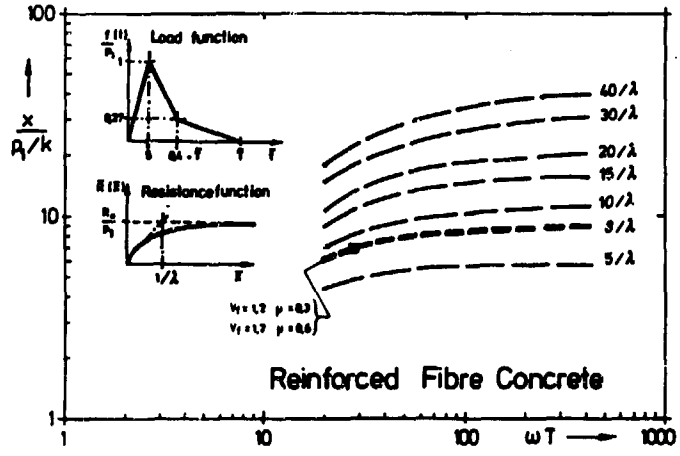

Fig. 10 Iso-damage curves for reinforced fibre concrete

In these diagrams the influence of fibre and steel content can be observed, based on the average of experimental results. The lower percentage of reinforcement leads to a higher working capacity of the slabs thus resulting in a higher deflection ratio for the ultimate load. The range of this ratio spans for the fibre concrete from $8/\lambda$ to $15/\lambda$, the precentage of the reinforcement varing from 2,4 % > V_f > 1,2 % (Fig.8). The influence of steel content presents Fig. 9 with 0,6 % < μ < 1,3 % and a corresponding deflection range from $15/\lambda$ to $5/\lambda$. The combination of fibre and steel reinforcement is displayed in Fig. 10. Here the fibre content is kept constant at V_f = 1,2 %, the steel reinforcement is varied from 0,3 % < μ < 0,6 %. This value has been chosen lower than in the cases before, because the use of fibre will only be reasonable for structures with low percentage of steel reinforcement as demonstrated in the static case. Comparing the deflection ratios as displayed in Fig. 9 the working capacity of the concrete reinforced by fibre and steel (Fig. 10) is improved. An ultimate deflection of $8/\lambda$ is obtained with a total reinforcement of 1,5 % < μ + V_f < 1,8 %, whereas in the case of Fig. 9 only $5/\lambda$ is reached with μ = 1,3 %.

For a ideal blast load and the global parameters as peak pressure P and impulse I, i.e. the integral of the pressure-time-function, a socalled P-I-diagram is developed (Fig.11). There is a transformation of a dimensionless deflection $\bar{x}$-$\bar{T}$- diagram(compare Fig. 7) carried through by $\bar{P} = 2/\bar{x}$ and $\bar{I} = \bar{T}/\bar{x}$ /3/. The lines of multiples of the elastic deformation are also displayed for the failure criteria as they are given by Fig. 8-10.

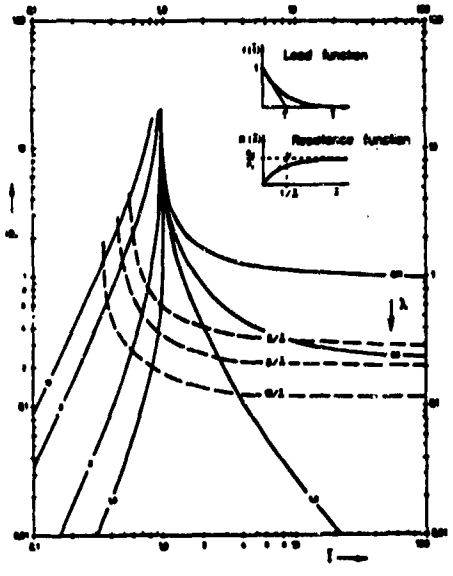

Fig. 11 Normalized P-I-diagram

Another importand difference between reinforced concrete and fibre concrete, the reducing of scabbing and spalling effects, is shown in Figs. 12 and 13.

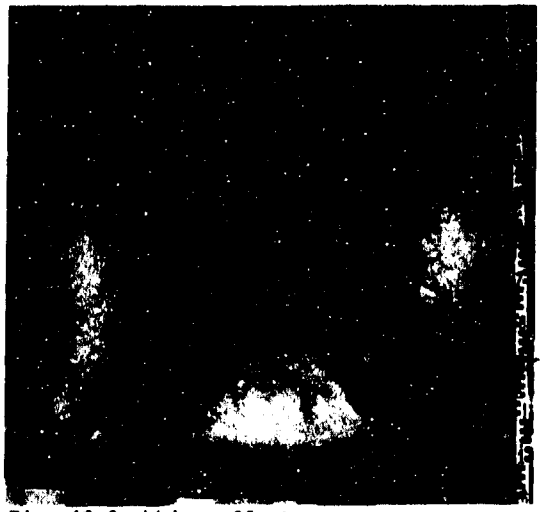

Fig. 12 Scabbing effect:
Conventional reinforced concrete

Fig. 13 Scabbing effect:
Fibre reinforced concrete

CONCLUSION

The experimental results for static and dynamic load, which have been presented here, show the advantages of fibre reinforcement for structural elements under multiaxial load and for low reinforcement ratios. The influence of fibre content has been discussed by introducing a efficiency factor $\varkappa$ for the static case. Here,ranges of interest for the use of fibre have been demonstrated for low percentage of steel reinforcement. The effect on the dynamic behaviour is presented combining the experimental results with those of a simplified numerical method. A dimensionless-P-I-diagram has been developed which allows the treatment of plates under ideal blast load.

BIBLIOGRAPHY

/1/ M.HUELSEWIG, C. MAYRHOFER
Endballistisches Verhalten von plattenförmigen Objekten aus Faserbeton bei punkt- und flächenhafter Belastung
E4/82, Ernst-Mach-Institut, Freiburg, März 1982

/2/ R.TEWES
LiteraturÜbersicht Faserbeton
Universität Stuttgart

/3/ W.E. BAKER, P.S. WESTINE, F.T. DODGE
Similarity Methods in Engineering Dynamics
Hayden Book Comp. Rochelle Park, New Jersey
(1973)

LINEAR SHAPED CHARGE PENETRATION, A PARAMETER STUDY

Charles E. Joachim

U. S. Army Engineer Waterways Experiment Station
Vicksburg, Mississippi

ABSTRACT

Research has shown that removal of large, partially damaged, concrete runway slabs is a major element in the time required to perform a runway repair operation. A rapid method for cleanly cutting away damaged sections would significantly reduce overall repair time. Shaped charges are potentially just such a rapid runway cutting technique. This paper presents the results of field tests designed to evaluate the effect of shaped charge parameters on runway cutting performance. A series of 39 explosive experiments was conducted on undamaged taxiway segments and aircraft shelter slabs constructed for a recent Air Force test program at the White Sands Missile Range, NM (WSMR). Additional tests were conducted on a runway slab constructed for another Air Force test program at Eglin AFB, FL. Parameters investigated include liner thickness, liner material, liner included angle, charge length, unit explosive loading, charge standoff, and, to a limited extent, runway material strength.

BACKGROUND

The U. S. Army Corps of Engineers is charged with responsibility for runway repairs at U. S. Air Force (USAF) airfields damaged by conventional attack when such repairs exceed USAF on-site capabilities. The importance of this wartime mission is obvious in light of our commitments in both Europe and the Near East, where rapid aerial reinforcement and resupply will be essential. Research on Repair and Restoration of Paved Surfaces (REREPS) has been conducted at the Waterways Experiment Station (WES) to develop an improved Army capability for rapid runway repair under combat conditions.

The REREPS research program has shown that removal of large, partially damaged, concrete runway slabs is a major element in the time required to perform a runway repair operation. A rapid method for cleanly cutting away the damaged portions of these slabs is needed to significantly reduce overall repair time. Initial investigations by the WES (Reference 1) demonstrated that linear shaped charges can successfully produce a rapid, relatively smooth cut through taxiways. This paper presents the results of later linear shaped charge tests designed to evaluate the effect of charge parameters on runway cutting performance.

OBJECTIVE

The study objective was to evaluate shaped charges as a means for rapidly cutting runways. Specific objectives were to evaluate the effect of: (1) liner parameters (thickness, material, and included angle), (2) charge variables (length, unit explosive loading, and standoff), and (3) target strength on linear shaped charge runway cutting performance.

APPROACH

The experiments described in this paper were performed on full-scale runway or taxiway pavements originally constructed for other test programs. A series of shaped charge pavement cutting tests was conducted on undamaged taxiway segments constructed for Air Force quantity-distance experiments on the White Sands Missile Range (WSMR), NM. Several WSMR tests were conducted on the intact floor slab of a full-scale aircraft shelter that had been destroyed. These taxiways and shelter floor slabs were built to design standards currently in use at USAF Europe Bases in Germany. Taxiway pavements consisted of 8-in.-thick unreinforced concrete slabs (6,000-psi unconfined compressive strength) overlain by 4 in. of asphalt, and underlain by a 6-in. stabilized aggregate base course over a compacted subgrade (Figure 1). The shelter floor slabs were 12-in.-thick unreinforced concrete (nominally 4,000-psi unconfined compressive strength) underlain by a 12-in. stabilized aggregate base course over a compacted subgrade (Figure 2).

The concrete runway segment tested at Eglin AFB was especially constructed for bomb penetration and cratering studies. The linear shaped charges were positioned to cut square holes through the pavement. In addition, one test was made to see how well the linear charges could be used to "square off" a small crater. The runway was 12 in. of unreinforced concrete (6,000-psi unconfined compressive strength) underlain by 6 in. of stabilized aggregate over a compacted subgrade (Figure 3).

The WSMR linear shaped charge parameter study investigated the effectiveness of nitromethane (NM) as the charge explosive. Charge containers 2, 3, and 4 ft long were used to evaluate the effect of charge length on penetration. The study also investigated the effect of liner thickness, liner

materials (aluminum, brass, and steel) and apex angles (60°, 90°, and 120°). In addition, one charge was scaled up in size to investigate scaling relations.

Initial runway cutting experiments at Eglin AFB were conducted with 4-ft-long linear shaped charges (Figure 4). Later tests used slightly larger steel-lined charges containing 20 lb/ft NM. Liner thickness was 1/4 in. Charges having 3/16-, 5/16-, and 3/8-in. liners were also tested to evaluate the effect of liner thickness on penetration.

RESULTS

Results of the linear shaped charge parameter study at WSMR, including shot geometry and penetration data, are presented in Table 1. Two experiments in this series were conducted with NM containers butted end-to-end (Shots 38 and 39). Only one container was boosted (on the end of the array) but the detonation was sustained through all the charges as shown by the relatively uniform cut over the entire length of the array.

The Eglin AFB runway cutting test results, including shot geometry and penetration, data are presented in Table 2. Initial tests using brass liners failed to completely cut the concrete. The penetrations shown in Table 2 are the average for the sides of the 4-ft-square cut. These shaped charges were less successful at cutting the concrete at the corners. (Note: Later tests with steel liners successfully cut the concrete all the way around the perimeter (6-ft square), including the corners.

The concrete slabs inside the square charge arrays were depressed 1 to 5 in. by the blast loads. This indicates that, although the brass-lined charges did not completely penetrate the runway, the unpenetrated concrete below the charges apparently failed in shear as a result of the load on the interior square. The depressed square was not severely fractured; in fact, it was too coherent to be removed with hand tools.

DISCUSSION AND CONCLUSIONS

The effect of normalized liner thickness (as a percentage of charge width) on scaled taxiway penetration is presented in Figure 5. These experiments were performed with brass liners having a 60° included angle. The charges were 4 in. wide by 3 ft long and were detonated at a 4-in. standoff. The height of the charge containers was varied to provide different explosive weights per unit charge length. Therefore, penetration data are scaled by dividing by the square root of the explosive weight per unit length. A single slab penetration datum point is included for comparison. The data shown in Figure 5 indicate little difference in penetration for brass liner thicknesses ranging from 3.1 to 6.3 percent of the charge width. A rapid decrease in penetration was noted for brass liners less than 3.1 percent of the charge width. Thus, the minimum thickness of brass liners for efficient penetration with NM linear shaped charges is 3.1 percent of the charge width.

The effect of liner material on penetration is presented in Figure 6. Three liner materials were investigated: steel, brass, and aluminum. Although the data are limited and there is some scatter, a general trend is indicated. Steel-lined charges produced greater penetration than either aluminum or brass for any liner thickness. The results also indicate that the aluminum liners may be more efficient than brass, but the data for the two materials show a great deal of scatter over the limited number of experiments performed. These data show that the minimum liner thickness for efficient cutting with steel and aluminum liners in NM linear shaped charges is approximately 4.7 percent of the charge width.

The influence of the included angle of the liner is presented in Figure 7. Charges used in this comparison were 3 ft long with a 0.1875-in.-thick brass liner (4.7 percent of the charge width). The curve shown in Figure 7 is drawn through the mean of the taxiway penetration data. Although there is considerable data scatter, the graph indicates a general trend of decreasing penetration as the liner included angle is increased.

Scaled penetration data from four brass-lined charges detonated on the concrete shelter slab are plotted in Figure 7 for comparison with the taxiway data. One charge design (60° liner included angle) was tested at two standoff distances, one and two charge widths above the shelter slab. Although these data are limited, a general trend can be seen: (1) increased standoff reduced penetration, and (2) shelter slab penetration tends to be greater than corresponding taxiway data.

The effect of the length of the linear shaped charge on penetration is presented in Figure 8. All charges used for this comparison have a 0.1875-in.-thick brass liner (4.7 percent of the charge width) and an included angle of 60°. The taxiway data shows an increase in scaled penetration with increasing scaled charge length up to a scaled length of 1.2 ft/lb$^{1/2}$. As the scaled charge length increases further, scaled penetration should approach a constant value. As shown in Figure 8, a maximum scaled penetration (dashed horizontal line) of 0.29 ft/lb$^{1/2}$ was assumed for the taxiway data. Although only two shelter slab penetration data points were obtained, a similar relation (dashed lines) was assumed as shown in Figure 8. Additional data are required to further refine these curves.

The curves shown in Figure 8 imply that the minimum charge length for complete pavement penetration is dependent on the pavement thickness. For example, assuming a maximum scaled penetration of 0.29 ft/lb$^{1/2}$, complete penetration of a 1-ft-thick taxiway requires an NM charge loading of $(1+0.29)^2$ = 11.9 lb/ft and a maximum charge length of $1.2(11.9)^{1/2}$ = 4.1 ft. Similarly, complete penetration of an 18-in. thick taxiway requires an NM charge loading of $(1.5+0.29)^2$ = 26.8 lb/ft and a

charge length of $1.2(26.8)^{1/2} = 6.2$ ft. Thus, increasing the pavement thickness requires a corresponding increase in the minimum charge loading and minimum charge length for efficient penetration.

Penetration is plotted versus explosive loading per unit length in Figure 9. Data from the 1982 (Reference 1) and 1983 WSMR tests are presented. The scaling relation suggested in Reference 1,

$$p = 0.29w^{1/2}$$

is included for comparison,

where:

p = penetration, ft
w = charge loading per unit length, lb/ft.

As shown here, the equation provides a reasonably good fit to the data. The shelter concrete slab penetration datum point falls slightly above the assumed relation, indicating less NM was required to breach the slab than the taxiway.

The effect of charge standoff on penetration is shown in Figure 10. Penetration data are scaled by the square root of the explosive weight per unit length to eliminate the effect of NM charge loading variations. All the NM charge containers were 4 in. wide, with the unit charge loadings varied from 7.0 to 12.7 lb/ft. An upper bound to the taxiway penetration data is presented in Figure 10. These data show that the NM linear shaped charge produced maximum penetration at one charge width standoff.

Dimensional analysis was applied to the data producing the dimensionless relation shown in Figure 11. The parameters involved in the relation are:

penetration, p, ft
liner thickness, t, ft
explosive detonation velocity, V, ft/sec
target unconfined compressive strength, σ, psf
charge explosive loading, w, lb (per foot of charge length)
charge length, l, ft
and target mass density, ρ, $lb/sec^2/ft^4$.

Figure 11 relates the penetration (dimensionalized) to explosive loading, charge geometry, and target characteristics. Although these data exhibit considerable scatter, a general linear trend can be seen. The curve shown in Figure 11 was obtained by least square fit.

REFERENCES

1. Joachim, Charles E. 1983 (May). "Rapid Runway Cutting with Shaped Charges," Symposium Proceedings, The Interaction of Non-Nuclear Munitions with Structures, U.S. Air Force Academy, Colorado Springs, CO.

TABLE 1

1983 WSMR Runway Breaching Study Test Plan and Results

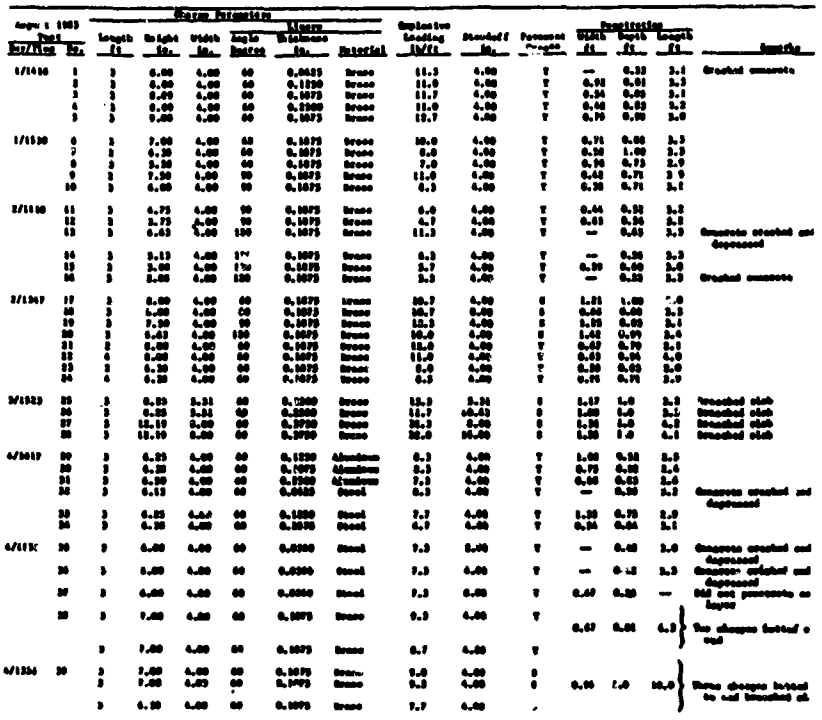

TABLE 2

EGLIN AFB RUNWAY BREACHING STUDY TEST PLAN AND RESULTS

Test No.	Test Date	Charge Parameters: Type*	Length ft	Height in.	Width in.	Liner: Thickness in.	Liner: Material	Explosive Loading lb/ft	Standoff in.	Penetration Depth ft	Remarks
1	9/27/83	MK	4	8	4	0.1875	Brass	11.1	4	0.79	4 charges, square array, center slab depressed 1 in.
2	9/27/83	MK	4	8	4	0.1875	Brass	~11	4	0.58	4 charges, square array, center slab depressed 2 in.
3	9/27/83	MK	4	8	4	0.1875	Brass	~11	4	0.67	4 charges, square array, center slab depressed 2 in.
4	9/27/83	MK	4	8	4	0.1875	Brass	~11	4	—	4 charges, two 8 ft perpendicular legs along edge of penetration crater, too close to crater, concrete shattered not cut
5	1/17/84	MK	3	11	3	0.250	Steel	~20	4	1.0	8 charges, 6 ft square array, center slab depressed 3 in.
6	1/18/84	MK	3	11	3	0.250	Steel	20	4	1.0	8 charges, 6 ft square array, center slab depressed 3 in.
		TOW			5††		Copper	5.4†	9.6**	0	Warhead at center of array, blown over before it detonated
7	1/18/84	TOW			5††		Copper	5.4†	0	>1.0	Warhead at center of slab cut by Test 6
8	1/18/84	MK	3	11	4	0.250	Steel	~20	4	1.0	8 charges, 6 ft square array, center slab depressed 3 in.
		TOW			5††		Copper	5.4†	9.6**	>1.0	Warhead detonated simultaneously at center of array, produced elongated hole 0.3 by 0.25 ft, long dimension parallel lead plates
9	1/19/84	MK	3	11	4	0.250	Steel	~20	4	—	8 charges, 6 ft square array, TOW detonated buried MK-82 GP bomb
		TOW			5††		Copper	5.4†	9.6	—	Warhead detonated simultaneously at center of array
10	1/19/84	MK	4	11	4	0.250	Steel	~26	4	1.0	5 charges end to end (20 ft), detonated from end of line
11	1/19/84	MK	4	11	4	0.1875	Steel	~20	4	1.0	2 in. wide uniform cut
		MK	4	11	4	0.313	Steel	~20	4	1.0	2 to 3 in. wide cut
		MK	4	11	4	0.375	Steel	~20	4	1.0	2 to 3 in. wide cut

* Types were either nitromethane (MK) linear shaped charges or Tube-launched, Optically-tracked, Wire-guided antitank warhead.
** Warhead taped between two lead plates (one-quarter of circumference each), plates 10 cm thick by 12 inches long.
† Composition B, total charge weight, lb.
†† Diameter, in.

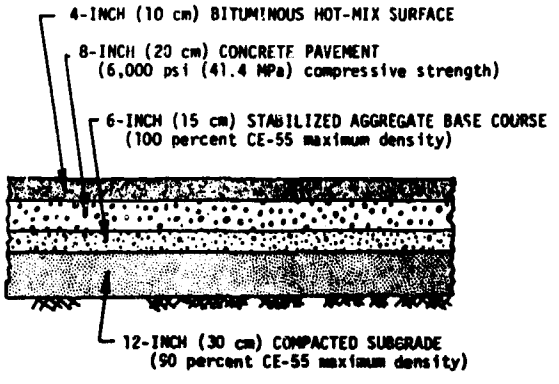

Figure 1. Typical DISTANT RUNNER taxiway cross-section. "CE-55" refers to a Corps of Engineers standard compactive effort.

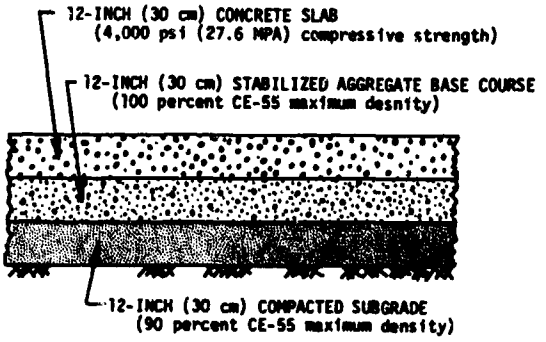

Figure 2. Typical DISTANT RUNNER shelter slab cross-section.

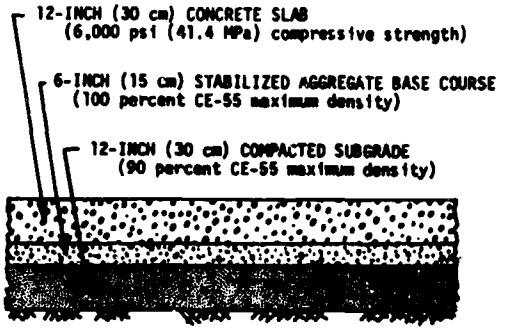

Figure 3. Typical runway cross-section, site C-72, Eglin AFB, FL.

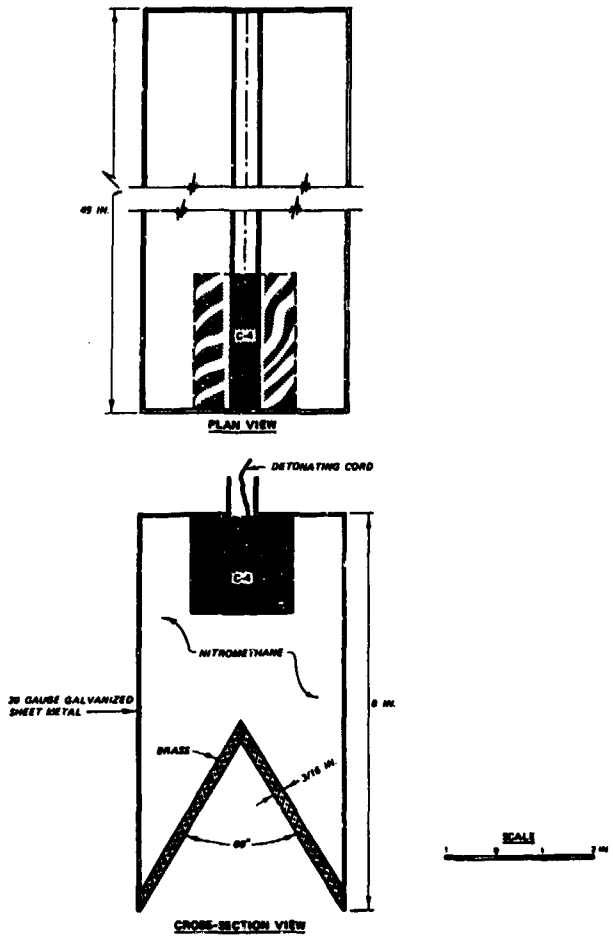

Figure 4. Design of 12-lb/ft (18 kg/m) NM linear shaped charge.

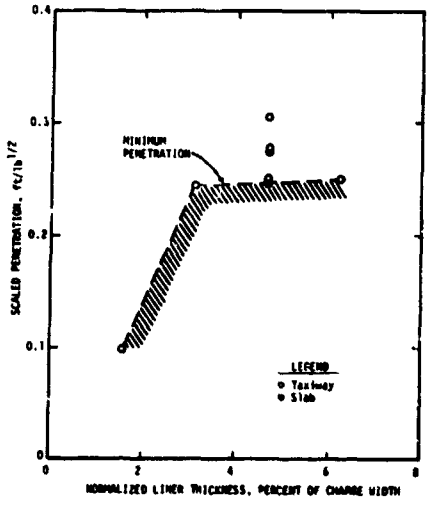

Figure 5. Effect of liner thickness on pavement penetration. The NM linear shaped charges were 3 ft long by 4 in. wide with brass liners and 60° included angle. Charge standoff was one charge width.

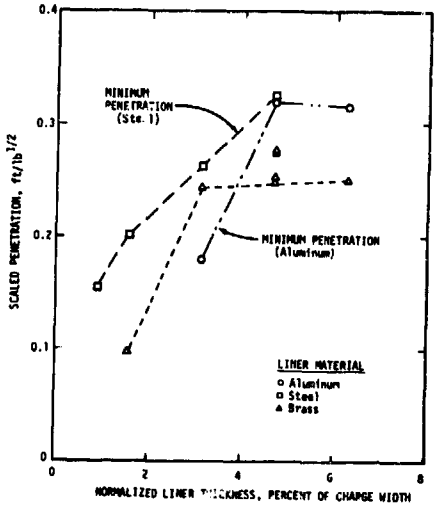

Figure 6. Effect of liner material on penetration. The NM linear shaped charges were 3 ft long by 4 in. wide with a 60° included angle. Charge standoff was one charge width above the taxiway surface.

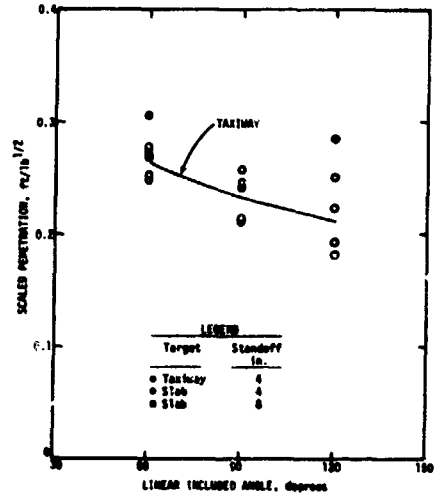

Figure 7. Scaled penetration versus liner included angle. The NM linear shaped charges were 3 ft long by 4 in. wide with brass liners 0.1875 in. thick.

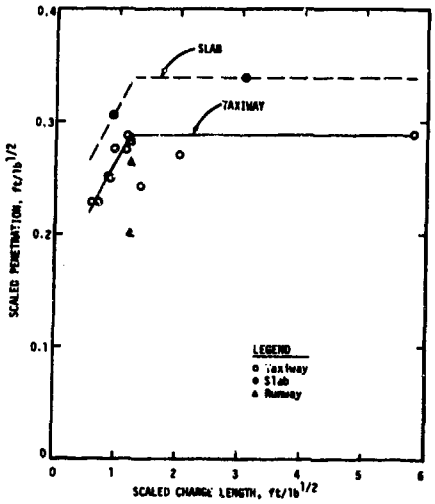

Figure 8. Scaled penetration versus charge length. The NM linear shaped charges were 4 in. wide with brass liners 0.1875 in. thick and an included angle of 60°. Charge standoff was one charge width.

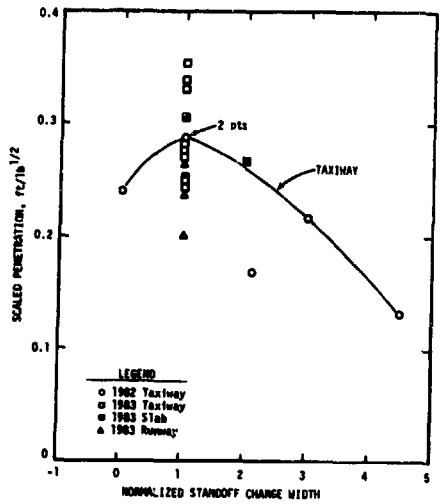

Figure 10. Scaled penetration versus normalized charge standoff. The NM linear shaped charges were 4 in. wide with brass liners 0.1875 in. thick and an included angle of 60°.

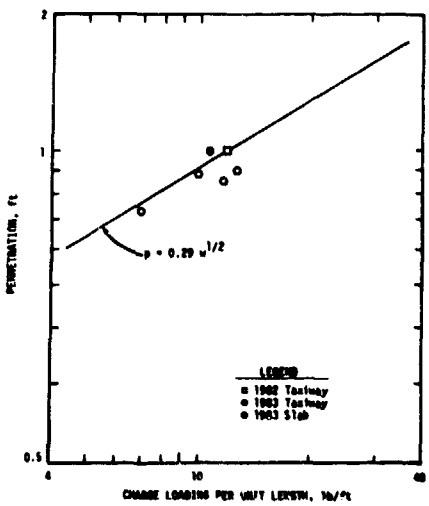

Figure 9. Penetration versus charge loading per unit length. The NM linear shaped charges were 4 in. wide with brass liners 0.1875 in. thick and an included angle of 60°. Charge standoff was one charge width.

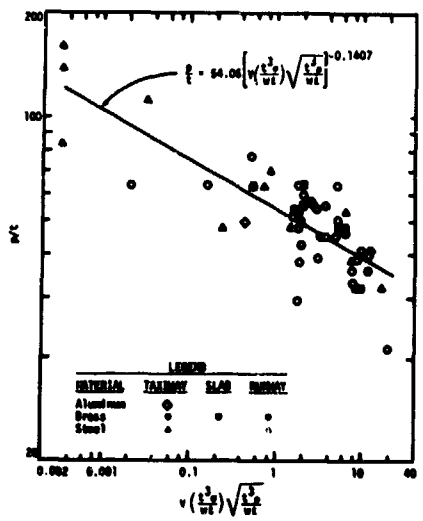

Figure 11. Nondimensional parameters relating penetration (p) to explosive properties (detonation velocity, V , and unit loading, w) charge geometry (liner thickness, t , and charge length, ℓ) and target material properties (uncomfined compressive strength, σ , and mass density, ρ .

OPTIMIZATION OF A 90 MM SHAPED CHARGE WARHEAD

David K. Davison

Physics International Company
San Leandro, California, USA

Bertil K. Arvidsson

Bofors Ordnance
Bofors, Swedan

ABSTRACT

Physics International's Reverse Engineering technique was applied to the design of a liner for a Bofors 90 mm shaped-charge warhead. A constrained optimization procedure was used in conjuction with the method to derive the unique liner shape and thickness profile that satisfied the specified constraints on performance.

Radiograph tests verified the significant increase in charge efficiency predicted by the calculations. Computed jet particle trajectories matched the observed trajectories very closely, and the expected jet velocity profile was confirmed.

The unique characteristics of the jet and the exceptional efficiency of the optimized charge make it an alternative candidate for applications where conventional shaped charges are inadequate.

The Reverse Engineering method used to design the Bofors 90 mm warhead is a universal technique in which targets are characterized by their shapes and their material properties. It is a method that can be adapted to the problem of defeating a variety of structures. Several examples are included for illustration.

INTRODUCTION

In the present paper we describe work that was performed to improve a Bofors charge with a baseline trumpet-shaped liner, designated the 77-3 design. We describe its optimization through Physics International's Reverse Engineering technique; we compare the methods used in fabricating the optimized liners; and we discuss the results of the tests that have been performed to verify the concept.

Figure 1 is a picture of the Bofors charge and a typical target arrangement. In the figure components are identified with generic categories that are factors in the derivation of optimized shaped charge designs. In the case of the 77-3 charge improvement, the goal was to replace the standard trumpet-shaped liner with an optimized one. Since the shape of the optimized liner was different from that of the standard one, the volume and the shape of the explosive changed as a result of the effort.

At Physics International (PI) the Reverse Engineering technique employs two optimization methods that make extensive use PI's proprietary computer programs and its database of charge designs and test results. The first optimization method, called

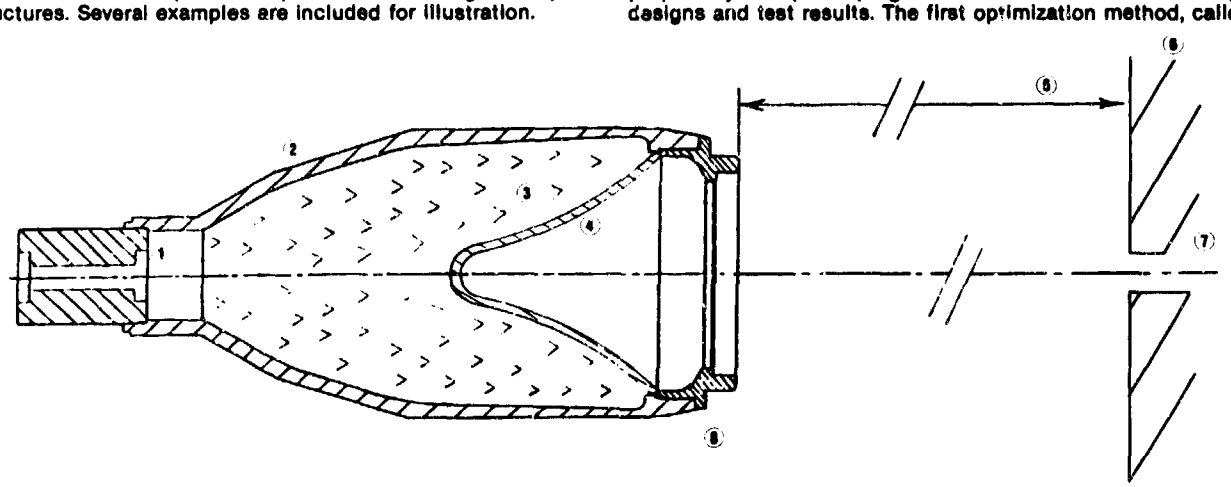

Figure 1. Parameters affecting the duality between a shaped charge warhead and its target:

Index	Description	Baseline 90 mm Warhead	Optimized 90 mm Warhead	
1	Initiation	Control, RDX Booster, 47 gm Plug	(same)	
2	Confinement	Steel, 1233 gm; Base Ring 190 gm	(same)	
3	Explosive	Octol, 1.82 gm/cc, 755 gm	(same)	1000 gm
4	Liner	Copper, Cold Forged, 325 gm	Copper	
5	Standoff	7.5 Caliber	9.0 Caliber	
6	Target	Armor, 2.5 cm plates	(same)	
7	Behind-Armor Effects	—	Maximum	
8	Symmetry	—	—	

Incremental Modification, obtains the required design by a small modification of an existing baseline warhead. It is a low-risk approach, but the improvement is limited by the characteristics of the baseline design. For the alternative Constrained Optimization method, the objective is the "best" charge for the application. A radical departure from the baseline is typical, but the charge efficiency is generally improved. It is a high-risk approach with a greater cost that is justified by projected performance improvement. It may require the use of Incremental Modification to arrive at the final design.

For the improvement of the 90 mm 77-3 design, the preliminary calculations showed a significant increase in performance when alternative liner shapes were tried. Hence it was decided that the use of the Constrained Optimization method was justified. A major criterion that guided the optimization task was the achievement of a maximum jet kinetic energy that was significantly greater than that of the baseline design of Figure 1. The damage that a jet can deliver to a target is proportional to its kinetic energy; the Target Inversion computer program provided the means by which the damage could be partitioned most effectively to achieve the desired residual effect.

The 90 mm warhead improvement effort described here is only one application of the Reverse Engineering method. For the 90 mm warhead the required performance could be characterized by damage to a thick steel target. When applied to the task of optimizing a design for defeat of typical structures, analogous criteria are applied. Several examples are described below.

DESIGN APPROACH

The objective of the program was to obtain an optimized liner design for the 90 mm Bofors Type 77-3 warhead capable of penetrating 70 cm (7.8 calibers) of armor at 9.0 calibers standoff with as large an exit hole as feasible. Maximum behind-armor spall damage is associated with a large exit hole. To achieve this goal a constrained optimization technique was used in conjunction with the PI-proprietary Target Inversion computer program. The resulting optimized liner was refined with an iterative scheme in which the liner thickness profile was varied until the computed PISCES 2D ELK (Reference 1) jet velocity profile matched the optimum one.

The optimization constraints were chosen to yield a design with a coherent jet of maximum kinetic energy that would be effective at the given standoff. The weights, jet energies, and liner inner surface shapes of the candidate designs were monitored to assure that the chosen design would be a practical concept. The outcome of the process was the simultaneous derivation of an optimum liner shape and an optimum jet velocity profile.

The optimum liner shape (outer contour) was not varied in the 2D ELK Iterative Refinement. After the initially-converged liner design had been tested, a second design with the same outer contour and with a modified thickness profile was derived to incorporate test observations and an improved jetting algorithm.

The initial tests verified the significant increase in charge efficiency predicted by the calculations, but the predicted penetration and hole diameter were not achieved. Future tests are planned to resolve this discrepancy.

TARGET INVERSION OPTIMIZATION

The Target Inversion computer program takes as input the charge description, except that only the outer contour of the liner is specified. It derives the liner thickness profile and inner contour from a specified hole shape and from conditions on the collapse and jet velocity at the apex of the liner.

Jetting values are computed by the analytical method described in Reference 2. The jet velocity V_j is the sum of the magnitudes v and V_c in Figure 2. The collapse velocity V_c is the velocity of the liner material as it strikes the axis of symmetry. The collapse angle is the angle β between the liner and the axis at the moment of impact.

The Target Inversion code uses a hydrodynamic penetration model (Reference 3) in which the incremental penetration Δp is given by

$$\Delta p = \Delta L_j / r\gamma \qquad (1)$$

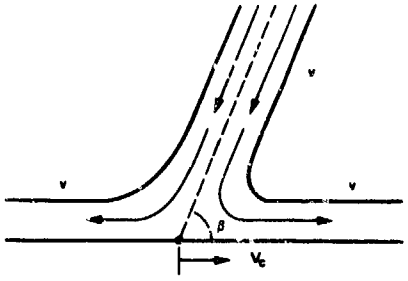

(A) DIAGRAM OF THE FLOW IN THE VICINITY OF THE COLLAPSE POINT.

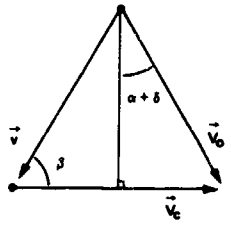

(B) VECTOR DIAGRAM FIXING THE RELATIONSHIP BETWEEN THE VECTORS $\vec{v}$, $\vec{V}_0$, AND $\vec{V}_c$, THE COLLAPSE ANGLE β, AND THE ANGLE $\alpha + \delta$, AT THE COLLAPSE POINT.

Figure 2. Collapse point geometry. $\vec{v}$ is the relative velocity of the liner material with respect to the collapse point, β is the collapse angle, V_c is the collapse point velocity, V_0 is the liner collapse velocity, α is the liner angle, and δ is the Taylor angle. Upper-case values are evaluated in a stationary frame. The lower-case relative velocity $\vec{v}$ is evaluating in a frame moving at the velocity $\vec{V}_c$.

where L_j is the length of the jet increment including air spaces (after breakup), r is the ratio of L_j to the length of the solid particles in the jet ($r \geq 1$), and $\gamma = \sqrt{\rho_t/\rho_j}$ for respective target and jet densities ρ_t and ρ_j. The rate of penetration is given by

$$u = V_j/(r\gamma + 1) \qquad (2)$$

When the penetration rate is small, the strength of the target material is greater than the dynamic pressure resulting from the jet impact, $\rho_j u^2/2$, and penetration ceases. This occurs when the jet velocity is small and when the breakup factor, r, is large. It is desirable to have as large a breakup time as possible, because the penetration increases when the breakup time increases.

The breakup time and the target's specific energy (ratio of jet energy to hole volume) were assumed to be constant. The use of a variable breakup time has been recently suggested (Reference 4) for liner optimization studies. The steel target specific energy was assumed to be 4000 Joule/cc.

For most of the calculations the breakup time was assumed to be 135 μs, relative to the time of initiation of the Octol explosive charge. The 135 μs breakup time is a nominal value for an optimized 90 mm charge when measured relative to the virtual origin time (Reference 5); analysis of the 77-3A jet retrospectively revealed that the choice was conservative.

For the inversion calculation the shaped charge is modeled as a sequence of disklike "slices," each of which can be treated as a one-dimensional problem insofar as the liner collapse is concerned. When a 2D ELK calculation of a similar shaped charge has been previously performed, the one-dimensional collapse velocities can be corrected to obtain a more accurate result. The estimated jet energy profiles in the one-dimensional calculations are in error when the correction factors are omitted. The 77-3 liner optimization was performed in three stages, each distinguished by the correction factor profile applied to the collapse velocities.

The design parameters computed by the Target Inversion program in the course of the optimization are listed in Table 1. Each design

is designated by a string of three symbols that respectively define the liner shape, the apex collapse and jet velocities, and the hole shape. Table 2 lists the liner shapes tried; the parameterization is illustrated in Figure 3. Tables 3 and 4 list the velocities and the hole shapes.

Experiments at Physics International of jets penetrating steel targets indicate that the target specific energy may be greater at the bottom of the hole than at the entrance. The reverse taper of the holes indexed 4 to 9 correspond accordingly to experimental holes that should be, at the worst, approximately constant in diameter to a depth of 70 cm and bulbous at the bottom. The energy distribution in a target with such a hole is concentrated deep inside, where it should be.

The collapse velocity correction factor profiles are illustrated in Figure 4. For the first stage of the optimization, the correction factor profile for the Bofors baseline trumpet design was used. Four favorable designs were obtained; they are indexed 7, 8, 16, and 20 in Table 1. All four designs had bell- or tulip-shaped liners. The D13 design (index 8) was considered the best of these, and a 2D ELK jetting calculation was performed to obtain an improved correction factor profile for the second stage of the optimization. In the second stage, several liner shapes were tried; the hole was made more narrow to improve the penetration; and the X55 design was selected for derivation of the correction factors to be used in the final stage of the optimization. In the final stage, the liner shape was fixed, and the apex velocities and the hole shape were varied to obtain the most suitable design.

Figure 5 shows six of the designs described in Table 1. Figures 5a, 5b, 5d, and 5e are the four designs derived in the first stage of the optimization. Figure 5c is an example of a trumpet-shaped liner. Trumpet-shaped liners gave low-energy jets in the study, and bell- or tulip-shaped liners were favored accordingly. Figure 5f is the design selected for Iterative Refinement and eventual fabrication.

The entries at the top of Table 1 are the optimization constraints. The limits are imposed to assure that the jet will be coherent, that the liner can be fabricated, that the computed penetration value is valid, and that the design satisfies the limits on weight, energy, and penetration. The optimimum X38A design derived from analysis of the entries in Table 1 was the unique "best" choice among those that were tried, and it was considered to be the candidate most likely to attain the required performance. The

Table 1. Summary table of computed values for the Target Inversion calculations. For designs indexed 1 to 20, the Baseline Trumpet collapse velocity correction factor profile was used (Figure 2); for designs indexed 21 to 37, the D13 correction factors; and, for designs indexed 38 to 49, the X55 correction factors. In the table headings maxima and minima are signified by respective up and down arrows (↑ and ↓). V_0 is the collapse velocity, V_j is the jet velocity, τ is the thickness, β is the collapse angle, v is the velocity relative to the collapse point, α_i is the slope angle of the inner (metal-air) surface of the liner, u is the rate of penetration, MHE is the high explosive mass, ML is the liner mass, MTOT is the total mass, KE is the jet kinetic energy (the number in parentheses is the ratio of the jet energy to the explosive chemical energy), and p is the penetration for the given hole shape. The numbers above the table headings are the optimization constraints. Designs are designated by a string of symbols. The first symbol describes the liner shape (Table 2); the second, the apex collapse and jet velocities (Table 3); and the third, the hole shape (Table 4). The tabulated explosive and liner masses include 26 gm each of material not included in the Target Inversion calculations.

I	Design	.40/.09 Vol/Vol (cm/μs)	1.10/.40 Vj↑/Vj↓ (cm/μs)	.50/.09 τ↑/τ↓ (cm)	-/25 β↑/β↓ (deg)	.44 v↑ (cm/μs)	2.0 α↑ (deg)	.10 u↓ (cm/μs)	MHE (gm)	ML (gm)	1050 MTOT (gm)	600 KE(%) (KJ)	70.0 p (cm)
1	A11	.39/.12	.98/.48	.34/.06	50/32	.42	3.1	.13	487	494	981	872(36)	70.8
2	A21	.40/.13	.98/.47	.31/.05	51/33	.44	3.4	.13	487	363	820	843(36)	71.8
3	B21	.39/.13	.98/.46	.34/.06	49/33	.44	2.3	.13	504	412	916	862(33)	72.6
4	B32	.36/.08	.90/.31	.68/.08	50/28	.40	-1.2	.07	504	715	1219	700(29)	81.5
5	B33	.16/.09	.90/.40	.55/.06	49/27	.40	-0.1	.11	504	626	1130	814(30)	71.8
6	C33	.31/.09	.90/.40	.49/.09	42/28	.42	1.7	.11	486	564	1050	817(31)	72.0
7	C13 +	.33/.11	.95/.43	.41/.09	43/30	.44	2.5	.12	486	473	959	847(33)	74.0
8	D13 + *	.35/.11	.95/.43	.41/.08	47/29	.43	2.4	.12	472	471	943	848(34)	74.1
9	E13	.36/.11	.95/.44	.38/.08	48/30	.43	1.6	.13	422	409	831	834(37)	73.2
10	F13	.33/.11	.95/.44	.38/.09	47/30	.44	1.8	.13	436	413	849	836(36)	73.2
11	F33	.31/.10	.90/.40	.46/.09	46/28	.42	1.1	.11	436	494	930	811(35)	71.5
12	G33	.30/.10	.90/.40	.44/.08	44/25	.43	1.4	.10	448	476	924	803(34)	71.0
13	G13	.31/.12	.95/.43	.36/.08	45/31	.46	1.9	.12	448	400	843	827(35)	72.7
14	H33	.30/.13	.93/.46	.49/.06	39/25	.45	6.7	.15	893	896	1299	721(19)	64.4
15	H13 #	.30/.15	.95/.47	.42/.06	37/27	.47	7.5	.15	893	518	1211	786(29)	68.0
16	I33 +	.30/.10	.90/.40	.46/.08	39/29	.43	4.8	.11	499	542	1041	809(30)	71.4
17	I13	.30/.11	.95/.43	.39/.08	40/30	.46	5.1	.12	499	458	957	839(31)	73.5
18	J33	.30/.12	.90/.47	.63/.06	39/23	.45	3.7	.16	843	754	1397	716(21)	64.6
19	K33	.30/.12	.90/.50	.73/.06	39/20	.45	-0.5	.19	883	785	1468	669(19)	60.2
20	L43 +	.34/.10	.93/.41	.43/.08	46/28	.42	2.5	.10	470	496	948	826(33)	72.6
21	M64	.22/.10	.90/.44	.35/.11	34/25	.43	6.7	.15	486	543	1029	847(25)	67.8
22	N64	.21/.10	.90/.44	.35/.10	34/25	.44	6.7	.15	493	543	1036	848(24)	67.8
23	O64	.20/.10	.90/.43	.39/.10	31/26	.44	6.1	.12	536	596	1132	836(22)	66.9
24	P64	.23/.10	.90/.44	.35/.11	36/25	.43	6.1	.15	466	519	985	848(26)	67.9
25	Q64	.21/.10	.90/.43	.40/.11	31/25	.43	6.1	.11	529	590	1128	838(22)	67.1
26	R64	.23/.10	.90/.46	.34/.11	37/25	.43	1.9	.16	441	478	919	843(27)	67.4
27	S64	.26/.10	.90/.43	.34/.11	41/25	.43	6.1	.15	399	432	831	831(30)	66.5
28	T64	.22/.10	.90/.45	.36/.11	34/25	.43	5.9	.15	486	550	1039	848(26)	67.9
29	U64	.23/.10	.90/.44	.35/.11	35/25	.43	3.8	.15	445	496	941	847(27)	67.8
30	V64	.23/.10	.90/.45	.36/.11	36/25	.43	2.9	.15	449	506	955	848(27)	67.9
31	W64	.23/.10	.90/.43	.33/.10	37/25	.43	6.5	.15	503	486	989	850(24)	68.7
32	X65	.23/.08	.90/.46	.42/.10	38/24	.43	6.2	.12	503	581	1084	826(23)	73.8
33	P66	.22/.08	.90/.40	.45/.11	36/23	.43	4.7	.13	486	616	1082	818(25)	73.3
34	W66	.25/.09	.90/.40	.39/.09	41/25	.43	6.6	.12	517	516	1033	834(23)	74.3
35	X66*	.25/.09	.90/.40	.40/.09	42/25	.43	4.6	.12	518	530	1048	837(23)	74.5
36	X66	.26/.09	.90/.41	.37/.09	42/25	.43	4.9	.13	518	496	1014	847(23)	73.1
37	X67	.25/.09	.90/.42	.38/.09	42/25	.43	4.9	.13	518	510	1028	843(23)	72.2
38	X56	.25/.08	.90/.40	.43/.10	42/24	.43	4.1	.11	518	570	1088	824(23)	76.5
39	X56	.25/.09	.90/.41	.39/.10	42/25	.43	4.4	.12	518	534	1052	836(24)	74.2
40	X66	.27/.10	.93/.43	.36/.10	43/25	.45	4.8	.13	518	470	987	851(24)	75.2
41	X76	.26/.09	.90/.40	.39/.09	42/25	.43	4.4	.12	518	530	1048	840(24)	74.3
42	X76	.26/.09	.90/.42	.36/.09	42/26	.43	4.8	.13	518	496	1014	878(24)	72.7
43	X74	.26/.10	.90/.43	.33/.09	42/27	.43	5.1	.14	518	466	984	888(25)	70.8
44	X86*	.26/.10	.91/.42	.36/.10	42/26	.44	4.9	.13	518	483	1001	881(24)	73.0
45	X84	.26/.10	.90/.43	.33/.08	42/27	.43	5.1	.14	518	483	981	897(25)	70.8
46	X76 A	.26/.09	.90/.41	.37/.09	42/26	.43	4.8	.12	518	506	1024	873(24)	72.5
47	X86 A	.26/.10	.91/.41	.36/.10	42/26	.44	4.7	.13	518	492	1010	878(24)	72.8
48	X86 B	.26/.09	.91/.38	.46/.10	43/26	.44	3.9	.10	518	527	1045	868(24)	72.0
49	X86 A	.25/.07	.91/.36	.50/.10	43/23	.44	2.1	.09	518	623	1141	837(23)	70.5

Suffix	Description
+	Favorable design from first series
*	Design computed with 2D ELK
#	Example of trumpet-shaped liner
A	Detonation point shifted from (-2.0 cm, 6.3 cm) to (-3.66 cm, 6.3 cm)
B	Breakup time changed from 136 μs to 126 μs

jet velocity profile of the X88A design was selected as the velocity profile toward which the 2D ELK Iterative Refinement would converge; it is shown in Figure 6.

Table 2. Liner shapes for the optimization calculations. The liner contours were continuous piecewise conics with continuous slope angles at single, intermediate join points. Liners H, J, and K had no join point. All liners extended from coordinate x = −1.0 cm to x = 11.9 cm; the radius at x = 11.9 cm was 3.9 cm, a constraint imposed by the hardware.

Liner Shape							
	Apex (x = -1.0cm)		Center			Base (x = 11.9cm) (r = 3.9cm)	
Symbol	r(cm)	α(deg)	x(cm)	r(cm)	α(deg)	α(deg)	Description
A	1.0	30	7.0	3.2	6	10	bell
B	1.0	30	7.0	3.0	6	12	bell
C	1.0	20	7.0	3.2	6	10	bell
D	1.0	25	7.0	3.2	6	10	bell
E	1.0	25	7.0	3.4	5	8	bell
F	1.0	20	7.0	3.4	5	8	bell
G	1.0	15	7.0	3.4	8	5	tulip
H	0.8	10	-	-	-	20	trumpet
I	1.0	15	7.0	3.2	10	8	tulip
J	1.2	10	-	-	-	20	trumpet
K	1.2	10	-	-	-	25	trumpet
L	1.0	30	2.4	2.2	14	5	tulip
M	1.2	15	7.0	3.2	10	8	tulip
N	1.2	12	7.0	3.2	10	8	tulip
O	1.2	12	7.0	3.0	10	8	tulip
P	1.2	15	6.5	3.2	10	8	tulip
Q	1.2	15	7.0	3.0	10	8	tulip
R	1.2	15	7.0	3.4	10	8	bell
S	1.2	15	6.0	3.4	10	8	bell
T	1.2	15	7.0	3.2	10	10	bell
U	1.2	15	6.0	3.2	10	8	bell
V	1.2	15	6.0	3.2	10	10	bell
W	0.8	15	7.0	3.2	10	8	tulip
X	0.8	15	7.0	3.2	8	10	bell

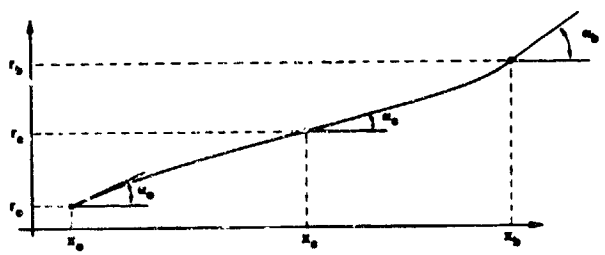

Figure 3. Liner shape parameterization. The liner contour is piecewire cubic between the indicated points. Parameter values are indicated in Table 2.

Table 3. Collapse velocities V_o and jet velocities V_j for the liner apex in the optimization calculations.

Index	Vo (cm/μs)	Vj (cm/μs)
1	0.300	0.950
2	0.300	0.980
3	0.300	0.900
4	0.280	0.925
5	0.200	0.900
6	0.200	0.930
7	0.210	0.900
8	0.200	0.910
9	0.220	0.900

Table 4. Hole shapes for the optimization calculations. d_1 is the diameter at the target surface; d_2 is the diameter corresponding to the penetration p_2; and d_3 is the diameter at the penetration of 100 cm.

Index	d_1(cm)	p_2(cm)	d_2(cm)	d_3(cm)
1	2.10	76	1.85	1.85
2	1.75	-	1.75	1.75
3	1.80	70	2.00	4.00
4	1.50	70	2.00	4.00
5	1.20	70	2.00	4.00
6	1.30	70	2.00	4.00
7	1.20	70	2.10	4.00
8	1.40	70	2.00	4.00
9	1.20	70	1.80	4.00

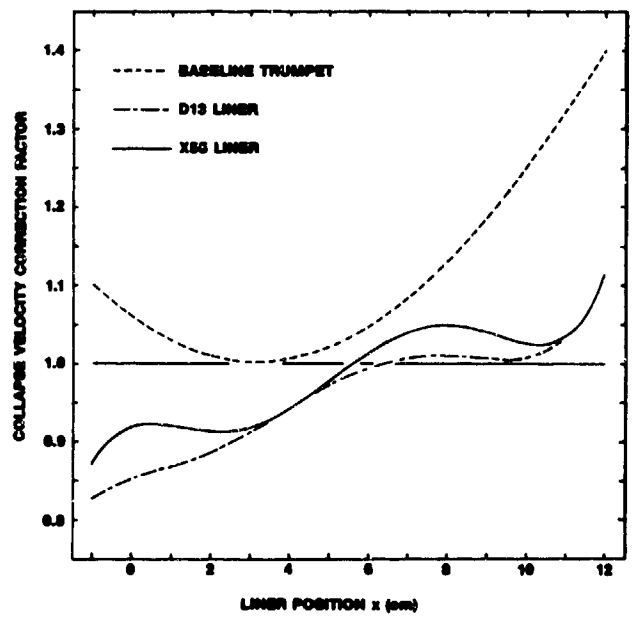

Figure 4. Collapse velocity correction factor profiles. Collapse velocity correction factors are ratios of collapse velocities in two-dimensional calculations to those in one-dimensional calculations.

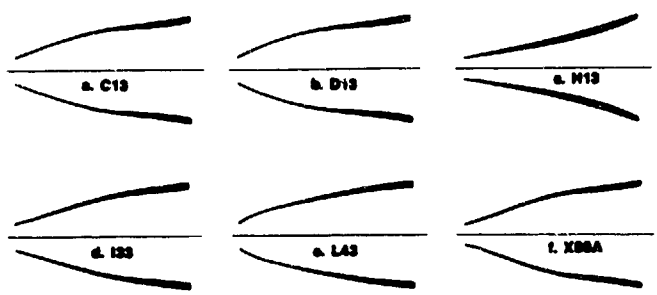

Figure 5. Selected liners derived by the Target Inversion/ constrained optimization technique.

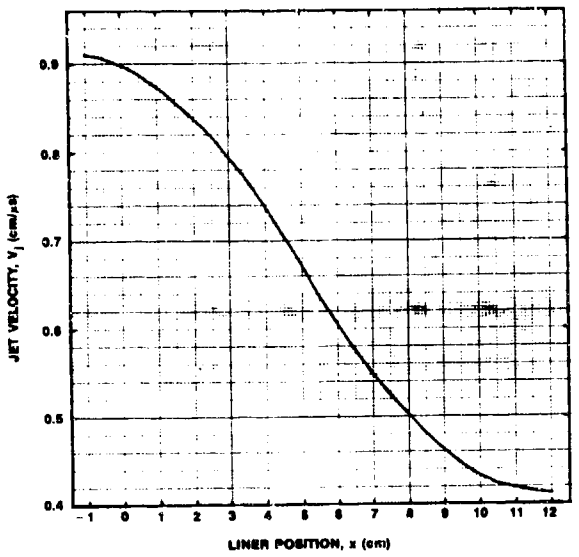

Figure 6. 2D ELK iteration convergence jet velocity profile.

2D ELK ITERATIVE REFINEMENT OF THE 77-3A AND 77-3H LINERS

The setup for the PISCES 2D ELK calculations is shown in Figure 7. The charge confinement and base ring were modeled with Lagrange zoning. The detonator plug was modeled as a rigid object, and the liner, as a jetting thin shell. The explosive is located in the Euler-zoned "background" mesh; the boundaries of the explosive within the mesh coincide with the appropriate boundaries of the previously mentioned objects. The explosive was allowed

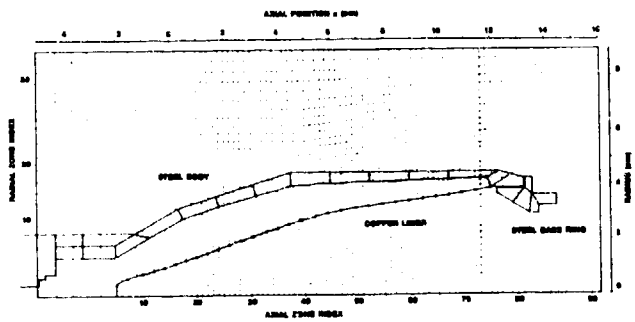

Figure 7. Setup for the PISCES 2D ELK iterative refinement calculations of the 77.3 charge.

to vent through the cracks between the components and through a hypothesized fracture at the base end of the confinement. The basic setup of Figure 7 was modified during the course of the refinement to accommodate changes in the initiation hardware and to speed up the calculations.

When the converged 77-3A liner thickness profile was obtained, it was altered at the base end as a conservative measure to compensate for the potential confining effect of a charge body that does not vent appreciably after detonation. Tests of the 77-3A liners indicated a moderate amount of venting through the aforementioned confinement fracture. The model was altered for the refinement of the 77-3H liner to simulate the observations; the 77-3H liner thickness profile was accepted without alteration. Figure 8 is a diagram of the 77-3H test assembly with the liner

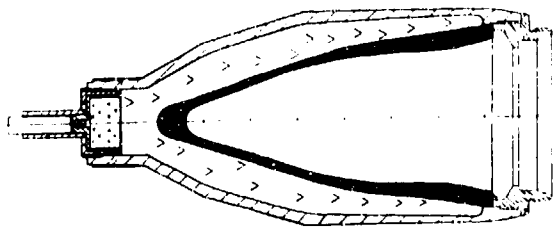

Figure 8. 77-3H test assembly.

in place. The computed masses, jet energies, and charge efficiencies are compared to those of the baseline 77-3 design below:

	Design		
	77-3	77-3A	77-3H
Explosive Mass (gm)	755	493	493
Liner Mass (gm)	325	591	617
Jet Energy (kJ)	568	639	694
Charge Efficiency (%)	14	25	27

The sum of the explosive and liner masses is slightly greater with the optimized designs, and, although the explosive mass decreased by 35 percent, the jet energy increased by 13 and 22 percent, respectively. The charge efficiency is the ratio of the jet energy to the explosive's chemical energy (5.3 kJ/gm for Octol explosive). The efficiency of the optimized design is significantly greater than that of the baseline.

ASPECTS OF LINER FABRICATION

There are several manufacturing techniques for liner fabrication. In a minor research program such as the 90 mm design improvement program, the object of the testing is to get only an approximate estimate of the penetration capability of the new shaped charge design; accordingly, not only the technical but also the economical aspects of the fabrication were considered.

The liners from the 77-3A and 77-3H tests reported here were machined from OFHC copper bar stock. The grain sizes were large, and they were thought to have preciptated an early breakup of the jet. The results of the limited number of tests with the machined liners justify the fabrication of a larger number of liners for future evaluation. It is planned that the liner grain size and other material properties be controlled to minimize their influence on the test results.

We considered machining more liners from small-grain bar stock, but we also examined other fabrication processes as well. The cold-forging process offers a method by which consistently high-quality liners can be fabricated, but the tooling costs were considered to be too great.

Computer-controlled shear-forming with intermediate heat treatments and a finish machining on both the outside and the inside of the liner was a very promising technique for making liners of sufficient quality for test evaluation. Accordingly, the 77-3H liners for the subsequent testing will be fabricated by this method. Grain size will be constrained to be less than 25μ; hardness, less than 50 V; and symmetry and wall thickness variation, less than 0.01 mm. Texture patterns will be obtained to document the preferred crystal lattice orientation, and microphotographs will be taken to determine the grain orientation and size. The liner material examination methods are described in Reference 6.

COMPARISONS OF CALCULATIONS AND EXPERIMENTS

The 77-3A and 77-3H charges with machined liners were fired against stacks of armor plates, and flash radiographs were taken of the charges and of their jets. The tests verified the computed shape of the expanding body and of the collapsing liner, and they confirmed the predicted jet trajectories and the jet velocity profile. The jet velocity/mass relationship agreed with the experiments, but there appeared to be additional material in the experimental jet that accounted, in part, for the conservative value computed for the jet kinetic energy. The computed penetration

depth and hole diameter were greater than observed; reasons for this inconsistency are explored below.

Figure 9 compares the computed outlines of the collapsing liner and of the expanding steel body to the outline observed on a radiograph taken 40 μs after zero time. On the radiograph it was observed that the explosive appeared to be venting through a gap near the base of the charge; the observed gap is represented by a dotted line in Figure 9c.

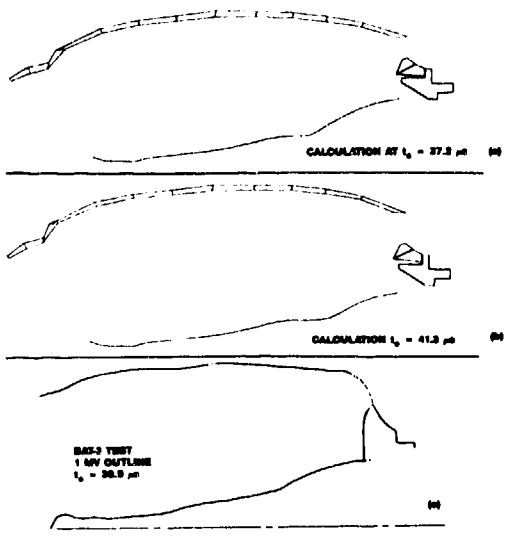

Figure 9. Comparison of calculated and experimental outlines of body and liner for the 77-3A design.

The trajectories of selected points on the computed jet are compared to observed particle positions in Figure 10. The Octol explosive was detonated at time zero in the calculation; in the experiment, detonation occurred 5.6 μs after zero time. The origin of the axis in the experiment is the base edge of the charge; this corresponds to position 14.5 cm in the calculation. Trajectories from the jetting calculation were shifted to the experimental frame by the indicated amounts before they were plotted on Figure 10.

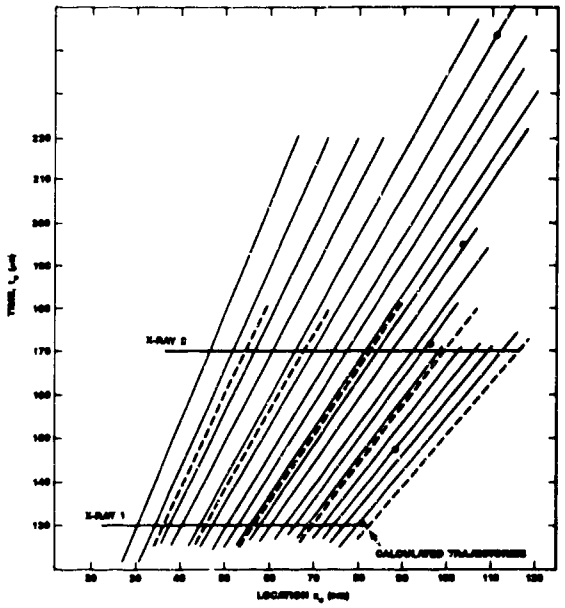

Figure 10. Comparison of trajectories of computed and experimental jet trajectories for the 77-3A design. Time-of-arrival data from range switches between armor plates is indicated by the points.

Trajectories of particles from the front, center, and rear of the jet were extrapolated to early time to estimate the position of the virtual origin. Intersections of the respective front-center, front-rear, and center-rear trajectories are (– 26.0 cm, 1.1 μs), (– 16.2 cm, 13.1 μs), and (– 10.4 cm, 27.6 μs). The centroid of these intersections is (– 17.5 cm, 13.9 μs). By comparison, the (shifted) centroid of selected trajectories from the jetting calculation was (– 20.9 cm, 7.5 μs).

When the time of liner collapse is plotted against the position of collapse, the curve that is generated is called the collapse locus. Each point on the collapse locus is associated with a unique point on the liner. Particle trajectories were extrapolated to the computed collapse locus to associate them with points on the liner. By this method jet velocities were assigned to points on the liner for comparison to the computed jet velocity profile (Figure 11). The solid line in the figure is the profile for the 77-3A design computed with an early jetting algorithm. The velocity of the tip of the jet matched the experimental value of 0.81 cm/μs when the improved algorithm was used instead. The 77-3H liner was derived with the improved algorithm; its tip velocity was measured to be 0.86 cm/μs, which was in better agreement with the 0.90 cm/μs value expected from the calculations.

Figure 12 shows that the computed relationship between cumulative jet mass and velocity for the 77-3A design was bracketed by curves derived from two of the experiments, but the observed jet mass was significantly greater than predicted. As a consequence the experimental jet kinetic energies were greater than expected. The kinetic energy of the 77-3A design was measured to be 689 kJ and 880 kJ in the two tests depicted in Figure 11; the computed jet kinetic energy was 639 kJ. By comparison, the observed jet energy for the baseline design was 500 kJ, and the computed value was 568 kJ.

Both of the optimized warheads, 77-3A and 77-3H, were fired into stacks of armor at moderate standoff. The holes were round and straight, suggesting good jet alignment and good dimensional control in the liner fabrication. Figure 13 is a comparison of the computed and the observed hole shapes. The volume of a hole in armor is proportional to the jet energy. It was expected that the hole volume would be greater than that computed because

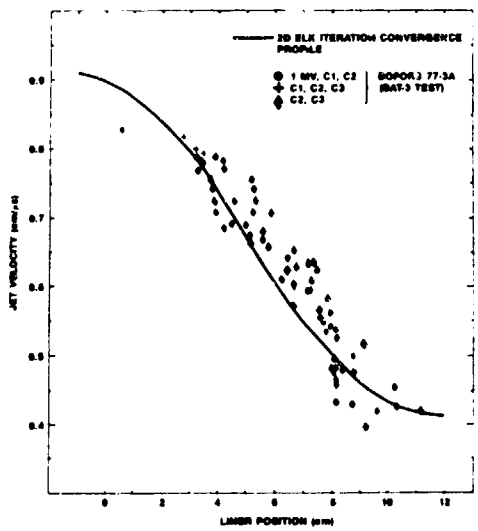

Figure 11. Comparison of calculated and experimental jet velocity profiles.

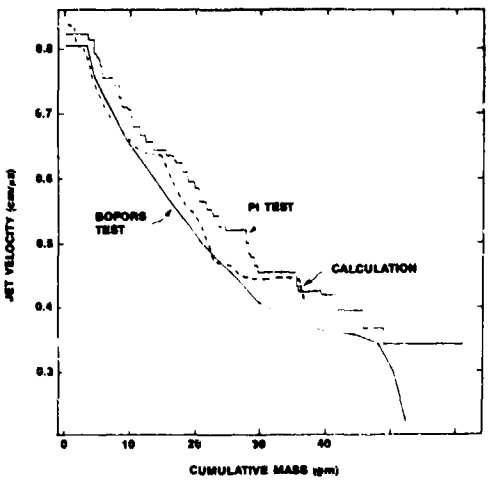

Figure 12. Relationship between jet velocity and cumulative mass for the 77-3A design.

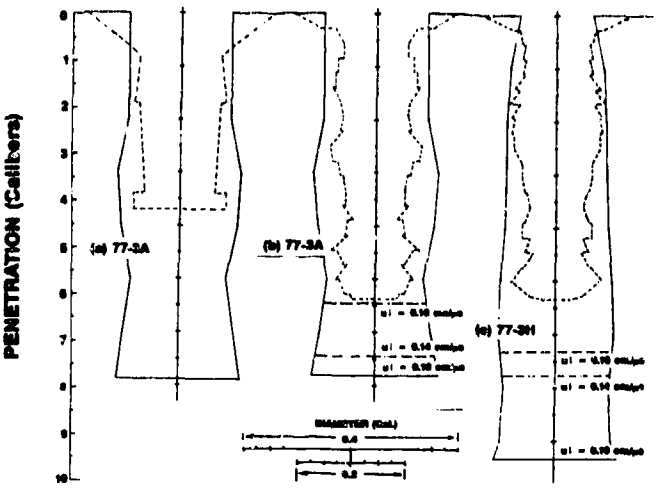

Figure 13. Comparison of calculated and experimental hole shapes in steel.

the experimental jet energies were greater than the computed ones, but the opposite was the case. The hole volume values are compared below:

Design	Standoff (Calibers)	Hole Volume (cc)	
		Calculation	Test
77-3A	9.0	161	68
77-3A	7.5	161	73
77-3H	7.5	174	61

By contrast the agreement between the computed hole shape and the observed hole shape for a 100 mm charge with a conical liner is much better (Figure 14).

The 100 mm charge was fired into a different type of steel armor than the optimized charges, and it is believed that the 3500 J/cc specific energy estimate is more accurate for that type of armor than was the 4000 J/cc estimate for the armor used in the tests illustrated in Figure 13. Other tests at Physics International suggest values as great as 7500 J/cc for the armor. For such a value the computed hole volumes in the table above are scaled by the factor 4000/7500 (53 percent).

The cutoff penetration velocity in the calculations was assumed to be 0.10 cm/μs. Figure 13 illustrates the influence of the cutoff velocity on the penetration. It appears that the discrepancy in the penetration can be resolved by assuming a value of 0.16 cm/μs; this also reduces the hole volume to a value close to that of the experiment. On the other hand the 0.16 cm/μs value is unusually high; other experiments with the armor indicate a value between 0.10 and 0.14 cm/μs. It should be noted that the computed penetration is greater for shorter standoffs when the cutoff velocity is greater than 0.10 cm/μs.

The jets were observed on the radiographs to be ragged, an occurrence that has been associated with large grains in copper shaped charge liners. The tail of the jet was also large in diameter, almost as large as the observed hole. A large-diameter, high-velocity tail was expected; it is consistent with the design requirement of a large exit hole. During target penetration gaseous material flows around the jet and out of the hole, and the shapes and sizes of the observed jet particles may have made them more susceptible to misalignment and disruption than otherwise. Misaligned and disrupted jets are inefficient; they give high values for the specific energy and low values for the penetration.

Figure 10 provides evidence of jet disturbance during penetration. The data for range switches located between three-inch-thick blocks of armor are superimposed on the jet trajectory data. From

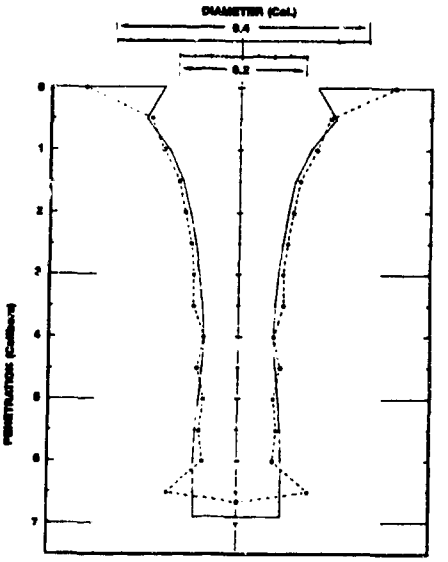

Figure 14. Comparison of calculated and experimental hole shapes in steel for 100 mm charge with conical liner.

this data and from measurements of the jet particle lengths, it was deduced that, whereas the cumulative jet particle length to penetrate the first 23 cm (nine inches) of armor was 18 cm, the length to penetrate the remaining 10 cm of armor was 36 cm.

Jets from shaped charges with liners made of copper with soft, small grains have smoothly-shaped particles that are more elongated than those observed in tests with material such as that used in the optimized liners. In view of the evidence of disruption and misalignment in the previous tests, it appears that a change in liner fabrication could improve the observed penetration performance of the optimized designs, because the factors that lead to the hypothesized degradation during penetration could be mitigated by this step.

The liners for the 100 mm shaped charge were fabricated by the cold-forging process, whereas the previously-tested 77-3A and 77-3H liners were machined from OFHC copper bar stock. The average grain size was 150 μ, significantly larger than that is typical of cold-forged liners; consequently, it is suspected that the material properties influenced the observed poor correlation illustrated in Figure 13 and the good correlation illustrated in Figure 14.

The radiographs and hole symmetry suggested good jet alignment, so poor dimensional control in fabrication has been ruled out as a factor in the tests of the optimized liners. As indicated above, additional tests are planned with shear-formed liners that will have smaller grains than the ones tested previously. The agreement between calculation and experiment is expected to improve accordingly.

REPRESENTATION OF STRUCTURES FOR DERIVATION OF OPTIMIZED CHARGE DESIGNS

Target defeat requirements are affected by system constraints such as attack obliquity, target spectrum, and method of operation and by countermeasures. Figure 15 shows the representation of a concrete/gravel target for a system with a nonzero attack obliquity; the thickness of the concrete layer is equal to the thickness along the line-of-sight of the jet. The representation is an axisymmetric idealization of the oblique target, and the effects of spall at the surface and of reflections at the interface are compensated by choosing a conservative diameter for the hole.

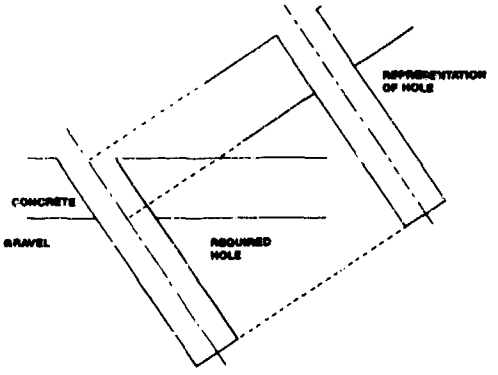

Figure 15. Schematic of concrete/gravel target with oblique hole.

Figure 16 is a typical spaced armor target; the target is represented by alternating layers of steel and air with line-of-sight distances more than twice the distances at normal obliquity. Spaced steel plates are countermeasures that are often very effective in reducing the performanced of a shaped charge.

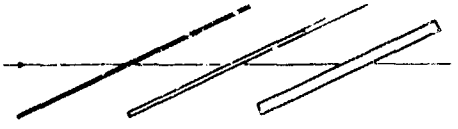

Figure 16. Typical spaced armor target.

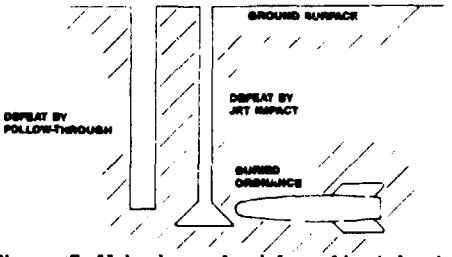

Figure 17. Hole shapes for defeat of buried ordnance by a follow-through charge or jet impact.

Buried ordnance can be defeated by destroying the fuzing mechanism through shock or by detonation of the main charge. For the first method there is less potential damage to the soil and surrounding structures, but the continued presence of the bulk of the explosive is a safety hazard that is not present when the ordnance is detonated. The choice of defeat mechanism affects the type of system to be developed and the size and shape of the hole required; typical hole shapes for the two applications are illustrated in Figure 17.

The warhead of Reference 7 was designed to make a large hole both in a thin steel plate and in a thick concrete slab. It was deduced that a charge capable of defeating the composite target of Figure 18 would be capable of the combined requirements. Hence the composite target was chosen as the target inversion hole description for derivation of the optimized liners.

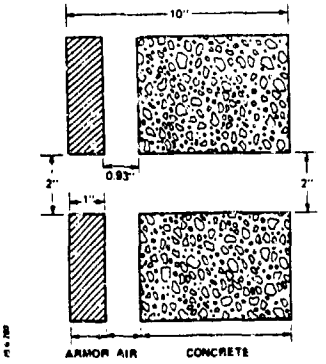

Figure 18. Composite target defeat constraint. A charge capable of defeating the target in the manner indicated will defeat, separately, a one-inch armor plate and a ten-inch concrete slab.

CONCLUSIONS

The Reverse Engineering method has been shown to be an effective technique for derivation of an optimized shaped charge liner design with significantly greater jet kinetic energy than the starting baseline design. The constrained optimization technique used in conjunction with the reverse engineering method was described by example for a 90 mm warhead improvement effort.

Conservative design practices were observed in the optimization task. Both calculations and experiments verified a significant increase in jet energy and charge efficiency for the optimized design, when compared to the baseline.

When the optimized designs were tested against armor targets, the performance was not as good as expected. It is believed that the penetration was degraded by the properties of the copper liner material. Further tests are planned to verify this assertion.

The Reverse Engineering method can be applied to the design of warheads to defeat structures other than the thick steel target for the 90 mm warhead. Examples of applications to other types of targets are included for illustration.

REFERENCES

1. M. Trigg, S. Hancock, and H. Hancock, "PISCES 2D ELK User's Manual (Version 4)," Physics International Company, 1984.
2. E.M. Pugh, R.J. Eichelberger, and N. Rostoker, "Theory of Jet Formation by Charges with Lined Conical Cavities," J. Appl. Phys. 23, 532, Jul 52.
3. G. Birkhoff, D.P. MacDougall, E.M. Pugh, and G. Taylor, "Explosives with Lined Cavities," J. Appl. Phys., 19, 563, Jun 48.
4. B.S. Haugstad and O.S. Dullum, "Optimization of Shaped Charges," J. Appl. Phys., 55, 100, Jan 84.
5. P.C. Chou, F. Hirsch, and W. Walters, "The Virtual Origin Approximation of a Shaped Charge Jet," Proc. Sixth International Symp. on Ballistics, ADPA, Oct 81.
6. B. Arvidsson, H.G. Ohlsson, F. Straumann, and E. Torok, "Investigation of Liners for Shaped Charges Manufactured from Copper Powder by X-ray Diffraction and Ultrasonic Techniques," Proc. Eighth International Symp. on Ballistics, ADPA, Oct 84.
7. D.K. Davison, "Interaction of High-Velocity Aluminum Shaped-Charge Jets With Finite Steel and Concrete Targets," Proc. Symp. on the Interaction of Non-Nuclear Munitions With Structures, USAF, Colorado Springs, CO, May 83.

DYNAMIC COMPRESSIVE TESTING OF CONCRETE

Lawrence E. Malvern, David A. Jenkins, Tianxi Tang, and C. Allen Ross

Engineering Sciences Department, University of Florida
Gainesville, Florida 32611

ABSTRACT

A Kolsky Apparatus (split Hopkinson's Pressure Bar System) with 3-inch diameter pressure bars has been built at the University of Florida for dynamic compression of specimens up to 3 inches (75 mm) in diameter. Equipment and procedures are described and some early results reported.

INTRODUCTION

Numerical finite-elements codes for analysis of reinforced concrete structural response incorporate the unconfined ultimate compressive strength f_c' of the concrete as a parameter. For dynamic impact loadings this parameter is sometimes increased by an arbitrary factor over the static value. The objective of the investigation reported here is to determine the strain-rate dependence of the ultimate strength of selected types of concrete at rates of interest for the structural response in order to permit a more rational correction of the static value, with a dynamic factor that may vary from element to element and with time during the deformation.

For over-all structural response (as distinguished from such intense local response as occurs in cratering, for example) the strain-rate range of interest is usually below 100 s^{-1}. In the range above 10 s^{-1}, wave propagation effects in the specimen and in a dynamometer mounted in tandem with the specimen complicate stress and strain determination.

The Kolsky Apparatus or Split Hopkinson's Pressure Bar (SHPB) system consists of two long strain-gaged pressure bars with a short specimen sandwiched between them. Analysis of the observed longitudinal elastic stress wave propagation in the two pressure bars furnishes information about both the force and displacement versus time at each specimen interface. The specimen is supposed to be so short that waves propagate back and forth between its two interfaces and achieve an approximately uniform state of stress and deformation along the specimen length, except during the initial rapid rise of the stress. Various versions of the SHPB system have been used in recent years for testing rock and fine-grained concrete. Most of the existing systems have a maximum specimen diameter of 25 mm. In structures of interest, concrete aggregate sizes up to 0.5 inch (12.5 mm) or even larger may be used. For such concrete, a larger specimen must be used in order to obtain representative properties of the composite material. The new system reported here, with 75-mm diameter pressure bars, was developed for this reason.

The larger specimen and larger-diameter pressure bars, however, introduce two problems. For specimens longer than about 1.5 inch (37.5 mm) the desired degree of uniformity along the length is not achieved. Maximum stresses are still reasonably well measured, but the stress-strain curve determination involves some uncertainty about what stress to associate with the average strain at each instant. The larger diameter also leads to more noticeable Pochhammer-Chree radial oscillations in the incident pressure bar, which interfere with the interpretation of the longitudinal strain measurement in the incident pressure bar and hence interfere with the force and displacement recording at the specimen's incident-bar interface.

Despite these problems, the SHPB system appears to be the best available system for determining dynamic compressive properties in the moderately high deformation rate range. For three-inch-long plain concrete specimens, the system to be described here has performed tests with strain rates at failure ranging from 10 to 100 s^{-1}.

BACKGROUND

Early work on rate effects in concrete was reviewed in a 1956 ASTM symposium [1]. At stress loading rates from 1 to 1000 psi per second in testing machines, compressive strength was reported to be a logarithmic function of the loading rate, with recorded strength increases up to 109% of the strength reported at "standard rates" (20 to 50 psi per sec). By using cushioned impact tests Watstein [2] obtained strengths 185% of the standard. Watstein also reported rate effects on the measured secant modulus of elasticity, energy absorption (up to 2.? times the static value) and strain to failure.

Read and Maiden [3] surveyed the state of knowledge on the dynamic behavior of concrete at high stress levels in 1971, including the data of Gregson [4], who used a gas gun to provide flyer plate impacts at pressures from 40 to 8,000 KSI.

Seabold [5] represented the rate effects on unconfined compressive strength in concrete up to strain rates of about 5 s^{-1} by an empirical formula containing both a linear term and a logarithmic term in the strain rate.

More recently Hughes and Gregory [6] have used a drop tester and concluded that the impact strengths averaged about 1.92 times the static compressive strength. For some of their "strong concretes" dynamic compressive strengths above 260 MPa (37.7 KSI) were found. Hughes and Watson [7] used a similar test technique and concluded that the percentage increase in compressive strength in dynamic tests over the static strength was greater for low-strength concrete than for high-strength concrete.

The compressive SHPB, introduced by Kolsky [8] is widely used for determining material properties in the strain-rate range from about 10^2 to 10^4 s^{-1}. See, e.g., Lindholm [9] and Nicholas [10]. Geotechnical materials and concrete have been investigated with SHPB. Christensen et al. [11] tested nugget sandstone specimens under confining pressures up to 30 KSI. They also used truncated-cone striker bars to spread out the rise time of the loading pulse in order to improve the accuracy and resolution of the initial portion of the stress-strain curves. Lindholm et al. [12] tested specimens of Dresser basalt under confining pressures up to 100 KSI at strain rates up to 10^3 s^{-1} and considered also temperature. They found unconfined strength variation by a factor of 3 over the range of rate and temperature examined. Lundberg [13] investigated energy absorption in dynamic fragmentation of Bohus granite and Solenhofen limestone. Specimen strain rates were not reported, but general fracture of the specimens occurred when the stress was about 1.8 times the static strength for Bohus granite and about 1.3 times for Solenhofen limestone.

Bhargava and Rehnström [14] found unconfined dynamic compressive strengths of 1.46 to 1.67 times the static strength in plain concrete and fiber-reinforced and polymer-modified concrete. Their failure strengths were identified as the maximum amplitude of short-pulse stresses that could be transmitted through the specimen and were more associated with the onset of failure than with complete crushing of the 100-mm diameter by 200-mm length cylinders. Their 250-mm-long striker bar gave a loading pulse duration only about twice the transit time through an elastic specimen.

At the University of Florida, Tang et al. [15], tested 28-day mortar specimens in a 3/4-inch diameter SHPB and found a linear dependence of maximum stress on the strain rate at the maximum stress at rates up to 800 s^{-1}. Few other applications of SHPB technology to concrete have been made. Kormeling et al. [16], adapted it for dynamic tensile tests. They reported dynamic tensile strengths of more than twice the static value at strain rates of approximately 0.75 s^{-1}.

Suaris and Shah [17] have recently surveyed mechanical properties of materials subject to impact and rate effects in fiber-reinforced concrete. Many investigators have found significant increases in impact tensile strength in fiber-reinforced concrete over that of plain concrete [18].

Radial inertia effects in geotechnical materials, which may be mistaken for strain-rate effects, were discussed by Glenn and Janach [19]. They observed high radial accelerations, which they attributed to dilatancy in their granite specimens, and suggested that the lateral confinement induced by this radial inertia causes the core of the cylinder to be more nearly in a state of uniaxial strain than uniaxial stress. Their tests involved direct impact of the striker against the specimen at such high speeds that failure occurred during the first transit of the wave through the specimen.

Young and Powell [20] investigated lateral inertia effects in SHPB tests on Solenhofen limestone and Westerly granite. By means of embedded wire loops and an externally applied longitudinal magnetic field they measured radial velocities, and hence determined radial accelerations and calculated radial-stress confinement in tests with loading pulse lengths of 50 microsec in specimens of length 46 to 52 mm. The impact speeds used (29.9 to 61.4 m/s) apparently caused failure during the first passage of the stress wave through the specimen. They concluded that the induced radial stress field is capable of producing a confining pressure sufficient to account for increases of compressive strength observed in SHPB experiments.

Bertholf and Karnes [21] made a two-dimensional numerical analysis of the SHPB system and concluded that with lubricated interfaces the one-dimensional elastic-plastic analysis was reasonable if limitations are imposed on strain rate and rise time in the input pulse and specimen length to diameter ratio is about 0.5.

EQUIPMENT AND PROCEDURES

The experimental facility consists of a gas gun, which propels a striker bar to impact axially the incident pressure bar, which transmits the loading pulse to the specimen sandwiched between the incident pressure bar and the transmitter pressure bar. Figure 1 is a schematic of

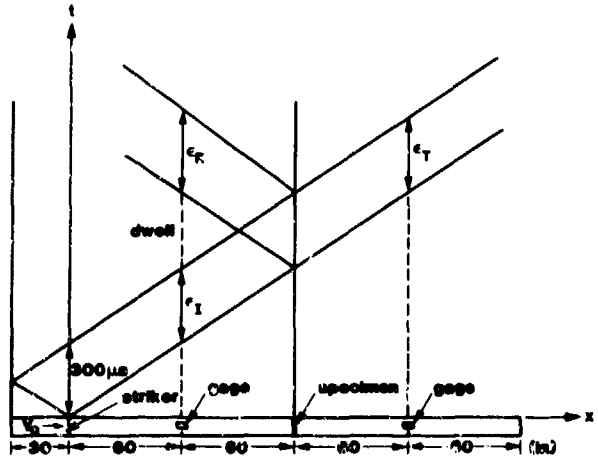

Fig. 1. Schematic of Bars and Lagrange Diagram.

the pressure bar arrangement, with a Lagrange diagram above it illustrating the elastic wave

propagation in the pressure bars. The gas gun was fabricated by Terra-Tek Systems, Inc. As currently configured, it fires a 30-inch-long, 3-inch-diameter 61.28-lb steel striker bar to impact at speeds V_o up to 50 ft/sec with firing chamber pressures up to 500 psi. Higher speeds are possible with a lighter impactor or a higher firing pressure. The propellant gas is furnished by a nitrogen bottle (2000 psi maximum). The firing chamber was proof tested to 3000 psi, but, as currently configured, a safety valve in the control panel limits the firing pressure to 750 psi to avoid damaging the pressure gauge. The whole system including gas gun, pressure bars and a shock absorber with 6.5-inch stroke at the far end is almost 30 feet long.

A full strain-gage bridge is permanently mounted on each pressure bar, 60 inches from the specimen interface. Each bridge consists of two double element strain gages (Micro-Measurements Type WA-06-250TB-350) mounted on opposite sides of the bar. The gage elements are oriented to coincide with the longitudinal and transverse directions of the bar. The amplified signals are recorded by a transient recorder consisting of a four-channel Nicolet 4094 digital storage oscilloscope. The recorded signals are displayed by the oscilloscope and also stored on floppy diskettes for subsequent analysis.

Figure 2 shows an example of the axial strain signals versus time, recorded by a Hewlett Packard 7470A digital plotter from the stored signals in the digital oscilloscope. Compressive

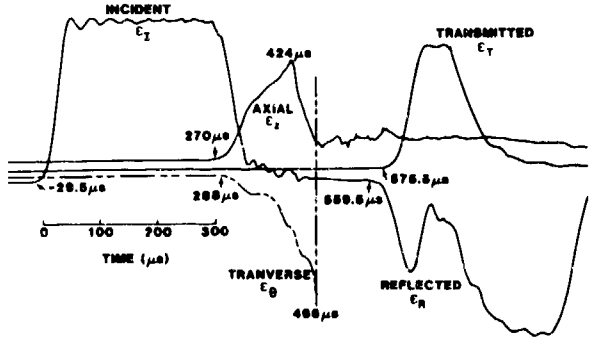

Fig. 2. Strain Pulses in Pressure Bars and Axial and Transverse Specimen Surface Strains.

strain is plotted upward. After the passage of the first incident pulse, of nominal length 300 microsec (from the beginning of the rise to the beginning of the fall), there is a dwell time before the arrival of the reflected pulse from the specimen, which is recorded at the same gage station as the incident pulse. Another channel shows the pulse transmitted through the concrete specimen into the transmitter bar. Because the two gage stations are equidistant from the specimen, the transmitted pulse arrives at the transmitter-bar gage station at approximately the same time as the reflected pulse arrives back at the incident-bar station, delayed only by the transit time of the leading edge of the pulse through the specimen. Also shown are records from two strain gages mounted on the specimen midway between its ends, one measuring axial surface strain ε_z and one measuring transverse (hoop) strain ε_θ. The drop in ε_z at 424 microsec corresponds to a failure in the specimen, but the gage continued to function. At 466 microsec the ε_θ gage failed.

For purposes of analysis, the digitally recorded pulses are time shifted, so that time zero coincides with the initial arrival at the specimen interface, as illustrated in Figure 3 where

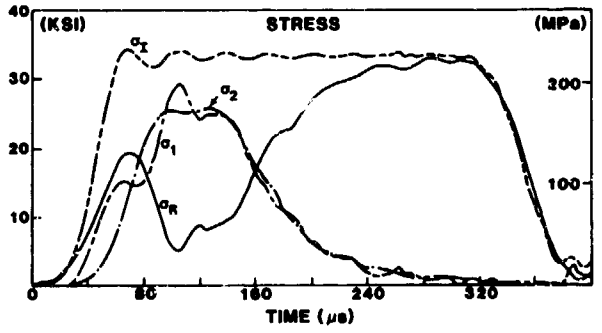

Fig. 3. Pressure Bar Interface Stresses (time-shifted) From Record of Fig. 2.

the pressure-bar strain pulses have been converted to stress pulses by multiplying by the elastic modulus of the steel. The reflected pulse σ_R is shown inverted, and all pulses have been shown as stresses in the pressure bars at the interfaces with the specimen. The total stress σ_1 at the incident interface, which is the sum of the incident σ_I and reflected σ_R is also plotted. The σ_1 record rises very slowly at first, and then rises smoothly until about 14 KSI, where something resembling a small step occurs. The reason for this is not certain, but it could be associated with three-dimensional effects at the pressure-bar end interacting with the axial stress waves propagating back and forth in the specimen. Since the specimen cross section is the same as that of the pressure bar, in the one-dimensional analysis the stress σ_1 is considered to be the specimen stress at the first interface, and the specimen stress σ_2 at the second interface is equal to the transmitted stress σ_T. For this 2.6-inch long specimen, σ_1 and σ_2 do not become equal before the maximum stress.

Figure 4 shows the stress σ_2, the average stress $\bar{\sigma} = \frac{1}{2}(\sigma_1 + \sigma_2)$, the average strain rate $\dot{\varepsilon}$ deduced from the difference in the two interface velocities as calculated from the one-dimensional elastic bar-wave analyses in the pressure bars, and the average strain ε obtained by numerical integration of the average strain rate, all plotted versus the time measured from the first pulse arrival at the first interface. Note that the strain rate is approximately constant in the vicinity of the maximum stresses,

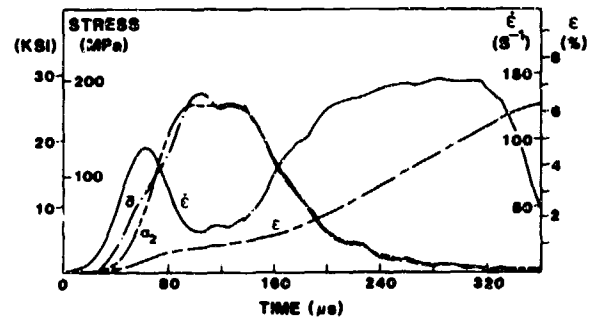

Fig. 4. Transmitted and Average Stresses, Strain Rate and Strain Versus Time.

except for some oscillations introduced by the oscillations in the incident pulse. Figure 5 shows $\bar{\sigma}$ and σ_2 versus the average strain ε.

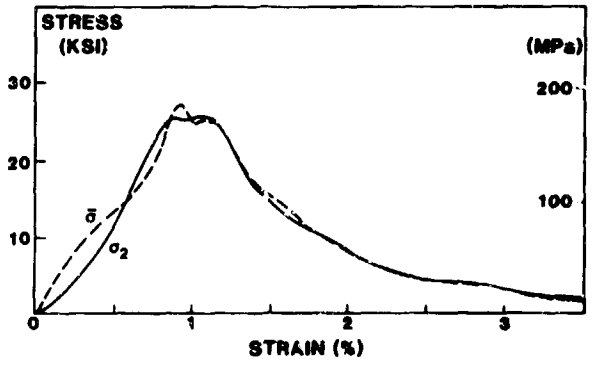

Fig. 5. Stress-Strain Curves.

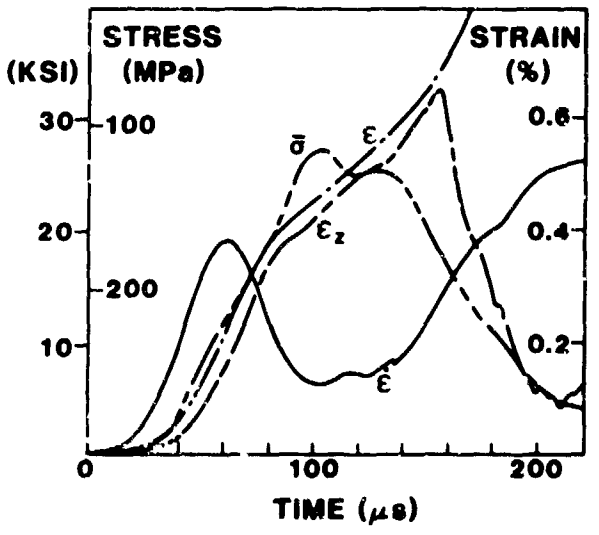

Fig. 6. Specimen Gage ε_z Compared with SHPB Determination of Average Strain ε.

Figure 6 compares the average strain ε to the specimen-gage strain ε_z, and also repeats the average stress and strain-rate curves. The drop in ε_z, which is attributed to a fracture in the specimen, occurs well after the maximum stress. The gage failure in ε_θ occurs still later. There is a plateau in the ε_θ record near the middle of the stress pulses. As may be seen in Figure 7 this plateau is near the maximum of $\bar{\sigma}$.

Figure 7 also shows the transverse strain rate $|\dot{\varepsilon}_\theta|$ obtained by numerical differentiation of a smoothed ε_θ record. Its rapid rise from

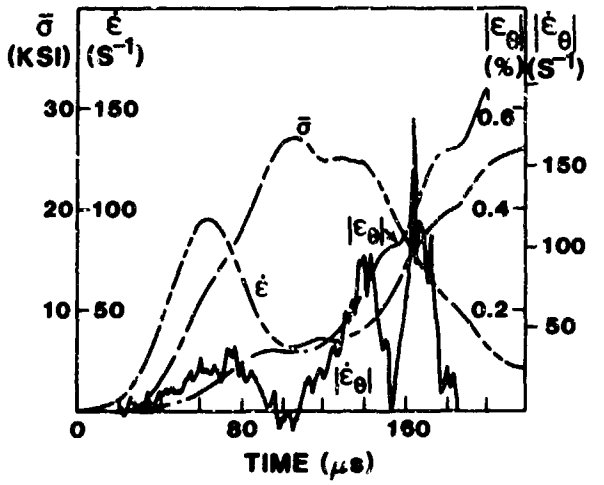

Fig. 7. Transverse Strain Rate Indicates That Significant Radial Acceleration Occurs Only After Maximum Stress is Reached.

about 100 to 140 microsec corresponds to a radially outward acceleration of the surface, which could cause lateral inertia confinement of the interior of the specimen. Since this only appears after about 100 microsec, it cannot account for the dynamic enhancement of the maximum stress that can be attained. The static strength of these specimens is not more than 15 KSI and σ_1, σ_2 and $\bar{\sigma}$ have all far exceeded this value well before the 100 microsec time at which radial inertia effects appear. In these tests at moderate impact speeds, failure occurs well after a single transit time of the stress wave through the specimen (of the order of 16 microsec). The rise time of the $\bar{\sigma}$ pulse is about 100 microsec.

RESULTS

Figures 8 and 9 summarize preliminary results on four types of high-strength concrete. The maximum value of $\bar{\sigma}$ attained is plotted versus the average strain rate at the maximum stress. The suitability of this choice of abscissa is open to question, but it seems to correlate the data. All four concretes have mix specifications [see Appendix] with water/cement ratio around 0.24 - 0.27 and are specified as 14 KSI concrete, based on standard static unconfined compression tests. They differ mainly in the type of aggregate used. Three of them were prepared, cured and cored from blocks by Terra Tek, Inc. of Salt Lake City. The three aggregates they used (maximum size 1/2 in.dia.) are

designated as Andesite, Seattle gravel, and a lightweight aggregate called Solite. The fourth material with a manufactured limestone aggregate (maximum size 3/8 inch) was prepared at the U. S. Army Waterways Experiment Station, cast in PVC pipe molds of three-inch diameter and cut to length after cure. They were further machined and ground at the University of Florida to ensure end face parallelism within 0.0005 inch.

Figure 8 shows Andesite and Seattle gravel specimen results. The 3-inch diameter by 3-inch long Andesite specimens had a static strength of 16.1 KSI and dynamic strengths varying from 20.4 up to 28.0 KSI at a strain rate of 77 s^{-1}.

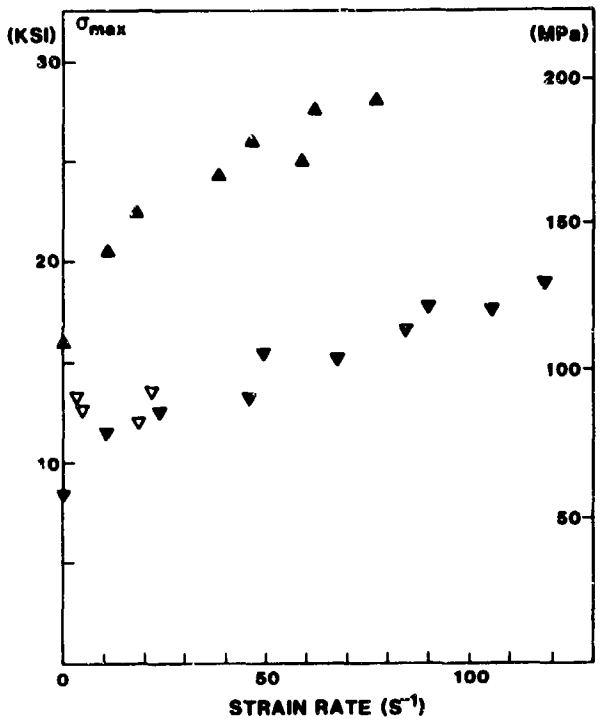

Fig. 8. Maximum Stress Versus Strain Rate at Maximum Stress: Andesite (upper) and Seattle Gravel Concrete (lower inverted triangles).

The inverted triangles in the lower group in Figure 8 represent specimens with Seattle gravel aggregate. The four hollow inverted triangles represent tests where the 120-inch-long incident bar impacted the specimen directly in order to provide a longer loading pulse. Two of these direct impacts induced failures at strain rates as low as 3 s^{-1} and 4.8 s^{-1}. The dynamic strengths by the conventional SHPB method varied from about 12 KSI at a strain rate of 10 s^{-1} to 18 KSI at 118 s^{-1}.

Figure 9 shows that the limestone aggregate specimens (solid circles) had dynamic strengths varying from 20.6 KSI at 9.31 s^{-1} to 29.9 KSI at 59.2 s^{-1}. One specimen (not shown) supported a dynamic stress of 19.2 KSI without fracture. The highest failure stress recorded in the Solite tests was 19.6 KSI.

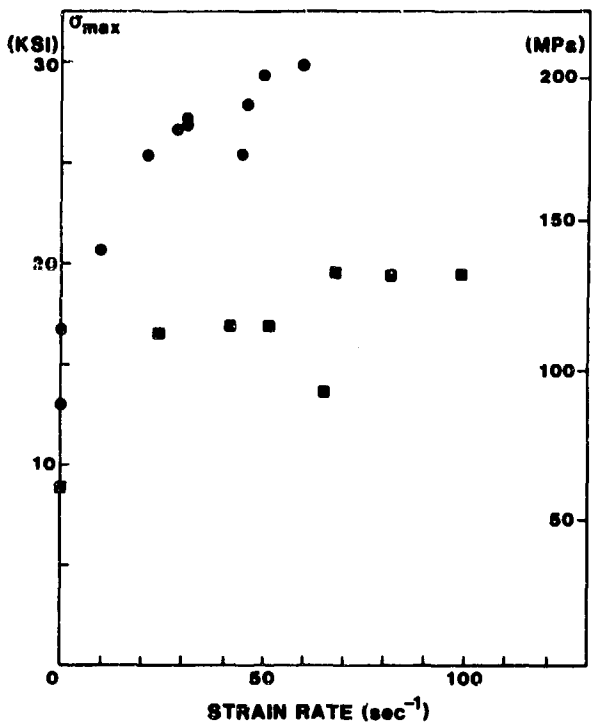

Fig. 9. Maximum Stress Versus Strain Rate at Maximum Stress: Limestone Aggregate (circles) and Solite Lightweight Aggregate (squares).

There are some very important questions involved in these dynamic tests for which we do not yet have answers. For example, what is happening in the limestone aggregate specimen of Figure 5 during the time from about 100 to 140 microsec where σ_2 and the average axial strain rate are approximately constant? This corresponds approximately to the previously mentioned interval of radially outward acceleration of the surface where lateral inertia confinement may be important, associated with the dilatancy in this part of the deformation. The end of this interval also matches approximately the drop in the recorded specimen axial strain at about 135 microsec, which we have attributed to a fracture where the part of the surface on which the axial strain gage was mounted broke off and was no longer subjected to the axial loads.

CONCLUSION

Despite the uncertainty in the interpretation of the later part of the deformation, it appears that the SHPB technique is a useful tool for determining the dynamic strength of concrete, at least at the moderate impact speeds leading to failure strain rates below about 100 s^{-1}. It appears that these maximum stresses cannot be attributed to lateral inertia confinement. The analysis of the part of the loading up to the maximum stress may be possible with some sort of damage-accumulation model, but this has not yet been attempted.

ACKNOWLEDGMENT

Research sponsored by the Air Force Office of Scientific Research, Air Force Systems Command, USAF, under contract Number AFOSR F49620-83-K-0007. The U. S. Government is authorized to produce and distribute reprints for Governmental purposes notwithstanding any copyright notation thereon.

REFERENCES

1. McHenry, D. and Shideler, J. J., "Review of Data on Effect of Speed in Mechanical Testing of Concrete," ASTM STP 185, pp 72-82, 1956.
2. Watstein, D., "Effect of Straining Rate on the Compressive Strength and Elastic Properties of Concrete," ACI Journal, Vol. 24, pp 729-744, 1953.
3. Read, H. E. and Maiden, C. J., "The Dynamic Behavior of Concrete," Topical Report 3 SR-707, Systems, Science and Software, La Jolla, CA, August 1971.
4. Gregson, V. G., Jr., "A Shock Wave Study of Fondu-Fyre WA-1 and a Concrete," General Motors Materials and Structures Laboratory, Report MSL-70-30, 1971.
5. Seabold, R. H., "Dynamic Shear Strength of Reinforced Concrete Beams--Part III", Technical Report R 695, Naval Civil Engineering Lab, Port Hueneme, CA, September, 1970.
6. Hughes, B. P. and Gregory R., "Concrete Subjected to High Rates of Loading in Compression," Magazine of Concrete Research, Vol. 24, pp 25-36, 1972.
7. Hughes, B. P., and Watson, A. J., "Compressive Strength and Ultimate Strain of Concrete Under Impact Loading," Magazine of Concrete Research, Vol. 30, pp 189-199, 1978.
8. Kolsky, H., "An Investigation of the Mechanical Properties of Materials at Very High Rates of Loading," Proc. Phys. Soc. (London) Ser. B., Vol. 62, pp 676-704, 1949.
9. Lindholm, U. S. "Some Experiments with the Split-Hopkinson's Pressure Bar," J. Mech. Phys. Solids, Vol. 12, pp 317-335, 1964.
10. Nicholas, T. in Impact Dynamics, eds. Zukas, J. A. et al., Wiley, New York, pp 277-332, 1982.
11. Christensen, R. J. Swanson, S. R. & Brown, W. S., "Split Hopkinson Bar Tests on Rock Under Confined Pressure," Experimental Mechanics, Vol. 12, pp 508-513, 1972.
12. Lindholm, U. S., Yeakley, L. M., & Nagy, A., "Dynamic Strength and Fracture Properties of Dresser Basalt," Int. J. Rock. Mech. & Mining Sci. & Geomech. Abstracts, Vol. 11, pp 181-191, 1974.
13. Lundberg, B., "A Split Hopkinson Bar Study of Energy Absorption in Dynamic Rock Fragmentation," Int. J. Rock Mech. & Mining Sci. & Geomech. Abstr., Vol. 13, pp 187-197, 1976.
14. Bhargava, J. & Rehnström, A., "Dynamic Strength of Polymer Modified and Fiber-Reinforced Concretes," Cement and Concrete Research, Vol. 7, pp 199-208, 1977.
15. Tang, T., Malvern, L. E. and Jenkins, D. A., "Dynamic Compressive Testing of Concrete and Mortar," Engineering Mechanics in Civil Engineering, eds. Boresi, A. P. and Chong, K. P., ASCE, New York, pp 663-666, 1984.
16. Kormeling, H. A., Zielinski, A. J., and Reinhardt, H. W., "Experiments on Concrete Under Single and Repeated Impact Loading," Report No. 5-80-3, Delft University of Technology, Stevin Laboratory, May 1980.
17. Suaris, W. and Shah, S. P., "Mechanical Properties of Materials Subjected to Impact," RILEM-CEB-IABSE-Interassociation Symposium on Concrete Structures Under Impact and Impulsive Loading, 33-62, Berlin, 1982.
18. Hoff, G. C., "Selected Bibliography on Fiber-Reinforced Cement and Concrete, Supplement No. 2, "Miscellaneous paper C-76-6, U. S. Army Waterways Experiment Station, Vicksburg, Miss. 1979.
19. Glenn, L. A. and Janach, W., "Failure of Granite Cylinders Under Impact Loading," International Journal of Fracture, Vol. 13, pp 301-317, 1977.
20. Young, C. and Powell, C. N., "Lateral Inertia Effects on Rock Failure in Split-Hopkinson-Bar Experiments," 20th U. S. Symposium on Rock Mechanics, 1979.
21. Bertholf, L. D. and Karnes, C. H., "Two-dimensional analysis of the split Hopkinson pressure bar system," Journal of the Mechanics & Physics of Solids, Vol. 23, pp. 1-19, 1975.

APPENDIX

Mix for Terra Tek High Strength Concretes
[0.75 Cubic Foot Mix (a)]

Water/Cement Ratio	0.26
Water (b)	7.52 lb @ 9°C
DARACAM 100 Superplasticizer (c)	425 cc
Type II Portland Cement	18.33 lb
Hana Microsilicate (Silica Fume)	3.9 lb
Flyash	3.9 lb
Fine Aggregate (#4 Concrete Sand)	39.9 lb
Coarse Aggregate (d)	41.67 lb

a - Slump varies from 4 to 9 inches.
b - Varies depending on water/cement ratio and absorption properties of aggregates rom 0.24 to 0.27
c - Varies from 400 to 550 cc.
d - Andesite or rounded river gravel

Mix for Waterways Experiment Station Concrete
[1 cubic yard] Slump 8.5 inches

Water/Cement Ratio (based on total cementitious material)	0.27
Type I Portland Cement	850 lb
Silica Fume	150 lb
Fine Aggregate (Manufactured limestone from Vulcan Materials, Calera, Ala.)	1860 lb
Coarse Aggregate (Manufactured limestone, maximum size 3/8 inch)	1008 lb
Water	270 lb
High Range Water Reducing Add Mixture	20 lb

DAXAD-19-2% by weight of cementitious material (superplasticizer).
Prepared by Concrete Technology Division, WES

EXPERIMENTAL PROGRAM TO INVESTIGATE RATE EFFECTS IN CONCRETE[1]

S. M. Babcock

New Mexico Engineering Research Institute
University of New Mexico
Albuquerque, New Mexico

ABSTRACT

Concrete structures and members are sometimes exposed to high rates of loading. The loads may be from earthquakes, explosively produced airblast or ground motion, or impact devices. The response of the material to high rates of loading must be known to provide an adequate design that is not overly conservative for these members or structures. The knowledge of material behavior is also important for the analysis of experimental data. To enlarge the currently inadequate data base required for the development of concrete constitutive models that incorporate strain rates up to 10/s, an experimental program was initiated. The data from the experimental tests will be used to advance the development of a viscoplastic model for frictional materials. This paper includes a detailed description of the new experimental device used in the program. Also included are preliminary uniaxial stress results. Limitations and extensions of the current device are discussed, as are the consequences of some design features. These features include the specimen size and the appropriate range of strain rates.

INTRODUCTION

Many of the mechanical properties of concrete are affected by the rate at which the concrete is loaded. The extent to which a property is affected depends on the property being considered and the method used to prepare and test the concrete. As the first step in the investigation of strain rate effects in concrete, a literature survey was performed (Ref. 1). The survey revealed a basic lack of experimental data that could be used for material model development. Although data from uniaxial stress tests at various strain rates are available, significant pieces of information, such as lateral strains and static behavior, are often missing. Almost no data exist for any other stress path.

A two-pronged approach that will help close the gap in the experimental data and provide adequate material models for frictional materials subjected to high rates of loading was proposed in Reference 1. The experimental program was to be conducted in conjunction with the development of a third-invariant plasticity model. The program was scheduled to consist initially of uniaxial stress tests, but the technique to be used was one that could be developed later for performing multiaxial stress tests at high rates of loading. The results of these tests were then to be used to verify the material model and to identify areas requiring improvement.

To accomplish these goals, the following tasks were scheduled for this work phase: complete the design of the experimental testing device, construct the device, and begin the evaluation tests. The evaluation tests were to be used to develop needed instrumentation, operation procedures, and apparatus configurations that would provide the required data. If the evaluation tests were successfully completed, production tests were to be initiated. In this paper, the progress made toward meeting these objectives is described.

DESIGN CONSIDERATIONS FOR EXPERIMENTAL TEST DEVICE

Concrete has been tested in uniaxial stress at high strain rates frequently enough that significant parameters are becoming apparent and a data base is being built. Data from multiaxial stress tests at high rates of strain, on the other hand, are virtually nonexistent. Because of the lack of multiaxial data, any attempt to model the multiaxial behavior of concrete requires that assumptions be made. The effects of high strain rates on the three-dimensional behavior of concrete are unknown. To fill this void, a relatively simple and inexpensive testing procedure is proposed.

Concrete is used in a number of applications that expose the concrete to high strain rates. Airblast and ground motion loadings from explosive shocks are two examples of such exposure. Other examples include the impact driving of concrete piles, the accidental dropping of concrete structural members during handling, high winds, earthquakes, and sudden increases in pressure in concrete vessels. Most of these events can involve strain rates ranging from virtually static (10^{-6}/s) to as high as 10^{6}/s. It has been shown that at

[1]The work is sponsored by the Air Force Office of Scientific Research, Contract No. F29601-81-C-0013.

strain rates of less than about 0.1/s, insignificant or confusing and unconfirmable results are obtained (Ref. 2). On the other hand, for the large majority of strain environments that structures are expected to survive, particularly airblast, ground shock, wind, and earthquake, the strain rates are less than 10/s. For these reasons, the strain rates sought in an experimental program should fall between 0.1/s and 10/s.

The rise-time to peak stress can be determined for a particular concrete once $\dot{\varepsilon}$ is given. The stress rate, $\dot{\sigma}$, can be approximated for uniaxial stress by

$$\dot{\sigma} = E\dot{\varepsilon}$$

where E is the modulus of elasticity. To find the approximate rise-time for a given strain rate, the stress rate is calculated, and the time required to reach f'_c can then be determined. For example, at a strain rate of 10/s and a compressive strength of 27.6 MPa (an average-strength concrete), E is calculated to be 2.5×10^4 MPa (Ref. 3), and $\dot{\sigma}$ is 25×10^4 MPa/s. Therefore, time to f'_c is 0.1 ms.

The size of the concrete test specimen is constrained by two factors. The minimum size is limited by the nonhomogeneous nature of concrete. The specimen must be large enough to ensure that the nonhomogeneities in the concrete can be neglected. Generally, the specimen must be at least 10 times the size of the largest aggregate in the mix. Usually, a 3/8-in coarse aggregate is used, which means that the minimum specimen size is about 100 mm. Conversely, to eliminate the effects of inertia the maximum specimen size must be limited in order to minimize the transit time of the wave (or to maximize the number of wave reflections). If the number of wave reflections is not sufficiently large during loading, the strain across the specimen cannot be considered uniform and the equations of motion will have to be solved and constitutive information backed out indirectly. For a large number of reflections the response can be considered homogeneous and quasi-static. The transit time is calculated from the wave speed in concrete (about 3000 m/s) and from the specimen size. The minimum specimen size of 100 mm gives a transit time of about 33 μs. With a strain rate of 10/s, the rise time is calculated to be 0.1 ms, and three reflections will occur before failure. A strain rate of 0.1/s requires a rise-time of 10 ms, and 300 reflections will occur before failure. Three hundred reflections are more than enough to ensure that the effects of inertia will not significantly affect the results; three reflections probably are not enough. The minimum number of reflections will have to be determined analytically by a comparison of the dynamic solution with the static solution. As an initial estimate, at least 25 to 50 reflections will be required, which would limit the highest quasi-static $\dot{\varepsilon}$ to about 1/s. If the specimen is loaded from both sides, which effectively reduces the transit time by one-half, a quasi-static $\dot{\varepsilon}$ of about 2/s could be obtained. Higher strain rates can be achieved, but the calculation of stress may involve the use of the equation of motion.

Figure 1 (Ref. 4) shows typical examples of pressure histories for some propellants. It is evident that rise-times of less than 10 ms can be achieved; thus, these materials could be used to obtain the required loading rates. Gunpowder, another readily available propellant, can produce a faster rise-time as well as higher pressures than those shown in Figure 1 and thus represents an option to be considered.

DESCRIPTION OF APPARATUS

Several designs for the testing device were considered. The final configuration consists of cylindrical segments bolted together with flanges. Figure 2 is a schematic view of the device. The overall height of the apparatus is about 1 m. Two chambers are included to provide more control over the burning of the propellant used as the driving force in the tests.

The walls of the barrel are made from 4142 steel tubing with a 10.2-cm (4-in) inside diameter and a 16.5-cm (6.5-in) outside diameter. The flanges are standard 1500-lb flanges. A plate is inserted between the top two flanges to close off the upper chamber. This plate is 2.54 cm (1 in) thick and has two safety rupture disc devices. The discs are calibrated to rupture in case the pressure should rise above 68.9 MPa (10,000 lb/in^2). Another plate is inserted between the lower chamber and the upper chamber. In this plate, which is also 2.54 cm (1 in) thick, are venting holes that allow the pressure created by the burning propellant to escape into the lower chamber, where the load cell and specimen are located. The venting has two purposes: (1) to reduce the temperature load on the cell, and (2) to provide some control over the rise-time. The second purpose is of particular interest if a high-density or a fast-burning propellant is used. These types of charges will give a very fast rise-time, and the venting plate can be used to reduce the rise-time to the desired value. However, the charge currently in use is producing an appropriate rise-time without the venting; therefore, the plate is used primarily to prevent the burning propellant from coming into contact with the load cell.

PROPELLANT CHARGE DESIGN

The Department of the Army has issued a propellant design handbook (Ref. 5) that includes an algorithm for determining the characteristics of burning propellants. The propellant parameters have been identified at arsenals where these propellants are in common use. The algorithm is coded to include a "closed bomb" configuration, which corresponds to rigid boundaries, and a configuration that permits displacements of the boundary based on the linear elastic constitutive properties of the material surrounding the propellant.

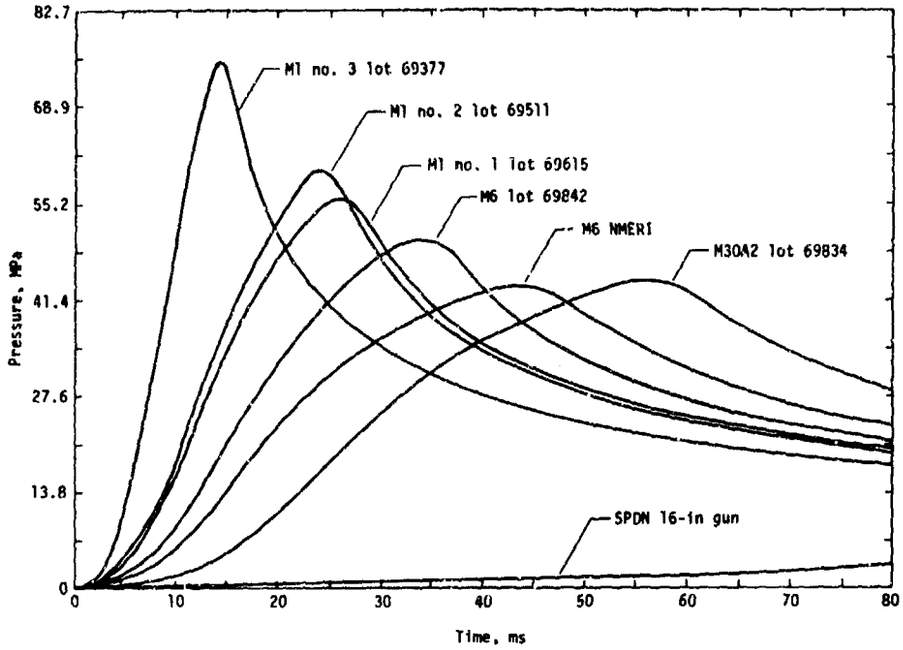

Figure 1. Pressure histories for some propellants (after Ref. 4).

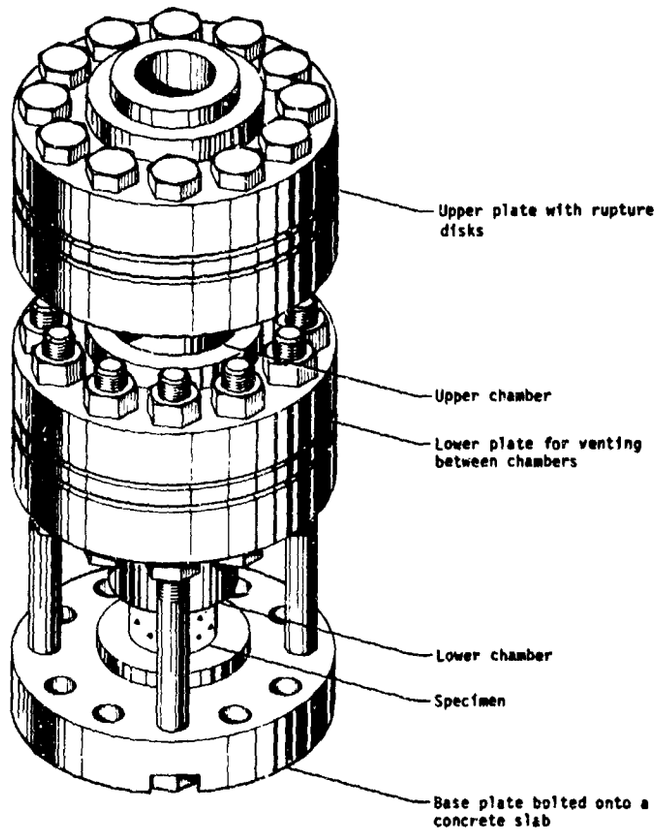

Figure 2. Isometric drawing of a rapid loading device.

Pressure histories, which are particularly relevant for observing rate effects in concrete, can be obtained for various propellants using the propellant burn algorithm. These histories indicate that the peak pressure in a chamber depends on the density of the propellant. Rise-times depend on both the initial density and the propellant type. Higher initial loading densities give faster rise-times and higher peaks. Iterating for different densities and propellants showed that for the desired pressure histories, a fast-burning propellant at a low density was required. The difficulty with low charge densities, however, is that the propellant may extinguish itself if any movement of the boundaries of the chamber occurs. This reaction is due to the interaction between pressures and burn rates for propellants. To ensure that the propellant would burn properly, a relatively high density (35 percent by weight) of a fairly large-grain, and therefore slow-burning, propellant was used. This charge gave too high a peak pressure--over 138 MPa (20,000 lb/in^2)--and too short a rise time and caused some minor damage to the device. Once the device had been repaired, lower charge densities were tried to determine whether the charges could maintain their burn. A small charge at a 5-percent density was tried next. Only the lower chamber was used in this test. One continuous solid steel cylinder was used to simulate the load cell and specimen in order to avert a cavity expansion that could cause the propellant to stop burning. The results of this test were encouraging, except that the top of the solid steel cylinder was scorched by the burning propellant.

In an attempt to reduce the heat load on the load cell, a plate was introduced between the upper and lower chambers. Vent holes in the plate allow the high-pressure gas to vent to the lower chamber where the load cell is located. Because the propellant actually burns in the upper chamber, away from the load cell, the cell is not subjected to the intense, direct heat. The propellant density was increased gradually over the next few experiments to bring the peak pressure up to about 41.4 MPa (6000 lb/in^2). The shortcoming of the current setup is the occurrence of leakage, which prevents the pressure from increasing to its full potential and also causes the pressure to decay to rapidly. In the next set of tests, gaskets will be used to reduce or prevent leakage.

A summary of the propellant type and charge density for each test fired to date is provided in Table 1. The peak pressures achieved, as measured by the pressure gage for the lower chamber, are also included. Typical pressure and concrete strain history plots are shown in Figure 3. Because of a time shift between the concrete strain record and the record of pressure in the lower chamber, no pressure-strain curve is included.

LOAD CELL DEVELOPMENT

Commercially manufactured load cells are not designed to be inserted into a cylindrical barrel. Therefore, a special developmental effort was conducted. Specifications for the cell included the following: it must be rugged enough to survive repeated tests; its physical dimensions are restricted; and it must provide linear response over the pressure range of interest.

The initial calibration tests indicated that the original load cell was linear and reliable up to the desired force level. To measure the Poisson effect, the cell was instrumented with two vertical and two horizontal semiconductor strain gages mounted on a column. The full bridge provided temperature compensation and a good response. The difficulty with this load cell was that because the gages and wires were exposed to the heat, gage survivability was poor.

To obtain better survivability, a second load cell was developed. On this cell the strain gages are mounted in the interior of a hole drilled part way through the wall of the aluminum cylinder. A side exit is provided for the wire, and a steel pipe screwed into the exit protects the wires from the heat. The first of this type of load cell was instrumented with U-shaped strain gages that could not provide linear results because of the curvature of the hole. In the next model, a straight strain gage that did not have to be curved around the hole was used.

Gage survivability for this load cell was adequate. However, the gage did not provide a linear response because of the response of the hole to compressive loads.

The third design was again a column-based load cell design. For better protection, a cover for the strain gages was added. Further tests will be conducted to verify the adequacy of the design.

EXTENSIONS

Because of the difficulty of developing an adequate load cell, production tests have not been accomplished. These tests will be made early in the new work phase, while a new device is being designed and built for biaxial testing. In addition to the experimental program, models will be developed from the data from the uniaxial stress tests and from biaxial stress data if available.

The design for the biaxial testing device will be based on the latest design for the uniaxial device. Essentially, two devices will be oriented to load orthogonal axes of a cubical specimen. Several difficulties that are immediately apparent include using a cylindrical barrel to load a square surface, instrumenting three-dimensional concrete specimens, and firing two devices simultaneously. These and other difficulties will be addressed as the designing of the device progresses.

ACKNOWLEDGMENTS

The work described in this paper was sponsored by the Air Force Office of Scientific Research. The author is also grateful for the aid and encouragement of Howard L. Schreyer of the New Mexico Engineering Research Institute.

TABLE 1. TEST SUMMARY

Test No.	Date	Propellant type	Charge density by volume, %	Total charge, kg (lb)	Specimen	Load cell	Peak pressure in lower chamber MPa (lb/in^2)	Comments
1	6-29-84	M5	35	2.27 (5)	Steel	Aluminum	138 (>20,000)	Damaged device
2	8-3-84	M5	5	0.16 (0.35)	Steel	Steel	[a]---	Small chamber only
3	8-31-84	M5	4	0.32 (0.70)	Steel	Steel	28.3 (4,100)	Larger chamber with vent plate
4	9-6-84	Black powder	4	0.39 (0.85)	Steel	Steel	31.7 (4,595)	Larger chamber with vent plate
5	9-13-84	Black powder	5.2	0.39 (0.85)	Concrete	Aluminum	26.9 (3,900)	Larger chamber with vent plate
6	10-5-84	Black powder	6.2	0.45 (1.0)	Concrete	Aluminum	20 (2,900)	Larger chamber with vent plate

[a]Propellant burn test; peak pressures not available.

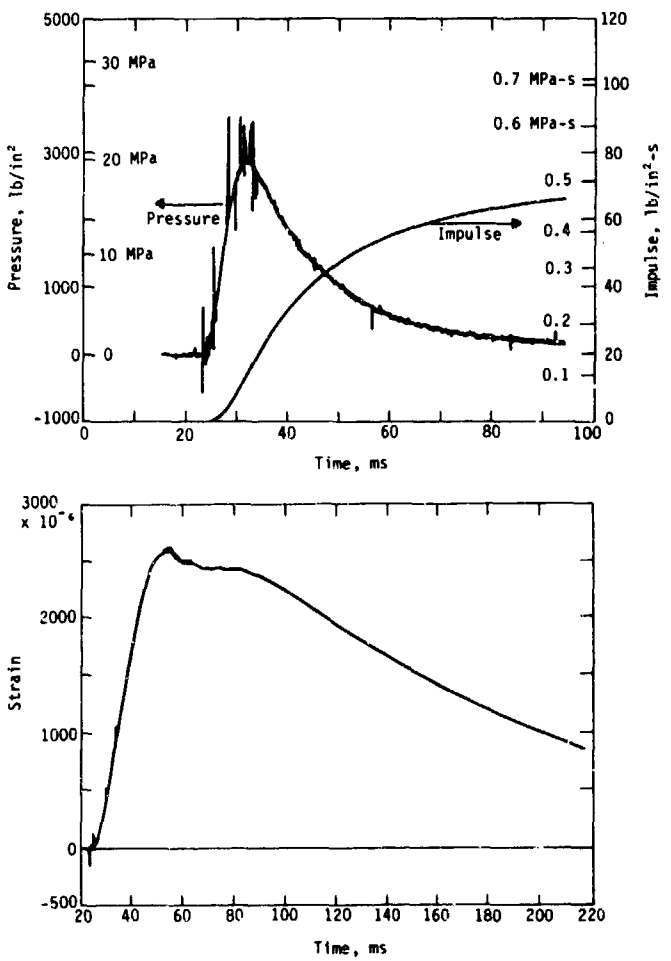

Figure 3. Typical plots of pressure versus time and concrete strain versus time.

REFERENCES

1. Schreyer, H. L., **Development of a Third-Invariant Plasticity Theory for Concrete and Soils**, AFWL-TR-83-119, Air Force Weapons Laboratory, Kirtland Air Force Base, New Mexico, October 1983.

2. Mainstone, R. J., "Properties of Materials at High Rate of Straining or Loading," **Materials and Structures**, Vol. 8, No. 44, March-April 1975.

3. **Building Code Requirements for Reinforced Concrete**, ACI Standard 318-71, American Concrete Institute, 1971.

4. Babcock, S. M., **Propellant-Driven Simulator Configuration Analysis**, AFWL-TR-83-21, Air Force Weapons Laboratory, Kirtland Air Force Base, New Mexico, February 1983.

5. **Engineering Design Handbook: Propellant Actuated Devices**, AMCP 706-270, Department of the Army, Headquarters, U.S. Army Materiel Command, Alexandria, Virginia, 30 September 1975.

A NEW TECHNIQUE FOR STUDYING THE DYNAMIC TENSILE RESPONSE OF CONCRETE

James K. Gran

SRI International Menlo Park, California 94025

INTRODUCTION

Tensile failure in concrete is produced by the nucleation, growth, and coalescence of microcracks. The tensile strength is the stress at which this process of accumulating damage becomes locally unstable. Once the material has become unstable, its resistance to further deformation quickly vanishes. An ideally brittle material would lose all its strength instantaneously. In real materials, including concrete, the strength reduction is a function of further accumulating tensile damage and requires a finite time to occur.

The objectives of this work were to develop and demonstrate experimental and analytical techniques to

(1) Obtain a measure of the tensile strength and the strength reduction as a function of accumulating tensile damage for concrete at strain rates of about 10/s.

(2) Study the effect of confining pressure on concrete tensile failure at these strain rates.

EXPERIMENTAL TECHNIQUE

The concept of the experiments is shown in Figure 1. A cylindrical rod is initially held in static compression, in both the axial and radial directions. The pressure at each end of the rod is

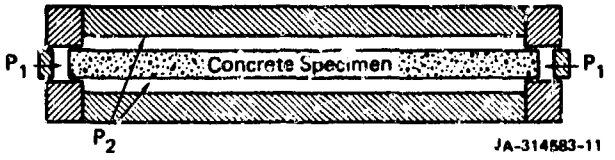

FIGURE 1 DYNAMIC TENSILE LOADING DEVICE

released simultaneously, sending axial relief waves toward the center. Individually, these waves bring the rod only to zero axial stress, but when they superpose at the midpoint, they bring the rod to a tensile stress equal to the original axial compression. Fracture occurs at the center of the rod if the original axial compression exceeds the tensile strength and if the rod is long enough that compressive reflections from the ends do not inhibit fracture.

A photograph of the tensile testing device with an unconfined specimen is shown in Figure 2.

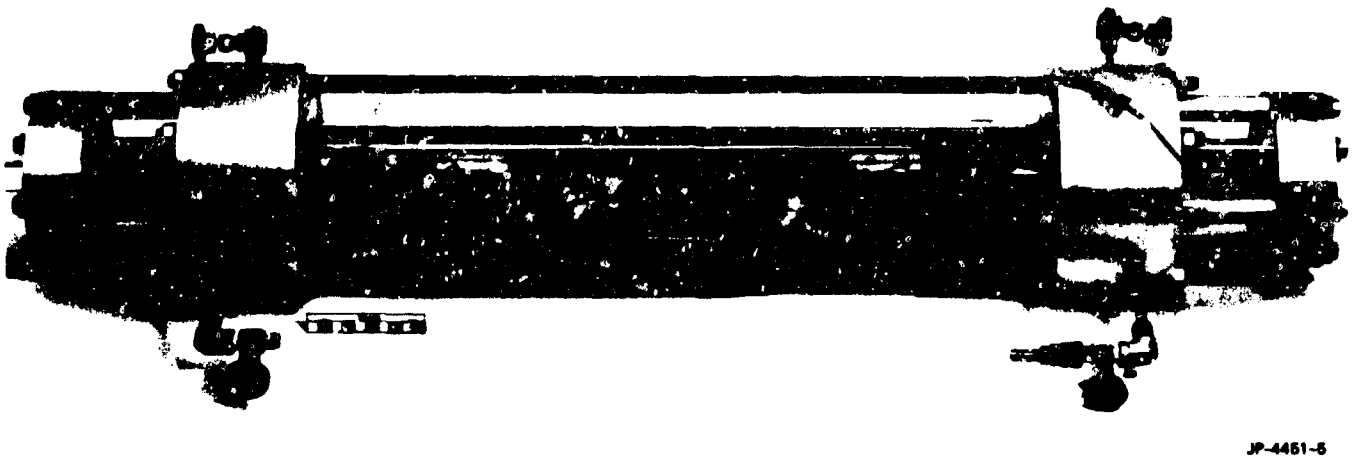

FIGURE 2 DYNAMIC TENSION TESTING WITH UNCONFINED CONCRETE ROD

The device tests 5.1-cm-diameter, 76.2-cm-long rods at stresses up to 20 MPa. The static end pressure is removed in about 30 μs, producing strain rates in concrete of about 10/s.

The essential component of the tensile testing apparatus is the relief wave generator at each end of the rod. A drawing of its design is shown in Figure 3. It consists of an aluminum bore block

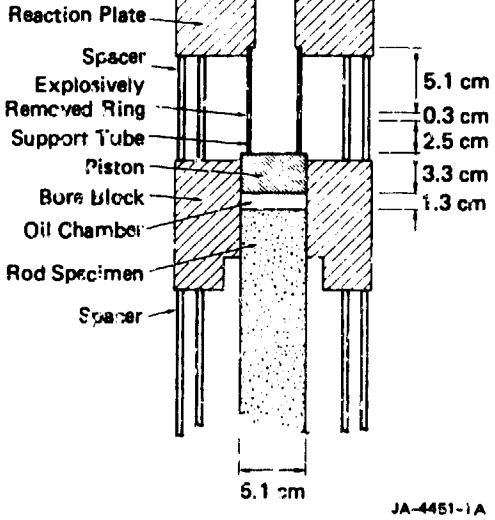

FIGURE 3 RELIEF WAVE GENERATOR

into which the end of a rod specimen and a plastic piston fit to form a chamber for oil. The oil is pressurized via a small orifice through the wall of the bore block. The rod and piston seal the pressurized oil in the chamber with rubber O-rings. The piston is held in place by a thin-walled steel support tube, which presses against a reaction plate bolted to the bore block. The rod is held in place by an identical unit at the other end, with the two bore blocks bolted together. The support tube comprises three sections, one of which is a segmented ring that is explosively driven inward to free the piston and initiate decompression of the oil. The rings in the support tubes are removed with an estimated simultaneity of less than 5 μs, using strands of sheet explosive.

The radial pressure (confinement) remains constant during an experiment, but is an independent parameter that can be varied. In experiments with confinement, an aluminum tube is used to hold the radial pressure and to space the bore blocks. In experiments without confinement, a Plexiglas tube is used.

To define the loads in these experiments, the pressure is measured in the chamber at each end of the rod and in the confining pressure chamber surrounding the rod. The measurements are made with commercially available diaphragm-type pressure gages. One gage is mounted in each bore block so that the sensing diaphragm is flush with the wall of the oil cavity. A single gage is also mounted at the midpoint of the confining pressure chamber, the diaphragm flush with the inside surface of the chamber (1.3 cm from the radial surface of the rod).

Axial and circumferential surface strains are measured at several locations on the rod, using commercially available 2.5-cm-long foil-type strain gages. Axial strain is measured at four locations: 10 cm from each end of the rod and 7.6 cm from the midpoint on both halves of the rod. Circumferential strain is measured only at the symmetric points 7.6 cm from the midpoint. At each measurement location, three gages are mounted at 120-degree intervals.

EXPERIMENTS ON UNCONFINED RODS

Test 42

Test 42 was a dynamic tension test of a concrete rod with no confinement and a static axial preload of 10.55 MPa. The static uniaxial tensile strength* of the concrete was about 3.5 MPa, the static uniaxial compressive strength† was about 50 MPa. The static elastic modulus was 24.1 GPa; Poisson's ratio was 0.2.†† The rod failed in dynamic tension at a single location, 0.46 cm from the midpoint, and no secondary damage was visible.

The axial strains at +/-7.6 cm are shown in Figures 4 and 5. In the time scale of these plots, the explosive charge was initiated at t = 0.100 ms. All the strain records were scaled to correspond to the average static elastic moduli. At both locations, the strains are fairly uniform even after the effects of tensile failure arrive.

The effects of dispersion are noticeable in the axial strains at +/-7.6 cm at the beginning of the pulse. At about t = 0.380 ms, these strains show the effect of tensile failure. The nominal wave speed, calculated from the times of arrival of the input and fracture waves at +/-7.6 cm, was 3.175 km/s. This is 5% lower than the bar speed computed from the measured density and static elastic modulus.

The strain rate at the front of the fracture signals is about 10/s, so the strain rate at the failure location was about 20/s. At -7.6 cm, 7.1 cm from the failure location, the peak average strain was 160 strain. At +7.6 cm, 8.1 cm from the failure location, the peak average strain was

---

* The tensile strength was determined from split-cylinder tests on samples taken from the rod after the dynamic tension test.

† The compressive strength was determined from tests on specimens taken from a companion rod.

†† The elastic constants were determined from the measurement of the static axial preload and the average initial strains.

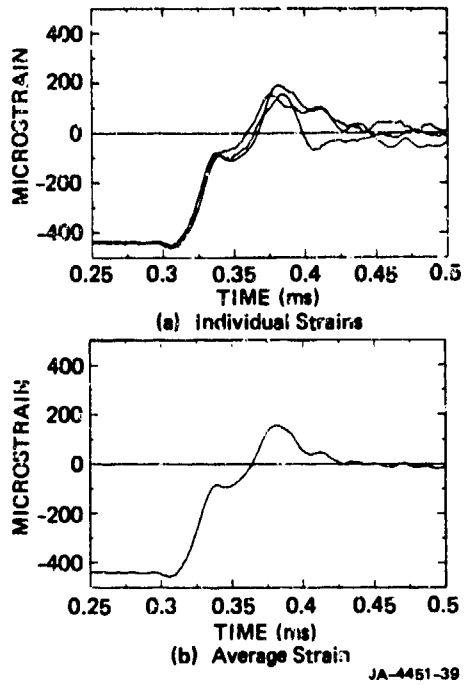

FIGURE 4 AXIAL STRAIN RECORDS AT -7.6 cm IN TEST 42

(7.1 cm from fracture location)

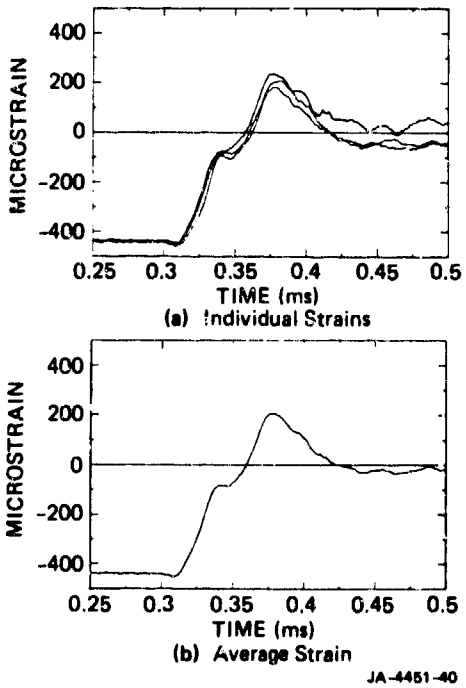

FIGURE 5 AXIAL STRAIN RECORDS AT 7.6 cm IN TEST 42

(8.1 cm from fracture location)

210 μstrain. The elastic axial stress computed from the highest measured strain is about 5 MPa, more than 40% higher than the static tensile strength.

Test 43

Test 43 was essentially identical to Test 42. It was conducted with no confinement and a static axial preload of 10.55 MPa. The specimen was made at the same time as the one tested in Test 42. The static uniaxial tensile strength of the concrete was about 3.75 MPa, the static uniaxial compressive strength was about 50 MPa. The static elastic modulus was 24.7 GPa; Poisson's ratio was 0.2. The rod failed in dynamic tension at a single location, only 0.10 cm from the midpoint, and no secondary damage was visible.

The individual axial strains at +/-7.6 cm are shown in Figure 6 and 7. The strains are not as uniform as in Test 42, especially after the effects of fracture arrive. However, the average strains are very nearly the same as in that test. The nominal wave speed was 3.243 km/s. This is about 3% lower than the bar speed computed from the measured density and state elastic modulus.

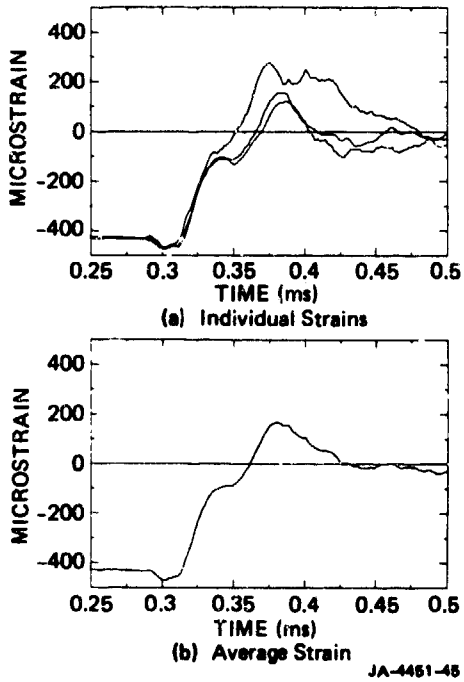

FIGURE 6 AXIAL STRAIN RECORDS AT -7.6 cm IN TEST 43

(7.5 cm from fracture location)

The strain rate at the front of the fracture signals is about 10/s, so the strain rate at the failure location was about 20/s. The peak average tensile strains at these locations are 170 and 190 μstrain, the higher of which corresponds to an elastic stress of about 4.7 MPa. This is about 25% higher than the static tensile strength.

EXPERIMENTS ON CONFINED RODS

Test 44

Test 44 was a dynamic tension test of a

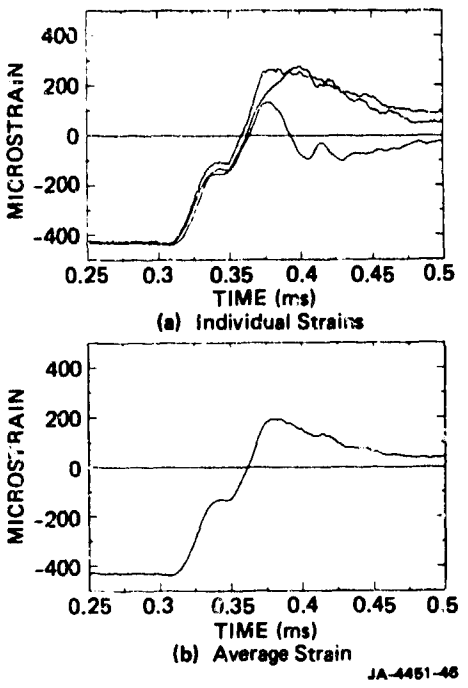

FIGURE 7 AXIAL STRAIN RECORDS AT 7.6 cm IN TEST 43

(7.7 cm from fracture location)

concrete rod with a hydrostatic preload of 10.31 MPa. The specimen was made at the same time as the ones tested in Tests 42 and 43. The static uniaxial compressive strength was about 50 MPa. The static elastic modulus was 28.4 GPa. The rod failed in dynamic tension at two locations, +2.2 cm and -15.2 cm. The fractures passed through the mortar, voids in the mortar, mortar/aggregate interfaces, and some of the larger aggregates. No large voids existed at either section.

The dynamic pressure histories are shown in Figure 8. The axial unloading occurs in about 25 μs and is simultaneous at the two ends. The radial pressure is constant until the stress waves in the rod reach the gage location (midpoint of the rod), and it remains within 1 MPa of the initial value. The variation in radial pressure appears to follow the circumferential strain (not shown), suggesting that the pressure variation is caused by volume changes in the specimen.

The average axial strain histories at +/-7.6 cm are shown in Figure 9. The records from the three gages at each location were averaged electronically before recording. The records were also scaled to correspond to the average static elastic moduli. Because the preload was hydrostatic compression, the initial strains are all equal and negative. The axial strain corresponding to zero axial stress is 145 μstrain. The nominal wave speed, calculated from the times of arrival of the input and fracture waves at +/-7.6 cm, was 3.544 km/s. This is 1% lower than the computed bar speed.

At about t = 0.380 ms, the axial strains at +/-7.6 cm showed the effect of tensile failure at +2.2 cm. Thereafter, the stress waves propagated and reflected in separate rod segments. The frequency of the reflections in the left half of the rod indicates that the fracture at -15.2 cm must have occurred when the tensile wave arrived there.

The strain rate at the front of the fracture signals was about 10/s, so the strain rate at the failure location was about 20/s. The peak average strain at +7.6 cm was 390 μstrain. At -7.6 cm it was 315 μstrain. These strains correspond to axial stresses of 6.9 MPa and 5.6 MPa, respectively. The higher of these stresses is about 90% greater than the static tensile splitting strength measured on sections of companion rods. It is also about 40% higher than the unconfined tensile strength at the same strain rate, observed in Tests 42 and 43.

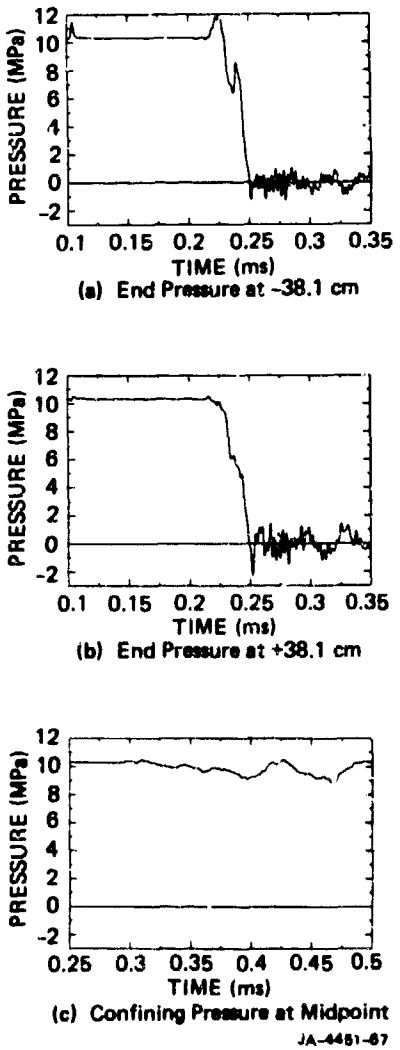

FIGURE 8 PRESSURE MEASUREMENTS IN TEST 44

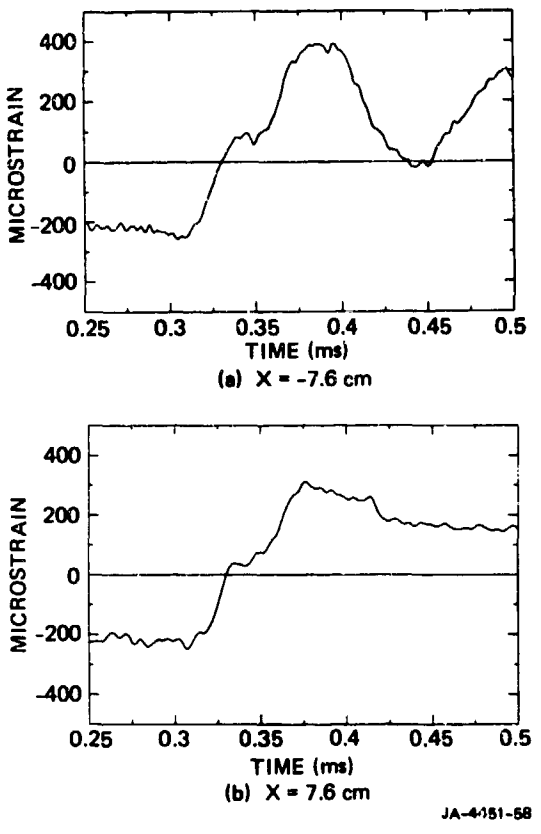

FIGURE 9 AVERAGE AXIAL STRAINS AT ± 7.6 cm IN TEST 44

CONCLUSIONS

The experimental techniques developed and demonstrated in this research effort provide a new method for studying the dynamic tensile response of concrete and, possibly, many geologic materials. In its present configuration, the tensile testing apparatus will produce up to 20 MPa tensile stress with up to 20 MPa confining stress at a strain rate of about 20/s. The primary failure location occurs within a few cm of the midpoint of the rod, and secondary failures can be inhibited by testing at load levels only slightly higher than the strength of the specimen. The boundary conditions are well-defined by the pressure measurements. The effects of fracture on the stress waves in the specimen are captured in the surface strain measurements.

Assuming the measured strains to be elastic, a first-order interpretation of the data indicates a significant enhancement of tensile strength at a strain rate of 20/s. The data also indicate a dependence of tensile strength on confining pressure. However, a wave analysis of the experiments (not shown) suggests that the response of the rod is inelastic even several centimeters from the failure location. Thus, to obtain a measure of the stress and fracture volume growth at the failure location requires an analysis beyond the classical Hopkinson bar wave-tracking approach.

ACKNOWLEDGEMENT

This work was supported by the U. S. Air Force Offfice of Scientific Research under Contract No. F49620-82-K-0021.

THE TENSILE STRENGTH OF CONCRETE UNDER DYNAMIC LOADING

J. Weerheijm
and
W. Karthaus

Prins Maurits Laboratory TNO
P.O. Box 45 2280 AA Rijswijk
The Netherlands

ABSTRACT

On the basis of the principles of fracture mechanics and the most significant properties of concrete, a new model has been developed which describes the failure under uniaxial tensile loading. Thanks to this model the strength can be determined as a function of the loading rate. The results are in very good agreement with the data of uniaxial tensile tests with loading rates of 10^4 to 10^{12} Pa/s.

1. INTRODUCTION

From recent investigations it appeared that in structures under impulse loading the force distribution differs a great deal from that under static loading. In the structure there appear to run high peaks of shear forces and moments (5). Since the numerical values of the corresponding stresses are high, the chance of failure under these loading conditions is expected to increase.

From experiments, however, the resistance of structures against explosion and impact loading is known to be higher than is to be expected from theoretical force distribution.

The strength of concrete is apparently greatly influenced by the loading rate. This influence of loading rate on the uniaxial tensile strength of concrete has been proven experimentally by several investigators. An increase in the loading rate from 10^4 to 10^9 Pa/s causes an increase in tensile strength of about 75%. The experiments of D.L. Birkimer have shown that the strength increases steeply at loading rates higher than 10^{11} Pa/s. To enable the loading rate to be taken into account in response calculations a model has been developed which describes the influence of the loading rate on the strength.

Concrete is a composite material with components of different stiffness. Because of this concrete is always more or less cracked and the mechanical behaviour is complex. In the model the internal damage is characterized by uniformly distributed cracks and the expansion of these cracks under dynamic loading is described by the principles of fracture mechanics. The speed of crack extension depends on the rate of energy supply which again depends on the loading rate. The way in which this enables the calculation of the uniaxial tensile strength of concrete as a function of the loading rate is presented in this paper.

2. TENSILE FRACTURE OF CONCRETE

Concrete is a composite material consisting of different sized aggregate particles embedded in cement paste. Because of the heterogeneity there are voids and cracks at all dimensional scale levels. Many of the microcracks are formed during the hardening process and therefore exist even before any load has been applied. The heterogeneity, the existing microcracks and voids and the differences in stiffness govern the mechanical behaviour of concrete.

Under tensile loading the stress-strain curve is linear up to a stress level of 60% of the ultimate tensile strength (f_c). Above this level the bond microcracks start to grow but due to crack arrest crack propagation remains stable.

Beyond a stress level of about 0,75 f_c the microcracks in the mortar start to grow and bridging of the bondcracks occurs; macrocracks are formed; crack propagation becomes unstable and finally one major crack develops.
To explain and determine the strength of a material like concrete fracture mechanics may be suitable as it considers materials that are not homogeneous and not continuously distributed. This gives the opportunity to describe the mechanical behaviour of materials with internal damage or of heterogeneous composition.

Fracture mechanics uses two criteria for crack propagation. The first is the strength criterion. The stresses in front of a crack tip must exceed a certain stress level to enable the crack to propagate. The second is the energy criterion which states that only when the strain energy release rate equals the energy required to separate the new crack surfaces is crack propagation possible. Application of fracture mechanics for a precise description of the behaviour of concrete until the ultimate strength is reached requires that the internal stress distribution and the energy demand for crack propagation are known at all dimensional scale levels. The above review of the behaviour and the composition of concrete shows that the

stress distribution and the energy demand cannot be described in detail.

The energy demand is not continuously distributed due to the heterogeneity of concrete, which reveals itself in crack arrest, and because the tensile fracture of concrete is not limited to one single crack. In front of the tip of a macro crack there exists a highly stressed zone with micro cracks. The expansion of these micro cracks determines the energy demand for the propagation of the macro crack. Due to this micro cracking and crack arrest the energy demand for expansion of the macro crack increases with increasing crack length. Although the fracture phenomena under tension are known quite well, modelling of the mechanical behaviour of concrete is only possible when it is focussed on the most significant features of the behaviour. These have been mentioned earlier. First of all there is the linear elastic behaviour until a stress level of 60% of the tensile strength (f_c). Apparently the criteria for crack propagation are fulfilled for the existing micro bond cracks with average size. The propagation of these cracks is hard to predict but the development of the final failure crack is determined by:

I: the number of cracks and their average size: the internal damage;

II: the quality of the undamaged material around the cracks;

III: the rate of energy supply.

The point mentioned as I, can be expressed in a geometrical parameter: the ratio of damaged and undamaged material ($\frac{a}{b}$).
The quality of the undamaged material (II) is characterized by the energy demand for crack propagation together with the stress level which must be exceeded. For determining the ultimate strength the average value of the energy demand between the onset of crack propagation and failure (G_{IC}) may be chosen as the characteristic parameter of material quality.
The loading rate ($\dot{\sigma}$) determines the rate of energy supply (III)

With the parameters ($\frac{a}{b}$), (G_{IC}) and ($\dot{\sigma}$) the expansion of the existing cracks can be modelled if the stress destribution is known. For describing the influence of the loading rate on the tensile strength the material around the cracks is assumed to be brittle and linear elastic so that the stress distribution can be determined with the Linear Elastic Fracture Mechanics (L.E.F.M.).

Although concrete is not linear elastic the L.E.F.M. has been chosen as a tool because of its simplicity and its possibility to take the parameters ($\frac{a}{b}$), (G_{IC}) and ($\dot{\sigma}$) into account. Furthermore the purpose of the model is to describe the strength of concrete which is specially governed by the resistence of the material to crack propagation on small-scale levels while the behaviour of concrete becomes more linear when the dimensional-scale level gets smaller.

3. LINEAR ELASTIC FRACTURE MECHANICS (LEFM)

Before the model is described a summary of the basic concepts of the L.E.F.M. will be given. As mentioned in 2 fracture mechanics deals with the balance of energies involved with the propagation of a crack. Griffith formulated this balance for crack propagation in a brittle material as follows. Propagation occurs when the strain energy release rate is at least equal to the rate of increase in the free surface energy due to the formation of new crack surface area.

In case of the basic problem of a single elliptical through thickness crack of length 2a in an infinite ideal Hookean plate subjected to a plane stress field (σ), the elastic strain energy (U) is given by:

$$U = \frac{\sigma^2 \Pi a^2}{E} \qquad (1)$$

Where E is the modulus of elasticity. In the energy balance the strain energy release rate per crack tip is used, defined by $\left[\frac{1}{2}\frac{\partial U}{\partial a}\right]$ and usually replaced by G which is also called the crack driving force. When G equals twice the specific surface energy (γ) of the crack surfaces, crack propagation is possible. So G must exceed a critical value (G_{IC}) for crack propagation to occur.

$$G_{IC} = \frac{\sigma_c^2 \Pi a}{E} = 2\gamma \qquad (2)$$

In this expression σ_c is the stress level in the critical situation.

Another criterion for crack propagation is the stress criterion. The stress field around the crack tip is determined by the stress intensity factor K_I. This factor is a measure for all stresses and strains in this zone. When the stresses, and so K_I, exceed a critical value crack propagation can occur. For the elliptical through thickness crack of length 2a in the infinite plate subjected to a plane stress field (σ), the critical value of K_I is given by:

$$K_{IC} = \sigma_c \sqrt{\Pi a} \qquad (3)$$

with σ_c the stress level at which the critical situation is reached.

Crack propagation will only occur when both the stress and energy criteria are fulfilled. For a linear elastic material these criteria are fulfilled simultaneously because:

$$K^2 = EG \quad \text{(plane stress)} \qquad K^2 = \frac{E}{(1-\nu^2)} \cdot G \quad \text{(plane strain)} \qquad (4)$$

For geometries different from the elliptical through thickness crack the stress distribution around the crack tip changes and equations (2) and (3) for the criteria and the stress field must be adjusted. In the model the geometry of a penny-shaped crack, of radius (a), in an infinitely long cylinder of radius (b) is used (Figure 1). In this case the criteria are given by (1)

$$K_{IC} = \frac{2}{\Pi} \sigma_c \sqrt{\Pi a} f(\frac{a}{b}) \qquad (5)$$

$$G_{IC} = \frac{K_{IC}^2}{E} (1 - \nu^2) \qquad (6)$$

where $f(\frac{a}{b})$ is a function which takes the finite dimensions of the cylinder into account (8). For a penny-shaped crack in an infinite medium the radius of the crack is the only relevant dimension of length. In case of the cylinder with internal crack the most relevant or characteristic dimension of length is the crack radius adjusted with the function $f(\frac{a}{b})$. The characteristic length is given by:

$$[a\ f^2(\frac{a}{b})]$$

4. DESCRIPTION OF THE MODEL

With the main features of the mechanical behaviour of concrete as described in section 2, and with the L.E.F.M. the influence of the loading rate on the tensile strength is modelled.
The concrete is schematized as a homogeneous material with penny-shaped cracks in the potential plane of failure. The cracks in the unloaded material have a radius (a) and the intermediate distance between the crack-centres is (2b). The geometry is given in Figure 1. The ratio $(\frac{a}{b})$ is characteristic for the degree of internal damage of the material.

The cracks with radius (a), representing the present cracks in the real material, start to extend at a stress level of 0,6 f_c.
The energy demand (G_{IC}) for crack extension is assumed to be constant during the extension.
The complex failure process of concrete can now be described by the crack extension in the given geometry by the L.E.F.M. The ultimate strength is reached when the radius of the cracks equals b.

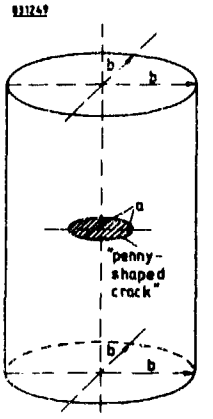

Figure 1a
Cylinder of undamaged material with one crack in the centre.

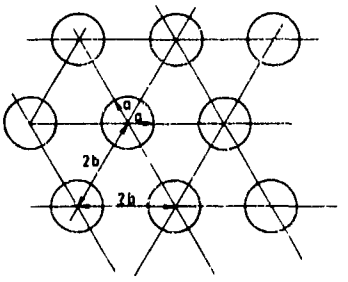

Figure 1b
Section through the cracks;
the potential plane of failure.

The criterion for crack extension is given by the energy or stress criterion. The extension itself is determined by the difference between the energy release rate (G_I) and the energy needed to form the new crack surfaces (G_{IC}). This difference equals the kinetic energy of the material around the crack tip.
When the radius of the crack increases from a_1 to a_2 the kinetic energy per unit length of the crack tip is given by:

$$E_{kin} = \int_{a_1}^{a_2} (G_I - G_{IC})\, da \qquad (7)$$

The displacement field ($\underline{u}$) around the crack tip, under constant loading, is given by:

$$\underline{u} = \underline{c} \cdot \frac{\sigma . a}{E} (1-\nu^2) \qquad (8)$$

where $\underline{c}$ is a vector which only depends on the point coördinates.
The kinetic energy of the material per unit length of crack tip is given by:

$$E_{kin} = \frac{1}{2}\rho \iint_A \left(\frac{\partial u}{\partial t}\right)^2 dA \qquad (9)$$

The integration area A is proportional to the square of the charateristic length of the problem

$\left[a\, f^2(\frac{a}{b}) \right]$. By using eqs. (8) and (9) in the case of a constant stress rate ($\dot{\sigma}$) the kinetic energy can be determined by:

$$E_{kin} = \frac{1}{2}\rho(\dot{a}+\frac{\dot{\sigma}}{\sigma}a)^2(\frac{\sigma}{E})^2(1-\nu^2)^2\ \lambda\cdot\{af^2(\frac{a}{b})\}^2 \quad (10)$$

with λ as an unknown constant.

The propagation velocity of the crack tip ($\dot{a}$) follows from eqs. (7) and (10). Substitution of eqs. (5) and (6) in (7) and (10) yields the expression:

$$\dot{a}=C_s\frac{2}{\sqrt{\Pi}\ af^2(\frac{a}{b})}\cdot\{a_c f^2(\frac{a_c}{b})(a_c-a)+g(\frac{a}{b})-g(\frac{a_c}{b})\}^{\frac{1}{2}}-\frac{\dot{\sigma}a}{\sigma} \quad (11)$$

with . $C_s = \sqrt{\frac{2E}{\rho\lambda(1-\nu^2)}}$

. $g(\frac{a}{b})-g(\frac{a_c}{b}) = \int_{a_c}^{a} af^2(\frac{a}{b})da$

. $f(\frac{a}{b}) = 1+\frac{1}{2}(\frac{a}{b})^2+0,21(\frac{a}{b})^4+1,74(\frac{a}{b})^6$

. $a_c = \frac{\Pi}{4}\cdot\frac{K_{IC}^2}{\sigma^2(t)}\cdot\frac{1}{f^2(\frac{a_c}{b})}$

Eq. (11) is valid until the velocity ($\dot{a}$) equals the Rayleigh wave velocity which is an upper boundary for the propagation velocity of the crack tip.

By integrating ($\dot{a}$) it can be verified whether the crack radius equals (b) in a certain time as a result of the loading $\sigma(t) = \dot{\sigma}\cdot t$. The unknown parameters in eq. (11) are the constant λ or C_s, the ratio $(\frac{a}{b})$ and K_{IC}

In the expression for ($\dot{a}$) the influence of the loading rate has only partly been taken into account. The influence of the stress or strain rate on the tensile strength has been investigated in several research programmes. It has been proven that for high stress rates the cracks extend not only through the cement matrix and along the bond surfaces but also through the aggregate particles. Since the specific surface energy of the aggregate is more than the surface energies of the cement matrix and the bond surfaces the critical value of the elastic energy release rate increases with increasing loading rate. Due to the increasing loading rate the inertia effects become more and more important. The stress field around the crack tip will change and fracture will not be limited to one main fracture plane but multiple cracking will occur. As a first approximation all these effects have been compressed in a parameter (α) and the propagation velocity of the crack tip is given by:

$$\dot{a}_d = \left(\frac{\dot{\sigma}_d}{\dot{\sigma}_s}\right)^{\alpha} \quad (12)$$

where index (d) stands for "dynamic" and (s) for "static". Parameter α will approach one because the average value of ($\dot{a}$) depends on the energy supply which is directly coupled to the loading rate ($\dot{\sigma}$). The average value of ($\dot{a}$) determines the time needed for the growth of the crack radius from (a) to (b), which interval is independent of the loading rate. As the strength increases with increasing loading rate, parameter α must not only be nearly-one but also smaller than one.

To determine the unknown parameters the model is fitted to the behaviour under static loading and to the composition of the concrete.
Constant K_{IC} is determined from the specific surface energy of the crack surfaces ($\underline{\delta}$) with the components of the matrix, bond and aggregate fracture.

Before loading ratio $(\frac{a}{b})$, damaged vs undamaged material is a parameter of the quality, the amount of cracks, voids and their size. For a great deal these are determined by the water-cement ratio and are expressed in the porosity (n). Ratio $(\frac{a}{b})$ is therefore estimated by $(n)^{1/3}$. The value of (a) for the unloaded concrete is equal to the critical radius (a_c) at a stress level of 0,6 f_{cs}, which is known from static tests. (f_{cs} is the static tensile strength)
Constant C_s follows from:

$$\int_{0,6t^*}^{t^*}\dot{a}dt = b-a(0,6t^*) \quad (13)$$

with $$t^* = \frac{f_{cs}}{\dot{\sigma}_s}$$

All parameters can be determined by means of the material properties under static loading except parameter α, which almost equals one.

5. COMPARISON OF THE THEORY WITH EXPERIMENTAL DATA

The tensile strength calculated with the model will now be compared with the available experimental data. The strength follows from:

$$b-a(t_o) = \int_{t_o}^{t}\dot{a}(a_c,a,b,\dot{\sigma},\alpha)dt \quad (14)$$

$$f_{cd} = \dot{\sigma}\cdot t.$$

with $a(t_o)$ the radius of the characteristic cracks in the material before loading and t_o the time when ($\dot{a}$) becomes positive.

Figure 2 gives an overview of experimental data of uniaxial tensile tests at different loading rates.

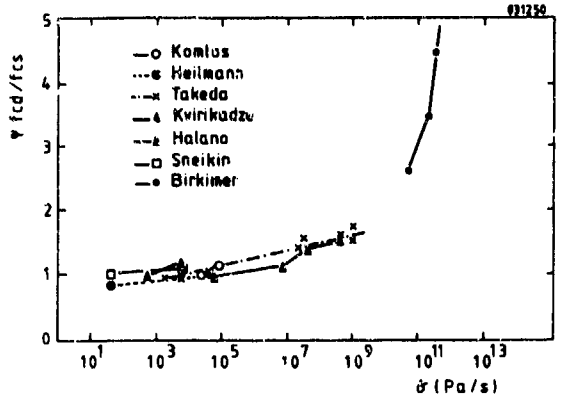

Figure 2 Relative tensile strength $\psi(\frac{fcd}{fcs})$ as a function of loading rate ($\dot{\sigma}$) (8)
-experimental data.

The results obtained by the model are given in the Figures 3 and 4. Figure 3 shows the influence of a change in the value of α and the good agreement with the experimental data for α=0,93 which is almost 1 as was expected. In Figure 4 the influence is shown of a change in material quality expressed in the parameter K_{IC}.
As the model is fitted on the static behaviour and the material properties the influence of a change in the parameters (K_{IC}) (Figure 4) and ($\frac{a}{b}$) is small as long as the crack velocity ($\dot{a}$) does not equal the Rayleigh wave velocity.

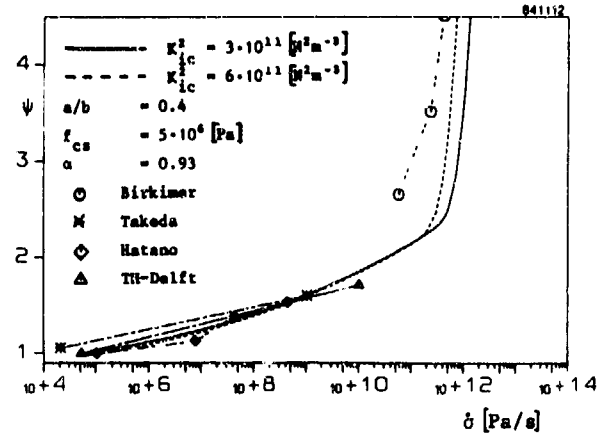

Figure 4 Relative tensile strength $\psi(=\frac{fcd}{fcs})$ as a funtion of loading rate ($\dot{\sigma}$)
-variation of K_{IC}

In spite of the simplifications and the assumptions made in the model the results demonstrate that the most relevant phenomena determining the influence of the loading rate on the failure process and ultimate strength have been taken into account. So the uniaxial tensile strength of concrete can be calculated for all loading rates using the approach of the extending characteristic cracks.

The influence of the loading rate on stress distribution, multiple cracking and crack surface are taken into account by just one parameter, α. Some remarks on this influence are in place.

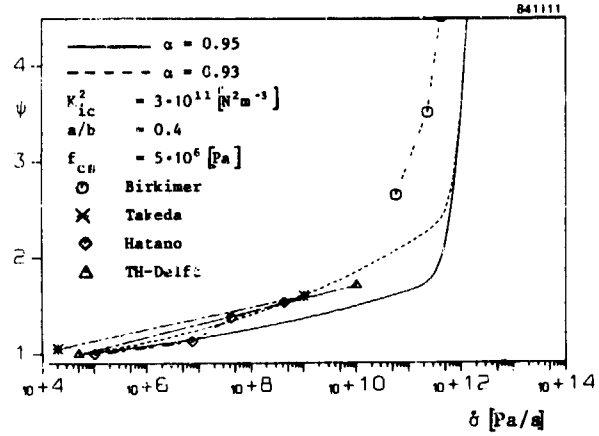

Figure 3 Relative tensile strength ψ $(=\frac{fcd}{fcs})$ as a fuction of loading rate ($\dot{\sigma}$)
-variation of α

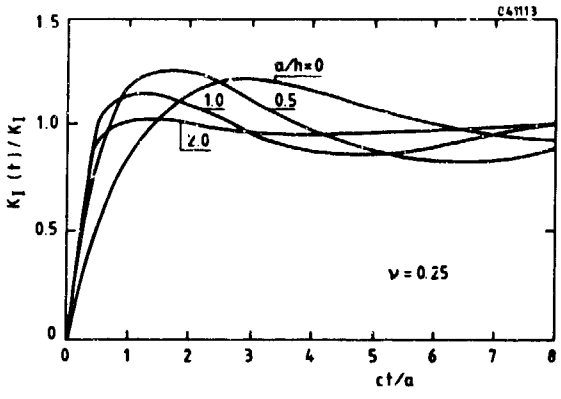

Figure 5 Dynamic to static stress intensity factor time for strip subjected to normal displacement (3)

In (3) the stress intensity factor K_I is given for the stress field around an elliptical crack of length 2a, in a strip with finite height (h) under sudden loading or displacement (Figure 5, with c the longitudinal wave velocity).

The stress distribution around the crack differs only a short time from the static stress field. The time delay by using the dynamic stress field in stead of the static field has the magnitude $O(\Delta t) = 10^{-5}$ sec so the influence on the maximum strength ($O(\Delta fc) = \dot{\sigma} 10^{-5}$ [Pa]) is relatively small. The influence of the increasing energy demand for crack propagation under increasing loading rates is shown in Figure 6 for an extreme case. It is assumed that under static loading there is no crack extension through the aggregate particles and at a loading rate of $\dot{\sigma} = 10^{11}$ [Pa/s] there is no bound cracking left.

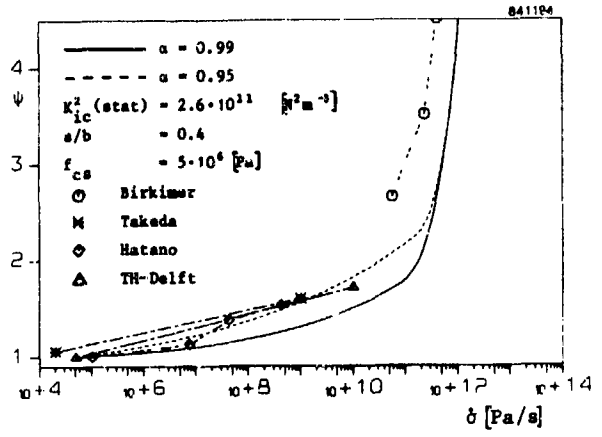

Figure 6 Relative tensile strength $\psi(=\frac{f_{cd}}{f_{cs}})$ as a function of loading rate ($\dot{\sigma}$)
$-K_{IC}$ as a function of $\dot{\sigma}$

The results of this extreme case show that when the influence of the changing energy demand (changing crack surfaces and multiple cracking) is taken into account more correctly the value of α almost equals one. Because of this and the negligible influence of the changing stress field under dynamic loading on the maximum strength the further development of the model will concentrate on a more precise description of the energy demand for crack propagation.

6. FINAL REMARKS

It can be concluded that the approach to determine the maximum tensile strength by describing the extension of characteristic cracks give good results for loading rates from $\dot{\sigma} = 10^4$ to 10^{12} [Pa/s]. The extension is determined by the energy demand for crack propagation (K_{IC}) and the rate of energy supply $\left(\frac{\dot{\sigma}_d}{\dot{\sigma}_s}\right)$.

Further the parameters used in the model described in this paper can be determined from the behaviour and properties of concrete under static loading. In practice the stress situation of uniaxial tensile stress is an exceptional case. In most cases there is a multiaxial loading condition of compression and tension (eg. shearing, spalling). To enable the strength criterion to be taken into account in response calculations the influence of the loading rate on the strength in multiaxial conditions must be known. Because of the good results for the uniaxial tensile case the same approach will be taken to uniaxial compression and the biaxial case of tension - compression.

LITERATURE

(1) Broek, D.
Elementary Engineering Fracture Mechanics.
Noordhoff International Publishing, Leyden 1974

(2) Chen, W.F., Saleeb, A.F.
Constitutive Equations for Engineering materials. Volume I: Elasticity and Modelling.
John Wiley & Sons, 1982.

(3) Chen, E.P., Sih, G.C.
Transient response of cracks to impact loads
In: Mechanics of fracture 4, Elastodynamic crack problems,
ed. G.C. Sih, Noordhoff, Leyden, 1977 pp 1-58

(4) Hillemeier, B.; Hilsdorf, H.K.
Fracture mechanics studies on concrete compound
Cement and Concrete Research, Vol. 7 1977, pp 523-536

(5) Karthaus, W., Leussink, J.W.
Dynamic Loading: More than just a dynamic load factor. Proc. of The Interaction of non-nuclear munitions with structures
US Air Force Academy, Colorado, May 10-13 1983

(6) Shah, P.; Asu, A.M.; Mc Garry, F.J.
Griffith fracture criterion and concrete
Journal of the Engineering Mechanics Division, Proc. ASCE, December 1971 pp 1663-1676

(7) Wittmann, F.H. ed.
Fracture Mechanics of Concrete
Elsevier, Amsterdam 1983

(8) Zielinski, A.J.
Fracture of Concrete and Mortar under Uniaxial Impact Tensile Loading.
Delft University Press, Delft, 1982.

Behavior of NIMS Composites During Impact Loading

William E. Wolfe and Robert L. Sierakowski
Department of Civil Engineering
The Ohio State University, Columbus, Ohio
and
Vincent P. Chiarito
U.S. Army Engineers Waterways Experiment Station
Vicksburg, Mississippi

ARSTRACT

New inorganic materials (NIMS) offer the promise of widespread useage in areas currently dominated by synthetic organic polymers and metals at substantially lower energy consumption for fabrication. One of these new materials is a hydraulic cement in which the forming process minimizes the size of the pore spaces. This paper describes the test procedure employed and presents some results obtained from a work effort designed to evaluate the stiffness and damping characteristics of one of these new inorganic products during an impact type loading. In this program, a force was applied to laboratory specimens using an instrumented impact hammer, and the amplitude of the resulting vibrations measured.

INTRODUCTION

Ordinary concrete is a common composite consisting of sand and gravel in a hydraulic cement matrix. Although it has long been a dominant material in the construction industry, a low strength to weight ratio and a low tensile strength has limited the range of problems for which concrete could be considered. In recent years there have been many attempts to increase the strength of concrete. As a result of some of these efforts, hydraulic cement concrete can now be routinely made with static compressive strengths of 5,000 psi (34.5 MPa) and, with the addition of plasticizers, strengths in excess of 10,000 psi (69.0 MPa) are commonly obtained. Recently a cement product manufactured by Imperial Chemical Industries (ICI) with the product name NIMS, for New Inorganic Materials, was introduced. Initial tests on NIMS specimens conducted at Ohio State by the Department of Civil Engineering and at the University of Florida have indicated that the material has a static compressive strength in excess of 43,000 psi (297 MPa) and a static tensile strength of approximately 9,000 psi (62 MPa). Some of the static properties obtained with these NIMS specimens are summarized in Table 1.

It is apparent that a material with the above strengths would be suitable in a wide range of applications previously not thought possible for a hydraulic cement product. Some of these applications have been discussed by Birchall and Kelly (1). Because initial tests cited above indicate that the NIMS material has several desirable static properties, laboratory programs seeking to fully characterize the behavior of this material have been started at Ohio State. This paper will describe the first results obtained in a test program designed to characterize the dynamic properties of NIMS, specifically its stiffness and material damping.

TEST PROGRAM

The test apparatus used is shown schematically in Figure 1 with the cantilever test sample included in the schematic. Sample size measured 178 mm long by 25 mm wide by 3 mm thick. A photograph of a typical specimen is shown in Figure 2. From this 178mm long sample, three cantilever beam lengths (152mm, 127mm, and 102mm) were tested. The experimental approach taken to obtain damping data was similar to that described by Suarez et. al. (2) in which they applied an impactive load to a sample fixed at one end. The specimen to be interrogated in the present tests was impacted by a hammer equipped with a force transducer located in the head which measured the magnitude and duration of the force pulse. The point of impact was approximately as shown in Figure 1. The resulting sample vibrations were monitored using a Bently Nevada 50mm probe and proximitor which operates by generating a magnetic field that induces eddy currents in a conducting target. The strength of the eddy currents is related to the distance separating the probe from the target. Because no transducer physically touches the vibrating beam, this type of recording device is well suited to the vibration tests conducted in this program. However, in order for the probe to be able to sense motion the target had to be conductive. This was accomplished by attaching a small aluminum foil strip to the free end of the beam.

Because of the small size of the aluminum target, the linear range of the displacement transducer in the experimental configuration used was only about 4.0 mm. Thus care had to be taken to keep the specimen at the proper distance from the probe. The outputs of the force transducer and of the displacement probe were sampled and recorded using a Zonic 6080 multichannel Structural Dynamics analyzer (5). Data collection was triggered off the force transducer. The data were displayed on a Zonic 6081 Real Time Display terminal and hard copies of screen displays produced by a Zonic printer/plotter.

TEST RESULTS

The usefulness of the impulse technique as a method for exciting structural components is primarily due to the ease with which tests can be performed and the quickness with which results can be obtained. In fact, the speed and simplicity of the test gives the experimenter the opportunity to overcome one of the test's chief weaknesses. As a result of an individual impact a relatively small amount of energy is imparted to the structure over a wide frequency range. This can result in any individual measurement being relatively noisy. By conducting several tests and averaging the response much of this random contaminating noise can be eliminated. A measure of the amount of noise remaining in the response can be made by calculating the coherence function between input and output signals. The coherence function which is defined as the ratio of the cross-spectrum to the power spectra of the two signals is equal to one when there is no noise and the system is linear. For a system with an output uncorrelated with the input, the coherence function is zero. A high value of coherence function over a wide range of frequencies such as the one shown in Figure 3 for a typical test sequence on the 127mm beams, indicates a relatively small amount of noise remaining and therefore a high degree of confidence that the measured system displacements are in response to the hammer impact.

Because the specimen is being impacted with a hand held device, it is not possible to precisely control the force applied. However by specifying the hammer weight and tip material reproducible results can be obtained. Due to the relatively small physical size of the samples, a small force was desired. In order to restrict the magnitude of the impulse, the hammer weight was kept to a minimum. By estimating the stiffness of the material an expected value of the system's fundamental frequency of vibration can be calculated (4). For the NIMS material, an estimate of the stiffness determined from the static tests gave a range of 50 to 70 Hz as the likely region for the fundamental frequency of the 152mm cantilever beam specimens and 100-130 Hz for the 127mm specimens, and 160-180Hz for the 102mm specimens being tested in this program. A plastic hammer tip was chosen to provide the best waveform over this frequency range. In a plot of the energy density for the plastic tipped hammer as measured by the force transducer located in the hammer tip (Figure 4), it can be seen that the energy content is fairly constant over the frequency range of interest.

Figure 5 shows plots of the applied load and tip displacement for a typical time history recorded when one of the 127mm long specimens was impacted. The average peak applied load was 2.84 kg (6.25 lbs), and a typical maximum tip displacement was 0.2 mm (0.008 inches).

The natural frequency of the concrete cantilever beam specimens was determined using plots of the real and imaginary portions of the frequency response (transfer) function. The FRF is defined as the ratio of the Fourier Transform of the output signal (displacement) over the Fourier Transform of the input signal (force). In actual calculation a less noisy signal will be obtained if the FRF is determined as the ratio of the cross spectrum between the input and output time histories over the power spectrum of the input (3). This is the method used to generate the graphs shown in Figure 6. In this figure are shown typical plots of the magnitude and phase of the frequency response function, determined by taking the ensemble average of ten individual impact events, as a function of frequency. The magnitude plots are given in terms of system stiffness. A point of minimum dynamic stiffness (maximum displacement per applied force) was observed at 172 Hz for the 102mm long beams (Fig. 6a) and 117 Hz for the 127mm beams (Fig. 6b). Additional tests gave maximum displacements at 62 Hz for the 152mm beams. Having measured the frequency of the damped free vibrations, the dynamic stiffness of the NIMS specimens was calculated. The stiffness was found to be between 31.7 and 35.9 kN/cm^2 (4.6 to 5.2 Mpsi).

Material damping was determined using the logarithmic decrement method. In this approach, the relative magnitudes of successive peaks in the response time history are compared. Specifically the logarithmic decrement, ζ, is equal to the natural log of the ratio of the amplitude of a response peak, x_t, to the amplitude of the next response peak, x_{t+1}. The damping, ξ, given in terms of a percentage of critical damping is related to ζ by:

$$\xi = \frac{\zeta}{\sqrt{4\pi^2 + \zeta^2}} \qquad (4)$$

A plot of beam tip displacement as a function of time as shown in Figure 5 was used to determine the logarithmic decrement from which damping was calculated. A good determination of the material damping can be made by this method when interrogating lightly damped systems. For the specimen tested the material damping was found to be approximately 2% of critical. A comparison of the properties of NIMS with other materials is given in Table 2.

SUMMARY

Vibration tests were performed in the laboratory on specimens of a new high strength hydraulic cement concrete. The results of the tests reported herein show that a flexural stiffness of approximately 32 to 36 kN/cm^2 with an internal damping on the order of 2% can be expected with this material. These values are similar to the values obtained for conventional concretes. While these results are only preliminary they are encouraging, since it appears that the high strength values which have been measured in static tests need not be accompanied by significant reductions in material damping.

ACKNOWLEDGEMENTS

The authors would like to thank Mr. E.L. Sadler of U.S.A. Waterways Experiment Station, Vicksburg, MS, who helped greatly with the test program. The NIMS materials were supplied by the University of Florida under a contract with AFESC Tyndall, AFB, Fl. The principle investigator at the University of Florida is Dr. L.E. Malvern. The program monitor at Tyndall is Mr. W. Buchholtz.

REFERENCES

1. Birchall, J.D. and Kelly, A., "New Inorganic Materials," Scientific American, Vol. 248, No. 5, (1983) 104-115.

2. Suarez, S.A., Gibson, R.F. and Deobald, L.R., "Development of Experimental Techniques for Measurement of Damping in Composite Materials," Proceedings, SESA, 1983 Fall Meeting, Salt Lake City, Utah, November 7-9, 1983.

3. Halvorsen, W.G., and Brown, D.L., "Impulse Technique for Structural Frequency Response Testing," Sound and Vibration, 11 (1977) 8-21.

4. Steidel, R.E., An Introduction to Mechanical Vibrations, New York, John Wiley and Sons, Inc. 1979.

5. Zonic Corporation, "6080/6081 User Manual", Zonic Corporation, Milford, Ohio 19 July 1983.

Compressive Strength	σ_c = 43,000 psi
Strain at failure (compression)	ϵ_{fc} = 4%
Tensile Strength	σ_t = 9,000 psi
Strain at failure (tension)	ϵ_{ft} = 0.4%
Flexural Strength	σ_f = 17,000 psi
Compressive Modulus	E_c = 1.5 x 10^6 psi
Flexural Modulus	E_f = 5 x 10^6 psi
Unit Weight = 146.8 lb/ft^3	= 2.35 g/cm^3

Table 1. Static Properties of NIMS

Material	Damping
Steel (cold rolled)	0.0006
Conventional Hydraulic Cement	0.02
Wood	0.003
Rubber	0.04

Table 2. Representative Damping Values for Selected Materials (4)

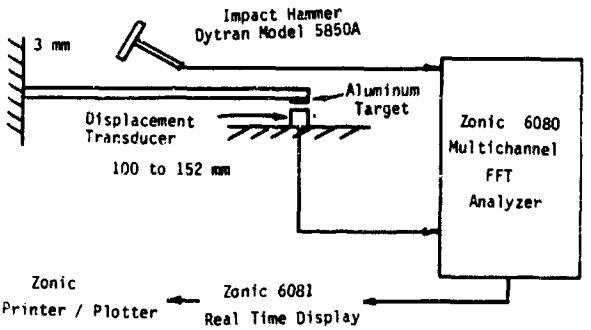

Figure 1. Schematic of Test Set-up.

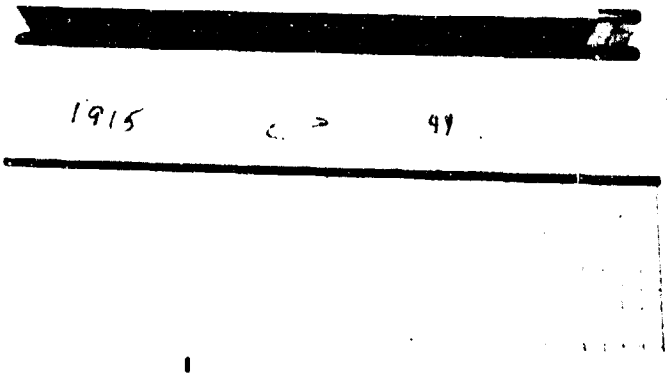

Figure 2. Typical Test Specimens

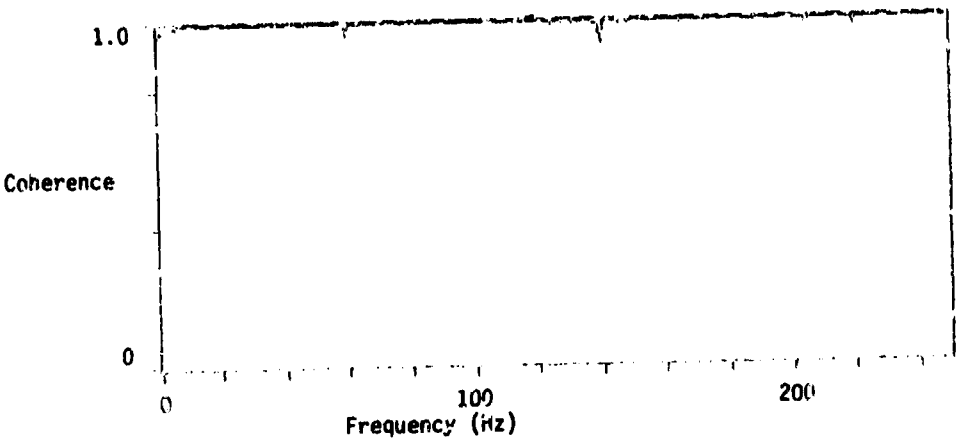

Figure 3. Coherence Function for Typical Test Series. (127 mm specimens)

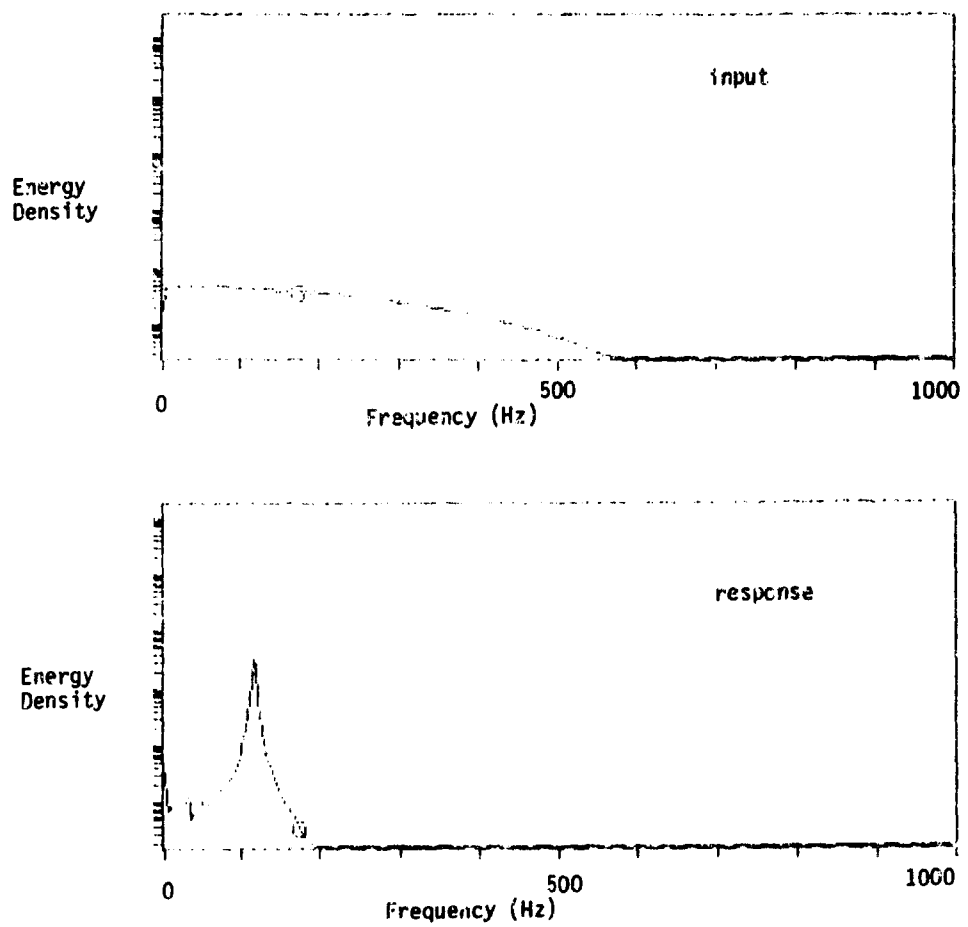

Figure 4. Energy Density Functions for Typical Test Series. (127 mm specimens)

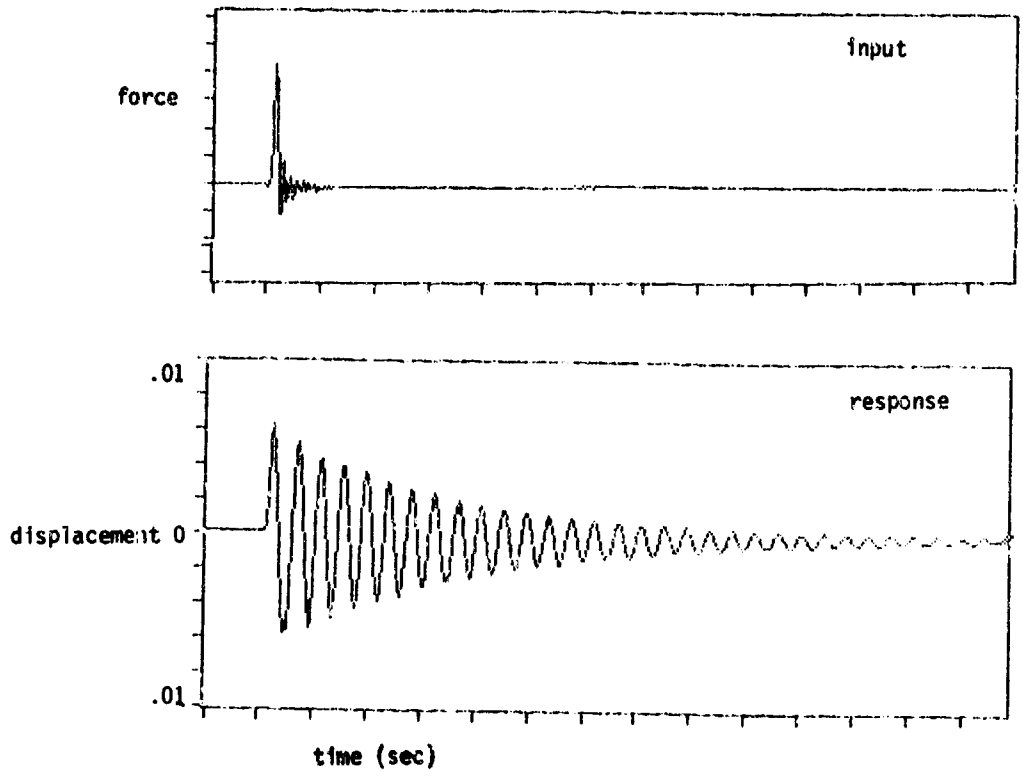

Figure 5. Time Histories of Applied Force and Beam Displacement for 127 mm Specimen.

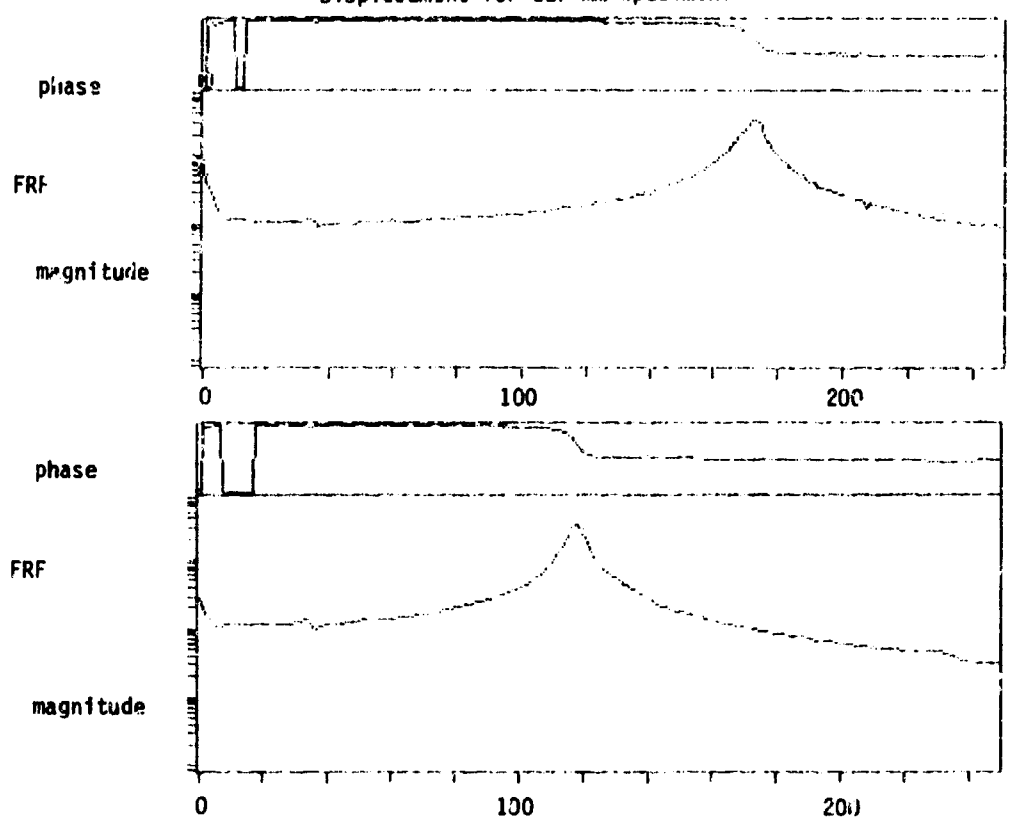

Figure 6. Frequency Response Functions for NIMS Specimens a) 102 mm specimens, b) 127 mm specimens.

HOPKINSON BAR SIMULATION USING DYNA2D*

Joseph A. Smith
and
Tracy A. Glover

Lawrence Livermore National Laboratory
Livermore, California

ABSTRACT

A finite-element simulation of a Split Hopkinson's bar (Kolsky apparatus) technique involving mortar specimens is accomplished with DYNA2D, an explicit two-dimensional finite-element code. Calculations are compared with experimental results contained in a University of Florida report Dynamic Response of Concrete and Concrete Structures, and with analytic solutions of the appropriate wave propagation problem.

INTRODUCTION

In 1982, personnel of the Department of Engineering Sciences, University of Florida, performed a series of split Hopkinson pressure bar (SHPB) tests on mortar specimens as part of an investigation into the dynamic response of concrete and concrete structures to impulsive loads. Results of these tests are presented in the first annual technical report of the three year program.[1] The aim of such an investigation was to develop representations of dynamic structural response of concrete that can be incorporated into structural analysis codes.

More recently, these tests have been modeled at Lawrence Livermore National Laboratory as the simplest of a series of benchmark calculations. The aim of these calculations is to demonstrate the growing accuracy with which the dynamic response of concrete can be predicted by DYNA2D as improved inputs to existing material models are developed. This report summarizes the results of the Hopkinson bar modeling.

THE EXPERIMENT MODELED

The SHPB test is used to obtain compression properties of mortar in the following manner. A sample of the material to be studied is placed between and in contact with two elastic rods of the same diameter (Fig. 1). A compression stress wave is initiated in the incident bar upon impact with a striker bar. This compression wave propagates along the rod causing multiple reflections in the sample, resulting in distorted waves reflected from the sample traveling back along the first rod and transmitted through the sample and into the second rod. Average stress can be found from the strain histories recorded in the two elastic rods if the following assumptions are maintained by the conditions of the experiment: (a) the specimen is in a state of one-dimensional stress, and (b) the stress and strain are uniform throughout the specimen.[2]

Average stress along the specimen length $(\sigma_s)_{avg}$ is computed from the following equations[1]:

$$
\begin{aligned}
(\sigma_s)_{avg} &= 1/2\ (\sigma_{sI} + \sigma_{sT}) \\
\sigma_{sI} &= E\ (A/A_s)(\varepsilon_I + \varepsilon_R) \\
\sigma_{sT} &= E\ (A/A_s)\ \varepsilon_T \\
\varepsilon_R &= \varepsilon_T - \varepsilon_I
\end{aligned}
\qquad (1)
$$

where ε_T and ε_I are the strain pulses recorded at the transmitter and incident bars, respectively, after these pulses have been translated in time to obtain the strain pulses which occur at the specimen edges. These waves are assumed to propagate without dispersion or attenuation in the elastic bars. The quantities A and A_s represent the cross-sectional areas of the elastic bars and the specimen, respectively.

In the University of Florida experiments,[1] cylindrical mortar specimens of diameter 19 mm and nominal length 10.16 mm were tested in a SHPB system using incident and transmitter bars of length 1.83 m, and a striker bar of length 0.584 m (Table 1). All three elastic bars had diameter 19 mm and were ETD-159 ground and polished, cold-finished steel bars, comparable in analysis

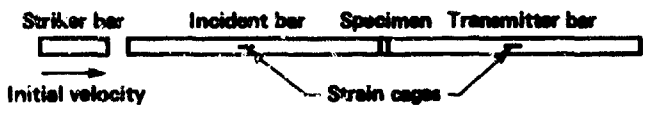

Figure 1. Hopkinson bar apparatus.

*Work performed under the auspices of the U.S. Department of Energy by the Lawrence Livermore Laboratory under contract number W-7405-ENG-48.

Table 1. University of Florida SHPB tests.

	Striker bar	Incident bar	Specimen	Transmitter bar
Initial velocity (m/s)	12.0	0.0	0.0	0.0
Length of bar (m), L	0.584	1.829	0.010	1.829
Diameter (m), D	0.019	0.019	0.019	0.019
Ratio L/D	30.7	96.3	0.5	16.8
Density (kg/m^3)	7.83E+03	7.83E+03	2.40E+03	7.83E+03
Young's modulus (Pa)	1.99E+11	1.99E+11	--	1.99E+11
Shear modulus (Pa)	--	--	1.36E+10	--
Rod wave velocity (m/s), C	5053	5053	--	5053
L/C (s)	1.16E-04	3.62E-04	--	3.62E-04
Mesh specifications				
No. Elts in axial dir., Nz	125	390	8	390
No. Elts in radial dir., Nr	16	16	16	16
No. of elements, (Nz x Nr)	1000	3120	64	3120
$\Delta L/\Delta D$ of elements	3.93	3.95	1.05	0.69
$\Delta L/C$ of elements (s)	9.2E-07	9.3E-07	--	9.3E-07

to 4140 steel. The mortar mix (by weight) was 0.55/2.5/1.0 water/sand/Portland Type I cement, with sand particles of maximum diameter less than 1/8 the specimen diameter. Strain gages were mounted on the lateral surface of the transmitter and incident bars, midway along their axes.

For the striker bar length above, Malvern and Ross,[1] report an interval of 230 μs for the elastic compression wave in the striker bar to return as an unloading tensile wave. A stress pulse of approximate amplitude 240 MPa [Ref. 3] was measured in the incident bar prior to reflection and transmission at the specimen. This pulse, as well as the subsequent pulses reflected in the incident bar and transmitted through the specimen into the transmitter bar (Fig. 2), are the object of the simulation.

ELEMENTARY THEORY OF LONGITUDINAL WAVES IN THIN RODS

Prior to interaction at the specimen boundary, wave motion in the elastic bars is approximated by the wave equation

$$\frac{\partial^2 u}{\partial t^2} = 1/C_0^2 \frac{\partial^2 u}{\partial t^2} \qquad (2)$$

where $C_0 = E/\rho$ is the rod wave velocity, $u = u(z,t)$ is the longitudinal displacement, E is Young's modulus, and ρ is the density of the rod. Several assumptions[4] have been made here, the validity of which will be discussed along with the results of the finite-element calculations. They are:

(i) The steel bars are elastic, of constant cross section, and homogeneous.

(ii) Plane, parallel cross sections remain plane and parallel.

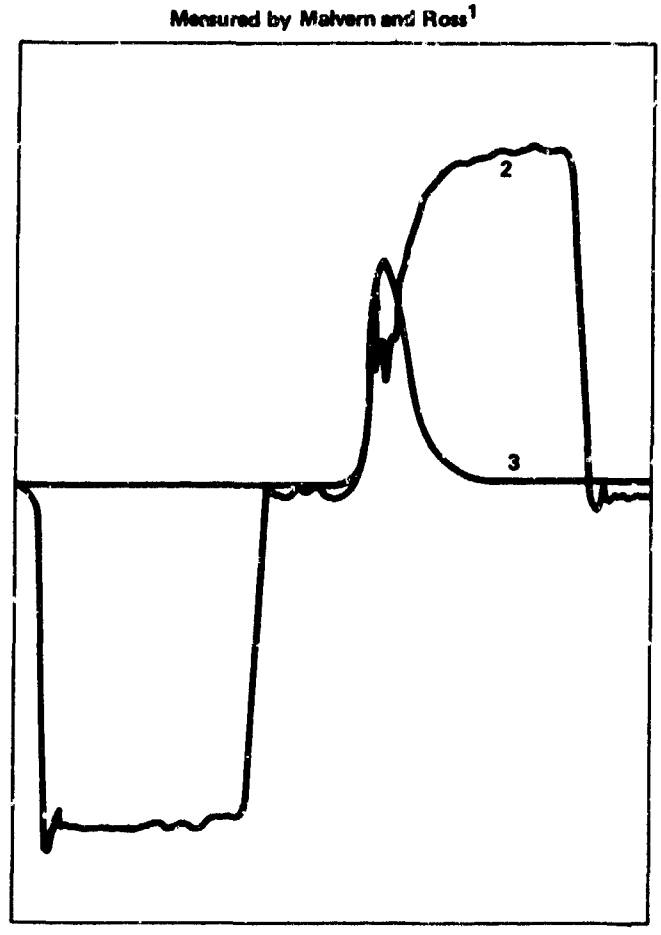

Figure 2. Strain histories--incident and transmitter bar gages as measured by Malvern and Ross (Ref. 1).

(iii) A uniform distribution of stress exists.

(iv) Uniaxial stress, but not uniaxial strain, is assumed. In other words, there exist lateral contractions and expansions arising from the axial stress, due to Poisson's effect, but the associated lateral inertia effects are neglected.

Based on D'Alembert's solution of Eq. (2), assuming a semi-infinite bar, the stress pulse which propagates in the incident bar after impact is rectangular with magnitude $\sigma = V_1\rho_1C_1/2$ and duration $T = 2L_1/C_1$, where 1 denotes properties of the striker bar. For the system under consideration, $L_1 = 0.584$ m, $V_1 = -12$ m/s, and $C_1 = 5053$ m/s so that this simple theory predicts a rectangular pulse of magnitude 237.4 MPa, duration 231.2 μs, and length 1.168 m. The ratio of bar radius to wavelength, R/Λ is 0.011.

In actual Hopkinson bar experiments, the measured pulse is usually found to have rounded corners, finite rise and fall times, and an oscillatory nature. The strain history of Fig. 2 affords an example. Graff[4] suggests that the imperfect contact surfaces of the impact bars and a finite response time of the measuring system cause these first two deviations. The oscillations of the curve about the straight line, which would be obtained for a distortionless bar, are shown by Davies[5] to be a consequence of the lateral inertia term $\partial^4u/\partial z^2\partial t^2$ neglected in the wave equation.

THE SIMULATION

DYNA2D is a vectorized, explicit, two-dimensional, axisymmetric and plane strain finite-element code for analyzing the large deformation dynamic and hydrodynamic response of inelastic solids. Spatial discretization is achieved by 4-node solid elements, and the equations of motion are integrated by the central difference method.[6] Again, the objective of the Hopkinson bar simulation is to determine the degree to which DYNA2D is capable of reproducing the results of an experiment involving concrete under significant dynamic stresses.

When the problem geometry is defined, the striker bar is modeled in addition to the elastic bars and the specimen, eliminating the need to specify an initial velocity or initial displacement curve at the incident bar boundary and thus ensuring a correct input pulse at the specimen edge. Axial symmetry is assumed so that the problem is two dimensional and only one half of the longitudinal cross section of the bars need be considered. MAZE, an input generator for DYNA2D, was used to discretize this cross section into a rectangular mesh with elemental length-to-diameter ratios of 1.96 in the striker, incident, and transmitter bars, and 1.06 in the specimen (Fig. 3). The resulting number of elements was 7304.

All nodes of the striker bar are given an initial velocity of 12 m/s towards the incident bar (in the negative z direction) and an initial position corresponding to a 0.0001 m spacing between the striker and incident bars, as seen in Fig. 1. In addition, all nodes along the axis of the elastic bars and of the specimen are constrained in the radial direction.

Slidelines are specified at all three interfaces, with an appropriate steel-concrete friction coefficient allowing for appropriate relative radial displacements of the bars and specimen. Intrusion of one bar into another is disallowed.

Extensive use of DYNA2D at Lawrence Livermore National Laboratory has verified DYNA2D's ability to correctly model events of metal plasticity involving inertial effects. The work with concrete under discussion is a comparatively recent event. It was found that this work required modification of an existing material model available within the code before correct calculation of the dynamic response of concrete could be obtained. The behavior of homogeneous concrete was originally modeled using an elastic-plastic isotropic hardening model with an associated tabulated compaction equation of state. The yield stress was modeled as a function of hydrostatic pressure using tabular values. This material model permitted plastic flow with strain and pressure hardening and also included a rudimentary description of material failure (spall) due to tensile stress. The behavior of concrete was not adequately represented by this model because fracture which occurs in the absence of tensile stress (i.e., deviatoric stresses) was not permitted. Similarly, the strain rate sensitivity of the yield stress was not represented. Fig. 4(a) illustrates the strain pulse calculated by DYNA2D with this original model. Here, the reflected and transmitted pulses (marked "2" and "3" in the figure) clearly do not accurately represent those of Fig. 4(c). This model was accordingly modified to reflect failure as a result of deviatoric stresses as well as rate sensitivity. The resulting equations are described below.

Dynamic yield stresses are calculated as follows:

$$\sigma_2 = [\sigma_0 + f_h(p) + E_p\varepsilon^p_{eff}] \times [1 + A(D_{ij}D_{ij})^n] \exp[-B(\varepsilon^*)^2] \quad ,$$

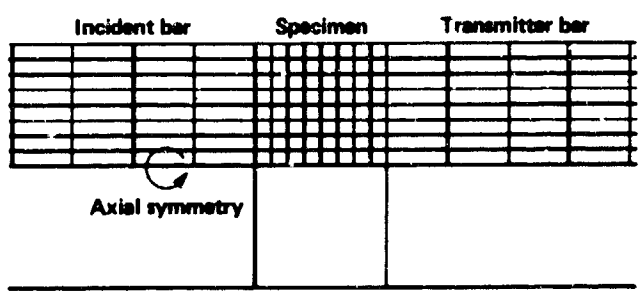

Figure 3. View of finite-element mesh near specimen.

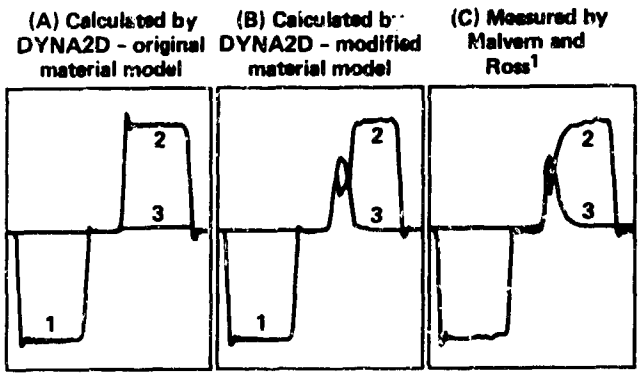

Figure. 4. Strain histories--incident and transmitter bar gages.

where

σ_0 = initial yield stress

f_h = hardening function

p = pressure

E = Young's modulus

E_T = tangent modulus

E_p = plastic modulus [= $E_T E/(E - E_T)$]

$$\dot{\epsilon}^p_{eff} = \int_0^t (2/3\dot{\epsilon}^p_{ij}\dot{\epsilon}^p_{ij})^{1/2}\, d\tau$$

ϵ^p_{ij} = plastic strain rate

A, m, B = constants (input to model)

D_{ij} = rate of deformation tensor

$$(\epsilon^*)^2 = \int_0^t D_{ij}D_{ij}\, d\tau$$

The hardening function, $f_h(p)$, may be specified in a tabular form with ϵ^p_{eff} or pressure as the independent variable. The rate sensitivity function $[1 + A(D_{ij}D_{ij})^m]$ is a slight modification of a standard form for rate sensitive materials.[7] The rate of deformation tensor is used in place of the strain rate $\dot{\epsilon}$ for programming conveniences as well as for tracking volumetric strain By selecting the appropriate constant in the exponential softening function $\exp[-B(\epsilon^*)^2]$, one may model psuedo fracture. The exponential form was selected to permit a reduction of strength over several calculational time steps. This approach reflects some of the features of "damage accumulation" models[8] as well as ensuring smooth changes of material strength. While this approach lacks the elegance of the more sophisticated models, it does permit an easily implemented simulation of fracture in concrete.

The material comprising both the striker bar and elastic bars on either side of the specimen is specified by an elastic-plastic model with mixed kinematic and isotropic hardening. Striker bar velocities are below the damage threshold, requiring that only the elasticity portion of this material model be exercised. As will be readily seen from the results, DYNA2D accurately reproduced the experimental response.

RESULTS OF THE SIMULATION

The initial strain pulse calculated by DYNA2D at the location of the incident bar strain gage is labeled "1" in Figs. 4(a) and 4(b). The experimental result of Fig. 4(c), which corresponds to the calculated incident pulse, has amplitude 1.18×10^{-3} and pulse length of 230 μs. Pulse length is measured from the initial incident pulse's downward movement to the end of the approximately flat maximum amplitude portion. These calculated and experimental pulses have amplitudes and pulse lengths which vary by at most 2% for this gage location, and remarkably similar pulse shapes. This pulse is identical in Figs. 4(a) and 4(b) because only the material model for steel is involved.

For similar runs with different element dimensions, the incident strain pulse was found to have slightly steeper sides and less rounded corners as the element size decreased. This is as expected because the homogeneity assumption in (i) is more nearly obeyed, and the finite response time of the measuring system minimized, in the limit of infinitesimal element areas. Pictures of the mesh in the elastic bars for various times also indicate that the cross sections of the bars remain plane and parallel as in assumption (ii). Plots of strain histories calculated along the incident bar at different radial and axial positions show that the assumption (iii) is similarly obeyed. As mentioned above, the deviation of the pulse from a rectangular shape, particularly its oscillatory nature, illustrates the inappropriateness of assumption (iv). The frequency of the first few oscillations following the initial rise of the incident pulse vary by no more than 10 percent between Figs. 4(b) and 4(c). Also observed are the curved initial portion of the pulse near the time axis which begins to rise slightly before the 181-μs time predicted by elementary theory. This phenomena was also predicted by Davies's analysis.

The reflected and transmitted pulses are those labeled "2" and "3" in Fig. 4, respectively. Strain pulses computed using the modified concrete material model show a vast improvement over those calculated with the original model. The maximum amplitudes of each pulse in Fig. 4(b) varies from its experimental counterpart in Fig. 4(c) by no more than 3 percent.

CONCLUSIONS

It has been shown that with fairly simple modifications, existing constitutive models in DYNA2D can effectively simulate one-dimensional wave propagation behavior in homogeneous

concrete. Good correlation for the incident compressive strain pulse with experimental results is observed. Calculations of increased accuracy have been obtained for the reflected and transmitted wave pulses as a result of improved concrete modeling capabilities, e.g., strain-rate and psuedo fracture effects, in DYNA2D.

REFERENCES

1. Lawrence E. Malvern and C. Allen Ross, Dynamic Response of Concrete and Concrete Structures - First Annual Technical Report, AFSOR TR-84-165, January 26, 1984.

2. L. D. Bertholf and C. H. Karnes, "Two-Dimensional Analysis of the Split Hopkinson Pressure Bar System," J. Mech. Phys. Solids, Vol. 23, 1974.

3. Telephone conversation of July 12, 1984, between Joseph Smith and Allen Ross.

4. Karl F. Graff, Wave Motion in Elastic Solids, Ohio State University Press, Northern Ireland, 1975.

5. R. M. A. Davies, "A Critical Study of the Hopkinson Pressure Bar," Phil. Trans. R. Soc., A240, 375-457 (1948).

6. John O. Hallquist, Theoretical Manual for DYNA3D, Lawrence Livermore National Laboratory, Livermore, CA, UCID-19401 (1983).

7. G. E. Dieter, Mechanical Metallurgy (McGraw Hill, New York, 1976), 2nd ed.

8. M. L. Wilkins et al., Cumulative Strain Damage Model of Ductile Fracture: Simulation and Prediction of Engineering Fracture Tests, Lawrence Livermore National Laboratory, Livermore, CA, UCRL-53058 (1980).

DISCLAIMER

This document was prepared as an account of work sponsored by an agency of the United States Government. Neither the United States Government nor the University of California nor any of their employees, makes any warranty, express or implied, or assumes any legal liability or responsibility for the accuracy, completeness, or usefulness of any information, apparatus, product, or process disclosed, or represents that its use would not infringe privately owned rights. Reference herein to any specific commercial products, process, or service by trade name, trademark, manufacturer, or otherwise, does not necessarily constitute or imply its endorsement, recommendation, or favoring by the United States Government or the University of California. The views and opinions of authors expressed herein do not necessarily state or reflect those of the United States Government thereof, and shall not be used for advertising or product endorsement purposes.

A METHOD FOR ESTIMATING ARRIVAL TIMES FOR WAVES PRODUCED BY A BURIED NON-SPHERICAL CHARGE

CAPTAIN STEPHEN R. WHITEHOUSE

Department of Engineering Mechanics
United States Air Force Academy, Colorado

ABSTRACT

This paper discusses the shock waves produced in soil by a buried non-spherical charge and provides techniques for estimating the time of arrival (TOA) for each type of wave. Although these techniques may have a variety of applications, they were developed primarily to assist the analyst in determining the sources of ground motions or soil stresses observed in data obtained from explosive field tests.

BACKGROUND

In general, the detonation of a non-spherical charge buried in soil of uniform geology generates two major types of waves: those produced directly by the detonation of the charge (source-generated waves), and those caused by the reflection of the source-generated waves at the soil's free surface (reflected waves).

As expected in any buried explosion, the detonation of a non-spherical charge produces a source-generated compressive longitudinal wave (P wave). In addition, the non-spherical geometry of such a charge gives rise to a source-generated shear wave (S wave).

A total of four reflected waves are produced by these source-generated waves at the free surface. The reflection of the source-generated compressive P wave results in a reflected tensile P wave (P-P wave) and a reflected S wave (P-S wave). In addition, the source-generated S wave also produces a reflected P wave (S-P wave) and S wave (S-S wave) at the free surface. Since P waves and S waves travel at different velocities, the TOA for each type of wave at a point of interest, such as a gage location, can be estimated if the P wavespeed, S wavespeed, charge location and the coordinates of the point of interest are known. This paper presents one method for estimating arrival times using this information.

APPROACH

As seen in Figure 1, the six waves considered in this paper can take a variety of paths to get to the point of interest. An arrival time for a wave can be calculated fairly easily if the length of each portion of the wave's path can be determined and if the velocity of the wave along each portion is known. The required calculations can be quite simple if the following assumptions are made.

1. The soil geology consists of one uniform layer of infinite depth. If this assumption is

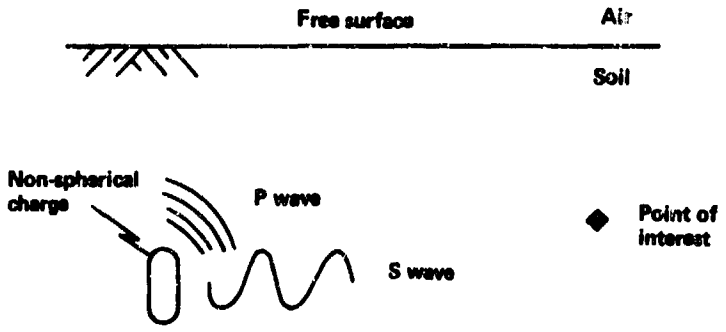

(a) Source-generaged waves.

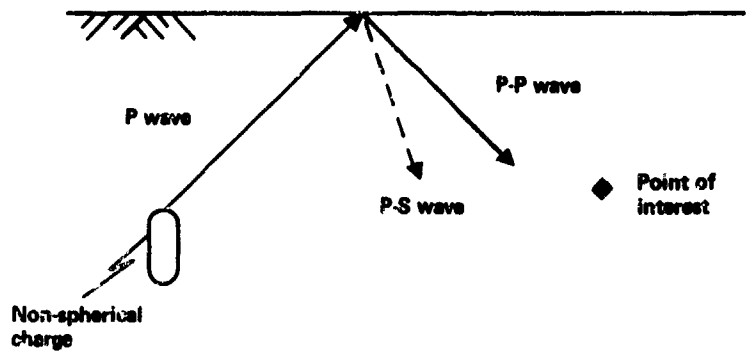

(b) Waves produced by the reflection of the P wave at the free surface.

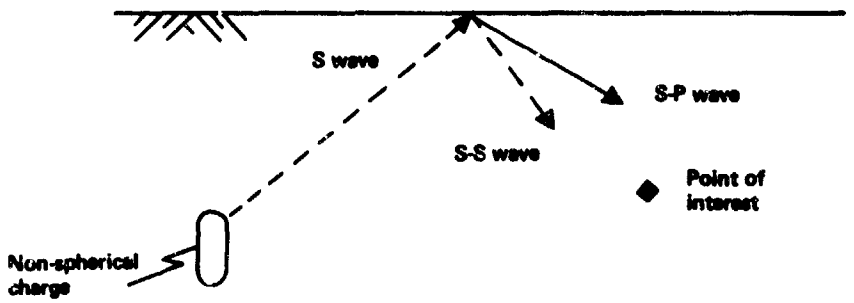

(c) Waves produced by the reflection of the S wave at the free surface.

Figure 1. Waves produced by a buried non-spherical charge.

made, wave reflection and refraction caused by multi-layered geologies can be ignored.

2. All waves emanate from one point in the charge. Rough estimates can be made using the charge's center of gravity (CG). However, more accurate results can be obtained if the point on the charge closest to the point of interest in the soil is chosen. If the CG is used, preliminary calculations indicate estimated arrival times will be within 5% of the correct answer for points of interest at least 10 charge lengths from the charge.

3. Arrival times are governed by seismic wavespeeds for P waves and S waves (C_p and C_s, respectively). Since Assumption 1 limits this discussion to a uniform layer, refraction caused by changes of C_p and C_s with depth are not considered in this paper. Therefore, the source-generated waves travel in straight lines between the charge and the point of interest. In addition, reflected waves travel in straight lines between the charge to the surface and from the surface to the point of interest.

Using these assumptions, the arrival times of the waves shown in Figure 1 can be estimated if the variables listed below are specified.

C_p: seismic P wavespeed
C_s: seismic S wavespeed
x_1, y_1 and z_1: coordinates of the appropriate point in the charge
x_2, y_2 and z_2: coordinates of the point of interest in the soil

WAVE PATHS

The coordinate system used to locate the charge and the point of interest is shown in Figure 2. Figures 3 through 6 illustrate the wave paths for the waves depicted in Figure 1.

As seen in Figure 3, the P wave and the S wave take the most direct route from the charge to the point of interest. The length of this path (R_0) is given by:

$$R_0 = \sqrt{(x_1 - x_2)^2 + (y_1 - y_2)^2 + (z_1 - z_2)^2} \quad (1)$$

A variable of interest in other wave paths is R_{xy}, which is the projection of the R_0 vector in the x-y plane. Its magnitude is given by:

$$R_{xy} = \sqrt{(x_1 - x_2)^2 + (y_1 - y_2)^2} \quad (2)$$

The wave path for the P-P wave and the S-S wave is given in Figure 4. An important characteristic of a P-P wave or S-S wave is that the reflected wave travels at the same velocity as its associated incident wave. Therfore, the angle of reflection (θ_2) is equal to the angle of incidence (θ_1), as is evident in Figure 4. Using other relationships given in this figure, the length of the incident portion (R_1) and reflected portion (R_2) of the P-P or S-S wave path can be determined using

$$R_1 = \sqrt{z_1^2 + d_1^2} \quad (3)$$

and

$$R_2 = \sqrt{z_2^2 + d_2^2} \quad (4)$$

where

$$d_1 = \frac{R_{xy}}{1 + \frac{z_2}{z_1}}$$

$$d_2 = \frac{R_{xy}}{1 + \frac{z_1}{z_2}}$$

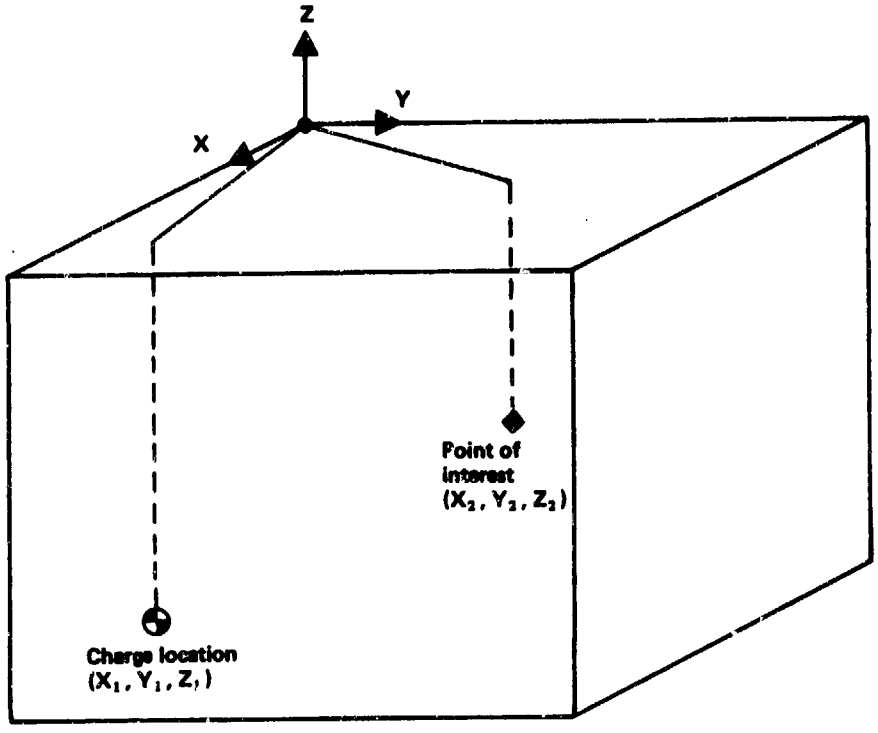

Figure 2. Coordinates of the charge and the point of interest.

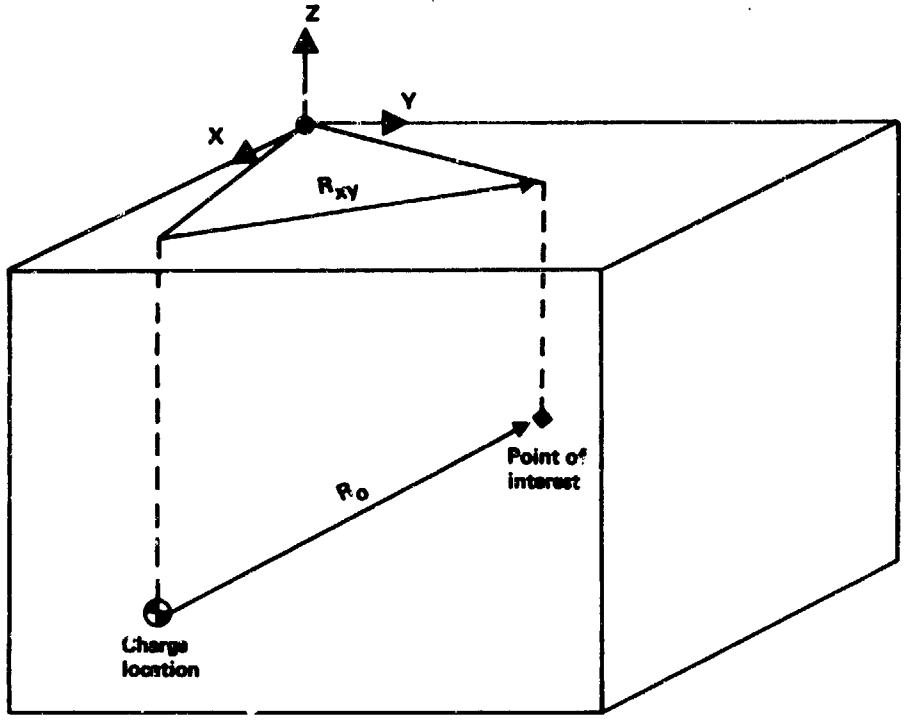

Figure 3. Wave path for source-generated waves.

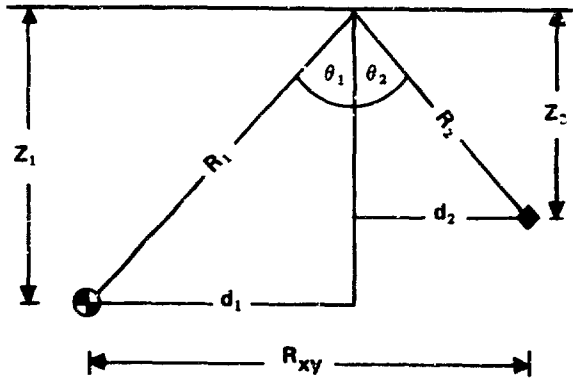

NOTE: Figures 4-6 show the plane perpendicular to the x-y plane which contains the charge location and the point of interest.

θ_1 = angle of incidence
θ_2 = angle of reflection

$$\theta_1 = \theta_2 \Rightarrow \tan\theta_1 = \tan\theta_2 \Rightarrow \frac{d_1}{Z_1} = \frac{d_2}{Z_2}$$

Also, $d_1 + d_2 = R_{xy}$

$$\therefore d_1 = \frac{R_{xy}}{1 + Z_2/Z_1} \qquad d_2 = \frac{R_{xy}}{1 + Z_1/Z_2}$$

Figure 4. Wave path for the P-P and S-S waves.

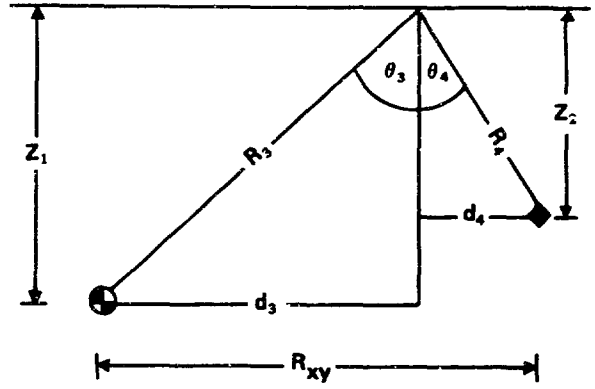

θ_3 = angle of incidence
θ_4 = angle of reflection

$$\frac{\sin\theta_3}{C_p} = \frac{\sin\theta_4}{C_s}$$

Let ϵ = specified tolerance

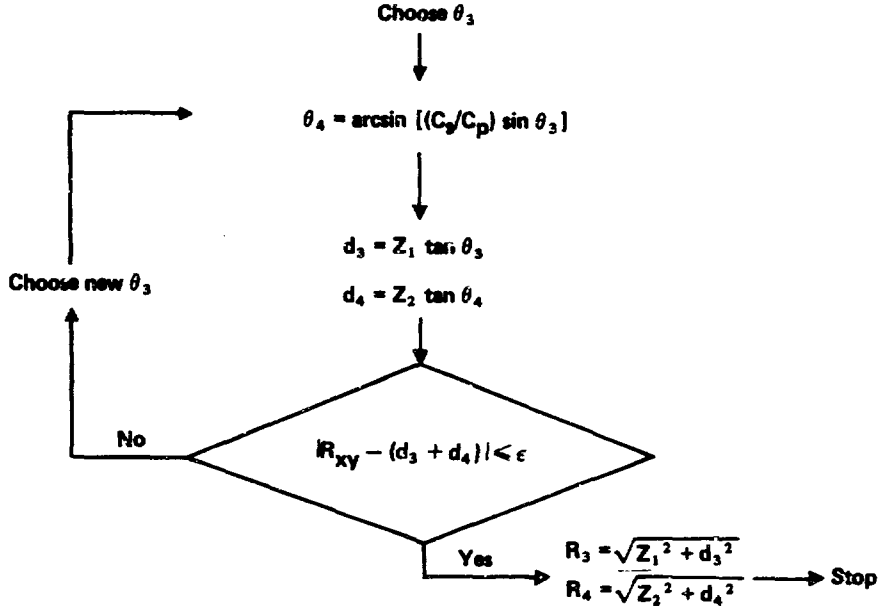

Figure 5. Wave path for the P-S wave.

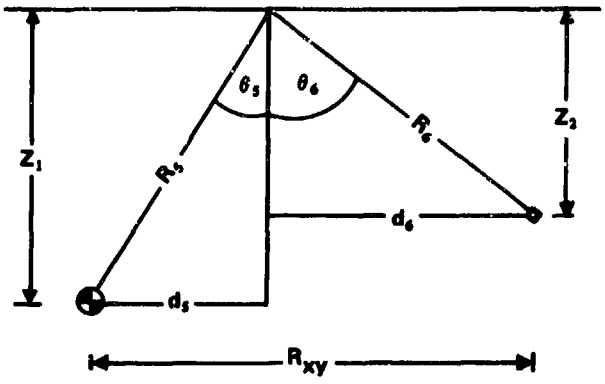

θ_s = angle of incidence
θ_s = angle of reflection

$$\frac{\sin\theta_s}{C_s} = \frac{\sin\theta_s}{C_p}$$

Let ϵ = specified tolerance

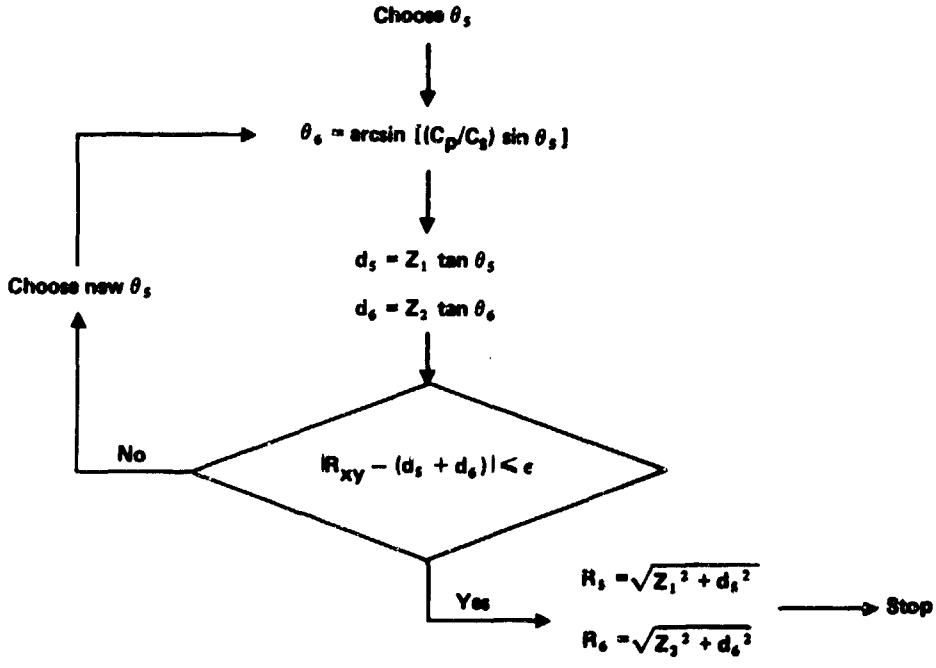

Figure 6. Wave path for the S-P wave.

The wave path for the P-S wave is shown in Figure 5. Since the P-wave and S-wave components of this wave travel at different velocities, the angle of reflection (Θ_4) does not equal the angle of incidence (Θ_3). The relationship between these angles is given by an adaptation of Snell's Law [1] given in Equation 5.

$$\frac{\sin \Theta_3}{C_p} = \frac{\sin \Theta_4}{C_s} \tag{5}$$

Because of this complication, the lengths of the P-wave and S-wave portions of the wave cannot be calculated in a straight forward manner. One possible calculation technique, presented in Figure 5, is summarized below.

1. Choose a value for Θ_3.
2. Use Equation 5 to calculate Θ_4.
3. Calculate d_3 and d_4 as shown in Figure 5.
4. Compare the sum of d_3 and d_4 with the value of R_{xy}.
5. If the difference between this sum and R_{xy} is not within the specified tolerance (ε), choose a new value for Θ_3 and return to Step 2. Repeat this process until acceptable values for d_3 and d_4 are found.
6. After d_3 and d_4 are obtained, use the following equations to calculate the lengths of the P-wave and S-wave portions of the wave path (R_3 and R_4, respectively).

$$R_3 = \sqrt{z_1^2 + d_3^2} \tag{6}$$

$$R_4 = \sqrt{z_2^2 + d_4^2} \tag{7}$$

The distance traveled by each portion of the S-P wave path, illustrated in Figure 6, can be determined in a similar fashion. Snell's Law for this path is:

$$\frac{\sin \Theta_5}{C_s} = \frac{\sin \Theta_6}{C_p} \tag{8}$$

Using this equation, d_5 and d_6 can be calculated using the iterative technique shown in Figure 6. Once acceptable values for these distances are found, the lengths of the S-wave and P-wave portions of the S-P wave path (R_5 and R_6, respectively) can be calculated using

$$R_5 = \sqrt{z_1^2 + d_5^2} \tag{9}$$

$$R_6 = \sqrt{z_2^2 + d_6^2} \tag{10}$$

TOA CALCULATIONS

After the lengths R_0 through R_6 have been determined, the arrival times for each wave can be calculated using the following equations.

$$T_p = \frac{R_0}{C_p} \tag{11}$$

$$T_s = \frac{R_0}{C_s} \tag{12}$$

$$T_{p-p} = \frac{R_1 + R_2}{C_p} \tag{13}$$

$$T_{s-s} = \frac{R_1 + R_2}{C_s} \tag{14}$$

$$T_{p-s} = \frac{R_3}{C_p} + \frac{R_4}{C_s} \qquad (15)$$

$$T_{s-p} = \frac{R_5}{C_s} + \frac{R_6}{C_p} \qquad (16)$$

where

T_p = P wave TOA T_s = S wave TOA
T_{p-p} = P-P wave TOA T_{s-s} = S-S wave TOA
T_{p-s} = P-S wave TOA T_{s-p} = S-P wave TOA

CONCLUSIONS

This paper presents convenient techniques for estimating arrival times of waves produced by a buried non-spherical charge. TOA estimates obtained using these techniques should be helpful in analyzing ground shock data. Although the required calculations can be made quite easily by hand, the equations given in this paper can be readily programmed on a hand-held calculator, making TOA estimation an even simpler task.

If these techniques prove useful, several subsequent efforts should be considered. First, the importance of assuming all waves emanate from the charge's CG rather than some other point in the charge should be investigated. In addition, techniques for calculating arrival times of waves from a buried non-spherical charge in a multi-layered geology should be developed. Finally, systematic methods of using TOA estimates to analyze ground shock data should be adopted and documented.

REFERENCE

1. Rinehart, John S., Stress Transients in Solids, published by Hyper Dynamics, Santa Fe, N.M., 1975.

SPATIAL AND TIME VARIATIONS OF LOADING ON BURIED STRUCTURES BY UNDERGROUND CYLINDRICAL EXPLOSIVES

C. A. Ross
E. L. Jerome
L. E. Malvern

University of Florida

Abstract

This study presents some discussion on spatial and time pressure variations of the loading on flat-sided buried structures when subjected to pressure waves from a general cylindrical-shaped underground explosive. Non-normal incidence, triaxial pressure conditions, and reflected/transmitted coefficients are discussed relative to pressure waves in soil impinging on buried flat concrete walls.

Introduction

Tests associated with measurement of pressure waves in soil are generally concerned with three pressures, namely a free-field pressure, a side-on pressure and a reflected pressure. The free-field pressure and the side-on pressure measurements are made with instruments whose pressure measuring faces are aligned normal and parallel respectively, with the pressure wave direction traveling radially from the explosive. These are shown schematically in Figure 1a. These devices are designed and mounted in such a manner so as not to interfere with the wave as it moves over the measuring devices. The normal reflected pressure measuring devices are rigidly mounted in such a fashion that the measuring face is normal to the wave direction as shown in Figure 1b.

In elementary wave mechanics analyses for normal reflections and transmissions, the free-field and the associated side-on pressures are usually denoted as the incident stresses, and the so-called reflected pressure equals the transmitted stress; while the true reflected stress wave which is reflected from the rigid face is usually not measured in soil.

If the pressure wave is truly hydrostatic, then the side-on pressure is equal to the free-field pressure. The assumption of a hydrostatic stress state in the wave at very high pressures is reasonable but at lower stress levels soils are known to exhibit shear resistance; therefore a triaxial stress condition is expected. Cristescu [1] reported that for pressure waves in soils the transverse or side-on pressure varies with the moisture content, and at low humidities of 5 to 7% the transverse pressure in sandy soils may be 30 to 40% of the free-field or radial pressure. Then for a plane or spherical pressure wave in soil a triaxial stress condition as shown in Figure 2 will exist, and the transverse stress σ_t may be expressed in terms of the free field or radial stress σ_r,

$$\sigma_t = k_t \sigma_r. \tag{1}$$

For fully saturated soils k_t would approach unity. Experimentally determined variations of k_t with moisture content are not available, but later in this paper this parameter variation will be investigated.

Experimentally determined and calculated radial stresses and transverse stresses for pressure waves in soils were reported by Baum et al [2]. In that study two types of stress gauges were used to measure normal pressures up to 5.0 MPa at three different orientations as shown in Figure 3. Results of both calculation and experiment showed normal pressures as a straight line variation of $\cos(2\theta)$, where θ is the angle between the normal to the gauge face and the impinging wave direction. This suggests a variation of the normal stress at the gauge, σ_n, with σ_r and σ_t as

$$\sigma_n = \frac{1}{2}(\sigma_r+\sigma_t) + \frac{1}{2}(\sigma_r-\sigma_t)\cos 2\theta, \tag{2}$$

where σ_n is the normal stress as shown in Figure 4. Equation (2) is an expression of the normal stress at an angle θ for a cylindrical stress state of principal stress σ_r and two equal principal stresses of σ_t. The shear stress on this plane is constant for a given θ and reaches its maximum value for $\theta=45°$. Experimental results of Ref. 2 indicate that the normal

stress measurement is relatively unaffected by the sliding of the soil along the gauge surface.

Using the identity $\cos 2\theta = (2\cos^2\theta - 1)$ and Eq. (1) in Eq. (2) yields an expression for the normal stress σ_n as

$$\sigma_n = \sigma_r (1-k_t) \cos^2\theta + k_t \qquad (3)$$

Reflected and Transmitted Stresses

For normal reflection and transmission from an interface, by using elementary wave mechanics, the reflected stress σ_R and the transmitted stress σ_T may be expressed in terms of the incident stress σ_I and the characteristic impedances of the media on opposite sides of the interface. For an incident stress σ_I, traveling in material 1 that impinges on an interface between material 1 and material 2, using equilibrium conditions, the stress ratios are given by Rinehart [3] as

$$\frac{\sigma_R}{\sigma_I} = \frac{\rho_2 c_2 - \rho_1 c_1}{\rho_1 c_1 + \rho_2 c_2}$$

$$\frac{\sigma_T}{\sigma_I} = \frac{2\rho_2 c_2}{\rho_1 c_1 + \rho_2 c_2} \qquad (4)$$

where ρ and c are density and stress-wave speed, respectively, for materials 1 and 2. For a soil/concrete interface the transmission ratio σ_T/σ_I varies from 1.43 for a saturated clay to 1.92 for a dry sandy soil. There appear to be no experimental data for transmission ratios in soil at other than normal incidence. Data presented by Kingery et al [4] for explosions in air show that conditions which produce normal transmission ratios of 2.0 also give transmission ratios of 2.0 on planes other than at normal incidence. Based on this it will be assumed that transmission ratios in soil are independent of the angle θ. Then the transmitted normal stress on a plane aligned at given angle θ will be equal to the incident normal stress on that plane times the transmission ratio for the soil/structure interface. The shear stress is assumed to be negligible in comparison to the normal stress.

Cylindrical Explosive Model

Free-field pressures from spherical explosive charges have been measured by many researchers and reported in detail in the classic HDRC document [4] and expanded by many others such as Drake et al [5]. The general expression for the free field pressure in soil is given in [5] as

$$\sigma_r = K(\rho c)(R/W^{1/3})^{-n} \qquad (5)$$

where K is a constant for a given depth of burial, a given explosive type and given units of ρc, R and W where

- ρ is soil density
- c soil sonic wave speed
- R standoff distance of explosive from point
- W explosive weight
- n negative slope of pressure vs $(R/W^{1/3})$ curve

A formula for the stress transmitted to a buried wall by the pressure wave from a buried conventional explosive will be developed using all the previous equations. This development is made for any explosive length; however, in practice only for close-in explosions is it necessary to account for explosive length. The following assumptions and procedure will be used.

1. Mathematically break the cylindrical charge into N parts, each weighing W/N pounds, where N is the closest odd integer to L/D, where L is the cylinder length, D is the cylinder diameter and W is the total explosive weight. Assume that the free-field pressure at any point contributed by each part can be calculated as though it were a spherical explosive.

2. Calculate the free field pressure according to Eq. (5) at a given point as a function of time for each part. Assume that the transverse pressure is of the form of Eq. (1) and that the normal pressure is given by Eq. (3), and apply the transmission factor of Eq. (4).

3. Assume that each part has its own peak pressure, transit time, pulse duration and attenuation, based on its individual weight, stand-off distance and wave speed in the soil.

4. At the desired point, sum all the pressures spatially and in proper time phase to give an overall pressure time function for each desired point.

For a given point (x,y) on a flat plane which is a known distance from a cylindrical explosive (Figure 5) the ith part of the explosive will produce a pressure time curve similar to the schematic of Figure 6. The following symbols are used in Figures 5 and 6 and in the development of expressions for stresses from a cylindrical explosion. Here, (x_i, y_i, z_i) are the relative coordinates of the point (x,y,o) relative to the center of the ith part.

$x_i = (x-X_1) - (X_2-X_1)(i-\frac{1}{2})/N$

$y_i = (y-Y_1) - (Y_2-Y_1)(i-\frac{1}{2})/N$

$z_i = Z_1 + (Z_2-Z_1)(i-\frac{1}{2})/N$

$R_i = (x_i^2 + y_i^2 + z_i^2)^{\frac{1}{2}}$

N = Nearest odd integer to (L/D)

X_1, Y_1, Z_1 Location of explosive ends

X_2, Y_2, Z_2 $Z_2 > Z_1$, $Y_2 > Y_1$, $X_2 > X_1$

t_{01} Time of arrival of first pressure pulse from the first element i = 1, time zero for structural response.

t_{0i} Time of arrival of pressure pulse from ith element

Δt_i Pulse length of pressure pulse from ith element

$\sigma(x_i,y_i,t_i)$ Pressure time function of pressure pulse from ith element at a point (x,y)

$F(t_i)$ Time function for a pressure pulse of ith element at a point (x,y)

$\sigma(x_i,y_i)$ Spatial function for a pressure pulse of ith element at a point (x,y)

α Time decay constant for pressure time curve

If σ denotes the normal stress transmitted to a buried concrete wall (z=0) from a buried explosive and σ_n the incident stress, the transmitted stress at a position (x,y) of Figure 5 from the ith element of the explosive is

$$\sigma(x_i,y_i) = \sigma_n(x_i,y_i)[\sigma_T/\sigma_I] \qquad (6)$$

If Eq. (3) is used for σ_n and Eq. (5) for s_r, Eq. (6) for the ith element becomes

$$\sigma(x_i,y_i) = K\rho_s c_s (R_i/W^{1/3})^{-n}[\sigma_T/\sigma_I]\cdot [(1-k_t)\cos^2\theta_i + k_t] \qquad (7)$$

Since $W_i = W/N$ and $\cos\theta_i = z_i/R_i$, Eq. (7) may be written as

$$\sigma(x_i,y_i) = K\rho_s c_s [(W/N)^{n/3}][\sigma_T/\sigma_I]\cdot [(1-k_t)(z_i^2/R_i^{n+2}) + k_t/R_i^n] \qquad (8)$$

The stress σ at (x_i,y_i) at time t_i is assumed to be given by a separated variable function

$$\sigma(x_i,y_i,t_i) = \sigma(x_i,y_i)\, F(t_i) \qquad (9)$$

where $F(t_i)$ is given as

$$F(t_i) = [1-(t-t_{0i})/\Delta t_i]\cdot \exp[-\alpha(t-t_{0i})/\Delta t_i]$$

for $(R_i-z_1)/c_s < t < (2R_i-z_1)/c_s$ (10)

and $F(t_i) = 0$

for $(R_i-z_1)/c_s > t > (2R_i-z_1)/c_s$

The arrival time t_{0i} is measured from the arrival time of the first pressure pulse at (x_1,y_1,o). The pulse duration is also assumed to be a function of pulse arrival time, based on experimental observation of Reference [5]. For these assumptions the arrival time and pulse duration become

$$t_{0i} = (R_i-z_1)/c_s \qquad (11)$$
$$\Delta t_i = R_i/c_s$$

These two items of Eq. (10) then set the range of time given in Eq. (10). Use of Eqs. (8), (9), (10) and (11) gives the stress transmitted to a structure at a point (x,y) at time t as

$$\sigma(x,y,t) = \Sigma\, \sigma(x_i,y_i,t_i) \qquad (12)$$

Soil/Structure Interaction

A method of accounting for motion of the structure is given in References [6] and [7]. The general procedure is to double the free field pressure value and then reduce this by a ρcV term, where V is the normal velocity of the structure. Doubling of the free field pressure assumes a completely rigid structure and a transmission ratio of 2.0. For the cylindrical model given, the pressure calculated by using Eq. (12) has already accounted for the transmission ratio; therefore this pressure may be corrected by using the following

$$\sigma_{ss}(x,y,t) = \sigma(x,y,t) - \rho_s c_s V, \qquad (13)$$

where $\sigma_{ss}(x,y,t)$ is the pressure transmitted to the wall, $\sigma(x,y,t)$ is given by Eq. (12) and V is the normal velocity of the wall.

Results

Eq. (12) is easily programmed, and distributions for transmitted stresses for any position (x,y) may be determined. A set of normalized pressure-time curves are given in Figures 8, 9, and 10 for an explosive positioned at some distance x = a, y = 0 of Figure 7. The curves are normalized by calculating the spatial distribution for a given time and dividing by the maximum peak pressure for $k_t = 1.0$. Figures 8, 9, and 10 are given for k_t = 1.0, 0.5 and 0.0 respectively at various times for variable x along the line y = 0. The effect of k_t on the peak pressures underneath the explosion at times immediately after detonation is almost negligible; however, increasing k_t tends to increase the pressure at points further away from the center of the explosion at later times. The peak of the curves show that for the assumed model the effect of the magnitude of the transverse stress is negligible, but variations due to time phasing should be accounted for since the entire surface is not loaded at zero time.

Discussion

The cylindrical explosive model is based on the spherical model of References [4] and [5]. Experimental data on cylindrical explosives which might be used to check the model predictions, is very scarce; however, an extensive set of experiments were conducted by Westine, et al [8]. Comparison of the data of Drake [5] and Westine [8] shows that the peak maximum pressure of Reference [5] is two to three times greater than the cylindrical data of Reference [8]. This is rather surprising since the data of Reference [5] is free-field data and that of Reference [8] is reflected pressure. These differences as yet are unexplained but some interesting curves result when they are compared in a normalized fashion. If d denotes the standoff distance from a flat plane as shown in Figure 11 and R the distance for a given angle θ, a normalized free-field pressure expression of Eq. [5] may be written as

$$\sigma_n/\sigma_o = (d/R)^n = (\cos\theta)^n, \qquad (14)$$

where σ_o is the pressure calculated using R = d in Eq. (5). If the transverse stress is taken into account, the normalized free field pressure expression becomes

$$\sigma_n/\sigma_o = (\cos\theta)^n\,[(1-k_t)\cos^2\theta+k_t]. \qquad (15)$$

Note that Eq. (15) reduces to Eq. (14) when $k_t = 1.0$

Eq. (15) is plotted in Figure 11 for the two extreme values of k_t and a constant value of $n = 3.25$. Also plotted is a normalized curve of the cylindrical data of Reference [8]. Except for the region near $\theta = 45°$, all the curves are very similar, and as d increases the cylindrical data of Reference [8] smooths out at the $\theta = 45°$ point.

The solid curves of Figure 11 using Eq. (15) are ratios of free-field pressures; however they could very well be ratios of transmitted pressures for a constant transmission ratio. The dashed curve of Figure 11 shows the ratio of transmitted pressure of Ref. [8] and except for the area near $\theta = 45°$ the curve falls within the bounds of the curves for the extremes of k_t. This may suggest that a smoothed curve of the reflected cylindrical data indicates a relatively constant transmission ratio. Because of the similarity of the two different types of curves of Figure 11 these observations may indicate that the differences in data of References [5] and [8] may just be that of a constant factor.

The assumption of a transmission coefficient independent of incidence angle is based on very limited experimental observations. Reflections and transmissions for soil/concrete interfaces at incidence angles greater than ten degrees of incidence are undefined using simple refraction laws of physics. This occurs due to the large differences in wave speeds of some soils and concrete. The major problem is that the simple laws based on light propagation do not hold for the complicated shock waves in soil and soil/structure interactions. Both experimental and analytical studies are needed to define soil/structure interaction at non-normal incidence angles.

Conclusions

A formula has been developed for the stress transmitted to a buried wall by the pressure wave from a buried conventional explosion of cylindrical shape. The formula seems to give reasonable predictions, but has yet to be checked against experimental results. Very few experimental results are available for pressure from a cylindrical explosive, and what is available seems to be inconsistent with the results for spherical explosives which were used as a basis for the model developed for the cylindrical charge. Additional experiments are needed before the validity of the model presented here can be considered verified.

Acknowledgement

Research sponsored by the Air Force Office of Scientific Research, Air Force Systems Command, USAF, under contract Number AFOSR F49620-83-K-0007. The U.S. Government is authorized to produce and distribute reprints for Governmental purposes notwithstanding any copyright notation thereon.

References

1. Cristescu, N., Dynamic Plasticity, North Holland Publishing Company, Amsterdam, 1967.

2. Baum, N., and Kovarna, J., "Dynamic Soil Stress - Its Calculation and Measurement," AFWL-TR-81-89, USAF Weapons Laboratory, Kirtland AFB, New Mexico, March 1981.

3. Rinehart, J. S., Stress Transients in Solids, Hyperdynamics, Santa Fe, New Mexico, 1975.

4. NDRC Summary Technical Report of the National Defense Research Committee, 1946.

5. Drake, J. L., and Little, C. D., Jr., "Ground Shock from Penetrating Conventional Weapons," Proceedings of the Symposium on the Interaction of Non-Nuclear Munitions with Structures, pp 1-6, USAFA, Colorado Springs, Colorado, May 1983.

6. Higgins, C. J., "Some Considerations in the Analysis and Prediction of Ground Shock from Buried Conventional Explosives," Proceedings (Part 2) of the Symposium on the Interaction of Non-Nuclear Munitions with Structures, pp 1-24, USAFA, Colorado Springs, Colorado, May 1983.

7. Wong, F. S., and Weidlinger, P., "Design of Underground Protective Structures," J. Structural Eng., Vol. 109, No. 8, pp 1972-1979, August 1983.

8. Westine, P. S., and Friesenhahn, G. J., "Ground Shock Loads from Buried Bombs and Ordnance Detonations," AFATL-TR-81-89, USAF Armament Laboratory, Eglin AFB, Florida, March 1982.

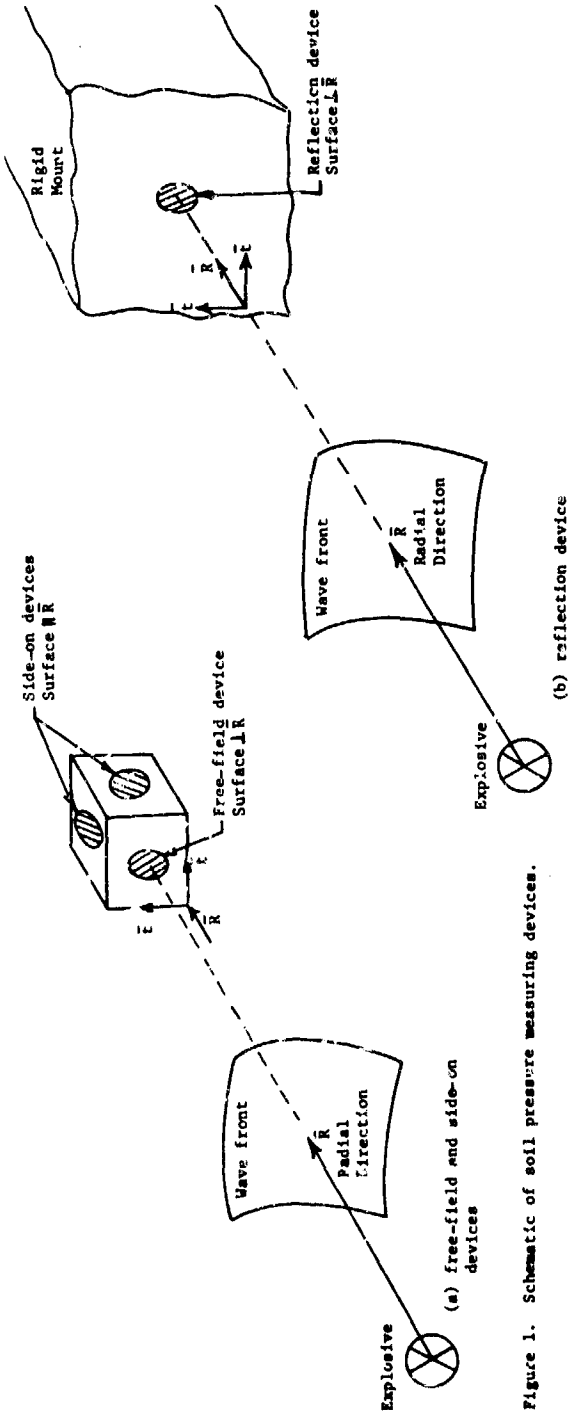

Figure 1. Schematic of soil pressure measuring devices.

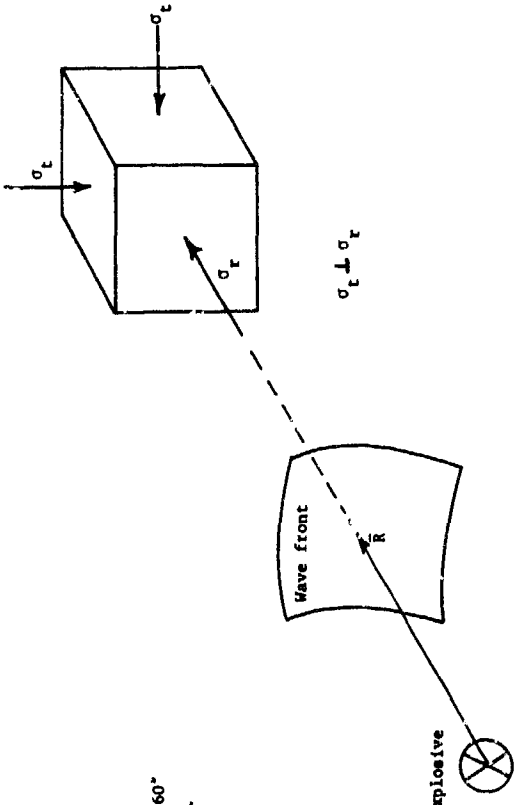

Figure 2. Schematic of triaxial stress condition for a pressure wave.

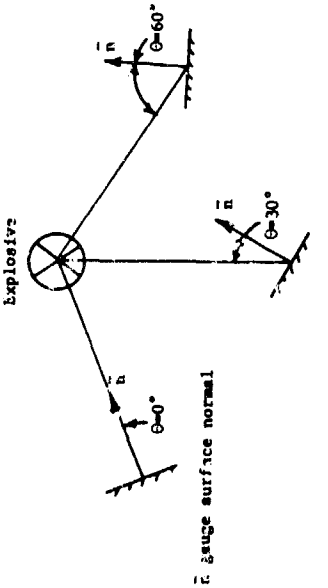

Figure 3. Pressure gauge orientation for shock tube tests of Reference 2. θ is angle between gauge normal and radial wave direction.

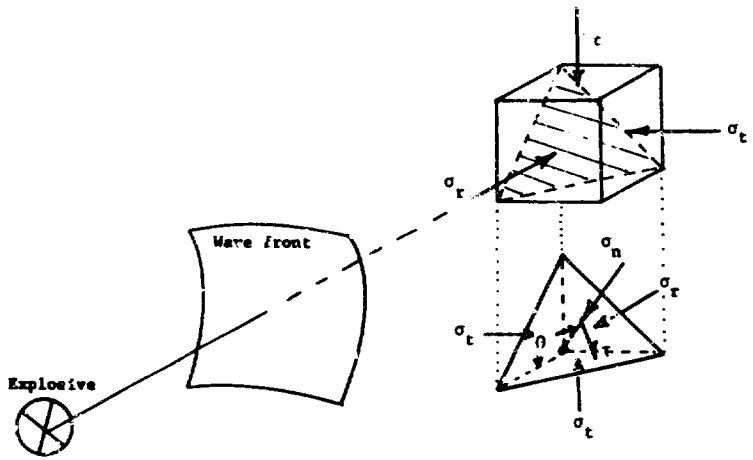

Figure 4. Cylindrical stress state of a minimum stress σ_r and two equal principal stresses σ_t.

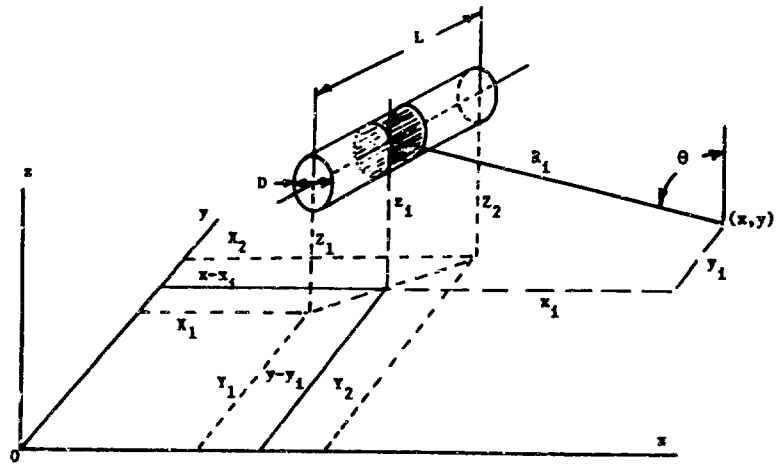

Figure 5. Schematic of cylindrical explosive.

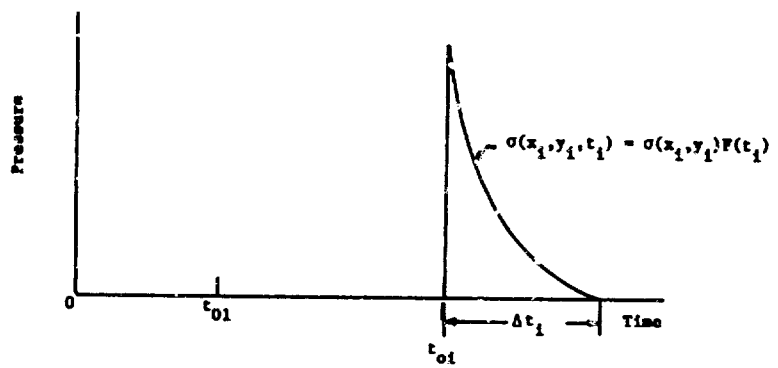

Figure 6. Schematic of pressure-time curve for ith element of Figure 5.

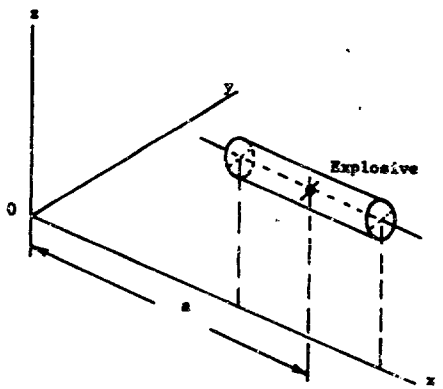

Figure 7. Position of cylindrical explosive for Figures 8,9, and 10. Explosive parallel to x axis.

240

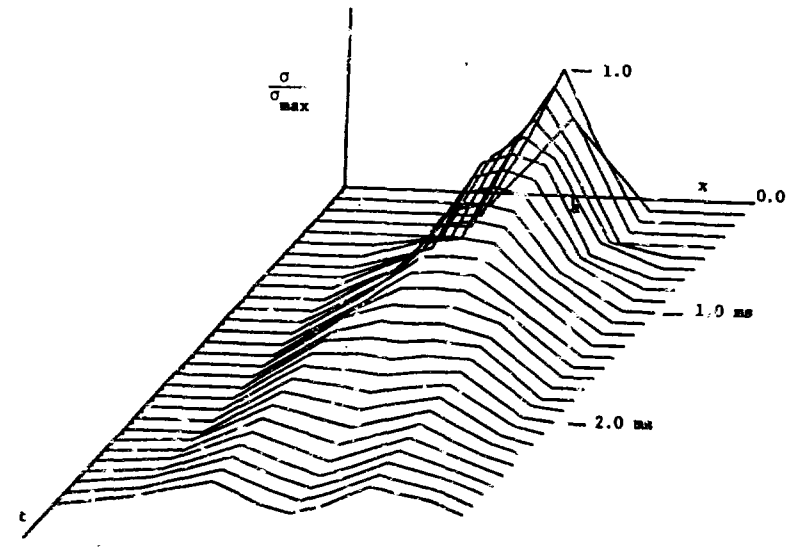

Figure 8. Normalized pressure-time curves for cylindrical explosive at x=s are shown for y=0.0. W=15.4 lb, L=2.24 ft, D=0.3 ft, ρ_s=3.168 lbf-sec^2/ft^4, c_s=1000 ft/sec, standoff=2.5 ft, k_t=1.0.

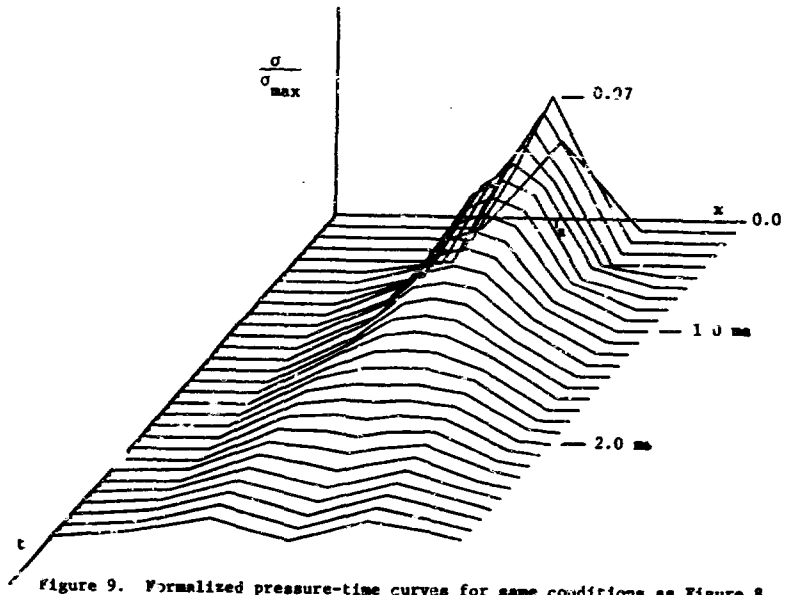

Figure 9. Normalized pressure-time curves for same conditions as Figure 8 except k_t=0.5.

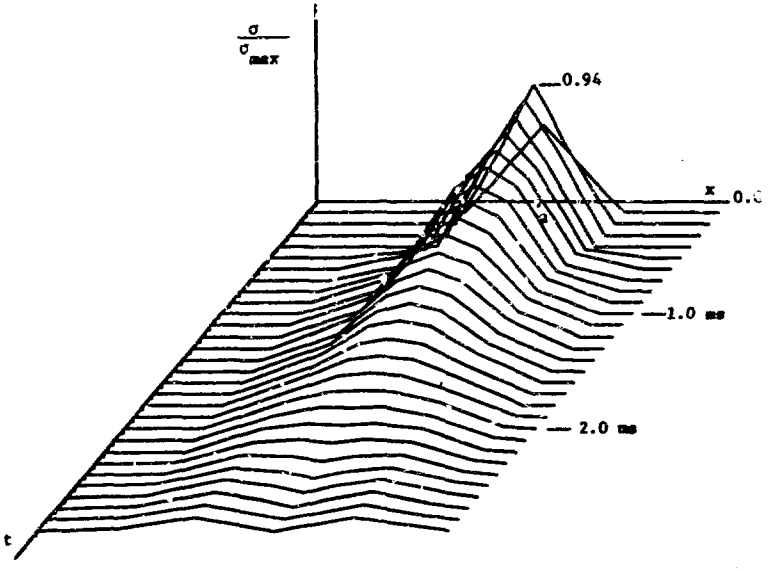

Figure 10. Normalized pressure-time curves for same conditions as Figure 8 except k_t=0.0.

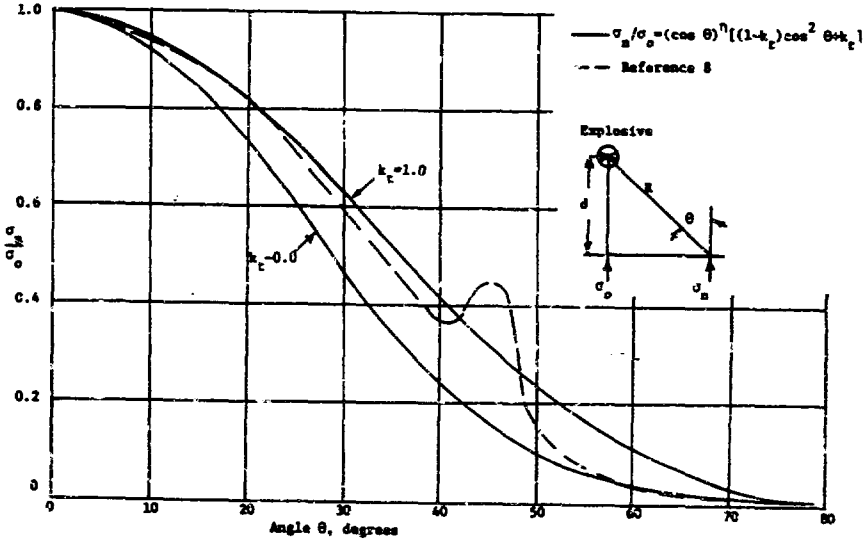

Figure 11. Normalized peak pressure curves vs θ.

PROPAGATION OF SHORT DURATION AIRBLAST INTO PROTECTIVE STRUCTURES

J. L. Drake and J. R. Britt

Applied Research Associates, Southern Division
Vicksburg, Mississippi

ABSTRACT

This paper describes a combined analytical and experimental effort to study blast wave propagation into the interior of rooms from short duration airblast produced by conventional weapons detonated near entrances to these facilities. Data from small-scale high-explosive tests were analyzed to study the effects of opening size, incident blast pulse duration and peak pressure levels on the blast transmitted into structures. Peak entrance pressures ranged from 0.07 to 1.5 MPa (10 to 220 psi). A computer code--CHAMBER--was developed based upon a modified ray theory combined with empirical formulae derived from the experiment and non-linear shock propagation and shock on shock addition rules to describe the diffracted shock at any point in the room. An existing code was incorporated to account for the quasi-steady flow. Calculated waveforms compare well with the measured blast pressure-time records, including high order reflections, with an accuracy comparable with the best 3-D hydrocode calculations.

INTRODUCTION

Personnel areas and equipment within hardened military facilities must be protected against the blast produced by explosions outside entrances and openings to these facilities. Methods for predicting the interior blast pressures are not well developed for short duration pulses characteristic of those from conventional weapons. Previous research by others [1] emphasized the quasi-steady gas flow (fill) through openings into rooms for long duration pulses, simulating airblast from nuclear weapons. Because the short duration diffracted pulses that accompany the filling process are not included in this technique, interior peak blast pressures can be grossly underestimated for conventional size threats.

The transmission of the blast environment starts with the diffraction of the incident shock wave through the opening of the building. This wave expands into the structure with a corresponding drop in pressure due to geometrical expansion and rarefactions. The pressure differential between the exterior and interior causes an inflow of air which results in an eventual equalization of the interior pressure with the exterior blast environment--so-called "filling". It is convenient to consider the shock propagation and subsequent internal reflections separately from the filling and mass flow, even though they occur simultaneously. The injury to personnel and damage to equipment within a structure associated with each of these components is dependent upon the position within the building, the magnitude and duration of the incident pressure, the room dimensions (volume), and size of the openings into the facility.

Airblast "filling" or "leakage" into chambers from long duration blast loads has been studied extensively and is well understood, particularly for large structures with small openings. Filling is essentially a quasi-steady process where a jet of air flows through the opening due to the difference in the interior and exterior pressure. Initially, the abrupt rise in exterior pressure causes a high velocity jet to enter the chamber. The average interior pressure gradually builds as additional air is forced into the structure until it eventually attains a near equilibrium condition with the outside blast environment. The time at which equalization occurs (fill time) may be estimated by the formula [1],

$$T_{fill}(\text{msec}) = \frac{V}{2A} \quad (\text{ft}) \qquad (1)$$

where V is the chamber volume and A is the area of the opening. Thus for small chamber volumes, equilibrium occurs almost immediately. An excellent review of the important research for the filling problem is given in Ref. [1] (Chapter 4). Coulter [2-3] performed experiments in a shock tube using model rooms to study the filling process. The volumes and entrance areas as well as the incident pressure and opening geometries were widely varied. Primary interest in most of these studies was on long duration pulses (typical of nuclear explosions) against civil defense-type structures such as basements and parking garages.

Several theoretical treatments of the filling process are available [1 and 7]. Most of these ignore the shock wave interaction problem and focus on the jet that forms at the entrance. Experimental verification of these computations is quite good for simple room and entrance geometries and for relatively small openings [1]. However, for large openings and for locations near the entrance, the interior pressure may be dominated by the shock propagation into the facility.

The incident shock generates a pressure wave at the opening that subsequently propagates into the facility. This wave expands geometrically into the interior, decays in amplitude, and reflects from internal surfaces. Decay rate and pulse duration of this wave are governed by the size of the openings into the structure. The attenuation of the peak is inversely proportional to the opening diameter (or mean opening dimension), while its duration is proportional to the opening diameter. Shock diffraction and interior reflection problem was recognized in early studies [1-3], but little experimental data were obtained on the propagation and attenuation of this wave into structures.

In this paper, a combined analytical and experimental effort is described that studied blast wave propagation into the interior of rooms from airblast waves incident to openings in rooms. Twenty-seven small-scale high-explosive tests were conducted to study the effects of opening size, incident blast pulse duration and peak pressure levels on the blast transmitted into a structure. Interiors of the model rooms were heavily instrumented to measure both the blast entering the room and the subsequent reflections at several locations on the walls. An analytical method was developed based upon a modified ray theory combined with nonlinear shock propagation and shock on shock addition rules to describe the diffracted shock at any point in the room. Empirical formulae for the nonlinear shock propagation were derived from fits to experimental data. An existing jet-fill theory was incorporated to account for the quasi-steady flow. Comparisons of calculated waveforms with measurements are given.

EXPERIMENTS

A series of high-explosive experiments was conducted during the period of July 1980 through September 1983 at the U. S. Army Waterways Experiment Station (WES) Big Black Test Site to study the propagation and subsequent multiple reflections of a diffracted shock into a room [4,5]. It was desired to model the short duration but high amplitude diffracted shock that would be present downstream from blast valves or transmitted through small penetrations from large explosions as well as the interior airblast produced by conventional size weapons detonated near entryways. In all, twenty-seven tests were conducted using C-4 and TNT charges ranging from 0.11 to 12.3 kg detonated outside small-scale instrumented rooms. The charge mass and stand-off distances were selected to provide the desired peak pressure and duration of the incident airblast at entrances to the test article. Entrance blast peak pressures from 0.07 to 1.5 MPa and pulse durations just outside the entrance ranging from 0.[illegible] to 2.8 msec were achieved.

Typically, the interior pressure history consisted of a rapid succession of short duration pressure pulses corresponding to superposition of multiple reflections from the interior walls. Normally, the first peak associated with the direct wave produced the greatest pressure. However, at some locations, constructive interference between reflected waves produced peak pressures greater than the direct pulse, Fig. 1 shows records taken inside the structure. Gage 1 shows the pressure pulse entering the room, and gages 2-6 illustrate the dramatic variation of the waveform at different locations in the facility.

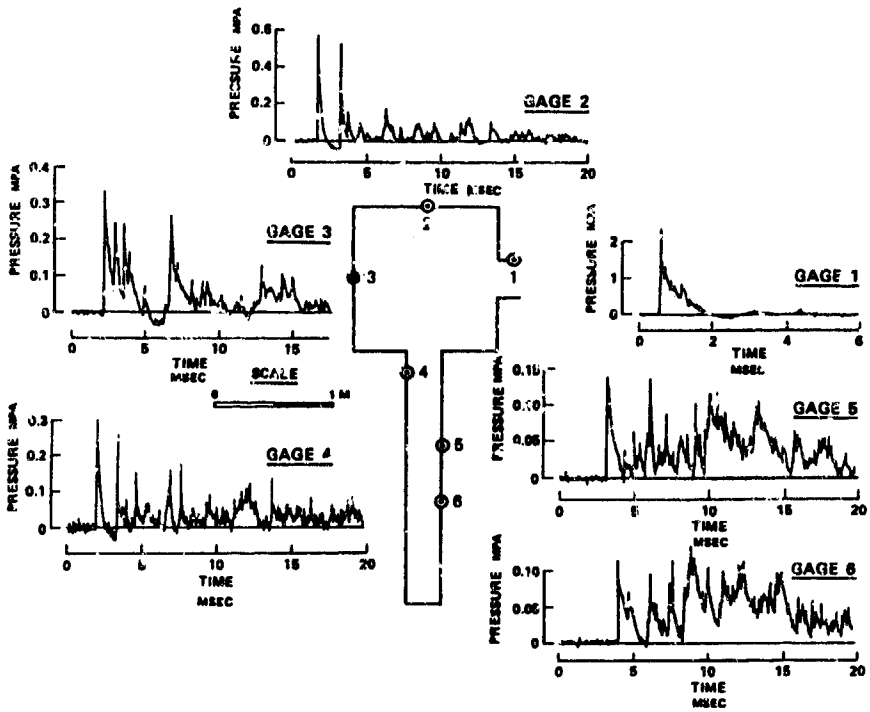

Figure 1. Typical pressure-time histories inside a structure with an interconnecting tunnel.

A plot of the side on peak pressures from the first test series normalized by the peak incident pressure in the tunnel is shown in Fig. 2 plotted as a function of the distance in tunnel diameters from the opening to the gages. The relationship between normalized pressure and range is

$$\frac{P_{max}}{P_o} = C(R/D)^{-1.35} \qquad (2)$$

where P_{max} is the peak side on pressure in the test structure, P_o is the entrance pressure, R is the distance from the center of the opening to the gage, and D is the entrance tunnel diameter. The coefficient C, was found to be a function of the angle α, between the normal to the center of the opening and the gage location as given by the expression,

$$C = 0.65\ (1-0.25\alpha) \qquad (3)$$

for α in radians.

The duration of the input shock was found to be controlled by the size of the opening. Rarefaction waves are developed at the edges of the opening that propagate across the entrance and drop the pressure behind the incident shock. This effect can be measured by the time the rarefaction wave takes to transit the opening. A linear relationship for the positive duration, t_+ , was obtained as

$$t_+ = \frac{D}{C_o} \qquad (4)$$

where C_o is the sound speed in air. If the exterior pulse duration, t_p , is less than D/C_o , then $t_+ = t_o$.

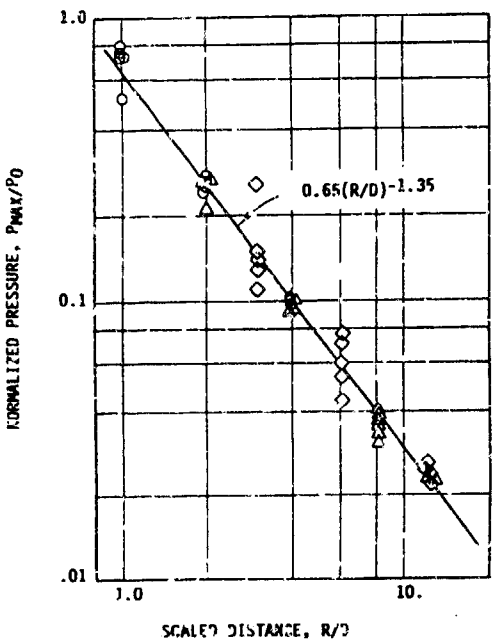

Fig.2. Peak pressure transmitted into the chamber as a function of distance from the entrance.

Eq. 2 fits the side-on pressure measurements within about ±20 percent. Because of instrumentation limitations associated with measurements of explosively generated airblast, such as the frequency response of gages and the recording system, gage overshoot, and vibration of gage mounts, this accuracy is within normal experimental scatter. Measurements of pulse duration have a much larger random scatter which is characteristic of most airblast data.

The analysis above treats only side-on blast which is equivalent to the free field blast in a chamber before reflections occur. All of the test records from the steel chamber and many from the wood chamber are reflected blast requiring a much more complex analysis procedure as discussed below.

SHOCK DIFFRACTION MODEL

A semi-empirical modified ray tracing procedure was developed to model shock wave diffraction through an opening into a room of rectangular cross-section. The blast at the opening is treated as originating from a point source located at the center of the entrance. Interior walls are assumed to be perfectly rigid reflecting planes. Each encounter with a wall generates a reflection which can be treated as a pulse originating from an "image source" located behind the wall. The pressure at any location in the room is then a nonlinear superposition of the direct shock and a contribution from an "image source" for each of an infinite series of reflections.

The outline of steps for computing a waveform is as follows: First, path lengths for rays of successively higher order reflections are generated. Arrival times are calculated by integrating the pressure dependent shock propagation velocity along the path. The shock wave pressure attenuation with distance for each ray is assumed to be the same as for the direct shock expressed by Eq. 2. Orders of reflections having arrival times greater than the times of interest do not contribute and are not computed. Next, pressure, particle velocity and density waveforms for each ray are calculated neglecting the presence of other rays. Finally, the pressure waveforms are combined using non-linear shock addition rules to produce the total diffracted pulse. Each of these steps is treated in detail below.

Path Lengths

An infinite number of ray paths are possible within the room due to combinations of reflections from the six walls. The order of the ray is defined as

$$N = \sum n_i \qquad (5)$$

where n_i is the order of the reflection in each of the rectangular coordinate directions, i = 1, 2, and 3. Let n_{N_i} be the components of the Nth order ray, then

$$r_{N_i} = X_i^1 - (-1)^{n_i} X_i^0 \pm n_i L_i \qquad (6)$$

where X_i^0 and X_i^1 are the coordinates of the source and receiver, respectively, and L_i is the dimension of the room in the i'th direction. Note that for each non-zero order of reflection, $n_i \neq 0$, two values of the ray component are possible; one from each of the opposite walls of the room in that plane, for example, floor and ceiling. When $n_i = 0$, then only one value is possible for the i'th ray component. The total ray length is found from all combinations of r_{n_i} as

$$R_N = \left(\sum_{i=1}^{3} r_{n_i}^2 \right)^{1/2} \qquad (7)$$

In general, six ray lengths are possible when $n_i \neq 0$ for $i = 1$, 2, and 3.

Pressure Histories

An examination of the measurements indicated that pressure histories for any ray can be adequately computed from the commonly used exponential formula

$$P_i(R,t) = P_{max}(R,\alpha)\,[1-(t-t_o)/t_+ \times \exp[-(t-t_o)/t_+] \quad \text{for } t > t_o \qquad (8)$$

where t_+ is the positive phase duration given by Eq. 4, and P_{max} is the peak overpressure given by Eq. 2. Peak pressure, $P_{max}(R,\alpha)$, is the only factor which changes in this expression for different rays and observation points. The total waveform is constructed by superposition of these pressure histories for all rays using the following non-linear shock addition formulae.

Shock Combining Rules

Non-linear shock rules were postulated by Needham [6] combining shocks at a point from multiple sources and incorporated into the LAMB model. While these shock addition rules cannot be supported from first principles, they have proved to be accurate in comparisons with measurements and hydrocode calculations for many shock combining situations. In this method the waveform for each ray is computed ignoring the presence of other shocks. These results are then combined using the three shock addition rules as follows:

Shock Addition Rule Number 1 - "Conservation of Mass"

It is assumed that at a point in space, the density, $\bar{\rho}$, is the ambient density, ρ_a, plus the sum of the overdensities, $\Delta\rho_i$, due to all shocks that have passed that point at a given time

$$\bar{\rho} = \rho_a + \sum_{i=1}^{N_s} \Delta\rho_i \qquad (9)$$

where N_s is the number of shocks.

Shock Addition Rule Number 2 - "Conservation of Momentum"

$$\bar{\rho}\,\vec{V} = \sum_{i=1}^{N_s} \rho_i \vec{V}_i \qquad (10)$$

where $\vec{V}$ is the total material velocity, ρ_i is the density for shock i, and $\vec{V}_i$ is the particle velocity for shock i.

Shock Addition Rule Number 3 - "Conservation of Energy"

The total overpressure from N_s shocks is

$$\bar{P} = \sum_{i=1}^{N_s} P_i + \left(\frac{\gamma_o+1}{2}\right)\left(\frac{1}{2}\sum_{i=1}^{N_s} \rho_i |\vec{V}_i|^2 - \frac{1}{2}\bar{\rho}|\vec{V}|^2\right) \qquad (11)$$

where P_i is overpressure for shock i.

Arrival Time

The arrival time, t_o, for each ray is evaluated by integrating the pressure dependent shock wave propagation velocity using a polytropic equation of state for air with a ratio of heat capacities, $\gamma = 1.4$.

Other Shock Wave Parameters

These shock combination rules require not only pressure, $P_i(t)$, waveforms, but also velocity, $V_i(t)$, and density, $\rho_i(t)$, waveforms. Experimental measurements provided only $P_i(t)$. Particle velocity, V_{max}, and density, ρ_{max}, at a shock front can be related to the pressure, P_{max}, through the Rankine-Hugoniot conditions. These conditions do not hold exactly behind the shock front.

In the current analytical model of the measured blast environment in a room at low to moderate overpressure ($0.07 < P_o < 1.5$ MPa) the following approximations (whose accuracies are supported by

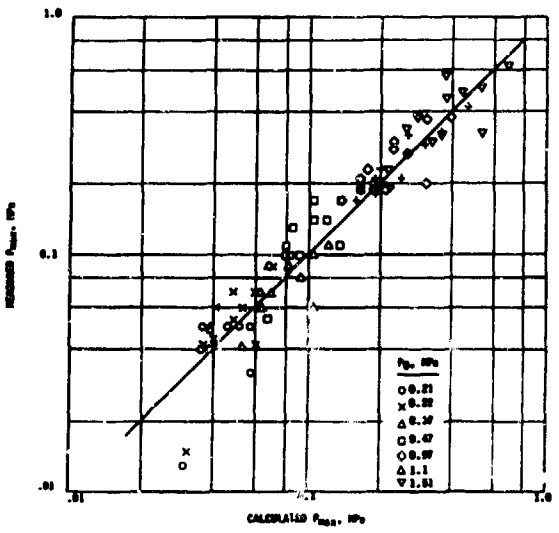

Figure 3. Calculated versus measured peak initial reflected pressures.

comparison of the calculated pressures with measurements) have been made to obtain parameters behind the shock front. First, assume adiabatic expansion behind the shock front to obtain the density

$$\rho_i(t) = \rho_{max}\left[\frac{P_i(t)+P_a}{P_{max}+P_a}\right]^{1/\gamma} \qquad (12)$$

where P_i is obtained from Eq. 8 for each shock wave and P_a is atmospheric pressure. Next, assume that the Rankine-Hugoniot relation for particle velocity applies, approximately, behind the shock front to obtain

$$V_i(t) \approx C_o\left[\frac{(1-\rho_a/\rho_i)P_i(t)}{P_a\gamma_o}\right]^{\frac{1}{2}} \qquad (13)$$

These approximations, along with the shock addition rules, provide a reasonable procedure for calculating the shock waveforms produced by the many reflections from the walls of a room. In the following section, the accuracy of this procedure is evaluated by comparison with measurements.

WAVEFORM CALCULATIONS

Using modified ray theory model discussed above for the diffracted pulse and the fill code of Ref. [3] a computer code, CHAMBER, was developed to calculate the combined pressure pulse in a room. This code was written in FORTRAN, originally for mainframe computers, but has been converted to run on a microcomputer. CHAMBER is an outgrowth of an earlier code, WESFILL, reported in Ref. [4] which treated only the low-pressure region where reflections can be treated acoustically.

Fig. 3 is a comparison of the CHAMBER computed values of the initial peak reflected shock wave ovepressure with the data measured in the steel chamber. The 45-degree line represents perfect agreement. The maximum deviations from this line for 90 percent of the data is about 35 percent which is within the normal experimental scatter for measurements of this type. Since the code uses

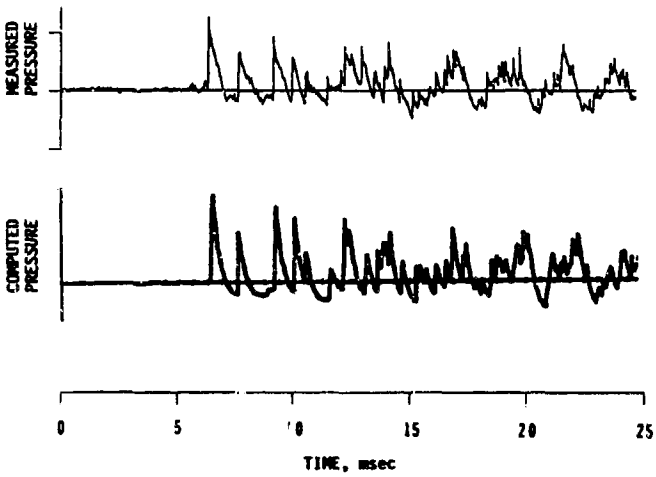

Fig. 4. Example of a calculation with measured pressure history at midpoint of the mid-plane wall for low pressures (P_{max}~14 KPa).

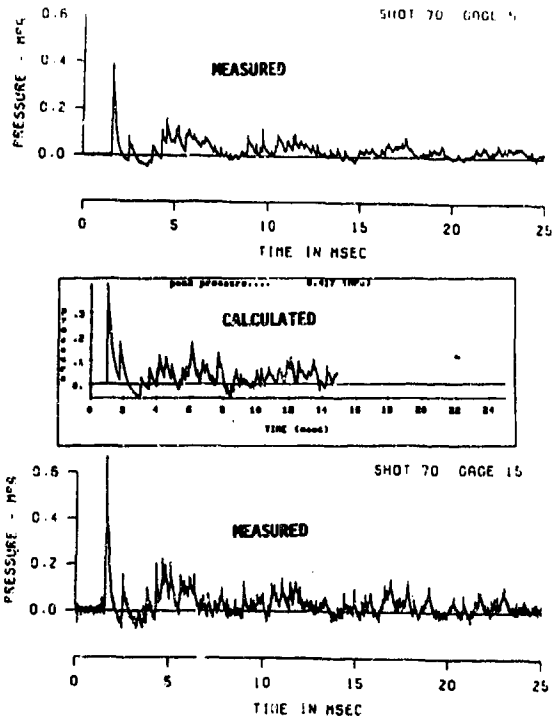

Figure 5. Comparison of calculations with measurements from symmetrically located gages.

Eqs. (2)-(4) derived from the measurements in the wood test structure, this comparison with data from the steel chamber provides an independent check on the generality of these formulae. Several test cases were run to verify the accuracy of the waveform computations. Fig. 4 is an example of the low pressure measurements made in the wooden structure. Agreement between the amplitude of the peaks, the time of the peaks, and apparent reverberations within the structure are reproduced well by the code. Fig. 5 is an example of comparisons with the high pressure measurements made in the steel chamber. Measured records from two symmetrically located gages are shown with the computed waveform. The calculated values are intermediate between the two measurements. Fig. 6 shows another comparison between calculated and measured records. The calculated curve and the input data at the top of the figure are from an actual CHAMBER run. In this case the second peak resulting from higher order reflections is greater than the first peak.

CONCLUSIONS

The explosive tests discussed in this paper provided an experimental basis for developing and verifying a semi-empirical calculational procedure for short duration blast entering a room through an opening. The code CHAMBER based on this procedure reproduces the blast pressure-time records, including high order reflections, with an accuracy comparable with the best 3-D hydrocode calculations. Further improvement of the procedure will require incorporating more expreimental data and more accurate formulae for density and particle velocity histories.

The analysis presented in this paper -- embodied in the CHAMBER code -- is in excellent agreement with measurements obtained in two experimental structures. While this analysis may not be applicable to all openings, the measurements on which the analysis is based cover a fairly broad range of parameters as follows: (a) the pressure pulse just outside the entrance ranged from 0.07 to 1.5 MPa, (b) the positive phase durations of the incident pulse ranged from 0.9 to 4.3 acoustic transit times across the opening, (c) the ratio of opening area to entrance wall area varied from .006 to 0.1, (d) the ratio of room volume to opening area ranged from 20 to 350 m, (e) the angle α with the entrance, described in Eq. (3), ranged from 0 to 69 degrees for the first arrival at gages.

For the short duration blast in our tests, the quasi-static fill contributed only a small fraction to the total internal pressure. However, for long duration blast incident on the entrance, fill will become a more dominant part of the total waveform. Since Coulter's fill model [3] is included in CHAMBER, calculations can be performed for long duration pulses. Fig. 7 is an example of computations compared with airblast measurements in a test structure on Operation Prairie Flat [8], a 500-ton (453,600-kg) surface tangent detonation. In this case the entrance area was 31 percent of the wall area, or three times greater than the openings used in our tests. The pressure pulse at the entrance had a peak of 4.7 psi (.032 MPa) and a duration of 250 msec, which is about 50 acoustic transit times across the opening. The circles on Fig. 7 were computed assuming an opening size equal to the square root of the entrance area, i.e., 4.5 ft on a side. The calculated values follow the shape of the measured curve, but the peak is 35 percent lower. The triangles, computed using an opening 5.5 ft on a side, are in better agreement with the peaks. This result suggests that for long, rectangular openings an effective opening size greater than the square root of the area should be used for the refracted shock calculations. The quasi-static fill contribution to the calculated pulse gradually rises to a maximum value

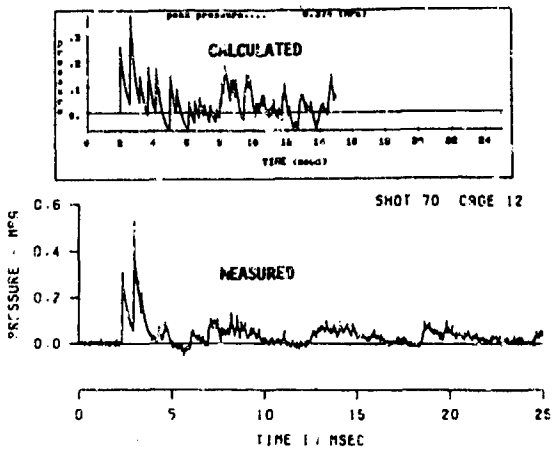

Figure 6. Comparison of calculated pressure with measurement showing constructive nonlinear reflections.

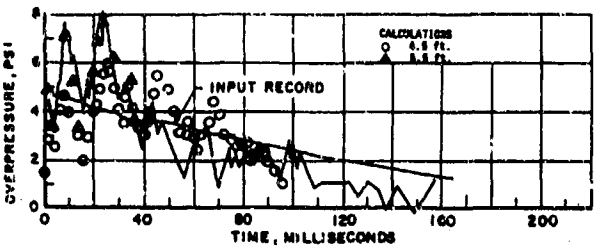

Figure 7. Pressure history for Prairie Flat structure.

of 3.7 psi at 30 msec and is approximately equal to the input record for later times. This part of the total pulse appears to be accurately computed.

ACKNOWLEDGEMENTS

The experimental work and much of the analysis were performed by the authors while employees of WES. Support for the project at WES was provided by the Air Force Engineering and Services Center at the Army Office, Chief of Engineers.

REFERENCES

1. A. R. Kriebel, "Airblast in Tunnels and Chambers," DASA 1200-II Supplement 1, Defense Nuclear Agency, Washington, DC, Oct 1972

2. G. A. Coulter, "Air Shock and Flow in Model Rooms," BRL MR 1967, U. S. Army Ballistics Research Laboratory, Aberdeen Proving Ground, MD, June 1969

3. G. A. Coulter, "Blast Loading in Existing Structures - Basement Models," BRL MR 2208, U. S. Army Ballistics Research Laboratory, Aberdeen Proving Ground, MD, Aug 1972

4. J. L. Drake and J. R. Britt, "Airblast Penetration into Semiherdened Structures," ESL-TR-80-60, Air Force Engineering and Services Center, Tyndal AFB, FL, Oct 1980

5. J. R. Britt and C. D. Little, "Airblast Attenuation in Entranceways and Other Typical Components of Structures: Small Scale Tests Data Report 1," Draft, USAE Waterways Experiment Station, Vicksburg, MS, 1983

6. S. Hikida and C. E. Needham, "Low Altitude Multiple Burst (LAMB) Model, Volume 1: Shock Description," DNA 5063Z, S-Cubed, Albuquerque, NM, June 1981

7. K. Kaplan, "Accidental Explosions and Effects of Blast Leakage into Structures," ARLCD-CR-79009, ARRADCOM, Dover, NJ, 1979

8. G. A. Coulter and R. L. Peterson, "Blast Fill Time of a One-Room Structure," Operation Prairie Flat Project Officers Report - Project LN 111, POR-2101, U. S. Army Ballistics Research Laboratory, Aberdeen Proving Ground, MD, Nov 1964

BLAST CHARACTERISTICS RESULTING FROM INTERNAL DETONATIONS INSIDE A BLAST CHAMBER

Larry Mars

Computer Sciences Corporation
NSTL, Mississippi

ABSTRACT

A series of tests were conducted in an effort to determine blast characteristics resulting from the detonation of a high explosive inside a blast chamber, which was designed to simulate conditions in a multiple bay underground structure. Test specimens of varying concrete strength and reinforced steel were tested to determine failure modes under interior blast loadings and to determine blast effects to an adjacent space. Test analysis, including a brief narrative discussion of the results and the anomalies are presented.

INTRODUCTION

The use of existing blast wave data is quite difficult for the practitioner. For free-air bursts and surface bursts, the effects of blast waves can be readily estimated from existing experimental data. However, when an explosion occurs within a structure, the use of existing data for estimation purposes is quite difficult. Furthermore, the resulting damage cannot always be clearly correlated with the values of peak overpressure and impulse.

When an explosion occurs within a structure, the peak pressures associated with the initial shock front (free-air pressures) may be extremely high, and in turn, may be reinforced within the structure. In addition, the gases from the explosion may exert additional pressures and increase the load duration within the structure. The combined effects of the shock front and additional pressures may eventually destroy the structure unless venting for the gas and the shock pressure is provided. The pressures reflected and reinforced within the structure could be referred to as interior-shock front pressures while those pressures produced by the accumulation of the gaseous products of the explosion could be identified as gas pressures.

Experimental data for comparison with theoretical data is not readily available. For this reason, a series of tests were designed by the Air Force Armament Laboratory and conducted by Computer Sciences Corporation to determine resulting damage from a partially confined explosion and some of the parameters associated with interior loading. In the early stages of test planning, it was decided to achieve some definite objectives in the preliminary testing:

1. Simulate an internal blast in an underground buried structure;
2. Construct a reuseable test fixture that would allow indefinite testing for a definite cost effectiveness;
3. Establish damage criteria for different design of reinforced concrete walls;
4. Measure the parameters associated with an internal blast.

It has been stated that when an explosive charge is detonated inside a structure, the initial shock wave is identical with an initial shock wave obtained in the open. When this shock wave strikes the wall that surrounds the charge, it is reflected, and the reflected wave bounds back and forth among the walls, the floor, and the roof until the wave's energy has been completely transformed into heat or until there are no longer confining walls, that is, until the structure is demolished.

Various approximate methods for the calculations of different parameters have been developed, and the structures are usually designed for impulse loading rather than for the peak pressures. The total impulse is assumed to be distributed uniformly, whereas the actual distribution of the blast impulse is highly irregular due to the multiple reflections and time phasing. Only recently has it been shown that a combination of peak overpressure and positive phase impulse is responsible for the damage.

TESTING PROCEDURES

To meet the need for experimental data, to make predictions for damage to reinforced concrete structures from internal blast and the resulting internal pressure associated with such a blast, it was determined that a blast chamber be designed and

built to contain such a blast. The assembled blast chamber is shown in figure 1.

There are three basic parts to the chamber: a bottom cylinder, top cylinder, and dome. The cylinders are 6-ft sections of 5-ft O.D. pipe with a 1-inch thick wall. Three cyclinders were constructed to be interchangeable, and three cylinders were constructed with flanges in order to hold a concrete specimen between them. A hemispherical dome was also constructed to sit atop the blast chamber to aid in uniformly distributing the blast load at the top of the cylinder.

The reinforced concrete test specimens were designed and constructed as shown in figures 2a and 2b. The concept was to have a target area 30 by 30 inches which would simulate a reinforced concrete wall. Fourteen concrete test specimens were constructed. The specification for each window design is given in table 1 below.

Table 1. Fabrication Details

Specimen	Bar Spacing #3 Bar (O.C. each way) (inches)	Fabrication Details* (welded)	Compressive Strength (psi)
1	3	Fully	3000
2	3	Fully	3000
3	3	Fully	3000
4	3	Partially	3000
5	6	Fully	3000
6	6	Fully	3000
7	6	Partially	3000
8	3	Partially	6000
9	3	Fully	6000
10	3	Fully	6000
11	6	Partially	6000
12	6	Fully	6000
13	6	Fully	6000
14	6	Fully	6000

*Fabrication details with reference to window reinforcement connection to rolled steel frame.

TEST RESULTS

A total of 17 tests were conducted. Initial tests were conducted with a 0.5 lb spherical pentolite charge at stand-off distances of 9, 12, and 15 inches. The basic premise is that if a shock wave strikes a wall, the wall can be subjected to a blast of constant pressure equal to the pressure in the shock wave. At some point the wall will collapse and the migration of pressure through the collapsed wall could be measured as well as the pressure rise in the adjoining area. Based on this reasoning, it is not possible to predict whether confined blasts with small bombs or external blasts with large bombs is the better choice. Experimental curves for free air bursts, surface bursts, and reflecting phenomena are readily available, and an attempt has been made to produce some experimental data for explosive bursts in enclosed rooms. Without reiterating established theory and experimental curves, bear in mind our attempt was to simulate an internal blast in a reuseable test fixture and observe the damage to determine how practical and useful this approach would be for future testing.

Radial distances of 9, 12, and 15 inches were initially determined to be the area of interest for the assessment of damage criteria. Damages on a reinforced concrete wall from nearby explosions may vary from minor cracks up to complete perforation. Our main objective was to get complete perforation, so we could get pressure migration to the bottom chamber and record the pressure. Simply stated, the desired result was to measure the area of damage at a certain distance for a certain weight of explosive. Using these radial distances and a charge weight of 0.5 lb would give scaled distances (Z) of approximately 1.57, 1.26, and 0.94. At a scaled distance of 1.57 using a 0.5 lb charge, there was no damage. At a scaled distance of 0.89 using approximately a 1.5 lb charge for the same specimen, there was no damage. At a scaled distance of 0.66 using 1.5 lb charge again with the same specimen, there was only spalling on the back side. Using the same specimen at a scaled distance of 0.44 and a 1.5 lb charge, there was a perforation. These tests were with a 3-inch spacing and 3000 psi compressive-strength concrete. Using the same size charge and the same stand off but with a 6-inch spacing and 6000 psi compressive-strength concrete, there was a perforation with spalling. Perhaps a significant development at this stage of close-in very near contact tests was the relationship observed for a spherical shock wave. That is, for a spherically shaped source, the front as it propagates through the medium, is the surface of a sphere. A second result was complete sealing of the test chamber was not achieved as expected.

Testing was continued in an effort to gain as much information as possible for future testing. This was done using different charge weights with different scaled distances in an attempt to generate some type of data base. There was a clear difference between the performance of the reinforced concrete specimens with a 6-inch spacing and those with a 3-inch spacing. However, to describe this performance adequately in terms of damage criteria for a simulated reinforced concrete wall is very difficult. For a contact explosion, the time integral of the total force exerted on the wall is the impulse. This includes both the intense instantaneous pressures and the longer lasting quasi-static pressures associated with a detonation. Conversely, for an indirect explosion in a confined space, the impulse is affected by this confinement, and the effect may appear to be a difference in behavior for the materials being tested. Thus, an ideal condition would be to determine the amplitude of an explosion, the amount of pressure delivered for a period of time, and the exact final condition of the structure. Thus, to correlate this type of testing with different, perhaps more realistic specimen designs, is a future task.

Table 2 gives a record of some of the parameters measured during the tests. Figures 3a through 16b are photographs showing the damage criteria with front and rear damage. In the initial design, it was decided to put pressure transducers in the concrete specimen where the reinforcement was greater to determine if it would be practical. Transducer stations in the side of the cylinder were based on all tests being conducted at either 9, 12, or 15 inches. Figures 17 through 25 show a sampling of pressure time histories. Also shown are some representative histories of pressure migration in the bottom cylinder.

Table 2. Damage Parameters Observed

Concrete Specimen (Test no.)	Explosive Weight lb (kg)	Distance Radial M (ft)	Distance Scaled	Compressive Strength	Bar Spacing (in)	Percent Reinforcement	Damage
1 (1)	0.5	1.25	1.58	3000	3	2	No damage
1 (2)	1.42	1.0	0.89	3000	3	2	No damage
1 (3)	1.46	0.75	0.66	3000	3	2	Spalling
1 (4)	1.46	0.5	0.44	3000	3	2	Perforation
6 (5)	1.48	0.5	0.44	3000	6	1	Perforation
8 (6)	4.09	0.75	0.47	6000	3	2	Perforation
12 (7)	4.13	2.1	1.31	6000	6	1	Perforation
11 (8)	4.26	3.2	1.97	6000	6	1	Perforation
9 (9)	3.01	2.36	1.53	6000	3	2	No damage
2 (10)	3.02	2.89	2.00	3000	3	2	No damage
3 (11)	3.03	1.91	1.32	3000	3	2	Light cracking
9 (12)	4.16	4.02	2.50	6000	3	2	Severe damage
14 (13)	4.17	4.82	3.00	6000	6	1	Perforation
7 (14)	4.18	5.6	3.50	3000	6	1	Perforation
10 (15)	4.19	5.6	3.50	6000	3	2	Severe spalling*
4 (16)	4.21	5.2	3.25	3000	3	2	Severe spalling*
2 (17)	4.17	4.4	2.75	3000	3	2	Severe spalling*

*No complete perforation.

CONCLUSIONS

No specific conclusions from the actual test series were made because of some of the variations in the results. However, an attempt will be made to describe these results in conjunction with our stated objectives:

1. There was a marked difference between the 0.5, 1.5, 3.0, and 4.0 lb explosive charges at approximately the same scaled distances. The effects could not be explained in simple charge weight differences, nor could they be explained in simple differences between the strength of the reinforced concrete specimens. Perhaps the fact that nearer the charge to the test specimen the less uniform the loading, while at greater distances, the more uniform the loading is a critical factor.

2. Spacing of the reinforcement steel relative to the thickness of the concrete specimen is a more critical factor than the compressive strength of the concrete.

3. There is a certain peak pressure apart from the total time phase which will perforate the reinforced concrete specimen.

4. No complete analysis could be made because of the disparity in the behavior of the two patterns to a blast.

5. Valuable information was gathered for future testing, and our basic objectives were accomplished: to construct a test fixture that could be used to simulate an internal blast and use concrete specimens to simulate reinforced concrete walls.

Based on the results obtained in this test series, a test program will be developed whereas the concrete specimens will be redesigned using various wall thickness, percent reinforcement, and different compressive-strength concrete. Test fixtures with a minor modification will be completely sealed. More sophisticated arrangement of instrumentation will be utilized. As a result, a practical means of predicting blast effects for confined detonations within a structure for static pressure, pressure migration, and damage criteria will be developed.

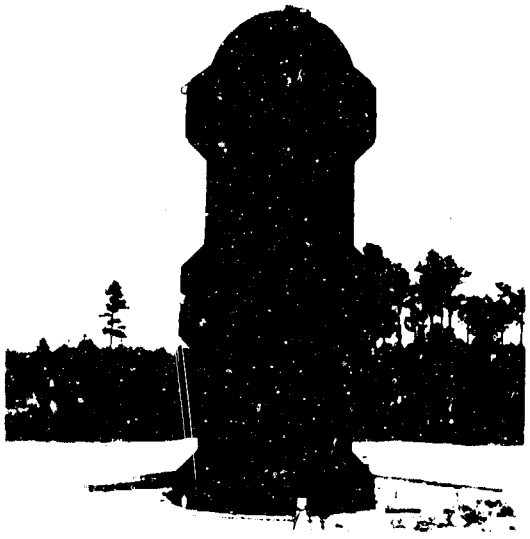

Figure 1.

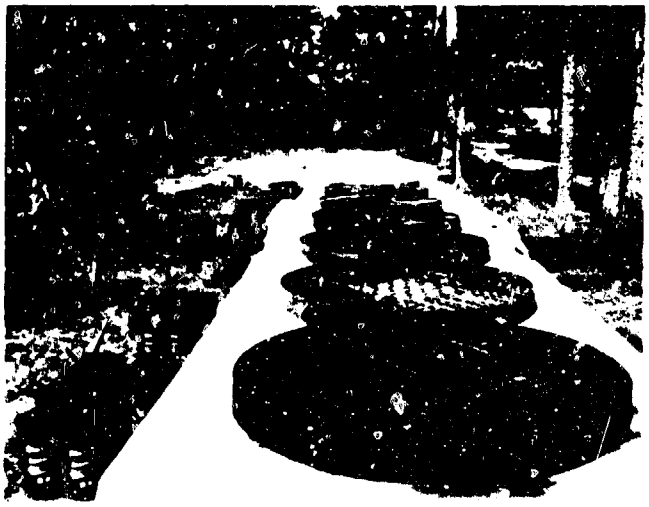

Figure 2a.

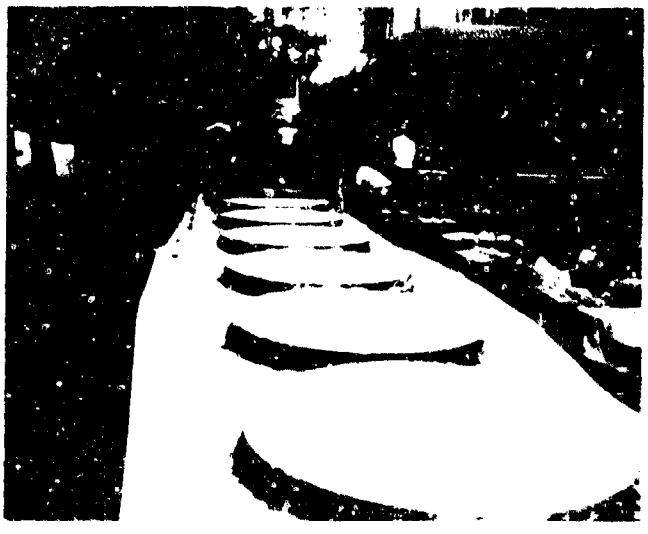

Figure 2b.

Figure 3a.

Figure 3b.

Figure 4a.

Figure 4b.

Figure 5a.

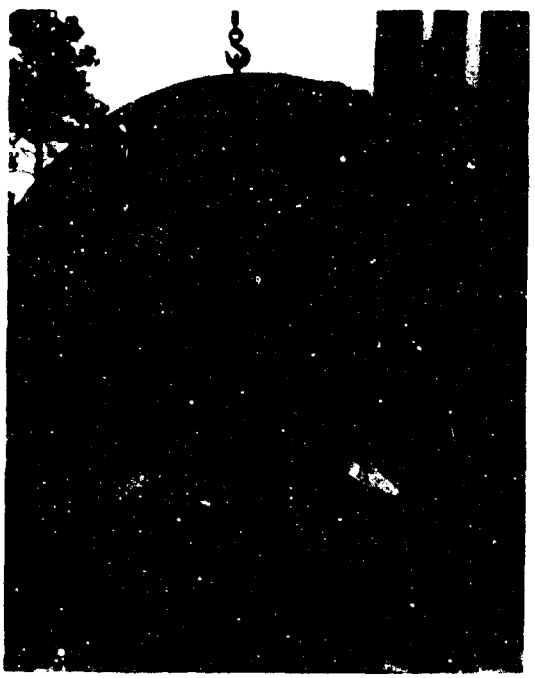

Figure 5b.

Figure 6

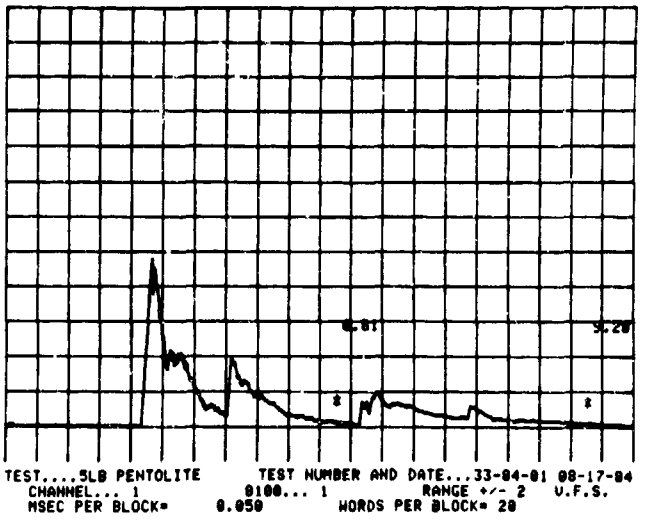

Figure 7

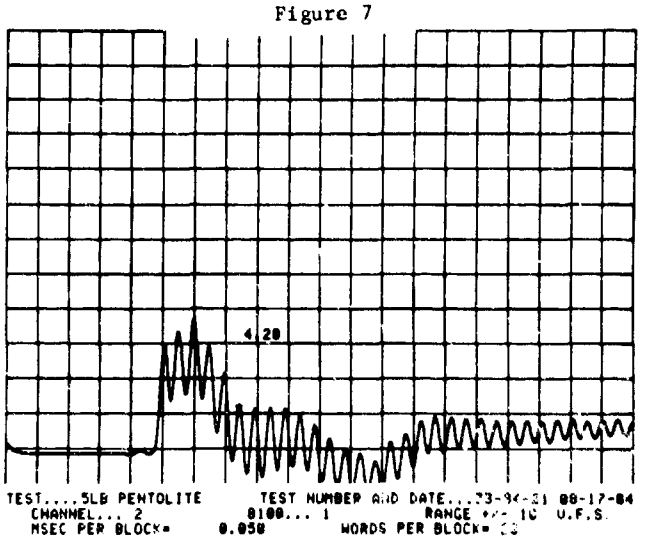

Figure 8

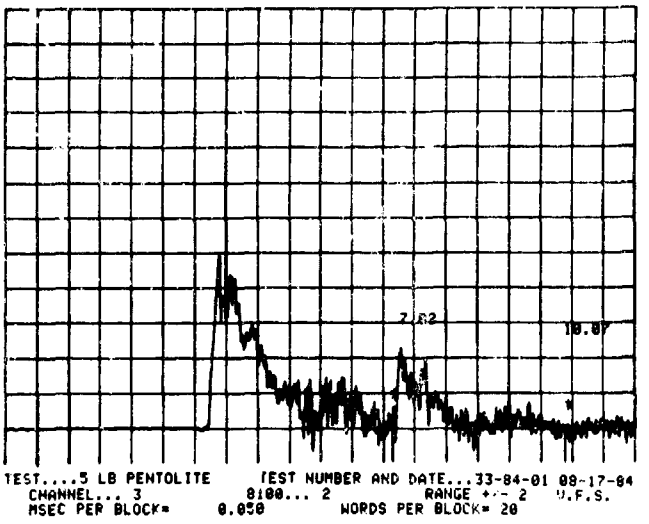

Figure 9

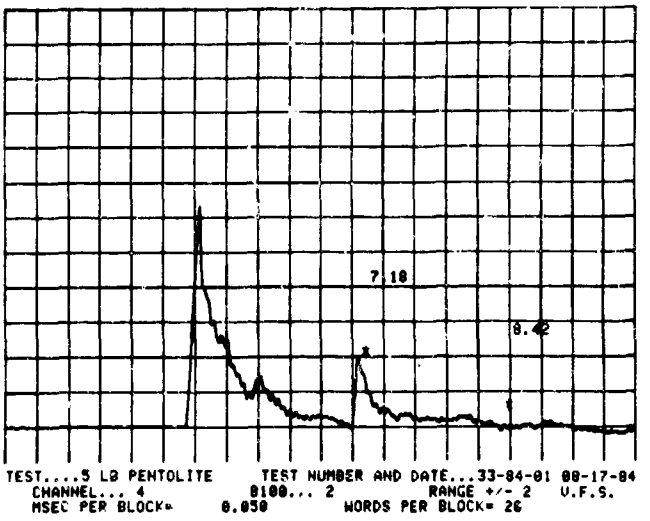

Figure 10

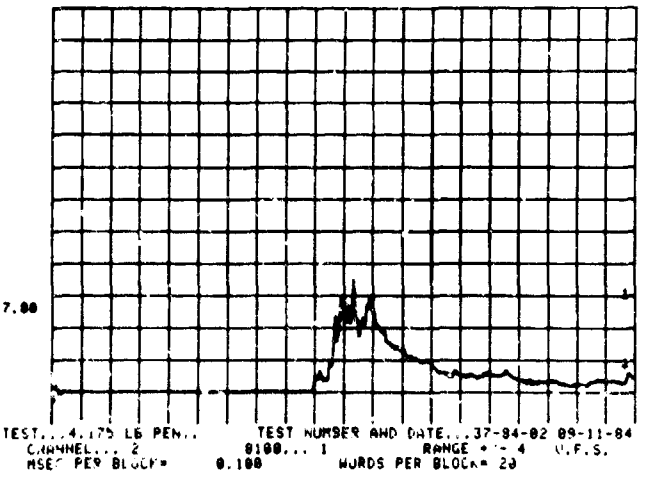

Figure 11

TESTS OF SHEAR FRACTURE AND STRAIN-SOFTENING IN CONCRETE

Zdeněk P. Bažant
and
Phillip A. Pfeiffer

Center for Concrete and Geomaterials
Northwestern University, Evanston, Illinois 60201

ABSTRACT

The paper reports fracture tests of double notched beam specimens of concrete and mortar loaded in shear. It is demonstrated that shear fracture propagation exists provided that there exists a concentrated shear zone. The results tend to confirm the maximum energy release rate criterion for fracture propagation. Tests of geometrically similar specimens yield maximum loads that agree with the recently established size effect law for blunt fracture, previously verified for Mode I. Preliminary results also indicate agreement with finite element analysis based on the strain-softening crack band model, in which the same material properties are assumed for fractures in Mode I and Mode II. The results are of particular interest for the failure of concrete structures subjected to blast loadings.

INTRODUCTION

Cracks in concrete or mortar have been generally assumed to propagate in the direction normal to the maximum principal stress, which represents the cleavage (or opening) fracture mode, designated as Mode I. This type of cracking has been verified even for the failure of many structures loaded in shear, e.g., the diagonal shear failure of beams, the punching shear failure of slabs, the torsional failure of beams, the shear failure of panels, etc. Ingraffea [1] showed recently that in a shear-loaded beam with a starter notch normal to the beam axis the crack does not propagate in this direction but roughly in the direction normal to the maximum principal stress. Thus, many investigators have thought that shear fracture does not exist, and even the claim that "shear fracture is a sheer nonsense" has been heard in some recent lectures.

Shear fractures are nevertheless observed in practice. For example, reinforced concrete slabs loaded by an intense short-pulse blast often fail by shearing off at the support along a crack normal to the slab. Penetration of projectiles into concrete also apparently involves shear-produced cracks. On the modeling side, applications of the recently developed crack band model with strain-softening [13,16,17,10] have indicated that the crack band which models fracture can propagate, under certain conditions, in the shear mode (Mode II).

Therefore, a program to investigate the shear fracture of concrete has been undertaken at Northwestern University, and presentation of the first results is the purpose of this paper.

TEST SPECIMENS

The test specimens were beams of constant rectangular cross section and constant length-to-depth ratio 8:3 (see Fig. 1). To determine the size effect, a crucial aspect of fracture mechanics, geometrically similar specimens of various depths, d = 1.5, 3, 6, d 12 in. (Fig. 2), were tested. The specimens of all sizes were cast from the same batch of concrete or mortar, and their thicknesses b were the same; b = 1.5 in.

For comparison of specimens of different sizes, the choice of their thicknesses is a subtle question which has no clear-cut answer. The question arises with respect to the effect of the probable variation of fracture energy along the crack edge across the thickness. This variation is principally due to two effects: 1) The fact that the crack front in the interior of the specimen is essentially in plane strain, while near the surface it is essentially in plane stress, which causes for elastic behavior an additional stress singularity at the surface termination of the crack edge [2]; and 2) The fact that nonplanar deformation at crack front near the surface may be caused by failures along planes nonorthogonal to the specimen sides, similarly to the shear-lip phenomenon in plastic fracture of metals [3,4,5]. The former effect would prevail for structures very large compared to the aggregate size, which would basically follow linear fracture mechanics. The latter effect seems to be more important for structures of normal sizes because the size of the fracture process zone affected by the surface would be proportional to the aggregate size and independent of the specimen size. Therefore, the latter effect was deemed to be more important, and this was the reason for choosing the same thickness for specimens of all sizes, ensuring the same thickness-to-aggregate size ratio.

A pair of symmetric notches, of depth d/6 and thickness 2.5 mm (same thickness for all specimen sizes) was cut with a diamond saw into the hardened specimens. (Compared to the specimen with a one-sided notch used before, the symmetrically notched specimen, in which two cracks propagate simultaneously, is simpler to analyze.) The specimens were cast with the side of depth d in a vertical posi-

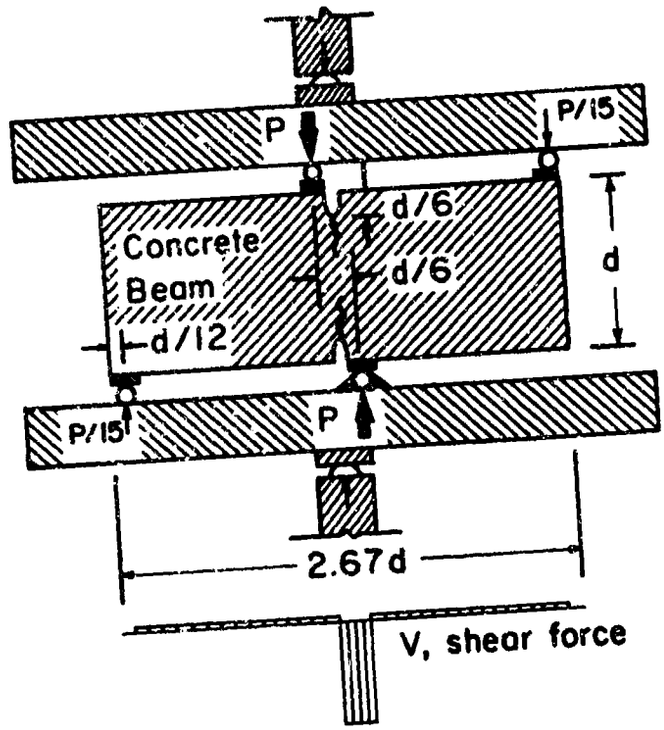

Fig. 1 - Mode II Fracture Specimen and Loading Apparatus.

Fig. 2 - Specimens of Four Different Sizes, after Mode II Fracture

Fig. 3 - MTS Testing Machine with Specimen (after Test).

tion, using a concrete mix with water-cement ratio 0.6 and cement-sand-gravel ratio of 1:2:2 (all by weight). The maximum gravel size was d_a = 0.5 in., and the maximum sand grain size was 0.19 in. Mineralogically, the aggregate consisted of crushed limestone and siliceous river sand. The aggregate and sand were air-dried prior to mixing. Portland cement C150, ASTM Type I, with no admixtures, was used.

To illustrate the effect of aggregate size, a second series of specimens was made of mortar, with water-cement ratio of 0.5 and cement-sand ratio of 1:2. The same sand as for the concrete specimens was used, the gravel being omitted. Thus, the maximum aggregate size for the mortar specimens was d_a = 0.19 in. The water-cement ratio differed from that for concrete specimens in order to achieve approximately the same workability.

Companion cylinders 3 in. in diameter and 6 in. in length were cast from each batch of concrete or mortar to determine the compression strength. After standard 28-day moist curing, the compression strength was f'_c = 5500 psi with standard deviation S.D. = 125 psi for the concrete specimens, and 7100 psi with S.D. = 107 psi for the mortar specimens (each value determined from 3 cylinders).

The specimens were removed from the plywood forms after 1 day and were subsequently cured until the moment of the test, for 28 days, in a moist room of 95% relative humidity and 78F temperature. Three identical specimens were tested for each type of test.

The tests were carried out in a 10-ton servo-controlled closed-loop MTS testing machine (Fig. 3). The laboratory environment had relative humidity about 65% and temperature about 78F, and the specimens were exposed to this environment approximately 3 hours before the start of the test.

The shear loading was produced by a system of steel beams shown in Fig. 1, which applied concentrated vertical loads onto the specimen. Three of the loads were applied through rollers, and one through a hinge, which produced a statically determinate support arrangement. The steel surfaces were carefully machined so as to minimize the friction on the rollers.

The distribution of shear force V in the vertical cross sections, produced by this load arrangement, is shown in Fig. 1. Note that the loads were applied relatively close to the notches, so as to produce a narrow region of a high shear force. However, the loads could not be too close to the notch, or else the concrete under the support would shear off locally before the overall shear fracture could be produced. To prevent this from happening, the load-distributing steel plate under the roller could not be too small, and after some experimentation a suitable size of the support plate was determined. For the four specimen sizes, the support plates under the rollers and the hinge had the widths of 0.25, 0.5, 1 and 2 inches. The distance of the loads from the notch axis was always kept as d/12. The thickness of all loading plates was 0.25 in.

The specimens were tested at constant displacement rate of the machine. For each specimen size the displacement rate was selected so as to achieve the maximum load in about 5 min. (±30 sec.).

TEST RESULTS

The measured values of the maximum load measured are given in Table 1 for all specimens of all sizes, along with the mean values.

Table 1. - Measured Maximum Loads

Type of Test	Depth d (in.)	Maximum Load P, (lb.)			Mean $\bar{P}$
		1	2	3	
Mode II Concrete	1.5	1380	1465	1475	1440
	3.0	2792	2816	3012	2873
	6.0	5300	5580	5590	5490
	12.0	9910	9990	10100	10000
Mode II Mortar	1.5	1700	1735	1755	1730
	3.0	3200	3300	3350	3283
	6.0	5280	5400	5500	5410
	12.0	9200	9700	10000	9633
Mode I Concrete	1.5	405	408	417	410
	3.0	676	705	710	697
	6.0	984	1034	1090	1036
	12.0	1715	1716	1750	1727
Mode I Mortar	1.5	456	508	543	502
	3.0	702	751	776	743
	6.0	999	1053	1098	1050
	12.0	1461	1559	1565	1528

The cracks propagate as shown in Fig. 1. This proves that shear fracture exists, i.e., the crack can propagate in Mode II. Microscopically, of course, the shear fracture is likely to form as a zone of tensile microcracks with a predominantly 45°-inclination which only later connect by shearing; but the fact is that in the macroscopic sense the observed fractures must be described as Mode II.

As already mentioned, the presently observed crack direction contrasts with that observed by Ingraffea [1] in his test sketched in Fig. 4a. This test differed by its wider separation of the loading points. Therefore, the present type of test was also made with a wider separation of the loading points. In that case the cracks propagated from the notch tip basically in the direction normal to the maximum principal stress, same as observed by Ingraffea; see Fig. 4b. In both the present type of test (Fig. 1) and the tests with the wide shear zone (Fig. 4a,b) the stress fields near the fracture front are similar. So the crack somehow senses the stress field remote from the cracks, and responds to it. Consequently, the stress field near the fracture front, as well as the strain and strain energy density fields near the fracture front, does not govern the direction of fracture propagation. What is then the governing law?

The answer is that a Mode I crack propagating sideway from the notch tip would, for the present type of test with a narrow shear force zone, quickly run into a low stress zone of the material, and would, therefore, release little energy. On the other hand, a vertically running crack (Mode II) continues to remain in the highly stressed zone of

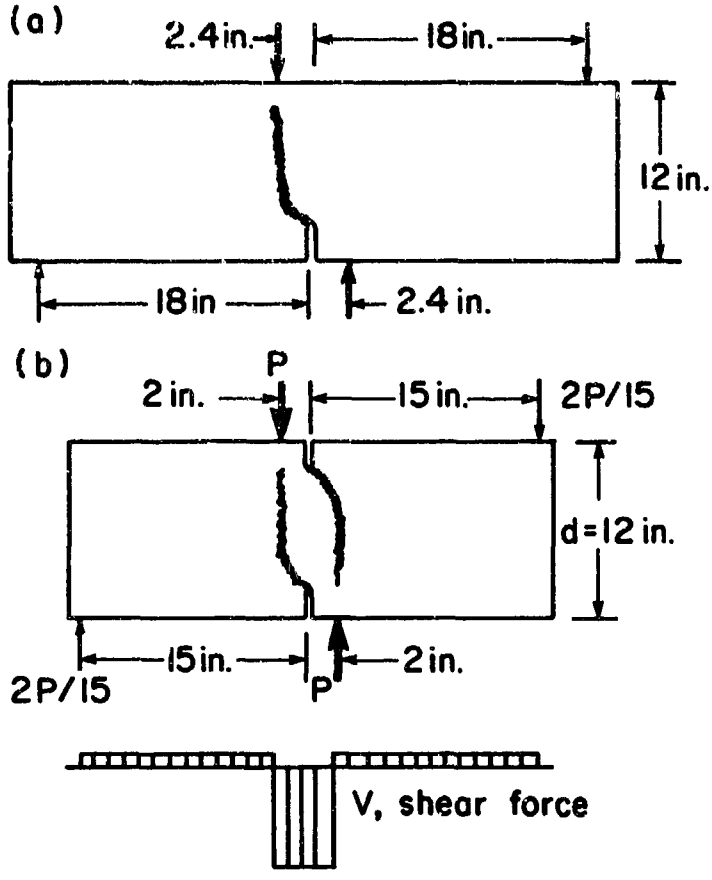

Fig. 4 - Crack Paths Obtained when Shear Zone is not Concentrated.

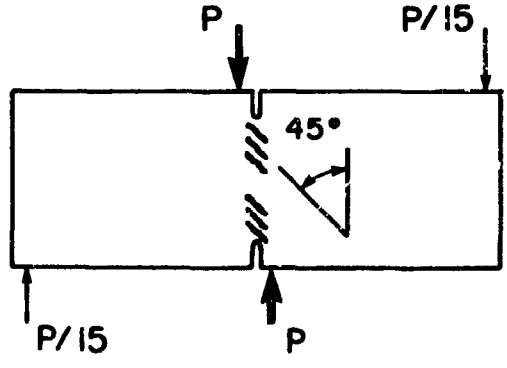

Fig. 5 - Mode II Fracture Arising from a Band of Mode I Microcracks.

the material, and can, therefore, cause a large release of strain energy. This appears to confirm that the fracture propagation direction is governed by the criterion of the maximum energy release rate. This criterion has been known in theoretical fracture mechanics and is in fact a direct consequence of the basic laws of thermodynamics.

The conclusion that the criterion of maximum energy release rate should govern the direction of crack propagation is confirmed by the finite element studies reported by Pfeiffer et al. [6-9]. In these studies, the crack band model was used, and among all finite elements adjacent to the crack band front the crack band was advanced into that element for which the energy release from the finite element system was maximum. These finite element simulations indicated the crack band to propagate sideway when the shear force zone was wide (Fig. 4b), and vertically when the shear force zone was narrow (Fig. 1), which is in agreement with the observed directions of crack propagation.

SIZE EFFECT AND FRACTURE ENERGY

The structural size effect, a salient aspect of fracture mechanics, is observed when geometrically similar structures of different characteristic dimensions d are compared. It can be described in terms of the nominal stress at failure, defined as $\sigma_N = P/bd$ where P = load at failure (maximum load) and b = structure thickness. While according to the strength or yield criteria used in plastic limit design or elastic allowable stress design, σ_N is independent of structure size d, in fracture mechanics σ_N decreases as the structure size increases. This is because fracture mechanics is based on energy criteria for failure.

Introducing an approximate but apparently quite reasonable hypothesis that the energy release caused by fracture is a function of both the fracture length and the area traversed by the fracture process zone, Bažant showed [10,11] by dimensional analysis and similitude arguments that, for geometrically similar structures of specimens,

$$\sigma_N = Bf_t'\left(1 + \frac{d}{\gamma_0 d_a}\right)^{-\frac{1}{2}} \qquad (1)$$

in which f_t' is the direct tensile strength of concrete, d_a is the maximum aggregate size, and d, γ_0 are empirical parameters characterizing the shape of the structure or specimen. According to this size effect law, the plot of log σ_N vs. log (d/d_a) represents a gradual transition from the strength criterion (i.e., σ_N proportional to strength f_t') to the failure criterion of the classical, linear elastic fracture mechanics (i.e., σ_N proportional to $d^{-\frac{1}{2}}$). This size effect law is verified, within the limits of inevitable statistical scatter, by all available Mode I fracture tests of concrete and mortar. Moreover, this size effect law has also been shown applicable to the diagonal shear failure of longitudinally reinforced beams without stirrups [12], and is probably applicable to all the so-called brittle failures of reinforced concrete structures. Does the size effect law also apply to shear fracture?

The measured maximum load values show that it does. They are plotted in Fig. 6 as the data points, while the size effect law is plotted as the smooth curve, and a good agreement is apparent. Parameters B and γ_0 of the size effect law can be most easily obtained by the linear regression plot in Fig. 6 because Eq. 1 can be rearranged as $Y = AX + C$ where $X = d/d_a$, $Y = (f_t'/\sigma_N)^2$, $C = 1/B^2$, $A = 1/(\gamma_0 B^2)$. This means that $B = 1/\sqrt{C}$, $\gamma_0 = 1/(AB^2)$ where A represents the slope of the straight regression line in Fig. 6 and C represents its intercept with axis Y.

An advantage of the regression plot is that it also yields statistics of the errors, i.e., of the deviations of the measured data points from the size effect law. As is clear from Fig. 6, these deviations are random rather than systematic, and their coefficient of variation is found to be $\omega_{Y|X} = 0.0911$, which is quite acceptable for a heterogeneous material with statistical properties such as concrete. This value is calculated as $\omega_{Y|X} = \{[\Sigma(Y - Y_{test})^2]/(N-2)\}^{\frac{1}{2}}/\bar{Y}$, which is an unbiased estimate; $Y - Y_{test}$ are the deviations of data points, N is the number of all data points, and $\bar{Y} = (\Sigma Y)/N$ = mean of all measured Y. When the statistics is based on the mean P for each specimen size, then $\omega_{Y|X} = 0.0668$.

To calibrate the size effect law once its validity is already accepted requires specimens whose sizes differ at least as 1:3. However, to verify the validity of the size effect law one needs a much broader range of sizes, at least 1:10. This necessitates inclusion of very large specimens in the test program. The smallest specimen is chosen as small as possible for the given size of aggregate. This is the reason for choosing the depth of the smallest specimen to be only $3d_a$. The largest practicable specimen for the available testing machine was then of depth d = 12 in. $(d/d_a = 24)$. For concrete, however, this size is not large enough to verify the size effect law (Eq. 1), since the last data points for concrete in Fig. 6 lie too far from the limiting inclined straight line of slope - 1/2 corresponding to linear elastic fracture mechanics. This was the main reason for adding a second series of mortar specimens, which makes it possible to extend substantially the range of relative sizes d/d_a without having to test still much larger specimens. Even though some additional error is no doubt introduced due to the differences between mortar and concrete other than those due to aggregate size d_a, the measured maximum loads for concrete and mortar, when put together, appear to follow quite well the size effect law (Eq. 1), and thus to verify its validity.

Note also that according to Fig. 6 linear fracture mechanics would govern the behavior of specimens with $d/d_a = 200$ or larger. This implies for concrete the beam depth of over 100 in., and for mortar over 40 in.

Another advantage of the size effect law is that it allows the simplest way to determine the fracture energy G_f. As recently shown [14],

$$G_f = \frac{g(\alpha_0)}{A\,E_c}\,(f_t')^2 d_a \qquad (2)$$

in which A = slope of the size effect regression

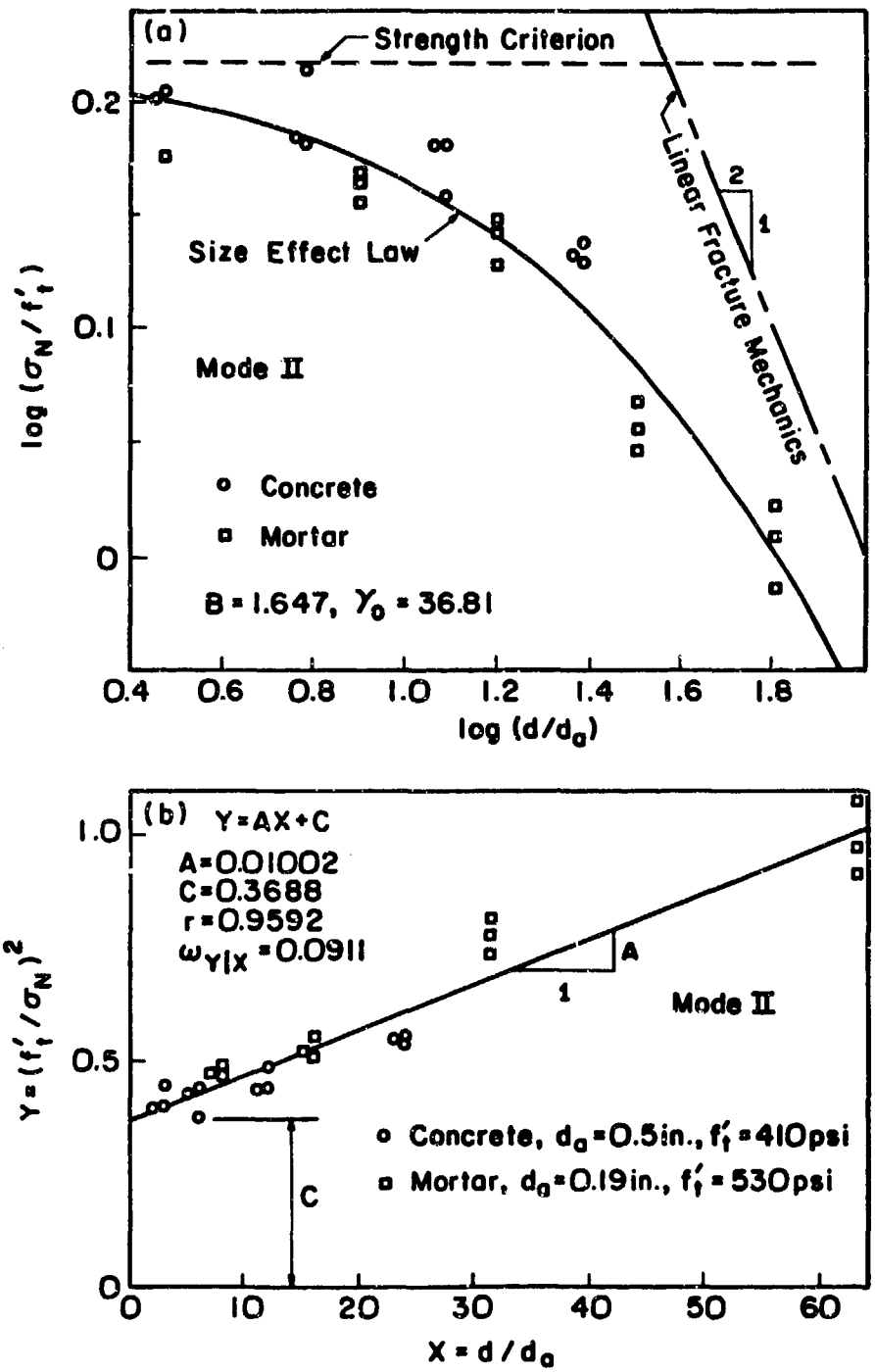

Fig. 6 - Test Results of Mode II (shear) Fracture Tests and their Regression.

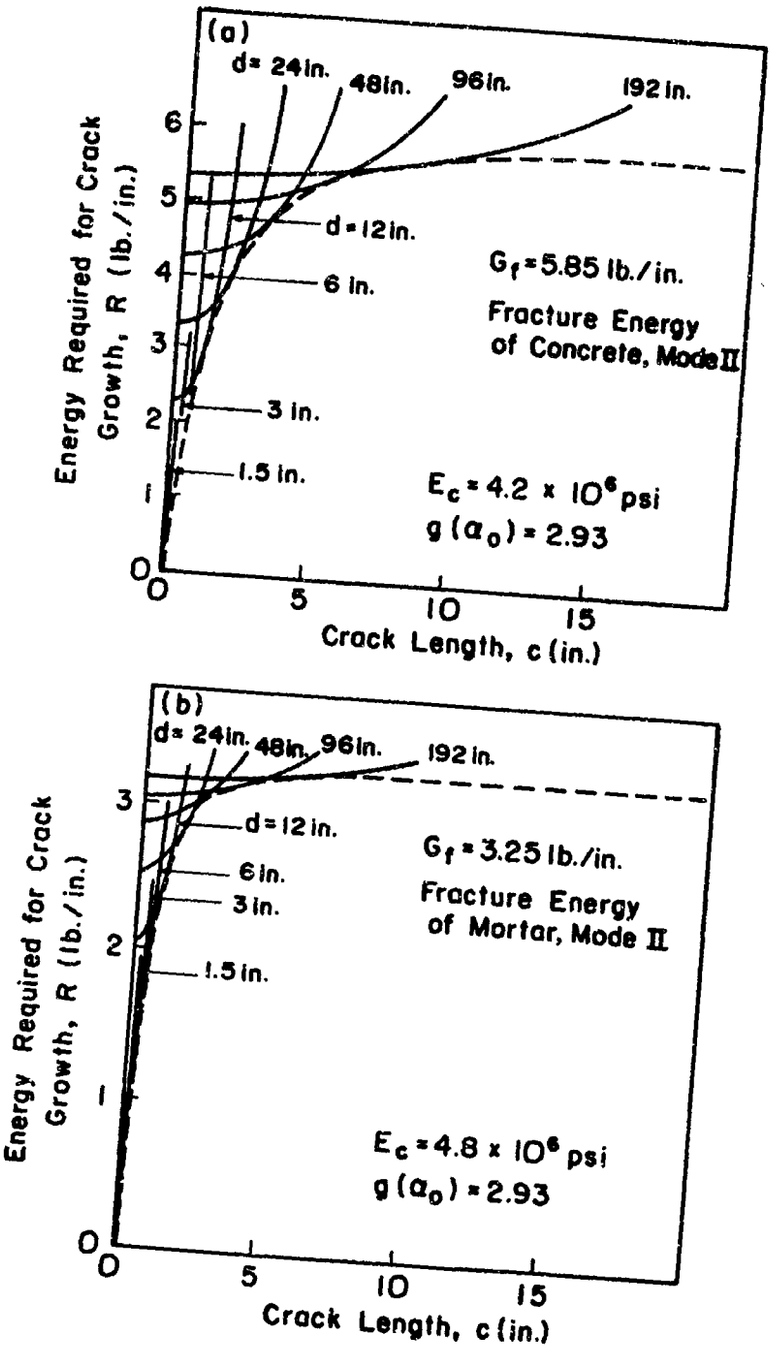

Fig. 7 - R-Curves Derived from Mode II Fracture Test Results

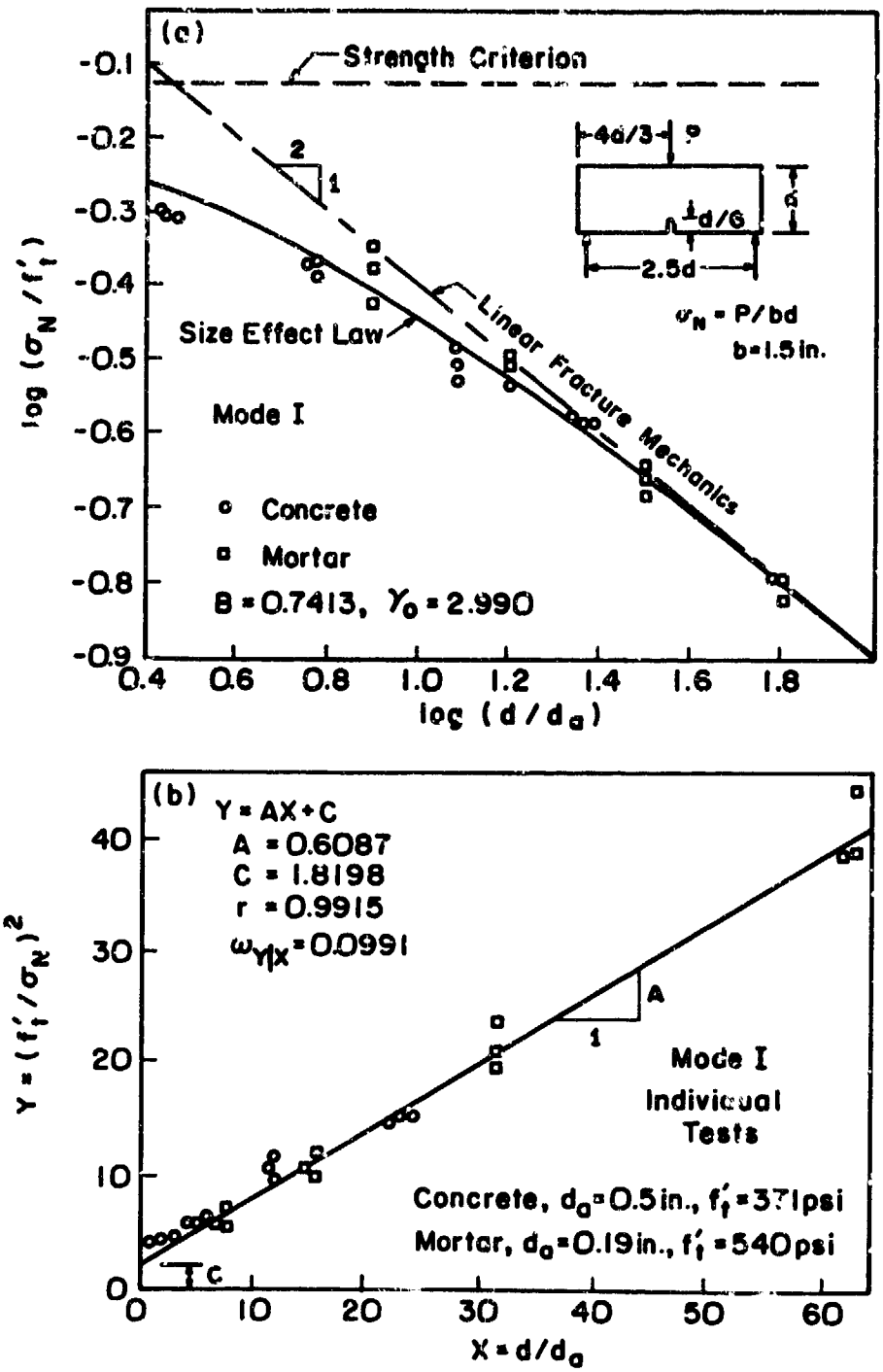

Fig. 8 - Test Results of Mode I Fracture Tests and Their Regression.

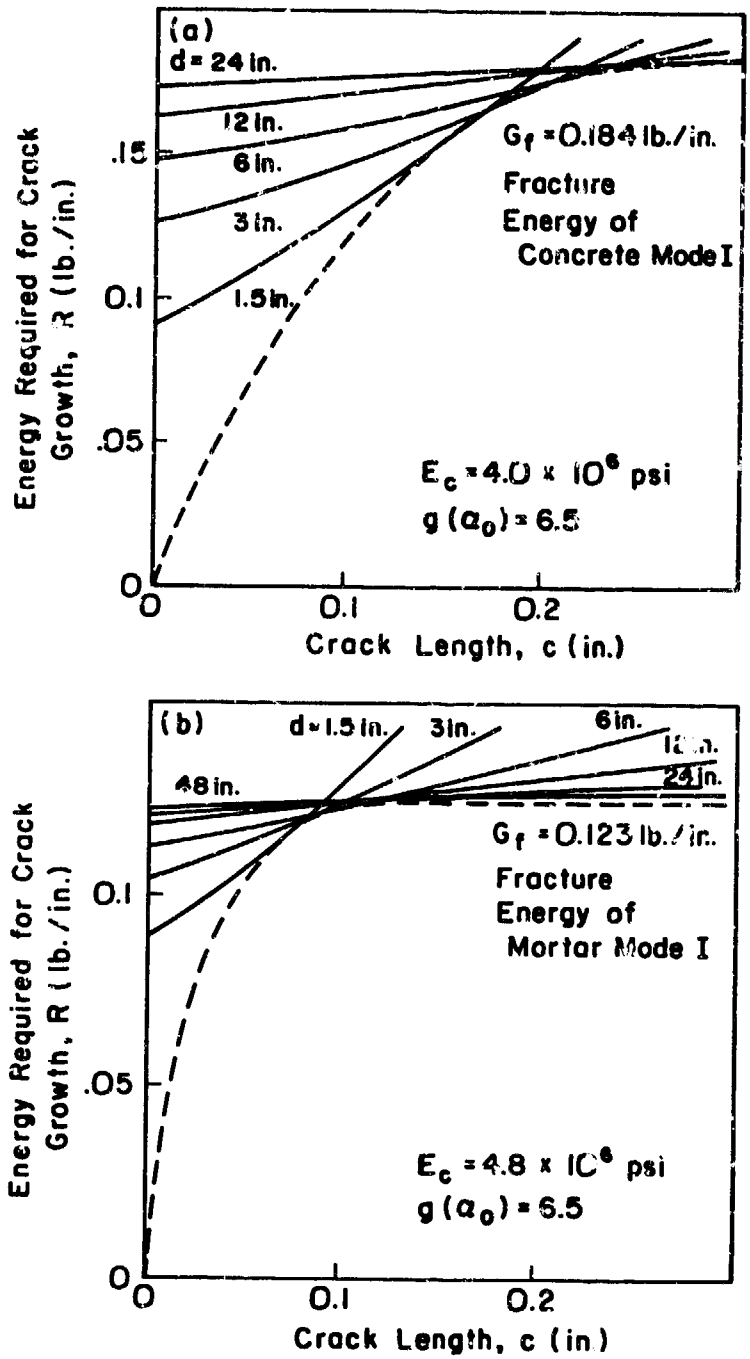

Fig. 9 - R-Curves Derived from Mode I Fracture Test Results.

line (Fig. 7b in the present case), E_c = elastic Young's modulus, and $g(\alpha_0) = G(\alpha_0)E_c b^2 d/P^2$; $G(\alpha)$ represents the linearly elastic energy release rate as a function of $\alpha = a/d$ where $a = a_0 + c$, a_0 = length of the notch and c = length of the crack from the notch tip, $G(\alpha_0)$ is the value of G evaluated for $a = a_0$, and $g(\alpha_0)$ with $\alpha_0 = a_0/d$ is the nondimensional energy release rate. The values of $G(\alpha_0)$ or $g(\alpha_0)$ can be found in handbooks [15] or textbooks [3,4,5] for many typical specimen geometries, however, not for the present specimen. Therefore, the value of $g(\alpha_0)$ was obtained by linear elastic finite element analysis; $g(\alpha_0) = 2.93$.

Note that f_t' and d_a are used in Eq. 2 because the regression plot in Figs. 6 and 7 is in nondimensional variables in order to allow comparing mortar and concrete. Alternately, the regression could be done in the plot of σ_N^{-2} versus d, and then $f_t'^2$ and d_a do not appear in Eq. 2. Therefore, the precise values of f_t' (and d_a) are immaterial for the value of G_f calculated in Eq. 2.

Application of Eq. 2 to the present data yields the following values for Mode II fracture energy $G_f = G_f^{II}$;

$$G_f^{II} = 5.85 \text{ lb./in. (1020 N/m) for concrete} \qquad (3)$$
$$G_f^{II} = 3.25 \text{ lb./in. (569 N/m) for mortar.}$$

From preliminary results of the companion Mode I test series for the same type of concrete and mortar, application of Eq. 2 (for the three-point bent specimen geometry) yields approximately the value $G_f^I = 0.184$ lb./in. (32.2 N/m) for concrete and $G_f^I = 0.123$ lb./in. (21.5 N/m) for mortar. The linear regression plot and size effect are plotted in Fig. 8 for individual maximum load values. The load values for Mode I fracture tests are given in Table 1.

It is striking how much larger the fracture energy is for Mode II as compared to Mode I. The ratio appears to be about 32 for concrete and 26 for mortar. This huge difference seems, however, explicable in terms of the crack band finite element model [16] which was shown to also describe correctly the crack shear resistance [17].

The results of tests and of preliminary finite element calculations compare as follows:

$$\text{Tests:} \quad G_f^I = 0.184 \text{ lb./in.}, \; G_f^{II} = 5.85 \text{ lb./in.} \qquad (4)$$
$$\text{Finite Elements:} \quad G_f^I = 0.236 \text{ lb./in.}, \; G_f^{II} = 5.02 \text{ lb./in.}$$

It must be emphasized that the same material properties, defined by the same tensile strain-softening diagram [16], were used both for Mode I and Mode II finite element simulations.

In Mode I fracture, the fracture energy is in the crack band model represented by the area under the tensile strain-softening diagram, multiplied by the width of the fracture process zone. In Mode II (shear) fracture, tensile cracking is not all that is needed for failure. The cracks produced by shear are inclined about 45°, and there remains a connection across the fracture after these cracks form, consisting of inclined struts between the cracks spanning across the fracture (Fig. 6).

The full shearing of the material also requires that these struts be broken by compression crushing (which would most likely consist in compression-shear failure of these struts). Therefore, the fracture energy for shear also includes the area under the compression stress-strain diagram for these inclined struts, including the strain-softening portion of this diagram, multiplied by the width of the fracture process zone. Now, the area under the complete compression stress-strain diagram is many times larger than the area under the complete tensile stress-strain diagram. Thus, it is not surprising that the G_f-values in Eq. 3 are far larger than those for Mode I fracture. It must be kept in mind, however, that these values of G_f^{II} include the energy to break the shear resistance due to aggregate interlock (crack surface roughness).

The size effect law also makes it possible to easily determine the R-curve, i.e., the plot of the energy required for crack growth as a function of the crack length, c (measured from the notch tip). As shown in Refs. 14 and 19, the R-curve represents the envelope of the fracture equilibrium curves of geometrically similar specimens of all sizes; see Figs. 7, 8 and 9, in which the convex curve for each specimen depth d can be plotted from the maximum load value, P [14,19]. It is essential to use for this purpose the maximum load values smoothed by the size effect law. If the use of unsmoothed, scattered data (as measured) is attempted, then the fracture equilibrium curves do not yield any envelope [14,19]. As already remarked, the limiting asymptotic value of the envelope, i.e., of the R-curve, is the fracture energy obtained from Eq. 2. Fig. 7 shows the R-curve for shear fracture obtained after smoothing with the regression line in Fig. 6. (Fig. 9 shows the R-curve for Mode I fracture from regression line in Fig. 9.) Availability of the R-curve makes it possible to approximately calculate failure loads of structures with an equivalent analysis based on linear elastic fracture mechanics, even though the fracture law is evidently highly nonlinear.

A more detailed study of the finite element modeling of shear fracture with the crack band model is planned for subsequent work. While the crack band model and the finite element models based on a stress-displacement relation for a line crack (Hillerborg's model, Refs. 18 and 19) are essentially equivalent for Mode I fracture tests of concrete and can represent them equally well, there appears to be a significant difference for shear fracture tests. It seems that both Mode I and Mode II fracture tests can be described with one and the same crack band model. This is not true for the model based on the stress-displacement relation, for which some additional rules apparently need to be added to make it work also for shear fracture and, in particular, to represent the contribution of surface roughness (aggregate interlock) to the shear fracture energy.

CONCLUSIONS

1. Shear fracture (i.e., Mode II fracture) of concrete exists.
2. The direction normal to the maximum principal stress cannot be considered in general as a

criterion of crack propagation direction in concrete. Rather, fracture seems to propagate in the direction for which the energy release rate from the fracture is maximized.

3. Like mode I fracture, the shear (Mode II) fracture follows the size effect law of blunt fracture [11]. This implies that a large fracture process zone must exist at the fracture front, and that nonlinear fracture mechanics should be used, except for extremely large structures.

4. The maximum aggregate size d_a appears acceptable as a characteristic length for the size effect law. This further implies that the size of the fracture process zone at maximum load is approximately a certain fixed multiple of the maximum aggregate size.

5. The shear (Mode II) fracture energy appears to be about 32-times larger than the cleavage (Mode I) fracture energy. This large difference may probably be explained by the fact that shear fracture energy includes not only the energy to create inclined tensile microcracks in the fracture process zone, but also the energy required to break the shear resistance due to interlock of aggregate and other asperities on rough crack surfaces behind the crack front.

6. The R-curve describing the shear fracture energy required for crack growth as a function of the crack extension from the notch, may be obtained from the size effect law. It results as the envelope of the fracture equilibrium curves for geometrically similar specimens of various sizes.

ACKNOWLEDGMENT

Partial financial support under U.S. Air Force Office of Scientific Research Grant No. 83-0009 to Northwestern University, monitored by L. Hokanson, is gratefully acknowledged.

REFERENCES

1. Arrea, M., and Ingraffea, A. R., "Mixed-mode Crack Propagation in Mortar and Concrete," Dept. of Structural Engineering, Cornell University, Report No. 81-13, 1982.

2. Bažant, Z. P., and Estenssoro, L. F., "Surface Singularity and Crack Propagation," *Int. J. of Solids and Structures, 15*, 1979, pp. 405-426, Addendum, *16*, pp. 479-481, Errata, *19*, p. 661.

3. Broek, D., *Elementary Engineering Fracture Mechanics*, Sijthoff and Noordnoff, Alphen aan den Rijh, Netherlands, 1978.

4. Knott, J. F., *Fundamentals of Fracture Mechanics*, Butterworths, London, England, 1973.

5. Rolfe, S. T., and Barsom, J. M., *Fracture and Fatigue Control in Structures*, Prentice-Hall, Englewood Cliffs, N.J., 1977.

6. Pfeiffer, P. A., "Blunt Crack Band Propagation in Finite Element Analysis for Concrete Structures," Argonne National Laboratory, RAS 83-10, March 1983.

7. Pfeiffer, P. A., Marchertas, A. H., and Bažant, Z. P., "Blunt Crack Band Propagation in Finite Element Analysis for Concrete Structures," *Transactions of 7th International Conference on Structural Mechanics in Reactor Technology*, Paper H5/2, North-Holland, Amsterdam, 1983, pp. 227-234.

8. Pan, Y. C., Marchertas, A. H., and Kennedy, J. M., "Finite Element of Blunt Crack Propagation, A Modified J-integral Approach," *Transactions of 7th International Conference on Structural Mechanics in Reactor Technology*, Paper H5/3, North-Holland, Amsterdam, 1983, pp. 235-292.

9. Pan, Y. C. Marchertas, A. H., Pfeiffer, P. A., and Kennedy, J. M., "Concrete Cracking Simulations for Nuclear Applications," *Theoretical and Applied Fracture Mechanics, 2*, No. 1, 1984, pp. 27-38.

10. Bažant, Z. P., "Fracture in Concrete and Reinforced Concrete," Preprints, IUTAM Prager Symposium on *Mechanics of Geomaterials: Rocks, Concretes, Soils*, ed. by Z. P. Bažant, Northwestern University, Sept. 1983, pp. 281-316.

11. Bažant, Z. P., "Size Effect in Blunt Fracture: Concrete, Rock, Metals," *Journal of Engineering Mechanics, ASCE, 110*, No. 4, 1984, pp. 518-535.

12. Bažant, Z. P., and Kim, J. K., "Size Effect in Shear Failure of Longitudinally Reinforced Beams," *Journal of the American Concrete Institute, 81*, No. 5, Sept.-Oct. 1984, pp. 456-468.

13. Bazant, Z. P., "Crack Band Model for Fracture of Geomaterials," Proc. 4th Intern. Conf. on Numer. Methods in Geomechanics," ed. by Z. Eisenstein, held in Edmonton, Alberta, 1982, Vol. 3, pp. 1137-1152.

14. Bažant, Z. P., Kim, J. K., and Pfeiffer, P., "Determination of Nonlinear Fracture Parameters from Size Effect Tests," NATO Advanced Research Workshop on *Application of Fracture Mechanics to Cementitious Composites*, ed. by S. P. Shah, Northwestern University, Sept. 4-7, 1984, pp. 143-169.

15. Tada, H., Paris, P. C., and Irwin, G. R., *The Stress Analysis of Cracks Handbook*, Del Research Corp., Hellertown, Pa., 1973.

16. Bažant, Z. P., and Oh, B. H., "Crack Band Theory for Fracture of Concrete," *Materials and Structures* (RILEM, Paris), *16*, 1983, pp. 155-177.

17. Bažant, Z. P., and Gambarova, P. G., "Crack Shear in Concrete: Crack Band Microplane Model," *Journal of Structural Engineering, ASCE, 110*, No. ST9, Sept. 1984, pp. 2015-2035.

18. Hillerborg, A., Modéer, M., and Petersson, P. E., "Analysis of Crack Formation and Crack Growth in Concrete by Means of Fracture Mechanics and Finite Elements," *Cement and Concrete Research, 6*, 1976, pp. 773-782.

19. Petersson, P. E., "Crack Growth and Development of Fracture Zones in Plain Concrete and Similar Materials," thesis presented to the Lund Institute of Technology, at Lund, Sweden, in 1981, in partial fulfillment of the requirements for the degree of Doctor of Philosophy.

A NONLINEAR THEORY FOR REINFORCED CONCRETE

G. A. Hegemier* and H. Murakami*

S-CUBED, A Division of Maxwell Laboratories, Inc.
San Diego, California

ABSTRACT

A nonlinear model for reinforced concrete is discussed. The theoretical framework is nonphenomenological in the sense that the global equations are synthesized from the properties of the constituents and constituent interfaces, and the component geometry. The model is cast in the form of a binary mixture which resembles the overlay of two continua: steel and concrete. Validation studies reveal good agreement between simulations and experimental data for both monotonic and hysteretic deformation histories.

INTRODUCTION

The nonlinear response of reinforced concrete is dominated by complex interactions between the steel and concrete. Such interactions have a major effect on structural characteristics such as stiffness, strength, damping, and ductility. Consequently, it is necessary that a model of reinforced concrete reflect these phenomena. Further, in an effort to minimize the number and type of tests necessary to define model parameters, it is desirable that the model be nonphenomenological, i.e., that the global properties of reinforced concrete be synthesized from the properties of the steel and concrete, the steel-concrete interface physics, and the steel geometry.

In this paper a candidate model is discussed that satisfies the foregoing requirements. The theoretical formulation is validated, in part, by detailed comparisons between numerical simulations and experimental data. These validations concern two primary steel-concrete interaction mechanisms: (1) The steel-concrete bond problem and (2) the steel-concrete dowel problem. Problem (1) plays a dominant role in the bending and the nonlinear stretching of reinforced concrete beams, plates, and shells. Problem (2) plays a major role in the transverse shear deformation of reinforced concrete beams, and the transverse and in-plane shear deformation of reinforced concrete plates and shells.

THEORETICAL

A large class of theoretical modeling problems concerning the constitutive description of reinforced concrete fall into the general category of "homogenization". The term, as used here, implies construction of the macro-constitutive relations via micromechanical considerations together with appropriate smoothing or averaging operations. The final result may, on the macroscale, be an "equivalent" single-phase, multi-phase, or non-local continuum.

As use of the prefixes "micro" and "macro" above imply, homogenization typically enters the picture when one wishes to determine the response of a continuum for which two widely differing length scales can be identified. The large scale, or macroscale, is determined by the specimen geometry and/or the loading condition; the small scale, or microscale, is determined by material heterogeneity. In the case of reinforced concrete, the typical steel spacing constitutes the appropriate microscale.

The homongenization problem is parameterized by the small ratio of the two length scales, ε. The fundamental problem is to determine the "proper" macroscopic response equation as $\varepsilon \to 0$. Once obtained, it is natural to introduce asymptotic (small ε) notions into the analysis to determine a physically meaningful sequence of equations ordered in powers of ε. The higher order equations are intended to provide additional simulation capability on the macroscale.

Using homogenization concepts, a nonlinear model of reinforced concrete with a "dense" unidirectional steel layout has been constructed. Typical such meshes are depicted in Figure 1. The construction technique was based upon the use of multivariable asymptotic expansions, a variational principle and certain smoothing operations. The resulting model has been cast in the form of a binary mixture which resembles an overlay of two continua: steel and concrete; these continua interact via body forces which are functionals of the relative

*Consultant, also Professor of Applied Mechanics, University of California, San Diego.

global displacements of the continua. A complete mathematical description of the model and the construction procedure can be found in Reference [1]. For brevity, remarks in this paper are focused primarily upon comparisons between theoretical simulations and experimental data in our effort to demonstrate the simulation capability of the model.

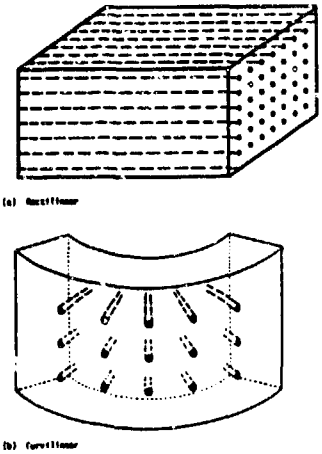

Figure 1. Unidirectional dense steel arrays.

STEEL-CONCRETE BOND PROBLEM

The steel-concrete bond problem concerns the manner in which normal forces are transferred across cracks in reinforced concrete, and the stiffness degradation that occurs due to progressive cracking. The phenomena considered include bond slip and degradation, concrete cracking, and yielding of the rebar. In the literature, problems of this type fall into the category of "tension stiffening".

Consider the problem of predicting the global response of a unidirectionally reinforced concrete specimen where a state of global uniaxial stress is applied in the steel direction, Figure 2. For small deformations, the theory developed in Reference [1] which is valid for multiaxial stress states and large deformations, reduces to the elementary relations:

$$N_{11,1}^{(1p)} + P_1 = 0 \quad , \quad N_{11,1}^{(2p)} - P_1 = 0 \quad , \qquad (1)$$

$$\dot{N}_{11}^{(\alpha p)} = n^{(\alpha)}\dot{N}_{11}^{(\alpha)} = n^{(\alpha)}E_{ep}^{(\alpha)}\dot{U}_{1,1} \quad , \qquad (2)$$

$$\dot{P}_1 = K_{ep}(\dot{U}_1^{(1)} - \dot{U}_1^{(2)}) = K_{ep}[\dot{U}_1] \quad . \qquad (3)$$

In the above, $\alpha = 1, 2$ refer to steel, concrete, respectively; $U_1^{(\alpha)}$, $N_{11}^{(\alpha)}$ denote axial displacement and axial stress (averages), respectively; $E_{ep}^{(\alpha)}$ and K_{ep} are tangent moduli; $n^{(\alpha)}$ denotes volume fraction of material α; and $(\,)_{,1} \equiv \partial(\,)/\partial x_1$, $\dot{(\,)} \equiv \partial(\,)/\partial t$ where t represents time.

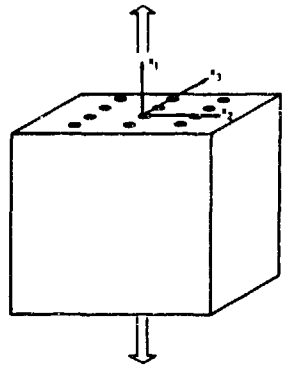

Figure 2. Global uniaxial loading.

Relation's (1) are the equilibrium equations for each material; the latter interact via the interaction body force P_1 which reflects interface shear transfer between the concrete and steel. Equation (3) shows that this interaction term depends upon the relative displacement history. Equations (2) represent the global constitutive relations for each material.

For the elastic response regime, the tangent moduli are determined, through a micromechanical analysis, to have the form:

$$E_{ep}^{(\alpha)} = (\lambda+2\mu)^{(\alpha)} - \lambda^{(\alpha)2}/(\lambda+\mu)^{(\alpha)} \equiv E^{(\alpha)} \quad , \qquad (4)$$

$$K_{ep}^{-1} = \frac{\ell^2}{8}\left(\frac{1}{\mu}\right)^{(1)} - \frac{[2+\mu^{(2)}+(2\ell n\, n^{(1)})/n^{(2)}]}{n^{(2)}\mu^{(2)}}\Bigg) \equiv K^{-1} \qquad (5)$$

where $\lambda^{(\alpha)}$, $\mu^{(\alpha)}$ denote Lamé constants of material α. Equation (5) implies that no slip occurs between steel and concrete.

When steel-concrete slip occurs, Equation (5) must be generalized. For monotonic global deformation, a simple elastic-perfectly plastic model is sufficient. For hysteretic deformation, detailed studies [2] of steel-concrete pull-out specimens have guided the construction of an elementary bond-slip model which is depicted in terms of the interaction term P_1 in Figure 3. For a wide range of concretes, the following selection of parameters is appropriate: $P_{cr} = 2\sqrt{n^{(1)}}(\sigma_{rx})_{cr}/\ell$, $-P_G = P_F = 0.8\,P_{cr}$, $P_{IJ} = 0.2\,P_{cr}$, $P_{DE} = -P_{GH} = 0.1\,P_{cr}$. The model shown in Figure 3 is easily placed in analytical incremental form. The description involves two parameters, K as defined by (5) and $(\sigma_{rx})_{cr}$ which represents a critical steel-concrete interface shear stress.

Global inelastic material behavior can, within the context of the problem under consideration, take place via cracking of the concrete or yielding of the rebar. Typical global tangent moduli for these phenomena are shown in Figure 4.

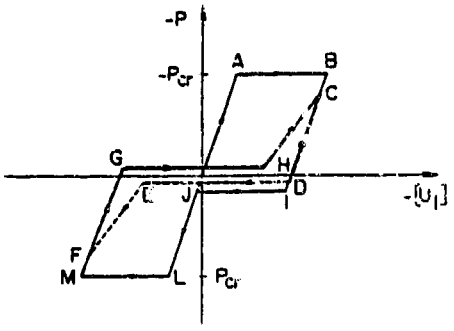

Figure 3. Bond-slip model.

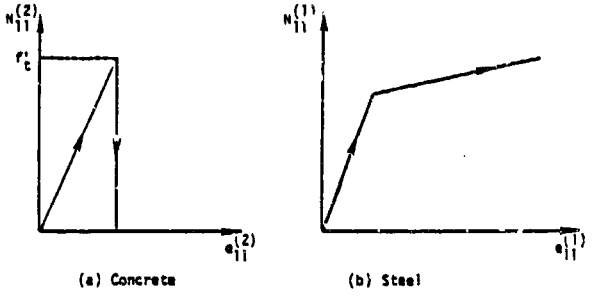

Figure 4. Behavior of constituents for monotonic extension example.

Consider now monotonic extension. For this case, an analytical solution of the foregoing model has been obtained [3]. with reference to Figure 5; the analysis reduces to the consideration of a typical "cell". Figure 5(a) is the starting condition; in Figure 5(b) the concrete has reached the tensile strength; the crack location is flaw-dominated and for convenience is placed at the specimen center; thereafter the theory predicts the appropriate crack location as deformation increases, Figures 5(b)-5(d). The mathematical boundary conditions and cracking sequence are shown in Figures 5(e)-5(h). Figure 6 shows the various response stages predicted theoretically; these consist of elastic response with no cracking, debonding, or slip (I), progressive cracking with debonding and slip (II), and slip only (III). Figure 7 shows a typical comparison between theory and experiment (scaled specimens, Somoyaji [4]). Agreement is observed to be good (stress drops were not clearly observed since the tests were conducted under load-control). The quantities $(e_e)_{cr}$, $(\sigma_e)_{cr}$, E_m in Figures 6 and 7 denote average strain, stress at first concrete cracking and mixture modulus; here $\sigma_e = n^{(1)}N_{11}^{(1)} + n^{(2)}N_{11}^{(2)}$ and $E_m = n^{(1)}E^{(1)} + n^{(2)}E^{(2)}$.

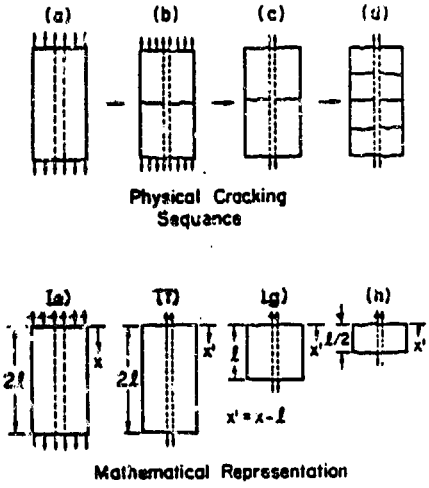

Figure 5. Cracking sequence assumed.

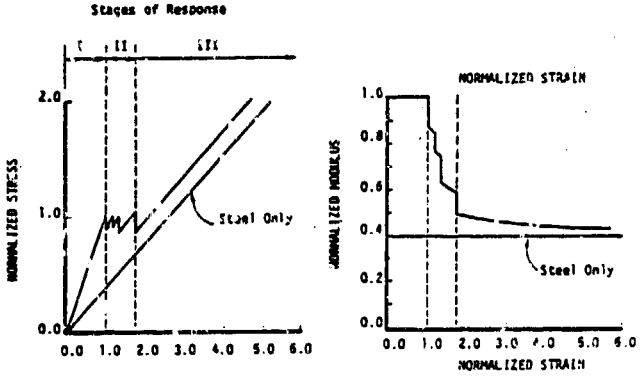

Figure 6. Stages of response predicted theoretically.

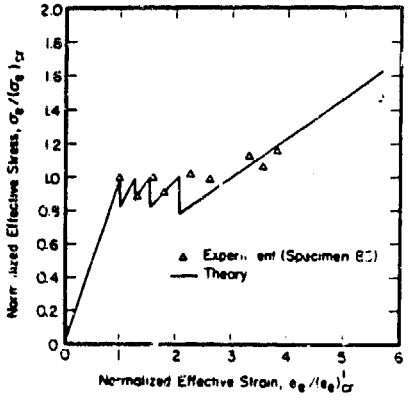

Figure 7. Comparison of test and simulation: tension specimen B3 from Somayaji [4].

A more critical test of the model concerns hysteretic deformation. A comparison of cyclic tension-compression test data by Hegemier, et al. [5] on full-scale reinforced concrete-type specimens and simulated test data is illustrated in Figure 8 for test panel No. 87. Shown here is the entire load-unload-reload history of the specimen as given by the experiment (Figure 8(a)) and as given by the simulation (Figure 8(b)). In Figure 9, the envelop of the experimental data has been superposed on the simulated data to illustrate model accuracy. The agreement is generally excellent. Figure 10 gives a closer look at the experimental and simulated response for the first and second cycles of Figure 8. The overall agreement is good although the experimental data indicates crack closure (i.e., steepening of the stress-strain curve) at larger strains than does the simulation. Possibly this difference is due to a mismatch of the asperities of the actual crack surfaces during reloading in compression. Hysteresis damping is apparent in the simulated response as well as the test data. The extent of this damping in both cases is clearly shown in Figure 11 in the reproduction of the third, fourth and fifth deformation cycles. Although the shapes of the hysteresis loops are not identical, the enclosed areas, which are a measure of the damping, are similar. Finally, the tangent stiffness degradation as a result of progressive damage was determined by measuring the average slope of the unload-reload curves. Excellent agreement between theory and experiment for the tangent stiffness degradation is shown in Figure 12.

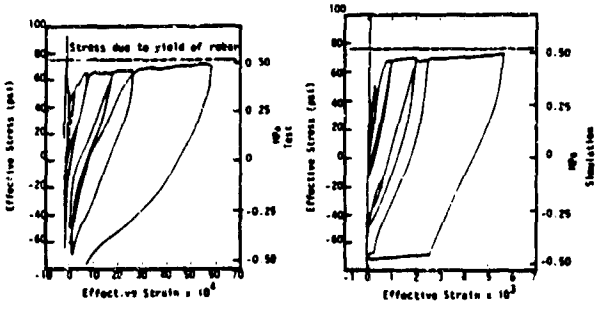

Figure 8. Comparison of test and simulation.

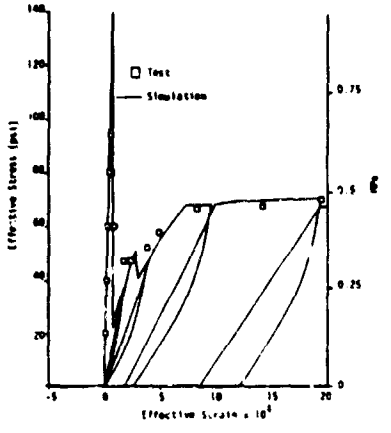

Figure 9. Comparison of test and simulation.

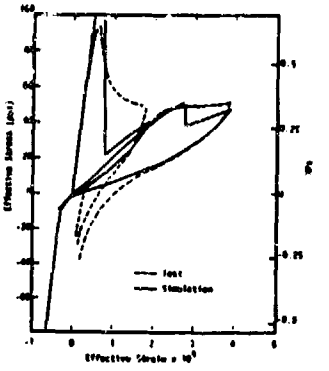

Figure 10. Comparison of test and simulation: σ_e-e_e curves for first two cycles.

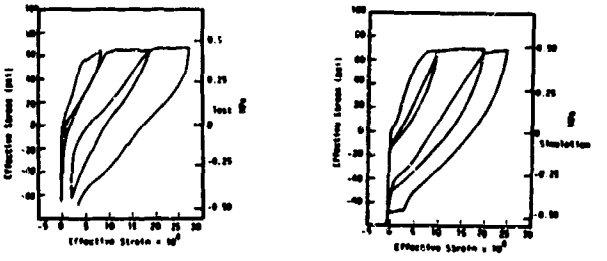

Figure 11. Comparison of test and simulation: σ_e-e_e curves for third, fourth and fifth cycles.

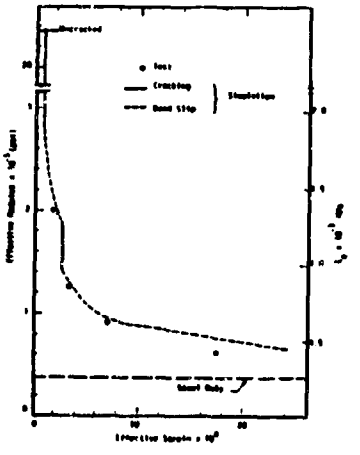

Figure 12. Comparison of test and simulation: tangent stiffness degradation due to cracking and debonding.

STEEL-CONCRETE DOWEL PROBLEM

The dowel problem concerns the manner in which shear forces are tranferred across cracks in reinforced concrete. Three distinct modes of shear transfer exist at a crack: (1) Interface shear transfer (IST) on the rough surfaces of

the crack; (2) dowel action (DA) in the reinforcement crossing the crack; and (3) components of axial forces in the reinforcing bars inclined to the crack direction. IST includes the effective frictional and bearing forces generated at a slightly open crack as the protruding particles on each side of the cracked surface come into contact. DA is induced by the shear and bending deformations experienced by the reinforcement when shear displacements are applied to the crack. Where the dowel transverse displacements become sufficiently large, axial forces in the rebars crossing the crack contribute to effective shear resistance. The example to follow focuses upon a single preexisting crack in the absence of IST with rebar initially normal to the crack surface.

The dowel problem is illustrated in Figure 13. Of interest here is the prediction of the global shear force or stress across the crack plane for a prescribed relative displacement of the concrete. To eliminate IST, it will be assumed that the crack surface is smooth and lubricated; thus the contact shear stress between concrete segments is assumed to be negligible. Under this condition, together with the assumed prescription of the average global concrete displacements, the theory developed in Reference [1] reduces to

$$N^{(1p)}_{11,1} + P_1 = 0 \ , \tag{6}$$

$$N^{(1p)}_{12,1} + (N^{(1p)}_{11} U^{(1)}_{2,1})_{,1} + P_2 = 0 \ , \tag{7}$$

$$M^{(1p)}_{11,1} - M^{(1p)}_{12} = 0 \ , \tag{8}$$

$$\dot{N}^{(1p)}_{11} = n^{(1)} A E^{(1)}_{ep} (\dot{U}^{(1)}_{1,1} + \dot{U}^{(1)}_{2,1} U^{(1)}_{2,1}) \ , \tag{9}$$

$$\dot{N}^{(1p)}_{12} = n^{(1)} A_u{}^{(1)} (\dot{U}^{(1)}_{2,1} + \dot{S}^{(1)}_1) \ , \tag{10}$$

$$\dot{M}^{(1p)}_{11} = \frac{\pi d^{(1)^4}}{64} E^{(1)}_{ep} \dot{S}^{(1)}_{1,1} \tag{11}$$

$$\dot{P}_1 = s_1[\dot{U}_1] \tag{12}$$

$$\dot{P}_2 = s_2[\dot{U}_2] \tag{13}$$

where $[U_i] = [U_i^{(2)} - U_i^{(1)}]$, $d^{(1)}$ is the diameter of the rebar, and A represents a certain "cell" area. In the above, $N^{(1p)}_{ij}$ is the partial stress associated with the steel, P_i is an interaction body force in the ith direction, and $M^{(1p)}_{ij}$ is a weighted stress average, i.e., a moment. Equations (6) to (8) are equilibrium relations while (9) to (11) are constitutive equations. An assumption of moderate rotations of the steel is implicit in these relations. Based in part on micromechanical considerations, the models shown in Figures 3 and 14 were utilized to represent the interaction relations (12) and (13). The boundary conditions of the problem depicted in Figure 12 correspond to

$$U^{(1)} = U^{(2)} = M^{(1p)}_{11} = 0 \quad \text{at } x_1 = 0 \tag{14}$$

$$N^{(1p)}_{11} = N^{(1p)}_{12} = M^{(1p)}_{11} = 0 \quad \text{at } x_1 = \ell/2 \ . \tag{15}$$

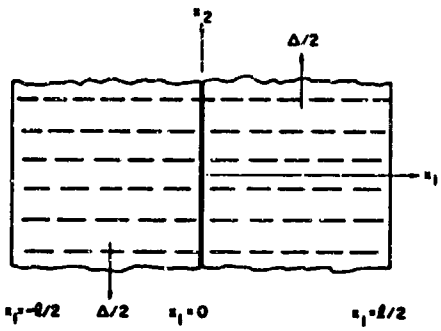

Figure 13. The dowel problem.

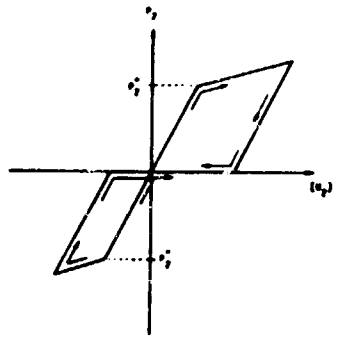

Figure 14. Interaction term P_2 for dowel problem.

With use of the above model, a simulation of the monotonic dowel tests by Pauley et al. [6] was performed. The test specimen and setup are illustrated in Figures 15 and 16; wax was used to lubricate the joint surface. A comparison of theoretical and experimental results are shown in Figure 16 for three different steel volume fractions. Agreement is observed to be good. The "shear stress" in Figure 17 is based on the specimen area.

A more critical test of the model simulation capability is represented by the cyclic experiments of Jimenez, et al. [7]. The specimen and test setup are illustrated in Figure 18. Thin brass sheets were used to lubricate the joint surface. A typical simulation versus experiment

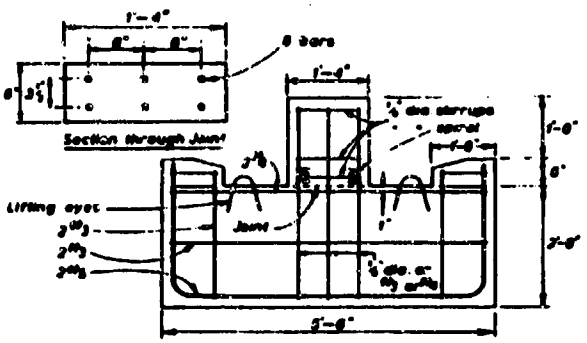

Figure 15. Details of test specimens, Paulay, et al. [6].

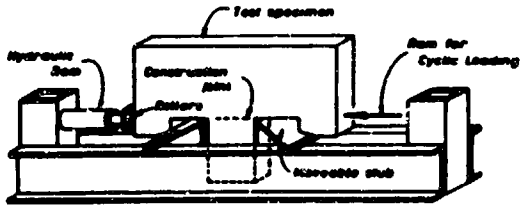

Figure 16. The test set up, Paulay, et al. [6].

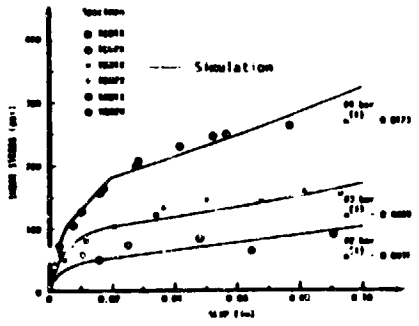

Figure 17. Load-slip relationship for the dowel test by Paulay, et al. [6].

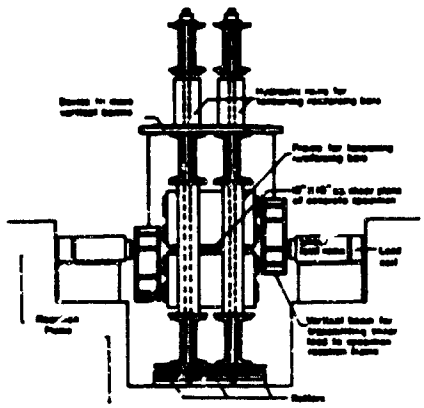

Figure 18. Test set up, Jimenez, et al. [7].

is shown in Figure 19. The agreement is observed to be good considering the complexity of the response.

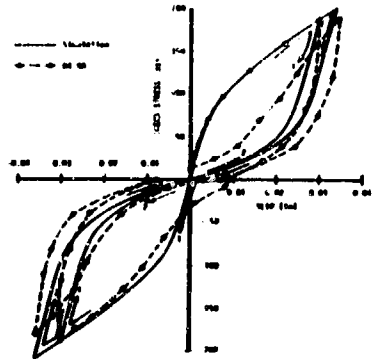

Figure 19. Load-slip relation for the dowel test by Jimenez, et al. [7].

CONCLUSION

An advanced nonlinear model for reinforced concrete has been developed for dense unidirectional steel layouts. The description takes the form of a binary mixture of concrete and steel. Validation tests performed to-date indicate that the model correctly simulates progressive concrete cracking, steel-concrete bond degradation and slip, and steel-concrete dowel action. Current efforts are focused upon extensions to include more general steel layouts and inclusion of a more accurate plain concrete model.

ACKNOWLEDGEMENT

This research was sponsored by the Air Force Office of Scientific Research (AFSC) under Contract F49620-84-G-0029.

REFERENCES

1. Hegemier, G. A., H. E. Read and H. Murakami, Development of Advanced Constitutive Model for Reinforced Concrete, Report SSS-R-84-6684, S-CUBED, La Jolla, CA., April 1984.

2. Hageman, L. J., "A Mixture Theory with Microstructure Applied to the Debonding, Cracking and Hysteretic Response of Axially Reinforced Concrete", Ph.D. Dissertation, University of California, San Diego, 1983.

3. Hegemier, G. A., H. Murakami, and L. J. Hageman, "On Tension Stiffening in Reinforced Concrete," submitted for publication, 1984.

4. Somayaji, S., "Composite Response, Bond Stress-slip Relationships and Cracking in Ferrocement and Reinforced Concrete," Ph.D. Dissertation, University of Illinois, Chicago Circle, 1979.

5. Hegemier, G. A., R. O. Nunn and S.K. Arya, Behavior of Concrete Masonry under Biaxial Stress," Proc. North American Masonry Conference, University of Colorado, Boulder, Colorado, August 1978.

6. Paulay, T., R. Park and M. H. Phillips, "Horizontal Construction Joints in Cast-In-Place Reinforced Concrete," ACI SP-42, Shear in Reinforced Concrete, Vol. 2, 1974.

7. Jimenez-Perez, R., P. Gergely and R. N. White, "Shear Transfer Across Cracks in Reinforced Concrete," Report No. 78-4, Department of Structural Engineering, Cornell University, Ithaca, New York, August 1978 (NTIS PB-288 885/RC).

A COMPOSITE FRACTURE MODEL FOR LOCALIZED FAILURE IN CEMENTITIOUS MATERIALS

Kaspar J. Willam
and
Stein Sture

University of Colorado at Boulder
Boulder, Colorado

ABSTRACT

Stroke-controlled post-peak experiments on cylindrical mortar and concrete specimens will be utilized to develop a continuum based model for localized strength degradation in cementitious materials. The resulting composite fracture formulation is based on the postulate that the fracture energy release rate G_f = const. which is implemented into a non-associated plasticity formulation with equivalent strain-softening properties. The non-local character of the size dependent constitutive relation will be verified with finite element convergence studies of different post-critical experiments.

INTRODUCTION

The response behavior of cementitious materials can be broadly classified into three regimes, (i) cleavage in the form of mode I type cracking, (ii) decohesion in the form of mode II type frictional slip, and (iii) compactive hardening due to pore collapse. The first type prevails in tension and leads to a predominantly brittle appearance of the load-deformation characteristics shown in Fig. 1 for the direct tension test of a cylindrical NX-size mortar specimen [1]. The second type exhibits in contrast far more ductile behavior with a softening post-peak regime which diminishes with increasing confinement. Figure 2 illustrates the hardening and softening behavior of a cylindrical NX-size concrete specimen which failed under increasing axial compression at constant confining pressure [2]. In contradistinction to the first two cases the third type does not exhibit any softening response whatsoever for highly confined compressive loading paths. In fact the volumetric response behavior of a cementitious material exhibits the typical compactive behavior of porous matter [3] when subjected to hydrostatic loading in compression.

Clearly, the safety of unconfined cementitious structures depends to a large extent on the ductility and thus on the underlying post-peak response characteristics. The principal thrust of this investigation is therefore directed towards the softening post-peak behavior and the transition from brittle cracking to ductile shear slip. Unfortunately, there are several problems that complicate the identification and the formulation of "proper" strain-softening properties:

- Triaxial post-peak experiements are extremely difficult to perform requiring sophisticated servo-control and sufficiently stiff test apparatus;
- The post-peak response is really a structural characteristic associated with particular specimen geometries and boundary conditions from which generic fracture properties are to be extracted, e.g. via inverse identification;
- The computational difficulties of post-critical response studies are compounded by the lack of normality and the progressive localization of local material instabilities into a structural failure mode.

In view of the overall objective of computational models for the failure analysis of complex three-dimensional structures we will pursue a triaxial fracture formulation based on a continuum approach. To this end we will resort to the basic postulate of a constant fracture energy release rate such that the work expended to generate a fracture surface per unit area will remain constant, G_f = const. The equivalent strain-softening model will be set within the framework of non-associated plasticity which leads to a non-local constitutive format in which the governing stress-strain law depends on the mesh size. Since the main focus concentrates on the post-peak behavior, hardening in the pre-peak regime will be neglected in favor of predictive studies of different post-peak models for tensile cracking and frictional slip.

Although substantial experimental evidence on post-peak behavior has been assembled for soils and rocks, there are very few test data available for cementitious materials. In fact most of the experimental results on mortar and concrete have been obtained within the scope of fracture mechanics studies on notched specimens. Only very recently have limited post-peak data been secured by van Mier [4], Mazars [5] and Hurlbut [2] on unnotched samples which can be used for continuum-based formulations of triaxial fracture. Figure 4 shows a conceptual plot of the triaxial failure surface in the Rendulic stress plane in which the residual post-peak strength values are inserted in

order to delineate the zones of tensile cracking and frictional slip. While fracture along the compressive meridian can be loosely related to tensile straining in two directions with associated distributed cleavage along orthogonal surfaces fracture along the tensile meridian is accompanied by tensile straining in a single direction that exhibits highly localized cracking along a single fracture plane. This broad classification is complicated by mode II type-fracture in compression which leads in our terminology to the formation of localized shear bands. In brittle materials this phenomenon is normally attributed to the coalescence of distributed initial tensile crack feathers which ultimately lead to continuous faulting. In the case of cementitious materials there is considerable controversy about the fundamental aspects of shear banding because of the complexities of matrix-aggregate interaction on the mesomechanical level. In this context the distributed damage formulation of interacting continua by Ortiz [6] should provide further insight into the underlying fracture mechanisms within the matrix-aggregate composite.

In this paper we will focus on the fracture mechanics interpretation of softening in the direct tension and the triaxial compression tests in terms of the fracture energy release rate concept. To this end we will incorporate this fracture postulate into an equivalent non-associated elastic-plastic strain-softening formulation which leads to a non-local size-dependent format of the resulting stress-strain law. In this sense the current composite fracture model bears similarities to the recent strain-softening proposal by Bazant and Belytschko [7] who resorted to non-local continuum theories.

COMPOSITE CRACK MODEL

The proposed formulation is best understood in terms of the uniaxial tension test. To this end we consider an elementary volume V composed of an elastic zone V_e and a localized crack band of width $2d_t$ and area $A_t = h_t t$ oriented normal to the direction of major principal stress. In the simple case of a linear degradation of the tensile strength σ_f the fracture energy release rate for cracking the cross-sectional area A_t results in

$$G_f^I = \frac{\sigma_f^2}{E_f} d_t = \frac{\sigma_f^2}{E} \ell_t \qquad (1)$$

where the characteristic length ℓ_t defines the range of interacting bond forces partaking in the separation of the specimen into two competent parts. Let us now consider the equivalent continuum element in wich the localized crack band is homogenized uniformly over the height b of the composite element $V = bA_t$. Equating the energy release in the crack band of the composite element with the energy dissipation characteristics of the equivalent continuum element the following elementary expression is obtained for the tensile softening modulus of the homogenized composite element

$$E_s = \frac{1}{\frac{2G_f^I}{\sigma_f^2}\frac{1}{b} - \frac{1}{E}} = \frac{E}{\frac{2\ell_t}{b} - 1} \qquad (2)$$

Generalization of the uniaxial relationship to three dimensions involves the elementary volume V defined by the determinant of the Jacobian in a finite element environment. This spherical interpretation of the fracture geometry leads directly to the scalar relationship developed previously by the authors [8] which does not account for the directionality of oriented microcracking.

Since the orientation of the crackband is defined by the direction of the principal stresses it is simply a question of refinement to account for the particular geometry of the elementary volume at a pivot point of the numerical integration scheme. The metric tensor of the Jacobian provides the necessary information to define the fracture surface area A_t and the range of debonding b within the elementary volume V. For the case of two-dimensional rectangular elements the geometric quantities have been previously detailed by the authors in [1]. Figure 4 illustrates the composite fracture model for tensile cracking of the rectangular elementary volume $V = abt$. This leads to the following generalization of the equivalent tensile softening modulus in Eq. 2

$$E_s = \frac{1}{\frac{2G_f^I}{\sigma_f^2}\frac{h_t}{ab} - \frac{1}{E}} = \frac{E}{\frac{2\ell_t h_t}{ab} - 1} \qquad (3)$$

This expression clearly demonstrates that the softening modulus of the equivalent continuum element depends not only on the fracture energy but also on the geometry of the elementary volume. In other words, E_s varies with the mesh size of the particular finite element lay-out if the fracture energy release rate G_f remains constant. As a result, the composite fracture model leads to a non-local format of the equivalent strain-softening formulation which is fundamentally different from traditional strain-softening plasticity and plastic fracturing theories.

Note that the composite fracture formulation reduces to the fictitious crack model of Hillerborg et al [9] when a displacement discontinuity is introduced along the fracture band which separates the elementary volume into two intact elastic portions interconnected by a degrading interface condition. The homogenization procedure above monitors the fracture energy release rate by equivalent strain-softening of the continuum element. Contrary to the previous blunt crack model of Bazant et al [10] the mesh lay-out is in our case independent of the orientation and the width of the crack band $2d_t$ providing full flexibility of the finite element idealization irrespective of the particular crack orientation. Therefore the composite fracture model results in a spatial mesh description of fracture in contra-

distinction to the material description of discontinuous macrodefects within the discrete fracture approach. In our case tensile cracking is entirely defined by two fracture parameters, the tensile strength σ_f and the critical fracture energy release rate G_f. In fact there is no need to speculate on the width $2d_t$ or the unknown softening properties E_f of the localized crack band.

Examination of the denominator in Eq. 2 leads to two important observations. There is no restriction on the minimum mesh size, i.e. any nonzero value of the element size can be adopted as long as the following condition is satisfied

$$0 < b_i < \frac{2G_f^I E}{\sigma_f^2} = 2\ell_t \qquad (4)$$

Equation 4 infers on the other hand that there is a restriction on the maximum mesh size, i.e. the height of the elementary volume b_i must remain smaller than two times the characteristic length ℓ_t partaking in the formation of the crack band. Figure 5 illustrates the equivalent strain-softening behavior for three idealizations of the uniaxial tension specimen with mesh lay-outs of constant cross-section and different heights. The plots clearly demonstrate the decrease of ductility with increasing mesh height necessary in order to maintain constant fracture energy release rates. For mesh heights $b_i > 2\ell_t$ we observe the dynamic "snap back" condition [11] which results in instabilities of the underlying strain driven computational strategy. For this reason it is recommended to resort to mesh lay-outs which satisfy the mesh size restriction in Eq. 4. Here we note that the equivalent reduction of the fracture strength σ_f can not be adopted in general without undue alteration of initiation and propagation of the fracture process.

The predictive value of the composite fracture model is illustrated in Fig. 6 with the results of a finite element convergence study of the direct tension test shown in Fig. 1. We observe little disagreement between the three mesh lay-outs of the cylindrical mortar specimen in spite of the severe strain localization during the formation of a tensile crack band through the cross-section. In fact, the results of the rectangular 4 x 2 mesh correspond closely to those of the square 2 x 4 and 4 x 8 idealizations in which the softening modulus is adjusted according to Eq. 3 in order to enforce the fracture energy release rate C_f = 44 N/m. In contrast the constant softening modulus formulation E_s = 0.82 E leads to post-critical response predictions which are perfectly brittle [1]. Consistent mesh-reinforcement of the direct tension test results in an excessive decrease of ductility because each element subdivision contains the fracture energy release rate of the entire specimen. Therefore, we cannot extract softening properties from a direct tension test with a single crack band which are expected to hold locally at every point of the specimen. In fact post-mortem inspection of the cracked specimen clearly illustrates that the tension specimen has separated into two competent parts. Therefore global softening at the structural level involves localization of a single crackband which cannot be translated into local strain-softening properties relating point measures of stress and strain.

COMPOSITE SLIP MODEL

The proposed fracture model is readily extended to include mode II type frictional slip. In this case the elementary volume is composed of the undamaged elastic region V_e and the localized shear band of width $2d_s$ with the surface area $A_s = h_s t$. Adopting the Mohr-Coulomb condition for frictional slip, the shear band is oriented at the angle $\theta = \phi/2 + \pi/4$ with regard to the major axis of principal stress. Figure 7 depicts the basic lay-out of the composite slip element for a rectangular geometry of the elementary volume. For linear softening of the shear strength at peak τ_f to the residual strength level τ_r, the fracture energy release rate for advancing the shear band by the surface area A_s is

$$G_f^{II} = \frac{(\tau_f - \tau_r)^2}{G_f} d_s = \frac{(\tau_f - \tau_r)^2}{G} \ell_s \qquad (5)$$

where the characteristic length ℓ_s defines the range of the decohesive force during the formation of the shear band. Equating the energy dissipation characteristics of the composite slip element with that of the homogenized continuum element the equivalent shear-softening modulus is analogous to Eq. 3

$$G_s = \frac{1}{\frac{2G_f^{II}}{(\tau_f - \tau_r)^2}\frac{h_s}{ab} - \frac{1}{G}} = \frac{G}{\frac{2\ell_s h_s}{ab} - 1} \qquad (6)$$

The shear softening modulus of the equivalent continuum element exhibits again a pronounced size effect because of its dependence on the geometric parameters ab and h_s of the elementary volume. In other words, G_s has to be adjusted to the particular finite element configuration under consideration in order to enforce a fracture energy release rate which remains invariant during the formation of shear bands within the stationary mesh lay-out. As a result the underlying fracture mechanics concept leads to a non-local format of the equivalent softening relations which differs fundamentally from the local constitutive theories of strain-softening plasticity and progressive fracture.

For the verification of the composite slip model let us consider the post-critical response behavior of the triaxial compression test reported previously for NX-size mortar specimens [1]. To this end let us compare the predictions of the constant fracture energy release formulation above with that of the smeared strain-softening approach in which G_s is assumed to be a mesh size independent property of distributed fracture G_s = 0.05 G. Figure 8 illustrates the computational

results of the non-associated Mohr-Coulomb formulation in which a plastic potential corresponding to the maximum strain condition has been used to account for splitting tensile failure. Previous convergence studies have indicated that both post-critical response predictions are virtually independent of the particular mesh lay-out. Similar to the results of the direct tension study the constant softening approach furnishes predictions that are far too brittle. On the other hand the results of the constant fracture energy release rate approach are on the ductile side.

The corresponding post-peak results are shown in Fig. 9 which illustrates the deformation and distribution of principal stresses and strains within the cylindrical specimen. We observe the formation of two elastic cones near the frictional end platens and the localization of conical shear faulting throughout the specimen because of the axisymmetric idealization. A close-up indicates that the shear band consists of distributed vertical tensile cracks due to radial splitting which results in an outward motion of the lateral surface. The fracture mode agrees with the accepted failure behavior of triaxial compression specimens when subjected to low confinement.

In conclusion let us consider the underlying issue of calibrating the critical fracture energy release rate G_f^{II} for the formation of shear bands. In our case we have assumed that failure of the cylindrical NX-specimen takes place in form of a single shear band inclined at the slip angle $\theta = \phi/2 + \pi/2$ with the major principal stress. Therefore the surface area A_s is of the same order of magnitude as the cross-sectional area in tension A_t. This leads to the fracture energy release rate $G_f^{II} = 2452$ N/m and the characteristic length for decohesion $\ell_s = 1.465$m because of the large amount of strain energy stored in compression. In view of the far smaller values for mode I type tensile cracking, $G_f^{I} = 44$ N/m and $\ell_t = 0.12$ m, the question arises if G_f^{II} is an independent fracture property or simply the result of our elementary interpretation of shear faulting. Clearly, in brittle materials shear fracture is initiated by distributed tensile cracking, thus the subsequent formation of a single shear band is the result of coalescing crack feathers along an inclined slip plane. Because of the limited resolution of our computational tools to trace each individual crack it is natural to lump distributed mode II type cracking into the faulting concept of an independent fracture energy release rate for shear banding.

CONCLUDING REMARKS

The composite fracture model above provides a systematic methodology to incorporate fracture energy concepts for the formation of localized crack and shear bands in the strain-softening formulation of an equivalent continuum. In contrast to the updating material description of single macrodefects within the discrete fracture approach, progressive fracturing is in this case accounted for by an equivalent non-local constitutive relation within a spatial description of the domain. The equivalent strain softening model involves the fracture energy release rates as well as the particular finite element geometry.

REFERENCES

[1] K.J. Willam, N. Bicanic and S. Sture, "Constitutive and Computational Aspects of Strain-Softening and Localization in Solids," ASME/WAM '84 Symposium, Volume GOO274, 1984, pp. 233-252.

[2] B. Hurlbut, "Experimental and Computational Strain Softening Investigation of Mortar and Concrete Specimens," M.S. Thesis, University of Colorado at Boulder, CEAE Dept., 1985.

[3] T. Stankowski, "Concrete under Multiaxial Load Histories", M.S. Thesis, University of Colorado at Boulder, CEAE Dept., 1983.

[4] J. G.M. van Mier, "Strain-Softening of Concrete under Multiaxial Loading Conditions", Ph.D. Dissertation at University of Technology, Eindhoven, The Netherlands, 1984.

[5] J. Mazars, "Application de la Mecanique de L'Endommagement au Comportment Non Lineaire at a la Rupture du Beton de Structure", Universite Pierre et Marie Curie, Paris, 1984.

[6] M. Ortiz and E.P. Popov, "Plain Concrete as a Composite Material", Mechanics of Materials, Vol. 1, No. 2, May 1982, pp. 139-150.

[7] Z.P. Bazant, T.B. Belytschko and T.-P. Chang," Continuum Theory for Strain-Softening," ASCE, J. Eng. Mech., Vol. 110, No. 12, Dec. 1984, pp. 1666-1692.

[8] K.J. Willam, "Experimental and Computational Aspects of Concrete Fracture", Comp.-Aided Analysis and Design of Concrete Structures, Pineridge Press, Swansea, 1984, pp. 33-70.

[9] A. Hillerborg, M. Modeer and P.E. Peterson, "Analysis of Crack Formation and Crack Growth in Concrete by Means of Fracture Mechanics and Finite Elements," Cement and Concrete Research, Vol. 6, 1976, pp. 773-781.

[10] Z.P. Bazant and B.H. Oh, "Crack Band Theory for Fracture of Concrete", RILEM, Materiaux et Constructions, Vol. 16, 1983, pp. 156-177.

[11] M.A. Crisfield, "Overcoming Limit Points with Material Softening and Strain Localization", Numerical Methods of Non-Linear Problems Pineridge Press, Swansea, 1984, pp. 244-277.

ACKNOWLEDGEMENT

This work was supported by the U.S. Air Force Office of Scientific Research under Contract AFOSR 82-0273 to the University of Colorado at Boulder.

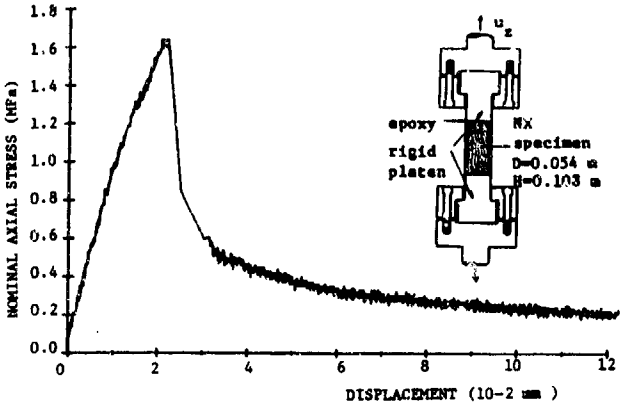

Fig.1 DIRECT TENSION EXPERIMENT

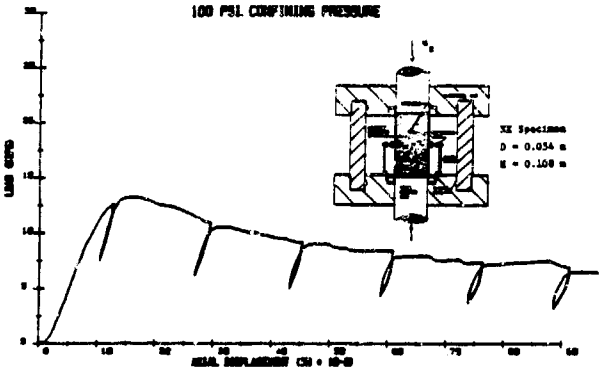

Fig.2 TRIAXIAL COMPRESSION EXPERIMENT

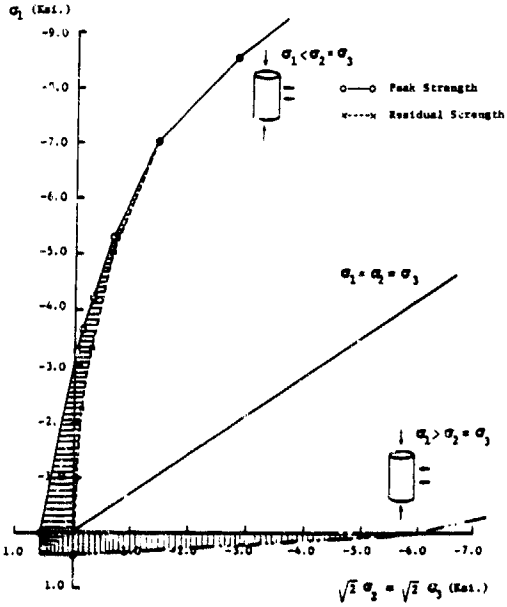

Fig.3 SOFTENING REGIMES IN BENDULIC PLATE

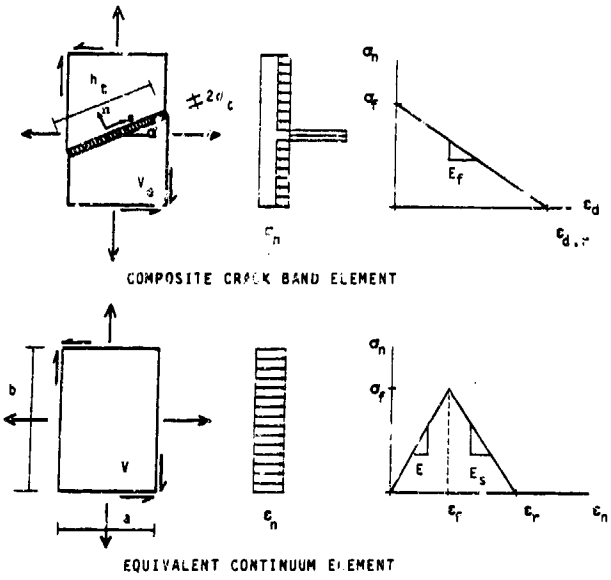

Fig. 4 COMPOSITE CRACK MODEL FOR TENSION

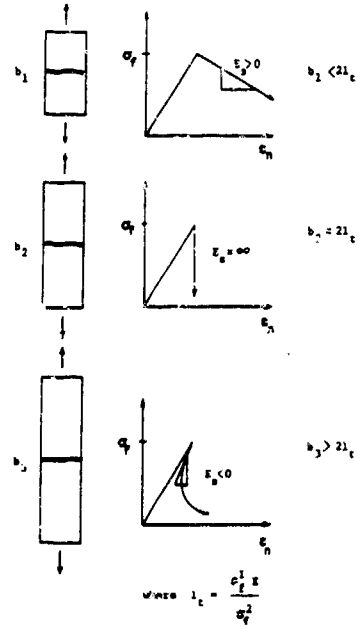

Fig.5 SIZE EFFECT OF SOFTENING MODULUS

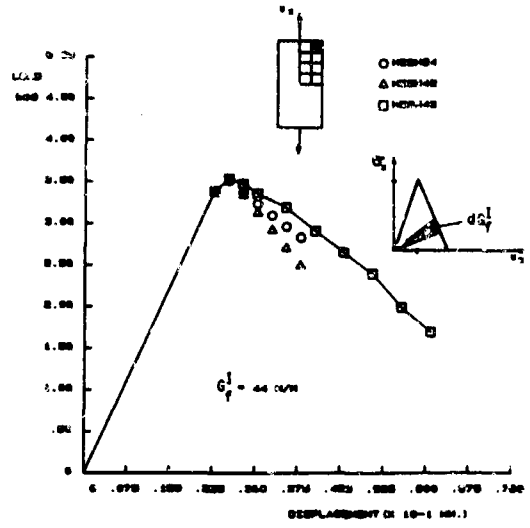

Fig.6 DIRECT TENSION TEST PREDICTIONS

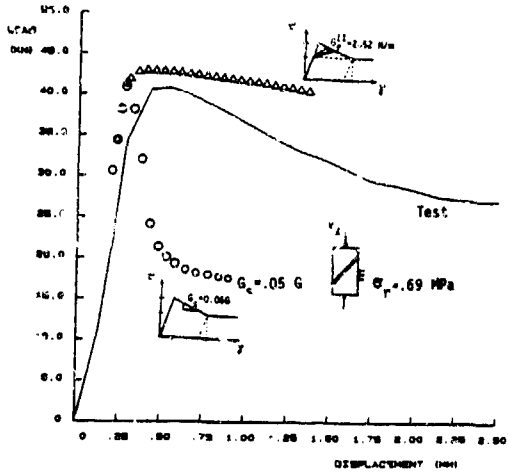

Fig.8 TRIAXIAL COMPRESSION TEST PREDICTIONS

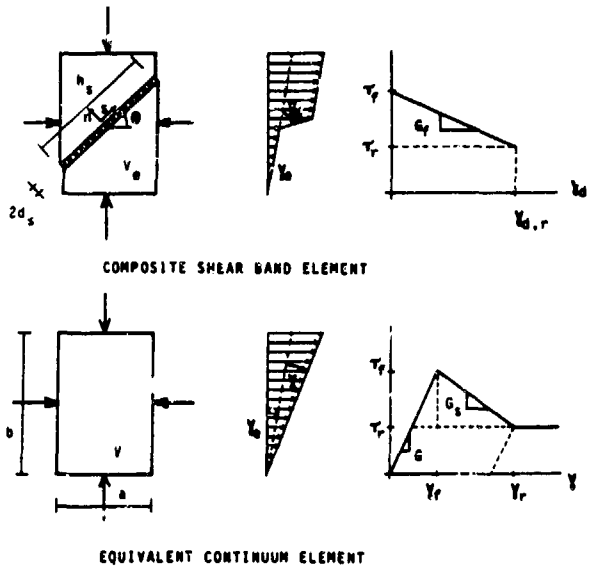

Fig.7 COMPOSITE SLIP MODEL FOR SHEAR FAULTING

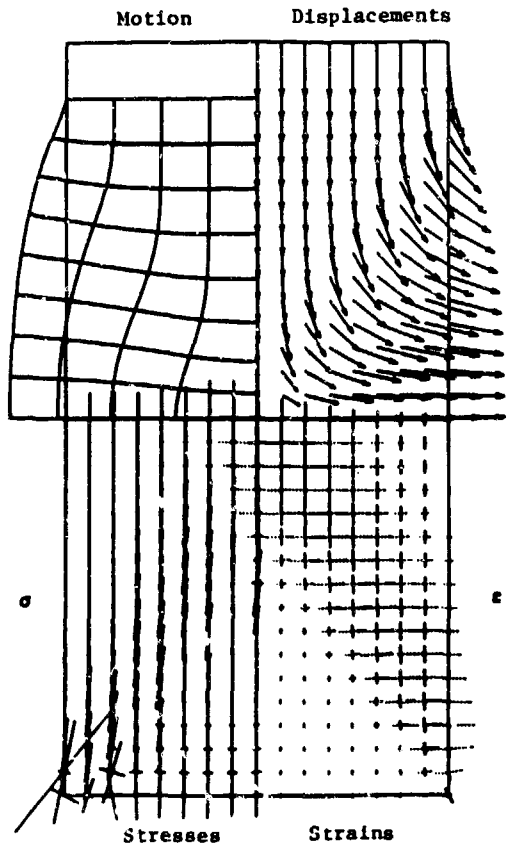

Fig.9 POST-PEAK RESPONSE BEHAVIOR

CONSTITUTIVE EQUATION FOR GEOLOGICAL MATERIALS UNDER HIGH DYNAMIC LOADING

J.K. Park and Y. Horie

Department of Civil Engineering
North Carolina State University, Raleigh, North Carolina

ABSTRACT

A constitutive formalism for geological materials has been tested by use of an elliptical and a lemniscate yield surface which include pore-related strain-hardening. We present a procedure for determining material coefficients through mechanistic modelling. The models have been used in numerical calculations for spherical blast wave propagation with an aim to study the stress-strain paths experienced by material elements.

INTRODUCTION

Continuum plasticity theory has long been used for modelling the mechanical behaviors of geological materials such as soils and rocks. Many of recent models [1,2] involve a complex combination of multiplastic potential surfaces and a non-associated flow rule. However, as the complexity of these models increases, so does the difficulty of determining their material parameters. For example, a recent model [3] for sand contained twenty adjustable parameters. Hence, the determination of parameters, such as the yield surface and the plastic potential as well as elastic moduli, is rarely complete when various paths in stress space are involved.

Recently, Swegle proposed a constitutive model for porous materials based upon the extension of the P-α model [4]. This extension is physically motivated and is simpler in the determination of the material parameters than many other plasticity models. The important features of this model are (1) that the overall stress components are described in terms of the stress in solid components and porosity, and (2) the plasticity behavior is described by a conventional closed yield surface and the associated hardening flow rule. We used this model to study the shock compaction of metal and ceramic powders and found it very effective [5]. This paper describes a further application of Swegle's formalism to the blast wave loading of geological materials and a mechanistic procedure for simplifying the determination of some of the material parameters involved in his model.

CONSTITUTIVE MODEL

The following is a summary of Swegle's model with an emphasis on the stress-strain relationship. Stress components σ_{ij} are determined by those of the solid component and the solid volume fraction α.

$$\sigma_{ij} = -P\delta_{ij} + S_{ij} \tag{1}$$

$$P = \alpha P_s = \alpha f(V_s, E) \tag{2}$$

$$S_{ij} = \alpha S_{ijs} \tag{3}$$

where P is pressure, $\alpha = V_s/V$, the subscript "s" stands for the solid, V the specific volume, E the internal energy and S_{ij} deviatoric stress components.
Strain increments are partitioned in terms of volume components.

$$d\epsilon_{ijs} = (d\theta_s/d\theta)d\epsilon_{ij} \tag{4}$$

where $d\theta = dV/V$ and $d\theta_s = dV_s/V_s$.

Elastic response is formulated by use of the P-α model and a frame indifferent isotropic Hooke's law. That is,

$$\left(\frac{d\alpha}{dP}\right)_{\text{elastic}} = \frac{1}{K_{os}h^2(\alpha)}\left(\frac{1}{\alpha} - 1\right), \tag{5}$$

where

$$h(\alpha) = 1 + \frac{1-\alpha}{1-\alpha_o}\left(\frac{C_o}{C_{so}} - 1\right),$$

K_{so} = solid bulk modulus at zero pressure,

C_o, C_{so} = sound velocities at zero pressure,

$$dS_{ijs} = 2G_s de_{ijs} + (\omega_{ik}S_{kj} - \omega_{kj}S_{ik})dt,$$

where G_s is the shear modulus of the solid component, and ω_{ik} are the components of the rotation tensor, and de_{ij} are the increments of deviatoric strain tensor defined by

$$de_{ij} = d\epsilon_{ij} - (d\theta/3)S_{ij}. \tag{7}$$

If Eq. (4) is used for the partition of the strain components, it can be shown that irrespective of deformation modes,

$$de_{ijs} = de_{ij}[1+(d\alpha/\alpha)(dV/V)^{-1}]. \quad (8)$$

Inelastic state of the material is determined by a yield function g such that the material is behaving plastically if

$$g = f(J_1, \sqrt{J_2'}, \alpha) = 0, \quad (9)$$

and elastically if

$$g < 0,$$

where

$$J_1 = \sigma_{KK} = -3P,$$

and

$$\sqrt{J_2'} = (1/2\ S_{ij}S_{ij})^{1/2}. \quad (10)$$

When a material is plastic according to Eq. (9), the increment of strain is defined by

$$d\varepsilon_{ij} = d\varepsilon^e_{ij} + d\varepsilon^p_{ij}, \quad (11)$$

where the superscripts describe the state of the material, and the plastic components are prescribed by the associated normality rule given by

$$d\varepsilon_{ij} = d\lambda \frac{\partial g}{\partial \sigma_{ij}}, \quad (12)$$

where $d\lambda$ is a non-negative scalar.
An expansion of Eq. (12) yields the increments of stress components,

$$dP = -Kd\varepsilon^e_{kk} = -K(d\varepsilon_{kk}-d\varepsilon^p_{kk}) = dP^e + 3Kd\lambda\left(\frac{\partial g}{\partial J_1}\right), \quad (13)$$

$$dS_{ij} = 2Gde^e_{ij} = 2G(de_{ij}-de^p_{ij}), = dS^e_{ij} - \frac{S_{ij}}{\sqrt{J_2'}} Gd\lambda\left(\frac{\partial g}{\partial \sqrt{J_2'}}\right), \quad (14)$$

where K and G are the elastic moduli of the medium as a whole, and dP^e and dS^e_{ij} could be looked upon as instantaneous elastic response of the medium as a whole. The shear modulus can be simplified by use of Eq. (3).

$$G = \alpha G_s[1+(d\alpha/\alpha)(dV/V)^{-1}] \quad (15)$$

The yield function g provides an additional incremental relation for the scalar parameter $d\lambda$. That is,

$$dg = 0 = \left(\frac{\partial g}{\partial J_1}\right)dJ_1 + \left(\frac{\partial g}{\partial \sqrt{J_2'}}\right)d\sqrt{J_2'} + \left(\frac{\partial g}{\partial \alpha}\right)d\alpha = 0. \quad (16)$$

$$d\alpha = (dP - \frac{\partial f}{\partial V_T}dV_T)/\left(\frac{\partial f}{\partial \alpha}\right). \quad (17)$$

Hence, one finds

$$d\lambda = \frac{\left(\frac{\partial g}{\partial J_1}\right)(-3dP^e)+\left(\frac{\partial g}{\partial \sqrt{J_2'}}\right)(d\sqrt{J_2'})^e+\left(\frac{\partial g}{\partial \alpha}\right)d\alpha}{9K\left(\frac{\partial g}{\partial J_1}\right)^2+G\left(\frac{\partial g}{\partial \sqrt{J_2'}}\right)^2}, \quad (18)$$

where

$$d\sqrt{J_2'}^e = \frac{GS_{ij}de_{ij}}{\sqrt{J_2'}}. \quad (19)$$

SELECTION OF MATERIAL PARAMETERS

An advantage of Swegle's model is that the elastic moduli can be independently and accurately determined through acoustic sound velocity measurements. Also, they are easily accessible in standard handbooks. Hence adjustable parameters deal only with yield criteria.

There are many yield criteria including the well known Mohr-Coulomb and Drucker-Prager models [2]. We considered two representative functions to examine the process of material-parameter determination. They are an elliptical and a lemniscate function [6] given in Eqs. (20) and (21), respectively.

$$g = (P/P_1(\alpha))^2 + (D/D_1(\alpha))^2 - 1 = 0, \quad (20)$$

$$g = (P-k(\alpha))^2 + D^2 - B^2(\alpha)\cos^{2n}(1/2\theta/\phi) = 0, \quad (21)$$

where $D = (3J_2')^{1/2}$, P_1, D_1, k, and B are parametric functions of the solid volume fraction α, and $\tan\theta = (3J_2')^{1/2}/(P-k(\alpha))$.

These selections have been made based upon the observations that they describe the general features of yield surfaces which are observed experimentally and that their parameters can be understood through mechanistic interpretation of flow mechanisms. For example, $P_1(\alpha)$, which is the hydrostatic inelastic compression of the porous material, can be determined by a spherical pore-collapse model [7]. Then,

$$P_1(\alpha) = \frac{Y}{\beta}[(1-\alpha)^{-2\beta/3}-1], \quad (23)$$

where Y and β are related to the cohesion C and the angle ϕ of shear resistance as follows.

$Y = 2C\cos\phi/(1-\sin\phi)$ and

$$\beta = 2\sin\phi/(1-\sin\phi). \quad (24)$$

Similarly $D_1(\alpha)$ can be estimated by model calculations [8,9]. However, the latter is not yet well developed as $P_1(\alpha)$. Hence, in this paper their interdependence is expressed by a polynomial function $Q(\alpha)$ [10] such that

$$Y_1(\alpha) = Q(\alpha)P_1(\alpha) = Q_0(1-\alpha)^m P_1(\alpha). \quad (25)$$

Similar interpretations can be made of the parameters in the lemniscate function. θ is related to the friction angle of the material, and the functions $k(\alpha)$ and $B(\alpha)$ express effective work hardening. We made the following identification of these functions.

$$k(\alpha) = k_0 + C_0 P_1(\alpha),$$
$$B(\alpha) = P_1(\alpha) - k(\alpha), \quad (26)$$

where $P_1(\alpha)$ is given by Eq. (23) and K_0 and C_0 are constants.

There are still four to eight parameters which are needed for describing plastic flow. But a significant reduction is achieved in the number of truly adjustable parameters.

SPECIFIC APPLICATIONS

The models have been applied to Kayenta sandstone. Table 1 summarizes the model coefficients which have been determined based upon static laboratory data shown in Fig. 1 during uniaxial strain loading of the sandstone [10]. No attempt has been made to optimize curve fitting, because the coefficients already describe important features of the stress path under the uniaxial loading. The purpose of this exercise is to investigate the loading characteristics of such model materials during spherical blast wave loading.

It has recently been recognized that standard hydrostatic, uniaxial-strain, and triaxial tests are not adequate for developing accurate constitutive models that are valid for the stress-strain paths experienced by material elements in actual field conditions [11]. Therefore, following Johnson's idea [11], we simulated the blast wave loading of the model materials through finite difference calculations of spherical wave propagation [12]. The results are shown in Figs. 2 through 8.

Figures 2 and 3 show elastic and elastic-plastic axial stress profiles resulting from a pressure wave,

$$\sigma_a = P_0\exp(-at)$$

applied at the cavity surface of radius ($=R_0$) of 1m in an infinite medium. The elastic-plastic solution is based upon the lemniscate yield function (21), and did not develop local stress maxima. The development of local maxima is apparently controlled not only by the blast wave decay constant a, but also by pore-related hardening.

Table 1. Material Coefficients for Model Sandstone

$P_{so} = 1/V_{so} = 2.7$ g/cm^3,
$P_0 = 2.0$ g/cm^3, $\alpha_0 = 0.74$
$K_s = 25$ GPa, $G_s = 18$ GPa,
$P_s = 25(V_{so}/V_s-1) + 68(V_{so}/V_s-1)^2$ GPa
$Y = 0.072$ GPa, $B = 4.0$
$D_1 = 0.48\ P_1 (P_1 < 0.72$ GPa)
$= 0.019\ (1-\alpha)^{-4}\ P_1 (P_1 > 0.72$ GPa)
$K_0 = 0.01$ GPa, $C_0 = 0.1$
$n = 0.5$
$\phi = 60°$

Figures 4 through 7 show the stress-strain paths generated from the numerical solution for the lemniscate yield criterion. The paths depend sensitively on the location of material elements and the decay constant. As is expected from the shape of the yield surface, the qualitative feature of the stress-strain paths are similar to those found for the Drucker-Prager model by Johnson et al. [11]. At $R = 1.5\ R_0$ and $R = 2.0\ R_0$ the stress paths intersect the failure surface during loading and remain in contact during unloading for certain durations. But at $R = 3.0\ R_0$, this phenomenon is no longer observed, and is already close to elastic loading. Initially, the loading is approximately uniaxial strain, but subsequent paths develop considerable transverse strain.

Figure 8 shows a feature of the stress-strain path for the elliptic yield surface at $R = 1.5\ R_0$. The intersection of the stress path with the failure surface is significantly different from that for the lemniscate function. However, such a difference cannot be discerned from the data during uniaxial-strain loading shown in Fig. 1.

These results illustrate the importance of determining, as accurately as possible, the in-situ stress history due to blast-wave loading.

REFERENCES

1. P.A. Vermeer et al., Deformation and Failure of Granular Materials, Proc. of IUTAM, Delft, 1982. Balkema, Rotterdam 1982.

2. C.S. Desai and H.J. Siriwardane, Constitutive Laws for Engineering Materials, Prentice Hall, 1983.

3. G.Y. Baladi, "An Elastic-Plastic Isotropic Constitutive Model for Sands," in Advances in the Mechanics and the Flow of Granular Materials. V. 2, Trans Tech Publications, 1983.

4. J.W. Swegle, "Constitutive Equation for Porous Materials with Strength," J. Appl. Phys. 51, 2574 (1980).

5. Y. Horie et al., "High Pressure Equation of State for Metal and Ceramic Powders," Final Report Part I, V. 2. Prepared for Lawrence Livermore Nat. Lab., Subcontract 6853501, Jan. 1984. North Carolina State University, Raleigh NC.

6. N.P. Suh, "A Yield Criterion for Plastic, Frictional, Work-Hardening Granular Materials," Int. J. Powder Metall., 5, 69 (1969).

7. M.M. Caroll and A.C. Holt, "Suggested Modification of the P-α Model for Porous Materials," J. Appl. Phys. 43, 759 (1972).

8. R.J. Green, "A Plasticity Theory for Porous Solid," Int. J. Mech. Sci. 14, 215 (1972).

9. J.F. Martynova and M.B. Shtern, "An Equation for the Plasticity of a Porous Solid Allowing for True Strains of the Matrix Materials," Poroshk. Metall. 181, 23 (1978).

10. Y. Corapcioglu and T. Uz, "Constitutive Equations for Plastic Deformation of Porous Materials," Powder Technology, 21, 269 (1978).

11. J.N. Johnson, R.K. Dropek, and D.R. Schmitz, "Simulation of the Load-Unload Paths Experienced by Rock in the Vicinity of Buried Explosions," TR 76-74, December 1976. Terra Tek. Inc., Utah. This report was kindly made available to us by Dr. Johnson of Los Alamos National Lab.

12. M.L. Wilkins, "Calculation of Elastic-Plastic Flow," in Methods in Computational Physics V. 3, Academic Press, 1964.

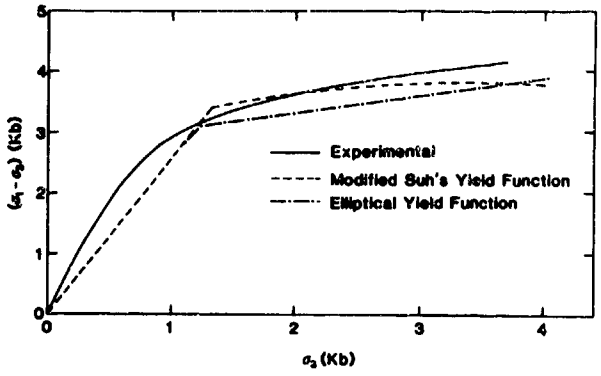

Fig. 1. Stress path during uniaxial loading of Kayenta sandstone. $\sigma_1(=\sigma_a) - \sigma_2(=P_c)$= Load L in the triaxial text configuration. σ_a is the axial stress and P_c the confining pressure.

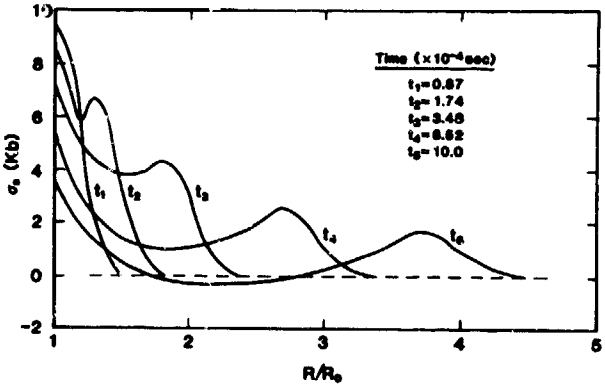

Fig. 2. Stress profiles in an elastic porous sandstone from a 1 GPa pressure pulse. 1/a=1 msec. σ_a is the axial stress.

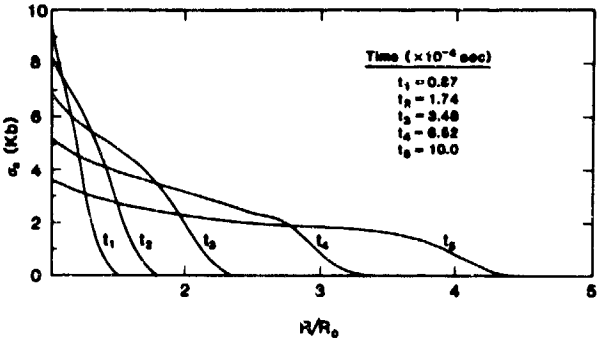

Fig. 3. Elastic-plastic stress profiles from a 1 GPa pressure pulse. 1/a=1 msec. The yield surface is given by a lemniscate function.

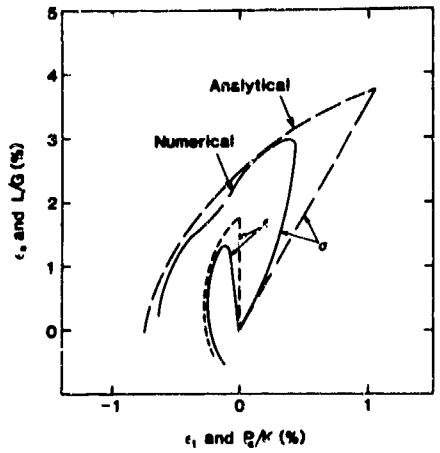

Fig. 4. Stress-strain paths for spherical wave propagation in a porous elastic medium. Analytical solutions are from [10] and are based upon K=9.5 GPa and G=6.375 GPa.

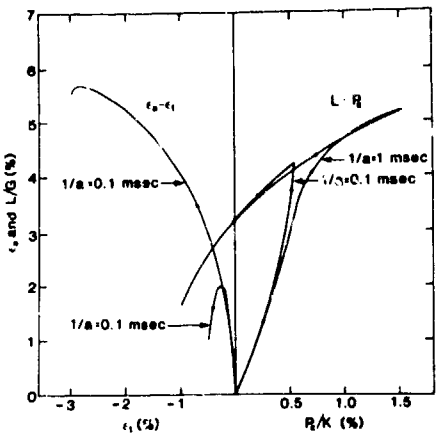

Fig. 5. Stress-strain paths at R=1.5 R_0. R_0=1m, P_0=1GPa, 1/a=1 msec or 0.1 msec. The yield surface is given by Eq. (21). ϵ_a and ϵ_t are axial and transverse strain components.

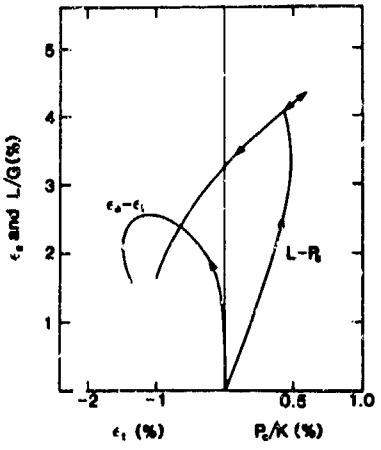

Fig. 6. Stress-strain paths at R=2.0 R_0. 1/a=1 msec, P_0=1 GPa. The yield surface is given by Eq. (21).

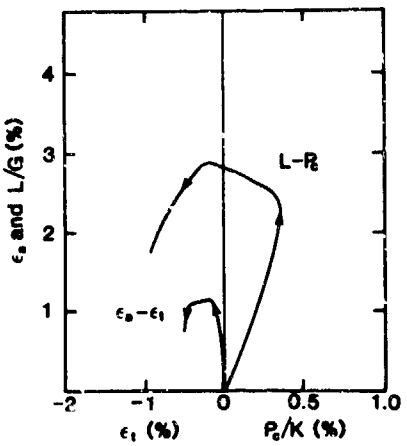

Fig. 7. Stress-strain paths at R=3.0 R_0. 1/a=1 msec, P_0=1 GPa. The yield surface is given by Eq. (21).

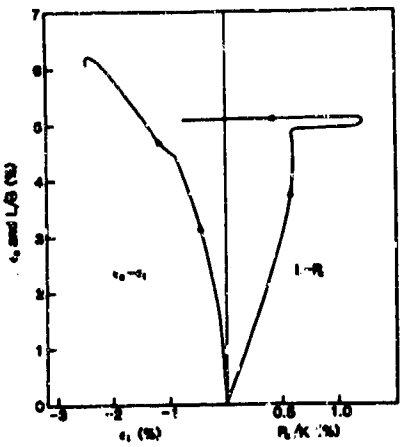

Fig. 8. Stress-strain paths at R=15 R_o. R_o=1 m, P_o=1 GPa, 1/a=1 msec. The yield surface is given by Eq. (20).

AN ENDOCHRONIC PLASTICITY THEORY FOR CONCRETE

K. C. Valanis* and H. E. Read

S-CUBED, A Division of Maxwell Laboratories, Inc.
San Diego, California 92121

ABSTRACT

An endochronic plasticity theory for plain concrete is developed which is intended to describe its nonlinear behavior over the stress range where significant cracking does not occur. The model is isotropic, rate-independent and thermodynamically sound. It exhibits the major features of concrete behavior, including shear-volumetric coupling, effect of hydrostatic compression on shear response, hardening, hysteresis and stress-path dependence. The theory is applied to, and successfully proof-tested against, an extensive set of complex multiaxial plain concrete data obtained by others using a true triaxial device.

INTRODUCTION

A new endochronic plasticity theory was developed by Valanis in 1979 [1] which has since been applied with remarkable success to various problems in metal plasticity [2,3] and geomaterials [4]. The theory is founded on the concepts of irreversible thermodynamics of internal variables and formulated on the hypothesis that the current state of stress in a material is a linear functional of the entire history of deformation, with the history defined with respect to a deformation memory scale, called intrinsic time, which is itself a property of the material at hand. Such a theory does not require the notion of yield surface nor the specification of unloading-reloading criteria; it predicts that plastic flow will occur from the onset of loading, a feature which makes the theory particularly attractive for describing plain concrete, which does not exhibit a well-defined yield point.

The purpose of this paper is to describe recent work that we have done [5] to explore the potential offered by the new endochronic plasticity theory for describing plain concrete behavior, with particular focus on the extensive data recently reported in Reference [6]. An endochronic model of plain concrete is developed which exhibits the major features of concrete behavior over the stress range where significant cracking does not occur. The model has been fit to a small subset of the data from Reference [6], and then exercised around a variety of complex non-standard stress paths also investigated in Reference [6] but not used in fitting the model. It is shown that the model can successfully predict the nonlinear behavior of plain concrete under these complex loading conditions.

The endochronic model presented here differs in a fundamental manner from previous endochronic models of plain concrete developed by others [7-9] on the bases of earlier versions of endochronic theory. In the present model, proper closure of hysteresis loops is guaranteed, so that artifices, such as the jump-kinematic hardening introduced in Reference [9], are not required. Also, the instantaneous response at points of unloading and reloading is elastic. Discussions of the basic inelastic properties of the new endochronic theory have been given recently by Trangenstein and Read [10] and Murakami and Read [11].

THEORY

In Reference [5], a comprehensive formulation of the governing equations of the new endochronic plain concrete model, starting from the concepts of the irreversible thermodynamics of internal variables, is given. The model portrays the major features of nonlinear inelastic behavior exhibited by plain concrete at stress levels where significant cracking does not occur; this includes shear-volumetric coupling, effect of hydrostatic compression on shear response, hardening, hysteresis and stress-path dependence. In that which follows, the basic equations of the model are given without derivation and the interested reader is referred to Reference [5] for further details. It is assumed that the material is isotropic, rate-independent and deforms isothermally. In this case, the governing equations for the new endochronic model of plain concrete are as follows:

$$\underset{\sim}{s} = \int_0^{z_s} \rho(z_s - z') \frac{d\underset{\sim}{e}^p}{dz'} \, dz' \qquad (1)$$

*Consultant; also, Professor of Mechanics, University of Cincinnati, Cincinnati, Ohio.

$$\sigma = \int_0^{z_H} \phi(z_H - z') \frac{d\varepsilon^p}{dz'} dz' \tag{2}$$

$$d\underset{\sim}{e}^p = d\underset{\sim}{e} - \frac{d\underset{\sim}{s}}{2\mu} \tag{3}$$

$$d\varepsilon^p = d\varepsilon - \frac{d\sigma}{K} \tag{4}$$

$$dz^2 = \|d\underset{\sim}{e}^p\|^2 + k^2 |d\varepsilon^p|^2 \tag{5}$$

$$dz_s = \frac{dz}{F_s} \; ; \; dz_H = \frac{dz}{kF_H} \tag{6a,b}$$

Here $\underset{\sim}{s}$ denotes the deviatoric stress tensor, σ is the hydrostatic stress (pressure), $\underset{\sim}{e}^p$ represents the plastic component of the deviatoric strain tensor $\underset{\sim}{e}$, while ε^p is the plastic component of the volumetric strain ε. Moreover, μ and K are, respectively, the shear and bulk moduli, while k is a constant which determines the magnitude of shear-volumetric coupling. The double bars surrounding a symbol denote its norm, while single bars denote absolute value. Furthermore, F_S and F_H are, respectively, shear and hydrostatic hardening functions which, in the present model, are taken in the form:

$$F_s = \delta + \gamma\sigma \tag{7}$$

$$F_H = 1 + \beta\varepsilon^p \tag{8}$$

where δ, γ and β are positive constants. In addition, z denotes the intrinsic time scale, while z_s and z_H are, respectively, the intrinsic times for shear and hydrostatic behavior. Finally, $\rho(z)$ and $\phi(z)$ are weakly singular kernel functions satisfying the condition $\rho(0) = \phi(0) = \infty$, but integrable in the domain $0 \leq z \leq \infty$. The weakly singular nature of the kernel functions is a crucial feature of the model for two reasons: (1) It provides for closure of hysteresis loops in the uniaxial or shear stress-strain space, however small they may be, and (2) it ensures that, at points of unloading or reloading, the response is always elastic. The specific forms of the kernel functions found to be appropriate for the present model:

$$\rho(z_s) = \sum_r A_r e^{-\alpha_r z_s} \tag{10}$$

$$\phi(z_H) = \sum_r B_r e^{-\beta_r z_H} \tag{11}$$

where the constants A_r, B_r, α_r and β_r are all positive and finite. With such forms, it can be shown [5] that each of the hereditary integrals in Eqs. (1) and (2) is reducible to a system of coupled linear ordinary differential equations; this greatly simplifies the computational strategy for dealing with the model. In the present study, it was found that sufficient accuracy could be obtained for present purposes by taking r = 2 in Eqs. (10) and (11).

MATERIAL PARAMETERS EVALUATION

The material parameters in the model described above were evaluated specifically for the plain concrete considered in Reference [6], which had an unconfined compressive strength (f'_c) of 3.65 ksi. Due to limitations on text length, the details of the procedures used to accomplish this will not be given here, since they can be found in Reference [5]. In general, this was accomplished in a direct fashion through the use of a relatively small amount of data from Reference [6], requiring only a virgin hydrostatic compression curve, data on the response to shear under several different fixed hydrostatic pressures, and triaxial failure data at various confining pressures. Also, an examination of the data from the shear tests at several fixed hydrostatic pressures revealed that the initial unloading slopes in the octahedral shear stress-octahedral shear strain space exhibited a nearly linear increase with the octahedral shear strain, γ_o. Accordingly, the shear modulus, 2μ, was taken to depend on γ_o in the form:

$$2\mu = 2\mu_o + m\,\gamma_o \tag{12}$$

On this basis, the following values of the material parameters were determined:

$K = 2.1 \times 10^3$ ksi	$\beta = 64.8$
$2\mu_o = 1.9 \times 10^3$ ksi	$m = 1.04 \times 10^6$ ksi
$\delta = 0.33$	$\gamma = 0.083$ ksi^{-1}
$A_1 = 1.46 \times 10^3$ ksi	$\alpha_1 = 100$
$A_2 = 19.0 \times 10^3$ ksi	$\alpha_2 = 6{,}554$
$B_1 = 1.55 \times 10^3$ ksi	$\beta_1 = 570$
$B_2 = 5.87 \times 10^3$ ksi	$\beta_2 = 2{,}224$
$k = 1.5$	

Examples of the extent to which the model with the above parameters describes the data to which it was fit are given in Figure 1. Here, σ_o and τ_o denote, respectively, the octahedral normal and octahedral shear stress, while ε_o and γ_o are, respectively the octahedral normal and octahedral shear strain.

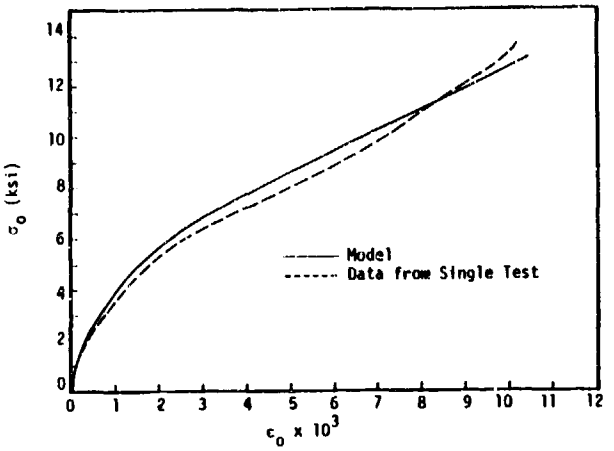

(a) Pure hydrostatic compression.

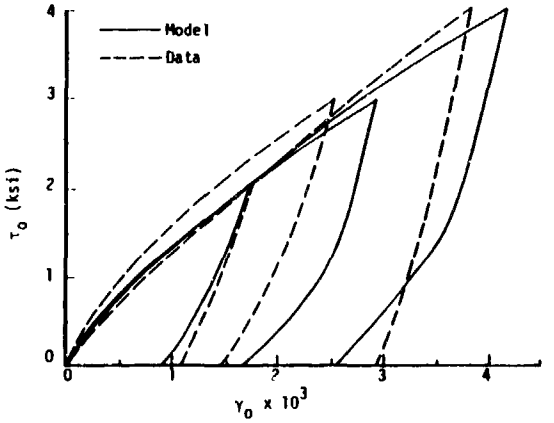

(b) Shear at fixed hydrostatic pressures of σ_o = 4, 6 and 8 ksi.

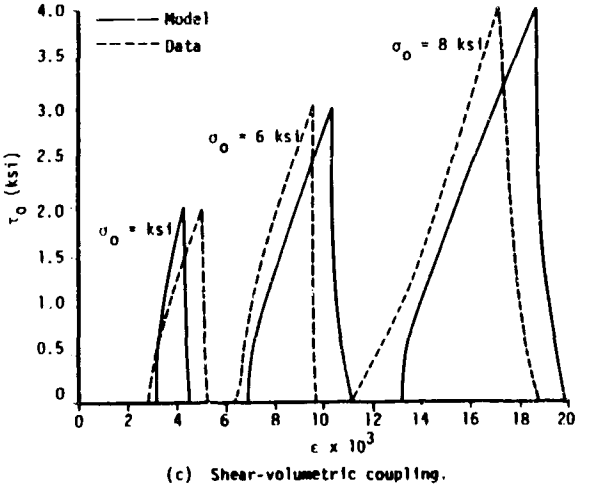

(c) Shear-volumetric coupling.

Figure 1. Capability of model to describe the data to which it was fit.

MODEL VALIDATION

In this section, the capability of the model described above to predict the measured behavior of plain concrete around stress paths that differ greatly from those used in fitting the model parameters is examined. For this purpose, a number of complex stress path tests conducted in the test program reported in Reference [6] is considered. The specific test cases selected for discussion here were chosen because they reveal a variety of different response features of plain concrete and exercise various features of the model. In that which follows, the test cases considered are referred to by the numbers assigned to them in Reference [6]. None of the tests considered below were used in fitting the model parameters, and no optimization techniques were employed to achieve the results presented below.

Test 1-1

This test was designed to explore the response of plain concrete to triaxial load cycles which do not exhibit stress reversals. The loading, shown in Figure 2(a and b), consisted first of cyclic hydrostatic loading up to 8 ksi, followed by cyclic deviatoric loading along the triaxial compression path, as depicted in Figure 2(b). The predicted and measured responses for this loading history are given in Figure 2(c). As this figure reveals, the predicted and measured responses are in good agreement, considering the data scatter, which is apparent from comparing the data from Test 1-1 with those from the replicate test, Test 1-10, given in Reference [6].

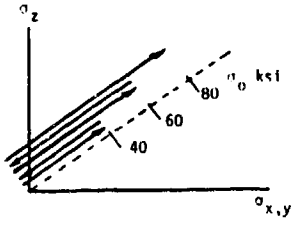

(a) Cyclic hydrostatic loading.

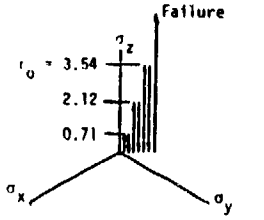

(b) Cyclic deviatoric loading along the triaxial compression path.

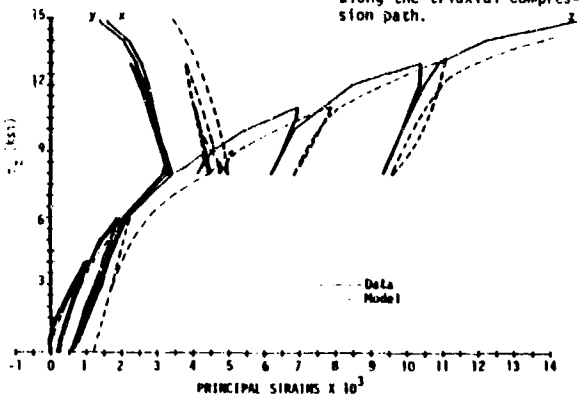

Figure 2. Cyclic triaxial loading (Test 1-1).

Tests 3-3 and 3-12

Test series No. 3 was designed to examine the behavior of plain concrete to circular stress paths in the deviatoric plane. The stress paths shown in Figure 3(a) consisted first of monotonic hydrostatic compression to some pressure σ_0, followed by a circular load path in the deviatoric at some fixed value of octahedral shear stress, τ_0. Comparisons between model predictions and data for the deviatoric loading portions of Tests 3-3 and 3-12 from this series are shown in Figures 3(b) and 3(c). The overall agreement is quite good. Also, it is of interest to note that the tests in this series apparently provide the first data on the response of concrete to "loading-to-the-side" [12], which the present model appears to describe it quite well.

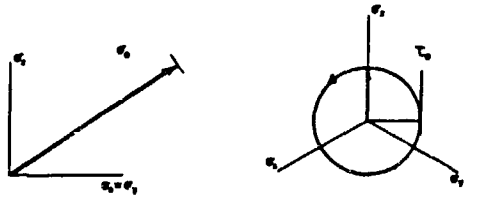

(a) Stress path

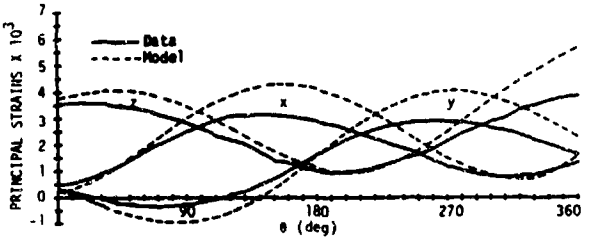

(b) Test 3-3 in which σ_0 = 4 ksi and τ_0 = 2 ksi.

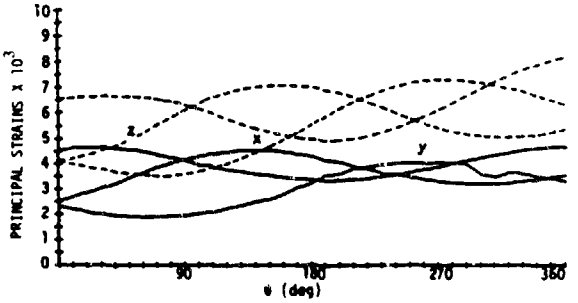

(c) Test 3-12 in which σ_0 = 8 ksi and τ_0 = 1.5 ksi.

θ (deg)

(c) Test 3-12 in which σ_0 = 8 ksi and τ_0 = 1.5 ksi.

Figure 3. Circular stress paths in the deviatoric plane.

Tests 4-11, 4-15 and 4-17

These tests were part of a larger group of tests designed to explore several aspects of response to complex stress paths for which two of the principal stresses were equal. While the stress paths for Tests 4-11, 4-15 and 4-17 were quite different, they nevertheless have a common stress state, i.e., σ_0 = 8 ksi and σ_0 = 4 ksi, thus permitting some insight into the stress-path dependence of response. Comparisons between the predicted and measured responses for Tests 4-11, 4-15 and 4-17 are given in Figures 4 to 6, where the applied stress histories are also shown. As an inspection of these figures reveals, the present model describes the measured response quite well, with an accuracy that appears to be well within the data scatter.

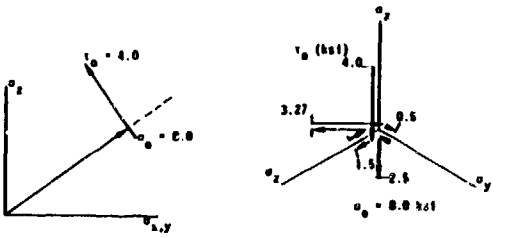

(a) Stress path

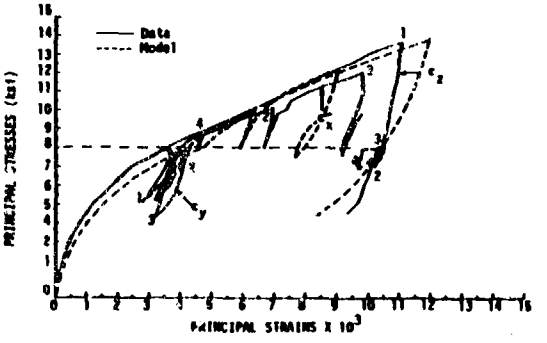

(b) Principal stresses versus principal strains.

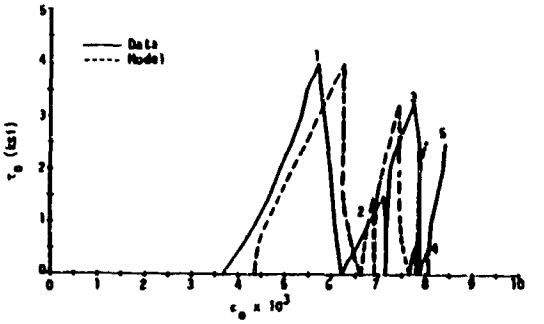

(c) Octahedral shear stress versus octahedral normal strain.

Figure 4. Complex stress paths in the deviatoric plane.

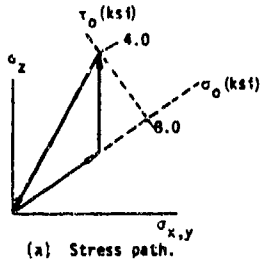

(a) Stress path.

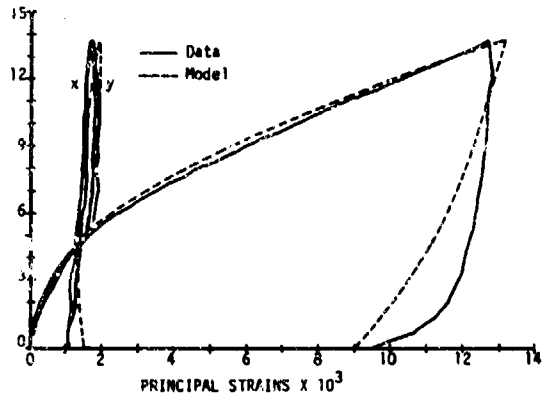

(b) Major principal stress versus principal strains.

Figure 5. Measured and predicted responses for Test 4-15.

Tests 5-1, 5-2 and 5-3

The purpose of these tests was to investigate the response of plain concrete to unsymmetric stress paths in a fixed deviatoric plane. The stress paths consisted of hydrostatic compression to the 4 ksi deviatoric plane, followed by proportional deviatoric loading paths which makes angles of 30°, 60° and 90° with the triaxial compressive axis, as shown in figure 7(a). The predicted and measured responses for these tests are shown in Figure 7(b,c,d); also included in the figures are corresponding predictions reported by Stankowski [12]. As indicated, the present model captures the measured responses very well, and is clearly superior to the Stankowski- Gerstle model [13].

Test 6-2

In Test 6-2, the response of plain concrete to the piecewise linear loading path shown in Figure 8(a) was explored. The loading was applied so that all possible uniaxial and equibiaxial stress states at a peak stress level of 3.6 ksi were achieved. The predicted and measured responses are depicted in Figure 8(b). In view of the typical scatter of concrete data, the agreement between model and experiment is considered excellent.

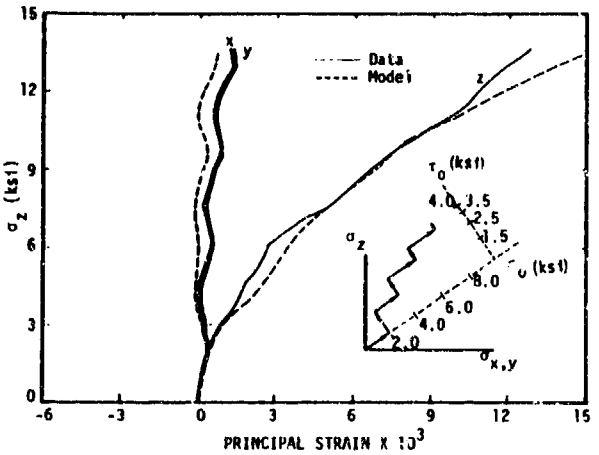

(a) Major principal stress versus principal strains.

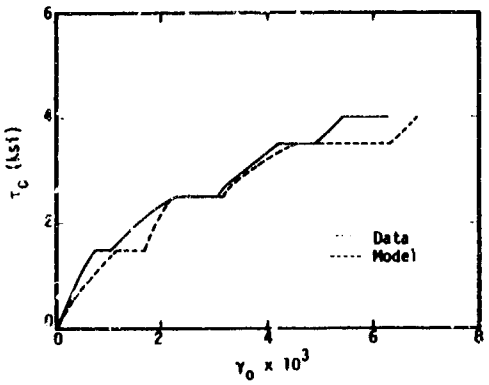

(b) Octahedral shear stress versus octahedral shear strain.

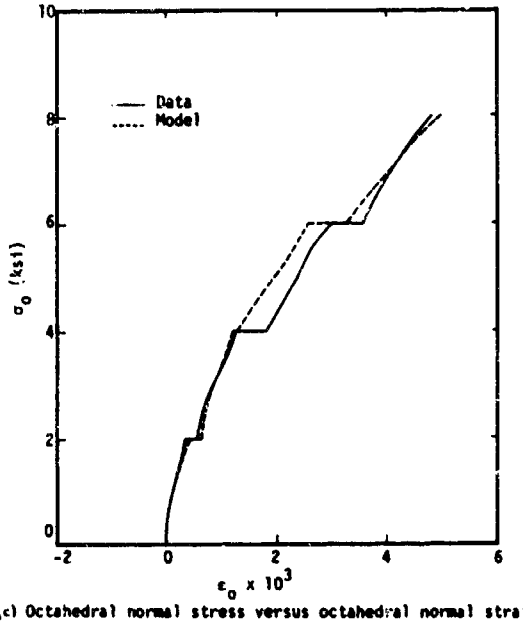

(c) Octahedral normal stress versus octahedral normal strain.

Figure 6. Measured and predicted responses for Test 4-17.

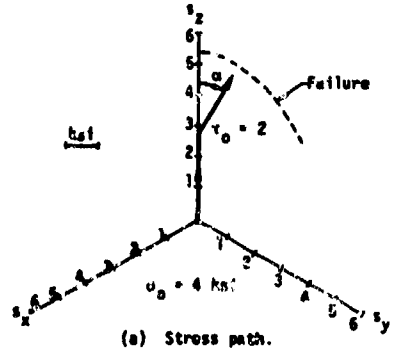

(a) Stress path.

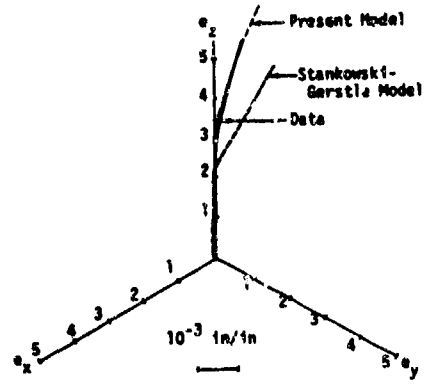

(b) Test 5-1 (α = 30°)

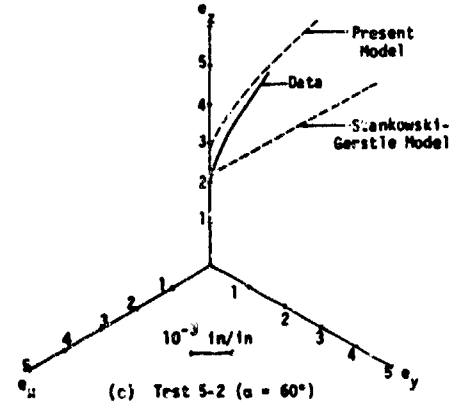

(c) Test 5-2 (α = 60°)

Figure 7. Measured and predicted responses for Tests 5-1, 5-2 and 5-3.

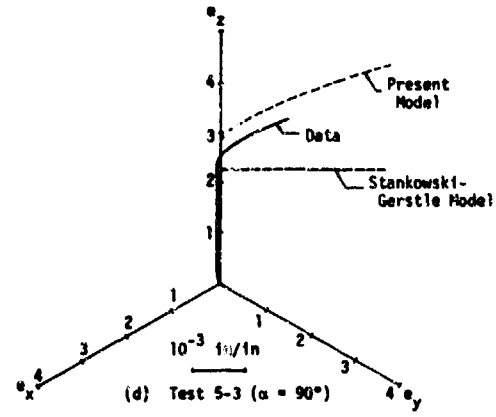

(d) Test 5-3 (α = 90°)

Figure 7. (Continued)

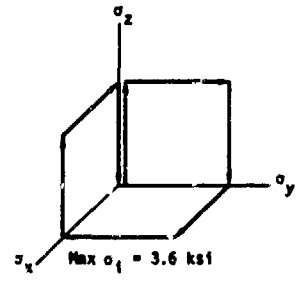

(a) Stress path

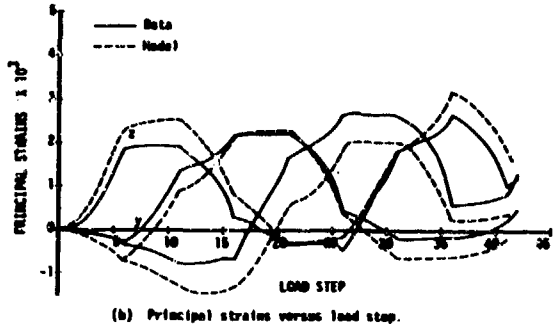

(b) Principal strains versus load step.

Figure 8. Measured and predicted responses for Test 6-2.

CONCLUSION

An advanced nonlinear constitutive model has been developed, on the basis of the new endochronic plasticity theory, to describe the general behavior of plain concrete over the range of stresses for which significant cracking does not occur. The model is isotropic, rate-independent and thermodynamically sound. The model exhibits shear-volumetric coupling in the form of shear compaction, dependence of shear behavior on hydrostatic pressure, hysteresis and stress-path dependence. The wide variety of proof-tests to which the model has been subjected clearly demonstrate that, over the intended range of application, the endochronic plasticity framework described above captures the essential features of the nonlinear behavior of plain concrete.

ACKNOWLEDGMENT

This research was jointly sponsored by the Air Force Office of Scientific Research (AFSC) (Contract F49620-84-C-0029) and the Defense Nuclear Agency (Contract DNA001-84-C-0127).

REFERENCES

1. Valanis, K. C., "Endochronic Theory with Proper Hysteresis Loop Closure Properties," S-CUBED, La Jolla, CA., Report SSS-R-80-4182, August 1979.

2. Valanis, K. C., and C. F. Lee, "Some Recent Developments of the Endochronic Theory with Applications," Nuclear Engr. Design, 69 (1982) 327.

3. Valanis, K. C., and J. Fan, "Endochronic Analysis of Cyclic Elastoplastic Strain Fields in a Notched Plate," J. Appl. Mech., 50 (1984) 789.

4. Valanis, K. C., and H. E. Read, "A New Endochronic Plasticity Model for Soils," in Soil Mechanics -- Transient and Cyclic Loads, G. N. Pande and O. C. Zienkiewicz, eds., John Wiley and Sons, Ltd., 1982.

5. Valanis, K. C., and H. E. Read, "An Endochronic Plasticity Theory for Concrete," S-CUBED, La Jolla, CA., Report SSS-R-85-7023, November, 1984.

6. Scavuzzo, R., T. Stankowski, K. H. Gerstle and H. Y. Ko, "Stress-Strain Curves for Concrete Under Multiaxial Load Histories," CEAE Department, University of Colorado, Boulder, 1983.

7. Bazant, Z. P., and P. C. Bhat, "Endochronic Theory of Inelasticity and Failure of Concrete," J. Engng. Mech. Div., ASCE, 102(EM4) (1976) 701.

8. Bazant, Z. P., and C. L. Shieh, "Endochronic Model for Nonlinear Triaxial Behavior of Concrete," Nuclear Engr. Design, 47 (1978) 305.

9. Bazant, Z. P., and C. L. Shieh, "Hysteretic Fracturing Endochronic Theory for Concrete," J. Engng. Mech. Div., ASCE, 106(EM5) (1980) 929.

10. Trangenstein, J. A., and H. E. Read, "The Inelastic Response Characteristics of the New Endochronic Theory with Singular Kernel," Intl. J. Solids Struct. 18(11) (1982) 947.

11. Murakami, H., and H. E. Read, "Some Basic Inelastic Response Features of the New Endochronic Theory," Presented at 21st Annual Meeting of Soc. Engng. Science, VPI, Blacksburg, VA, October 15-17, 1984.

12. Stankowski, T., "Concrete Under Multiaxial Load Histories," M. S. Thesis, CEAE Department, University of Colorado, Boulder, 1983.

13. Stankowski, T., and K. H. Gerstle, "Simple Formulation of Concrete Behavior Under Load Histories," submitted to J. Amer. Conc. Inst. for publication.

A POLYMER PRESSURE GAGE FOR DYNAMIC PRESSURE MEASUREMENTS

Anthony J. Bur and Steven C. Roth

Polymers Division, Center for Materials Science,
National Bureau of Standards, Gaithersburg, MD 20899

ABSTRACT

The construction, calibration and use of a polymer pressure gage is described. The transducer material in this gage is polyvinylidene fluoride (PVDF) which becomes piezoelectrically and pyroelectrically active when subjected to a large electric field (2 MV/cm at room temperature). The sensitive region of the gage consists of two 12 μm thin films of PVDF for which the active area is 1 cm in diameter. These films are laminated together and subsequently sandwiched between two protective layers of polycarbonate. Compensation for signals generated by temperature changes is described and demonstrated.

INTRODUCTION

The pressure sensing element of the pressure gage, polyvinylidene fluoride (PVDF), has been the subject of many laboratory studies and has been used in many applications during the past decade [1-5]. PVDF is available as thin films or sheets which become piezoelectrically and pyroelectrically active by "poling" a specific region of it with a large electric field (2 MV/cm at room temperature). Upon removal of the field PVDF possesses a permanent electric polarization. Switching from the unpoled to the poled state is viewed as a ferroelectric transition [6].

A model of transducer response to changes in hydrostatic pressure and temperature was developed by Broadhurst et al [1]. In the model, the polarization of the sample changes in response to changes in volume and dimensions of the PVDF transducer when stressed, the dipole moment per unit volume changes because of the volume change, but the dipole moment remains constant. This effect is called secondary piezoelectricity.

In Figure 1, a permanently polarized sample is shown with the polarization vector in the 3 direction. The 1 and 2 directions are equivalent as is approximately the case for the pressure gages which we describe here. The change in the polarization P in the i^{th} direction produced by an applied stress T is given by

$$\Delta P_i = \sum_{j=1}^{6} d_{ij} T_j \quad , \quad E_i = 0 \qquad (1)$$

where i=1, 2 and 3 corresponds to the directions

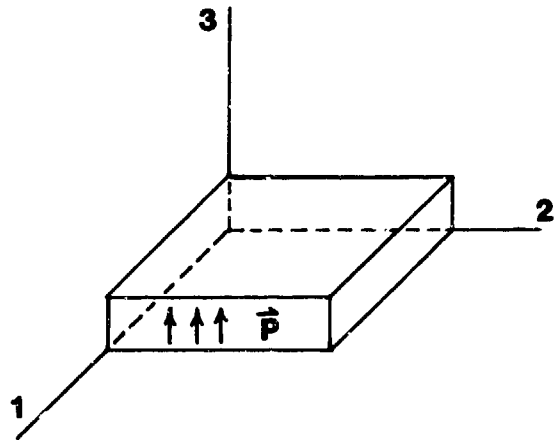

Figure 1. The coordinate system for a polarized PVDF sample is shown. P, the polarization vector, is in the 3 direction.

of the coordinate system, d is the piezoelectric coefficient and E is the macroscopic electric field which must be zero for equation (1) to be true. The six j indices correspond to three tensile stresses and three shear stresses.

By inspection and by carrying out gedanken experiments involving the application of individual stresses to the polarized specimen of Figure 1, it is found that the d matrix contains only five non-zero coefficients. Thus,

$$d = \begin{bmatrix} 0 & 0 & 0 & 0 & d_{15} & 0 \\ 0 & 0 & 0 & d_{24} & 0 & 0 \\ d_{31} & d_{32} & d_{33} & 0 & 0 & 0 \end{bmatrix} . \qquad (2)$$

If electrodes are placed on the transducer normal to the 3 direction, changes in P_3 can be detected as charge or current in an external circuit. From equations (1) and (2),

$$\Delta P_3 = d_{31} T_1 + d_{32} T_2 + d_{33} T_3 \quad . \qquad (3)$$

If hydrostatic conditions prevail, then $T_1 = T_2 = T_3$ and d_h, the hydrostatic d coefficient, is equal to $d_{31} + d_{32} + d_{33}$.

It must be emphasized that the d matrix of equation (2) is the result of the model; experimental verification is incomplete. The coefficients d_{31}, d_{32} and d_{33} have been measured but the values of the other 15 coefficients remain unknown. In particular, the effect of shear stresses on the piezoelectric response of PVDF or of a pressure gage made from PVDF has not been reported.

Since the poled active material is both pyroelectric and piezoelectric, measurements are usually carried out in an isobaric or isothermal environment so that only one effect is activated. For the measurement of dynamic pressures, an isothermal environment is not always present because pressure pulses will be accompanied by temperature pulses due to adiabatic compressional heating. This effect was discussed by DeReggi et al. who considered the relative time effects of pressure induced temperature changes in PVDF and temperature changes which occur in the surrounding medium [7]. Adiabatic heating of the PVDF will occur in coincidence with its pressure change. When adiabatic heating of the surrounding medium occurs, the thermal time constant, τ, for diffusion of heat into the transducer will determine its pyroelectric response as a function of time. If the temperature changes in PVDF and its surroundings are identical, then there will be no heat transfer and the pyroelectric response will be due to adiabatic heating of the PVDF only. Calculations for this special case show that the pyroelectric charge signal is approximately 8% of the piezoelectric charge [7]. In general, adiabatic heating in both PVDF and its surroundings along with the time scale of each effect must be considered. For pressure measurements at $t \ll \tau$ temperature compensation can be achieved by applying the 8% correction to the transducer signals. For longer times the conduction of heat from the surroundings must be measured in order to apply the appropriate correction to the electrical signal from the PVDF gage.

Since τ depends on the dimensions of the transducer, it is often possible to adjust τ in accordance with the requirements of the measurement. For thin film transducers, τ, as determined from the solution to the heat flow equation in one dimension, depends on the square of the thickness, ℓ, of the transducer. For example, for a PVDF transducer with $\ell = 0.7$ mm, $\tau \approx 1$s. We will show that accurate pressure measurements for $t < \tau/20$ are possible without active compensation.

We will also demonstrate in this paper a method of active compensation for some applications for which it is not appropriate to change ℓ in order to accommodate the time scale of the measurement. For this situation, $t \geq \tau$. Compensation is achieved by using a thermocouple with a fast response time to measure temperature changes in the PVDF gage. The dynamic range of the compensated measurement can be as broad as 0.1 Hz to 10^5 Hz. Pressure measurements at higher frequencies, up to 10^8 Hz, can also be corrected with the 8% temperature compensation.

TEMPERATURE COMPENSATION

The method of active temperature compensation we have chosen is: (a) to measure the temperature change of the PVDF transducer using a thermocouple; (b) to amplify the thermocouple voltage to equal that generated by the pyroelectric response of the gage; and (c) to add the transducer voltage to the amplified thermocouple voltage yielding a corrected transducer voltage. This corrected output is proportional to the pressure which is applied to the active area of the transducer.

In Figure 2 we illustrate a skeleton diagram of the compensation circuit. Since the PVDF transducer is a charge generating device, its signal is converted to a voltage via a feedback capacitor C_f, in a charge amplifier. When the transducer responds to both temperature and pressure simultaneously, the transducer charge, q_t =

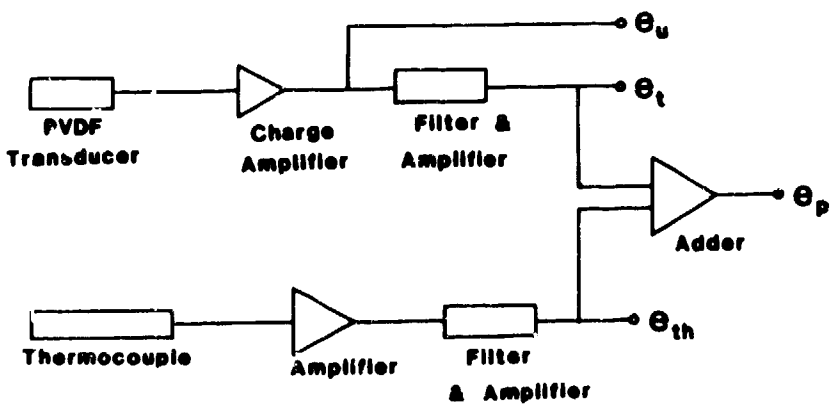

Figure 2. A skeleton diagram of the compensation circuit is shown. Here, e_u is the uncompensated output of the charge amplifier ; e_t is called the transducer voltage; e_{th} is proportional to the thermocouple voltage; and e_p is the output of the compensation circuit and is proportional to the pressure applied to the transducer.

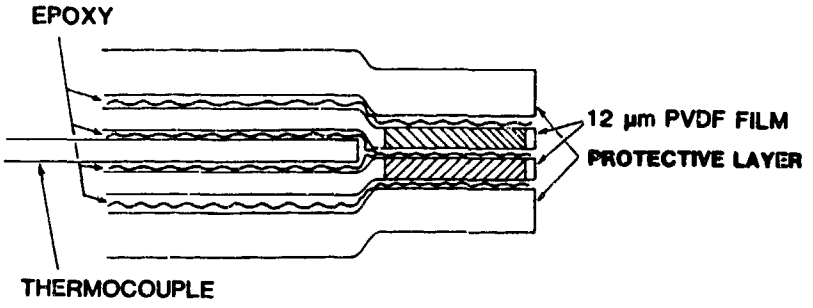

Figure 3. A cross section of the PVDF transducer is shown. The shaded areas are the piezoelectrically active regions. The outer protective layers can be PVDF or another material. The aluminum and indium electrodes are not shown.

$q_p - q_{th}$, where q_p is the charge proportional to pressure and q_{th} is the charge proportional to temperature. These charges combine out of phase because a positive pressure and a positive temperature will generate charges of opposite sign. After inverting the output of the charge amplifier, we have $e_t = q_p/C_f - q_{th}/C_f = e_p - e'_{th}$ where e'_{th} is the voltage proportional to the temperature change ΔT, e_p is a voltage proportional to the pressure change ΔP, and e_t is the output (transducer) voltage as shown in Figure 2. In terms of pyroelectric and hydrostatic piezoelectric coefficients λ and d_h we have

$$q_p = d_h A_e \Delta P \tag{4}$$

$$q_{th} = -\lambda A_e \Delta T, \tag{5}$$

where A_e is the area of electrodes. Equations (4) and (5) define the coefficients λ and d_h.

The thermocouple junction, which is positioned close to the active area of the transducer as shown in Figure 3, provides a voltage, $V_{th} = K\Delta T$ where K is the thermocouple constant. V_{th} is amplified to equal the quantity e_{th} by an amplification factor, A_f, so that $e_{th} = A_f V_{th}$. When e_{th} is set equal to e'_{th} by adjusting A_f and when e_t and e_{th} are added, we have

$$e_t + e_{th} = e_p - e'_{th} + e_{th} = e_p. \tag{6}$$

Since e_p is proportional to pressure only, compensation is achieved.

The amplification factor A_f of the thermocouple circuit is established by subjecting the transducer to a temperature change at zero pressure change. Under these conditions e_p should be zero. The procedure consists of immersing the transducer into warm or cold water and adjusting A_f until e_p is zero. For $C_f = 10^4$ pf, A_f is of the order of 10^4. Details regarding the compensation circuit and calibration procedures can be found elsewhere [8,9].

DESIGN OF THE TRANSDUCER

The PVDF transducer with thermocouple is shown in Figure 3. It is made from four sheets or films of polymeric material which have been laminated together using epoxy. The inner two films are each 12 μm thick biaxially oriented PVDF films. The shaded regions of Figure 3 are the active areas on which electrodes of 10^2 nm aluminum followed by 10^2 nm indium have been deposited. The active area is 1 cm in diameter. The outer two layers, whose thickness is adjusted in order to achieve a particular value of τ, can be PVDF or another material such as polycarbonate. A commercial copper-constantan thermocouple junction, made with 12 μm (0.5 mil) metal strips, is placed between the inner two sheets and within 2 mm of the active transducer area. Prior to lamination the electroded regions are made piezoelectrically active by poling them at room temperature with an electric field of 2 MV/cm. Other details regarding gage construction can be obtained from published reports [10,11].

In the symmetric geometric configuration of Figure 3, the transducer charge $q_t(t)$ and the thermocouple voltage, $V_{th}(t)$, have nearly the same response time to a change in external temperature. We have used the heat flow equation in one dimension to analyze the two functions. The solutions are that $V_{th}(t)$ an $q_t(t)$ are expressed as a Fourier series both of which contain the same dominant time constant,

$$\tau = \frac{\ell^2}{\pi^2 \kappa} \tag{7}$$

where κ is its thermal diffusivity [12].

EXPERIMENTAL APPARATUS AND RESULTS

Two experiments were used to examine tranducer behavior. One is designed to investigate transducer response to pressure changes in the time regime, $t \geq \tau$, and the other is concerned with $t \ll \tau$.

For the $t \geq \tau$ experiments, the outer two layers of the gage are each 25 μm thick films of PVDF and the overall thickness is 0.13 mm. This gage is placed in a steel pressure chamber which is filled with oil at room temperature. A pressure pulse is initiated by dropping a 16 kg mass onto a plunger in the chamber. Typical pulses have peak values up to 2.8×10^7 Pa (4000 psi) and a half width of

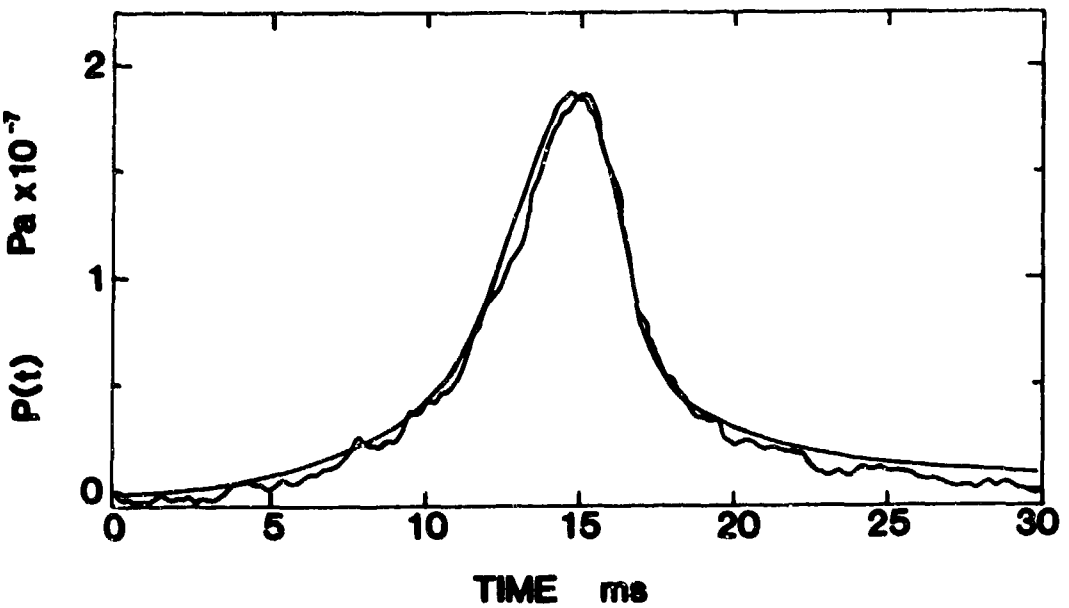

Figure 4. Pressure pulses from the compensated PVDF transducer, $P_c(t)$, and from the reference pressure gage, $P_r(t)$, are shown. The curve having the larger noise component is $P_r(t)$; the source of the noise is the thermocouple amplifier.

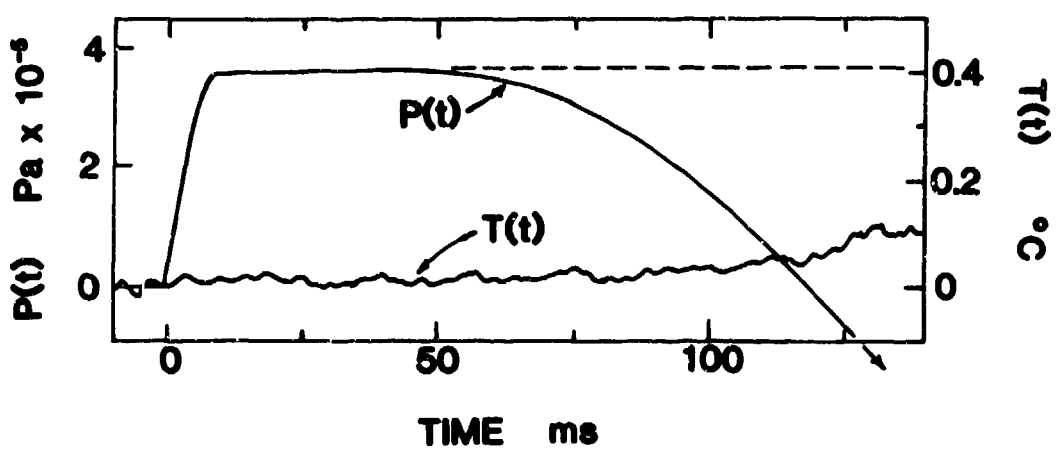

Figure 5. The pressure response, P(t), of a PVDF transducer to a step function applied pressure is shown. Also, the temperature, T(t), at its center is shown. The transducer has polycarbonate protective layers which are 375 μm (15 mil) thick. Its thermal time constant is 1.36 s. The dashed line is the actual pressure.

10 ms. A reference pressure gage, which is a resistive device having a response time of 60 μs, is positioned in the chamber. Pressure can also be measured using an accelerometer which is mounted on the drop weight. Signals from the transducer and thermocouple are fed into the compensation circuit; its output, e_p, along with the signals from the pressure gage and the accelerometer are captured by a digital signal processing system.

Using a value of the hydrostatic piezoelectric coefficient, d_h, which is obtained from a static measurement (described elsewhere [11]), the transducer or gage pressure $P_t(t)$ is calculated from e_p and compared with the reference pressure $P_r(t)$. The data are shown in Figure 4; $P_t(t)$ is the noisier of the two curves. The source of the noise is the inherent noise of the thermocouple amplifier. (In subsequent work, the noise has been decreased by a factor of 3; this is seen in the data of Figure 5.) A maximum temperature change of 0.5 °C accompanied the pressure pulse for which the compensation correction was 15% of the generated transducer charge. The accuracy of the pressure measurement is estimated to be ± 10%.

For $t \ll \tau$, we used a transducer with outer layers which were each 375 μm (15 mil) sheets of polycarbonate and the overall thickness of the transducer was 825 μm. The thermal time constant was calculated to be 1.36 s, which means that the approximate range of time for accurate pressure measurements is up to 70 ms. A value of d_h for this transducer was obtained from an independent measurement, either the drop test or the static measurement.

The transducer was placed in an air pressure chamber in which the pressure of the air was changed in a step function manner. The resultant transducer temperature and pressure (as calculated from its charge output) are plotted versus time in Figure 5. We note that the pressure is constant at 3.5×10^5 Pa as long as the temperature remains unchanged. As the temperature increases due to adiabatic compressional heating of the air the pressure appears to decrease as the pyroelectric charge begins to accumulate. At $t \approx 70$ ms, 10% of the piezo-charge has been neutrallized by the opposite polarity pyro-charge. For $t > 117$ ms, the pyro-charge so dominates the transducer output that the apparent pressure becomes negative even though the real pressure has been held constant at 3.5×10^5 Pa. This transducer can be used for satisfactory dynamic pressure measurements if $t < 70$ ms.

We have demonstrated two types of temperature compensation. For $t \geq \tau$, an active temperature compensation circuit is used. For $t \ll \tau$, temperature effects are avoided by adjusting the thickness of the transducer.

In other published work [8,9], we have reported the linearity of the piezoelectric response up to 1.8×10^7 Pa (2600 psi). At higher pressures, non-linear response is due to a decrease in the compressibility of PVDF as pressure increases. Calibration of the gage in the non-linear regime is being carried out.

REFERENCES

1. M. G. Broadhurst, G. T. Davis, J. E. McKinney and R. E. Collins, J. Appl. Phys. 49, 4992 (1978).
2. R. G. Kepler and R. A. Anderson, J. Appl. Phys. 49, 4490 (1978).
3. R. J. Shuford, A. F. Wilde, J. J. Ricca, and G. R. Thomas, Polym. Eng. Sci. 16, 25 (1976).
4. N. Takahashi and A. Odajima, Ferroelectrics 32, 49 (1981).
5. Michael Marcus, Ferroelectrics 40, 239 (1982).
6. M. G. Broadhurst and G. T. Davis, Ferroelectrics 32, 177 (1981).
7. A. S. DeReggi, S. Edelman, S. C. Roth, National Bureau of Standards Internal Report, NBSIR 76-1078, June 1976.
8. A. J. Bur and S. C. Roth, National Bureau of Standards Internal Report, NBSIR 84-2862, April, 1984.
9. A. J. Bur and S. C. Roth, J. Appl. Phys. 57, 113 (1985).
10. J. M. Kenney and S. C. Roth, J. Res. Nat'l. Bur. Stds. 84, 447 (1979).
11. M. G. Broadhurst, W. P. Harris, F. I. Mopsik, and C. G. Malmberg, in Electrets, Charge Storage and Transport in Dielectrics, M. M. Perlman, Ed., Electrochemical Soc., Princeton, NJ, p. 492 (1973).
12. Conduction of Heat in Solids, by H. S. Carslaw and J. C. Jaeger, Oxford University Press, Amen House, London, 1948, p. 79.

This work has been supported in part by the U. S. Air Force, Eglin AFB, Florida and by the Defence Nuclear Agency.

LABORATORY EVALUATION OF AN NBS POLYMER SOIL STRESS GAGE

Riley M. Chung and Anthony J. Bur
National Bureau of Standards, Gaithersburg, Maryland

and

J. R. Holder
Eglin Air Force Base, Florida

ABSTRACT

The NBS polymer gage, which is made of thin sheets of polyvinylidene fluoride (PVDF) sandwiched between polycarbonate sheets, has been tested extensively at the National Bureau of Standards to evaluate its ability to measure soil dynamic stresses due to blast loading.

The present gage design, which has an aspect ratio of 0.024 and a modulus ratio of at least 35 provides an excellent dimensional and physical characteristics to assure good soil stress measurement. A linear relationship between input stress and gage output has been established for stress levels up to 2000 psi. This relationship is not affected by the location of gage placement, the thickness of the protective cover, the frequency of impact load, and the length of cable used for signal meaurement.

INTRODUCTION

Many studies have been conducted in the past to develop stress gages to properly measure soil stresses. Most of the research was focused on gage development for measurement of static loads, e.g., the work reported in refs. 1, 8, 6, 14, 17, 10, 18. A very comprehensive review and summary of these studies is provided in ref. 18. In recent years, gage design has also concentrated on its capability to measure stresses due to impact and dynamic loads such as result from blasting. Examples are listed in refs. 2, 4, 9, 11, and 16.

A number of factors should be considered in gage design. They are the aspect ratio, the ratio of total gage thickness, T, to total gage diameter, D; the modulus ratio, the ratio of gage modulus, E_g , to soil modulus, E_m ; gage deflection and arching; stress distribution over the gage surface; lateral stress rotation; methods of gage placement; methods of gage calibration; necessity for temperature compensation; capability of the gage to resist adverse environments; natural frequency of the gage; inertia force due to the weight of the gage; and gage response time.

The most important factors are the aspect ratio, the modulus ratio, and the uniformity of stress distribution over the gage surface. A Waterways Experiment Station study in 1944 recommended an aspect ratio of less than 1/5 and this criterion has since been followed by the gage designers. Studies have also been conducted to establish the relationship between the aspect ratio and the modulus ratio (15, 12). Figure 1 shows a revised plot from Loh's work (12) where a typical Poisson's

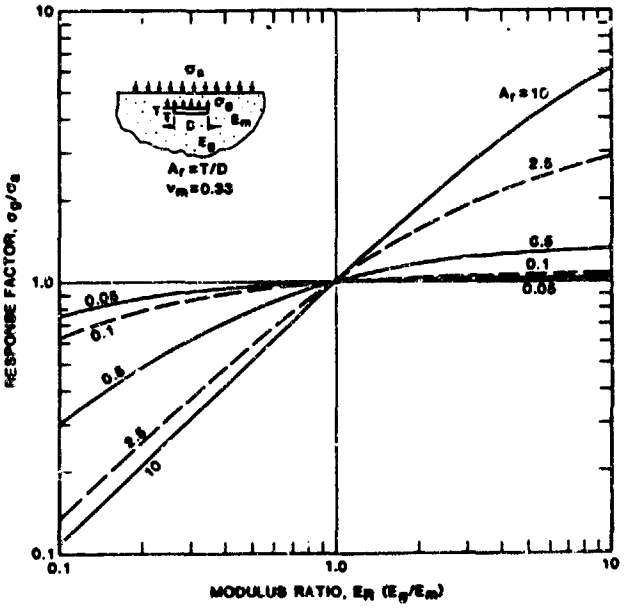

Figure 1 Theoretical Soil Stress Gage Response (Ref. 12)

ratio for sandy soils is used in the formulation. The figure suggests that good stress measurement can be expected from a gage with an aspect ratio less than 1/10 and a modulus ratio greater than unity. Research on stress uniformity over the gage surface led to the recommendation that the sensitive area of the gage be less than 45 % of its total area to avoid stress over-registration (13). Another factor influencing the stress distribution over the gage surface is the possibility of measuring point loads due to the particulate nature of soil. A criterion requiring the ratio of active gage diameter to mean soil grain size to be at least 10 was suggested in ref. 18 to keep the error from point loads to less than 3%.

At present, two types of gages are commonly used for in-situ soil stress measurement during blast testing: The WES-SE gage is a diaphragm type gage with an aspect ratio of about 0.1 (11) and the SRI gage is a high modulus and low aspect ratio gage consisting of a piezoresistance foil made of ytterbium (9). The NBS stress gage uses different principles for its operation than either of these two gages. These principles and the gage calibration and testing are briefly presented in the following sections.

THE NBS POLYMER GAGE

The NBS gage is made of a polymer material called polyvinylidene fluoride (PVDF). Properties of the PVDF material and methods of gage fabrication are described in a companion paper by the second author (3). Several versions of the gage were developed and tested during the program. The final gage design is shown schematically in figure 2, and a photograph of the gage in figure 3. It consists of two layers of PVDF sheets, each of them contains an active area 10 mm in diameter. The overall diameter of the gage is 15 mm. Both aluminum and indium are deposited over the PVDF surfaces as electrodes and a thermocouple is placed in between the two PVDF sheets before they are epoxied together. Two polycarbonate sheets are used to cover the gage surface to improve its ruggedness. Overall thickness of the gage is about 0.35 mm.

An assessment of this gage is made with respect to the important factors listed earlier. The gage, with T = 0.35 mm and D = 15 mm, has an aspect ratio, T/D, of 0.024. Using a gage modulus of 2 x 10+6 psi (1.4 x 10+4 MPa) and a soil modulus of 5.7 x 10+4 psi (4 x 10+2 MPa), typical of sandy soil (determined considering impulse load condition), a modulus ratio of 35 is obtained. Referring to figure 1, it is seen that this design offers excellent dimensional characteristics that assure good stress measurement. The ratio between the sensitive area of the gage and the total gage area is 0.44 which is less than 0.45 and is satisfactory. It should be noted that the dimension of both the sensitive area and the total area of the gage has been fixed for the convenience of laboratory soil testing. These dimensions can be made to any size and any shape to fit the specific need for which the gage is used. Thus, a ratio much less than 0.44 can be accomplished with no difficulty. The ratio between the diameter of the active area and the mean grain size (0.30 mm) for the fine to medium sandy soil used in testing is 33, which far exceeds the value of 10, recommended in ref. 18.

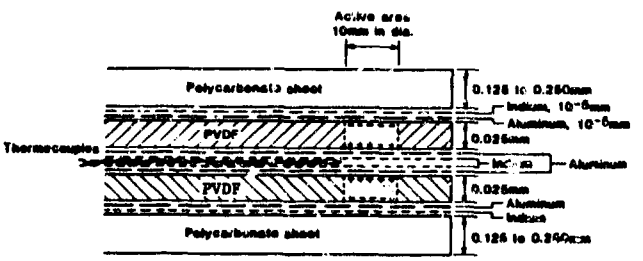

Figure 2 Schematic View of The Present NBS Polymer Gage

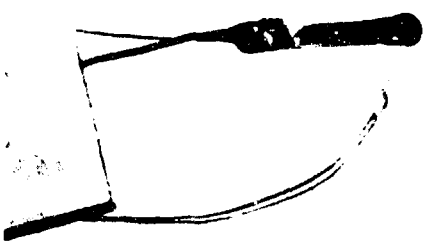

Figure 3 An NBS Polymer Gage

The gages were fabricated in the laboratory of NBS Polymers Division. Pyroelectric characteristics of the gage have also been studied in detail to develop a compensation amplifier for temperature compensation. Methods for temperature measurement and hydrostatic gage calibration using a drop test set-up are presented in the companion paper by the second author (3). It should be noted that temperature compensation is important when the gage is used for air pressure measurement due to blasting. However, as will be shown later, temperature correction is not required for the stress level tested (up to 2000 psi) when the gage is used for dynamic soil stress measurement since the temperature rise in an embedded gage is very small (about 0.6 °F).

GAGE TESTING IN GEOTECHNICAL LABORATORY

A typical sandy soil obtained from the future field test site at Eglin Air Force Base, Florida was used in testing and is referred to as Florida sand. It is reddish brown in color and was slightly moist when received with an average moisture content of 6.0 %. The soil can be described as fine to medium sand, trace to some fines or SP-SM under the Unified Soil Classification System. It has a maximum dry density of 114.5 pcf at an optimum moisture content of 12.5 %.

A number of test variables were included in the test program including gage type, gage location, type of protective cover, cable length, frequency, and mold insulation. An overall view of the test set-up is given in figure 4 and a close-up view is given in figure 5. Figure 6 presents a schematic drawing of the test cylinder and its accessories.

Two arrangements were used to test gages in the test cylinder. In the first arrangement, a concrete pedestal was placed into the test cylinder and the gage was then inserted through a slot cut in the test cylinder to rest on the surface of the pedestal. The space above the pedestal was filled with Florida sand and compacted to the top of the test cylinder for testing. In the second arrangement, Florida sand was poured into the test cylinder and compacted to the slot level to receive the gage. The gage was then covered with additional sand as in the first arrangement. The compacted density of the Florida sand was about 95 pcf.

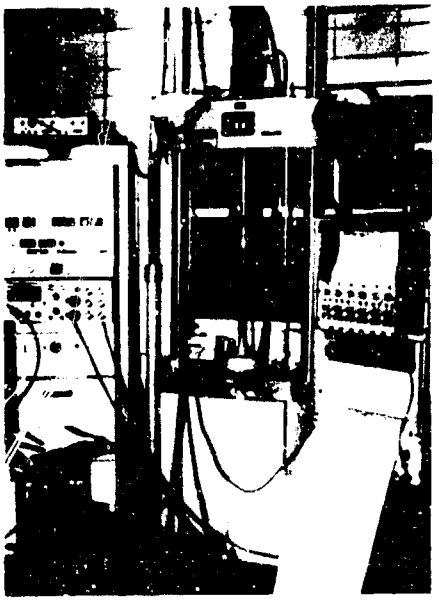

Figure 4 Overall View of NBS Polymer Gage Test Set-up

An impact load consisting of a half cycle inverted sine waveform was dialed in through the use of an MTS testing system. The magnitude of the input load as well as the specimen deformation were recorded on channels 3 and 4 of a strip chart recorder. Refer to figure 5, the gage output was connected to the input port of a compensation amplifier, which is the aluminum box shown next to the test specimen. Outputs from the compensation amplifier, which include the temperature measurement from the thermocouple, and the corrected and uncorrected gage responses with respectto temperature, were recorded on channels 5, 1, and 2, respectively of the same recorder. A typical strip chart output from an impact load test is shown in figure 7.

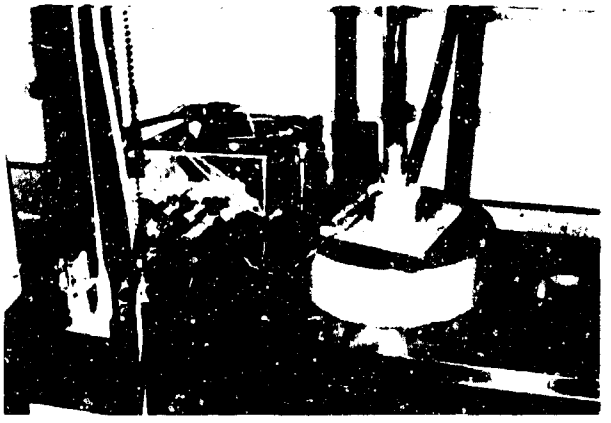

Figure 5 Close-up View of NBS Polymer Gage Test Set-up

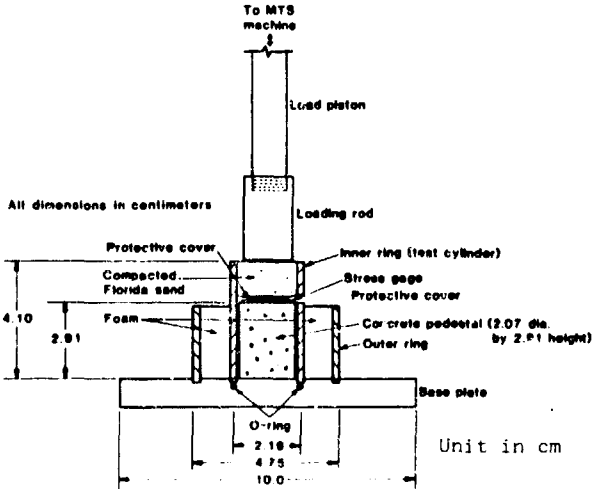

Figure 6 Schematic Drawing of The Test Cylinder and Its Accessories

In most tests, loading-unloading-reloading characteristics of gage response to impact loads were studied. The task was carried out by applying impact loads to the test specimen in successively greater increments up to 2000 psi. Unloading was conducted by reducing the impact load magnitude in decrements to an equivalent stress level close to 20 psi. Reloading was conducted in the same manner as in initial loading. Most of the impact loads were applied at a frequency of 50 Hz; however, the frequency was varied between 5 and 40 Hz in some cases to study the possible effect on gage response.

Initial tests were conducted with the test cylinder wrapped with insulation tape to evaluate its possible effect on temperature rise and therefore the gage response. Some tests were also conducted using a 150-ft long co-axial cable to find out whether the length of cable (capacitance) had any effect on the gage signal output. Several types of gages, combined with a number of gage protection measures were experimented in the test program which led to the final gage design as shown in figures 2 and 3. Details of these studies are documented in an NBS report entitled "Development of an NBS Polymer Gage for Dynamic Soil Stress Measurement."(5)

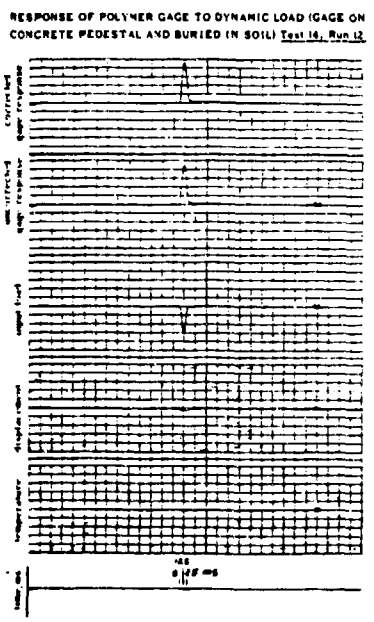

Figure 7 Typical Strip Chart Output

TEST RESULTS

Figures 8 and 9 show typical plots of test results. Plots presenting the results of other test variables studied are included in the report cited above. It was found that a linear relationship between the input stress and the gage output signal can be established throughout the stress range used in tests. Although corrected gage output signals were used in plotting, the strip chart outputs in figure 7 actually indicate that the difference between the corrected and uncorrected signals is very small. This is to say that for soil stress measurement, a gage without thermocouple can be used to yield equally satisfactory results. Figure 8 plots all the data obtained from impact load tests with a frequency of 50 Hz. For each strip chart output as shown in figure 7, one data point in figure 8 was plotted. Note that test 42 was conducted by having the gage placed on the concrete pedestal, whereas the other three tests were carried out having the gage embedded in soil to simulate the free field condition. Results of the same tests conducted using impact loads at various frequencies are given in figure 9. Frequencies at 5, 10, 20, 30, 40, and 50 are noted and show no effect on the linear relationship established in the figure.

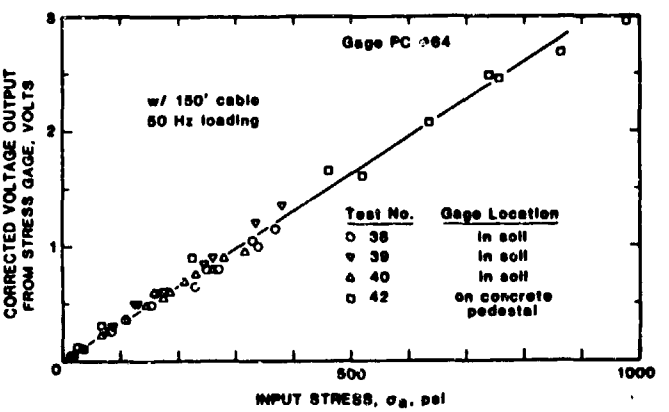

Figure 8 NBS Polymer Gage Test Result, Gage PC #64

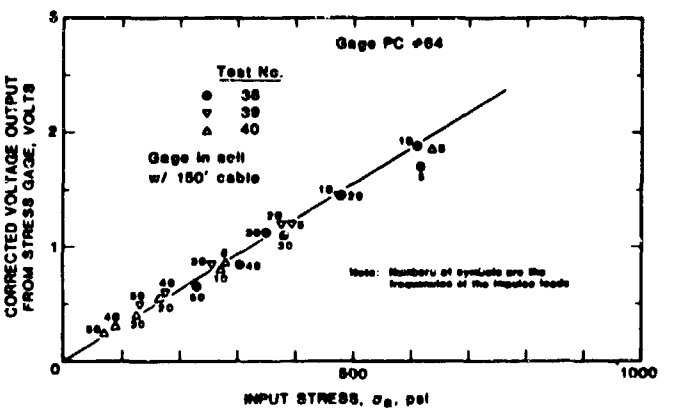

Figure 9 NB Polymer Gage Test Result, Gage PC #64 (Effect of Frequency)

We should mention that four gages, PC #49, 54, 58, and 64, were tested in the laboratory to establish the relationship between voltage output and stress similar to that shown in figures 8 and 9. These gages were used in a field test program conducted at the Eglin Air Force Base, Florida in June, 1984. The field test program and results are presented in a companion paper at this conference.(7)

SUMMARY AND CONCLUSIONS

The following summary and conclusions may be advanced from the results of the test program:

1. A gage made of two thin sheets of PVDF material, a thermocouple, and two thin polycarbonate sheets for gage surface protection, has been developed to reliably measure dynamic soil stresses up to 2000 psi due to impact load.

2. The gage design, which has an aspect ratio of 0.024 and a modulus ratio of at least 35, satisfies dimensional and physical requirements for accurate stress measurement.

3. The gage design further offers the flexibility and feasibility to build the gage with any aspect ratio and shape required for its specific use.

4. The pyroelectric nature of the gage has been considered in designing the gage. Temperature correction is necessary when air pressure measurement is of interest. Gage signal output does not need to be compensated for temperature if the gage is embedded in soil for stress measurement (to the stress level tested in the program) because the temperature rise in the gage is small.

5. A linear relationship between the input stress and gage output can be established through the data points derived from the loading-unloading-reloading sequences of specimen testing. This relationship is not affected by the placement of the gage (whether on a concrete pedestal or freely in soil) nor by the frequency of the impact loads applied to the specimen.

REFERENCES

1. Abbott, P.S., Simmons, K.B., Reiff, C.M.,and Mitchell, S., "Recent Soil Stress Gauge Research," Proc. Int. Sym. on Wave Propagation and Dynamic Properties of Earth Materials, U. of N.M., 1967

2. Baum, N. and Kovarna, J., "Dynamic Soil Stress - Its Calculation and Measurement," Contract Report AFWL-TR-81-89, U. of N. M., 1982

3. Bur, A. J. and Roth, S., "A Temperature Compensated Polymer Pressure Gage," This conference

4. Burcham, R. L., "Evaluation of Piezoelectric Polymer Soil-Stress Gage," Contract Report to AFWL, U. of N. M., 1974

5. Chung, R. M., Bur, A. J., and Reasner, E., "Development of an NBS Polymer Gage for Dynamic Soil Stress Measurement," An NBSIR publication, in preparation

6. Hamilton, J.J., "Earth Pressure Cells: Design Calibration and Performance," Tech. Paper 109, Division of Building Research, NRC, Canada, 1960

7. Holder, J. R., Chung, R. M., and Bur, A. J., "Field Evaluation of the Polymer Soil Stress Gage," This conference

8. Ingram, J.K., "The Development of a Free Field Soil Stress Gauge for Static and Dynamic Measurements," ASTM, STP 392, 1965

9. Keough, D., Decarli, P., and Rosenberg, J.T., "Development of a High Modulus, Piezoresistance Gage for Dynamic In-situ Soil Stress Measurement," Contract Report to DNA, Proc., Conf. on Instrumentation for Nuclear Weapons Effects, 1982

10. Krizek, R.J., Farzin, M.H., Wissa, A.E.Z., and Martin, R.T., "Evaluation of Stress Cell Performance," J. GED, ASCE, Vol. 100, GT12, 1974

11. Labreche, D., Beam, J., Baum, N., and Boor, D., "Soil Stress Gage Placement and Testing," Contract Report AFWL-TR-80-126, U. of N.M., 1981

12. Loh, Y.C., "Internal Stress Gauges for Cementitious Materials," Proc. Society for Experimental Stress Analysis, Vol. XI, No. 2, 1954

13. Monfore, G.E., "An Analysis of the Stress Distribution In and Near Stress Gauges Embedded in Elastic Solids," Structural Laboratory Report SP26, Bureau of Reclammation, 1950

14. Selig, E.T., "A Review of Stress and Strain Measurement In Soil," Proc., Sym. on Soil-Structure Interaction, Tucson , AZ, 1964

15. "Soil Pressure Cell Investigation," Tech. Memo 210-1, Waterways Experiment Station, Vicksburg, MS, 1944

16. Tracy, H. A., "Piezoelectric Polymer Transducers," Contract Report to The Air Force Armament Test Laboratory, 1983

17. Triandafilidis, G.E., "Soil-Stress Gauge Design and Evaluation," J. Testing and Evaluation, ASTM, 1974

18. Weiler, W.A. and Kulhawy, F.H., "Factors Affecting Stress Cell Measurements in Soil," J. GED, ASCE, Vol.108, GT12, 1982

Field Evaluation of the Polymer Soil Stress Gage

J. Rick Holder

USAF Armament Laboratory
Vulnerability Assessments Branch
Eglin AFB, Florida 32542-5000

and

R. M. Chung and A. J. Bur
National Bureau of Standards
Gaithersburg, Maryland

ABSTRACT

The feasibility of a new type of pressure gage to measure dynamic soil stresses was evaluated. The pressure gage is made from thin sheets of polyvinylidene flouride (PVDF) sandwiched between polycarbonate sheets. Tests were conducted to measure dynamic soil stresses and stresses on buried structures resulting from the detonation of buried high explosive charges. The work was conducted by the laboratories of National Bureau of Standards, under the sponsorship of the Air Force Armament Laboratory, Eglin AFB Florida. This paper presents the field test results of this gage when subject to high intensity blast loadings. The paper was prepared in conjunction with those being presented by Dr Riley Chung and Dr Anthony Bur entitled "Laboratory Evaluation of an NBS Polymer Soil Stres Cage," and "Development of a Polymer Pressure Gage with Temperature Compensation," respectively.

INTRODUCTION

Background

The Air Force Armament Laboratory (AFATL) has responsibility within the Air Force for the lethality evaluation of conventional munitions against ground and air targets. Hardened, high value targets such as radar sites, airfields, and command and control centers represent high priority threats in a tactical scenario, and are consequently of considerable importance in current Air Force munition development programs. Part of the engineering knowledge necessary to evaluate the lethality of conventional munitions against high value targets includes near-field explosive blast effects against concrete structures. Problems presently exist with the methods of measuring blast impulse and pressures on underground structures. For example, gages must be placed on mounting brackets inserted in holes drilled through the structure wall. As a result, the structure is weakened. A need exists to develop a flush mounted pressure gage that permits the measurement of blast loads on a buried structure. In turn this will allow accurate vulnerability evaluations to be made of structural targets attacked with massive unitary warheads without weakening the targets with the instrumentation.

In response to this need, the USAF Armament Laboratory and the National Bureau of Standards jointly developed a flush mounted pressure gage to measure dynamic blast pressure in a soil medium, as well as at a soil and concrete interface. The polymer gage is shown in figure 3. It is made from four sheets of PVDF which have been laminated together using epoxy. The inner two sheets (12.0 μm thick) contain active areas on which aluminum electrodes have been deposited. The outer two layers (25.0 μm thick) serve as protection for the inner two so that the gage can be used in environments requiring mechanical ruggedness. The overall thickness of the transducer is approximately 0.35 mm. Prior to lamination the electroded regions are made piezoelectrically active by poling them at room temperature with an electric field of 2.0 mv/cm. The active areas are then laminated face-to-face so that the polarization vectors in each element point in opposite directions. In this bilaminate pattern, the ground electrodes are on the exterior surface and the inner electrodes carry the signal potential. This paper describes the results of field testing the gage at Eglin AFB range facilities.

Objective and Approach

The objective of the field tests was to evaluate the gage in the fields environment when dynamically loaded. The loading of the gages was accomplished with explosive charges detonated at different distances from the emplaced gages. Two PVDF gages were attached to a buried concrete wall and two were placed in free soil near the explosive charge. All test gages were calibrated in the laboratory up to 1000 psi. With this limitation on the dynamic range, the field tests were designed to encompass pressure loading up to 500 psi.

EXPERIMENTAL PROCEDURES

Test Configuration

Two successful field tests took place. Both tests took place in the same geographic location. The test setups are shown in Figures 1 and 2. Both figures show a plan and side view of a buried 1/3 scale reinforced concrete structure. The figures

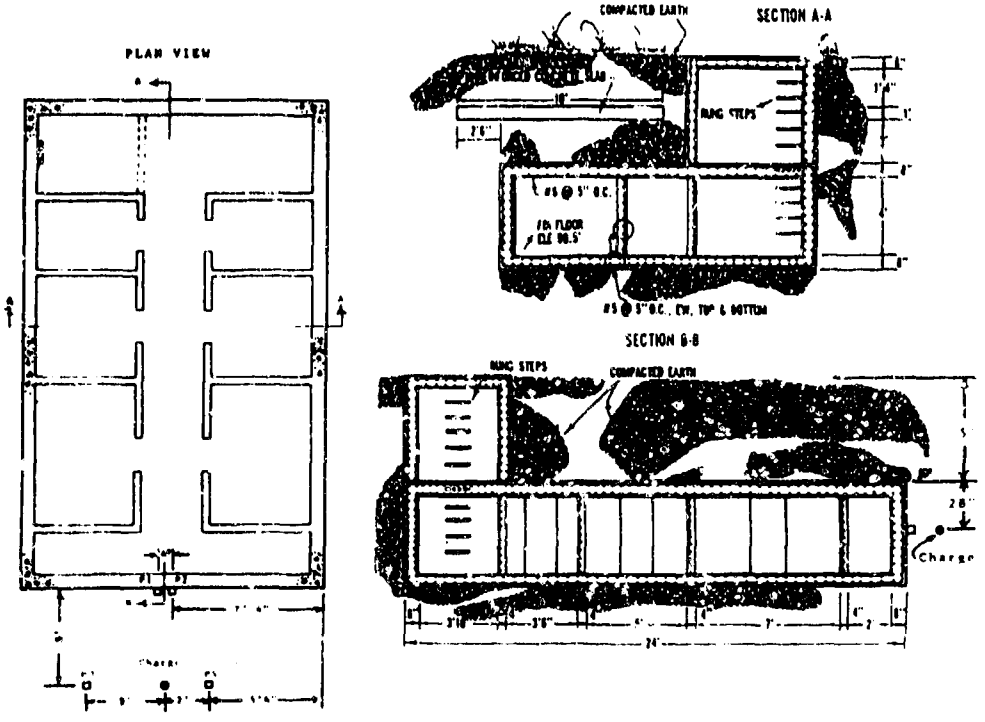

Figure 1 Gages and charge location for test 1

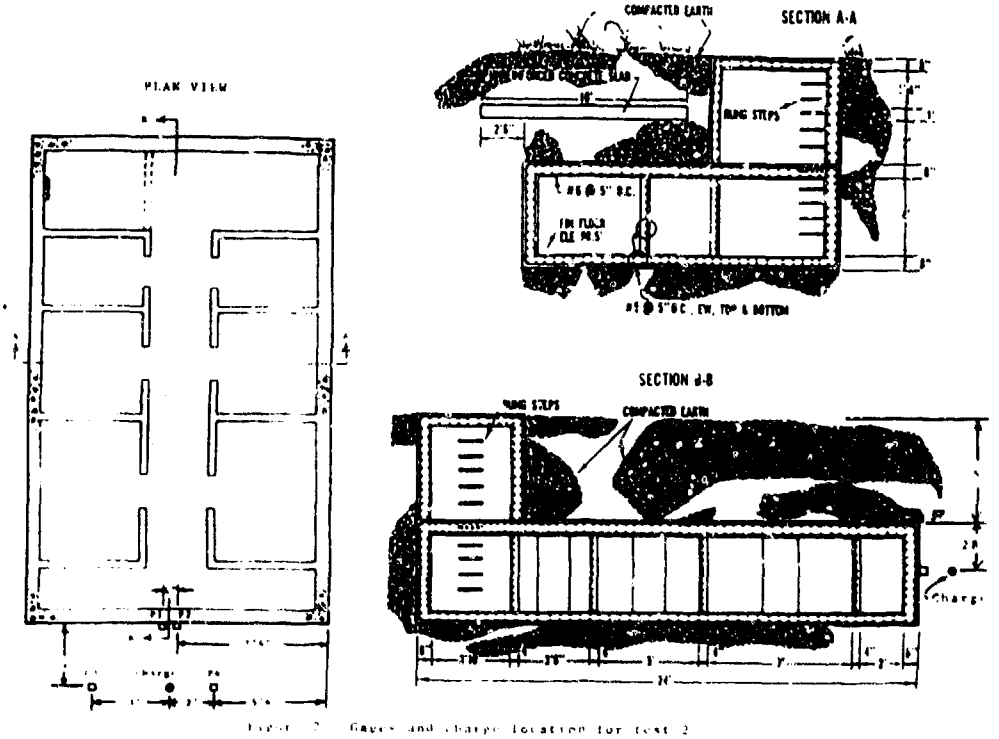

Figure 2 Gages and charge location for test 2

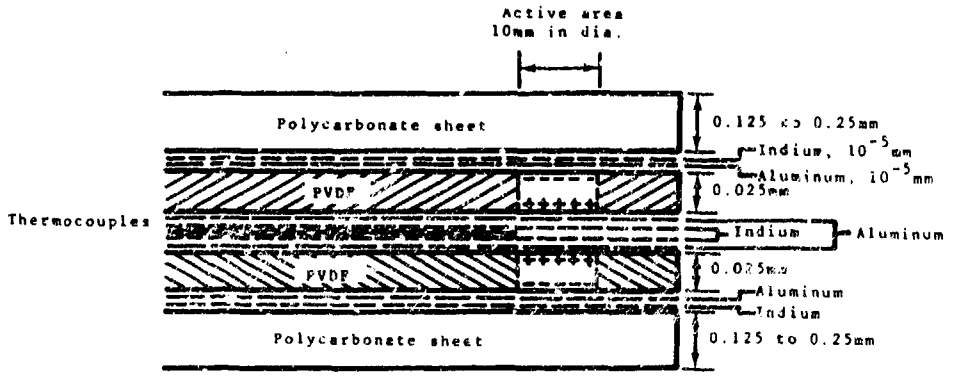

Figure 3. Construction drawing of typical gage

Photo 1. Two gages installed on concrete wall

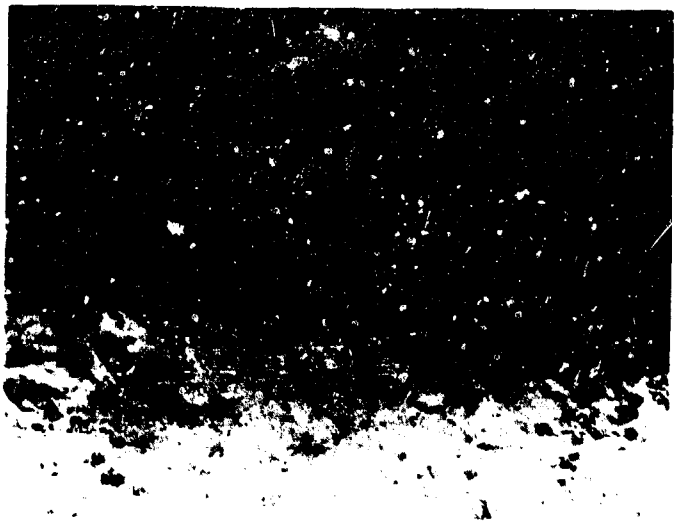

Photo 2. Test layout

show the different standoffs each gage has in respect to the charge. All gage's sensing elements were buried at the same depth, 28.0 inches below the top surface of the buried structure. The 5 foot compacted fill over the structure in the test area was removed so as to maintain uniform depth of burial. The gage sensing elements were positioned roughly perpendicular to the charge. Thus reflective pressure was expected. Four gages were used during each test. Two were placed in the free field, and two were attached to the exterior wall of the buried concrete structure. The two gages placed in the soil were positioned to the proper depth and hand compacted to allow free field movement. The remaining two gages were attached to exterior wall of the concrete structure by positioning to the proper depth and taping them directly to the wall with reinforced nylon strapping tape. The sensing element of P1 gage was placed 2.0 inches to the left of a perpendicular line drawn from the charge to the concrete wall and the sensing element of P2 gage was 2.0 inches to the right of the same line. The soil was composed of fine, uniform sand with a void ratio of approximately 0.7 and a unit weight of approximately 104.0 pounds per cubic foot. The sand was dry with some moisture during the day of the tests. Swiss Hammer tests indicated the concrete wall compressive strength was 6800 psi. Photo 1 shows the two gages installed against the concrete wall. The soil was carefully backfilled and brought back to normal compaction conditions before each test. Photo 2 shows the layout of the test. The hole in the soil shows the position of the charge.

Explosive Charge

All charges were fabricated by forming composition C-4 explosive into a sphere weighing two pounds. Each charge's center of gravity was positioned at a depth of 28.0 inches (same level as the sensing elements of the gages).

Instrumentation

The four gages were attached to RG-62 coaxial cable which ran approximately 300 feet to the following recording sequence:

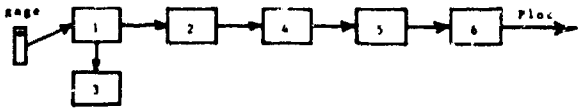

1. PCB 463A Charge Amplifier
2. VR 3700B-Wide Band Group II-Frequency Modulator Tape Recorder
3. Bell and Howell 5-133 Oscillograph
4. Hewlett Packard 5180 Waveform Recorder
5. Hewlett Packard 9825 Computer
6. Hewlett Packard four-pen plotter

When the charge was detonated a loading was placed through the soil and impacted the concrete wall. The gage reacted from being compressed causing an electrical signal to move through the cable to the charge amplifier. At this point, the signal is amplified and moved to the frequency modulator and oscillograph. The oscillograph allows a quick look at the wave form. The frequency modulator stores the signal on antilog tape. At this point, the signal is transferred from the tape to the computer where its software calculates the pressure-time history curve and impulse. Peak pressure and impulse are also determined by the computer program. This data is then plotted for permament record.

Test Results

Before each test two pressure measurements were predicted for each polymer gage location. The predictive equations used were developed at Southwest Research Institute (Reference 3) and US Army Engineer Waterways Experiment Station (Reference 4). The following tables indicate the pressures predicted and the pressures measured at the individual polymer gage location.

TEST 1

Gage No	Predictive Pressure (PSI) SWRI	WES	Polymer Gage (PSI)
P1	20	17	89
P2	20	17	42
P3	102	102	89
P4	375	439	413

TEST 2

Gage	Predictive Pressure (PSI)		Polymer Gage
NO	SWRI	WES	(PSI)
P1	41	37	40
P2	41	37	29
P3	102	102	101
P4	375	439	*

* Gage saturated, No data.

SUMMARY and CONCLUSIONS

1. The test results indicate that the polymer gages perform well. As presented in the tables, the pressures obtained are reasonably close to predicted

values for the soil type, standoff, depth of burial, and charge weight.

2. Figure 4 indicates the relationship between peak stress and scaled range for free-field data and interface pressure data on the concrete wall. The graph of the test data falls in the region of each of the predictive equation curves using the same criteria. Therefore the accuracy of the polymer gages is comparable with the accuracy of the PCB gages used by Southwest Research Institute and the WES-SE gages used by US Army Engineer Waterways Experiment Station.

3. The gage design offers unlimited use as a flush mounting gage. The gage was extremely easy to install and would result in no structural damage to any structure due to installation. Placement of the gage in free-field was unconstrained. No special mounting support was required. The gage design further offers the flexibility and feasibility to build the gage with any aspect ratio and shape required for its specific use.

4. The tests showed that the gage's construction was rugged. Thus allowing the gages to be dropped, bent, and handled not so carefully yet continue to be operationable.

5. The laboratory tests indicate the polymer gage will be as operationable in wet soil as it is in dry soil.

6. The polymer gage has a fast response time and produces a clear signal. Thus the gage performs well in the dynamic soil loading case for both free-field and interface with concrete measurements.

7. The polymer gage is more flexible, easier to install and use, and rugged in design than existing gages used for the same purpose.

8. Finally, by no means do two field tests indicate final conclusions in regards to gage accuracy. However the gage results from the field tests were encouraging. Additional tests should be conducted including comparison of the polymer gage to other ground shock gages, as well as expanding the dynamic range of the measurements.

REFERENCES

1. Bur, A.J. and Roth, S.C., "Development of a Polymer Pressure Gage with Temperature Compensation," National Bureau of Standards, Gaithersburg, Maryland, April 1984.

2. Chung, R.M., Bur, A.J., and Holder, J.R., "Laboratory Evaluation of an NBS Polymer Soil Stress Gage," This conference.

3. Westine, P.S. and Friesenhahn, G.J., "Free-Field Ground Shock Pressures from Buried Detonations in Saturated and Unsaturated Soils," presented at the interaction of Non-Nuclear Munitions with Structures Symposium, 10-13 May 1983, US Air Force Academy, Colorado.

4. Drake, J.L. and Little, C.D. Jr., " Ground Shock from Penetrating Conventional Weapon," presented at the interaction of Non-Nuclear Munitions with Structures Symposium, 10-13 May 1983, US Air Force Academy, Colorado.

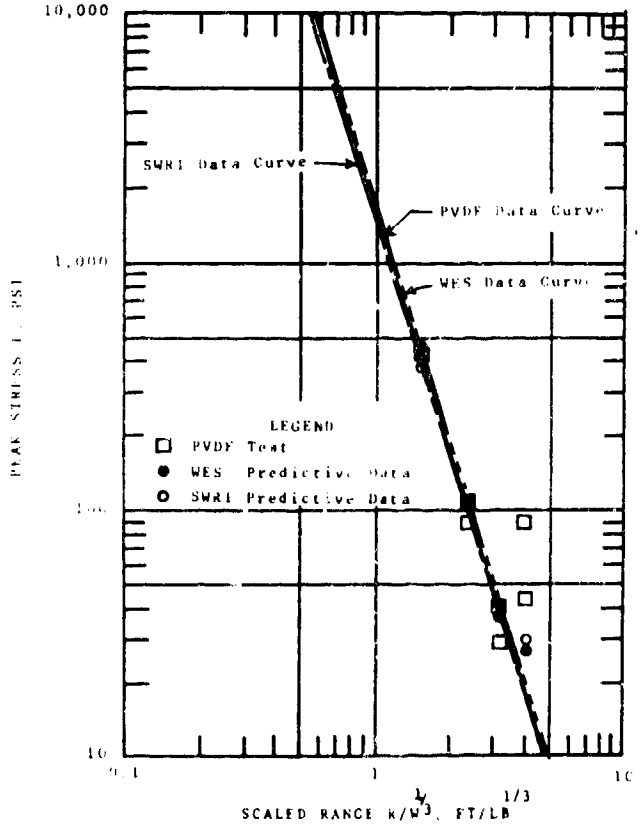

Figure 4 Relation between peak stress and scaled range free-field data and interface pressure data on the concrete wall.

ACCURACY OF ANALOG-TO-DIGITAL CONVERTERS USED FOR BLAST DATA

Gary P. Ganong

R and D Associates
Albuquerque, New Mexico

ABSTRACT

Previous analyses of the accuracy of analog-to-digital converters by Stough and this author used simulated gauge records for a particular record from the MISERS BLUFF test series. To increase our understanding of the accuracy of converters, accelerometer records from a small gauge calibration test have been analyzed. This paper will show that 12 and 16 BIT systems can produce very high accuracies, using only a small percent of the full scale range of the system. Eight BIT systems may produce as much as 10 percent error in final displacement, using the entire full scale range. Six BIT systems produce very large errors in velocity and displacement even when the entire full range of the system is used.

INTRODUCTION

In recent years, some organizations have collected blast data in digital form directly in the field, rather than converting analog records in a laboratory. This permits experimenters to quickly process and display their results. Data systems can be adjusted and follow-on tests can proceed more rapidly.

Previous analyses of the accuracy of analog-to-digital converters by Stough (Ref. 1) and this author (Ref. 2) used simulated gauge records for a particular record from the MISERS BLUFF test series. To increase our understanding of the accuracy of converters, four accelerometer records from a small gauge calibration test have been analyzed. These records were provided to me by Mr. R. C. Baer of the University of New Mexico and are shown in Figures 1 through 4.

All successive approximation analog-to-digital (A/D) converters have an inherent quantization error of ±½ least significant BIT(LSB). The LSB is defined as the full scale range divided by 2 to the power of the number of BITS. Thus, a six BIT system has an inherent quantization error of ±0.78%. This assumes that the experimenter can exactly predict the necessary range of his data and use 100% of the full scale range. If he uses only 10% of the full scale range, his error is ten times larger (±7.8%).

When accelerometer records are integrated to obtain velocities and displacements, the errors produced can far exceed the inherent quantization errors. Stough (Ref. 1) analyzed a simulated MISERS BLUFF gauge record and incorrectly concluded that only a 14 BIT word size would be sufficiently accurate for single and double integration of blast data. This author analyzed a simulation of the same record (Ref. 2) and concluded that 5% accuracy in displacements is possible from 8 BIT accelerometer data, using 80% of the available range.

ANALYSIS OF FOUR GAUGE RECORDS

The previous analysis assumed that experimenters would be willing to use 80% of the full scale range. It was also based on the use of a simulated gauge record. It did not answer two questions: Does the conclusion hold for real gauge records? How much of the full scale range must be used to get adequate results?

To answer these questions, this author analyzed the four records provided by Baer. The records were digitized on a computer with 40 BIT precision, and then truncated to achieve desired accuracy. In equation form, this operation can be written:

Digital Value = Digital Increment x Integer (Analog Value/Digital Increment +½)

The value of the digital increment was the full scale range divided by 2 to the power of the number of BITS: 1000 data pairs were used for each record. For each record, the errors were computed for 6, 8, 12, and 16 BITS and for ratios of signal amplitude to full scale range of 0.01 to 0.99.

RESULTS

Tables 1, 2, and 3 summarize the results of the error analysis. The values in the tables were obtained from 72 graphs of percent error vs. signal amplitude. Since the tables were assembled from graphical data rather than printed values, only one significant figure is used for each value. Percent error does not monotonically decrease as the ratio of signal amplitude to full scale range increases. There are many local maximums and minimums for each record. The tables do not show local minimums, but instead show the maximum error when at least that fraction of the full scale range is used.

Peak velocity (Table 1) was always adequately computed by 12 and 16 BIT systems. Eight BITS provided sufficient accuracy (4% error) when 50% of the full scale range was used. Six BITS was always unsatisfactory for record MN08.

Peak displacement (Table 2) had only small errors for 12 and 16 BIT systems. Eight BIT systems were adequate when 70% of the full scale range was used. Six BIT systems could not provide sufficient resolution for records MN07 and MN08.

Final displacements (Table 3) were the most severe test of A/D systems. Twelve and 16 BIT systems always proved to be satisfactory. Eight BITs produced 10% error for record MN07 even when the entire full scale range was used. Six BIT systems failed to provide adequate resolution for records MN07, MN08, and MN17.

CONCLUSIONS

Assuming that the four selected records are typical of blast applications, one could draw the following conclusions:

1. The records from 6 BIT systems cannot be singly and doubly integrated with sufficient accuracy to adequately describe velocities and displacements.

2. When 70% of the full scale range is used, accurate peak velocities and peak displacements can be derived from 8 BIT accelerometer data.

3. Accurate velocities and displacements can be obtained from 12 BIT systems even when as little as 10% of the full scale range is used.

REFERENCES

1. T. A. Stough, "Effect of Digital Word Size on Precision of Data Recovery From Field Instrumentation," DNA 5510T, November 1980, approved for public release, distribution unlimited.

2. G. P. Ganong and S. L. Humphreys, "Accuracy of Analog-to-Digital Converters Used for Blast Data," 8th Military Applications of Blast Simulation Symposium, June 1983, approved for open publication.

TABLE 1
Percent Errors In Peak Velocity

Number of Bits	Record	Fraction of Full Range Used				
		0.9	0.7	0.5	0.3	0.1
		% Errors in Peak Velocity				
6	MN 07	2.	2.	2.	2.	2.
	MN 08	20.	30.	50.	60.	60.
	MN 10	1.	1.	1.	1.	10.
	MN 17	2.	2.	2.	6.	40.
8	MN 07	0.2	0.3	0.8	2.	2.
	MN 08	1.	2.	4.	8.	60.
	MN 10	0.4	0.4	0.4	0.4	1.
	MN 17	1.	1.	1.	1.	5.
12	MN 07	0.02	0.02	0.02	0.05	0.08
	MN 08	.01	.01	.01	.01	1.
	MN 10	.01	.02	.02	.03	.07
	MN 17	.02	.03	.06	.06	0.2
16	MN 07	.0006	.001	.001	.002	.005
	MN 08	.002	.002	.002	.006	.02
	MN 10	.0005	.001	.002	.002	.008
	MN 17	.001	.002	.002	.002	.002

TABLE 2
Percent Errors In Peak Displacement

Number of Bits	Record	Fraction of Full Scale Range Used				
		0.9	0.7	0.5	0.3	0.1
		% Errors in Peak Displacement				
6	MN 07	90	100	100	300	300
	MN 08	10	20	40	50	50
	MN 10	3.	3.	7.	40	100
	MN 17	2.	2.	4.	10	50
8	MN 07	2.	4.	10.	20.	200
	MN 08	1.	1.	2.	4.	40.
	MN 10	2.	2.	2.	3.	7.
	MN 17	1.	1.	2.	3.	8.
12	MN 07	0.1	0.1	0.1	0.1	1.
	MN 08	0.01	0.01	0.01	0.01	0.05
	MN 10	0.04	0.1	0.1	0.1	0.4
	MN 17	0.02	0.05	0.07	0.07	0.2
16	MN 07	.006	.006	.006	.01	.03
	MN 08	.002	.003	.003	.005	.01
	MN 10	.002	.002	.008	.008	.04
	MN 17	.001	.001	.003	.003	.01

TABLE 3
Percent Errors In Final Displacement

Number of Bits	Record	Fraction of Full Scale Range Used				
		0.9	0.7	0.5	0.3	0.1
		% Error in Final Displacement				
6	MN 07	200	200	300	500	700
	MN 08	10	20	40	50	50
	MN 10	3	3	8	40	100
	MN 17	8	8	20	50	300
8	MN 07	10	20	70	200	400
	MN 08	1.	1.	2.	4.	40
	MN 10	2.	2.	2.	3.	7.
	MN 17	3.	3.	5.	6.	20.
12	MN 07	0.3	0.5	0.6	1.	4.
	MN 08	0.1	0.1	0.1	0.1	0.3
	MN 10	0.04	0.1	0.1	0.1	0.4
	MN 17	0.1	0.2	0.3	0.4	0.7
16	MN 07	0.03	0.03	0.03	0.05	0.2
	MN 08	0.002	.003	.003	.005	0.01
	MN 10	0.002	.002	.008	.008	0.04
	MN 17	.008	.008	0.01	0.01	0.03

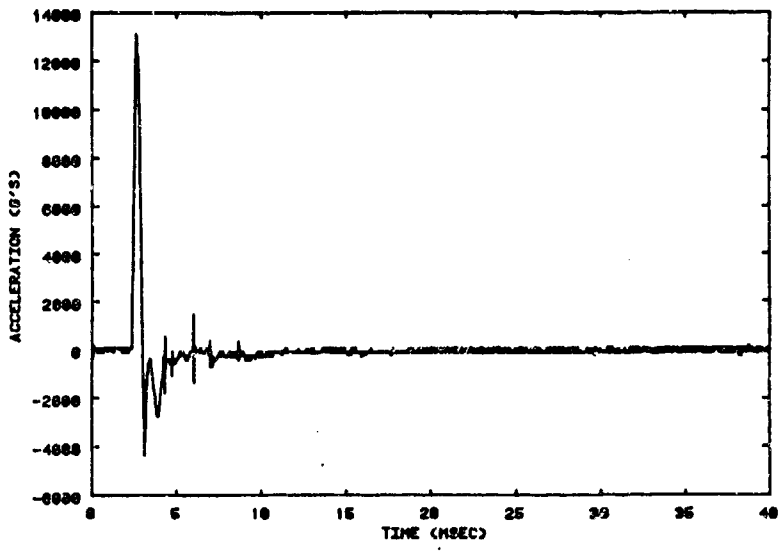

FIGURE 1. DATA RECORD MN07

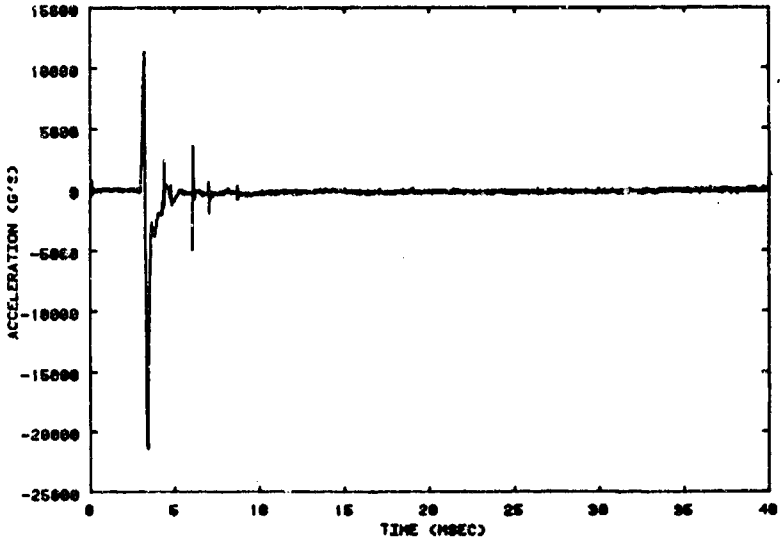

FIGURE 2. DATA RECORD MN08

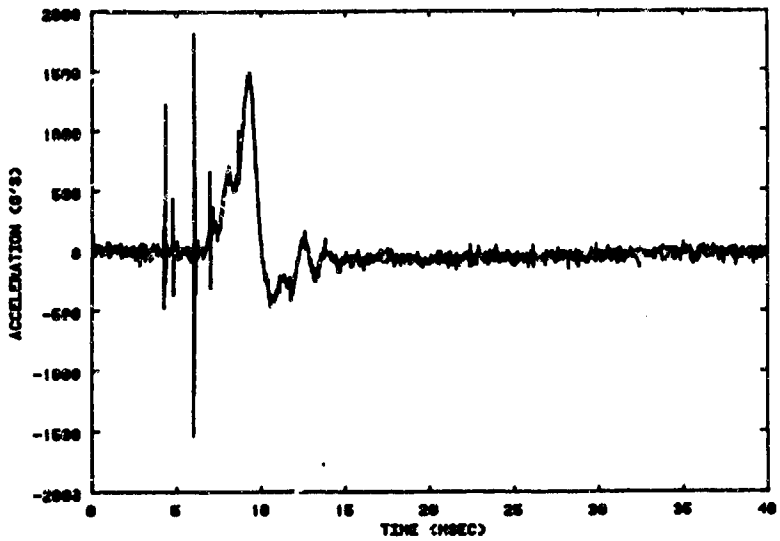

FIGURE 3. DATA RECORD MN10

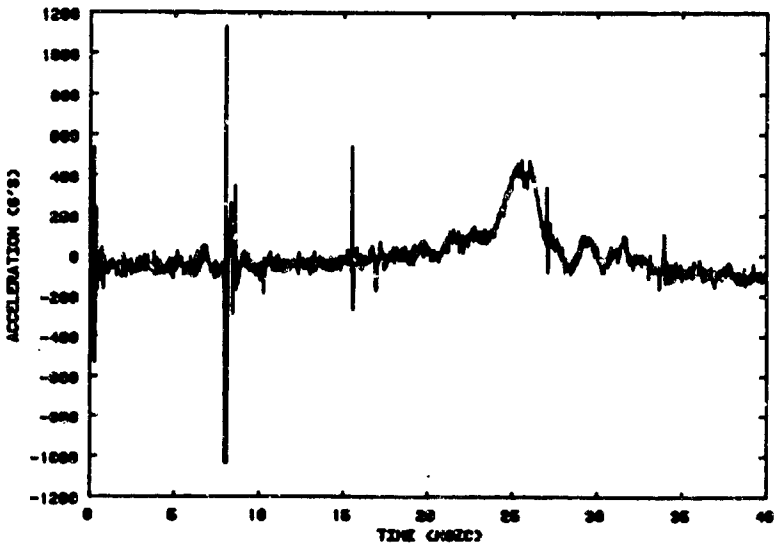

FIGURE 4. DATA RECORD MN17

CALIBRATION TESTS OF PRESSUREMETER IN CLAY

An-Bin Huang, Robert D. Holtz, and Jean-Lou A. Chameau

Purdue University
West Lafayette, Indiana

ABSTRACT

A calibration chamber has the unique capability of subjecting a soil sample to known stress history and boundary conditions. Although the technique has been used with success in cohesionless soils, its use in cohesive soils is unprecedented. This paper presents the laboratory equipments built to perform chamber calibration tests of model pressuremeters in clay. Due to the cohesive nature of clay soils, special considerations are necessary to insure that the test is performed under favorable conditions. Those include procedures of constructing high quality clay specimens, optimum sizes of the sample, and techniques for pore pressure measurements. A double-wall calibration chamber which can accommodate a clay sample 20 cm in diameter and 34 cm high, a slurry consolidometer, needle piezometers, and scaled down model pressuremeters are described. The performance of this experimental system is evaluated based on preliminary test results.

INTRODUCTION

A research program on "Fundamental Aspects of Pressuremeter Testing" is underway at Purdue University. The goal of this study is to determine why and how the nature and characteristics of different soils can explain their response under the loading conditions imposed by the pressuremeter. Phase I of the research involves a series of chamber pressuremeter tests in cohesive soils under known stress history and boundary conditions. A calibration chamber system has been designed and built to perform these tests.

The aim of this paper is to present the capabilities and features of the calibration chamber system, including the pore pressure monitoring devices and the scaled down, single cell, model pressuremeters. Preliminary results are used to evaluate the performance of the system and future improvements are indicated.

PREVIOUS EXPERIENCE IN CHAMBER TESTING

There are basically two alternate designs for calibration chambers, rigid-wall (such as a test pit) or flexible-wall chamber. The rigid-wall chamber imposes a boundary condition corresponding to zero lateral strain. To minimize the effects of this boundary condition, the sample size must be significantly larger than that of the device to be calibrated (Chapman, 1974). Therefore, testing is costly and time consuming.

In a flexible-wall chamber, the sample is encased in a soft membrane and confined with air or water. It provides several types of boundary conditions (Table 1) which makes the simulation of field tests possible, even with relatively small samples. Several large scale calibration chambers of this type have been built throughout the world (Belloti et al., 1982, Jewell et al., 1980, Chapman, 1974, and Laier et al., 1975). These chambers were used primarily to perform calibration tests in sands. The sand was deposited into the chamber through a carefully controlled pluvial process to provide a highly reproducible and uniform sample with a desired density. Diameters of 1 to 1.5 meters and heights of less than 2 meters were the usual dimensions of these samples.

A CHAMBER SYSTEM FOR CLAYS

The main capability of this system is to create a uniform and reproducible cohesive soil sample around a testing device, such as a pressuremeter, with known stress conditions and essentially no soil disturbance. The time required to consolidate clay samples is orders of magnitude longer than for sands. In addition, the handling of a large clay sample comparable to the ones mentioned above would be difficult if not impossible. Thus, it was decided to build a small scale chamber system and to use scaled down model pressuremeters. The design was based on a sample size of 20 cm in diameter and 34 cm in height. The experimental system consists of a slurry consolidometer, a double wall calibration chamber, model pressuremeters, and needle piezometers.

The basic concept behind this design is to consolidate a clay sample in two stages. During the first stage, the slurry is consolidated into a clay sample inside the consolidometer. This technique is known to provide high quality samples of cohesive soils (Krizek and Sheeran, 1970). Following the consolidometer stage, the sample is placed in a chamber and consolidated to a higher pressure. A model pressuremeter and needle piezometers are inserted in the slurry before consolidation. Since there is no need

of boring the soil for pressuremeter insertion, the main source of soil disturbance is eliminated. The pressuremeter test follows immediately after consolidation. Details of these equipments and techniques are described in the following sections.

The Slurry Consolidometer

This device (Figure 1) is used to consolidate a slurry from an initial maximum height of 90 cm to a final height of slightly more than 34 cm. It is made of a nickel plated steel pipe with two compartments. Both compartments have an inside diameter of 20 cm. A pressuremeter is fastened to the center of a chamber top cap together with five needle piezometers. This top cap is placed at the bottom of the lower compartment as a base. A filtered piston placed on top of the slurry is pressed by a 1 ton capacity rolling diaphragm piston.

The lower compartment has the same height as the soil sample after consolidation (34 cm). It is split longitudinally into two halves which are bolted together. The interior is lined with a sheet of sandpaper facing a rubber membrane. The sandpaper prevents slippage of the membrane caused by adhesion between clay and membrane as consolidation proceeds. The upper compartment which provides additional space for the slurry in the early stage of consolidation is bolted to the lower one. The rubber membrane extends out of the lower compartment and provides a sealing between the two.

Upon completion of slurry consolidation, the sample is confined in the lower compartment and encased in the rubber membrane. This arrangement eliminates the need of trimming the sample and therefore minimizes the chance of disturbance.

The Double Wall Calibration Chamber

The double wall calibration chamber is shown in Figure 2. The device can accommodate a sample 20 cm in diameter with a maximum height of 34 cm. Figure 3 shows the arrangement of the calibration chamber and its control system. The vertical stress is provided by a piston at the bottom of the chamber. This piston has the same diameter as that of the sample. The sample is encased in a 0.0635 cm thick, custom made latex membrane. The annular space between the sample and the chamber wall is filled with deaired water. Since both ends of the sample are isolated from the cell water, the stresses in the vertical and horizontal directions can be controlled independently. Porous discs are placed at both ends of the sample to permit double drainage. The chamber is installed in a constant temperature room. The variation of temperature in this room is less than 1° F.

Four different boundary conditions (Table 1) can be imposed on a soil sample. The condition of zero vertical strain can be imposed by locking the piston. The condition of zero lateral strain is maintained by balancing the chamber cell pressure and that between the two walls, while locking the cell drainage. The balanced pressure insures a stationary position of the inner wall (Figure 2) and simulates a rigid system.

Note that, with the boundary condition BC3 (Table 1), a sample can be consolidated under a K_o condition. The loss of sample volume due to consolidation is replaced by the piston movement, therefore allowing consolidation in the vertical direction only.

Table 1. Boundary Conditions in a Calibration Chamber Tests.

1. BC1: constant vertical stress and constant lateral stress.
2. BC2: zero vertical strain and zero lateral strain.
3. BC3: constant vertical stress and zero lateral strain
4. BC4: zero vertical strain and constant lateral stress.

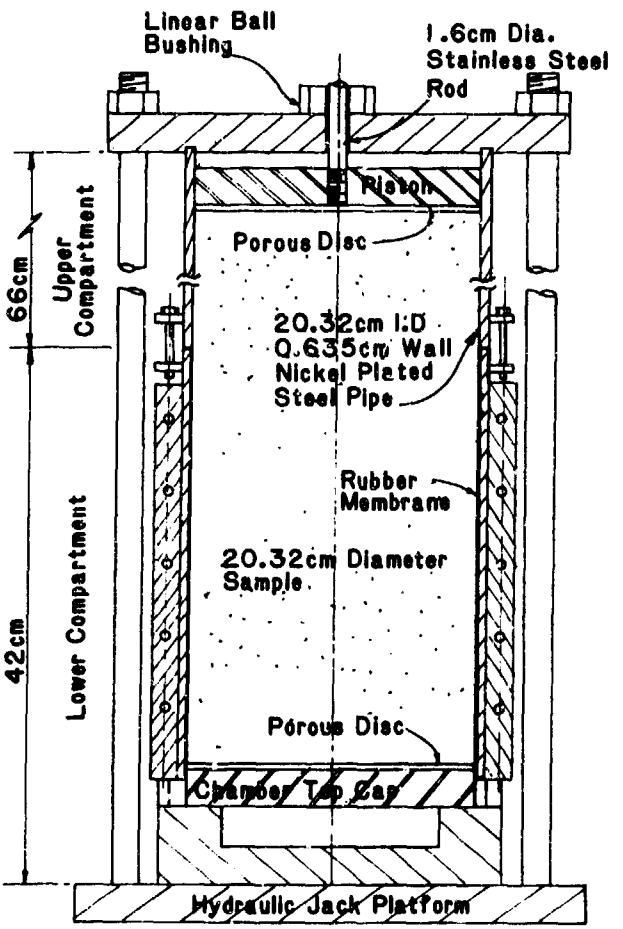

Figure 1 SCHEMATIC DIAGRAM OF THE CONSOLIDOMETER FOR CHAMBER TEST SAMPLES

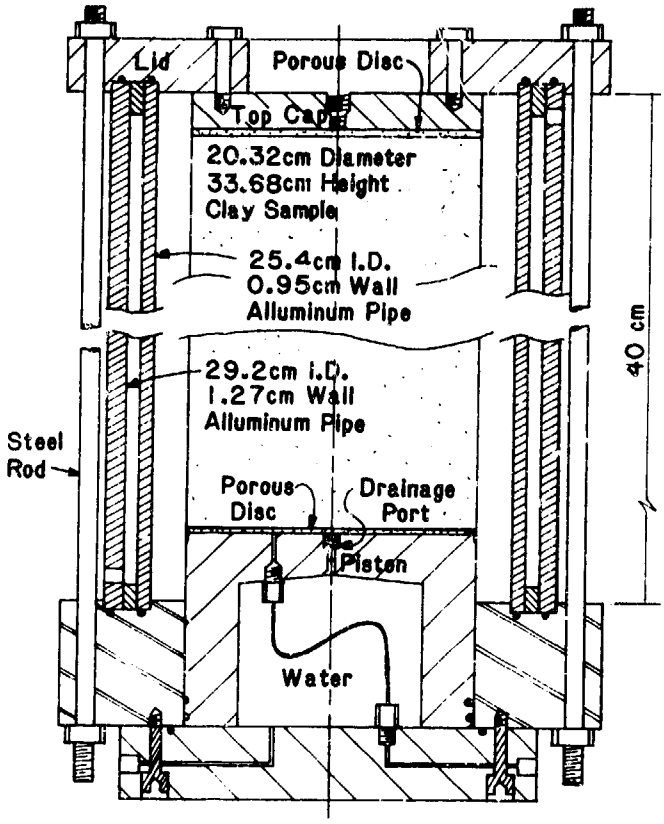

Figure 2 OVERVIEW OF THE DOUBLE WALL CALIBRATION CHAMBER.

The Model Pressuremeters

Two single cell, water inflated model pressuremeters were built for the research. Figure 4 shows a schematic diagram of the model pressuremeter. The measurement probe (central section of the pressuremeter) has a diameter of 1.11 cm and a length of 11.1 cm. Latex tubing of 1.11 cm O.D. and 0.24 cm wall was utilized as the probe membrane.

The design concept of the model pressuremeters is similar to a commercial single cell pressuremeter made by OYO Corporation, Tokyo, Japan (Suyama et al., 1982). It recognizes that head losses occur as the fluid is forced to flow through tubings and fittings before it reaches the probe. Thus, in order to obtain accurate pressure readings it is essential to measure the fluid pressure within the measurement probe. To achieve this, the pressuremeter is equipped with a piezometer which extends to the center of the probe. The piezometer is connected directly to a pressure transducer (Figure 4).

The pressuremeter test can be performed either stress controlled or strain controlled. In the case of stress controlled test, the volume change of the pressuremeter probe is monitored by a glass burette with a sensitivity of 0.03155 cm^3/cm. An increase of 10% of the probe radius would correspond to a drop of burette reading of 72 cm. For strain controlled pressuremeter tests, the fluid is pumped into the probe by a high accuracy flow pump system similar to the one proposed by H.W. Olsen (Yoo, 1984).

The Needle Piezometers

Five miniature piezometers were specially designed to monitor the variation of pore pressure within the soil sample during a test. They are installed at distances of 0.3 to 9 cm from the pressuremeter. The piezometer tips are at the same level as the center of the pressuremeter probe. Each piezometer consists of a 0.0762 cm O.D. stainless

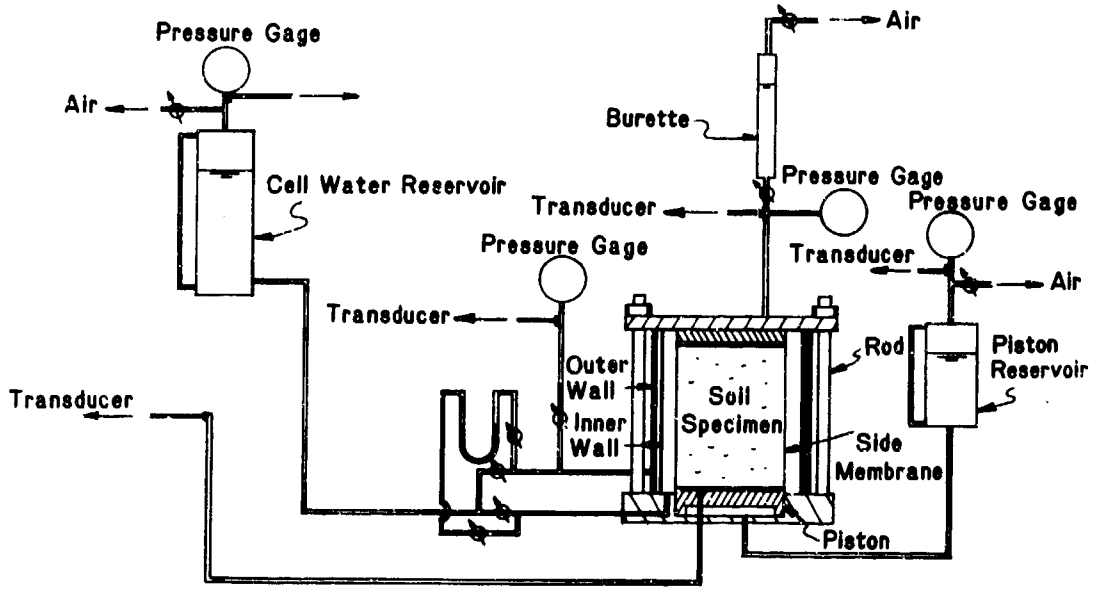

Figure 3 ARRANGEMENT OF THE CALIBRATION CHAMBER.

steel tubing soldered to a transducer port. The tip of the piezometer is filtered with strings of very fine bronze fiber. The transducer ports were custom made to minimize the volume of fluid in the sensing system. All the transducer ports together with the model pressuremeter are fastened to the top cap of the chamber.

PERFORMANCE OF THE SYSTEM

Before making extensive use of this new equipment in the research, a preliminary testing program is currently (December, 1984) underway to asses the performance of the different components of the system. A chamber pressuremeter test has been performed using Georgia kaolinite (specific gravity=2.57, PL=28, LL=63). Powdered kaolinite was mixed with deaired, deionized water to form a slurry with a water content of 150 %. The slurry which had an initial height of 76 cm in the consolidometer, was consolidated under a pressure of 2.25 kg/cm^2. Upon completion of the first stage consolidation, it was placed in the chamber and saturated under a back pressure of 7 kg/cm^2. Consolidation of the sample was performed under a K_o condition following the procedures suggested by Campanella and Vaid (1972). The vertical (piston) and horizontal (cell) pressures were increased to 9.84 kg/cm^2 simultaneously. Double drainage was then allowed while maintaining the boundary condition BC3 (Table 1) under a back pressure of 7 kg/cm^2. The cell pressure (sample lateral stress) decreased as consolidation continued and stabilized at the end of consolidation. The degree of consolidation was monitored by taking pore pressure readings through needle piezometers extended to the center of the sample.

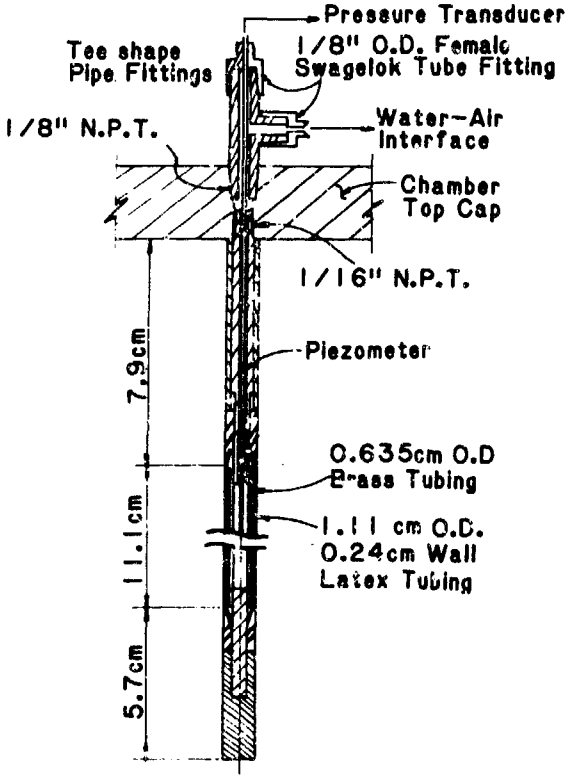

Figure 4 SCHEMATIC DIAGRAM OF THE MODEL PRESSUREMETER

A stress controlled pressuremeter test was performed immediately after consolidation. The boundary condition BC4 (Table 1) was applied during the test by maintaining the lateral stress reached at the end of consolidation. The probe pressure was increased in two minute intervals.

Sixteen days were required to complete the test, 8 days for slurry consolidation, and 8 days for chamber saturation, consolidation, and pressuremeter test. The slurry consolidation can be conducted simultaneously with chamber testing and thus, two tests can be completed in 16 days. The sample weighs approximately 20 kg and is easily portable while confined in the lower compartment of the slurry consolidometer.

At the end of chamber consolidation and pressuremeter test, samples were taken from different locations. Averaged water contents in a range of 42.9% to 43.6% were obtained. There was no clear trend of water content variation as a function of distance to the pressuremeter or locations within the sample. These water contents are essentially the same as those recorded during K_o triaxial tests performed earlier. The triaxial tests used the same kaolinite, consolidated under the same procedures. The water content measurements show that the chamber consolidated sample is uniform and the procedures should be repeatable as indicated by comparing with previous data.

It is well recognized that significant soil disturbance is very difficult to avoid in field tests even with the self-boring pressuremeter. The disturbance can cause variations in horizontal stresses and mask the soil response under the pressuremeter loading conditions. It is of great interest to perform chamber pressuremeter tests under a "disturbance free" condition. The pressure and radial strain values recorded during the pressuremeter test are given in Figure 5 ("raw data"). The data points represent not only the response of soil under the applied pressure, but also the effects of the pressuremeter system compliance and membrane stiffness. To measure these, a pressuremeter test was performed in an empty chamber under essentially the same lateral stress (cell pressure) and conditions as in the previous test. The pressures and radial strains measured during this test are also given in Figure 5 ("empty test"). The data show a clear breaking point as the probe pressure reaches the cell pressure (8.44 kg/cm^2). To the left of this point, the curve corresponds to system compliance and the rest of the curve represents membrane stiffness effects. The corrected pressuremeter data are obtained by subtracting the "empty test" values from the raw data ("net" values in Figure 5). The net pressure-strain curve (Figure 5) shows a sharp "lift off" point as the probe pressure reaches the soil lateral stress (cell pressure). This feature indicates that a "disturbance free" condition, at least in a sense of no lateral stress variation, was present during the chamber test.

The piezometers were located at distances of 3.12 cm to 7.7 cm from the center of pressuremeter probe. The pore pressure readings were found very sensitive to the chamber pressure variations. The pore pressure variations measured during the pressuremeter test are plotted versus the radial strains in Figure 6. The pore pressure increases are more significant towards the probe as predicted theoretically (Carter et al., 1979). Quantitative interpretation of these pore pressure changes as a function of the soil characteristics will be an essential part of our research program.

Two undesirable features were noticed during the chamber test. The measured K_o value of this normally consolidated sample was 0.53 at the end of consolidation. This value was lower than those obtained from K_o triaxial tests (0.56) performed on the same material. A slight bulging was noticed at the center of the sample. This is a strong indication that the sample may have yielded locally during K_o consolidation. For an ideal performance, the net pressure-strain curve (Figure 5) should indicate zero strain before the lift-off point. However, the results showed a positive strain immediately after the beginning of the test which increased with probe pressure. This is most likely due to some air trapped in the pressuremeter system.

CONCLUDING REMARKS

A calibration chamber system has been developed to perform model pressuremeter tests in cohesive soils. This system includes a slurry consolidometer, a double wall calibration chamber, scaled down model pressuremeters, and needle piezometers. A preliminary test was performed to evaluate the performance of this system. Based on the available experience, the following conclusions are made:

1. A uniform sample can be made using the slurry and chamber consolidation system. The complete consolidation cycle to create a sample from slurry took approximately 16 days.

2. The test result indicated a clear "lift off" point which corresponds to the soil lateral stress. This is a strong indication that a disturbance free condition, at least in a sense of no lateral stress variation, can be accomplished in the chamber.

3. The performance of the pore pressure measurement system (needle piezometers) was excellent. However, further improvements are in order to insure complete saturation of the pressuremeter system.

4. Slight bulging was noticed at the center of the sample. It is likely that the bulging was caused by yielding of the soil during chamber consolidation. Further considerations should be given to the K_o consolidation process in the chamber. The possibility of a multi-stage chamber consolidation procedure will be studied.

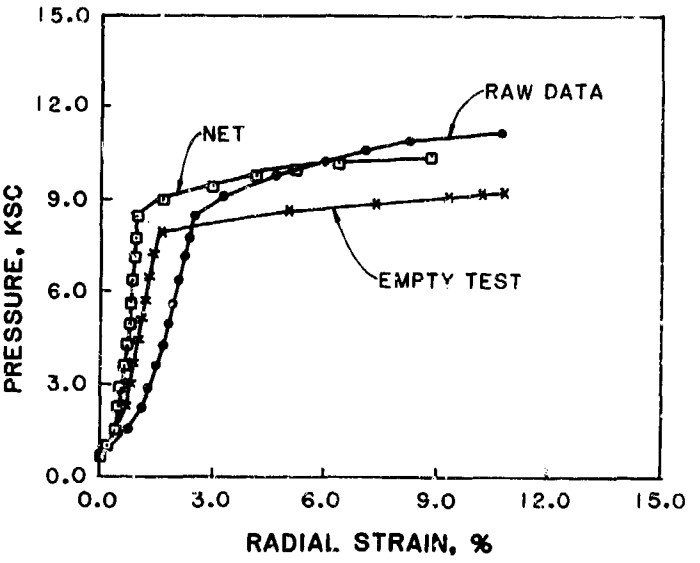

Figure 5. PROBE PRESSURE vs. RADIAL STRAIN

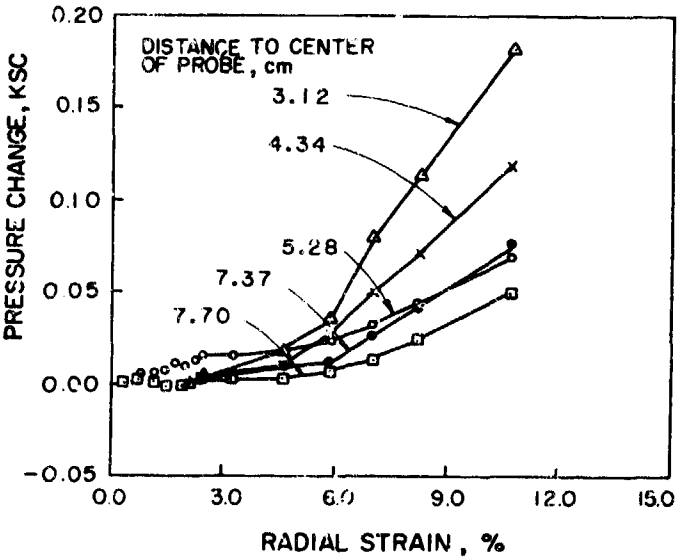

Figure 6. PORE PRESSURE CHANGE vs. RADIAL STRAIN

ACKNOWLEDGEMENTS

This research is sponsored by the Air Force Office of Science Research, Air Force System Command, U.S.A.F., under grant number AFOSR-84-0330. The U.S. government is authorized to reproduce and distribute reprints for governmental purposes notwithstanding any copyright notation thereon. Financial support was also provided by the National Science Foundation, under grant number CEE-8416360, and the Fukada Geological Institute of Japan. Personal interest and support provided by Mr. S. Ohya, President of OYO Corp. in Houston, Texas are greatly appreciated.

REFERENCES

Bellotti, R., Bizzi, G., and Ghionna, V. (1982) "Design, Construction and Use of a Calibration Chamber" Proceedings of the Second European Symposium on Penetration Testing, Amsterdam.

Campanella, R.G. and Vaid, Y.P. (1972) "A Simple Ko Triaxial Cell", Canadian Geotechnical Journal, Vol.9, pp249-260.

Carter, J.P., Randolph, M.F., and Wroth, C.P. (1979) "Stress and Pore Pressure Changes in Clay during and after the Expansion of a Cylindrical Cavity" International Journal for Numerical and Analytical Methods in Geomechanics, Vol.3.

Chapman, G. (1974) "A Calibration Chamber for Field Testing Equipment", Proceedings of the European Symposium on Penetration Testing, Stockholm.

Jewell, R.J., Fahey, M., and Wroth, C.P. (1980) "Laboratory Studies of the Pressuremeter Test in Sands" Geotechnique, Vol.30, No.4.

Krizek, R.J., and Sheeran, D.E. (1970) "Slurry Preparation and Characteristics of Samples Consolidated in the Slurry Consolidometer" Technical Report No.2, Contract No. DACW 39-70-C-0053, U.S. Army Corps of Engineers Waterways Experiment Station, Vicksberg, Mississippi.

Laier, J.E., Schmertmann, J.H., and Schaub, J.H. (1975) "Effects of Finite Pressuremeter Length in Dry Sand" Proceeding of the ASCE Specialty Conference on In-Situ Measurement of Soil Properties, Vol.1, Raleigh, North Carolina.

Suyama, K., Imai, T., and Ohya, S. (1982) "Lateral Load Tester (LLT). Its Method and Accuracy" Symposium on the Pressuremeter and Its in Marine Applications, Paris.

Yoo, N.-J. (1984) "Development of K_o Consolidation Testing Technique by Means of a Flow Pump" M.S. Thesis, Department of Civil, Environmental and Architectural Engineering, University of Colorado, Boulder, Colorado.

APPLICATION OF THEORIES OF MIXTURES TO BEHAVIOR OF FLUID-SATURATED DEFORMABLE POROUS MEDIA

Mahantesh S. Hiremath and Ranbir S. Sandhu

The Ohio State University
Department of Civil Engineering
Columbus, Ohio

ABSTRACT

Various approaches to description of motion as well as formulation of the equations of balance of mass, momentum, and energy for a mixture are discussed with special reference to the mechanics of fluid-saturated porous solids.

INTRODUCTION

Terzaghi[56]'s theory of one-dimensional consolidation was extended [40] to the case of variable material properties and later to finite strain [23]. Biot [6-11] proposed theories for three-dimensional problems of fluid-saturated solids based on certain postulates. Theories of interacting continua, based on principles of mechanics and thermodynamics, first proposed by Truesdell[57-59], were further developed by several investigators [1-5,13,25-32,36,45] and applied to the problem of flow of a fluid through an elastic solid [16,51,55].

Various investigators have used different sets of assumptions to develop self-consistent theories. The notion of the motion of the mixture as a single material is often introduced. This is open to objection except for certain special cases. Some investigators(e.g., Green and Naghdi) assume partial stresses in the constituents to be additive. Others (e.g., Truesdell) would so define the mechanical quantities that the form of the equations of the mixture be same as for a single material. Still others consider the notion of the partial stresses to be irrelevent to the development of a consistent theory for the mixture. Truesdell assumed the sum of internal and kinetic energy of the mixture to be the sum of all such quantities for the constituents. Green has derived a relationship between the energies of the constituents and that of the mixture consistent with his set of assumptions. The quantities for which constitutive relations are required are identified by considering the energy equality. Different notions regarding diffusive resistance have been proposed. Recent work [13,15,42-44,49,60] has extended these applications to finite deformations and nonlinear constitutive laws. Other theories of mixtures have been proposed. Gurtin[33,34], Oliver[46,47], Williams[61] and Sampaio[50] used a different approach to the theory of mixtures. In the so-called volume fraction theories, in addition to usual variables of classical theory, volume fractions of the constituents are taken as variables.

In developing a rational theory of mixtures, Truesdell[59] laid down the following 'metaphysical principles'.

1. All properties of mixture must be mathematical consequence of properties of the constituents.
2. So as to describe the motion of a constituent we may in imagination isolate it from the rest of the mixture, provided we allow properly for the action of the other constituents upon it.
3. The motion of the mixture is governed by the same equations as a single body.

Green and Naghdi[27,29,31], however, used different set of assumprions in developing balance laws for multicomponent mixture.

In this brief review, we outline various schemes to describe the motion of a multi-constituent material and to set up equations of balance of mass, linear momentum, angular momentum and energy. Our interest is primarily in mixture of immiscible constituents so that the results might be applicable to the problem of fluid-saturated soils. The relationship of quantities associated with the constituents and with the mixture as a whole is reviewed.

KINEMATICS

To apply the principles of continuum mechanics, it is customary to regard a fluid-saturated solid as superposed continua. The mixture is defined by the current coincident configurations of the constituents. It is assumed that, in the current configuration, each point is occupied by a particle of each of the constituent. This necessitates the introduction of 'bulk' description of the materia, instead of the 'intrinsic' description, which would apply if the material were the single constituent of a body.

a. Density of each constituent and the mixture

For each constituent to fill the body, a 'bulk' description of density is used [4,5,13,16,17,18,25-32,42-44,48,49,54,58,60]. Thus,

$$\rho = \Sigma \rho^{(k)} \tag{1}$$

where $\rho^{(k)}$ is the bulk density of the constituent $s^{(k)}$ and ρ is the density of the saturated solid. The bulk densities are related to the intrinsic or true densities $\rho^{(k)*}$ [13,14,20,42-44,48] as

$$\rho^{(k)} = n^{(k)} \rho^{(k)*} \tag{2}$$

where $n^{(k)}$ represents the volume fraction of the constituent $s^{(k)}$ in the current configuration. Combining (1) and (2), for a binary mixture,

$$\rho = n^{(k)} \rho^{(1)*} + n^{(k)} \rho^{(2)*} = \Sigma n^{(k)} \rho^{(k)*} \tag{3}$$

Terzaghi's theory differs from most others in that $n^{(2)} = 1$ and, therefore, the solid has the 'buoyant' bulk density

$$\rho^{(1)} = \rho - \rho^{(2)*} = n^{(1)} (\rho^{(1)*} - \rho^{(2)*}) \tag{4}$$

b. Motion of the constituents

Several approaches have been used to describe the motion of constituents. One is to refer the motion of each constituent to its reference configuration, another is to refer to the motion of each constituent to the current configuration of the solid and often it is convenient to refer to the current configuration of each constituent. If $x_i^{(k)}(\tau)$ is the place occupied at time τ by the material particle described by $X_j^{(k)}$ in the reference configuration for the constituent $s^{(k)}$, the displacement gradient is [13,16,17,27]

$$F_{ij}^{(k)} = \partial x_i^{(k)} / \partial X_j^{(k)} = x_{i,j}^{(k)} \tag{5}$$

with

$$\det \| F_{ij}^{(k)} \| > 0 \tag{6}$$

The velocity vectors are derived from $x^{(k)}$ as

$$v_i^{(k)} = (D/Dt) \; x_i^{(k)} = (\partial/\partial t + v_j^{(k)} \; \partial/\partial x_j^{(k)}) \; x_i^{(k)} \tag{7}$$

where

$$v_j^{(k)} = \partial x_j^{(k)} / \partial t \tag{8}$$

An Eulerian description of motion too has been used [15].

The acceleration vector at time t for constituent $s^{(k)}$ is denoted by

$$f_i^{(k)} = [D^{(k)}/Dt] \; v_i^{(k)} \tag{9}$$

Components of the rate of deformation tensor, for the material $s^{(k)}$, at time t are defined by [16]

$$d_{ij}^{(k)} = [D^{(k)}/Dt] \; F_{ij}^{(k)} = [D/Dt] \; x_{i,j}^{(k)} = v_{(i,j)}^{(k)} \tag{10}$$

Westmann[60] and others[e.g.15] have used Eulerian description of deformation. Vorticity tensor is the anti-symmetric part of spatial velocity gradient tensor $L_{ij}^{(k)}$ and is represented by

$$\Gamma_{ij}^{(k)} = L_{[i,j]}^{(k)} \tag{11}$$

where the square bracket around the pair of indices denote 'anti-symmetric part'. Often, a mean or barycentric velocity for the mixture in terms of velocities $v_i^{(k)}$ of the constituents is introduced by

$$v_i = \Sigma \rho^{(k)} \; v_i^{(k)} / \rho \tag{12}$$

Atkins[4] noted that the mixture velocity has no particular meaning in continuum mechanics. This is because a mixture defined by (3) is a set of centers of mass and cannot be regarded as a set of material particles in motion [52] except in the case of no relative motion between the constituents. A material rate, executed on the mixture is defined by [53]

$$\rho [D/Dt] = \Sigma \rho^{(k)} \; [D^{(k)}/Dt] \tag{13}$$

Another quantity, found convenient, is the diffusive velocity. This is the velocity of a constituent relative to that of the mixture i.e.

$$u_i^{(k)} = v_i^{(k)} - v_i \tag{14}$$

Biot[10], for the case of binary mixture of a solid and a fluid, introduced a nominal relative velocity viz.,

$$w_i = n^{(2)} (v_i^{(2)} - v_i^{(1)}) \tag{15}$$

This and its invariants were used by Ghaboussi and Wilson[21,22], Krause[39] and Kenyon[37,38] among others.

BALANCE LAWS

a. Treusdell's theory

For each constituent of the mixture, Truesdell postulated the balance laws in point form. This was, using notation of [31],

i. Continuity of mass[59]

$$(\partial/\partial t) \; \rho^{(k)} + (\rho^{(k)} \; v_i^{(k)})_{,i} = \rho \, c^{(k)} \tag{16}$$

where $\rho^{(k)}$, $c^{(k)}$ are, respectively, the density and mass production fraction of the constituent $s^{(k)}$. Indices following the subscripted comma denote the spatial derivative with respect to the space coordinates.

ii. Balance of linear momentum[59]

$$(\partial/\partial t)\,(\,\rho^{(k)}\,v_i^{(k)}\,) + (\,\rho^{(k)}\,v_i^{(k)}\,v_j^{(k)}\,)_{,j} - t_{ji,j}^{(k)} = \rho\, m_i^{(k)} + \rho^{(k)}\, b_i^{(k)} \qquad (17)$$

Here $t_{ji}^{(k)}$, $\rho^{(k)}\, b_i^{(k)}$ $\rho m_i^{(k)}$ are, respectively, the components of the partial Cauchy stress tensor, the body force vector per unit mass and the partial momentum supply density for the constituent.

iii. Balance of momentum of momentum[59]

$$t_{ij}^{(k)} - t_{ji}^{(k)} = M_{ij}^{(k)} \qquad (18)$$

Here M_{ij} are components of the skew-symmetric tensor describing the partial production density of the moment of momentum of the constituent.

iv. Balance of energy rates[59]

$$\rho^{(k)}\,[D^{(k)}/Dt]\,U^{(k)} + q_{i,i}^{(k)} - \rho^{(k)}\, r^{(k)} = t_{ij}^{(k)}\, v_{(i,j)}^{(k)} + \rho\, \Delta\, U^{(k)} \qquad (19)$$

where

$$\Delta\, U^{(k)} = e^{(k)} - [\,U^{(k)} - 1/2\, v_i^{(k)}\, v_i^{(k)}\,]c^{(k)} - v_i^{(k)}\, m_i^{(k)} - 1/2\, M_{ij}^{(k)}\, v_{j,i}^{(k)} \qquad (20)$$

Here $U^{(k)}$, $q_i^{(k)}$, $r^{(k)}$, $e^{(k)}$ are, respectively, the specific internal energy, components of the partial heat flux vector, the partial energy supply and the partial energy production density of the constituent $s^{(k)}$. Bowen[12] wrote the energy rate balance equation for a fixed volume in the form,

$$(\partial/\partial t)\int_V \rho^{(k)}\,[U^{(k)} + 1/2\, v_i^{(k)}\, v_i^{(k)}]\,dV + \int_A \rho^{(k)}\,[U^{(k)} + 1/2\, v_i^{(k)}\, v_i^{(k)}]\, v_j^{(k)}\, n_j\, dA = \int_A [t_{ij}^{(k)}\, v_i^{(k)} - q_j^{(k)}]\, n_j\, dA + \int_V [\rho^{(k)}\, r^{(k)} + \rho^{(k)}\, v_i^{(k)} b_i^{(k)} + \rho\, e^{(k)} + \rho v_i^{(k)}\, m_i^{(k)} + \rho\, c^{(k)}\{U^{(k)} + 1/2\, v_i^{(k)}\, v_i^{(k)}\}\,]\,dV \qquad (21)$$

Application of the divergence theorem and substitution of equations of mass and linear momentum give the point form

$$\rho^{(k)}\,[D/Dt]U^{(k)} + q_{j,j}^{(k)} - \rho^{(k)}\, r^{(k)} = t_{ij}^{(k)}\, v_{i,j}^{(\kappa)} + \rho e^{(k)} \qquad (22)$$

Several alternative forms of the above equation can be stated [12,59]. Truesdell postulated balance equations for the mixture as well. These equations can be derived by summing over the equations of the constituents. Truesdell introduced the following quantities to ensure that the resulting equations for the motion of the mixture have the same form as the equations of motion of a single constituent.

Specific internal energy of the mixture

$$\rho[U + 1/2\, v_i\, v_i] = \sum_1^n \rho^{(k)}\,[U^{(k)} + 1/2\, v_i^{(k)}\, v_i^{(k)}] \qquad (23)$$

Total stress tensor

$$t_{ij} - \rho v_i\, v_j = \sum_1^n [t_{ij}^{(k)} - \rho^{(k)}\, v_i^{(k)}\, v_j^{(k)}] \qquad (24)$$

Total heat flux vector

$$q_i + \rho\, v_i[U + 1/2\, v_j\, v_j] - t_{ij}\, v_j = \sum_1^n [q_i^{(k)} + \rho^{(k)}\, v_i^{(k)}\{U^{(k)} + 1/2\, v_j^{(k)}\, v_j^{(k)}\} - t_{ji}^{(k)}\, v_j^{(k)}] \qquad (25)$$

Specific energy supply

$$\rho(r + b_i\, v_i) = \sum_1^n \rho^{(k)}\,[r^{(k)} + b_i^{(k)}\, v_i^{(k)}] \qquad (26)$$

Further, it was asumed that the mixture is thermodynamically isolated i.e.

$$\sum_1^n c^{(k)} = 0,\ \sum_1^n m_i^{(k)} = 0,\ \sum_1^n M_{ij}^{(k)} = 0,\ \sum_1^n e^{(k)} = 0 \qquad (27)$$

Summing the equations of balance of the constituents over all of them gives, in view of the definitions introuduced for the total quantities

v. Balance of mass for the mixture

$$(\partial\rho/\partial t) + (\rho v_i)_{,i} = \sum_1^n \rho c^{(k)} = 0 \qquad (28)$$

vi. Balance of linear momentum for the mixture

$$(\partial/\partial t)(\rho v_i) + (\rho v_i\, v_j)_{,j} = t_{ji,j} + \sum_1^n \rho^{(k)}\, b_i^{(k)} \qquad (29)$$

Bowen[12] introduced a body force for the mixture

$$\rho\, b_i = \sum_1^n \rho^{(k)}\, b_i^{(k)} \qquad (30)$$

Then the equation of balance of linear momentum is

$$(\partial/\partial t)\,(\rho v_i) + (\rho v_i\, v_j)_{,j} = t_{ji,j} + \rho\, b_i \qquad (31)$$

vii. Balance of angular momentum for the mixture

$$t_{ij} = t_{ji} \qquad (32)$$

i.e. the total stress tensor is symmetric. It also follows from (23)

$$\sum_1^n t_{ij}^{(k)} = \sum_1^n t_{ji}^{(k)} \qquad (33)$$

viii. Energy balance for the mixture

$$\rho(DU/Dt) + q_{i,i} - t_{ij}\, v_{i,j} = \rho r - \sum_1^n \rho^{(k)}\,[r^{(k)} + b_i^{(k)}\, u_i^{(k)}] \qquad (34)$$

An alternative derivation of the equations of mass, momentum and energy balance for the mixture was presented by considering a volume V of the mixture bounded by an arbitrary fixed surface A [36,59,31,12]. The conservation of mass is expressed by

$$(\partial/\partial t)\int_V \sum_1^n \rho^{(k)}\, dV + \int_A \sum_1^n n_j\, \rho^{(k)}\, v_j^{(k)}\, dA = 0 \qquad (35)$$

This is equivalent to (28) upon use of divergence theorem. Equating the linear change of momentum to

the force exerted on the material inside the region V, Green and Naghdi[31] obtained in point form the balance of momentum as,

$$\rho D/Dt\ v_i + \sum_1^n (\rho^{(k)} u_i^{(k)} u_j^{(k)})_{,j} = \sum_1^n \rho^{(k)} b_i^{(k)} + \sum_1^n t_{ji,j}^{(k)} \quad (36)$$

Green and Naghdi[31] pointed out that (36) is same as (29). However, if total stress is taken as equal to sum of partial stresses, (36) reflects the fact that the total rate of increase of linear momentum is not equal to the barycentric rate of increase of momentum of continuum of density moving with velocity v_i.

b. Green and Naghdi's theory

The theory for a mixture of two constituents originally presented by Green and Naghdi[27,29], was generalized by Mills[41] to the case of multicomponent mixtures. Green and Naghdi proposed that the total stress and total heat flux for the mixture should be equal to the sum of the corresponding quantities for the constituents. Thus,

$$t_{ij} = \sum_1^n t_{ij}^{(k)},\ q_i = \sum_1^n q_i^{(k)},\ r_i = \sum_1^n \rho^{(k)} r_i^{(k)}/\rho \quad (37)$$

Green and Naghdi[29] stated that Truesdell's equations were correct but found it difficult to accept the interpretation for some of the terms. These are of special significance if boundary conditions on the surface of the mixture involve total stress and total heat flux. In Green and Naghdi's theory, the equations of mass and momentum balance are derived from the material frame invariance of a rate of energy equality. For a volume V enclosed by a fixed surface A, Green and Naghdi[31] wrote

$$(\partial/\partial t)\int_V \rho[U + 1/2\ v_i\ v_i]\ dV + \int_A \rho n_j\ v_j\ [U + 1/2\ v_i\ v_i]\ dA = \int_V \sum_1^n \rho^{(k)}\ [r^{(k)} + b_i^{(k)}\ v_i^{(k)}]\ dV + \int_A [t_{ji}\ v_j - q_j]\ n_i\ dA \quad (38)$$

Here the left hand side represents the rate of change of energy in volume V bounded by a fixed surface A plus the energy flux of the mixture across the boundary. Green and Naghdi[31] accept the form of (38) and (34) but not the interpretations associated with some of the quantities occuring in them.

Green and Naghdi[27] gave energy equality in the form

$$(\partial/\partial t)\int_V [\rho U + 1/2 \sum_1^n \rho^{(k)}\ v_i^{(k)}\ v_i^{(k)}]\ dV + \int_A [U \sum_1^n \rho^{(k)}\ v_j^{(k)} + 1/2\ \rho^{(k)}\ v_i^{(k)}\ v_i^{(k)}\ v_j^{(k)}]\ n_j\ dA = \int_V [r\rho + \sum_1^n \rho^{(k)}\ b_i^{(k)}\ v_i^{(k)}]\ dV + \int_A \sum_1^n [t_j^{(k)}\ v_i^{(k)} - q]\ dA \quad (39)$$

Allowing for interactions between constituents, the energy equality was restated as [29],

$$(\partial/\partial t)\int_V \rho^{(k)}\ [U^{(k)} + 1/2\ v_i\ v_i]dV + \int_V \rho^{(k)}\ n_j\ v_j^{(k)}[U^{(k)} + 1/2\ v_i^{(k)}\ v_i^{(k)}]\ dA = \int_V \rho^{(k)}\ [r^{(k)} + b_i^{(k)}\ v_i^{(k)}]\ dV + \int_A [t_i^{(k)}\ v_i^{(k)} - q_i^{(k)}]\ dA + \int_V [\alpha_i^{(k)}\ v_i^{(k)} + \lambda_{ij}^{(k)}\ \Gamma_{ij}^{(k)} + \psi^{(k)}]\ dV - \int_A \bar{q}^{(k)}\ dA \quad (40)$$

where $\alpha_i^{(k)}$, $\lambda_{ij}^{(k)}$ are the internal force and couple acting due to interactions and $\psi^{(k)}$, $\bar{q}^{(k)}$ represent contributions to the balance of energy arising out of interactions of n constituents. Also,

$$\sum_1^n \alpha_i^{(k)} = 0,\ \sum_1^n \lambda_{ij}^{(k)} = 0,\ \sum_1^n \bar{q}^{(k)} = 0 \quad (41)$$

(39) can be writen as [53]

$$\int_V [\rho\ DU/Dt - \rho r + \sum_1^n \rho^{(k)}\ v_i^{(k)}\ (f_i^{(k)} - b_i^{(k)})\ dV + \int_V \sum_1^n \rho c^{(k)}\ [U + 1/2\ v_i^{(k)}\ v_i^{(k)}]\ dV = \int_A \sum_1^n [t_i^{(k)}\ v_i^{(k)} - q]\ dA \quad (42)$$

Invariance of the energy equality under superposed uniform translational velocities yields, for arbitrary volume V

$$\int \rho c^{(k)}\ dV = 0 \quad (43)$$

i.e. the mass elements of the mixture are conserved. (10) yields

$$D\rho/Dt + \rho v_{i,i} = 0 \quad (44)$$

Also,

$$\int_V \sum_1^n [\rho^{(k)}\ (b_i^{(k)} - f_i^{(k)}) - \rho c^{(k)}\ v_i^{(k)}]\ dV + \int_A \sum_1^n t_i^{(k)}\ dA = 0 \quad (45)$$

Applying (45) to an arbitrary tetrahedron gives generalization of Cauchy's stress principle viz.,

$$\sum_1^n t_i^{(k)} = \sum_1^n t_{ji}^{(k)}\ n_j \quad (46)$$

Use of (46) in (45) and of divergence theorem yields

$$\sum_1^n [\rho^{(k)}(b_i^{(k)} - f_i^{(k)}) - \rho c^{(k)} v_i^{(k)} + t_{ji,j}^{(k)}] = 0 \quad (47)$$

(47) has same form as (31). Replacing f_i in (47) we get [53]

$$\sum_1^n \rho^{(k)}\ b_i^{(k)} - (\partial/\partial t)\rho^{(k)}\ v_i^{(k)} - (\rho^{(k)}\ v_i^{(k)}\ v_j^{(k)})_{,j} + t_{ji,j}^{(k)}] = 0 \quad (48)$$

This is the equation of linear momentum balance for an arbitrary fixed volume. Now (42) can be restated as [53]

$$\int_V [\ \rho DU/Dt - \rho r + h_{j,j} - \sum_1^n \theta_i^{(k)}\ v_i^{(k)} + \sum_1^n 1/2\ \rho c^{(k)}\ v_i^{(k)}\ v_i^{(k)} - \sum_1^n t_{ji}^{(k)}\ v_{i,j}^{(k)}]\ dV = 0 \quad (49)$$

where we define

$$\theta_i^{(k)} = t_{ji,j}^{(k)} + \rho^{(k)}[b_i^{(k)} - f_i^{(k)}] \quad (50)$$

In consequence of (47)

$$\sum_1^n \theta_i^{(k)} = \sum_1^n \rho c^{(k)}\ v_i^{(k)} \quad (51)$$

Invariance of (50) under a superposed uniform rigid body angular velocity gives

$$\sum_1^n t_{[ji]}^{(k)} = 0 \quad (52)$$

i.e. the sum of partial stresses is symmetric. The partial stresses do not have to be symmetric. In view of (28), (43), (51) and (52), application of (49) to arbitrary volume gives

$$\begin{aligned}\rho DU/Dt &= \rho r + h_{j,j} - \sum_1^n t_{(ji)}^{(k)}\ d_{ij}^{(k)} \\ &\quad - \sum_1^{n-1} t_{[ji]}^{(k)}\ (\Gamma_{ij}^{(k)} - \Gamma_{ij}^{(n)}) \\ &\quad - \sum_1^{n-1} p_i^{(k)}\ (v_i^{(k)} - v_i^{(n)})\end{aligned} \quad (53)$$

where

$$\begin{aligned}p_i^{(k)} &= t_{ji,j}^{(k)} + \rho^{(k)}(b_i^{(k)} - f_i^{(k)}) \\ &\quad - 1/2\ c^{(k)}\ (v_i^{(k)} - v_i^{(n)})\end{aligned} \quad (54)$$

For binary mixture, this is same as given by [28]. Green and Naghdi[31] established a relationship between internal energies of the constituents and that of the mixture. They wrote the rate of energy equality in terms of the energies of the constituents, ignoring external body couples, as follows

$$\begin{aligned}(\partial/\partial t)\int_V \sum_1^n [\ \rho^{(k)}\ U^{(k)} + 1/2\ \rho^{(k)}\ v_i^{(k)}\ v_i^{(k)}]\ dV \\ + \int_A \sum_1^n n_j[\ \rho^{(k)}\ v_j^{(k)}\ U^{(k)} \\ + 1/2\ \rho^{(k)}\ v_i^{(k)}\ v_i^{(k)}\ v_j^{(k)}]\ dA \\ = \int_V \sum_1^n \rho^{(k)}\ [r^{(k)} + b_i^{(k)}\ v_i^{(k)}]\ dV \\ + \int_A \sum_1^n [\ t_i^{(k)}\ v_i^{(k)} - q^{(k)}]\ dA\end{aligned} \quad (55)$$

Let ρU^* be the sum of the energies of the constituents i.e.

$$\rho U^* = \sum_1^n \rho^{(k)}\ U^{(k)} \quad (56)$$

Also define, [31]

$$K = [\ \rho^{(k)}\ u_i^{(k)}\ U^{(k)}]_{,i} \quad (57)$$

Then it can be shown [53] that

$$\begin{aligned}(\partial/\partial t)\int_V \sum_1^n \rho^{(k)}\ U^{(k)}\ dV + \int_A \sum_1^n \rho^{(k)}\ v_i^{(k)}\ U^{(k)}\ n_i\ dA \\ = \int_V [\ \rho\ DU^*/Dt + K\ ]\ dV\end{aligned} \quad (58)$$

Define the total energy of the mixture so that [31]

$$\rho\ DU/Dt = \rho\ DU^*/Dt + K \quad (59)$$

Then (55) becomes

$$\begin{aligned}\int_V [\ \rho\ DU/Dt - \sum_1^n \rho^{(k)}\ (\ r^{(k)} + b_i^{(k)}\ v_i^{(k)}) \\ \sum_1^n \rho c^{(k)}(U + 1/2\ v_i^{(k)}\ v_i^{(k)}) + \sum_1^n \rho^{(k)}\ v_i^{(k)}\ f_i^{(k)}\ ]\ dV \\ = \int_A \sum_1^n (t_i^{(k)}\ v_i^{(k)} - q^{(k)})\ dA\end{aligned} \quad (60)$$

This is identical to (42). (59) defines the relationship between the specific energies of the constituents and that of the mixture for the two rate of energy equalities (42) and (55) to be equivalent.

c. Other work

i. Mass continuity equation using relative velocity

Krause[39], referring to fixed volumes in space, for continued saturation, wrote,

$$\sum_1^n n^{(k)} = 0 \quad (61)$$

Using (16) and (2) and assuming intrinsic density to be specially constant, mass continuity equation becomes

$$\dot{n}^{(k)} + [n^{(k)}\ v_j^{(k)}]_{,j} = 0 \quad (62)$$

For binary mixture (61) and (62) give

$$[\ v_j^{(1)} + n^{(2)}\ (v_j^{(2)} - v_j^{(1)})]_{,j} = 0 \quad (63)$$

Using (15), (63) can be rewriten as [37,38]

$$[v_j^{(1)} + w_j]_{,j} = 0 \quad (64)$$

Hsieh and Yew[35] added the equations (16) for the constituents of a binary mixture and for no chemical reaction obtained

$$\dot{\rho} + (\ \rho\ v_i^{(1)})_{,i} + (\ \rho^{(2)}\ w_i)_{,i} = 0 \quad (65)$$

as the mass continuity equation.

ii. Mass balance in terms of porosity

Fukuo[19] used the equations of the mass balance to set up equations in terms of volume fractions of the constituents. Using intrinsic densities mass balance equation is writen as

$$\dot{n}^{(k)}\rho^{(K)*} + n^{(k)}\dot{\rho}^{(k)*} + (n^{(k)}\rho^{(k)*}v_i^{(k)})_{,i} = 0 \quad (66)$$

Fukuo used Gibson's[23] approach of referring to the set of particles in the reference configuration to get

$$n_0^{(i)}\ \rho_0^{(1)*} = n^{(1)}\ \rho^{(1)*}\ \det\ [F_{ij}] \quad (67)$$

For small volumetric deformations in solid it was shown [53]

$$n_0^{(1)}\ e_{jj}^{(1)} = (n^{(2)}\ v_i^{(2)})_{,i} \quad (68)$$

Hsieh and Yew[35] considered a porous solid saturated with incompressible fluid and undergoing small deformations. They established a compatibility condition of volume change of a fluid-saturated porous medium as

$$(\partial/\partial t)\,(n^{(2)} - n_0^{(2)}) + n_0^{(2)}\,(\partial/\partial t)\,e_{jj}^{(1)} + w_{i,i} = 0 \qquad (69)$$

iii. Energy balance in terms of porosity (Volume fraction theory)

Goodman and Cowin[24] postulated the equation of energy balance for a porous material with porosity n in local form as

$$n\rho^*\,(\partial U/\partial t) = t_{ij}\,v_{(i,j)} + S_j\,(\mathring{n})_{,j} - n\rho^*\,g\,(\partial n/\partial t) - h_{j,j} + n\rho^*\,r \qquad (70)$$

where g is the intrinsic equilibrated body force and S_i are components of the equilibrated stress vector.

iv. Alternative form of linear momentum balance equation

Hsieh and Yew[35] obtained for a binary mixture, with no body forces,

$$\rho(Dv_i^{(1)}/Dt) + \rho^{(2)}\,[(\partial/\partial t)v_i + v_j^{(2)}\,v_{i,j} + v_j\,v_{i,j}] = t_{ji,j} \qquad (71)$$

v. Other forms of the energy balance equation

Bowen[12] postulated the point form of the rate of energy equality as

$$\rho\,(\partial/\partial t)\,[U + 1/2\,v_i\,v_i] = [t_{ji}\,v_j - q_i]_{,i} + \rho r + \sum_1^n \rho^{(k)}\,v_i^{(k)}\,b_i^{(k)} \qquad (72)$$

Bowen[12] pointed out that if all second order terms in the diffusion velocities are neglected then (24), (25), (26) reduce to (37). Neglecting products of the diffusion velocities with their time and space derivatives, the energy equality in (72) becomes

$$\rho(\partial U/\partial t) = t_{ji}\,v_{j,i} - q_{i,i} + \rho r + \sum_1^n \rho^{(k)}\,u_i^{(k)}\,b_i^{(k)} \qquad (73)$$

Interpretation of quantities in (72) and (73) is quite different. Green and Naghdi[31] used the same form as (73), but their formulation was based on different definitions for the quantities associated with the mixture.

Morland[43] stated the energy balance equation for the mixture as

$$\sum_1^n [\,\rho^{(k)}\,(D^{(k)}/Dt)\,U^{(k)} - t_{ij}^{(k)}\,v_{i,j}^{(k)} + q_{i,i}^{(k)}] = 0 \qquad (74)$$

Discussion

Truesdell's theory requires that the form of the equations for the mixture to be the same as for a single material. For the case of no relative motion between the constituents, mixture will have motion and deformation as a material body. However, if relative motion is present, the mixture does not satisfy the axioms of continuity and its corollary, the principle of impenetrability. Hence, the 'third metaphysical princple' stated by Truesdell[59] appears irrelevant. We also note that the sum of the internal energies of the constituents does not equal the internal energy of the mixture. The balance equations due to Truesdell and to Green and Naghdi have similar form and are essentially equivalent but the quantities appearing in the two sets have different interpretations based on the relationships postulated between the quantities associated with the constituents and with the mixture. The equations energy balance contain scalar products of the corresponding quantities. This indicates the quantities for which constitutive relationships would be required. Some investigators, considering the special problems of flow through porous media, have attempted to write the balance equations in terms of relative motion and porosity, which is essentially a measure of relative deformation. It would appear that a theory based upon the balance equations written for a reference set of particles of the porous solid would be the most appropriate for this case. For one-dimensional case, Gibson developed such a theory for the quasi-static problem. This needs to be developed further to include inertia effects and a generalization to three-dimensional problem. This would require a convected coordinate description for the stresses and deformations in the porous solids.

ACKNOWLEDGEMENTS

This work is part of a research program supported by the Air Force Office of Scientific Research, Air Force Systems Command, USAF under Grant Number AFOSR-83-0055. The U. S. Government is authorized to reproduce and distribute reprints for Governmental purposes notwithstanding any Copyright notation therein. The assistance provided by the Instruction and Research Computer Center, The Ohio State University, is gratefully acknowledged.

REFERENCES

1. Adkins, J. E., Phil. Trans. Roy. Soc. Series A, 255, 607-650, 1963.
2. Adkins, J. E., Arch. Rat. Mech. Anal., 15, 222-234, 1964.
3. Aifantis, E. C., Acta Mechanica, 27, 265-296, 1980.
4. Atkin, R. J., ZAMP, 18, 803-825, 1967.
5. Atkins, R. J., and Craine, R. E., Quar. J. Mech. App. Math., 29 Pt.2, 209-244, 1976.
6. Biot, M. A., J. App. Phy., 12, 155-164, 1941.
7. Biot, M. A., J. App. Phy., 26, 182-185, 1955.

8. Biot, M. A., J. App. Phy., 26, 459-467, 1956.
9. Biot, M. A., and Willis, D. G., J. App. Mech., ASME, 594-601, 1957.
10. Biot, M. A., J. App. Phy., 33, 1482-1498, 1962.
11. Biot, M. A., Indiana Univ. Math. J., 21, 597-620, 1972.
12. Bowen, R. M., Continuum Physics, III, 1-127, 1976.
13. Bowen, R. M., Int. J. Engrg. Sci., 20, 697-735, 1982.
14. Carroll, M. M., J. Geophy. Res., 84, 7510-7512, 1979.
15. Carter, J. P., Small, J. C., and Booker, J. R., Int. J. Solids Struct., 13, 467-478, 1977.
16. Crochet, M. J., and Naghdi, P. M., Int. J. Engrg. Sci., 4, 383-401,1966.
17. Demiray, H., Int. J. Engrg. Sci., 19, 253-268, 1981.
18. Firoozbakhsh, K., Int. J. Solids Struct., 12, 649-654, 1976.
19. Fukuo, Y., Bull. Dias. Prev. Res. Inst.,Japan, 18, Pt.4, No. 146, 1-15, 1969.
20. Garg, S. K., and Nur, A., J. Geophy. Res., 78, 5911-5921, 1973.
21. Ghaboussi, J., and Wilson, E. L., Report, UCSESM 71-12, University of California, Berkeley, California, 1971.
22. Ghaboussi, J., and Wilson, E. L.,J. Soil Mech. Found. Div., ASCE, 99, No. SM10, 849-862, 1973.
23. Gibson, R. E., England, G. L., and Hussey, M. J. L., Geotechnique, 17, 261-273, 1967.
24. Goodman, M. A., and Cowin, S. C., Arch. Rat. Mech. Anal., 44, 249-266, 1972.
25. Green, A. E., and Adkins, J. E., Arch. Rat. Mech. Anal., 15, 235-246, 1964.
26. Green, A. E., and Rivlin, R. S., ZAMP, 15, 290-292, 1964.
27. Green, A. E., and Naghdi, P. M., Int. J. Engrg. Sci., 3, 231-241, 1965.
28. Green, A. E., and Steel, J. R., Int. J. Engrg. Sci., 483-500, 1966.
29. Green, A. E., and Naghdi, P. M., Arch. Rat. Mech. Anal., 24, 243-263, 1967.
30. Green, A. E., and Naghdi, P. M., Int. J. Engrg. Sci., 6, 631-635, 1968.
31. Green, A. E., and Naghdi, P. M., Quar. J. Mech. App. Math., XXII, Pt.4, 427-438, 1969.
32. Green, A. E., and Naghdi, P. M., Acta Mechanica, 9, 329-340, 1970.
33. Gurtin, M. E., and De La Penha, G., Arch. Rat. Mech. Anal., 36, 390-410, 1972.
34. Gurtin, M. E., Oliver, M. L., and Williams, W. D., Quar. J. App. Math.,30, 527-530, 1973.
35. Hsieh, L., Yew, C. H., J. App. Mech., ASME, 873-878, 1973.
36. Kelly, P. D., Int. J. Engrg. Sci., 2, 129-153, 1964.
37. Kenyon, D. E., Arch. Rat. Mech. Anal., 62, 131-147, 1976.
38. Kenyon, D. E., J. App. Mech., ASME, 45, 727-732, 1978.
39. Krause, G., Die Bautechnik, 95-103, 1977.
40. Mikasa, M., Civil Engineering in Japan, JSCE, 21-26, 1965.
41. Mills, N., Quar. J. Mech. App. Math., 20, 499-508, 1967.
42. Morland, L. W., J. Geophy. Res., 77, 890-910, 1972.
43. Morland, L. W., Geophy. J. Roy. Astro. Soc., 55, 393-410, 1978.
44. Morland, L. W., Geotechnical and Environmental Aspects of Geopressure Energy, Ed. S. Saxena, Engineering Foundation, New York, 363-366, 1980.
45. Muller, I., Arch. Rat. Mech. Anal., 28, 1-39, 1968.
46. Oliver, M. L., Arch. Rat. Mech. Anal., 49, 195-224, 1973.
47. Oliver, M. L., and Williams, W. D., Quar. App. Math., 33, 81-86, 1976.
48. Pecker, C., and Deresiewicz, H., Acta Mehcanica, 16, 45-64, 1973.
49. Prevost, J. H., Int. J. Engrg. Sci., 18, 787-800, 1980.
50. Sampaio, R., Arch. Rat. Mech. Anal., 62, 99-116, 1976.
51. Sandhu, R. S., Fluid Flow in Saturated Porous Elastic Media, Ph.D. Thesis, Univ. of California at Berkeley, 1968.
52. Sandhu, R. S., and Liu, H., Numerical Methods in Geomechanics, Aachen, 1969, Ed. W. Wittke, Balkema, 1255-1263, 1979.
53. Sandhu, R. S., Mechanical Behaviour of Saturated Soils, Report OSURF-715107-84-1, The Ohio State University, Columbus, Ohio, (To be published).
54. Shi, J. J., Rajgopal, K. R., and Wineman, A. S., Int. J. Engrg. Sci., 19, 871-889, 1981.
55. Tabaddor, F., and Little, R. M., Int. J. Solids Struct., 7, 825-841, 1971.
56. Terzaghi, K., Theoretical Soil Mechanics, Wiley, 1943.
57. Truesdell, C., and Toupin, R. A., Handbuch der Physik, III/1, Ed. S. Flugge, Springer-Verlag, 1960.
58. Treusdell, C., J. Chem. Phys., 37, 2336-2344, 1961.
59. Truesdell, C., Rational Thermodynamics, McGraw-Hill, 1969.
60. Westmann, R. A., Nonlinear Three Dimensional Theory of Consolidation, Unpublished Report, 1967.
61. Williams, W. O., Arch. Rat. Mech. Anal., 51, 239-260, 1973.

DAMAGE PREDICTION FOR IMPACTED CONCRETE STRUCTURES

H. Adeli*, A.M. Amin**, and R.L. Sierakowski***

Department of Civil Engineering, The Ohio State University
470 Hitchcock Hall, 2070 Neil Avenue
Columbus, Ohio 43210

ABSTRACT

Available formulae for predicting the penetration depth, scabbing thickness, and perforation thickness of concrete structures impacted by solid missiles are summarized, reviewed, and compared. In addition, based on quadratic and cubic regression analysis of existing data, two new formulae are proposed for predicting the penetration depth of concrete due to the impact by solid missiles. The new penetration equations are compared statistically with NDRC penetration formula and two other recent penetration formulae.

INTRODUCTION

Effects of impact of solid missiles on concrete structures can be classified into local effects and global dynamic response of the structure. If the kinetic energy transmitted through the zone of impact by the missile is considerably smaller than the strain energy capacity of the structure, the local effects will probably be governed by this consideration. This paper is concerned with local effects of solid missile impact on concrete structures.

The problem of impact of missiles on concrete structures is extremely complicated. A complete physical modeling of the problem has yet to be developed. However, for design of concrete structures against impact, simple but reliable equations are urgently needed. At present it appears that only empirical and semi-empirical equations have been developed for design purposes. In the following sections, available formulae for predicting the penetration depth, scabbing thickness, and perforation thickness of concrete structures impacted by solid missiles are summarized, reviewed, and compared.

*Associate Professor, ** Graduate Student,

***Professor and Chairman

MODIFIED PETRY FORMULA

The Modified Petry Formula developed originally in 1910, predicts the penetration depth in inches as follows [1 and 15]:

$$X_p = 12\, K_p\, A_p\, \mathrm{Log}_{10}(1.0 + V^2/215000) \qquad (1)$$

Where V is the impact velocity in ft/sec, A_p is the weight of missile per unit projected area in lb/ft^2, and K_p is a coefficient taking into account the effect of reinforcement. It has the value of 0.00799 for massive concrete, 0.00426 for normal reinforced concrete, and 0.00284 for specially reinforced concrete. The coefficient K_p has been modified to account for the effect of concrete strength by Amirikian [1]. The modified K_p is a function of f'_c, the compressive strength of concrete. When Eq. (1) is used with the original values of K_p, we call it Modified Petry 1, and when it is used with the values represented by the curve in Ref. [1], we call it Modified Petry 2. Also, Amirikian [1] suggested that perforation thickness be determined by

$$d_p = 2\, X_p \qquad (2)$$

and the scabbing thickness be determined by

$$d_s = 2.2\, X_p \qquad (3)$$

ARMY CORPS OF ENGINEERS FORMULA

In 1946, the following formula for penetration was developed by the Army Corps of Engineers [2]:

$$\frac{X_p}{D} = \frac{282W}{D^{2.785} f'_c{}^{0.5}} \frac{V^{1.5}}{1000^{1.5}} + 0.5 \qquad (4)$$

where D is the diameter of the missile in inches, W is the weight of the missile in pounds, and f'_c is the compressive strength of concrete in psi. In 1943, high-velocity ballistic tests were carried out on 38, 76, and 155 mm steel cylindrical missiles and the following relationships for scabbing and perforation were obtained using regression analysis:

$$\frac{d_s}{D} = 2.12 + 1.36\,\frac{X_p}{D} \qquad 0.65 \leq \frac{X_p}{D} \leq 11.75 \qquad (5)$$

$$\frac{d_p}{D} = 1.32 + 1.24\,\frac{X_p}{D} \qquad 1.35 \leq \frac{X_p}{D} \leq 13.5 \qquad (6)$$

MODIFIED NATIONAL DEFENSE RESEARCH COMMITTEE (NDRC) FORMULA

In 1946, the National Defense Research Committee (NDRC) proposed the following formula for predicting the penetration depth [12]:

$$\frac{X_p}{D} = \left[\frac{4\,K\,K_1\,W}{D\,(1000D)^{1.8}}\,V^{1.8}\right]^{0.5} \qquad \text{for } \frac{X_p}{D} \leq 2.0$$

$$\frac{X_p}{D} = 1. + \frac{K\,K_1\,W}{D\,(1000D)^{1.8}}\,V^{1.8} \qquad \text{for } \frac{X_p}{D} > 2.0 \qquad (7)$$

Where K_1 is the concrete penetrability factor and is given as a function of concrete strength f'_c as follows:

$$K_1 = 180/\sqrt{f'_c} \qquad (8)$$

As defined previously K is the missile nose shape factor. It is equal to 0.72 for flat-nosed missile, 1.00 for average bullet nose (spherical end), 0.84 for blunt-nosed bodies, and 1.14 for very sharp nose. All the quantities are expressed in U.S. customary units. Kennedy and Chelapati [11] proposed the following equations for scabbing and perforation thickness for use in conjunction with Eqs. (7) and (8):

$$\frac{d_s}{D} = 7.91\,\left(\frac{X_p}{D}\right) - 5.06\,\left(\frac{X_p}{D}\right)^2 \qquad \frac{X_p}{D} \leq 0.65 \qquad (9)$$

$$\frac{d_p}{D} = 3.19\,\left(\frac{X_p}{D}\right) - 0.718\,\left(\frac{X_p}{D}\right)^2 \qquad \frac{X_p}{D} \leq 1.35 \qquad (10)$$

AMMANN AND WHITNEY FORMULA

The following formula has been developed to predict the penetration depth of small explosively generated fragments traveling over 1000 ft/sec [17]:

$$\frac{X_p}{D} = \frac{282\,K\,W\,V^{1.8}}{D\,(f'_c)^{0.5}\,(1000D)^{1.8}}$$

THE BALLISTIC RESEARCH LABORATORY FORMULA (BRL)

The Ballistic Research Labs (BRL) have proposed the following formula to predict directly the perforation thickness for concrete walls having an ultimate compressive strength of 3000 psi [6]:

$$\frac{d_p}{D} = 7.8\,\frac{W}{D^{2.8}}\,\frac{V^{1.33}}{1000^{1.33}}$$

This equation has been extended for other values of the ultimate compressive strength as follows:

$$\frac{d_p}{D} = \frac{427\,W}{D^{2.6}\,f'^{0.5}_c}\,\frac{V^{1.33}}{1000^{1.33}}$$

The scabbing thickness d_s can be obtained from:

$$d_s = 2\,d_p$$

BECHTEL CORPORATION FORMULA

The Bechtel Corporation has proposed an empirical formula for calculating the scabbing thickness of concrete panel under the impact of cylindrical hard missiles as follows [13 and 14]:

$$d_s = \frac{15.5\,W^{0.4}\,V^{0.6}}{f'^{0.5}_c\,D^{0.2}}$$

STONE AND WEBSTER CORPORATION FORMULA

Stone and Webster have proposed a formula for predicting the scabbing thickness for a concrete panel under the impact of solid missiles as follows [9]:

$$d_s = \left(\frac{W\,V^2}{c}\right)^{1/3}$$

where c is a coefficient that depends on the ratio of the target thickness to the diameter of the missile. The ranges of test parameters for this formula were: 3000 psi $\leq f'_c \leq$ 4500 psi and $1.5 \leq d/D \leq 3.0$.

COMMISSARIAT A L'ENERGIE ATOMIQUE-ELECTRICITE DE FRANCE (CEA-EDF)

In 1977, Berriaud et al. [3] proposed the

following empirical formula for calculating the perforation thickness of concrete on the basis of experiments carried out in France by CEA-EDF:

$$d_p = 0.765\ (f_c')^{-0.375}\ V^{0.75}\ (\frac{W}{D})^{0.5}$$

The limits of validity of this formula are:

1. Reinforcing steel = 9.34 - 18.68 lb/ft^3.
2. Concrete compressive strength f_c' = 4300 - 7300 psi.
3. Missile impacting velocity V=82-1476 ft/sec.
4. Ratio of target thickness to missile dimeter d/D = 0.349 - 4.17.

KAR FORMULA

In 1978, using regression analysis, Kar revised the NDRC formula to account for the size of aggregates and the type of missile material. His equation for penetration depth is as follows [10]:

$$\frac{X_p}{D} = [\frac{4\ K\ K_1}{D}(\frac{E}{E_m})^{1.25}\ \frac{W\ V^{1.8}}{1000D^{1.8}}]^{0.5} \qquad \frac{X_p}{D} \leq 2.$$

$$\frac{X_p}{D} = \frac{K\ K_1}{D}(\frac{E}{E_m})\ \frac{W\ V^{1.8}}{1000D^{1.8}} + 1 \qquad \frac{X_p}{D} > 2.$$

Where E is the modulus of elasticity of the missile material and E_m is the modulus of elasticity of mild steel. The shape factor K equals 0.72 for flat-nosed hard missiles. For missiles with special noses, it is calculated from the following equation:

$$K = 0.72 + 0.25\ (n - 0.25)^{0.5} \leq 1.17$$

in which n is the ratio of the radius of the nose to the diameter of the missile. Kar stated that the factor $(E/E_m)^{1.25}$ is approximate; its use is recommended until sufficient test data is available for making necessary changes, and for most practical cases $E \approx E_m$. In this case, his penetration equation for flat nosed solid cylindrical missiles becomes identical with the NDRC formula. He also proposed the following scabbing and perforation equations:

$$b\ \frac{d_s - a}{D} = 7.91\ \frac{X_p}{D} - 5.06\ (\frac{X_p}{D})^2 \qquad \frac{X_p}{D} \leq 0.65$$

$$b\ \frac{d_s - a}{D} = 2.12 + 1.36\ \frac{X_p}{D} \qquad 0.65 \leq \frac{X_p}{D} \leq 11.75$$

$$\frac{d_p - a}{D} = 3.19\ \frac{X_p}{D} - 0.718\ (\frac{X_p}{D})^2 \qquad \frac{X_p}{D} \leq 1.35$$

$$\frac{d_p - a}{D} = 1.32 + 1.24\ \frac{X_p}{D} \qquad 1.35 \leq \frac{X_p}{D} \leq 13.5$$

where:

$$b = (E_m/E)^{0.2} \qquad (24)$$

and a is half the concrete aggregate size.

DEGEN FORMULA

In 1980, based on statistical analysis, Degen proposed the following perforation formula [5]:

$$\frac{d_p}{D} = 0.69 + 1.29\ \frac{X_p}{D} \qquad 2.65 \leq \frac{d}{D} \leq 18$$

$$\frac{d_p}{D} = 2.2\ \frac{X_p}{D} - 0.3\ (\frac{X_p}{D})^2 \qquad \frac{X_p}{D} \leq 1.52$$

The test data from which Degen statistically derived his equation cover the following ranges of variables:

Reinforcing steel: 9.97 - 21.8 lb/ft^3.

82	≤	V	≤	1023	ft/sec.
33	≤	W	≤	756	lb.
4116	≤	f_c'	≤	6245	psi
6	≤	d	≤	24	in.
4	≤	D	≤	12	in.
0.5	≤	d/D	≤	27	

CHANG FORMULA

In 1981, using Bayesian statistics and classical mechanics principles, Chang [4] proposed the following two formulae for evaluating scabbing and perforation thicknesses of a concrete panel:

$$d_s = 1.84\ (\frac{200}{V})^{0.13}\ \frac{(M\ V^2)^{0.4}}{D^{0.2}\ f_c'^{0.4}}$$

$$d_p = (\frac{200}{V})^{0.25}\ (\frac{M\ V^2}{D\ f_c'})^{0.5}$$

The test data from which Chang developed his equation cover the following ranges:

55	$\leq$	V	$\leq$	1023	ft/sec.
0.24	$\leq$	W	$\leq$	756	lb.
2	$\leq$	d	$\leq$	24	in.
0.79	$\leq$	D	$\leq$	12	in.
3300	$\leq$	f'_c	$\leq$	6600	psi.

HALDAR & MILLER FORMULA

Introducing the impact factor

$$I = \frac{12 \times 0.72}{32.2} \frac{W V^2}{D^3 f'_c}$$

where the units are the same as those of the NDRC formula, Haldar & Miller [7] found the following equations for penetration based on a bi-linear regression analysis and connecting the resulting two lines by a third intermediate line.

$$\frac{X_p}{D} = -0.02725 + 0.22024\ I \qquad 0.3 \leq I \leq 2.5$$

$$\frac{X_p}{D} = -0.592 + 0.446\ I \qquad 2.5 \leq I \leq 3$$

$$\frac{X_p}{D} = +0.53886 + 0.06892\ I \qquad 3.0 \leq I \leq 21.$$

Where $X_p/D \leq 2.0$.

HUGHES FORMULA

In 1983, assuming a parabolic impact force-penetration depth relationship, Hughes developed three formulae for predicting penetration depth, scabbing thickness, and perforation thickness [8]. He defined an impact factor in terms of the concrete tensile strength, f_r:

$$I' = \frac{M V^2}{f_r D^3}$$

He proposed the following formula for predicting the penetration depth:

$$\frac{X_p}{D} = 0.19\ K'\ I'/S$$

Where K' is the nose shape factor and equal to 1.00 for flat nosed missiles, 1.12 for blunt nosed missiles, 1.26 for average bullet nose (spherical end), and 1.39 for very sharp nose; and

S=strain-rate factor = 1.+12.3 Ln (1. + 0.03 I').

His equations for scabbing and perforation are as follows:

$$\frac{d_s}{D} = 1.74 \frac{X_p}{D} + 2.3 \qquad \frac{X_p}{D} > 0.7$$

$$\frac{d_s}{D} = 5.0 \frac{X_p}{D} \qquad \frac{X_p}{D} < 0.7$$

$$\frac{d_p}{D} = 1.58 \frac{X_p}{D} + 1.4 \qquad \frac{d}{D} > 3.5$$

$$\frac{d_p}{D} = 3.6 \frac{X_p}{D} \qquad \frac{d}{D} < 3.5$$

ADELI - SIERAKOWSKI - AMIN (ASA) FORMULAE

The present authors noticed a proportional relationship between the observed penetration depth X and the dimensionless impact factor I defined as follows:

$$I = \frac{K W V^2}{g D^3 f'_c}$$

After using the least squares technique and trying various forms for this unknown relationship, quadratic and cubic polynominals were found to best fit the test data. Using the test data from the test programs conducted in Europe and U.S.A. during the last 10 years [16], the following two equations for estimating the penetration depth of the concrete are proposed:

$$\frac{X_p}{D} = 0.0416 + 0.1698\ I - 0.0045\ I^2$$

$$\frac{X_p}{D} = 0.0123 + 0.196\ I - 0.008\ I^2 + .0001\ I^3$$

COMPARISON OF PENETRATION EQUATIONS

In 1976, Kennedy compared the modified Petry, ACE, NDRC, and Ammann and Whitney penetration equations with the experimental results available at that time [11]. He found the NDRC equations to be the best among the concrete penetration equations available in 1975. These equations along with other recent penetration equations i.e., those of Haldar and Miller, Hughes, and ASA were compared in this work using the recent experimental results compiled by Sliter [16]. The recent concrete penetration equations along with the available data are shown in Fig. 1. Figure 2 shows scatter diagrams for X_p/X (X is the experimentally observed depth) versus X/D. The following observations are made:

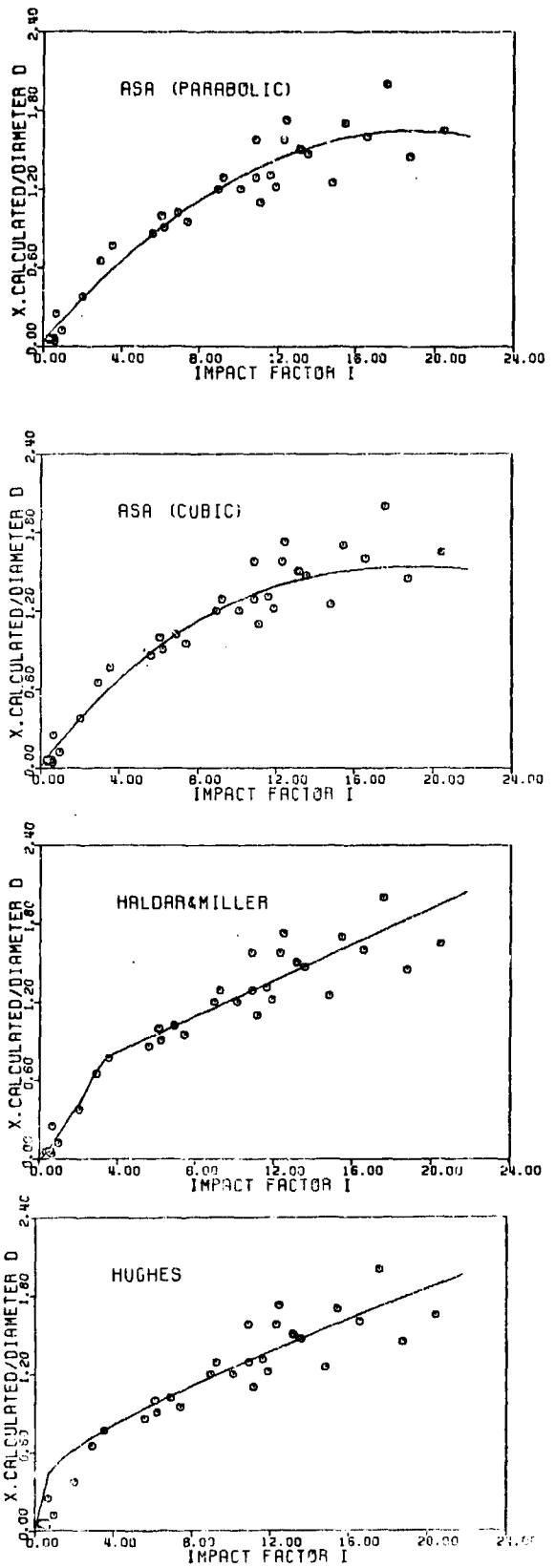

Figure 1

1. For X/D > 0.6, Modified NDRC, Haldar & Miller, Hughes and the ASA formulae tend to agree with the experimental results within ±25%.

2. For X/D < 0.6, Modified Petry 2, Haldar & Miller, and ASA formulae agree with experimental results better than the other ones.

3. ACE formula and Modified Petry 1 practically overpredict the penetration depth with a big margin.

Generally, Hughes, Haldar & Miller, and ASA formulae predict the penetration depth better than other predictors. Therefore, two statistical comparisons were carried out on these particular formulae. In each comparison, the variance and the coefficient of variation have been calculated. The first comparison was carried out on all data points (33 points). The second comparison was carried out for high velocity data points (velocity > 475 ft/sec) (22 points).

In the first comparison, when all data points were used, ASA quadratic formula gave the least coefficient of variation of 0.1433, then ASA cubic formula, Haldar & Miller, NDRC, and Hughes gave coefficients of variation of 0.1444, 0.1506, 0.1803 and 0.1956, respectively. For data points with velocity > 475 ft/sec., the coefficients of variation of 0.1203, 0.1299, 0.131, 0.1476, 0.1481 were obtained by NDRC, ASA quadratic ASA cubic, Haldar & Miller, and Hughes formulas, respectively.

COMPARISON OF SCABBING EQUATIONS

The Modified Petry, ACE, NDRC BRL, Bechtel Corporation, Chang, and Hughes scabbing formulae were compared with the data compiled by Sliter [16]. The results are summarized below

1. The Modified Petry and BRL formulae provide the worst fit with the experimentally obtained data for scabbing thickness and underestimate the scabbing thickness in many cases.

2. The Hughes scabbing formula is the most conservative equation in predicting the scabbing thickness and overestimates the scabbing thickness sometimes by a factor of three.

3. The ACE, NDRC, Bechtel, and Chang formulae in general predict the scabbing thickness safely with a few exceptions, however, the NDRC and ACE equations give more conservative results than the other two. In terms of closeness of fit, the Bechtel formula appears somewhat better than the other equations.

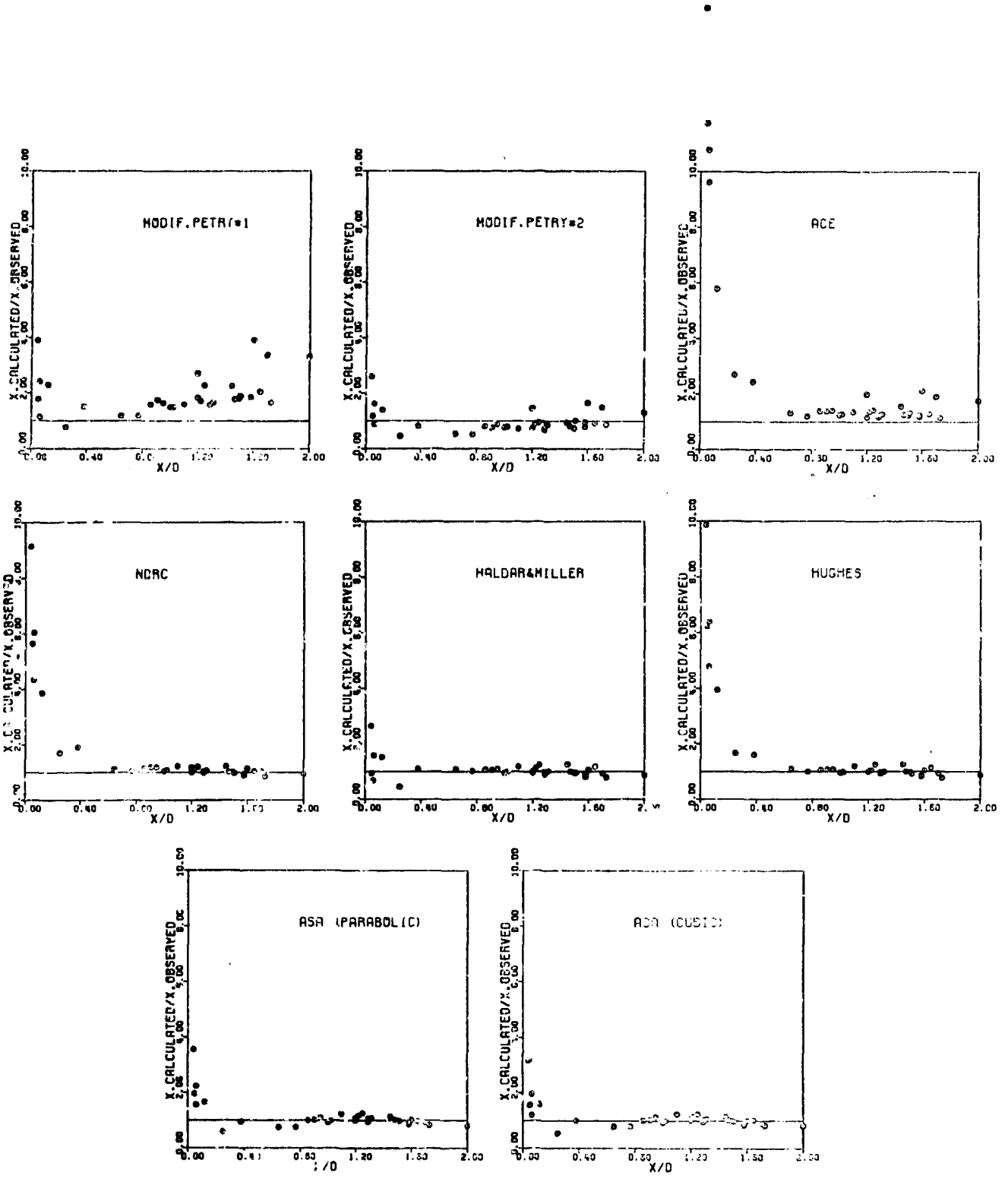
MODIF.PETR(*1
MODIF.PETRY*2
ACE
NCRC
HALDAR&MILLER
HUGHES
ASA (PARABOLIC)
ASA (CUBIC)
X.CALCULATED/X.OBSERVED
X/D

Figure 2

COMPARISON OF PERFORATION EQUATIONS

The Modified Petry, ACE, NDRC, BRL, CEA-DEF, Degen, Chang, and Hughes perforation formulae were compared with the data compiled by Sliter [16]. The results are summarized in the following paragraphs:

1. The Modified Petry and BRL formulae have the worst fit with the experimentally obtained data and underestimate the perforation thickness in many cases.

2. The Hughes perforation formula in general overestimates the perforation thickness more than the other equations.

3. The CEA-DEF, Degen, and Chang formulae have the best fit for perforation thickness followed by the NDRC formula.

REFERENCES

1. Amirikian, A., "Design of Protective Structures", Report NT-3726, Bureau of Yards and Docks, Department of the Navy, August 1950.

2. ACE, "Fundamentals of Protective Design", Report AT120 AT1207821, Army Corps of Engineers, Office of the Chief of Engineers, 1946.

3. Berriaud, C., Sokolovsky, A., Gueraud, R., Dulac, J., and Labrot, R., "Local Behavior of Reinforced Concrete Walls Under Missile Impact", Nuclear Engineering and Design, Vol. 45, pp. 457-470, 1978.

4. Chang, W.S., "Impact of Solid Missiles on Concrete Barriers", Journal of the Structural Division, ASCE, Vol. 107, No. ST2, pp. 257-271, February 1981.

5. Degen, P.P., "Perforation of Reinforced Concrete Slabs by Rigid Missiles", Journal of the Structural Division, ASCE, Vol. 106, No. ST7, pp. 1623-1642, July 1980.

6. Gwaltney, R.C., "Missile Generation and Protection in Light Water-Cooled Reactor Power Plants", ORNL NSIC-22, Oak Ridge National Laboratory, Oak Ridge, Tennessee, September 1968.

7. Haldar, A. and Miller, F.J., "Penetration Depth in Concrete for Nondeformable Missiles", Nuclear Engineering and Design, Vol. 71, pp. 79-88, 1982.

8. Hughes, G., "Hard Missile Impact on Reinforced Concrete", Nuclear Engineering and Design, Vol. 77, pp. 23-35, 1984.

9. Jankov, Z.D., Shanahan, J.A., and White, M.P., "Missile Tests of Quarter-Scale Reinforced Concrete Barriers", Proceedings of the Symposium on Tornadoes, Assessment of Knowledge and Implications for Man, Texas Tech University, Lubbock, Texas, June, 1976.

10. Kar, A.K., "Local Effects of Tornado-Generated Missiles", Journal of the Structural Division, ASCE, Vol. 104, No. ST5, pp. 809-816, May 1978.

11. Kennedy, R.P., "A Review of Procedures for the Analysis and Design of Concrete Structures", Nuclear Engineering and Design, Vol. 37, 1976, pp. 183-203.

12. NDRC, "Effects of Impact and Explosion", Summary Technical Report of Division 2, National Defense Research Committee, Vol. 1, Washington, D.C., 1946.

13. Rotz, J.V., "Results of Missile Impact Tests on Reinforced Concrete Panels", 2nd ASCE Specialty Conference on Structural Design of Nuclear Plant Facilities, New Orleans, Louisiana, December 1975.

14. Rotz, J.V., "Evaluation of Tornado Missile Impact Effects on Structures", Proceedings of the Symposium on Tornadoes, Assessment of Knowledge and Implications for Man, Texas Tech University, Lubbock, Texas, June 1976.

15. Samuely, F.J. and Hamann, C.W., Civil Protection, The Architectural Press, 1939.

16. Sliter, G., "Assessment of Empirical Concrete Impact Formulas", Journal of the Structural Division, ASCE, Vol. 106, No. ST5, May 1980, pp. 1023-1045.

17. "Structures to Resist the Effects of Accidental Explosions", TM 5-1300, Department of Army, Washington, D.C., July 1965.

PENETRATION OF FRAGMENTS INTO SAND

A. Stilp, E. Schneider
and
M. Hülsewig

Ernst-Mach-Institute, Freiburg, FRG

ABSTRACT

Penetration mechanics of steel fragments into sand have been experimentally investigated for a range of impact velocities between 100 m/s and 3500 m/s. In order to obtain systematic results, idealized fragment geometries have been chosen, i.e. spheres and cylinders were used as projectiles. The results obtained show that sand is well suitable as a protective medium against fragment threat, however, it is not useful as a diagnostic recovery material for fragments. Impact velocities of fragments cannot be derived from penetration depths.

INTRODUCTION

In the field of fragment ballistics, material properties of fragment catcher media are interesting with respect to the following aspects:

1) Protection properties
2) Soft recovery of fragments
3) Diagnostic properties concerning kinetic fragment parameters

For shelter purposes the overall stopping efficiency of a given material is of primary importance, i.e. short penetration paths, deformation, erosion and shattering of fragments are highly desirable.

A different problem arises, if soft fragment recovery is desired, for example if mass, shape, and spatial distributions of fragments are to be measured. In this case, fragments must not be affected during their deceleration within the catcher material. In addition, it is very advantageous, if relations between penetration depths and impact velocities can be established. Taking these aspects into account, sand as a cheap and widespread material has been experimentally studied.

EXPERIMENTS AND RESULTS

Idealized fragments, steel spheres with a diameter of 1 cm (mass 4.07 g) and steel cylinders with length-to-diameter-ratios of 1, 5 and 10 and masses between 10 g and 50 g have been used as projectiles. They were accelerated within closed launch facilities. Depending on the velocity range, the launchers can be operated as compressed air/powder/and light gas guns. They are equipped with velocity measurement stations and flash-X-ray channels. Dry, loose sand with a density of 1.8 g/cm^3 and maximum grain sizes of 1.05 mm and 2 mm, respectively, were used as target materials. It has been placed within a box sufficiently large in order to avoid confinement influences on the penetration process. The sand box had an entrance opening for the projectile, closed by a paper strip, and was set up within the target chamber.

1) RESULTS FOR SPHERE PROJECTILES (Schneider and Stilp 1977)

The steel spheres were shot into the sand target at velocities between 118 m/s and 3553 m/s.

Depending on the impact velocity the following processes have been observed: Up to a few hundred m/s the projectiles are decelerated by sand displacement and compaction. The kinetic projectile energy is dissipated as internal friction energy. Slight scratches are observed at the front side of the projectiles (fig. 1 a).

Starting at about 400 m/s, sand grains become fragmented, projectile erosion effects and mass losses occur. Fig. 1 b shows a projectile after penetration at an impact velocity of 1745 m/s. Projectile material is eroded up to a distinct boundary line. Agglomerates of fine fragmented sand at the projectile are observed.

For comparison fig. 1 c shows a sphere which had been annealed prior to the experiment. The velocity was 1746 m/s.

Much more material is eroded in this case, since the projectile had a considerably lower hardness.

At impact velocities beyond about 1000m/s the projectiles break into parts (fig. 1 d ... h).

The sharp boundary lines between the eroded and uneroded parts of the projectiles indicate that the projectiles remain strictly oriented during the penetration, at least as long as material erosion processes take place. Fig. 2 shows a flash X-ray photograph of a sphere during penetration. A cavity-like transient penetration channel is formed behind the projectile.

Fig. 3 presents the penetration curve for spheres into sand. The penetration depth normalized by the projectile diameter is plotted versus the impact velocity. The curve reflects the penetration behaviour already described qualitatively. Up to about 400 m/s a steep increase of penetration depths is obtained. Between 400m/s and about 2000 m/s the penetration depths increase by only a factor of about 1.6. The data scatter considerably. Above 2000 m/s the penetration depths are steeply decreasing which is due to projectile fragmentation. The data points marked by crosses are penetration depths of annealed spheres. They are not fragmented, but become much more eroded than the harder spheres. Fig. 4 shows a diagram, where the absolute mass loss of the projectiles is plotted versus the impact velocity. Starting at about 500 m/s the mass loss increases nearly linearly.

2) RESULTS FOR STEEL CYLINDERS (Hülsewig and Stiip, 1978)

In a similar way steel cylinders have been shot into the sand targets at velocities between 93 m/s and 1400 m/s. The results obtained can be characterized qualitatively as follows:

a) The penetration depths increase steeply up to an impact velocity of about 400 m/s.

b) Between 400 m/s and about 1000 m/s the depths of penetration increase only very weakly.

c) Beyond about 1000 m/s the penetration depths decrease again due to projectile deformation and erosion.

d) In all cases, considerable scattering of penetration data has been observed.

Fig. 5 shows how cylindrical projectiles are deformed and eroded with increasing impact velocities. The projectile mass was 48.8 g with a length-to-diameter ratio of L/D = 1. They become "mushroom-shaped". As a consequence the cross sectional area increases which leads to higher deceleration forces.

In the diagram of fig. 6 the penetration depths normalized by the projectile diameter are plotted versus the impact velocities for cylinders with a mass of 10.54 g (L/D = 1). These experiments have been performed using two types of sand targets with maximum grain sizes of 2 mm and 1.05 mm, respectively. No grain size effects have been found for such projectile sizes. Fig. 7 shows the residual masses normalized by the original projectile mass for the same projectiles at velocities of up to 1345 m/s. Fig. 8 shows the respective normalized residual projectile lengths. Within this range of impact velocities, the length reduction is predominantly caused by deformation and not by erosion.

Figs. 9 ... 11 present normalized penetration depths, residual masses and lengths for cylinders with L/D = 5 and masses of 10, 20, and 50 g. The scatter of the data is enormous. The data points in brackets within fig. 10 refer to projectiles which have been accelerated without a fixed pusher plate at the rear end of the projectile.

Figs. 12 ... 14 present the same plots for cylinders with L/D = 10 and masses of 10 g and 20 g. The penetration depths in this case show a steep decrease at about 800 m/s impact velocity. This decrease is caused by bending of the projectiles, leading to high yaw angles and deflections from the original trajectory. Above about 1000 m/s also breaking of the projectiles has been observed.

For comparison a test series has also been performed involving natural fragments with L/D ratios of about 1 and masses between 2 g and 14 g. Fig. 15 shows their normalized penetration depths versus their impact velocities. The scattering is very big and a velocity dependence of the penetration values between 100 m/s and 1200 m/s cannot be established.

DISCUSSION

The existence of maxima in the penetration curves of idealized fragments into sand as well as the occurence of projectile deformation, erosion and fragmentation during the penetration process, characterize sand as material which can

be used very effectively for protection against fragment threat, e. g. shelter constructions. For the same reasons, however, it is not appropriate as a diagnostic fragment recovery material, since projectile masses and shapes are not preserved, especially fragment velocities cannot be estimated from penetration depths.

LITERATURE

E. Schneider, A. Stilp
Verhalten von Sand als Auffangmaterial für Stahlsplitter
EMI-Bericht E 13/77, Juli 1977

M. Hülsewig, A. Stilp
Untersuchung über das Eindringverhalten von Splittern in Sand verschiedener Körnung
EMI-Bericht V 1/78, Januar 1978

FIGURES

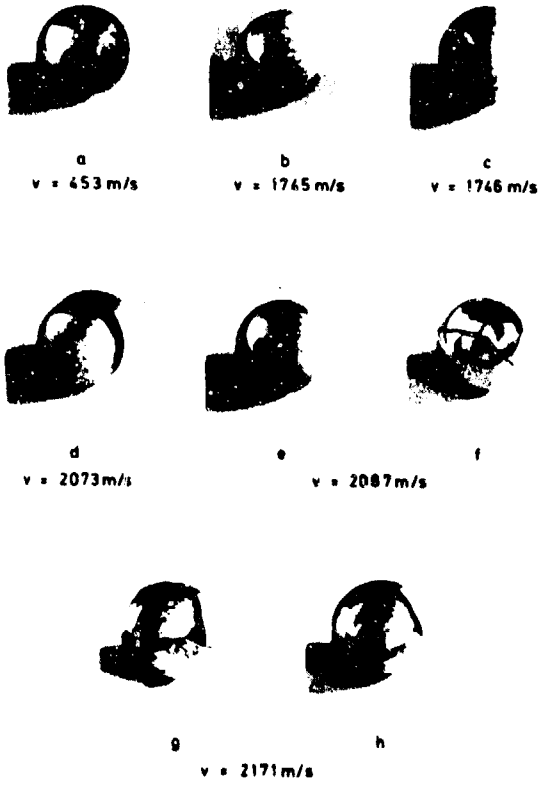

Fig. 1: Steel spheres after penetration into sand

Fig. 2: Flash X-ray photograph of a sphere during penetration

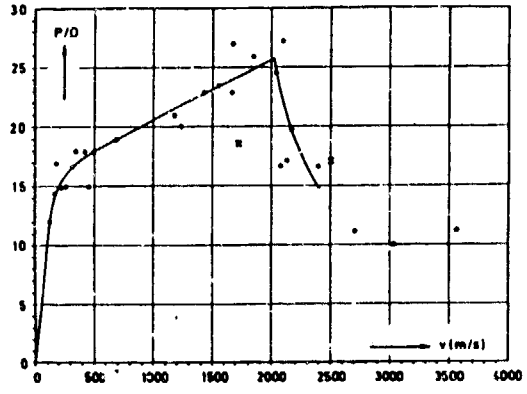

Fig. 3: Penetration curve for spheres

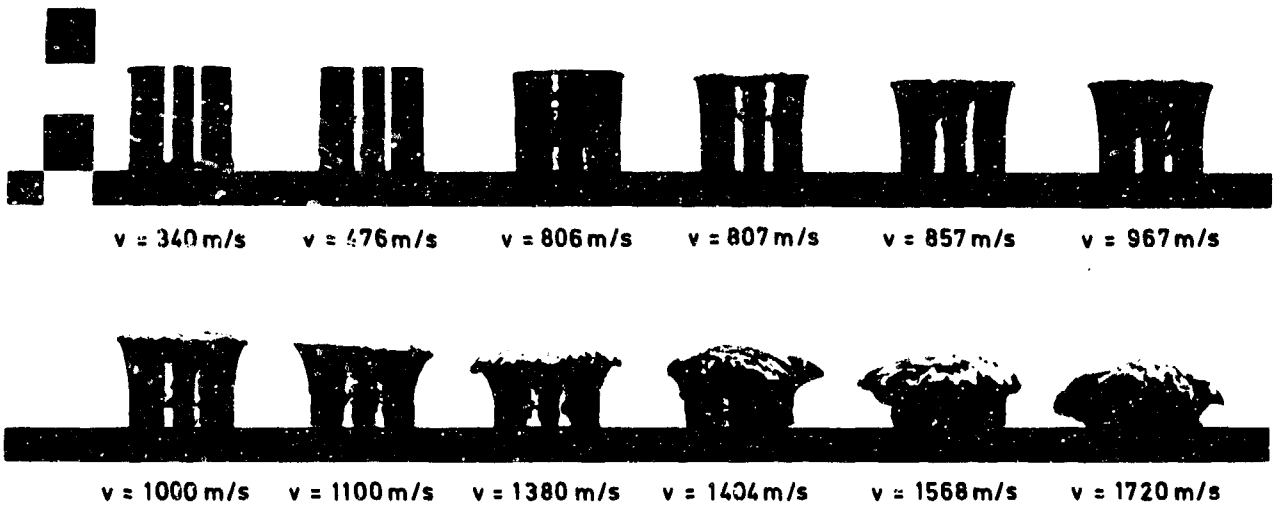

Fig. 5: Deformation and erosion of cylindrical projectiles

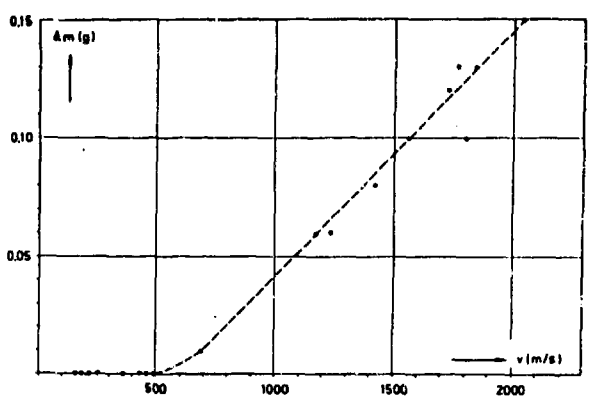

Fig. 4: Absolute mass loss of spheres as function of the impact velocity

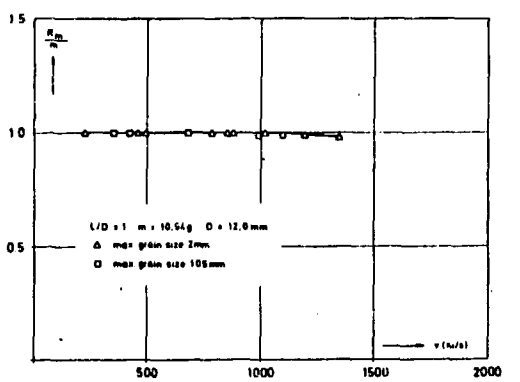

Fig. 7: Normalized residual projectile masses for L/D = 1 cylinders

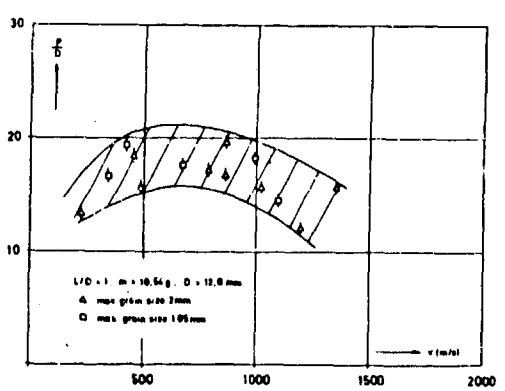

Fig. 6: Penetration depths for cylinders with L/D = 1

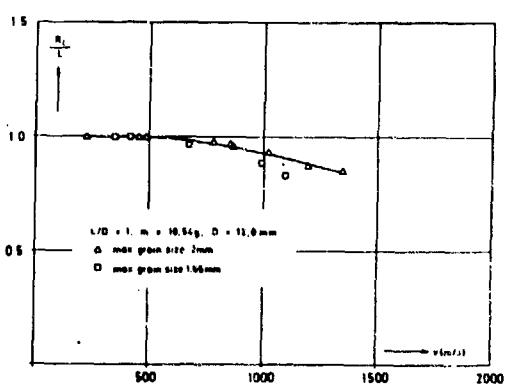

Fig. 8: Normalized residual projectile lengths for L/D = 1 cylinders

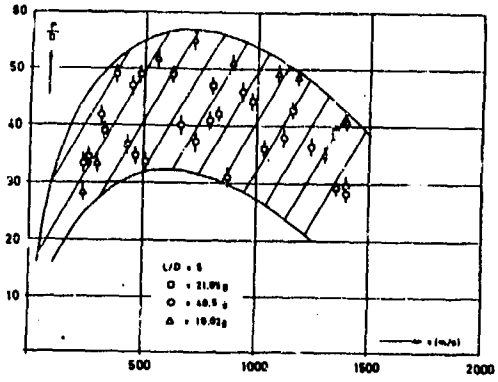

Fig. 9: Penetration depths for cylinders with L/D = 5

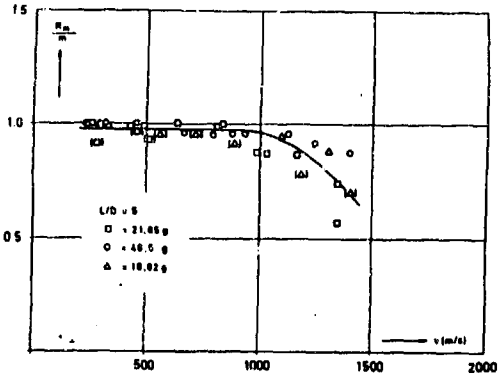

Fig. 10: Residual projectile masses for L/D = 5

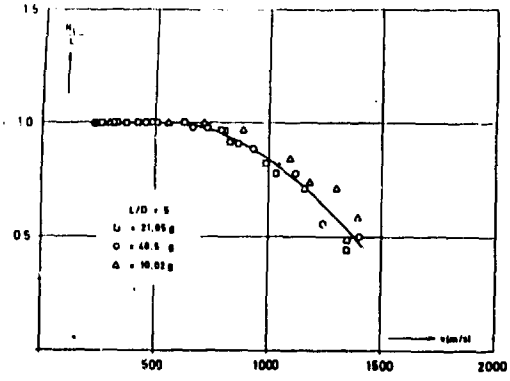

Fig. 11: Residual projectile lengths for L/D = 5 cylinders

Fig. 15: Penetration depths for natural fragments with L/D ~ 1 ⟶

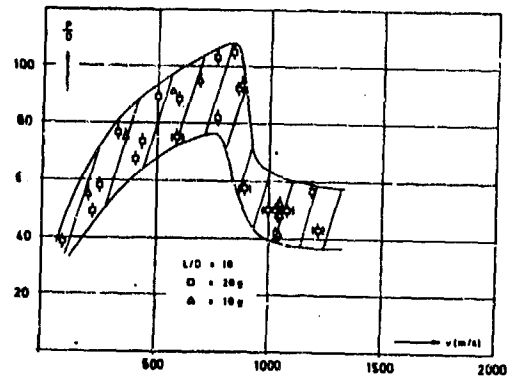

Fig. 12: Penetration depths for cylinders with L/D = 10

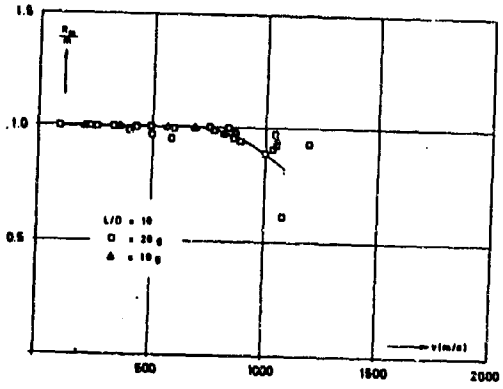

Fig. 13: Residual projectile masses for L/D = 10 cylinders

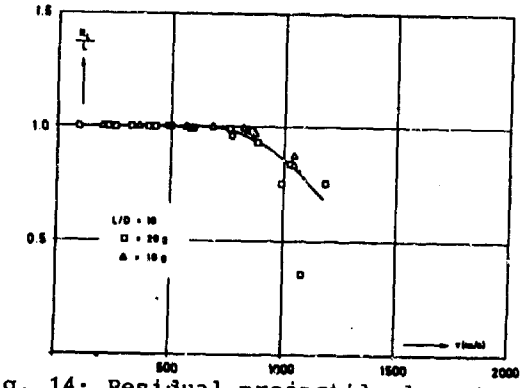

Fig. 14: Residual projectile lengths for L/D = 10 cylinders

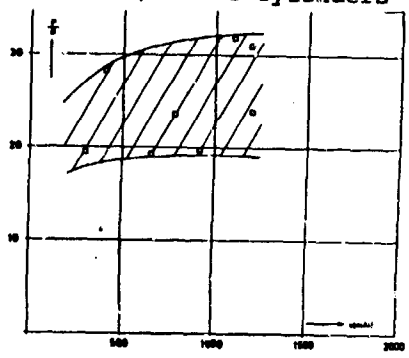

ANALYSIS OF RANDOM IMPACT LOADING CONDITIONS

L. A. Twisdale

Applied Research Associates, Inc.
4917 Professional Court
Raleigh, North Carolina 27609

ABSTRACT

Probabilistic methods are developed for the analysis of random impact loading conditions that arise from oblique, noncollinear, and spinning missile impacts. Models are developed for the analysis of impact orientation of rotating objects; expected values of effective impact velocity are numerically calculated for randomly oriented rod-type missiles; and a probability model of multiple missile impact effects is presented. An integrated methodology is outlined for the general treatment of random impact loading conditions.

INTRODUCTION

Impact loads form an important class of loading conditions in the analysis and design of structures for non-nuclear munitions effects. The sources of these loads include munition fragmentation loads, direct impact loads from unexploded bombs and projectiles, and secondary missile impact produced by scabbing or spalling of structures and protected facilities. In general, these sources of impact loads are highly variable with respect to time, position, and the conditions of the fragment or missile on impact with the barrier or component. Hence, the loading conditions are fundamentally stochastic in several parameters, including geometry, mass, orientation, velocity, angular velocity, and load position.

In view of the fundamental uncertainty in characterizing these types of multiple, random impact loads, probabilistic formats are relevant for survivability/vulnerability analysis. In general, however, conventional analysis and design procedures treat certain important aspects of impact loading conditions deterministically. This includes the conventional assumption that missile impact occurs in a normal, collinear orientation with no angular velocity. Such impact conditions are relatively unlikely for fragmentation type loads. Hence, questions arise as to what effect these assumptions have on survivability/vulnerability calculations. Estimation of the relative likelihood of near normal, collinear impact and the effects of oblique, spinning, and noncollinear impacts in reducing the impact velocity that is effective in damaging the barrier are thus critical to an accurate and realistic analysis of random impact loads.

This paper presents a collection of probability formulations and analysis of several problems that arise in certain classes of fragment and missile impact loads. It will report the results of research into probabilistic safety analysis of nuclear power plant structures subjected to fragment and secondary missile impact. The general formulations and results should provide insights to impact, penetration, and survivability analysis of protective structural design, particularly above-ground hardened and semi-hardened structures. In this paper, the term random is used to denote stochastic behavior of the missile orientation and velocity vectors in space and time. The emphasis is on slender rigid body missiles ($L/d \geq 4$) and local effects target response, although most of the results are independent of the specific mechanistic model of response (penetration, perforation, scabbing, overall dynamic response). The effect of missile rotation on impact orientation for rod-shaped missiles is developed. Estimations of the effects of oblique, spinning, and noncollinear impacts in reducing the impact velocity that is effective in damaging the barrier are made using the normal impulse model developed in Refs. 1 and 2. A probabilistic formulation of the potential for a number of missiles to impact a barrier randomly and induce cumulative damage effects is also developed. Finally, an integrated methodology is outlined for the general treatment of random impact loading conditions.

IMPACT ORIENTATION OF TUMBLING MISSILES

A convenient starting point for the analysis (and eventual simplification) of missile impact conditions is an assessment of the effects of angular velocity on impact orientation. Such an analysis provides a basis for determining whether or not angular velocity can be neglected in the development of a probability density function (pdf) of missile impact orientation. A general

formulation is developed for a rod-type missile with missile center line vector $\underset{\sim}{M}$ undergoing general motion in space. Results are illustrated for a rod-type missile and an irregular fragment.

Model Formulation. The notation for the scalars that define the vectors for the missile, $\underset{\sim}{M}$, translational velocity, $\underset{\sim}{V}_i$, and angular velocity, $\underset{\sim}{\Omega}_i$, is given in Fig. 1. For convenience, spherical coordinates are used to specify vectors--i.e., $\underset{\sim}{M} = (L,\theta,\phi)$, $\underset{\sim}{V}_i = (V,\theta',\phi')$, and $\underset{\sim}{\Omega}_i = (\Omega,\theta'',\phi'')$. Also shown in Fig. 1 are the angles γ and τ, where γ is the angle of yaw (the angle between $\underset{\sim}{M}$ and $\underset{\sim}{V}_i$) and τ is the angle between $\underset{\sim}{M}$ and $\underset{\sim}{\Omega}_i$. All of these variables are functions of time, t, and, hence, represent a family of stochastic processes that describes the instantaneous orientation and motion of the missile. In the analysis that follows, $\underset{\sim}{V}_i$, $\underset{\sim}{\Omega}_i$, and τ are assumed to remain constant constant for

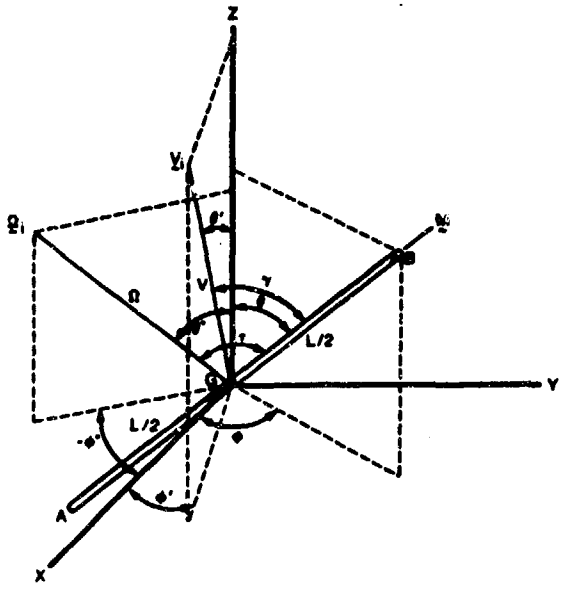

Figure 1. Notation for Missile, Velocity, and Angular Velocity Vectors

any arbitrarily small time increment, δt. However, during this time increment, the angular position of the missile is not fixed but is assumed to change by the angle $\Omega\delta t$, which is measured about the instantaneous axis of rotation defined by $\underset{\sim}{\Omega}_i$.

To determine the probability of impact orientation for a rotating missile as it approaches the target, the hit probability within time interval δt is assumed to be proportional to the distance the leading edge of the missile travels toward the surface. This concept is easily visualized in the planar example illustrated in Fig. 2, in which the leading tip motion of a missile with $V/L\Omega = 1.6$ is plotted vs time. For a missile translating with fixed orientation in the Z direction (normal to the target surface), the forward tip Z coordinate would be represented as a

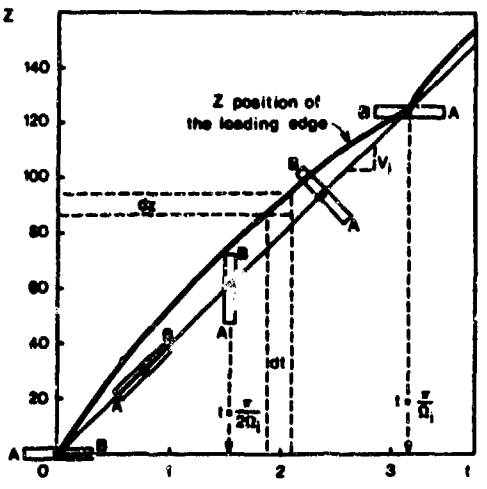

Figure 2. Motion of the Leading Edge of a Spinning Missile

function of time by a straight line with slope V. Hence, the hit probability would be equally likely for any time, t, and any fixed orientation since the slope of all such lines, dz/dt, is constant. However, if the missile is also rotating, the leading tip Z coordinate is given by the curve in Fig. 2 (for $d \ll L$). The hit probability is no longer uniform in time since the advancement of the leading edge is not a linear time function, but has sinusoidal characteristics and a period of π/Ω for slender bodies with nondistinguishable ends A and B. It is proportional to dz/dt over the time interval (t_1,t_2) during which the leading edge is advancing toward the surface and the forward Z position has not been previously reached. Mathematically, these conditions in terms of an arbitrary time t^* are written as

$$f_{t|\underset{\sim}{V}_i,\underset{\sim}{\Omega}_i,\tau}(t|\underset{\sim}{V}_i,\underset{\sim}{\Omega}_i,\tau) \propto \frac{dz}{dt} \quad , \tag{1a}$$

$$\text{if} \quad \begin{cases} \left.\dfrac{dz}{dt}\right|_{t^*} \geq 0 \\ z(t > t^*) > z(t < t^*) \end{cases}$$

$$f_{t|\underset{\sim}{V}_i,\underset{\sim}{\Omega}_i,\tau}(t|\underset{\sim}{V}_i,\underset{\sim}{\Omega}_i,\tau) = 0 \quad , \text{otherwise} \quad , \tag{1b}$$

where $f_{t|\underset{\sim}{V}_i,\underset{\sim}{\Omega}_i,\tau}(t|\underset{\sim}{V}_i,\underset{\sim}{\Omega}_i,\tau)$ denotes the probability density function of t, given $\underset{\sim}{V}_i$, $\underset{\sim}{\Omega}_i$, and τ.

The parametric equations of motion of the leading edge of the missile provide the relationship for dz/dt in Eqs. 1. Using the notation in Fig. 1 (where Z is assumed to be the outward normal from the target surface), the Z position of the leading tip is

$$z = Vt\cos\theta' + \frac{L}{2}(\cos\theta^* \cos\tau + \sin\theta^* \sin\tau \sin\Omega t) \quad , \tag{2}$$

where $Vt\cos\theta'$ is the position of the body center at time t and thus

$$\frac{dz}{dt} = V\cos\theta' + \frac{L}{2}\Omega \sin\theta^* \sin\tau \cos\Omega t \quad . \tag{3}$$

The condition that the leading edge advances (the first inequality of Eq. 1a) is satisfied when

$$\frac{2V}{L\Omega} \geq \frac{\sin\theta^* \sin\tau}{\cos\theta'} \tag{4}$$

in which case the position time curve of the leading edge is similar to Fig. 2 for the entire period $t = \{0,\pi/\Omega\}$. If Eq. 4 is not satisfied, then a time interval exists within which the leading edge recedes, as is illustrated in Fig. 3,

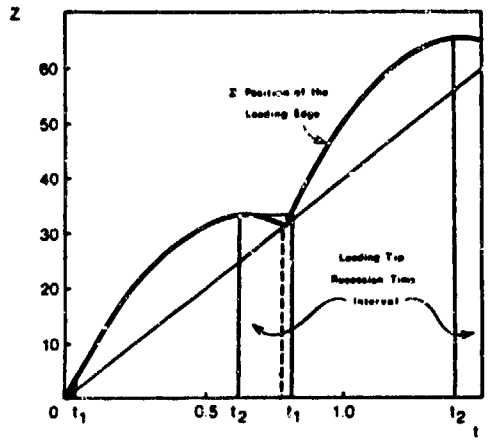

Figure 3. Motion with Leading Edge Recession

which is based upon the same parameters as Fig. 2 except that $V/L\Omega = 0.4$. To determine the time interval, $\{t_1,t_2\}$, in which the missile advances (and, hence, to satisfy the second inequality of Eq. 1a), t_2 is obtained from the condition $dz/dt = 0$. Thus,

$$t_2 = \frac{1}{\Omega}\cos^{-1}\left(\frac{-2V\cos\theta'}{L\Omega \sin\theta^* \sin\tau}\right) \quad . \tag{5}$$

Then t_1 is obtained by solving the transcendental equation

$$z(t1) = z(t2) - z\left(\frac{\pi}{\Omega}\right) \quad , \tag{6}$$

where $z(t)$ is given by Eq. 2.

Once the $\{t_1,t_2\}$ interval is known, the pdf $f_t(t)$ is easily calculated. First, for those cases in which Eq. 4 is satisfied, the normalization constant, k, of $f_t(t)$, is determined from

$$k = \left[\int_0^{\pi/\Omega} \frac{dz}{dt}\, dt\right]^{-1} = \frac{\Omega}{\pi V\cos\theta'} \tag{7}$$

which is simply the inverse of the path length traced by the leading edge. From Eqs. 1, 3, and 7, the conditional pdf is

$$f_{t|\underset{\sim}{V}_i,\underset{\sim}{\Omega}_i,\tau}(t|\underset{\sim}{V}_i,\underset{\sim}{\Omega}_i,\tau) = k\frac{dz}{dt} = \frac{\Omega}{\pi} + \frac{L\Omega^2 \sin\theta^* \sin\tau}{2\pi V\cos\theta'}\cos\Omega t \quad , \quad 0 \leq t \leq \pi/\Omega \quad . \tag{8}$$

The development of a general closed-form pdf for the case in which Eq. 4 is not satisfied is not possible because of the transcendental characteristic of Eq. 6. However, the procedure is similar to that developed above; that is,

$$k = \left[\int_{t_1}^{t_2} \frac{dz}{dt}\, dt\right]^{-1} = \frac{1}{z(t_2) - z(t_1)} \quad , \tag{9}$$

and an expression similar to Eq. 8 is developed that applies to the interval $\{t_1,t_2\}$. Outside this interval, the probability density is zero.

For given $\underset{\sim}{V}_i$, $\underset{\sim}{\Omega}_i$, and τ, Eq. 8 (or its equivalent developed using Eqs. 1, 3, and 9) is used to determine the pdf of the angular position Ωt of the missile by a transformation of variables [e.g., 5],

$$f_{\Omega t|\underset{\sim}{V}_i,\underset{\sim}{\Omega}_i,\tau}(\Omega t|\underset{\sim}{V}_i,\underset{\sim}{\Omega}_i,\tau) = \frac{1}{\Omega} f_{t|\underset{\sim}{V}_i,\underset{\sim}{\Omega}_i,\tau}(t|\underset{\sim}{V}_i,\underset{\sim}{\Omega}_i,\tau) \quad . \tag{10}$$

Two final relationships are needed for the conversion from Ωt to the impact orientation relative to the barrier normal. For angular position Ωt the orientation of the missile is determined from

$$\theta = \cos^{-1}(\cos\tau \cos\theta^* + \sin\tau \sin\theta^* \sin\Omega t) \tag{11a}$$

and

$$\phi = \tan^{-1}[(\tan\tau[\cos\phi^* \cos\Omega t + \cos\theta^* \sin\phi^* \sin\Omega t] - \sin\theta^* \sin\phi^*) / (\tan\tau[\sin\phi^* \cos\Omega t - \cos\theta^* \cos\phi^* \sin\Omega t] + \sin\theta^* \cos\phi^*)] \quad . \tag{11b}$$

Expected Angular Orientation for Rod Missile Impact. Using the previously developed relationships, the probabilities of missile impact orientation are illustrated for a rod-type missile for specified values of $\underset{\sim}{V}_I$, $\underset{\sim}{\Omega}_I$, and τ.

As a first example, consider the conditions illustrated in Fig. 2 with $\theta' = 0°$ and $\theta^* = 90°$. Hence, the missile is translating directly towards the barrier and rotating about an axis parallel to the barrier surface. Equation 4 is satisfied and thus the relevant pdfs are given by Eqs. 8 and 10. Figure 4(a) shows the pdf as a function of

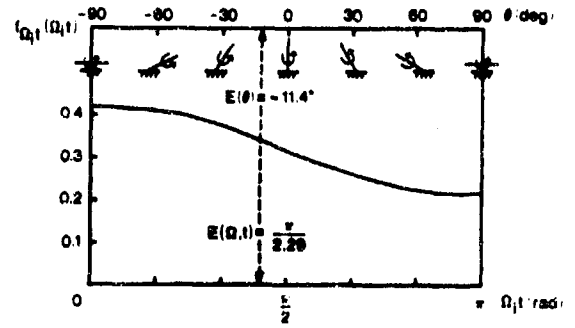

(a) No Recession Time Interval (Ω_I = 1 rad/sec)

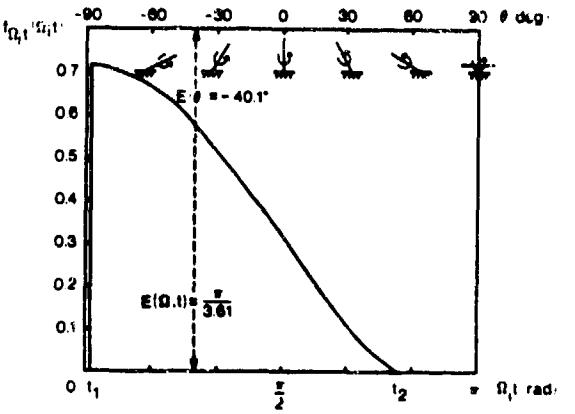

(b) Recession Time Interval (Ω_I = 4 rad/sec)

Figure 4. Probability Density Functions of Missile Impact Orientation

orientation angle. The most likely impact orientation is $\theta = -90°^+$, when the velocity of the leading edge (point A in Fig. 2 for $t = 0$) toward the surface is maximum. Correspondingly, the least likely orientation is $\theta = 90°^-$ (point B in Fig. 2 for $t = \pi/\Omega$), as the leading edge is rotating away from the surface. The orientations $\theta = -90°$ and $\theta = 90°$ define the same condition; i.e., the missile impacts perfectly flatly. Thus, as the missile rotates through this orientation, there is a step change in the pdf from maximum to minimum.

The expected value of missile position as defined by Ωt can be expressed in closed-form for those cases in which Eq. 4 is satisfied. From Eqs. 8 and 10 and the definition of expected value, one obtains

$$E(\Omega t) = \frac{\pi}{2} - \frac{L\Omega \sin\theta^* \sin\tau}{\pi V \cos\theta'} \quad , \qquad \frac{2V}{L\Omega} \geq \frac{\sin\theta^* \sin\tau}{\cos\theta} \quad . \tag{12}$$

Similarly, for the variance $\sigma^2[\Omega t]$, the following expression can be derived:

$$\sigma^2(\Omega t) = \frac{\pi^2}{12} - \frac{L^2\Omega \sin^2\theta^* \sin^2 \tau}{\pi^2 V^2 \cos^2\theta'} \quad , \qquad \frac{2V}{L\Omega} \geq \frac{\sin\theta^* \sin\tau}{\cos\theta'} \quad . \tag{13}$$

For this example, the expected value of missile orientation is $E(\Omega t) = 1.37$ rad, or $E(\theta) = -11.4°$ as shown in Fig. 4(a), and $\sigma^2(\Omega t) = 0.783$ rad^2. Thus, the effect of rotation is to bias the impacts toward orientations in which the missile edge is rotating into the surface; i.e., $\theta < 0$. As noted in Refs. 1 and 2, the effects of rotation add to the normal impulse for $\dot{\theta} < 0$ (missile edge rotating into the surface) and subtract for orientations in which $\dot{\theta} > 0$ (missile edge rotating away from surface). Since the above analysis shows that $\theta < 0$ impact orientations are more likely, the total effect of rotation on the expected normal impulse would be an increase over the case in which $\dot{\theta}$ effects are neglected.

As a second example, consider the motion in Fig. 3, which illustrates an interval of leading edge recession. From Eq. 5, we find that $t_2 = 0.625$ sec, which corresponds to $\Omega t_2 = 2.50$ rad, or $\theta = 53.1°$. With Eq. 6, t_1 is determined to be 0.012 sec, corresponding to $\Omega t = 0.048$ rad, or $\theta = -87.25°$. Thus, as shown in Fig. 4(b), the probability of impact orientations outside the interval $-87.25° \leq \theta \leq 53.1°$ is zero, and from Eqs. 7, 8, and 9, the probability density of Ωt is

$$f_{\Omega t}(\Omega t) = 0.318 + 0.398 \cos\Omega t \quad ,$$

$$0.048 \leq \Omega t \leq 2.50 \quad .$$

The most likely and least likely orientations occur at the lower and upper limits of Ωt, respectively. The expected value of missile orientation is $E(\Omega t) = \pi/3.61$ rad, or $\theta = -40.1°$, which indicates an increased bias toward advancing oblique orientation over the case where $\Omega = 1$ rad/sec.

These simple cases illustrate the effect of rotation on the impact position for a spinning missile translating towards a target. For small $\Omega L/V$, the impact orientation is nearly uniform over the complete interval ($\theta = -90°$ to $\theta = 90°$). As the relative angular velocity increases, bias

toward $\theta = -90°$ occurs as noted in Fig. 4(a). When the relative angular velocity is increased to the point that Eq. 4 is not satisfied, certain impact orientations become physically impossible. As illustrated in Fig. 4(b), this further shifts the expected impact orientation. Further increases in ΩL cause Ωt_2 to approach $\pi/2$ from the right and Ωt_1 to approach (more slowly) $\pi/2$ from the left. For example, for $\Omega = 100$ rad/sec in the above problem, $\Omega t_1 = 65.9°$ and $\Omega t_2 = 91.8°$. As $\Omega L/V \to \infty$, a spike forms at $\Omega t = \pi/2$, and only normal impact orientations are possible.

Distribution of Angular Orientation for Fragment Missile. For nonslender body fragment-type missiles, the previously developed solution is complicated by the shifting (both continuously and in steps) of the impact point of the leading edge. A combined analytic and numerical solution has been developed by applying the previous method to a failed sector of a large steam turbine disc [3]. Figure 5 shows the resulting pdf on θ for a

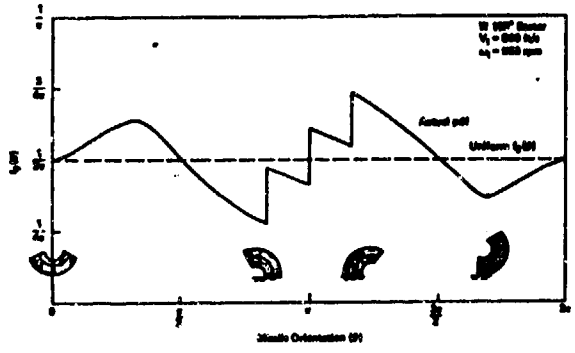

Figure 5. Probability Density Function of Turbine Fragment Orientation

120° sector disc translating at 500 ft/sec (152 m/s) towards a barrier and spinning at 900 rpm in a plane normal to the barrier. The three steps in the function correspond to shifts in the leading edge from the outside rim to the inside hub at $\theta = 150°$, from one inside hub to the other inside hub at $\theta = 180°$, and from the inside hub to the outside rim at $\theta = 210°$. The results indicate that the most likely impact orientation (at $\theta = 210°$) is about 2.7 times more probable than the least likely orientation at $\theta = 150°$. Also shown is a uniform distribution, which tends to underpredict the peak of the actual pdf by about 50 percent and overpredict the minimum by about 78 percent. If Ω is increased, the deviation from uniform would be greater and, similar to the rod example, the e would be some impact orientations that would not be possible.

PROBABILITY DISTRIBUTIONS OF EFFECTIVE IMPACT VELOCITY

In conventional design for missile impact, the missile is often assumed to strike the barrier at its most vulnerable positions with maximum velocity, with the velocity vector oriented normally to the barrier surface, with the major axis of the missile oriented normally to the barrier surface, and with zero rotational velocity. For many impact loads, except perhaps certain ballistic targeting situations, the probability of all of these conditions being met simultaneously at the instant of impact is quite low. Hence, typical impact conditions include off-normal missile orientation, oblique velocity vector, and nonzero rotational velocity.

To account for conditions of oblique, noncollinear, and rotating missile impact for probabilistic assessments of random impact loads, an effective velocity relationship for local effects damage assessment of slender body type missiles was derived in Refs. 1 and 2. This relationship was developed using impulse analysis methods assuming inelastic interaction between the target and the surface. The effective impact velocity function, g, is defined by $g = V'/V$, where V' = effective velocity. For primatic rod-type missiles, this analysis reduces to

$$g(L\dot{\theta}/V,\theta,\phi,\theta',\phi') = \left(1 - \frac{3}{4}\sin 2\theta\right)\cos\theta'' - \frac{L\dot{\theta}}{8V}\sin\theta + \frac{3}{4}\cos\theta\sin\theta\sin\theta'\cos(\phi' - \phi) \qquad (14)$$

and the equivalent impact velocity, V', is thus determined from

$$V' = V\, g\,(L\dot{\theta}/V,\theta,\phi,\theta',\phi') \quad . \qquad (15)$$

Equations 14 and 15 provide a means to predict the effects of oblique, noncollinear, and spinning impacts in terms of V' for local effects damage assessment. Evaluation of Eq. 15, based upon known or assumed pdfs of $L\dot{\theta}/V$, θ, ϕ, θ', and ϕ', enables probability estimates of barrier impact with velocities greater than a specified equivalent normal collinear velocity, V'. If the angular velocities are high relative to the component of translational velocity that is normal to the surface, then, as developed previously, the effect of rotation on biasing the impact orientation should be considered. In cases where $\Omega L/V$ is small and can be neglected, special solutions of Eq. 14 are possible, as noted in the following paragraphs.

Probability Distribution Function for Equally Likely Orientations. Of general interest is the case in which $\tilde{V}_t$ and $\tilde{M}$ have independent and equally likely directions in a three-dimensional half space relative to the impact surface. For this case the input pdfs are $f_\theta(\theta) = \sin\theta$,

$\theta \in [0,\pi/2]$; $\theta'(\theta') = \sin\theta'$, $\theta' \in [0,\pi/2]$; and $f_{\phi-\phi'}(\phi-\phi') = 1/\pi$, $\phi-\phi' \in [-\pi/2,\pi/2]$, where the orientation of the XY axes on the impact surface is assumed to be arbitrary and, hence, only the relative azimuthal angle ($\phi-\phi'$) is needed (see Fig. 3). Using these pdfs and Eq. 14, the cumulative pdf, $F_g(g)$, can be calculated numerically. These results are shown in Fig. 6 and indicate

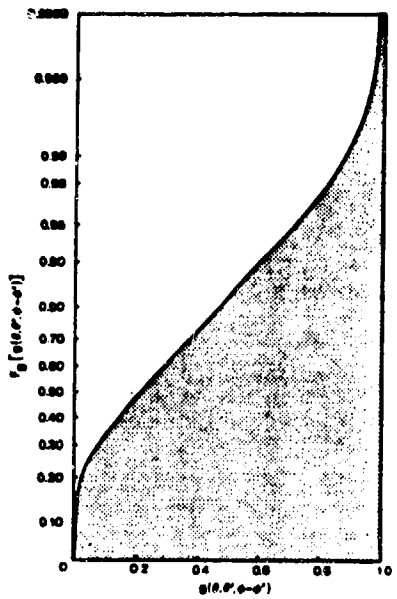

Figure 6. Probability Distribution Function of $g(\theta,\theta',\phi-\phi')$

that there is a 50 percent chance that a random impact will result in an impulse that is less than 20 percent of a normal collinear impact in which $g = 1$, a 75 percent chance that the impulse is less than 41 percent of a normal collinear impact; and a 90 percent chance that the impulse is less than about 60 percent of the normal collinear case. Hence, for equally likely solid angle directions on $\underset{\sim}{V}_i$ and $\underset{\sim}{M}$ nine out of ten (independent) missiles would impact the surface with an effective impact velocity less than 60 percent of a normal collinear impact. The expected value of g, denoted E(g), integrated over all directions, is 0.2658. A table of exceedance probabilities, $1 - F_g(g)$, of the effective impulse is summarized in Table 1. These values indicate, for example, that the probability of a single random missile impacting with $g > 0.90$ is 0.00562.

Expected Impulses for Collinear Impacts. Another special application of the impulse equation exists for no-spin collinear impacts; i.e., $\dot{\theta} = 0$, $\theta' = \theta$, and $\phi' = \phi$. In this case, which is characteristic of ballistic impact problems, g reduces to $g(0,\theta'=\theta,\phi'=\phi) = \cos\theta$ and solutions of the expected value normal impulse are calculated by

$$E(g) = \int\int \cos\theta \, f_\theta(\theta) \, f_\phi(\phi) d\theta \, d\phi \quad . \qquad (16)$$

For equally-likely solid angle $\underset{\sim}{V}_i$ direction in space, one obtains $E(g) = 0.5$. If the plane of missile trajectory (plane Z $\underset{\sim}{V}_i$ in Fig. 1) is is limited to a plane normal to the surface, $E(g) = 2/\pi = 0.637$. Table 2 summarizes these results as Case 2 and indicates about a 100 percent increase in E(g) over Case 1, which is the general case that includes noncollinear $\underset{\sim}{M}$ described in the preceding section.

Also given in Table 2 are several results for ballistic-type trajectories in which the missile pdf on θ is approximated by $f_\theta(\theta) = \sin\theta$ in which the reference Z axis is normal to ground surface (as opposed to the impact surface). For this class of problems (Case 3 in Table 2), expectations on normal impulse indicate that $E(g) = 1/2$ for random $\underset{\sim}{V}$ over a half space for both horizontal and vertical surfaces, an apparently paradoxical result in view of the preference for horizontal direction ($f_\theta(\theta)$ is maximum at 90°) for the assumed pdf. However, the solid angle integration in both cases reduce to identical forms, which are also equivalent to the general collinear situation (Case 2). These results for the horizontal and vertical surfaces are actually special cases for a surface rotated through an angle ξ from the Z axis. Case 3c in Table 2 summarizes the general results for an arbitrarily inclined plane, which reduces to a vertical and horizontal plane in the limits ($\xi = 0$ and $\xi = \pi/2$, respectively). The resulting E(g) expectations are a function of ξ. For a half space, plots of E(g) indicate that E(g) is insensitive to the angle ξ. E(g) varies from 0.5 to about 0.48, with the minimum attained at about 45 degrees. For normal plane trajectories, E(g) increases monotonically from 1/2 at $\xi = \pi/2$ to $\pi/4$ at $\xi = 0$ and thus the results are more sensitive to ξ.

MULTIPLE IMPACT PROBABILITIES

The potential for multiple impacts, produced by random loading processes, introduces the risk of enhanced target damage from cumulative local damage effects, i.e., the potential for accumulation of damage from succeeding impacts at the same location on the target. This type of damage may take the form of increased penetration depth, additional back-face scabbing, complete barrier perforation, or increased vulnerability to overall response damage mechanisms. The probability of cumulative impact damage from random impact loads is dependent on the number of impacts, the target size and the effective damage area of each impact. The following analysis presents a simple model of these effects.

TABLE 1. Exceedance Probabilities for Random Impact Orientation

Equivalent Velocity Coefficient $g(\theta,\phi,\theta',\phi')$	Exceedance Probability $1 - F_G(g) = P[g > g(\theta,\phi,\theta',\phi')]$
0.01	0.8386
0.10	0.7164
0.21[1]	0.5000
0.25	0.4334
0.27[2]	0.4210
0.50	0.1619
0.75	0.0368
0.90	0.00562
0.95	0.00139
0.99	0.0000514
0.999	0.0000013

[1] Median of g = 0.21.
[2] Mean of g = 0.27.

TABLE 2. Expectations of Normal Impulse for Random Impact

Case	$g(\theta,\phi,\theta',\phi')$	E(g) Half Space	Normal Trajectory
1. Uniform Noncollinear	Eq. 14	0.27	--
2. Uniform Collinear	$\cos\theta$	1/2	2/π
3. Ballistic Collinear			
a. Horizontal Surface	$\cos\theta$	1/2	1/2
b. Vertical Surface	$\sin\theta\sin\phi$ $\sin\theta$	1/2 --	-- π/4
c. Inclined Surface	$\sin\theta\sin\cos\xi$ $-\cos\theta\sin\xi$	$[2(\pi-\xi)\cos\xi + 2\sin\xi\cos^2\xi]$ $+ \pi\sin^3\xi]/[2\pi(1+\cos\xi)]$	--
	$\sin\theta\cos\xi$ $-\cos\theta\sin\xi$	--	$[\sin\xi + (\pi-\xi)\cos\xi]/$ $[2(1+\cos\xi)]$

Probabilistic Formulation. The probability of cumulative damage is formulated for the case in which the impact points of the missiles are uniformly distributed over the barrier's surface. This assumption simplifies the analysis and, in addition, a barrier can generally be partitioned into regions such that, within each, the impact distribution is approximately uniform. Denote the damage probability of a single random missile on target A as P(A). The probability that at least one cumulative damage impact occurs out of N missiles, $P^N(A^C)$, can be expressed as

$$P^N(A^C) = \sum_{j=2}^{N} \binom{N}{j} P(A)^j [1-P(A)]^{N-j} P(A^C|j) \quad , \quad N \geq 2 \quad , \tag{17}$$

where $P(A^C|j)$ is the probability of at least one impact that induces cumulative damage effects out of a total of "j" impacts on target A.

The assessment of $P(A^C|j)$ requires assumptions on the geometry and characteristics of the missile-induced damage area and a proximity relationship for cumulative effects. For a simple parametric analysis of Eq. 18, the dimensionless parameter, δ, is defined as the ratio of damage area, a_d, for a single missile to the barrier surface area (or subarea), A. Thus, $\delta = a_d/A$ is a measure of the vulnerability of a barrier to cumulative damage from multiple independent impacts. Small values of δ indicate a small damage-influence area compared to the subarea A, and, as δ approaches unity, cumulative damage

becomes more likely to occur on succeeding impacts. For $\delta = 1$, $P(A^c|j) = 1$ for $j \geq 1$ since the influence area equals the target area.

For a given target, A, a_d may be defined to correspond to the penetration zone, the zone of scabbing, or the cracked region. For example, in Fig. 7, the parameter a_d is represented as a

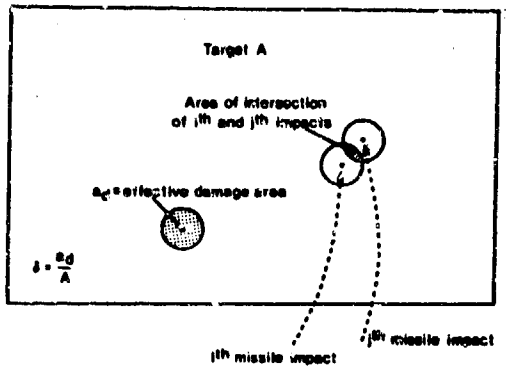

Figure 7. Cumulative Missile Impact ($\delta = 0.01$)

circular area corresponding to the case in which $\delta = 0.01$. For this case, the probability of cumulative damage on the second impact is 0.01. A conservative upperbound estimate to $P(A^c|j)$ is given by

$$P(A^c|j) \leq 1 - \prod_{k=2}^{j} [1 - (k-1)\delta] \quad , \tag{18a}$$

$$2 \leq j \leq \frac{1}{\delta} + 1$$

$$P(A^c|j) \leq 1 \quad , \; j > \frac{1}{\delta} + 1 \quad , \tag{18b}$$

if the areas of intersection of effective impact areas are counted more than once (see Fig. 8). For two missiles, Eqs. 17 and 18 combine to yield the exact cumulative damage probability, that is $\delta \cdot P(A)^2$.

Example Calculation. Figure 8 illustrates conservative estimates of cumulative impact damage probabilities for $N \cdot P(A) > 1$. This range is of practical interest in the evaluation of cumulative damage probabilities for the case in which a single impact is incapable of causing damage. However, if two impacts within a damage area a_d by this missile could damage the target, Fig. 8 can be used to estimate the upperbound cumulative damage probability as $P^N(A) \to 1$. For example, if P(A) is 0.01 and if 200 such missiles are available, $P^N(A)$ is about 0.87; if $\delta = 0.1$, the upperbound probability estimate of cumulative damage effects is 0.16.

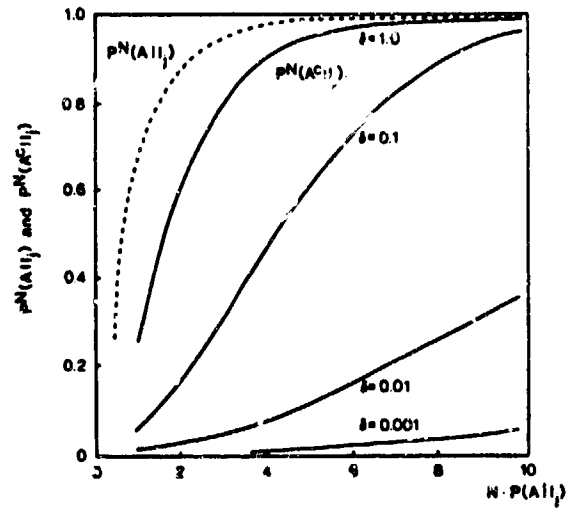

Figure 8. Multiple Missile and Cumulative Impact Probabilities

GENERAL METHODOLOGY FOR RANDOM IMPACT LOADS

The collection of topics presented herein form a basis for an integrated approach to the probabilistic analysis of random impact loads. A general approach is useful when a probability density function of the load (effective impact velocity) is desired separately from, or as an input to, the target damage assessment.

Figure 9 outlines the approach for integrating impact orientation, effective impact velocity and offset impact relationships. With the missile transport characteristics defined by $f_{\underset{\sim}{V}_1,\underset{\sim}{\Omega}_1,\tau}(\underset{\sim}{V}_1,\underset{\sim}{\Omega}_1,\tau)$, the first step involves the development of the joint density function, $f_{\underset{\sim}{V}_1,\underset{\sim}{\Omega}_1,\tau,t}(\underset{\sim}{V}_1,\underset{\sim}{\Omega}_1,\tau,t)$, that defines the angular position of the missile at the instant of impact. From Eq. 10 and the geometrical relationships defined by Eqs. 11, the joint density function of impact variables defined in Fig. 1 is developed. Once $f_{\underset{\sim}{V}_1,\underset{\sim}{\Omega}_1,\underset{\sim}{M}(\underset{\sim}{V}_{i_2},\underset{\sim}{\Omega}_{i_2},\underset{\sim}{M})}$ is defined, probabilities of particular impact conditions such as $\underset{\sim}{V}_1^*$, $\underset{\sim}{\Omega}_1^*$, $\underset{\sim}{M}^*$ can be calculated can be calculated in the standard manner. From Eq. 14, the normal impulse associated with the orientation can be determined, and, hence, the probability density function of the equivalent velocity function, $f_g(g)$, can be derived. This function can then be used with a deterministic or probabilistic damage model to determine the required barrier or target properties for specified risk levels.

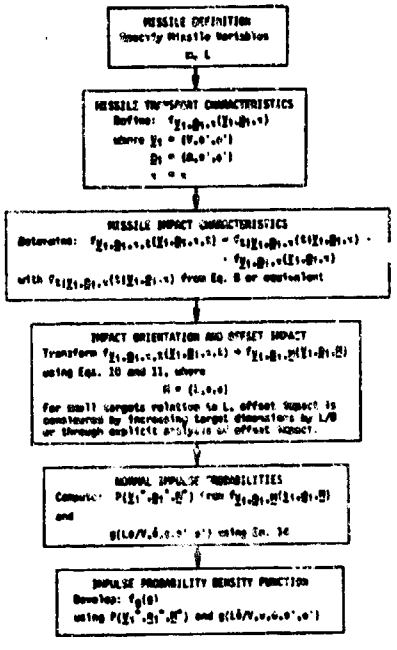

Figure 9. General Methodology for Impact Velocity Loading Function

SUMMARY

By virtue of their loading generation and transport mechanisms, impact loads are fundamentally stochastic with respect to missile orientation, velocity, angular velocity, and position of impact. However, conventional methods of analysis and design generally treat these loads as deterministic with worst case impact conditions (normal, collinear, no-spin, midspan impacts). Several models have been developed herein to assess the effects of random impacts on conventionally assumed impact conditions. Some of the key results include:

(1) The effect of missile angular velocity Ω is to bias the impact orientation of a spinning missile toward orientations in which the loading edge is rotating into the surface. With increasing Ω certain impact orientations become impossible; as ΩL/V → ∞, the probability distribution function reduces to a unit impulse correspond to normal missile orientations.

(2) The effect of oblique, noncollinear orientations is to reduce the velocity of the missile that is effective in damaging the barrier. Using an impulse model, the expected value of the normal impulse for a missile with random orientation and velocity vector is 27 percent of that produced by a normal collinear impact. The probability of a single random impact with an effective velocity > 90 percent is about 0.006.

(3) The potential for cumulative damage from multiple impacts are modeled using conditional probabilities with the binominal distribution. Curves of the probability of cumulative effects are given in terms of a dimensionless damage area ratio δ and the expected number of impacts N·P(A). As δ·N·P(A) → 1, these curves approach unity.

An approach for integrating these elements into a comprehensive methodology for analysis of random impact loading conditions has also been outlined.

REFERENCES

1. Twisdale, L. A., and Dunn, W. L., "Tornado Missile Simulation and Design Methodology," Vols. 1 and 2, EPRI Final Report NP-2005, Electric Power Research Institute, Palo Alto, California, August 1981.

2. Twisdale, L. A., et al., "Tornado Missile Risk Analysis," EPRI NP 768 and 769, Electric Power Research Institute, Palo Alto, California, May 1978.

3. Yoshimura, H. R., and Schmaun, J. T., "Preliminary Results of Turbine Missile Casing Tests," EPRI RP 399, Electric Power Research Institute, Palo Alto, California, October 1978

CALCULATION OF IMPACT- AND PENETRATION-EFFECTS ON HARDENED REINFORCED CONCRETE STRUCTURES

R. Schwarz, P. Foros, F. Scharpf

Industrieanlagen-Betriebsgesellschaft mbH, West Germany

ABSTRACT

The evaluation of the survivability of hardened structures against conventional weapons essentially requires the realistic calculation of impact and penetration effects.

With respect to the large number of influencing parameters on one hand, and the capacity of current computersystems on the other hand, there is a real necessity for the simulation of impact and penetration processes by means of advanced continuum-mechanical codes able to solve complex problems.

The specific objective of this work is to demonstrate the efficiency of the numerical simulation of weapon effects including the interaction of projectile and impacted target with respect to the design of protective structures.

INTRODUCTION

Within this computational study the response of structural reinforced concrete members to high velocity impacts of postulated missiles is simulated using the fully 3D-code DYSMAS/L, extended for a realistic modelling of the material behavior of reinforced concrete. Conforming to available experimental data a nonlinear stress-strain curve and a continuous triaxial failure-surface is composed to include nonlinear behavior of concrete, cracking of concrete in the tensile region, the inelastic response in the compressive mode and the mixed modes of failure.

The interaction between projectile and concrete structure is considered by a 3D-multibody contact processor which calculates geometry and exchange of momentum in the contact zone, based on a generalized master-slave algorithm.

The application of the code is demonstrated by simulations of projectile impact and penetration of different configurations of shelter doors made of reinforced concrete and steel components. For some realistic parameters, the deformation and damage of the target, the stressing of bending and shear reinforcement, the failure of concrete elements as well as the deformation and stress behavior of the impacting projectile is shown for a better understanding of the ballistic resistance of the respective components and their interaction.

THE NUMERICAL MODEL

The numerical simulations are based on the 3D-Lagrangean code DYSMAS/L, a code developed for calculating the response of structures under extremely dynamic loading as e.g. high velocity impact or nonlinear shockwave propagation by means of continuum mechanical relationships and numerical solution algorithms /1/. The appendix /L refers to the Lagrangean description of the physical process within a time dependent, material fixed reference frame. The spatial discretization is accomplished by dividing the structure into finite elements; the discretization in time results from subdividing the time domain into adequate time steps.

Within the time loop the direct integration of the equations of motion of the finite system is carried out by means of a central difference scheme /2/. For this the element masses are proportionately assigned to the corresponding nodal points supplied by potentially additional nodal masses ('lumped mass model'). Referring to stability the explicit scheme demands for a time step less than a critical value. As however explicit methods facilitate the description of nonlinearities and arbitrary constitutive equations, and as the analysis of shock wave propagation calls for small time steps anyway, the conditional stability of the chosen scheme appears not too restrictive.

Using the kinetic quantities of the nodal points the element strains and - based on the corresponding constitutive laws - the element stresses resulting from straining and damping are calculated. The resulting element stresses are assigned to the nodal points in terms of inner forces to enter the integration within the next time step.

MATERIAL MODELS

Due to the intense stressing of material during impact and penetration the numerical model has to include the entire domain of deformation characterized by linear elastic behavior, nonlinear beha-

vior as well as failure- and post-failure-behavior of the respective materials.

The models implemented in DYSMAS/L use a fully incremental plasticity model, capable of strain hardening, for the representation of arbitrary stress-strain relationships for ductile and brittle materials. This model describes the arbitrary material behavior by means of mechanical sublayers. Each sublayer has a different yield stress and cross-sectional area in order to force the material to conform the input stress-strain relationship for the uniaxial case. The stress calculation is performed independently for the respective layers. The resulting stress is calculated by a weighted summarizing of the sublayer stresses.

YIELDING CONDITIONS

Within the sublayer model according to MROZ /3/ yield stresses are defined only for the individual sublayers with ideal-elastic-plastic characteristics. The yield stress of the one-dimensionally loaded cross-section corresponds to the yield surface within the domain of principal stresses in the case of triaxial straining. The yield surface encloses the regime of ideal-elastic material behavior, i.e. a stress pattern within the surface effects ideal-elastic deformation. States of stress on the yield surface indicate plastic deformation whereas states of stress outside the yield surface are not allowed. Generally the yield surface is related to the first invariant of the stress tensor, i.e. the hydrostatic pressure, as well as to the second and third invariant of the deviatoric stresses.

The yield surfaces implemented in the code DYSMAS/L with respect to the penetration of reinforced concrete structures are the yield surfaces according to v. MISES and to WILLAM/WARNKE. The former, appropriate for steel, represents a function of the second deviatoric invariant I_2 of the stress deviator $\underline{s}$ and of the octahedral shear stress τ_o respectively:

$$\bar{I}_2 - \frac{1}{3}\cdot\sigma_F^2 = -\frac{3}{2}\cdot\tau_o^2 - \frac{1}{3}\cdot\sigma_F^2 = 0$$

This formulation is independent from the hydrostatic pressure. In the domain of principal stresses this yield surface constitutes a circular cylinder with the radius r and the axis as equisectrix (fig. 1):

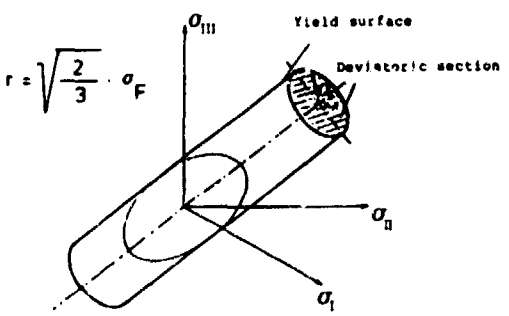

Fig. 1: Yield surface according to v. Mises

Contrary to steel the stress-strain relation of concrete is dependent on the hydrostatic pressure /4/. The application of the 'MROZ' sublayer model to this relation leads to yield surfaces in the principal stress space which are dependent on the hydrostatic pressure and moreover are affine to the failure surface for concrete - here modelled according to WILLAM/WARNKE /5/.

Consequently the yield surface - geometrically similar to the failure surface - represents an elliptic paraboloid with the axis as the equisectrix of the principal stress space and with the apex in the region of hydrostatic tension (fig. 2).

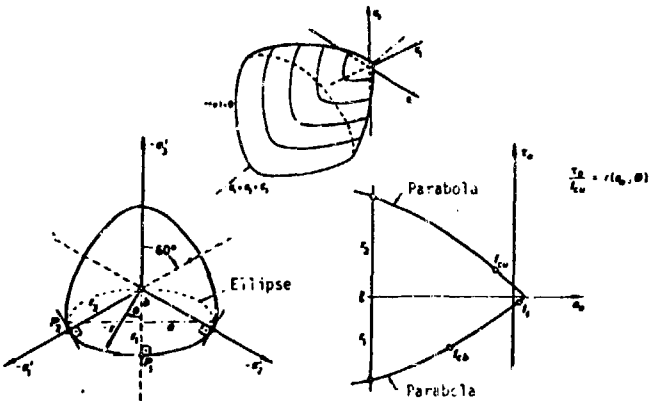

Fig. 2: Yield surface accord. to Willam/Warnke

The hydrostatic section consists of two different parabolas above and below the equisectrix. The position within the principal stress space is determined by the angle θ. The shape of the parabolas is defined by five parameters, collectively related to the uniaxial compressive strength of concrete:

- biaxial compressive strength	f_{cb}/f_{cu}
- uniaxial tensile strength	f_t/f_{cu}
- hydrostatic stress	$\xi_1 = p/f_{cu}$
- average shear stress	$r_1(\xi_1,\theta=0^\circ)=\tau_{o1}/f_{cu}$
- average shear stress	$r_2(\xi_1,\theta=60^\circ)=\tau_{o2}/f_{cu}$

Moreover both parabolas are required to pass through a common apex at the equisectrix thus providing another constraint condition for the description of the hydrostatic section along the 'tensile' ($\theta = 0^\circ$) and and the 'compressive' ($\theta = 60^\circ$) meridian.

The deviatoric trace is composed of triple-symmetric elliptic sections defined by the position vectors $r_1(\xi,\theta=0^\circ)$, $r_2(\xi,\theta=60^\circ)$. Consequently the position vector r in the deviatoric section of the paraboloid results as

$$r = r\ (\theta, r_1(\xi), r_2(\xi))$$

The surface composed in this way is still independent from the uniaxial compressive strength of the concrete f_{cu} in case of a failure surface, or from the sublayer yield-stress $\bar{\sigma}_i$ in case of a yield surface according to to the 'MROZ' sublayer model respectively.

According to /5/, the position vector r is proportional to the octahedral shear stress τ_o of the yield state:

$$r = \sqrt{\frac{3}{5}} \cdot \frac{\tau_o}{\bar{\sigma}_i}$$

The octahedral shear stress τ_o again is directly proportional to the equivalent stress σ_v according to the hypothesis of minimization of deformation energy:

$$\tau_o = \frac{2}{3 \cdot \sqrt{2}} \cdot \sigma_v$$

Herewith the uniaxial equivalent stress σ_F can be assigned to any state of stress on the yield surface described by the position vector r:

$$\sigma_F = \sqrt{\frac{15}{2}} \cdot r \cdot \bar{\sigma}_i$$

Consequently there is yielding within a sublayer if the equivalent stress, calculated from the actual state of stress, exceeds the yield-criterion.

FLOW RULE

If the stress pattern violates the yielding criterion a redistribution is accounted for when calculating the internal forces. The redistribution requires additional information concerning the relation between increments of plastic strain, stress and stress increment in order to describe the plastic behavior of the material.

In the case of material flow, defined by the occurrence of an inadmissible state of stress outside the yield surface, the stress vector will be set back to the yield surface, splitting the state of strain into an elastic and a plastic part. Plastic straining does not contribute to the elastic strain energy; only the elastic part contributes to a stress increment. Moreover it is assumed that the stress deviator resulting from the elastic part is proportional to the strain deviator.

According to HENCKY, the instantaneous state of plastic straining is determined directly from the elastic state; contrary to the also implemented formulation of PRANDTL/REUSZ, hysteresis connected with cyclic loading cannot be described with this type of flow rule. The updated state of stress is assumed to be the intersection between the stress increment $\Delta\underline{\sigma} = \underline{\sigma}_2 - \underline{\sigma}_1$ and the yield surface which leads to the following distribution of the strain tensor $\underline{\varepsilon} = \underline{\varepsilon}_M + \underline{\varepsilon}_{pl}$ with the elastic part $\underline{\varepsilon}_{el}$ and the plastic part $\underline{\varepsilon}_{pl}$:

$$\underline{\varepsilon}_{el} = \frac{F}{V} \cdot \left(\underline{\varepsilon} - \frac{e}{3} \cdot \underline{1}\right) + \frac{e}{3} \cdot \underline{1} \quad ; \quad \underline{\varepsilon}_{pl} = \left(1 - \frac{F}{V}\right) \cdot \left(\underline{\varepsilon} - \frac{e}{3} \cdot \underline{1}\right)$$

Herein σ_v represents the equivalent stress calculated from the state $(\underline{\sigma}_1, \underline{\varepsilon}_1)$ and from the dilatation of volume e.

The flow rule according to PRANDTL/REUSZ is based on the normality principle which means, that the plastic strain increment is normally, the elastic strain increment tangentially directed to the yield-surface, defined in the stress-domain; this is prerequisite for the description of elasto-plastic redistribution of stresses.

FAILURE- AND POST-FAILURE-BEHAVIOR

As in penetration processes the material straining generally leads not only to plastic deformation, but also causes material failure, the code is supplied with different fracture models. The respective concepts however do not simulate the formation and propagation of cracks in a pure fracture mechanical sense, but rather enable a more global description of the post-failure material behavior adequate to the problem.

Material failure occurs, if an appropriate measure for strain exceeds a certain value. In the post-failure regime the steel is capable of carrying hydrostatic pressure, whereas hydrostatic tension cannot be transferred. Therefore failure in the tensile region causes the stress tensor to be set to zero, whereas in the compressive mode only the deviatoric components are set to zero with remaining hydrostatic pressure. For concrete the calculation is continued with reduced sublayer yield-stresses. After severe element distortions in the post-failure regime, the element is removed from the structure distributing its nodal masses to newly generated nodes; the kinetic energy is kept within the system during the further computation, as the newly generated nodal points preserves the coordinates and velocities of the corresponding nodes of the remaining structure. Moreover a contact-problem for the resulting structural surface and the additional nodes will be defined such, that the fragments will be able to interact with arbitrary parts of the residual structure.

An alternate concept allows the opening of the structure at the boundaries of failed elements; in this case the generation of new nodal points and the definition of contact-zones between disconnected elements prevents an overlapping of the structural parts in the case of repeated contact.

CONTACT PROCESSOR

To model the interaction between projectile and concrete structure during the impact and penetration process a 3D-multibody contact-processor describes the structural removal within the contact zones, effects the exchange of momentum between the structures in contact and finally determines the contact forces. The nodes in contact are assumed to strike fully plastically. The springback is accomplished by the elastic reaction of the elements behind the contact zone. The procedure is based on a generalized master-slave algorithm. For the bodies in contact, master planes and slave points are defined. The slave points of one body may not intersect the master planes of any other body. During time integration the contact processor controls whether different structural parts are overlapping each other. In case of a dynamic contact the state of motion is modified in such a manner, that nodal points belonging to one of the structures in contact, which have passed through the interface, are reset. Furthermore the velocities of the nodal points are corrected with regard to the conservation of momentum, and the contact forces are calculated according to the dynamic equilibrium. During the penetration pro-

cess elements showing large deformations are eliminated; new master surfaces and slave points arising from this elimination process are created by the contact processor autonomously.

STRAIN-RATE DEPENDENCY OF MATERIAL STRENGTH

High rates of straining which may be significant for impact and penetration processes, affect the strength behavior of most materials and consequently to a certain extent the dynamic response of structures too. As far as experimental results are available, the shock- and penetration-model accounts for these effects by the application of a relevant set of stress-strain curves depending on the rate of straining.

APPLICATION OF THE CODE

The application of the code described above is demonstrated by the simulation of projectile impact and penetration into different configurations of shelter gates made of reinforced concrete and steel components involving the interaction between penetrator and target.

FE-MODEL OF PROJECTILE AND TARGET

To enable advantageous axisymmetric simulations, the shelter gates are represented by circular plates with radius R and thickness T, modelled with hinged supports at the boundaries. The concrete of the gates is modelled by solid elements characterized by 8 nodal points and 12 integration points. The bending reinforcement - arranged at the outer and inner concrete elements - is described by means of membrane elements with each 4 nodal- and integration points. The shear reinforcement is represented by bar elements defined by two nodes and one integration point. According to the concrete grid which becomes coarser with increasing distance from the rotational axis, the cross-sectional area of the bar elements increases. The steel plates covering the inside and the lateral faces of the second gate-type are modelled by plate elements supplied with a moment-curvature relationship. In table 1 the characteristic quantities of the analysed gate types are summarized.

Parameter	Abbrev.	Dim.	Gate I	Gate II
Gate thickness	T	m	1.40	0.68
Thickness of concrete layer	TC	m	1.40	0.46
Outer radius of plate	R1	m	4.00	1.85
Inner radius of plate	R2	m	2.00	1.20
Thickness of inside steel plate St520	TSI	m	-	0.02
Thickness of outside steel plate St520	TSA	m	-	0.12
Bending reinforcement inside BSt 420/500	FBI	cm^2/m	20.1	49.2
Bending reinforcement outside BSt 420/500	FBA	cm^2/m	7.7	10.1
Shear reinforcement BSt 420/500	FS	cm^2/m^2	6.8	78.5
Compressive strength of concrete	σ_{cu}	N/mm^2	33	33

Table 1: Characteristics of the gate discretizations

The casing of the assumed representative AP-projectile is idealized by means of 4-node-plate elements with again four integration points respectively. The explosive charge -in the simulation supposed to be inert - is modelled by 8-node solid elements with 12 integration points respectively. The characteristic values of the projectile are shown in table 2.

Parameter	Dim	Value
Overall length	m	1.00
Max. diameter	m	0.36
Total mass of structure	kg	450

Table 2: Characteristic values of the projectile

MATERIAL PARAMETERS

The concrete's uniaxial stress-strain relationship is derived from the parabolic-quadrilateral diagram which is basic for the German standards. For both gate-types an uniaxial compressive strength 33 N/mm^2 is assumed. The parameters for the failure surface according to Willam/Warnke are taken from /5/. For the sublayers yield surfaces are used which are affine to the failure surface. Table 3 contains a summary of the respective input values.

Concerning steel, the stress-strain relations are characterized by the strain-values within the region of reduced cross-sectional area and consequently by the inherent 'true' stresses. The true stress-strain relation is supplied in terms of a polygonal function with the following data base (0, 0), $(\epsilon_F, \sigma_F), (\epsilon_G, \sigma_G), (\epsilon_{BE}, \sigma_{BE})$. Table 4 shows the

Parameter	Abbrev.	Dim.	Gate I,II
Young's modulus	E	N/mm^2	3.0E04
Poisson's ratio	ν	-	0.2
Strain 1	ϵ_1	-	0.0008
Stress 1	σ_1	N/mm^2	24.6
Strain 2	ϵ_2	-	0.0020
Stress 2	σ_2	N/mm^2	32.0
Ultimate strain	ϵ_{Br}	-	0.0100
Uniaxial compressive strength	f_{cu}	N/mm^2	33.0
Concrete model acc. to WILLAM/WARNKE:			
biaxial compressive strength	f_{cb}/f_{cu}	-	1.80
tensile strength	f_t/f_{cu}	-	0.15
hydrostatic pressure	ξ_1	-	3.67
mean shear stress	$\tau_1(\xi_1,\theta=0°)$	-	1.59
mean shear stress	$\tau_2(\xi_1,\theta=60°)$	-	1.94

Table 3: Stress-strain curves for concrete

general pattern of the stress-strain diagram and contains the parameters for the respective sorts of steel.

For the explosive charge of the projectile ideal-elastic-plastic behavior is assumed with the parameters from /6/.

Parameter	Abbrev.	Dim.	Rein-forcement	Steel plates	Projectile's hull
Sort of steel		N/mm²	BSt420/500	St520	St1200
Young's modulus	E	N/mm²	2.1E10	2.0E10	2.1E10
Yield limit	σ_F	N/mm²	420	330	1150
Nom. ultimate stress	σ_B	N/mm²	500	520	1200
Yield strain	ε_F	-	0.002	0.002	0.006
Techn. ultimate strain	ε_B	-	0.150	0.220	0.100

Table 4: Param. of the stress-strain curves for steel

RESULTS OF NUMERICAL SIMULATION

For gate-type I, fig. 3 shows the penetration process - characterized by an impact velocity of 250 m/s of the projectile - at different times. The corresponding time history of the projectile's kinetic energy shows a first strong decay down to 20% of the initial value within the first two ms; this is followed by a less inclined part which finally leads to a nearly total exchange of the initial kinetic energy into deformation energy

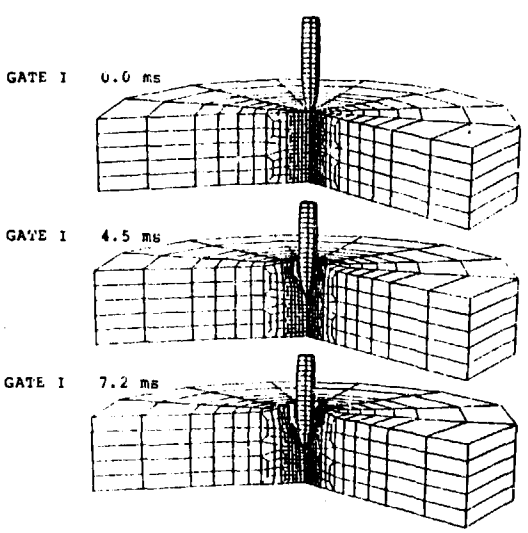

Fig. 3: Penetration of Gate I

after about 6.5 ms. The reduction of kinetic energy is plotted versus the depth of penetration in fig. 4. Fig. 5 pictures the time dependent failure sequence of the concrete elements; the elements inside the gate near the rotational axis are failing later than the more distant situated elements, i.e. a cone-shaped failure surface results. Although there is no perforation, the concrete at the inside of the door is severely damaged. The interactive stressing of the projectile's hull is

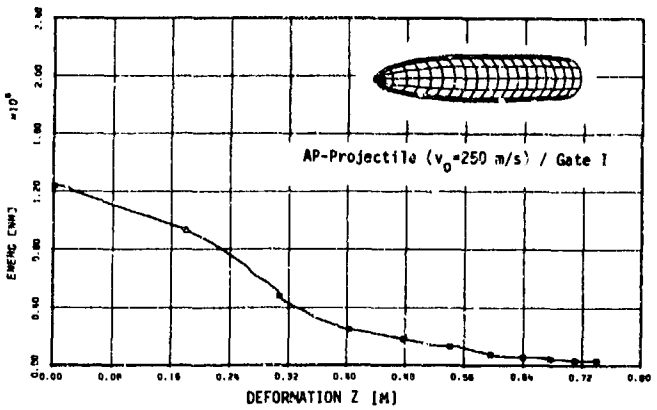

Fig. 4: Kin. energy of projectile during penetration

demonstrated by the time history of the equivalent stress and strain at it's tip (fig. 6). In this case the equivalent strain reaches 25% without exceeding the ultimate strain after all. The stressing of the rear of the projectile remains within the elastic region. For time intervals of 0.45 ms, the respective states of deformation of the gate-inside are drawn on fig. 7. During the first 4.5 ms the maximum values of deformation are located

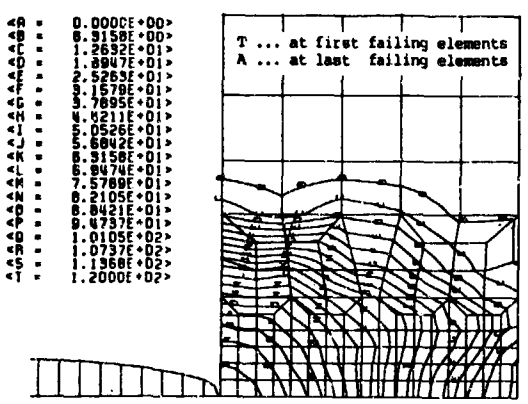

Fig. 5: Sequence of failing concrete elements

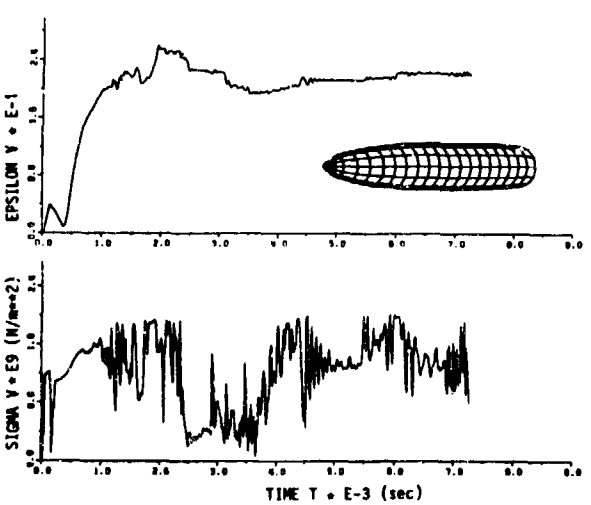

Fig. 6: Equivalent stress and strain (projectile tip)

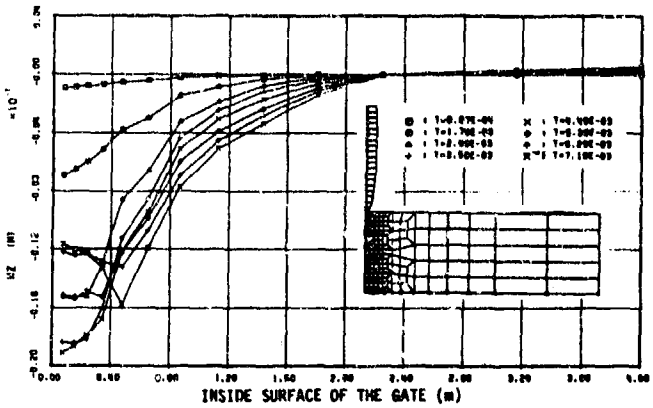

Fig. 7: States of deformation for the gate-inside

in the axis of the penetrator; later they are transferred to the outer regions, effected by the failure-induced vibrations of the center of the gate. The inside positioned bending reinforcement is stressed up to the yield-point reaching an equivalent strain of 1.2% in the elements near the axis, which indicates plastic deformation (fig. 8). However the bending reinforcement on the impacted face is destroyed by exceeding the ultimate strain within the impacted region.

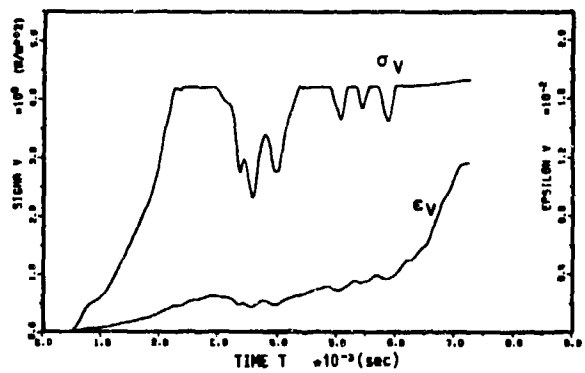

Fig. 8: Equiv. stress/strain for inner reinforcement

For gate II, characterized by an additional steel shielding at the impacted face, the impact and penetration process is shown for intervals of 0.50 ms (fig. 9). In this case the gate is considerably deformed especially within the impacted region, the projectile however is unable to further penetration; it's hull is destroyed within the ogival zone, recognizable by the intensive folding. The time-history of the projectile's kinetic energy firstly reveals a weak, then an increasing linear decay to 23 % of the initial value at 0.38 ms. Subsequently the kinetic energy is reduced in a parabolic manner to 43 % of the original amount. The remaining energy does not render possible further penetration of the projectile, but leads rather to the extensive destruction of it's hull. The bending of the inside surface increases up to a final value 2.4 cm. Comparable to gate I a failure region of conical shape is proceeding with an inclination of 30° to the impact axis. The time-histories of equivalent stress and strain for the bending reinforcement indicate elastic stressing for the elements arranged at the inside of the gate. Table 5 summarizes the essential results for the evaluation of survivability.

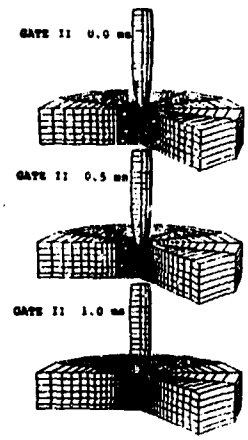

Fig. 9: Penetration of Gate II

	GATE I	GATE II
Penetration depth of the projectile (cm)	75	10.5
Max. deformation at the inner side of the gate (cm)	2	2
Stressing:		
Outer bending reinforcement	failure	yielding
Inner bending reinforcement	yielding	elastic behavior
Hull (ogival zone)	yielding	failure
Remaining kinetic energy of the projectile (%)		
after 1.2 ms	50	46
after 2.5 ms	17	—
after 5.0 ms	4	—
Perforation of the gate probable?	no	no

Table 5: Summary of results

CONCLUSION

The efficiency of numerical methods for the simulation of impact and penetration processes is demonstrated by means of the code DYSMAS/L, especially developed for the analysis of extremely dynamic continuum mechanics problems. The presented numerical results just give an insight into the extensive possibilities of the use of adequate code formulation especially in connection with experiments and model testing.

REFERENCES

/1/ The Program Family DYSMAS, B-TF-V197, IABG, Munich (1984)

/2/ Belytschko, T. Explicit Time Integration of Structure-Mechanical Systems, published in: 'Advanced Structural Dynamics', JRC of the Commission of the European Communities, Ispra, Italy (1978)

/3/ Mroz, Z. On the description of Anisotropic Work Hardening, J. of Mathematics and Physics of Solids, Vol. 13, 1957, pp.163-173

/4/ Schickert, G., Winkler, H. Versuchsergebnisse zur Festigkeit und Verformung von Beton bei mehraxialer Druckbeanspruchung , DAfStB, Heft 227,(1977)

/5/ Argyris, J.H., Faust, G., Szimmat, J., Warnke, E.P., Willam, K.J. Finite Element Ultimate Load Analysis of Three-Dimensional Concrete Structures ISD Lecture held at Jablonna, Poland (1974)

/6/ Schwarz, R., Scharpf, F. Fachband 'Durchdringungsuntersuchungen' zur Studie 'Simulationsmodell für Kernkraftwerke' IABG-B-TF-1286/01, Munich (1982)

Flash X-Ray Pseudocinematography of the Penetration Process of Bomb-Models in Concrete

A. J. Stilp, M. Hülsewig and E. Schneider

Ernst-Mach-Institute Freiburg i. Br., FRG
Terminal Ballistics and Impact Physics Division
H. Pahl, NATO Brüssel, Air Field Section

ABSTRACT

This paper summarizes some experimental work on penetration of GP-bomb-models in concrete slabs. The objectives of these tests were to study the deformation behaviour of the bomb-case during penetration, and to measure the X-t-diagram of the bomb nose in the first phase of penetration. These laboratory scale experiments were devised in order to complement field tests to verify design assumption of burster slabs for Avionics. For these tests an impact velocity of about 300 m/s was of interest.

Flash X-ray pseudocinematography was used to measure the penetration depth-time-diagram and the case failures at the beginning of the penetration. This method can be applied, because the impact process can be repeated in exactly the same manner.

The test results show that on the bomb-model no case failures are observable during the first 1000 sec after impact.

BACKGROUND

NATO countries are vitally concerned with the protection of Avionics - buildings against direct hits of conventional weapons. Several test programs (NWS, Meppen, Eglin AFB, ect.) have been undertaken to determine the level of protection provided by various overlay systems. As antipenetration systems concrete burster slabs with different thicknesses and rock/rubble burster slabs are in discussion.

The purpose of our effort was to verify thickness assumptions of the concrete slabs, and to study the behaviour of the bomb-case failure and the penetration depth-time function within the first phase of penetration. To perform such tests with large caliber projectiles against concrete slabs in full scale, means high costs, and they are time-consuming. Therefore, we have performed our test program on a model scale. The scale factor in our laboratory tests was 1 : 4.5. At such a relatively small scaling factor we expect no significant scaling effects.

FACILITY DESCRIPTION AND EXPERIMENTAL SET-UP

The launcher system consists of the energy reservoir, the hydrolic cuppling device, and the 100 mm diameter smoothbore launch tube. For low impact velocities (up to 250 m/s), compressed air is used as driver gas. For higher velocities a powder chamber replaces the air pressure reservoir. Energy reservoir and launch tube are coupled together with a hydrolic clamp. The launcher is mounted on a stable support without a recoil system (Fig. 1).

The gun fires into a closed range consisting of two parts, the blast-tank with the velocity measurement system and the sabot catcher, and the impact chamber. Fig. 2 shows a schematic drawing of the range.

The projectile velocity was measured by two exact positioned velocity pins at the muzzle of the launch tube or by two direct shadowgraph stations. The projectile velocity is determined to an accuracy of about 1 %.

The sabot catcher in the blast-tank is built up by bundles of strong chains hanging from the top to the bottom of the blast tank (Fig. 3). The bundles of chains have a low drag against the muzzle blast, but they are able to stop the sabot parts.

The impact tank, an octogonal steel construction with windows on each side, has a large door at the rear side to insert the concrete slab. The largest target size which we can insert into the chamber has a dimension of 1 m x 1 m x 0.5 m.

Impacts in concrete or rocks produce a lot of dust during projectile penetration; therefore, high speed photographic methods using visible light sources fail after a short duration of the impact event. This is the reason why we used the method of flash X-ray cinematography, especially the method of pseudocinematography. This method consists of repeating the whole phenomenon, with gradually increasing delays between the beginning of the process and the time of X-ray flashes. This method can be applied if the phenomenon to be studied is exactly reproducible. For the cinematography of the penetration of the bomb-model in the concrete target, three separate flash-X-ray sources are used. The frame separation is achieved by a simple arrangement of X-ray tubes and film cassettes as shown in Fig. 4. The X-ray sources (180 kV Field Emission tubes) are triggered successively. Tube axis are oriented in the direction of the concrete plate at grazing incidence with respect to the target front side. The X-ray tubes are located outside the impact tank and radiate through X-ray transparent windows into the tank interior. The film cassettes are arranged inside the tank, fairly close to the target, in order to obtain sharp shadowgraphs of the penetrating bomb.

The first flash tube is triggered by a contact foil at the front side of the target. Fiducial marks are installed to measure exactly the position of the bomb model during penetration. The delay time between the flash X-ray bursts is measured by electronic counters on the same time base.

At the rear side of the concrete slabs, thin strips of cupper foils are glued to the surface. If cracks run over the foils, electric circuits are interrupted. The electric signals indicate the beginning of crack formations at the rear side of the target.

TEST PROGRAM

The type of projectile used in the program is shown in fig. 5. It is a subscale (1 : 4.5) model of the GP-bomb MK83. The laboratory projectiles were fabricated of a steel with a tensile strength larger than 800 N/mm^2. Only the main dimensions of the bomb are scaled exactly, details like fins, fuses, support elements, etc. have been ignored. The bomb-models are loaded with a resin quartz powder mixture having roughly the same mechanical properties as the explosive filler composition B of the MK83-GP-bomb.

A four piece styrofoam sabot with a polyethylen pusher is used for launching the projectiles (Fig. 6). For the measurement of the depth of the penetration the case was equipped with thin brass rings at exact measured positions. On the X-ray shadowgraphs these rings can easily be seen.

All targets were constructed of concrete using a mix design intended to yield a compressive strength of BN35 quality. The slabs have a low reinforcement with one mat each at the front and at the rear side. The details of the projectiles and targets are summarized in the following table I. The impact velocity for all tests was about 248 m/s $\pm$ 10 m, and the angle of incident for all tests was Nato 0°.

TABLE I

parameters of concrete slabs

	model	original
dimension:	80 x 80 x 30 cm	320 x 320 x 120 cm
	80 x 80 x 35 cm	320 x 320 x 140 cm
	80 x 80 x 40 cm	320 x 320 x 160 cm
reinforcement:	one mat each at front-and rear side	
thickness of reinforcement	4 mm	16 mm
mesh distance	5 cm	20 cm
compression strength	BN 35	BN 35
max. grain size	8 mm	32 mm

parameters of the bomb type MK 83

	model	original
dimension:		
length	42.6 cm	191.7 cm
diameter	7.9 cm	35. cm
loading	resin and quartz powder	composition B
tensile strength	≥ 800 N/mm^2	≥ 800 N/mm^2

RESULTS

A typical series of flash X-ray pictures with the reconstruction of the penetrated part of the projectile in the concrete slab is presented in Fig. 7. From this series and from others no case failures were detected.

The flash X-ray pictures with the position of the projectile, and the measured time delay between contact and exposure are the fundamental basis for the calculation of the X-t-diagram. Such a X-t-diagram is shown in Fig. 8. The vertical dashed line indicates the occurence time of the first cracks at the rear side of

the target. At thicknesses of 30 respectively 35 cm, that means in full scale 120 respectively 140 cm, the bomb-model perforated the burster slabs with a surplus of residual kinetic energy. The consequence of this was a large deformation of the bomb noses caused by an impact on a steel plate catcher behind the target (Fig. 9 left). At a burster slab thickness of 36 cm (original 160 cm) the bomb-model can perforate the slab with a small surplus of residual kinetic energy. In this case, no significant case failures were observed on the recovered bomb-model (Fig. 9 right).

The typical target damage is shown in Fig. 10 a - d) with photographs from the front and the rear side.

SUMMARY

* The accordance of our results with full scale tests is satisfactory.

* A target thickness of about 36 cm (original 160 cm) guarantees a sufficient protection level against MK83-bomb threat at impact velocities lower than 250 m/s and attack angles larger than zero degree.

* No significant case failures were observable at impact velocities smaller than 250 m/s.

* The method of flash X-ray cinematography is applicable for concrete penetration tests.

FIGURES

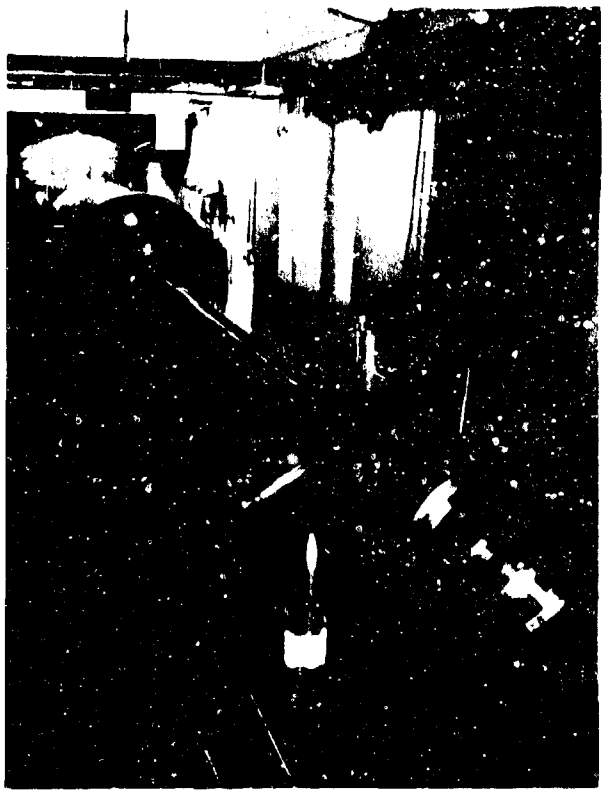

Fig. 1: Photograph of the launcher

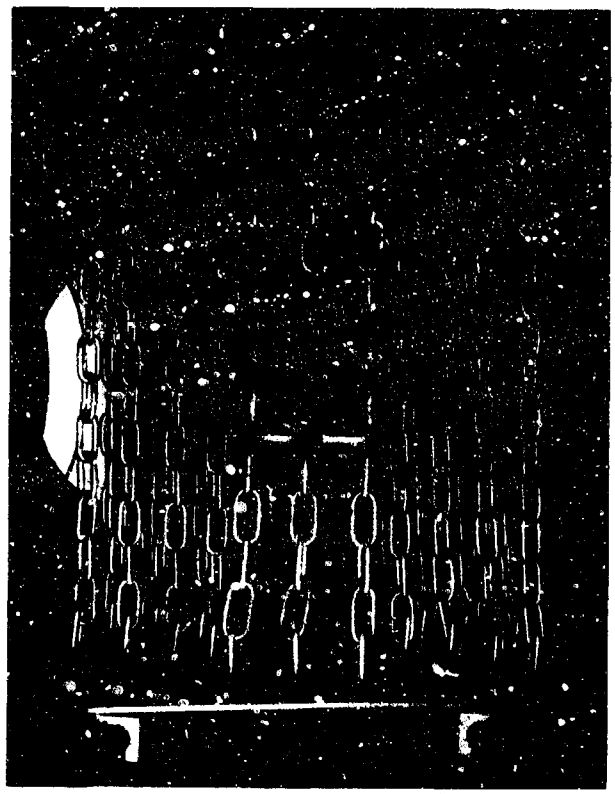

Fig. 3: Sabot catcher

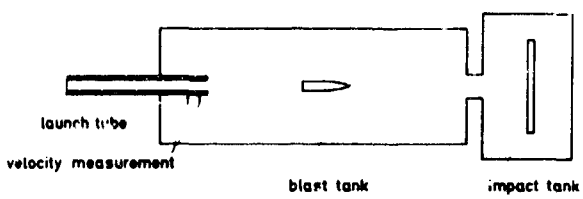

◀ Fig. 2: Schematic drawing of the range

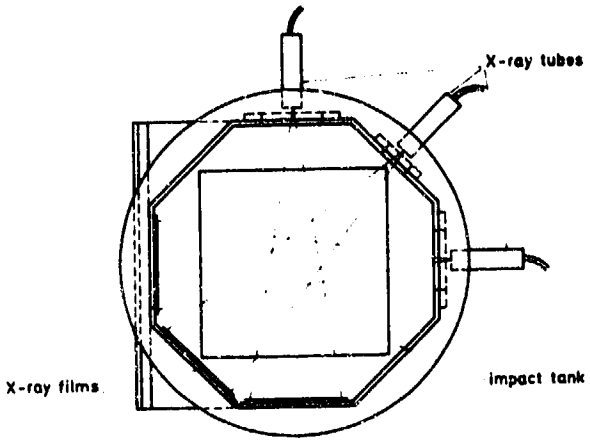

Fig. 4: Arrangement of the X-ray tubes

Fig. 6: Bomb-model with sabot ▶

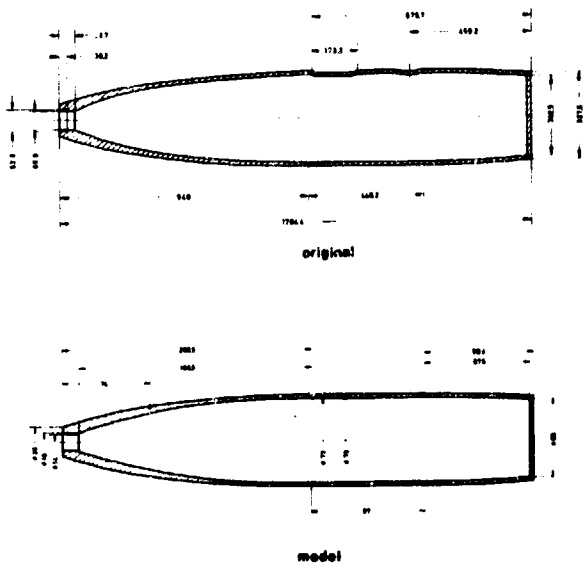

Fig. 5: Dimension of the original and the model

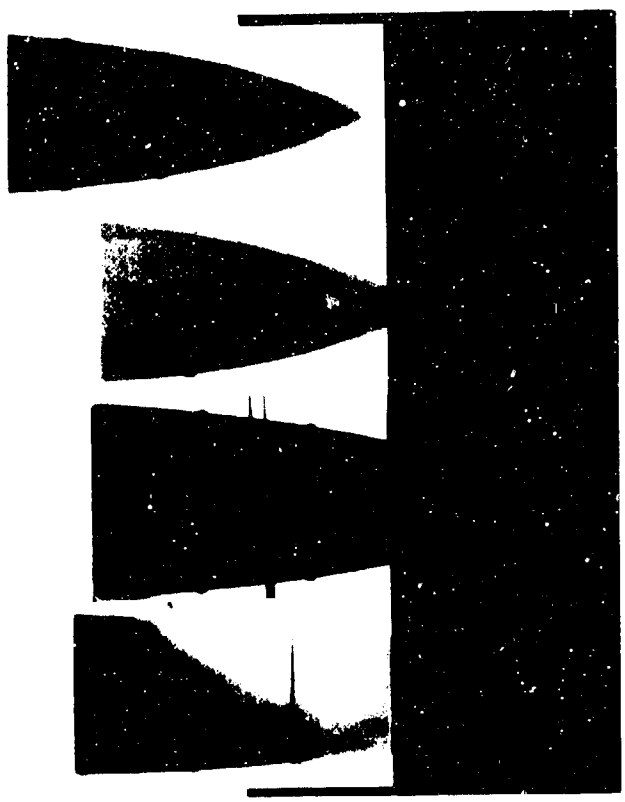

Fig. 7: Series of flash-X-ray pictures ▶

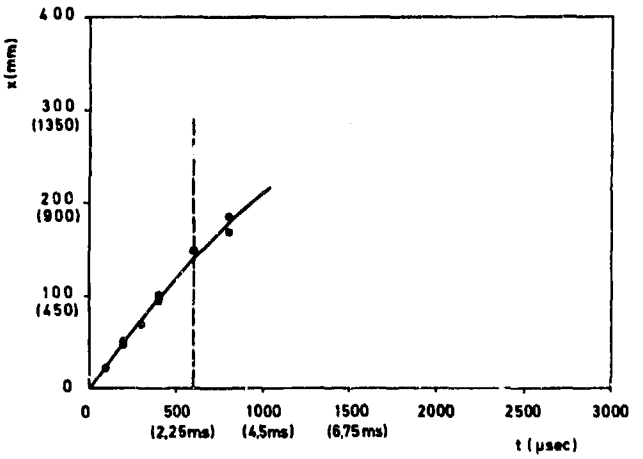

Fig. 8: X-t-diagram

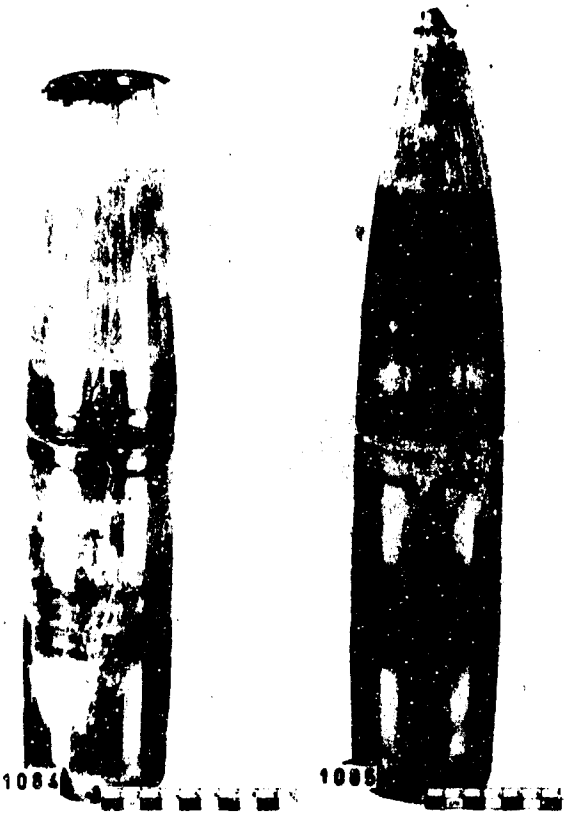

Fig. 9: Recovered bomb-models

Fig. 10 a - d: Target damage

EFFECT OF STRESS STATE ON VELOCITIES OF LOW-AMPLITUDE COMPRESSION AND SHEAR WAVES IN DRY SAND

K.H. Stokoe, II, S.H.H. Lee, and H.Y.F. Chu

Department of Civil Engineering
The University of Texas at Austin

ABSTRACT

The effect of state of stress on compression and shear wave velocities was examined for waves propagated as body waves through a dry sand mass. Testing was performed in a large-scale triaxial device in which cubic soil samples measuring 7 ft on a side were loaded in isotropic, biaxial, and triaxial states of stress. Compression and shear waves were propagated along principal stress axes of the sample over a range in pressure from 10 to 40 psi. All testing was performed at low-amplitude strains (less than 0.001 percent) and at wave frequencies less than 3000 Hz. Compression wave velocity was found to depend almost solely on the principal stress in the direction of wave propagation. Shear wave velocity was found to depend about equally on the principal stresses in the directions of wave propagation and particle motion and was determined to be relatively independent of the third principal stress.

INTRODUCTION

Shear and compression wave velocities of soils are often obtained from field testing or laboratory measurements. Once velocities are determined, shear, constrained and Young's moduli of the soil can be calculated. These soil moduli are used in dynamic soil-structure interaction analyses for small strain problems such as machine foundations and as reference values for larger-strain problems such as earthquake shaking or blast loading. A thorough understanding of the interelationship between wave velocity and state of stress is, therefore, required for the prediction of ground response under dynamic loading

With funding from the U.S Air Force Office of Scientific Research (AFOSR), a large-scale triaxial testing device for seismic wave propagation studies has been designed and constructed [References 1 and 2]. The device is used to load 7-ft cubes of dry sand under various states of triaxial stress with principal effective stresses ranging from 10 to 40 psi. Measurements of velocities of compression (P) and shear (S) waves propagating through the sand skeleton are performed with accelerometers embedded within the sand body. Wavelengths and frequencies are generally in the range of 0.5 to 1.5 ft and 500 to 1500 Hz, respectively. Strains in the soil skeleton are less than 0.001 percent.

An overview of the second series of tests with this device are presented herein. These tests were performed to study the behavior of P- and S-waves polarized along principal stress directions; that is, the seismic waves were excited so that the directions of wave propagation and particle motion were always parallel to principal stress directions. Results from the second series of tests were selected for presentation because of the more extensive testing performed in this series of tests as compared with the first test series.

LARGE-SCALE TRIAXIAL DEVICE

The large-scale triaxial testing device is a free-standing, heavily-reinforced steel box with interior dimensions of 7 ft on a side. The purpose of the device is to confine dry soil under triaxial states of stress. A sketch of the device with soil and some instrumentation in place is shown in Fig. 1. To date, the only soil tested has been dry sand. Equipment associated with the device is used to: 1. place sand into the device, 2. pressurize the sand mass to the desired stress state, 3. generate compression or shear waves in the sand mass, 4. monitor and digitally record these waveforms, and 5. monitor stress and strain throughout the sand sample during testing.

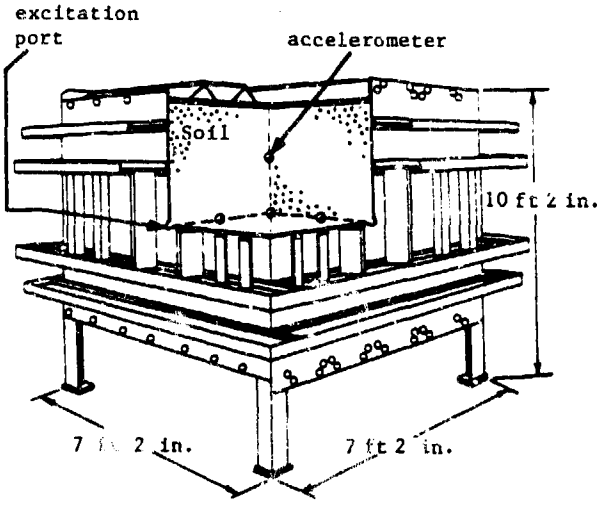

Fig. 1 - Cut-Away, Isometric View of Large-Scale Triaxial Device. (Reference 1).

Each wall of the triaxial device is designed to represent a principal plane so that axes perpendicular to the walls of the device represent principal directions. To permit independent control of the pressure in each of the three principal directions, confining pressures are applied to the soil mass using three membranes (water pressure bags) placed on the inside of the triaxial device; one on the top and one on each of two adjacent sides. Each membrane has two ports located at opposite corners so that water can be allowed to fill up or drain from the membrane. When the membranes are full of water, air pressure is used to pressurize them. To protect the membranes from damage by soil particles and to minimize any friction (hence shearing stresses) at the soil-membrane interface, several layers of plastic sheets with grease between them are placed between the soil and each membrane.

In the center of each wall not covered by a membrane, ports have been constructed so that mechanical coupling can be made between the soil in the device and mechanical exciters outside. Mechanical impulses applied at the ports are used to excite P- and S-waves in the soil. A single impulse parallel to the axis of the device is used to generate P-waves. A single impulse perpendicular to the axis (parallel to the wall of the device) is used to excite shear waves. However, two different shear waves can be excited. The waves have the same direction of propagation which is parallel to a principal axis but have different directions of particle motion. Particle motion of the first S-wave is polarized parallel to one principal stress axis while particle motion of the second S-wave is polarized parallel to the other principal stress axis. All of these waves, excited at one port, are shown in Fig. 2.

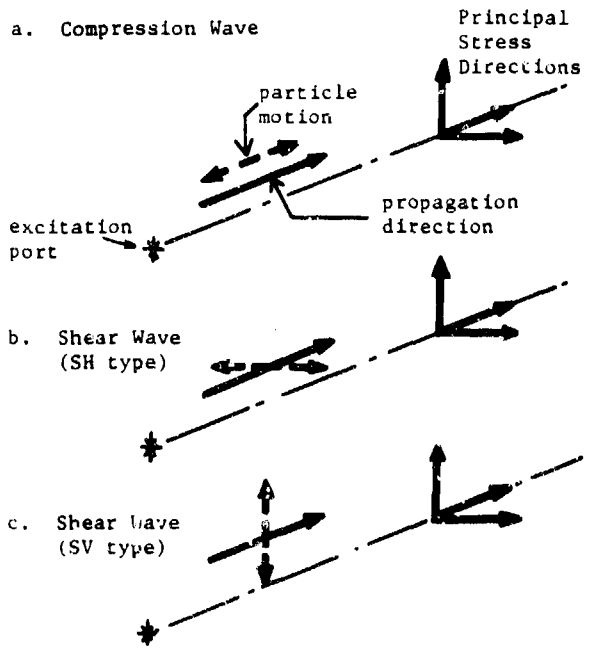

Fig. 2 - Types of Seismic Waves Generated at One Excitation Port.

The generated waves in the soil mass are recorded and interpreted with various electronics. An array of 24, low-frequency, high-sensitivity piezoelectric accelerometers has been used. These accelerometers, packaged in 3-D configurations, are placed in the soil mass during construction. The pattern inside the soil mass used in these tests is illustrated in Fig. 3. Two digital storage oscilloscopes with floppy disks for permanent storage were used to record the accelerometer signals.

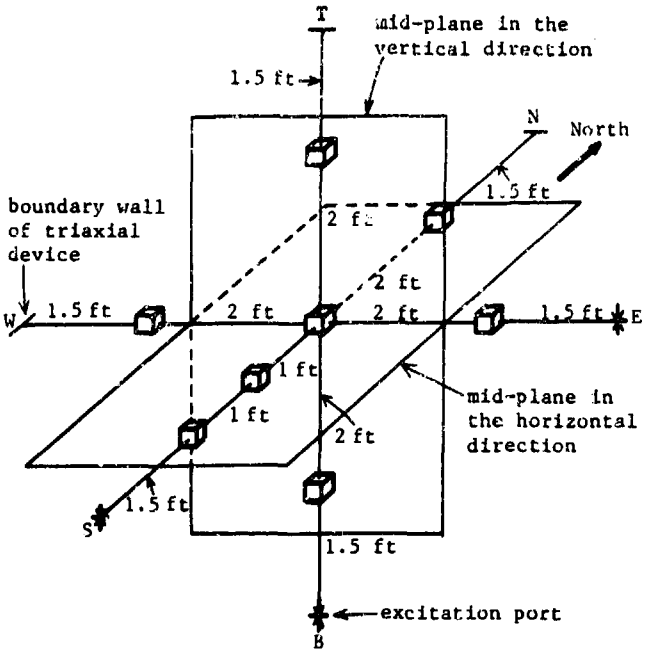

Legend: 1. NS = north-south principal axis
EW = east-west principal axis
TB = vertical (top-bottom) principal axis
2. S, E and B are locations of excitation ports.

Fig. 3 - Schematic View of 3-D Accelerometer Locations.

SOIL TESTED

The soil used in these tests is a medium dense, washed mortar sand which classifies as SP in the Unified Soil Classification System. The sand has a specific gravity of 2.67 and a mean grain diameter of about 0.46 mm. This sand was selected for several reasons. First, it is easy to handle and place, and when placed by the raining technique, uniform medium-dense samples can be obtained which can be duplicated from one test series to the next. Second, the static and dynamic properties of the sand are essentially independent of time of loading which means testing can proceed as rapidly as data can be gathered. Third, seismic waves transmitted through the dry sand evaluate properties of the soil skeleton which is the purpose of this project. Finally, the dynamic properties of dry sand are insensitive to frequency and number of cycles of loading in and below the strain and frequency ranges in these tests.

The sand sample was constructed by raining the soil through air (pluviation). This technique was chosen over other methods because of the efficiency and uniformity of placement attainable with this technique. Raining sand through air yields uniform, medium-dense samples when the height of fall is a few feet. A 7-ft wide rainer was therefore constructed. The rainer travelled in the east-west direction on a collar which elevated the rainer 3 ft above the top of the triaxial device. With this rainer, a uniform sand sample was constructed with an average density of 101.8 pcf and a standard deviation of 2.0 pcf. Instrumentation was placed in the sample at the desired elevations by simply stopping the filling process at those elevations.

TESTING SERIES

Once the sample was constructed, wave propagation measurements were performed under various states of stress. The first step was to perform tests with isotropic confinement ($\bar{\sigma}_1=\bar{\sigma}_2=\bar{\sigma}_3$). This state of confinement is the simplest state that can be applied with the triaxial device, and the effect of stress state on velocity is the easiest to analyze. Moreover, this state of confinement eliminates stress as a contributing factor for different values of P- and S-wave velocities measured along each of the principal axes at a given stress. Thus, this state permits evaluation of structural anisotropy (also called inherent anisotropy) and stress history.

After studying the effect of isotropic confinement on wave velocities, an exhaustive set of tests with biaxial confinement was performed. Conditions of biaxial confinement were obtained by keeping the intermediate principal effective stress equal to either the minor principal effective stress ($\bar{\sigma}_1>\bar{\sigma}_2=\bar{\sigma}_3$) or the major principal effective stress ($\bar{\sigma}_1=\bar{\sigma}_2>\bar{\sigma}_3$). The complete set of biaxial tests was composed of two test series: the first with confining stress varying in only one principal direction and the second with confining stress varying in two principal directions. Only a few of the results are presented herein because of space considerations. Also, testing with triaxial states of stress are not presented herein because of space limitations.

WAVE VELOCITY MEASUREMENTS

Waveforms of compression and shear waves were monitored under each confining pressure and were recorded on magnetic disks using the two digital oscilloscopes. These records were then analyzed for propagation velocities, frequencies, and strain amplitudes. However, only wave velocities are discussed herein. The other information is found in References 1 through 4.

Determination of wave velocity was quite straightforward. With known distances between accelerometers (measured during sample construction) and measured travel times of the waves, wave propagation velocities were simply calculated by dividing the distances by the corresponding travel times. The waveforms recorded on the magnetic disks were recalled using the same digital oscilloscopes used in monitoring the waves, and travel times were estimated from first arrivals of the waves at each accelerometer.

ISOTROPIC CONFINEMENT

An initial series of tests was performed under isotropic loading to evaluate any effect of stress history. Confining pressures were increased from 10 to 40 psi. The sand specimen was then unloaded to 10 psi. At each state of isotropic confinement, P- and S-wave velocities were determined as the average of two interval velocities along each of the principal axes, except for the north-south axis along which three interval velocities were used. Average interval velocities were then plotted against the corresponding confining pressure on log-log paper for each of the principal axes.

The variation in P-wave velocity with isotropic confinement is shown in Fig. 4. Compression wave velocity increases as confining pressure increases, with the relationship well represented by a straight line. A least-squares method was used to fit the data for loading and unloading separately. The unloading data exhibit slightly flatter slopes than those for the loading data. The slope of each log V_p - log $\bar{\sigma}_0$ relationship is denoted as m (n for the S-wave). The hysteresis effect shown in Fig. 4 results in wave velocities being slightly larger

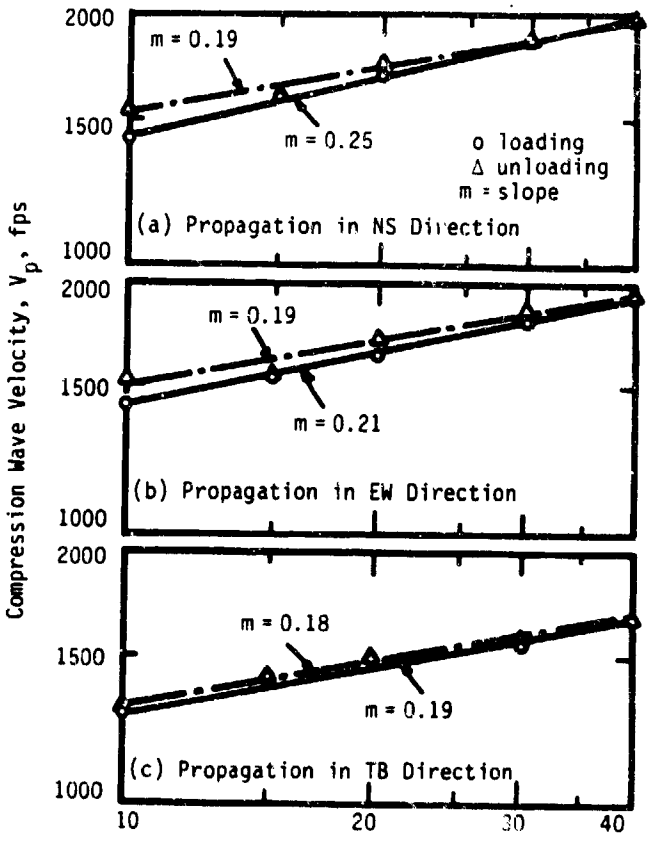

Fig. 4 - Variation of P-wave Velocity with Isotropic Confining Pressure.

upon unloading. This effect is most important at the lowest pressure. However, the largest variation in wave velocity upon loading and unloading was only 6 percent for the P-wave and only 5 percent for the S-wave. The hysteresis effect upon velocity was, therefore, not significant, and averages of values obtained from both loading and unloading were used in all analyses.

Results from shear wave tests are more complicated to present than the P-wave results because six shear waves were mesured at each confining pressure. Therefore, only averages of velocities for loading and unloading are shown in Fig. 5. Inserts in the figure illustrate the six waves. The nomenclature used for each shear wave consists of four symbols. The first two symbols denote the direction of wave propagation and the second two symbols denote the direction of particle motion. Therefore, the shear wave denoted as NSEW, for instance, represents a wave propagating in the north-south (NS) direction with particle motion polarized along the east-west (EW) direction.

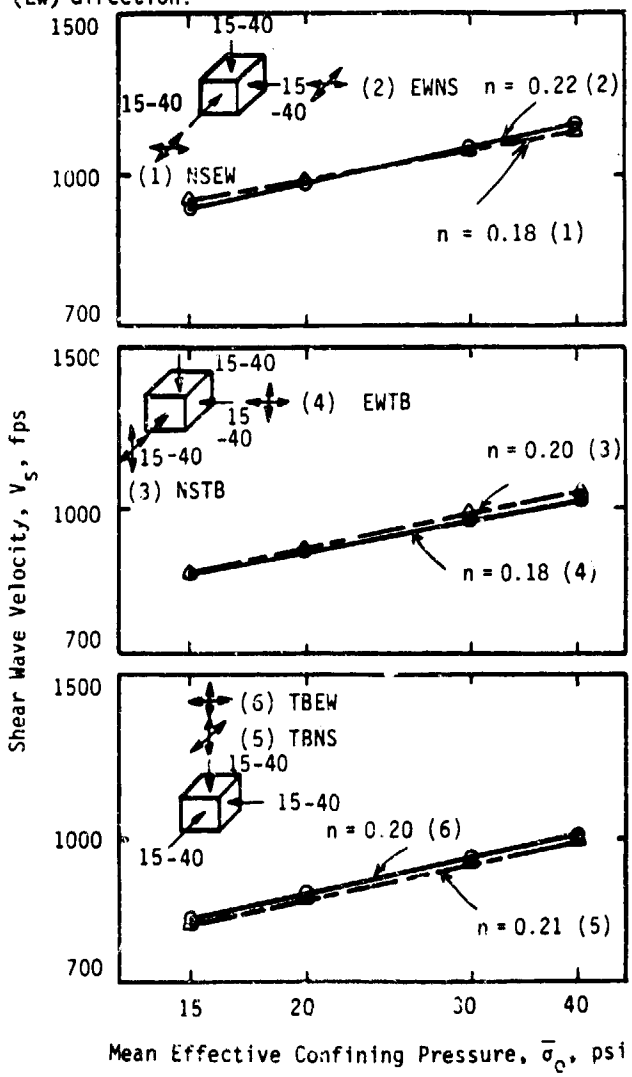

Fig. 5 - Variation of Shear Wave Velocity with Isotropic Confining Pressure.

As seen in Fig. 5, the log V_s - log $\bar{\sigma}_0$ relationships can be represented by straight lines just as in the P-wave case. Also, the slopes (n) of these relationships for the shear wave are nearly the same as those found for the P-waves. Only the values of wave velocity differ, with $V_s < V_p$.

Structural anisotropy is the inherent anisotropy in the soil skeleton which causes a difference in soil properties (including wave velocities) in different directions under isotropic loading. (Soil properties will vary with direction if the stresses vary, and this is referred to as stress-induced anisotropy). A certain amount of structural anisotropy was believed to have been induced in the sample as a result of the raining operation used to build the sample. Therefore, it was necessary to evaluate the magnitude and importance of the effect of structural anisotropy on P- and S-wave velocities before the general effect of isotropic confinement could be studied.

Average P-wave velocities are plotted against isotropic confining pressure using logarithmic paper in Fig. 6 (top three curves). The resulting curves are represented by three best-fit straight lines that are almost parallel. The curves fall into two groups: 1. for waves propagating along horizontal directions (NS and EW) in which case the velocities are within 3.5 percent, and 2. for waves propagating along the vertical direction which falls below the other two curves. As such, structural anisotropy is essentially not present in the horizontal plane but does exist between the horizontal and vertical directions. This condition is often modelled with a cross-anisotropic model.

Shear wave velocities shown in the lower part of Fig. 6 for the six shear waves also group according to what would be expected for a cross-anisotropic model. The two waves in the horizontal plane (NSEW and EWNS) exhibit nearly the same velocity while the four waves in the vertical plane (EWTB, NSTB, TBNS and TBEW) show some scatter in velocities but are more nearly similar.

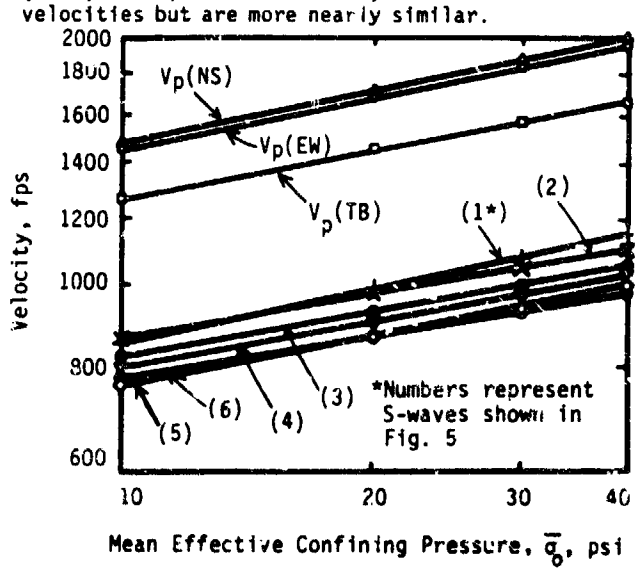

Fig. 6 - Effect of Structural Anisotropy on Variation of P- and S-Wave Velocities with Isotropic Confining Pressure.

The variation in wave velocities with isotropic confinement can then be represented by linear relationships on a log-log plot in a power form as:

$$V_p = C_1 \bar{\sigma}_o^m \quad (1)$$

$$V_s = C_2 \bar{\sigma}_o^n \quad (2)$$

where:

V_p = P-wave velocity, in fps,
V_s = S-wave velocity, in fps,
$\bar{\sigma}_o$ = isotropic confining pressure, in psf,
C_1 = constant ($C_1 = V_p$ when $\bar{\sigma}_o = 1$ psf),
C_2 = constant ($C_2 = V_s$ when $\bar{\sigma}_o = 1$ psf),
m = slope of straight line for P-wave, and
n = slope of straight line for S-wave.

The general form of the equations is unaffected by structural anisotropy, which only affects the constants C_1 and C_2.

BIAXIAL CONFINEMENT

Numerous tests were conducted using biaxial confinement. For the series presented herein, testing started at an isotropic state of stress of 15 psi. The stress in the vertical (TB) direction was then increased from 15 to 40 psi. Finally, the vertical stress was unloaded from 40 to 15 psi. The two horizontal stresses were held constant at 15 psi during the entire series.

The variation in velocities of P-waves propagating along each principal axis for these biaxial loading conditions are shown in Fig. 7. All wave velocities are plotted against the confining stress in the TB direction in the figure. Compression wave velocities under isotropic conditions (assuming that the isotropic pressure equals the pressure in the TB direction) are also shown in the figure for comparison purposes.

As shown in the upper portion of Fig. 7, P-wave velocity in the direction of increasing confining stress under biaxial confinement varies with stress in essentially the same manner as under isotropic confinement. These results suggest that the relationship between wave velocity and confining stress for biaxial confinement can be patterned after Eq. 1 for isotropic confinement if $\bar{\sigma}_a$ (stress in the direction of wave propagation) is substituted for $\bar{\sigma}_o$ (isotropic confining stress). The resulting equation is:

$$V_p = C_1 \bar{\sigma}_a^m \quad (3)$$

This equation for biaxial confinement only relates P-wave velocity to the stress in the direction of wave propagation, stresses in the other two principal directions perpendicular to the direction of propagation have very little effect on P-wave velocity. This behavior is clearly shown in the middle and bottom portions of Fig. 7. Compression wave velocities along directions of constant stress are essentially constant.

As with isotropic confinement, the behavior of the shear wave under biaxial confinement is more complex than the P-wave. To discuss this behavior, it is first necessary to develop a notation for the stress components. The notation is:

$\bar{\sigma}_a$ = effective principal stress in direction of wave propagation,
$\bar{\sigma}_b$ = effective principal stress in direction of particle motion, and
$\bar{\sigma}_c$ = effective principal stress in out-of-plane direction (the direction perpendicular to the $\bar{\sigma}_a$ and $\bar{\sigma}_b$ directions).

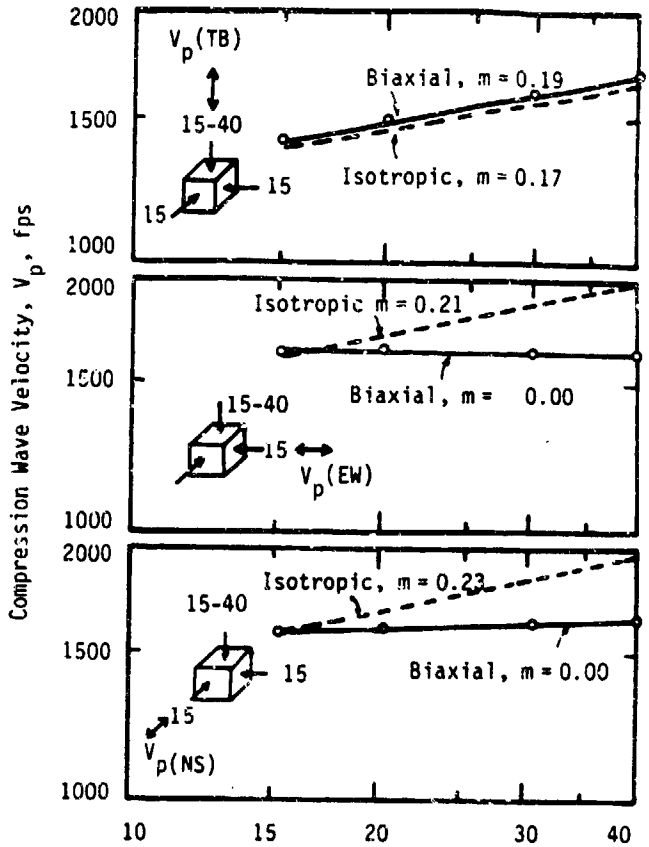

Fig. 7 - Variation in P-Wave Velocities Under Biaxial Conditions for Stress Increasing along TB Direction.

The variations in shear wave velocity with $\bar{\sigma}_a$ and $\bar{\sigma}_b$ are shown by the solid lines in the lower and middle portions of Fig. 8, respectively. In each case, the slope of the log V_s - log $\bar{\sigma}_a$ or - log $\bar{\sigma}_b$ relationship is about half of that found under isotropic confinement. The dashed lines in the figure shows the behavior of each shear wave under isotropic confinement, if the isotropic stress is assumed equal to the stress in the TB direction. The effect of $\bar{\sigma}_c$ on shear wave velocity is shown in the upper portion of Fig. 8. As can be seen, $\bar{\sigma}_c$ has essentially no effect on velocity. This behavior leads to the following equation [after Reference 5]:

$$V_s = C_2 \bar{\sigma}_a^{na} \bar{\sigma}_b^{nb} \quad (4)$$

where:

C_2 = constant
$n\bar{a}$ = slope of log V_s - log $\bar{\sigma}_a$ relationship, and
nb = slope of log V_s - log $\bar{\sigma}_b$ relationship.

In this equation, the mean effective principal stress is replaced by the stress components (expressed in psf) for shear wave motion. Ideally, the sum of the slopes for each stress component (ma + mb) should equal the slope m in Eq. 2 (slope of the log V_s - log $\bar{\sigma}_o$ relationship for isotropic confinement) for each shear wave type. The constant, C_2, represents the physical characteristics of the sand used in testing, including the structural anisotropy of the sand sample.

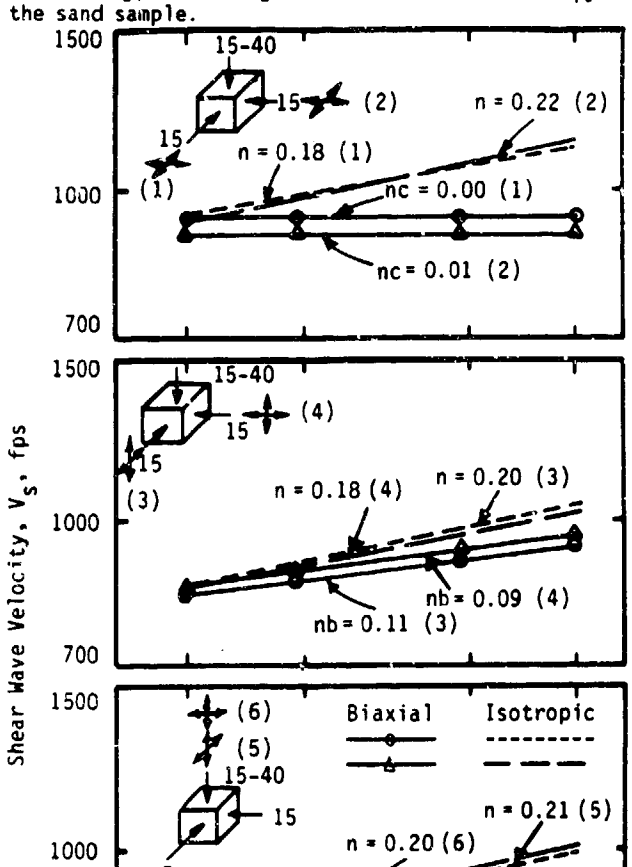

Fig. 8 - Variation in Shear Wave Velocity under Biaxial Conditions for Stress Increasing along TB Direction.

TRIAXIAL CONFINEMENT

Numerous tests were also conducted under triaxial confinement. Unfortunately, space limitations preclude presentation. The results did show, however, that Eq. 3 holds for P-waves and Eq. 4 holds for S-waves.

CONCLUSIONS

One sample of dry sand was tested in the large-scale triaxial device. Extensive tests were performed under isotropic, biaxial and triaxial states of stress. In each case, velocities of P- and S-waves propagating along all principal stress directions were measured. Results from these tests lead to the following conclusions: 1. the effect of stress history on P- and S-wave velocities is negligible, 2. the sample can be treated as a cross-anisotropic material under isotropic confinement due to structural anisotropy, 3. complete anisotropy resulted by the coupling of stress anisotropy and structural anisotropy, 4. P-wave velocity depends on the principal effective stress in the direction of propagation, with principal stresses perpendicular to the direction of propagation having a negligible effect on velocity, and 5. S-wave velocity depends about equally on the principal effective stresses in the directons of wave propagation and particle motion and is essentially independant of the third principal stress.

ACKNOWLEDGMENTS

The authors would like to to thank AFOSR, Bolling Air Force Base, for supporting this research. Major John J. Allen was the initial project manager after which Lt. Col. Dale Hokanson assumed the project management. The support, encouragement and guidance of the project managers is greatly appreciated.

REFERENCES

(1) Kopperman, S.E., Stokoe, K.H., II, and Knox, D.P. (1982), "Effect of State of Stress on Velocity of Low-Amplitude Compression Waves Propagating Along Principal Stress Directions in Dry Sand," Report GR82-22, Civil Engrg. Dept., Univ. of Texas at Austin.

(2) Knox, D.P., Stokoe, K.H., II, and Kopperman, S.E. (1982), "Effect of State of Stress on Velocity of Low-Amplitude Shear Waves Propagating Along Principal Stress Directions in Dry Sand," Report GR82-23, Civil Engrg. Dept., Univ. of Texas at Austin.

(3) Chu, H.Y.F., Lee, S.H.H., and Stokoe, K.H., II (1984), "Effects of Structural and Stress Anisotropy on Velocity of Low-Amplitude Compression Waves Propagating Along Principal Stress Directions in Dry Sand," Report GR84-6, Civil Engr. Dept., Univ. of Texas at Austin.

(4) Lee, S.H., and Stokoe, K.H., II (1985), "Effects of Structural and Stress Anisotropy on Velocity of Low-Amplitude Shear Waves Propagating Along Principal Stress Directions in Dry Sand," Report GR85-4, Civil Engrg. Dept., Univ. of Texas at Austin. (In progress)

(5) Roessler, S.K. (1979), "Anisotropic Shear Modulus Due to Stress Anisotropy," Journal of the Geotechnical Engineering Division, ASCE, Vol. 105, No. GT5, July, pp. 871-880.

ANALYSIS OF RESPONSE OF SATURATED SOIL SYSTEMS SUBJECTED TO DYNAMIC LOADING

Ranbir S. Sandhu, S.J. Hong, and Baher L. Aboustit

The Ohio State University
Department of Civil Engineering
Columbus, Ohio 43210

ABSTRACT

Biot's equations of wave propagation in fluid-saturated elastic solids allowing for relative motion between solid and fluid were implemented in a finite element computer program. Nodal values of the solid displacement and relative displacement of the fluid were used as the unkown quantities. The program was applied to several one-dimensional dynamic problems for which the exact solutions are available. The results showed excellent agreement between the numerical and the exact solutions.

INTRODUCTION

Most analytical solutions for the initial boundary value problem of wave propagation through saturated porous media provide only the harmonic component of the solution. Deresiewicz [5,6] obtained solution for the reflection of plane waves [2] and Love waves at a free plane. Garg et al.[8] presented the exact solutions for transient as well as the steady state compressional wave propagation through a porous elastic solid and developed finite difference procedures for numerical solution. Chakraborty and Dey [4] obtained the solution for Love waves in saturated media underlain by heterogeneous elastic media.

Although the finite element method has been extensively used for analysis of quasi-static consolidation problems, e.g. Sandhu [13], its application to the dynamic response of saturated soils is still in its infancy. Ghaboussi and Wilson [9] used Sandhu and Wilson's [12] approach to construct a variational principle, of the Gurtin type, equivalent to Biot's [3] field equations including initial as well as boundary conditions. The β-γ-θ method was used for the time domain integration. In the spatial discretization, a one-dimensional element was used with nodal values of the solid displacement and the relative displacement of the fluid as generalized coordinates. Ghaboussi and Wilson [9] did not present any comparison with an exact solution. Prevost [11] used the Galerkin approach for spatial discretization and Hughes' [10] implicit-explicit algorithm for time-domain integration. Bilinear four-node isoparametric elements were used with nodal point values of displacement of the solid and the fluid as the unknown parameters. Assumption of Newtonian fluid behavior led to nonsymmetric damping matrices. The methodology developed for solution of two-dimensional problems was used to solve a one-dimensional problem with finite length. For relatively large permeability, Prevost compared his results with the exact solution for a solid with no pores.

As part of an ongoing research effort at the Ohio State University, a finite element computer program based on the Biot's theory was developed and evaluated against analytical solutions. A Galerkin approach was used to set up the semi-discrete matrices spatially and, following Ghaboussi and Wilson [9], the β-γ-θ algorithm was used for the time domain integration. Nodal values of the solid displacement and relative displacement of the fluid with respect to the solid skeleton were used as the unknown quantities. A computer program was written to handle one-dimensional as well as plane-strain problems. One-dimensional linear element and four node and eight node isoparametric two-dimensional elements were included. The program was applied to several one-dimensional dynamic problems for which exact solutions are available. Herein, we report some results.

DYNAMIC EQUATIONS OF FLUID-SATURATED ELASTIC SOILS

Biot's [3] equations of motion for an elastic porous medium saturated with a compressible fluid may be written in standard indicial notation as;

$$[E_{ijkl}u_{k,l} + \alpha M(\alpha u_{k,k} + w_{k,k})\delta_{ij}]_{,j} + \rho f_i = \rho \ddot{u}_i + \frac{1}{f}\rho_2 \ddot{w}_i \qquad (1)$$

$$[M(\alpha u_{k,k} + w_{k,k})]_{,i} + \frac{1}{f}\rho_2 f_i = \frac{1}{f}\rho_2 \ddot{u}_i + \frac{1}{f^2}\rho_2 \ddot{w}_i + \frac{1}{K}\dot{w}_i \qquad (2)$$

where u_i, w_i, f_i, E_{ijkl} denote the cartesian components, respectively, of the solid displacement vector, the relative fluid displacement vector, the body force vector per unit mass and the isothermal elasticity tensor. ρ is mass density of the saturated soil and ρ_2 that of water per unit bulk volume. f, K, α, M are, respectively, the porosity, the permeability, the solid compressibility and the fluid com-

pressibility. The superposed dot implies a time derivative. All the functions are defined over the cartesian product $Rx[0,\infty)$ where R is the spatial region of interest and $[0,\infty)$ is the positive interval of time. With these field equations, we associate the following boundary conditions.

$$u_i(t) = \hat{u}_i(t) \quad \text{on } S_{1i} \tag{3}$$

$$t_i = \tau_{ij} n_j = (E_{ijkl} u_{k,l} + \alpha \pi \delta_{ij}) n_j = \hat{t}_i \quad \text{on } S_{2i} \tag{4}$$

$$\pi(t) = M(\alpha u_{k,k} + w_{k,k}) = \hat{\pi}(t) \quad \text{on } S_3 \tag{5}$$

$$w_i(t) = \hat{w}_i(t) \quad \text{on } S_4 \tag{6}$$

where S_{1i}, S_{2i} are complementary subsets of the boundary S of the spatial region of interest and so are S_3, S_4. The initial conditions for the problem are given by:

$$u(\underline{x}, 0) = u_o(x)$$

$$\dot{u}(\underline{x}, 0) = \dot{u}_o(x)$$

$$w(\underline{x}, 0) = w_o(x)$$

$$\dot{w}(\underline{x}, 0) = \dot{w}_o(x)$$

FINITE ELEMENT FORMULATION

a. Spatial Discretization

Spatial discretization of the governing equations for the two-field formulation leads to the following matrix equations;

$$\begin{bmatrix} K_{ss} & K_{sf} \\ K_{sf}^T & K_{ff} \end{bmatrix} \begin{bmatrix} u \\ w \end{bmatrix} + \begin{bmatrix} 0 & 0 \\ 0 & C_{ff} \end{bmatrix} \begin{bmatrix} \dot{u} \\ \dot{w} \end{bmatrix} + \begin{bmatrix} M_{ss} & M_{sf} \\ M_{sf}^T & M_{ff} \end{bmatrix} \begin{bmatrix} \ddot{u} \\ \ddot{w} \end{bmatrix} = \begin{bmatrix} R_s \\ R_f \end{bmatrix} \tag{7}$$

The elements of these matrices and the load vector are:

$$K_{ss} = \int_v [E_{ijkl} \phi^N_{,l} \psi^N_{,j} + \alpha^2 M \delta_{ij} \psi^M_{,j} \psi^N_{,k}] dv \tag{8}$$

$$K_{sf} = \int_v \alpha M \delta_{ij} \psi^N_{,k} \phi^M_{,j} \, dv \tag{9}$$

$$K_{ff} = \int_v M \phi^N_{,k} \phi^M_{,j} \, dv \tag{10}$$

$$M_{ss} = \int_v \rho \psi^N \psi^M \, dv \tag{11}$$

$$M_{sf} = \int_v \frac{1}{f} \rho_2 \phi^N \psi^M \, dv \tag{12}$$

$$M_{ff} = \int_v \frac{1}{f^2} \rho_2 \phi^N \phi^M \, dv \tag{13}$$

$$C_{ff} = \int_v C_{jk} \phi^N \phi^M \, dv \tag{14}$$

$$f_s = \int_{S_3} \hat{\pi} n_j \phi^M \, dS + \int_v \frac{1}{f} \rho_2 f_j \phi^M \, dv \tag{15}$$

$$F_s = \int_{S_{2i}} \hat{t}_i \psi^M \, dS + \int_v f_i \psi^M \, dv \tag{16}$$

in which ψ^M, ϕ^M denote the test functions for Equations (1) and (2), and ψ^N, ϕ^N the interpolating functions for the solid displacement and the relative displacement of fluid, respectively.

Equations (1) and (2) assume no inherent damping in the system as a whole. The only damping component is associated with relative motion. Rayleigh type damping for the system, introduced by Ghaboussi and Wilson [9], has the form

$$C_{ss} = a_1(M_{ss} - f^2 M_{ff}) + a_2(K_{ss} - \alpha^2 K_{ff}) \tag{17}$$

where a_1, a_2 are constants and f, α have been defined previously. The structural damping matrix is a linear combination of the mass and the effective stiffness of the soil. Comparing with Equation (1), $(K_{ss} - \alpha^2 K_{ff})u$ to corresponds to $(E_{ijkl}u_{k,l})_{,j}$. The quantity M_{ss} corresponds to ρ in Equation (1) and M_{ff} to ρ_2/f^2 in Equation (2). Hence, $M_{ss} - f^2 M_{ff}$ corresponds to ρ_1.

b. Time Domain Integration

Introducing structural damping defined in Equation (17), the discretized equations of motion, Equation (7), can be rewritten as

$$M\ddot{U} + C\dot{U} + KU = R \tag{18}$$

in which

$$U = \begin{bmatrix} u \\ w \end{bmatrix} \quad M = \begin{bmatrix} M_{ss} & M_{sf} \\ M_{sf}^T & M_{ff} \end{bmatrix} \quad C = \begin{bmatrix} C_{ss} & 0 \\ 0 & C_{ff} \end{bmatrix}$$

$$K = \begin{bmatrix} K_{ss} & K_{sf} \\ K_{sf}^T & K_{ff} \end{bmatrix} \quad R = \begin{bmatrix} R_s \\ R_f \end{bmatrix} \tag{19}$$

Wilson's β-γ-β algorithm was used to integrate the equations of motion. For the choice of these parameters, Zienkiewicz [14] has given the following conditions for analysis of undamped response of a linear system.

$$\gamma > 1/2$$

$$\beta > 1/4(1/2 + \gamma)^2 \qquad (20)$$

$$1/2 + \beta + \gamma > 0$$

RESULTS OF NUMERICAL IMPLEMENTATION

Two one-dimensional problems for which the analytical solutions are known were used to check the validity of the code. These include an elastic column of single material and the fluid-saturated soil layer solved by Garg et al. [8], and Ghaboussi and Wilson [9]. All the problems are concerned with compressional wave propagation in an initially undisturbed, homogeneous, isotropic, elastic system subjected to spatially uniform surface traction q(t).

(a) An Elastic Column of Single Material

An elastic layer under spatially uniform excitation applied to its surface can be regarded as an elastic column, constrained in its lateral dimensions and subjected to excitation at the free end. The characteristics used in the finite element model were;

Total length	$L = 500$ mm
Number of nodes	$= 51$
Number of elements	$= 50$
Length of each element	$= 10$ mm
Modulus of elasticity	$E = 20000$ kg/mm^2
Poisson's ratio	$\nu = 0$
Density	$\rho = 0.0008$ kg.m.sec^2/mm^4
Wave velocity	$C_o = [(2\mu + \lambda)/\rho\ ]^{1/2}$ $= 5000$ mm/msec
Time interval	$\Delta t = 0.002$ msec
Number of time steps	$= 50$

where μ, λ are Lame's constants for isotropic linear elastic material. The following two types of loading at the free end were considered.

i. Steady state response

A sinusoidal loading in the form

$$q(t) = q_o \sin(40\pi t) \qquad (21)$$

was applied to one end of the bar with the other end fixed.

ii. Response to step load

A load was suddenly applied and allowed to stay, i.e.

$$q(t) = q_o H(t) = \rho C_o H(t) \qquad (22)$$

where H(t) is the Heaviside function. It should be noted that the loading in Equation (22) will induce a unit particle velocity [1]. The analytical solution for this problem which contains both the harmonic and the transient solution is well known [7].

Figures 3(a) through 3(c) illustrate the stress response when fixed at one end and subjected to sinusoidal loading at the free end at time stages 0.038, 0.064 and 0.10 second. The numerical solution was based on values of q_o=-4, β=0.25, γ=0.5 and θ=1.0. Good agreement was shown between the finite element solution and the analytical solution throughout the spatial as well as the temporal domains. At the point y/L=0.99, the error at t=0.03 and 0.05 second was 4.6 and 5.4 percent, respectively. But at the other time stages it was less than 1.0 percent.

Figures 4(a) through 4(c) illustrate the displacement, velocity and stresses along the elastic column under unit step load at the free surface, at time t=0.08 sec, i.e. after 40 time increments. Two different time integration schemes were used viz, β=0.167 and β=0.25. For both the schemes, θ=1.0 and γ=0.5. Figure 4 shows that both schemes give almost the same displacement response. However, β=0.167 was better for velocity and β=0.25 better for stress distribution. Despite this fact, large error around wave front is observed and numerical results are not reliable.

(b) Response of a Fluid-Saturated Soil Layer (Garg's Problem)

In the example, the exact solution for wave propagation in a one-dimensional fluid-saturated porous soil layer was found by Garg [8]. The material properties were assumed to be the same as used by Garg [8]. The finite element model for this problem was;

Total length	$L = 50$ cm
Number of nodes	$= 51$
Number of elements	$= 50$
Length of each element	$= 1$ cm
Modulus of elasticity	$E = 0.2319 \times 10^{12}$ dyn/cm^2
Poisson's ratio	$\nu = 0.171$
Mixture mass density	$\rho = 2.3612$ gm/cm^3
Fluid mass density	$\rho_2 = 0.18$ gm/cm^3
Porosity	$f = 0.18$
Fluid compressibility	$M = 0.102 \times 10^{12}$ dyn/cm^2
Lower bound of wave velocity	$C_o = 354875$ cm/sec
Upper bound of first kind wave velocity	$C_+ = 358193$ cm/sec
Upper bound of second kind wave velocity	$C_- = 127941$ cm/sec

The velocities C_o, C_+, C_- were defined by Biot [2] and Garg [8]. Using the notation of this report, these quantities are given by the following expressions [8].

$$C_o^2 = (\lambda + 2\mu + \alpha^2 M)/\rho$$

$$C_1^2 = (\lambda + 2\mu + M(\alpha - f)^2)/\rho_1$$

$$C_2^2 = Mf^2/\rho_2$$

$$C_{12}^2 = Mf(\alpha - f)/\rho_1$$

$$C_{21}^2 = Mf(\alpha - f)/\rho_2$$

$$2C_\pm^2 = C_1^2 + C_2^2 \pm [(C_1^2 - C_2^2)^2 + 4C_{12}^2 C_{21}^2]^{1/2}$$

Here, $\rho_1 = \rho - \rho_2$ is the bulk mass density of the soil. These velocities are applicable to one-dimensional compressive wave propagation. A unit particle velocity for each phase was imposed at the free surface, i.e.,

$$\dot{u}(L,t) = H(t) \qquad (23)$$

$$\dot{w}(L,t) = 0 \tag{24}$$

Equation (24) implies "strong" coupling at the free surface. In reality, this may not be true. However, for the purpose of comparison with Garg, the same assumptions were made. As reported by Garg [8], as permeability $K \rightarrow 0$, the relative motion between the two constituents vanishes and phase velocity $C \rightarrow C_0$. This is termed "strong coupling". In this case the material behaves as a single continuum whose properties are combination of those of the two constituents. On the other hand, as $K \rightarrow \infty$, the coupling between the two constituents vanishes and $C \rightarrow C_+$. This extreme is termed "weak coupling". The boundary condition given by Equation (23) can be replaced by the traction boundary condition, while the boundary conditions expressed by Equation (24) can be replaced by the displacement boundary condition, i.e.

$$q(L,t) = \rho C H(t) \tag{25}$$

$$w(L,t) = 0 \tag{26}$$

where $q(L,t)$ is the traction applied to the free surface. In order to investigate the effect of fluid-soil interaction on wave propagation, two different values of the permeability coefficient were selected to approximate "strong" and "weak" coupling extremes described by Garg [8]. The numerical values for the permeability and the time steps corresponding to strong and weak couplinge were;

i. Strong Coupling (Low Permeability)

$K = 0.148 \times 10^{-8}$ cm^3/gm sec
Δt = 1 micro sec
Number of time steps = 50

ii. Weak Coupling (High Permeability)

$K = 0.148 \times 10^{-2}$ cm^3/gm sec
Δt = 2.4 micro sec
Number of tme steps = 50

Figures 5(a) and 5(b) show the velocity of both the solid and fluid at 10 cm from the traction boundary in the case of "strong coupling". The numerical results are based on calculations with $\theta = 1$, $\gamma = 0.6$, $\beta = 0.3025$. Reasonable agreement is seen between the finite element and the analytical solutions. But while the exact solution has the sharp discontinuity in the wave front, numerical one was diffused. A single wave front exists. The wave is propagating with velocity $= C_0$, and the solid velocity is the same as the fluid velocity. This is because, for this problem, relative velocity $\dot{w}$ approaches zero and the two constituents effectively act as a single continuum.

Figures 6(a) and 6(b) shows the results for "weak" coupling. The values of β, γ, θ were the same as for the "strong" coupling. The results for a station 10 cm away from traction boundary (y=40cm) are quite close to Garg's analytical solution [8]. Existence of two wave fronts travelling with speeds C_- and C_+ is noticed.

Pore pressure distribution at different times for the two extremes of "strong" and "weak" coupling are plotted in Figure 7(a) and 7(b). A single phase description is seen in Figure 7(a), in which the pressure wave is propagating with speed C_0. Figure 7(b) clearly demonstrates the existence of two waves travelling with speed C_- and C_+, in the fluid and the solid, respectively.

(c) Response of a Fluid-Saturated Soil Layer (Ghaboussi and Wilson's Problem)

The final example was the problem of a saturated half-space subjected to a unit step load. Ghaboussi and Wilson [9] obtained a numerical solution of the problem, but did not present any comparison with analytical solution. The finite element model had the following properties.

Total length	L= 50 cm
Number of nodes	= 51
Number of elements	= 50
Length of each element	= 1 cm
Modulus of elasticity	E= 0.2319×10^{12} dyn/cm^2
Poisson's ratio	ν= 0.171
Mixture density	ρ= 3 gm/cm^3
Fluid density	ρ_f= 0.18 gm/cm^3
Porosity	f= 0.18
Fluid compressibility	M= 90×10^{11} dyn/cm^2
Solid compressibilty	α= 1
Wave velocity for the mixture (no relative motion)	$C_o = [(2\mu+\lambda+\alpha^2 M)/\rho]^{1/2}$ = 1.755895×10^6cm/sec
Coefficient of permeability	K= 0.19×10^{-6} cm/sec
Time interval	Δt= 1 micro sec

Generally, the solid density of soil falls between the range of 2.0-2.7(gm/cm^3) and the compressibility of pure water is 2.0×10^{10}(dyn/cm^2). Thus, it should be noted that mixture density and the fluid compressibility given above are far from real soil properties, but were taken to match the problem solved by Ghaboussi and Wilson [9]. The values of k and f, not given explicitly in [9], were chosen to represent the mixture of very fine sand and silt in very dense state.

Figure 8 presents the pore pressure distributions at several time stages. In this figure, the non-dimensional pore pressure π/q is plotted against $y^* = y/(KC_0)$. For $\alpha = 1$ and $M \rightarrow \infty$ the pore pressure should be equal to the applied traction. This does not match Ghaboussi and Wilson [9].

CONCLUSIONS

Results of the analyses indicate the following:

1. The integration parameters β, γ and θ should be carefully selected to avoid oscillatory error.
2. The scheme, with proper selection of β, γ and θ showed exellent agreement with the analytical solutions.
3. The numerical and analytical results show the importance of the role of permeability in single or double phase description for fluid-saturated porous media. For low permeability, there is little relative motion and the strong coupling on single material description would be valid. For high permeability, the two phase description is necessary.
4. The computer code was checked only for one-di-

mensional problems. Its effectivenos for two-dimensional (plane strain) problems is yet to be established.

5. Further investigation in the choice of damping matrices is required. The solution process for a few idealized problems has been checked, but the assumptions regarding various couplings may not represent actual soil behavior.

6. The computer code implemented Ghaboussi and Wilson's version of Biot's theory. The entire fluid mass is expected to be in relative motion. In other theories, an interaction mass is introduced. This would imply a "partial" coupling somewhere between the "strong" and "weak" coupling defined by Garg [8]. Some work to quantify this coupling has been done and will be reported in the near future.

7. The computer code needs to be extended to propagation of shear waves and Love and Rayleigh waves. Studies are needed to allow for reflection and refraction of waves at interfaces or boundaries. Dynamics of nonhomogeneous, anisotropic and nonlinear soils needs to be investigated.

ACKNOWLEDGEMENTS

The work reported herein is part of a research program supported by the Air Force Office of Scientific Research, Air Force Systems Command, USAF, under Grant No. AFOSR-83-0055. The U.S. Government is authorized to reproduce and distribute reprints for Governmental purposes notwithstanding any copyright notation therein. The assistance provided by the Instruction and Research Computer Center, The Ohio State University is gratefully acknowledged.

REFERENCES

1. Achenbach, J.D.; 1973, Wave Propagation in Elastic Solids, North-Holland Publishing Company, Amsterdam, New York, Oxford.
2. Biot, M.A.; 1956, J. the Acous. Soc. Amer., 28, No.2, 168-178.
3. Biot, M.A.; 1961, J. Appl. Phys., 33, No.4, 1483-1498.
4. Chakraborty, S.K., and Dey, S.; 1982, Acta Mechanica, 44, 169-176.
5. Deresiewicz, H.; 1960, Bull. Seis. Soc. Amer., 50, 599-607.
6. Deresiewicz, H.; 1960, Bull. Seis. Soc. Amer., 51, 51-59.
7. Flugge, W.; 1966, Handbook of Engineering Mechanics, McGraw-Hill, New york, N.Y.
8. Garg, S.K., Nayfeh, A.H., and Good, A.J.; 1974, J. Appl. Phys., 45, 1968-1974.
9. Ghaboussi, J., and Wilson, E.L.; 1973, Amer. Soc. Civ. Engrs., 98, J. Engrg. Mech. Div., 947-963.
10. Hughes, T.J.R., Pister, K.S., and Taylor, R.L.; 1979, Comp. Meth. Appl. Mech. Engrg., 17/18, 159-182.
11. Prevost, J.H.; 1982, Comp. Meth. Appl. Mech. Engrg., 30, 3-18.
12. Sandhu, R.S., and Pister, K.S.; 1970, Int. J. Engrg. Sci., 8, 989-999.
13. Sandhu, R.S.; 1982, "Finite Element Analysis of Subsidence due to Fluid Withdrawal", Forum on Subsidence due to Fluid Withdrawal, Fountainhead State Resort, Oklahoma.
14. Zienkiewicz, O.C.; 1979, The Finite Element Method, 3rd Ed., McGraw-Hill, London.

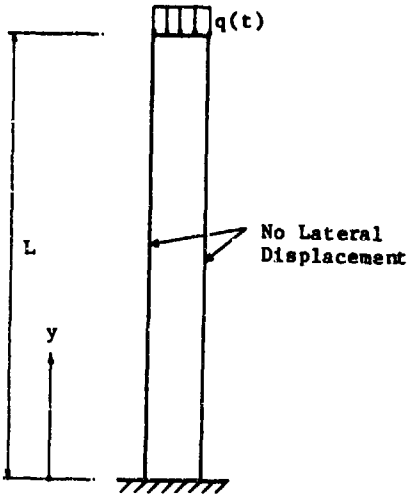

Figure 1: An Elastic Column Subjected to Dynamic Loading

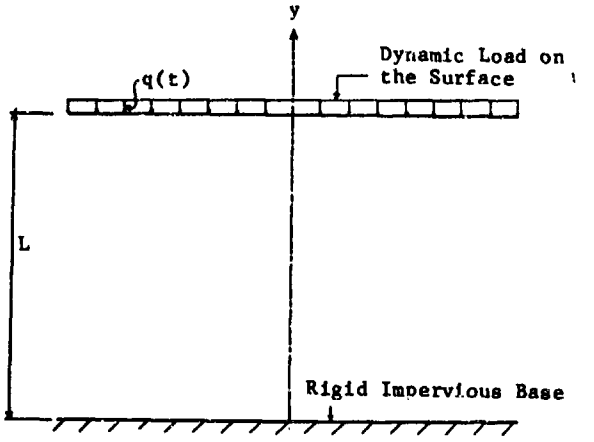

Figure 2: Soil Layer Subjected to Surface Traction

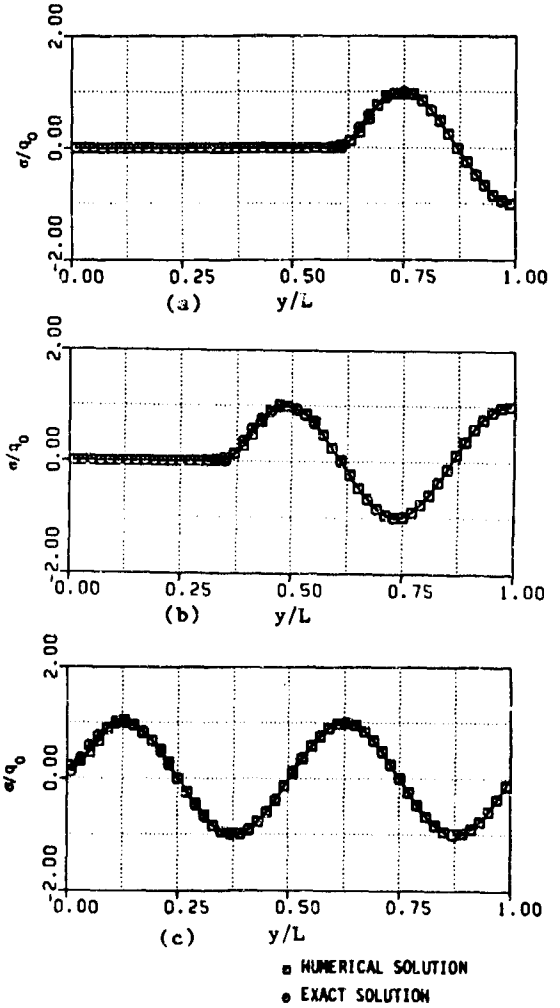

Figure 3: Stress Distribution in an Elastic Column Subjected to Sinusoidal Load at the Free Surface; (a)t=0.038 sec, (b)t=0.064 sec, (c)t=0.1 sec

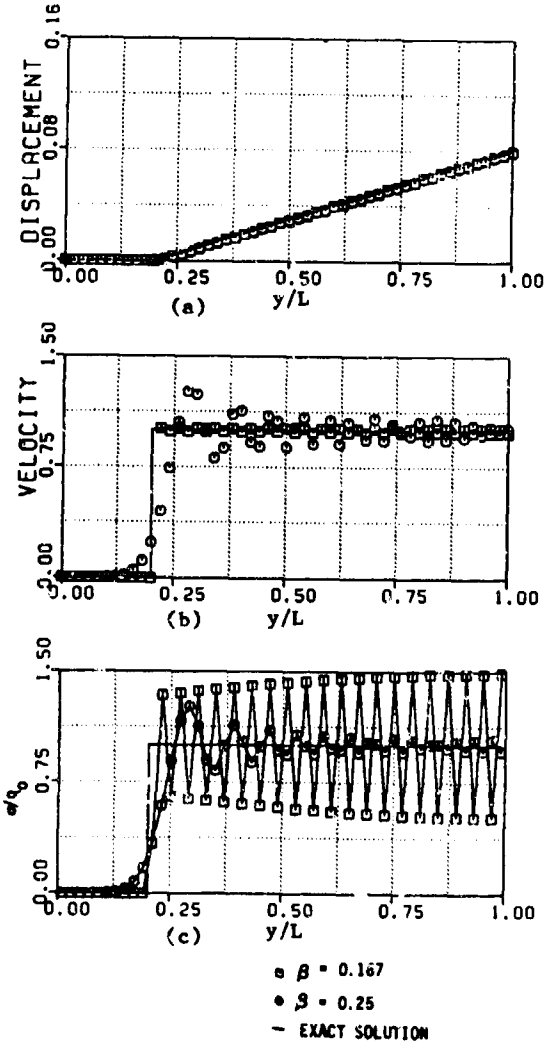

Figure 4: (a)Displacement, (b)Velocity, (c)Stress Distribution in an Elastic Column under Unit Step Load at Free Surface at time= 0.08 sec

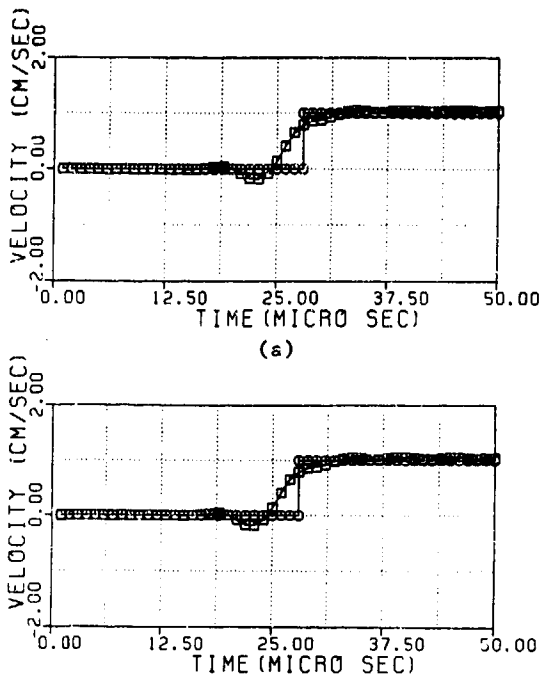

Figure 5: Garg's Problem for Strong Coupling; Velocity History of (a)Solid, (b)Fluid at 10cm from the Traction Boundary

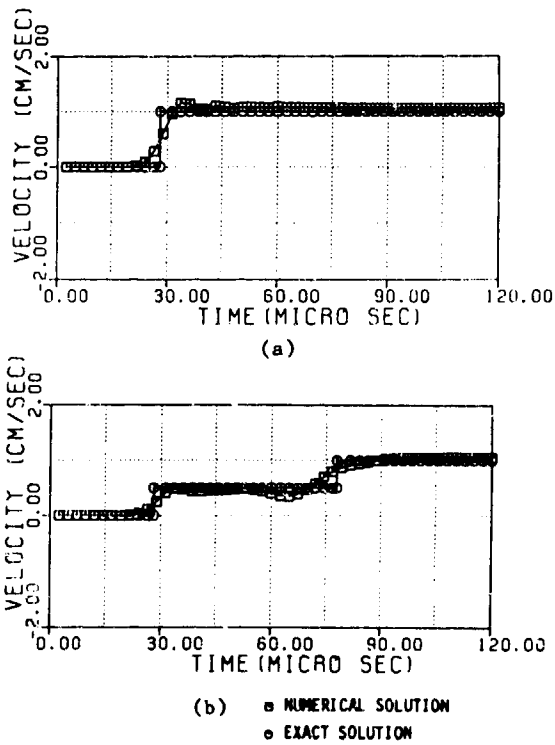

Figure 6: Garg's Problem for Weak Coupling; Velocity History of (a)Solid, (b)Fluid at 10cm from the Traction Boundary

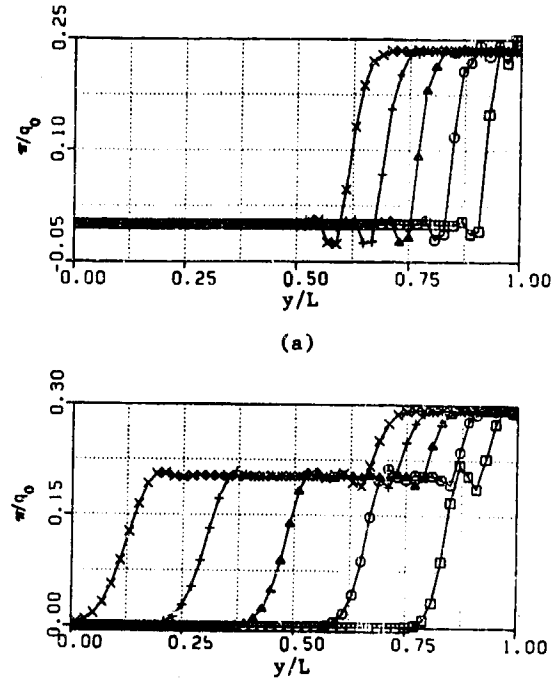

Figure 7: Pore Pressure Distribution of Garg's Problem (a)Strong, (b)Weak Coupling

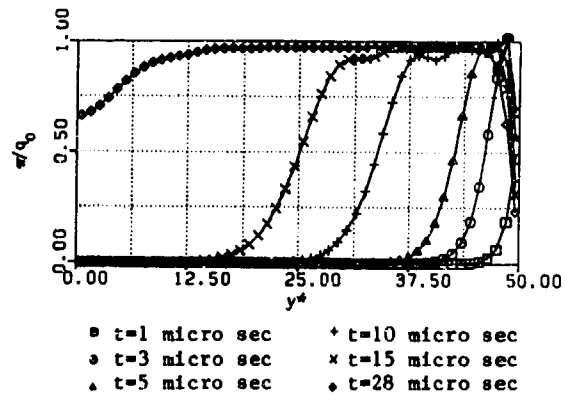

Figure 8: Pore Pressure Distribution of Ghaboussi's Problem

DYNAMIC PORE PRESSURE RESPONSE OF SATURATED SOIL UNDER SHOCK LOADING

Wayne A. Charlie
Steven R. Abt
George E. Veyera

Department of Civil Engineering
Colorado State University
Fort Collins, Colorado

ABSTRACT

This paper describes an experimental laboratory testing program which is subjecting water saturated sands to shock loadings. The study is being conducted to evaluate potential blast induced short- and long-term changes in porewater pressure and soil shear strength. The laboratory data obtained to date indicates that residual porewater pressure increases and soil shear strength decreases may occur under shock loads if peak compressive strains exceed 10^{-2} percent.

INTRODUCTION

Explosive induced ground motion prediction models and engineering designs presently incorporate the assumption of little or no blast induced soil property changes. However, Charlie et al. (1981) report that blast induced soil property changes, such as fairly long-term decreases in shear strength, shear wave velocity, and damping, as a result of fairly long-term increases in water pressure have occurred after blasting in loose saturated granular soils. Therefore, blasting near slopes may result in inducing sufficient residual excess porewater pressures to reduce the soil's shear strength for a period of time which may be long enough to allow gravity to fail the slopes. Residual porewater pressures may also lead to flotation, sinking, or differential movements of structures.

For porewater pressure response, the three stages of interest which may occur as a result of blasting are:

- The millisecond transient response directly associated with the stress wave.
- The residual response shortly after the passage of the stress wave.
- The longer-term dissipation of the residual porewater pressures.

Of major concern for the stability of earth structures and foundation behavior is the residual porewater pressure occurring after the stress wave has passed. The resulting decrease in effective stress would lead to a decrease in the soil's shear strength. Blast induced residual porewater pressure increases have been reported by Terzaghi (1956), Florin and Ivanov (1961), Kummeneje and Eide (1961), Lyakhov (1961), Puchkov (1962), Ivanov (1967), Damitio (1972), Langley et al. (1972), Perry (1972), Banister and Ellett (1974), Yamamura and Koga (1974), Charlie (1977), Studer and Prater (1977), Rischbieter (1977), Arya et al. (1978), Charlie (1978), Damitio (1978), Kok (1978), Marti (1978), Studer and Kok (1980), Charlie et al. (1981), Long et al. (1981), Prakash (1981), Fragazzy et al. (1983), Veyera (1983), Charlie et al. (1983,1985), and other researchers. Such soil behavior may indicate that liquefaction may have occurred at these sites. As such, an explosive detonated in a soil having a high liquefaction potential could result in damage disproportionate to the energy released.

EXPLOSIVE INDUCED GROUND MOTIONS

For a deeply buried charge or a HEST charge layout, most of the wave energy is in the form of a compressional stress wave. For rock, clay and unsaturated granular soils, the compression pulse from a single charge detonation typically has one sharp peak of acceleration with a duration near the blast on the order of a few milliseconds for rock and tens of milliseconds for soil (Stagg and Zienkiewicz, 1968; SME, 1973). For a single charge detonated in loose saturated granular soils and sensitive marine clays, the compression pulse typically has one sharp peak of acceleration followed by a period of low frequency oscillation (Charlie et al., 1980). After the stress wave impinges upon interfaces, such as soil-rock boundaries, the water table or the earth's surface, reflections produce compression (or tensile), shear and surface waves.

EXPLOSIVE INDUCED RESIDUAL POREWATER PRESSURES

For two-phase materials that are vibration sensitive, such as loose saturated sands, the fluid phase may act elastically while the sand skeleton acts plastically, resulting in a residual increase in porewater pressure after passage of the stress wave. The state-of-the-art for assessing blast induced residual porewater pressure increases and liquefaction potential is limited at best. The literature indicates that nonsensitive cohesive soils are least affected by vibrations while loose saturated cohesionless soils are most sensitive to

saturated cohesionless soils are most sensitive to vibrations. Theoretical approaches are almost nonexistent and have not been verified by experimental testing (Charlie et al., 1981). Empirical scaling factors have been derived from a limited number of field tests. A logical approach would be to determine possible threshold particle velocities, stresses or strains below which blast induced porewater pressure increases should not occur. It is emphasized that such threshold values would be for soils having a high blast induced residual porewater pressure increase potential.

Marcuson (1982) suggests that liquefaction should not occur where the peak particle velocity is less than 2.5 cm per second. Sanders (1982) related earthquake induced liquefaction to peak particle velocity indicating that a threshold particle velocity of 5 to 10 cm per second was a value that may also hold for underground blasts. Charlie (1983) suggests that residual porewater pressure increases should not occur in saturated loose sands and silts if the peak particle velocity is kept below 1 cm per second.

A few field tests have been conducted where porewater pressure responses induced by contained explosives have been measured. Lyakhov (1961) noted that blast induced liquefaction did not occur in water saturated sand with densities greater than 1.6 gm per cubic cm. For saturated soils at lower densities, Puchkov (1962) found that soils did not liquefy below a peak particle velocity of 7 cm per second. Ivanov (1967) and Studer and Kok (1980) have reported empirical relationships to predict the maximum radius of liquefaction from contained point charges. These relationships indicate liquefaction may occur in loose saturated sands if peak particle velocities exceed 4 cm per second. Residual porewater pressures from other contained explosive tests have been reported at peak particle velocities as low as 1 cm per second (Charlie et al., 1985). Residual porewater pressures have also been generated by surface explosions. For a 450,000 kg TNT surface explosion, Langley et al. (1972) measured residual porewater pressure increases exceeding 75 KPa in saturated glacial deposits out to distances where the estimated peak airblast over pressure and peak compression strain was 350 KPa and 10^{-2} percent, respectively.

Perry (1972) conducted shock tube tests and determined that a loose saturated sand could be liquefied at peak over pressures as low as 600 KPa (estimated peak compression strain of 1.5×10^{-2} percent). Fragazzy et al. (1983) report that in centrifuge modeling of blast induced liquefaction, residual porewater pressure increases occurred in water saturated sands at scaled distances ($R/W^{1/3}$) from buried charges as large as 20 (estimated peak particle velocity of 13 cm per second). Liquefaction occurred at scaled distances as large as 15 (estimated peak particle velocity of 20 cm per second). The tests were run on sand placed at relative densities of 50 percent and saturation of 97 percent.

Charlie et al. (1983,1985) suggest that a threshold strain approach may prove very useful for assessing blast induced residual porewater pressure increases. Shear strains of less than 10^{-2} percent are generally considered to be elastic (Dobry et al., 1982). Under elastic plane strain conditions, the peak shear strain is equal to the peak compression strain (Timoshenko and Goodier, 1970). Therefore, compressive strains of less than 10^{-2} percent should also be elastic and not induce residual porewater pressure after passage of the stress wave. Utilizing equations given by Rinehart (1975) and Richart et al. (1970), a compression strain of 10^{-2} percent in water saturated soils at a void ratio equal to one corresponds to about 15 cm per second peak radial particle velocity. Table 1 presents several empirical scaling factors based on threshold strain, particle velocity and field tests to determine the potential radius of liquefaction and residual porewater pressure increases for various charge weights. Although

Table 1. Predicted Maximum Radius of Liquefaction and Residual Porewater Pressures for a Single Contained Point Charge Detonated in Loose Saturated Cohesionless Soils (Charlie et al., 1985)

Charge Weight TNT (kg)	Predicted Maximum Radius (meters)(1)						
	Liquefaction(2)				Porewater Pressure Increase(3)		
	Russian(4) Peak Particle Velocity 7 cm/sec	Russian(5) $R_{max} = k_3 W^{1/3}$ Relative Density 0%	Relative Density 40%	Liq.(6) Coef. 1.0	Comp.(7) Strain 10^{-2}%	Liq.(8) Coef. 0.1	Peak(9) Particle Velocity 2 cm/sec
1	6	25	8	2	4	15	12
10	18	55	20	5	12	20	40
100	40	120	40	15	40	50	120
1,000	180	250	80	—	120	—	400
10,000	600	540	170	—	400	—	1200
100,000	1800	1200	370	—	1200	—	4000

Notes:
(1) Predicted maximum radius may be higher under multiple detonations and some geologic and confinement conditions.
(2) Maximum radius for the residual porewater pressure increase equal to the initial effective vertical stress.
(3) Maximum radius for some increase in residual porewater pressure.
(4) Estimated peak particle velocity and Puchkov (1962) for threshold velocity.
(5) Ivanov (1972).
(6) Studer and Kok (1980).
(7) Estimated assuming a compression wave velocity of 1500 meters per second and a void ratio of one.
(8) Studer and Kok (1980).
(9) Estimated peak particle velocity.

there are differences in the predictions, residual porewater pressure increases occur where predicted compressive strains exceed 10^{-3} percent, an order of magnitude less than expected by considering only compression wave induced strains. This may indicate that other factors such as shear wave induced strains, multiple strains and other factors are also important.

LABORATORY FACILITY AND INSTRUMENTATION

Laboratory testing is currently being conducted at Colorado State University to evaluate

the empirical scaling factors presented in Table 1, to evaluate the effects of multiple shock loadings and to extend the state-of-the-art in understanding stress wave mechanics of two-phase materials. The objectives of the program are to generate and determine the number of axial compressive stress pulses required to induce liquefaction in saturated cohesionless soils as a function of: initial relative density, initial effective stress, peak particle velocity, peak compressive strain amplitude and peak compressive stress amplitude. Since little or no drainage would occur in deep field deposits of saturated soils during the passage of the stress wave, the laboratory tests are undrained. The laboratory facility is shown schematically in Figure 1. It consists of separate

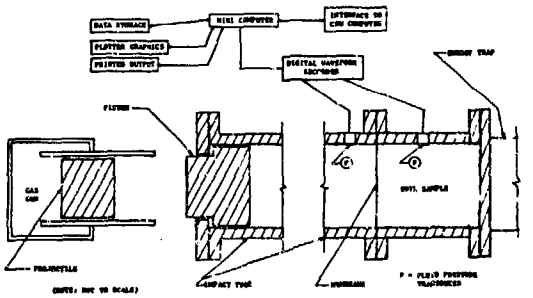

Figure 1. Schematic of laboratory facility to study shock-induced liquefaction.

but intimately related elements which include a gas-charged cannon, a fluid-filled stainless steel tube, a rigid sample container, a flexible interface membrane, an electronic control system and an electronic recording and monitoring system. The membrane is utilized to apply the confining pressure to the soil sample and allow variations in effective stress (depth). The cannon is designed to fire a projectile which impacts a piston which imparts the stress wave to the confining fluid which in turn applies the compressive shock pulse to the soil sample. To minimize reflections, an energy trap, which consists of a polyvinyl chloride (PVC) rod, is utilized. In current testing procedures, the energy trap is placed at the end of the sample container. A pressure transducer, positioned just upstream of the soil sample, is used to determine the intensity of the applied compressive stress. A second pressure transducer is located in the wall of the sample container and is used to measure both the peak and long-term transient porewater pressure response in the soil. The pressure transducers (ENDEVCO Model 8511A-5kM1) have a resonant frequency greater than 500 KHz over a pressure response range of from 0 to 35,000 KPa.

LABORATORY SHOCK TESTING

Tests have been conducted on saturated sand at densities ranging from 1.4 to 1.7 grams per cubic cm (0 to 100 percent relative density). Initial effective confining stresses are being varied from 100 to 1000 KPa. All tests to date have been conducted using water saturated Monterey No. 0/30 sand. Figures 2 and 3 show the response of the porewater pressure as a result of the input stress

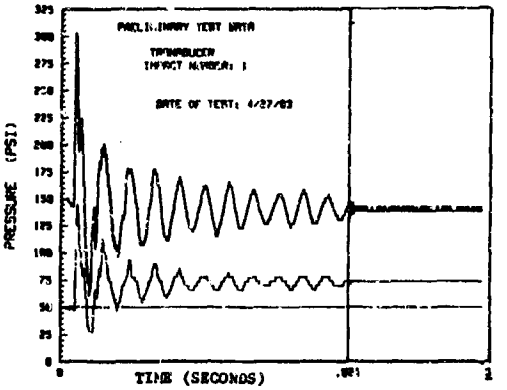

Figure 2. Response of the sample's porewater pressure leading to limited increase in residual porewater pressure under the first shock loading: initial effective stress of 690 KPa (1 psi = 6.895 KPa).

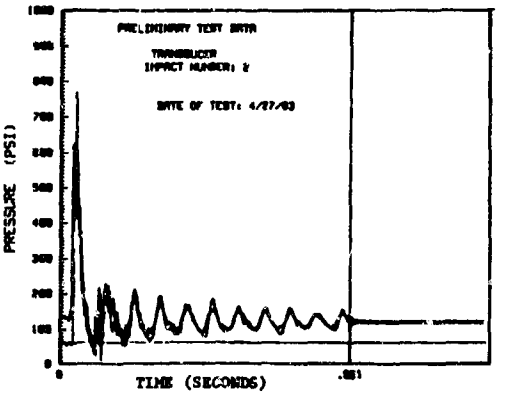

Figure 3. Response of the sample's porewater pressure leading to liquefaction under the second shock loading: initial effective stress of 690 KPa (1 psi = 6.895 KPa).

wave for the saturated sand at a dry density of 1.47 grams per cubic cm under an initial confining stress of 6.90 KPa. Each plot combines both the input shock and the sample's porewater pressure response. Figure 2 shows the sample's residual porewater pressure increased by 200 KPa after being subjected to a peak strain of 2×10^{-2} percent. This porewater increase is about 30 percent of the increase required to cause liquefaction. Figure 3 shows that the same sample liquefied when subjected to a second peak strain of 7×10^{-2} percent. The relationships given earlier in this paper predict residual porewater increases at these peak strains. The results of 20 test series are currently being analyzed.

CONCLUSIONS

Today's understanding of blast induced porewater pressure increases has advanced only slightly beyond the point of recognition of its existence. The possibility exists that an explosive detonated in a soil having a high liquefaction potential could cause fairly long-term decreases in

the shear strength resulting in damage disproportionate to the energy released. Documented occurrence, although sketchy and often incomplete, is available in the open literature. Although considerable work remains to be done in projecting this information into a comprehensive method of predicting liquefaction for actual or hypothetical blasts, the limited data indicates that residual porewater pressure increases should not occur in soils subjected to strains of less than 10^{-2} percent. In soils subjected to plane strain compression wave loading, peak radial particle velocities below 15 cm per second for saturated silts and sands should limit compressive strains to less than 10^{-2} percent. In soils also subjected to shear wave loading, field data indicates that peak particle velocities below 2 cm per second should limit shear strains to the elastic range. Liquefaction induced by single point explosions has not been reported in the literature for peak particle velocities below 7 cm per second. The limited data indicates that liquefaction can be induced at lower peak particle velocities under multiple shock loadings. Tests also indicate that more energy is required to cause liquefaction as the soil's initial effective stress or relative density is increased. Extraordinary situations may require more conservative criteria.

The following preliminary conclusions pertain to the laboratory shock tests on saturated Monterey No. 0/30 sand conducted by the authors at Colorado State University.

- For compressive strains less than approximately 10^{-2} percent, residual porewater pressures increases did not occur regardless of the number of shocks, soil density or initial effective stress.
- For compressive strains greater than approximately 10^{-2} percent, residual porewater pressure increases occurred.
- For compressive strains greater than approximately 10^{-1} percent, liquefaction could be induced under one shock load at all densities and initial effective stresses used for the testing program.
- For compressive stresses between approximately 10^{-2} percent and 10^{-1} percent, liquefaction could be induced by subjecting the sample to multiple shock loadings.

The results of the laboratory shock testing for peak compressive strains between approximately 10^{-2} to 10^{-1} percent are currently being analyzed to obtain the actual relations between peak strain, number of shock loads, initial effective stress and density.

ACKNOWLEDGEMENTS

Research sponsored by the Air Force Office of Scientific Research, Air Force Systems Command, USAF, under grant No. AFOSR-80-0260.

REFERENCES

1. A. S. Arya, P. Nandakumaran, V. K. Puri, and S. Mukerjee, Verification of liquefaction potential by field blast tests. Proc. of the 2nd Int. Conf. on Microzonation, Vol. II, San Francisco, California, November-December (1978).

2. J. R. Banister and D. M. Ellett, Pore pressure enhancement observation on Rio Blanco. Report SLA-74-032, Test Effects Department 1150, Sandia Laboratories, Albuquerque, New Mexico, August (1974).

3. W. A. Charlie, Liquefaction potential of soils under blast loads. U.S. Air Force Office of Scientific Research, Bolling Air Force Base, Washington, D.C., Report No. 40, 2, AFOSR-TR-78-0349 (1977).

4. W. A. Charlie, The dial pack event. Int. Workshop on Blast-Induced Liquefaction, Organized by Dames and Moore, London, and sponsored by U.S. Air Force Office of Scientific Research, Bolling Air Force Base, Washington, D.C., Job. No. 10926-002-86, January 1979, Maidenhead, United Kingdom, September (1978).

5. W. A. Charlie, J. Shinn, S. Melzer, and J. Martin, Blast induced soil liquefaction: phenomena and evaluation. Int. Sym. on Soils Under Cyclic and Transient Loads, Univ. College of Swansea, Swansea, United Kingdom, January (1980).

6. W. A. Charlie, T. A. Mansouri, and E. R. Ries, Predicting liquefaction induced by buried charges. Proc. of the 10th Int. Conf. on Soil Mechanics and Foundation Eng., Stockholm, Sweden, June (1981).

7. W. A. Charlie, Predicting porewater pressure increases induced by construction blasting: potential hazards to earthfill dams. Report, U.S. Dept. of Interior, Bureau of Reclamation, D-1541, Denver, Colorado (In press-1983).

8. W. A. Charlie, G. E. Veyera, S. R. Abt, and H. D. Patrone, Blast induced soil liquefaction. Proc. of the Symp. on the Interaction of Non-Nuclear Munitions with Structures, coordinated by Univ. of Florida Graduate Eng. Center, Eglin AFB, Florida, USAF Contract No. FOB635-81-C-0302, U.S. Air Force Academy, Colorado Springs, Colorado, May (1983).

9. W. A. Charlie, G. E. Veyera, and S. R. Abt, Predicting Blast induced porewater pressure increases in soils, J. of Civil Eng. for Practicing and Design Engineers, Vol. 4, No. 3, February (1985).

10. C. Damitio, La consolidation des sols sans cohesion par explosion. Construction, 27 (In French), Paris, France (1972).

11. D. Damitio, Field experience on blast-induced liquefaction. Int. Workshop on Blast-Induced Liquefaction, Organized by Dames and Moore, London, and sponsored by U.S. Air Force, Maidenhead, United Kingdom, September (1978).

12. R. Dobry, R. S. Ladd, F. Y. Yokel, R. M. Chung and D. Powell, Prediction of pore water pressure buildup and liquefaction of sands during earthquakes by cyclic strain method. NBS Building Science Series 138, National Bureau of Standards, Washington, D.C., July (1982).

13. V. A. Florin and P. L. Ivanov, Liquefaction of saturated sandy soils. Proc. Fifth Int. Conf. Soil Mechanics and Foundation Engineering (ICSMFE) 1, 107, Paris, France (1961).

14. R. J. Fragazzy, M. E. Voss, R. M. Schmidt, and K. A. Holsapple. Eighth International Symposium on Military Applications of Blast Simulation, Spiez, Switzerland, June (1983).

15. P. L. Ivanov, Compaction of Noncohesive Soils by Explosions, Izdatel'stvo Literatury Po Stroitel'stvu, Leningrad, Translated from Russian by the Indian National Scientific Documentation Center, New Delhi, Published in 1972 for the U.S. Dept. of Interior, Bureau of Reclamation and the National Science Foundation, Washington, D.C. (1967).

16. L. Kok, Empirical predictions of blast-induced liquefaction. Proc. Int. Workshop on Blast-Induced Liquefaction, Organized by Dames and Moore, London, Maidenhead, United Kingdom (1978).

17. D. Kummeneje and O. Eide, Investigation of loose sand deposits by blasting. Proc. 5th Conf. Soil Mechanics and Foundation Engineering, 1, Paris, France (1961).

18. N. P. Langley, C. R. Smith, and W. Pfefferle, Dial pack event - soil pore pressure and shear strength test. Aerospace Corp. Report No. TOR-0172 (S2970-20)-1, February (1972).

19. J. H. Long, E. R. Ries, and A. P. Michalopoulos, Potential for liquefaction due to construction blasting. Proc. Int. Conf. on Recent Advances in Geotech. Eng. and Soil Dynamics, Univ. of Missouri-Rolla, St. Louis, Missouri (1981).

20. G. M. Lyakhov, Shock waves in the ground and the dilatancy of water saturated sand. Zhurnal Prikladnoy Mekhanik; i Tekhnicheskoy Fiziki, 1, 38, Moscow, Russia (1961).

21. W. Marcuson, U.S. Army Waterways Experiment Station, Vicksburg, Mississippi, Personal Communication, July (1982).

22. J. Marti, Blast-induced liquefaction: a survey. Report by Dames and Moore for the U.S. Air Force Office of Scientific Research, Bolling Air Force Base, Washington, D.C., Report No. TR-78-3, May (1978).

23. E. B. Perry, Movement of variable-density inclusions in wet sand under blast loading. U.S. Army Eng. Waterways Experiment Station, Vicksburg, Mississippi, Misc. Paper S-72-37, September (1972).

24. S. Prakash, Soil Dynamics. McGraw-Hill Book Company, New York (1981).

25. S. V. Puchkov, Correlation between the velocity of seismic oscillations of particles and the liquefaction phenomenon of water-saturated sand. Issue No. 6, Problems of Engineering Seismology, Study No. 21, Edited by S. V. Medvedev, translated by Consultants Bureau, New York (1962).

26. F. E. Richart, J. R. Hall, and R. D. Woods, Vibrations of Soils and Foundations, Prentice-Hall, New Jersey (1970).

27. J. S. Rinehart, Stress Transients in Solids, Hyperdynamics, Santa Fe, New Mexico (1975).

28. F. Rischbieter, Soil liquefaction: a survey of research. Proc. of the Fifth Int. Symp. on Military Applications of Blast Simulation, Organized by the Royal Swedish Fortifications Administration, Stockholm, Sweden, May (1977).

29. S. G. Sanders, Assessment of the liquefaction hazards resulting from explosive removal of the Bird's Point - New Madrid Fuze Plug Levee, Misc. Paper GL-82-5, U.S. Army Eng. Waterways Exp. Station, Vicksburg, Mississippi, April (1982).

30. SME, SME Mining Engineering Handbook, Society of Mining Engineers of the American Institute of Mining, Metallurgical and Petroleum Engineers, Inc., New York, New York (1973).

31. K. G. Stagg and O. C. Zienkiewicz, Rock Mechanics in Engineering Practice, John Wiley and Sons, London, United Kingdom (1968).

32. J. Studer and L. Kok, Blast-induced excess porewater pressure and liquefaction experience and application. Int. Symp. on Soils under Cyclic and Transient Loading, Swansea, United Kingdom, January (1980).

33. J. Studer and E. G. Prater, An experimental and analytical study of the liquefaction of saturated sands under blast loadings. Proc. of Dynamical Methods in Soil and Rock Mechanics, Vol. 2, Karlsruhe, Germany, A. A. Balkema, Rotterdam (1977).

34. K. Terzaghi, Varieties of submarine slope failures. Proc. of the Eighth Texas Conf. on Soil. Mech. and Fdn. Eng., Univ. of Texas, Austin, Harvard Soil Mechanics Series, No. 52, Cambridge, Massachusetts, September (1956).

35. S. P. Timoshenko and J. W. Goodier, Theory of Elasticity, McGraw-Hill, New York, New York (1970).

36. G. E. Veyera, Blast-Induced Liquefaction: Mechanisms and Experience, Final Report, Contract No. F49620-82-C-0035, USAF-SCEEE Graduate Student Summer Support Program, U.S. Air Force Office of Scientific Research, Bolling Air Force Base, Washington, D.C. (1983).

37. K. Yamamura and Y. Koga, Estimation of liquefaction potential by means of explosion test. Proc. of the Sixth Joint Panel Conf. of the U.S.-Japan Coop. Program in Natural Resources, National Bureau of Standards, Washington, D.C., May (1974).

FINITE ELEMENT ANALYSIS OF FLOW AND DEFORMATION IN SATURATED SOILS

Ranbir S. Sandhu, Baher L. Aboustit, and S.J. Hong

The Ohio State University
Department of Civil Engineering
Columbus, Ohio 43210

ABSTRACT

Finite element solution for the consolidation of the saturated soils are reviewed. For the spatial discretization, Sandhu's 8-4 element and Ghaboussi's formulation are compared. Performance of "singularity elements" designed to improve the accuracy of pore pressure distribution near the loaded surface right after loading is discussed.

INTRODUCTION

Since the first application of the finite element method to the coupled problem of flow and deformation [1,2], considerable progress has been made. Recent advances include variational formulations admitting limited smoothness of finite element bases [3,4], experimentation with several different spatial interpolation schemes and investigation of various temporal approximation methods [5-15]. It has been difficult to reproduce accurately the pore fluid pressure distribution near loaded free-draining boundaries immediately after application of the load. Special elements capable of modeling linear singularities have been proposed to overcome this difficulty.

In spatial discretization, Sandhu [1] proposed that the order of terms appearing in a convolution product in the variational principle be the same. This produced the "composite" element in which the order of polynomial interpolation for displacements was higher than that for fluid pressures. The composite element first proposed by Sandhu [1,2], and used by Hwang [16] and others, was the "63" element with quadratic interpolation for displacements and linear interpolation for fluid pressures over triangular regions. Later, Sandhu [7,17] introduced the "84" element which had eight point biquadratic interpolation for displacements and was a four point isoparametric quadrilateral for fluid pressures. This element was also used by Runesson [13]. Buchmaier [18] experimented with five, six and seven point quadrilaterals for fluid pressure as transition elements near loaded surfaces.

Several spatial interpolation schemes, besides the composite elements, have been tried by various investigators. Ghaboussi [5] used four point isoparametric quadrilaterals for both the fields. However, an additional incompatible mode was included in the displacement approximation. This element has the economy while the additional "local" mode gives it the character of a "higher order" scheme. Smith's [19] formulation was similar to Ghaboussi's except that no incompatible modes were used. Prevost [9] proposed cautious use of "reduced integration" in conjuction with Smith's "44" element. Yokoo [20] and Vermeer [21] used triangular elements with linear interpolation for both the displacement and the fluid pressure fields. Other interpolation schemes, based on use of quadrilaterals built up from linear four- or five-point triangles were tried by Sandhu [8].

In evaluating various candidate schemes, Sandhu proposed that an acceptable method meet the following requirements in addition to efficiency and accuracy.

i. The interpolation scheme must conform with the assumptions regarding continuity and differentiability used in setting up the governing variational formulation.
ii. It should be possible to generate the "undrained" solution, i.e. the state of fluid pressures and displacement at time $t = 0+$.
iii. For sufficiently small time steps, the scheme should be insensitive to the choice of the time-step size.

Elements "63" and "84" satisfy these requirements. However, the composite elements are too expensive to be used in large problems. This has discouraged extension of the analysis to three-dimensions, and to nonlinear and dynamic problems. The 4-4 element is more economical but was found by Sandhu [8] to have spatially and temporally oscillating errors. The "63" element has been widely used because it was the first one to be introduced and gave satisfactory results in most cases. However, the 8-4 element gives results almost identical to those from the "63" element but is more economical as it requires fewer nodal points and has smaller band-width.

Immediately after application of a surface load to a free-draining boundary, the excess pore water pressure remains zero at the surface but has a very steep gradient and rises, over an extremely short distance into the soil mass, to a magnitude comparable with the applied stress. Finite element interpolations commonly used cannot model this locally high

pore pressure gradient near the surface. Yokoo's [19] formulation, not requiring the fluid pressure to satisfy the prescribed boundary condition at the free-draining boundary gave good solution immediately after loading. Buchmaier's [18] studies showed that transition elements, using higher order interpolation, near loaded boundaries had only limited success. Vermeer [21] suggested that the fluid pressure boundary condition be enforced as a "ramp" condition to limit the error.

In this paper, we compare Ghaboussi's element (hereafter referred to 6-4 element) with the 8-4 element. Terzaghi's problem of one-dimensional consolidation and Gibson's problem of a half-space under a strip load were taken as the example problems. To simulate consolidation of the half-space by a finite domain model, an approximation to the conditions at infinity is required. Three alternative assumptions regarding the "cut-off" boundary were considered. To satisfactorily model the pore-pressure distribution in the vicinity of free-draining loaded surfaces, "singularity" elements were developed by Lee [22]. Several variants of the scheme in solution of one-dimensional consolidation were discussed in [23] and [24]. Herein, we summarize some of this work as well.

EQUATIONS GOVERNING SOIL CONSOLIDATION

For linear elastic soils, the equations of force equilibrium of elementary volumes and mass continuity, over the spatial region of interest R, may be written in standard indicial notation as

$$[E_{klij}u_{k,l}]_{,i} + \alpha\pi_{,j} + f_j = 0 \tag{1}$$

$$[K_{ij}(\pi_{,i} + \rho_2 f_i)]_{,j} + u_{j,j} = \frac{1}{M}\dot{\pi} \tag{2}$$

where u_i, f_i, E_{klij}, K_{ij}, denote the cartesian components, respectively, of the displacement vector, the body force vector per unit mass, the isothermal elasticity tensor and the permeability tensor. ρ is the mass density of the saturated soil and ρ_2 that of water. π is the pore water pressure, α is the solid compressibility and M is a measure of fluid compressibility. Equation (2) is for compressible fluids. For incompressible fluid, $M \to \infty$ and consequently the right side vanishes. With these field equations we associate the following boundary conditions;

$$u_i = \hat{u}_i \qquad \text{on } S_{1i} \tag{3}$$

$$t_i = \tau_{ij}n_j = \hat{t}_i \quad \text{on } S_{2i} \tag{4}$$

$$\pi = \hat{\pi} \qquad \text{on } S_3 \tag{5}$$

$$Q = q_i n_i = \hat{Q} \quad \text{on } S_4 \tag{6}$$

Here, t_i, q_i are components of the traction and fluid flux vectors associated with surfaces embedded in the closure R. τ_{ij} are components of the total stress tensor. S_{1i}, S_{2i} are complementary subsets of the boundary of the spatial region of interest and so are S_3, S_4. Even though the equations given above apply to compressible fluids, the applications reported herein assumed incompressible fluid i.e. $M \to \infty$. The initial conditions for the problem are

$$u_i(x_j, 0) = u_i(0) \qquad \text{on R}$$

$$\pi(x_j, 0) = \pi(0) \qquad \text{on R}$$

SPATIAL DISCRETIZATION

Discretization of the governing function for the two-field formulation followed by application of the variational principle [3] leads to the following matrix equation.

$$\begin{bmatrix} K_{uu} & K_{pu} \\ K_{pu}^T & K_{pp}^* \end{bmatrix} \begin{bmatrix} u(t_1) \\ \pi(t_1) \end{bmatrix} + \begin{bmatrix} 0 & 0 \\ -K_{pu}^T & K_{pp}^{**} \end{bmatrix} \begin{bmatrix} u(t_o) \\ \pi(t_o) \end{bmatrix} = \begin{bmatrix} P_1 \\ P_2 \end{bmatrix} \tag{7}$$

where (t_o, t_1) is the single time step of interest, and

- $\{u(t_1)\}, \{u(t_o)\}$ = vectors of nodal point values of the components of the displacement at time t_1, t_o, respectively.
- $\{\pi(t_1)\}, \{\pi(t_o)\}$ = vectors of nodal point values of the pore water pressure at time t_1, t_o, respectively.
- $\{P_1\}$ = the vector of nodal point loads including applied nodal loads, boundary tractions, body forces, initial stresses and effect of displacement constraints.
- $\{P_2\}$ = the vector of nodal point fluxes including applied nodal fluxes, boundary fluxes, body force effects and effects of specified pore water pressures.
- $[K_{uu}]$ = the spatial "stiffness matrix" for the elastic soil.
- $[K_{pp}]$ = the spatial "flow matrix" for the compressible fluid and $\Delta t = 1$.
- θ = the coefficient characterizing single-step temporal discretization.
- $[K_{pu}]$ = the coupling matrix representing the influence of pore pressure in the force equilibrium equation.
- $[K_{pu}]^T$ = the coupling matrix representing the influence of soil volume change upon the nodal point fluid pressure.
- $[C_{pp}]$ = the spatial fluid compressibility matrix.

The matrix $[K_{uu}]$ depends on the interpolation scheme for displacements and $[C_{pp}]$, $[K_{pp}]$ depend upon the interpolation scheme for the pore-water pressures. The coupling matrix $[K_{pu}]$ involves spatial interpolation for both the field variables. The temporal discretization for the single step scheme is reflected in the value of the coefficient θ. For linear interpolation $\theta = 0.5$. Elements of matrices are defined as

$$K_{uu} = \int_{-1}^{1}\int_{-1}^{1} \underline{B}_e^T \underline{D} \underline{B}_e \, J \, d\xi dt \tag{8}$$

$$K_{pp} = \int_{-1}^{1}\int_{-1}^{1} \underline{B}_q^T \underline{k} \underline{B}_q \, J \, d\xi dt \tag{9}$$

$$K_{up} = \int_{-1}^{1}\int_{-1}^{1} \underline{B} \underline{N}_\pi^T \, J \, d\xi dt \tag{10}$$

$$C_{pp} = \int_{-1}^{1}\int_{-1}^{1}\frac{1}{M}\,\underset{\sim}{N}_{\pi}\,\underset{\sim}{N}_{\pi}^{T}\,J\,ds\,dt \qquad (11)$$

$$K^{*}_{pu} = [-\theta\Delta t K_{pp} - C_{pp}] \qquad (12)$$

$$K^{**}_{pu} = [-(1-\theta)\Delta t K_{pp} + C_{pp}] \qquad (13)$$

$$\{P_i\} = \{M_1\} + \{M_3\} \qquad (14)$$

$$\{P_2\} = \theta\Delta t\{M_2(t_1) + (1-\theta)\,\Delta t M_2(t_o)\} - \theta\Delta t\{M_4(t_1)\} - (1-\theta)\,\Delta t\{M_4(t_o)\} \qquad (15)$$

where
$$\{M_1\} = \int_{-1}^{1}\int_{-1}^{1}\underset{\sim}{N}_u\,\{\rho f\}\,J\,ds\,dt \qquad (16)$$

$$\{M_2\} = \int_{-1}^{1}\int_{-1}^{1}\underset{\sim}{N}_q\,\underset{\sim}{k}\,\{\rho f\}\,J\,ds\,dt \qquad (17)$$

$$\{M_3\} = \int_{-1}^{1}\int_{-1}^{1}\underset{\sim}{N}_u\,\underset{\sim}{N}_t^{T}\,\{t\}\,dS_{21} \qquad (18)$$

$$\{M_4\} = \int_{-1}^{1}\int_{-1}^{1}\underset{\sim}{N}_{\pi}\,\underset{\sim}{N}_q^{T}\,\{Q\}\,dS_4 \qquad (19)$$

and
$$\Delta t = t_1 - t_o$$

Here D, k are matrices describing the elastic properties and the permeability, respectively, of the porous material. f is assumed to be constant over each element. $\underset{\sim}{N}_t$, $\underset{\sim}{N}_q$, $\underset{\sim}{N}_u$, $\underset{\sim}{N}_{\pi}$ represent interpolating functions for boundary tractions, boundary flux, displacements of the solid and fluid pressures, respectively. The interpolating functions $\underset{\sim}{N}$, $\underset{\sim}{N}_{\pi}$ for the consolidating region and for its boundary will be different.

Equation (7) includes the "natural" boundary conditions expressed by Equation (4) and (6). Equations (3) and (5) are satisfied by explicitly requiring $u_i = \hat{u}_i$ on S_{1i} and $\pi = \hat{\pi}$ on S_3. As the fluid is assumed to be incompressible in both the example problems, the matrix C_{pp} is zero. It is included in the theoretical discussion for completeness.

INTERPOLATION FUNCTIONS OF SINGULARITY ELEMENT

To set up singularity elements, Lee [22] used special interpolation schemes following the procedures given by Hughes and Akin [25]. In the present work, only line singularity was considered in the context of a two-dimensional problem. Consider the sequence of functions

$$f_n(x) = 1 - x^n \qquad (20)$$

over the domain [0,1]. In the limit as $n \to \infty$, $f_n(x) = 1$ for x in the interval [0,1) and equals 0 at x=1. This is the type of discontinuity encountered in consolidation analysis.

i) One-Dimensional Elements

(a) The two-node singularity element
In one dimension, over range [0,1], the singularity element would use interpolation functions

$$1-x^n, \quad x^n$$

where n is sufficiently large. For n=1, this reduces to linear interpolation. Noting that the error in pore water pressures near loaded free-draining boundaries is of relevance only immediately after loading and decays with advance in the time domain, it appeared reasonable to use a composite element which would approximate the singularity for small values of the "elapsed time" after loading and reduce to linear interpolation for large values of the time variable. This led to use of variants of the type

$$f_n(x) = 1 - ax - (1-a)x^n \qquad (21)$$

where a=0 approximate the singularity element and a=1 gives linear interpolation. Thus, the coefficient a has to be assighned a value growing with time from 0 to 1. The scheme investigated was based on

$$a = 1 - \exp(-m\tau) \qquad (22)$$

in which m is a scalar coefficient and the non-dimensional "time-factor". The investigation covered a range of values of n and m.

(b) The three-node singularity element
This element would directly involve three functions, viz.,

$$1, \; x, \; x^n$$

where n is sufficiently large. This was expected to include linear interpolation and approximation of the singularity at the same time.

ii) Two-Dimensional Elements

Corresponding to the two types of one-dimensional elements, for the two-dimensional case, two types of elements were considered. The displacement interpolation was the same as for the two element, viz. the same as in 8-4 element. The pore pressure interpolation corresponded to the two cases discussed in the preceding paragraph. Fig.1 shows the arrangement for the two elements. The line singularity implies singularity in one variable only. In the following, we assume this to be the variable t. For the 8-4 element the interpolating functions are [22];

$$\{N\} = \begin{Bmatrix}(1-s)(1-t^n)\\ s(1-t^n)\\ s\,t^n\\ (1-s)t^n\end{Bmatrix} \qquad (23)$$

where the range of s, t is [0,1]. If the variant expressed by Equation (21) is employed;

$$\{N\} = \begin{Bmatrix} (1-s)\{1-at-(1-a)t^n\} \\ s\{1-at-(1-a)t^n\} \\ s\{at+(1-a)t^n\} \\ (1-s)\{at+(1-a)t^n\} \end{Bmatrix} \quad (24)$$

For the 8-6 element the interpolating functions are;

$$\{N\} = \begin{Bmatrix} (1-s)\{(1-t)^n)-(2-b)M\} \\ s\{(1-t^n)-(2-b)M\} \\ s\{t^n-bM\} \\ (1-s)(t^n-bM) \\ 2sM \\ 2(1-s)M \end{Bmatrix} \quad (25)$$

where $b = 2^{1-n}$

$$M = (t-t^n)\{1-2(.5)^n\}$$

NUMERICAL EXPERIMENTS

Terzaghi's one-dimensional consolidation problem and Gibson's problem [26] of a half-space under a strip load were solved using Sandhu's 8-4 element and Ghaboussi's 6-4 element. Fig.2 and Fig.3 show the dimensions and element mesh used in the analyses. In Gibson's problem, the infinite domain is required to be modelled by a finite one for numerical implementation. Three alternative boundary conditions were considered to represent the "far" boundary where the half-space is cut off.

Case (a) Pore fluid pressure and horizontal displacement prescribed.
Case (b) Fluid flux and horizontal displacement prescribed.
Case (c) Pore pressure and traction prescribed.

In order to model the singularity, the 8-4 element was modified and applied to Terzaghi's problem. Throughout the numerical experiments, material properties for the test problems were assumed to be as follows:

Modulus of elasticity E=6000
Poisson's ratio ν=0.4
Permeability coefficient $k=4\times10^{-6}$

For Terzaghi's porblem, soil and water particles were assumed to be incompressible, i.e. α=1 and M->∞ while for Gibson's problem linear variation in displacement and pore pressure was assumed, i.e. θ=0.5.

a. Comparative results of 8-4 and 6-4 elements.

In solving Terzaghi's problem, Fig.2, CPU time was 13.92 seconds for 8-4 element while for the 6-4 element it was 10.03 seconds. The response of the two elements practically coincided throughout the time domain and was in good agreement with the analytical solution, except at early time, i.e. $t < 0.1$. The pore-pressure distribution generated by the two elements for different time steps is shown in Fig.4 The vertical axis shows the ratio of depth below surface to the total height h of the soil column considered. The horizontal axis gives the pore fluid pressure as a fraction of the intensity of the constant surface load. The plots are for values of time variable equal to 0.000001, 11.1, 201.1, and 901.1 corresponding to non-dimensional time factor $\tau = \bar{C}t/h^2$ of 0.1×10^{-8}, 0.01165, 0.2110, 0.9195 where $\bar{C} = 2Gk$ and k is the coefficient of permeability. The plots of pressure distribution history generated by the two schemes coincide. At early stages, the error in the pore pressure at points near the loaded surface is quite large for both the schemes. This is a feature of the popular spatial interpolation schemes mentioned earlier [8].

In solving the half-space problem, the CPU time for 8-4 element was 315 seconds while for the 6-4 element it was only 33 seconds. For the settlement and pore pressure history, good agreement between the results for the two finite element procedures is seen at all time stages regardless of "cut-off" boundary conditions. Fig.5 compares the settlement and pore pressure history for cases (a) and (b), using the 6-4 element under different conditions at the "cut off" boundary. A non-dimensional measure of the settlement is introduced as Gu/aq where G is the shear modulus, a the half-width of loaded strip and q the intensity of load per unit width of the strip. The fluid pressure is represented by the fraction π/q. The quantities are tabulated for dimensionless time given by $\tau = \bar{C}t/h^2$. Table 1 shows that the location of the "far" boundary was selected far enough so that, for the case where horizontal displacements are assumed to vanish at this distance, prescribing vanishing fluid pressure or fluid velocity at this boundary had little effect on the displacements and fluid pressures near the center of the loaded area.

Comparing Case (c) with Case (a), i.e. considering the effect of prescribing traction or displacements at the "far" boundary for prescribed fluid pressure, it was found, Fig.5, that the settlement in the early stage of loading was significantly affected. The solution for Case (c) was in excellent agreement with Gibson's [26] theoretical solution.

b. Pore pressure distribution by singularity element

Fig.6 shows the history of pore water pressure using the 8-4 element with functions of the type expressed by Equation (20) at depth 0.03h below the top free-draining boundary of the soil column of height h. Results show that the "immediate" pore water pressure obtained by this method was more accurate than by using the 8-4 element. However, the pore pressure dropped sharply after application of the load and accuracy in pore pressures was worse than that of the 8-4 element in later time stages. Apparently, the error in pore pressure at later time stages was due to the abscence of the linear term from the interpolation scheme. For time factor values upto 0.03, the error reduced with n increasing upto 5.0. For time factor values greater than 0.3, the error increased with increasing n. Fig.7 and 8

represent, respectively, the results at a point 0.06h and 0.09h below the loaded surface. As would be expected, the error at these points is throughout smaller than that at 0.03h. The pattern of dependence upon n and the value of the time factor is essentially the same.

To combine the ability of the singurality interpolation to give more accurate "immediate" pore pressures and the accuracy of the 8-4 element for later time stages, it appeared reasonable to set up shape functions such that the element has the characteristics of the singularity element at early stages and has those of the 8-4 element as time increases. The shape functions given by Equation (21) would accomplish this. A parametric study was carried out to investigate the effect of variation in m for values of n. Fig.9 compares the results for various values of n paired with the optimal (out of the set tried) value of m in each case. The least error in initial pore pressures was realized for n=48, m=40. However, the error was seen to grow with time. The best overall accuracy was obtained for n=30, m=32.5. For this case, maximum error was less than 3%.

CONCLUSIONS

Ghaboussi and Wilson's 6-4 element and Sandhu's 8-4 element were applied to Terzaghi's and Gibson's problem for which exact solutions are available. To overcome the inadequacy of commonly used spatial interpolation schemes for the pore pressure distribution near free-draining loaded surface right after loading, singularity elements were introduced and applied to Terzaghi's problem. Results of these limited numerical tests show [22,23,24];

i. The 6-4 element gave a solution identical to that given by the 8-4 element but with significant savings in computational time.

ii. The 6-4 element as well as the 8-4 element predicted the solution (t = 0+). However, at early stages of loading, both elements gave unsatisfactory results. Apparently, special singularity elements [22,23,24] are required near loaded drained surfaces.

iii. The conditions at the "cut off" boundary for the finite domain considered in the finite element model must be carefully defined. The solution near the loaded region was not sensitive to whether the fluid flux or fluid presure was prescribed. However, prescribed displacement or tractions had significant influence. This is in line with Sandhu and Schiffman's experience [27].

iv. Using the 8-4 element to generate the solution at time t=0+, numbering of the nodal points has to be carefuily ordered to avoid zeroes on the diagonal of the matrix. However, Ghaboussi and Wilson's 6-4 element is free from this defect. This is because, in eliminating the additional degrees of freedom, the static condensation would, in general, result in non-zero diagonal quantities.

v. Accuracy in pore pressure at all time satges can be achieved using the 8-4 "singularity" element whose shape functions are based on $f(x)=1-ax-(1-a)x^n$ in which the coefficient $a=1-\exp(-m\tau)$. This combines the best characteristics of the singularity element with those of the 8-4 element.

In summary, for the soil consolidation analysis, Ghaboussi's 6-4 element appeared distinctively superior to the 4-4 element in that it gives the solution at time=0+ and does not have the oscillating error. It is also superior to the 8-4 element in that it generated numerical solutions which were as accurate but were an order of magnitude more economical to obtain. This advantages make the Ghaboussi and Wilson's 6-4 element be a good candidate for nonlinear and dynamic analysis as well as for extension to three dimensional applications. Use of singularity elements was successful in modelling the pore pressure distribution in the vicinity of free-draining loaded boundaries. However, only one-dimensional problem was considered. It is necessary that the procedures be extended to problems of two and three dimensions (point singularity as well as surface singularity) before firm recommendations for routine use of certain elements can be made. More investigation is also needed in the selection of indices n and m used in the formulation. Further, realizing that the consolidation of soils is a decay process, use of more than one exponential terms in the time domain could possibly enhance accuracy.

ACKNOWLEDGEMENTS

The work reported herein is part of a research program supported by the Air Force Office of Scientific Research, Air Force Systems Command, USAF, under Grant No. AFOSR-83-0055. The U.S. Government is authorized to reproduce and distribute reprints for Governmental purposes notwithstanding any copyright notation therein. The assistance provided by the Instruction and Research Computer Center, The Ohio State University is gratefully acknowledged.

REFERENCES

1. Sandhu, R.S.: 1968, Fluid Flow in Saturated Porous Elastic Media, Ph.D. Thesis, University of California at Berkeley, Berkeley, California.
2. Sandhu, R.S., and Wilson, E.L.: 1969, J. Engrg. Mech. Div., Am. Soc. Civ. Engrs., 95, 641-652.
3. Sandhu, R.S.: 1975, Variational Principles for Soil Consolidation, Report OSURF-3570-75-2 to National Science Foundation, Dept. of Civil Engrg., The Ohio State University., Columbus, Ohio.
4. Sandhu, R.S.: 1976, "Variational Principles for Soil Consolidation", in Numerical Methods in Geomechanics, Proc., 2nd Intl. Conf. Numer. Methods in Geomech., Ed. C.S. Desai, Am. Soc. Civ. Engrs., 1, 20-40.
5. Ghaboussi, J., and Wilson, E.L.: 1973, Int. J. Num. Methods in Engrg., 5, 419-442.
6. Smith, I.M.: 1978, "Transient Phenomena of Offshore Foundations", in Numerical Methods in Offshore Engineering, Eds. O.C. Zienkiewicz, R.W. Lewis, and K.G. Stagg, J. Wiley, 483-513.
7. Sandhu, R.S., Liu, H., and Singh, K.J.: 1977, Int. J. Num. Anal. Methods in Geomech., 1, 177-194.
8. Sandhu, R.S, and Liu, H.: 1979, "Analysis of Consolidation of Viscoelastic Soils", in Numerical Methods in Geomechanics, Proc., 3rd.

Int. Conf. Numer. Methods in Geomech., Ed. W. Wittke, A.A Balkema, 1255-1263.
9. Prevost, J.H.: 1981, J. Engrg. Mech. Div., Am. Soc. Civ. Engrs., 107, 169-186.
10. Booker, J.R.: 1973, Quar. J. Mech. Appl. Math, XXVI, 4, 445-470.
11. Booker, J.R., and Small, J.C.: 1977, Int. J. Solids Struct., 13, 137-149.
12. Smith, I.M., Siemieniuch, J.L., and Gladwell, I.: 1977, Int. J. Num. Anal. Methods in Geomech., 1, 57-74.
13. Runesson, K.: 1978, On Nonlinear Consolidation of Soft Clay, Publ. 78-1, Dept. Struct. Mech., Chalmers Institute of Technology, Goteborg, Sweden.
14. Carter, J.P., Booker, J.R., and Small, J.C.: 1979, Int. J. Num. Anal. Methods in Geomech., 3, 107-129.
15. Suklje, L.: 1978, Int. J. Num. Anal. Methods in Geomech., 2, 129-158.
16. Hwang, C.T., Morgenstern, N.R., and Murray, D.W.: 1971, Canadian Geotech. J., 8, 109-118.
17. Sandhu, R.S.: 1976, Finite Element Analysis of Soil Consolidation, Report OSURF-3570-76-3 to National Science Foundation, Dept. of Civ. Engrg., The Ohio State University, Columbus, Ohio.
18. Buchmaier, R.: 1980, Personal Communication.
19. Smith, I.M., and Hobbs, R.: 1976, Geotechnique, 26, 149-171.
20. Yokoo, Y., Yamagata, K., and Nagaonka, H.:1971, Soils and Foundations, 11, 29-46.
21. Vermeer, P.A., and Verruijt, A.: 1981, Int. J. Num. Anal. Methods in Geomech., 5, 1-14.
22. Lee, S.C.: 1982, Special Finite Elements for Analysis of Soil Consolidation, M.S. Thesis, The Ohio State University, Columbus, Ohio.
23. Sandhu, R.S., Lee, S.C., and The, H.: 1983, Special Finite Elements for Analysis of Soil Consolidation, Report OSURF-715107-83-2 to Air Force Office of Scientific Research, Dept. of Civil Engineering, The Ohio State University, Columbus, Ohio.
24. Sandhu, R.S., Lee, S.C., and The, H.: 1985, Int. J. Num. Anal. Methods in Geomech (in press).
25. T.J.R. Hughes, and J.E. Akin: 1980, Int. J. Numer. Meth. Engrg., 15, 733-751.
26. Gibson, R.E., Schiffman, R.L., and Pu, S.L.: 1970, Quar. J. Mech. Appl. Math., 16, 34-50.
27. Sandhu, R.S., and Schiffman, R.L.: 1977, Implementation of Computer Program RC63 and FECONB for Plane Strain and Axisymmetrical Consolidation of Elastic Solids, Norges Geotekniske Institutt, Report No. 51405-10.

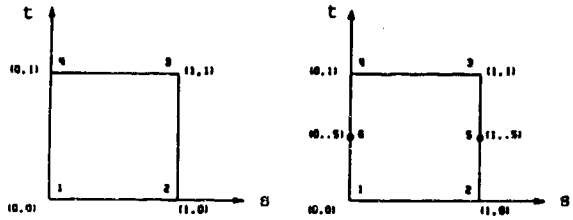

Figure 1: Singularity element-singularity along axis t at edge 3-4

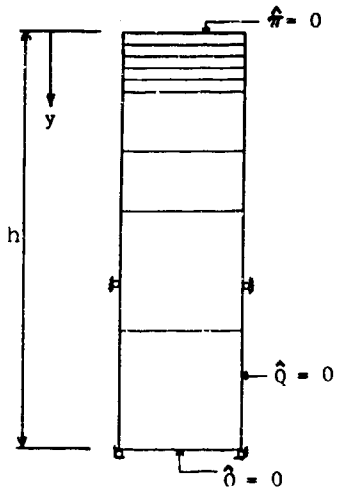

Figure 2: Finite element model of Terzaghi's problem

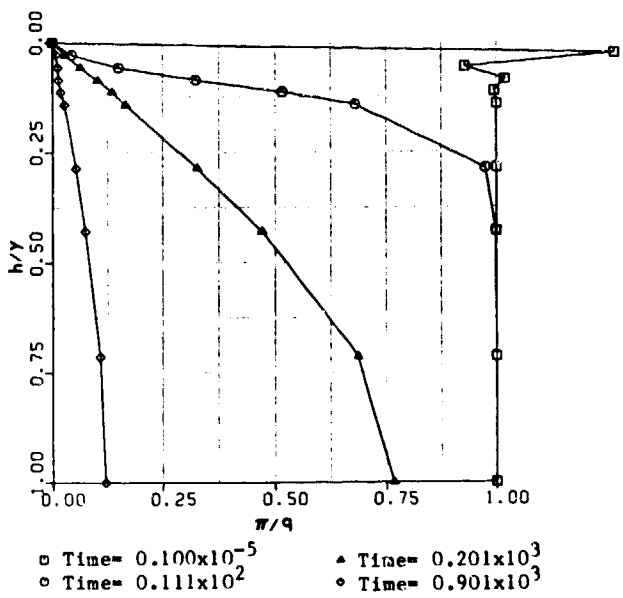

Figure 4: Fluid pressure distribution at various time stages

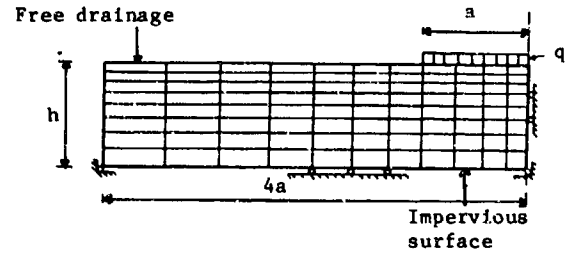

Figure 3: Finite element mesh for Gibson's problem

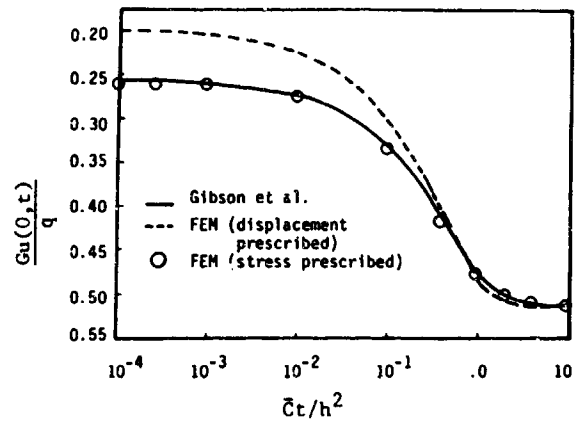

Figure 5: Influence of "far" boundary conditions on surface settlement history

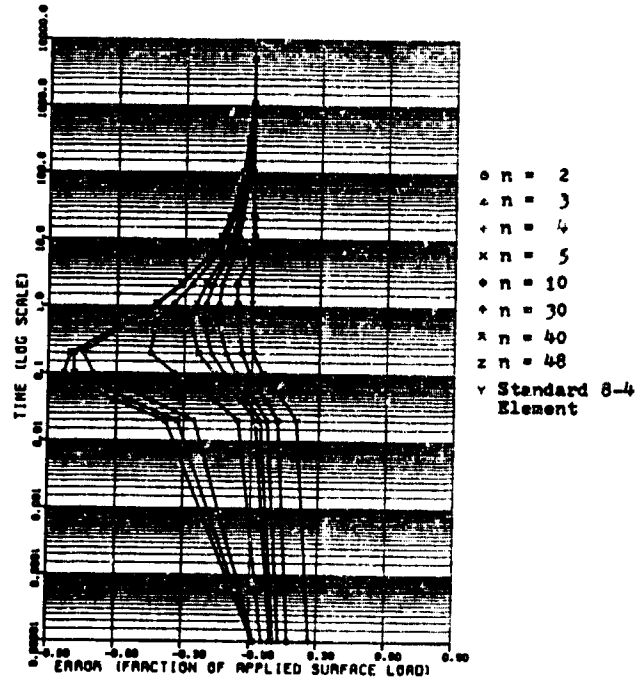

Figure 6: Distribution of the 'relative' error in pore pressure (8-4 singularity element, shape function based on $f(x) = 1-x^n$) at 0.03h

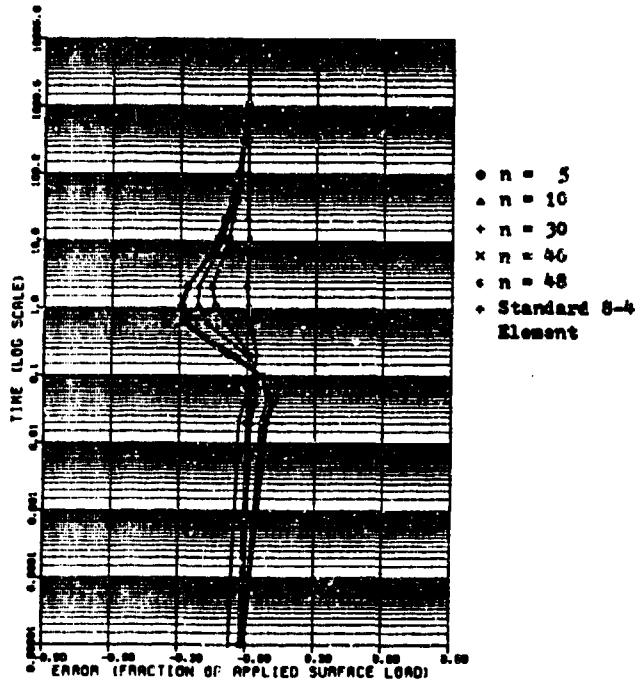

Figure 7: Distribution of the 'relative' error in pore pressure (8-4 singularity element, shape function based on $f(x) = 1-x^n$) at 0.06h

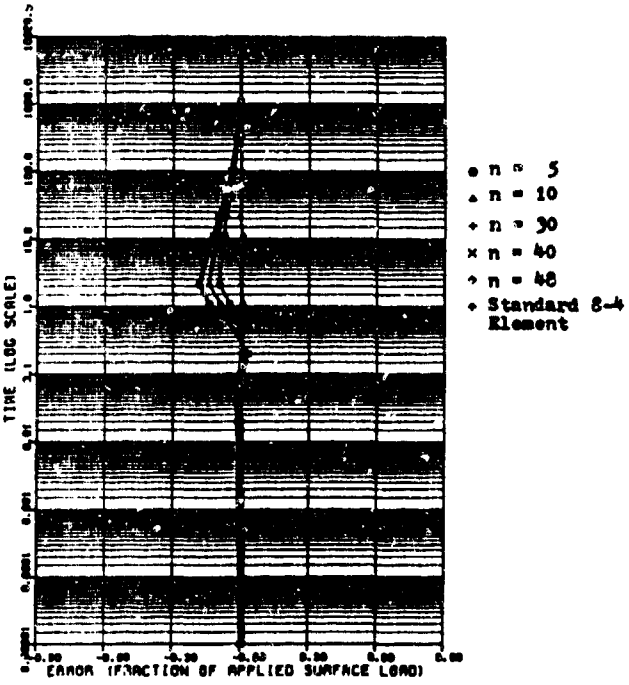

Figure 8: Distribution of the 'relative' error in pore pressure (8-4 singularity element, shape function based on $f(x) = 1-x^n$) at 0.09h

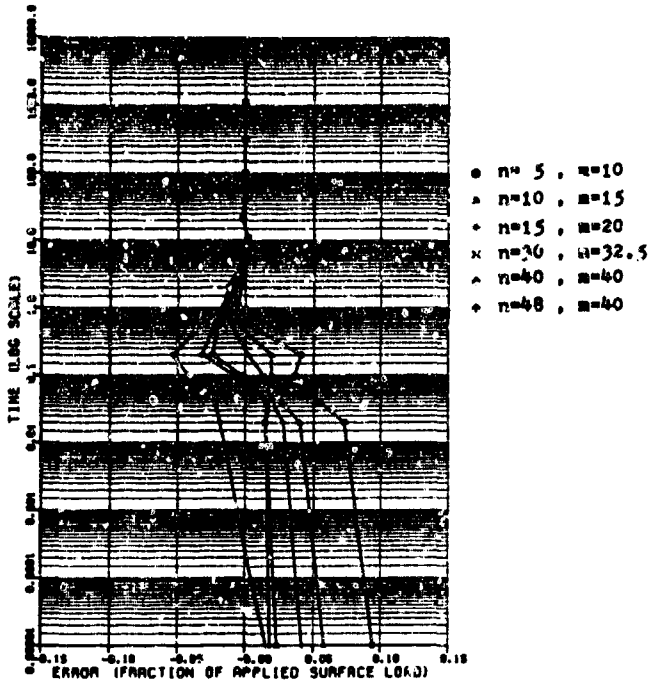

Figure 9: Distribution of the 'relative' error in pore pressure (8-4 singularity element, shape function based on $f(x)=1-ax-(1-a)x^n$, $a=1-\exp(-mt)$) at 0.03h 0.03h

Table 1: Comparison of cases (a) and (b); Vertical displacement and pore pressure at 0.094a below the center of the loaded area

$T = \frac{Ct}{h^2}$	Gu/aq		W/q	
	Case a	Case b	Case a	Case b
3.6×10^{-5}	0.17855	0.177012	0.89619	0.90026
9.6×10^{-4}	0.17926	0.17769	0.73221	0.73562
0.01056	0.192738	0.191256	0.32014	0.32164
0.04896	0.229206	0.22779	0.16341	0.16434
0.10656	0.265962	0.264534	0.11456	0.11526
0.87456	0.433548	0.434202	0.017178	0.016863
1.06656	0.445332	0.445914	0.011439	0.011163

A VISCOELASTIC CONSTITUTIVE RELATION FOR COMPACTED COHESIVE SOIL

S.V. Ramaswamy
and
M.R.M. Alwahhab

Yarmouk University
Irbid, Jordan

ABSTRACT

A constitutive relation is suggested to characterise the nonlinear viscoelastic behaviour of compacted cohesive soils based on triaxial compression creep and relaxation tests conducted at different water contents and confining pressures. The material behaviour was characterised by two functionals, nonlinear creep compliance and equivalent Poisson's ratio. The nonlinear creep compliance was found to be a power function of time and was expressed as a function of linear creep compliance and stress dependent parameters independent of time. Poisson's ratio was found to be almost time independent, but highly stress dependent.

INTRODUCTION

In order to obtain acceptable results in estimating stresses and deformations in soil masses due to changes in load, a reasonable characterisation of all aspects of the stress-strain behaviour of the soil is essential. Numerous research efforts in recent years have led to the development of a number of comprehensive constitutive laws for soils based on concepts from elasticity, viscoelasticity and plasticity theories. These models delineate the nonlinear stress-dependent inelastic behaviour of soils. Generally greater attention has been devoted to elasto-plastic deformations and major proportion of these models do not include the time dependent bahaviour. But creep and relaxation behaviour of earth materials are to be taken into consideration in the analysis and design of a number of practical problems in geotechnical engineering such as long term deformation of earth embankments, stability of excavations and tunnels, relaxation of stress in the anchorages for retaining structures, displacement of piles driven in clay and a variety of other soil-structure interaction problems.

Compacted soils are extensively used in the construction of embarkments, highways, airfields and railroads. They have been considered as nonlinear elastic materials in the analysis of soil engineering problems. However their behaviour under load is complex and they exhibit plastic and viscoelastic bahaviour also. When a compacted clay sample is subjected to a load, the total deformation under the load is substantially larger for the first cycle of loading than for the subsequent cycles of loading (4,9). The deformation under the first cycle of loading is the sum of plastic and viscoelastic deformations while plastic deformation is essentially absent in second and subsequent cycles of loading. In this paper a constitutive relation proposed by Schapery (8) is used to describe the nonlinear viscoelastic behaviour of compacted cohesive soils in triaxial compression creep tests under second cycle of loading. The experimental results of an earlier investigation is used in this analysis (4).

Sections 2 and 3 summarise the properties of the soil used in this investigation and the experimental procedure for triaxial compression creep tests. Section 4 analyses the time-dependent and stress-dependent characteristics of the viscoelastic parameters for the compacted soil based on experimental observations. Section 5 gives a brief description of the proposed nonlinear viscoelastic characterisation. The magnitudes of the viscoelastic parameters and the influence of stress level and other factors are discussed in section 6. Conclusions for the investigation are given in section 7.

SOIL PROPERTIES

The soil used in this study was Edgar plastic kaolin. Its liquid limit was 59%, plastic limit 37% and clay fraction 81%. Test specimens of 1.31 cm diam. and 2.81 cm height were prepared at different water contents by kneading compaction which was accomplished with a Harvard miniature compaction equipment. Specimens were compacted in five layers with twenty tamps of spring loaded compactor per layer, compactive force being 27.3 kg. The optimum water content was 27.5% and the maximum dry unit weight, 1.77 g per cm^3. The specimens thus prepared were assumed to be homogeneous and isotropic.

EXPERIMENTAL PROCEDURE

The compression creep tests were carried out in a Norwegian triaxial chamber which had rotating ball bearings for reducing the piston friction. The loading on the specimen was by dead weights, which was transferred to the specimen as an

instantaneous step load by a hydraulic jack and a loading platform.

In the tests reported herein, the specimens were allowed to creep for one hour under the step load and then to relax for 30 min. Two cycles of such creep and relaxation tests were conducted at each stress level before increasing the load to next higher stress level. The process was repeated until the desired stress level was reached, a single specimen being used at all stress levels. Both axial and lateral strains were continuously measured and recorded with time. After the creep and relaxation tests were completed the strength of each specimen was determined. The creep tests were conducted at various confining pressures with different water contents. Further details about the materials and testing procedures are available elsewhere (5,6).

VISCOELASTIC PARAMETERS

Elastic and Viscoelastic Strains

The relation between total shear strain and time was found to obey a power law with time for compression creep tests of longer duration on compacted clays (4). Similar relations have been observed by other investigators for triaxial creep tests on saturated clays (10) and compacted clays (7) and for torsional shear creep tests on compacted clays (2).

In this investigation, the total axial strain, $\varepsilon(t)$, was considered as the sum of initial elastic strain, $\varepsilon(0)$, and the net creep strain, $\varepsilon(c)$. The strain measured at a very small time (0.02 or 0.04 min.) was assumed to be equal to $\varepsilon(0)$. A power law relation was fitted to correlate $\varepsilon(c)$ and time, t. Hence,

$$\varepsilon(t) = \varepsilon(0) + At^n \qquad (1)$$

where A and n are constants for particular stress level. A and n were determined for each creep test by the method of least squares. The magnitudes of n varied from 0.15 to 0.35 with the majority of values between 0.2 and 0.3. There was no systematic influence of water content or stress levels on n. The average of n values was found to be 0.26 and this can be considered as a material constant for kneading compacted specimens.

Creep Compliance

The creep compliance, D(t), at any time can be defined as the ratio between total axial strain, $\varepsilon(t)$ and the principal stress difference, $(\sigma_1-\sigma_3)$. This can be considered as the sum of initial elastic compliance, D(0) and net creep compliance, D(c),

$$D(t) = D(0) + D(c) = \frac{\varepsilon(0)}{\sigma_1-\sigma_3} + \frac{\varepsilon(c)}{\sigma_1-\sigma_3} \qquad (2)$$

Figure 1 shows the relation between D(c) and time for various stress levels and the relation can be expressed as,

$$D(c) = k_1 t^n \qquad (3)$$

where k_1 is constant for a particular stress level, confining pressure and water content. Both D(0) and D(c) are functions of water content, confining pressure and stress level.

Equivalent Poisson's Ratio

Two material functions are required to characterise the load-deformation-time behaviour of an isotropic homogeneous material. The second parameter proposed in this investigation is the principal strain ratio or the equivalent Poisson's ratio, $\mu(t)$, which is defined as the ratio between the lateral strain, $\varepsilon_3(t)$ and the total axial strain, $\varepsilon(t)$. Figure 2 shows the relation between Poisson's ratio and time for various stress levels. The magnitude of Poisson's ratio increased with time at higher stress levels and decreased with time at lower stress levels. However, the magnitude of the increase or decrease was found to be comparatively small. Hence Poisson's ratio can be reasonably assumed to be independent of time. However it is highly stress dependent.

CONSTITUTIVE RELATION

A general nonlinear viscoelastic constitutive relation derived from thermodynamic principles proposed by Schapery (8) is used to characterise the time dependent behaviour of compacted clay. For uniaxial loading, the relation can be written as

$$\varepsilon(t) = g_0 D_L(0)\sigma + g_1 \int_0^t D_L(c)(\Psi-\Psi^1) \frac{dg_2\sigma}{d\tau}\, d\tau \qquad (4)$$

where $D_L(0)$ and $D_L(c)$ are the initial elastic and transient creep components of linear viscoelastic creep compliance, $D(\Psi)$.

$$\Psi = \Psi(t) = \int_0^t \frac{dt'}{a_\sigma} \; ; \; \Psi' = \Psi(\tau) = \int_0^\tau \frac{dt'}{a_\sigma} \qquad (5)$$

g_0, g_1, g_2 and a_σ are stress dependent material properties. The equation contains one time dependent parameter $D_L(c)$, one time independent parameter $D_L(0)$, both independent of stress level and four stress dependent parameters g_0, g_1, g_2 and a_σ. These four parameters tend to unity at low stress levels and equation 4 reduces to the superposition integral of linear behaviour.

The transient creep component of the linear creep compliance, $D_L(c)$ can be expressed as a power function of time for the compacted soil,

$$D_L(c) = Ct^n \tag{6}$$

where C and n are material constants. Hence in a creep and recovery test, where the stress, σ is removed after a time t_1, the total axial strain, $\varepsilon(t)$ and the recovery strain, $\varepsilon_r(t)$ can be obtained by,

$$\varepsilon(t) = \left[g_0 D_L(0) + C\left(\frac{g_1 g_2}{a_\sigma^n}\right) t^n \right] \sigma \tag{7}$$

$$\varepsilon_r(t) = \frac{\varepsilon(c)}{g_1} \left[(1 + a_\sigma \lambda)^n - (a_\sigma \lambda)^n \right] \tag{8}$$

where $$\lambda = \frac{t - t_1}{t}$$

$$\varepsilon(c) = C\left(\frac{g_1 g_2}{a_\sigma^n}\right) t_1^n \sigma \tag{9}$$

The nonlinear viscoelastic parameters can be evaluated from the results of creep and recovery tests using a graphical shifting procedure (3). The results of unconfined compression creep tests on compacted clays have been analysed in an earlier investigation (6).

PARAMETERS FOR COMPACTED SOIL

Creep

An examination of equation 7 shows that the nonlinear viscoelastic creep compliance can be written as,

$$D(t) = g_0 D_L(0) + \left(\frac{g_1 g_2}{a_\sigma^n}\right) Ct^n \tag{10}$$

n can be assumed a constant for a particular type of compaction for the soil and its magnitude is equal to the average of n values for all the tests in this series 0.26.

A parameter, stress-strength ratio, SSR, is defined as the ratio between the principal stress difference $(\sigma_1-\sigma_3)$ and the principal stress difference at failure $(\sigma_1-\sigma_3)_f$ for the same confining pressure

$$SSR = \frac{(\sigma_1-\sigma_3)}{(\sigma_1-\sigma_3)_f} \tag{11}$$

The material behaviour was assumed to be linear viscoelastic at the lowest magnitudes of stress-strength ratio, which was about 0.1. The average values of $D_L(0)$ and C determined for these tests in addition to n were taken to be the parameters needed to characterise the linear viscoelastic behaviour of compacted clays.

$$D_L(0) = \frac{\varepsilon(0)}{(\sigma_1-\sigma_3)}; \; C = \frac{A}{(\sigma_1-\sigma_3)} \tag{12}$$

$D_L(0)$ was found to be equal to 44.7×10^{-5} cm^2/kg and C equal to 5.8×10^{-5} cm^2/kg in this investigation. The magnitudes of g_0 and $(g_1 g_2/a_\sigma^n)$ were found from substituting the values of C and $D_L(0)$ into equation 10. It has been observed (7) that the range of scatter was relatively small upon expressing the viscoelastic parameters as a function of SSR for different confining pressures and water content values thus normalising their effects. The stress dependent parameters g_0 and $(g_1 g_2/a_\sigma^n)$ are plotted against SSR in figures 3(a) and 3(b). The magnitudes of these parameters approach unity at the lowest stress levels and show an increasing trend with increasing SSR. They can be approximately considered as linear functions of SSR beyond the linear viscoelastic range.

Poisson's Ratio

Poisson's ratio, μ, has been shown to be almost independent of time (figure 2) and it increases with increasing stress level as observed by Daniel and Olsen (1). The Poisson's ratio can also be considered as a constant in the linear viscoelastic range. At higher stress levels it can be expressed as a function of the initial Poisson's ratio, μ_0, as

$$\mu = m_0 \mu_0 \tag{13}$$

The magnitude of m_0 at different stress levels for all the tests in the series was determined and m_0 is plotted against SSR in figure 3(c). The magnitude of Poisson's ratio increased from about 0.03 in the linear range to about 0.24 near failure. The Poisson's ratio and SSR can be correlated by a linear function beyond the linear viscoelastic range.

Recovery

The parameters required for predicting the recovery deformation are the net creep strain $\varepsilon(c)$ and the parameters g_1 and a_σ as shown in equation 8. The shifting procedure (3) to determine g_1 and a_σ makes use of a master recovery curve for the particular n. The parameters were determined from the recovery tests on two similar specimens. The average n value obtained from the creep tests, 0.245, was used to draw the master recovery curve by setting $g_1=1$ and $a_\sigma=1$. The master recovery curve and the shifted recovery curve are shown in figure 4. After obtaining the values of g_1 and a_σ by the shifting procedure, the magnitudes of g_2 can be determined from the creep strain for these tests, using equation 9. The magnitudes of g_1, g_2

and a_σ are plotted against SSR in figure 5. While g_1 and a_σ show a decreasing trend with increasing SSR, g_2 increases in magnitude as SSR increases.

CONCLUSION

A nonlinear viscoelastic relation is suggested to describe the creep and relaxation behaviour of compacted cohesive soil. The nonlinear creep compliance, D(t) derived from the proposed relation is composed of an initial elastic component, D(0) and viscoelastic component, D(c). The nonlinear components are expressed as functions of linear viscoelastic components, $D_L(0)$ and $D_L(c)$ and $D_L(c)$ and stress dependent parameters, g_0, g_1, g_2 and a_σ.

It was found that the nonlinear creep compliance for compacted soils can be expressed as a power function of time. The stress dependent parameters were considered as functions of a parameter, stress-strength ratio $(\sigma_1-\sigma_3)/(\sigma_1-\sigma_3)_f$. It was observed that the effects of water content and confininf pressure on the parameters g_0 and $(g_1 g_2/a_\sigma^n)$, needed to define the creep behaviour can be approximately accounted for by this procedure. These parameters can be approximately considered as linear functions of SSR in the nonlinear range. The stress dependent parameters g_1 and a_σ were found to be decreasing functions of SSR while g_2 was an increasing function of SSR.

The equivalent Poisson's ratio was almost independent of time for compacted soils and an approximate linear relation is valid between μ and SSR beyond the linear viscoelastic range.

REFERENCES

1. Dan el, D.E., and Olsen, R.E., (1974), "Stress-Strain Properties of Compacted Clays," Journal of Geotechnical Engineering Division, ASCE, Vol. 100, No. GT10, pp. 1123-1126.
2. Lara-Tomas, M., (1962), "Time Dependent Deformation of Clay Soils under Shear Stress," Proceedings, First International Conference on the Structural Design of Asphaltic Pavements, Ann Arbour, U.S.A.
3. Lou, Y.C., and Schapery, R.A., (1971), "Viscoelastic Characterisation of a Nonlinear Fiber-Reinforced Plastic," Journal of Composite Materials, Vol. 5, pp. 208-234.
4. Ramaswamy, S.V., (1971), "Creep of Compacted Clay," Ph.D. Thesis, Purdue University, Indiana, U.S.A.
5. Ramaswamy, S.V., (1973), "Anisotropic Properties of Compacted Clays, "Proceedings, Seminar on Pavement Design and Construction of Roads and Airfields, Institution of Military Engineers, Poona, India, pp. 77-82.
6. Ramaswamy, S.V., (1975), "Deformation Studies of Compacted Clay, "Proceedings, Fifth Asian Regional Conference on SM & FE, Bangalore, India, pp. 91-94.
7. Ramaswamy, S.V., (1984), "Time Dependent Characterization of Compacted Clay," ASCE-EMD Speciality Conference, Laramie, U.S.A.
8. Schapery, R.A., (1969), "On the Characterisation of Nonlinear Viscoelastic Materials," Polymer Engineering and Science, Vol. 9, pp. 295-310.
9. Seed, H.B., Chan, C.K., and Monismith, C.L., (1955), "Effects of Repeated Loadings on the Strength and Deformation of Compacted Clay, "Proceedings, Highways Research Board, Vol. 34, pp. 541-558.
10. Singh, A., and Mitchell, J.K., (1968), "General Stress-Strain-Time Function for Soils," Journal of Soil Mechanics and Foundations Division, ASCE, Vol. 94, No. SM1, pp. 21-46.

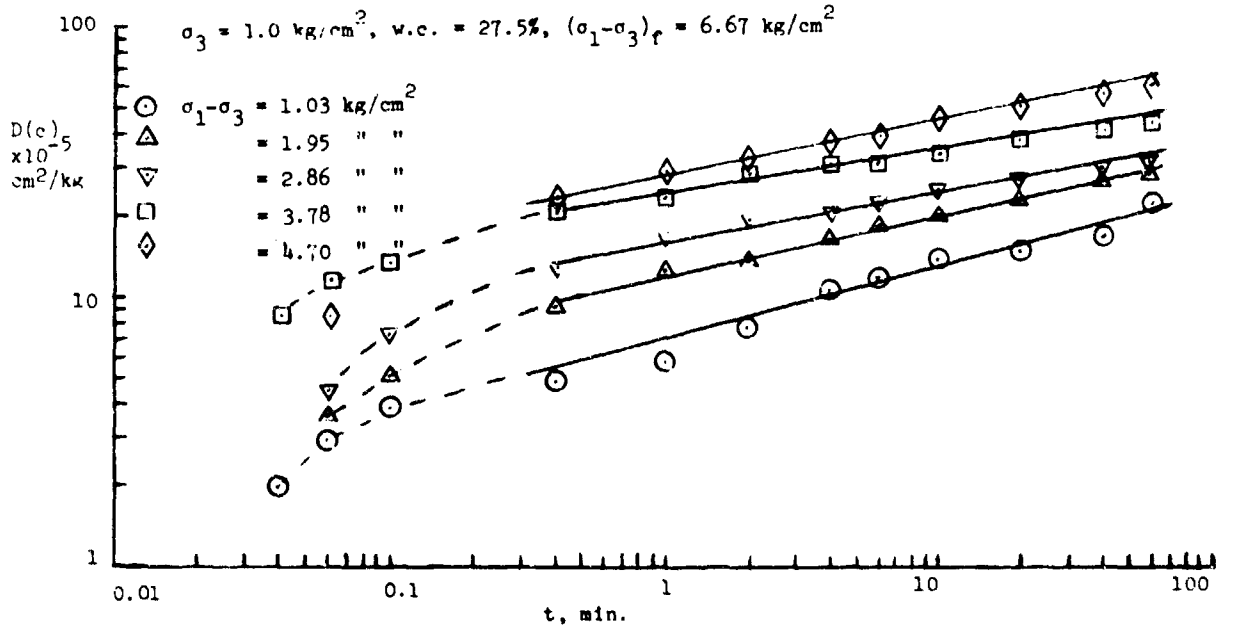

Fig. 1. Relation between net creep compliance and time.

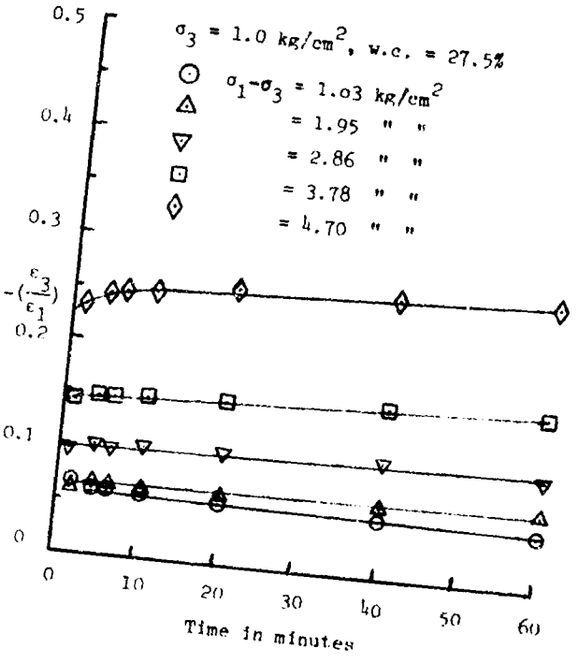

Fig. 2 Poisson's ratio vs. time at different stress levels.

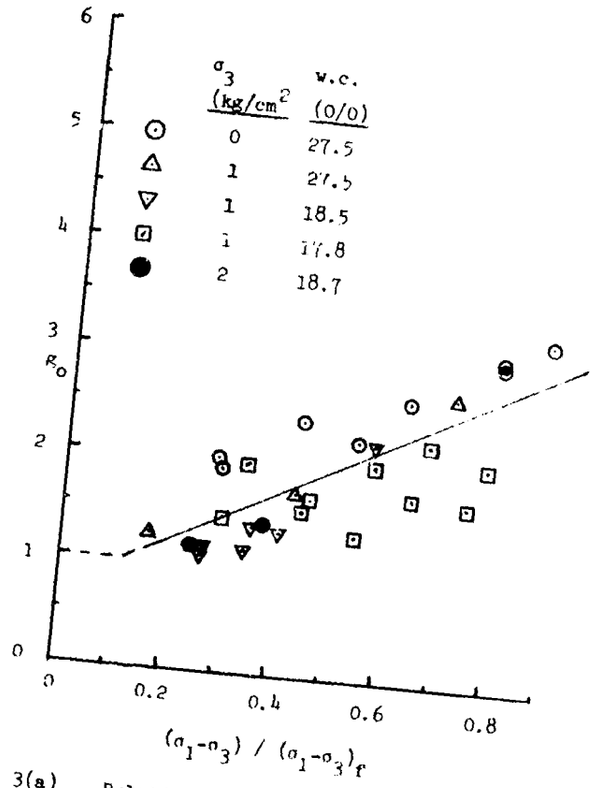

Fig. 3(a) Relation between E_o and SSR.

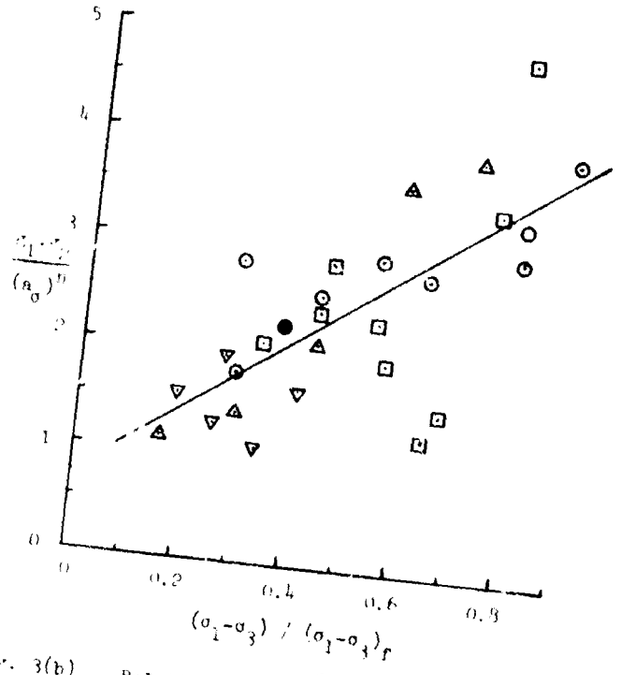

Fig. 3(b) Relation between $\frac{\varepsilon_1-\varepsilon_2}{a_\sigma^n}$ and SSR.

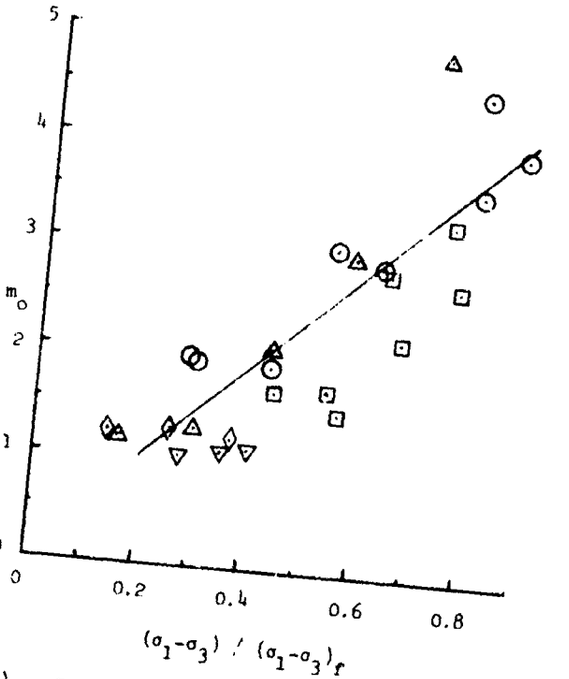

Fig. 3(c) Relation between m_o and SSR.

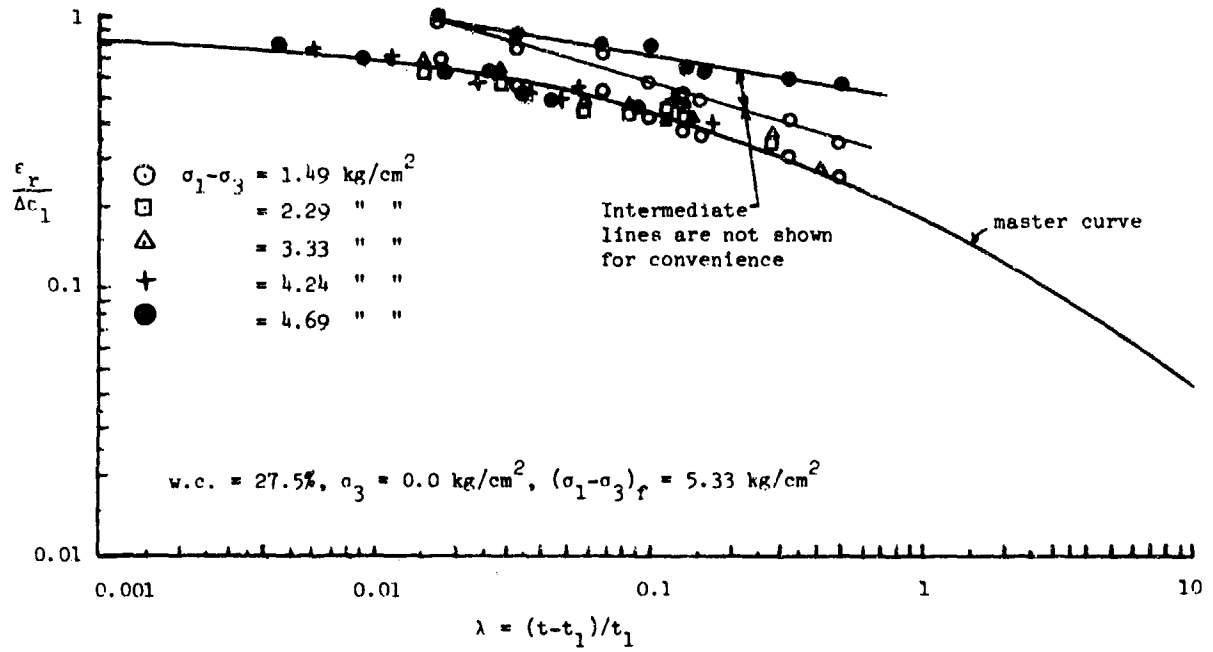

Fig. 4 Master recovery curve and shifted data.

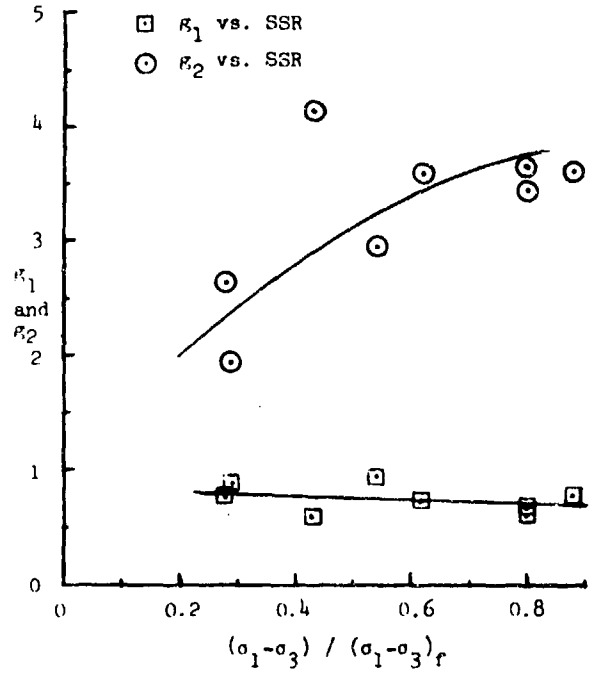

Fig. 5(a) Influence of stress level on β_1 and β_2.

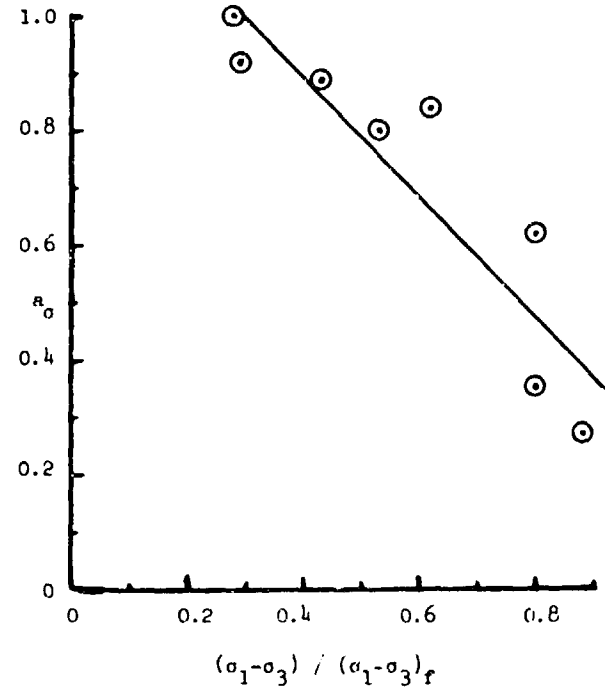

Fig. 5(b) Influence of stress level on a_σ.

AN INVESTIGATION INTO THE HIGH STRAIN-RATE BEHAVIOR OF COMPACTED SAND USING THE SPLIT-HOPKINSON PRESSURE BAR TECHNIQUE

C. W. Felice*, J. A. Brown+, E. S. Gaffney+ and J. M. Olsen‡

*Capt., USAF, Air Force Institute of Technology, Wright-Patterson AFB, OH 45433
+Earth and Space Sciences Division, Los Alamos National Laboratory, Los Alamos, NM 87545
‡University of Utah, Salt Lake City, UT 84112

ABSTRACT

The results of compressive high strain-rate experiments on compacted sand are presented. Experiments were conducted on a 60.3 mm split Hopkinson pressure bar (SHPB). The experiments showed that the assumptions necessary for a valid SHPB experiment are satisfied when using compacted sand samples constrained to a nearly uniaxial strain state. Results show that the sample stress-strain response is governed principally by the initial sample gas porosity, and that no strain-rate dependence is exhibited at sample strains less than the initial gas porosity. Several stress-strain curves are presented for samples prepared at several combinations of moisture content and density with applied stresses and strain rates up to 520 MPa and 4000 sec^{-1}, respectively.

INTRODUCTION

This paper presents the results of a laboratory investigation into the high strain-rate behavior of compacted soil using the split Hopkinson pressure bar (SHPB) technique [1]. This work has been performed using a 60.3 mm SHPB which is located at the Los Alamos National Laboratory, Los Alamos, New Mexico [2].

For the experimental program, samples were statically compacted into thick-walled confining cylinders at lengths of 6.35 mm and 12.7 mm. The thick-walled confining cylinder provided a means of containing the sample and producing a condition of nearly uniaxial strain during the experiment. The compaction moisture and density combinations ranged from drier than to wetter than optimum conditions as determined by the Harvard compaction test. The applied stresses and strain rates ranged from 240 MPa to 520 MPa and 1000 sec^{-1} to 4000 sec^{-1}, respectively.

CONFINING SYSTEM

To achieve a nearly uniaxial strain environment for the experiments, the soil samples were compacted into thick-walled bearing-bronze cylinders. The dimensions of these cylinders were 60.35 mm inside diameter, 102 mm outside diameter, and 44.5 mm in length. These confining cylinders served two purposes; first, to contain the soil sample itself, and second, to cancel the effects of radial inertia, forcing the sample to experience a state of nearly uniaxial strain. Thus, sample distortion or barrelling was prevented by the elimination of friction at the specimen/bar interfaces.

When the confining cylinder containing the sample was placed in the bars, approximately 19 mm of the cylinder overlapped the bars on each end. To determine if the confining cylinder was transferring any stress to the transmitter bar, a test was conducted with the bars separated a distance of 3.0 mm (a distance greater than the anticipated displacement of the incident bar) and the confining cylinder placed over the air gap between the bars. If the confining cylinder did transfer stress to the transmitter bar a signal would be recorded at the transmitter bar strain gage; if not, the strain gage record would be flat. The results indicated that the confining cylinder did not transfer any measurable stress to the transmitter bar.

SAMPLE PREPARATION

The clayey sand (SC, Unified Soil Classification System) was obtained in bulk quantities from the McCormick Ranch test site located on Kirtland Air Force Base (KAFB), New Mexico. In order that the soil be as free of organic material as possible, the surface vegetation was removed and the samples were taken at a depth of 1 to 2 meters. After arriving at the University of Utah soils laboratory, the material was slaked to achieve a uniform mixture as well as to break apart large clumps of soil.

The majority of samples were prepared near the optimum moisture content (13.3%) and dry density (1.87 g/cc) as determined by the Harvard miniature compaction test (see Figure 1). To achieve as uniform conditions among samples as possible, the soil was mixed in batches of enough material to prepare a minimum of five experimental samples. Before the addition of water, the soil was passed through a No. 4 sieve (4.75 mm opening). The soil was then carefully weighed and placed in a large flat pan. The correct amount of moisture was added by using a spray bottle so that an even distribution could be obtained. The sample material was then mixed thoroughly. After mixing, a damp cover was placed over the soil for a period of 20 minutes to allow the soil-water mixture to stabilize. Following the stabilization period, the sample was again mixed to ensure that an even mixture was obtained.

The individual experimental samples were then prepared by removing the appropriate soil mass from the batch mix to yield a given volume when compacted. The samples were statically compacted in the confining cylinders by using a hydraulic press with spacer rings to control the sample length (and hence, density). Two sample lengths were used: 12.7 mm and 6.35 mm. Each sample was then sealed in a plastic bag to reduce any moisture loss that might occur prior to the actual experiment. The same procedure was followed for samples prepared on the wet and dry side of optimum conditions.

EXPERIMENTAL PROGRAM

The information reported here represents the results of twenty-six experiments. In most cases, a minimum of two experiments were conducted at each combination of moisture content and density, in order that data replication could be obtained. Due to the nature of the specific Hopkinson bar apparatus used, the seating strains could not be controlled with great accuracy, hence the pre-experiment sample length differed from sample to sample affecting the ability to achieve exact experiment replication. In addition, there existed a friction force between the launch tube and the striker bar such that it was difficult to achieve duplicate impact velocities. The applied stresses (i.e., the amplitudes of the incident waves in the bar) ranged from 240 MPa to 520 MPa. At the completion of the experiment, the sample was removed from the confining cylinder and a post-experiment moisture content determined.

EXPERIMENTAL ASSUMPTIONS

In analyzing the strain gage data recorded in the SHPB experiment, several assumptions need to be addressed. These are:

1) That there exists a uniform distribution of axial stress over the length of the sample;

2) That there exists a uniform distribution of radial stress over the length of the specimen;

3) That the interfaces between the bars and the samples are frictionless.

Assumptions two and three will be addressed first, followed by assumption one.

A nearly uniaxial strain state is forced upon the sample by the fact that it is contained in a thick-walled confining cylinder. As the nominal inside diameter of the confining cylinder is the same as the diameter of the bar, the stress applied to the sample will be constant across the sample diameter (provided that the stress is constant over the diameter of the bar) [2]. This configuration will also constrain the sample such that there will be no appreciable radial strain.

As briefly mentioned earlier, this configuration will prevent sample distortion or barreling during the experiment. In the traditional SHPB experiment a sample with a diameter slightly less than that of the bars is placed between them. This is to allow the sample to expand radially during the experiment while not exceeding the diameter of the bar. As stress is applied to the sample, radial shear forces are created between the bars and the sample. These have commonly been referred to as "end effects" or "friction effects." A result of these end effects is that the sample tends to be clamped at the specimen/bar interfaces [3]. This prevents the sample from expanding uniformly; hence, barreling of the sample is observed. By preparing the sample at the same diameter as that of the bars and confining it so that no radial expansion is allowed, these "end effects" are eliminated.

An analytic method for determining when stress uniformity is achieved in an SHPB sample was developed by Davies and Hunter [4] based on energy considerations and use of the Taylor-von Karman theory for the plastically deforming sample. This expression is written as follows:

$$\frac{d\sigma}{d\varepsilon} > \frac{\pi^2 \rho_s l^2}{T^2}$$

where $d\sigma/d\varepsilon$ is the slope of the stress-strain curve, ρ_s is the density of the specimen, l is the length of the specimen, and T is the time required for the stress to equilibrate in the sample. Figure 2 shows results from a typical experiment. Using the above expression with the stress-strain curve (Fig. 2a) and the appropriate sample length and density, T is computed to be 66 microseconds. From Fig. 2b, it can be determined that after about 65 microseconds the stresses at the two interfaces are indeed approximately equal. The stress difference across the interfaces as a function time is shown in Fig. 2c. If axial inertia forces are absent, this stress difference should be zero. It can be seen that after about 65 microseconds the stress difference is very small.

EXPERIMENTAL RESULTS

Figures 3 and 4 show typical stress-strain curves for sample lengths of 12.7 mm and 6.35 mm, respectively, over a range of applied stresses. The experimental conditions are given in Table 1. In both figures, the initial portions of the curves are slightly concave toward the stress axis. The average stress experienced by the specimen increased with increasing applied stress independent of the sample length. The stress-strain response was very similar for applied stresses up to 400 MPa with some increase in stiffness observed at higher applied stresses. For all applied stress levels, the samples began to stiffen at strains approximately equal to the gas porosity. For both sample lengths and at all applied stresses, the strain at peak stress experienced by the sample exceeded the gas porosity of the material. This discrepancy will be addressed in the next section.

To observe how moisture content variations affect the stress-strain response of the soil, samples were prepared at the following nominal moisture contents; 7 percent, 13 percent and 15 percent (see Figure 1 for relationship to the Harvard compaction curve). Figures 5 and 6 show the effect of moisture content on stress-strain response for sample lengths of 12.7 mm at an applied stress of 400 MPa, and 6.35 mm at an applied stress of 250 MPa, respectively. From Figure 5, there is a clear indication that the average stress experienced by the samples increased with

TABLE 1
Summary of experimental conditions.

Experiment Number	Sample length (mm)	Water content (%)	Gas porosity (%)	Wet density (Mg/m^3)	Applied stress (MPa)
112	6.44	11.8	7.9	2.09	425
113	6.45	12.1	7.7	2.09	385
114	6.55	12.1	9.2	2.05	386
115	6.45	11.4	10.6	2.04	395
116	6.37	11.2	8.1	2.10	243
117	6.35	10.7	8.5	2.10	268
118	6.45	10.6	10.3	2.07	244
119	6.45	10.4	9.9	2.08	246
131	13.13	12.4	9.6	2.04	387
132	12.69	12.5	6.9	2.10	375
133	12.91	12.4	8.0	2.07	368
134	12.59	12.4	5.8	2.12	399
135	13.07	7.0	23.4	1.84	385
136	12.23	15.1	5.2	2.08	397
138	5.96	13.0	4.9	2.13	251
139	6.09	7.0	17.7	1.98	249
145	12.65	11.8	6.2	2.13	269
146	12.67	11.9	6.3	2.13	523
147	6.36	11.9	6.6	2.12	237
148	6.31	14.4	7.4	2.04	249
162	6.29	13.0	4.4	2.14	519
163	6.31	12.9	4.8	2.13	522
164	12.98	12.9	7.5	2.07	507
165	12.89	12.7	7.1	2.09	254
166	6.24	14.0	4.4	2.12	261
167	6.22	14.0	4.1	2.12	261

increasing moisture content (Table 1). Also the samples became stiffer with increasing moisture content, and the strain at peak stress experienced by the sample decreased with increasing moisture content. As with the other stress-strain curves shown, there is a marked break in slope near the gas porosity. This change is slope is not observed for the dry sample (experiment 135). The strain experienced by the sample at peak stress decreased with increasing water content. The 6.35 mm samples also became stiffer with increasing moisture content with a change in slope near the gas porosity (Figure 6). However, this change in slope is less abrupt than observed in the thicker samples. As with the 12.7 mm sample, the 6.35 mm samples experienced decreasing strain at peak stress with increasing moisture content.

There is a difference in the response of the dry sample for the two sample lengths. The 12.7 mm sample, which had a gas porosity of 23.4 percent, experienced very little build up of stress at the maximum strain of 16 percent. For the 6.35 mm sample, which had a gas porosity of 17.7 percent, the accumulated strain approached that value with a substantially higher build up of stress. Therefore, it appears that stiffening begins at strains slightly less than the initial gas porosity.

Another major interest of this research was whether or not a sufficient degree of experimental replication could be achieved. Figure 7 demonstrates the success of this effort. There is virtually no observable difference between the four experiments in this figure, except that one sample (experiment 117) received an impact stress somewhat higher than the other three.

To determine the strain-rate sensitivity of the compacted soil, stress-strain rate curves were constructed at constant strain levels. Such a plot is shown in Figure 8 for 6.35 mm samples compacted to moisture and density conditions near optimum. The dashed lines show the stress-strain rate trajectories averaged for each of two sets of experiments conducted at the same applied stress. The solid lines connect points of constant strain between the two sets. From Figure 8, it can be seen that there is no strain-rate dependence at strains less than the initial gas porosity. This is in accord with the findings of Gaffney et al. [2] that strain-rate dependence effects on loading occurred in dry alluvium only at strain rates above 5000 sec^{-1}.

DISCUSSION

In most cases, the strains experienced by the samples exceeded the initial gas porosity. Several phenomena may work together to account for this observed discrepancy: 1) Water compression, 2) Radial expansion of the confining cylinder, 3) Water loss, and 4) Soil loss. The first three have the potential to be examined quantitatively, while the last can be looked at qualitatively, at best. Addressing the potential strain contribution of the above factors individually and then summing their contributions would seem a natural approach to the problem. However, the experimental environment complicates this approach. At the incident bar/sample interface the initial compressive stress wave is reflected as a tensile wave due to the lower impedence of the sample relative to the bar. This tensile wave travels back down the bar toward the end at which impact occurred. As the impact end of the bar is now a free end, the tensile wave is reflected as a compressive wave travelling once again toward the sample, and hence, reloading the sample. Because of this multiple impact situation, there is no way to determine the contribution from water loss and soil loss during the period of the first applied pulse alone (about 150 μs).

Because a sample moisture was determined before and after each experiment, a measure of the amount of moisture loss is available. The average moisture loss for all the experiments was 11.0 percent. Also, it can be observed that some soil mass is lost from the confining cylinder during the experiment. However, there is no way of measuring how much is lost or the distribution of the loss (if the loss occurs during the period of the first applied pulse or later in the experiment). It is also certain that the pore water does compress and the confining cylinder does experience radial expansion.

Because of the uncertainty in the evaluation of the strain contribution from the above-mentioned factors individually, a gross strain adjustment has been made even though it is possible to calculate the effect of water compression and cylinder expansion. This was accomplished by plotting the difference between the strain at maximum average stress and the initial gas porosity against the average force (computed as the maximum average stress multiplied by the area of the sample). A

simple linear regression line was then fit to the data for samples prepared near optimum water content (Figure 7). Using the regression line and the average force experienced by the sample, a systematic strain correction was then computed for each experiment. The strain correction was then added to the sample gas porosity to yield an accountable sample strain which could be compared to the strain experienced by the sample at the maximum average stress. The discrepancy between the accountable strain and the strain at maximum stress is then used as a measure of the success of the correction (Table 2).

TABLE 2
Accountable strain for sample at optimum conditions

Test No.	Gas porosity (%)	Strain correction (%)	Sum (%)	Strain at peak stress (%)	Balance (%)
112	7.9	7.87	15.77	19.79	4.02
113	7.7	7.67	15.37	17.40	2.03
114	9.2	7.61	16.81	19.60	2.79
115	10.6	8.07	18.67	18.03	-0.64
116	8.1	4.98	13.08	14.24	1.16
117	8.5	6.54	15.04	14.50	-0.54
118	10.3	5.18	15.48	14.06	-1.42
119	9.9	4.93	14.83	14.07	-0.76
131	9.6	6.10	15.70	12.68	-3.02
132	6.9	6.43	13.33	10.67	-2.66
133	8.0	5.52	13.52	12.52	-1.00
134	5.6	6.57	12.37	12.22	-0.15
138	4.9	5.75	10.65	11.80	1.15
145	6.2	3.51	9.71	10.12	0.41
146	6.3	9.41	15.71	13.30	-2.41
147	6.6	4.78	11.38	12.99	1.61
162	4.4	9.74	14.14	20.60	6.46
163	4.8	12.52	17.32	15.27	-2.05
164	7.5	9.28	16.78	12.43	-4.35
165	7.1	2.70	9.70	9.27	-0.43

After making the strain adjustment, experiment 162 is the only experiment that has a significant discrepancy remaining. The stress-strain curve for that experiment (Figure 10) suggests that a greater amount of soil and water extrusion may have occurred in that experiment than in the other experiments. At about 270 MPa, the sample begins to accumulate strain with very small changes in stress. Similar behavior is not observed to this extent in any other sample, and we believe that it can be attributed to excessive extrusion of soil and water during the course of the experiment.

It was observed in Figure 8 that as the accumulated sample strain approached and exceeded the initial gas porosity a dependence on strain-rate seemed to develop. However, this apparent behavior should be viewed with some caution for two reasons. First, the constant strain curves used to show this apparent strain-rate dependence are only rough averages developed from a few data points. Second, the factors identified to account for the discrepancy between the strain at maximum stress and the initial gas porosity cannot be quantified with the necessary accuracy to determine their effect on the apparent strain-rate dependence.

CONCLUSIONS

From the results of this experimental study conducted on compacted sand samples at strain rates up to 4000 sec^{-1}, we draw the following conclusions.

a) The assumptions necessary for a valid SHPB experiment can be satisfied for compacted sand samples constrained to a nearly uniaxial strain state.

b) Experimental replication can be achieved if sufficient care is taken in sample preparation and generation of the incident stress wave.

c) The stress-strain response of the soil studied is governed principally by the initial gas porosity of the sample.

d) Compacted clayey sand samples appear to be insensitive to strain rate (at least up to 4000 sec^{-1}) so long as the strain experienced is less than the initial gas porosity. At strains in excess of that value, there is an apparent strain-rate dependence; however, caution is recommended until further experimental confirmation of this apparent behavior can be obtained.

REFERENCES

[1] Kolsky, H. An investigation of the mechanical properties of materials at very high rates of loading. Proc. Phys. Soc. B62, 676-700 (1949).

[2] Gaffney, E. S., J. A. Brown and C. W. Felice, Soils as samples for the split Hopkinson bar. This volume.

[3] Green, S. J., and R. D. Perkins, Uniaxial compression tests at strain rates frome 10^{-4}/sec to 10^{4}/sec on three geologic materials. DASA 2199, Defense Atomic Support Agency (now Defense Nuclear Agency), Washington (1969).

[4] Davies, E. D. H, and S. C. Hunter, The dynamic compression testing of solids by the method of the split Hopkinson pressure bar. J. Mech. Phys. Solids 11, 155-179 (1963).

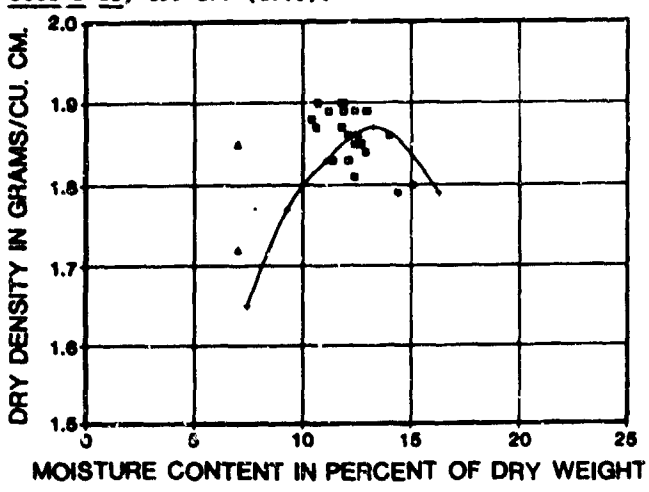

Figure 1. Sample moisture and density in comparison to the Harvard compaction curve. + Harvard compaction data, o wet of optimum, Δ dry of optimum, □ near optimum.

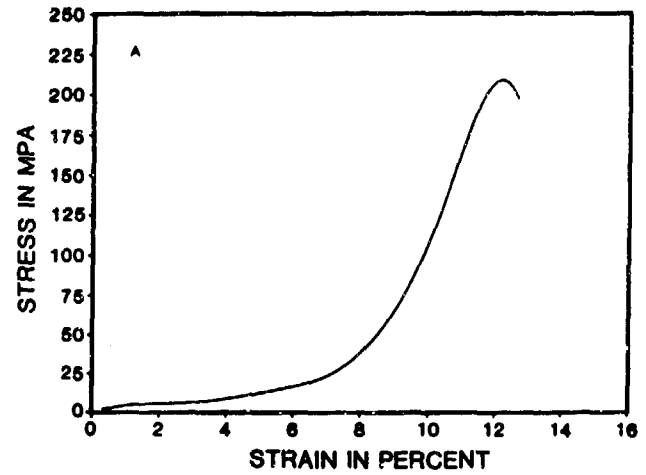

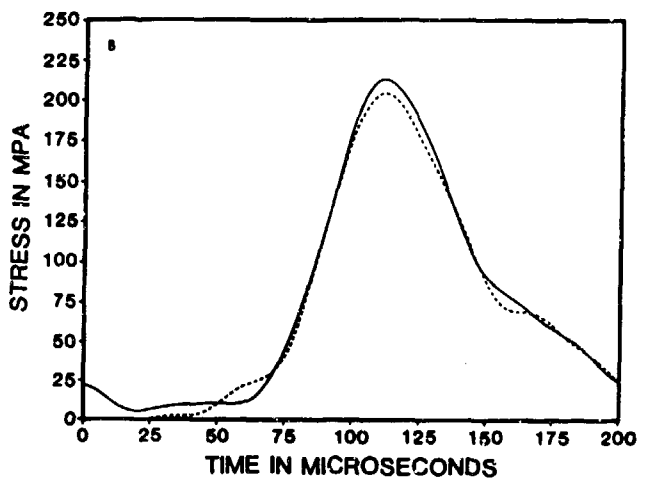

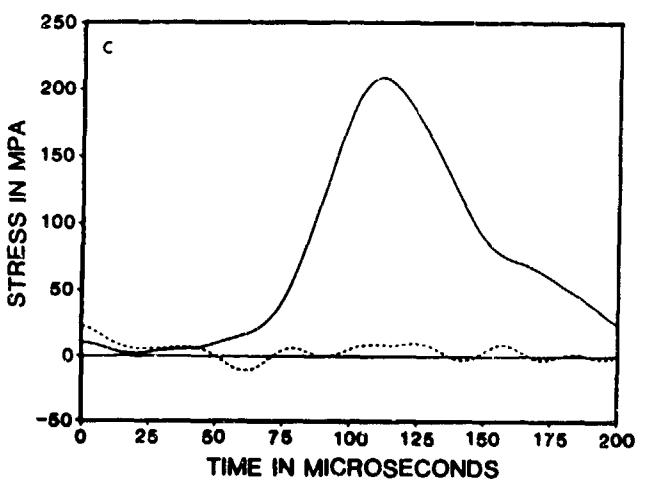

Figure 2. Typical experimental results for a 12.7 mm sample with an applied stress of 400 MPa.

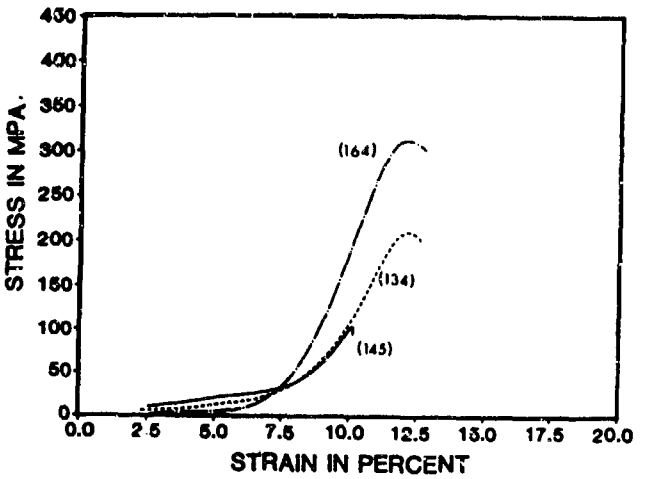

Figure 3. Experimental results for a 12.7 mm sample over a range of applied stresses. 269 MPa, solid; 399 MPa, dashed; 507 MPa, chain-dotted.

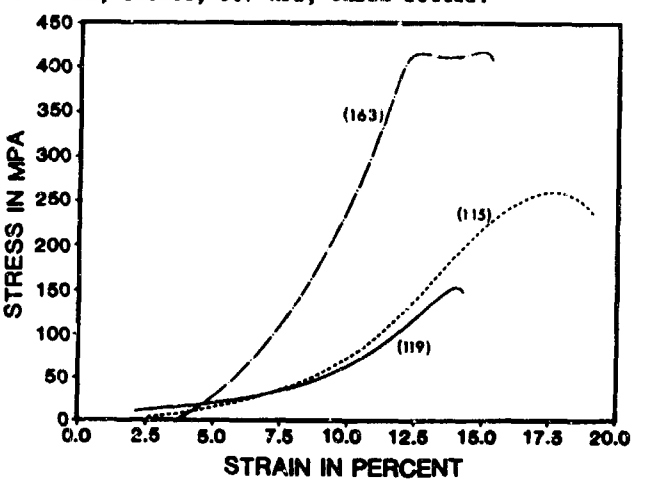

Figure 4. Experimental results for a 6.35 mm sample over a range of applied stresses. 246 MPa, solid; 395 MPa, dashed; 522 MPa, chain-dotted.

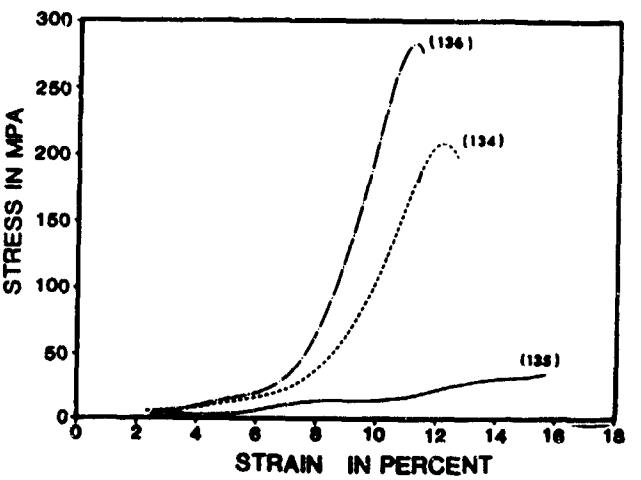

Figure 5. Experimental results for a 12.7 mm sample prepared at nominal moisture contents of 7 percent (solid), 13 percent (dashed) and 15 percent (chain-dotted).

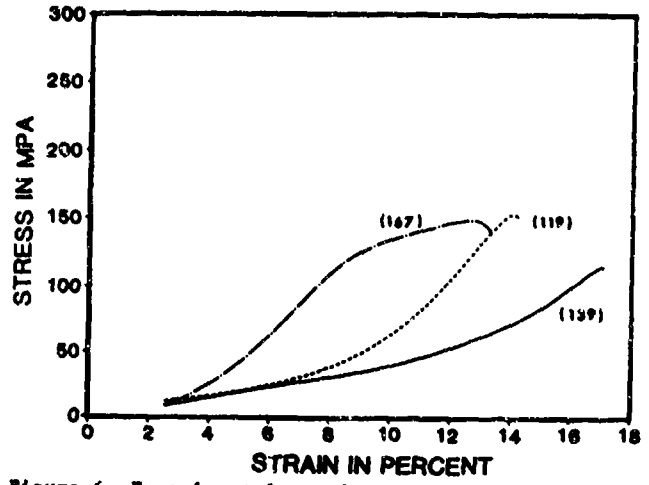

Figure 6. Experimental results for a 6.35 mm sample prepared at nominal moisture contents of 7 percent (solid), 13 percent (dashed) and 15 percent (chain-dotted).

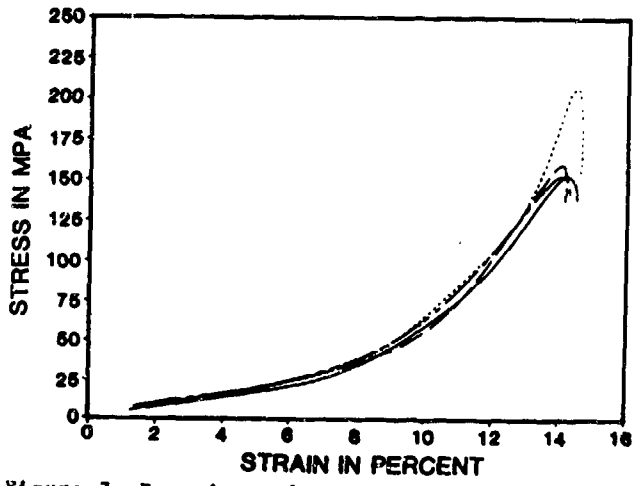

Figure 7. Experimental replication for 6.35 mm samples. The experiments are 116 (solid), 117 (dashed), 118 (chain-dotted), 119 (chain-dashed).

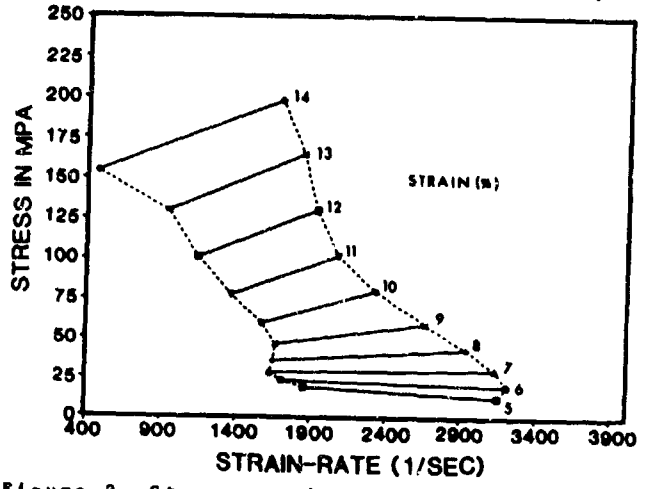

Figure 8. Stress-strain rate plot for 6.35 mm samples compacted to near optimum conditions.

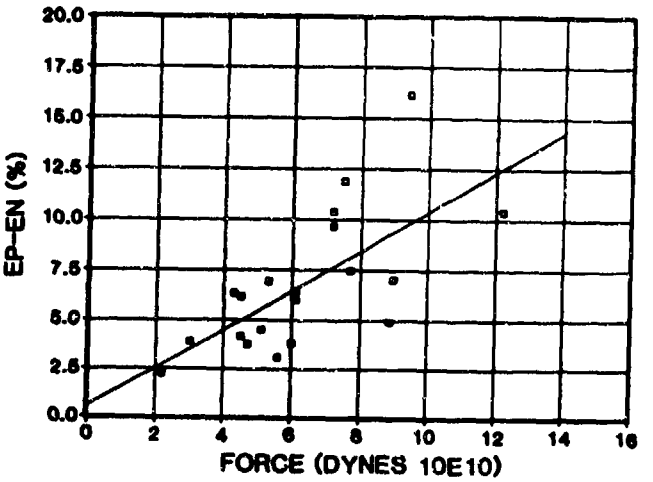

Figure 9. Linear regression fit to data for all samples compacted to near optimum conditions used in the systematic strain adjustment discussed in text.

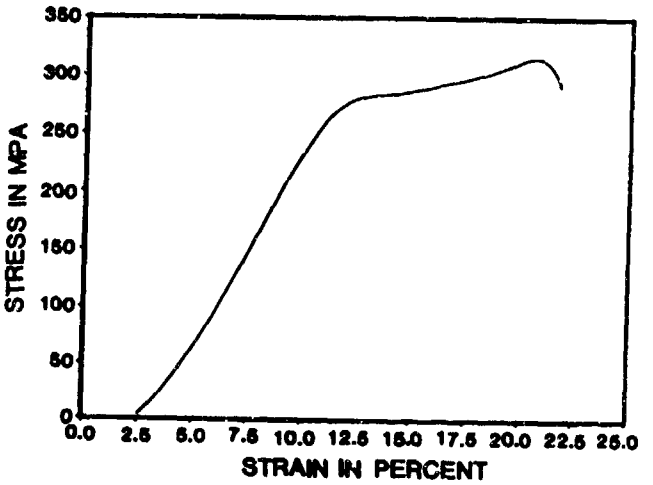

Figure 10. Stress-strain response for experiment 162.

SOILS AS SAMPLES FOR THE SPLIT HOPKINSON BAR

E. S. Gaffney, J. A. Brown, and C. W. Felice*

Earth & Space Sciences Div., Los Alamos National Laboratory, Los Alamos, NM 87545
*U. S. Air Force Institute of Technology

ABSTRACT

Soils frequently exhibit one or more of the following characteristics which complicate analysis of data from split Hopkinson bar tests or make test setup and execution difficult: low wave speed, high attenuation of acoustic energy, or insignificant structural strength. Low wave speed invalidates the assumption that the sample is deformed uniformly by the load at early times; but, use of a Lagrangian wave propagation analysis permits derivation of useful information from the standard suite of data. Use of gauges within the sample would facilitate this technique. High attenuation requires thin samples, which restricts the strain paths which can be achieved. The weakness of non-cohesive soils presents difficulties in preparation, handling and control of boundary conditions. One simple solution is to support the sample in a rigid sleeve; this results in a uniaxial strain experiment so that the results are directly comparable to shock wave data.

INTRODUCTION

For the past 35 years, the split Hopkinson bar has been used to measure the high-strain-rate mechanical behavior of many materials. Kolsky's pioneering work in 1949 [1] investigated elastomers and metals in very thin discs. Later work treated similar materials in other shapes (e.g., [2]) and extended the work to other metals and to ceramics and rocks (e.g., [3]). Some work has even been reported on very low density foams [4]. In recent years, there has been interest in the possibility of applying the split Hopkinson bar to the determination of the high-strain-rate response of soils. The driving force for most of this interest has been the need to develop predictive methods for estimating structural damage to military systems in or on soil. However, information on the high strain rate deformation of soils is potentially useful in other technical areas such as mining, overburden removal, earthquake engineering, containment of underground nuclear tests, and the study of impact and explosion cratering phenomena.

In the past two years we have conducted over 150 tests of soil specimens in a split Hopkinson bar at Los Alamos National Laboratory. These tests have provided a considerable challenge and a substantial learning process. The purpose of this paper is to share with the community some of the peculiarities of testing soils with the Hopkinson bar and the techniques we have used to overcome of the difficulties. A more detailed discussion of the dynamic behavior of a particular soil is given in a companion paper [5], but most of the examples here are taken from a Los Alamos report describing the dynamic behavior of a dry desert alluvium [6].

THE SPLIT HOPKINSON BAR

A typical arrangement for the split Hopkinson bar, or Kolsky apparatus, is shown schematically in Figure 1. The system consists of two long cylindrical bars: the incident or input bar and the transmitter or output bar. For compression testing, the cylindrical specimen is placed between the two bars and a compressive stress pulse is generated at the end of the incident bar by impact of the projectile or striker bar. The amplitude of the incident stress pulse is determined by the impact velocity and the material properties of the projectile and the incident bar, while the duration of the pulse is dependent on the length and modulus of the projectile.

The stress pulses incident on and reflected from the incident bar/specimen interface are recorded with strain gauges mounted at some point along the incident bar sufficiently distant from either end to prevent overlap of wave trains. The stress transmitted through the specimen is monitored by similarly mounted gauges on the transmitter bar. A momentum-absorbing arrangement at the end of the transmitter bar prevents multiple reflections of the transmitted stress wave. It is assumed that the bars remain elastic during the passage of the stress wave so that, except for the dispersive effects discussed below, the strain gauges accurately reproduce the appropriate stress histories in the bars.

The split Hopkinson bar apparatus operated by the Geophysics Group at Los Alamos National Laboratory consists of incident and transmitter bars as described above supported by a massive reaction frame and includes several other features. The bars are 60.3 mm diameter, 1.22 m long, Vascomax 350 maraging steel heat treated to a yield stress of about 2 GPa (300 ksi). Teflon bushings in the cross members of the reaction frame support the bars at about half meter intervals. For control of specimen pore pressure, each bar is provided with a 3.2 mm diameter axial hole vented radially about 0.3 m from the specimen end. When not required, the cone-shaped openings of these

holes at the specimen ends of the bars are plugged with matching cones of the same steel. Stress waves in the bars are monitored by strain gauge pairs mounted 0.61 m from the specimen ends. The pairs are used in a half-bridge configuration to null bending strains.

The incident stress pulse is generated by impact of a projectile from a small gas gun. Projectiles are available to generate pulses with nominal durations of 50, 100, and 200 μs. Projectile velocity is measured just prior to impact by three pairs of diode lasers and photodetectors mounted in the muzzle of the gun.

A static pre-load of up to 200 MPa (30 ksi) can be applied by a hydraulic ram located at the downstream end of the transmitter bar. Finally, a momentum-trapping steel slug is attached to the rear of the ram by a breakaway bolt and allowed to fly off into a rag-filled basket.

Transient signals from the two continuously-powered strain gauge bridges are filtered and preamplified, then routed to the data acquisition and control area in the adjacent room. The signal conditioning amplifiers also have a provision for switching to a calibration signal which verifies the overall gain of the data acquisition system. Further amplification is provided as required prior to digital recording of the signals. The analog bandwidth of the signal recording system is 1 MHz, to prevent aliasing of the digital records.

The data are recorded by CAMAC (IEEE-583) based waveform digitizers. The incident and transmitter bar records are recorded on separate channels with 8-bit resolution. At the usual rate of 0.5 μs per point, a total of 8 ms of data are recorded per channel, and a timing signal derived from the projectile velocity measuring system is used to position the useful data appropriately within this window. The data are automatically read by a small microcomputer and stored on flexible disk for later processing on a larger machine.

In the standard analysis of Hopkinson bar data [3], the stress at the incident bar/sample interface is calculated as

$$\sigma_i = E(I+R),$$

where E is Young's modulus for the bar, I is the incident strain and R is the reflected strain; the stress at the sample/transmitter bar interface is

$$\sigma_t = E(T),$$

where T is the transmitted strain; and the strain rate in the specimen is given by

$$\dot{\epsilon} = C_o(I-R-T)/l_o,$$

where $C_o^2 = E/\rho$, ρ is the density of the bar, and l_o is the initial sample length. In order to get stress-strain paths for the deformation, the stress is calculated as the average of the stress at the two interfaces and the strain is the time integral of the strain rate.

In the above expressions, all the strain pulses are shifted in time to coincide with the transit time to or from the center of the sample. Propagation of rod waves is dispersive [7,8], so we must correct the measured strain histories for dispersion in addition to shifting them in time. A method has been described by Follansbee and Frantz [9] which is very easy to implement in a numerical data reduction code. They have approximated the dispersion relation for maraging steel, which is derived in terms of Bessel functions, as a polynomial:

$$\frac{C(\frac{r}{\lambda})}{C_o} = 0.5764 + \frac{0.4236}{22.(\frac{r}{\lambda})^4 + 12.8(\frac{r}{\lambda})^3 + 2.77(\frac{r}{\lambda})^2 + 0.92(\frac{r}{\lambda})^{1.5} + 1}$$

where r is the radius of the bar and λ is the wavelength. In our standard data reduction, we make this correction by transforming the measured pulses to the frequency domain, applying the desired phase shift, and inverting the transform. This procedure also removes the high frequencies in the data which are mostly digitizing noise.

SOILS AS SAMPLES

Soils frequently exhibit one or more properties that make them difficult materials for Hopkinson bar testing. They often have so little strength that even putting them into the bars is not trivial. Soils with substantial fraction of air-filled void volume have very low wave speeds and very high rates of attenuation; these properties limit the sample thickness and/or complicate the data analysis. And, of course, the usual difficulties of getting samples that are characteristic of *in situ* behavior to the laboratory apply to Hopkinson bar tests as to most other laboratory tests of soil samples.

Except for very cohesive, clayey soils or soils that are very well-indurated, it is usually necessary to provide radial support to a soil sample merely to keep it in position for the test. The most obvious choice of support is one that is as compliant as possible in hopes that the lack of radial confinement of the standard Hopkinson bar test could be reproduced. However, when one considers even the flimsiest of sleeves they still provide a radial restraint that would be significant relative to the strength of most soils. The opposite extreme of a very stiff radial support is easy to implement and has the added advantage of providing a strain path that can be easily duplicated at both higher and lower strain rates--uniaxial strain. This strain path also facilitates data analysis, as we shall see below. A third alternative is to provide some intermediate degree of confinement; however, in that case it would be necessary to determine the radial strain and stress histories so that the overall strain path and stress history is known.

For soils with several percent or more of air-filled porosity, it can be shown that radial strain is negligible when a thick-walled metal sleeve is used to confine the specimen. Figure 2 shows the sample holder configuration we have used at Los Alamos. The holder is a cylinder of bronze or steel with an axial hole just slightly larger than the diameter of the bar. The sample is compacted into a disc of the desired thickness at the center of the holder, and then the holder is slipped over one bar and the other bar is moved into the free

end. Tests with no sample have shown that the sleeve carries substantially less than 0.1 percent of the pulse during dynamic loading. The radial expansion, Δr, of a tube of modulus E, Poisson's ratio 0.3, inside diameter r, outside diameter R and radial stress P is given by

$$\frac{\Delta r}{r} = \frac{P}{E}\,\frac{(0.7-1.3R^2/r^2)}{(1-R^2/r^2)}$$

For our sample sleeves, this formula gives a radial strain of 1.6×10^{-11}/Pa. This will actually be an overestimate because the internal load is not applied over the entire length of the cylinder. The extreme case occurs when the soil has no shear strength so that the radial stress P is equal to the axial stress measured by the bars. For our typical soils, axial strains of 10 percent or more are attained at only a few tens of MPa so that the radial strain is less than 0.1 percent of the axial strain. In some of the experiments described by Felice et al. [5], stresses were hundreds of MPa and radial strains may have been as high as a few percent of axial.

The low wave speed and high attenuation in dry soils lead to another sample constraint--that the sample be thin. Because we are deforming the soils in uniaxial strain we do not have to worry about friction effects at the ends of the bars or radial inertia as were considered in detail by Davies and Hunter [2]. The low wave speed limits sample length in two ways. First, thick samples will never reach equilibrium because of the low wave speed; the Hopkinson bar test will then be a wave propagation experiment rather than a homogeneous deformation experiment. Fortunately, for uniaxial strain we can still derive useful information from such a test (see below). The second, and frequently more limiting, result of low wave speed is that the amplitude of the stress wave delivered to the incident bar/sample interface will be very low. If the amplitude of the incident wave in the bar is P_o and the impedence of the bar and soil are $\rho_b D_b$ and $\rho_s D_s$, respectively, the stress of the first wave through the soil will be approximately $P=2P_o\rho_s D_s/\rho_b D_b$. For our dry alluvium [5], we find $P=0.02P_o$. Subsequent reflections between the bars increase the amplitude, but very many reflections would be needed before P approached even half of P_o.

The high attenuation rate of dry soils also limits us to thin samples. The stress incident to the sample, which is already low, will decay as it propagates through the sample. Thus the stress at the sample/transmitter bar interface will be very low and subject to measurement errors. Furthermore, the variability of all these properties makes it difficult to set measurement levels so as to precisely measure transmitter bar signals.

DATA ANALYSIS FOR SOILS

With soils as specimens, the conditions assumed for the reduction of data from the ideal split Hopkinson bar experiment may not be met. In particular, the wave speeds in dry soils at low stress levels (which may still be large enough to achieve considerable pore collapse) may be very low; values of about 200 to 250 m/s are common. As mentioned above, the deformation is very nearly uniaxial if the sample is confined in a massive sleeve, so we can adopt a data analysis technique originally developed for shock wave experiments which also produce uniaxial-strain loading. In that case, the equations of motion of the soil can be cast into a form wherein the stress is expressed in terms of the velocity and the temporal and spatial derivatives of velocity. Seaman [10] has developed a method which uses Lagrangian measurements of stress or velocity to estimate the temporal and spatial derivatives of the measured quantity. This method, called Lagrangian analysis, is particularly developed for analysis of uniaxial strain waves which attenuate as they propagate. Because the calculation of the stress at the incident interface of the sample involves subtraction of two large numbers, better accuracy can be obtained by analysing the velocity at both sides of the sample than could be obtained with stress data. The velocity calculated in the standard analysis for the incident interface is Lagrangian, but that for the other interface is definitely not. Nevertheless, we can estimate the Lagrangian wave amplitudes from the measured ones if we can determine the reflection properties at this interface.

Consider the experiment in pressure-particle velocity space as illustrated in Figure 3. If the impedence of the wave reflected back into the sample at the transmitted interface is equal to that of the wave incident on that interface, the ratio of the Lagrangian particle velocity, u_L, to the measured particle velocity, u_m, can be calculated from the geometric relations: $(u_L/u_m) = (\rho_b D_b/2\rho_s D_s)+1/2$, where ρ is density, D is wave speed, and subscripts b and s refer to the bar and the soil, respectively. As a check, we can also note that the pressures are related by $(P_L/P_m) = (\rho_s D_s/2\rho_b D_b)+1/2$. If, on the other hand, the impedence of the reflected wave is n times that of the incident wave (as illustrated, for example, by the dashed lines in Figure 3), we find that the ratios are $(u_L/u_m) = (\rho_b D_b/(n+1)\rho_s D_s)+n/(n+1)$ and $(P_L/P_m) = (n\rho_s D_s/(n+1)\rho_b D_b)+1/(n+1)$. It is usually possible to determine the velocity of the first loading wave and the first reflection from the Hopkinson bar data; we have occasionally detected the second arrival at the transmitter bar.

The technique outlined in the preceding paragraph will work well as long as the crush curve of the soil is fairly smooth and the two waves are both compressive. However, in two situations of interest the procedure will break down. First, if the crush curve of the soil is not smooth, the reflection coefficient will not be nearly constant, and a simple multiplicative factor will not represent the true variability of the Lagrangian wave form. This might occur if the soil has a very sharply defined yield point or if all of the gas-filled porosity is crushed out. In the former case the reflection coefficient may decrease dramatically as the yield point is exceeded, whereas in

the other case it may increase sharply. Second, if the incident wave has a rarefaction phase, this will likely have a substantially higher impedence than the compression which would occur upon its reflection from the transmitter bar. The result would be a very complicated geometric configuration in the pressure-particle velocity plane. Although a scheme comparable to the one described above could probably be developed, this has not been done to date. Consequently, we present data below only for the initial loading portion of the experiment.

To illustrate this method, consider the data from four experiments on a very dry (about 3 percent water by dry weight) desert alluvium from Luke Air Force Base, AZ, shown in Figure 4. The incident wave amplitudes are all within 2 percent of the same value; two of the experiments used a sample 25 mm thick (22 and 24) and the other two used a 13 mm sample. The data taken from experiments 21, 23 and 24 show that reflections from the transmitter bar interface travel about 1.6 times faster (Lagrangian wave speed) than the wave incident on that bar through the sample so we have used n=1.6 in our data reduction. There are two ways in which the data from the four experiments could be grouped for Lagrangian analysis; we could either analyse each experiment separately or we could analyse both experiments with the same projectile as a unit. We have adopted the latter approach, using the incident interface velocity as the first gauge, the transmitted interface velocity from the 13 mm sample as the second gauge and the transmitted velocity from the companion 25 mm experiment as the third gauge. The amplitude of the second transmitted velocity record was scaled up or down by the amount necessary to bring the incident signal of the second experiment into coincidence with that of the first.

The results of the Lagrangian analysis of the initial loading portions only of the four experiments are shown in Figures 5 and 6. As can be seen from Figure 5, the strain rates actually experienced are 1800 to 5000 sec^{-1}, about twice as great as those determined from the standard analysis. This is because the deformation is not distributed uniformly through the sample during the wave propagation portion of the experiment (which is represented by the initial loading). The differences between the loading paths for the two experiments (Figure 6) are probably not significant.

Figure 7 compares the stress-strain paths for the Hopkinson bar experiments with those from gas gun experiments and a quasistatic uniaxial strain test on the same material. The strain rates for the gas gun tests are in the range of 10,000 sec^{-1} to 30,000 sec^{-1} as compared with 1800 sec^{-1} to 5000 sec^{-1} for the Hopkinson bar. There is apparently a considerable effect on the loading modulus when the strain rate is increased from 5000 sec^{-1} to 10,000 sec^{-1}. The gas gun data were for continuous compression over several microseconds, not for discontinuous shock waves; the gas gun stress-strain paths are, therefore, true loading paths and not just Rayleigh lines connecting some initial and final states. The stress-strain path for loading in the quasistatic test ($\dot{\varepsilon}=5\times10^{-3}$ sec^{-1}, 2.8 percent water) is indistinguishable from those of the Hopkinson bar loading over almost all of the range of the data and coincide with the unloading data from the gas gun tests. We conclude, therefore, that the onset of strain-rate effects is rather sudden, affecting the loading path (but not the strain at peak stress) for strain rates above 5000 sec^{-1}. We also note that the dynamic unloading path is considerably less stiff than the quasistatic unloading indicating that the strain-rate effect is also present on unloading for strain rates as low as 2000 sec^{-1}. Our present inability to reduce data for the unloading portion of the Hopkinson bar test prevents us from locating more precisely the lower limit strain rate for which strain-rate effects are important on unloading.

ALTERNATIVE MEASUREMENTS

In addition to the above techniques which we have used to obtain valid data from Hopkinson bar experiments in soils, there are several other techniques which might be applied, but have not yet been (to our knowledge). These include Lagrangian measurements within the sample, use of stress gauges at the interfaces between the bars and the sample, and alternative methods of support.

We have conducted a few experiments with stress gauges embedded in a Hopkinson bar specimen. These experiments have included carbon foils in a thick stack of electrolytic grade mica (muscovite) and strain gauges potted into a cylinder of polymeric material. Both types of experiment yielded good data, but, as of this writing, analysis of these experiments is not complete. Furthermore, neither of these types of gauges could be used in soil with our current massive containment method.

Quartz stress gauges have been used between the specimen and the bar to measure directly the stress at the sample/bar interfaces in Hopkinson bar tests of foam materials [4]. These foams present problems of low wave speed and high attenuation comparable to those encountered in dry soils but do not have the added complication of lack of shear strength. As with the truly Lagrangian measurements of the preceding paragraph, it would be very difficult to combine this approach with the massive containment.

Ways can certainly be found to provide sufficient radial support to keep the sample in place for the dynamic load without resorting to massive containment. As mentioned in a previous section, confinement per se does not invalidate the Hopkinson bar test. If the radial stress and strain can be measured, it would be possible to derive stress-strain relations for strain paths intermediate between uniaxial stress and uniaxial strain. Such information would be very valuable in deriving constitutive models for general deformation paths. There are several possible ways to approach this problem, and we are pursuing some of them. Relaxation of our current massive containment conditions will also facilitate the use

of Lagrangian gauges which we have shown in the previous section will permit the use of very powerful analytic tools.

REFERENCES

[1] Kolsky, H., An investigation of the mechanical properties of materials at very high rates of loading. Proc. Phys. Soc. B62, 676-700 (1949).

[2] Davies, E. D. H., and S. C. Hunter, The dynamic compression testing of solids by the method of the split Hopkinson pressure bar. J. Mech. Phys. Solids 11, 155-179 (1963).

[3] Lindholm, U. S., Some experiments with the split Hopkinson pressure bar. J. Mech. Phys. Solids 12, 317-335 (1964).

[4] Hoge, K. G. and R. J. Wasley, Dynamic compressive behavior of various foam materials. Appl. Polymer Symp. 12, 97-109 (1969).

[5] Felice, C. W., J. A. Brown, E. S. Gaffney and J. M. Olsen, An investigation into the high strain-rate behavior of compacted McCormick Ranch sand using the split Hopkinson pressure bar technique. This volume.

[6] Gaffney, E. S., and J. A. Brown, "Dynamic material properties for Dry CARES alluvium." LA-UR-84-3795 (1984).

[7] Pochhammer, L., On the propagation velocities of small oscillations in an unlimited istropic circular cylinder. J. Reine Ange. Math. 81, 324-326 (1876).

[8] Chree, C., The equations of an isotropic elastic solid in polar and cylindrical coordinates, their solutions and applications. Traus. Cambr. Phil. Soc. A 14, 250-369 (1889).

[9] Follansbee, P. S., and C. Frantz, Wave propagation in the split Hopkinson pressure bar. J. Eng. Mater. Tech. 105, 61-66 (1983).

[10] Seaman, L., Lagrangian analysis for multiple stress or velocity gauges in attenuating waves. J. Appl. Phys. 45, 4303-4310 (1974).

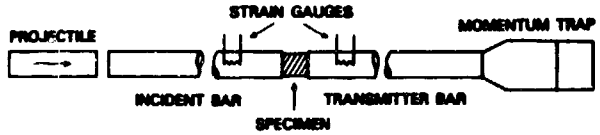

Figure 1. Schematic drawing of split Hopkinson bar apparatus.

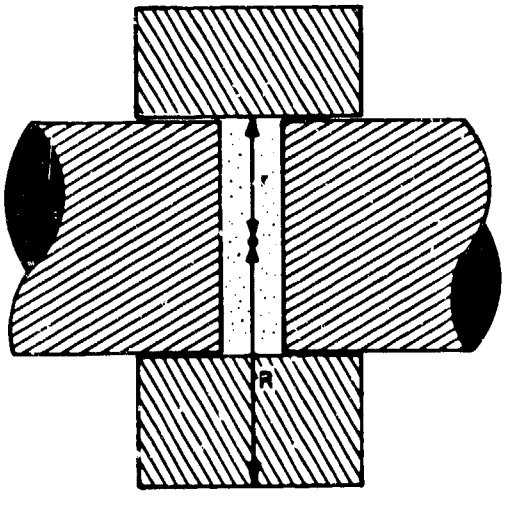

Figure 2. Sample containment scheme used to conduct uniaxial strain tests of soils in the split Hopkinson bar.

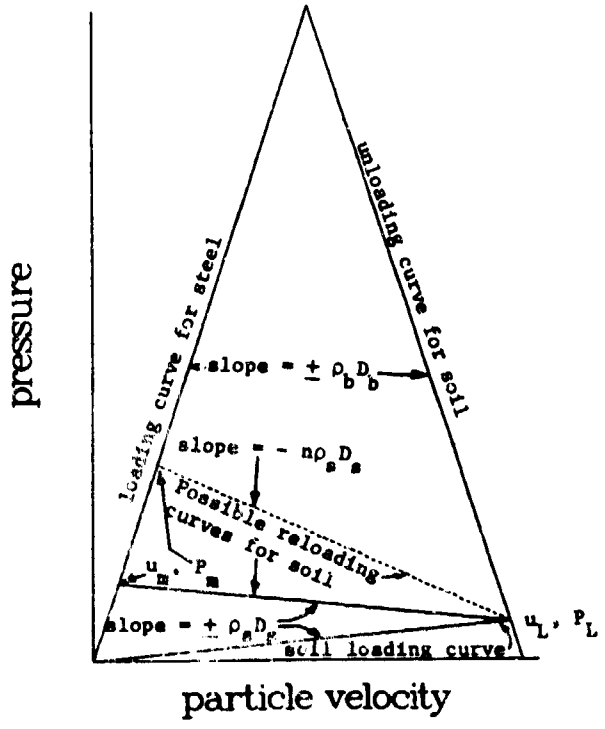

Figure 3. Pressure-particle velocity plot of split Hopkinson bar experiment showing relations used in converting transmitter bar data to free-field Lagrangian equivalent. See text for discussion.

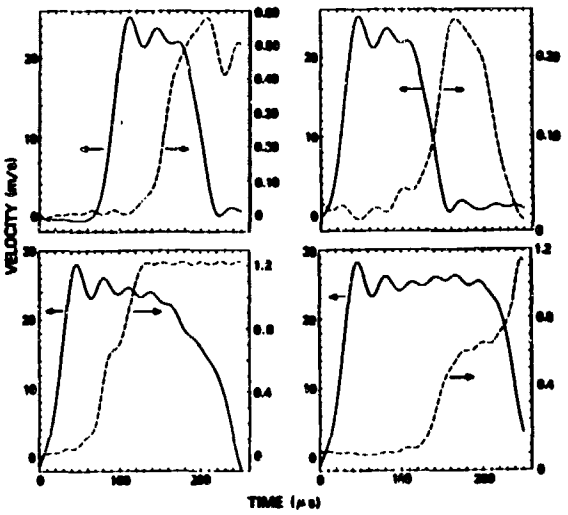

Figure 4. Interface velocity histories for four Hopkinson bar tests of dry desert alluvium [6].

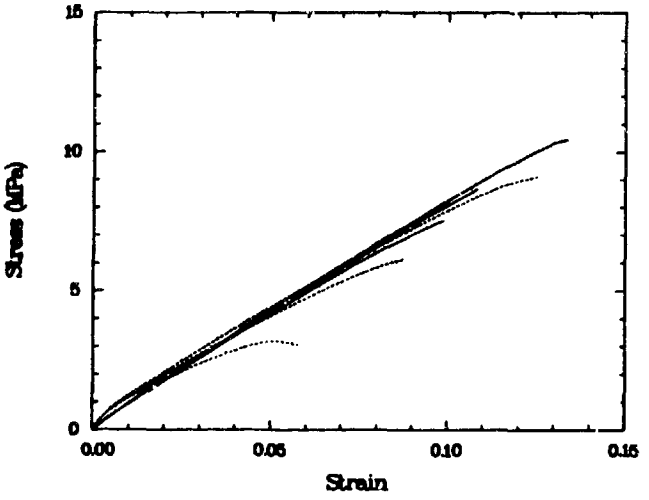

Figure 6. Stress-strain paths derived for initial loading of desert alluvium in Hopkinson bar.

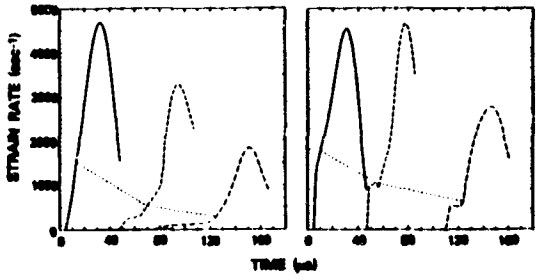

Figure 5. Strain-rate histories derived from data in Figure 4.

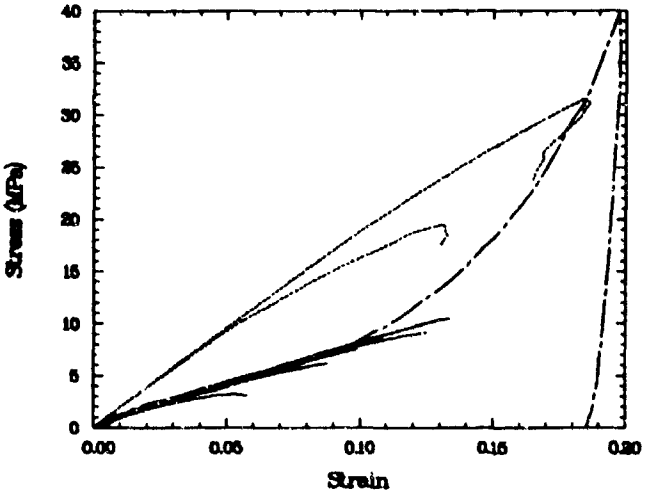

Figure 7. Stress-strain paths for several types of uniaxial strain deformation of dry CARES alluvium: dashed = gas gun, solid = Hopkinson bar, chain dash = quasistatic.

IMPULSE RADAR FOR DETECTION OF INTERNAL DAMAGE AND SOIL FEATURES

John G. Lyon
Dept. of Civil Engineering, The Ohio State University
Columbus, OH 43210

and

Ted Zobeck
Agricultural Research Service, U.S. Dept. of Agriculture
Big Spring, TX 79720

ABSTRACT

Impulse radar can help locate and determine the extent of internal damage or cracking in structures. Radar data can be interpreted for damage such as broken rebar, cracks in concrete or delamination, and the presence and size of voids. Radar systems are useful for location of buried structures, and for accurate measurement of depth to sewers, tunnels, and plastic pipe.

A project at OSU evaluated capabilities of radar for detection of objects buried in soils [17]. Radar data were used to discriminate soil features such as clayey and rocky layers, and to precisely measure depth to targets including air filled voids and steel pipe. Targets buried in a meter of wet, silty soil were measured with a precision of plus or minus 1.2 cm.

Analysis of literature and results of our projects indicate radar can locate cracks and voids in materials above and below ground, and radar is potentially valuable for measurement of damage.

INTRODUCTION

Evaluation of internal damage is difficult because it is often hidden by materials. For concrete, internal damage can be examined by serial sectioning or coring. This alters the integrity of the structure, and makes it difficult to evaluate effects of multiple damage. Hence, methods for nondestructive evaluation (NDE) are necessary for determinations of internal damage.

Impulse radar is a promising technique for nondestructive evaluations. These systems differ from conventional aircraft radar in several ways. The impulse radars are operated near or on the ground, and are used to evaluate features or structures near the unit. A relatively short nanosecond pulse with frequency between 10 and 1000 MHz is used to obtain good penetration and resolution of internal features. The returned radar wave is altered by varying conditions of materials and produces a signal which can be interpreted for anomolous structures or damage.

Radar has proven useful for applications requiring measurement of internal conditions of structures and ground probing of buried structures and objects. Radar applications include detection of cracks and voids in concrete pavements [3, 10, 4] and airport runways [1]. Radar has also proven valuable for locating underground voids such as mine shafts and sinkholes [5, 13], mapping the position rock fractures [11, 5], determination of the positions of drums in hazardous waste sites [7, 15], detection of soil features [12, 17], and location of buried plastic and concrete pipe have been determined [6, 2].

Laboratory and field tests have demonstrated the capability of radar and other NDE instruments for detection of structural damage [14, 8, 9]. These studies compared the capabilities of radar to other devices including chain drag, acoustics, electrochemical methods, and thermal infrared sensors. Evaluation of sensors in the above projects and work at OSU [6, 2, 17] indicate radar capabilities were very good in comparison to other sensors.

The capability for precise and accurate measurements of varying conditions of materials makes radar a potentially valuable NDE method for determinations of internal damage. Radar data can be used for classifying cracks and voids into damage classes and for determining serviceable concrete structures and damaged ones.

Radar and other NDE techniques are useful components of a multiple-test approach for determination of internal damage in structures [9]. The multiple-test approach includes visual inspection, selective sectioning of the damaged structure, and an electromagnetic technique such as radar.

BACKGROUND

Radar responds to inhomogeneity of the materials in the crack. Cracks are apparent as radar return altered from the normal response by differences in dielectric properties of air or water in the crack. Concrete has an approximate dielectric constant of 6, water is 81, and air is 1. The difference between the materials affects the radar signal returned from the material with cracks. The resulting altered signal can be interpreted for the location and size of damaged areas.

The radar signal also responds to reflection of radiation at the crack interfaces. Ray analysis can explain part of the signal returned to the radar. Both dielectric constant and radar reflection characteristics may be used to detect fractures.

Impulse radar systems operate in the time domain and distances to internal features are calculated from the time of return of signals. The time history of radar returns is displayed as a wave with varying amplitude, whose peak height is associated with the strength of signal returned. The characteristics of the signal amplitude and position of peaks are used to locate cracks.

The results of lab tests have shown that radar can measure the separation between concrete slabs at small increments from 0.0 to 30.0cm [1]. For separations of 0.0 to 7.5 cm between two similar materials, the change in amplitude of radar signal is proportional to the change in space between slabs. As the space increases in increments to 15.0 cm, the peak increases primarily in width. For spaces greater than 15.0 cm, the radar signal splits into two separate waveforms, thereby resolving the reflection from upper and lower boundaries of the crack. These signal characteristics allow location and identification of crack sizes or size classes.

THE EXPERIMENT

This study determined some capabilities and precision of radar for evaluation of mineral soils with numerous coarse fragments (soil 1) and soils derived from till and loess (soil 2). Careful determination of precision was necessary to ensure proper interpretations and to facilitate measurements of depth to subsurface features from radar traces. This study was part of a larger project to evaluate radar in the variable soil conditions common to glaciated and unglaciated regions of Ohio.

The impulse radar system has been described [12, 17]. For this project, the Geophysical Survey Systems radar (Hudson, NH) and ARS operator (J. Doolittle) were moved to Ohio and the system was operated as described.

Radar scans were made on undisturbed soil next to the face of a pit 1.5m deep. Markers were placed at different levels in the pit to calibrate radar measurements of depth. A 4.5 cm diameter bucket auger was used to bore horizontal holes at selected depths in the face of pits. Radar scans were repeated with the steel auger in each hole. Two depths (60.9 cm, 101.6 cm) were tested in soil 1 at the Coshocton site and in a pit of soil 2 at the Wooster site (50.8, 101.6 cm).

RESULTS AND DISCUSSION

The precision of the radar system was very good as judged by depth measurements. For soil 1, the radar measured depths were 60.9 cm and 60.8 cm as determined from two different scans of the pit. The actual depth of the marker was 61.0 cm. The difference in measurements was 0.3%. For the second calibration the radar depth measurements were 101.7 cm and 101.6 cm. They compared well with actual depth of 101.6 cm measured in the pit.

Radar traces from the Wooster pit (soil 2) indicated a similar capability for measuring depth. The first calibration depth was measured from the radar trace and calculated to be 48.0 cm, compared to the actual depth of 50.8 cm. The second calibration depth was measured and calculated to be 100.5 cm, as compared to the actual value 101.6 cm. The values for both soil 1 and 2 varied no more than 5.0% from the actual depth. The radar system was generally precise to plus or minus 1.2 cm in the silt or clay loam soils evaluated in the study.

CONCLUSIONS

Impulse radar systems can be used to measure depth of subsurface features *in situ* with good precision under suitable soil conditions. For soils tested, the precision of measuring depth to a metal auger or air void was within 5% of the absolute measurement value, or within plus or minus 1.2 cm of a given depth measurement. Results of this experiment are representative of the capabilities of radar for subsurface measurements.

Radar has potential as a nondestructive evaluation technology for assessment of damage to structures. Impulse radar systems can help to locate damage and assist prioritization of areas for further detailed examination.

FUTURE WORK

The experiment illustrated some of the precision of radar systems. These capabilities have been used with good success in studies mentioned here. Our work is directed to greater applications of radar for evaluation of damage in materials. We are currently developing a program of research in that area.

The program of research involves testing of materials and enhancement of radar scans to improve interpretation and measurement of internal features. This involves use of signal and image processing technologies developed at Ohio State [2, 16, 17] to enhance signals, reduce artifacts, and present data as profiles or map-like products (Fig. 1).

ACKNOWLEDGMENTS

The authors wish to thank James Doolittle, Soil Scientist, Agricultural Research Service (ARS), USDA, Florida, for his assistance in operating the radar and other technical assistance. Appreciation is extended to the staff at the North Appalachian Experimental Watershed,

ARS, USDA, Coshocton, OH, soil scientists from SCS, USDA, Ohio, OARDC, Wooster, OH, Department of Agronomy, OSU, and Ohio Department of Natural Resources, Division of Soil and Water Conservation for their generous support and hospitality.

The assistance of John Young and Ross Caldecott of The Ohio State University Electroscience Laboratory is also gratifully acknowledged.

BIBLIOGRAPHY

1. Alongi, A., T. Cantor, C. Kneeter and A. Alongi, Jr., 1982. Concrete Evaluation by Radar: Theoretical Analysis. Transportation Research Board, Record 853, National Academy of Sciences, Washington, DC, p. 31-37.

2. Caldecott, R., A. Terzuoli and J. Hall, 1979. An Underground Mapping System Using Impulse Radar. 7th IEEE/PES Transmission and Distribution Conference and Exposition, April, 9 pp.

3. Cantor, T. and C. Kneeter, 1982. Radar as Applied to Evaluation of Bridge Decks. Transportation Research Board, Record 853, National Academy of Sciences, Washington, DC, p. 37-42.

4. Clemena, G., 1983. Nondestructive Inspection of Overlaid Bridge Decks with Ground-Penetrating Radar. Transportation Research Board, Record 899, National Academy of Sciences, Washington, DC, p. 21-32.

5. Cook, J., 1974. Ground Probing Radar. Proceedings of the Conference of Subsurface Exploration for Underground Excavation and Heavy Construction, ASCE, p. 172-194.

6. Eberle, A. and J. Young, 1977. Development and Field Testing of a New Locator for Buried Plastic and Metal Utility Lines. Transportation Research Board, Record 631, National Academy of Sciences, Washington, DC, 19 pp.

7. Glaccum, R., R. Benson and M. Noel, 1981. Improving Accuracy and Cost Effectiveness of Hazardous Waste Site Investigation with a New Generation of Geophysical Methods. Presented at National Water Well Association Education Session, Kansas City, MO.

8. LaCroix, J., 1981. Bridge Deck Condition Survey. Report FHWA/IL/PR-094, Bureau of Materials and Physical Research, Illinois Department of Transportation, Springfield, IL, 42 pp.

9. Manning, D. and F. Holt, 1982. Detecting Deterioration in Asphalt-Covered Bridge Decks. Report ME-82-03, Research and Development Branch, Ontario Ministry of Transportation and Communications, Downsview, Ontario, 23 pp.

10. Manning, D. and F. Holt, 1983. Detecting Deterioration in Asphalt-Covered Bridge Decks. Transportation Research Board, Record 899, National Academy of Sciences, Washington, DC, p. 10-20.

11. Moffat, D. and R. Puskar, 1976. A Subsurface Electromagnetic Pulse Radar. Geophysics 41:506-518.

12. Shih, S. and J. Doolittle, 1984. Using Radar to Investigate Organic Soil Thickness in the Florida Everglades. Soil Sci. Soc. Am. J. 48:651-656.

13. Ulriksen, C., 1982. Applications of Impulse Radar to Civil Engineering. Doctoral Dissertation, Lund University of Technology, Dept. of Engineering Geology, Sweden, Coden:Lutudg/(TVTG-1001), 175 pp.

14. Weber, W., P. Grey and P. Cady, 1976. Rapid Measurement of Concrete Pavement Thickness and Reinforcement Location: Field Evaluation of Nondestructive Systems. Transportation Research Board, Program Report 237, National Academy of Sciences, Washington, DC, 63 pp.

15. Yaffee, H., N. Cichowicz and R. Pease, 1981. Evaluation of Abatement Alternatives Through the Use of Remote Sensing Devices. EPA Project Summary, EPA-600/S2-81-185, 7 pp.

16. Young, J., 1982. Comparative Performance Testing of Two Radar Pipe Locator Systems. Proceedings of the Workshop for Gas Distribution and Safety Instrumentation. Institute of Gas Technology, Kissimmee, FL, Feb., 19 pp.

17. Zobeck, T., and J. Lyon, 1985. Calibration and Interpretation of Ground Penetrating Radar Signals. Unpublished Note, Submitted for Journal review, 12 pp.

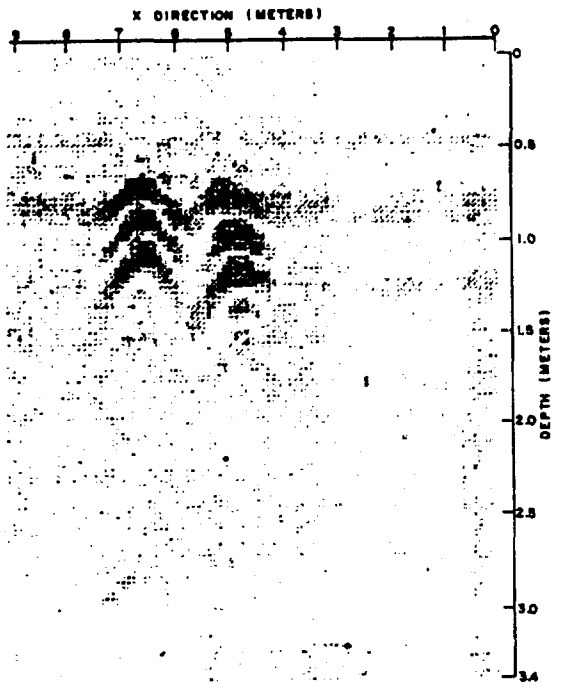

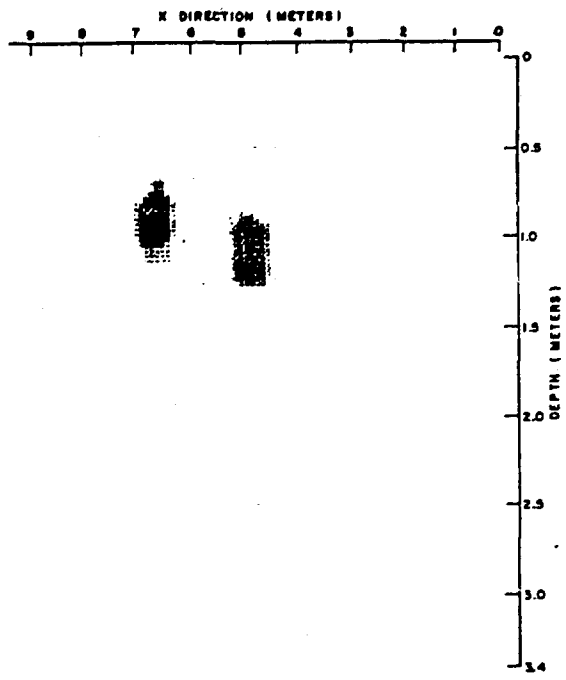

Fig. 1 a) Raw radar data scan of buried pipes. b) Scan after enhancements by OSU Electroscience Lab [2, 16]. c) Simulated map of plan view of damaged areas from radar transects of a pavement [17], d) Simulated three dimensional plot of damaged areas in c). The last three figures were developed to enhance the value of radar imagery for the operational user.

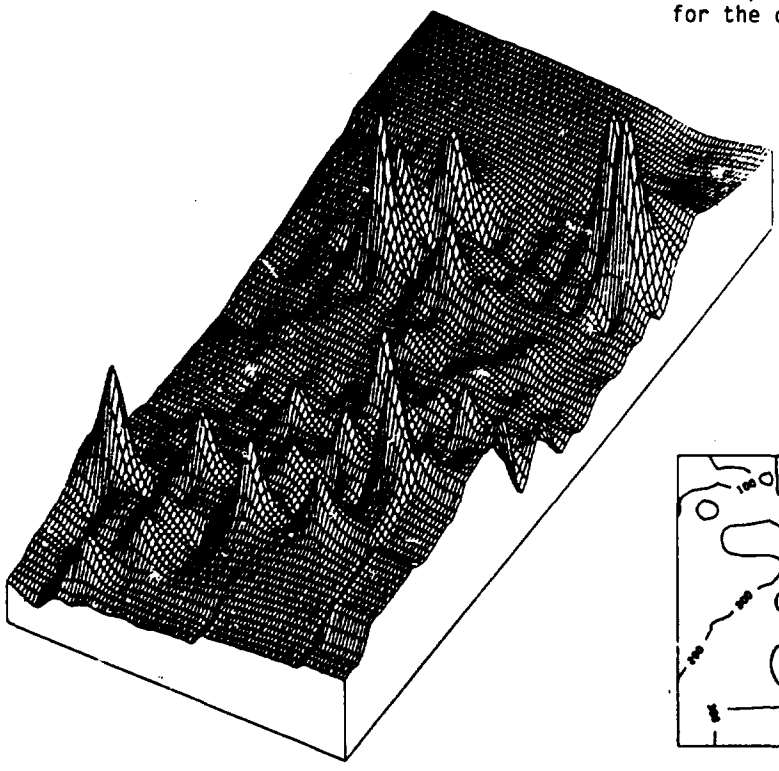

EFFECTS OF STRESS STATE AND STRAIN AMPLITUDE ON SHEAR MODULUS OF DRY SAND

K.H. Stokoe, II and S.H. Ni

Department of Civil Engineering
The University of Texas at Austin

ABSTRACT

The effect of stress state on the nonlinear shear modulus of the soil skeleton was examined for a dry sand. Testing was performed using a resonant column device with which isotropic and biaxial states of stress can be applied. Both solid and hollow specimens were used. Testing was performed over a range in shearing strains from 0.0005 to 0.2 percent and over a range in major principal stresses from 3 to 48 psi. This work was performed to determine if the behavior found in the large-scale triaxial device (described in a companion paper) could be duplicated with the resonant column. These tests confirmed the finding from the large-scale triaxial device that low-amplitude shear wave velocity, and hence shear modulus, depends about equally on the principal stresses in the directions of wave propagation and particle motion. Additionally, the tests show that the resonant column can be employed to study the effects of stress state and strain amplitude on shear modulus and material damping.

INTRODUCTION

The effect of stress state on the low-amplitude stiffness in shear and compression of the soil skeleton has recently been studied with the large-scale triaxial device. These tests resulted in the new finding that, when low-amplitude body waves are propagated along principal stress directions, only stresses in the directions of wave propagation and particle motion affect the waves. Wave velocities are essentially unaffected by principal stresses perpendicular to these directions. Unfortunately, only small strains could be generated in the sand specimens in the large-scale triaxial device. Therefore, a torsional resonant column has been developed with which larger strains can be generated. In addition, the effects of stress state and strain amplitude on material damping can simultaneously be studied. Results from initial tests with this equipment are presented herein.

RESONANT COLUMN

Resonant column equipment used in this research is of the fixed-free type. In this configuration, the bottom of the soil specimen is rigidly fixed to the base while the top (free end) is connected to a drive system that is used to vibrate the specimen in torsional motion. The soil specimens have the shape of a right circular cylinder and may be solid or hollow. The basic operational principal is to excite the cylindrical specimen in first-mode torsional motion. Once first mode is established,measurements are made of the resonant frequency, amplitude of vibration and free-vibration-decay curve. These measurements are then combined with equipment characteristics and specimen size to calculate shear wave velocity, shear modulus and shearing strain amplitude using elastic theory [Reference 1]. Material damping ratio is calcuated from measurement of the free-vibration-decay curve.

Fixed-free resonant column devices have been used at The University of Texas at Austin for over a decade. Each device consists of a confining pressure system, height-change measurement system, drive system, and response measurement system. However, several modifications were made for this project. First, a computer was added to the system so that data collection and reduction was completely automated. Second, the top cap and base pedestal of the resonant column were modified to permit the soil specimen to be loaded isotropically or anisotropically. Anisotropic loading was accomplished by adding an additional vertical load to an isotropically confined specimen through a thin central steel wire. Figure 1 shows the anisotropic mechanism axially loading a hollow specimen. The central wire was used so that boundary conditions independent of stress state remained essentially unchanged. The performance of the thin wire was verified by a series of analytical and experimental tests [Reference 2].

DATA REDUCTION

Calculation of shear wave velocity and shear modulus in the resonant column is based upon the theory of elasticity. By using the wave equation, the basic data-reduction equation can be expressed as [Reference 1]:

$$I/I_0 = (\omega l/V_s) \tan (\omega l/V_s) \qquad (1)$$

where

I = mass moment of inertia of soil specimen,
I_0 = mass moment of inertia of drive plate,
ω = resonant circular frequency,
l = length of the specimen, and
V_s = shear wave velocity.

Once the value of shear wave velocity is determined from Eq. 1, shear modulus, G, is calculated from:

$$G = \rho \times V_s^2 \qquad (2)$$

where

ρ = mass density of the soil.

By assuming a viscous material, material damping in shear is calculated from a decay of free vibrations. Because of space limitations, damping calculations and measurements are not presented.

Values of shearing strain, γ, are presented as single-amplitude values. For solid specimens, γ was calculated at 0.67 times the radius of the specimen. For hollow specimens, γ was calculated at the average of the inside and outside radii.

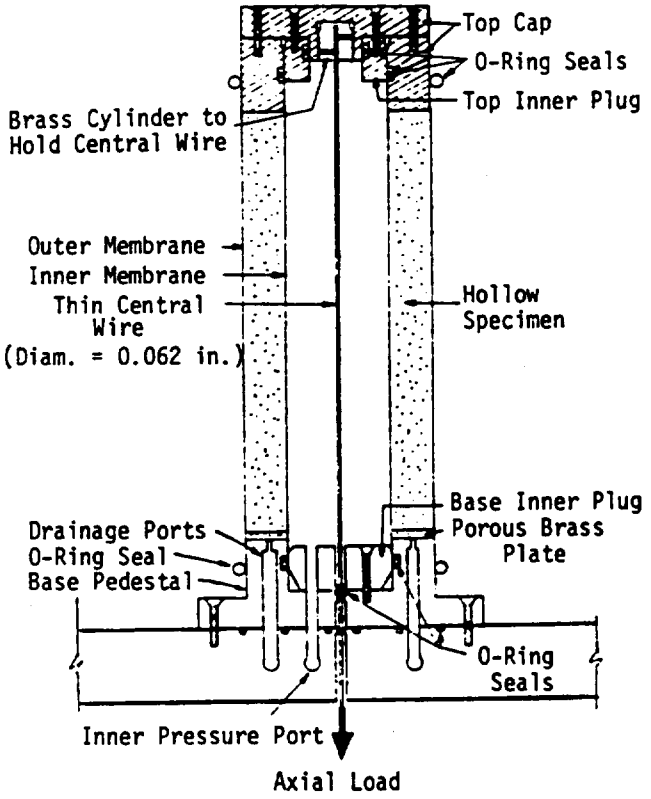

Fig. 1 - Anisotropically Loaded Hollow Soil Specimen.

SOIL SPECIMENS

The soil used in this research is air-dried sand which was also used in the study with the large-scale triaxial device. The sand is a medium to fine, washed mortar sand with a specific gravity of 2.67. The sand classifies as SP in the Unified Soil Classification System. Based on the average of five grain size analyses, the sand has an effective grain size, D_{10}, of 0.28 mm and a uniformity coefficient, C_u, of 1.71.

Two types of sand specimens were used. The first was a hollow specimen with nominal dimensions of: 1.43-in. inside diameter, 2.5-in. outside diameter and 5.6-in. height. The second type was a solid specimen with nominal dimensions of: 2.0-in. diameter and 4.0-in. height. An outer split mold was used to build the solid specimens. Two split molds, inner and outer, were required to build the hollow specimens. The inside diameter of the hollow specimens was controlled by the inner mold which was covered by an inner membrane during construction. The inner split mold has a small gap which allows the mold to collapse slightly upon withdrawal so that any friction between the inner split mold and inner membrane is nearly eliminated when it is pulled from the specimen.

Both types of specimens were constructed layer by layer with the "undercompaction" method described in Reference 3. Specimen information is included in Table 1. The average void ratio of all specimens is about 0.69 with a standard deviation of 0.01.

Table 1 - Summary of Specimens

Specimen No.	Specimen type	Dry unit weight, γ_d, pcf	Void ratio, e
S1	solid	98.7	0.69
S2	solid	98.4	0.69
S3	solid	99.8	0.67
H1	hollow	98.4	0.69
H2	hollow	98.0	0.70
H3	hollow	98.2	0.69
H4	hollow	99.7	0.68
H5	hollow	99.0	0.68
H6	hollow	98.3	0.70

STRESS NOTATION

The confining stresses applied on an element of soil during resonant column testing with anisotropic loading are shown in Fig. 2. The major principal effective stress, $\bar{\sigma}_1$, is applied in the vertical direction. This is also the direction of wave propagation which is denoted as $\bar{\sigma}_a$. The effective intermediate and minor principal stresses, $\bar{\sigma}_2$ and $\bar{\sigma}_3$, are equal and are applied in the lateral directions, circumferential and radial. Particle motion occurs in the circumferential direction and the stress in this direction is denoted as $\bar{\sigma}_b$. The stress in the third direction, the radial direction, is called the out-of-plane stress and is denoted as $\bar{\sigma}_c$.

TEST PROCEDURE

Stage testing was employed in all low-amplitude testing. Low-amplitude tests are defined as those tests in which shearing strains did not exceed 0.001 percent. Each low-amplitude test series was composed of three major stages on a loading pressure sequence. Shear modulus and material damping ratio were evaluated at each pressure. The first stage involved isotropically loading the specimen at 3, 6 and then 12 psi. The second stage involved increasing $\bar{\sigma}_a$ while holding $\bar{\sigma}_b$ constant. This was accomplished by increasing the load applied by the central wire while simultaneously keeping the lateral pressure constant. Vertical stresses of 14, 18 and then 26 psi were typically used. The third and final stage involved increasing $\bar{\sigma}_b$ while holding $\bar{\sigma}_a$ constant. Lateral stresses of 14, 18 and 26 psi were used. Stages 2 and 3 represent anisotropic loading of the specimen.

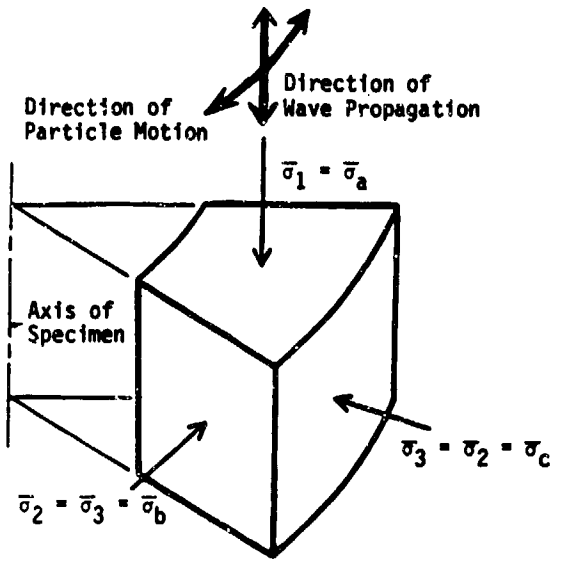

$\bar{\sigma}_a$: Effective principal stress in direction of wave propagation
$\bar{\sigma}_b$: Effective principal stress in direction of particle motion
$\bar{\sigma}_c$: Effective principal stress in out-of-plane direction (the direction perpendicular to $\bar{\sigma}_a$ and $\bar{\sigma}_b$ directions)

Fig. 2 - Principal Stress Directions and Associated Wave Movements.

After this first cycle of stage loading was completed, some specimens were loaded isotropically up to 48 psi. Other specimens were loaded with another anisotropic stage test between 26 and 48 psi. After testing at the final pressure was completed, all specimens were isotropically unloaded to 12 and 3 psi to evaluate any effect of overconsolidation.

High-amplitude tests were performed after all low-amplitude testing was completed. The same anisotropic stage loading sequence was used as in the low-amplitude tests. Both hollow and solid specimens were used. However, only hollow specimens were used in the high-amplitude anisotropic tests.

LOW-AMPLITUDE TESTS

Low-amplitude measurements were performed at shearing strains on the order of 0.0005 percent. At these strains, the shear modulus is essentially independent of strain amplitude and is commonly denoted as G_{max}. The notation of G_{max} is used because the magnitude of modulus decreases at strains above about 0.001 percent, and therefore the largest value of modulus is measured at small strains.

The variation in G_{max} with isotropic confinement is shown in Fig. 3. Tests with both hollow and solid specimens are shown. Shear moduli measured with either type of specimen are statistically the same within the bounds of experimental scatter. A linear log G_{max} - log $\bar{\sigma}_o$ relationship was obtained from a least-squares fit and is shown as the solid line in the figure. The equation of the straight line can be expressed as [Reference 4]:

$$G_{max} = \frac{S}{0.3 + 0.7e^2} \bar{\sigma}_o^{\,n} P_a^{\,1-n} \qquad (3)$$

where
S = material stiffness constant,
e = void ratio,
n = slope of log G_{max} - log $\bar{\sigma}_o$ line, and
P_a = atomospheric pressure.

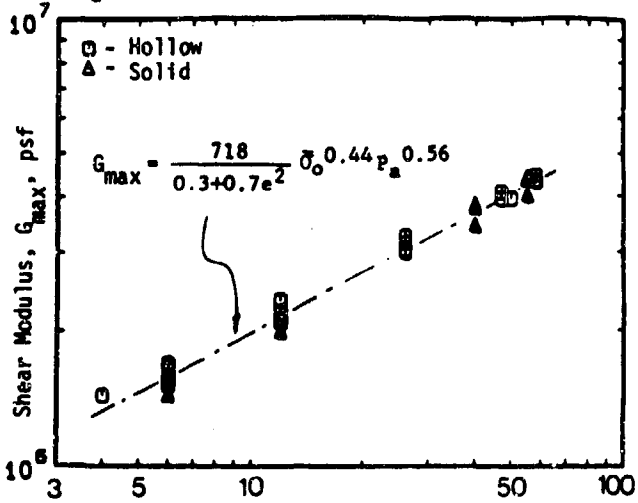

Fig. 3 - Variation in Shear Modulus with Isotropic Confining Pressure.

From isotropic tests, it is not possible to investigate the effect on G_{max} of the three principal effective stresses independently. As such, anisotropic tests were conducted in which the axial and lateral stresses were varied separately. However, only biaxial loading was performed in which $\bar{\sigma}_a$ and $\bar{\sigma}_b (= \bar{\sigma}_c)$ were varied independently. [The assumption was made that G_{max} was unaffected by $\bar{\sigma}_c$.] Typical results from these tests are shown in Fig. 4. The variation in G_{max} with stress in the direction of wave propagation, $\bar{\sigma}_a$, is shown in Fig. 4a. The log of shear modulus increases linearly with the log of axial stress, with the slope, na, equal to 0.22. On the other hand, the relationship between G_{max} and the stress in the direction of particle motion, $\bar{\sigma}_b$, is shown in Fig. 4b. The relationship between the log of shear modulus and log $\bar{\sigma}_b$ is also linear with the slope, nb, equal to 0.23.

A summary of the anisotropic test results is given in Table 2. The values of na and nb were calculated by the least squares method. As shown in the table, values of na and nb are not significantly affected by stress level, and little scatter is present. This scatter probably came from experimental scatter and/or multi-stage loading effects. It is reasonable to conclude that na and nb are independent of stress level. By taking average values for all stress levels employed, na equals 0.216 while nb equals 0.226. In the isotropic loading case, the average value of n equals 0.443. Therefore, the results from the anisotropic tests correctly predict the behavior under isotropic loading; that is, na plus nb equals n. [The assumption is made that nc

equals zero which seems reasonable from these results.] This is an important finding because it allows the conclusion to be made that shear modulus is dominated by two stress components, e.g. $\bar{\sigma}_a$ (the stress in the direction of wave propagation) and $\bar{\sigma}_b$ (the stress in the direction of particle motion). This finding agrees with a similar conclusion drawn from tests with the large-scale triaxial device in a companion paper.

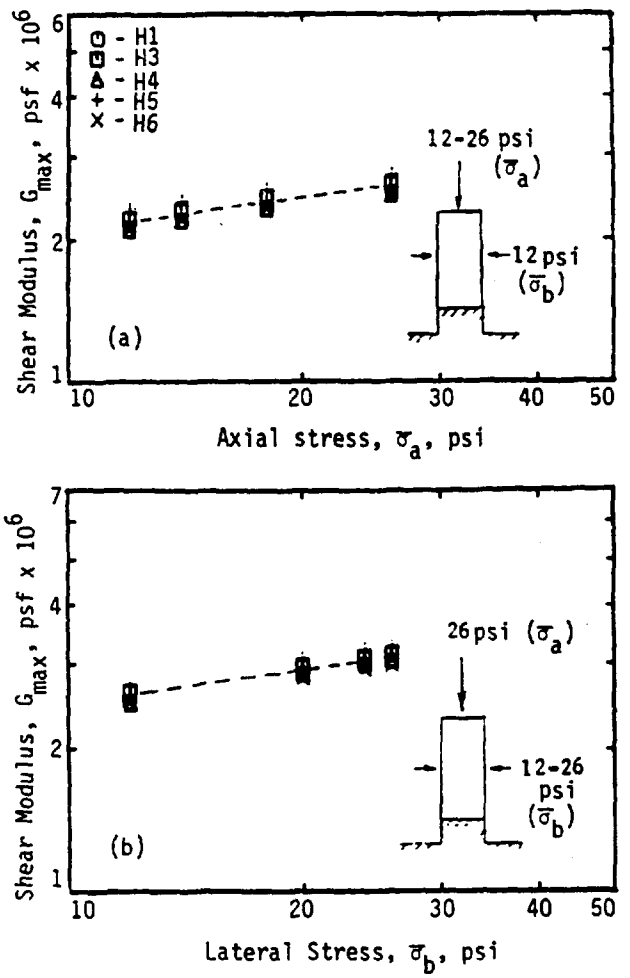

Fig. 4 - Variation in Shear Modulus Under Anisotropic Loading.

Table 2 - Summary of Anisotropic Test Results

σ_a (psi)	σ_b (psi)	na	nb	Specimen No.
6 - 12	6	0.22	----	H5, H6
12	6 - 12	----	0.23	H5, H6
12 - 26	12	0.22	----	H1 - H6
26	12 - 26	----	0.23	H1 - H6
26 - 47	26	0.21	----	H1, H3, H4
47	26 - 47	----	0.22	H1, H3, H4

From these results, the empirical equation recommended by Hardin [Reference 4] should be modified as:

$$G_{max} = \frac{S}{0.3 + 0.7e^2} \bar{\sigma}_a^{na} \bar{\sigma}_b^{nb} p_a^{1-na-nb} \qquad (4)$$

S is a function of soil type, grain size characteristics etc. Typical values of S for sands and silty sands are from about 400 to 800. In these tests, S equals 721 for the anisotropic tests and 718 for the isotropic tests. The stress index factors, na and nb, seem to vary only slightly with soil type. From these tests, average values are: na = 0.217, and nb = 0.228. It seems reasonable to assume that na equals nb, and, in this case, the value is 0.22. Therefore, Eq. 4 could be written as:

$$G_{max} = \frac{S}{0.3 + 0.7e^2} \bar{\sigma}_a^{0.22} \bar{\sigma}_b^{0.22} p_a^{0.56} \qquad (5)$$

The relationship between shear modulus and $(\bar{\sigma}_a \cdot \bar{\sigma}_b)^{0.22}$, is shown in Fig. 5. It is well defined by a straight line as predicted by Eq. 5. Also, moduli measured with both solid and hollow specimens are shown.

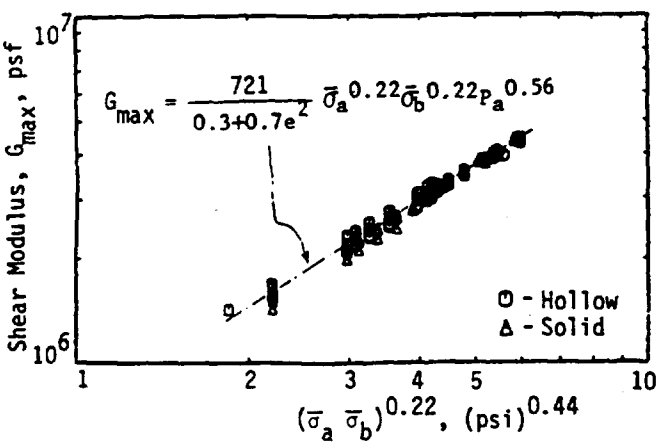

Fig. 5 - Relationship between Shear Modulus and Anisotropic Stress State.

A comparison between shear moduli measured in this study and moduli measured in other studies is shown in Fig. 6. The agreement in both trends and absolute values is good, and, when comparisons are made with other researchers, the scatter results mainly from variations in soil type.

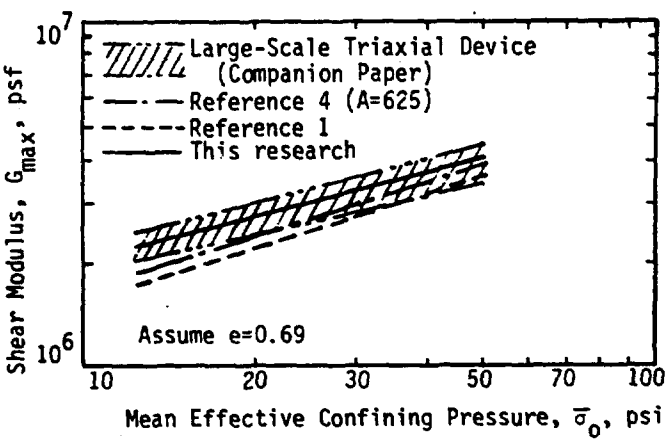

Fig. 6 - Comparison of Moduli from This and Other Studies.

HIGH-AMPLITUDE TESTS

High-amplitude measurements of shear moduli were performed at shearing strains above 0.001 percent. One set of tests with isotropic confinement is shown in Fig. 7. A second set of tests with anisotropic confinement is shown in Fig. 8. As shown in the figures, shear modulus decreases as shearing strain increases above a threshold strain of about 0.001 percent. This type of behavior has been well documented in many other studies [Reference 5]. However, these tests show the feasibility of using anisotropic resonant column tests to study this behavior.

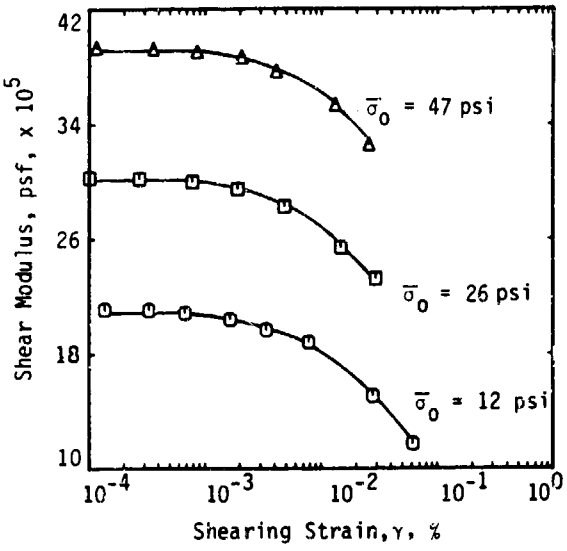

Fig. 7 - Variation in Shear Modulus with Shearing Strain under Isotropic Confinement.

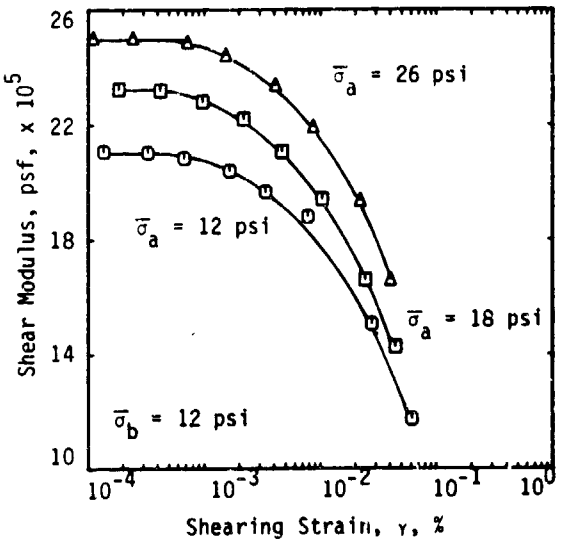

Fig. 8 - Variation in Shear Modulus with Shearing Strain under Anisotropic Confinement.

One convenient way of presenting the effect of strain amplitude on modulus is in terms of normalized modulus, G/G_{max}, versus the logarithm of shearing strain. The results presented in Fig. 7 are shown replotted in this fashion in Fig. 9. The value of G_{max} used at each confining pressure was simply the value of modulus measured at 0.0005 percent strain. Definition of a threshold strain below which modulus is constant is now clearly evident, and an approximate value of 0.001 percent is observable. In addition, it can be seen that for the value of normalized modulus at ay strain above the threshold strain increases as isotropic confining pressure increases. This behavior is typical of sands [Reference 6].

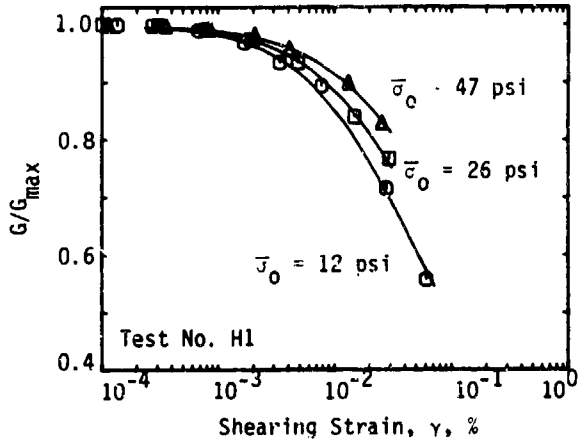

Fig. 9 - Variation in Normalized Shear Modulus with Isotropic Confining Pressure.

The data shown in Fig. 8 for anisotropic loading has not been plotted in Fig. 9 because there would be too much data in one figure. The data falls between the two curves for isotropic pressures of 12 and 26 psi as expected. It seems to indicate at this point that anisotropic loading is more important in affecting G_{max} than the G/G_{max} versus log γ curve. However, more work is required.

Although space considerations preclude a detailed presentation of the high-amplitude tests, it was found that Eq. 4 could be modified to predict the behavior shown in Figs. 7 and 8. The general equation with which modulus at high-amplitude strains can be predicted is:

$$G = \frac{\bar{S}}{0.3 + 0.7e^2} \bar{\sigma}_a^{\bar{na}} \bar{\sigma}_b^{\bar{nb}} p_a^{1-\bar{na}-\bar{nb}} \qquad (6)$$

in which $\bar{S}$, $\bar{na}$ and $\bar{nb}$ are the same factors as in Eq. 4 except that each one now varies with strain amplitude. The values of the parameters and their variation with strain are easily determined by using a Ramberg-Osgood curve fitting technique as discussed in Reference 5. Variations of $\bar{S}$, na, and $\bar{nb}$ with strain amplitude as shown in Figs. 10, 11, and 12, respectively. It is interesting to note that the effect of strain amplitude is most pronounced on $\bar{S}$. Values of $\bar{na}$ and $\bar{nb}$ exhibit some scatter, but the general trend of na and nb increasing with increasing strain amplitude is clearly evident. This behavior is consistent with that predicted by Mohr-Coulomb failure criterion. These results also

show the potential of the resonant column for investigating nonlinear behavior under anisotropic loading.

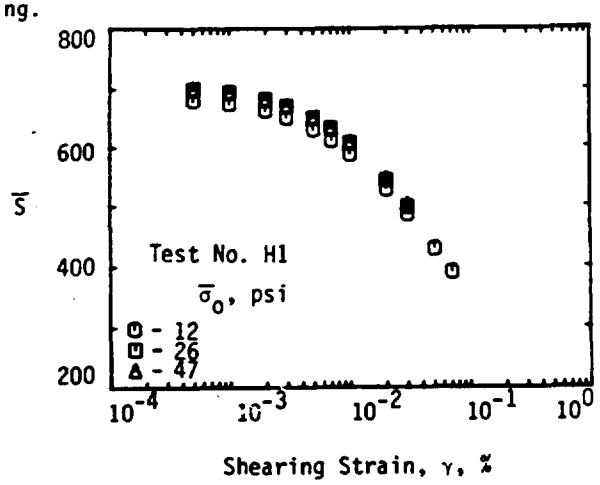

Fig. 10 - Influence of Strain Amplitude on $\bar{S}$ Under Isotropic Loading.

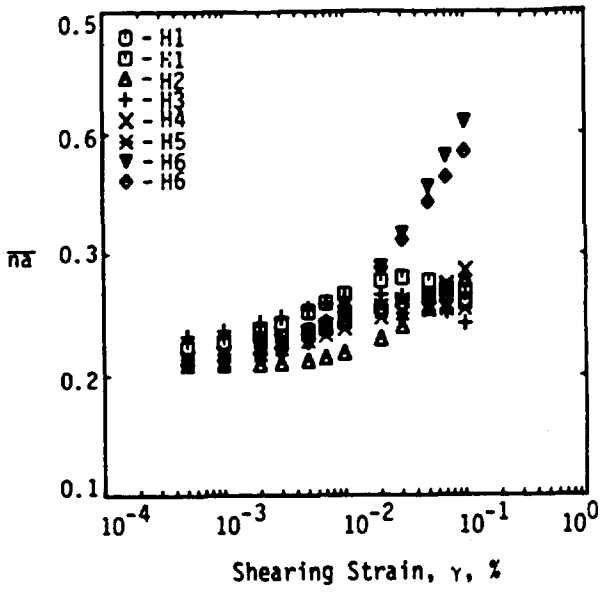

Fig. 11 - Influence of Strain Amplitude on $\overline{na}$ Under Anisotropic Loading.

CONCLUSIONS

A resonant column device was developed with which hollow or solid cylindrical soil specimens can be loaded either isotropically or biaxially. The resonant column is used to excite soil specimens in first-mode torsional motion from which shear modulus and material damping are evaluated. With this equipment, the shear modulus at small strains, G_{max}, of one sand was found to depend about equally on the principal stresses in the directions of wave propagation and particle motion (as defined by Eq. 5). These tests confirm similar findings with the large-scale triaxial device. In addition, the tests also demonstrate the feasibility of using anisotropic resonant column tests to investigate modulus and damping at higher strains.

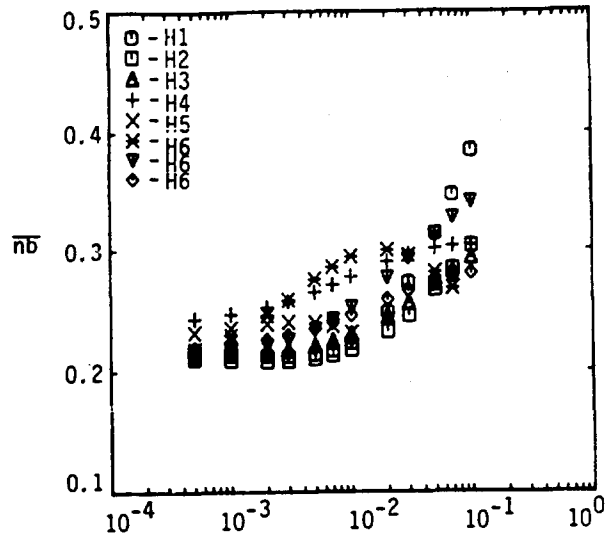

Fig. 12 - Influence of Strain Amplitude on $\overline{nb}$ Under Anisotropic Loading.

ACKNOWLEDGEMENTS

The authors would like to thank the U.S. Air Force Office of Scientific Research, Bolling AFB, for supporting this research. Lt. Col. Dale Hokanson was the project manager and his support and guidance are sincerely appreciated.

REFERENCES

(1) Richart, F.E., Jr., Hall, J.R., Jr., and Woods, R.D., (1970), Vibrations of Soils and Foundations, Prentice Hall, 414 p.

(2) Allen, J.C., and Stokoe, K.H., II, (1982), "Development of Resonant Column Apparatus with Anisotropic Loading," Report GR82-28, Civil Engrg. Dept., Univ. of Texas at Austin.

(3) Ladd, R.S., (1978), "Preparing Test Specimens Using Undercompaction," Geotechnical Testing Journal, ASTM, Vol. 1, No. 1, March, pp. 16-23.

(4) Hardin, B.O., (1978), "The Nature of Stress-Strain Behavior of Soils," Proc. Earthquake Engineering and Soil Dynamics Conf., ASCE, Vol. I, June, pp. 3-90.

(5) Woods, R.D., (1978), "Measurement of Dynamic Soil Properties," Proceedings of the Geotechnical Division Specialty Conference on Earthquake Engineering and Soil Dynamics, ASCE, Pasadena, California, pp. 91-178.

(6) Seed, H.B. and Idriss, I.M., (1970), "Shear Moduli and Damping Factors for Dynamic Response Analyses," Earthquake Engineering Research Center, University of California at Berkeley, California, Report No. EERC70-10.

(7) Ni, S.H., and Stokoe, K.H., II, (1985), "Evaluation of Anisotropic Shear Modulus with Resonant Column Device," Report GR85-3, Civil Engrg. Dept., Univ. of Texas at Austin. (In progress)

MEASUREMENT OF GROUND SHOCK IN EXPLOSIVE CENTRIFUGE MODEL TESTS

E. S. Gaffney, K. H. Wohletz and R. G. McQueen

Los Alamos National Laboratory, Los Alamos, NM 87545

ABSTRACT

Los Alamos National Laboratory has begun a project to simulate the formation and collapse of underground cavities produced by nuclear explosions using chemical explosions at much smaller scale on a large geotechnical centrifuge. Use of a centrifuge for this project presents instrumentation challenges which are not encountered in tests at similar scale off of the centrifuge. Electromagnetic velocity measuring methods which have been very successfully applied to such models at 1 g would be very difficult, if not impossible, to implement at 100 g. We are investigating the feasibility of other techniques for monitoring the ground shock in small-scale tests including accelerometers, stress gauges, dynamic strain meters and small, mutual-inductance particle velocity gauges. Initial results indicate that some of these techniques can be adapted for centrifuge applications.

INTRODUCTION

Los Alamos National Laboratory recently began a project to investigate some of the phenomena which are associated with the containment of underground nuclear tests. The experimental goal is to use small chemical explosive charges buried in simulated rock and soil on a centrifuge [1]. Although the ultimate objective of this project may be outside the scope of this conference, many of the experimental techniques that will be used are directly applicable to the simulation of the effects of non-nuclear munitions using centrifuge models. Because this program has just begun, this paper will focus on general considerations regarding the measurement of ground shock on the centrifuge; however, we will briefly discuss the results of some preliminary tests.

Explosives have been used for many years on centrifuges. One of the most extensive applications has been the investigations of explosively produced craters by Schmidt and various co-workers [e.g., 2-5]. One of us has also been involved in this and similar studies [6,7]. However, almost all such investigations have involved no in situ measurements of the ground shock that is the mechanism by which the explosive does its work. We have found only one report of a centrifuge investigation in which the ground shock amplitude has been measured [8]. In order to have confidence in the fidelity of scaled model simulations of explosive effects on structures, it is essential that the ground shock be measured in the free field and in the immediate vicinity of the structure. Only if we are correctly simulating the source of the loads on the structure can we be assured that measured structural responses will be similar to the responses of the full-scale structure.

BASIC GROUND SHOCK MEASUREMENT TECHNIQUES

Numerous techniques have been developed to measure many parameters of ground shock in a variety of environments including nuclear explosions, large high explosive (HE) field tests and smaller HE tests in a laboratory environment. In this section we review some of those methods without direct consideration of their adaptability to centrifuge testing; that adaptibility will be discussed in the next section.

Accelerometers have been successfully applied to the measurement of ground shock from large scale explosive events for many decades. In their most straightforward application, the acceleration is the measured quantity, but it is possible to integrate the basic output of the transducer to obtain both velocity and displacement. The integration can be done as a data reduction step after the experiment or in real-time, either in a circuit packaged with the transducer or in a seperate package removed from the ground shock environment. Real-time, close-coupled integration to velocity has the advantages that the signal to be transmitted is lower frequency (which will usually be easier to separate from noise) and that the velocity is frequently the ground shock parameter most needed in the application. Experience shows that, unless the accelerometer and its cabling are extremely stiff, accelerometers follow the motion of the surrounding medium faithfully.

One difficulty of accelerometers is that they do not return good data when the inverse of the ground shock rise time is near or above the resonant frequency of the transducer. Typically, accelerometers capable of measuring very high accelerations are small and have high resonant frequencies (e. g., Endevco 2291 rated at 1×10^7 m/s^2 with a resonance at >230 kHz). Accelerometers are designed to be sensitive to motion in a particular direction, but packages can be obtained with three devices mounted so that their sensitive

axes are mutually perpendicular. They typically have a sensitivity to transverse acceleration of a few percent of their nominal sensitivity. Another difficulty with accelerometers is occasional occurrence of drift and zero shift. Finally, accelerometer housings must be able to withstand the pressure that accompanies the acceleration in a ground shock pulse. However, despite their difficulties, accelerometers are unquestionably the mainstay of ground shock instrumentation for large scale events.

Induced electromotance is the basis of most techniques which directly measure the particle velocity in ground shock. The Lorentz force on electrons in a conductor moving in a uniform magnetic field was used by Zaitsev et el. [9]. When a large electromagnet is used to produce a uniform magnetic field perpendicular to the direction of the anticipated motion, the Lorentz force produces a current in a wire perpendicular to both the field and the motion. The current is proportional to the velocity of the wire which is small enough that it moves with the surrounding medium. More recent experiments have employed a cylindrical version to measure the azimuthal average of the radial velocity produced by a spherical charge [10]. This azimuthal averaging can be very useful in reducing the scatter of ground shock data caused by the inevitable variability of geologic materials. An electromagnetic particle velocity gauge has been developed in which the field is produced by a small permanent magnet rather than by a large electromagnet [11]; but the response of this gauge is highly non-linear, and it has not been employed in divergent flow.

Mutual inductance has also been used to measure particle velocity. Using two coils, both with their axes parallel to the direction of expected particle motion but separated in that direction, the velocity can be measured if a current is supplied to the upstream coil and the current is monitored in the downstream one. If the ground shock enveloping the source coil will sever the leads providing the current, a conductive plate can be placed inside the source coil to trap the flux for a duration dependent on its skin depth and thus prolong the useful life of the gauge [12]. After the shock envelops the outer coil, this gauge will only give a record of the relative velocity of the two coils.

Yet another electromagnetic velocity gauge consists of two long, thin coils wound together with the long direction being the expected direction of particle motion; a constant current is put through one of the coils and the current in the other is measured. As the end nearest the source begins to move, the area of the two coils decreases which produces a current in the pickup coil proportional to the rate of change of the area. If the flow is not significantly divergent, the result will be a measure of the particle velocity of that end of the gauge. As in the previous example, when the ground shock arrives at the end of the coils the gauge measures the relative velocity of the two ends [13].

The FDR displacement gauge is a gauge which directly measures the dynamic displacement in ground shock and has been used in large HE and nuclear tests. The gauge is essentially a coaxial cable aligned parallel to the direction of measurement; a frequency domain reflectometer is used to determine the length of the cable [14]. If the cable is very long and the upstream end is well coupled to the flow in the ground shock, the change in the length of the cable is the Lagrangian displacement at that end of the cable. For shorter cables, the gauge will measure displacement until the wave has encompassed both ends, and will measure the relative displacement of the two ends thereafter.

Almost all of the above described displacement, velocity and acceleration measuring systems have the potential of measuring strain, strain rate or strain acceleration as well. In some cases, such as the mutual inductance types of velocity gauge and the FDR displacement gauge, the potential can be achieved by using a smaller gauge and/or modifying the orientation. In most of the other cases, two separate gauges must be used and the strain derived by dividing the difference in their displacement by their separation.

In addition to parameters directly describing the flow field, measurement of the stress driving it is also desirable. Most measurements of stress in ground shock are accomplished with Lagrangian gauges which have transducers that are either piezoresistive or piezoelectric. The most common piezoresistive materials are foils of manganin, ytterbium or carbon-loaded polymer. Piezoelectrics include quartz, ceramics like lead zirconate titanate (PZT), lithium niobate, and recently polyvinylidene flouride (PVF_2).

In order to use these transducers successfully to measure ground shock, they must be packaged and emplaced to survive the flow and to deliver the proper stress to the transducer. The foil materials (the piezoresistives and PVF_2) can be made into very survivable flat-pack designs which will transmit the stress at the gauge surface to the transducer. Unfortunately, for the metals there is a considerable sensitivity to shear stresses which may also be delivered to the transducer. Carbon gauges have been shown to be sensitive only to the component of stress normal to the foil [15], so they should give reliable results in a flat-pack design.

The most critical requirement of stress gauges is that they be emplaced in such a manner that the free-field stress is also the stress measured by the transducer. This was discussed in a paper delivered at the first symposium in this series [16]. The flat pack design was specifically selected for this quality. However, that design only guarantees that the stress measured is that in the medium immediately outside the gauge package. If the gauge has been emplaced in a hole drilled into the free-field medium, stress bridging may still occur around the emplacement hole and its contents.

CONSIDERATIONS FOR CENTRIFUGE IMPLEMENTATION

Not all of the above-described types of gauge will be usable for measuring ground shock in a centrifuge test and others may require substantial modification. The centrifuge environment differs from the field and static laboratory environment in

that there are limitations on the mass and physical dimensions of the test, the entire experiment is rotating about the axis of the machine, and the initial accelerations are much greater than 10 m/s^2. These differences will make some of these methods impossible to deploy and will degrade or invalidate the performance of other techniques.

Use of accelerometers to measure ground shock in centrifuge model tests is very appealing because of the long history of their successful application to full scale measurements. However, their use in the centrifuge environment will necessarily involve some effort. Integration of acceleration records to get velocity and displacement is obviously sensitive to any initial acceleration; thus care must be taken that the test acceleration not interfere. Use of ac coupling schemes should permit the dynamic signal to be recorded without interference from the test acceleration. This consideration will apply to accelerometers in any orientation because of the transverse sensitivity of the transducers. The small scale of the model experiment can also present problems. First, because the experiment dimensions are small, risetimes will be proportionately shorter if hydrodynamic similitude is maintained. This may lead to accelerometers approaching their resonant frequencies. Second, the size of the accelerometer package may be large enough to perturb the flow field. For comparison to the same problem at full scale, consider a half-centimeter accelerometer encapsulated in a 2 cm package for a 100 g test. This would be equivalent to a 2 meter package at full scale.

All electromagnetic velocity gauges may be affected by the rotation of the centrifuge if the ambient magnetic environment is poor. The earth's magnetic field per se is probably so weak as to be no problem for gauge response, but the presence of large masses of magnetic steel moving either relative to the test or relative to the earth's field may prove troublesome. Sensitivity to this possibility will have to be determined on a case by case basis. If the rotation produces a problem of varying background field large enough to compromise gauge performance, ac coupling may be useful in eliminating the spurious signal.

Some of the electromagnetic techniques will not be useful in centrifuge experiments because of their requirement for large electromagnets. For example the coils used to produce the magnetic field for a recent series of meter-scale tests with explosive sources in soil conducted at Livermore National Laboratory [17] employed a pair of coils about 3 m high and weighing several tons. We feel confident in predicting that these coils will not be used in any centrifuge testing program; in view of the considerable success of this technique for measuring ground shock in model tests at 1 g, this is unfortunate.

Fortunately, particle velocity gauges of the mutual inductance type seem to offer excellent potential for application to the centrifuge environment. The only anticipated difficulty is that scaling them down will entail the use of thinner gauge wires which will be more fragile. Nonetheless, this type of gauge will almost certainly figure prominently in future centrifuge modelling programs.

The FDR displacement gauge also seems to be a likely candidate. The most apparent difficulty also seems to be the trade-off between size and fragility.

Stress gauges should experience little difficulty due to either the static acceleration or the rotation of the centrifuge. Size may be some problem, but both carbon and PVF_2 are available in very small (< 3 mm) sizes. Obtaining the desired sensitivities from small transducers of other types may not be possible.

PRELIMINARY TEST RESULTS

The objective of our work so far has been to test various gauge designs that may be adaptable to the centrifuge environment. We have tested various package designs for manganin and carbon stress gauges and have identified several potential problems for obtaining good records. We are currently testing accelerometers to identify design considerations. The goals have been to develop stress gauge packages that (1) create a minimum of reflected waves by good impedance matching with test materials, (2) ensure a gauge life that is greater than that of stress signals associated with shock waves, (3) are easily emplaced in heterogeneous materials such as alluvium and grout, and (4) can protect the gauge element from the test material.

Our initial tests used gauge packets placed in a tank of water with spherical high explosive charges. The charges were 1 and 2 inch (25 and 51 mm) diameter spheres of C-4 high explosive initiated by Reynolds RP-87 detonators. This approach allowed experiments to be setup easily and provided a harsher test for most gauges than would soil. Use of C-4 permitted quick molding of the charge to the desired size while saving expense. Presently we are experimenting in a sand bed, which is also relatively simple for experimental setup. Simple design encourages the repetition of many shots in preparation for the limitations imposed by the centrifuge.

Figure 1 illustrates a design for the manganin gauge package that, so far, has met our goals. The manganin gauge is mounted on a polycarbonate support with the sensitive element at right angles to the Kapton-coated leads. A coaxial cable is attached to the back of the gauge. A shorting pin extends about 1 mm in front of the sensing element; this pin is also attached to a coaxial cable. The whole assembly is potted in epoxy, which can be doped with corundum powder to obtain the desired density. The package is placed perpendicularly to the shock front. Upon contact, the shorting pin triggers an oscilloscope trace. The wave, with reflections of minimum amplitude, will then pass through the gauge along the axis of the wire leads. In this manner, the wave must travel several centimeters before it can shear the gauge leads; hence a relatively long record is achieved. A desirable feature of using the oscilloscope trigger is that the scope can be set to a fast measuring window, which allows detail of the wave profile to be obtained. With other recording techniques this pin might be redundant. Figure 2 shows two typical records for different charge sizes and different

gauge ranges in water. Note that the gauge orientation affects the shape of the measured signal.

We have also used carbon gauges in a flat pack design. Figure 3 shows the gauge sensitive element and leads encapsulated between two 1 mm thick sheets of mica. The gauge leads and mica plates are strengthened by potting in epoxy well away from the sensitive element. This design allows us to place the gauge perpendicular to the direction of stress wave propagation. The lifetime of the gauge is maximized by its tangential length, which determines the amount of time the shockwave must travel to reach the leads after hitting the gauge element. Figure 4 is a typical stress record obtained with a flat pack gauge in water.

Since the carbon gauge placement we employ is much different than that used for manganin, different geometrical problems (e. g., reflections, gauge motion and bridging across the gauge altering the free-field stresses) arise for each gauge. Shear strength in tuff and grouts used to simulate it is expected to be a major problem to overcome in achieving good stress records. The radial versus tangential arrangements described above are hoped to give us maximum gauge life.

We have experienced problems with electromagnetic noise from the detonator because it produces over 100 millivolts of moderate frequency (5 to 10 MHz) noise in unshielded leads. This noise may be an artifact of our simple charge design. However, we have found that by using coaxial leads wherever possible and aluminum foil shields around the gauge packages, the noise can be reduced to less than 10 millivolts. With further grounding of the shielding and use of better, cast charges,we are certain that the noise can be reduced to negligible levels.

FUTURE PLANS

Our program to measure ground shock produced from small HE explosions on a centrifuge has just begun. There is still much to be done at 1 g in the line of selecting and perfecting proper techniques before moving onto the centrifuge. As mentioned above, we are beginning to conduct tests in soil-like material. We expect to conduct tests in grouts designed to simulate the porous tuffs which occur at the Nevada Test Site. However, the primary thrust of these early experiments is upon measurement techniques, not on materials. During the coming months we plan to try several other stress and velocity gauges. In particular, we will investigate the feasibility of using the long electromagnetic particle velocity gauges and stress gauges using PVF_2 sensitive elements. Other plans include attempts to measure hoop stresses (with the carbon gauge described) and strains (with the FDR gauge and a strain-rate version of the long electromagnetic gauge). We hope that within the next year we will begin testing with fully confined bursts on a centrifuge.

REFERENCES

[1] E. S. Gaffney and J. A. Cheney, Containment science on a centrifuge. Proc. 2nd Symp. Containment of Underground Nucl. Expl., Kirtland AFB, NM, 2-4 Aug, 1983, Vol. II, 365-378, CONF-830882, Defense Nucl. Agency, Kirtland AFB (1983).

[2] Holsapple, K. A., and R. M. Schmidt, On the scaling of crater dimensions, 1, explosive processes. J. Geophys. Res. 85, 7247-7256 (1980).

[3] Holsapple, K. A., and R. M. Schmidt, On the scaling of crater dimensions, 2, impact processes. J. Geophys. Res. 87, 1849-1870 (1982).

[4] Housen, K. R., R. M. Schmidt and K. A. Holsapple, Crater ejecta scaling laws: Fundamental forms based on dimensional analysis. J. Geophys. Res. 88, 2485-2499 (1983).

[5] Schmidt, R. M., "Gravity Effects in Cratering", Bimonthly Prog. Rep. 2, January 15 1983, Boeing Aerospace Company on contract DNA001-82-C-0301 (1983).

[6] E. S. Gaffney, Effects of gravity on explosion craters. Proc. Lunar Planet. Sci. Conf. 9th, 3831-3842 (1978).

[7] E. S. Gaffney, H. K. Brown and J. A. Cheney, Explosion craters in ice at large scaled yields. Lunar and Planet. Sci. XIV, 233-234 (1983).

[8] P. L. Rosengren, Jr., Centrifuge modeling techniques. Symp. Proc., Pt. 2, Interaction of Non-nuclear Munitions with Structures, U. S. Air Force Academy, CO, 10-13 May, 1983, 25-28 (1983).

[9] V. M. Zaitsev, P. F. Pokhil and K. K. Shvedov, An electromagnetic method for measuring the velocity of detonation products. Doklady Akad. Nauk SSSR, 132 (6), 529-530 (1339-1340 in Russian) (1960).

[10] A. L. Florence, J. C. Cizek and C. E. Keller, Laboratory experiments on explosions in geologic materials. Shock Waves in Condensed Matter--1983, J. R. Asay, R. A. Graham and G. K. Straub, eds., Elsevier, New York (1984).

[11] J. N. Fritz and J. A. Morgan, An electromagnetic technique for measuring material velocity. Rev. Sci. Instr. 44, 215-221 (1973).

[12] P. L. Coleman, Development of the Kratz particle velocity gauge. Conf. on Instr. for Nucl. Weapon Effects, Mar 30-Apr 1, 1982, DNA-TR-82-17, pp. 137-148, Defense Nuclear Agency, Washington (1982).

[13] A. L. Florence, D. D. Keough and R. Mak, Calculational evaluation of the inclusion effect on stress gauge measurements in rock and soil. Symp. Proc., Pt. 2, Interaction of Non-nuclear Munitions with Structures, U. S. Air Force Academy, CO, 10-13 May, 1983, 7-11 (1983).

[14] T. O. Summers, The FDR particle displacement gage electronics. Proc. 30th Intern. Instrum. Symp.-Denver, Colorado, 647-654, Intrum. Soc. Am. (1984).

[15]. W. D. Williams, D. J. Fogelson and L. M. Lee, Carbon piezoresistive stress gauge. Shock Waves in Condensed Matter-1983, J. R. Asay, R. A. Graham and G. K. Straub (eds.), 121-124, Elsevier, New York (1984).

[16] C. W. Smith, D. E. Grady, L. Seaman and C. F. Petersen, Constitutive relations from in situ Lagrangian measurements of stress and particle velocity. DNA-2883I, Defense Nuclear Agency, Washington (1972).

[17] Don Larsen, personal communication (1984).

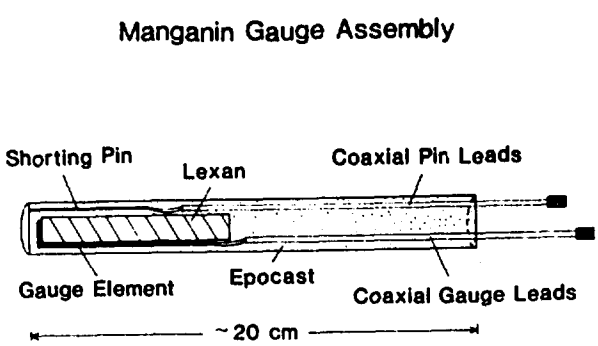

Figure 1. Sketch of manganin gauge assembly.

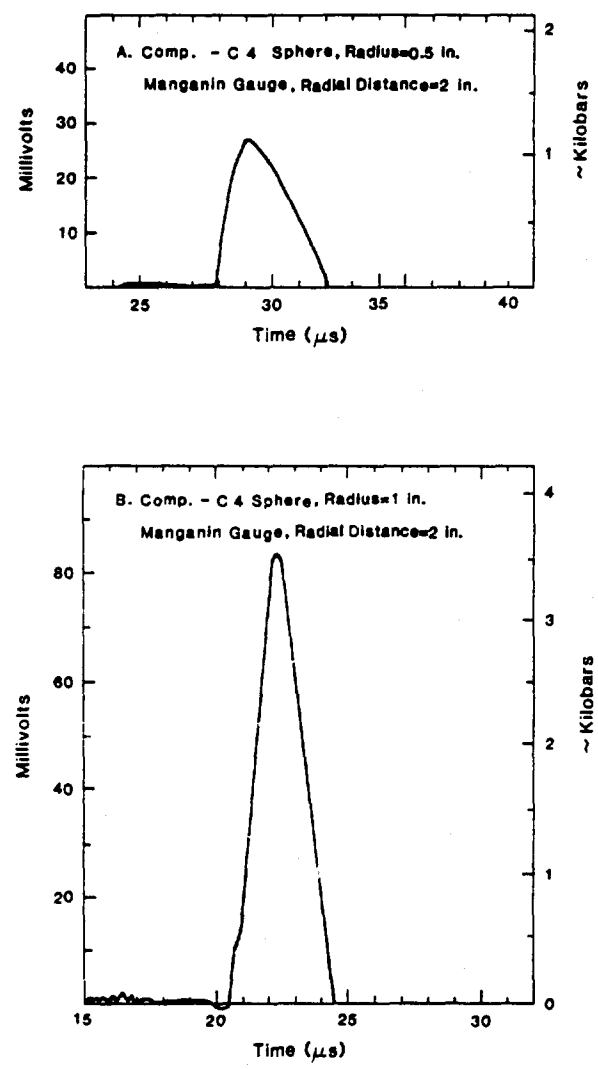

Figure 2. Pressure histories recorded from manganin gauges. (a) Charge diameter, 25.4 mm; gauge range, 50.8 mm. (b) Charge diameter, 50.8 mm; gauge range, 50.8 mm.

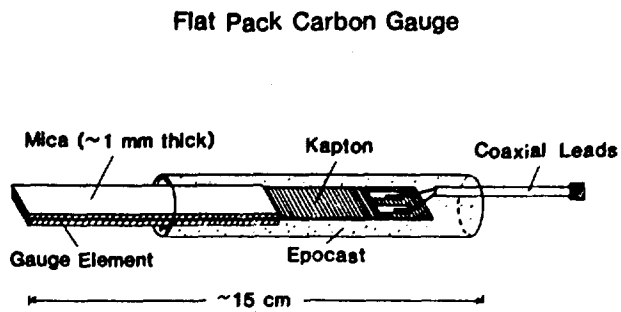

Figure 3. Carbon flat pack gauge assembly.

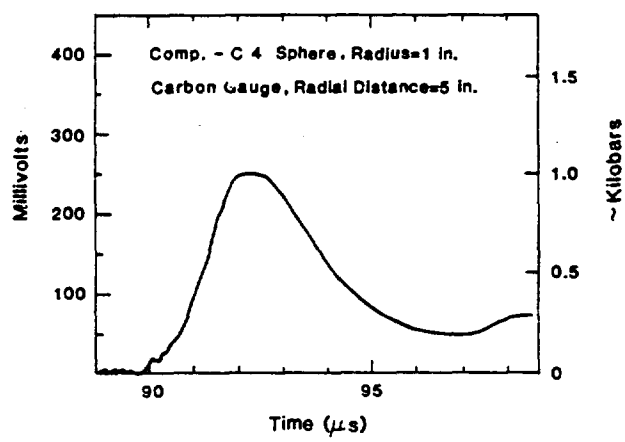

Figure 4. Pressure trace measured by carbon gauge at a range of 127 mm from a 50.8 mm diameter charge of C-4.

CENTRIFUGE MODELING OF ADVECTION AND DISPERSION PROCESSES DURING POLLUTANT TRAVEL IN SOIL

K. Arulanandan, P. Y. Thompson*, N. J. Meegoda, B. L. Kutter and R. B. Krone

Department of Civil Engineering, University of California, Davis, CA 95616
*Tyndall Air Force Base, Panama City, Florida 32403

ABSTRACT

The processes that occur during the movement of chemicals through soils are outlined. Feasibility of accelerating the transport of chemicals in the centrifuge is studied by performing 'modeling of model' tests. The influence of stress level on chemical dispersion and advection is studied. The results show the potential applicability of centrifugal modeling for the acceleration of transport process during chemical travel.

INTRODUCTION

Movement of liquid pollutants into soil and water bearing strata from spills, waste disposal ponds, and landfills is governed by the processes of advection, dispersion, adsorption, and degradation. The first three of these processes are strongly affected by the character of the soil, particularly the grain size distribution, aggregation of particles, mineral composition, soluble salt type and amount, and the pore size distribution and shape. Adsorption and degradation depend on properties of the polluting compound as well as the character of mineral surfaces and possibly soil organic matter. It follows that typical heterogenous soils, having strata of differing characteristics, provide very complex media for the transport of pollutants. Prediction or evaluation of the movement of pollutants in such soils requires consideration of all the processes described above for the complex soil system.

Analyses of problems of this nature are currently carried out using mathematical simulation studies (Javandel et al. (1984), Orlob (1984)). The accuracy of the mathematical simulation studies depends, among other factors, on the accuracy of the input parameters. For example, many investigators have concluded that values of longitudinal and transverse dispersivities in field systems are significantly larger than those values obtained in laboratory experiments on homogeneous materials or on materials with simple heterogeneities. The determination of input parameters such as permeability and diffusion coefficients in the laboratory for use in mathematical models must be such that they represent the in situ stress conditions which are very difficult to simulate in the laboratory.

Predictive methods, e.g. mathematical models, are used to indicate the major changes and the possible magnitude of the changes during the transport process, but these have been difficult to verify, due largely to lack of adequate data. Simulation costs are often high for the more complex models such as two or three dimensional models, since the time horizon of interest may span decades of real time. Detailed representation of geological structure, also possible in such models, adds to the difficulty of simulation of the transport of pollutants.

Certain of these difficulties may potentially be overcome by the use of centrifuge modeling. In particular, it should be feasible by such models to greatly accelerate the transport processes that govern the fate of pollutants as they move through soils and aquifers. This should greatly enhance general predictive capability and also improve and verify the capabilities of mathematical models now being used.

PHYSICAL TRANSPORT PROCESSES

The common starting point in the development of differential equations to describe the transport of solutes in porous materials is to consider the flux of solute into and out of a fixed elemental volume within the flow domain. A conservation of mass statement for this elemental volume is

$$\begin{bmatrix}\text{net rate}\\ \text{of change}\\ \text{of mass}\\ \text{of solute}\\ \text{within the}\\ \text{element}\end{bmatrix} = \begin{bmatrix}\text{flux of}\\ \text{solute}\\ \text{out of}\\ \text{the}\\ \text{element}\end{bmatrix} - \begin{bmatrix}\text{flux of}\\ \text{solute}\\ \text{into}\\ \text{the}\\ \text{element}\end{bmatrix} \pm \begin{bmatrix}\text{loss or}\\ \text{gain of}\\ \text{solute}\\ \text{mass}\\ \text{due to}\\ \text{reactions}\end{bmatrix}$$

The physical processes that control the flux into and out of the elemental volume are advection and hydrodynamic dispersion.

Advection is the component of solute movement attributed to transport by the flowing water. The rate of transport is equal to the average linear water velocity, $\bar{v}$, where $\bar{v} = v/n$, v being the specific discharge and n the porosity. There is a tendency, however, for the solute to spread out from the path that it is expected to follow according to the advection hydraulics of the flow system. This spreading phenomenon is called hydrodynamic dispersion. It causes dilution of the solute. It occurs because of mechanical mixing during fluid advection and because of molecular diffusion due to the thermal kinetic energy of the solute particles.

Our purpose here is to examine first as to whether the physical processes (advection and dispersion) can be modelled in the centrifuge. The objectives of this paper are: 1) to examine the validity of centrifugal modeling by performing 'modeling of model' tests and 2) to examine the influence of gravity on advection and dispersion processes.

The physical processes of advection and dispersion in a salt water bearing sand strata subjected to leaching by fresh water is examined.

SCALING LAWS

One-dimensional expressions for advection, dispersion, adsorption, and degradation for a saturated, homogeneous, isotropic medium, where the flow is in a steady state and where Darcy's Law is applicable can be written as

$$\frac{\partial C}{\partial t} = D_\ell \frac{\partial^2 C}{\partial \ell^2} - \bar{v}_\ell \frac{\partial C}{\partial \ell} - \rho/n \frac{\partial s}{\partial t} - k_d C \qquad (1)$$

where C = concentration of the chemical in the pore fluid
D_ℓ = longitudinal coefficient of dispersion
v_ℓ = average linear velocity along the flow line
ℓ = the coordinate direction along the flow line
ρ = bulk mass density of the porous medium
n = the porosity of the medium
s = the mass of the chemical constituent adsorbed on a unit mass of the solid part of the porous medium
t = time
k_d = the degradation coefficient of the chemical in the porous medium

Advection The second term on the right hand side describes advection of the pollutant through soil by the movement of pore fluid. Advection in a saturated soil depends on the following factors:

permeability of the soil, k (cm/s),
pressure gradient, I,
concentration, C (grms/cm^3)
cross-sectional area perpendicular to the flow, A (cm^2)
time t, (seconds)

The mass flow rate f(w/t) = f(k,I,C,A) where w is the total mass flowing in time t. Using dimensional analysis, considering (kI), C and A as parameters influencing mass flow rate (w/t) it can be written

$$w/t = M^1L^0T^{-1} = A^bC^c(kI)^d = M^cL^{2b-3c+d}\ T^{-d}$$

$$\text{i.e. } M^1L^0T^{-1} = M^cL^{2b-3c+d}\ T^{-d}$$

therefore c=1, d=1, and 2b-3c+d=0 and hence

b = 1. The non-dimensional constant becomes
w/t = A (kI) C or

$$\left[\frac{A(kI)Ct}{w}\right]_m = \left[\frac{A(kI)Ct}{w}\right]_p$$

where the subscript m refers to the model and p refers to the prototype.

But if $k_p=k_m$ i.e. same stress level, porosity, viscosity and mass density and if we maintain $I_m=I_p$, i.e. same pressure head in both model and prototype, and if we could model the amount of pollutant, i.e. $w_p/V_p = w_m/V_m$, which means mass of pollutant in unit volume of the soil is the same, then $C_p = C_m$ and we could now write

$$\frac{A_m k_m I_m C_m t_m}{w_m} = \frac{A_p k_p I_p C_p t_p}{w_p}$$

substituting $A_p=N^2A_m$, $V_p=N^3V_m$, $k_p=k_m$, $C_p=C_m$ and $w_p=V_p/V_m\ w_m$ we obtain $\underline{t_p = N^2 t_m}$, (2)

where N is the scale factor.

Dispersion The first term of the equation (1) describes the longitudinal mixing processes that result from the travel of pollutant by paths through the pores having different lengths and molecular diffusion. This representation, often called "Fick's Law", holds well in media where the diffusion coefficient D is constant. The factors that affect this term are:

diffusion coefficient, D (cm^2/sec)
cross sectional area perpendicular to the flow, A(cm^2)
concentration gradient, $\partial c/\partial x$ (grm/cm^4)
and time, t (sec)

The mass flow rate f(w/t) = f(D,A,$\partial c/\partial x$)
Using dimensional analysis, considering A,D, and $\partial c/\partial x$ as basic parameters influencing mass flow rate (w/t), one can write

$$w/t = M^1L^0T^{-1} = A^b(\partial c/\partial x)^c\ D^d$$

$$\text{i.e. } M^1L^0T^{-1} = L^{2b-4c+2d}\ M^c\ T^{-d}$$

therefore c=1, -d=-1, 2b-4c+2d=0 and hence b=1. The non-dimensional constant becomes

$$\frac{t\ AD\ \partial c/\partial x}{w}$$

and we can write

$$\left[(t/w)AD\left(\frac{\partial C}{\partial x}\right)\right]_m = \left[(t/w)AD\left(\frac{\partial C}{\partial x}\right)\right]_p$$

At the same stress level $D_m=D_p$ and if the mass of pollutant per unit volume of soil is the same i.e. $w_p/V_p = w_m/V_m$, then $C_p = C_m$

We can therefore write

$$t_m A_m D_m C_m / w_m x_m = t_p A_p D_p C_p / w_p x_p$$

Substituting $A_p=N^2A_m$, $x_p=Nx_m$, $V_p = N^3V_m$, $D_m=D_p$, $C_p=C_m$ and $w_p = V_p/V_m\ w_m$
we obtain $\underline{t_p = N^2 t_m}$ (3)

The scaling calculations above show that time would scale with N^{-2} for the process of advection and dispersion described by equation (1). Pollutant travel would scale N^2 faster in a physical model than in the prototype.

PHYSICAL ASPECTS OF MODELING

In addition to the similarity conditions established above for diffusion and advection processes, it is

necessary to maintain the validity of Darcy's Law. This can be maintained if the Reynolds number $R_e = \frac{vd}{\nu} \leq 1$

where v = the velocity of seepage
d = diameter of the soil grains
ν = kinematic coefficient of viscosity.

For the condition where $R_e = 1$, $\nu/d = v_{max}$

$$v_{max} = \frac{10^{-6}}{d} \frac{m}{sec} \quad \text{where } \nu = 10^{-6} \text{ meters}^2/\text{sec}$$

The rate of seepage in soil = $\frac{kI}{n}$

where k = permeability meters/sec
I = hydraulic gradient
n = porosity

$$v_{model} = \frac{kNI}{n}$$

For $v_{max} = v_{model}$

$$N = \frac{10^{-6}\, n}{kdI}$$

The maximum permissible scale factor for a clay with $k = 10^{-9}$ meters/sec, n = 0.5, I = i, and $d = 10^{-6}$ meters is

$$N = \frac{(10^{-6})(0.5)}{(10^{-9})(10^{-6})(1)} = 5 \times 10^{8}$$

Even for a fine sand with $k = 10^{-5}$ meters/sec, n = 0.5, I = 1, and $d = 10^{-4}$ m, the maximum permissible scale factor is

$$N = \frac{(10^{-6})(0.5)}{(10^{-5})(10^{-4})\ 1} = 500$$

Therefore the requirements of laminar flow will not be a significant problem for soils having effective grain sizes finer than fine sand.

TESTING PROGRAM AND RESULTS

Four sand models (referred to as models 1, 2, 3 and 4) varying in heights of 8.23, 6.18, 5.14 and 3.88 inches were prepared by pluviating and vibrating a fine sand (a uniform sand with a mean grain diameter of 0.42 mm) into a 0.08N salt water solution contained in a 5.0 inch diameter plastic cylinder (see Fig. 1). The modelled sand layer was prepared at a void ratio of 0.48. The permeability of the sand layer under 1 g condition was determined as 10.25×10^{-3} cm/sec. Models 1, 2, 3 and 4 were subjected to centrifugal accelerations of 25 g, 33.3 g, 40 g and 53 g respectively in the Schaevitz centrifuge (Figs. 2 and 3). Fresh water was allowed to seep through the models under a simulated excess head of 20.63 inches in all cases.

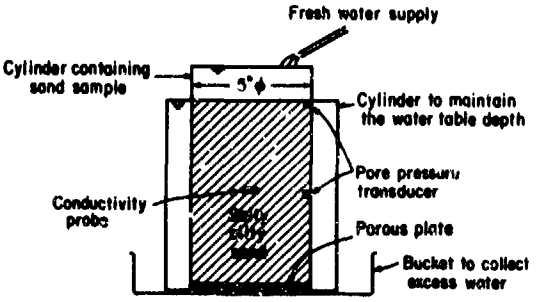

FIG. 1. Model setup used in the centrifuge for the four sand models

FIG. 2. Recording and display equipment setup.

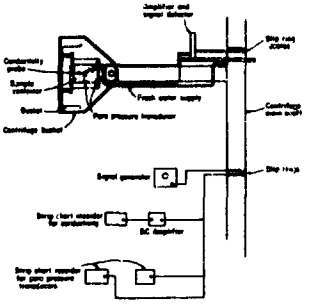

FIG. 3. Schematic diagram of experimental setup.

The change in concentration of the pore fluid at the mid depth of each model was monitored as a function of time utilizing a conductivity measuring system as shown in Fig. 4. The conductivity cell consisted of a

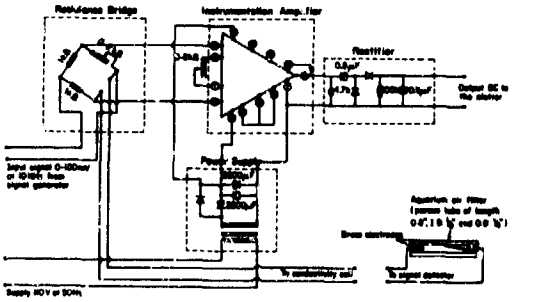

FIG. 4. Circuit diagram for the conductivity measuring system.

porous filter (diameter of the pores of about 2-5 μ) and the dimensions of the cell are shown in Fig. 4. The change in conductivity and the pressure heads were monitored on strip chart recorders. The schematic diagram of the experimental setup is shown in Fig. 2 and a photograph of the setup is shown in Fig. 5.

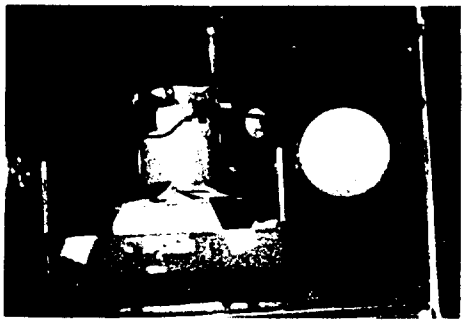

FIG. 5. Model setup in the Schaevitz centrifuge.

The column of sand contained in a plastic cylinder modelled the sand layer. The prototype dimensions are as shown in Fig. 6.

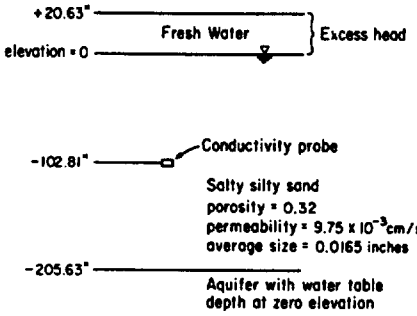

FIG. 6. Simulated prototype of the four sand models.

The ratio of the concentration C/C_o measured in terms of conductivity as a function of model time for the four models is shown in Fig. 7. The relationship

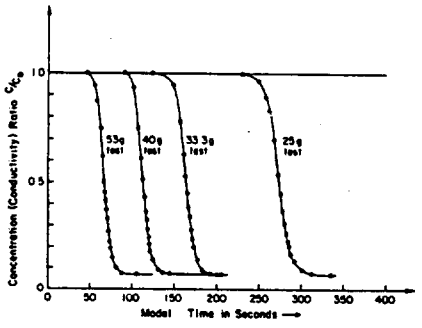

FIG. 7. The ratio of concentration C/C_o as a function of model time for the four sand models.

between the ratio of C/C_o versus prototype times shown in Fig. 8 for the four models are seen to be approximately identical with the greatest deviation occuring in the lower portion of the breakthrough curves. A plot of

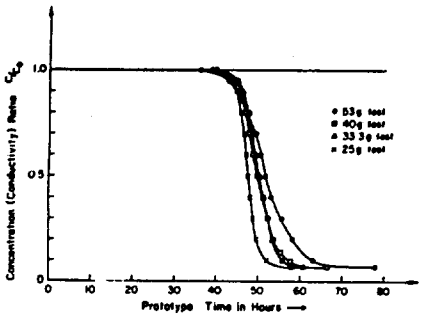

FIG. 8. The ratio of concentration C/C_o as a function of prototype time for the four sand models.

log t_m (model time) for 50% reduction in concentration ratio versus log N is shown in Fig. 9. This result can be interpreted as $t_p = N^{1.96} t_m$.

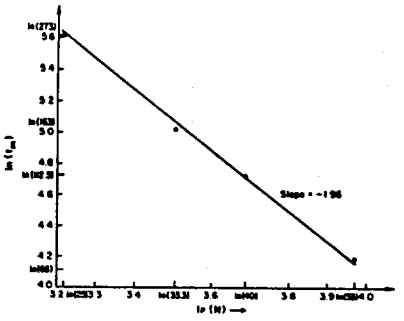

FIG. 9. Logarithmic model time for 50% reduction in concentration ratio vs logarithmic g level.

The influence of g level on the breakthrough curve was investigated by comparing a 1 g test data with the model test at 53 g. In the 1 g test a sample height of 3.88 inches was used. The height of the sample and the excess pressure heads and the location of the conductivity probe were identical in the 1 g and 53 g tests. The model behavior based on the 1 g and 53 g tests are compared in Fig. 10. The breakthrough curves are shown to be different with the time for 50% reduction in concentration ratio for 1 g tests being less than that for the 53 g tests.

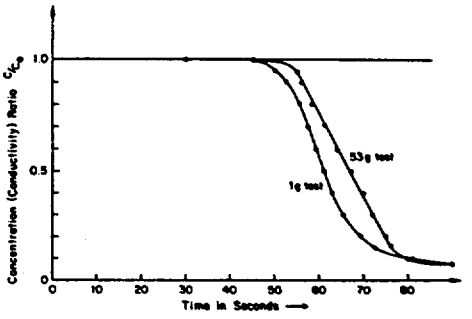

FIG. 10. The ratio of concentration C/C_o as a function of model time for 1 g and 53 g tests.

Comparison of 1 g test and 53 g test to study the influence of g level

The conventional approach for the determination of breakthrough curve is to perform a longitudinal dispersion test of a tracer passing through a column of porous media. The breakthrough curve is used to calculate dispersion coefficient (D_ℓ) and the average velocity ($\bar{v}$). The calculated values of D_ℓ and $\bar{v}$ are used to predict the breakthrough curve for any depth in the prototype.

For advection and diffusion processes for any given boundary conditions the solution of the basic differential equation for the concentration ratio can be shown to be functions of nondimensional parameters ($\bar{v}\ell/D_\ell$) and $\{(\ell \pm \bar{v}t)/2(D_\ell t)^{1/2}\}$. For the same concentration ratios for a model of size 1/N and a prototype, which has corresponding velocities of ($N\bar{v}$) and $\bar{v}$ (this condition could be obtained if the model and prototype have the same excess pressure head) it should satisfy the following:

$$\bar{v}_m \ell_m / D_{\ell m} = \bar{v}_p \ell_p / D_{\ell p}$$

and

$$(\ell_{im} \pm \bar{v}_m t_m)/2(D_{\ell m} t_m)^{1/2} = (\ell_p \pm \bar{v}_p t_p)/2(D_{\ell p} t_p)^{1/2}$$

but $\ell_p = N\ell_m$, $\bar{v}_p = \bar{v}_m/N$ and $D_{\ell p} = D_{\ell m}$

Therefore

$$\bar{v}_m \ell_m / D_{\ell m} = N\bar{v}_p * (\ell_p/N)/D_{\ell p} = \bar{v}_p \ell_p / D_{\ell p}$$

and

$$(\ell_m \pm \bar{v}_m t_m)/2(D_{\ell m} t_m)^{1/2} = \left(\frac{\ell_p}{N} \pm \bar{v}_p N t_m\right)/2(D_{\ell p} t_m)^{1/2}$$

$$= [\ell_p \pm \bar{v}_p (N^2 t_m)]/2[D_{\ell p} (N^2 t_m)]^{1/2}$$

$$= (\ell_p \pm \bar{v}_p t_p)/2(D_{\ell p} t_p)^{1/2}$$

Therefore to have the same concentration ratio

$$t_p = N^2 t_m$$

Therefore the breakthrough curve for the corresponding point in prototype could be obtained if the model breakthrough curve is scaled up by N^2.

The prototype breakthrough curves predicted at middepth from 1 g and 53 g tests which simulate the real behavior are plotted in Fig. 11. The shape of the breakthrough curve for the 1 g test is seen to be steeper and faster than that for the 53 g test. This would be expected if permeability decreases as confining pressure increases. The centrifuge provides correct prototype stress levels in the model, which are higher than the stress levels in the small model test at 1 g.

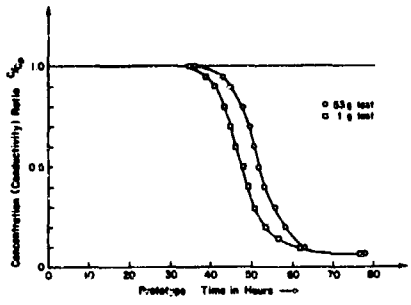

FIG. 11. The ratio of concentration C/C_o as a function of prototype time for 1 g and 53 g tests.

DISCUSSION AND CONCLUSIONS

Modelling of model tests performed to assess the validity of centrifuge modelling with regard to physical processes of advection and diffusion show the time for prototype behavior scales closely as N^2 as predicted by scaling laws (see Fig. 9).

The lack of exact similarity of the predicted prototype behavior by different models may be attributed to the following reason. As the time for the breakthrough curve is so short due to high velocities, the response time of the conductivity cell which is of the order of a second would contribute to the discrepancy, especially for higher g-level tests. The error may be of the order 1 hour (in prototype time) for 53 g test compared to 0.2 hrs for the 25 g test. This contribution to observed deviations may become insignificant for a fine grained soil such as silt with a very low permeability and a low Peclet number. The Reynolds number ranges from 0.11 to 0.21 for the four tests thus ensuring laminar flow.

There is an influence of stress level on advection as well as diffusion processes as seen from the results in Fig. 11. The self weight may have an effect of reducing the average velocity and the permeability, and thus affecting the diffusion coefficient. The changes in the above properties will show a difference in the shape and position of the breakthrough curve.

This study shows that advection and diffusion processes can be modelled in the centrifuge. If future studies on fine grained soils show that the physical processes of advection and diffusion, and chemical processes of adsorption can be modelled in the centrifuge, this technique will have a significant application to the study of the processes affecting the pollutant travel in soils and the prediction of pollution travel. The length and time of travel can be accelerated and the dispersivities in different directions can be included as long as the prototype conditions can be simulated in the centrifuge.

SUMMARY

Four centrifuge tests were carried out on four sand models, 8.23, 6.18, 5.14, and 3.18 inches, accelerated to g levels of 25, 33.3, 40 and 53. The results on the sand models contained in a 5 inch diameter plastic cylinder

were used to examine the validity of scaling relations for advection and diffusion processes during pollutant travel in soils. The prototype time is shown to scale as N^2 times the model time.

The breakthrough curves obtained in a 1 g and a 53 g test were analyzed to examine the influence of self weight on the advection and diffusion processes. The results indicate that self weight has an influence in the physical processes involved in the transport of pollutants in soil, and therefore the use of diffusion coefficients measured in 1-g tests may be incorrect.

The results also suggest that the centrifuge may have significant application in the study of pollutant travel in soil.

ACKNOWLEDGEMENTS

This research was supported by Tyndall AFB and forms part of a larger study and this support is gratefully acknowledged. Special thanks are given to K. Muraleetharan for his assistance in the conduct of the centrifuge model tests.

REFERENCES

1. Javandel, I., Doughty, C., and Tsang, C.F. (1984). "Ground Water Transport; Handbook of Mathematical Models", American Geophysical Union, 2000 Florida Ave., N.W. Washington, D.C. 20000.

2. Orlob, G.T. (1984). "Mathematical Modeling of Water Quality", International Institute for Applied Systems Analysis.

3. Perkins, T.K. and O.C. Johnston (1963). A review of diffusion and dispersion in porous media. J. Soc. Petrol. Eng., 3, pp. 70-83.

4. Freeze, R.A. and J.A. Cherry (1974). "Groundwater", Prentice-Hall, Inc., Englewood Cliffs, NJ 07632.

5. Bear, J. (1972). "Dynamics of fluids in porous media", American Elsevier Publishing Company, Inc., N.Y.

DIFFICULTIES IN THE SIMULATION OF DYNAMIC EVENTS IN A CENTRIFUGE

[1]A. Anandarajah, [2]K. Arulanandan and [3]J. Hutchinson

[1]The Johns Hopkins University, [2]University of California, Davis,
[3]University of California, Davis

ABSTRACT

This paper presents: (1) an analytical method of evaluating the error introduced by Coriolis acceleration on the centrifuge model data, and (2) a method of simulating a controllable arbitrary earthquake motion in a centrifuge. The Coriolis error is evaluated by Newmark's sliding block analysis and it is shown that the Coriolis acceleration may have a significant influence on the observed model behavior. A piezoelectric shaker is used in the feasibility study of simulating a given variable frequency earthquake motion in a centrifuge and the results are reported.

INTRODUCTION

The centrifuge modeling technique was introduced to the geotechnical engineering community by Bucky in 1931 and independently by Pokrovsky in 1933. Since then, the technique was used in the study of certain mining problems, but was not pursued to any significant degree for geotechnical modeling in the U.S. and in Europe. In the past ten years, it has received a remarkable recognition in the U.S. and around the world.

The centrifuge provides a unique means of increasing the gravity in the form of centrifugal acceleration and thereby enables small scale soil models be tested at prototype stress levels. For example, the stress level in a 100 foot tall soil structure would be identical to those in a 1 foot tall geometrically similar model when tested under 100 g centrifugal acceleration. The scaling laws associated with the quantities of interest can be derived by using the principles of dimensional analysis. A summary of model laws is presented in Table 1.

The simulation of dynamic events in the centrifuge requires that certain similitude conditions be satisfied. Considering the simulation of an acceleration history in a centrifuge at a centrifugal acceleration of Ng: (1) model frequency is N times larger than the prototype frequency, (2) Model amplitude is N times larger, and (3) model duration is N times shorter. Moreover, the energy in the model is N^3 times smaller than that in the prototype. Hence, in simulating an explosive loading in a centrifuge model, the weight of explosive required would be N^3 times smaller than that used in the field, provided identical explosive types are used. For example, a field explosive with 8000 pounds of PETN can be simulated in the centrifuge with 3.65 grams of PETN at a centrifugal acceleration of 100g.

TABLE 1. SCALING RELATIONS

Quantity	Full Scale (Prototype)	Centrifugal Model at n g's
Linear Dimension	1	1/n
Area	1	$1/n^2$
Volume	1	$1/n^2$
Time		
In Dynamic Terms	1	1/n
In Diffusion Cases	1	$1/n^2$
In Viscous Flow Cases	1	1
Velcity (Distance/Time)	1	1
Acceleration (Distance/Time^2)	1	n
Mass	1	$1/n^3$
Force	1	$1/n^2$
Energy	1	$1/n^3$
Stress (Force/Area)	1	1
Strain (Displacement/Unit Length)	1	1
Density	1	1
Energy Density	1	1
Frequency		
In Dynamic Problems	1	n

A great upsurge in the centrifuge activity has taken place during the past few years in the study of dynamic geotechnical engineering problems. Active research has been pursued in the areas of earthquake response and earthquake-induced liquefaction (Anandarajah, 1980; Arulanandan et al., 1982; Kutter, 1984; Prevost et al., 1983, Zelikson, 1981). Schmidt and Holsapple reported a comprehension series of model studies dealing with explosive as well as impact craters (15, 16). Nielson (1983) has recently conducted a series of experiments to study the attenuation of dynamic stress waves generated from an explosion. Scott (1977) and Row et al. (1976) demonstrated the feasibility of modeling foundatin vibration problems in a centrifuge. Ortiz et al. (1981) reported model experiments performed in a centrifuge to study the dynamic behavior of cantilever retaining walls.

There are, however, many difficulties and uncertainties associated with dynamic centrifuge modeling which require further research and development. The purpose of this paper is to address two such problems, namely the error introduced by the Coriolis acceleration, and the difficulties related to the simulation of a variable frequency earthquake motion in a centrifuge.

INFLUENCE OF CORIOLIS ACCELERATION ON CENTRIFUGE DATA

Figure 1. shows the velocity and acceleration fields of a rotating mass where the component $2\omega v$ is the Coriolis acceleration. Thus, any dynamic excitation occurring in the plane of rotation or any movement ocurring within the soil model would give rise to Coriolis acceleration. Pokrovsky (1975), by requiring that radial Coriolis acceleration be less than 10 percent of the centrifuge acceleration, gave an upper bound to the dynamic velocity as: $v < 0.05\omega r$. Also by considering the motion of a particle under the influence of Coriolis acceleration, Pokrovsky suggested that the error can be neglected if $v > 2\omega r$ for high-velocity events (eg: cratering event). Thus an acceptable range of velocity according to Pokrovsky is $2\omega r < v < 0.05\omega r$. The Coriolis effect is unknown in the intermediate range of velocities.

In order to evaluate the extent of Coriolis effect, a cohesionless centrifuge model embankment subjected to an earthquake base motion in the plane of rotation is analyzed by the Newmark's sliding block method. Goodman and Seed (1966) have shown that the sliding block analysis yields reasonable predictions for the earthquake induced displacements. The analysis assumes that the rigid mass begins to slide down the slope when the earthquake acceleration exceeds a certain threshold value known as the yield acceleration. The movement of the sliding mass upward on the slope is neglected.

The accelerations and forces acting on the sliding mass, m, are shown in Fig. 2, where ω = angular velocity of the centrifuge; a = amplitude of earthquake acceleration; v = amplitude of earthquake velocity; r = radius of centrifuge arm, $\mu = \tan\phi$; ϕ = friction angle of soil; and x, $\dot{x}$ and $\ddot{x}$ are displacement, velocity and acceleration of the sliding mass respectively. Observe that $2\dot{x}\omega$ is the Coriolis acceleration caused by the downhill velocity of the sliding mass and $2\omega v$ is the Coriolis acceleration due to the earthquake velocity. For simplicity, a sinusoidal earthquake motion, $a = Fg \sin\omega_e t$, is considered

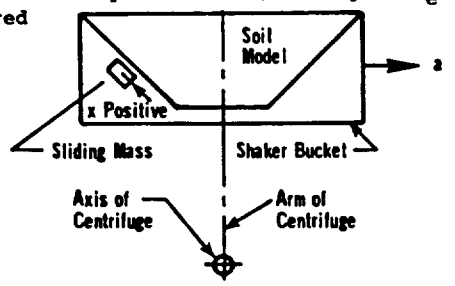

Figure 2.a

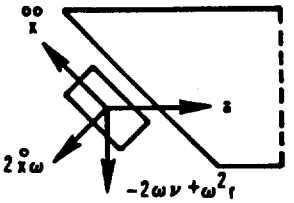

Figure 2.b Acceleration

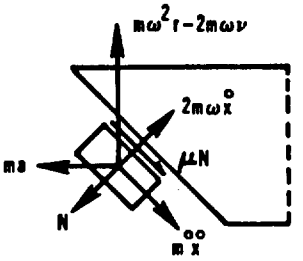

Figure 2.c Forces

Figure 2. Accelerations and Forces Acting on the Sliding Mass for Case (1)

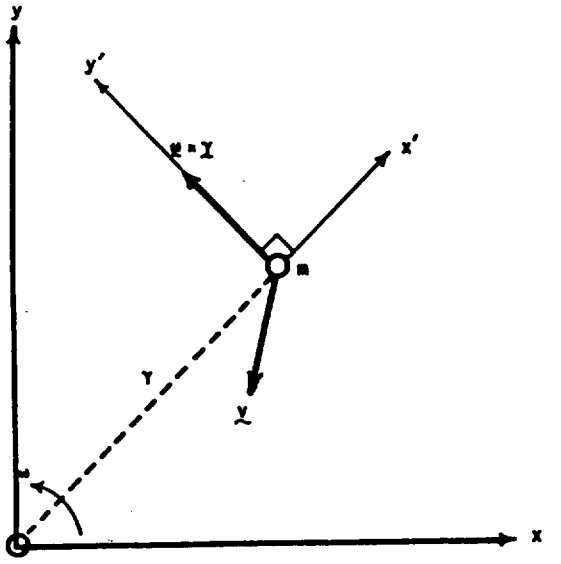

1a. Velocities

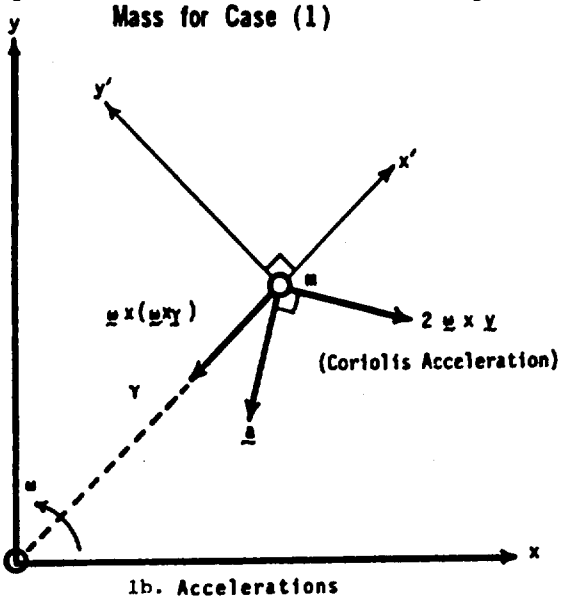

1b. Accelerations

Figure 1. Velocity and Acceleration Components of a Rotating Mass, m

By considering the dynamic equillibrium of mass m and eliminating the normal force, N:

$$\ddot{x} + 2\omega\mu\,\dot{x} = B(x)\,F \sin \omega_e t$$

$$- \frac{2\omega}{\omega_e} B(x)\,F \tan(\phi-\alpha) \cos \omega_e t$$

$$- \frac{B(x)\omega^2 r}{g} \tan(\phi-\alpha) \qquad (1)$$

where $B(x) = g(\cos\alpha + \mu \sin\alpha)$

The minimum value of F that satisfies the condition $\dot{x} = \ddot{x} = 0$ yields the following expression for the coefficient of yield acceleration:

$$k_y = \frac{\omega^2 r \tan(\phi-\alpha)}{g(1 + c^2 \tan(\phi-\alpha))}$$

where $c = 2\omega/\omega_e$. By combining the homogeneous and particular solutions, the general solution to equation 1 is:

$$x = D_1 + D_2 e^{-2\mu\omega t} + A_1 t +$$

$$A_2 \sin \omega_e t + A_3 \cos \omega_e t$$

where

$$A_1 = - \frac{k_y B}{2\mu\omega}$$

$$A_2 = - BF \frac{\omega_e^2 + 4\mu\omega^2 T}{4\mu^2\omega^2\omega_e^2 + \omega_e^4}$$

$$A_3 = 2\,BF\omega \frac{T - \mu}{4\mu^2\omega^2\omega_e + \omega_e^3}$$

and $T = \tan(\phi-\alpha)$.

The constants D_1 and D_2 can now be evaluated by imposing the intitial conditions that $x = \dot{x} = 0$ at $t = \beta/\omega_e$ (Fig. 3) where $\beta = \sin^{-1}(k_y/F)$.

A parametric study was carried out considering one cycle of input motion for the two cases: (1) incorporating the Coriolis accelerations in the analysis, and (2) neglecting the Coriolis accelerations. From this, the relative error caused by the presence of Coriolis acceleration was evaluated. Typical variations of errors with the model frequency are shown in Figs. 4-6. Further results and discussion can be found in Ref. (2). For the range of parameters considered, it was found that the error on displacement results could be as much as 18 percent.

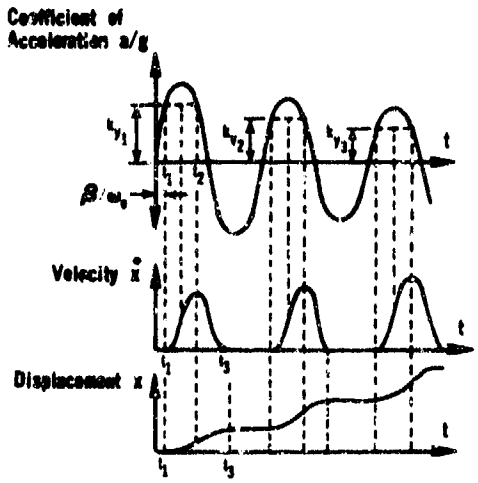

Figure 3. Integration of Accelerograms to Determine Downslope Displacements.

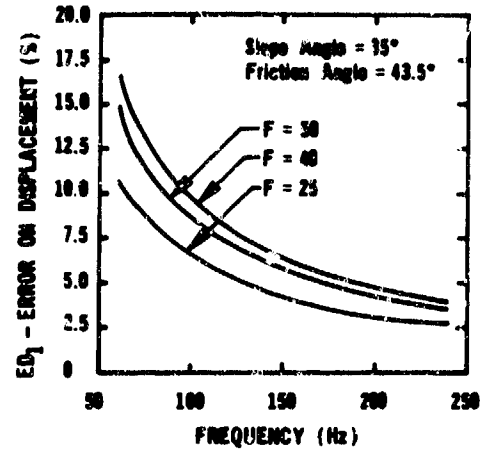

Figure 4. Error on Displacement for Slope Angle 35° and Friction Angle 43.5°.

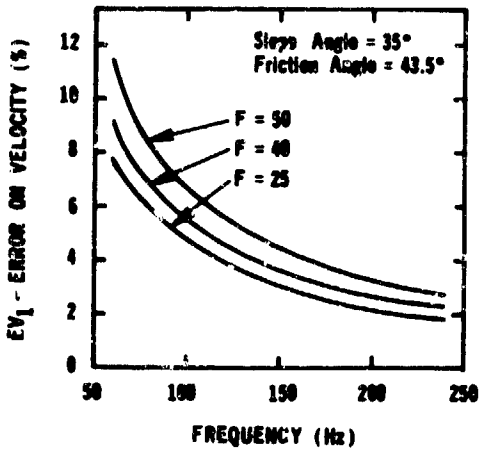

Figure 5. Error on Velocity for Slope Angle 35° and Friction Angle 43.5°.

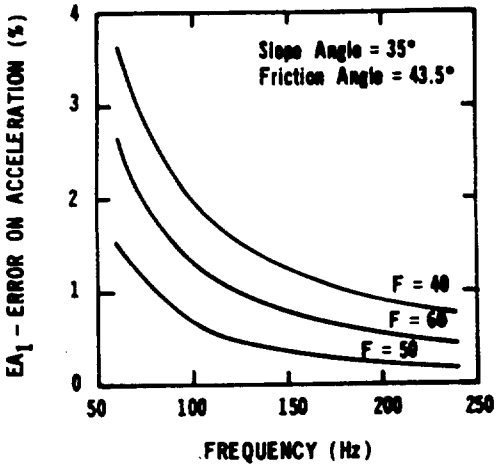

Figure 6. Error on Acceleration for Slope Angle 35° and Friction Angle 43.5°.

SIMULATION OF A VARIABLE FREQUENCY EARTHQUAKE MOTION IN A CENTRIFUGE

During the past few years there has been a considerable development of the technology for earthquake motion simulation in a centrifuge. The range of predominant frequencies and amplitudes of commonly used design earthquake accelerations are: f_p = 10 HZ to 0.33 HZ and F_p = 0.2g to 0.6g as high as 1.0g. The corresponding model values of f and F at, for example, 100g centrifugal acceleration would be: f_m = 1000 HZ to 33 HZ and F_m = 20g to 60g as high as 100g. It is well known that the frequency content of earthquake motion has a significant influence on the response of structures. Due to non-linear stiffness properties and damping of soils, it is further required that exact prototype dynamic stresses and strains be induced in the corresponding centrifuge model. Thus, it is apparent that it would be highly desirable to have the capability of reproducing the exact shape and amplitude of any selected arbitrary motion or response spectra at the base of centrifuge bucket.

Various methods of earthquake excitation are presently used (4,7,8,13,20) and the exact simulation of any aribtrary motion can not, at the present time, be achieved by using these methods. A critical evaluation of the merits and limitations of the existing systems can be found in Reference 19, and the discussion here would be limited to the piezoelectric shaking system (4).

A piezoelectric ceramic element is an artifically polarized wafer which deforms when an electric field is applied across its surface. The magnitude of the strain is directly proportional to the magnitude of the applied electric field. The range of displacement can be extended by stacking several piezoelectric elements together. A piezoelectric shaker-payload box system is shown in Fig. 7. Since the strain is related to the applied electric field, the motion may be controlled by varying the electrical input. The present system, however, functions on the basis of electrical resonance and thus the input signal

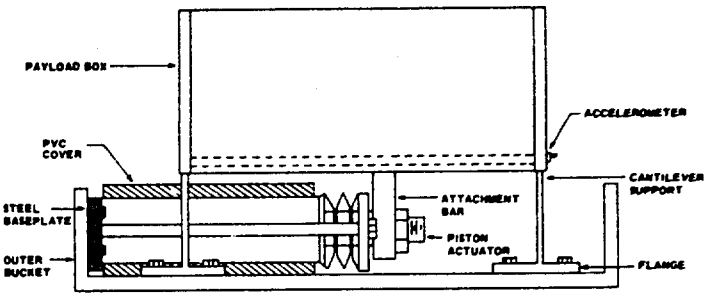

FIG 7. SIDE VIEW OF PIEZOELECTRIC SYSTEM SHOWING ATTACHMENT OF THE PISTON ACTUATOR TO THE PAYLOAD BUCKET. NOT SHOWN ARE STIFFENING RIBS WHICH ARE WELDED TO THE ATTACHMENT BAR AND THE BOTTOM OF THE PAYLOAD BUCKET

must be a sine wave with a certain frequency that matches the impedence of the circuit in order to give rise to resonance. The required shaking capability is obtained when the system is at resonance. The system can easily be modified to produce any arbitrary earthquake motion by directly inputing a voltage of any arbitrary pattern. A large capacity power supply is required in this case to obtain the required shaking capability. One problem associated with this method is that the dynamic characteristics of the shaker-bucket-soil model system will modify the input voltage pattern as it is fed through the system and consequently the bucket base motion would differ in shape from the input voltage. This problem can be overcome by using the methods of system identification and one possible method is proposed here.

In Figure 8, the shaker-bucket-model arrangement represents the system and $a_1(t)$ and $a_2(t)$ represent respectively the input voltage signal to the piezoelectric shaker and the bucket base acceleration.

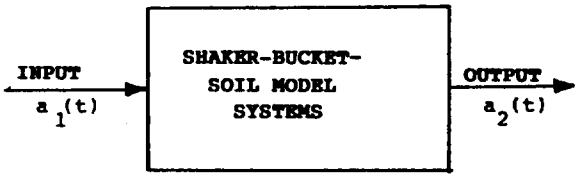

Figure 8. The Input and Output Response of Shaker-Bucket Model System

Step 1

In the analysis presented here, the system is assumed to be linear. The functions $g_1(s)$ and $g_2(s)$ represent the Lapalce transforms of $a_1(t)$ and $a_2(t)$ respectively; i.e.;

$$g_1(s) = L\{a_1(t)\} \; : \; g(s) = L\{a_2(t)\}$$

The transfer function of the system can be determined knowing the impulse response, I(t) as follows:

$$T(s) = L\{I(t)\}$$

Then, $g_2(s) = T(s)\, g_1(s)$

and, $g_1(s) = \dfrac{g_2(s)}{T(s)}$

and by inverse transform,

$$a_1(t) = L^{-1}\left\{\frac{g_2(s)}{T(s)}\right\}$$

The impulse response can be derived from a step response as follows:

$$I(t) = \frac{d}{dt} A(t)$$

It is relatively easier to apply a unit step voltage input signal than an impulse signal. In summary, the procedure includes the following steps: (1) find step response A(t) experimentally, (2) derive I(t) from A(t), (3) evaluate T(s) and $g_2(s)$, and (4) evaluate $a_1(t)$ by inverse transform. Special attention should be paid to any possible system noise and when T(s) = 0.

Step 2

Since the system may exhibit some non-linearity due to the presence of soil model and the possible non-linear nature of the shaker and bucket, the procedure described in Step 1 may not yield the required results. The results may be improved by a trail and error procedure as follows:

The input motion, $a_1(t)$ can be expressed in a fourier series as follows:

$$a_1(t) = \Sigma a_n \sin(\omega_n t + \phi_n)$$

Let a(t) be the required base acceleration, and $s(\omega)$ and $s_2(\omega)$ be the acceleration response spectra of a(t) and $a_2(t)$ respectively. The input motion $a_1(t)$ is modified as follows:

$$a_1(t) = \Sigma a_n^* \sin(\omega_n t + \phi_n)$$

where, $a_n^* = \frac{S(\omega_n)}{S_2(\omega_n)} a_n$

This procedure is repeated until $S_2(\omega)$ is reasonably close to $S(\omega)$.

The entire procedure described in Step 1 and Step 2 can be carried out automatically by using a suitable computer set up. It should be recognized that this calibration procedure should be repeated for different centrifuge tests with different models. Nevertheless, the dynamic characteristics of the system must be accounted for in obtaining the required base motion. The simplicity and controllability of piezoelectric shaker system enable the system identification procedure such as the one proposed here to be performed quite easily.

A preliminary study was conducted using the piezoelectric system available at the University of California, Davis. A comparison between the required response spectra and the observed response spectra is presented in Figure 9. The test was performed at 1g level and without the payload. The apparent good comparison indicates the feasibility of adopting the proposed method for the simulation of a given variable frequency earthquake motion in a centrifuge.

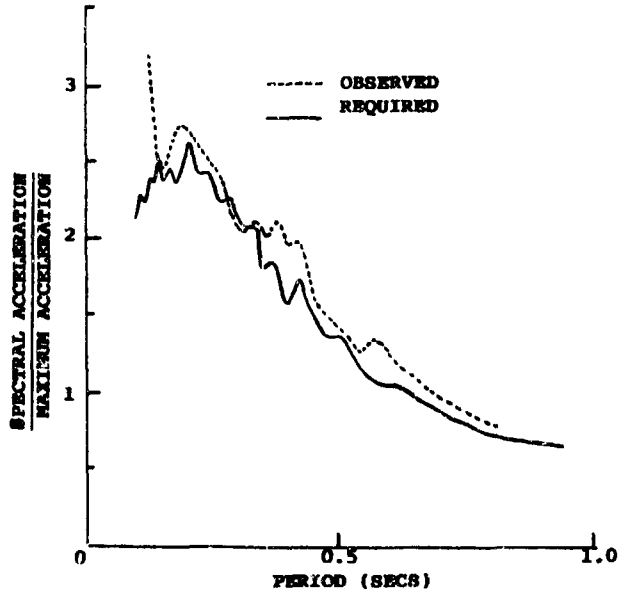

Figure 9. Comparison Between The Observed and Required Spectral Accelerations at Base of Payload Bucket.

SUMMARY AND CONCLUSIONS

The centrifuge modeling technique has a tremendous potential for experimentally determining the behavior of soils and soil/structure interactions under dynamic loading conditions. Discussed in this paper are two common problems encountered in the simulation of dynamic events in a centrifuge: the error due to Coriolis accelerations and the difficulties of simulating a given variable frequency earthquake motion in a centrifuge.

An analysis based on the Newmark's sliding block method was carried out in order to quantify the effect of Coriolis acceleration on the behavior of cohesionless embankments subjected to a base shaking. It was shown that Coriolis acceleration might introduce a significant error on the observed behavior.

A method of simulating a variable frequency earthquake motion in a centrifuge is proposed. A preliminary test was conducted using a piezoelectric shaker system. The results indicate the feasibility of simulating a given variable frequency motion by adopting the proposed system identification procedure.

REFERENCES

1. Anandarajah, A. "Centrifuge Modeling of Earthquake Response of Embankments," thesis presented to the University of California, Davis, California, in 1980 in partial

fulfillment of the requirements for the degree of Master of Science.
2. Anandarajah, A., Hutchinson, J. and Arulanandan, K. "The Effect of Coriolis Acceleration on the Accuracy of Centrifuge Model Test Results," Report No. 81-01, Department of Civil Engineering, University of California, Davis, 1981.
3. Arulanandan, K., Anandarajah, A., and Abghari, A. "Centrifuge Modeling of Liquefaction Susceptibility," ASCE, J. of the Geotechnical Engineering Division. Volume 109, No. 3, March 1983.
4. Arulanandan, K., Canclini, J., and Anandarajah, A. "Simulation of Earthquake Motions in the Centrifuge," ASCE J. of the Geotechnical Engineering Division, May 1982, Vol. 108, No. GT5, pp. . 730-742.
5. Bucky, P. B. (1931), "Use of Models for the Study of Mining Problems," American Institute of Mining and Metallurgical Engineers, Technical Publication No. 425, pp. 3-28.
6. Goodman, R. E., and Seed, H. B. "Earthquake Induced Displacements in Sand Embankments," ASCE, Vol. 92, No. SM2, March 1966, pp. 125-146.
7. Kutter, B. L. (1984), "Earthquake Deformation of Centrifuge Model Banks," ASCE, Journal of Geotech. Eng. Div., V110, No. 12, December.
8. Morris, D. V., "The Centrifugal Modeling of Dynamic Soil-Structure Interaction and Earthquake Behavior," Thesis, Presented to the University of Cambridge, Cambridge, England, in 1979, in Partial Fulfillment of the Requirement of Doctor of Philosophy.
9. Nielson, John P., "The Centrifugal Simulation of Blast Parameters, ESL-TR- 83-12, Engineering and Services Laboratory, AF Engineering and Services Center, Tyndall AFB, FL 32403, Dec. 1983.
10. Ortiz, L. A., Scott, R.F. and Lee, J. (1981), "Dynamic Testing of a Cantilever Retaining Wall," Report, Soil Mechanics Laboratory, CIT, Pasadena, CA.
11. Pokrovsky, G. and Fyodorov, I., "Centrifuge Model Testing in the Construction Industry," Vol. 1 and 11, Draft Translation prepared by Building Research Establishment Library Translation Service, Great Britain, 1975.
12. Pokrovsky, G. I., "On the Use of a Centrifuge in the Study of Models of Soil Structures," Technical Physics, Vol. 14, No. 4, 1933.
13. Prevost, J. H. and Scanlan R. H., (1983), "Dynamic Soil-Structure Interaction: Centrifugal Modeling," Report 83-SM-1, Civil Engineering, Princeton University.
14. Rowe, P. W., and Graig, W. H., "Studies of Offshore Caissons Founded on Oosterschelde Sand," Design and Construction of Offshore Structures, ICE, London, 1976.
15. Schmidt, R. M., "Centrifuge Simulation of the JOHNIE BOY 500 Ton Cratering Event," Proceedings of the Lunar Planet Science Conference, 1978, pp. 3877-3889.
16. Schmidt, R. M. and Holsapple, K. A. (1981), "An Experimental Investigation of Transient Crater Size (Abstract)," Lunar and Planetary Science XII, Lunar and Planetary Institute, Houston, TX, pp. 934-936.
17. Scott, R. F., Liu, H. P., and Ting. J., "Dynamic Pile Tests by Centrifuge Modeling," Paper 4-50, Proc. Sixth World Conference on Earthquake Engineering, New Delhi (January, 1977).
18. Whitman, R. V., Lambe, C. E. and Akiyama, J., "Yielding of Sand Slopes During Earthquakes," ASCE Annual Conference, Las Vegas, Nevada, April 26-30, 1982. Preprint 82-063.
19. "Workshop For Development of Specifications For A Ground Motion Simulator For Centrifuge Modeling in Geotechnical Engineering," Workshop held at MIT Endicott house, Dedham, Mass., 6-7 June 1983, Org. by J. A. Chaney and R. V. Whitman.
20. Zelikson, A., Devaure, B., and Badel, D., "Scale Modeling of Soil Structure Interaction During Earthquakes Using a Programmed Series Explosions During Centrifugation," Int. Conf. on Recent Advances in Geotechnical Engineering, University of Missouri at Rolla, 1981, Vol. 1, pp. 301-366.

MODEL TESTS FOR DESIGN OF CENTRIFUGE SAFETY BARRIER

Bruce L. Kutter

University of California
Davis, California

ABSTRACT

A model test series was conducted to verify the design of a barrier around a large geotechnical centrifuge. Two "worst case" parts of the centrifuge were assumed to detach from the centrifuge at maximum speed. The model tests showed the barrier to be adequate with some modifications to the design. The barrier is designed to resist oblique impact of irregularly shaped steel objects of 5,000 and 20,000 lb mass with a 400-530 ft/s horizontal velocity. The impact occurs near the free surface of the barrier. It is argued that physical model tests are particularly useful for complex problems where analytical methods are unavailable, inadequate, or unverified.

INTRODUCTION

A model test series has been conducted to evaluate the adequacy of a proposed gravel barrier around a large geotechnical centrifuge. The tests were conducted for the purpose of engineering design, and they were therefore designed to provide a conservative, rather than accurate, evaluation of the barrier adequacy. The results reported here show an example of the use of model tests to assist in the solution of practical engineering problems, where available calculation methods give inadequate or conflicting results.

A large centrifuge, designed to train astronauts, was constructed to simulate takeoff and landing of an Apollo capsule at NASA Ames Research Center, Moffett Field, California. It was located above ground directly adjacent to an office building. Since the completion of the Apollo project, the centrifuge was not used. NASA Ames and UC Davis then commenced on a project to make use of the facility by modifying it to provide a facility for geotechnical centrifuge modeling. The drive motor, power supply, buildings, and signal slip rings could be used for the modified centrifuge, but the centrifuge rotor arm had to be replaced and a speed increaser was added to enable testing geotechnical models of 4 tons mass at up to 300 g accelerations at a 29 ft radius.

The new centrifuge arm is much more massive (it weighs about 100 tons) and would spin at much higher velocities (with tip speeds of 530 ft/sec) than the original arm which, of course, was designed to carry humans. This raised new questions regarding the safety of personnel in the adjacent offices. If a heavy part of the new centrifuge were to fail at high speed it would become a projectile and serious damage and injury could occur. It was decided that a barrier wall should be constructed around the centrifuge that would contain a "worst case" projectile. Since the new centrifuge arm has a smaller radius than the old arm, it was proposed to construct a gravel barrier 22 ft thick and 18 ft high inside the existing building in an annulus around the centrifuge. A diagram of the centrifuge and proposed barrier is shown in Figure 1.

A report by Southwest Research Institute (1983) identified the 4,700 lb counterweight plates with approximate dimensions of 6" x 36" x 102" as the most dangerous projectiles in terms of their penetration capability. Another potentially dangerous object is the fully loaded swinging platform which weighs 20,000 lbs, but has a much larger cross-sectional area. It is roughly 60" x 74" x 84" with an irregular shape.

At the maximum speed of the centrifuge (174 rpm) the counterweight plates would have a velocity of 402 ft/sec and the swinging platform would have a velocity of 530 ft/sec. The counterweight and platform would impact obliquely at 30 and 45° respectively from the normal. They also would impact near the top of the barrier, with their centroids at 4.5 ft and 6 ft below the sand surface respectively. The proximity to the surface was a major concern. Would the projectiles veer upward and escape from the surface of the gravel barrier? Hopefully they would stay in the gravel so that we could take advantage of the full barrier thickness to stop them.

Preliminary calculations based on empirical penetration equations proposed by Young (1969) were conducted by the writer and other calculation procedures proposed by Backman (1976), and Healey et al. (1975) were conducted by Baker et al. (1983). The calculations resulted in widely varying evaluations of the proposed barrier's adequacy. This is, no doubt, due to the fact that the empirical equations were being used to predict penetration of centrifuge parts with shapes, sizes, and velocities very different from the projectiles that were tested to develop the empirical equations. Some of the equations predicted complete perforation and others predicted that the barrier would be thick enough. But none of the equations accounted for the proximity of the sand surface. They were primarily based on data from normal (non-oblique) impact of axisymmetric projectiles downward into a soil layer.

Because the empirical equations could not be relied upon, it was decided to conduct a series of scale model tests that could account for the three-dimensional nature of the problem.

MODEL TESTS

Ideally, scale model tests of geotechnical structures should be conducted on a centrifuge in order to properly simulate self-weight stresses in the soil mass. Since the centrifuge was not yet running, we could not do the model tests there, and no machine large enough was conveniently available. We therefore decided to test the models in earth's gravity using a 6" diameter gas gun at NASA Ames Research Center to project scaled facsimilies of the critical centrifuge parts into the model barriers. A total of twelve tests were conducted.

Apparatus

Figure 2 shows the general test setup and Figure 3 shows the dimensions of the model and prototype centrifuge parts. Referring to the numbers on Figure 2, the projectiles (1) were loaded into an aluminum cylindrical sabot (2) that fit like a bullet shell in the 6" diameter gun barrel (3). Mylar diaphragms (4,5) allowed evacuation of the barrel. The pressure chamber (6) was then clamped to the barrel and pressurized to between 50 and 200 psi depending on the desired projectile velocity. After starting the video (7) and high speed movie cameras (8), the diaphragm (5) was broken by a hot wire and the pressure accelerated the model projectile down the barrel and through diaphragm (4). The sabot stripper (9) stopped the sabot but allowed the projectile to escape the barrel. The projectile then broke the breakwires (10) which allowed determination of the projectile velocity. The projectile then penetrated the model barrier (11) with the event being monitored by the movie and video cameras.

Details of Model Barrier

Figure 4 shows a model barrier wall. The scale for the tests was selected to be as large as possible subject to the limitation of the size of the gun barrel. For the tests on the counterweight the scale was 1/8 of full-scale and for the model of the loaded swing platform the scale was 1/20.

The model barrier consisted of a rectangular box made from a steel frame with reinforced concrete front and back walls to represent the inner concrete block masonry wall and the original building wall. The walls were cast from micro-concrete with embedded wire mesh reinforcement. Two layers of 2" x 3" x 16 gauge steel wire mesh were used in the 1/8 scale tests while for the 1/20 scale tests, an appropriate amount of 20 gauge hexagonal wire mesh (chicken wire) was used to simulate the prototype reinforcing bars. Table 1 summarizes the model and prototype concrete wall dimensions. For practical reasons, it was decided that the curvature of the actual wall could be neglected and hence the model walls were cast as flat plates. However, as shown in Figure 5, the angle of impact, θ, and the thickness of the barrier in the direction of the projectile velocity, ℓ, was scaled precisely. As shown in Figure 4, the depth of sand, d, above the impact point was also scaled precisely. The projectiles were shot so they would impact with the minimum frontal area. The grain size of the gravel in the barrier was scaled down in the model tests. Monterey #30 sand was used to simulate the pea gravel that was selected as the fill for the prototype barrier.

In some of the later tests a heavily reinforced concrete slab was placed on top of the sand in an attempt to deter the projectile from veering upward out of the sand. The model and prototype dimension of these slabs is also summarized in Table 1.

TEST RESULTS

The twelve tests that produced useful data are summarized in Table 2. The tests at 1/8 scale represent models of impact of the counterweight plates and the tests at 1/20 scale represent models of impact of the swinging platform. Using the scale factors summarized in Table 3 the impact velocities should be identical in model and prototype. The impact velocities corresponding to full centrifuge speed are 402 ft/sec and 530 ft/sec for the counterweight and swinging platform respectively. Tests in Group I (18C,19C,38,30,31A) represented tests of the final safety barrier design with a concrete cap on top of the gravel. Tests in Group II (15C,16C,37,37A) represented tests without the cap on top. Tests in Group III (17C,34,36) were conducted with no sand fill.

The Group II and III tests were conducted to determine whether an incomplete barrier would be adequate for containing centrifuge parts at less than maximum speed. It was hoped that we could use the centrifuge at low speeds before completion of the barrier. The Group III tests suggest (see Table 2) that a maximum counterweight speed of 102 ft/sec may be permissible, even without any fill, but this only corresponds to a centrifugal acceleration of about 20 g. Test 37A in Group II illustrated that without a concrete slab on top of the barrier, the counterweight may escape if it veers upward with an impact velocity as low as 260 ft/sec (which corresponds to only 125 g).

Group I Test Results

The mode of behavior during impact of the counterweight plate models into a barrier with fill and a slab on top was the punching of a hole in the front wall and then veering through the sand in a direction determined by its orientation at impact. The projectile then either escaped the barrier surface, impacted the back wall, or came to a stop near the back wall. The back wall often cracked but very little spalling occurred. As the projectile entered the sand the entire slab that covered the gravel developed cracks as it lifted about 6" off the sand surface.

The tests at 1/20 scale of the impact of the swing platform yielded a different type of behavior. A large hole was broken out of the front wall and the projectile decelerated much more rapidly. The model concrete caps were blown vertically off the top of the sand and were followed by the model projectiles which then escaped with a low vertical velocity and almost no horizontal velocity. The back walls were distorted in bending over a large area and extensive cracks appeared, but it was not perforated. The concrete caps and the projectiles raised about 2 to 5 ft in the air and then fell down.

All of the tests indicate that if the projectile veers downward, the model barrier is adequate. It was intended that the model projectiles impact without an upward or downward tilt. However, observations of data from the high speed cameras showed that there was a small random tilting of model projectiles of ±10°, and this tilt was responsible for the tendency of the counterweight model projectiles to veer up or veer down in the sand. If the projectiles had a downward angle of attack they veered down in the sand and vice versa. Two tests of the counterweight impact into a capped barrier were conducted for which the model projectiles had an upward angle of attack on impact (tests 19C and 38). Test 19C had an undersized concrete cap which allowed the projectile to barely escape with a very low velocity. Test 38, however, had a properly sized concrete cap and this resulted in satisfactory containment for an impact velocity of 398 ft/sec which was very close to the desired velocity of 402 ft/sec.

INTERPRETATION OF RESULTS

The model tests suggest that the barrier design is adequate, but perhaps marginally so. It is therefore necessary to show that the models represent a conservative simulation of the prototype barrier. In summary, the tests on the final barrier configuration (Group I) gave some results that required further analysis:

1) In the 1/8 scale test 18C the counterweight model did escape (albeit with a low velocity).

2) In the 1/8 scale test 38 the back wall was damaged.

3) In the 1/20 scale tests 30 and 31A, the model swing platforms escaped and the concrete slab on the sand surface were blown vertically off the sand surface.

The above concerns are answered in the following sections.

Undersized Slab in Test 18C

Tests 18C and 19C were conducted using an ad hoc arrangement. While the front and back walls were of properly scaled thickness, the back wall was made from two separate slabs and the cap was made from a slab that was meant to be a front wall and hence a significant portion of the surface was not covered. The paths of the projectiles is approximately shown in Figure 6. In test 18C the projectile impacted with a downward angle of attack and buried itself safely in the barriers.

In test 19C the projectile exhibited an uncanny attraction toward the path of least resistance. The projectile was tilted upward on impact, it veered up and out of the uncapped area of the sand. It then squeezed through the crack between the two back walls breaking the edges of each back wall slab without tearing a bit of the reinforcing wire.

In test 38 a properly sized cap and back wall successfully contained a model counterweight during a similar impact. This indicated that the escape of the projectile in test 19C would have been prevented if a properly sized cap was used.

Damage to Back Walls

In many tests, the exterior concrete walls were damaged. This is a major concern since the centrifuge rotunda is directly adjacent to an office building. The damage consisted of extensive cracking over a large length of the wall but very little spalling. This suggests that the gravel successfully distributes the load over a large area, which tends to cause a bending failure of the outer wall rather than perforation or spalling.

The damage to the outer wall consisted of cracking and in one case (test 38) the projectile actually struck the back wall and a few small chunks of concrete spalled off the back wall without breaking any of the re-bar in the wall. However, it can be strongly argued that the penetration resistance of sand or gravel depends on the confining pressure. Since the models were tested at reduced scale, the confining pressures in the tests were much lower than those in full-scale structure. The strength, stiffness, and shear wave velocity will all be higher in the prototype barrier. All of the above factors would tend to cause the hardness and safety provided by the prototype gravel fill to be greater than the model sand.

The influence of scale effects and the above arguments are supported by data from Schmidt (1980) who conducted impact tests at 1 g and on a centrifuge at elevated accelerations. He conclusively showed that for high velocity impact, crater dimensions (both depth and radius) varied in proportion to $L(\frac{gL}{Qe})^{\beta}$, where $0.146 < \beta < 0.21$ and L is a characteristic dimension of the projectile. In other words, if L is reduced by a factor N and g is increased (as in centrifuge modeling) by a factor N, then the crater radius will be reduced by the same factor N, and proper modeling is achieved. However, if g is not increased, the crater dimensions, r, in the model would differ from perfect scaling by a factor of N^{β}.

Adopting $\beta = 0.17$ as a value intermediate between the extremes measured by Schmidt and assuming this (N^{β}) error factor would apply to the barrier wall model tests at 1/8 to 1/20 scale, we expect an error in crater dimensions in the models by a factor of $8^{0.17} = 1.42$ and $20^{0.17} = 1.66$ respectively.

In a properly scaled model test, all dimensions should scale by the same factor. We therefore expect penetration distances to be in error by a similar factor, and hence, we expect prototype penetrations to be about 42% and 66% smaller than those directly scaled up from the model tests at 1/8 and 1/20 scale respectively.

It should be noted that Schmidt's findings were based on hyper-velocity impact (6,000 to 81,000 ft/sec) much higher than our maximum centrifuge velocity of about 500 ft/sec. It is known that as velocity decreases, target density becomes less important and target strength becomes more important.

Newton's law of motion applied to the projectile yields

$$R(v) = m \frac{dv}{dt}$$

where R(v) is the drag force as a function of velocity and m is the projectile mass. Allen et al (1957) suggested that R(v) could be expressed as

$$\frac{R(v)}{m} = \alpha v^2 + \beta v + \gamma$$

where α, β, and γ are constants that depend on the projectile shape, size, and soil properties. The first term (αv^2) is related to momentum transfer and particle crushing. The βv term is related to viscous effects which are small for sands. And the γ term is related to strength of the barrier. It is apparent that at high speeds, the αv^2 term will dominate and at low speeds the γ term will dominate. Since sand strength depends on overburden and confinement, the γ term will be less significant in our model tests than in the prototype.

Data from Schmidt (1980) and the above arguments prove that the model tests are conservative from the point of view of penetration resistance. Hence, it is concluded that though the damage to the back wall in the model tests was only marginally acceptable, the inherent conservatism of the model tests indicates that the prototype barrier is adequate.

Scaling Trajectories After Impact

The test results from the 1/20 scale tests raised concern due to the relatively high trajectories of the model concrete cap and the model projectiles after impact. However, the trajectories of objects cannot be simulated in scale test at 1 g.

Consider an object in the prototype with a vertical velocity v. According to the modeling laws summarized in Table 3, the velocity in the model is the same as the velocity in the prototype. Since they both exist in a 1 g environment the prototype and model objects will both reach an altitude of $h = \frac{v^2}{2g}$. This presents a contradiction in the scaling for tests at 1 g. The scaling law for length should be that h in the model is N times smaller than h in the prototype, however, the height of a trajectory of a flying object will be the same in model and prototype if velocities and g are the same in model and prototype. So, it is expected that since the model projectiles in tests 30 and 31A escaped with a vertical velocities of 20 and 10 ft/sec respectively, the prototype projectiles would escape with a similar vertical velocity. The height of both the model and prototype trajectories would be h = 8 ft and 2 ft for v = 20 ft/sec and 10 ft/sec respectively. While this height of climb results in complete escape of the model projectiles, a similar climb would not allow the prototype projectiles to escape, since the impact point for the prototype barrier is about 7 ft below the barrier surface.

VELOCITY-PENETRATION DATA

The model tests were filmed by a high speed movie camera at about 5,000 frames/sec. The films were then analyzed to provide the velocity versus penetration distance relations shown in Figure 8. The data shown corresponds to the time from the first impact until the projectiles disappeared into the barrier. Points of interest include:

1) The swing platform models decelerated much more rapidly than the counterweights since they had a much larger frontal area and a lower density.

2) The concrete walls, without gravel fill caused a very small drop in velocity of the counterweight models.

3) Test 37 shows a significant reduction in the deceleration at the end of the data shown. This is probably caused by the fact that the projectile was approaching the surface of the barrier, and there was no concrete cap.

CONCLUSIONS

A set of model tests has been conducted to evaluate the adequacy of a safety barrier to resist impact of high speed parts of a large geotechnical centrifuge in case of accident. The tests confirmed the adequacy provided that one modification was made. That is, a concrete slab should be placed on the gravel fill to prevent escape from the sand surface and to increase penetration resistance.

The tests represent an example of the use of model tests to assist in the design of engineering structures. The use of model tests in design is particularly helpful in problems for which analytical solutions are unreliable or unavailable. The oblique impact of irregularly shaped projectiles parallel to a nearby free surface is a highly three-dimensional dynamic problem for which available analytical solutions are wholly inadequate.

As many features were incorporated in the model tests as practical. Two "most dangerous" centrifuge parts were identified as potential projectiles. They were fired at an oblique angle near the surface of the barrier. The inherent rotation of the projectiles before impact was ignored, and the projectiles were shot into the model barriers with minimum frontal area.

The use of physical model tests for design should be similar in philosophy to the use of analytical methods in design. That is, while conservative assumptions are made when carrying out calculations, conservative facsimilies of the prototype should also be used in the model, material strengths, dimensions, and the failure models tested should represent "worst case" conditions.

ACKNOWLEDGMENTS

Several students have assisted in conducting the tests reported herein: Jin Song Tsai, Chaney Darlington, Julie Lewis, and Michael Ralph deserve thanks for their contributions. J. A. Cheney at UC Davis and J. A. Hallam, T. Trower, D. Englebert, K. Mort, and D. Matsuhiro at NASA Ames contributed to the planning and helped to provide the required facilities and assistance.

REFERENCES

1. Allen, W. A., Mayfield, E. B., and Morrison, H. L., "Dynamics of a Projectile Penetrating Sand," Jour. Appl. Phys., Vol. 28, No. 3, pp. 370-376, 1957.

2. Backman, M. E., "Terminal Ballistics," Naval Weapons Center, Technical Publication No. 5780, China Lake, Calif., February 1976.

3. Baker, W. E., Hokanson, J. C., and Bowles, P. K., "An Evaluation of the National Geotechnical Centrifuge Safety Barrier," Report to NASA Ames Res. Ctr. and Beam Engr., SWRI Project 06-7532, May 1983.

4. Cheney, J. A. and Hallam, J. A., "Study of the Safety Barrier Impact Resistance," Dept. of Civil Engr., UC Davis, June 1982.

5. Healey, J., Werner, H., Weissman, S., Dobbs, N., and Price, P., "Primary Fragment Characteristics and Impact Effects on Protective Barriers," Picatinny Arsenal Technical Report No. 4093, Ammann and Whitney, Consulting Engineers, New York, N.Y., December 1975.

6. Kutter, B. L., "The Adequacy of the NGC Safety Barrier," Dept. of Civil Engr., UC Davis, January 1983.

7. Schmidt, R. M., "Meteor Crater: Energy of Formation - Implications of Centrifuge Scaling," Proc. Lunar Planet. Sci. Conf. 11th, pp. 2099-2128, 1980.

8. Young, C. W., "Depth Prediction for Earth-Penetrating Projectiles," Journal of the Soil Mech. and Found. Div., ASCE, Vol. 95, SM3, pp. 803-817, 1969.

Table 1

SOME MODEL DIMENSIONS
(refer to Fig. 4 for definition of t_1, t_2, t_3, d)

Test	t_1	t_2	t_3	d
Group I				
18C, 19C	1.75	1.75	1.75	6.75
38	1.75	1.45	1.0	6.75
30	0.70	0.58	0.44	3.6
31A	0.70	0.58	0.60	3.6
Group II				
15C, 16C	1.75	1.75	-	6.75
37, 37A	1.75	1.45	-	6.75
Group III				
17C	1.75	1.75	-	-
34, 36	1.75	1.45	-	-

Table 2

SUMMARY OF TESTS

Shot #	Impact Velocity (ft/sec)	Scale Factor	Remarks
Tests with concrete cap (Group I)			
18C	420	1/8	Veered down, contained
19C	380	1/8	Veered up, barely, escaped, undersized concrete cap
38	398	1/8	Veered up slightly, damaged back wall, contained
30	545	1/20	Escaped with low vertical velocity, almost no horizontal velocity back wall cracked, no spalling
31A	525	1/20	
Tests with sand fill but no cap (Group II)			
15C	360	1/8	Veered up, missed short back wall, escaped
16C	390	1/8	Veered down, contained
37	300	1/8	Veered down, contained
37A	260	1/8	Veered up, not contained
Tests with no sand, just concrete walls (Group III)			
17C	350-380	1/8	Sailed through, tore steel guard plate
34	135	1/8	Veered up, missed short back wall, escaped
36	102	1/8	Contained but damaged back wall

Table 3

SCALE FACTORS FOR MODEL TESTS

Dimension	Model Dimension / Prototype Dimension
Mass	$1/N^3$
Density	1
Length	1/N
Velocity	1
Acceleration	N
Gravity	1
Strength of Concrete	1

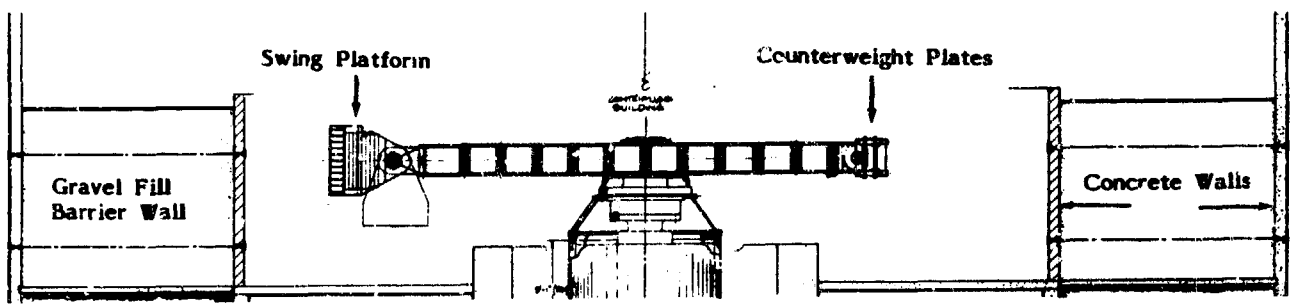

Figure 1. Cross-section of National Geotechnical Centrifuge and proposed barrier wall.

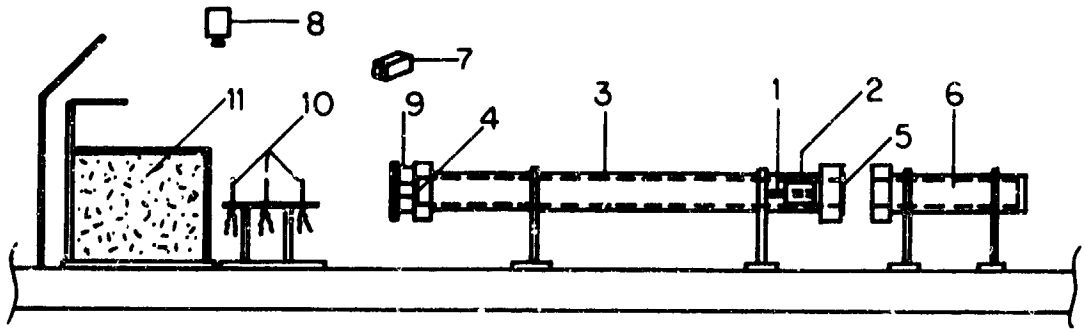

Figure 2. Model test setup.

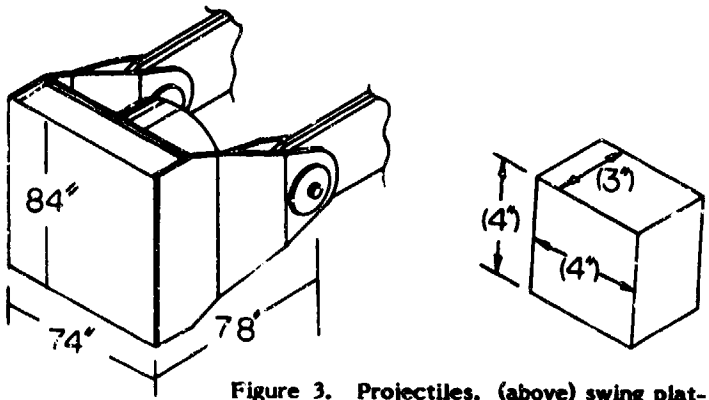

Figure 3. Projectiles. (above) swing platform and (below) counterweight plate (model dimensions in parentheses).

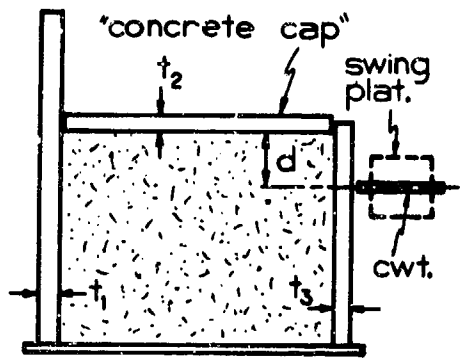

Figure 4. Model Barrier Wall

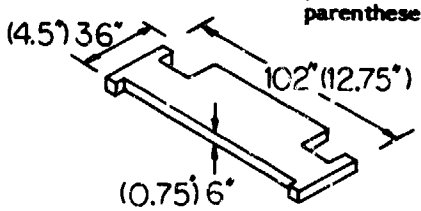

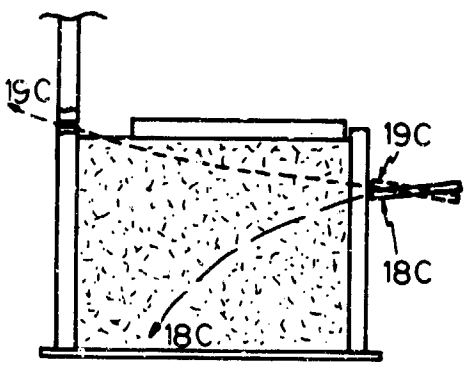

Figure 6. Projectile paths in tests 18C and 19C.

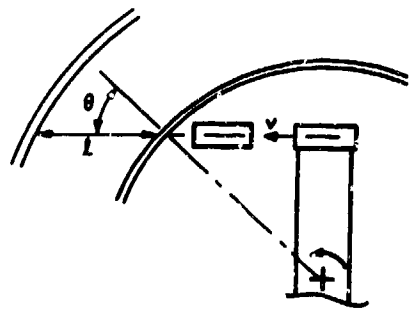

Figure 5. (above) Projectile path and angle of impact.

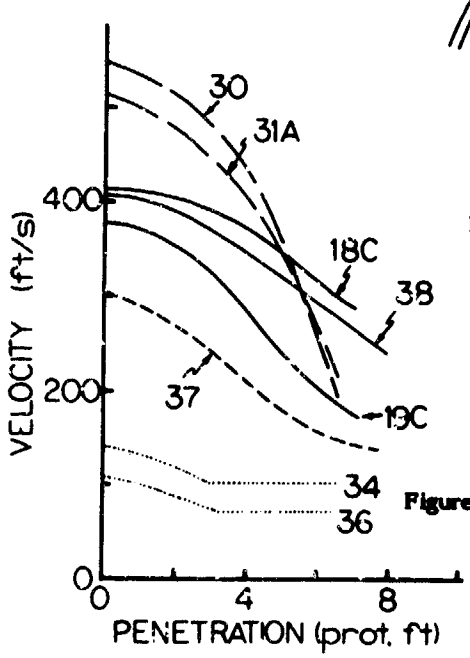

Figure 7. (left) Velocity penetration data.

CENTRIFUGE MODELING OF BURIED STRUCTURES

Hon-Yim Ko
Chin-Kuan Ni
and
Stein Sture

University of Colorado
Boulder, Colorado

ABSTRACT

The complex problem of the reaction of a buried structure to loads applied at the ground surface is studied using physical modeling in a geotechnical centrifuge. Centrifuge testing provides the opportunity to collect performance data on scale models of buried structures under conditions simulating the prototype, since the increased body forces in the centrifuge model make it possible to simulate the self-weight induced stresses that control the stiffness and strength of the soil. The data collected by centrifuge testing under controlled laboratory conditions are used as the basis for calibrating numerical models in which a major input component is the constitutive properties of the soil.

The centrifuge experiments are conducted in the 10 g-ton machine at the University of Colorado. A four-inch diameter pipe is tested at 50 g, representing a 1/50-th scale model of a horizontal missile shelter. The model is instrumented with strain gages to measure the stresses in the pipe and with LVDT's to measure the pipe deflections. The behavior of the test model under surface applied pressure is described.

INTRODUCTION

In geotechnical engineering, the deformations and stability of structures built in, and of, earth materials are of primary concern. In the analysis, design and construction of earth structures, the conventional approach employs the following steps:

(1) Investigate the site conditions.
(2) Obtain material properties from field testing or laboratory testing of representative samples.
(3) Cast the material properties into constitutive models suitable for incorporation into analysis.
(4) Perform the analysis, usually in a numerical fashion, for the prediction of the response of the structure being designed.
(5) Evaluate the adequacy of the design on the basis of past experience with similar structures and modify the design as necessary.
(6) Construct the structure according to an acceptable design.

In spite of the sophistication in computer modeling techniques, the predictions made often prove inadequate, primarily due to a poor understanding and representation of the complex constitutive properties of earth materials which exhibit nonlinear, time-dependent and inelastic behavior. Calibration of proposed constitutive models and the methods of analysis, by comparing predictions against measured prototype structural response, is often hampered by a poor understanding of the site characteristics including the local geology and, more importantly, by the high costs and grave consequences involved in loading a structure to failure.

Structures with economic or safety importance, such as earth dams, underground facilities, nuclear power plants, or offshore drilling platforms, and structures with defense applications, such as missile silos, are often unique in design because of the prevalent site conditions and unprecedented loading conditions. In dealing with these structures, there is usually a scarcity of data on similar prototype structures that have been built and monitored to provide a guidance to the selection of the proper design. This problem becomes much more acute in situations where dynamic loadings are involved, such as blast and earthquake excitation.

The difficulty can be largely overcome by model testing, as is traditionally carried out in hydraulic engineering and in the aircraft industry. The laws of similitude must be followed if model testing is to provide meaningful results. For geotechnical structures, the primary loading function is derived from the self weight of the materials. In addition, the behavior of soil materials is stress dependent, making it necessary to simulate the stress level in soil masses if the correct structural response is desired. To simulate correctly the stresses in the prototype, a geometrically similar model must be subjected, in a centrifuge, to an increased gravity whose ratio to earth's gravity is the inverse of the length scale by which the model is scaled down from the prototype. And if the same prototype material is used in the model, the same strains will be obtained in the model as in the prototype. The full structural response will then be observed.

There are many other advantages in testing scaled centrifugal models; for example, the time scale for diffusion phenomena such as consolidation and heat conduction is reduced by a factor of n^2, where n is the gravity ratio, and the forces required for loading are also similarly reduced. On the other hand, the time scale for dynamic phenomena is reduced by a factor of n.

In order to model actual prototypes which are sometimes quite large, centrifuges of a very large capacity may be required. The high costs involved with maintaining, and testing in, such facilities make it impractical to base our design procedures entirely on the findings of centrifuge modeling. On the other hand, if centrifuge modeling is employed in conjunction with constitutive modeling and numerical analyses, it becomes possible to utilize the centrifuge test results as a basis for calibrating the numerical modeling. As illustrated in Fig. 1, the numerical modeling technique can be first applied to predict the behavior of centrifuge models by duplicating all the details in the latter, including the material properties, and boundary and loading conditions. Only after satisfactory verification of the accuracy of the numerical modeling technique has been obtained through comparison with the centrifuge test data will it be applied to full scale structures. In adopting this philosophy, the question of utilizing a very large centrifuge is bypassed, although it is still necessary to maintain a reasonable resemblance to the types of problems being studied by employing centrifuges of a sufficient capacity to reach the stress levels experienced by the prototypes under consideration.

MODELING OF BURIED STRUCTURES

Behavior of buried structures is governed by the interaction between the soil and the structure. For instance, if a pipe buried in the ground deflects against the surrounding soil, the resisting soil pressure increases as a function of deflection and cannot be predetermined without analyzing the combined interaction of the two components. Soil-structure interaction analysis, particularly under dynamic loads derived from a surcharge, or stress waves propagating from a ground shock nearby or from earthquake excitation, is a complex undertaking and requires consideration of the properties of both the soil and the pipe material as well as the interface conditions between the two. Many computer codes have been developed for such analyses, e.g., the CANDE code for static analysis, and numerous codes used in the defense industry for analyzing ground shock loading on underground missile silos. The accuracy of these analyses can best be verified by comparison with measurements on the full scale prototype. However, as mentioned previously, such measurements are often difficult and costly, for instance, when explosive loading is involved. On the other hand, measurements taken on reduced scale models tested under normal gravity can be misleading because the stress level due to loading by the soil's self weight is not properly simulated.

It would seem reasonable, then, to expect centrifugal modeling to provide an attractive alternative for gathering data for validating analytical results. Centrifugal test results can be obtained to a high degree of accuracy, especially by employing the modeling of models technique in which several models of different scales are used to model the same "prototype" by testing them at the respective gravity level to bring each into similitude with the prototype and with each other. By exercising the analytical procedure, whether in closed form or by numerical solution (e.g., finite elements, finite difference, or boundary integral methods), to analyze the centrifuge test in the exact manner by duplicating the boundary and loading conditions as well as the material properties, then the accuracy of the analytical procedure can be verified against the centrifuge test results.

Based on the above philosophy, a research program has been started to develop techniques of testing models of buried structures in a geotechnical centrifuge under static and dynamic loadings. Concurrent with the centrifuge testing program are efforts to model the constitutive behavior of the soil used in the experiments and to numerically model the experiments. The primary objective is to collect the necessary data on the performance of buried structures so as to identify the pertinent features of behavior and to validate the accuracy of the available computer codes. This paper gives a progress report of these research efforts.

EXPERIMENTAL PROGRAM

The experimental program of centrifuge testing is designed on the premise of modeling a horizontal missile shelter with a 16.7 ft. O.D. and buried 8.3 ft. below the ground surface. Using a length scale of 50, the configuration shown in Fig. 2 is adopted for the centrifuge tests to be carried out at 50 g in the 10 g-ton geotechnical centrifuge at the University of Colorado.

This centrifuge has a radius of 53.5 in. to the surface of the swing basket which can carry a payload measuring 18 in. by 18 in. in base dimensions. Its rated capacity allows a 200 lb. payload to be accelerated to 100 g. It has 56 electrical slip rings for power and instrumentation signal transmission, and 2 hydraulic rotary joints for hydraulic or pneumatic power and fluid transmission. The experiment is monitored by inflight closed circuit television and on-board still photography under remote control.

The size of the payload shown in Fig. 2 is governed by the available space on the centrifuge basket. The presence of the soil container boundaries on the soil mass may not be representative of prototype conditions, but are easily duplicated in any analysis (e.g., finite elements) of the experiment. In fact, the possibility of exactly duplicating the boundary conditions allows for the close scrutiny of the performance of the numerical algorithm and the constitutive model in the analy-

sis. Similarly, the choice of the pipe thickness for these experiments might not simulate the actual conditions in the prototype missile shelter, but it allows the soil-structure interaction aspects of the experiment to be fully exploited. Future experiments on thicker pipes can be easily conducted by using the methodology described herein.

The soil used in these experiments was a typical silty, clayey sand found in the valleys in the Nevada desert. This soil had been previously used in missile site selection studies such that its basic mechanical properties are already available.

The model pipe was made of an aluminum sheet, bent and soldered along a longitudinal seam. The total length of the pipe was 15.9 in., leaving 0.05 in. of gap from the end walls of the soil container. As shown in Fig. 3, 11 pairs of strain gages were placed around the pipe at the mid-section, to measure the strains developed on the inside and outside surfaces of the pipe due to surface loading. The gages were located at spacings of 18° or one side of the pipe, and symmetry is assumed. In addition, 12 LVDT's were used to measure the deflections of the pipe. They were mounted on a strong rod which was anchored on the end walls of the soil container and was, therefore, independent of the movement of the pipe. These LVDT's were aligned radially in order to detect the radial deflections, and were spaced all around the pipe in several longitudinal sections near the mid-plane of the pipe. However, by assuming symmetry and by neglecting end effects, the 12 deflections measured by the LVDT's are interpreted as if they were obtained on one side of the pipe in one single section. Under such interpretation, the LVDT locations used in the experiments are shown in Fig. 3.

The interaction between the soil and the buried pipe is influenced by the embedment conditions around the pipe. To simulate construction conditions in the field, the soil used in these centrifuge experiments was statically compacted in layers to 95% compaction. The soil sample was prepared in two halves, separated at the level of the springline of the pipe. A special soil cutting tool was used to carve out a semi-cylindrical trough in each half, so that when the two halves were put together a cylindrical opening was formed to accommodate the 4-in. diameter pipe with a snug fit. Successive experiments on samples prepared in this fashion produced repeatable results, indicating this procedure to be successful.

The loading was applied to the soil surface by pneumatically pressurizing a silicon rubber membrane confined within a metal frame which was mounted on the soil container, as shown in Fig. 2. In the experiments conducted so far, the pressure was applied over a 2.9-in. wide strip of the surface symmetrically directly over the pipe location. Variations of this loading to include asymmetrical loading will be used in future experiments. This loading was statically applied in steps. Methods of dynamic loading are also being developed for future use.

Signal conditioning units for the LVDT's and strain gages were mounted on the centrifuge arm. The signals were amplified to the ±10V range before transmission through the slip rings. In this way, the slip ring noise problem was bypassed. The signals were acquired by a microcomputer based data acquisition system for storage and subsequent analysis.

EXPERIMENTAL RESULTS

Only a few experiments have been performed to date. They involved static, symmetrical loading on a flexible buried pipe. Typical response of the pipe is given in Figs. 4, 5, 6 in which the bending moments, hoop stresses and pipe deflections are shown in polar plots around the pipe. The bending moment at a location is calculated from the difference of the inside and outside strain gage readings there, while the hoop stress is calculated from the sum of these readings. The patterns shown in Figs. 4, 5, and 6 were obtained under four pressure increments of 10 psi each and they indicate that nonlinear response had developed under the higher pressures. Loading of the pipe to failure had not been carried out, since it was tedious and expensive to manufacture and instrument a new model.

ANALYTICAL MODELING

The analytical work being pursued consists of finite element modeling in which the soil properties are modeled by elastoplastic constitutive relations. The interface conditions between the soil and the pipe will also be modeled, since it is felt that this may be a crucial factor that influences soil structure interaction, particularly near failure state of the pipe.

In previous research in which numerical models were validated against centrifuge test results, it was possible to differentiate between different constitutive models in terms of their effectiveness in capturing the soil structure response. For instance, in the modeling of soil excavation, it was found that it was futile to use nonlinear hyperbolic stress-strain relations, since strain increments experienced during excavation were generally not aligned with the prevalent stress directions. It was necessary to employ incremental plasticity to duplicate the observed deformation pattern. It is anticipated similar considerations will be made in the modeling of buried structures, leading to conclusions regarding the accuracy of the numerical analysis including the soil material characterization.

ACKNOWLEDGEMENT

This work is being supported by a grant from the Air Force Office of Scientific Reserch, No. AFOSR84-0300. This support is gratefully acknowledged.

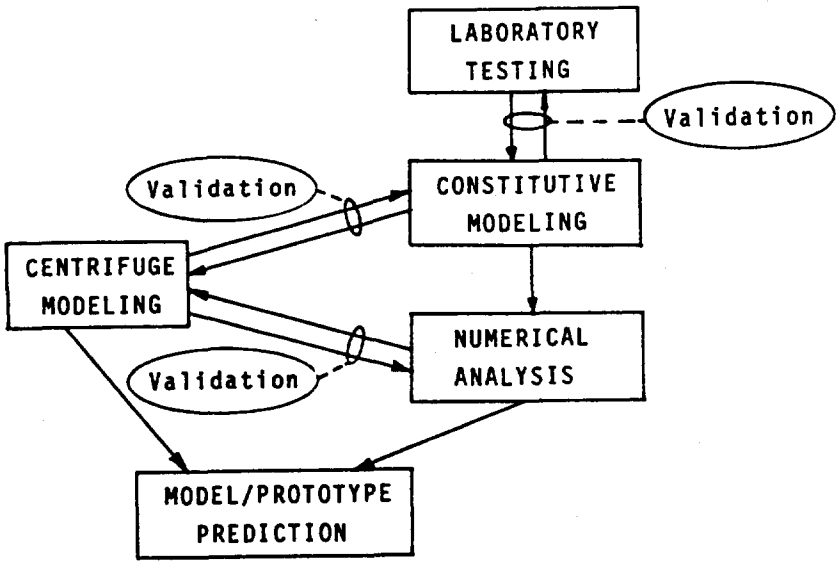

Fig. 1. Validation of Design and Analysis Procedure

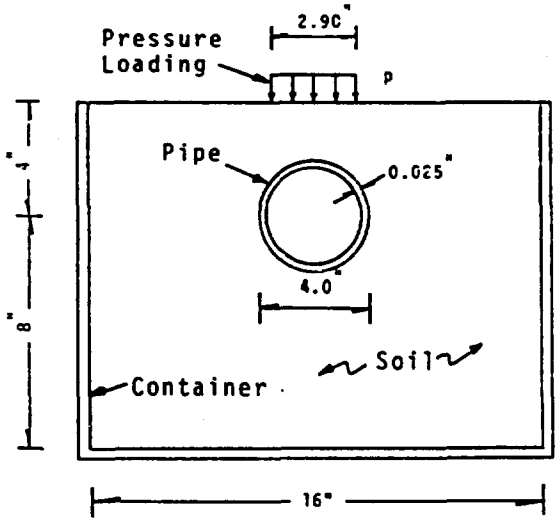

Fig. 2. Centrifuge Test Package of Buried Pipe

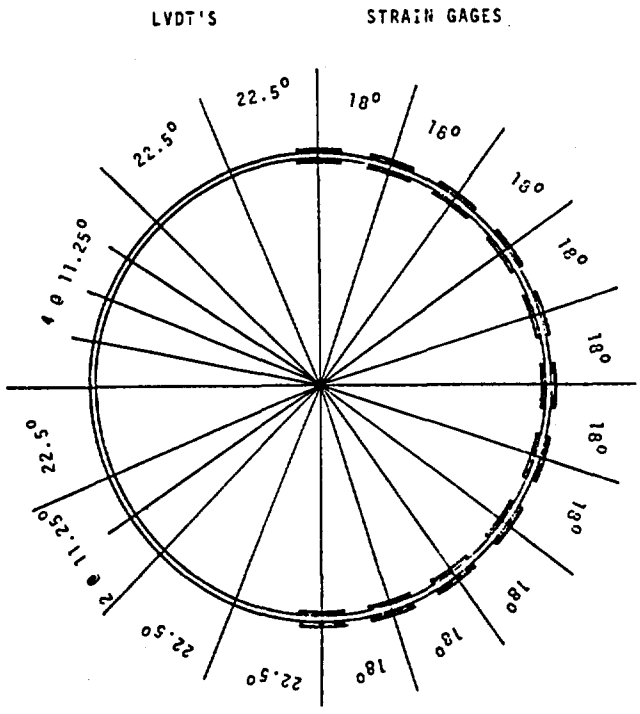

Fig. 3. Location of Instrumentation on Model Pipe

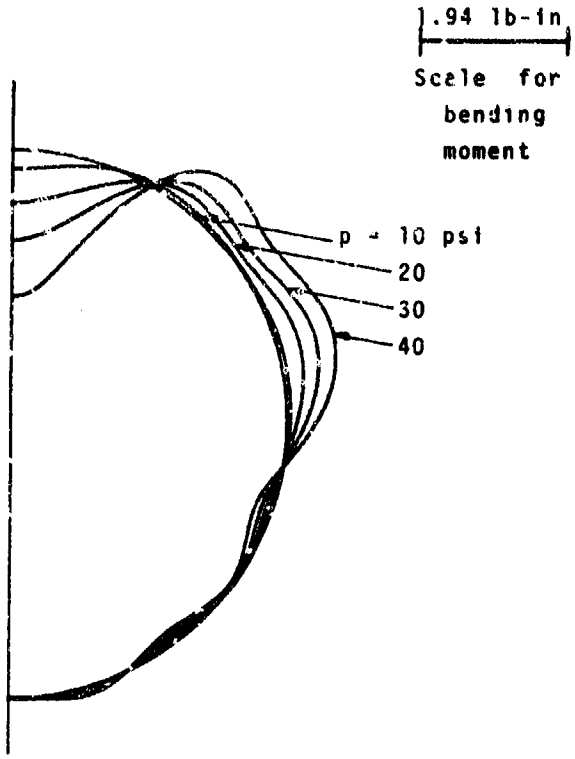

Fig. 4. Bending Moment Around Pipe

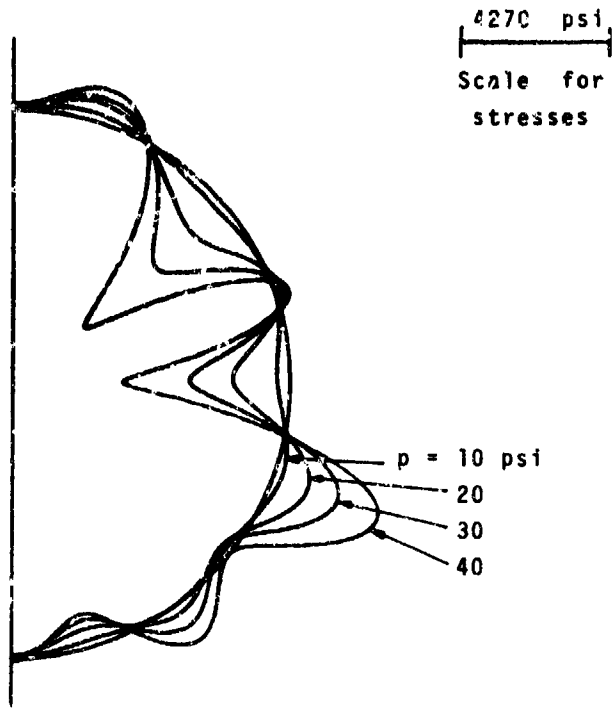

Fig. 5. Hoop Stress Around Pipe

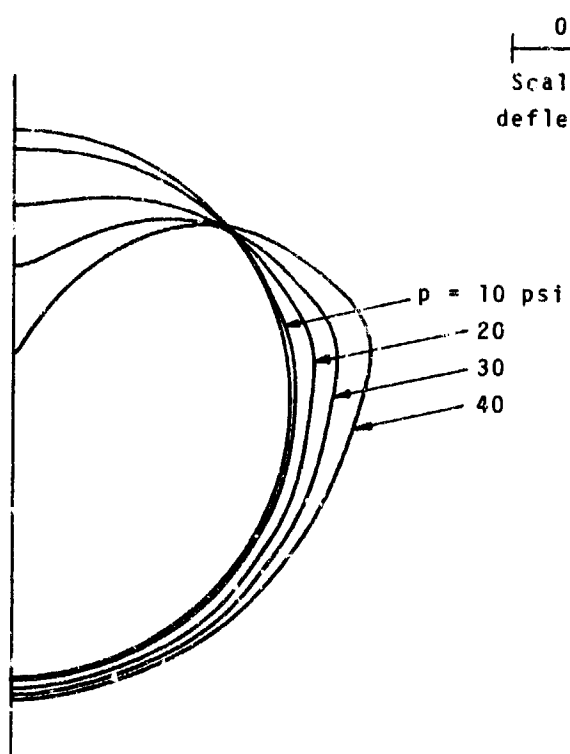

Fig. 6. Pipe Deflections

VERIFICATION OF IN SITU PREDICTION OF STRESS-STRAIN BEHAVIOR BY LABORATORY AND CENTRIFUGE TESTS

Namunu J. Meegoda[1], A. Anandarajah[2], and Kandiah Arulanandan[1]

[1]University of California, Davis, California and [2]John Hopkins University, Baltimore, Maryland

ABSTRACT

The input properties for the determination of stress-strain behavior of a soil using the bounding surface plasticity model were predicted by in situ nondestructive testing. The predicted stress-strain behavior was compared with that measured using undisturbed Shelby tube samples.

The validity of the in situ prediction of the stress-strain behavior was also checked for remolded soil and compared with laboratory measurements. The accuracy of the predicted strength was further checked by studying the stability of a slope in the centrifuge.

INTRODUCTION

The application of any constitutive model for the prediction of field performance requires input properties that are representative of field conditions. In situations where undisturbed samples are difficult to obtain without destroying the cementation or structure, input parameters need to be obtained by in situ tests.

This paper has the following objectives: 1) a comparison of the stress-strain behavior obtained from nondestructive in situ tests with that obtained on undisturbed Shelby tube samples, and 2) a validation of the use of in situ tests by obtaining input parameters for the prediction of stress-strain behavior on remolded samples and utilizing the predicted stress-strain behavior to examine the stability of a slope tested in the centrifuge.

BOUNDING SURFACE PLASTICITY MODEL

A bounding surface plasticity model has been developed by Dafalias (1979) to describe the stress-strain behavior of fine grained soils under a variety of loading conditions.

One of the desirable features of this approach is that the plastic deformation takes place within the bounding surface unlike the classical plasticity theory where the behavior is fully elastic within the yield surface. This feature of the model yields realistic predictions for overconsolidated soils and under cyclic loading conditions.

The bounding surface concept is that the plastic modulus of the material at a given stress state can be determined knowing the stress state, a distance from a point on the bounding surface (defined by means of a suitable mapping rule) to the point representing the current stress state, a plastic internal variable to account for the past loading history and the plastic modulus corresponding to the projected point on the bounding surface.

The detailed description of the theory could be found in Dafalias et al. (1979,1980). The information required for the prediction of stress-strain behavior of normally consolidated soils are (1) the slope of isotropic consolidation line, λ, in the $e - \log_e p$ space, where p = mean normal pressure; (2) the slope of isotropic swelling line, κ, in the $e - \log_e p$ space; (3) the slope of critical state line, M, in the $q - p$ space, where q = deviatoric stress; (4) the parameter, R which is defined as the ratio of the mean normal pressure, p_0 at which the bounding surface intersects the p - axis and the mean normal pressure, p_1 at which the bounding surface intersects the critical state line ($R = 2.72$ in Cam-Clay theory (Schofield et al., 1968); (5) the initial void ratio, e_o; and (6) the preconsolidation pressure, p_0.

PREDICTION OF INPUT PARAMETERS FOR THE BOUNDING SURFACE MODEL

The conductivity, σ, and the dielectric constant, ε, of granular soils are shown to be independent, whereas σ and ε of cohesive soils are shown to vary with the frequency of the alternating current (Arulanandan et al., 1983). The above electrical behavior has been used to quantify the compositional and heterogeneous nature of particulate systems (Arulanandan et al., 1973, 1978,1979,1982).

The granular soils are characterized by the formation factor $F = \sigma_{solution}/\sigma_{sample}$ and the average formation factor $\bar{F} = 1/3\ (F_V + 2F_H)$ is shown to be uniquely related to porosity. The electrical anisotropy index A, where $A^2 = F_V/F_H$ is used to characterize the orientation of particles, where F_V is the vertical formation factor and F_H is the horizontal formation factor. The shape of the particles are quantified by $\bar{f} = -\log \bar{F}/\log n$, where n is the porosity of the sample. The aggregate and grain properties of a granular media could be quantified by ($\bar{F}$, A) and $\bar{f}$ respectively.

A three element electrical network model is used to quantify the inter- and intra-cluster void ratios of

cohesive systems (Arulanandan et al., 1985). The significance of intra-cluster void ratio to swelling is shown in Fig. 1 by a correlation between the swell index κ and e_I/e_T, where e_I and e_T are the intra-cluster and total void ratios respectively (Arulanandan et al., 1983).

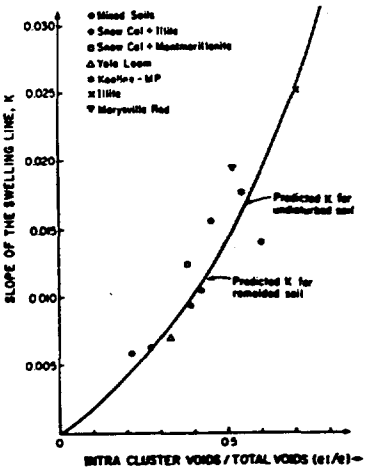

FIG. 1. Correlation between slope of the swelling line (κ) and ratio of intra-cluster to total voids.

The magnitude of dielectric dispersion which is dependent on the compositional and heterogeneous nature of the cohesive system is shown to be directly related to the compression index λ, as shown in Fig. 2 (Arulanandan et al., 1983).

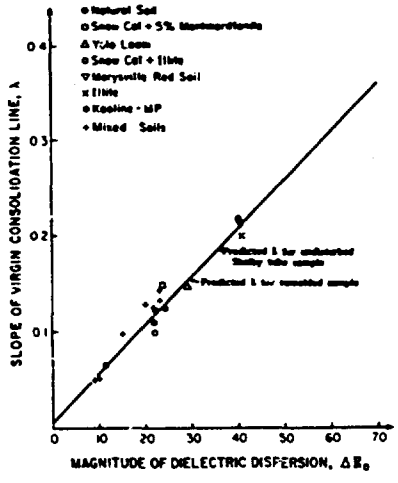

FIG. 2. Correlation between slope of the compression line (λ) and the magnitude of dielectric dispersion.

A combination of the parameters 'A' and $\bar{f}$ of cohesive systems is shown to be uniquely related to M, the slope of the critical state line in the bounding surface model, as shown in Fig. 3 (Arulanandan et al., 1983). Correlations of κ, λ, and M with electrical parameters have been extensively studied by Anandarajah (1982), Meegoda (1983), Abdullah (1983), and Arulanandan et al. (1983).

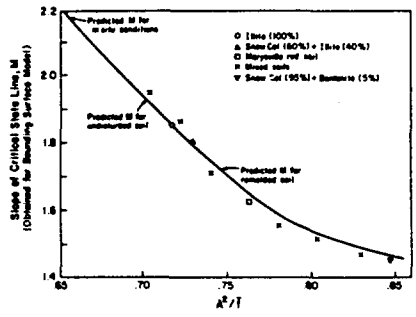

FIG. 3. Correlation between the slope of the critical state line (M) in the bounding surface model and the electrical index A^2/f.

FIELD TESTING AND RESULTS

In situ electrical measurement and water contents were determined at a site containing copper mine tailings. The in situ water contents as a function of depth were determined in three bore holes which were spaced at a distance of fifteen feet apart. The soil profiles, the water table depth, and the average distribution of water content as a function of depth are shown in Fig. 4. The water content decreases with depth with a maximum value of about 65 percent at the water table depth to a value of 50 percent at a depth of 40 feet below the surface.

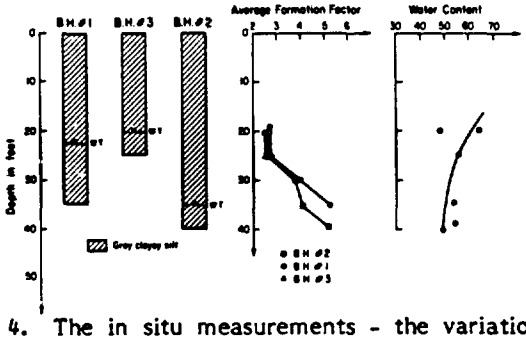

FIG. 4. The in situ measurements - the variation of formation factor and water content with depth.

The in situ formation factors determined by the use of an electrical probe (Geoelectronic Model GE100) in the horizontal and vertical directions, at different depths, are plotted in Fig. 4. The average formation factor is seen to increase with depth. The method of determining the in situ vertical and horizontal formation factors are described elsewhere, Arulanandan et al. (1979,1982), Ertec Western, Inc. (1982), and Arulmoli et al. (1985). Using the in situ formation factor and the in situ water content, the in situ shape factor $\bar{f}$ is estimated using the relationship $\bar{f} = -\log \bar{F}/\log n$. Using the in situ values of A and $\bar{f}$, the slope of critical state line (M) is estimated with the aid of Fig. 3.

It was found that the predicted stress-strain curve and stress path using bounding surface model (Herrmann et al., 1980) is not significantly affected by slight variation in λ and κ values. Hence the values of λ and κ used in the prediction of stress-strain relationship are the values determined on Shelby tube samples. The estimated void ratio and pressure relationship for the in situ state is shown in Fig. 5.

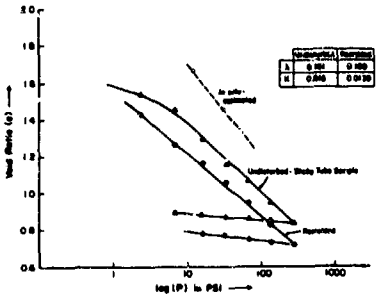

FIG. 5. Relationship between vertical pressure (p) and void ratio (e) for remolded and undisturbed samples.

A computer program utilizing the bounding surface plasticity theory (Herrmann et al., 1980) is used to obtain the predicted stress-strain relationship as shown in Fig. 6.

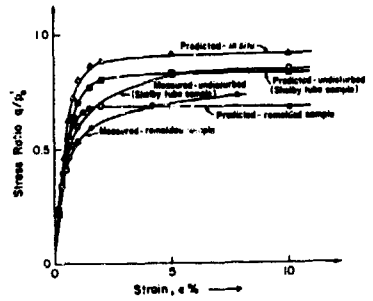

FIG. 6. The normalized stress vs. strain relationship (measured and predicted) for in situ, undisturbed and remolded states.

LABORATORY TESTING AND RESULTS

In order to validate the procedure used to predict the in situ stress-strain behavior, laboratory tests on undisturbed and remolded samples were carried out. Remolded sample in the form of a slurry was prepared and electrical conductivity and dielectric constant as a function of frequency in the radio frequency range were measured at each state of consolidation. A typical set of electrical dispersion curves are plotted in Fig. 7.

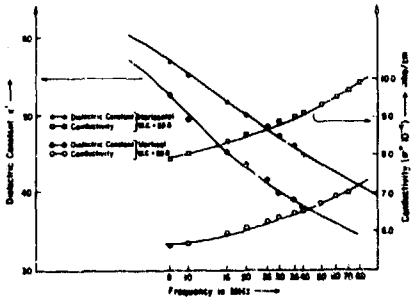

FIG. 7. Electrical dispersion data for remolded soils at 1.119 psi.

Similarly, Shelby tube samples were cut and trimmed to the size of electrical measuring cells and electrical measurements were made.

The physical properties, the consolidation and rebound characteristics, the permeability characteristics, the stress-strain behavior of undisturbed samples obtained from Shelby tube, and remolded samples were determined. The properties are tabulated in Table 1. The consolidation and rebound characteristics of undisturbed and remolded samples are compared in Fig. 5. An estimated in situ consolidation behavior based on in situ water content and overburden pressure is also shown in Fig. 5. Significant differences in the consolidation characteristics of in situ, Shelby tubes, and remolded samples are seen to exist.

Using the measured values of A and f for remolded and Shelby tube samples, the slope of critical state line (M) is estimated with the aid of Fig. 3.

The electrical dispersion data for remolded and Shelby tube samples were used to obtain the intra-cluster void ratio and the magnitude of dielectric dispersion.

Using Fig. 1 and Fig. 2 the λ and κ values for remolded and Shelby tube samples were obtained.

The values of λ, κ, and M were used in the bounding surface plasticity model (Herrmann et al., 1980) to predict the stress-strain behavior. The predicted results are compared in Fig. 6 with the measured results. The measured and predicted electrical and mechanical properties are summarized in Table 1.

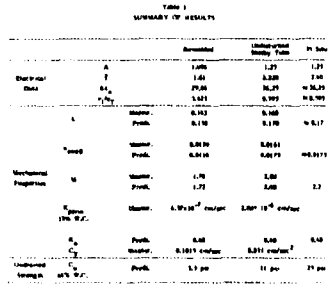

DISCUSSION OF IN SITU AND LABORATORY TEST RESULTS AND STRESS-STRAIN BEHAVIOR

The difference in the formation factors measured in situ and that measured on remolded samples at the same porosity is a clear indication of the structure sensitivity of the soil. The structure is partially disturbed even in a conventional undisturbed Shelby tube sample as reflected by the difference in formation factors of in situ and undisturbed sample. The distinct difference in the strength (stress-strain behavior) measured in the laboratory on the undisturbed and remolded soil confirm the structure sensitivity of the soil.

Cementation is a possible cause for the high strength behavior of the in situ soil. The shape factor for undisturbed soil is about 2.22 compared to that of the remolded soil of about 1.61. This difference is mainly due to the cementation and fabric anisotropy. Cementation produces a higher shape factor and is evident from the work of Willey and Gregory (1953). The values of bounding surface M of 1.72 for remolded soil predicted from laboratory measurements compared

to that of 2.2 for undisturbed soil predicted from in situ electrical measurements shows the need for nondestructive testing to assess in situ soil behavior.

The reasonably close agreement between the predicted stress-strain behavior for remolded and Shelby tube samples using the electrical measurements and the bounding surface plasticity theory with the measured stress-strain behavior validates the method of predicting the in situ stress-strain behavior.

The predicted differences in the mechanical behavior of undisturbed and in situ samples show the influence of disturbance during sampling, transportation, and testing. It is clearly evident that nondestructive testing is a necessary prerequisite for the proper prediction of in situ mechanical behavior of structure sensitive soils. Destructive methods of testing are inadequate to predict in situ behavior especially in soils that are structure sensitive such as copper mine tailings.

CENTRIFUGE TESTS AND RESULTS

In order to further validate the accuracy of the predicted in situ stress-strain behavior, a centrifuge model behavior was analyzed using the predicted strength (stress-strain behavior). Initially the sample was mixed with water to form a slurry of uniform consistency. The sample was then poured into the centrifuge bucket (1' x 1' x ½') and allowed to settle under its own weight for one day. Then the soil was consolidated under a twenty-six pound load for one day. The sample was then mounted in the centrifuge and was accelerated to fifty times the acceleration of gravity. After four hours of consolidation at 50 g's the centrifuge was stopped and a 30° slope was cut with a metal template. The photograph of the finished slope is as shown in Fig. 8, where the dimensions of the slope are given in Fig. 10.

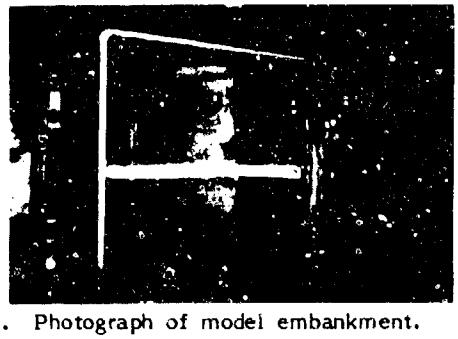

FIG. 8. Photograph of model embankment.

The cut sample was covered by two lines of chalk dust to aid in the detection of a crack. The slope was accelerated at 20 g's for ten minutes with no failure. The acceleration was increased to 30 g's and after three minutes a crack formed (see Fig. 10). The sample was kept at 30 g's for another 12 minutes but the crack did not progress. It was then accelerated to 40 g's and immediately the slope failed with a tension crack formed across the top of the sample. The failed embankment was allowed to dry in order to examine the mode of failure. A circular arc toe failure was observed (see Fig. 10).

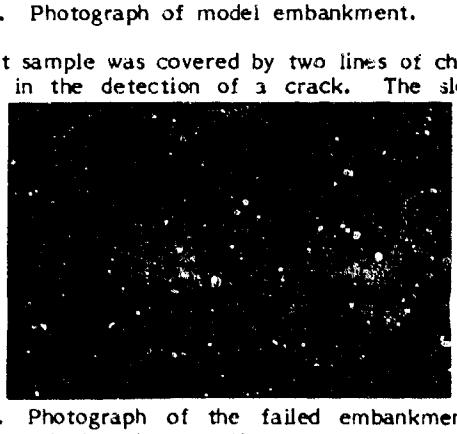

FIG. 9. Photograph of the failed embankment after spinning the centrifuge.

The q/p value at failure for the remolded soil (see Fig. 6) was used to obtain the value of C_u (see Table 1). The value of p was estimated from the measured water content.

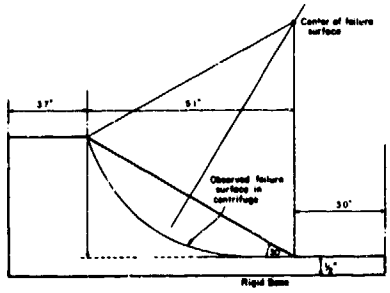

FIG. 10. Dimensions of the embankment with the observed failure surface.

ANALYSIS AND DISCUSSION OF THE CENTRIFUGE TEST RESULTS

A total stress slope stability analysis was carried out for the configuration of the slope as shown in Fig. 8. The value of c = 3.30 psi (at an average water content of 46 percent as determined from samples obtained in the model at different depths) and values of $\alpha = 30°$, r = ½' as observed in the model test were used to determine the critical height at which a factor of safety of one was obtained.

The distance from the center of the rotation to the center of gravity of the slipped mass, $\bar{x}$, can be shown to be equal to

$$\bar{x} = \frac{r/2\ (1 - \cos 2\alpha)}{\alpha - \frac{1}{2} \sin 2\alpha}$$

For the equilibrium of the slide

$$r^2(\alpha - \tfrac{1}{2} \sin 2\alpha)\rho\ (Ng)\ \bar{x} \sin \alpha = 2\alpha r^2 c$$

The value of N corresponding to a factor of safety of one is seen to be 41. The slope failed in the centrifuge test at an N value of 40. Thus the critical height of the slope ($\alpha = 30°$) can be shown to be equal to 10 feet. This research provides a valid justification for use of in situ testing by electrical method to predict the stress-strain behavior.

If the predicted soil strength, c = 11 psi, corresponding to the "undisturbed" sample is used for the slope stability analysis the critical height would be about 33 feet. For the predicted in situ strength of c = 23 psi, the critical height is about 71 feet.

The above analysis demonstrates the importance of nondestructive in situ testing to obtain input parameters for use in constitutive relationships to predict deformation behavior. This is particularly important in soils which are structure sensitive such as in mine tailings. It is very difficult to predict the in situ stress-strain behavior of structure sensitive soils by destructive in situ testing. The difficulty of obtaining undisturbed samples poses problems of predicting in situ stress-strain behavior by laboratory testing.

SUMMARY AND CONCLUSIONS

In situ testing using the nondestructive electrical method of soil characterization was used to predict in situ stress-strain behavior of copper mine tailings.

Laboratory electrical and mechanical tests on undisturbed and remolded samples of copper mine tailings were used to validate the nondestructive testing method. The measured stress-strain behavior is in reasonable agreement with that predicted using nondestructive electrical method and boundary surface plasticity model.

Centrifuge model behavior of the slope stability was analyzed using input parameters predicted by the electrical method to further validate the procedure used to predict the in situ stress-strain behavior. The stable height of the embankment evaluated using the predicted strength (stress-strain behavior) was in accordance with the observed.

This study shows that the electrical method of nondestructive testing to obtain input parameters for the use in constitutive relationships is very effective in structure sensitive soils such as copper mine tailings.

The stable height obtained from analysis of an embankment composed of mine tailing vary from 10 feet, 33 feet, and 71 feet when results of remolded, undisturbed (Shelby tube samples) and in situ properties using the electrical method respectively are used.

In structure sensitive soils nondestructive methods of soil testing are essential.

ACKNOWLEDGMENTS

The facilities provided by Geoelectronics are greatly appreciated.

REFERENCES

1. Abdullah, A. (1983), "A Fundamental Approach for the Characterization of Mixed Soils to Predict Stress-Strain Behavior In Situ." Dissertation presented to the University of California, Davis, in partial fulfillment of the requirements for the degree of Doctor of Philosophy.

2. Anandarajah, A. (1982), "In Situ Prediction of Stress-Strain Relationships of Clays Using a Bounding Surface Plasticity Model and Electrical Methods," Dissertation presented to the University of California, Davis, California, in 1982, in partial fulfillment of the requirements for the degree of Doctor of Philosophy.

3. Arulanandan, K. and Smith, S. S. (1973), "Electrical Dispersion in Relation to Soil Structure," Journal of the Soil Mechanics and Foundation Division, ASCE, Vol. 99, No. SM12, Proc. Paper 10235, December.

4. Arulanandan, K. and Kutter, B. (1978), "A Directional Structural Index Related to Sand Liquefaction," Proceedings on the Specialty Conference on Earthquake Engineering and Soil Dynamics, ASCE, Pasadena, CA, June, pp. 213-229.

5. Arulanandan, K. and Dafalias, Y. F. (1979), "Significance of Formation Factor in Sand Structure Characterization," Letters in Applied and Engineering Sciences, Vol. 17, pp. 109-112.

6. Arulanandan, K., Arulmoli, K., Dafalias, Y. F., and Herrmann, L. R. (1982), "In Situ Prediction of Shear Wave Velocities and Stress Strain Relationship of Soils," Report to the Air Force Office of Scientific Research.

7. Arulanandan, K., Anandarajah, A., Dafalias, Y. F., and Herrmann, L. R. (1982), "In Situ Characterization of Soils for Prediction of Stress Strain Relationship of Soft Clay," Report to the Air Force Office of Scientific Research.

8. Arulanandan, K., Anandarajah, A., and Meegoda, N. J. (1983), "Soil Characterization for Non-Destructive In Situ Testing," Symposium Proceedings Part 2, The Interaction of Non-Nuclear Munitions with Structures, U.S. Air Force Academy, Colorado, pp. 69-75, May.

9. Arulanandan, K., Anandarajah, A., and Meegoda, N. J. (1985), "Quantification of Inter and Intra Cluster Void Ratios Using Three Element Electrical Model," UCD Report to be Published.

10. Arulmoli, K., Arulanandan, K., and Seed, H. B. (1985), "New Method for Evaluation Liquefaction Potential," In Press, ASCE, GT., to be published in January 1985.

11. Dafalias, Y. F. (1979), "A Model for Soil Behavior Under Monotonic and Cyclic Loading Condition," Trans., 5th SMRT, K 1/8, Berlin, Germany.

12. Dafalias, Y. F. and Herrmann, L. R. (1980), "Bounding Surface Formulation of Soil Plasticity," Soils Under Cyclic and Transient Loading, Swansea, U.K., pp. 335-345.

13. Ertec Western, Inc. (1982), "In Situ Prediction of Shear Wave Velocity."

14. Herrmann, L. R., Dafalias, Y. F., and DeNatale, J. S. (1980), "Bounding Surface Plasticity for Soil Modeling," Final Report to Civil Engineering Laboratory, Naval Construction Battalion Center, Port Hueneme, CA, October.

15. Herrmann, L. R. and Mish, K. D. (1983), "Finite Element Analysis for Cohesive Soil, Stress and Consolidation Problems Using Bounding Surface Plasticity Theory, Final Report to Naval Construction Battalion Center, Port Hueneme, CA.

16. Meegoda, N. J. (1983), "Prediction of in Situ Stress State Using Electrical Method," Thesis submitted in partial satisfaction of the requirements for the degree of Masters of Science in Engineering, University of California, Davis, March.

17. Schofield, A. N. and Wroth, C. P. (1968), "Critical State Soil Mechanics," McGraw-Hill, London.

18. Smith, S. S. and Arulanandan, K. (1981), "Relationship of Electrical Dispersion to Soil Properties," J. of Geotechnical Engineering Division, ASCE, Vol. 107, No. GT5, May.

19. Wyllie, M. R. J. and Gregory, A. R. (1953), "Formation Factors of Unconsolidated Porous Media: Influence of Particle Shape and Effect of Cementation," Petroleum Trans., AIME, 198, pp. 103-110.

MODELING OF EXPLOSIVE-STRUCTURE INTERACTION EFFECTS IN A LARGE CENTRIFUGE

George B. Clark

National Technical Systems
Redondo Beach, California

ABSTRACT

Small and large geotechnical centrifuges have been used extensively for body force studies of soils and to a lesser degree for rock structures. Investigations of explosive cratering, body force loading of rock masses, and gravity simulation of underwater explosions have demonstrated the viability of experimentation for modeling explosive phenomena in multiple gravity fields. Testing of a variety of structures and materials in large centrifuges has proven the usefulness and the other advantages of modeling of (1) explosive cratering covering several orders of magnitude, (2) simulated sustained pulse loading of underground rock structures, and (3) accurate modeling of underwater explosion bubble behavior. These basic methods and techniques of experimentation, as well as of the analyses of results, are applicable to other related dynamic explosion-structure problems of current interest.

INTRODUCTION

Research utilizing large centrifuges for the loading of geo-engineering structures has increased rapidly in recent years especially in static soil mechanics, but to a lesser degree in rock mechanics and rigid structures; and in specialized areas in the dynamic mechanics of explosion processes such as intense earth waves impinging on underground structures, apparent cratering of soils, and underwater explosions.

Viable physical modeling has both marked economic and scientific advantages and investigations of applicability of centrifugal modeling of studies of effects of intense waves impinging on underground openings, explosive cratering, and effects of underwater explosions, indicate that the technique of centrifugal modeling is likewise applicable to other appropriate problems of explosive-structure interaction. Experience has also shown that the centrifuge may be used effectively (1) for similitude studies, (2) as a testing machine, and (3) to verify mathematical modeling studies. The review below of the use of basic principles of physical modeling in the above dynamic processes gives a good indication of its applicability in other related areas of research interest. One unique and scientifically usable capability of centrifugal loading is that, in contrast to a universal type testing machine, the body force load on the structure is maintained before, during, and after failure (Clark, 1984a, 1984b, 1985).

DEEP BASED STRUCTURES

Although not a subject of direct interest in this conference on nonnuclear impact and response of structures, the methods and techniques of hardening, and experimentation to determine the resistance to large yield weapons have many factors in common with it. Some of these response factors can be effectively examined and evaluated by modeling of loading in a centrifuge. One such experimental program was carried out in the 7 ft diameter centrifuge at the University of Missouri-Rolla (Haas and Clark, 1970).

Various background studies have indicated that an intense plane wave of long duration impacting unlined and lined tunnels in elastic geologic media can be represented by a unit step pulse or a continuous static load. The investigation by Haas and Clark (1970) was designed to test tunnel structures under plane stress and plane strain conditions in a universal testing machine as well as four models under body force loading in a centrifuge, the latter primarily to measure strain (stress) distribution and to observe failure processes.

Two types of carefully designed artificial rock materials were used, a mix of plaster of low modulus and strength and a mix of higher modulus and strength of Portland cement, all pertinent mechanical properties being measured. The stress field intensity caused by body forces was increased above normal by placing several inches of lead sheet on top of the centrifugal model, but lead shot may be preferable for uniform load distribution.

The radial stress field in the model in a centrifuge (Hoek, 1965) is given by (Figure 1):

$$\sigma_r = \omega^2 \rho_{pb} \int_{r_1}^{r_2} r\,dr + \omega^2 \rho_{pl} \int_{r_2}^{r} r\,dr$$

$$= \frac{\omega^2}{2} \rho_{pb} [r_2^2 - r_1^2] + \frac{\omega^2}{2} \rho_{pl} [r^2 - r_2^2] \quad (1)$$

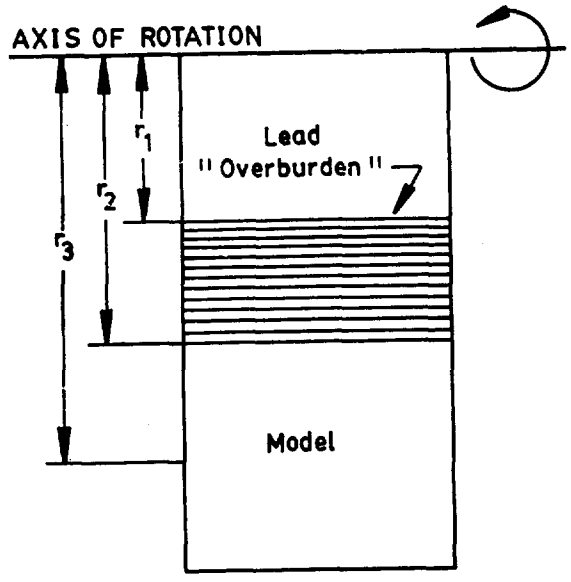

Figure 1. Tunnel Model with Lead "Overburden."

where

ω = angular velocity

r, r_1, r_2 = radii

ρ_{pb} = density of lead

ρ_{pl} = density of plaster model

If the model is restrained laterally then the strain in this direction is zero and the stress is some fraction of the radial stress, depending upon Poisson's ratio.

As a first approximation the stresses around the tunnel can be taken as those for the average value of the stress field at the center evaluation of the model. The above development is for an uniaxial stress field, but the model and holder can be designed to create biaxial or triaxial stress fields in the model and consequent conditions of plane stress or plane strain. Of primary importance is that the centrifuge creates body force loading which is similar to that in the earth's crust, explosive loading can be superimposed, and the loading can be continued after initial failure. In a conventional testing machine, stiff or not, the loading may drop to zero or a low value with initial failure in the model (Figure 2). Continued scaled gravity loading in the whole model or in a single broken or isolated member of the structure is simulated in a centrifuge, which also produced the same action as found in a prototype tunnel structure.

In the similitude study of Haas and Clark (1970) approximately 50 tests were made on models with applied loads to simulate plane stress and plane strain, and four on 12 x 12 x 2 inch models loaded in the centrifuge. A total of 17 strain measurements were made at 8 positions in each model. Side restraint was supplied with bolts, friction minimized at the base of the model with Teflon, and all models carefully machined for precise fitting on the bearing surfaces.

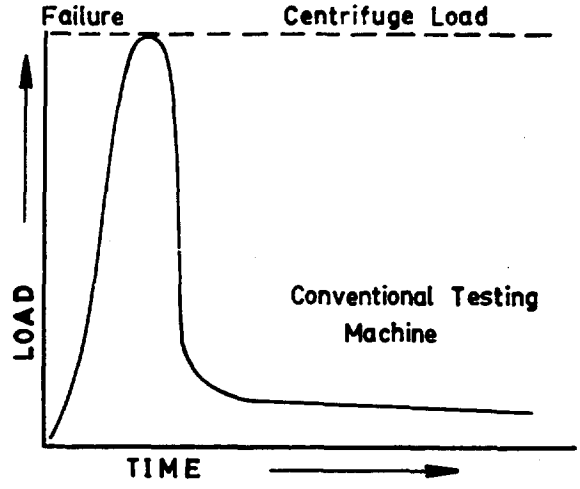

Figure 2: Loading Comparison: centrifuge and conventional testing machine.

The behavior of the models with body force loading prior to failure was similar to those tested with applied static loading in a conventional testing machine. The failure mechanism of the model material was brittle, catastrophic, and explosive in nature. Special sensors will be required to instrument and observe the initiation and progress of such failure, the energy release accompanying failure, and also the degree and type of failure must be controlled to prevent damage to the centrifuge rotor.

In summary, the viability and applicability of centrifugal testing to the investigation of the stability of underground openings under explosive attack are indicated by:

1. Long pulses can be simulated by body force loading.
2. Body force loading on elements and separated parts of the structure are simulated.
3. Loading after initial failure is maintained and simulated, a critical factor.
4. Plane stress and plane strain can be simulated.
5. Photoelastic models can be studied for stress distribution and structural failure.
6. Photostress coating may be used on artificial or natural rock models.
7. Complex rock defects and structure may be

modeled, which cannot be done with mathematical modeling.
8. Failure mechanisms may be observed and photographed.
9. Dynamic loading can be modeled with explosives.
10. Hardening studies can be simulated.

CRATERING

The cube root law of real cratering for single point explosive charges is a well known principle, i.e., that crater dimensions for charge weights (energies) in the range to several tons will scale according to the cube root law, that is, the cratering curves for various linear dimensions scale as the cube root of the charge weight, the areas as the weight to the 2/3 power, and the volume as the first power of the weight of the explosive. However, for apparent cratering, both gravity and the charge weight affect the depth of the crater, the larger the charge weight, the greater percentage fall back into the crater, which reduces the relative size of the apparent crater, especially for large yield nuclear craters.

One possible advantage of experimentation in modeling of effects of munitions (explosives) on structures, or other material masses made up of gases, liquids, or solids, is that some of the behaviorisms may be self-similar. Sedov (1949) shows that certain wave propagation processes in gasses are self-similar, i.e., that velocity and other parameters can be expressed in terms of ordinary linear differential equations. Also, for ejection of soil from a crater by explosive energy for mechanical energy transferred to the solid, E, a crater depth h, and density ρ

$$E = c\rho g h^4 \tag{2}$$

Thus, the relation between the volume V of soil ejected and the mechanical energy is

$$E = c_{\ell}(c)V^{4/3}\rho g \tag{3}$$

That is, under the assumptions made for the derivation of the above equations the specific energy required to produce an apparent crater is the function of the size of the event. For a true crater gravity has little effect on the volume of material broken, but it does determine the size of the apparent crater.

In commercial blasting in Sweden (Langefors, 1978), it was found that the effective breakage and throw of rock by explosives could be expressed by a mathematical series

$$Q = k_2\ell^2 + k_3\ell^3 + k_4\ell^4 \tag{4}$$

where

ℓ = linear dimension of blast

$K_{2,3,4}$ = factors which are variable functions of ℓ

Q = energy of explosive

The above equation may also be written:

$$Q/\ell = k_2/\ell + k_3 + k_4\ell \tag{5}$$

where the first term is associated with crushing rock and other energy losses, the second to the cube root law, and the third with heave or work against gravity.

Holsapple and Schmidt (1979) in definitive model cratering studies in the centrifuge found that for cohesionless material (sand) the cratering efficiency or scaled apparent volume of the crater may be expressed by:

$$(V_{\rho}/W) \propto [g/Q_e)(W/\delta)^{1/3}]^{-\alpha} \tag{6}$$

which is equivalent to the third term of Langefors equation. The following term governs for the cube root regime

$$(\frac{V\rho}{W}) \propto (\frac{c}{\rho Q_e})^{-\alpha} \tag{7}$$

while the following takes the strength (cohesion) of the soil into account

$$(\frac{V\rho}{W}) \propto [(\frac{g}{Q_e})(\frac{W}{\delta})^{1/3}(0.1 + \tan\theta]^{-\alpha} \tag{8}$$

where

V = apparent crater volume
ρ = density of sand
g = gravity
W = wt of explosive
Q_e = specific energy of explosive
δ = density of explosive
θ = angle of friction
α = an exponent

Schmidt and Holsapple (1980) made a detailed analysis of the similitude factors which might apply, including eight field equations, but found that if the same earth materials and explosives are used in the model and the prototype that the apparent cratering process scales accurately within well defined limits. Thus with the centrifuge crater modeling, it has been possible to define quite explicitly the mechanisms of apparent cratering which have earlier been only empirically known, (Figure 3).

Both the true and apparent crater volumes are dependent upon the size of the charge, the depth of burial, and the physical properties of the medium, as are the amounts of energy that are partitioned into that required for breaking the ground, and ejecting the crater material. That is, these factors also determine the amount of energy that is transmitted as wave energy into the ground below the crater. Vital factors that can be examined in centrifugal testing are the relationships of the above and related parameters to the hardening of underground structures.

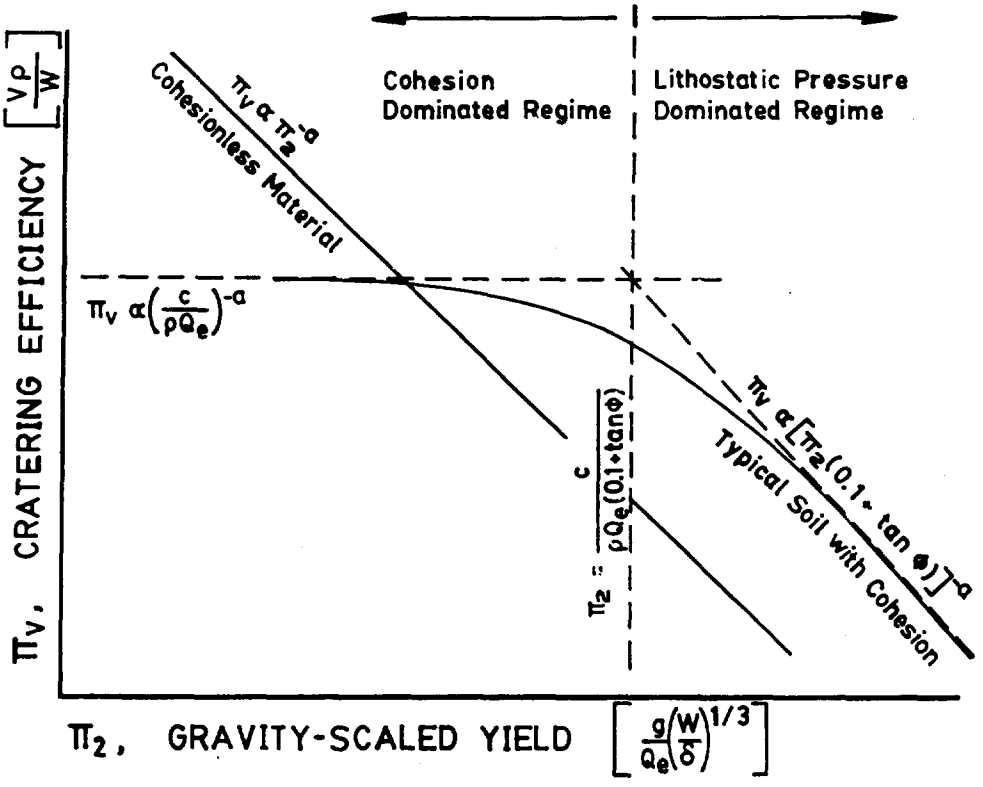

Figure 3. General form of cratering efficiency versus gravity-scaled yield for a typical soil.

UNDERWATER EXPLOSIONS

Scaling or model relationships for a wide range of underwater explosions under high-gravity conditions (Zuke, 1962) are based on either two or three similitude criteria, including (1) Froude scaling of the bubble migration, (2) near surface similarity, and (3) scaling of minimum bubble radius. Critical parameters for simulation (coefficients J_m, K_m, and N_m, where J and K are coefficients defined by equations (14) and (15), N = ratio of max and min bubble radius), were defined by experiments with underwater explosions in a small evacuable tank where approximate scaling of bubble behavior was done by adjusting the air pressure, charge weight and depth, and the water temperature. For more nearly correct scaling, centrifugal loading gives a pressure of more realistic scaled buoyancy characteristics to utilize for scaling of both HE and nuclear explosives:

a. Geometric similarity of bubble and water surface, at maximum expansion.

b. Similarity of the ratio of maximum to minimum bubble radius.

c. Froude scaling at maximum bubble expansion.

The maximum bubble radii of the model are scaled to the depth of the explosion:

$$\frac{A_{max\ m}}{A_{max\ p}} = \frac{d_m}{d_p} \tag{9}$$

where A_{max} is the maximum bubble radius and d is the charge depth. The subscripts m and p refer to the model and prototype. Also model and prototype bubbles have the same ratio of A_{max}/A_{min} at corresponding times, or

$$\frac{A_{min\ m}}{A_{max\ m}} = \frac{A_{min\ p}}{A_{max\ p}} \tag{10}$$

Further, experimental evidence indicates that

$$\frac{A_{min}}{A_{max}} \times \frac{1}{Z^{1/3}} = N \tag{11}$$

where N is approximately constant for a given explosive and Z is the total hydrostatic pressure at the charge depth.

Equations (2) and (3) give

$$\left(\frac{Z_m}{Z_p}\right)^{1/3} = \frac{N_p}{N_m} \tag{12}$$

Thus, for the same explosive, the ratio of hydrostatic pressures is a constant determined by N_m

and N_p. However, N for nuclear explosions is not known but N's for many high explosives are nearly the same.

Froude or gravitational scaling defines bubble migration where the hydrostatic pressure, which produces the buoyant force, is caused by gravity:

$$\frac{A_{max\ m}}{g_m T_m^2} = \frac{A_{max\ p}}{g_p T_p^2} \tag{13}$$

where T is the period for the first bubble oscillation and g the acceleration of gravity.

Expressions (9), (12), and (13) are the scaling relationships which must be satisfied in gravity scaling. In (9) and (13), the A_{max} and T may be expressed in terms of the variables and explosion coefficients. The following equations result in terms of the radius coefficient, J, and the period coefficient, K, which are experimentally determined:

$$A_{max} = J\left(\frac{W}{Z}\right)^{1/3} \tag{14}$$

$$T = K\frac{W^{1/3}}{Z^{5/6}} \tag{15}$$

where A_{max} is in feet; W, the weight of the explosive, is in pounds; T is in seconds; and Z is in feet of water. For one g, Z is defined as

$$Z = P + d \tag{16}$$

where P is the air pressure in feet of water (equal to 33 feet of salt water or 34 feet of fresh water for atmospheric pressure at sea level) and d is the charge depth in feet.

Equations (14) and (9) yield mathematical law for geometric scaling of the bubble maximum:

$$\frac{J_m}{J_p}\left(\frac{W_m Z_p}{W_p A_m}\right)^{1/3} = \frac{d_m}{d_p} \tag{17}$$

Similarly, Equations (13), (14), and (15) give the expression for Froude scaling:

$$\frac{J_m}{J_p} = \frac{g_m}{g_p}\left(\frac{K_m^2}{K_p}\right)^2\left(\frac{W_m}{W_p}\right)^{1/3}\left(\frac{Z_p}{Z_m}\right)^{4/3} \tag{18}$$

In prototype explosions, J_p is assumed to be constant for a given explosion; K_p, however, is dependent on surfaces in all six coordinate directions from the charge as well as the type of explosive, and mathematical-experimental adjustments must be made for both of these factors in the model for surface and wall proximity.

Further, in a centrifuge, the pressure due to the head of water at a depth d_m is assumed to be $d_m \times g_m/g_p$. (Actually, the pressure, Equation 16, varies as d_m^2, but the difference is small.) However, the air pressure in a closed gravity tank has a negligible increase with increasing acceleration, and total hydrostatic pressure is due to water pressure and air pressure is approximated by:

$$Z_m = d_m g_m/g_p + P_m \tag{19}$$

In a closed centrifuge tank the pressure at the bubble surface and the vapor pressure are increased. The rate of evaporation also depends on vapor pressure, water temperature and pressure; hence, a low temperature, such as 48°F, tends to minimize the evaporation effects. Table I summarizes the ranges of the variables which were proposed for the gravity test tank as determined from the above equations.

Table I

ESTIMATED RANGE OF GRAVITY TANK VARIABLES

Variable	From	To
g_m	1 g	250 g
d_m	0.25 ft	2.0 ft
P_m	3 ft H_2O	99 ft H_2O
W_m	0.2 gm or 4.4×10^{-4} lb lead azide	
t	Approximately 48° F	

With the above relationships, preliminary experimental conditions for scaled explosions in a high gravity tank were calculated. The expressions for J_m and K_m, and A_{max}/A_{min} coefficients, and N for the gravity tank were based on observations of the bubble behavior in free water and in the small vacuum tank at one g.

The range of prototype explosions which could be scaled was determined largely by the tank limitations. The variables in the laboratory are g_m, d_m, P_m, W_m, and water temperature, T. An estimate of the maximum experimental (centrifuge) acceleration for a tank two feet in diameter containing three feet of water was about 250 g. Values of J_m used were determined in a vacuum tank at depths between 0.5 and 2.0 feet. The range of charge depths was to be from 2.25 to 2.0 feet. A test tank was to be designed to withstand two or three atmospheres pressure, (68 to 102 feet of fresh water absolute), the lower limit being the vapor pressure of the water (about 0.5 feet of fresh water). These ranges of model values determined the limits of the prototype conditions W_p and d_p which can be scaled (Price, Zuke, and Infosino, 1964).

It is difficult to derive analytical expressions for one tank variable in terms of the other two, but some of the coefficients were known

for some explosives (Table II).

Table II

EXPLOSIVE COEFFICENTS FOR SELECTED EXPLOSIVES

	Lead Azide	HBX-1	TNT
J_p	9.32	14.3	12.6
$K_{m\infty}$ or $K_{p\infty}$	3.23	5.10	4.35
N_p or N_m	0.0258	0.0252	0.0228

In various methods, including the iterative approach to solution, combinations of d_m, g_m, and P_m may be used and for each combination d_p is evaluated along with K_p, K_m, and J_m to determine explosive weights and depths, programmed for computer calculation. The predictive study for gravity studies by Zuke (1962) was based on model explosion data obtained in a small stationary vacuum tank at NOL with gravity and size corrections applied where possible.

The required methods of scaling of two or three criteria were met, geometric scaling at two different times, and Froude scaling. The range weight of prototype explosions scaled in a high-gravity tank may be limited and restricted to HE modeling. With the second method, which satisfies only two criteria, geometric scaling at one point in time and Froude scaling, the range of prototype shots scaled is larger, and may include nuclear weapons. The three criteria scaling could not be applied to nuclear weapons because of prototype information for the A_{max}/A_{min} ratio was lacking.

Some conclusions were: A centrifugally accelerated test tank can be used for model bubble-explosion studies. A variety of shots was fired and except for an under-ice shot, the difficulties were minor. The control of tank conditions attained was satisfactory and the centrifugally accelerated test tank for model explosion studies proved a practical method. The data obtained indicate that the systems of scaling, especially the three criteria method, may be applied over a wide range of conditions.

Seven series of shots were investigated (Price, Zuke, and Infosino, 1964):

1. General Information
   a. Effects of tank size or "wall effect."
   b. Effects of charge depth, tank acceleration, and air pressure.
2. Scaling of Specific Prototypes
   a. Forms of bubble scaling.
   b. High explosive prototype shots, in deep water and on the bottom.
   c. Under-ice explosions.
   d. Shallow underwater nuclear explosions.
   e. Deep underwater nuclear explosions.

Preliminary research in static tanks at NOL and on a small NOL centrifuge included engineering problems of (1) a layout of optical and mechanical plan, (2) tank design, (3) windows and access ports, (4) mirror, (5) beam for support of tank (5) fairing structure, (6) camera and mounting, and (7) other equipment illumination. For most of the deep shots, the maximum explosion bubble radius, A_{max}, and its first period, T, were measurements of primary interest, and those of secondary interest were the growth of the surface water mount and plume development. For shallow shots the surface phenomena were of primary importance.

Problems encountered in experimental procedures included the determination of the water surface position over the charge, location of optical axes, and determination of radial distance from the centrifuge axis to the water surface. The windows bulged during acceleration, acting as lenses, and the undersurface of the water acted as a mirror, diverting light paths.

The number and nature of parameters which must be carefully controlled in the modeling of underwater explosion bubbles is probably more critical than most other types of centrifugal modeling. These include charge depth, water volume and level, acceleration control and evaluation, air pressure control, and water temperature.

The data points obtained from tests were in agreement with prediction curves. These tests represented the initial explosion experiments in an accelerated test tank in a centrifuge. The accuracy of predictions was evlauated by:

$$I_A = \frac{A_{max\ m}\text{measured}}{A_{max\ m}\text{calculated}} \tag{20}$$

$$I_T = \frac{T_m\text{measured}}{T_m\text{calculated}} \tag{21}$$

For these indices, unity indicates agreement of the prediction with a measurement. For 54 shots, the average I_A was 0.990 with a standard deviation of ±.039 while I_T was 0.994 ± .045. The standard deviation shows 68% of the $A_{max\ m}$'s were within about ±4% of expected values and 68% of the T_m's within about ±4.5%.

Since the calculated $A_{max\ m}$'s and T_m's were based on measurements, the indices indicate the reliability of predictive equations in the high-gravity tank. However, they do not indicate the

degree of experimental control or the errors of interpolation and extrapolation resulting from the use of charts for d_m, a_m, and P_m.

FUTURE RRESEARCH

As with underwater explosions and cratering some of the effects of chemical explosions scale and some can be modeled with conventional modeling techniques. This holds for true cratering, but for apparent cratering gravity effects dominate for large explosions. Full scale experiments have been very costly, and significant gravity effects can be modeled with accurate simulation in a centrifuge at a small fraction of the cost in time and effort. In most model tests in the application of centrifugal loading, it is desired to simulate the effects of gravity. In apparent cratering the solid particles generated by an explosion are propelled into a trajectory by the explosive force and move in a gravitational force field created by their planetary movement caused by the centrifuge rotor. Stress or pressure fields in solids (soil and rock and water) are developed by the centrifugal gravitational field. The earth's field gravity is constant, while in the centrifuge it varies as the radial distance. However, this can be compensated by calculations or by the adjustment of given parameters where necessary.

For experimentation in the research area of munitions-structures effects, a primary use of centrifugal testing will be to simulate stress and failure effects due to combined gravity and blast effects. Other structural tests requiring body force loading are also possible. Areas for research include:

1. Continued investigations of true and apparent cratering in soil and rock, and energy partitioning as a function of critical parameters.

2. Research in rock burst effects, stress, strain and energy release, relation to military structures.

3. Failure of surface and deep structures due to gravity and explosion effects.

4. Buried structures in soil, combined effects

5. Failure of shallow and deep unsupported structures in rock.

6. Failure of shallow and deep supported structures in rock.

7. Failure of surface or near-surface protective structures.

8. Arching of soils, broken and natural rock, static and dynamic effects.

9. Shallow buried cylinders.

Some of the related basic technical subjects which require investigation are:

1. Wave propagation and attenuation on a small scale, modeling of the same.

2. Mechanics or geologic structure failure under gravitational force.

3. Mechanics of static and dynamic arching of natural materials.

4. Identification of structures affected by gravity.

5. Identification of applications of body force testing, non-simulation.

6. Effects of explosive loading on centrifuge rotor and bearings, etc.

7. Mechanics of response of domes, cylinders, slabs, and composite elements.

8. Frequency response, single and multiple degrees of freedom.

9. Equipment response under gravity and shock loading.

10. Shock isolation under model gravity loading.

APPLICABLE PRINCIPLES

1. Body force and dynamic loading of geologic sections.
    a. Simulated a long period pulse with one, two, and three directional effects.
    b. Body force loading producing a simulated earth gravity stress field.
    c. Sustained realistic load before, during, and after initial failure.
    d. Creation of local load weight effects on gravity members, in addition to the self weight due to gravity stress field.
    3. Superimposed explosive-gravity loading.
2. Model apparent cratering.
    a. Non-trivial dynamic similarity: size, density, and time.
    b. Complete and exact dynamic similarity by use of same material which is rate independent.
    c. Ottawa sand provides reproducibility for apparent cratering phenomena ±4%.
    d. Coriolis effects are negligible.
    e. Large explosive (nuclear) yield can be simulated with small scale charges.
    f. Gravity parameter $(g/Q)(Q/\delta)^{1/3}$ gives quantitative agreement for four explosives.

g. π_2 parameter includes g,Q,W,δ, and strength of material.

h. Defines two regimes, cohesion and lithostatic pressures, i.e., defines scaling effects of earth's crust.

i. Gravity scaling 1/3.6 instead of 1/4 root scaling as predicted by Sedov and others.

3. Model underwater explosions.

a. Geometric similarity attained for (1) bubble-water surface, and (2) bubble radii ratios.

b. Froude (gravity) scaling applicable for centrifugal modeling of bubble behavior.

c. Correction methods defined for scaling in a tank: (1) radius coefficient, and (2) time coefficient obtained from small static tank tests.

d. Water pressure scaling for gravity by means of Froude number.

4. Other areas of research.

a. Situations requiring body force loading.

b. Modeling of complex structures.

c. Complement mathematical modeling.

d. Modeling of physical properties.

e. Self-similar processes.

f. Simultaneous static and dynamic effects.

g. Studies of skin and internal friction.

h. Egress studies.

REFERENCES

Clark, George B., (1984a), Modeling in Rock Mechanics and Geology, The Application of Centrifuge Modeling to Geotechnical Design, Univ. of Manchester, W. H. Craig, Ed., 16-18 April 1984.

Clark, George B., (1984b), Factors in the Design of a Rock Mechanics Centrifuge for Strong Rock, Symposium on Centrifugal Testing, U. of Cal-Davis, June 1984.

Clark, George B., (1984), State of the Art of Centrifugal Modeling in Rock Mechanics, Int'l Meet ISSMEF San Francisco.

Haas, C., and Clark, G. B., (1970), Experimental Investigation of Small Scaled Lined and Unlined Cylindrical Cavities in Rock-Like Materials, UMR-Rolla, AWFL TR 70-58.

Hoek, E., (1965), The Design of a Centrifuge for Simulation of Gravitational Force Fields in Mine Models, Jl. of S.A. Inst. of Min & Met., Volume 65, Number 9.

Holsapple, K. A., and Schmidt, R. M., (1979), A Material-Strength Model for Apparent Crater Volume, Proc. Lunar Sci. Conf. 10th, pp. 2757-2777.

Langefors, U., and Kihlstrom, B., (1963), The Modern Technique of Rock Blasting, Wiley & Sons, Inc., New York.

Price, R. S., Zuke, W. G., and Infosino, C., (1964), A Study of Underwater Explosions in a High Gravity Tank, NOL TR 63-125, June 5, 1964.

Schmidt, R. M., and Holsapple, K. A., (1980), Theory and Experiments on Centrifuge Cratering, Jl. of Geoph. Research, Volume 85, Number 81, January 10, 1980.

Sedov, L. E., (1959), Similarity and Dimensional Methods in Mechanics, Academic Press.

Zuke, W. G., (1962), Underwater Explosion Scaling Predictions for an Accelerated Test Tank, NAVORD Report 6794, 4 January 1962.

IMPACT AND PENETRATION TESTING OF MODELED LAYERED PAVEMENT SYSTEMS

Phillip T. Nash
Gerard J. Friesenhahn
and
Patricia C. Suggs

Southwest Research Institute, San Antonio, Texas
Southwest Research Institute, San Antonio, Texas
Engineering and Services Laboratory, Tyndall AFB, FL

ABSTRACT

Experimental data on large bombs impacting and penetrating layered pavement systems are very scarce due to the exteme costs of both target construction and testing. Past attempts to model physically the penetration of geological targets at sub-scale have shown that simple replica modeling is not satisfactory. In this study, a dissimilar material technique was applied to the modeling of pavement penetration by large bombs. Two runway types were modeled, a rigid and flexible surface. Runway material included clay, gravel, crushed stone, concrete, and asphalt. Special procedures were used to monitor subsurface material properties during runway construction and ensure modeling requirements were being met. The deforming steel bomb case was modeled with a special tin-antimony alloy. The modeled bomb was instrumented with accelerometers mounted on the bomb nose and tail during testing. This paper presents the modeling techniques and typical test results.

INTRODUCTION

Projectile penetration into concrete and geologic materials is a very complicated process dependent upon characteristics of the target, projectile and impact conditions. Intense dynamic stresses are developed locally at the impacted target region and can produce crushing, cratering, shear failure and tensile fractures. The target materials are usually highly nonhomogeneous with wide variations in properties, thus limiting the application of computational mechanics for predicting penetrations. [1]. Early research and development of penetration prediction techniques was primarily based on empirical data [2]. The development of depth of penetration formulas is usually systematic and evolves by choosing parameters considered pertinent to the penetration process being modeled, deriving penetration formulas from the available data base, and later refining formulas by including additional parameters [3].

Predicting penetration depths into layered geologic targets by large projectiles involves additional difficulties. Targets contain a number of layers of materials each subject to large variations and nonhomogeneities. Modeling of layered target systems has also been predominantly empirical. However, for large projectiles, tests are expensive and can require great efforts in target construction and projectile delivery. Scale modeling offers a useful alternative to full-scale penetration testing. Because penetration into geologic targets does not scale in a simple geometric way [4], subscale test design is critical and requires special considerations. The objective of this paper is to present techniques used in modeled penetration testing of layered pavement systems by large, deformable bombs.

SCALE MODEL ANALYSIS

Previous studies have shown depth of penetration into concrete and geologic targets increases with projectile impact energy and decreases with target resistance. Many empirical relationships are available with some variation in governing parameters. The parameters basic to most penetration formulas include projectile velocity, weight and dimensions, and target strengths, densities and dimensions. Refinements can include nose shape factors, aggregate size, moisture content and others [3]. To model projectile penetration into the layered pavement system, the projectile, runway surface and subsurface layers were described with 37 parameters. Details of the model analysis are available in Reference 5. Some of the basic parameters considered are shown in Figure 1 and include:

Projectile

- ρ_p - Case density
- σ_p - Case strength (yield, ultimate, etc)
- E_p - Case elastic modulus
- ℓ_i - Characteristic length
- d_p - Diameter
- V_o - Impact velocity
- β - Impact angle

Target

- ρ_s - Surface Density
- σ_s - Surface strength (yield, ultimate, etc)

h_s - Layer thickness

d_s - Particle size (aggregate)

ρ_g - Base course or subgrade

g - Gravity

h_g - Layer thickness

d_g - Particle size

Projectile Response

A - Deceleration

V - Velocity

X - Position

t - time.

Strength, density and geometric dimensions are given for both the projectile and target. Gravity was considered for the target subgrade to account for its penetration resistance derived from dead weight of overburden.

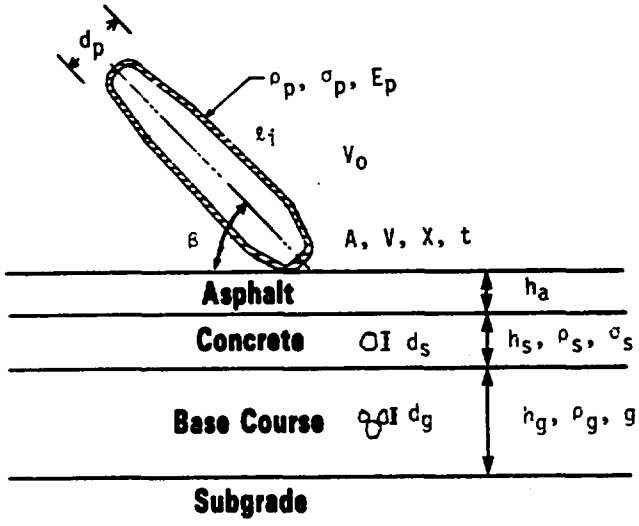

Figure 1. Projectile Penetration Parameters

Dimensionless ratios were obtained using the pi theorem [6]. The model analysis resulted in 34 pi terms which were categorized as nondimensional parameters and self-similar geometries, densities, strengths and response terms. Some of the pi terms containing parameters of Figure 1 are:

$$\left(\beta, g, \frac{\ell_i}{d_p}, \frac{\rho_p}{\rho_c}, \frac{\sigma_p}{\sigma_c}, \frac{X}{d_p}\right)$$

The two pi terms which determined the model law were:

$\frac{gd_p}{V_o^2}$ - Froude Number

$\frac{\rho_c V_o^2}{\sigma_c}$ - Cauchy Number

The Froude number is the ratio of gravitational effects to inertial effects. When multiplied and divided by ρ_c, the numerator becomes potential energy per unit volume and the denominator becomes kinetic energy per unit volume. The Cauchy number is the ratio of inertial effects to inherent strength or constitutive effects. Three physical processes (gravitational, inertial and constitutive effects) are related to one another through these two pi terms.

If the model and prototype are to be similar, the dimensionless ratios must be the same in model and prototype systems. To reduce the size of the modeled system, a scale factor λ is defined as

$$\lambda = \frac{d_p \text{ (Model)}}{d_p \text{ (Prototype)}} \qquad (1)$$

Using the subscript m for model and p for prototype, the Froude number requires similar ratios:

$$\frac{d_{pm}}{d_{pp}} = \frac{V_{om}^2}{g_p} \frac{g_m}{V_{op}^2} = \lambda \qquad (2)$$

Unless the acceleration of gravity is increased by special techniques such as a centrifuge, the ratio of g_m to g_p is fixed at 1 which thus requires

$$\frac{V_{om}^2}{V_{op}^2} = \lambda \qquad (3)$$

and

$$V_{om} = \sqrt{\lambda}\, V_{op} \qquad (4)$$

Then, from the Cauchy number

$$\left(\frac{\rho_{cp}}{\rho_{cm}}\right)\left(\frac{\sigma_{cm}}{\sigma_{cp}}\right) = \lambda \qquad (5)$$

The relationship in Equation 5 can be satisfied best by maintaining a material density ratio of 1 and selecting model materials with strengths weaker by the scale factor λ. This technique of dissimilar material modeling was used in the penetration study and requires careful selection of materials for both projectile and target.

SCALE MODEL DESIGN AND CONSTRUCTION

Candidate projectile materials were selected based on prototypical properties and limitations of test facilities. Model projectile material properties determined the scale factor, and targets were constructed according to model laws. Impact velocities were also scaled according to Equation 4.

Tin alloys have been used in past research to simulate steel structures and were chosen as primary candidates for modeling the steel projectile. Materials, compositions and properties were compiled for a variety of tin alloys. White metal (92% Sn, 8% Sb) was selected as the best material for simulating the projectile steel casing primarily because of its high Izod value (measure of material toughness). In previous research, White metal was used to model responses of steel ship hull bottoms to dynamic loadings [7]. Several tin alloys were tested in the previous research for the dissimilar material requirements. White metal was found to be the best alloy for modeling the steel at high strain rate loadings. Other alloys proved too brittle. White metal properties are:

Modulus of Elasticity - 5.25×10^6 psi

Density - .260 psi

Static Yield - 6400 psi

Dynamic Yield - 10,000 psi.

Based on the ratio of moduli of elasticity for steel and white metal, a geometric scale factor (λ) of 1/6 was chosen.

Scale factors derived from the model analysis were used within practical limits, for designing both a rigid and thin asphalt modeled runway. Linear dimensions such as slab sizes, layer thicknesses and aggregate diameters were scaled by λ for the asphalt, concrete and granular materials. Dimensions and materials of the scaled rigid runway and thin asphalt surface designs are given in Figure 2. Material strengths were scaled according to the previously derived modeling relationships. Asphalt and concrete strengths were scaled by λ. CBR ratios for the subsurface materials were equated to modulus of subgrade reaction (k) values using relationships found in Reference 8. A scaled plate bearing test was devised and used to monitor subsurface material properties during scaled runway construction. During the scaled plate bearing tests, a steel plate five inches in diameter was loaded to a bearing stress of 1.66 psi. Required deflections for the various materials were determined from the relationship:

$$\Delta = \frac{p}{k} \qquad (6)$$

where: Δ = deflection (inches)
p = bearing stress (1.66 psi)
k = desired modulus of subgrade (pci)

The concrete slabs were cast in four foot square sections. In order to simulate construction details for the modeled runway, the sandy soil at the test location was excavated and replaced with clay. The clay subgrade was placed in layers and conditioned to meet the appropriate scaled material properties. Placing the scaled runway sections required conducting appropriately scaled plate bearing tests to make sure scaled material properties were developed. Above the clay subgrade, the runway sections have different base courses. The main runway section has a gravel base course, sand when geometrically scaled, while the redundant surface has a crushed stone base and gravel subbase. The concrete runway was formed in the four foot square sections and the base course was hand screeded for leveling at the required thickness. The base course was compacted to meet specifications, as were all layers of the runway construction. Concrete, designed with scaled strength and aggregate size, was then placed and leveled. Finally, the asphalt overlay was placed on the main runway section and compacted to finish runway construction.

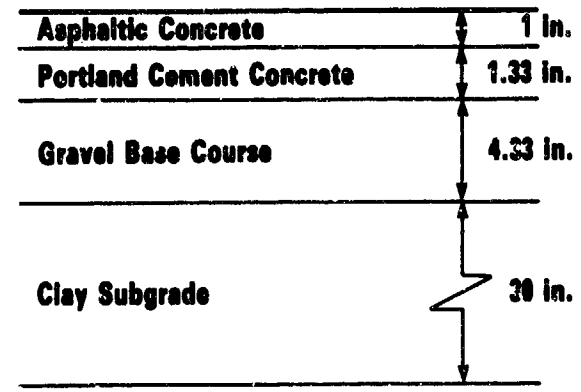

a) Rigid Pavement

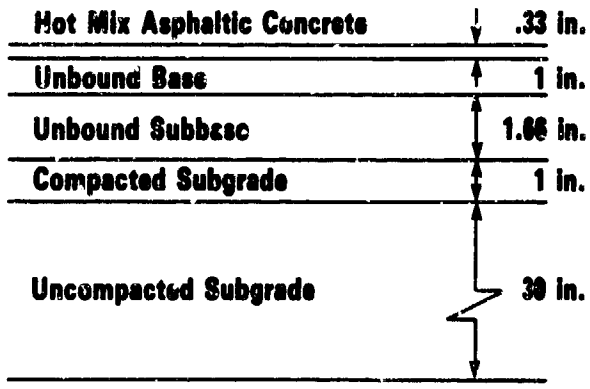

b) Thin Asphalt Surface

Figure 2. Pavement Design (1/6 Scale)

TEST RESULTS

A total of 46 baseline penetration experiments were accomplished. Two tests against the rigid pavement and one test against the thin asphalt surface were performed with instrumented projectiles. Accelerometers were attached to the nose and tail of the projectiles. Typical accelerometer data from the instrumented tests are shown in

Figure 3. The large difference in nose and tail deceleration is obvious in the acceleration-time histories for penetrations into the rigid pavement. The accelerometer data were numerically integrated and used to compare velocity-time and displacement-time records as well as total depth of penetration. Results are shown in Figure 3. Plastic deformation of the projectile is evident. The nose and tail have different velocity and displacement histories. A simple computational technique was developed and compared with the experimental results. Since the computational model considered a rigid projectile, the predicted values should be compared to the average of the nose and tail values. As such, the results appear very good. Also, the differential displacement of the projectile nose and tail was determined to be 0.8 inches from integration of the acceleration-time curves. Deformations on the projectile were measured and matched the calculated 0.8 inches. The computational model was exercised using both modeled and prototype dimensions and results matched expectations from the modeling laws. An important observation from Figure 3 is the bulk of the penetration resistance occurs when the projectile is penetrating through the concrete which is the strongest layer. Observations showed failure of the concrete by plugging before the projectile completely penetrated through the concrete layer. Figure 3 reveals a rapid decrease in deceleration corresponding to concrete plugging. The weaker subgrade offered little resistance to penetration.

SUMMARY

Using dissimilar modeling techniques, an experimental program was designed and conducted to study penetration of layered pavement systems by large projectiles, The modeling laws required reducing projectile and target strengths and impact velocities. Instrumented projectiles resulted in valuable insight to target penetration resistances. Experimental results compared favorably with a computational technique at both subscale and full-scale.

REFERENCES

[1] Sliter, G. E., "Assessment of Empirical Concrete Impact Formulas," ASCE Journal of the Structural Division, May 1980.

[2] "Effects of Impact and Explosion," Summary Technical Report of Division 2, National Defense Research Committee, Vol 1, Washington, DC, 1946.

[3] Sierakowski, R. L., Ross, C. A., and Milton, J. E., "Investigation of Warhead Ricochet, AFATL-TR-82-11, February 1982.

[4] Gurson, A. L., Miller, C. W., and Pepe, R. D., "Penetration Modeling Feasibility Study," ESL-TR-83-20, September 1983.

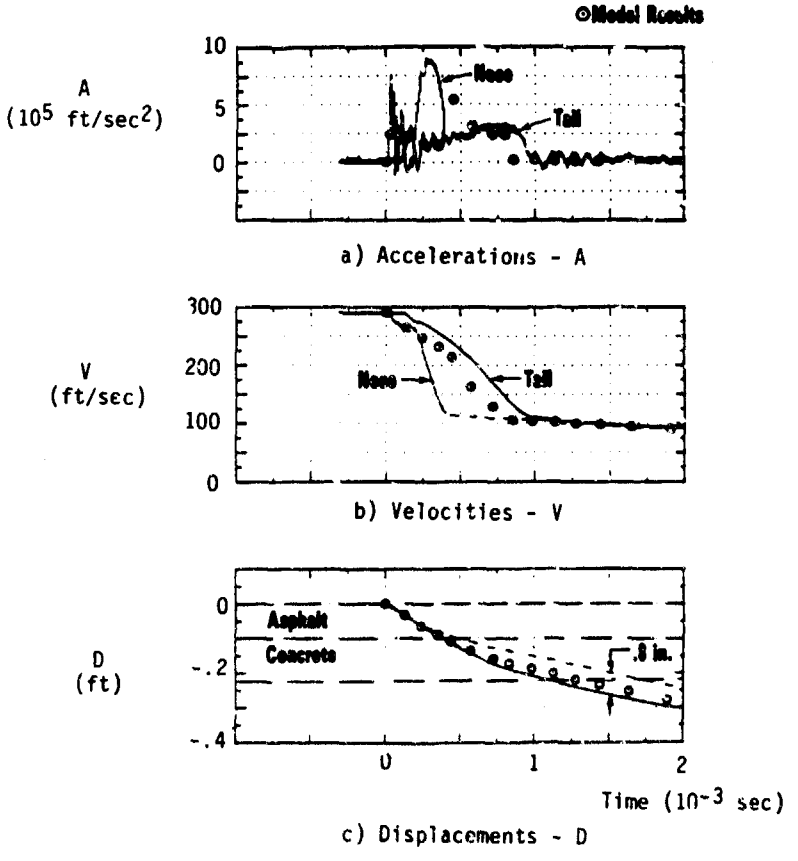

Figure 3. Instrumented Projectile Experimental Results (Rigid Pavement)

[5] Nash, P. T., Wilbeck, J. S., Westine, P. S., and Friesenhahn, G. J., "Damage-Resistant Runway Concept Development," ESL-TR-85-02, In Publication.

[6] Baker, W. E., Westine, P. S., and Dodge, F. T., Similarity Methods in Engineering Dynamics, Theory and Practice of Scale Modeling, Spartan Books, 1973.

[7] Ransleben, Guido, E., Jr., "Construction of Dynamic Models of Ship Hull Bottoms," Construction Report, Contract No. N00189-68-C-0538, SwRI Project No. 02-2343, 15 October 1969.

[8] Hennes, Robert, G. and Ekse, Martin, "Fundamentals of Transportation Engineering," McGraw-Hill Book Company 1969.

ACKNOWLEDGEMENTS

Research reported in this paper was sponsored by the Engineering and Services Laboratory, Tyndall Air Force Base, Florida.

LABORATORY MEASUREMENT OF WAVE PROPAGATION IN SOILS

James S. Wilbeck
Southwest Research Institute, San Antonio, Texas

Paul Y. Thompson
USAF Engineering and Services Laboratory, Tyndall AFB, Florida

C. Allen Ross
Ross Engineering Associates, Inc., Valparaiso, Florida

ABSTRACT

Considerable scatter is evidenced in the data obtained when pressure measurements are made in the vicinity of underground explosions of moderate size. A research program is currently underway to identify and understand the reasons for this scatter. In this program, a compression split-Hopkinson pressure bar apparatus is being used for identifying those soil parameters which are most responsible for variations in soil pressures measured during high amplitude, short duration loading. An investigation is also being conducted using existing pressure transducers to identify the sensitivity of various transducers to those soil parameters. Based upon parameters identified and experimental results, existing theories for wave transmission through a granular media will be extended or new models developed. This paper discusses results from initial testing and plans for future tests. A description is also given of the new wave propagation test facility to be utilized in these tests.

INTRODUCTION

In conducting underground explosion tests of moderate size, reproducibility of measurements from one explosion to another using the same location, measuring device and so called "identical charge size" is not usually the norm. Standard deviations as high as 150 percent have been reported [1]. Though methods of calculating these deviations may be debatable, reported variations in measurements are quite high [2-4]. Assuming proper use of the pressure measuring instruments, this scatter is too great to have been caused by errors in measurement precision or signal transmission. Scatter is more likely to have been due to variations in soil properties between tests or differences in contact between the soil and the pressure transducer in use.

A number of researchers have investigated elastic wave transmission through granular media both analytically and experimentally [5-10]. Reasonable correlation between theory and experiment has been shown for the ranges of the test data. However, for high amplitude, short duration pulses near high explosive sources, which can drastically alter material properties of the soil medium, large variations can occur in pressure measurements. It is apparent that carefully controlled, laboratory experiments are necessary to isolate and study those parameters or properties which influence pressure wave characteristics in soils. Pressure waves need be studied beyond the seismic levels previously tested and extended to magnitudes where significant alterations of soil properties can be expected.

This paper discusses an ongoing research program aimed at investigating, both experimentally and analytically, the effects of soil properties on the transmission of pressure pulses through the soil and their effects on the soil-structure interface pressure measurements. The main instrument being used in this study of wave propagation is the split Hopkinson pressure bar. The main objective of the program is to identify those soil parameters which are most responsible for variations in soil pressures measured during high amplitude, short duration loading events and to better understand their effects. Initial experiments were performed with an existing 0.5-inch diameter split Hopkinson bar to determine if it could be used to transmit pressure pulses into the soil specimens. A two-inch diameter bar was then fabricated to provide a larger bearing area for the granular specimens and to accommodate various transducers for measuring pressures at the soil-steel bar interface.

Split Hopkinson Pressure Bar Apparatus

In order to examine effects of soil properties on pressure measurements, a device was needed which could generate a known pressure pulse into a soil sample. The choice of instruments for this program was a split Hopkinson pressure bar apparatus which uses the impact of one bar onto another to generate a pressure wave and then uses this pressure wave to load a specimen sandwiched between two identical bars. A schematic is presented in Figure 1 showing the apparatus configured to study the propagation of compression waves. Referring to Figure 1, the operation of the system for a linear elastic material specimen is as follows:

- A striker bar is put in motion by a launcher and it impacts the incident bar with a velocity V.

- The impact produces an almost rectangular stress pulse of magnitude $\rho cV/2$ in the striker bar and the incident bar. The pulse length in time is $t_s = 2L_s/c$; ρ is the bar density, c is the bar elastic stress wave speed and L_s is the striker bar length.
- The compressive stress pulse propagates away from the impacted ends of each bar at a speed of c. When the stress wave reaches the free end of the striker bar it is completely reflected as a tensile wave and it travels back toward the impacted end. This tensile wave unloads the ends of the striker bar and the incident bar and the bars separate.
- The compressive pulse travels down the incident bar and impinges on the sample sandwiched between the incident bar and the transmitter bar. Depending on the physical properties of the sample, portions of the stress pulse are reflected back into the incident bar and portions are transmitted into the transmitter bar. The reflected and transmitted portions of the stress pulse are proportional, respectively, to the strain and stress in the specimen.
- Strain gages, located equidistant from the specimen to provide time coincident pulses, are used to measure the magnitude and duration of the incident, reflected and transmitted pulses. It can be shown that the integral of the reflected pulse is proportional to the strain in the specimen and when displayed along with the transmitted pulse (proportional to stress in the specimen) a dynamic stress-strain curve can be determined.

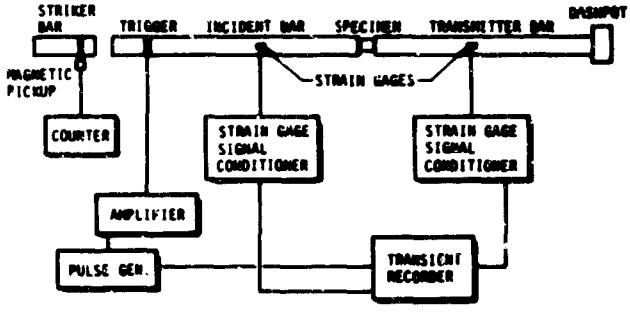

Figure 1. Schematic View of Split-Hopkinson Pressure Bar

Questions concerning how much of the pressure pulse is transmitted to the test sample and in turn how much of the stress pulse in the sample is transmitted to the transmitter bar may be addressed most easily using one-dimensional elastic stress wave propagation theory. When a wave is travelling in a medium of acoustic impedence $\rho_1 c_1$ and encounters an interface of another material of impedance $\rho_2 c_2$, the stress magnitude of the transmitted pulse σ_T and reflected pulse σ_R can be written in terms of the incident pulse σ_I. Using Figure 2 and Reference [11], the following expressions may be found.

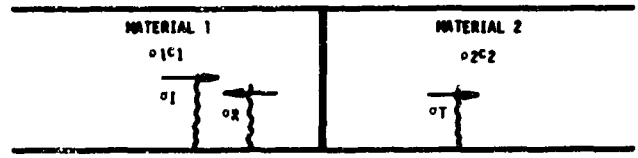

Figure 2. Schematic of interface between materials 1 and 2. Initial incident stress σ_I moving to the right.

$$\frac{\sigma_R}{\sigma_I} = \frac{(\rho c)_2 - (\rho c)_1}{(\rho c)_1 + (\rho c)_2} \qquad (1)$$

$$\frac{\sigma_T}{\sigma_I} = \frac{2(\rho c)_2}{(\rho c)_1 + (\rho c)_2} \qquad (2)$$

If two elastic materials go to infinity in both directions, a simple reflection and transmission takes place, and this phenomenon may be treated as a simple stress wave propagation problem with the resulting reflected and transmitted wave forms almost completely independent of the incident length. A rough approximation of typical ratios of transmitted stress (σ_T/σ_I) and reflected stress (σ_R/σ_I) for a steel incident bar and typical soil samples are given in Table 1. (The reader is reminded that these predictions assume that the soil samples are responding as linear elastic materials). Further details on principles of operation and description of the compression Hopkinson bar may be found in several publications such as References [12, 13].

Experimental Set-Up

The 0.5-inch diameter split Hopkinson bar used in initial experiments is similar in layout to the schematic of Figure 1 and are shown in Figure 3. The target materials, which are granular media and soil samples, are encased in a hollow cylindrical sleeve that fits over the ends of the incident and transmitter bars. The specimen holder in all tests was a 3-inch long PVC pipe with a 0.20-inch wall thickness. The incident end was closed with a 0.001-inch thick steel shim circular sheet, 0.5-inch diameter, and the transmitter end was closed with a 0.75-inch long steel bar, 0.5 inch diameter. It was necessary to limit the thickness of closure sheets on the incident side of specimen, to prevent "wave trapping" in the closure sheet. During the feasibility test program, both bars were solid. In subsequent testing, a pressure transducer will be placed in the front end of the transmitter bar next to the sample (Figure 4) or actually embedded within the soil sample. Details of the transmitted pulse will be measured with a strain gage mounted on the transmitter bar as well as with the pressure transducer. Thus, the use of a pressure transducer

Table 1. Material Properties and Stress Ratios

Material Properties [14]			
Material	Density, ρ g/cm^3	Wave Speed, c (10^5) cm/sec	ρc $(10^5) g/cm^2/sec$
Sandy Top Soil (dry)	1.39	0.23	0.32
Clayey Top Soil (dry)	1.63	0.51	0.82
Clay (wet)	1.99	1.37	2.73
Steel	7.84	5.08	39.83

Stress Ratios			
Incident Bar	Soil	σ_T/σ_I	σ_R/σ_I
Steel	Sandy	.02	.98
Steel	Clayey	.04	.96
Steel	Clay	.13	.87

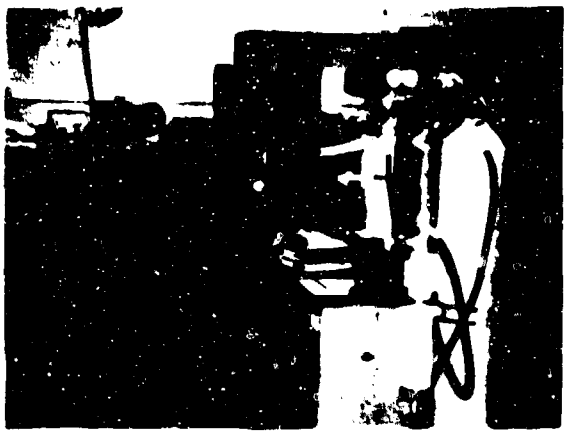

(a) View From Launcher End

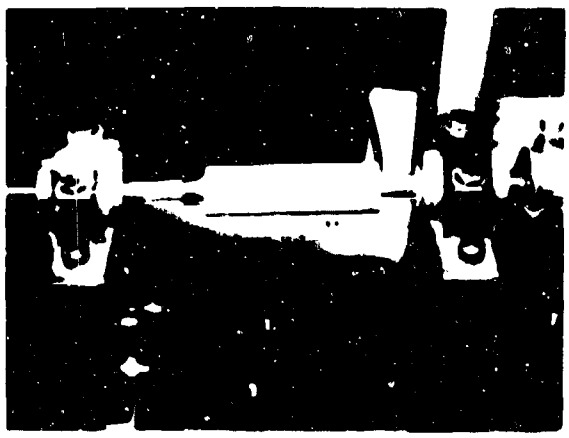

(b) Soil Specimen in Hollow Tube

Figure 3. Split Hopkinson Bar Test Setup (0.5 inch diameter)

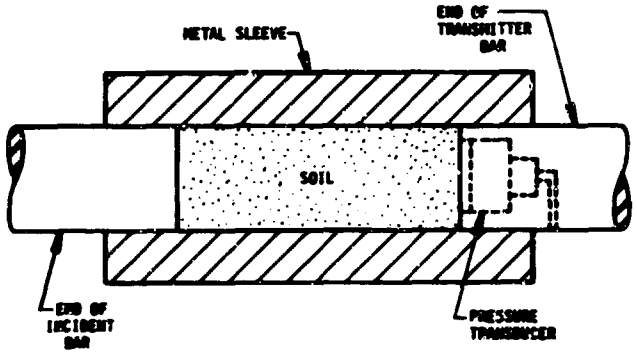

Figure 4. Schematic of Soil Specimen

should allow an independent check of the details of wave transmission.

In contrast to usual split Hopkinson bar testing, the samples in this program are long relative to the length of the incident stress pulse, so that studies can be performed on the propagation of a single wave through a soil medium. By using a constant impact bar velocity and resulting constant incident bar stress, specimen properties can be varied and their effects on the transmitted pressure magnitude and time duration evaluated. Tests can be run with and without the transducer in place to determine the affects of the specimen properties on measurements made by the transducer. Using this type of test device, the properties of the soil can be varied systematically to various stress levels by simply changing the striker bar velocity. Pulse duration can also be varied by changing the striker bar length. In addition, pulse shapes can be altered by introducing different types of buffer materials at the impact end of the incident bar.

Feasibility Test Program

Initially, thirty experiments were conducted using the 1/2-inch split Hopkinson pressure bar apparatus shown in Figure 3. Three different types of soil specimens with significant differences in grain size were utilized: Texas ball clay, sand, and 3mm glas beads. Typically, impact speeds of the striker bar were 1060 feet per second (fps), resulting in stress waves of approximately 78,000 psi propagating into the incident bar. Most material specimens were 2 inches in length and material densities were varied as follows:

Texas Ball Clay	γ = 81.9 - 96.3 pcf
Sand	γ = 91.7 - 112.7 pcf
3mm Glass Beads	γ = 85.2 - 95.6 pcf

The strain gage signals were recorded and translated into corresponding stress levels. Typical traces (Test 20) are given in Figure 5. The top portion of the figure presents the stress-time history of the incident bar and the bottom portion corresponds to the transmitter bar. The first pulse in the incident bar, designated by (A), corresponds to the initial compressive wave caused by impact with the striker bar. The second wave, designated by (B), is the reflection of the initial wave off the interface of the incident bar and test specimen. The wave shown in the transmitter bar is the stress wave "transmitted" through the interface of the test specimen and the transmitter bar. This figure presents both the experimentally measured stress waves and the waves predicted using one-dimensional wave theory and assuming linear elastic target material response. Since the wave speed in the clay was unknown, a value of 1000 fps was selected for comparisons.

The close match between predicted and measured stress wave profiles in the incident bar was expected since the magnitude of the stresses was well below the yield point in the steel bar and elastic-wave propagation in long bars is essentially a one-dimensional phenomenon. However, the predicted and measured values of the wave profile in the transmitter bar seem to show little resemblance. Again, this was expected since soils do not behave as linear elastic materials at stresses on the order of 1000 psi. It is, in fact, one of the main objectives of this program to better understand wave propagation through the soil specimen, so that the actual transmitted stress profile can be predicted.

Measured values of peak transmitted stress, comparable to wave (C) of Figure 5, are plotted in Figure 6, as a function of initial soil specific weight. For the sand and clay specimens, the measured peak stress is seen to increase with increasing density. This should be expected since the amount of stress transmission is proportional to the impedance of the soil, which is the product of the soil's density and local sound speed. Likewise, a plot of the measured values of the specific impulse of each wave (the integral of the stress-time curve) is given in Figure 7 and similar increases are seen for the sand and clay samples.

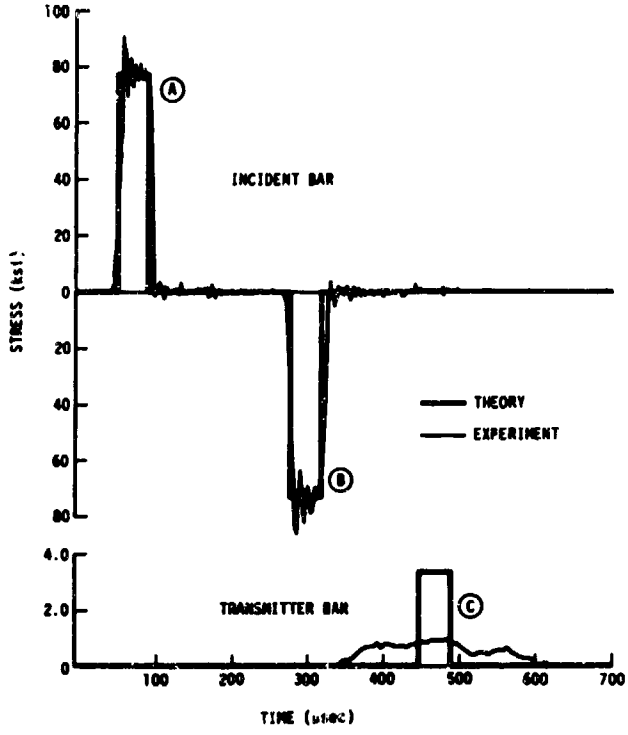

Figure 5. Typical Stress-Time History (0.5 inch diameter bar)

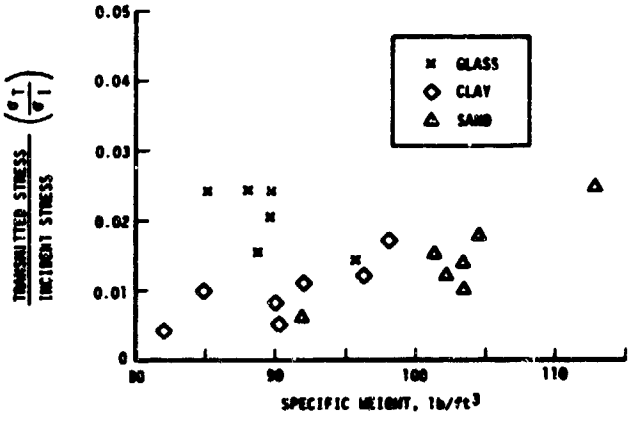

Figure 6. Stress Ratio versus Specific Weight

It should be noted in both Figures 6 and 7 that the stress wave transmission of the glass bead specimens differs from that of the other two materials. Large scatter in the data is evident and no increase is seen with increasing density. This behavior was probably due to the large size of the glass particles relative to the bar diameter (3mm vs. 12.7mm). Such large particles would

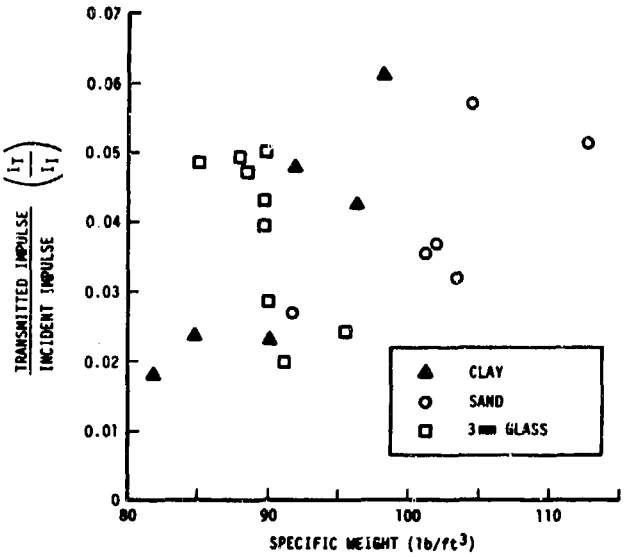

Figure 7. Specific Impulse Ratios Versus Specific Weight

not be packed efficiently in the specimen holder and the amount of contact area between these beads and the bar would be small. These results clearly demonstrate the need for a much larger diameter Hopkinson bar system for testing large granular soils.

The normal rule for soil pressure measuring devices is to keep the ratio of the diameter D of the measuring device to that of the particle diameter d above 50 for cylindrical measuring devices and above 10 for diaphragm devices (Reference 15). Table 2 lists the diameter ratios for the specimens in the 0.5-inch bar experiments and corresponding diameter ratios for future testing with the 2-inch bar. A 2-inch diameter bar was chosen for the large split Hopkinson bar in order to provide enough surface area for typical dynamic soil stress gages. A larger diameter bar could be used, but increases in bar diameter also increase two-dimensional effects which complicate interpretation of pressure transmission pulses. The 2-inch diameter bar is shown in Figure 8. Stainless steel bars age-hardened to 140 ksi yield strength and 162 ksi ultimate strength were used for the split Hopkinson bar. Both the incident and transmitter bars are nominally eleven feet long. Three projectiles 16-, 8- and 4-inches long are available and are launched with a compressed gas gun.

Table 2. Diameter Ratios for Bars and Soil Particles

Particle	d(mm)	D/d(D=12.7)	D/d(D=50.8)
Glass Bead	3.0	4.2	16.9
Sand	2.0 - 0.6	6.4 - 21.1	25.4 - 84.8
Clay	0.01	1270	5080

(a) View Towards Launcher

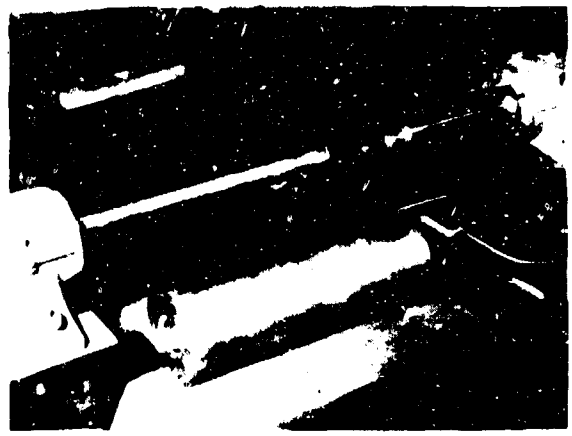

(b) Soil Specimen Holder

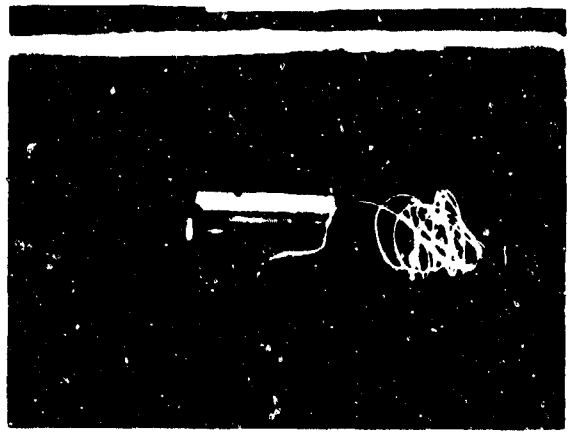

(c) Soil Pressure Gage Mount

Figure 8. Split Hopkinson Bar Test Setup (2 inch Diameter)

Future Efforts

The large split Hopkinson bar will first be used to measure the effect of variations in soil conditions on pressure wave transmissions. Soil parameters to be varied include particle size and moisture content. A variety of pressure gages will be included for comparing transducer measurements with Hopkinson bar measurements. The laboratory experimental program will be complemented with an analytical study using classical wave propagation theories for multi-phased media. Once a clear understanding of pressure wave transmission and soil variation relationship is achieved, procedures will be developed for designing soil systems to better mitigate expected pressure loadings on buried structures. Experimental techniques developed will also be applicable to a variety of other geologic materials.

REFERENCES

1. Westine, P. S. and Friesenhahn, G. J., "Close-In Ground Shock Loads from Buried Bomb and Ordnance Detonations," in progress report Contract No. FO8635-80-C-0174.

2. Ingram, J. K., "CENSE Explosion Test Program," Report 2 Tech Rpt N-77-6, Weapons Effects Lab., U.S. Army Engineer Waterways Experiment Station, Vicksburg, MS, December 1977.

3. Kiger, S. A. and Albritton, G. E., "Response of Buried Arch Structure to the Effects of Localized Explosions," Tech Report No. SL-79-13 Structures Lab., U.S. Army Engineer Waterways Experiment Station, Vicksburg, MS, December 1979.

4. Kiger, S. A. and Albritton, G. E., "Response of Buried Box Structures to the Effects of Localized Explosions," Tech Report No. SL-80-1, Structures Lab., U.S. Army Engineer Waterways Experiment Station, Vicksburg, MS, March 1980.

5. Brandt, H., "A Study of the Speed of Sound in Porous Granular Media," J. Appl. Mech., Trans. ASME, Vol. 22, No. 4 (Dec) pp. 479-486, 1955.

6. Deresiewicz, H., "Stress-Strain Relations for a Simple Model of a Granular Medium," J. Appl. Mech., Trans. ASME, Dec, pp. 402-406, 1958.

7. Duffy, J., and Mindlin, R. D., "Stress-Strain Relations of a Granular Medium," J. Appl. Mech., Trans. ASME, Dec, pp. 585-593, 1957.

8. Hall, J. R., Jr., and Richart, F. E., Jr., "Dissipation of Elastic Wave Energy in Granular Soils," J. Soil Mech. and Found. Div., Proc. ASCE, Vol. 89, No. SM 6, Nov, pp. 27-56, 1963.

9. Hardin, B. O., and Richart, F. E., Jr., "Elastic Wave Velocities in Granular Soils," J. Soil Mech. and Found. Div., Prov. ASCE, Vol. 89, No. SM 1, Feb, pp. 33-65, 1963.

10. Digby, P. J., "The Effective Elastic Moduli of Porous Granular Rocks," J. Appl. Mech., Vol. 48, p. 803, Dec, 1981.

11. Rinehart, J. S., Stress Transients in Solids, Hyperdynamics, Santa Fe, NM, 1975.

12. Lindholm, U. S., "Some Experiments with the Split Hopkinson Bar," J. Mech. Phys. Solids 12, 317, 1965.

13. Sierakowski, R. L., Malvern, L. E. and Ross, C. A., "Compression Testing of Metals at Elevated Temperature," AFATL-TR-80-76, Air Force Armament Lab., Eglin AFB, FL, Oct, 1981.

14. NDRC, Effects of Impact and Explosions, Summary Tech. Report of the Nat. Def. Res. Comm. Div. 2, 1946, AD 221586.

15. Weiler, W. A., Jr., and Kulhawy, F. H., "Factors Affecting Stress Cell Measurements in Soil," J. Geo. Eng. Div., Proc. ASCE, Vol. 108, No. GT12, Dec, pp. 1529-1548, 1982.

The work reported in this paper was conducted for the USAF Engineering and Services Laboratory, Tyndall Air Force Base, under Contract No. FO8635-84-K-0153. The permission of the Air Force for publication is gratefully acknowledged.

ATTENUATION OF SHORT DURATION BLAST IN ENTRANCEWAYS AND TUNNELS

J. R. Britt

Applied Research Associates, Inc.
Vicksburg, MS

ABSTRACT

Experimental results of small-scale explosive tests treating the attenuation of short duration airblast in entranceways and tunnels are reviewed and analyzed. These tests modeled the attenuation characteristics of blast produced by conventional sized high explosive bombs in the 100-1000 kg range as contrasted with the attenuation of longer duration blast produced by nuclear detonations. Formulae for scaling the results to other structures and explosions and for predicting blast pressure and impulse in tunnels are presented.

INTRODUCTION

This paper presents an analysis of small scale explosive tests (References [1 and 2]) conducted at the U. S. Army Engineer Waterways Experiment Station (WES) in 1981-1982 to obtain measurements of short duration, high explosive blast penetrating into relatively large tunnels.

Before these tests a large amount of research had been conducted on the attenuation of long duration blast pulses in tunnel systems, but only a small amount of information was available for the propagation of high pressure, extremely short duration, pulses produced by conventional explosives detonated near a tunnel entrance.

The WES experimental program consisted of a series of 99 spherical charges ranging from 113 to 907 g of composition C-4 explosive detonated outside and inside the entrance of tunnels of circular and square cross-sections. The model structures were about 30 cm in diameter and from 4 to 24 tunnel diameters long. Both end-on and side-on burst configurations were used. Blast pressure was measured at locations ranging from 1/6 to 24 diameters from the entrance. Included in the program were tests of blast propagation in a long straight tunnel, blast reflection at the end of short tunnels, blast attenuation in side tunnels and "t" tunnels, blast propagation in 45 and 90 degree bends and blast suppression with a vented expansion chamber. This paper treats only blast attenuation in a long straight tunnel. Measurements presented in Reference [1] for this configuration are reviewed and formulae for scaling the results to other structures are presented.

BACKGROUND

The object of the WES test program was to obtain fundamental blast propagation information for typical tunnel structure components. The primary range of interest was approximately $1 < W^{1/3}/\sqrt{A} < 4$ kg$^{1/3}$/m where W is the charge mass in kg T.N.T. and A is the cross-sectional area of the tunnel. (We have used $D = \sqrt{A}$ as an extended definition of "diameter" to refer to structures of square and rectangular as well as circular crosssection.) Pressure measurements from near the entrance to at least 20 tunnel diameters were needed. Pressures at the tunnel entrance ranging from about 0.34 MPa (50 psi) to 40 MPa (5800 psi) were of interest, as well as, explosions inside the entrance.

The work of Itschner and Anet [3] provides some excellent data on blast attenuation in a straight tunnel using the same basic configuration of the WES tests. Pressure measurements were made at distances of 0.5 to 80 diameters within the tunnel, but the range of the tests, about $26 < W^{1/3}/\sqrt{A} < 33$ kg$^{1/3}$/m , is almost an order of magnitude larger than our needs. This difference in scale causes some very significant differences in blast attenuation. Gürke and Scheklinski-Glück [4] obtained pressure measurements in long straight tunnels in the desired $W^{1/3}/\sqrt{A}$ range, but had no pressure sensors closer than 10 diameters from the entrance. They also used cylindrical rather than spherical charges and a slightly different entrance configuration.

EXPERIMENTAL FACILITIES

The test structures were fabricated from steel plate and heavy wall (0.95 cm thickness) steel tubing of both round and square cross-sections. The straight tunnel arrangement is shown in Figure 1. Explosive charges were detonated in both end-on and side-on configurations. Piezoresistive pressure transducers were mounted from the outside of the tunnel so that the sensing surface was flush

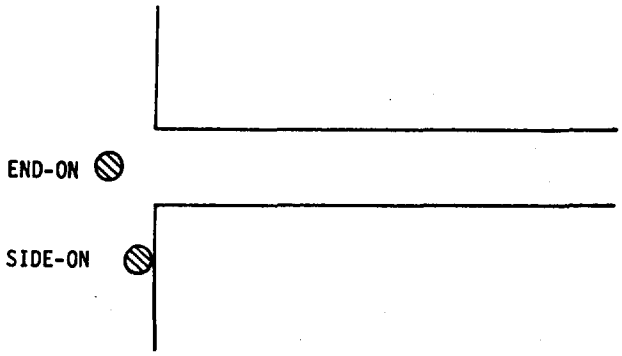

Figure 1. Tunnel Blast Configurations

with the inside wall to obtain side-on blast measurements. Gages were also located facing the blast on the plate surrounding the entrance. The analog signals from the sensors were recorded on FM magnetic tape records with 80 kHz frequency response, and the data was digitized at 500 kHz for processing on a digital computer.

EXPERIMENTAL RESULTS

Experimental results are presented for long straight tunnels with circular cross-section. The diameter is 0.3048 m. Figure 2 is a plot of peak overpressure measurements from three tests at the 3.45 MPa entrance pressure level as a function

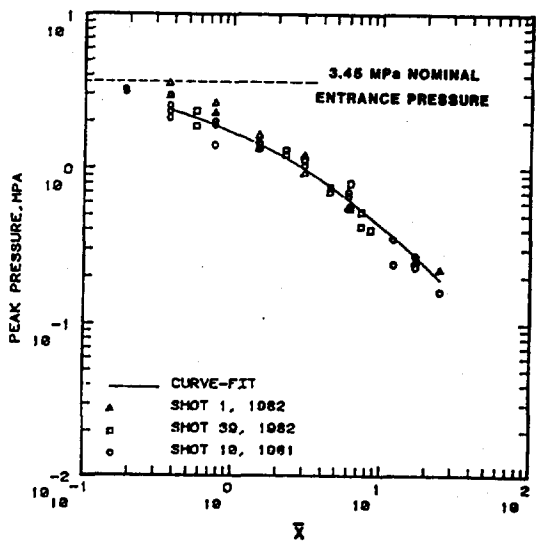

Figure 2. Peak Pressure as a Function of Scaled Distance for 3.45 MPa Entrance Pressure from a 340.2 g Explosive Charge for End-On Bursts

of the scaled distance $\bar{x} = x/\sqrt{A}$, where x is the distance from the entrance and A is the cross-sectional area of the tunnel. 340.2 g charges were detonated in the end-on configuration. The measurements show a pressure decay and duration increase down the tunnel similar to that observed in References [3] and [4] but with the following differences: (a) Pressure decays monotonically down the tunnel. A pressure increase at two to ten tunnel diameters of up to 1.6 times the free-field value seen in both shock tube measurements [5] and in the tests of Itschner and Anet [3] does not occur in the WES experiments. (b) The simplified characteristic solutions used by Coulter and Clark [5] and [6] and Itschner and Anet [3] do not accurately model the pressure attenuation and pulse duration of these tests.

Figure 3 shows attenuation of pressure with scaled distance for 340.2 g charges detonated directly in front of the entrance. The parameter is the nominal (predicted) free-field overpressure at the entrance assuming 0.75 kg composition C-4 is equivalent to 1.0 kg of T.N.T. The upper curve resulted from the explosion of a charge half inside the entrance suspended at the center of the opening.

Figure 4 compares the pressure decay down the tunnel for three charge sizes detonated to produce the same nominal 3.45 MPa entrance pressure. As observed in previous shock tube and explosive tests there is more rapid attenuation for the smaller charges which generate shorter duration pressure pulses and shock fronts with greater curvature.

Figures 5-7 are plots of the positive impulse (time integral of the overpressure) as a function of the scaled distance $\bar{x}$ in the tunnel corresponding to the pressure plots Figures 2-4. The impulse is either nearly constant, or initially decays slightly and then slowly increases.

Explosions were also detonated in a side-on configuration. Figure 8 shows the measured peak overpressure attenuation with scaled distance for 340.2 g charges. Shots 1 and 3 were fired in contact with the steel entrance plate and 61.0 cm from the center of the entrance. The nominal pressure at the center of the entrance was 3.45 MPa. Shot 8 was located 15.2 cm out from the plate and 58.5 cm measured along the plate to produce the same pressure. From the entrance to about one tunnel diameter the measurements separate into two groups. In the upper group the transducers were on the side of the tunnel opposite from the explosion and received a head-on blast component. In the lower group of measurements the gages were on the side of the tunnel nearest the explosion and received primarily side-on blast. These two groups converge at a distance of about one diameter into the tunnel.

Figures 9 and 10 show pressure and impulse attenuation for five entrance pressure levels for 340.2 g charges detonated in the side-on configuration. Pressures at one diameter correlate well with transmitted pressures measured in shock tubes, Reference [5], for blast side-on to a tunnel entrance.

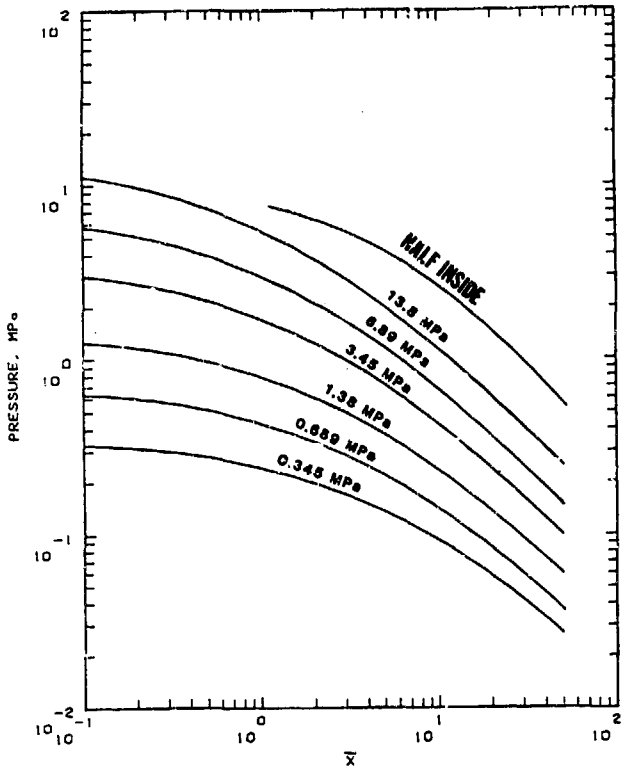

Figure 3. Blast Attenuation for 340.2 g Charge and Several Entrance Pressure Levels for End-On Bursts

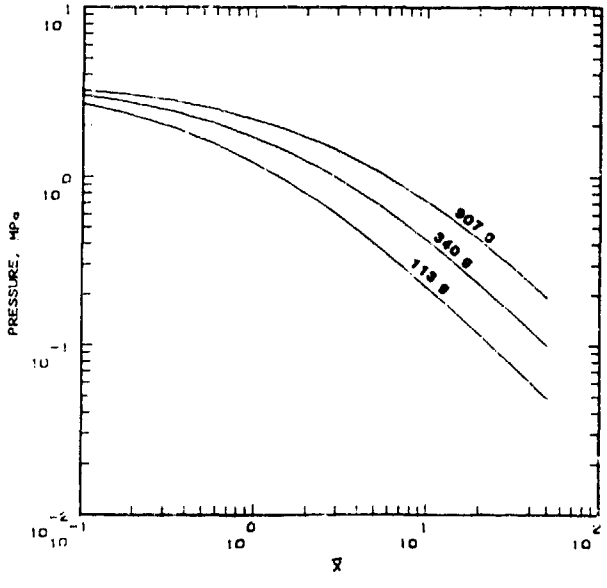

Figure 4. Blast Attenuation for 3.45 MPa Entrance Pressure and Three Charge Sizes for End-On Bursts

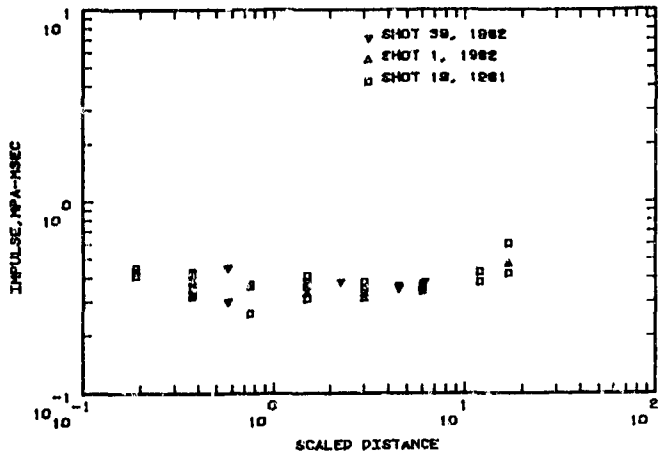

Figure 5. Impulse Measurements for 3.45 MPa Entrance Pressure and 340.2 g Explosive for End-On Bursts

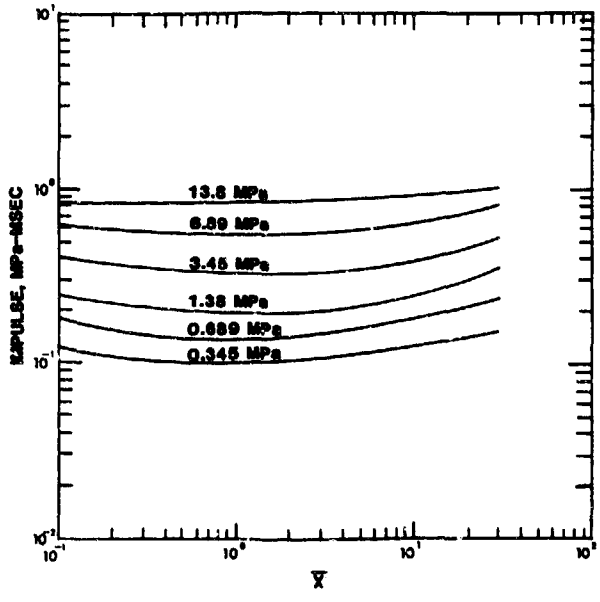

Figure 6. Impulse of 340.2 g Explosive Charges for Six Entrance Pressure Levels as a Function of Scaled Distance for End-On Bursts

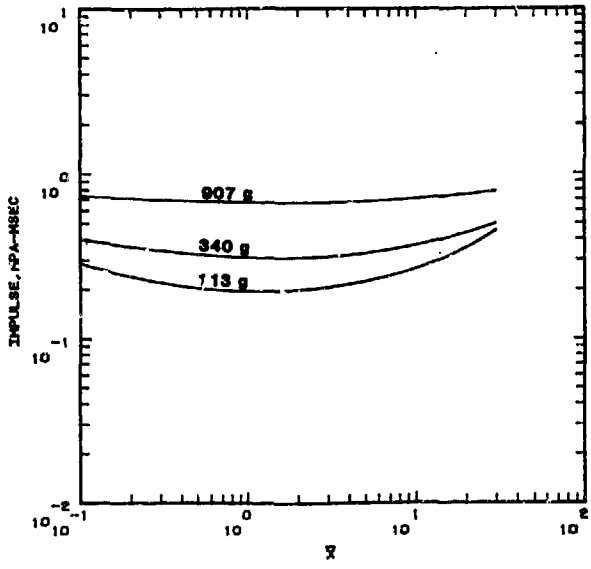

Figure 7. Impulse for Three Charge Sizes as a Function of Scaled Distance, at 3.45 MPa Entrance Pressure Level for End-on Bursts

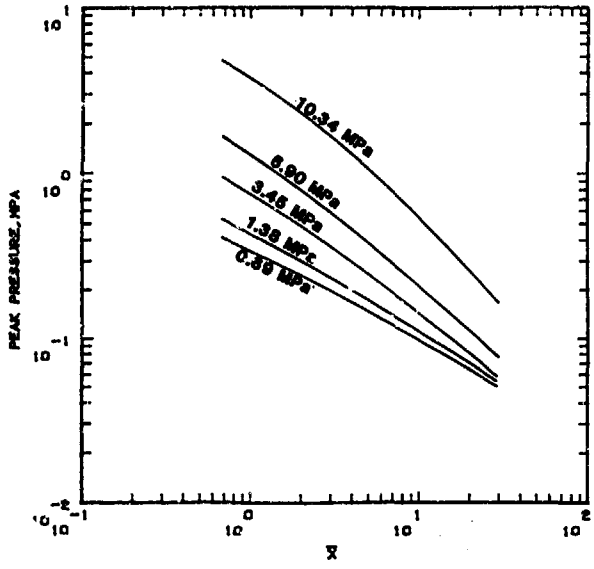

Figure 9. Pressure Attenuation From Side-On Bursts

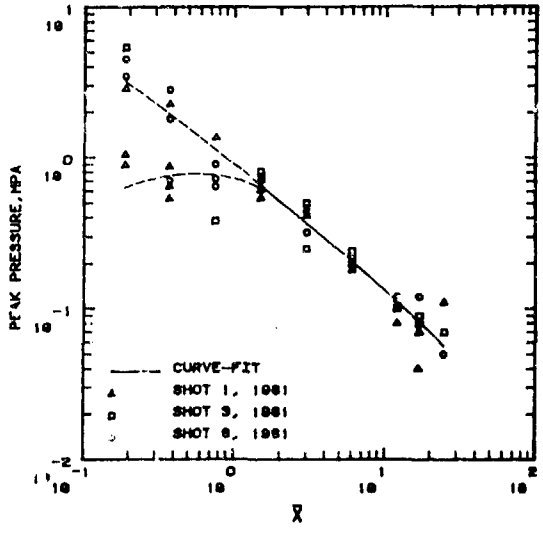

Figure 8. Blast Attenuation for Side-On Configuration

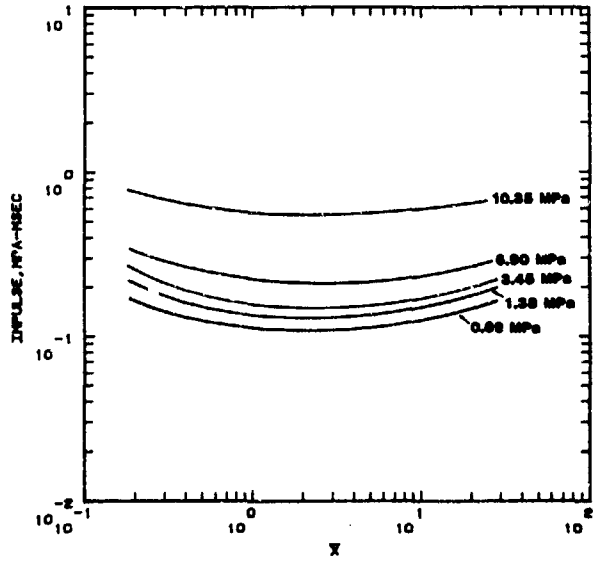

Figure 10. Impulse as a Function of Scaled Distance from Side-On Bursts

SCALING RELATIONS FOR A LONG STRAIGHT TUNNEL

The results of the WES tests were analyzed to develop simplified peak pressure and impulse formulae suitable for engineering design of tunnel-like protective structures. The peak pressure attenuation with distance in a tunnel was fit to the following modification of the Broh Equation given in Reference 8:

$$P = P_i / \{1 + \tan [(\pi/2)\, \bar{x}/(\bar{x} + \bar{E})]\} \qquad (1)$$

where P = pressure at distance x inside tunnel
P_i = pressure at tunnel entrance
x = distance from entrance
A = cross-sectional area of the tunnel
$\bar{x}$ = $x/\sqrt{A}$ scaled distance from entrance
$\bar{E}$ = dimensionless empirical decay parameter

For the end-on burst configuration $\bar{E}$ is given by

$$\bar{E} = K_e\, (W^{2/3}/A)\, (P_o/P_i)^{0.4} \qquad (2)$$

where W = charge weight
P_o = atmospheric pressure in same units as P_i
K_e = 0.586 for W in kilograms and A in square meters
K_e = 3.72 for W in pounds and A in square feet

For the side-on burst configuration $\bar{E}$ is given by

$$\bar{E} = K_s\, (W^{2/3}/A)\, (P_o/P_i)^{0.8} \qquad (3)$$

where K_s = 2.26 for W in kilograms and A in square meters
K_s = 14.4 for W in pounds and A in square feet

For design purposes impulse, I, in the tunnel is essentially constant with distance into the tunnel, except at the ends of the tunnel. For the end-on burst configuration the impulse

$$I = I_{oe}\, W^{1/3}\, (W^{1/3}/A^{1/2})^{1/2}\, (P_i/P_o)^{0.6} \qquad (4)$$

where I_{oe} = 0.0420 for I in MPa·msec, W in kg and A in m^2.
I_{oe} = 7.43 for I in PSI·msec, W in lbs and A in ft^2.

For side-on bursts the impulse is

$$I = I_{os}\, W^{1/3}\, (W^{1/3}/A^{1/2})^{1/2}\, (P_i/P_o)^{0.2} \qquad (5)$$

where I_{os} = 0.0756 for I in MPa·msec, W in kg, and A in m^2.
I_{os} = 13.4 for I in PSI·msec, W in lbs, and A in ft^2

The ranges of validity of these equations are approximately $1 < W^{1/3}/\sqrt{A} < 4$ kg$^{1/3}$/m and 0.3 MPa $< P_i <$ 40 MPa for end-on bursts and 0.6 MPa $< P_i <$ 11 MPa for side-on bursts. There were insufficient measurements to determine the charge weight dependence for side-on bursts. Equations (3) and (5) assume the same yield scaling as for the end-on bursts. Further experimental work is needed to verify this assumption.

CONCLUSIONS AND RECOMMENDATIONS

Formulae for calculating peak blast overpressure and impulse in tunnels for explosions near the entrance have been presented. These results are considerably different from the shock tube work which modeled blast from nuclear detonations and, hence, should be used instead of the nuclear blast formulae when designing protective structures for blast from non-nuclear explosions. Several weaknesses of the experimental data base were identified in the course of this analysis: (a) Tests with different charge weights are needed, particularly for side-on bursts. (b) Measurements with different diameters and other cross-sectional shapes (such as rectangles) are needed. (c) Tests with near prototype size structures are needed to verify scaling. Additional experimental work at WES has been conducted which partially addressed these needs but the results are not yet available.

ACKNOWLEDGEMENT

The analysis presented in this paper was supported, in part, under contract with the U. S. Air Force Engineering and Services Center.

REFERENCES

1. Britt, J. R., "Attenuation of Short Duration Airblast in Tunnel Systems," Proceedings Eighth International Symposium on Military Applications of Blast Simulation, Spiez, Switzerland, 1983.

2. Britt, J. R. and Little, C. D., "Airblast Attenuation in Entranceways and other Typical Components of Structures: Small Scale Tests Data Report 1," TR-SL-84-22, USAE Waterways Experiment Station, 1984.

3. Itschner, D. and Anet, B., "Entry and Attenuation of Shock Waves in Tunnels," Proceedings Fifth International Symposium on Military Applications of Blast Simulation, Stockholm, 1977.

4. Gurke, G. and Scheklinski-Gluck, G., "An Investigation of Blastwave Penetration into a Tunnel Entrance," Report E 7/80, Ernst-Mach-Institut der Fraunhofer-Gesellschaft, Freiburg, Germany, 1980.

5. Coulter, G., "Information Summary of Blast Patterns in Tunnels and Chambers, BRL MR 1390, Ballistic Research Laboratories, 1962.

6. Clark, R. O., "Theory for Viscous Shock Attenuation in Ducts Based on the Kinetic Theory of Gases Experimentally Verified to a Shock Strength of 68," AFWL-TR-65-204, Air Force Weapons Laboratory, 1966.

7. Coulter, G., "Blast Loading in Existing Structures - Basement Models," BRL MR 2208, Ballistic Research Laboratories, 1972.

8. Coulter, G., "Attenuation of Peaked Air Shock Waves in Smooth Tunnels," Memorandum Report 1809, U. S. Army Ballistic Research Laboratories, 1966.

SOIL PROPERTIES AT DEPTH FROM SURFACE MEASUREMENTS

Robert Douglas & George Eller

North Carolina State University
Raleigh, NC

ABSTRACT

The use of soil-matrix overburden and sidefill as protective multi-layer structures to protect critical installations calls for a regular inspection schedule. Means must be developed for determining quantitatively whether such actions as settlement, freeze and thaw, microseisms, etc., have caused the structure to alter its character excessively. Several possibilities for such tests are described that are based on wave propagation methods: seismic refraction, Rayleigh wave dispersion analysis, and signature evaluation. Current research by the authors is described, with examples of several experiments similar in character to conditions possible to soil-matrix protective structures.

INTRODUCTION

Specially designed soil-matrix structures are used as overburden or sidefill to protect critical installations against attack by explosives or heavy projectile penetration. They are used in an arrangement described in mechanics as a layered medium. At least some of the layers will be of local materials, soil, aggregate, rock, in various combinations and sizes. One or more layers may be of concrete, reinforced or not, the layers of thicknesses and combinations selected by the designer to best defeat attack by rapidly absorbing mechanical energy and by diverting, turning, or breaking up a projectile so that its energy and momentum may be brought within acceptable limits.

Once in place, the passive armor represented by the soil structure will begin to alter. Settlement, infiltration and diffusion, rain, freeze and thaw, expansion and contraction, local seismic activity of whatever scale, these will combine to change the original system to a blurred copy, almost certainly changed in the direction of decreased effectiveness.

Such a system must be examined from time to time to determine whether it still is capable of performing its function or whether it should be reinforced or rebuilt, for unlike exposed structures of concrete and steel, visual examination of the surface will not give an indication of the general condition of this layered system. There should be an initial inspection soon after construction, with a quantitative evaluation to establish a basis for later comparison, and definite provision and established means for inspection.

CHARACTERIZATION

In determining a suitable inspection means it is useful to observe that adjacent layers of these protective structures may be expected to have quite different properties in order to maximize changes in impedance. The designer will characterize the properties of a layer in such terms as a density parameter, apparent or equivalent shear and bulk moduli, particle size, perhaps a strength characteristic associated with individual particles, etc. The response to attack will involve extensive motion, permanent deformation, and fracture and distortion at many levels of size. In spite of the many levels of response intended, it is probable that the instantaneous conditions of the various layers can be defined adequately, for time-dependent comparisons, in terms of the gross mechanical behavior of each layer.

WAVE PROPAGATION METHODS FOR EVALUATION OF LAYERED SOLIDS

If the early, low-stress portions of the constitutive relationships for a material define it adequately, if the properties of concern are sufficiently related to the values of elastic moduli, then wave propagation methods should be considered. Non-destructive methods of evaluation are coming to be based more and more on wave propagation rather than upon simulations of service conditions, for the particular reason that the results of wave propagation tests are specifically related to fundamental mechanical parameters such as the elastic moduli, the density, and particle size. Furthermore, impulsive sources of very low magnitude are sufficient and tests can be made easily in a horizontal plane, on vertical faces, even overhead.

The waves generally used as diagnostic invaders are the longitudinal wave, the shear wave, the Rayleigh wave, and the Lamb waves. The phenomena invoked with them are reflection, refraction, dispersion, and scattering. The quantities computed from test results differ with the geometries of individual structures, but generally consist first of finding the velocities of one or more types of waves or of individual frequencies, or of determining the stripping of portions of the frequency spectrum of the original signal. The determination of mechanical parameters comes as a second series of computations and requires that there be a sufficient number of quantities determined from tests to provide the number of equations needed.

The Possibilities, The Difficulties.

Reflection Studies. From advertisements and commercials by oil companies and publicity about the CAT-scans of medical programs, even the lay public have some appreciation for reflection studies. An impulsive source at the surface, Fig. 1, sends waves to the layers below. Reflection takes place at each interface between layers of different densities and wave velocities and a picture can be formed of the layering. While the method (1) does describe the layering and does give an idea of layer thicknesses and changes in thickness, the reflection method does not, of itself, provide much quantitative information. Actual layer thicknesses and wave velocities must come from other sources.

Seismic Refraction Studies. Where a system is such that each successively deeper layer has a higher wave velocity than those above (normal geological structure), the method of choice is seismic refraction (1,2), whether layers are thousands of feet deep, or only a few feet in depth. Only the instruments and frequencies change.

A point source, Fig. 2, generates longitudinal waves (and others) which expand outward beneath the surface like half a bubble. Some of the rays of the wavefront are certain to encounter each successively deeper layer at the critical angle. Refraction from the slower into the faster layer will cause the wave to travel along the layer boundary, but in the faster (and deeper) layer and at the wavespeed of the faster layer. As the critically refracted wave travels on in that layer, it will continually refract energy back toward the surface through the layers above in the continuously generated wave known as "kopfwelle".

The essence of quantitative use of the seismic refraction method is that of first return. If there is a string of transducers at the surfact, each will detect and record all ground motion within its sensitivity. For transducers quite near the source, the first signal received will be that coming straight through the surface layer from the source. Farther away, a transducer will receive and display as first signal the return from the second layer. Farther away yet, some even more distant transducer will receive and display a first return from the third layer, and so on. The characteristic way of presenting the information is shown in Fig. 3, a plot of first arrival time vs. position. From such a plot, from such information alone, the thickness of each layer and the longitudinal wave speed in each layer may be computed.

In a similar way, a surface source of dominant shear waves might generate first arrival versus position data for shear waves and provide the shear wave speed in each layer. The equations relating the experimentally obtained wave velocities to the elastic moduli E, and G of a layer are:

$$c_\ell = \sqrt{[(1-\nu)(1+\nu)^{-1}(1-2\nu)^{-1}E\rho^{-1}]} \qquad [1]$$

$$c_s = \sqrt{[G\cdot\rho^{-1}]}$$

where c_ρ, c_s are longitudinal and shear wavespeeds

ρ is the density
ν is Poisson's ratio.

Refraction studies have two restrictions: first, layering must be of "normal" geologic sort, wave speeds must increase as depth increases; second, it must be possible to assign approximate values for the density and for Poisson's ratio to solve equations [1] and [2] for the moduli.

Rayleigh Wave Dispersion. Layered structures used as armor cannot be expected to be of normal geological type. The faster layers may be on top, there may be multiple inversion, or there may be interleaving of layers of different properties.

Less well known than seismic refraction is a method based on the dispersion of Rayleigh waves. These are surface waves, extending into the medium to a depth that is dependent upon the wavelength. If the medium is not layered, and if the properties do not change, Rayleigh waves are not dispersive and all frequencies travel with the same speed, somewhat less than the speed of the shear wave. If the medium is layered and the wavelengths are long enough to extend into other layers, then the propagation is dispersive and wave speeds are not the same for all frequencies. This phenomenon, presents an opportunity to develop means with which to determine the velocities of buried layers when there is inversion or interleaving, and when added to the capabilities present in the reflection and refraction methods, it gives to wave propagation studies a useful range of types of tests that may be combined as needed.

A dispersion test involving Rayleigh surface waves requires an impulsive source of waves and one or more accelerometer pairs placed along the surface away from the source, each pair serving to define a gagelength. A test begins with a pulse. As the signal passes each one of an accelerometer pair, its shape is recorded as a function of time. Each of the two signal shapes, if not in the near-field, is subjected to analysis by a discrete finite Fourier transform, Eqn. [3], to obtain the frequency domain results of magnitude vs. frequency, Eqn. [4] and, the essential information,

phase angle vs. frequency, Eqn. [5]. The two sets of results from the accelerometer pair then are evaluated to find the phase change (phase difference) $\Delta\phi_x$ between them at each frequency of the transform

$$F_{re}(X) = \sum_{n=o}^{n-1} f(n)\cos\left(\frac{nX}{N} \cdot 2\Pi\right); F_{im}(X) = -\sum_{n=o}^{n-1} f(n)\sin\left(\frac{nX}{N}2\Pi\right) \quad [3]$$

$$|F(X)| = \sqrt{[F_{re}(X)]^2+[F_{im}(X)]^2} \quad [4]$$

$$\theta_x = \tan^{-1}[F_{im}(X)/F_{re}(X)] \quad [5]$$

For each frequency, since its period T is known automatically, and the distance of travel GL (gagelength), and the phase change $\Delta\phi$, the velocity possibilities for each frequency (or wavelength) may be computed by the deceptively simple equation [6] below.

$$v_x = [2\Pi GL]/[\Delta\theta_x T] \quad [6]$$

Next, the dispersion curve can be plotted, Fig. 4, relating velocity to wavelength. The forms of dispersion curves differ considerably, for they depend upon the relative thicknesses of the layers, the number of layers present, their relative and absolute properties, the condition of each, and to what extent they are "welded" together.

Dispersion analysis of Rayleigh surface waves was the subject of considerable attention in England and in this country in the 1960's because of its potential application to the same problems with pavements that now appear with respect to the soil-matrix structures used as armor: how to determine instantaneous condition; beyond that, how to predict remaining life. The theory for this application of dispersion analysis was established (3,4) at that time.

Airfield Pavements. Engineering work in the USAF, associated with airfield pavements, was turned toward dispersion analysis and tests in the late 1960's. In the late 70's, to boot dispersion analysis into practice, the USAF embarked on a plan of simultaneous hardware development and development of analysis and interpretation, a plan that is reaching maturity now with results that may be useful to inspection of soil-matrix armor.

The problems have been how to move from the broad statements of theory to the realities of field practice. In this work, the problems come about largely from the differences between the layered half-space of the applied mathematician or mechaniker and the layered system of the airfield, where the surface layer often is made up of slabs that are less than 25 ft. on a side.

The statements of theory, for the testing of soil-matrix armor as well, are these, that dispersion analysis may be able to provide the following:

1. the shear or Rayleigh wave speeds for each of several buried layers;
2. that from a single test, both the speed of the longitudinal wave and the speed of the shear wave can be found for a buried layer;
3. that the test can distinguish between "welded" layers and layers that over time have become degraded;
4. that although there is not sufficient information to compute the moduli without at least a guessed value of the density, the values of the wave speeds themselves for each layer will serve as accurate descriptors to tell whether or not the mechanical properties of the buried layers have changed.

We are involved in this work, concerned with the problem of how to instrument and conduct dispersion tests in such a way that the promise of theory can be realized. We also are investigating the subsequent problems of analysis and interpretation. Our subject has been the airfield runway, the inverted system in which the surface layer is often concrete over a crushed stone base, then over soil. The slabbed surface creates a series of problems:

1. The lateral boundaries are so close that reflections return quickly to the accelerometers during a record and alter the phase information.
2. The slabs are small yet of comparable magnitude to the wavelengths of interest, so that many of the accelerometer pairs must be on the same slab with the source. Immediately one is dealing with a mixed near-field, far-field problem.

Our work has been built about model studies of laboratory scale. The models are made up of layers of polymeric materials to provide a variety of wave speeds. The models serve as useful testbeds for the development of instrumentation and methods, and for reproducing problems of analysis met in the field. They may be used to quickly create structures of whatever configurations are desired. Of primary importance, we are able to compare easily the results of mathematical analysis with the actual structure of the particular model being studied in the laboratory, as we seek to improve the analysis and to extend interpretation beyond its present state.

Approach to the problem of reflections requires understanding of the conduct of an experiment together with appreciation of the analysis that follows. We have devised several ways to overcome the reflection problem. The best to date is one that combines a time-frame window with choice of the spectral content of the input signal. It is in only minor contradiction with a beautiful feature implicit in dispersion analysis, that it is not necessary to reproduce test conditions closely to be able to reproduce the results. It is not necessary to reproduce the shape of the input signal exactly, merely necessary that repeated inputs contain all the same frequencies as the original

signal. It is not even the phase angle that counts, only the phase differences.

Instead of a single input pulse, we now use two or three different ones. Each contains a different group of principal frequencies so that there may be high, medium, and low frequency pulses. Dispersion in this layered system has high frequencies generally traveling most rapidly. By selecting the interval within the accelerometer record (the time-frame windowing) according to the nature of the pulse, we are able to minimize the way in which reflections of one group of frequencies masquerade as part of a different group.

The near-field problem is a different matter altogether and leads first to consideration of altered analysis rather than altered experiment. The form of the solution to the problem (5) is as shown below:

$$\phi_n = \int_0^\infty Q_n J_o(kr)\exp[-\nu(z-h)]dk \qquad [7]$$

so that now we are working to apply the Hankel transform based on the Bessel functions for near-field analysis rather than Fourier analysis of sines and cosines. We look ahead to the probability that we will end up using a hybrid of the two transforms.

Experiments related to inspection of soil-matrix structures. In the course of the work above, experiments have been conducted that may prove of use for the evaluation of soil-matrix armor.

Fig. 5 shows a dispersion curve in which both the longitudinal wave speed and the shear wave speed are displayed at the same time for a buried layer. This is the first time we have been able to produce this phenomenon and we look forward to learning how to do it regularly.

Fig. 6 shows the results of several experiments using Rayleigh wave dispersion to examine inverted systems for several conditions of layering. In our work they represent several comparable structures that may exist after a pavement has been resurfaced. From the standpoint of soil-matrix structures, three layerings are shown that could represent stages of decay of an original system. The question is, can we distinguish the structures, one from another, and in a meaningful way.

In all structures (cross-sections in Fig. 6) the same two types of materials were used: first, one-inch layers of styrene-butadiene-rubber (SBR) used as separate layers in Fig. 6b and 6c, bonded together in Fig. 6a; second, three inches of foam rubber (FR) made up of one-inch and two-inch layers. The SBR has wave speeds several times higher than FR, so SBR represents a "stiff" material, concrete, whereas FR would represent a soil. This simple physical modeling has proven effective; results compare well with those from full-scale structures.

In all experiments the same entering pulse shape was employed. Despite the tenet that pulse shape has no effect in dispersion analysis, we have seen that changing the shape markedly can bring entire new behavior modes into the dispersion field, therefore are careful to change the shape cautiously in model experiments.

Fig 6a shows the result of two SBR layers cemented together to form a single thick surface layer. The behavior is discontinuous: the SBR layer acts independently, and both Lamb waves appear. Higher wave speeds than customary are coaxed out of the FR base, probably an interface wave created by the lower surface of the SBR plate.

The second, Fig. 6b, differs in that the two SBR layers are not bonded together. Their behavior is more independent of one another. Some minor slippage is possible at all the interfaces and the overall behavior is more continuous and representative more of a somewhat stiffer single plate over a less stiff one than the extreme condition above. There is only a hint of the truly independent behavior that is seen next.

In Fig. 6c the two SBR layers are separated from each other by a one-inch layer of FR and are much more free of one another. The two humps that are clearly visible, that were just discernible in 6b, show the two SBR layers each behaving independently within an overall continuous behavior for the entire structure.

The sensitivity of dispersion analysis is such that it can indeed respond to changes of structure at the level of structural degradation.

Signature. When overburden or sidefill is used as armor, it may be possible to mount instruments temporarily within the protected structure. In this case the concept of signature, of change in wave shape *per se* may be may be used to detect changes in the properties of the overburden. Fig. 7 shows experiments on a different set of models using combinations of the same materials described earlier. A uniformly reproducible pulse, necessary for signature studies, was created at the top of the overburden, with an accelerometer placed on the underneath side to record the shape of the in-coming longitudinal wave. Fig. 7 shows the layering arrangements together with the shapes of the respective pulses as received (tracings from oscilloscope photos).

The signatures obviously are quite different. Regardless of which type of layering arrangement might be more desirable, it is clear that changing the arrangement changes the nature of the transmitted pulse markedly.

Even at this level of modeling with continuum layers, the consequences of design choices can be seen. The structure of Fig. 7c results in a pulse that is briefer in duration than the others, of higher magnitude, with more high frequencies in it. The other extreme (of these three choices) is Fig. 7a, which results in the pulse of lowest

amplitude, greater duration, loading most slowly. Since all the initial pulses had the same shape, the designer is able to judge the response against the material properties at his disposal.

Conclusions. Although it is unlikely that any single wave propagation method can provide all the information desired to evaluate the mechanical state of a protective layered medium, it is entirely possible that a single method will be able to provide clear evidence that there has, or has not been a change in condition. Where additional or more complete information is desired, several wave propagation methods can be tailored to the particular type of layering involved and the information needed.

Acknowledgement. The experiments described here have been conducted in connection with work under AF Contract FY 8952-83-60056 for Hq AFESC, Tyndall AFB. That support is acknowledged here with appreciation.

References.

1. Dobrin, M. B., Introduction to Geophysical Prospecting, McGraw-Hill, 1976.

2. Redpath, B. B., "Seismic refraction exploration for engineering site investigations," U.S. Army Engineer Waterways Experiment Station, May 1973 (AD 768 710 NTIS).

3. Jones, R., "Surface wave technique for measuring the elastic properties and thickness of roads: Theoretical development," Brit. J. Appl. Phys. 13, 21, 1962.

4. Vidale, R. F., "The dispersion of stress waves in layered media overlying a half-space of lesser acoustic rigidity," Ph.D. dissertation, U. Michigan, 1964.

5. Ewing, W. M.; Jardetsky, W. S.; Press, F.; Elastic Waves in Layered Media, McGraw-Hill.

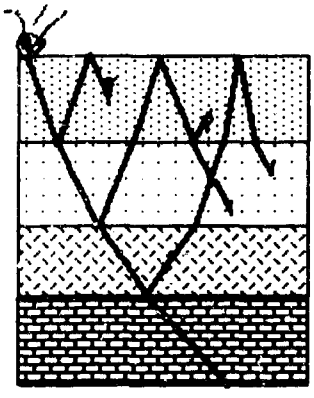

Fig. 1 Seismic Reflection

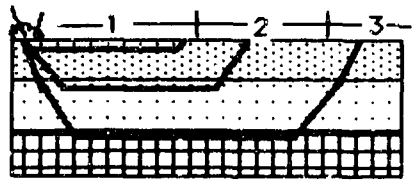

Fig. 2 Seismic Refraction

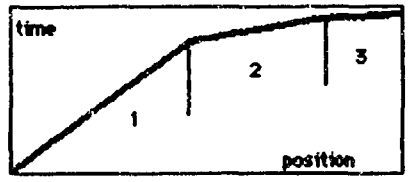

Fig. 3 Arrival time vs. position

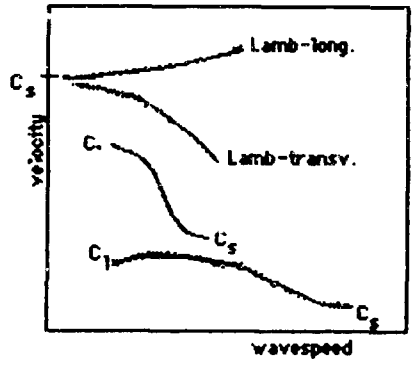

Fig. 4 Dispersion curve

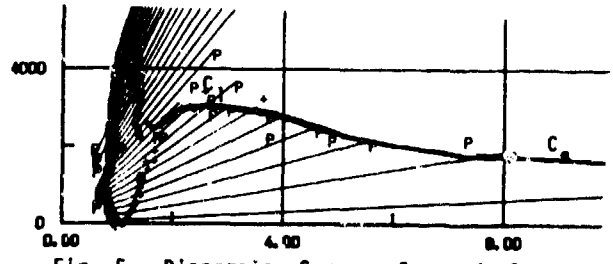

Fig. 5 Dispersion Curve: C_l and C_s

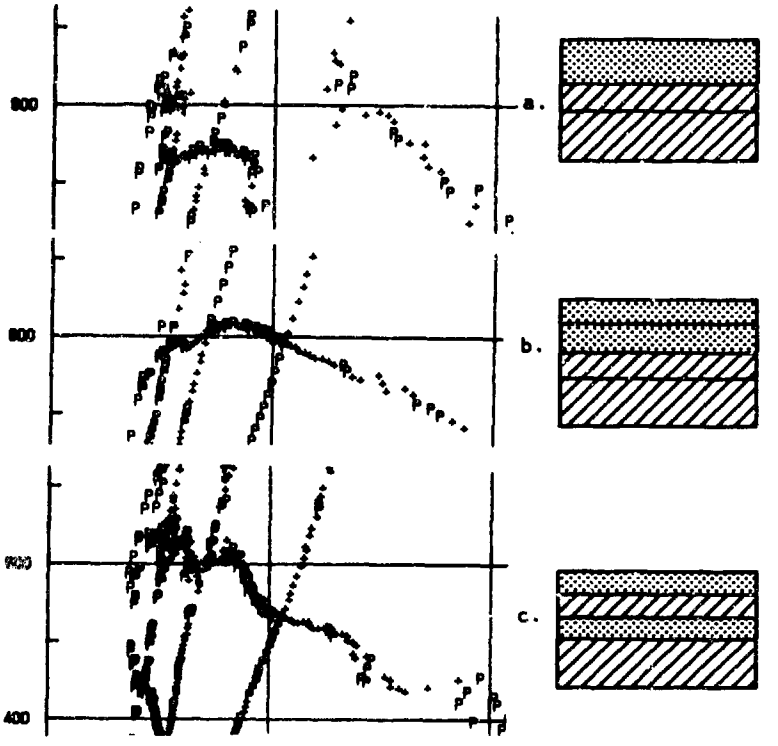

Fig. 6 Dispersion Curves. Lamb-transverse

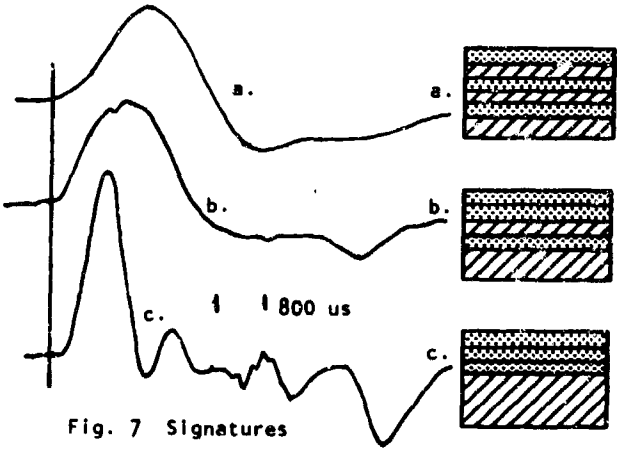

Fig. 7 Signatures

HIGH-PRESSURE BLAST DOOR AND BLAST VALVE DESIGNS

David W. Hyde and Sam A. Kiger

U. S. Army Engineer Waterways Experiment Station
Vicksburg, Mississippi

ABSTRACT

Design concepts for blast doors and blast valves capable of surviving the airblast and fragmentation effects of general purpose bombs are developed. Maximum blast pressures ranging from 500 psi to 8000 psi, along with the associated fragmentation effects, were used in the design calculations. Three general concepts for blast doors were investigated: (1) a heavily reinforced concrete door protected from fragmentation by a blast wall; (2) a steel plate stiffened with angles also protected by a blast wall; and (3) a massive steel and concrete door with steel plates on each face and with concrete confined by additional transverse plates. Each of the blast valve concepts examined must be protected from fragmentation and extreme pressures by a blast screen or wall.

BACKGROUND

Although extensive research programs have been conducted to determine the survivability of blast doors and blast valves when subjected to a nuclear detonation, the response of these structural components to conventional weapons effects is largely unknown.

Blast door design parameters include the location and orientation of the door relative to the weapon, the size of the door opening, frequency of use, and allowable damage criteria. Blast valve design parameters include the location and orientation of the valve relative to the weapon, the airflow capacity of the structure's ventilation system, the sensitivity of the ventilation system to airblast, and the amount of floor space available for additional airblast attenuating devices, e.g., an expansion chamber.

The design threat for this project is a general purpose bomb detonated at near-miss distance. The blast doors and blast valves must protect the occupants of the structure from the extreme pressures and fragmentation associated with this detonation. In addition, the doors should remain operable after the explosion, and both the doors and the valves should be capable of surviving multiple hits. The objectives for the blast doors may be met in one of two ways. The door may either be strong enough to withstand direct exposure to the detonation, or it may be shielded from the explosive source by a blast wall, which will attenuate the pressure to a lower magnitude and defeat the fragmentation effects. The physical characteristics of active blast valves require that they be shielded from fragmentation. The valve mechanism must be light enough to close very quickly, yet strong enough to survive the extreme pressures.

BLAST DOOR REQUIREMENTS

Each of the blast doors evaluated for this project provides a clear opening 55 inches wide by 83 inches high. The doors are required to remain gas tight during the explosion and to be operable after the detonation. The doors must also be able to prevent fragment perforation.

The "average" pressure and impulse distributions from the Series II NATO Semihardened Wall Tests (Reference 1) were used to approximate the airblast loading of the unprotected door. Reference 2 was used to determine the impulse distribution across the door due to fragmentation. The "ANSWER" computer code was used to predict the loading history for the protected doors. This code was developed at WES and is based on modifications of the work found in References 3, 4, and 5. Fragmentation effects for the protected doors were neglected, and predicted impulses and durations at various points on the doors were averaged to obtain an equivalent uniform pressure across the door.

Each of the doors were represented by an equivalent single-degree-of-freedom (SDOF) system for analysis purposes. The deformed shape of the doors was considered identical to the deformed shape of a uniformly loaded simply supported slab. For the unprotected door, the load distribution was considered uniform across the width of the door, with a step decrease in load of 33 percent at 60 percent of the door height (see Figure 1). This step load is an approximation of the high reflected pressures near the bottom of the door plus the loading due to fragmentation, which acts primarily on the lower half of the door. The protected doors were considered uniformly loaded across the entire face. Procedures for the SDOF analysis performed are given in Reference 6.

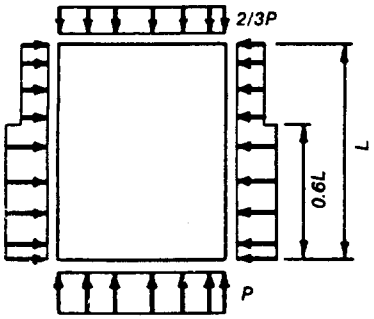

Figure 1. Idealized load function

FINAL DOOR DESIGNS

A. Unprotected door.

A massive steel and concrete door with steel plates on each face was selected for testing against direct exposure to the design threat. See Figure 2a. This door is 7 inches thick and has a 1-inch-thick, 50-ksi steel plate on either face. The outside plate serves primarily as protection against fragmentation, although it also provides additional flexural capacity. It is attached to the door with welded shear connectors, which provide shear reinforcement and insure that the plate and the body of the door act compositely during bending. Additional transverse plates are welded to the inside plate at 12-inch spacings. These transverse plates confine the concrete and allow larger plastic deformations than would otherwise be possible. The total weight of this door is about 6300 pounds, and the predicted maximum deflection when exposed to the design threat is about 1.2 inches. The outside plate is expected to be severely damaged by fragmentation but should be relatively easy to repair by patching any holes or deep pits with additional plates welded to the door's exterior. Preliminary analysis indicates that some of the shear connectors will break due to the horizontal shear at the plate/concrete interface. The effect this will have on the response due to a second detonation will be investigated experimentally.

B. Protected Doors.

Several European firms now manufacture a gas-tight 20-cm reinforced concrete blast door. This door is lightly reinforced and was conceived for a nuclear threat with a reflected pressure of 132 psi. The addition of a 10-mm mild steel plate has been proposed as an added protective measure. The section selected for testing will consist of a 20-cm (7.87-inch) reinforced concrete section sandwiched between the two 10 mm (0.4-inch) plates, which are anchored to the concrete with shear connectors spaced uniformly across each plate (Figure 2b). The weight of this door is about 5500 pounds, and the predicted maximum deflection when protected by a blast wall is about 0.5 inch.

As an alternative to the 20-cm (7.87-inch) door, a lighter section with a higher steel percentage was selected. This door is a total of 4.625 inches thick with a 0.25-inch plate attached with shear connectors to each face. This door weighs about 3000 pounds and has a predicted maximum response of 0.3 inch (Figure 2c).

The simplest of the protected doors selected for testing consists of a 0.75-inch, 50-ksi steel plate with 3-inch steel angles welded to the inside face at 12-inch spacings. The angles add little additional flexural capacity, but alter the stiffness of the door by an order of magnitude. If protected by a blast wall, the predicted maximum deflection of this door is about 1.4 inches. The total door weight is about 1500 pounds (Figure 2d).

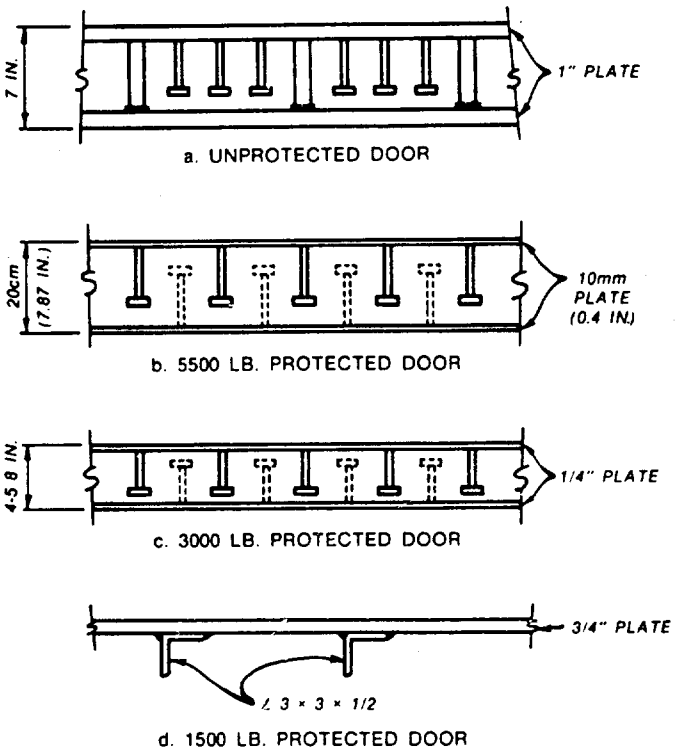

Figure 2. Blast door cross-sections

DOOR HARDWARE

When a blast door, or any structure loaded dynamically, reaches its maximum deflection, it has energy stored in it and tends to deflect in the opposite direction. For pressure durations that are long relative to the natural period of the door or when large plastic deformation occurs, this rebound is generally negligible. However, for elastic response and short-duration loads, the ratio of required rebound resistance to yield resistance approaches 1.0 (Fig. 9-14, Ref. 7).

There are two consequences of severe rebound loads: (1) the negative reinforcement of a simply supported door must nearly equal the positive reinforcement, (2) more important for a hinged door, either the hinges or the latch mechanism

must be capable of resisting the rebound forces. For the severe loads expected, no reasonable hinges are capable of resisting the rebound load. Therefore, the latch mechanism is designed to resist all of the rebound force so that the hinges are only required to perform their primary function.

As shown in Figure 3, the latch mechanism consists of three movable steel plates, each 1.0 inch thick for the heavier doors and 0.75 inch thick for the lighter doors, which interact with a steel catch welded to the exterior of the door frame. One latch plate is mounted on the hinged side of the door between the hinges and the other two plates on the opposite side. The plates are caused to move by a rotating cam which is welded to the shaft of the latch handle. The cam is designed so that the plates move in the horizontal direction only - they are not required to move vertically. The weight of each plate is supported by a steel angle welded to the door's exterior.

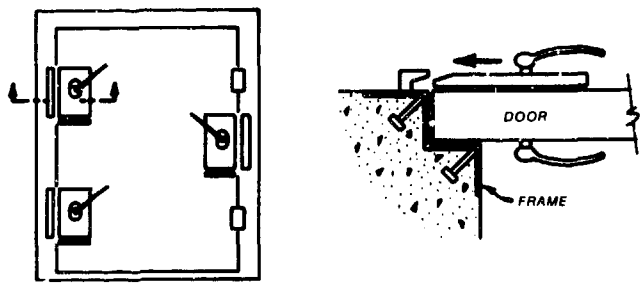

Figure 3. Latch mechanism

BLAST VALVES

Several international firms currently manufacture blast valves to protect mechanical systems from blast damage; however, most of these valves are designed for the long-duration, relatively low-pressure environment associated with nuclear explosions. It is uncertain if these blast valves will operate satisfactorily in the short-duration, high-pressure environment of conventional explosions. The blast valve mechanism must operate quickly enough to prevent a large-magnitude impulse from passing through.

A large variety of blast- and blast sensor-actuated valves were designed, built, and tested in the 1950's and early 1960's under the sponsorship of various U.S., Canadian, and European government agencies. Many of these valve designs were evaluated by Los Alamos National Laboratory in 1982 (Ref 8). Unfortunately, many of them were never put into production or have since ceased production. Several of the valve designers recognized the inherent difficulty in manufacturing a valve mechanism both light enough to move rapidly and strong enough to survive high pressures. Many of the valve designers solved, or attempted to solve, this problem by forcing the shock front to bypass the valve opening as the valve mechanism closed, so that by the time the shock front arrived at the opening the valve was completely closed.

One of the valves utilizing this concept which has been selected for further testing is shown in Fig. 4. This valve consists of three concentric pipes, with a piston that closes off the innermost pipe when activated by the pressure of an airblast wave. During normal operations, air flows through the outer pipe, into the middle pipe, and finally into the inner pipe before reaching the ventilation equipment. However, when a shock front enters the valve inlet and strikes the piston, by the time the shock front has traveled through the first two pipes the valve piston is closed. Given the predicted peak pressure, duration, and shock front velocity, this valve can be proportioned to allow no damaging impulse to pass through to the ventilation equipment.

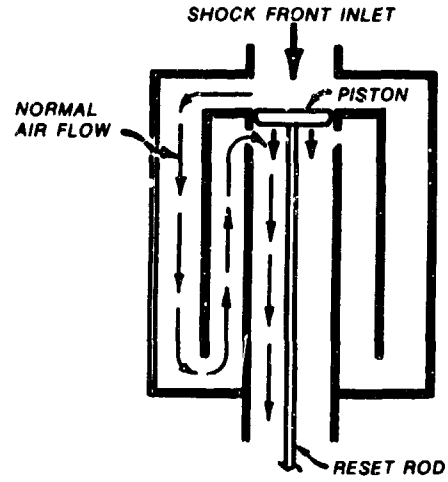

Figure 4. Pipe valve

CLOSURE

Current plans are to test each of the blast door concepts and the pipe valve, along with several commercially available valves, in a full-scale test at Tyndall AFB in October-November 1985.

REFERENCES

1. D. R. Coltharp, K. P. Vitaya-Udom, and S. A. Kiger; "Response of Semihardened Facilities Walls to Nearby Detonations"; Final Report, USAE Waterways Experiment Station, Vicksburg, MS. (In preparation)

2. J. T. Baylot, et. al.; "Fundamentals of Protective Design for Conventional Weapons"; 1984, U.S. Army Waterways Experiment Station, Vicksburg, MS.

3. G. A. Coulter; "Attenuation of Peaked Air Shock Waves in Smooth Tunnels"; BRL Report No. 1809, November 1966; Ballistics Research Laboratories, U. S. Army Research and Development Center, Aberdeen Proving Ground, MD.

4. G. A. Coulter; "Blast Loading in Existing Structures - Basement Models"; Memorandum Report No. 2208, August 1972; Ballistic Research Laboratories, U.S. Army Research and Development Center, Aberdeen Proving Ground, MD.

5. S. Hikida and C. E. Needham; "Low Altitude Multiple Burst (LMAB) Model, Volume 1: Shock Description"; Report No. S-CUBED-R-81-5067, DNA #58632, June 1981; Systems, Science, and Software, Albuquerque, NM.

6. J. M. Biggs; "Introduction to Structural Dynamics"; 1964, McGraw-Hill Book Company, New York, NY.

7. Committee on Structural Dynamics, Engineering Mechanics Division, American Society of Civil Engineers; "Design of Structures to Resist Nuclear Weapons Effects"; Manuals of Engineering Practice No. 42, 1961; American Society of Civil Engineers, New York, NY.

8. C. C. Cappiello; "Review of Ventilation System Fast-Closing Valves"; 1982; Los Alamos National Laboratory, Los Alamos, NM.

NUMERICAL AND CENTRIFUGAL MODELLING OF BURIED STRUCTURE RESPONSE TO NEAR FIELD BLAST

F. C. Townsend[1], M. C. McVay[2], D. M. Bradley[3]
C.H. Cunningham[4], and D. J. Yovaish[4]

University of Florida

ABSTRACT

Centrifugal modelling is a method of accounting for gravity effects on laboratory scale models and evaluating numerical predictions of these model responses. The objectives of this research were (a) to develop centrifugal model scaling relationships, (b) a micro-concrete with miniaturized reinforcement, and (c) to incorporate a nonlinear soil model into NONSAPC.

Dimensional analyses identified a set of scaling laws and indicate that similitude can be achieved if both prototype and model materials are comparable and blast yields are scaled. A micro-concrete with miniaturized reinforcement was developed using gypsum mortar and downsized sand gradation, and serrated steel wire. Testing of revealed this composite material compares favorably with prototype predicted by NONSAPC. Comparisons between linear and nonlinear representations of both concrete and soil materials revealed much higher stresses and peak displacements occurred for nonlinear modelling.

INTRODUCTION

Background - Economic design and survival of buried structures subjected to blast loadings requires a thorough knowledge of the stress loadings created by the weapon and generated response. In the case of DOD protective structures, the degree of uncertainty must be quite narrow and the simple application of safety factors is not sufficient.

Hence, in order to evaluate design assumptions and computer models, full scale testing of the structure over a variety of geological sites is attractive and has been done in several instances, but at considerable cost and safety risk. Presently, designs are based upon emperical correlations of these field studies and some numerical analyses of structural components. However, variations in geological sitings, structural design details, weapons, stand-off distances, etc. are precluding full-scale field tests for numerical validation and/or improvement. Accordingly, to reduce testing costs and safety risks, laboratory scale models provide a viable method under controlled conditions for evaluating numerical models, provided that the dead load effects of the structure and surrounding soil can be accounted for. Unfortunately, these dead load effects are not appropriately handled in one gravity testing and thus, centrifugal modelling offers an alternative testing procedure with substantial potential for cost reduction.

Faced with these concerns, the Air Force initiated an investigation of the feasibility of using centrifugal modelling as an alternative testing procedure and a substantial potential for cost reduction for evaluating buried structures subjected to blast loadings.

Objectives - From these considerations, the objectives of the research reported herein were: (a) to evaluate centrifugal model scaling relationships pertinent to blast loadings, (b) to develop a micro-concrete with miniaturized reinforcement to construct 1/50th or smaller scale models, and (c) to incorporate a nonlinear soil model into an existing numerical finite element code (NONSAPC) to be compared with centrifugal models.

Scope of Work - These objectives were accomplished by performing dimensional analyses using Buckingham Pi Theory which resulted in a computer code PISETS. Trial mixes using gypsum mortar and sand scaled to follow prototype gradations were used to develop a micro-concrete. Deformed steel wire was used to model reinforcement. A nonlinear soil model (Modified Duncan) was inserted into NONSAPC to represent the stress dependent behavior of soils. Subsequent numerical analyses of the structure were performed to evaluate the sensitivity of the structure to linear or nonlinear analyses.

(1) Professor & (2) Assistant Professor, Dept. of Civil Eng., Univ. of Fla., Gainesville, Fla. 32611
(3) Captain, U.S. Air Force
(4) Grad. Ass't., Dept. of Civil Eng., Univ. of Fla., Gainesville, Fla 32611

Table 1. Listing of parameters for dimensional analyses of blast loadings [After (6)]

	Dependent Parameters								System Parameters														
	Stress	Displacement	Acceleration	Pressure	Impulse	Energy	Radius	Thickness	Mass density - concrete	P wave speed concrete	Strength - concrete	Modulus - concrete or steel	Strength - steel	Area - steel	Mass density - soil	P wave speed - soil	Modulus - soil	Soil Cohesion	Preconsolidation Pressure	Permeability	Gravity	Time
	σ	d	a	P_o	I	E_n	R	H	ρ_c	C_c	F'_c	E_c	F_{ST}	A_{ST}	ρ_s	C_s	E_s	c	P_c	k	g	t
M	1	0	0	1	1	1	0	0	1	0	1	1	1	0	1	0	1	1	1	0	0	0
L	-1	1	1	1	1	2	1	1	-3	1	-1	-1	-1	2	-3	1	-1	-1	-1	1	1	0
T	-2	0	-2	-2	-1	-2	0	0	0	-1	-2	-2	-2	0	0	-1	-2	-2	-2	-1	-2	1

Centrifugal Model Scaling Relationships

Dimensional Analyses - Table 1 presents the dependent parameters of interest (stress, displacement, and acceleration) and 19 independent parameters used for determining scaling relationships. In order to solve this dimensional matrix, three repeating parameters; inpulse, height, and concrete modulus were used to generate the π terms listed in Table 1. Note that many of the π terms are dependent upon the material properties. Contingent on using the same material in model and prototype, the scaling relationships in Table 2 result. It is important to observe that π_{11}, energy, scales as n^3, that is to say, small blast energies or charges in a high g centrifuge environment can simulated high yields (6).

Scaling and Equipment Difficulties - The major problem stems from the conflict between satisfying geometric scaling laws while maintaining the material properties. For soils a reduced grain size drastically changes its material properties; i.e., modulus, stength, dilational wave speed, permeability, etc. Hence, it is appropriate to ignor geometric reduction of soil particles and assume consistent properties between model and prototype. For reinforced concrete, similar material properties pertubations occur in that aggregate and reinforcement sizes must be scaled to construct a model. Accordingly micro-concrete and miniaturized reinforcement duplicating prototype properties are dictated. In the case of explosives since energy scales at $1/n^3$ that of the prototype energy, very small explosive quantities are required for a model blast loading. Nielson (10) has proposed that RDX could be used to model explosives and estimated 2.0 gms of RDX in a 60 g environment would model a 1000 lb. bomb. Hence, downsizing explosive quantities may require special considerations.

The scale to which a buried structure can actually be tested is dependent upon the radius, acceleration level and payload of the centrifuge.

Avgherinos and Schofield (3) have suggested that due to the radial nature of centrifugal accelerations applied to a model within a centrifuge, the gravitational forces on the model will vary across its base and height unlike that of the prototype. Hence, to limit this effect, the height of the model should be limited to $\pm$ 1/10 of the radial arm of the centrifuge. Similarly, Bassett (5) suggests that length be no longer than the cord of a 15° section with a radius equal to the centrifuge's arm. In addition to these model size limitations, allowances must be made for boundary effects. Based upon centrifugal model footing experiments, Bagge and Christensen (4) have suggested that container diameters should be greater than five times that of the model diameter ($D_c > 5D_m$). Faced with these model size criteria, one must also consider the payload weight capacity versus g level of a specific centrifuge.

Micro-concrete and Miniaturized Reinforcement Developement

Faced with the requirement of scaling both aggregate and reinforcement to construct reinforced concrete models for centrifugal testing, the objective of this phase was to develop a micro-concrete and miniaturized reinforcement. Accordingly, a micro-concrete was developed after numerous trials consisting of high strength gypsum, and fine sand; the recipe of which is one part gypsum, 0.25 parts water, and 0.8 parts sand. After forming the mix, specimens were cast, allowed to cure 48 hours and then coated with shellac to cease curing of the gypsum. This procedure produced a micro-concrete

Table 2. Pi Sets of Blast Load Dimensional Analysis [After (6)]

π Terms	Scaling Relationship at N g's
$\pi_1 = d/h$	$d_m = d_p/n$
$\pi_2 = R/H$	$R_m = R_p/n$
$\pi_3 = A_{ST}/H_z$	$A_{STm} = A_{STp}/n^2$
$\pi_4 = F'_c/E_c$	$F'_{cm} = F'_{cp}$
$\pi_5 = F_{ST}/E_c$	$F_{STm} = F_{ST\,p}$
$\pi_6 = E_s/E_c$	$E_{Sm} = E_{sp}$
$\pi_7 = C/Ec$	$C_m = C_p$
$\pi_8 = P_c/E_c$	$P_{cm} = P_{cp}$
$\pi_9 = \sigma/E_c$	$\sigma_m = \sigma_p$
$\pi_{10} = P_o/E_c$	$P_{om} = P_{op}$
$\pi_{11} = E_n/H^3E_c$	$E_{nm} = E_{np}/n^3$
$\pi_{12} = aI^2/H^5E_c^2$	$A_m = na_p$
$\pi_{13} = H^6\rho_c E_c/I^2$	$\rho_{cm} = \rho_{c\,p}$
$\pi_{14} = IC_c/H^3E_c$	$C_{cm} = C_{cp}$
$\pi_{15} = H^6E_a\rho_s/I^2$	$\rho_{sm} = \rho_{sp}$
$\pi_{16} = IC_s/H^3E_c$	$C_{sm} = C_{sp}$
$\pi_{17} = Ik/H^3E_c$	$k_m = k_p$
$\pi_{18} = I^2g/H^5E_c^2$	$g_m = n\,g_p$
$\pi_{19} = E_cT\,H^2/I$	$T_m = T_p/n$

with the following properties: compressive strength = 4100 psi, tensile strength = 310 psi, unit weight 136 pcf, and 50% fc' secant modulus = 3.3×10^6 psi.

Black annealed steel wire (22 gage) is used for miniaturized reinforcement in the following fashion: (a) the wire is passed through a knurling machine which makes serrations on the wire similar to re-bar, (b) the wire is then stressed to 40,000 psi to remove kinks, bends, etc. and (c) the wire is placed in the model. An $E = 29 \times 10^6$ psi and tensile strength of 50,000 psi results from this procedure. The slightly lower yield strength of the wire is accounted for in the models by increasing the area of steel reinforcement.

Figure 1 presents the results of a miniaturized reinforced beam (.6" x 1.0" x 7.25") subjected to third point loading, and the corresponding numerical prediction (NONSAPC) using a nonlinear, concrete model. As shown, the prediction is quite good and the properties of this miniaturized reinforced micro-concrete are quantified; thus providing the means for constructing centrifugal models.

Numerical Modelling of Buried Structure Response to Blast Loadings

Background - Complimenting centrifugal model tests are numerical models, which when properly "calibrated" and accurate material properties described can greatly extend our abilities to evaluate designs. In fact, the testing philosophy adapted at UF is to use centrifugal test results of generic simple prototypes to validate and improve numerical models. In this context, the objective of this phase is to evaluate the NONSAPC (nonlinear elastico dynmaic finite element program) (2) for predicting the response of the structure to blast loadings. Accordingly, the stability and convergence of the program was studied, a nonlinear soil model

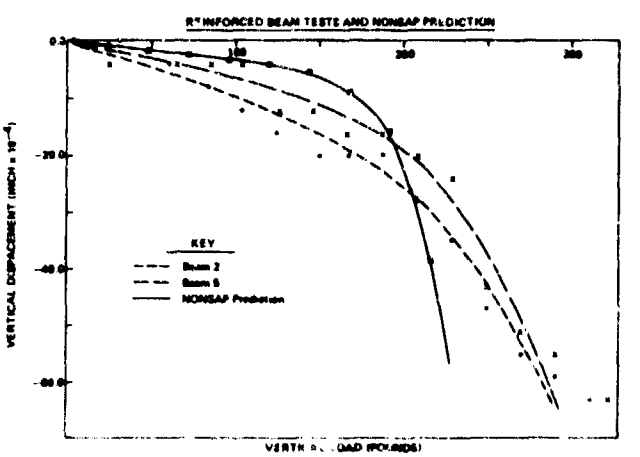

Figure 1. Predicted and Laboratory Test Results of Reinforced Micro-Concrete

implemented, and lastly comparisons between linear and nonlinear representations of both concrete and soil models were performed.

Soil Model - The NONSAPC program, as received originally, did not contain a material model that could represent the nonlinear stress-dependent behavior of soils. The Modified Duncan Model (9), an outgrowth of the Duncan-Chang Model (8), was added to NONSAPC in order to model the characteristically nonlinear stress-strain behavior of soils observed in the laboratory. The model, being incremental elastic, was adaptable to the solution scheme of NONSAPC and utilizes input parameters obtainable from conventional laboratory triaxial tests.

Input Preparation - Due to the size and complexity of the buried structure to be analyzed, symmetry was assumed and only one quarter was discretized. As shown in Figure 2, the structure consists of a burster slab and buried three bay facility. Loading of the structure was calculated based upon a 1000 lb. spherical charge detonated five feet above the burster slab centerline. Shock wave parameters and reflective pressure coefficients (12) were used to determine the pressure time load history for the structure at selected nodal points.

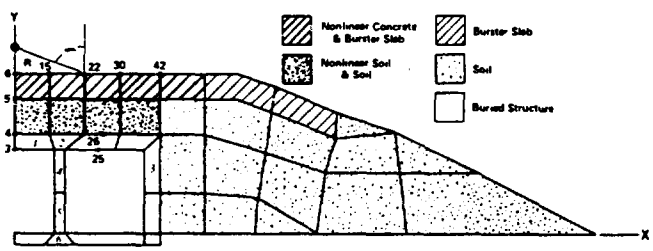

Figure 2. Finite Element Idealization of the Soil-Structure-System

In the linear analysis of the structure, all the soil and concrete materials were modelled as linear elastic, with $E_c = 5.76 \times 10^8$ psi (1) and for the soil $E = B = 13{,}039.6\,(\sigma_o)^{1/2}$ (11). The estimated value of σ_o was based upon gravity and blast loadings, with the blast loading calculated as P_o (psf) = $39{,}905{,}539\,(R)^{-2.75}$, where R = distance from explosion (ft.) (7). In the case of nonlinear analyses, the Modified Duncan model was used to represent the sand, while an orthotropic variable modulus model (2) was used to represent the nonlinear concrete behavior. Since the actual placement of the reinforcing steel is not represented in this model, a smeared (composite) modulus based upon concrete and steel moduli was used for the appropriate element. The sand was represented by dynamic soil parameters inserted in the Modified Duncan model (9).

Analysis and Results of Numerical Modelling

General - Four complete finite element analyses, one linear and three nonlinear, were performed on the soil-structure system. The first analysis utilized all linear elements and a time step of integration of 0.1 milliseconds, while the three nonlinear analyses used nonlinear elements and time steps of 0.025, 0.05, and 0.1 milliseconds respectively. Figure 2 presents the linear and nonlinear material elements, and nodes examined for stresses and time displacements, respectively. The material model parameters used are described in detail in Reference 13.

Figure 3 presents a comparison of peak stresses in the soil (independent of time) along the structure top in the x-y plane. As shown, smaller time steps produced the highest peak stress, with the effect greatest nearest the point of loading. This effect is due primarily to the nonlinear stress dependency of the soil in regions of high stress gradients (near the charge). At lower stress gradients further from the detonation time step sensitivity decreases. Predictions using the following equation are quite unconservative (7):

$$P_o = f \cdot (P_c) \cdot 160 \cdot (R/W)^{1/3})^{-n}$$

where f = coupling factor (0.14), P_c = acoustic impedence (22), R = distance from explosion, ft, W = weight of charge (1000), and n = attenuation coefficient (2.75). Thus, it is concluded that an improved numerical analysis using smaller time steps and/or finer descretization near the detonation would better predict the high stress gradients in this region.

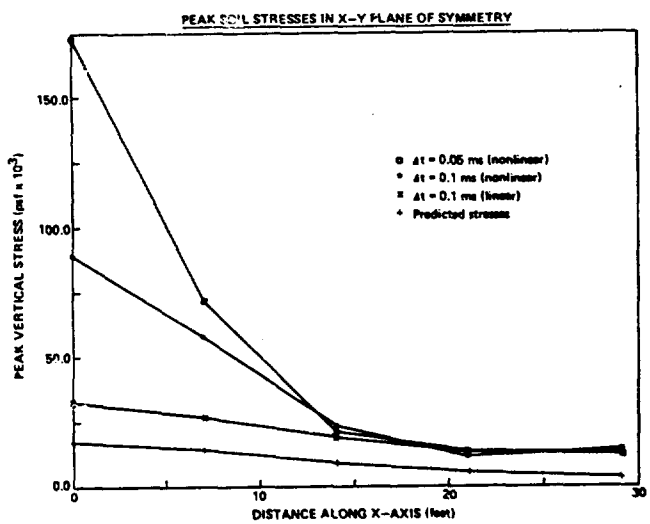

Figure 3. Peak Vertical Stress, in the X-Y Plane of Symmetry, On the Structure

Figure 4 presents the time displacements of node 5 (Figure 2) as an example. As shown, displacements were greatest nearest the detonation for the nonlinear analyses using the smallest time step. The increasing peak displacements with decreasing time steps indicates that convergence has not been achieved and a finer time step and/or finer discretization may be appropriate.

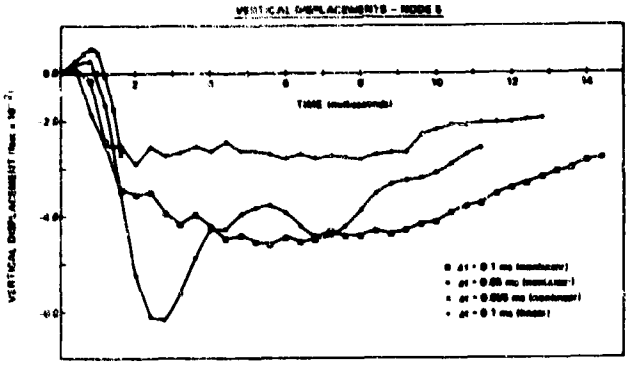

Figure 4. Time Displacements for Node 5 Under Burster Slab

Also shown is that the linear analysis displacements near the detonation are much lower than those of the nonlinear analyses. Additional comparisons (not presented) between linear and nonlinear analysis revealed that when the distance from the blast increased, the effects of material nonlinearity and reduced time steps on peak displacements decreased. Specifically, the time displacements of nodes 22, 25, 26, 30, and 42 of Figure 2 exhibit little differences, thus, suggesting nonlinear material characterization and small time steps are not necessary at great distances from the blast.

Elements exhibiting exceptionally high stresses compared to the strength of concrete are numbered in Figure 2, and undoubtably would exhibit a nonlinear behavior resulting in damage to the structure. In all cases, the nonlinear analyses calculated higher stresses than the linear analyses, primarily due to the nonlinear behavior of the soil model.

Conclusions

1. Centrifugal modelling is a viable technique for evaluating the response of buried structures to blast loadings, and similitude can be achieved if both prototype and model materials have the same properties and yields are scaled.
2. Micro-concrete consisting of gypsum mortar and sand and miniaturized reinforcement of knurled anealed steel wire can successfully simulate reinforced concrete.
3. Nonlinear numerical analyses of a buried structure subjected to blast loading produces much higher stresses and corresponding displacements than linear analyses, and as much as 10 times greater than those of emperical design methods. However, sensitivity to time step and nonlinear material formulations decreased with distance from the point of detonation.

Acknowledgements

This research was sponsored by USAF/AFESC/RDCS, Tyndall AFB, Florida under Task order 83-1 "Similitude in Centrifuge Testing." The cooperation and guidance provided by Capt. Paul L. Rosengren is greatly appreciated. The assistance of Profs. J.L. Davidson and F.E. Fagundo, Univ. of Florida, contributed substantially to this project and is recognized.

References

1. ACI COMMITTEE 318, Building Code Requirements for Reinforced Concrete (ACI 318-77), American Concrete Institute, Detroit, Michigan, p. 26, 1977.

2. Anderson, C.A., P.D. Smith, and L.M. Carruthers, "NONSAPC: A Nonlinear Stress Aalysis Program for concrete Contaminents Under Static, Dynamic, and Long Term Loadings," NUREG/CR-0416, Rev. 1 LA-7496-MS, Los Alamos National Laboratory, Los Alamos, NM.

3. Avgherinos, P.J. and A.N. Schofield (1969), "Drawdown Failure of Centrifuged Models," Proc. 7th Int. Conf. on Soil Mech. & Fdn. Engr.

4. Bagge, G. and S.H. Christensen (1977), "Centrifuge Testing on the Bearing Capacity of Circular Footings on the Surface of Sand," Dialog 77 Denmark Ingeniorakademi, Lyngby, Denmark.

5. Bassett, R.H. (1973), "Centrifugal Model Tests of Embankments on Soft Alluvial Foundations," Proc. 8th Int. Conf. on Soil Mech. and Fdn. Engr. Vol. 2.2.

6. Bradley, D.M., F.C. Townsend, F.E. Fagundo, and J.L. Davidson (1984), "Centrifugal Scaling Laws for Ground Launch Cruise Missile Shelter," ESL-TR-84-07, AFESC, Tyndall AFB, Florida.

7. Drake, J.L. and C.D. Little, Jr., "Ground Shock From Penetrating Conventional Weapons," U.S. Army Engineers Experiment Station, Vicksburg, Mississippi, 1982.

8. Duncan, J.M. and Chin-Yung Chang (1970), "Nonlinear Analysis of Stress and Strain in Soils," JSMFD, Vol. 96, SM5.

9. Duncan, J.M., P. Byrne, K.S. Wong, and P. Mabry (1980), "Strength, Stress-Strain and Bulk Modulus Parameters for Finite Element Analysis of Stresses and Movement in Soil Masses," UCB/GT/80-01, Univ. of California - Berkeley.

10. Nielson, J.P. (1983), "The Centrifuge Simulation of Blast Parameters," ESL-TR-83-12, AFESC, Tyndall AFB, Florida.

11. Richart, F.E. Jr., J.R. Hall, Jr., and R.D. Woods, Vibration of Soils and Foundations, Prentice Hall Inc., Englewood Cliffs, New Jersey, 1970.

12. U.S. Army Engineer Waterways Experiment Station, Fundamentals of Protective Design for Conventional Weapons, Report for Office, Chief of Engineers, U.S. Army, June, 1982; available through the Office , Chief of Engineers, U.S. Army, Washington, D.C.

13. Yovaish, D.J. and M.C. McVay (1984), "Dynamic Analysis of Buried Structures Subject to High Impulse Loads of Short Durati ," ESL-TR-84-??, AFESC, Tyndall AFB, Florida.

CONCRETE BREACHING DATA BASE SEARCH AND CONCRETE PENETRATION ANALYSIS

J. R. WOLFERSBERGER

GOODYEAR AEROSPACE CORPORATION

ABSTRACT

The data base search summarized below was performed under Air Force Contract FO-8635-83-C-0557. The analyses described in this paper were performed using IR&D funds supplied by Goodyear Aerospace Corporation. A complete description of the search and the analyses is contained in document ESL-TR-84-37, published by the Engineering and Services Laboratory, Air Force Engineering and Services Center, Tyndall Air Force Base, Florida.

1. PURPOSE OF DATA BASE SEARCH

The need for a data base search can be seen from the graph presented in Figure 1 (References 1 and 2), which shows that there are substantial differences among concrete scabbing and breaching estimators. There are a variety of plausible explanations for some of these differences: target properties, interpretations of damage, and experimental methods. One specific intent of this data base search was to locate and acquire, if possible, the data used to formulate the officially sanctioned concrete breaching and scabbing estimators set forth in the Joint Munitions Effectiveness Manual (JMEM). Given these data, it was felt that it would be possible to either resolve the differences in scabbing/breaching estimators by means of analysis or determine if specific experimental programs would be required to provide a sound basis for the estimation of concrete scabbing and breaching.

a. Focus of Contractor's Search Report

It was known at the outset of the search effort that the data base for hard target vulnerability assessments was largely generated during the 1940's. Because the Vulnerability Assessments Branch (DLYV) already had in its possession or could readily acquire concrete scabbing and breaching data generated during the past twenty years, this search concentrated on locating and acquiring data generated during the 1940's.

b. Results of Search Effort

A major objective of the search was to locate and acquire the 14 key reference documents that provide the basis for official concrete scabbing and breaching estimators (Reference 3). Eight of the 14 references

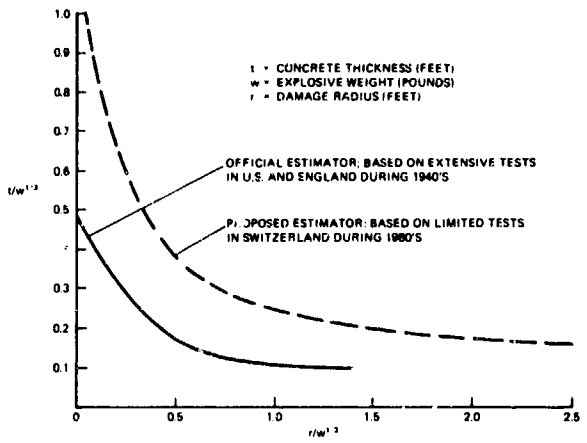

Figure 1 - Comparison of Official and Proposed Estimators for Breaching Damage to Reinforced Concrete Wall Panels

were acquired; the missing references are all British documents. Multiple copies of these documents were sent to the United States during the 1940's, and were at one time in the library established by the National Defense Research Committee (NDRC). Despite an exhaustive search that involved numerous telephone calls and on-site searches at the National Archives, Military Archives, and United States Air Force (formerly Albert Simpson) Historical Research Center, these documents were not located. The search did yield, however, the location and acquisition of a large amount of reference material needed for hard target vulnerability assessments. Twenty-two valuable references on the subjects of concrete penetration, scabbing, and breaching were acquired for the program sponsor and 20 other important references for vulnerability assessments were located and reviewed. Bibliographies of the Textbook of Air Armament and the summary reports of the United States Strategic Bombing Survey were also prepared.

2. EFFECT OF CONCRETE COMPRESSIVE STRENGTH ON PENETRATION

a. Introduction

It is an established fact that the compressive strength of concrete increases with age. Typical rate of strength developments and compressive strengths at various

ages are shown in Figure 2 (Reference 4). It is also a fact that several widely used concrete penetration equations contain a target properties term that has the form $KS^{-1/2}$, where S is concrete compressive strength and K is an experimentally determined constant, usually at small scales. A final fact important in considering the influence of concrete properties on penetration is that there is an inevitable dispersion in concrete penetration data, regardless of the care exercised in performing concrete penetration experiments. Tests of identical projectiles at identical velocities against the same concrete target should produce identical penetrations; sometimes this occurs, but most of the time it does not. Typical data dispersion for .50-caliber tests against massive concrete targets is shown in Figure 3. These were well controlled penetration experiments, yet the width of the band containing all the data ranges from 0.5 to 0.82 calibers. Thus when seeking to demonstrate that some parameter or concrete variable has a small but predictable effect on penetration, somehow one must separate the signal from the noise; as noted in Reference 5: "A graph of penetration versus one of the concrete variables does not necessarily imply a unique relationship."

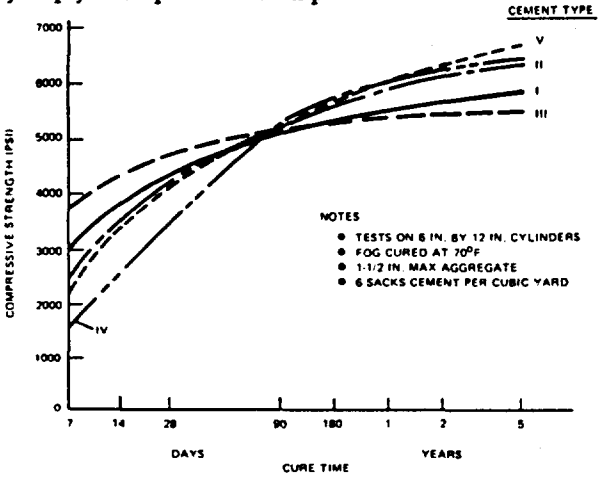

Figure 2. Rates of Compressive Strength Development for Various Concretes

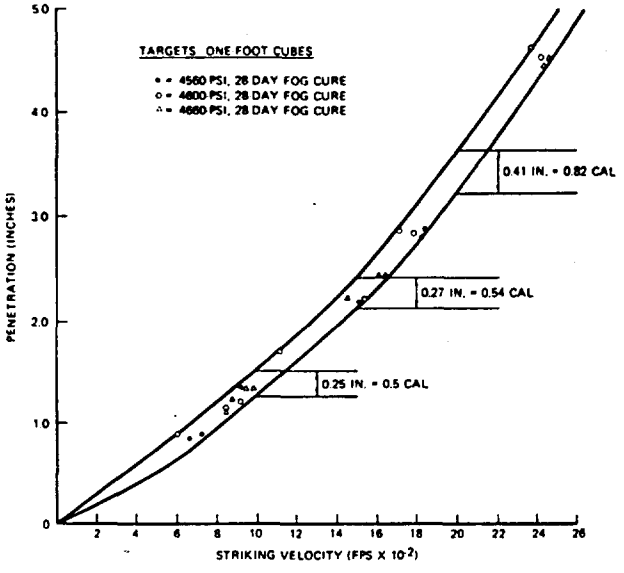

Figure 3. Experimental Data Dispersion For .50-Caliber Penetration Tests Against Massive Concrete Targets

b. Analysis

Large differences in concrete compressive strengths produce large differences in the penetration of identical projectiles, as is clearly shown in Figure 4. (Note that the ages of the targets are the same.) Now if compressive strength is strongly related to penetration resistance, one should be able to prepare accurate estimates of penetration into a 10,000 psi target, given the observed penetration into a 5000 psi target. The accuracy of such estimates can best be checked, of course, by conducting penetration tests against both targets using identical projectiles and striking velocities. If this is done and if a concrete properties term of the form $KS^{-1/2}$ is valid, penetration into the 10,000 psi target will be $[(5000/10{,}000)]^{1/2}$ times the penetration into a 5000 psi target or P(10,000 psi target) = P(5,000 psi target) x $(0.5)^{1/2}$. Figure 5 shows an interesting test of this hypothesis. The shaded circles are the actual penetration measurements for the .50-caliber tests against a 9450 psi target with a 365 day cure. The open circles are estimates formed by multiplying the .50-caliber test data for a 4115 psi target by $[(4115/9450)]^{1/2}$. Note that these data points would define a penetration curve for the 9450 psi target that would be essentially identical to the curve defined by the actual tests against this target. This same "test" can be applied to Figure 4. That is, assume only the data for .50-caliber tests against the 4115 psi target is available. Multiply each point by $[(4115/1895)]^{1/2}$ and generate estimated penetration points for an 1895 psi target, then multiply the same points by $[(4115/8240)]^{1/2}$ and generate an estimate for the 8240 psi target. After completing this exercise it will be clear that the concrete properties term in major penetration equations, $KS^{-1/2}$, accurately depicts the resistance of massive concrete to penetration.

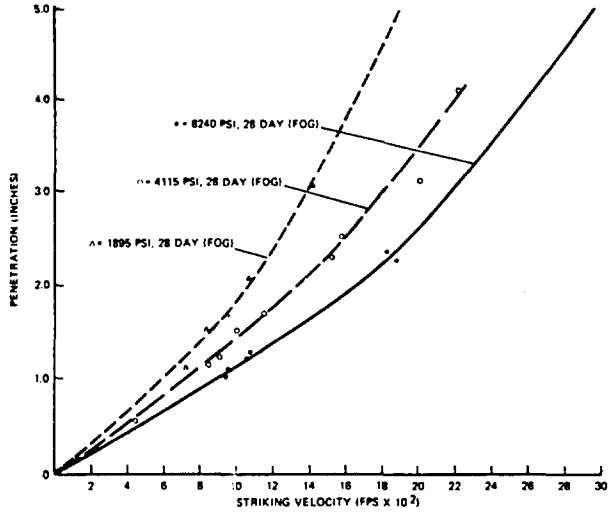

Figure 4. Effects of Compressive Strength on Penetration (.50 Caliber Tests)

Now consider briefly the problem of proving conclusively that an individual concrete variable significantly affects penetration. Figure 6 shows an apparent age effect. Since the targets do not have identical compressive strengths, a slight adjustment must be made to remove the compressive strength effect. Even if this is not done, note that when striking velocities are nearly identical, some sets of points indicate that there is a significant age effect while some sets of points indicate that there is little if any effect. Add to this the

data dispersion shown previously and one can at best suggest that these data show some indication that concrete age, per se, affects penetration. It certainly is not possible with these data to unambiguously establish a specific relation between concrete target age and penetration.

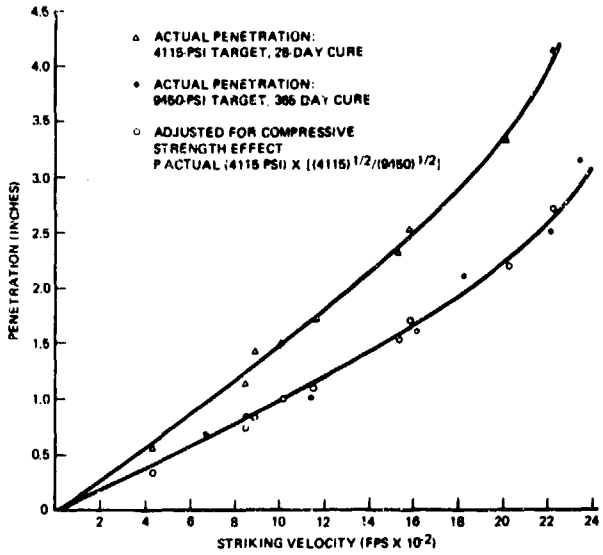

Figure 5. Compressive Strength Accounts for Age Effect in Concrete Penetration

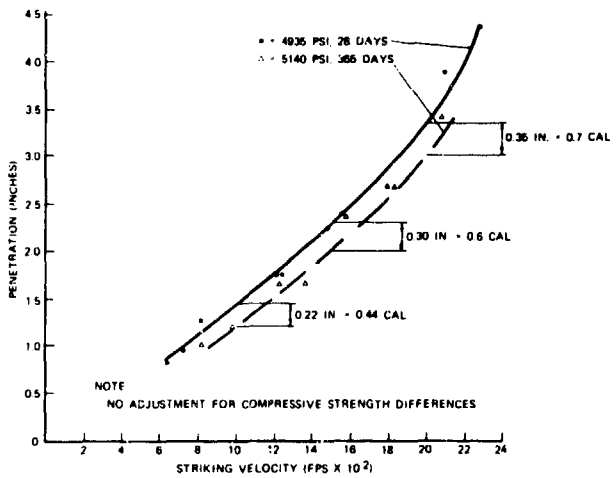

Figure 6. Effect of Target Age on Concrete Penetration

3. ANALYSIS OF PREDICTIVE ACCURACY OF TWO CONCRETE PENETRATION EQUATIONS

a. Introduction

The purpose of this analysis is to illustrate a use for the concrete penetration data acquired during the data base search and to provide a partial analysis of the predictive capabilities of two concrete penetration equations for massive penetration events. The data used in this analysis were drawn exclusively from Interim Report No. 20 (Report I - Data), Committee on Fortification Design (CFD), National Research Council (Reference 6). The tests reported in this document were performed to add to the massive concrete penetration data base and to develop concrete scabbing and perforation limits for .50-caliber, 37 mm, 75 mm, 3-inch, and 155 mm projectiles. Lateral target dimensions varied from 7 by 7 feet (small projectile tests) to 28 by 30 feet for the large projectile tests. Multiple shots were conducted against targets with no overlap of impact craters. All targets were reinforced; ages at test varied from 63 to 260 days; compressive strengths varied from 3800 psi to 6600 psi, with most targets being in the 5000 psi, 180-day cure regime. Complete details on the targets and tests are set forth in Interim Report 20.

Since this analysis is concerned exclusively with massive concrete penetration, it is worthwhile to clearly define the terms massive concrete target and massive penetration event. A concrete target is massive only with respect to a particular projectile and penetration event. If the impact and penetration of projectile P into concrete target T do not produce edge effects or rear face damage to the target, this constitutes a massive penetration event and the target is considered a massive target for this projectile and event. The most beneficial way to consider concrete penetration is in terms of massive penetration events, which, to repeat, are terminal ballistic events in which the target does not suffer either edge effects or rear face damage. The absolute size of the target is irrelevant; the only concern is that the target does not suffer edge effects or rear damage. Clearly, then, the same concrete target can be massive for projectile P_1 and not massive for projectile P_2. For the same projectile, the target can be massive for Event A and not massive for Event B.

b. Analysis

(1) General

Two concrete penetration equations were analyzed, an NRDC equation (Reference 7) and a British equation. The NRDC and British concrete penetration equations were selected for analysis because they are based on very large numbers of tests. These equations were developed during the 1940's. In the United States, a large portion of the concrete penetration work was supervised by the National Research Council.

The final NDRC equation is not evaluated since it contains a partially defined target properties term, and thus is not particularly useful. To the best of this analyst's knowledge, the British equation evaluated is the final British concrete penetration equation developed by the Road Research Laboratory.

Figure 7 provides a good indication of the need for an analysis of the predictive capabilities of concrete penetration equations. For impact velocities below about 1500 fps, the equations considered provide nearly identical penetration estimates. However, there are substantial differences in these estimates beyond 1500 fps. For example, for a 10,000 psi target at 2500 fps striking velocity, there is a 3-caliber difference in estimates. In a vulnerability assessment, this could easily equate to a zero-one situation; that is, estimate 1 would say the target was defeated; estimate 2 would say the target received slight damage.

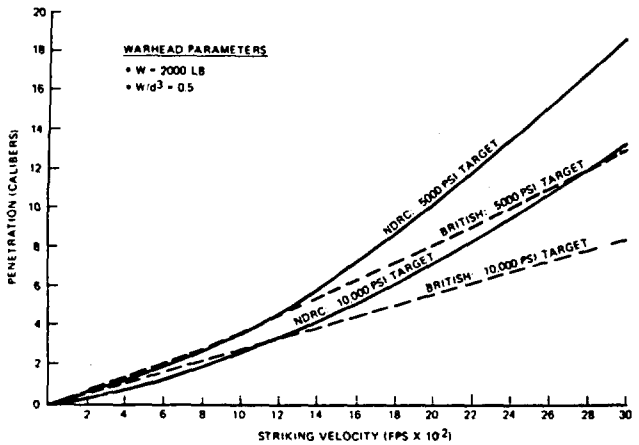

Figure 7. Differences in Two Massive Concrete Penetration Predictors

The NRDC equation is:

$$Z = \frac{1}{2} + \left(\frac{282}{S^{1/2}}\right)\left(\frac{W}{d^3}\right)\left(d^{0.215}\right)\left(V_o^{1.5}\right) f(\theta)$$

where:

- Z = penetration (calibers)
- S = compressive strength (psi)
- W = projectile/warhead weight (pounds)
- d = projectile/warhead diameter (inches)
- V_o = striking velocity, fps/1000
- $f(\theta)$ = obliquity correction (1.0 at zero degrees; 0.85 at 15 degrees; 0.60 at 30 degrees)

The one-half is an impact adjustment term that was used for only low velocity events in this analysis. Initial analysis indicated that an impact adjustment term would improve the predictive capabilities of the NDRC equation if applied only to low velocity impacts. So a 0.25-caliber impact adjustment term was used for penetration events at ≤1000 fps.

The British equation is not set forth because it is still classified, but it is basically similar to the NDRC equation; an important difference is that to convert concrete compressive strength by standard United States cylinder tests to British compressive strengths, the United States value must be multiplied by 1.39 for tests using 4-inch cubes and 1.33 for tests using 6-inch cubes. Most British compressive strength tests refer to 4-inch cubes; in this analysis, compressive strengths used in evaluating the British equation are 1.39 times United States compressive strengths.

(2) Data and Accuracy Criteria

The predictive accuracy of these two equations for massive penetration events was evaluated with respect to data from the following tests:

1. Thirty-three all-velocity, 37 mm tests against three massive concrete targets with essentially identical compressive strengths. First, a simple, semi-quantitative comparison of the equations was made using these data. This preliminary analysis indicated a need for a more definitive analysis of these equations.

2. Twenty-four all-velocity, 37 mm tests against two massive target with substantially different compressive strengths.

3. Thirteen all-velocity, 155 mm massive penetration tests.

4. Twenty low-velocity (≤1000 fps), 155 mm massive penetration tests.

For the main quantitative analysis of the equations, the predictive accuracy criteria utilized were caliber error, average caliber error, and mean absolute error. Caliber error is defined as actual (measured) penetration minus estimated penetration. Caliber errors are summed algebraically, and then averages are derived for several combinations of the separate sets of data; namely, all 37 mm data; all 37 mm plus the all-velocity 155 mm data; the low-velocity 155 mm data; and all 155 mm data. Absolute error is simply the absolute value of the difference between actual penetration and estimated penetration. Mean absolute error is then simply the sum of absolute errors divided by the data points in a particular set; for example, all 37 mm data. A sample of the data used is given in Table 1. The predictive errors are summarized in Table 2. The patterns of the predictive errors for the all-velocity data are shown in Figures 8 and 9.

TABLE 1 - BRITISH EQUATION 37 MM DATA

Target 6C, 4562 psi (67 days)				Target 6D, 6160 psi (266 days)			
Striking velocity (fps)	Actual pentr (cal)	Est. pentr (cal)	Error (cal)*	Striking velocity (fps)	Actual pentr (cal)	Est pentr (cal)	Error (cal)*
3027	12.90	11.90	+1.00	2979	11.56	9.59	+1.97
3006	13.66	11.80	+1.86	3097	11.39	10.02	+1.37
2452	9.31	9.24	+0.07	2488	7.94	7.85	+0.09
2446	9.21	9.22	-0.01	2476	7.81	7.81	0.00
1942	7.32	6.99	+0.33	2013	5.93	6.20	-0.27
1939	7.16	6.98	+0.18	2002	5.08	6.16	-1.08
1424	3.95	4.82	-0.87	1404	3.36	4.15	-0.79
1407	3.99	4.75	-0.76	1385	3.64	4.09	-0.45
985	2.59	3.10	-0.51	1199	2.52	3.48	-0.96
983	2.95	3.09	-0.14	961	2.22	2.72	-0.50
660	1.78	1.91	-0.13	671	1.53	1.83	-0.30
639	1.67	1.84	-0.17	671	1.40	1.83	-0.43

*Error = actual penetration minus predicted penetration

TABLE 2 - SUMMARY OF PREDICTIVE ACCURACY FOR NDRC AND BRITISH CONCRETE PENETRATION EQUATIONS

	Average errors (calibers)				
Equation	37 mm, 57 tests	155 mm 13 tests*	37 mm + 155 mm, 70 tests*	155 mm, 20 tests+	All 155 mm, 33 tests
NDRC	+0.0033	+0.059	+0.0136	+0.185	+0.135
British	-0.0723	+0.064	-0.0470	-0.083	-0.0251
	Mean absolute errors (calibers)				
Equation	37 mm, 57 tests	155 mm 13 tests*	37 mm + 155 mm, 70 tests*	155 mm, 20 tests+	All 155 mm, 33 tests
NDRC	0.437	0.393	0.429	0.299	0.336
British	0.646	0.215	0.566	0.219	0.217

*All velocity; +low velocity.

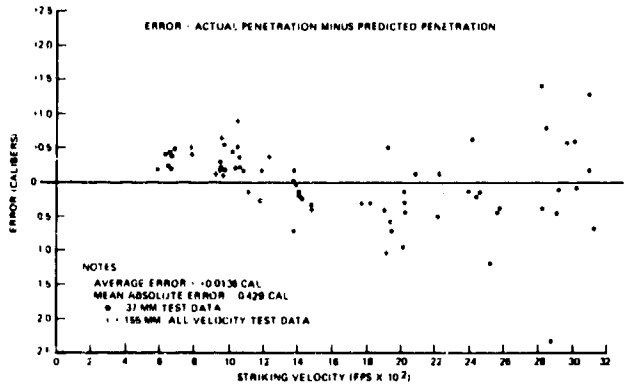

Figure 8. Pattern of Predictive Errors: NDRC Concrete Penetration Equation

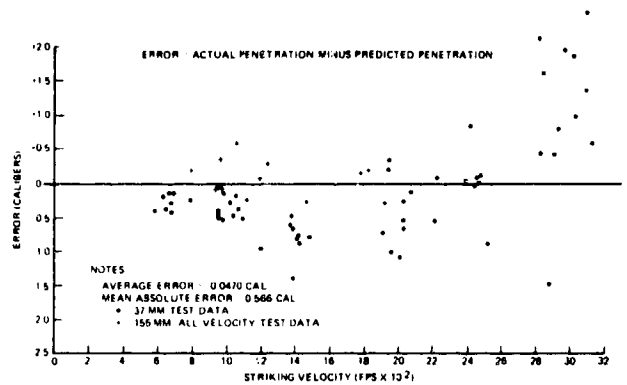

Figure 9. Pattern of Predictive Errors: British Concrete Penetration Equation

Figure 8 shows that, for the all-velocity data, the NRDC equation has a definite bias for striking velocities below about 1000 fps. Figure 9 shows that the British equation is a reasonably unbiased predictor for the velocity range of greatest interest, up to about 2400 fps. At the highest velocities, the British equation also has a bias. The all-velocity displays suggest an obvious correction for the NDRC equation; utilize a 0.25-caliber impact adjustment for velocities that are $\leq$1000 fps. The result of using such an adjustment is that, for the low-velocity 155 mm data, the NDRC equation has an average error of +0.185 caliber without an impact adjustment. With a 0.25-caliber adjustment, the average error is -0.065 caliber, which is about equal to the average error of the British equation (-0.083 caliber) for the low-velocity 155 mm data.

For the totality of the all-velocity data (70 data points), the NRDC equation, without an impact adjustment, has a remarkable average error of +0.0136 caliber and a mean absolute error of 0.429 caliber. The British equation has a respectable average error of -0.0470 caliber for the all-velocity data, with a mean absolute error of 0.566 caliber. For the 155 mm data alone, the British equation is a good predictor, with a -0.0251 average error and a 0.217 mean absolute error. The NDRC equation is only a good predictor for 155 mm data if the 0.25-caliber impact adjustment is used for low-velocity impacts; it then has an average error of +0.135 and a mean absolute error of 0.336.

There does not appear to be a single numeric that will produce an adequate evaluation of the predictive merits of empirical concrete penetration equations. An ideal penetration predictor would have small absolute errors with no biases. Average error can be a deceptive criterion if used alone. One could have a penetration predictor that produced a very small average error even though absolute errors are large; that is, the average of +2.5- and -2.6-caliber errors is -0.05 caliber. The error patterns of penetration predictors (see Figure 8 and 9) plus their mean absolute errors, in combination, appear to provide a sound basis for identifying a preferred concrete penetration predictor.

It is worthwhile to note that no rational concrete penetration equation could accurately predict many of the data points given in Table 2. There are almost always apparent anomalies in concrete penetration data regardless of the care exercised by test personnel. Thus, according to current theory one cannot have a penetration of Z calibers at V_1 feet per second and $Z + \Delta Z$ at V_2 feet per second in which $V_1 > V_2$ and the tests are done with identical projectiles against the same target. There are a variety of explanations for these anomalies, such as measurement errors, projectile yaw, and target variances.

d. Conclusions

Due to the scarcity of high-quality, large-scale concrete penetration data, it is not possible to perform a totally satisfactory analysis of concrete penetration equations. However, since prediction of penetration into concrete is a fundamental necessity in most hard target vulnerability assessments, it appears clearly worthwhile to extend this analysis if possible. One way to do this is to consider other equations and other measures of predictive ability. Of greatest importance, however, is to perform an analysis similar to that given above using all the high-quality, large-scale data that can be compiled. Until such an analysis is performed, the facts reported in the previous paragraph can be used to guide vulnerability assessments. The most important are that the NDRC equation without an impact adjustment is slightly better than the British equation as an all-velocity penetration predictor, and that the margin of superiority is lost for the largest scale data where even with a 0.25-caliber impact adjustment the British equation is superior. On the basis of this analysis, it is clear that one can obtain good predictive accuracy for massive penetration events by using either the British equation as is or the NDRC equation with a 0.25-caliber impact adjustment for impacts in the $<$1000 fps regime.

It is worthwhile to note that the differences between the equations evaluated herein are only large for high-velocity impacts. However, if deep penetration into heavy concrete targets is or becomes important, then penetration at high velocities will be important. As noted in the introduction, estimates of concrete penetration produced by major equations differ significantly for such events. Thus, if high-velocity impacts ($\geq$2000 fps) become of interest for large-caliber projectiles, it may be necessary to revise the available penetration predictors or develop a new predictor. High-quality, large-scale massive penetration data is scarce; it is essentially nonexistent for high velocities. Thus, the merits of trading warhead weight for propulsion weight (increase impact velocity) for large-caliber warheads cannot be adequately evaluated with available penetration data.

REFERENCES

1. "Effects of Impact and Explosions," Summary Report of Division 2, National Defense Research Committee, Washington, D.C., 1946.

2. "Effects of Bare and Cased Explosive Charges on Reinforced Concrete Walls," Ernst Basler and Partners, Zurich, Switzerland, (Technical paper published in 1983).

3. "Study of the Physical Vulnerability of Military Targets to Various Types of Aerial Bombardment," NDRC A-385 (OSRD-6444), Weapon Effects Group, Princeton University, January, 1946.

4. "Concrete Manual," United States Department of Interior, 1966.

5. "Concrete Properties Survey," Interim Report 27 (with Appendices A and B), Committee on Fortification Design, National Research Council, June 1944.

6. "Pentration and Explosion Tests on Concrete Slabs," Interim Report 20, Part I - Data, Committee on Fortification Design, National Research Council, January 1943.

7. "Terminal Ballistics," Final Report, Volume II, Part 1, Lehigh University, Bethelehem, Pa., 1949.

DESIGN AND APPLICATION OF REINFORCED CONCRETE-ARMOURED DOORS

H.J. Hader

Ernst Basler & Partners
Consulting Engineers
CH-8029 Zurich/Switzerland

SUMMARY

In recent years, the use of reinforced concrete-armoured doors as closing equipment for shelters has expanded significantly. Protection requirements can often be met more economically by such concrete doors than by steel doors, in particular if standardized equipment can be used.

A typical example is the shelter door program according to the standards set by the Swiss Civil Defence Authority (Ref. 1). These doors were originally developed for civil defence shelters, but are also extensively adopted for military structures in Switzerland and in many other countries.

In order to achieve a balanced protection for shelters, the analysis of the vulnerability of the entrances is of particular importance.
In this paper, recommendations on design and proper application of reinforced concrete-armoured doors and data on typical protection characteristics of existing door types are presented.

1. PROTECTION REQUIREMENTS FOR SHELTERS

Before going into details of the door design, some comments on protection requirements shall be made. According to the importance or target attractivity of a hardened structure, the requirements concerning the range and level of protection may vary within very wide limits. For very important targets not only large, but also very precise weapons have to be considered. Entrances to such facilities may represent an interesting subtarget, and therefore direct hits on these parts are to be assumed (see Figure 1).

However, there are also other structures such as civil defence shelters which, in general, are not to be regarded as primary targets of an enemy attack (see Figure 2). Such shelters are usually designed for a limited level of protection in order to reduce the extent of collateral damage to the civil population at minimum cost. As an example, Swiss civil defence shelters are designed to provide reasonable protection against a wide range of different weapon effets, whereby particular importance is given to weapons which can affect large areas at once, such as chemical and nuclear weapons. The standardized protection levels are characterized by incident blast-pressures of 1 bar (14 psi) or 3 bar (43 psi) respectively.

Threat to important targets

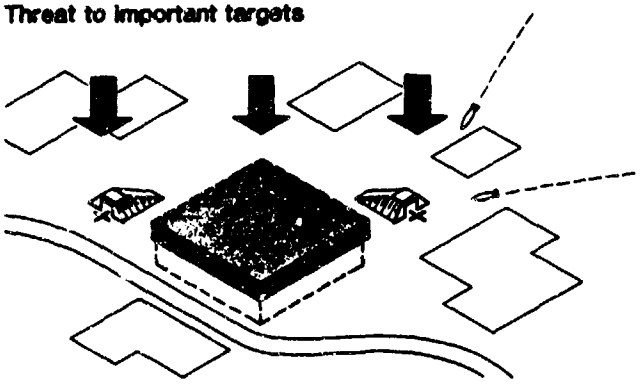

Figure 1: Example of an important protective structure; illustration of possible attack on selected parts such as entrance ways using heavy, precisely placed weapons

Threat to large areas

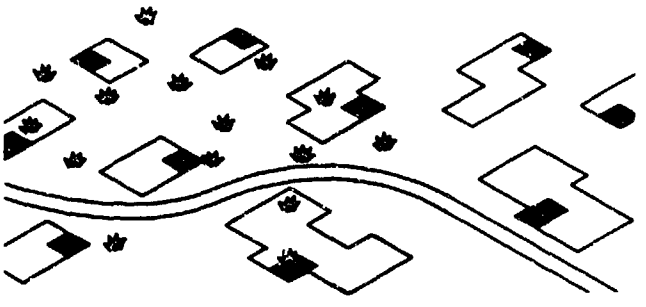

Figure 2: Example of distributed civil defence shelters for protection against collateral damage; uniform threat to entire area is assumed

The protection against the effects of conventional weapons comprises - since these shelters are located below ground level - all types of flat-trajectory fire and stand-off detonations of weapons with high impact angles. The critical stand-off distance at which a weapon breaks a shelter, varies within certain limits, depending, e.g., on the surrounding backfill or parts of buildings located over the shelter.

The protection level of the entrances is determined by the standardized 0.2 m (8 in) thick reinforced concrete-armoured doors and the geometry of the entrance passway. Further data on the protection characteristics of these doors will be given later on.

The two mentioned shelter examples are of course representing extremes of rather high and low levels of protection. Ordinary military protective structures usually range somewhere in between these limits.

We should be aware of the fact that for shelters of higher protection levels, the protection requirements and design problems for the entrance facilities are, in general, growing faster than those of the protective structure itself. This applies particularly to military protective structures, for which the threat due to conventional weapons is more imporant than for civil defence shelters. Thus, the relatively cheap standardized armoured doors and other components designed for civil defence purposes may be adopted for military structures only after proper examination of the relevant protective properties.

2. PROTECTIVE FEATURES OF SWISS CIVIL DEFENCE-ARMOURED DOORS

In this paragraph, I shall briefly discuss the protective features of Swiss civil defence armoured-doors with regard to conventional weapons. Moreover, I shall make some comments on possible improvements, if higher protection requirements are to be fulfilled.

2.1 Standard Types and Dimensions

Figure 3 shows examples of Swiss civil defence doors. All standard doors are hinged and have a 0.2 m thick door plate of reinforced concrete. This thickness has been chosen to ensure a fair protection against blast, flying fragments, nuclear radiation and thermal effects and to permit manual operation. The doors are to be mounted into the forms and cast with concrete on site together with the walls of the shelter.

2.2 Blast Resistance

According to the minimum requirements, a blast load as shown in the diagram of Figure 4 has to be considered (Ref. 1). It is obvious that this pressure/time configuration has been derived from a large nuclear weapon. The first peak having a duration of 30 ms is a simplified approach to the reflected

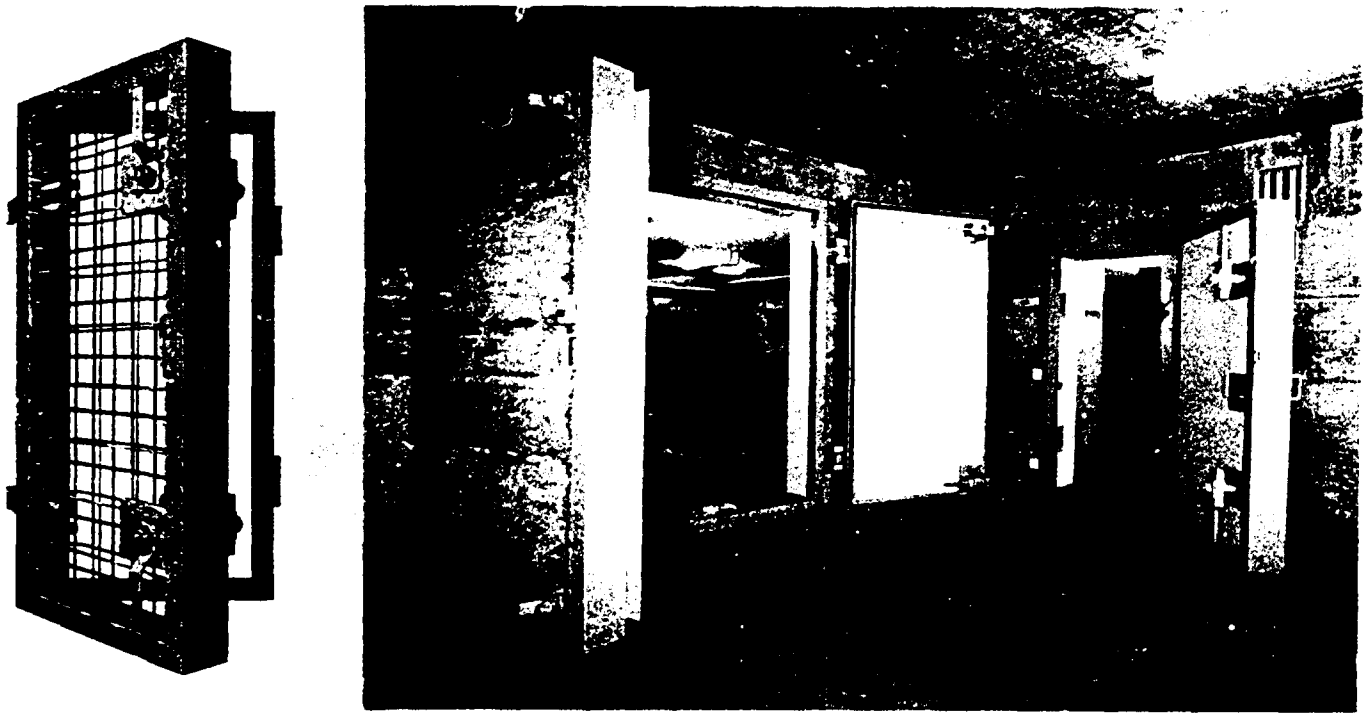

Figure 3: Examples of Swiss civil defence armoured doors, standard dimensions:
Personnel doors PT 1: 0.80 x 1.85 m
PT 2: 1.00 x 1.85 m
PT 3: 1.40 x 2.20 m
Escape hatch PD: 0.60 x 0.80 m
(not illustrated)
Equipment double-door: 2.40 x 2.10 m

pressure acting on a building façade. Conventional weapons can, under certain circumstances, produce similar pressure/time histories, e.g. at the end of a long entrance tunnel. But for common entrance configurations, the positive pressure duration from conventional weapons is much shorter even in case of detonation of relatively large bombs.

The natural period of the door plate has been measured to be about 8 ms. The reaction to the design load (Figures 4) is of quasi-static nature, whereas blasts from conventional weapons would act as impulsives loads. In Figure 5, the blast resisting capacity of a typical standard armoured door is shown in terms of a P-/I-diagram. The three curves indicate the elastic realm (λ = 1), the limit for minor permanent deflections at which a reasonable degree of tightness is still assured (λ = 5) and the limit for serious destruction (λ = 20). For reasons of comparison, the pressure/impulse combinations from the surface burst of a high-explosive charge (approximately equal to the net explosive weight of a 1000 lb GP bomb) at different distances from a door are also shown. As can be read from this diagram, the door plate remains in the elastic realm for a detonation at 15 m (50 ft) and would still not be destroyed by the blast at a distance of 6 m (20 ft) from the charge.

The blast resistance of these doors has been tested in full scale at the experiment station of the Royal Swedish Fortifications Administration at Märsta (Ref. 2). The blast loads were produced in a shock tube by means of high explosive charges up to 15 kg, whereby peak pressures of up to 12 bar with durations of more than 200 ms were obtained. All doors withstood the design load without any premature failures. Permanent deflections between 2 and 4 mm were observed at midpoint of the door plates.

A detailed dynamic structural analysis is somewhat complicated due to the changing support conditions. When the doors are subjected to small loads, they behave like slabs supported along one edge and on two points (i.e. the hinges) at the opposite edge. At higher loads deformations will take place at the hanger side, whereafter the doors will behave as simply supported along all four edges. For the assessment of the ultimate resistance against reflected blast pressure from outside, only this latter behaviour is relevant.

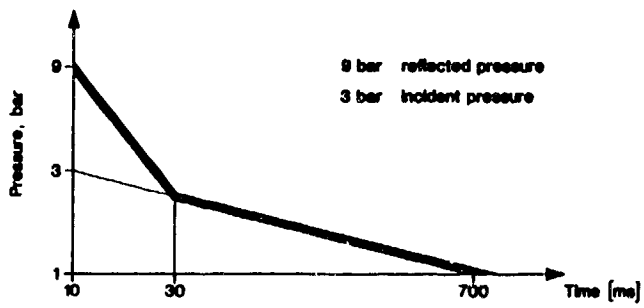

Figure 4: Design load for blast pressure

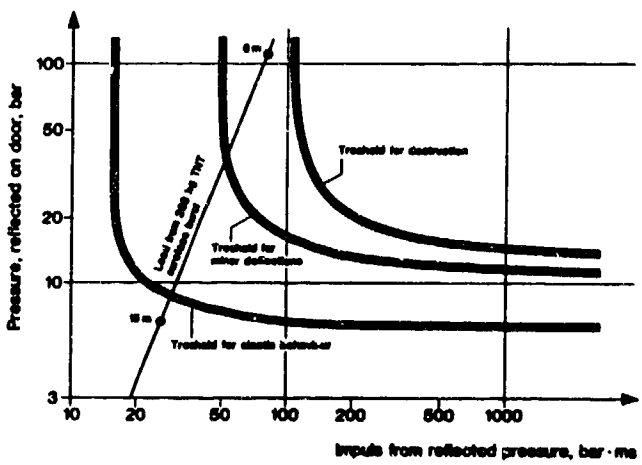

Figure 5: Pressure/impulse diagram showing the bearing capacity of personnel door PT 1

2.3 Rebound

For the rebound cycle the door slab is supported on four points. The minimum requirements stipulate that the doors resist to rebound forces equivalent to an inside dynamic overpressure of

$$p = \frac{6}{\sqrt{2 \cdot \frac{Y_{max}}{Y_{el}} - 1}} \text{ (bar)}; \quad p > 2 \text{ bar}.$$

It is a significant advantage of reinforced concrete doors that the rebound energy which is contained in the door plate can be absorbed by yielding of rebound reinforcement of a relatively low load capacity. By limiting the load capacity of the door plate in the opposite direction to e.g. 30 % of the positive bearing capacity, the loads on locks and hinges are limited correspondingly.
Steel doors, on the contrary, usually have door plates of about the same ultimate bearing capacity in positive and negative direction. Therefore, the rebound supports, i.e. the locks and hinges, have to be designed for approximately the same loads as the positive load supports.

Since the pressure loads from conventional weapons may include a large number of pressure peaks of short duration when acting on doors in entrance ways, sufficient resistance to rebound effects is very essential

2.4 Shock Loadings

If a shock is transmitted from a detonating weapon to a shelter, acceleration forces act on the hinges (see Figure 6).

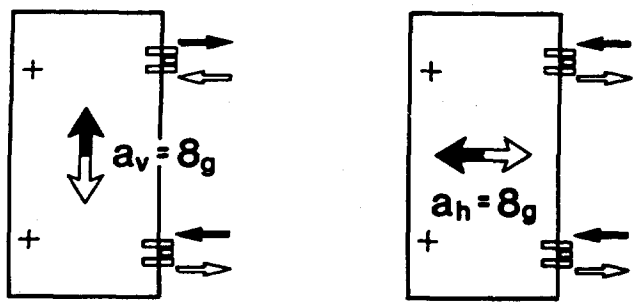

Figure 6: Support acceleration acting on door hinges

All doors and hatches can resist acceleration forces up to 80 m/s^2 quasi-statically. In case of higher shock loadings, permanent deflections up to 10 mm in horizontal and vertical direction may occur without jeopardizing the operability of the doors.

2.6 Flying Fragments

The most destructive effects from grenades or bombs detonating close to reinforced concrete walls are the flying fragments from the casing. As it has been concluded from investigations presented already to the first of these symposia (Ref. 3), fragments may perforate concrete structures, even at distances from the weapon where the blast damage is almost negligible.

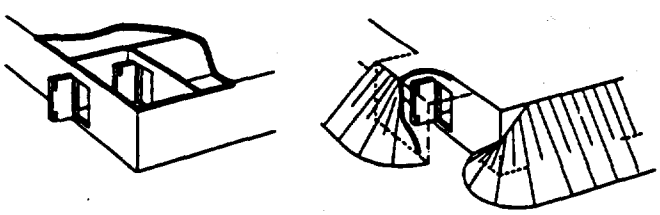

Figure 7: Examples of entrances with improved fragment protection

With door plates of 0.2 m of reinforced concrete, the mentioned armoured doors provide protection against artillery rounds up to calibre 155 mm detonating at 3 m or more from the door. However, the protection provided against flying fragments is lower than that regarding blast overpressure. In case of the example of a 1000 lbs GP bomb at 6 m mentioned earlier, to which the doors resist regarding blast pressure, a relevant portion of large fragments may perforate the door plate. Adequate protection against such weapons may be achieved either if two doors are being arranged in tandem or if the door is protected from direct fragment hits by the geometry of the entrance way (see Figure 7). Antiscabbing plates which may be welded onto the inner face of the door plate are of some value in protecting personnel and equipment. If door thickness and weight increase significantly for better fragment protection, all parts of the door have to be redesigned - particularly the locks and hinges - in order to resist increased rebound and shock forces.

2.5 Imperviousness

Shelter doors must seal tightly in order to avoid penetration of blast pressure and toxic gases from chemical warfare or fires.

In the full-scale shock tube tests carried out with armoured doors of the size 0.8 x 1.85 m approximately 0.03 m^3 m of air penetrated the leaking chamber when the doors were loaded with a triangular blast of 4 bar and 100 ms duration. This leakage is negligible for practical purposes.

For the protection against toxic gases, a minimum overpressure of filtered air has to be maintained inside the shelters. In case of the supply of filtered air being stopped, the infiltration of toxic gases from the outside surroundings must be kept within acceptable limits. The minimum requirements on imperviousness for shelter doors therefore depend on the capacity of the air supply system and the shelter's volume.

The minimum requirements for the mentioned civil defence armoured doors stipulate a maximum air leakage of 20 m^3/h at an inside overpressure of 2.5 mbar. Therefore, rubber seals are fitted into the grooves along the four edges of the door slab. The proper contact between the seals and the bearing faces may be ensured by adjusting the locks.

The best protection is achieved if an air lock is formed employing two consecutive doors.

2.7 Thermal Resistance

Because of the relatively short burning time of incendiary weapons, reinforced armoured doors are generally insensitive to their direct effects. A more critical situation can arise if large amounts of flammable material in the surroundings catch fire. The protection provided by the standard doors is again determined by the reinforced concrete door plate. A thermal load of 300 °C on the outside surface for two hours leads to a temperature rise on the inner surface of approximately 15 °C only. It is required that under these conditions no hazardous gases are released from the seals. This thermal resistance is adequate for most practical applications. If a shelter should become heated up above an acceptable temperature under extreme conditions, reasonable time is gained for the evacuation of its occupants.

2.8 Rescue Devices

Entrances of shelters may be blocked up, e.g. by ejecta material from bomb craters or debris from collapsed structures (see Figure 8). Rescue of occupants should therefore be made possible from outside as well as from inside without special tools.

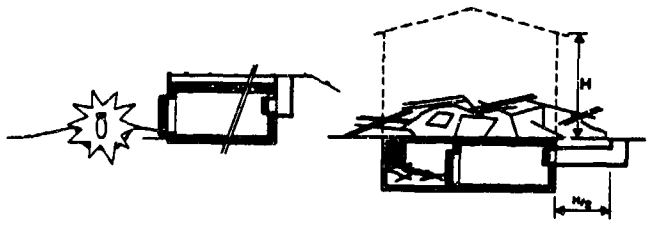

Figure 8: Shelter doors blocked up by crater material or debris

In the case of Swiss civil defence shelters, this is achieved by observing the following principles for the arrangement and equipment entrances:

.1 At least two independent escape ways shall be provided for each shelter.

.2 One of these escape ways shall be closed by an escape hatch which opens towards the inside of the shelter. This gives occupants a chance to escape even if the escape shaft is partly filled with loose material.

.3 If a shelter is located under a multi-storey building, escape tunnels shall be provided beyond the area expected to be covered by heavy debris.

.4 Each shelter has to be equipped with a so-called "self-rescue device". This is a simple mechanical jack which serves to open armoured doors in case of the exit being blocked with debris from outside. With this device the armoured door can be pushed open by a force of about 5 kN (1100 lbs) to make a passage way of a foot's width.

.5 All locks may be taken apart from inside as well as from outside by the same wrench which is included in the self-rescue device. This permits the unlocking of doors even if the locks cannot be turned open for any reason.

If additional security locks are installed for reasons of peace-time use of such shelters, care should be taken that the above rescue possibilities are not jeopardized.

3. OTHER TYPES OF REINFORCED CONCRETE-ARMOURED DOORS

Besides the above-mentioned standard types many other reinforced concrete-armoured doors are in use, in particular as closures for large openings. Depending on the space which is available, both wing doors and sliding doors have also been used for such large openings.

In the case of large public shelters which are often used as car parkings or warehouses, large entrances are needed for peace-time use. Such openings are equipped with so-called armoured sliding walls (see Figure 9). These sliding walls remain closed when the structure is used as a shelter and other entrances equipped with standard doors have to be provided, too. Since these sliding walls are to be moved very seldom in this application, they are usually operated manually by rope and winch.

Figure 9: Sliding wall for the closure of large openings in public shelters, which are used as car parking lot

4. RECOMMENDATIONS FOR THE APPLICATION

The first point to be specified for an armoured door is of course the range and level of protection. The comments made in this paper may be used to check whether all relevant protection requirements are clearly specified.

Regarding the cost of armoured doors, the operational requirements such as size, allowable effort and time for the operation of doors are very important.

The main limitations for the application of reinforced concrete-armoured doors are their weight and the space required for the body of the doors. The

standardized doors, as shown before, may be manually operated by one person with a force of less than 200 N (44 lbs). However, for frequent and rapid operation as well as for larger doors, a power drive may be required.

Reinforced concrete-armoured doors offer a number of advantages over steel doors, if they meet the operational requirements:

- The range of protection corresponds better to the protective structure (e.g. flying fragments, heat, all kinds of radiation)
- Intermediate and high levels of protection may often be achieved at significantly lower cost.

Depending on individual circumstances, other aspects such as the smaller transport weight or the characteristics of concrete as compared to those of steel with respect to self-guided warheads may also be of importance.

Whatever type of armoured door is used, particular care should be employed as to ensure that the door fits the protective structure in all respects, i.e. from protection requirements up to all details of forces transmitted to the supporting structure.

REFERENCES

1. "Technische Weisungen des Bundesamtes für Zivilschutz betreffend Mindestanforderungen und Zulassungsprüfungen von Schutzraumabschlüssen"; Swiss Federal Office of Civil Defence, Berne, Switzerland, 1967

2. "Experiences from Tests with Swiss Civil Defence Doors"
   Royal Swedish Fortifications Administration, Rapport No. 115:9, Stockholm, Sweden, 1974

3. "Effects from Bare and Cased Explosive Charges on Reinforced Concrete Walls"; paper presented to the First Symposium on the Interaction of Non-Nuclear Munitions with Structures in Colorado Springs, U.S.A., 1983

4. "Standard Design for Shelter Doors", Report Nr. 560.40-1 (in German) prepared by E. Basler & Partners, Consulting Engineers, Zurich, for the Swiss Federal Office of Civil Defence, Berne, Switzerland, 1976